Analysis of Cable Effects in Portable Antennas

Xinxin Lu, Yang Liu, and Hyeongdong Kim
Department of Electronics and Computer Engineering, Hanyang University, Seoul, Korea

Abstract— Ground plane may act as a main radiator in most portable antennas. Various cables connected with the ground plane, such as FPCB, speaker wire, and coaxial cables for measurement, can affect the radiation performances of the antenna significantly. In this paper, we use a loop-type ground antenna to examine the cable effects and analyze the effects by an EM simulator HFSS. The loop-type ground antenna is printed on a ground plane that measures 50×20 mm and is required a ground clearance of 4×6 mm. The antenna is operated at Wi-Fi (2.4–2.5 GHz) band. Without any extra cable effects, the resonant frequency is at 2.46 GHz. With extra cable connected to the different points on the ground plane, simulation results show that the resonant frequency and input impedance varies. Based on analysis, we demonstrate that the cable near the electric field maxima on the ground plane has strong influence on the resonant frequency and impedance of the ground antenna.

1. INTRODUCTION

The ground plane plays important roles in most of the mobile antennas. The size and shape of the ground plane can determine the ground mode (characteristic mode) and hence for the antenna performance. Antenna passive measurements for the return loss and input impedance are generally obtained by connecting the antenna to the network analyzer using coaxial cables. The coaxial cables change the shape and size of the ground plane, giving many difficulties to achieve the accurate measurement results [1]. Under this consideration, the position of connecting the coaxial cable becomes important. The cable effects on the different types of antenna, such as monopole, PIFA, dipole ultra wideband (UWB) antennas have been analyzed in several literatures [1–3]. In this paper, we use a loop-type ground antenna [4] to investigate the cable effects. The existence of the cables can alter the resonant frequency and antenna input impedance. The purpose of this article is to find a proper position to avoid error of the measured antenna. An EM simulator HFSS has been utilized to analyze the cable effects.

2. ANTENNA STRUCTURE

The loop-type ground antenna is designed for Wi-Fi (2.4–2.5 GHz). The geometry of the antenna is shown in Fig. 1. The ground antenna is rectangular in shape and the clearance area is 5×6 mm, which is printed on a 1 mm-thick FR-4 substrate ($\epsilon_r = 4.4$, $\tan\delta = 0.02$). The size of ground plane is 20×50 mm. A 4.5 mm long coplanar waveguide with ground (CPWG) is used as feed structure. The gap width of CPWG is 0.2 mm. Two capacitors C_R and C_F are used to adjust resonance frequency and input impedance respectively. The capacitance values we used here are

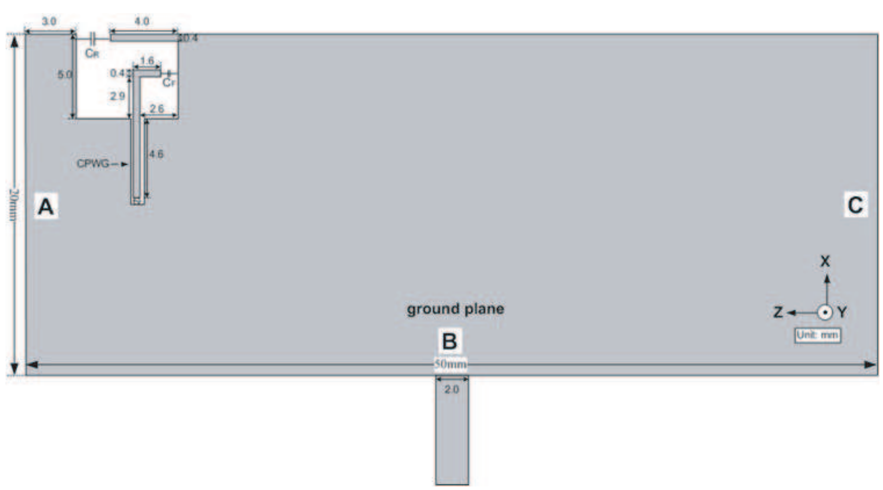

Figure 1: Configuration of loop-type ground antenna.

$C_F = 0.34\,\text{pF}$ and $C_R = 0.23\,\text{pF}$. Input impedance can also be controlled by the size of the feeding loop that connected with C_F. Current loop formed by the C_F drives the loop formed by the C_R to radiate. We use a rectangular metal sheet (2 mm for width, various lengths from 10 mm to 30 mm) to represent the coaxial cable effect in the simulation. The cable effect on the antenna performance has been analyzed at three different positions of the ground plane.

3. ANTENNA TEST AND RESULTS

The ground antenna is measured using Agilent 8753ES network analyzer. In order to clearly show the cable effect, we make some changes of the position and length of the cable. Placing the cable in the vertical direction of the board, measurement results are much closer to the isolated case [2], but in the actual measurement, antenna should be measured with the plastic shell cover and it is difficult to realize. For this consideration, the cable is placed in the same horizontal plane to the ground. As shown in Fig. 2, the center frequency of the antenna is at 2.46 GHz without the cables. With same length of cable (10 mm) in different positions, the response of position B is almost unchanged with the reference that without cable. In the Position A, obvious frequency shift can be observed, in which the center frequency is shifted to 2.49 GHz. In the Position C, the center frequency is shifted to 2.47 GHz, as well as with impedance variation.

Figure 3 shows the antenna return loss when increasing the length of cable with the interval of 5 mm. In Fig. 3(a), as the cable length is increased, the shift of the center resonance frequency is obvious. The center frequency of 10 mm cable is at 2.49 GHz, when the cable is increased to 30 mm, the center shits to 2.54 GHz. In Fig. 3(b), even change the length of cables, center frequencies are unchanged. Results of cable connected in Position C are shown in Fig. 3(c), following the cable length, frequency changes are not obvious, but the input impedance is significantly changed. With the cable length of 10 mm, bandwidth of the antenna at -10 dB is more than 100 MHz. When the length is increased to 30 mm, the bandwidth is reduced to 60 MHz.

In passive measurement, measured antenna is connected to the network analyzer via coaxial cable and ground shape will be changed. Fig. 4(a) shows the measured and simulated (without

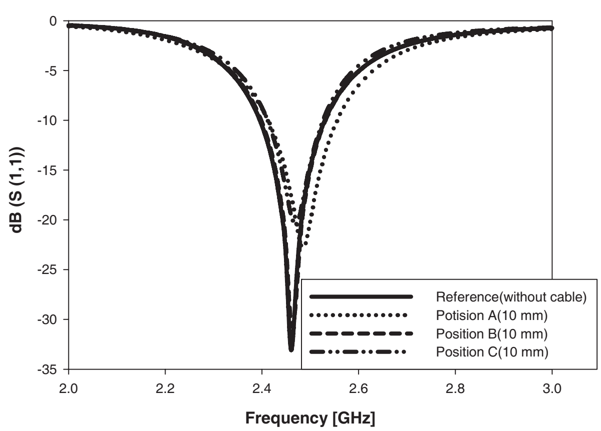

Figure 2: Simulated return loss of 10 mm cable at different positions.

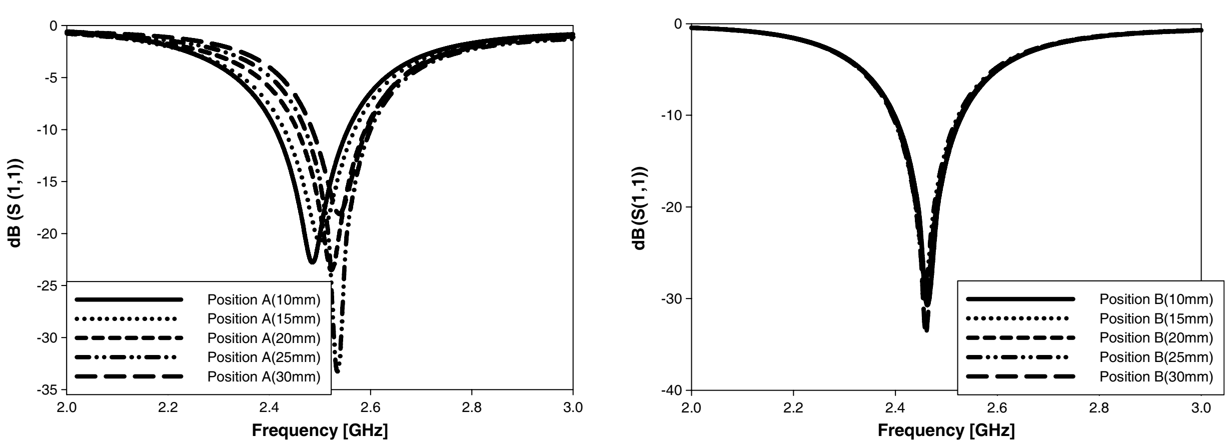

(a) (b)

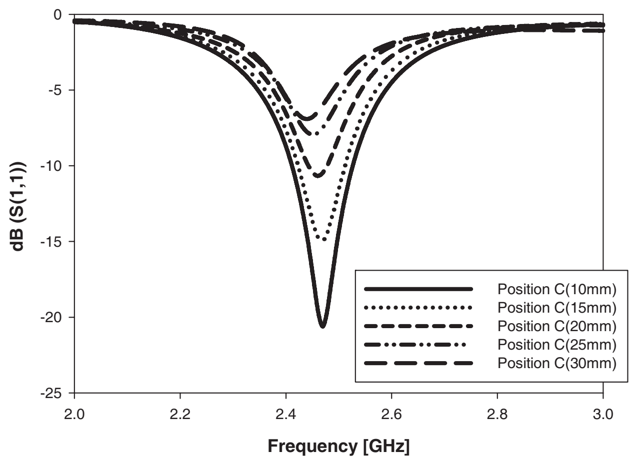

(c)

Figure 3: Simulated return loss at different positions with variation of cable length. (a) Cable length variation in Position A. (b) Cable length variation in Position B. (c) Cable length variation in Position C.

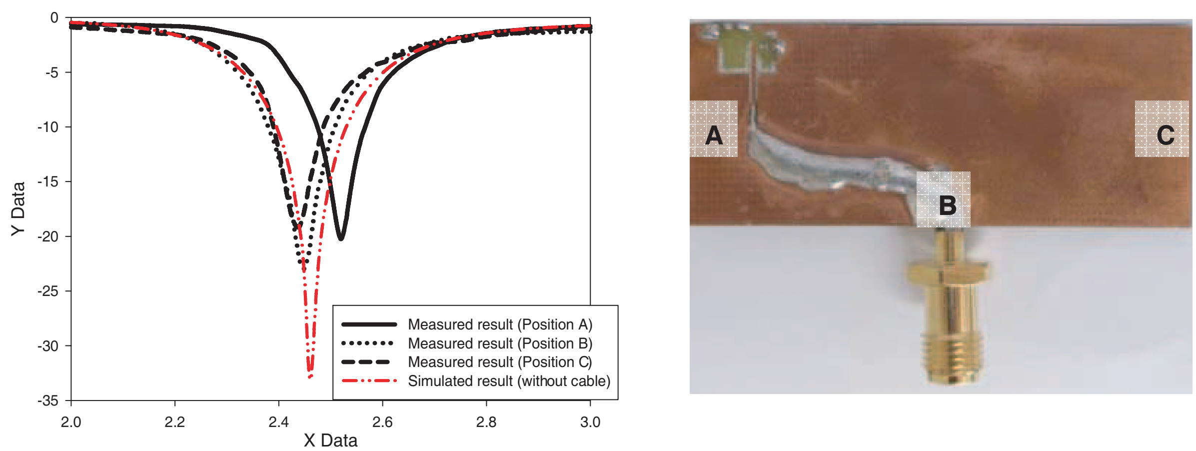

(a) (b)

Figure 4: (a) Measured return loss at different positions and (b) prototype antenna board.

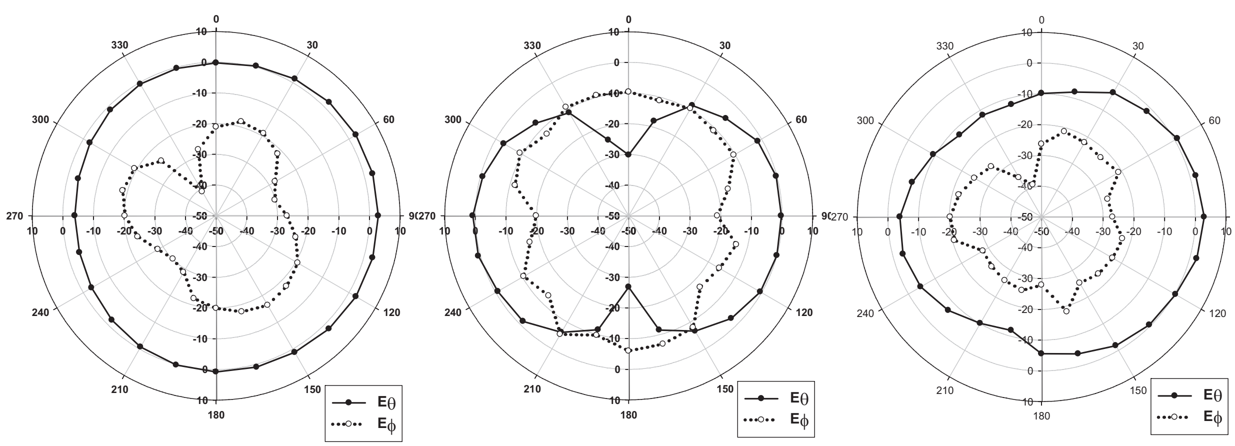

(a) (b) (c)

Figure 5: Measured radiation patterns. (a) x-y plane. (b) x-z plane. (c) y-z plane.

cable) return loss. Cable connected in position A has the most obvious frequency shift. Comparing Fig. 3 and Fig. 4, we find that the return loss produced when the cables in Position B and C are close to the simulation result without cable (in Fig. 2) Cable connected in Position A is similar to the simulated result when the cable length is 20 mm. Fig. 4(b) shows the prototype of the ground antenna. Fig. 5 shows the measured radiation patterns in xy-, xz-, yz-planes for the frequency at

2.45 GHz.

4. CONCLUSIONS

In this paper, a loop-type ground antenna is used to analyze the influence of the existence of coaxial cables. According to the analysis of different cable lengths and positions on the ground plane, the optimum position is observed. Placing the cable in the center of the long edge shows the most accurate results that close to the simulated result without cable.

ACKNOWLEDGMENT

This work was supported by the National Research Foundation of Korea (NRF) grant funded by the Korea government (MEST) (No. 2011-0015540).

REFERENCES

1. Massey, P. J. and K. R. Boyle, "Controlling the effects of feed cables in small antenna measurements," *The Institute of Electrical Engineers*, 561–564, 2003.
2. Saario, S., D. V. Thiel', J. W. Lu, and S. G. O'Keefe, "An assessment of cable radiation effects on mobile communications antenna measurements," *Proc. 1997 IEEE Int. Symp. Antennas Propagat.*, 550–553, Montreal, Canada, 1997.
3. Kwon, D.-H. and Y. Kim, "Suppression of cable leakage current for edge-fed printed dipole UWB antenna using leakage-blocking slots," *IEEE Antennas and Wireless Propagation Letters*, Vol. 5, 183–186, 2006.
4. Liu, Y., X. Lu, H. Jang, H. Choi, K. Jung, and H. Kim "Loop-type ground antenna using resonated loop feeding, intended for mobile devices," *Electronics Letters*, Vol. 47 No. 7, March 31, 2011.

Size Reduction of Patch Antenna Array Using CSRRs Loaded Ground Plane

H. A. Jang, D. O. Kim, and C. Y. Kim
School of Electronics Engineering, Kyungpook National University, South Korea

Abstract— Recent theoretical and experimental studies have shown that microstrip patch antennas loaded by ground plane partially filled with a negative permeability metamaterial may in principle provide a resonant radiating mode, even if the size of the patch antenna is smaller than the wavelength of operation. However, those studies have investigated only a single microstrip patch antenna. To extend the research for patch antenna with metamaterial, this paper offers a novel patch array antenna mounted with the rectangular complementary split ring resonators (CSRRs). The antenna consists of two patch arrays, and they are constructed on Rogers4003 substrate with the thickness of 0.812 mm and relative permittivity of 3.55. The CSRRs are arranged on area of the ground plane surrounding the radiating patch. The designed and fabricated antenna has the operating frequency of about 3.8 GHz, whereas the resonant frequency of an ordinary array antenna having the same patch size without the CSRRs is about 5 GHz. It means that the occupied area of our suggested array antenna can be reduced by 47% to that of the ordinary one. The miniaturized antenna maintains the high directivity performance required by an array antenna, which are confirmed by both simulation and measurement.

1. INTRODUCTION

In modern wireless communication systems, the microstrip patch antennas are commonly used in the wireless devices. Therefore, the miniaturization of the patch antenna has become an important issue in reducing the volume of entire communication system. The common method for reducing the microstrip patch antenna size is to utilize a high permittivity dielectric substrate. But, the antennas are more expensive, less radiation efficiency, and have narrow bandwidth. To overcome the above drawbacks, many design techniques of the patch antenna have already been proposed. These antennas have the inserted slot [1], the corrugation structure [2], the iris structure [3], and the shorting pin [4]. However, all of these design strategies have limitation in their design, which are a complex structure and low performance for miniaturization. So, the design methods of the miniaturized patch antenna with metamaterial technology have been reported on some authors, recently [5, 6]. These would include the SRR or CSRR on the microstrip patch, although those antennas have been restrictively researched in single patch antenna. In other words, achievement of size reduction of antenna with the SRR or CSRR has a special meaning in the field of array antenna. In this paper, the miniaturized 2-elements patch array antenna with CSRRs is presented. The proposed antenna takes an advantage over the previously published miniaturized patch array antennas

2. ANTENNA CONFIGURATION

The SRR was originally proposed by Pendry in 1999, and is the metamaterial resonator having the negative permeability [7]. The SRR structure is formed by two concentric metallic rings with a split on opposite sides. This behaves as an LC resonator with distributed inductance and capacitance that can be excited by a time-varying external magnetic field component of normal direction of resonator. This resonator is electrically small LC resonator with a high quality factor. Based on the Babinet principle and the duality concept, the CSRR is the negative images of SRR, and the basic mechanism is the same to both resonators except for excited the axial electric field. With adjustment of the size and geometric parameters of the CSRR, the resonant frequency can be easily tuned to the desired value. Figure 1 shows the geometry and dimensions of the finalized design CSRR.

Figure 2 shows the finalized shape and dimension of antenna with CSRRs. This antenna is constructed on Rogers 4003 dielectrics substrate with 0.812 mm thickness, a relative permittivity of 3.35, and a loss tangent of 0.0027. The top plane of the proposed antenna was designed by forming typical 2 elements microstrip patch array antenna which has operating band at 5 GHz. The bottom plane of antenna is periodically etched the CSRRs on ground plane. The T-junction power divider is applied to the feeding line of the proposed antenna, which consists of transmission

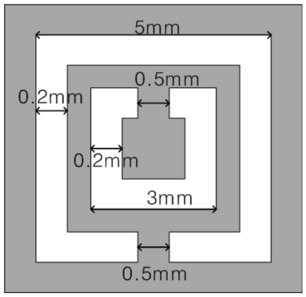

Figure 1: Geometry and dimensions of the proposed CSRR.

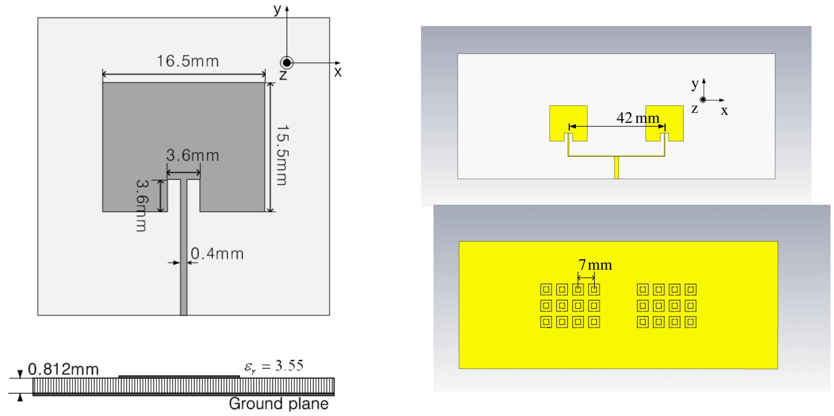

(a) (b)

Figure 2: Geometry and dimensions of antenna (a) unit patch antenna, (b) top and bottom view.

Figure 3: Photograph of the fabricated antenna.

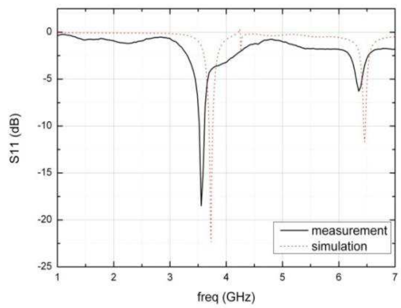

Figure 4: Simulated and measured return loss of the antenna.

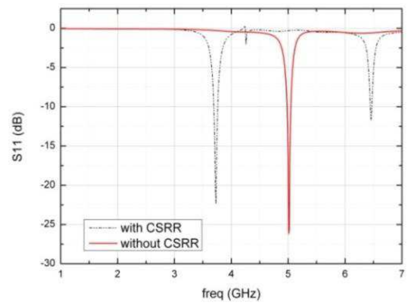

Figure 5: Return loss of antenna with CSRR or without CSRR.

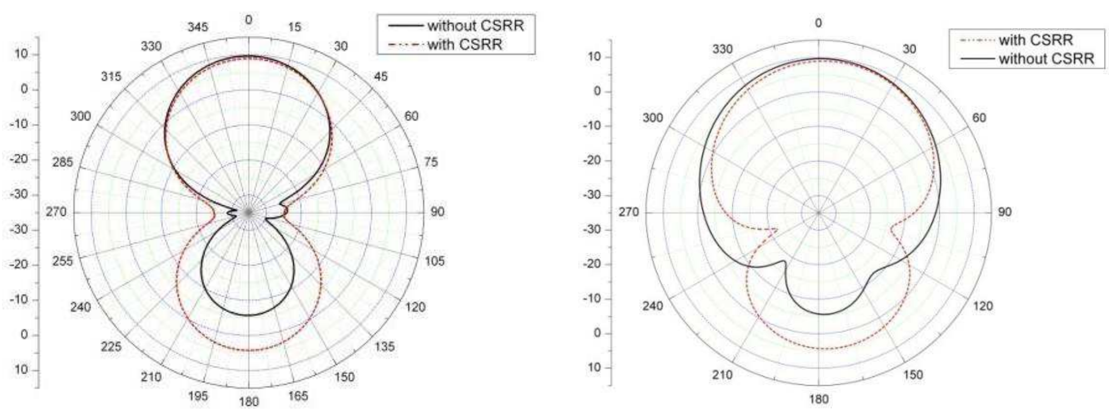

(a) (b)

Figure 6: Radiation pattern of antenna with CSRR or without CSRR (a) xz plane, (b) yz plane.

line of the characteristic impedance $50\,\Omega$ and $100\,\Omega$. The distance between two patch elements is 47 mm that corresponds to the electrical length of $0.7\lambda_g$. The etched CSRRs are finitely arranged around the radiating patches because the axial electric field to drive the CSRRs is produced only around radiating patches. Strong mutual coupling between negative permeability resonator and antenna patch is yielded by arranging of CSRRs, and it becomes typical high impedance structure. The physical insight for our configuration is similar to the mechanism of electric length reduction on high impedance substrate of [8].

3. SIMULATED AND MEASURED RESULTS

Figure 4 shows the simulated and measured return loss results for the fabricated antenna. The relatively good agreement is seen between the measured and simulated return loss curves. The measurement and simulation were performed by an Anritsu 37397C network analyzer and the Microwave Studio of CST, respectively. Figure 5 shows the return loss of the patch array antenna with and without the CSRRs inclusions. By adding the CSRRs, resonant frequency 5 GHz of typical patch array antenna is shifted to 3.8 GHz without changing the size of radiating patch. From these results, the proposed antenna achieves size reduction of 47% for antenna patch. Figure 6 indicates the radiation pattern of the miniaturized antenna with and without the CSRRs at 3.8 GHz. The antenna peak directivity of the typical array antenna without the CSRRs is 9.7 dB, and the designed antenna with the CSRRs is 8.9 dB which is about 0.8 dB below that of the typical antenna. This result exhibits that the proposed antenna maintains the inherent performance of array antenna.

4. CONCLUSION

This paper proposes a miniaturized 2-elements microstrip patch array antenna without changing the size and dimensions of typical patch array. To realize the size reduction, the CSRRs having the negative permeability characteristics are etched on the ground plane of the antenna. The proposed antenna achieves a 47% size reduction comparison with original patch antenna. To demonstrate the usefulness of the proposed design method, the performance parameters of antenna is simulated and measured. In spite of size reduction of radiating patch, antenna directivity of proposed antenna is only decreased within 1 dB. This reveals that the proposed antenna has more excellent performance compared to other miniaturized array antenna, and it might be useful for constructing the compact 3 GHz WiMAX communication system.

REFERENCES

1. Wong, K. L. and J. Y. Wu, "Single-feed small circularly polarized square microstrip antenna," *Electronics Letters*, Vol. 33, 1833–1834, October 1997.
2. Lee, S., J. Woo, M. Ryu, and H. Shin, "Corrugated circular micro-strip patch antennas for miniaturization," *Electronics Letters*, Vol. 38, No. 6, 262–263, 2003.
3. Seo, J. and J. Woo, "Miniaturization of microstrip antenna using iries," *Electronics Letters*, Vol. 40, 718–719, 2004.
4. Waterhouse, R., "Small microstrip patch antenna," *Electronics Letters*, Vol. 31, 604–605, 1995.
5. Zhao, X., Y. Lee, and J. Choi, "Design of compact patch antenna using split-ring resonator embedded substrate," *Microwave and Optical Technology Letters*, Vol. 53, No. 12, 2789–2790, December 2011.
6. Lee, Y., S. Tse, Y. Hao, and C. G. Parini, "A compact microstrip antenna with improved bandwidth using complementary split-ring resonator (CSRR) loading," *IEEE Antennas and Propagation Society International Symposium*, 5431–5434, Honolulu, HI, June 2007.
7. Pendry, J. B., A. J. Holden, D. J. Robbins, and W. J. Stewart, "Magnetism from conductors and enhanced nonlinear phenomena," *IEEE Transactions on Microwave Theory and Techniques*, Vol. 47, No. 11, 2075–2084, November 1999.
8. Mosallaei, H. and K. Sarabandi, "Antenna miniaturization and bandwidth enhancement using a reactive impedance substrate," *IEEE Transactions on Antennas and Propagation*, Vol. 52, No. 9, 2403–2414, September 2004.

Design of Internal Multi-band Mobile Antenna for LTE700/WCDMA/UMTS/WiMAX/WLAN Operation

D.-G. Yang, D.-O. Kim, and C.-Y. Kim
School of Electronics Engineering, Kyungpook National University, South Korea

Abstract— In this paper, an internal multi-band antenna is proposed for use with the LTE700/-WCDMA/UMTS/WiMAX/WLAN bands. The proposed antenna was configured to have three radiating elements. These elements were the folded loop line, rectangular patch inserting meandered slit, and L-shaped ground branch closely coupled to the feeding line. The antenna was constructed on a substrate FR4 with a relative permittivity of 4.5. The antenna operated at a lower band to cover the LTE700 operations and at a wide upper band to cover the WCDMA/ UMTS/WLAN operations. In addition, this antenna could also provide another upper band at about 3.5 GHz to cover WiMAX operations. By inserting the folded loop line and L-shaped ground branch, the LTE700 operations had VSWR ≤ 2.5 and RL ≤ -8 dB, while the WiMAX operations had VSWR < 2 and RL < -10 dB. By adding the rectangular patch with a meander slit, WCDMA/UMTS/WLAN band operations had VSWR < 2 and RL < -10 dB. The return loss and radiation patterns of the suggested antenna were simulated by commercial EM tool software by SEMCAD X. The computed results show both a good omni-directional radiation pattern and a moderate amount of radiation gain. According to the results mentioned, the proposed antenna can be applied to mobile handset using the LTE700/WCDMA/UMTS/WiMAX/WLAN bands.

1. INTRODUCTION

The rapid progress in mobile communications requires that a mobile device should have many functions and a compact size. To provide multimedia services, a compact mobile device has to achieve many features, such as high data rates, low power consumption, and multi-band characteristics, etc.. Presently, 3G mobile communication has accelerated data transfer velocity and improved communication quality with the commercialization of UMTS, WCDMA, HSPA and HSPA+. The long term evolution (LTE) which is 4G mobile communication has attracted much attention for its high data rate communication technology because the data transfer velocity of the 3G mobile communication is not sufficient to satisfy consumers. This system can use satellite networks, WLAN, and wireless internet with only one mobile device while the maximum data transfer velocity of this is 10 times faster than the 3G mobile communication IMT-2000. To perform the various multimedia functions of a compact device, recent mobile antenna may require the performance of wideband and multi-band and yet maintaining the space restriction of the device. For the past few years, many antenna engineers have configured the planar inverted-F antenna (PIFA) and folded monopole antenna in devices to efficiently utilize the limited space in a mobile device [1, 2].

In this paper, a multi-band antenna for the next generation wireless communication system is presented. The proposed antenna provides 5 operating bands, covering the LTE700 bands (700–730 MHz) [3, 4], Wideband Code-Division Multiple Access (WCDMA) bands (2100–2170 MHz), Universal Mobile Telecommunications System (UMTS) bands (2300–2400 MHz), Wireless Local Area Network (WLAN) bands (2400–2497 MHz), and World Interoperability for Microwave Access (WiMAX) system bands (3300–3790 MHz), simultaneously. To obtain the penta-band operation, the radiator section of the antenna is embedded in the structure of the folded loop line, the rectangular patch inserting slit [5], and the L-shaped ground branch. The measured return loss and impedance bandwidth results of the antenna satisfied the LTE 700 band (VSWR < 2.5, RL < -8 dB) WCDMA/UMTS, WLAN, and WiMAX bands (VSWR < 2, RL < -10).

2. ANTENNA GEOMETRY

This section presents the design strategy of the proposed antenna and discusses its return loss, surface current, and radiation pattern. Figure 1 shows the geometry and dimensions of the proposed antenna which is comprised of a thin metal plate with a single-side layer and a lossy FR-4 substrate (with thickness $= 0.4$ mm, $\varepsilon_r = 4.5$, $\tan\delta = 0.025$).

The antenna radiator consists of the folded loop line, rectangular patch inserting slit, and L-shaped ground branch. The folded loop line operates the LTE700 band with a 1 mm width and

112 mm (0.7 GHz, $0.25\lambda_0$) total length. This line is a new design structure by comparison with the meander line of the conventional structure of the LTE700 antenna. The rectangular patch inserting slit into the antenna is the WCDMA/UMTS/WLAN bands with a 0.3 mm slit width. To achieve WiMAX band performance, the L-shaped ground branch with a 1 mm width employed a coupling feed structure, which has a 0.5 mm distance between the branch and feeding line. The coupling feed structure plays a role in the internal impedance matching circuit with coupling capacitance. With the use of the coupling feed, the large reactance at around the WiMAX band can be decreased; it is possible to generate the desired resonant frequency and its bandwidth [6].

Figure 2 shows the simulated and measured return loss of the final proposed multi-band antenna. The simulation and measurements were performed by the SEMCAD-X with a Speag and Anritsu

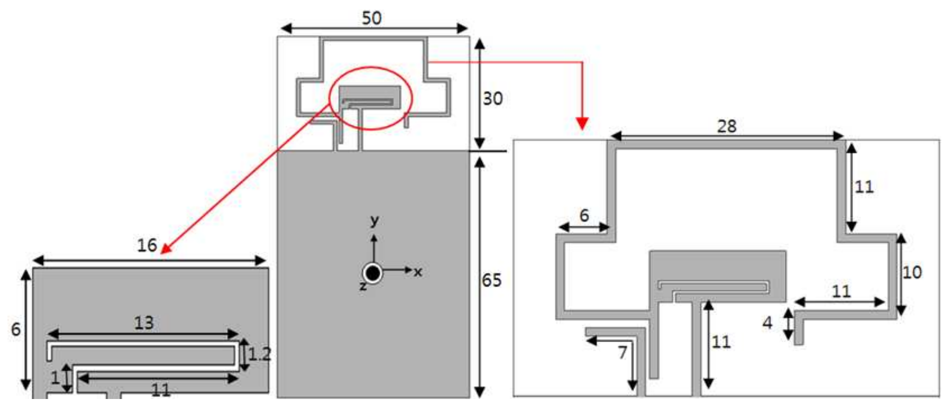

(a)

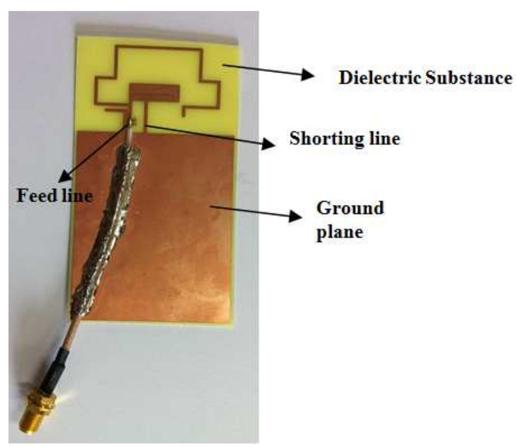

(b)

Figure 1: Geometry and dimensions of the multi-band antenna. (a) Top view. (b) Fabrication.

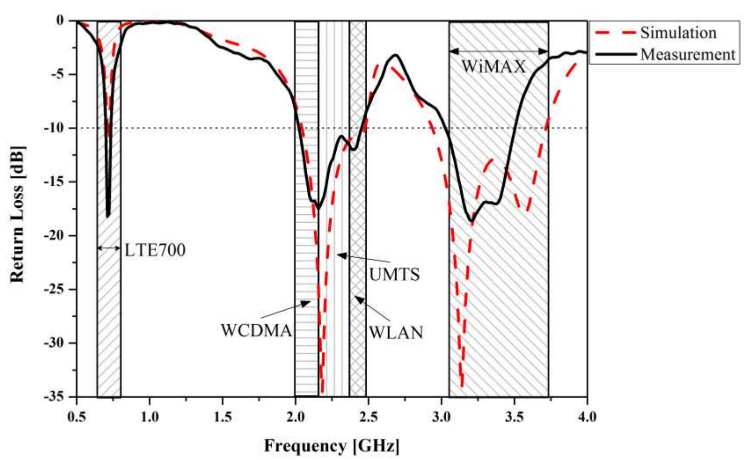

Figure 2: Return loss of the multi-band antenna.

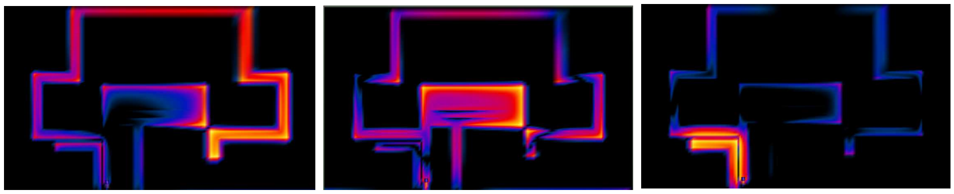

(a) (b) (c)

Figure 3: Surface current distribution at (a) 0.7 GHz, (b) 2.4 GHz, (c) 3.5 GHz.

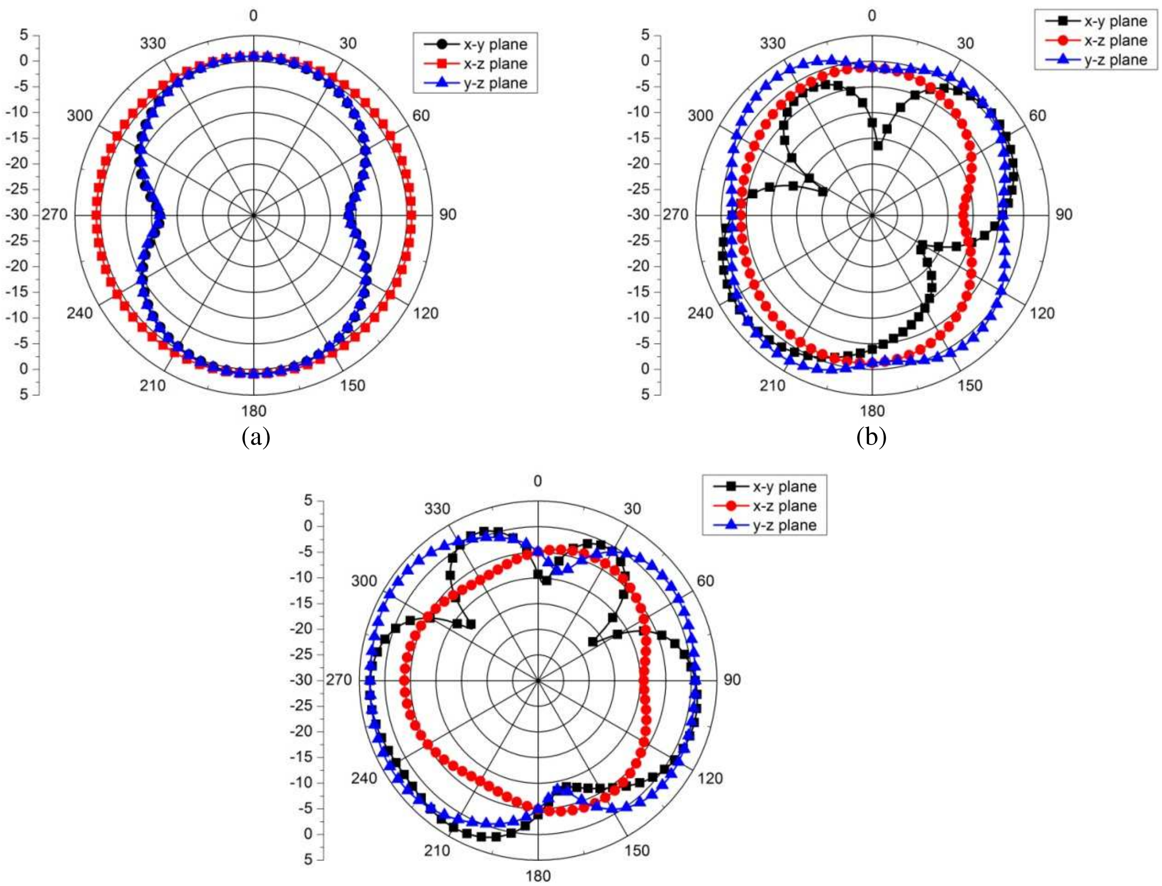

(a) (b)

(c)

Figure 4: Radiation Patterns. (a) 0.7 GHz, (b) 2.4 GHz, (c) 3.5 GHz.

37397C network analyzer, respectively. As shown in Figure 2, the return loss results cover the LTE 700, WCDMA/UMTS, WLAN and WiMAX bands. Figure 3 shows the simulated surface current distributions at each resonant frequency. The large resonant current distribution is indicated by the light color, and the small one is the dark color. This reveals that the proposed antenna has the independency on the resonant current path on the antenna radiator. Based upon the aforementioned independency, we can easily design and tune the multi-band antenna to satisfy the bandwidth and frequency required.

The simulated radiation pattern of the proposed antenna at each resonant frequency of 700 MHz, 2.4 GHz, and 3.5 GHz are illustrated in Figure 4. Notice that the patterns are almost an omnidirectional pattern suitable for mobile device.

3. CONCLUSIONS

This paper presents a multi-band antenna for the next generation wireless communication system including the LTE700 band, which provides simple control over the aimed operating bands. By applying three radiating elements of the folded loop line, rectangular patch inserting slit, and L-shaped ground branch, the LTE700, WCDMA/UMTS band, WLAN band, and WiMAX band as operating bands are obtained. To demonstrate the performance of the proposed antenna, return loss and radiation pattern were simulated and measured. And the resonant modes of the antenna were verified with the surface current distribution of the radiating elements. These results will be helpful in the design of multi-band antennas used for mobile communication systems

ACKNOWLEDGMENT

Thanks to SPEAG for providing the free license for SEMCAD X used in this study.

REFERENCES

1. Kärkkäinen, M. K., "Meandered multiband PIFA with coplanar parasitic patches," *IEEE Microwave and Wireless Components Letters*, Vol. 15, No. 10, 630–632, 2005.
2. Chi, Y. W. and K. L. Wong, "Very-small-size printed loop antenna for GSM/DCS/PCS/UMTS operation in the mobile phone," *Microwave and Optical Technology Letters*, Vol. 51, No. 1, 184–192, 2009.
3. Bhatti, R. A., S. Yi, and S. O. Park, "Compact antenna array with port decoupling for LTE-standardized mobile phones," *IEEE Antennas and Wireless Propagation Letters*, Vol. 8, 1430–1433, 2009.
4. Lizzi, L., "Dual-band printed fractal monopole antenna for LTE applications," *IEEE Antennas and Wireless Propagation Letters*, Vol. 10, No. 00, 760–763, 2011.
5. Wong, K. L., G. Y. Lee, and T. W. Chiou, "A low-profile planar monopole antenna for multiband operation of mobile handsets," *IEEE Transactions on Antennas and Propagation*, Vol. 51, No. 1, 121–125, 2003.
6. Wong, K. L. and C. H. Huang, "Compact multiband PIFA with a coupling feed for internal mobile phone antenna," *Microwave and Optical Technology Letters*, Vol. 50, No. 10, 2487–2491, 2008.
7. SEMCAD X by SPEAG, www.speag.com.

Planar UWB Antenna with WLAN/WiMAX Dual Band-notched Characteristics Using the Hilbert-curve Slots

D. O. Kim and C. Y. Kim
School of Electronics Engineering, Kyungpook National University, South Korea

Abstract— In this paper, a compact ultra-wideband (UWB) antenna with dual band-notched design is proposed. The antenna consists of a rectangular metal patch and a 50 ohm coplanar waveguide (CPW) transmission line. By etching both the first iteration and the third iteration Hilbert-curve slots on the radiating patch, band-rejected filtering properties in the WiMAX/WLAN bands can be obtained. Furthermore, each notched band can be easily tuned by adjusting the length of each Hilbert-curve line segment because the sum of whole line segment controls the corresponding resonance frequency. The proposed antenna is simulated, designed, and measured showing a broadband matching and a stable radiation performance over the entire UWB frequency range, which prospects the deployment in the UWB system. As will be seen, the operation bandwidth of the antenna is from 2.5 to 10.6 GHz for VSWR < 2, in which two frequency rejection bands from 3.3 to 3.7 GHz and from 5.4 to 6 GHz for VSWR > 2 can be achieved. The measured results agree well with the simulation by the Microwave Studio of the CST. Based on the simulated and measured results, the newly proposed antenna by this paper can be found its application on the design of multi-band rejection characteristics with broadband antenna technology.

1. INTRODUCTION

Ultra-wideband (UWB) is a short range communications technology having high data rates with low power consumption. Since the Federal Communications Commission (FCC) permitted the marketing and operation of UWB within the range 3.1 to 10.6 GHz in 2002, it has attracted much attention for next generation data communication. Furthermore, this technology has given rise to much interest in designing wideband antennas with performances of the broadband impedance matching, omnidirectional radiation pattern, constant group delay, and compact size. However, over the allocated bandwidth (7.5 GHz) of the UWB system, there exists some narrow bands for other data communication standards, such as 3.4–3.69 GHz for WiMAX (World Interoperability for Microwave Access), 5.15–5.825 GHz for WLAN (Wireless Local Area Network), which may be cause electromagnetic interference with the UWB system. Because of the existence of other wireless standards an additional requirement for UWB antennas is to reject some multi-bands within the UWB passband. Typical band rejection methods reported in the literature that can be applied to a UWB antenna include etching a slot of different shapes on the radiating patch [1–3]. To achieve the band notch function in this study, the Hilbert-curve slot (HCS) which is a fractal curve is used on a typical UWB antenna. Using the fractal structure with the UWB antenna to obtain the band notch characteristics, is to the best of our knowledge, the first time to be reported on for such an application. In this paper, we explore the ability of having multi-band notch function in which the fractal structure in the antenna is placed. The aforementioned key point of this study is differentiated from other dual-band notched UWB antennas.

2. ANTENNA CONFIGURATION

Figure 1 shows some iterations-order of the Hilbert-curves. It is clear that as the iteration order increases, the total length of the line segment is increased. In this article, the first order ($n = 1$) and third order ($n = 3$) iterations of the Hilbert-curve were used as the band notching elements. Figure 2 shows the configuration and dimension of the primitive UWB antenna before implementing the HCS. The coplanar waveguide fed is applied to the UWB antenna, which is constructed on Rogers 4003 substrate with a thickness of 0.812 mm, a relative dielectric constant of 3.55, and a loss tangent of 0.0027. Figure 3 shows the geometry and dimension of the finalized dual-band notched UWB antenna loaded by two HCSs. The overlapped dimensions between the proposed dual-band notched UWB antenna and the primitive UWB antenna have the same geometrical value. The embedded first order HCS is positioned near the top edge of antenna, the third order HCS is near the center of the antenna between a feedline part and a radiation patch. The low rejection frequency of WiMAX band 3.5 GHz comes from the first order HCS. The high rejection

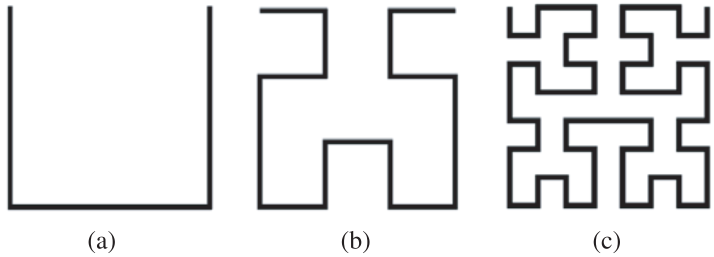

Figure 1: The Hilbert-curve shape in terms of order number, (a) first order, (b) second order, (c) third order.

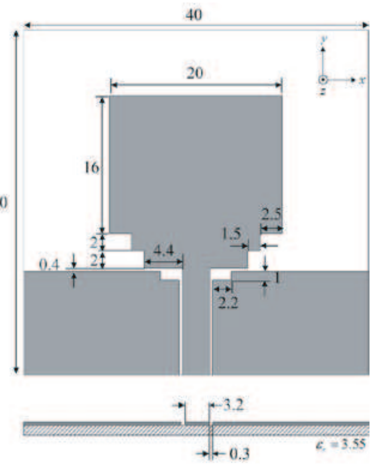

Figure 2: Geometry and dimension of the primitive UWB antenna.

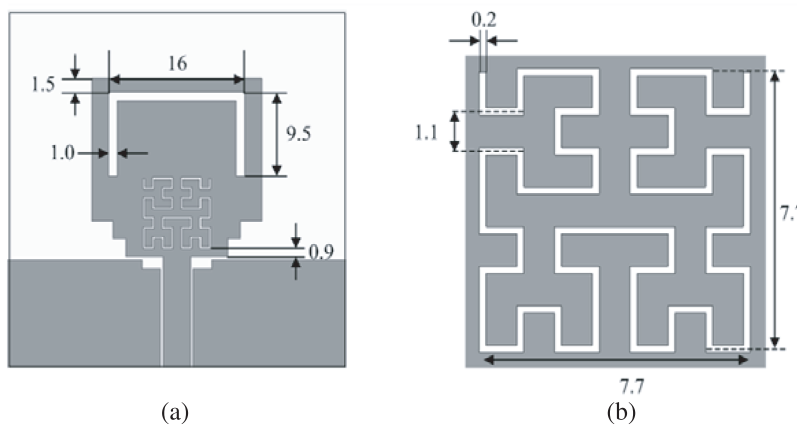

Figure 3: Geometry and dimensions of (a) the proposed dual-band notched UWB antenna, (b) Hilbert-curve slot.

frequency of WLAN band 5.5 GHz is attributed to the third order HCS. Each HCS works like the LC resonator whose resonance frequency depends on its geometrical size. The notched frequencies of the proposed antenna are forced to be the resonance frequency of the each HCS.

3. SIMULATION AND MEASUREMENT

Figure 4 shows the simulated and measured voltage standing wave ratio (VSWR) of the proposed antenna. The VSWR results were obtained using an Anritsu vector network analyzer 38397C and computed by 3D EM simulator of Microwave Studio of CST and HFSS of Ansoft. From the result shown in Figure 4, it is observed that an impedance bandwidth with good matching for VSWR < 2 is from 2.7 to 10. 6 GHz in which two rejected bands (VSWR > 2) from 3.3 to 3.7 GHz and from 5.4 to 6 GHz have been achieved.

To demonstrate the band notch characteristics of the HCSs, the VSWR results of the proposed antenna with and without the HCSs are plotted in Figure 5. In this figure, the solid line is indicated in the VSWR result of the primitive UWB antenna without HCSs, the dash-dotted line is the VSWR result of the singleband notched UWB antenna with only the third order HCS, and the dotted line is the VSWR result of the dual-band notched UWB antenna with the first and third order HCSs as shown in Figure 4. This reveals that the first order and third order HCSs carried out the band notch function at WiMAX and WLAN bands, discretely. In addition, Figure 6 shows the surface current distribution at rejected bands 3.5 GHz and 5.5 GHz. It is observed that the resonant currents are highly concentrated on each HCS corresponding to notched bands. It means that a large portion of electromagnetic field energy of the antenna at these bands has been stored in the HCSs so that the radiation efficiency declined drastically at these bands. The results of Figure 6 are able to sustain the independence of between the first order HCS and the third order HCS, too. The measured E-plane and H-plane radiation patterns are illustrated in Figure 7. A nearly omnidirectional radiation pattern can be observed over the whole UWB frequency range.

As the UWB communication has been based on impulse radio, it is necessary to consider the impulse distortion of the time-domain response of the proposed antenna. Fidelity factor F, defined

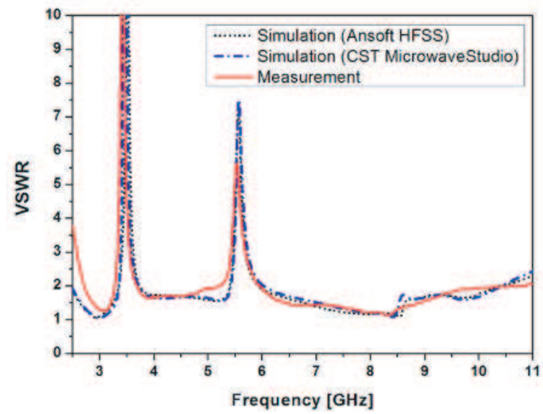

Figure 4: Measured and simulated VSWR results.

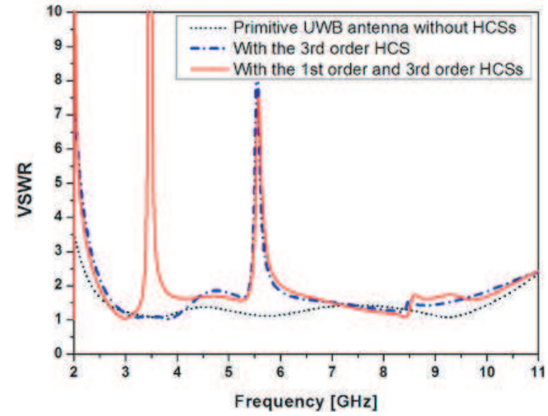

Figure 5: VSWR results of the proposed antenna with and without the Hilbert-curve slots (HCSs).

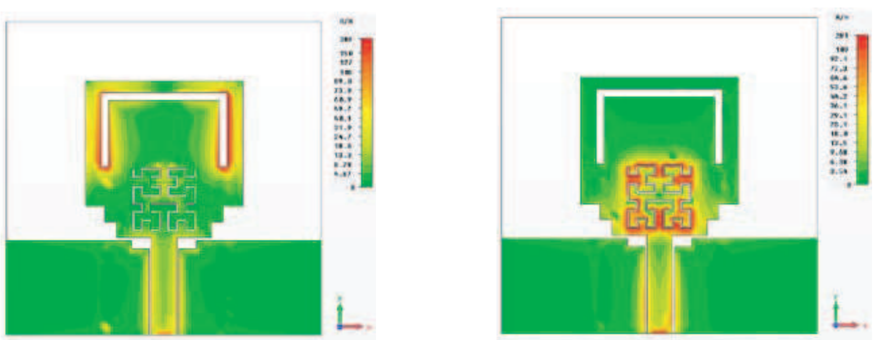

(a) (b)

Figure 6: Surface current distribution at (a) 3.5 GHz, (b) 5.5 GHz.

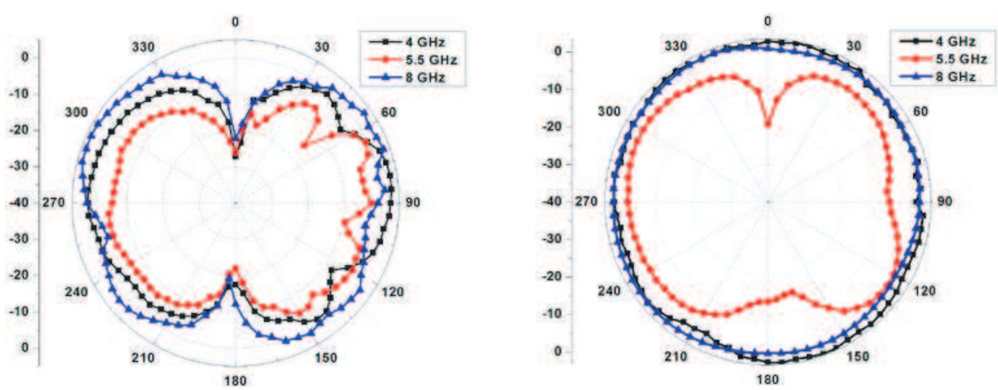

(a) (b)

Figure 7: Measured radiation pattern. (a) E-plane (yz-plane), (b) H-plane (xz-plane).

as Equation (1) of the proposed antenna is studied in this paper [4]

$$F = \max_\tau \int_{-\infty}^{\infty} S_r(t-\tau)S_t(t)dt \tag{1}$$

To calculate the fidelity factor of the proposed dual-band notched UWB antenna, it is assumed that the two proposed antennas in Figure 3 play the role of the transmitting antenna and receiving antenna. The two antennas are aligned pointing face-to-face with a distance of 300 mm. The input signal $S_t(t)$ form of the Gaussian pulse can be excited to transmitting antenna, then receiving pulse signal $S_r(t)$ can be obtained to receiving antenna. This pulse simulation is performed by a

CST Design Studio simulator. By substituting the two normalized pulse signal in Equation (1), we can calculate the fidelity factor F which is the maximum correlation coefficient between two pulse signals. The antenna having $F = 1$ indicates a perfect match between $S_t(t)$ and $S_r(t)$, without distortion in the transmission system of the pulse signal. The fidelity factor F of the proposed dual-band notched UWB antenna is 0.92, it is evident that the proposed UWB antenna exhibits a good time domain performance in the view of operating UWB communication systems [5, 6].

4. CONCLUSIONS

This paper presents a new design method on how to impose the dual-band rejection property with HCSs to the typical UWB antenna. Etched first order HCS and the third order HCS on the primitive UWB antenna worked as band notching elements for the WiMAX band and WLAN band, respectively. To verify the performance of the proposed dual-band notched UWB antenna, notably, VSWR, radiation pattern, surface current distribution, and fidelity factor are computed and measured. From these results, the proposed antenna is supposed to be suitable for deployment in UWB communication system.

REFERENCES

1. Kim, D.-O., N.-I. Jo, D.-M. Choi, and C.-Y. Kim, "Design of the ultra-wideband antenna with 5.2 GHz/5.8 GHz band rejection using rectangular split-ring resonators (SRRs) loading," *Journal of Electromagnetics Waves and Applications*, Vol. 23, No. 17–18, 2503–2512, 2009.
2. Lee, W. S., D. Z. Kim, K. J. Kim, and J. W. Yu, "Wideband planar monopole antenna with dual band-notched characteristics," *IEEE Trans. Microwave Theory Tech.*, Vol. 54, No. 6, 2800–2806, 2006.
3. Kim, D. O. and C. Y. Kim, "CPW-fed ultra-wideband antenna with triple-band notch function," *Electronics Letters*, Vol. 46, No. 18, 1246–1248, 2010.
4. Li, X., S. C. Hagness, M. K. Choi, and D. W. Weide, "Numerical and experimental investigation of an ultrawideband ridged pyramidal horn antenna with curved launching plane for pulse radiation," *IEEE Trans. Antennas Propaga.*, Vol. 56, No. 9, 259–262, 2003.
5. Kim, D.-O., N.-I. Jo, H.-A. Jang, and C.-Y. Kim, "Design of the ultrawideband antenna with a quadruple-band rejection characteristics using a combination of the complementary split ring resonators," *Progress In Electromagnetics Research*, Vol. 112, 93–17, 2011.
6. Kim. D. O., C. Y. Kim, J. K. Park, and N. I. Jo, "Compact band notched ultra-wideband antenna using the Hilbert-curve slot," *Microwave and Optical Technology Letters*, Vol. 53, No. 11, 2642–2648, 2011.

Reconfigurable Omnidirectional Loop Antenna with Left-handed Loading for RFID Applications

E. Serrano[1], **E. Diaz**[2], **A. Belenguer**[1], **J. Cascón**[1], **H. Hesteban**[2], **and A. L. Borja**[1]

[1]E. Politécnica de Cuenca, Universidad de Castilla-La Mancha, Campus Universitario 16071 Cuenca, Spain
[2]Instituto de Telecomunicaciones y Aplicaciones Multimedia, Universidad Politécnica de Valencia
Camino de Vera s/n 46022 Valencia, Spain

Abstract— This letter presents an omnidirectional horizontally polarized planar printed loop antenna using left handed CL loading with $50\,\Omega$ input impedance. The antenna gives an omnidirectional pattern in the plane of the loop, whilst working in an $n = 0$ mode at 868 MHz. In addition, reconfigurable responses can be achieved by using hard wire switches or diode varactor components. Finally, the antenna is compared with other right-handed conventional antennas i.e., a straight dipole, a folded dipole and a microstrip patch antenna working at the same frequency. Design details, simulated results and a fabricated prototype are presented. The concept significantly extends the design degrees of freedom for RFID antennas.

1. INTRODUCTION

As it has been demonstrated during the past years, antennas using a ladder network with left-handed loading can gain various operating modes [1–3]. Specifically, the zero order mode gives rise to omnidirectional pattern in the plane of the loop, with a circumference of one wavelength and good impedance [4]. In this particular case, the left-handed loading concept has been applied to loop antennas to investigate its performance for RFID applications.

2. LEFT-HANDED LOOP ANTENNA

In this section, both the design and performance of the antenna are presented. The loop antenna, loaded by a left-handed ladder network composed of 4 unit cells, is shown in Fig. 1(c). The unit

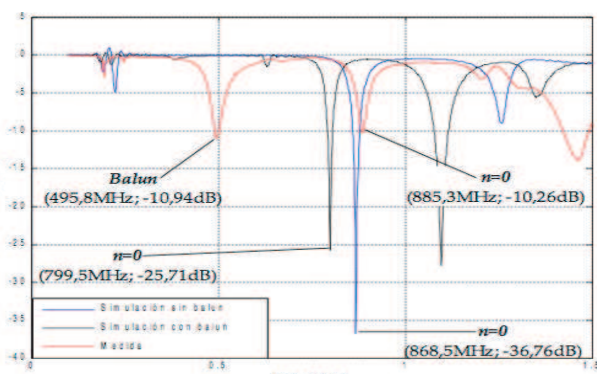

(a)

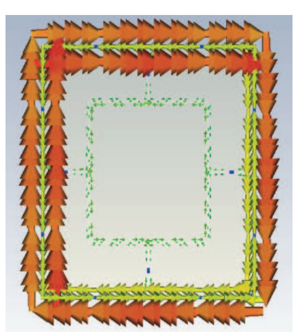

(b)

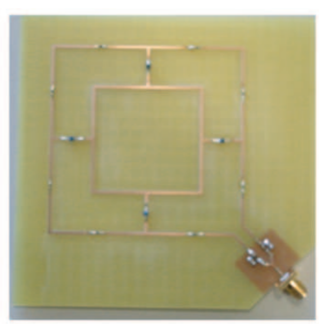

(c)

Figure 1: (a) Response of the left-handed loop antenna. (b) $n = 0$ mode with unidirectional currents. (c) Photograph of the loop antenna.

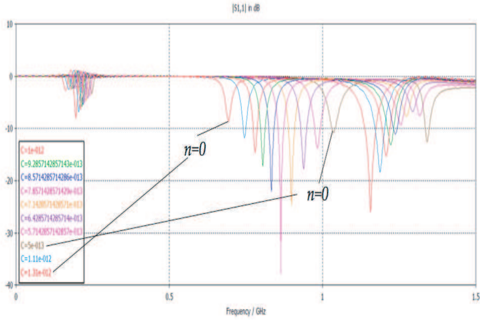

(a)

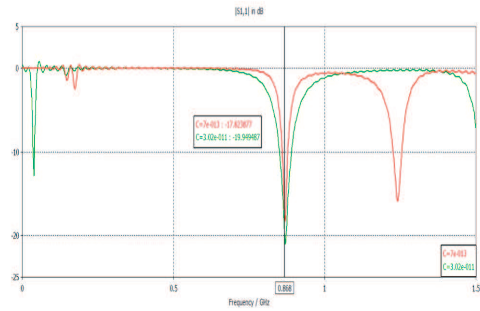

(b)

Mode	Current distribution at 868 MHz	Near H-field distribution at 868 MHz	Cap.
n=0	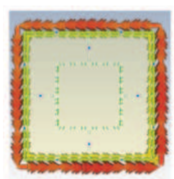	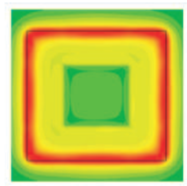	C_L= 0.7 pF
n=2	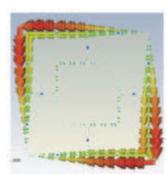	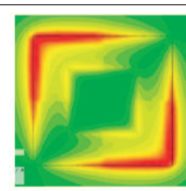	C_L= 30.2 pF

(c)

Figure 2: (a) Tunable Left-Handed loop response. (b) Tunable dual mode Left-Handed loop response. (c) Current and near H-field distributions for the tunable dual mode Left-Handed loop.

cell has a shunt inductor and two series capacitors.

These components determine the operating mode at a given frequency, where phase constant can be negative, zero, or positive. A resonance in the $n = 0$ mode (unidirectional currents) was observed at 885 MHz for measurement and at 868 and 799 MHz for simulation, see Figs. 1(b) and (a). The performance of the antenna was investigated numerically using the commercial simulator CST.

3. RECONFIGURABLE LEFT-HANDED LOOP ANTENNA

In the following, a reconfigurable and dual mode reconfigurable loop antenna with left handed loading for RFID applications is presented. In this first design, the capacitors are replaced by varactors, where an external DC voltage can control its capacitance value. As a consequence a tunable response can be obtained over a wide frequency range, see Fig. 2(a). Moreover, in a second design, different operation mode ($n = 0$ or $n = 2$) can be obtained at the same frequency range by tuning the value of loading components. To this end, hard wire switches can exchange to different capacitor values by simply moving the wires. Fig. 2(b) depicts the reflection parameter achieved for two different capacitor values, so that the antenna operation mode can switch from the $n = 0$ mode (red line) to the $n = 2$ mode (green line). Therefore, constant or two peak current and near H-field distributions can be achieved, as showed in Fig. 2(c).

4. CONCLUSIONS

In this contribution, a loop antennas using a ladder network with left-handed loading has been proposed. The antenna having a circumference of one wavelength, and working in an $n = 0$ mode presented an omnidirectional pattern in the plane of the loop. Moreover, two tunable left-handed antennas have been studied. The first one is a left-handed loop with reconfigurable response due to the presence of diode varactors. The tuning of this antenna is achieved by simply varying an external DC voltage. The second antenna is a left-handed loop working at two operating modes i.e., $n = 0$ or $n = 2$. These sort of small antennas can be foreseen in many applications, notably for RFID environments.

ACKNOWLEDGMENT

This work has been supported by Ministerio de Ciencia e Innovación, Spanish Government, under Research Project TEC2010-21520-C04-03, and by the Autonomous Government of Castilla-La Mancha under Research Project PPII10-0047-0220.

REFERENCES

1. Iizuka, H., P. S. Hall, and A. L. Borja, "Dipole antenna with left-handed loading," *IEEE Antenna and Wireless Propagation Letters*, Vol. 5, No. 12, 483–485, Dec. 2006.
2. Liu, Q., P. S. Hall, and A. L. Borja, "Dipole with left-handed loading with optimised efficiency," *2nd Eur. Conf. Antenna Propagation*, Edinburgh, UK, Nov. 2007.
3. Liu, Q., P. S. Hall, and A. L. Borja, "Efficiency of electrically small dipole antenna with self-complementary structure," *IEEE Transaction on Antennas and Propagation*, Vol. 57, No. 10, 3009–3017, 2009.
4. Borja, A. L., P. S. Hall, H. Iizuka, and Q. Liu, "Omnidirectional loop antenna with left-handed loading," *IEEE Antenna and Wireless Propagation Letters*, Vol. 6, 495–498, 2007.

Millimeter-wave Design of Broadband Active Integrated Microstrip Patch Antenna

Mohammad Mahdi Honari, Abdolali Abdipour, and Gholamreza Moradi
Microwave/Millimeter Wave and Wireless Communication Research Lab
Department of Electrical Engineering, Amirkabir University of Technology
Tehran 15914, Iran

Abstract— In this paper, a broadband active integrated antenna in millimeter wave frequency band is presented. For the direct integration, the output matching network is omitted so the microstrip antenna operates as an output matching network of the power amplifier and radiator. The power amplifier and microstrip antenna are designed to operate in wide bandwidth. The output power of the amplifier is obtained about 19.94 dBm for optimized load by load pull analysis. In this design, it is employed aperture-stacked patch microstrip antenna due to its wide bandwidth and isolation with the power amplifier by the ground. The simulated input impedance, radiation pattern and cross polarization of the aperture-stacked antenna are adequate within impedance bandwidth of 24 to 32 GHz.

1. INTRODUCTION

Active integrated antennas (AIA's) make available a new prototype for designing millimeter wave architecture, satellite communications and modern microwave. Integration of the antenna can result in lower insertion loss, smaller size and weight, lower cost and greater efficiency as compared to conventional system. The amplifier-type active antenna has been a main issue in recent researches [1]. In [2], a novel fully integrated active antenna using the direct integration between power amplifier and antenna is proposed to obtain high PAE and compact RF-front end because of omitting interconnecting elements between the amplifier and antenna. On the other hand, there is a growing interest in communication systems that operates in the millimeter wave frequency band in order to take advantage of the wider bandwidth that is accessible at the high frequencies [3]. However, it is well known that at high frequencies dielectric and conductor losses are significant, mainly in great systems, and this reduces the overall gain performance. In a broadband AIA, the antenna design in wide bandwidth as well as the amplifier. In recent years, much effort has been devoted on the advance of wideband antenna for modern communication systems. Using the aperture-stacked patch (ASP) antennas increase bandwidth because it utilizes a resonant aperture with stacked patches [4]. Furthermore, the ASP antennas provide more parameters for designing.

In this paper, we design a broadband AIA in millimeter wave frequency band. In our design, without any output matching network, the transistor of the power amplifier is connected to the antenna directly. The both of power amplifier and antenna are designed to operate in wide bandwidth. The harmonic balance analysis by ADS simulator is used for designing the power amplifier. The input impedance of the ASP antenna is adjusted to be optimized output impedance of the power amplifier, obtained by load pull analysis. Finally, the simulation of the ASP antenna by HFSS simulator is done that it shows good cross polarization and radiation pattern.

2. CONFIGURATION

The active integrated antenna consists of three parts: the power amplifier, the antenna, and the integration of these two parts as the AIA. One of the most famous features of the AIA is that the power amplifier and antenna are treated as a single unit. This is different from the design method of conventional wireless and communication systems, where the RF front-end and antenna are separate units, matched to 50-ohm.

In this work, we design the class-A power amplifier and antenna with together as AIA for broadband application in mm-wave frequency band. The power amplifier as well as the antenna are designed on Rogers's TMM 4 substrate with 4 mil substrate height and dielectric constant of 4.5.

2.1. The Power Amplifier

The selected power transistor of amplifier is TRW's 0.15 µm InGaAs/AlGaAs/GaAs pseudomorphic high electron-mobility transistor (pHEMT) that the linear equivalent-circuit parameters and asymmetric Curtice nonlinear model of it, has been given in [5]. To achieve the maximum PAE and output power, we do load pull analysis at centre frequency of 28 GHz then we optimize input matching network and load impedance for broadband operation. By adding the antenna instead of the load of the power amplifier, it maybe limits bandwidth of the power amplifier so before designing the antenna, we do load sensitivity analysis for the amplifier. In this analysis, we optimize input matching network so that, in the broad bandwidth, we reduce load sensitivity over frequency range. By reducing the load sensitivity, we can design the antenna so much easier than before because, input impedance of the antenna can change more much range in the bandwidth The overall schematic of designed broadband class-A power amplifier structure is shown in Fig. 1. It is seen that the power amplifier is connected to the antenna directly. Element values of power amplifier and optimized load are given in Table 1.

2.2. The Antenna

The aperture-stacked configuration is selected for antenna in view of its intrinsic advantages in active device integration as compared to the other feed structures. On the other hand, this structure has wide bandwidth. In the aperture antenna, the most common technique of controlling the coupling to the feed line is to change the size of the aperture [4]. But, in the aperture-stacked patch antenna, the aperture is employed as a radiator so its size cannot be varied alone and the coupling to the feed line must be controlled in the other method. To achieve this, we use feed line shaping under aperture. Fig. 2 shows the proposed ASP antenna. It must be notice that the antenna is designed for the optimized load of the power amplifier in addition to the adequate gain, radiation efficiency, radiation pattern and, cross-polarization over the bandwidth.

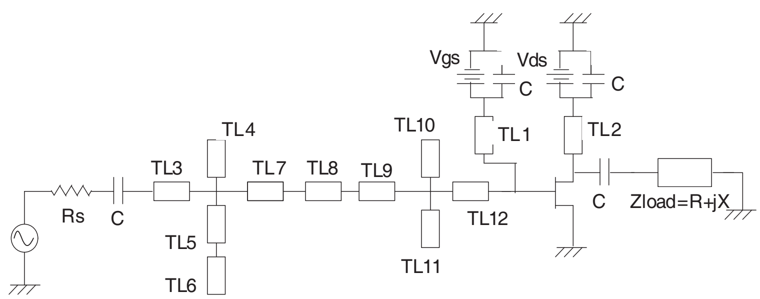

Figure 1: The schematic of broadband class-A power amplifier.

Table 1: Element values of the power amplifier.

parameters	*Values*	*parameters*	*Values*
W1	*2* mil	*L4*	*18.6* mil
W2	*2* mil	*L5*	*29.2* mil
W3	*4* mil	*L6*	*63.9* mil
W4	*4* mil	*L7*	*31.6* mil
W5	*4* mil	*L8*	*42.9* mil
W6	*1* mil	*L9*	*55.4* mil
W7	*2.9* mil	*L10*	*49.1* mil
W8	*1* mil	*L11*	*15.1* mil
W9	*4* mil	*L12*	*9* mil
W10	*4* mil	*Vgs*	*– 0.15* volt
W11	*4* mil	*Vds*	*5.5* volt
W12	*1* mil	*Rs*	*50* ohm
L1	*58.6* mil	*C*	*10* pf
L2	*58.6* mil	*R*	*36* ohm
L3	*1* mil	*X*	*50* ohm

3. SIMULATION RESULTS AND DISCUSSIONS

In this section, we consider simulation results of the power amplifier, antenna and AIA. The part of amplifier and antenna is discussed separately and then the monolithic AIA is considered.

3.1. The Power Amplifier

The power amplifier is design to operate at the centre frequency of 28 GHz. The harmonic balance technique by ADS simulator is used for analyzing the circuit. Fig. 3 shows the variation of PAE of the power amplifier, as function of the input power at the centre frequency of 28 GHz. It is seen that the input power of 5-dBm nearly is the best bias point.

We use the class-A power amplifier so, it is expected that the power of second and third harmonics of the load, be low. Fig. 4 depicts the output power and gain of the load respect to the frequency. A 0.5-dB ripple output power bandwidth of 25% from 24.5 to 31.5 GHz is achieved. The maximum output power of the amplifier is obtained about 19.94 dBm. The average gain of the amplifier is 16-dB. Figs. 4 and 5 show the main harmonic of the output power is at least 18-dBm better than the second and third harmonics over the bandwidth.

Finally, the stability test shows that at least the resistance of the load must be 18-ohm over bandwidth. In the part of antenna, we must be careful that input impedance of the antenna be greater than 18-ohm. This condition will secure the system from instability and oscillation.

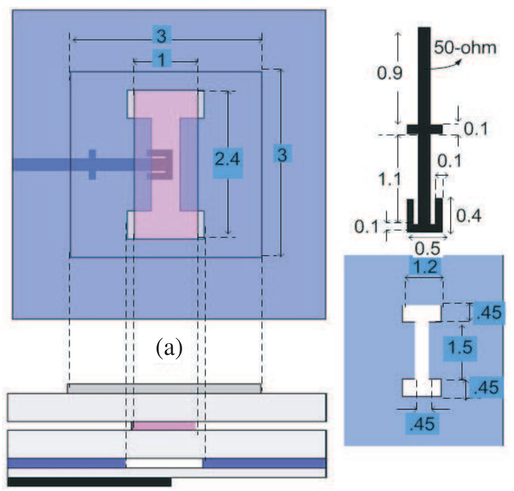

Figure 2: The ASP antenna. (a) Top view. (b) Side view. (c) The aperture and transmission line of antenna. (All units are in mm)

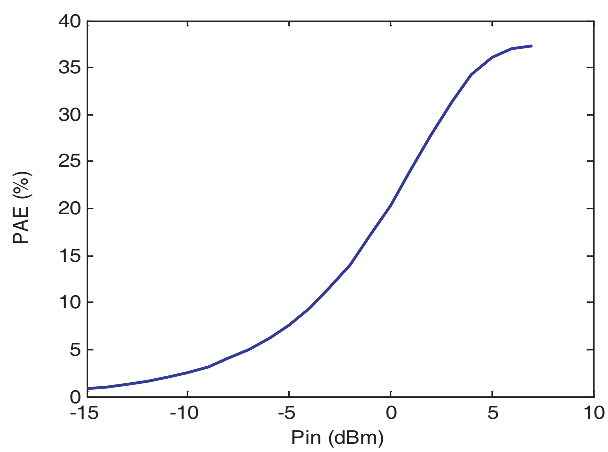

Figure 3: PAE of the power amplifier respect to the input power at centre frequency of 28 GHz.

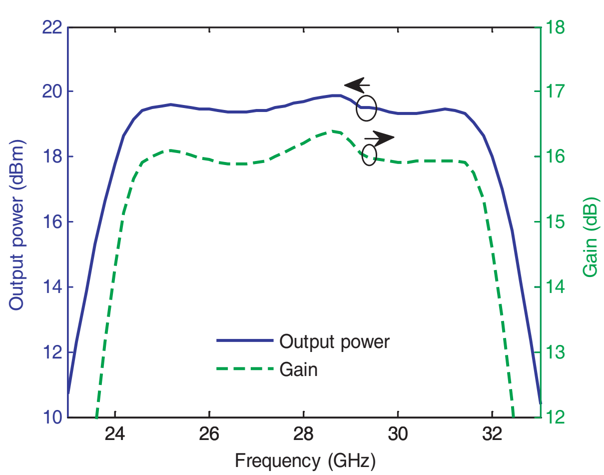

Figure 4: The output power and gain of amplifier.

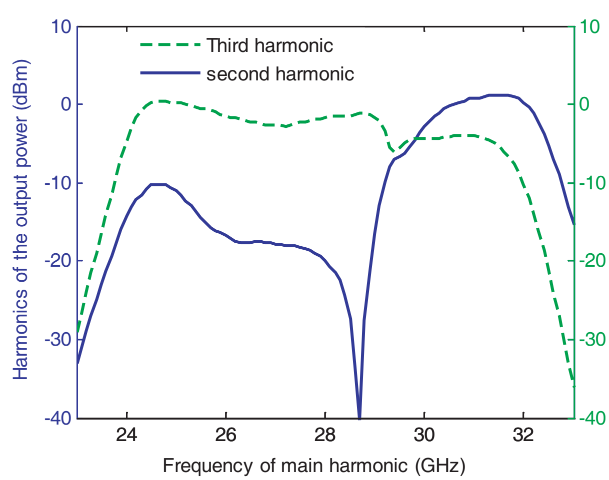

Figure 5: The amount of second and third harmonics over the bandwidth range of first harmonic.

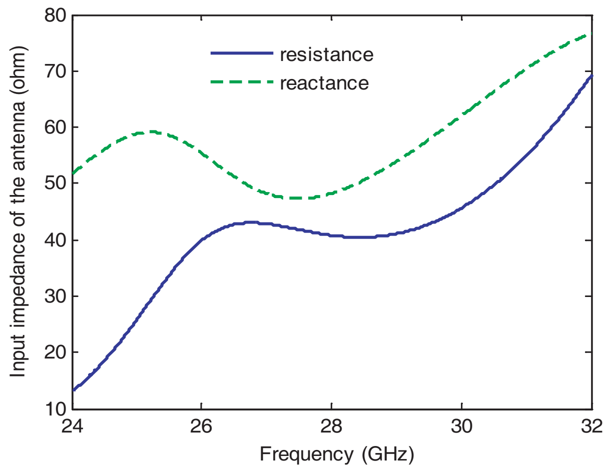

Figure 6: The input impedance of the ASP antenna.

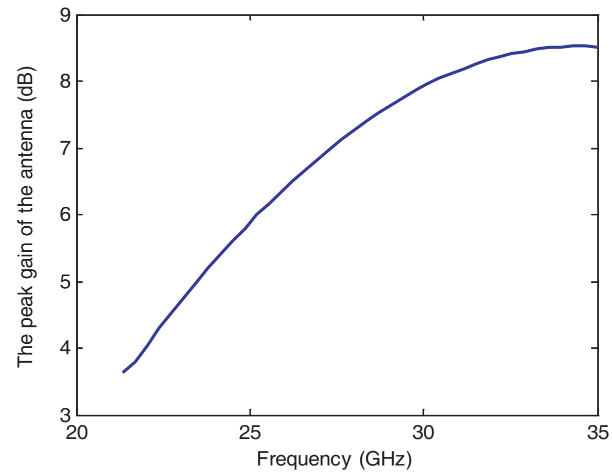

Figure 7: The peak gain of the ASP antenna.

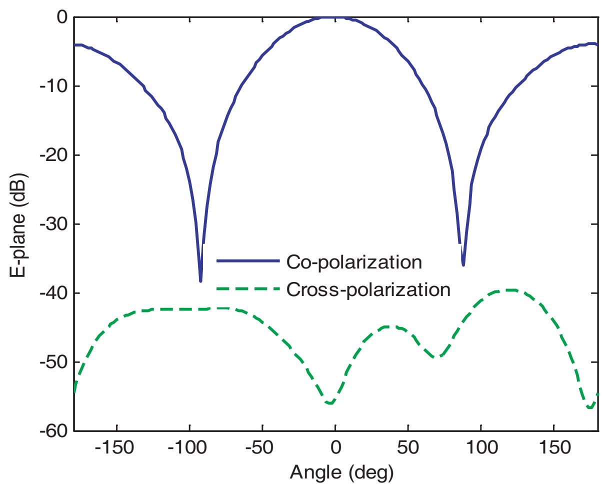

Figure 8: The E-plane of ASP antenna.

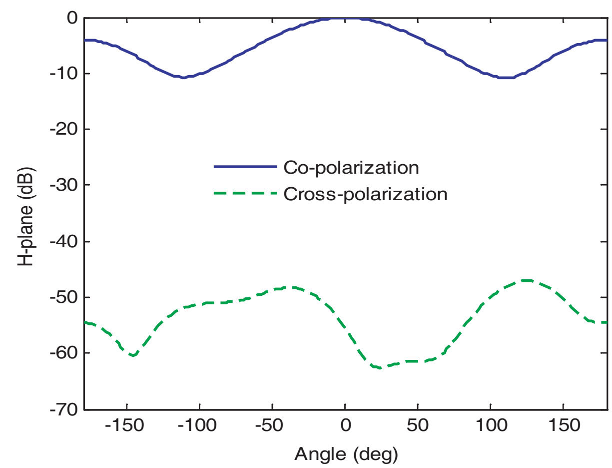

Figure 9: The H-plane of ASP antenna.

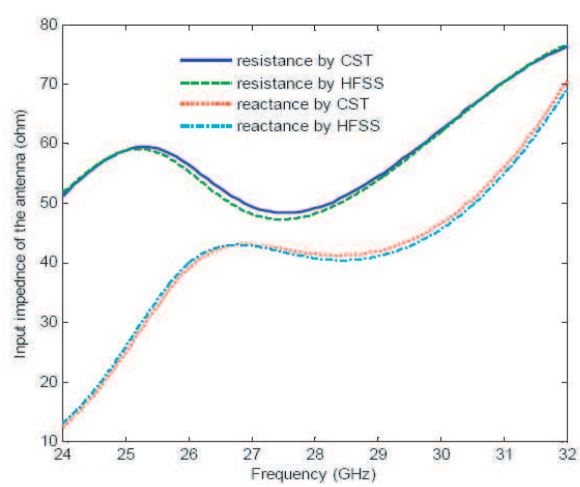

Figure 10: Input impedance of the antenna calculated by CST and HFSS simulators.

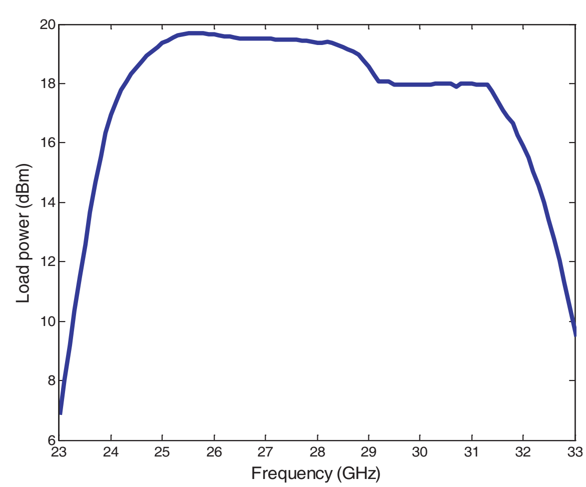

Figure 11: The load power of AIA.

3.2. The Antenna

We try to design the antenna for the optimized load but this is not practical so we did sensitivity analysis to design the antenna easier. Ansoft HFSS is used for simulating the antenna. Fig. 6 shows the input impedance of ASP antenna. The input impedance of antenna is not the optimized load of the amplifier so the bandwidth of amplifier will reduce. Also it is seen that the input impedance of antenna is in stable area of the bandwidth of the amplifier from 24.5 to 31.5 GHz.

In addition to the input impedance of antenna, the radiation specifications of designed ASP antenna must be acceptable. Figs. 7, 8 and 9 show the peak gain, E-plane and H-plane of the antenna, respectively. The peak gain is suitable over the bandwidth of the amplifier. A good radiation pattern is obtained in E-plane and H-plane. Cross-polarization in the 3-dB beamwidth is 44 dB below the co-polarization in the E-plane and 45 dB below the co-polarization in the H-plane for the ASP antenna. Finally, as shown in Fig. 10, we compared input impedance of the antenna calculated by CST and HFSS simulators, showing good agreement.

3.3. The AIA

The AIA consists of the designed power amplifier and antenna. Due to the input impedance of the antenna is not the optimum of load impedance of amplifier, the bandwidth of amplifier will decrease. Fig. 11 shows the bandwidth of AIA. A 2-dB ripple bandwidth of 25% is achieved.

4. CONCLUSION

In this paper, a broadband active integrated antenna in millimeter wave was presented. The power amplifier was design to operate in broad bandwidth. The transistor of the amplifier was connected to the antenna directly. The load pull analysis was applied to optimize the load impedance. We did load sensitivity analysis for the amplifier thus designed the antenna so much easier. The gain, radiation pattern and cross-polarization of the antenna were adequate in the bandwidth. A 2-dB bandwidth of 25% was achieved. In next step, we intend to fabricate our designed AIA in the future.

REFERENCES

1. Karnfelt, C., P. Hallbjorner, H. Zirath, and A. Alping, "High gain active microstrip antenna for 60-GHz WLAN/WPAN Applications," *IEEE Trans. Microwave Theory* & *Tech.,* Vol. 54, No. 6, 2593–2603, June 2006.
2. Kim, H., I. J. Yoon, and Y. J. Yoon, "A novel fully integrated transmitter front-end with high power-added efficiency," *IEEE Trans. Microwave Theory* & *Tech.*, Vol. 53, No. 10, 3206–3214, October 2005.
3. Keller, M. G., D. Roscoe, Y. M. M. Antar, and A. Ittipiboon, "Active millimetre-wave aperture-coupled microstrip patch antenna array," *Electronic Letters*, Vol. 31, No. 1, 2–4, January 2006.
4. Targonski, S. D., R. B. Waterhouse, and D. M. Pozar, "Design of wide-band aperture-stacked patch microstrip antennas," *IEEE Trans. Antenna* & *Propagation*, Vol. 46, No. 9, 1245–1251, September 1998.
5. Siddiqui, M. K., A. K. Sharma, L. G. Callejo, and R. Lai, "A high-power and high-efficiency monolithic power amplifier at 28 GHz for LMDS applications," *IEEE Trans. Microwave Theory* & *Tech.*, Vol. 46, No. 12, 2226–2232, December 1998.

A Dual Bevel Compact Planar Monopole Antenna for UHF Application

M. Jusoh[1], **M. F. Jamlos**[1], **M. R. Kamarudin**[2], **Z. A. Ahmad**[1], **M. A. Romli**[1], **and Naseer Sabri**[1]

[1]School of Computer and Communication Engineering
Universiti Malaysia Perlis (UniMAP), Malaysia
[2]Wireless Communication Centre, Faculty of Electrical Engineering
Universiti Teknologi Malaysia, Malaysia

Abstract— This paper presented a novel dual bevel planar monopole antenna with the ability to operate from 470 MHz to 1100 MHz. The compact planar monopole antenna consists of radiating element perpendicular to ground plane with dimension of 148 mm × 64 mm and 80 mm square respectively. The proposed monopole antenna employing FR4 substrate and implementing beveling technique as well reflect to the low cost and high bandwidth intention. By introducing a dual bevel, an enhancement of 100% impedance bandwidth can be achieved compare to a single bevel with the same bevel angle of 10°, 20°, 30°, 40° and 50°. Moreover, the dual bevel antenna capable in producing divisive radiation patterns with linear polarization at three different frequencies of $f_1 = 500$ MHz, $f_2 = 700$ MHz and $f_3 = 900$ MHz. The measured outputs have shown the same behaviour with the simulation results. The proposed antenna has a great potential as a spectrum sensing device for cognitive radio application in the future.

1. INTRODUCTION

The idea of Cognitive Radio (CR) was first introduced officially in an article by Joseph Mitola in 1999. It was a novel approach in wireless communication [1]. CR technology approach has ability to overcome the spectrum allocation congestion with reflect to the rapid wireless communication growth. The CR antenna system must be able to sense, adapt and communicate without interrupting the primary user. Yet, no CR antenna standard and guideline released. Paper [2] has discussed that a wideband CR antenna is necessary for the spectrum scanning purpose.

A lot of techniques have been proposed on the wideband planar monopole antenna such as notches, lumped circuit, bevel and shorting pin [3–6]. In [7], the conical monopole antenna with an enhancement of bevel has successfully overcome the weaknesses in [6] but only managed to cater for a low frequency range. Additionally, both methods have increased the antenna complexity and the physical dimension.

Instead of proficient in covering a wideband frequency, the proposed antenna is clearly small compared to the conventional planar monopole antennas [6, 7]. In this paper, the behavior of planar monopole antenna with single and dual beveling technique has been analyzed. The fabricated antenna with a 50° dual bevel angle has a very compact size of 64 mm × 146 mm radiating element and 80 mm squared ground plane. Hence, the proposed beveling technique has increase the impedance bandwidth significantly with dual bevel has two times greater bandwidth compared to single bevel. A prototype antenna was designed, fabricated and measured performance are presented. All designs and simulations have been done using CST Microwave Studio and the measurements performed by ZVL Rohde & Schwarz Network Analyzer.

2. ANTENNA DESIGN

Figure 1 and Figure 2 visualized the proposed simulated and fabricated wideband planar monopole antenna respectively. Figure 1(a) illustrated the highlighted radiating element which constructed with a rectangular and a half triangle shape. The divisive radiation pattern is accessible by totally removed all the copper at the backside of the substrate.

Instead of single bevel, dual bevel angle with dotted line as depicted in Figure 2(a) has been introduced to enhance the antenna bandwidth. An optimum reflection coefficient achievable at A is 50° angle. The planar monopole antenna is fabricated on the FR4 substrate with a 0.8 mm of thickness, 4.5 of dielectric constant and 0.019 of tangent loss. Theoretically the ground plane of planar monopole antenna is the tuning circuit of the matching network. The dimension of the ground plane is set in a way to increase the antenna efficiency. The 50 Ω subminiature (SMA) is

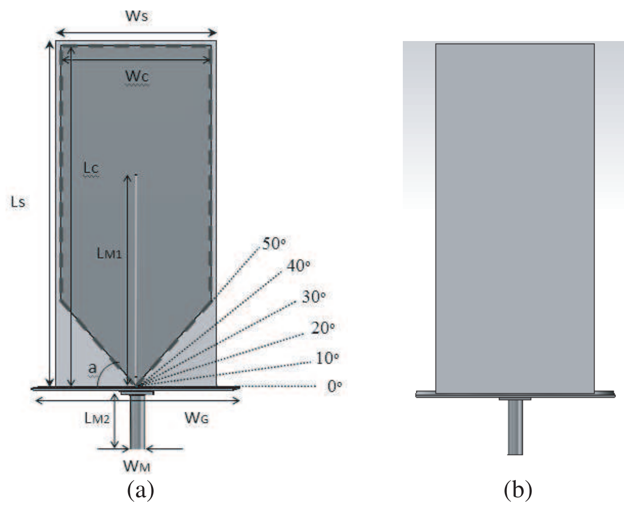

Figure 1: The structure of the simulated antenna (a) front view, (b) side view and (c) layout view.

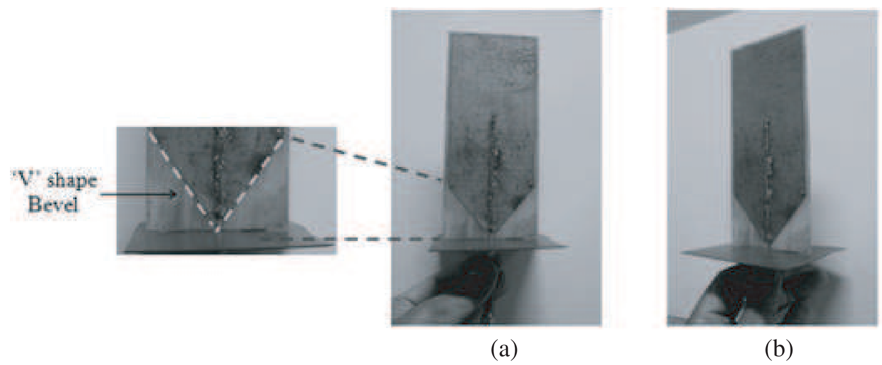

Figure 2: The structure of the fabricated antenna (a) front view and (b) side view.

placed in the middle of the ground plane. Such a way that current will be excited from the bottom of the antenna.

With a lot of optimization routine, the final geometric results are obtained as $W_S = 64$ mm, $L_S = 146$ mm, $W_C = 60$ mm, $L_C = 143$ mm, $W_G = 80$ mm, $L_G = 1$ mm and $a = 50°$.

3. RESULTS AND DISCUSSION

The simulation study has been made on the effect of single and dual bevels towards the input impedance matching (S_{11}). The analysis is performed from 400 MHz up to 1100 MHz with varieties angle (10°, 20°, 30°, 40° and 50°). For single bevel, the bandwidth is achievable from 36% up to 47% under the acceptable reflection coefficient of -6 dB. Whereas the dual bevel obtained two times greater bandwidth compared to the single bevel. Table 1 clearly summarized the comparison of both bevel.

Figure 3 discussed on the significant of the bevel angle towards the type of bevel, single and dual. The ultimate goal of the research is to increase the operating frequency of the antenna. Numerically, the escalating of the height antenna will influence the low frequency shifted to the left and improve the impedance matching, converse to the unaffected of high frequency. However, this will increase the surface wave effect which degradation the antenna efficiency. Surface wave can be prohibited by implementing the dual bevel technique as visualized in Figure 3(b).

Refer to Table 1 and Figure 3; the bevel angle should be between 30° to 50° in order to enhance the entire bandwidth for a planar monopole antenna. From there, a 50° is chosen as the bevel angle in this study.

Figure 4 compared the return loss (RL) of the measurement and simulation result for the proposed planar monopole antenna with 50° dual bevels. The impedance bandwidth is determined under -6 dB of RL (VSWR = 3) which gives 75% power transmitted and 25% reflected. The measured and simulated divergence results are caused by the performance of the network analyzer, the

Table 1: Comparison of single and dual bevel techniques.

Bevel Technique	A (bevel angle)	BW (MHz, %)	f_r (MHz)
Single	10	249.8, 36.7	681.4
	20	277.2, 40.7	681.4
	30	297.8, 43.7	680.7
	40	317.6, 46.9	677.2
	50	315.3, 47.4	664.6
Dual	10	335.9, 49.5	677.9
	20	442.5, 65.8	672.3
	30	559.8, 84.6	661.1
	40	574.3, 89.3	642.9
	50	593.3, 95.9	618.4

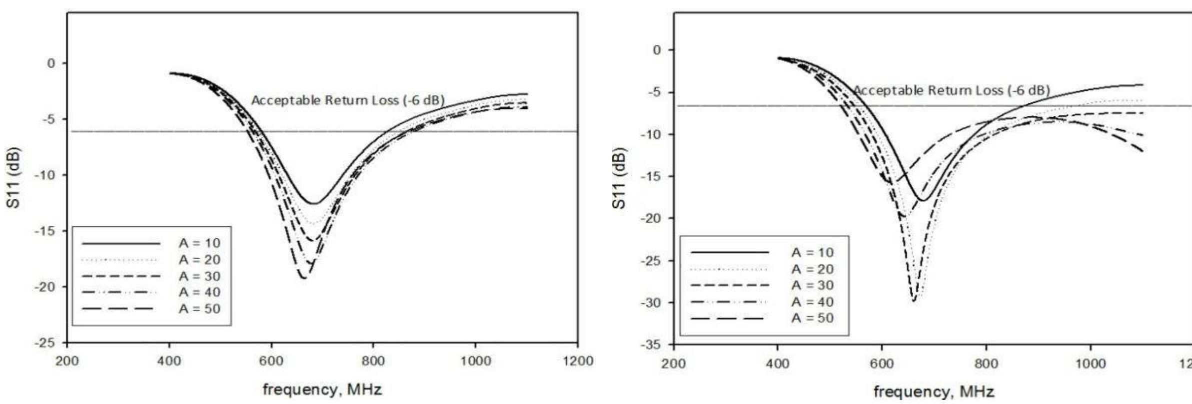

(a) (b)

Figure 3: The bevel angle effect on the presented antenna (a) single bevel and (b) dual bevel.

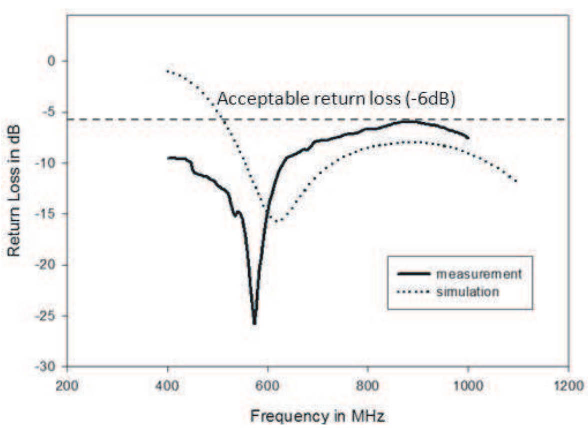

Figure 4: Simulated and measured return loss result of dual bevel planar monopole antenna.

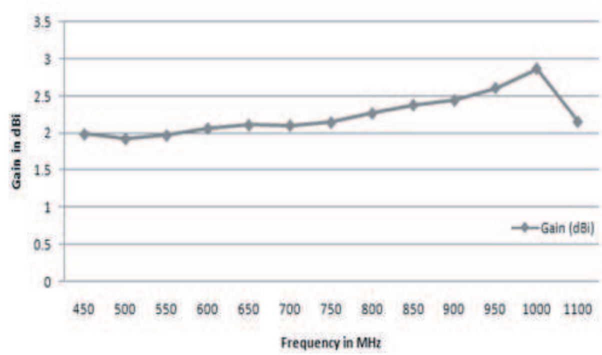

Figure 5: Simulated gain of the antenna.

unnoticeable errors during fabrication process, quality of the etching chemical liquid the soldering technique.

Figure 5 indicates the simulated gain of the small size planar monopole antenna. It can be seen that the gain of the antenna is comparatively small. The numerical radiation patterns for planar monopole antenna with dual bevel are simulated at particular frequencies which are $f_1 = 500\,\text{MHz}$, $f_2 = 700\,\text{MHz}$ and $f_3 = 900\,\text{MHz}$. The patterns are called divisive since they are consists of two main lobes as shown in Figure 6. The energy distributed is equal which is right lobe in magnitude is comparable to the left lobes.

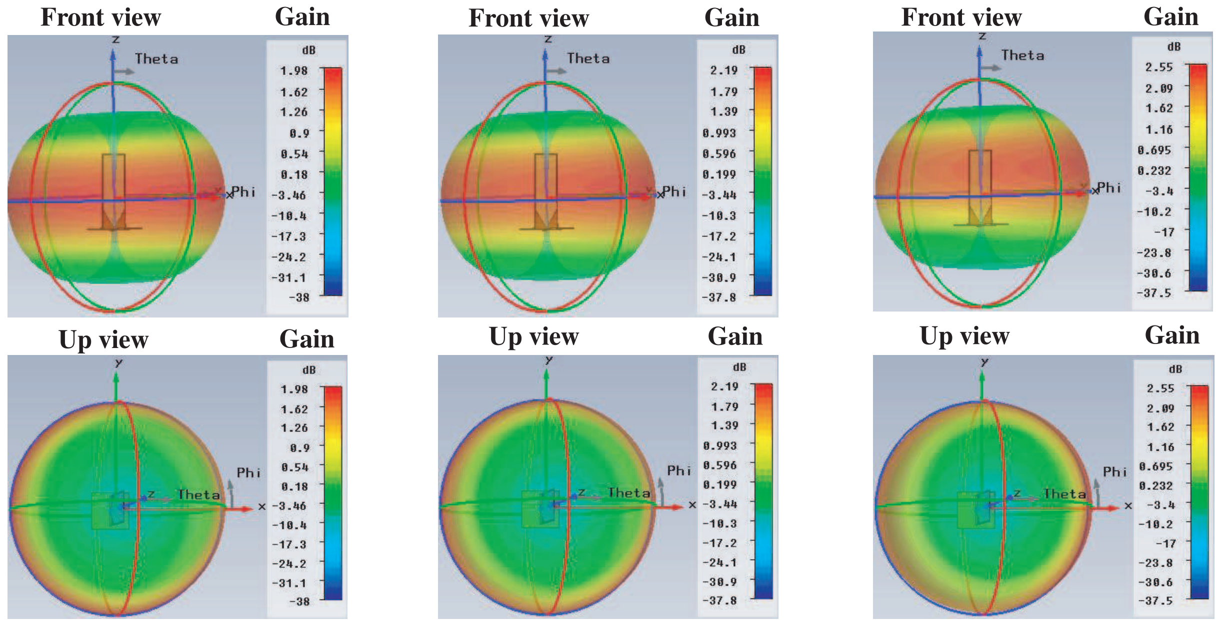

(a) (b) (c)

Figure 6: Simulated radiation pattern of the proposed antenna. (a) 500 MHz, (b) 700 MHz, (c) 900 MHz.

4. CONCLUSIONS

The physical dimension of the planar monopole antenna presented is considered compact and wideband. The implementation of 50° dual bevel angle has achieved a very wideband impedance bandwidth of approximately more than 90%. In addition, the antenna is easy to be fabricated. The antenna has capability to operate for the VHF spectrum, the targeted white spaces (broadcasting spectrum). These increase the value of the antenna for the cognitive radio applications in the future.

REFERENCES

1. Mitola, III, J. and G. Q. Maguire, Jr, "Cognitive radio: Making software radio more personal," *IEEE Personal Communications*, August 1999.
2. Kelly, J. R., E. Ebrahimi, P. S. Hall, P. Gardner, and F. Ghanem, "Combined wideband and narrowband antennas for radio applications," *Cognitive Radio and Software Defined Radios: Technologies and Techniques*, IET, 2008.
3. Lee, W.-S., D.-Z. Kim, K.-J. Kim, and J.-W. Yu, "Wideband planar monopole antennas with dual band-notched characteristics," *IEEE Transactions on Microwave Theory and Techniques*, Vol. 54, 2800–2806, June 2006.
4. Chakravarty, T., S. M. Roy, S. K. Sanyal, and A. De, "A novel microstrip patch antenna with large impedance bandwidth in Vhf/Uhf rang," *Progress In Electromagnetics Research*, Vol. 54, 83–93, 2005.
5. Ammann, M. J. and Z. N. Chen, "A wide-band shorted planar monopole with bevel," *IEEE Transaction Antennas Propagation*, Vol. 51, 901–903, April 2003.
6. Chu, J., C. Ruan, X. Liao, and Y. Cui, "A small size broadband antenna used in VHF/UHF band," *8th International Symposium on Antennas, Propagation and EM Theory, 2008, ISAPE 2008*, 254–256, 2008.
7. Kyi, Y. Y., L. Jianying, and G. Y. Beng, "Study of broadband small size conical antenna," *IEEE Antennas and Propagation Society International Symposium 2006,* 2025–2028, 2006.

A UWB MIMO Spatial Design Effect on Radiation Pattern

M. Jusoh[1], **M. F. Jamlos**[1], **M. R. Kamarudin**[2], **Z. A. Ahmad**[1], **M. A. Romli**[1], **and S. H. Ronald**[3]

[1]School of Computer and Communication Engineering
Universiti Malaysia Perlis (UniMAP), Malaysia
[2]Wireless Communication Centre, Faculty of Electrical Engineering
Universiti Teknologi Malaysia, Malaysia
[3]School of System Electrical Engineering, Universiti Malaysia Perlis (UniMAP), Malaysia

Abstract— Attractive features of emerging Ultra-wideband (UWB) and Multi-Input Multi-Output (MIMO) technique are outlined and special design effects are described. The proposed antenna is basically comprised of two patch elements integrated on the same substrate. In the sense of optimum inter-element spacing, initial analysis on antenna configuration has been made towards the reflection coefficient, mutual coupling and correlation coefficient. Furthermore, a proposed spatial design antenna on radiation pattern effect also has been presented. The proposed antenna design achieved the required impedance bandwidth over the entire frequency range of 3.1 GHz to 10.6 GHz under the acceptable S_{11} of less than -10 dB.

1. INTRODUCTION

Recently, ultra wideband (UWB) with the integration of Multiple-Input Multiple-Output (MIMO) technology has obtained a great attention among the researchers. UWB itself has a unique compensation such as license exemption operating at 3.1 GHz to 10.6 GHz, high bandwidth of 7.5 GHz and low power spectral density of -41.3 dBm/MHz. Hence MIMO enhanced the value added of UWB by improving the capacity as well as resistance to multipath propagation [1].

In designing MIMO antenna, there are few significant parameters to be considered such as a reflection coefficient, mutual coupling and correlation coefficient [2–5]. There are intimately engaged to the inter-element spacing (IES). However, the selection of IES must fit the physical dimension of the wireless communication device.

Power transmission and reflection is expressed by the reflection coefficient parameter. It indicates by the return loss (S_{11}) graph. Mutual coupling is the presence of the electromagnetic interactions between adjacent antenna elements. It can be attaining directly from the S_{12} or S_{21}. The correlation coefficient determined the degree of antenna diversity, such in MIMO systems. Instead of using radiation pattern, the scattering parameters also are able to intended correlation coefficient via Eq. (1).

$$\rho = \frac{|S_{11} * S_{12} + S_{21} * S_{22}|^2}{(1 - (|S_{11}|^2 + |S_{21}|^2))(1 - (|S_{22}|^2 + |S_{12}|^2))} \tag{1}$$

Based on the author knowledge consent so far, to design MIMO antenna the S_{11}, S_{12} and correlation coefficient need to be analyzed collectively as they are inter-connected to each other. Hence, this paper proposed three different cases which are reflection coefficient, mutual coupling and correlation coefficient with IES varying from 0 mm to 40 mm in the sense of obtaining an ultimate antenna configuration. Ultimately, this research focused on the UWB MIMO's special design effect on radiation pattern.

2. ANTENNA DESIGN

The proposed UWB MIMO antenna with a special design is illustrated clearly in Fig. 1. Special design means an identical antenna dimension that is redesign repetitively. This paper considered for two elements merely. The antenna developed by a combination of seven small circles surrounded single middle circle with a diameter of $R_s = 6$ mm and $R_{in} = 12$ mm respectively. Both elements excited by a 50 Ω microstrip feed line with 5 mm width. Fabrication is done on a Taconic TLY5 substrate with specifications as 1.5748 of thickness, 2.2 +/− 0.02 of dielectric permittivity and 0.0009 of tangent loss.

In this research, the inter-element spacing (IES) symbolized by D in Fig. 1 will be analyze with an ultimate goal of achieving low mutual coupling as well as low reflection coefficient which reflect to the minimum correlation coefficient by conserving UWB frequency band standard. All the design has been performed using CST Microwave Studio simulation software.

3. RESULTS AND DISCUSSION

This paper analyzes the MIMO antennas parameters (reflection coefficient, mutual coupling and correlation coefficient) towards the various D of 0 mm, 6 mm, 10 mm, 15 mm, 20 mm and 40 mm. Fig. 2 depicted an efficient return loss throughout the entire required operating band. The presented antenna has three dominant frequencies resonant for all D values.

The forward transmission coefficient, S_{12} put a value of lower than -10 dB for the various D values as shown in Fig. 3. The bigger the D reflected to the lower of mutual coupling eventually result to radiation efficiency improvement. However, $D = 15$ mm shows a good mutual coupling of less than -15 dB compared to other D's.

The lower value of correlation is significant to improve the diversity performance of the MIMO

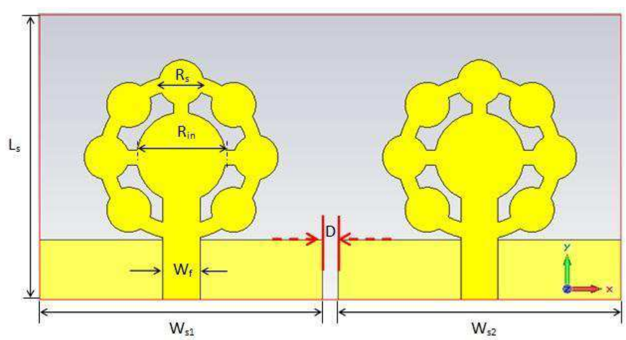

Figure 1: The simulated geometry of the proposed UWB MIMO antenna.

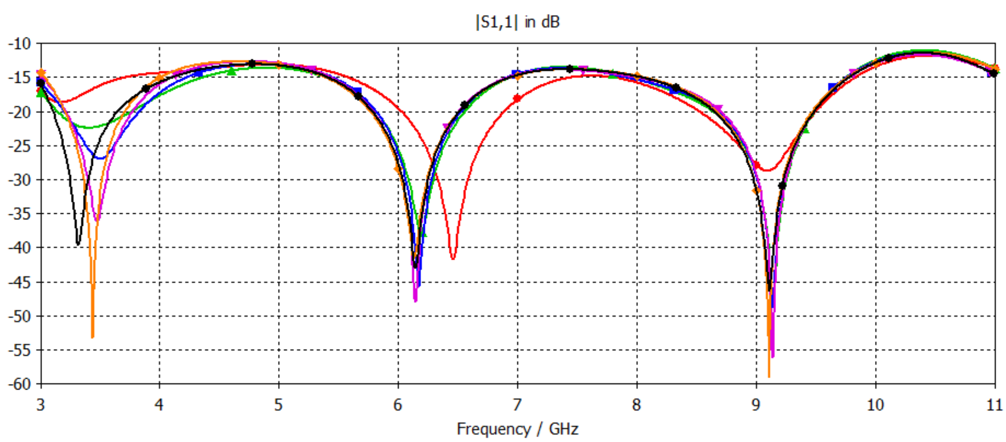

Figure 2: Simulated reflection coefficient of the proposed antenna.

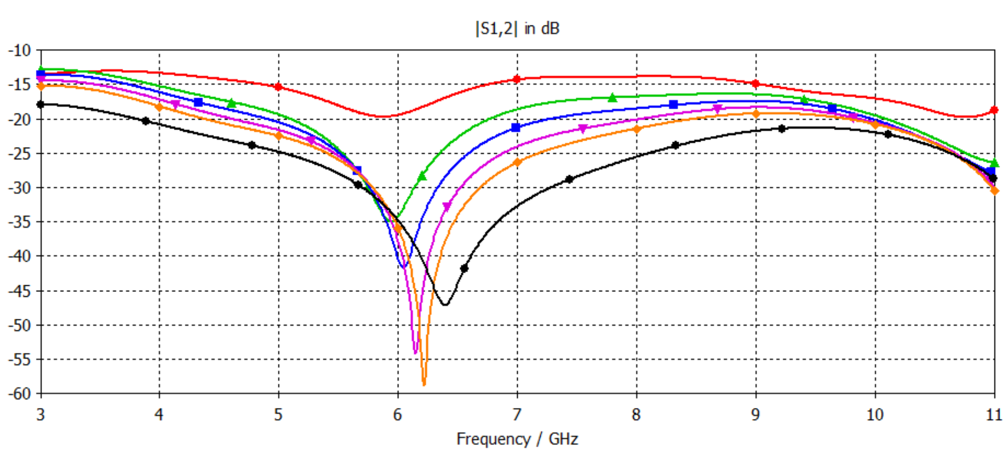

Figure 3: Simulated mutual coupling of the proposed antenna.

system [3]. Fig. 4 demonstrates that correlation between the various D differs significantly. Those figures revealed that S_{12} decreases as the IES increases. It can be seen that $D = 40\,\text{mm}$ has a minimum value of correlationz coefficient for the targeted operating frequency except at frequency resonant 6.2 GHz. Hence the mutual coupling of $D = 40\,\text{mm}$ is also the lowest among other D's. Even though the D increment will reflect to the decrement of S_{12} and correlation coefficient, this however will contribute to the bigger antenna dimension. Moreover, the acceptable value of D needs to reconsider in order to preserve the efficiency of MIMO antenna performance and antenna compaction as well. Therefore based on parameters deliberation, the ultimate D value is 15 mm with a minimum correlation coefficient value of $-100\,\text{dB}$.

Figure 5 indicates simulated 3D radiation pattern at 3 GHz of the proposed antenna. It is notable that the proposed MIMO antenna has significant gain improvement of 3.414 dBi compared to single antenna of 2.3 dBi. This is due to the influenced radiation intensity effect from the adjacent element that helps to boost up the gain. Moreover, MIMO antenna has better radiation efficiency of 90.6% and total efficiency of 86.48% against the single radiating element.

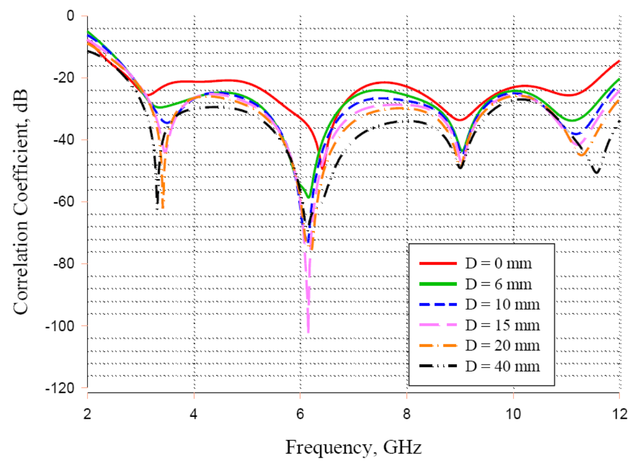

Figure 4: Calculated correlation coefficient of the proposed antenna.

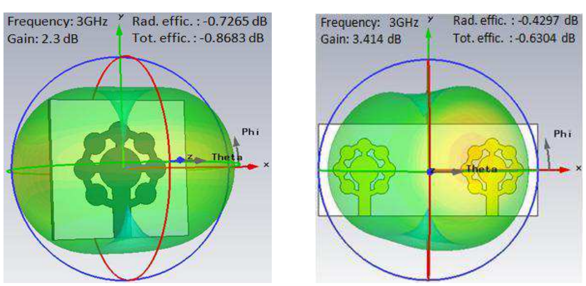

(a) (b)

Figure 5: Simulated radiation of the proposed antenna. (a) Single element antenna. (b) Proposed MIMO antenna.

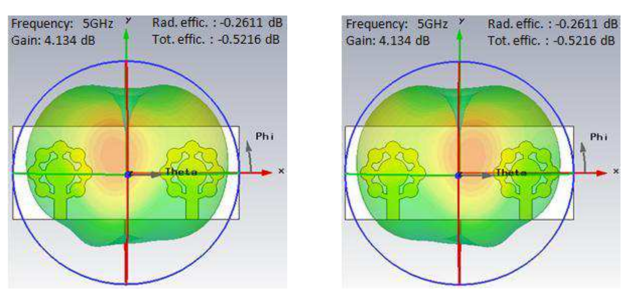

(a) (b)

Figure 6: Simulated 3D simulated radiation patterns at 5 GHz. (a) SMA 1. (b) SMA 2.

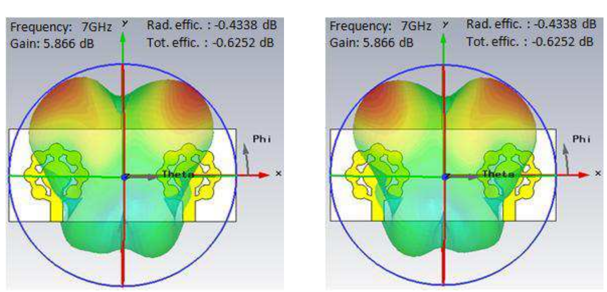

(a) (b)

Figure 7: Simulated 3D simulated radiation patterns at 7 GHz. (a) SMA 1. (b) SMA 2.

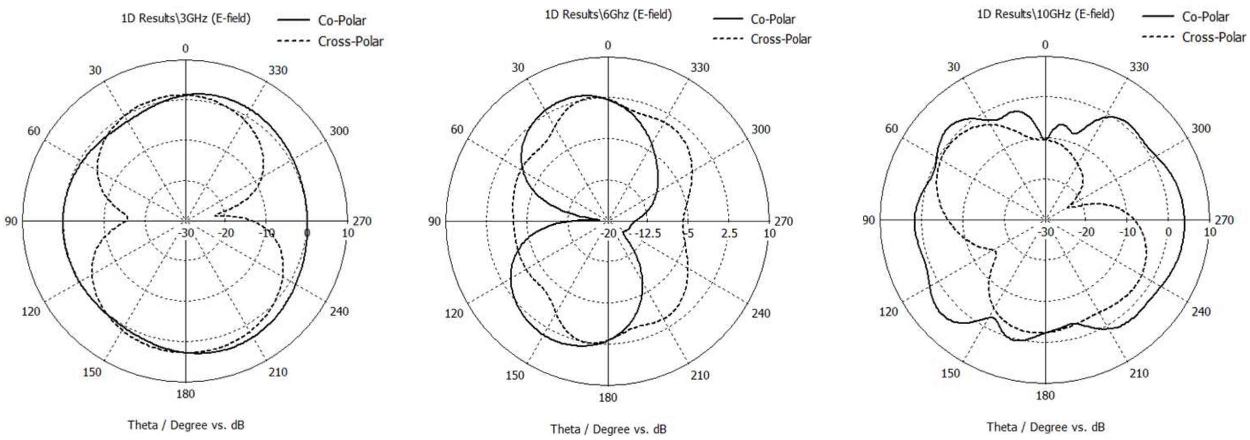

(a) (b) (c)

Figure 8: The simulated E-plane radiation pattern of the presented antenna. (a) 3 GHz. (b) 6 GHz. (c) 10 GHz.

The simulated 3D radiation pattern of the proposed MIMO as in Fig. 6 and Fig. 7 show that the two antenna elements work separately. Both figures illustrate that the identical element excited by two SMA (subminiature) shared the same performance of gain, radiation pattern and total efficiency at specified frequencies of 5 GHz and 7 GHz.

Figure 8 visualized the simulated radiation pattern in correspondence to three frequencies points which are $f_1 = 3\,\text{GHz}$, $f_2 = 6\,\text{GHz}$ and $f_3 = 10\,\text{GHz}$). From the figure, it can be seen that the presented antenna has relative stable radiation patterns at the particular frequencies.

4. CONCLUSION

This research proposed a special design of two identical patch elements on a single substrate. The proposed antenna achieved to cater UWB frequency resonant of 3.1 GHz to 10.6 GHz. The presented MIMO antenna accessible an optimum inter-element spacing with minimum reflection coefficient of −10 dB, low mutual coupling less than −15 dB and low correlation coefficient as well. Moreover, the effect of UWB MIMO antenna design on radiation pattern at three specified frequencies has been discussed.

REFERENCES

1. Dong, L., H. Choo, R. W. Heath, Jr., and H. Ling, "Simulation of MIMO channel capacity with antenna polarization diversity," *IEEE Transactions on Wireless Comm.*, Vol. 4, No. 4, Jul. 2005.
2. Manteuffel, D., "MIMO antenna design challenges," *2009 Loughborough Antennas & Propagation Conference*, Loughborough, UK, Nov. 16–17, 2009.
3. Zhou, X., R. L. Li, and M. M. Tentzeris, "A compact broadband MIMO antenna for mobile handset applications," *Antennas and Propagation Society International Symposium (APSURSI)*, 2010.
4. Najam, A. I., Y. Duroc, and S. Tedjini, "Design & characterization of an antenna system for UWB-MIMO communications systems," *Proceedings of the Fourth European Conference European Conference on Antennas and Propagation (EuCAP)*, 2010.
5. See, T. S. P., A. M. L. Swee, and Z. N. Chen, "Correlation analysis of UWB MIMO antenna system configurations," *Proceedings of the 2008 IEEE International Conference on Ultra-Wideband (ICUWB2008)*, Vol. 2, 2008.

Harmonic Rejection Triangle Patch Antenna

M. S. Bin-Melha[1], **R. A. Abd-Alhameed**[1], **C. H. See**[1], **M. Usman**[2], **I. T. E. Elfergani**[1], **and J. M. Noras**[1]

[1]Mobile and Satellite Communications Research Centre, University of Bradford, Bradford, UK
[2]Department of Electrical Engineering, University of Hai'l, KSA

Abstract— A triangular patch harmonic-rejecting antenna at 0.7 GHz is proposed. Simulated results obtained using HFSS software show that a triangular antenna with shorting pin feed, and of compact size, exhibits high reflection coefficients at the second and third harmonics (-0.12 dB at 1.4 GHz and -0.16 dB at 2.1 GHz) respectively.

1. INTRODUCTION

Patch antennas, based on printed circuit technology, are flat radiating structures on top of ground-plane-backed substrates, and have the advantages of being compact antennas with low manufacturing cost and high reliability. However, there are difficulties in practice in achieving high bandwidth and efficiency. Nevertheless, improvements in the properties of suitable dielectric materials and in design techniques have led to an enormous growth in popularity of microstrip patch antennas, and there are now a large number of commercial applications. Many shapes of patches are possible, with varying applications, but the most popular are rectangular, circular or thin strips [1].

Patch antennas are typically light in weight, low in cost, and widely used in communications. On the downside, they suffer from excess harmonic radiation. Fortunately, many methods have been developed for suppression of these harmonics. One effective approach to suppress harmonics in microstrip patch antennas (MPA) is to use electromagnetic band gap structures (EBG) [2–5].

In Ref. [1], periodic slots are etched in the ground plane of a MPA, which behave as EBG structures. Higher order harmonics fall in the stop band of the EBG and are suppressed. Another approach is to use defected ground structures (DGS) on microstrip feed lines. Up to third order harmonic rejection was reported combining DGS and EBG structure [4]. However, a problem for the EBG structure is backside radiation due to the etched slots just beneath the radiating patch [2–4]. The radiation pattern differs significantly from that of a single MPA. Recently, another approach is reported which used a 1-D Photonic Band Gap (1-D PBG) structure with a DGS on the feed line for impedance matching and harmonic rejection [5]. Up to second harmonic rejection was reported.

Additionally, a method involving a low-pass filter composed of a circular head dumbbell shaped DGS structure and a circular head shunt open microstrip stub on the feed line was able to suppress up to the fourth harmonic effectively [6]. Finally, second and third harmonics have been eliminated with a microstrip patch antenna with a proximity coupled feeding line by adjusting the length of feed line and introducing one resonant cell [7].

A triangular patch antenna with shorting pin used for suppressing the harmonics is proposed in this paper. This work is very similar to [8], but its performance has been optimized to serve its application.

2. ANTENNA DESIGN CONCEPT

The geometry of the proposed antenna is shown in Fig. 1. This triangular patch is designed on a FR4 substrate of thickness 1.6 mm and relative permittivity of 4.4, mounted over the ground plane. The sizes of the printed antenna patch and the ground plane are $90 \times 25\,\mathrm{mm}^2$ and $135 \times 65\,\mathrm{mm}^2$ respectively. The co-axial or probe feed technique is adopted on this antenna so that the feed point can be placed at any place in the patch to match its 50 ohm input impedance.

3. RESULT AND DISCUSSIONS

Figure 2 shows the simulated reflection coefficient of the proposed antenna. As can be seen, the antenna is designed to operate at 700 MHz and its corresponding second and third harmonics, at 1.4 GHz and 2.1 GHz, were eliminated. By adjusting the location of shorting pin good impedance matching can be easily obtained at the fundamental frequency. As can be seen, the suppression of the harmonics does not produce any harmful effects on the impedance matching at the fundamental frequency. The simulations were carried out using the HFSS simulator [9].

To overcome the spurious radiation problem, it is necessary to control the input impedance of the antenna and create a reactive termination at harmonic frequencies. The input impedance of the proposed antenna was investigated over a wide frequency band as shown in Fig. 3. The input impedance of this antenna at the fundamental operating frequency and its first two harmonics shows that almost perfect matching to 50 ohm was attained at the fundamental frequency, while fairly small resistive impedances at harmonic frequencies were observed.

Figures 4 and 5 show the corresponding harmonic current distributions on the patch. The position of the shorting pin is optimally set adjacent to a point of maximum voltage, which corresponds to a point of minimum current distribution on the patch.

The radiation patterns in the xz and yz planes for the antenna shown in Fig. 1 is presented in Fig. 6, at the fundamental, second and third harmonic frequencies. The results confirm viable

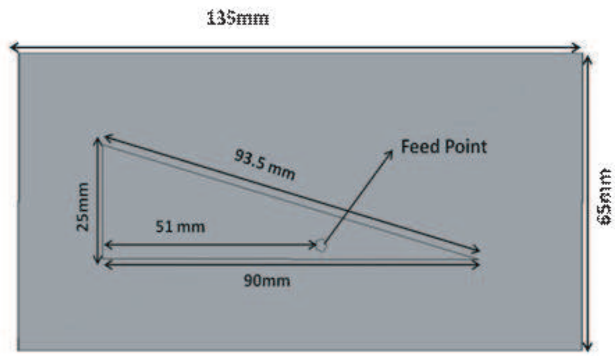

Figure 1: Basic geometry of the proposed antenna.

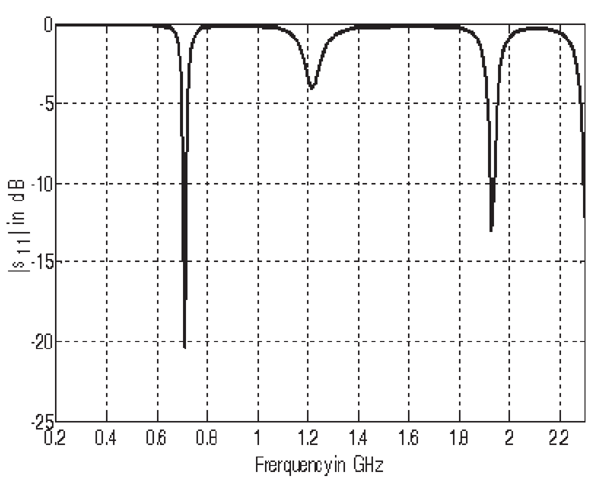

Figure 2: Reflection coefficient of the antenna, and its harmonics.

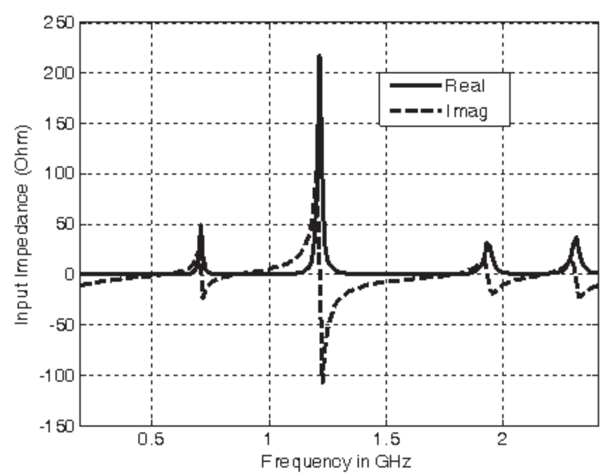

Figure 3: The input impedance of the proposed patch antenna.

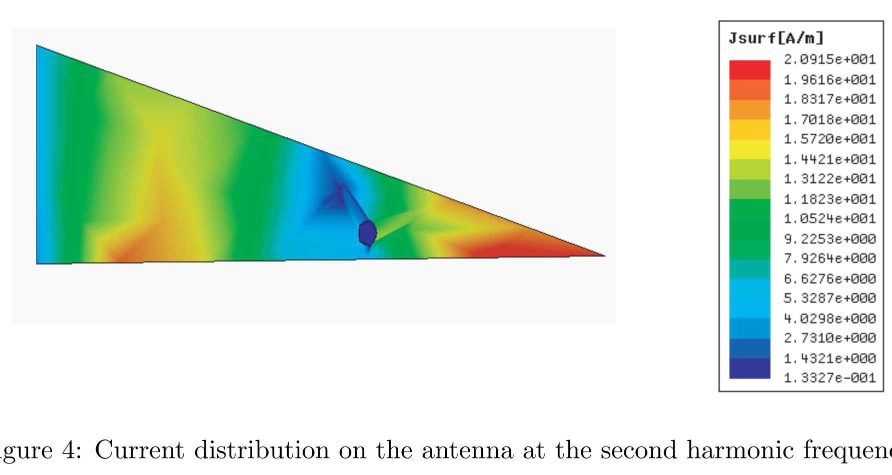

Figure 4: Current distribution on the antenna at the second harmonic frequency.

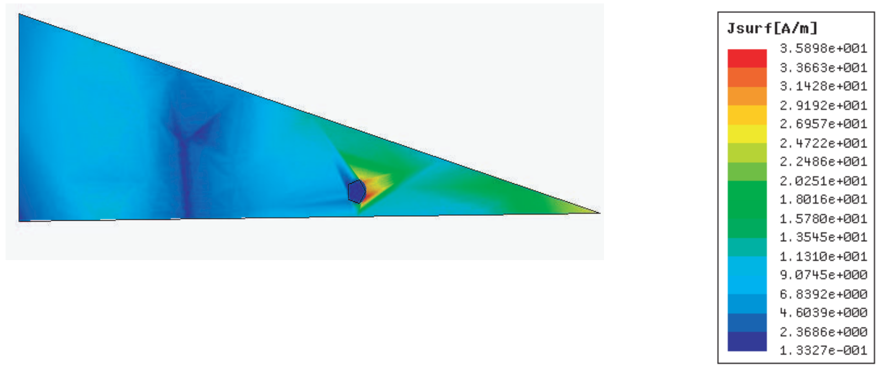

Figure 5: Current distribution on the patch at the third harmonic frequency.

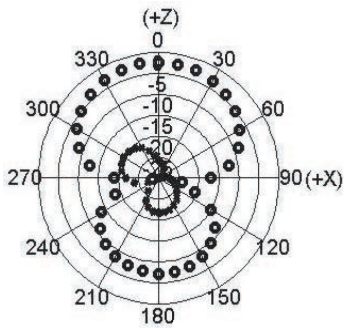
xz plane 700 MHz

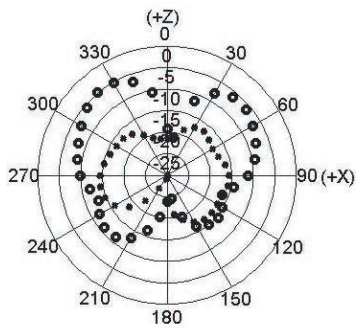
xz plane 1400 MHz

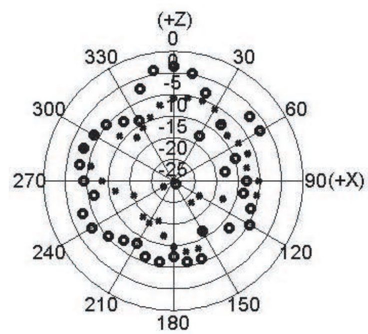
xz plane 2100 MHz

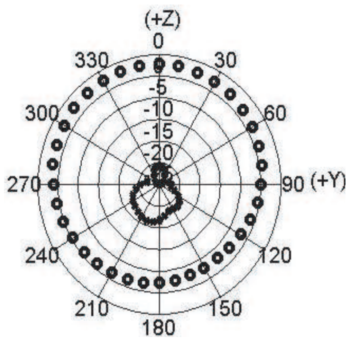
yz plane 700 MHz

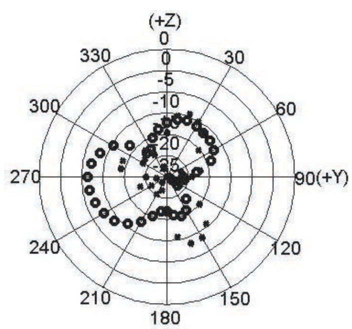
yz plane 1400 MHz

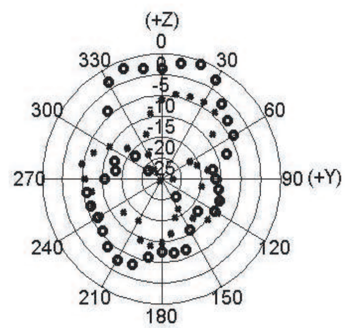
yz plane 2100 MHz

Figure 6: Radiation patterns of antenna design at fundamental, second and third harmonic frequencies. 'ooo': Simulated co-polar, '***': Simulated cross-polar.

levels of suppression of harmonics. In other words, these results show that the radiation patterns at the harmonic frequency are acceptably suppressed.

4. CONCLUSION

In this paper, a shorting pin technique for designing a triangular patch with suppression characteristics over harmonic frequency bands has been proposed and investigated. The reflection coefficient was about -0.12 dB at the second harmonic and -0.16 dB at the third harmonic. According to the results obtained, this antenna with its simple harmonic suppression structures is quite effective. Therefore, the proposed antenna can be suitable for active integrated antenna.

REFERENCES

1. Saunders, S. R. and A. Aragon-Zavala, *Antenna and Propagation for Wireless Communication Systems*, John Wiley & Sons, England, 2007.
2. Horri, Y. and M. Tsutsumi, "Harmonic control by photonic bandgap on microstrip patch antenna," *IEEE Microwave Guided Wave Lett.*, Vol. 9, 13–15, 1999.

3. Sung, Y. J., M. Kim, and Y. S. Kim, "Harmonics reduction with defected ground structure for a microstrip patch antenna," *IEEE Antennas Wireless Propag. Lett.*, Vol. 2, 111–113, 2003.
4. Liu, H., Z. Li, X. Sun, and J. Mao, "Harmonic suppression with photonic bandgap and defected ground structure for a microstrip patch antenna," *IEEE Microwave Wireless Compon. Lett.*, Vol. 1, 55–565, 2005.
5. Sung, Y. J. and Y.-S. Kim, "An improved design of microstrip patch antennas using photonic bandgap structure," *IEEE Trans. Antennas Propag.*, Vol. 53, 1799–1804, 2005.
6. Mandal, M. K., P. Mondal, S. Sanyal, and A. Chakrabarty, "An improved design of harmonic suppression for microstrip patch antennas," *Microwave and Optical Technology Letters*, Vol. 49, No. 1, 103–105, January 2007.
7. Luis, I.-S., J.-L. Vázquez-Roy, and E. Rajo-Iglesias, "Proximity coupled microstrip patch antenna with reduced harmonic radiation," *IEEE Transactions on Antennas and Propagation*, Vol. 57, No. 1, 27–32, January 2009.
8. Olaimat, M. M. and N. I. Dib, "A study of 15°–75°–90° angles triangular patch antenna," *Progress In Electromagnetics Research Letters*, Vol. 21, 1–9, 2011.
9. *Ansoft High Frequency Structure Simulator v10 Uses Guide*, CA, USA.

A New Fractal Based Printed Slot Antenna for Dual Band Wireless Communication Applications

Jawad K. Ali and Emad S. Ahmed
Department of Electrical and Electronic Engineering
University of Technology, Baghdad, Iraq

Abstract— Different fractal based structures have been widely used in numerous antenna designs for various applications. In this paper, a printed slot antenna has been introduced as a candidate for use in the dual band wireless communication applications. The antenna slot structure is in the form of a Sierpinski gasket of the first iteration. The antenna has been fed with 50 Ohm microstrip transmission line, and the slot structure is to be etched on the reverse side of the substrate. Performance evaluation of the proposed antenna design has been carried out using a method of moments based EM simulator, IE3D. Simulation results show that the resulting antenna exhibits an interesting dual frequency resonant behavior making it suitable for dual band communication systems including the dual band WLAN applications. Parametric study has been carried out to explore the effects of antenna parameters on its performance.

1. INTRODUCTION

The pioneer work of Mandelbrot [1] in fractal geometry had stimulated microwave circuits and antenna designers, in their attempts to realize miniaturized circuits and components, to seek out for solutions by investigating different fractal geometries. However, the recent developments in modern wireless communication systems have imposed additional challenges on microwave antenna and circuit designers to produce new designs that are miniaturized and multiband. Fractal curves are characterized by a unique property that, after an infinite number of iterations, their length becomes infinite although the entire curve fits into the finite area. This property can be exploited for the miniaturization of microstrip antennas, resonators, and filters. Due to the technology limitations, fractal curves are not physically realizable. Pre-fractals, fractal curves with finite order, are used instead [2, 3].

Slot antennas based on fractal curves such as Koch, Sierpinski and others have attracted the researchers to achieve antenna miniaturization with multiple resonances [4–11]. Sierpinski gasket fractal has been reported in [4] to model a dual band microstrip line fed slot antenna for GSM and 2.4 GHz WLAN bands. In [5], a Koch fractal slot antenna has been proposed to construct a CPW fed slot antenna for the two bands WLAN and WiMAX applications. Fractals generated from many Euclidean geometries such as the circle, triangle and others, have been employed to produce dual band antennas for a variety of communication applications [6–10]. Circular and half circular fractal shaped dual band antennas have been reported in [6] and [7] respectively for use in dual bands WLAN. Triangular based fractal based antenna has been proposed in [8] for GSM and DSC applications. Elliptical fractal patch antenna has been investigated a candidate for use in dual band communications [9]. Moreover, a quasi-fractal based slot geometries have been successfully used in different ways to form parts (or the whole) of the ground plane of dual band antenna [10].

In this paper, a new electromagnetically coupled microstrip-fed printed slot antenna design based on the first iteration of Sierpinski gasket fractal geometry has been presented as a dual band printed antenna for the 2.4/5.2 GHz bands WLAN applications.

2. THE PROPOSED ANTENNA STRUCTURE

The Sierpinski triangle or gasket is obtained by repeatedly removing (inverted) equilateral triangles from an initial triangle of a unit side length. For many purposed it is better to think of this procedure as repeatedly replacing an equilateral triangle by three triangles of half the height [11]. Figure 1 demonstrates the fractal generation process of the Sierpinski gasket up to the second iteration.

The geometry of the proposed Sierpinski gasket based slot antenna is shown in Figure 2. The first iteration Sierpinski gasket based slot structure has been constructed on, on the ground plane side of a dielectric substrate. The dielectric substrate is supposed to be the FR4 with a relative dielectric constant of 4.4 and thickness of 1.6 mm. The slot antenna is fed by a 50 Ω microstrip line printed on the reverse side of the substrate. A microstrip line, with a width of about 3.0 mm is placed on the centreline of the slot structure (x-axis). This type of feeding have been found to be more reliable for fractal slot antenna application [12, 13].

3. THE ANTENNA DESIGN

A printed slot antenna, based on the first iteration Sierpinski gasket, has been designed to resonate at 2.4 GHz. After suitable dimension scaling, the resulting antenna slot side length has to be determined. Observing the influence of the various parameters on the antenna performance, it has been found that the dominant factor in the antenna is the slot side length in terms of the guided wavelength λ_g.

$$\lambda_g = \frac{\lambda_0}{\sqrt{\varepsilon_{eff}}} \tag{1}$$

where ε_{eff} is the effective dielectric constant.

Then the lowest resonant frequency, f_{0L}, relative to the slot side length is formulated by

$$f_{0L} = \frac{2C_o}{3a\sqrt{\varepsilon_{eff}}} \tag{2}$$

where C_o is the speed of light in free space, and a is the slot side length. Higher order resonances are attributed to the smaller self-similar structures, as will be seen later.

The Sierpinski fractal slot antenna with the layout depicted in Figure 3, has been modeled and analyzed using the method of moments (MoM) based electromagnetic (EM) simulator IE3D [14].

4. PARAMETRIC STUDY AND PERFORMANCE EVALUATION

According to (2), the modeled antenna slot side length, a, that matches the specified frequency, has been found to be of about 47.23 mm, with a microstrip feed line length of about 9.2 mm, measured from the origin. The antenna exhibits a dual band response, centered on 2.4 and 5.2 GHz. The lower resonant band, which is mainly attributed by the slot side length, has good match. However, it has been found that the position of the upper resonant band is sensitive to the feed line length. This band is with relatively low match as compared with the lower one. Figure 4 shows the return loss responses corresponding to different values of feed line length increments, of 0.5, 1.0, 1.25, and

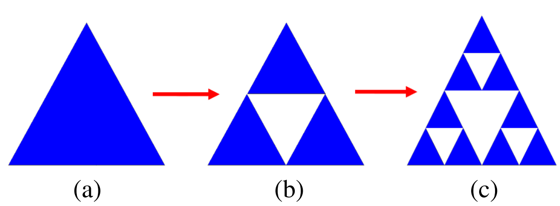

Figure 1: The generation of the Sierpinski gasket. (a) The zero iteration, $n = 0$, (b) the 1st iteration, $n = 1$, and (c) the 2nd iteration, $n = 2$.

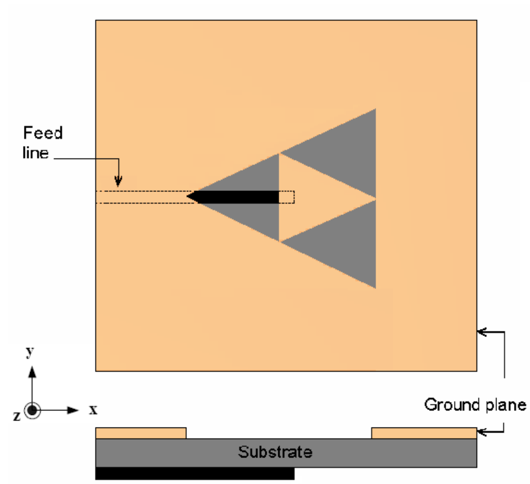

Figure 2: The geometry of the proposed 1st iteration Sierpinski gasket printed slot antenna.

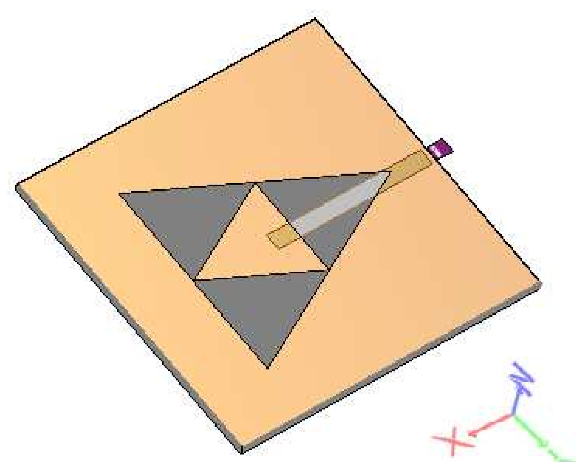

Figure 3: The layout of the modeled antenna with respect to the coordinate system.

2.0 mm, along the x-axis. It is clear that, how the feed length affects the position and the matching of the upper band, while it has a very slight effect on the lower band.

In order to enhance the matching and tuning the position of the upper band, a small vertical stub has been attached to the feed line. The position of this stub has a considerable effect on the matching of the upper resonant band, while, again, it has almost a slight effect on the lower band. Figure 5 demonstrates the return loss responses corresponding to different values of the vertical stub positions, in steps of 0.2 mm, along the x-axis and keeping the feed line length unchanged.

The optimal microstrip feed line length and stub position achieving a good impedance match of the 2.4 and 5.2 GHz WLAN bands have been found to be of 11.43 mm and 0.52 mm respectively, away from the origin. The resulting resonant frequencies are $f_{0L} = 2.408$ GHz, and $f_{0U} = 5.247$ GHz, with corresponding bandwidths (for $S_{11} \leq -10$ dB) of about 8.47%, and 8.80% respectively. Figure 6 shows the simulated 3D electric field patterns, E_θ at 2.4 and 5.2 GHz. With regard to the resulting gain, it is 2.11 dB and 3.72 dB in the lower and upper bands respectively.

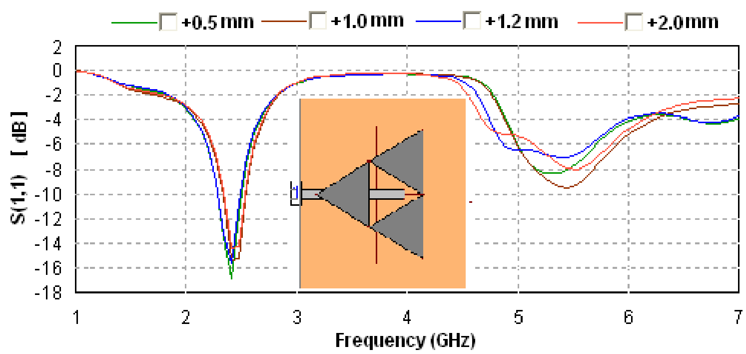

Figure 4: Return loss responses of the modeled antenna with the feed line length increment as the parameter.

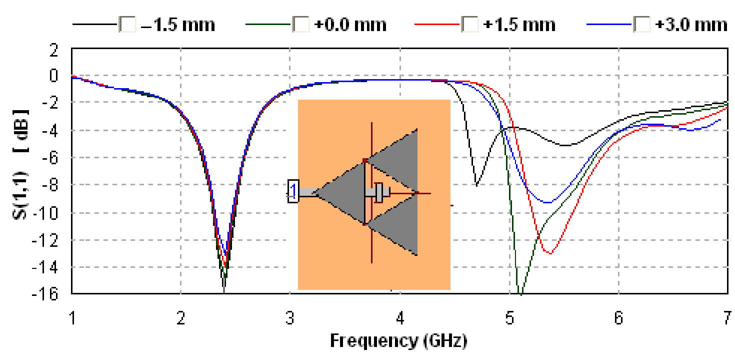

Figure 5: Return loss responses of the modeled antenna with the stub position on the feed line as the parameter.

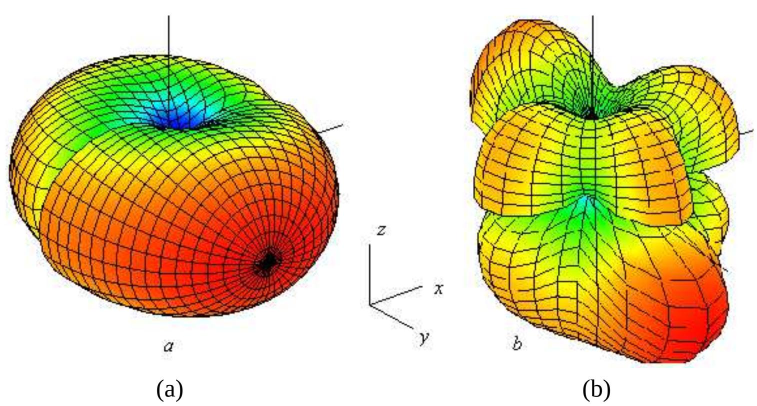

Figure 6: Simulated 3D electric field, E_θ patterns at (a) $f_{0L} = 2.4$ GHz, and (b) $f_{0U} = 5.2$ GHz.

5. CONCLUSIONS

A microstrip line fed printed slot antenna, with slot structure based on the first iteration Sierpinski gasket, has been presented in this paper. The antenna has been analyzed using a method of moments based EM simulator, IE3D. Simulation results showed that the antenna possesses a dual band resonant behavior meeting the requirements of the 2.4/5.2 GHz WLAN. A parametric study has been conducted to explore the effects of the most effective antenna parameters on its overall performance. The lower resonance has been found to be dominantly attributed by the side length of the slot structure, while the length of the feed affects, to certain extents, the position and the matching of the upper resonant frequency. It has been found that adding a vertical stub, at a proper position on the feed, will facilitate better matching and precise allocation of the second resonant frequency. Making use of this feature, the proposed antenna offers, it might be useful for many dual band communication applications.

REFERENCES

1. Mandelbrot, B. B., *The Fractal Geometry of Nature*, W. H. Freeman, San Francisco, CA, 1982.
2. Gianvittorio, J. P., *Fractals, MEMS, and FSS Electromagnetic Devices: Miniaturization and Multiple Resonances*, Ph.D. Thesis, University of California, Los Angeles, USA, 2003.
3. Gouyet, J., *Physics and Fractal Structures*, Springer, New York, 1996.
4. Krishna, D. D., A. R Chandran, and C. K. Anandan, "A compact dual frequency antenna with sierpinski gasket based slots," *Proceedings of the 10th European Conf. on Wireless Technology*, EuMA, Munich, Germany, Oct. 2007.
5. Krishna, D. D., M. Gopikrishna, and C. K. Anandan, "CPW-fed Koch fractal slot antenna for WLAN/WiMAX applications," *IEEE Ant. and Wireless Propag. Lett.*, Vol. 7, 389–392, 2008.
6. Chang, D.-C., B.-H. Zeng, and J.-C. Liu, "CPW-fed circular fractal slot antenna design for dual-band applications," *IEEE Trans. Ant. and Propag.*, Vol. 56, No. 12, 3630–3636, Dec. 2008.
7. Choukiker, Y. K., S. Rai, and S. K. Behera, "Modified half-circle fractal antenna using DC theorem for 2.4/5.2 GHz WLAN application," *Proceedings of National Conference on Communication*, IISc, Banglore, Jan. 2011.
8. Aziz, R. S., M. A. Alkanhal, and A. F. A. Sheta, "Dual band fractal monopoles," *Proceedings of Saudi Int. Electronics, Comm. and Photonics Conf., SIECPC*, Riyadh, Saudi Arabia, Apr. 2011.
9. Arora, P. and B. S. Dhaliwal, "Parameter estimation of dual band elliptical fractal patch antenna using ANN," *Proceedings of Int. Conf. on Devices and Comm., ICDeCom*, Mesra, Feb. 2011.
10. Hong, T., S.-X. Gong, Y. Liu, and W. Jiang "Monopole antenna with quasi-fractal slotted ground plane for dual-band applications," *IEEE Ant. and Wireless Propag. Lett.*, Vol. 9, 595–598, 2010.
11. Falconer, K., *Fractal Geometry: Mathematical Foundations and Applications*, 2nd Edition, Wiley, 2003.
12. Sayem, A. T. M. and M. Ali, "Characteristics of a microstrip-fed miniature printed hilbert slot antenna," *Progress In Electromagnetics Research*, Vol. 56, 1–18, 2006.
13. Ali, J. K., "A new microstrip-fed printed slot antenna based on moore space-filling geometry," *Proceedings of Loughborough Ant. and Propoag. Conf., LAPC*, Loughborough, UK, Nov. 2009.
14. *IE3D User's Manual*, Release 12.3, Zeland Software, Inc., Fremont, CA, 2007.

Performance Evaluation of Three Rectangular Patch Element Array Antenna Conformed on Small Radius Cylindrical Surface

Emad S. Ahmed and Jawad K. Ali
Department of Electrical and Electronic Engineering, University of Technology, Baghdad, Iraq

Abstract— The cylindrical geometry can offer certain desirable antenna characteristics that are not provided by planar elements. In this paper, a three-element cylindrical conformal array antenna has been presented as a candidate for use in wireless communications and Radio Frequency Identification (RFID). Each element in the array is a microstrip fed rectangular patch antenna designed to resonate at 2.4 GHz. Once the desired results were obtained for a single element, each element in the conformal cylindrical array has been then designed using the same dimensions and parameters. Modeling and performance evaluation of the array has been carried out using the commercially available electromagnetic software CST Studio Suite^{TM} 2009. Simulations have been conducted to study the performance of the proposed conformal array as well as the effects of small radius cylinder on mutual coupling and the radiation pattern of the array. The cylindrical radii in consideration are of about one quarter wavelengths or slightly more. The radius of cylinder used in simulation is taken to be 0.24λ and 0.32λ. Compared with the existing cylindrical conformal antenna, the proposed array antenna possesses a reduction in cylindrical structure radius with acceptable ominidirectionality and gain needed for wireless communications and RFID applications.

1. INTRODUCTION

Miniaturization in the integrated circuit technology and advancement in signal and data processing have opened prospects for wide spectrum of applications which uses densely packed terminals placed in little volume. That is why such applications depend on availability of conformal shaped antennas, ensuring required directions of radio wave propagation and enabling hidden terminal mounting. The range of applications spans from sensors goes through wireless access modes and then up to modern miniaturized spacecraft [1].

One of the most important innovations in modern antenna technology is the conformal antenna array. Conformal arrays have good potential for application in aerospace vehicles with excellent aerodynamic characteristics. Cylindrical antenna arrays have attracted the greatest attention amongst conformal antennas and their applications include mobile cellular base stations, airborne radar and mobile satellite communication terminals [2, 3].

Microstrip antennas are often used because of their thin profile, light weight and low cost. Furthermore, they can be made conformal to the structure. When the radius of the curved structure is large, the antenna can be analyzed as the planar one. However, for structure with smaller radii, more rigorous analysis methods should be used. If the antenna has a cylindrical shape, i.e., if one principal curvature is zero, the antenna can be analyzed as a circular-cylindrical one. In the case were both principal curvatures are different from zero, the antenna can be analyzed as a spherical one [4].

The use of cylindrical substrate for microwave design is generally driven by the physical attributes of the system rather than by choice, since the analysis and fabrication are more complicated than for a comparable planar implementation. However, the cylindrical geometry can offer certain desirable antenna characteristics that are not provided by planar elements. There are also variety of configurations that can be realized, for example cylindrical conformal patch and slot antennas [5–7], microstrip [8], and coplanar transmission lines [9]. Cylindrical conformal structures, with radii greater than one half wavelengths, have been proposed for use as prospective candidates for mobile communications systems, cellular base stations, and Telemetry, Teleranging and Telecommand (TTC) communication that is essential to maintain space missions due to their full field of view advantage [1, 10, 11].

In this paper, a microstrip fed rectangular patch antenna resonates at 2.4 GHz is considered. The proposed planar patch antenna is used in array consisting of three equally spaced elements. The proposed antenna array is conformed on a finite cylindrical substrate of 1.57 mm thickness and relative permittivity of 2.2. Two different radii for the cylindrical structure are simulated using CST Microwave Studio simulator. Results obtained on return loss, coupling between elements and radiation pattern are presented and discussed.

2. ANTENNA DESIGN AND CONFIGURAIONS

2.1. Single Element Antenna Structure

The configuration of the rectangular patch antenna is shown in Figure 1(a). The patch has been modeled in CST Studio and its dimensions have been adjusted to resonance at 2.4 GHz. A quarter-wave transformer was used to match 343 Ω input impedance to a 50 Ω system. The final dimensions of the entire microstrip patch are given in Table 1. Figure 1(b) shows the return loss response of the patch element antenna. It can be clearly indicated that the antenna was resonates at 2.4 GHz with return loss of less than −10 dB within 40 MHz bandwidth.

2.2. The Proposed Conformal Antenna Array Structure

Three patch elements were equally spaced on cylindrical substrate. The substrate material used for modeling has a thickness of 1.57 mm. The dielectric constant of the substrate is $\varepsilon_r = 2.2$. The conductive material in the model is of 70.0 µm thick copper. The radius of the cylinder is comparable to one quarter wavelength and the height is $H = 90$ mm. Inside the cylinder there is a

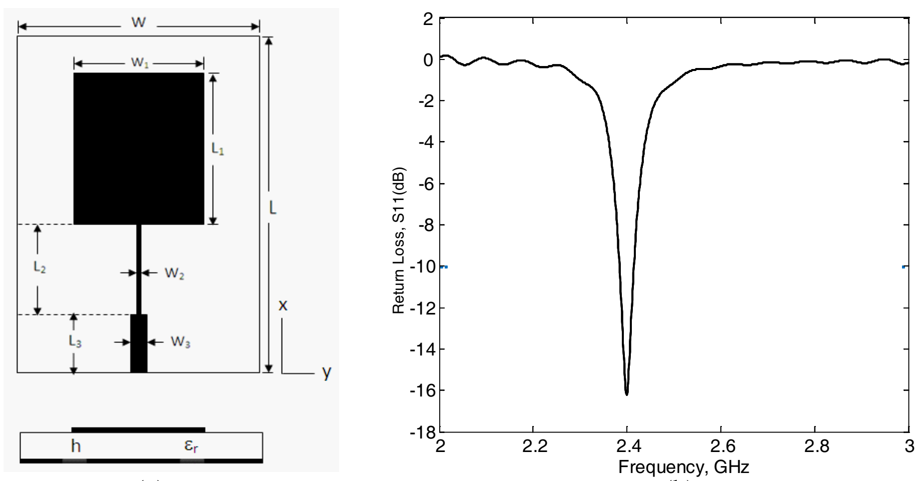

(a) (b)

Figure 1: (a) The layout of single element patch antenna structure, and (b) is its return loss S_{11} (dB) response for single element patch antenna.

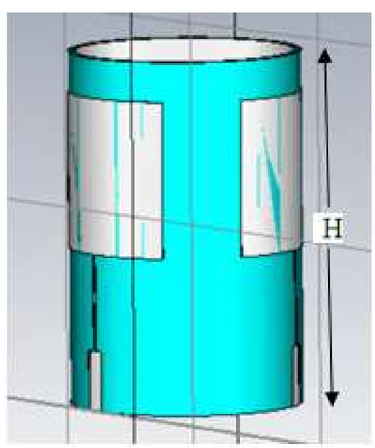

Figure 2: A 3-D view of the modeled 3-element array.

Table 1: Antenna dimensions in mm.

W	L	W_1	L_1
60	88	41.08	39.03
W_2	L_2	W_3	L_3
0.72	24.05	4.84	15

continuous ground plane of 70.0 μm thick copper. The model of the antenna array taken from the simulation software is shown in Figure 2.

3. PERFORMANCE EVALUATION

The cylindrical structure of Figure 2 has been modeled through a commercially available finite element package CST Studio Suite. Cylinders with radii 30 and 40 mm (0.24 and 0.32λ) have been analyzed while keeping the rest of the antenna parameters fixed. The simulation results of return loss of all of the ports of the array and the coupling among the antenna elements are shown in Figure 3.

From Figure 3, it's clearly observed that the coupling between elements for 30 mm (0.24λ) radius cylinder is about -1 dB, while for cylinder of 40 mm (0.32λ) radius, the coupling is less than -18 dB. The small radius of the cylinder results in decreasing the spacing between the elements so the mutual coupling between elements is increased.

Simulated radiation patterns at 2.4 GHz for single element and 3-element array are illustrated in Figure 4.

The radiation patterns are significantly affected. In the elevation direction, the radiation pattern

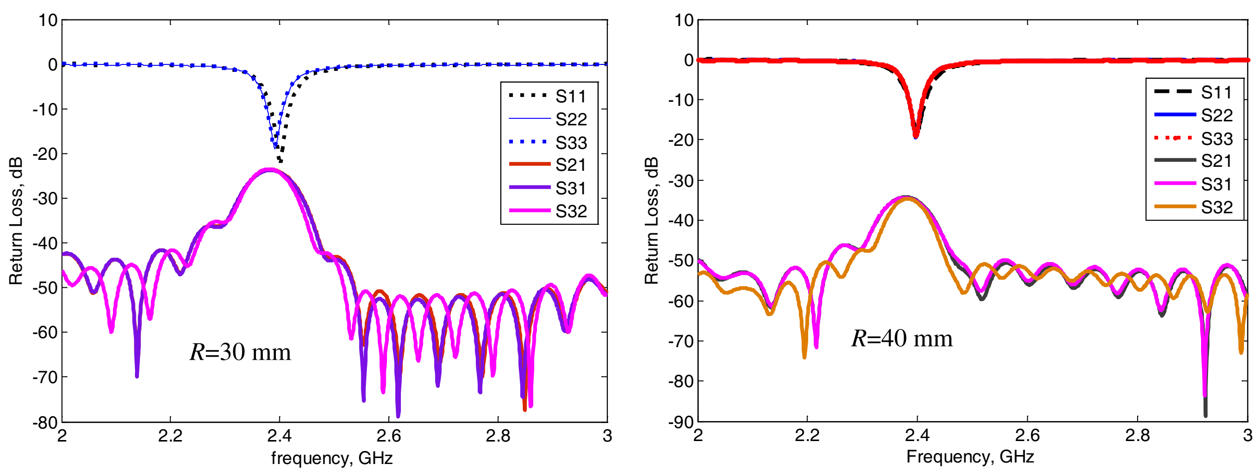

Figure 3: Simulated coupling of the 3-element array conformed on cylinders with radii of 30 mm (0.24λ) and 40 mm (0.32λ).

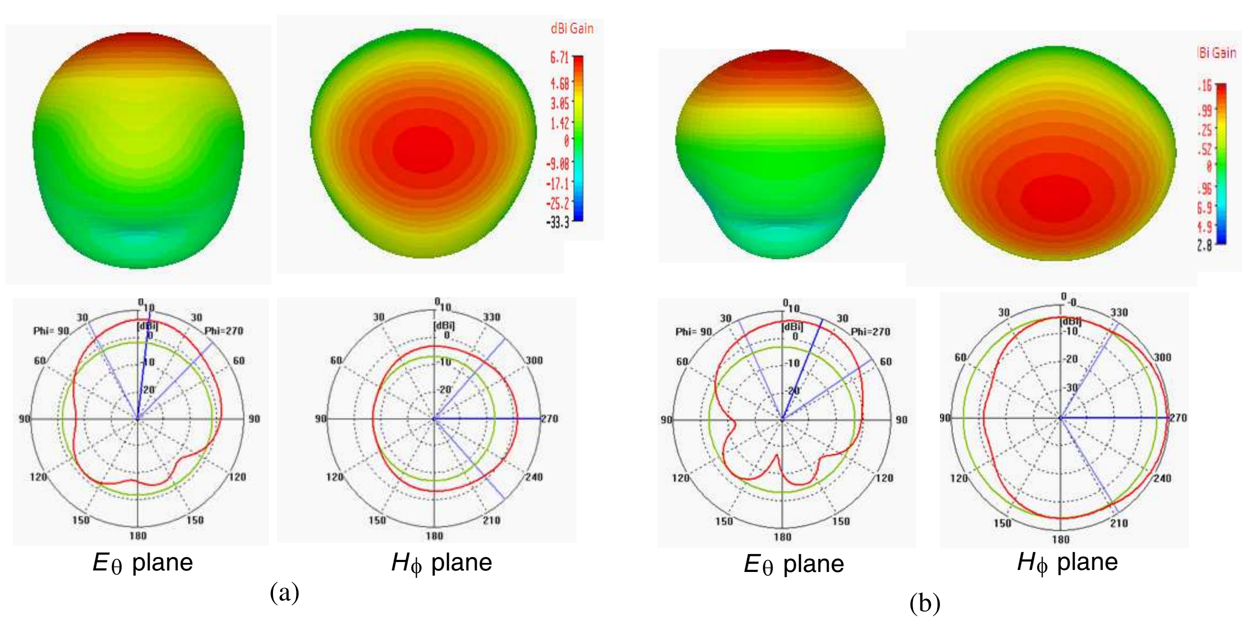

Figure 4: Radiation patterns: (a) for element in cylindrical array, the radius of cylinder is $R = 30$ mm (0.24λ) and (b) radius of cylinder is $R = 40$ mm (0.32λ).

is strongly dependant on the cylinder radius but much less so in the azimuth direction. The E plane (E_θ) and H plane (H_ϕ) fields, depicted in the figure, reveal that they still have an acceptable quasi ominidirectional radiation pattern.

4. CONCLUSION

This paper presents detailed performance evaluation concepts of a three rectangular patch element conformal antenna arrays. There are few issues that should be taken into consideration when designing such antennas. Firstly the curvature of the cylindrical array affects the radiation pattern of the antenna and the optimal radius should be found depending on the application on hand. Secondly the spacing between elements is very important to consider as it affects the level of mutual coupling in the array. An acceptable mutual coupling was obtained for cylinder radius greater than one quarter wavelength. The result shows that the resonant frequency is not affected by curvature however the radiation patterns are significantly affected. The radiation pattern in the elevation direction is strongly dependant on the cylinder radius but much less so in the azimuth direction. Simulation results shows that the proposed array antenna possesses an acceptable ominidirectional radiation pattern needed for most wireless communications and RFID applications.

REFERENCES

1. Pawel, K., O. Przemyslaw, and H. Pawel, "TTC patch antennas made in a conformal form with small radius," *Proceeding of 'Eu CAP 2006'*, Nice, France, Nov. 6–10, 2006.
2. Wang, Q. and Q.-Q. He, "An arbitrary conformal array pattern synthesis method that includes mutual coupling and platform effects," *Progress In Electromagnetics Research*, Vol. 110, 297–311, 2010.
3. Josefsson, L. and P. Persson, *Conformal Array Antenna Theory and Design*, Wiley-Inter Science, 2006.
4. Niksa, B. and S. Zvonimir, "Radiation properties of spherical and cylindrical rectangular microstrip patch antennas," *Automatika Journal*, Vol. 43, No. 1–2, 69–74, 2002.
5. Jain-Ming, J., J. A. Berrie, R. Kipp, and S. Lee, "Calculation of radiation patterns of microstrip antennas on cylindrical bodies of arbitrary cross section," *IEEE Transaction, Antennas and Wave Propagation*, Vol. 45, No. 1, 126–132,
6. Ho, C. H., P. K. Shmaker, K. Smith, and J. W. Liao, "Printed cylindrical slot antenna for commercial applications," *Electronic Letters*, Vol. 32, No. 3, 151–153, 1996.
7. Pirai, M. and H. R. Hassani, "L-probe fed circular polarized wideband planar patch antenna on cylindrical structure," *Progress In Electromagnetics Research C*, Vol. 3, 161–167, 2008.
8. Huang, J., R. Vahldieck, and H. Jin, "Microstrip discontinuities on cylindrical surfaces," *IEEE MTT-S Symposium*, Vol. 3, 1299–1302, Jun. 1993.
9. Su, H. and K. Wong, "Dispersion characteristics of cylindrical coplanar waveguides," *IEEE Trans. Microwave Theory and Techniques*, Vol. 44, No. 11, 2120–2122, 1996.
10. Ning, Y., S. Y. Tat, N. Xiao-Chun, and L. Le-Wei, "Analysis of probe-fed conformal microstrip antennas on finite grounded substrate," *IEE Trans. Ant. and Propag.*, Vol. 54, No. 2, 554–562, 2006.
11. Geng, J. P., J. J. Li, R. H. Jin, S. Ye, X. L. Liang, and M. Z. Li, "The development of curved microstrip antenna with defected ground structure," *Progress In Electromagnetics Research*, Vol. 98, 53–73, 2009.

A New Fractal Based PIFA Antenna Design for MIMO Dual Band WLAN Applications

Ali J. Salim[1], **Raad S. Fyath**[2], **Adil H. Ahmad**[1], **and Jawad K. Ali**[1]

[1]Department of Electrical and Electronic Engineering, University of Technology, Baghdad, Iraq
[2]Department of Electronic and Communication Engineering, University of Nahrain, Baghdad, Iraq

Abstract— This paper introduces the design of a dual-band internal F-PIFA (Fractal Planar Inverted F-antenna) as a candidate for use in the dual band WLAN (wireless local area network) MIMO (multi-input multi-output) applications. At first, the 4th iteration Koch's fractal geometry has been applied to the edges of the conventional rectangular patch structure to design a single compact antenna with a dual band resonant behavior. The radiating fractal based patch has been printed on a substrate with relative permittivity of 4.1 and thickness of 0.9 mm, and the antenna has been fed with $50\,\Omega$ probe. This antenna is located at the corner of a copper ground plane of 0.05 mm thickness and dimensions of $110 \times 70\,\text{mm}^2$. It has been found that the resulting F-PIFA has the dimensions of about 21 mm $\times$ 15 mm $\times$ 6.2 mm, making it suitable for mobile terminal applications. Furthermore, the proposed antenna offers a dual band resonance with a frequency ratio of about 2.41; resulting in bandwidths, for return loss ≤ -10 dB, covering the two WLAN band standards. Modeling and performance evaluation of the proposed antenna have been carried out using the CST Microwave Studio. The modeled antenna has been applied to a 4 by 4 MIMO system suggested for use in dual band WLAN applications. Simulation results show that the suggested system offers ≤ -10 dB impedance bandwidths of about 300 MHz with an isolation of about 12 dB, for the lower band, and 570 MHz with an isolation of higher than 22 dB, for the upper band. This makes the proposed system suitable for use in MIMO dual band WLAN applications.

1. INTRODUCTION

When a multiple-element antenna array embeds into the small mobile terminal, it should be small as much as possible. Some additional requirements should be met, e.g., good isolation (low mutual coupling) and diversity performance for multiple antennas besides the usual requirements of a conventional single antenna such as compact structure, light weight, low profile and robustness. The antennas are required to be small and yet their performances have to be maintained [1]. Therefore, in designing the antenna for the mobile terminal, it is important to balance the trade-off between size and performance [2]. In MIMO (multi-input multi-output) systems, multiple antenna elements are required at both transmitter and receiver. The multiple antennas at the both ends of the systems provide independent paths in the multipath fading environment [3]. As a result, the design of two or more antennas on a small mobile terminal for the MIMO systems is more challenging compared to the design of a single conventional antenna in the mobile terminal [4].

Inserting developments in the field of antenna miniaturization have been introduced in the form of fractal antennas. A fractal is a self-similarity structure, which means that a small part of the structure is a scaled-down copy of the original structure. The term fractal means broken or irregular fragments to describe complex shapes that possess an inherent self-similarity or self-affinity in their geometrical structures [5]. There are a few researches on the combination of fractal and PIFA (Planar Inverted-F Antenna) topology. A miniaturized PIFA has been proposed for dual-band mobile phone application by employing Hilbert geometry [6]. A Fractal PIFA antenna based on the Sierpinski carpet has been presented in [7] to obtain a multiband antenna. The proposed antenna achieved -6 dB return loss at the required GSM (Global System for Mobile Communications), UMTS (Universal Mobile Telecommunications Systems) and HiperLAN frequencies. A combination of microstrip patch antenna with a Koch pre-fractal edge and a U-shaped slot has been proposed for multi-standard use in GSM1800, UMTS, and HiperLAN2 [8]. Making use of a PIFA structure, the multi-band behavior has been obtained with broadened the lower resonant band covering GSM 1800 and UMTS. The HiperLAN2 band has been covered by insertion of a U-slot structure. An antenna arrangement of two Koch fractal patch PIFA elements has been studied.

2. ANTENNA STRUCTURE

In this paper, Koch fractal geometry is applied on the edges of the radiating plate. This concept has a considerable effect on the resonant length of the antenna structure. The design of this antenna is mainly based on the PIFA antenna. The performance of the modified PIFA depends on number of structure parameters, such as antenna height, H, radiating plate length, L and radiating plate width, W as illustrated in Figure 1. The dimensions of the ground plane (L_G and W_G) for this antenna are similar to those of most mobile terminal like personal digital assistant (PDA) or handset. The optimized dimensions of the proposed PIFA model are shown in Table 1. The radiating fractal based plate is printed on a substrate with relative permittivity of 4.2 and thickness of 0.9 mm, and the antenna is fed with a 50 Ω probe.

Applying fractal geometry on PIFA antenna configuration yields fractal (FPIFA) antenna. Fractal PIFA antenna can be miniaturized by adding indentations along all the edges of the radiating plate. These edges represent the resonant length of the plate used to miniaturize the size as shown in Figure 1(a). The fractal radiating plate, shown in Figure 2(b), is generated with four iterations. This is the result of adding the indentations along the resonant length of the radiating plate in the first iteration and repeating the process at similar scale. The FPIFA antenna on a ground plane is illustrated in Figure 3.

The simulation results indicate that the proposed antenna can achieve a bandwidth, for ($S_{11} < -10$ dB), of about 300 MHz (2.2174–2.521 GHz) at 2.4 GHz and 570 MHz (5.5317–6.1052 GHz) at 5.8 GHz as shown in Figure 4. The radiation patterns of the proposed antenna at the two resonance frequencies; 2.4 GHz and 5.8 GHz are illustrated in Figure 5. These patterns are presented for two elevation planes; XZ ($\varphi = 0°$) and YZ ($\varphi = 90°$), and for the azimuth XY plane ($\theta = 90°$). In the higher band one can note that the electric field approximately has an equal value at all points in XY plane more than those in the lower band. Maximum values of the field stretching

Table 1: Dimensions of the reference PIFA antenna.

Parameter	L	W	H	L_G	W_G
Value (mm)	21	15	6.2	110	70

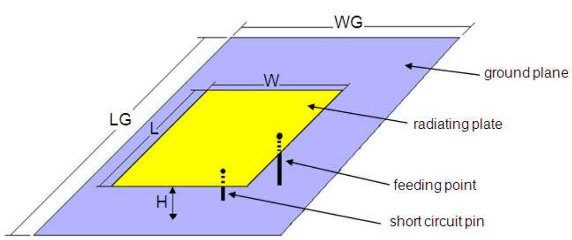

Figure 1: Schematic diagram of the PIFA antenna.

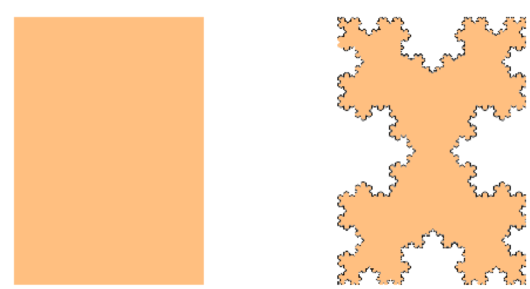

(a) (b)

Figure 2: (a) The rectangular radiating plate, and (b) the Koch fractal based radiating plate.

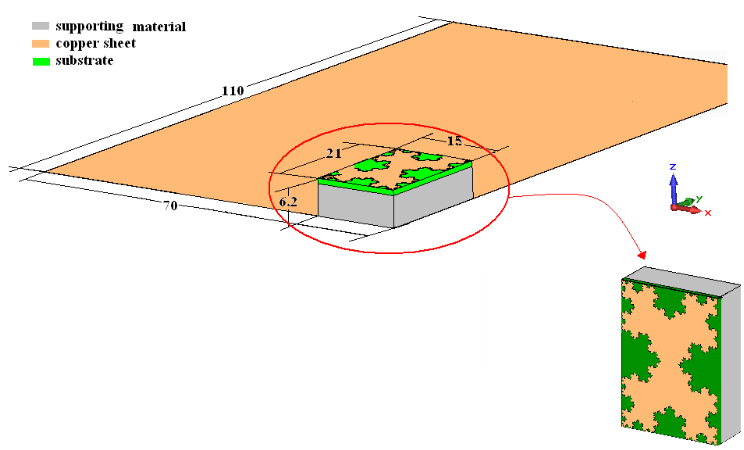

Figure 3: Schematic diagram of the FPIFA antenna; (all dimensions in mm).

from the direction 30° of the 60° in the upper half of the lower band in the YZ plane, while the highest values in the upper band are confined in the direction of 60° to 90°. Good omnidirectional radiation patterns at the two frequencies are obtained. The whole shapes of the radiation patterns are suitable for modern terminals. This antenna almost provides the same radiation pattern at the two resonant frequencies.

3. FOUR-ELEMENT DIVERSITY FPIFA DESIGN

In this section, a four-element diversity antenna based on the proposed FPIFA is designed on the same ground plane. The proposed design involves four elements of FPIFA antennas being located in each corner of the ground plane. The diversity antenna array has to be carefully designed to achieve low correlation as much as possible between the antennas. Since the proposed FPIFA antenna has the property of dual polarization, therefore mutual coupling between the antennas can be reduced by arranging the antennas. The optimized design of the diversity antenna array is shown in Figure 6.

The distance between antennas 1 and 2 (3 and 4) is approximately 40 mm which corresponds to

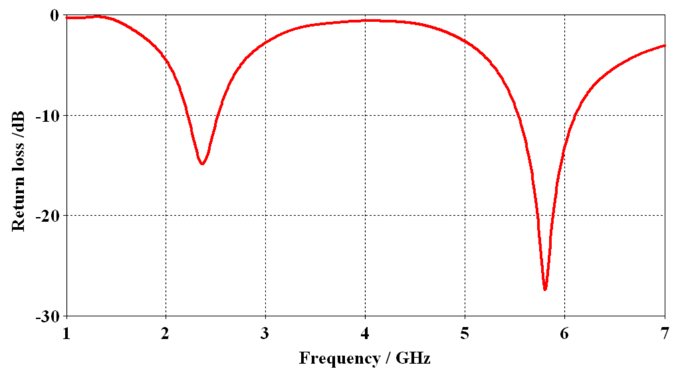

Figure 4: Simulated return loss of the FPIFA antenna.

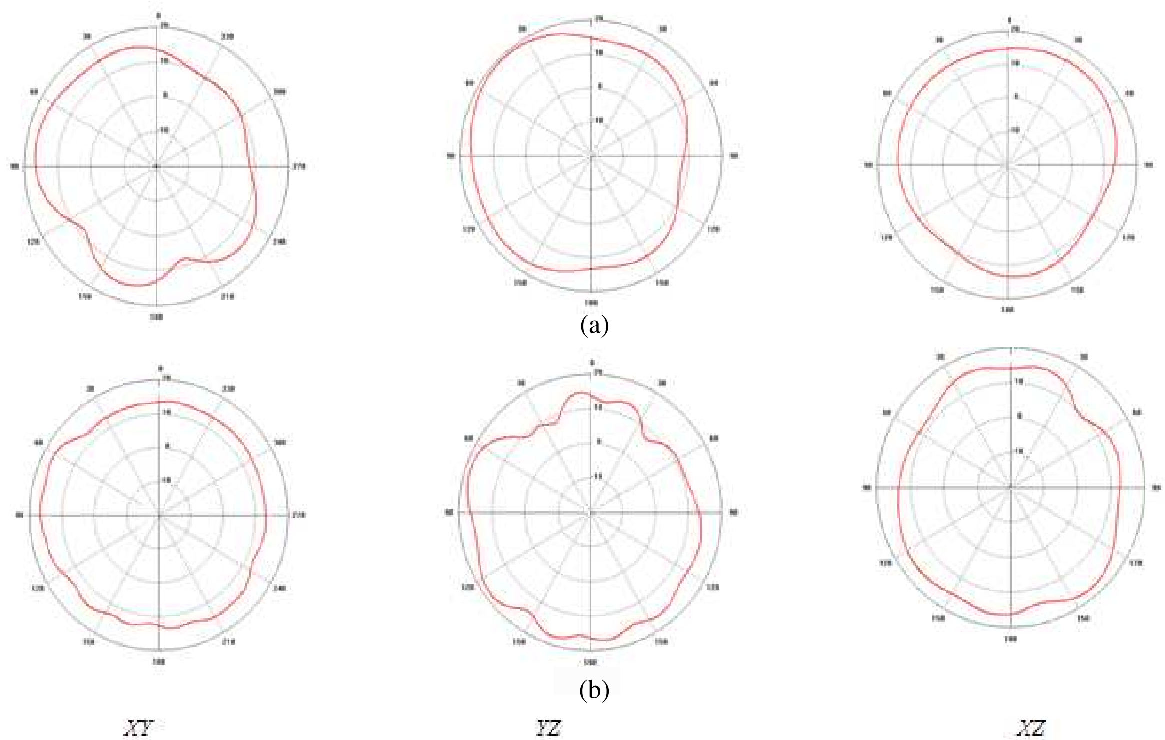

Figure 5: Simulated radiation patterns in the XY, YZ and XZ planes at (a) 2.4 GHz, and (b) 5.8 GHz for the single FPIFA.

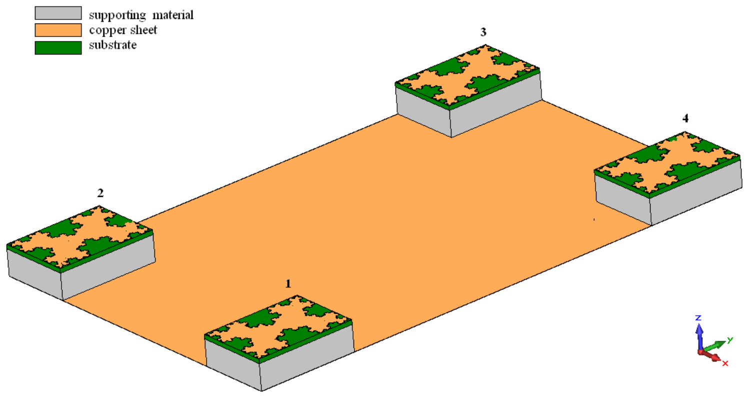

Figure 6: Schematic diagram of four-element diversity FPIFA antenna array placed on the same ground plane.

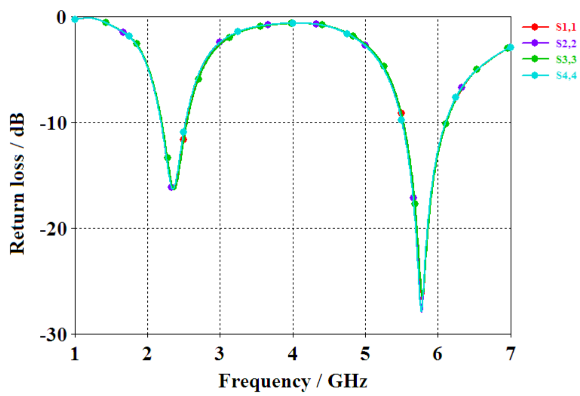

Figure 7: Return loss characteristics from the simulated results of the FPIFA antenns1, 2, 3, and 4.

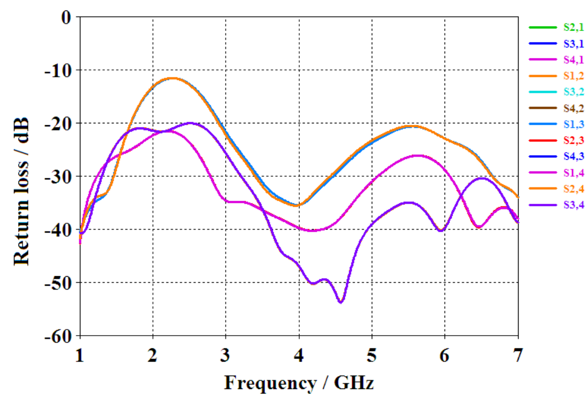

Figure 8: Isolation between each pair of antennas on the diversity FPIFA antenna array.

0.32 λ at 2.4 GHz, while the distance between antenna 1 and 4 (2 and 3) is 68 mm which corresponds to 0.54λ at 2.4 GHz. Although the spacing between antennas does not exceed half wavelength, the obtained results show good isolation between antennas. The simulated return loss performance of each antenna of the four-element diversity antenna array is plotted in Figure 7. The simulated S_{11}, S_{22}, S_{33} and S_{44} are exactly identical due to the optimization process used for choosing the positions of the feed and the shorting pin for each antenna. It is clear that the bandwidths of the antennas are the same.

Despite the fact that the antennas share the same ground plane; there is no any individual ground plane for each antenna, the simulation results show that the isolation between elements is low which means an acceptable value for good diversity performance. This is attributed to the spread surface current on the ground plane which leads to an increase in the mutual coupling between elements. Figure 8 shows the isolation between each pair of antennas obtained from the simulations. Isolation of more than 12 dB for each pair of antennas (1, 3) and (2, 4) is achieved in the lower band and more than 20 dB in the higher band. Isolation for other pairs is higher than 22 dB in the two bands. In other words, mutual coupling is relative very low between the antennas. Therefore, a low correlation between the antennas could be realized and would lead to well diversity performance.

4. CONCLUSIONS

A fractal based PIFA configuration has been investigated, in this work, to design MIMO antennas for 2.4 GHz and 5.8 GHz bands. Reduction of antenna size has been performed by means of applying Koch fractal geometry. This reduced the size of the radiating patch of antenna by a 33% as compared with conventional patch. Furthermore, the space diversity has been adopted and applied to the proposed antenna. According to simulation results the suggested system offers ≤ -10 dB impedance bandwidths of about 300 MHz with an isolation of about 12 dB, for the lower band, and

570 MHz with an isolation of higher than 22 dB, for the upper band.

REFERENCES

1. Costa, J. R., E. B. Lima, C. R. Medeiros, and C. A. Fernandes, "Evaluation of a new wideband slot array for MIMO performance enhancement in indoor WLANs," *IEEE Trans. Antennas Propag.*, Vol. 59, No. 4, 1200–1206, 2011.
2. Fujimoto, K., *Mobile Antenna Systems Handbook*, 3rd Edition, Artech House, Inc. 2008.
3. Zhang, S., P. Zetterberg, and S. He, "Printed MIMO antenna system of four closely-spaced elements with large bandwidth and high isolation," *Electron. Lett.*, Vol. 46, No. 15, 1052–1053, 2010.
4. Jensen, M. A. and J. W. Wallace, "A review of antennas and propagation for mimo wireless communications," *IEEE Trans. Antennas Propag.*, Vol. 52, No. 11, 2810–2824, 2004.
5. Habib, L., "Fractal monopole antenna," U.S. Patent, No. 7, 248, 223, B2, July 24, 2007.
6. Azad, M. Z. and M. Ali, "A miniaturized hilbert PIFA for dual-band mobile wireless applications," *IEEE Antennas Wireless Propag. Lett.*, Vol. 4, 59–62, 2005.
7. Saidatul, N. A., A. H. Azremi, R. B. Ahmad, P. J. Soh, and F. Malek, "Multiband fractal planar inverted F antenna for mobile phone application," *Progress In Electromagnetics Research B*, Vol. 14, 127–148, 2009.
8. Guterman, J., A. A. Moreira, and C. Peixeiro, "Microstrip fractal antennas for multistandard terminals," *IEEE Antennas Wireless Propag. Lett.*, Vol. 3, 351–254, 2004.

A New Compact Ultra Wideband Printed Monopole Antenna with Reduced Ground Plane and Band Notch Characterization

Jawad K. Ali, **Mahmood T. Yassen**, **Mohammed R. Hussan**, **and Mohammed F. Hasan**
Department of Electrical and Electronic Engineering, University of Technology, Baghdad, Iraq

Abstract— In this paper, a printed monopole antenna with reduced ground plane has been presented as a candidate for use in ultra-wideband applications. The monopole antenna structure is a nearly square shaped with m-slot embedded in it. A 50 Ω microstrip line is used to feed the proposed antenna. The proposed antenna has been supposed to be etched using a substrate with relative permittivity of 4.6 and thickness of 1.6 mm. Modeling and performance evaluation of the proposed antenna have been carried out using a method of moments based EM simulator, IE3D. Results show that the proposed antenna has a compact size of 20 mm × 25 mm. The resulting antenna has been found to possess an impedance bandwidth, for voltage standing-wave ratio less than 2, covering the required impedance bandwidth for UWB applications with 5/6 GHz band notch characteristics. Simulation results show that the lower frequency is primarily determined by the monopole radiating element perimeter, while the slot has an effective role to allocate the position of the band notch. A parametric study has been conducted to provide more understanding of the effects of antenna parameters on its performance. Besides the reasonable performance, the simple structure of the proposed antenna will make it an attractive choice for the antenna designers.

1. INTRODUCTION

Recently, ultra-wideband (UWB) systems have attracted much attention because of the need of exchanging huge quantity of information at high transfer rates in modern communication systems [1, 2]. Consequently, an increased interest has been reported to the UWB antenna design. For portable devices, an additional challenge is encountered; the antenna has to be miniaturized. The printed UWB antenna has been found to be a good option because it can be easily embedded into wireless devices or integrated with other RF circuits [3]. In 2002, the Federal Communication Commission (FCC) officially released the regulations for UWB technology with allocated spectrum from 3.1 to 10.6 GHz for unlicensed UWB indoor medical, measurement and communication applications. Since then, intensive research work has been devoted to the UWB antenna design.

Regarding the purpose of reducing the potential interference between the UWB system and others operating at 5/6 GHz, the antennas reported in the literature can be classified into three categories. The first one includes antenna that are not characterized with a band notch in their return loss, or VSWR, responses [2–5]. In this context, microstrip fed printed monopole antennas having radiators with E-shape [2], swan-like shape patch with reduced ground plane [3], circular shape monopole with trapezoid shape ground [4], and octagon shape [5], are presented for UWB applications. In the other hand, the CPW feed line has been also used for UWB antennas with various possible slotted patch structures [6, 7].

The UWB antennas of the second category are characterized with a single 5/6 GHz band notch in their return loss responses [8–12]. Again, almost similar techniques have been adopted to achieve the UWB impedance bandwidth. Slotted elements of various shapes have been added to create the required notch in the antenna response. In addition, the use of the electromagnetic-bandgap (EBG) structure is proven to be effective create the required band notched response [13]. Elliptical monopoles with CPW feeds were fabricated on liquid crystal polymer (LCP) with reconfigurable 5/6 GHz band-notch characteristics has been presented in [14].

In the third category, antennas are characterized with two band notches in their return loss, or VSWR, responses [15–20]. In most of these antennas, an additional notch has been added to prevent the interference of the UWB system with WiMax [15–18]. However, in [19], the proposed antenna has two narrow band notches within the 5/6 GHz band itself. Special band notch requirements might be needed, besides the 5/6 GHz notch as reported in [20]. In all of the reported antenna structures, the dual band notch has been attributed by two different elements resulting in antennas with complicated structures.

In this paper, a new microstrip fed compact printed monopole antenna with reduced ground plane has been proposed as a miniaturized antenna for UWB applications. It has simple struc-

Table 1: Summary of the Ref. Ant. dimensions, in mm.

L_G	W_G	S	L_E	W_E	L_{MS}	L_{TS}	W_{MS}	W_T
19.90	9.20	1.25	13.45	14.55	9.05	1.50	6.25	1.70

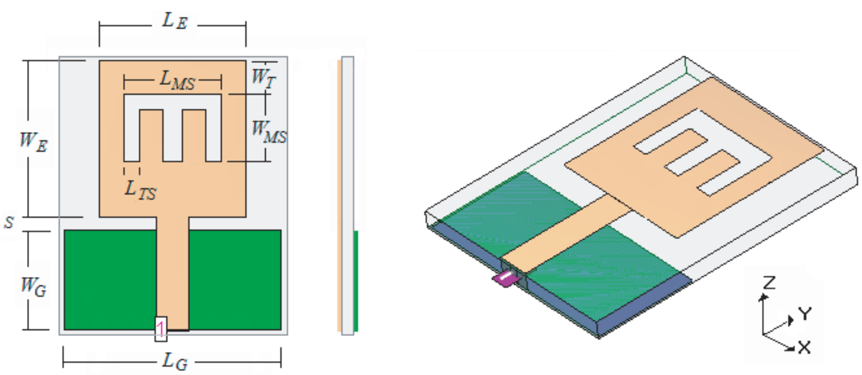

(a) (b)

Figure 1: (a) The proposed m-slot printed monopole antenna structure, and (b) its layout with respect to the coordinate system.

ture with 5/6 GHz band notch. The notch band position can be controlled via an m-shaped slot embedded in the radiating element of the printed monopole structure.

2. THE PROPOSED ANTENNA STRUCTURE

The geometry of the proposed UWB printed monopole antenna is shown in Figure 1(a). The antenna is to be modeled using an FR4 substrate with thickness of 1.6 mm and relative permittivity of 4.6. On the front surface of the substrate, a rectangular radiating patch with initial dimensions of $13.45 \times 14.55\,\text{mm}^2$, has been etched. For design convenience, the proposed antenna is fed by a 50 Ohm microstrip line printed on the radiator side of the substrate. The feed line width is of about 3 mm, and is symmetrically located with respect to both the radiating element and the ground plane. On the other side of the substrate, a conducting ground plane of $19.90 \times 9.20\,\text{mm}^2$ is placed. An m-slot is etched on the rectangular radiating element with slot width, $W_{MS} = 6.25$ mm, slot length, $L_{MS} = 9.05$ mm, and slot trace width, $L_{TS} = 1.5$ mm. The slot is symmetrically cut in the X-axis, while it is away from the upper edge of the radiating element by a distance, $W_T = 1.70$ mm.

Figure 1(b) shows the antenna layout with respect to coordinate system. This initial design has been found to almost meet the ultrawideband bandwidth requirements with the 5/6 GHz band notch. This antenna, with the depicted parameters, has been referred to as a (Ref. Ant.), in the parametric study to be later conducted. The proposed printed monopole antenna structure, shown in Figure 1, has been modeled using the commercially available method of moments based EM simulator, IE3D [21]. Table 1 summarizes the detailed dimensions of the Ref. Ant. parameters as labeled in Figure 1(a).

3. THE ANTENNA DESIGN

A printed monopole antenna with m-slot has been designed to resonate with the lower frequency is located at 3.1 GHz, as a starting step. After suitable dimension scaling, the resulting antenna radiating element length, L_E, has to be determined. Observing the influence of the various parameters on the antenna performance, it has been found that the dominant factor in the antenna is the monopole element perimeter, $2(L_E + W_\text{E})$, in terms of the guided wavelength λ_g.

$$\lambda_g = \frac{\lambda_0}{\sqrt{\varepsilon_{eff}}} \tag{1}$$

where ε_{eff} is the effective dielectric constant.

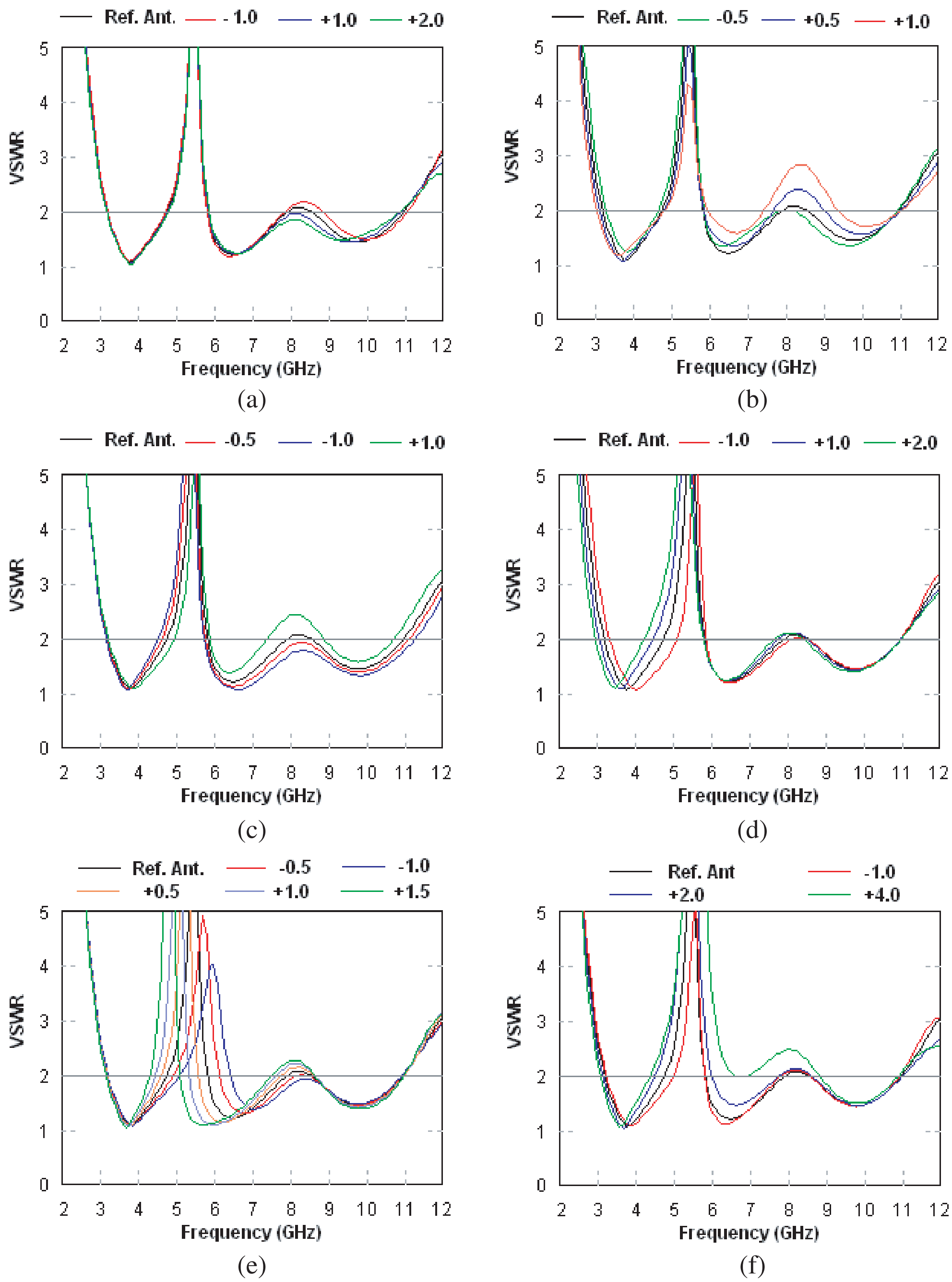

Figure 2: Simulated VSWR responses of the modeled antenna corresponding to the variations of: (a) L_G, (b) S, (c) L_E, (d) W_E, (e) W_{MS}, and (f) W_T.

Then the lower resonant frequency, f_L, relative to the radiating element length is formulated by

$$f_L \approx \frac{C_o}{2(L_E + W_E)\sqrt{\varepsilon_{\mathit{eff}}}} \tag{2}$$

where C_o is the speed of light in free space. Other antenna parameters, such as S, W_{MS}, and W_T, have only little effect on f_L, as will seen later.

4. ANTENNA PERFORMANCE EVALUATION

According to (2), the Ref. Ant., with the parameters depicted in Table 1, has been modeled. The antenna exhibits an UWB response with an impedance bandwidth, for VSWR ≤ 2, extending from 3.1 to 11.01 GHz and a band notch, centered on 5.438 GHz, and extending, for VSWR ≥ 2, from 4.755 to 5.825 GHz. An interesting parametric study has been conducted to demonstrate the effects of the variations of various antenna parameters on its performance in terms of the VSWR responses. Figure 2 summarizes the results of this study. Brief comments will be presented herein. In Figure 2(a), the effect of the variation of the ground plane length, L_G, has been presented. The ground plane length has been reduced to 20 mm due to the existence of the slot structure in the monopole radiating element. This supports the findings reported in [3]. The variation of L_G does not affect both f_L and the position of the notched band. Without the slot structure, it has been found that, not shown here to save space, the required ground plane length to achieve appropriate matching is of about 23 mm. The space width, S, between the radiating element and the ground plane top edge has a considerable effect on antenna response, as shown in Figure 1(b). Good matching has been achieved with $S = 0.75$ mm.

The effects of variations of the radiating element dimensions, W_E and L_E, are shown Figures 2(c) and 2(d) respectively. The variation of L_E has a slight effect on f_L, but it has a noticeable effect on width of the notched band; larger W_E results in narrower notched bands. However, the centers of the corresponding notch bands are little affected. Better matching can be achieved with smaller values of L_E. On other hand, the variation of W_E has a considerable effect on f_L as Equation (2) implies. The same effect, as in the case of varying L_E, has been noticed regarding the width of the notched band.

Variation of the m-slot structure width, W_{MS}, results in an interesting feature that the proposed antenna possesses, to control the position of the notched band, as shown in Figure 2(e). The position of f_L in the resulting responses has not been affected, but smaller values of W_{MS} leads to better matching.

Another interesting result is shown in Figure 1(f), where the variation of the slot position, W_T with respect to the top edge of the radiating element is investigated. The variation of W_T has a little effect on f_L, but it has a noticeable effect on width of notched band with its position remains unchanged. However, smaller values of W_T, leads to better matching. The variation of L_{TS} (not shown in Figure 2) has very slight effect on f_L; but it affects the width of the notched band.

In summary, it has been shown that the proposed antenna offers many degrees of freedom to the antenna designer to select from, to produce an antenna meeting the requirements of the UWB systems with the 5/6 GHz band rejection. Figure 3 shows the simulated current distributions on the surface of the proposed antenna at 3.5, 5.5, 8.0, and 10.0 GHz. At 3.5, 8.0, and 10.0 GHz, the current mainly flows along the microstrip feed line, while low current densities around the m-slot.

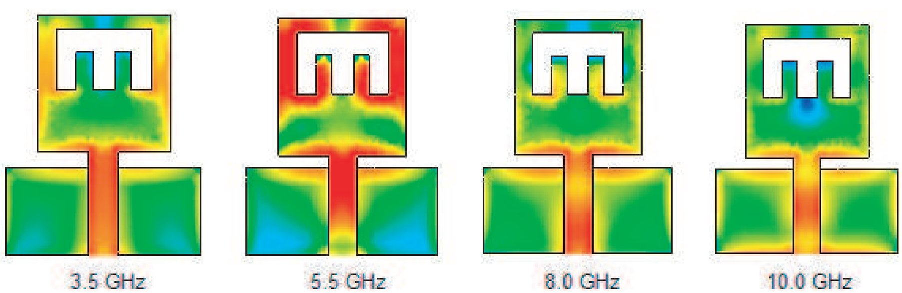

Figure 3: Simulated current distributions on the surface of the proposed antenna at different frequencies.

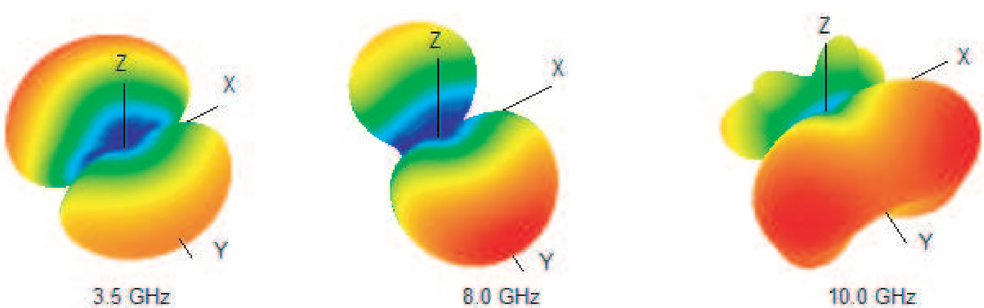

Figure 4: Simulated 3D total electric field patterns of the proposed antenna at 3.5, 8.0, 10.0 GHz.

On the contrary, the current distribution on the antenna surface at 5.5 GHz is heavily concentrated around the slot. As a matter of fact, the excitation of the 5/6 GHz notched band is attributed to the surface current density produced by the slot at this band. The 3D radiation patterns corresponding to 3.5, 8.0, and 10.0 GHz are shown in Figure 4. An average gain of about 2 dB has been offered by the proposed antenna at these frequencies.

5. CONCLUSIONS

A compact microstrip line fed printed monopole antenna, with an m-slot structure and 5/6 GHz band notch characterization, has been presented in this paper as a candidate for use in UWB applications. The antenna has been analyzed using a method of moments based EM simulator, IE3D. Simulation results showed that the antenna possesses resonant behavior meeting the requirements of the UWB systems with notched band at 5/6 GHz. A detailed parametric study has been conducted to explore the effects of the most effective antenna parameters on its overall performance. The lower resonant edge of the UWB response has been found to be dominantly attributed by the length of the monopole radiating element. The position of notch band can be controlled by the slot structure dimensions, while its width is highly sensitive to the position of slot structure relative to the monopole radiating element. It is hopeful that the simple structure of the proposed antenna, its compact size, and the degrees of freedom of its design, will make it an attractive choice for the UWB antenna designers.

REFERENCES

1. Habib, M. A., A. Bostani, A. Djaiz, M. Nedil, M. C. E. Yagoub, and T. A. Denidni, "Ultra wideband CPW-FED aperture antenna with WLAN band rejection," *Progress In Electromagnetics Research*, Vol. 106, 17–31, 2010.
2. Ali, J. K. and A. S. Hussain, "A new miniaturized E-shaped printed monopole antenna for UWB applications," *PIERS Proceedings*, 1273–1276, Suzhou, China, September 12–16, 2011.
3. Chen, Z. N., T. S. P. See, and M. X. Qing, "Small printed ultrawideband antenna with reduced ground plane effect," *IEEE Trans. Ant. and Propag.*, Vol. 55, No. 2, 383–388, 2007.
4. Zhang, Y., Y. Sakurai, and T. Miyashita, "Small planar UWB antenna with a trapezoid shape ground," *Proceedings of China-Japan Microwave Joint Conf., CJMW*, Hangzhou, China, April 2011.
5. Ren, W., "Compact microstrip-fed monopole antenna for UWB applications," *Advances in Information Sciences and Service Sciences, AISS*, Vol. 3, No. 8, 146–153, 2011.
6. William, J. and R. Nakkeeran, "CPW-fed UWB slot antenna with triangular tuning stub," *International Journal of Computer and Electrical Engineering*, Vol. 2, No. 4, 1793–8163, 2010.
7. Morales-Silva, C. and J. Wang, "CPW-fed arrow-shaped slot antenna design for ultra wideband (UWB) applications," *Proceedings of 10th Annual Wireless and Microwave Technology Conf., WAMICON*, Clearwater, USA, April 2009.
8. Zamel, H. M., A. M. Attiya, and E. A. Hashish, "Design of a compact UWB planar antenna with band-notch characterization," *Proceedings of National Radio Science Conf., NRSC 2007*, Cairo, Egypt, March 2007.
9. Amini, F., M. N. Azarmanesh, and M. Ojaroudi, "Small Semi-circle-like slot antenna for ultra-wideband applications," *Progress In Electromagnetics Research C*, Vol. 13, 149-158, 2010.
10. Lizzi, L., G. Oliveri, P. Rocca, and A. Massa, "Planar monopole UWB antenna with UNII1/UNII2 WLAN-band notched characteristics," *Progress In Electromagnetics Research B*, Vol. 25, 277–292, 2010.
11. Naghshvarian-Jahromi, M., "Compact UWB bandnotch antenna with transmission-line-fed," *Progress In Electromagnetics Research B*, Vol. 3, 283–293, 2008.
12. Bao, X. L. and M. J. Ammann, "Printed UWB antennas with coupled slotted element for notch-frequency function," *International Journal of Antennas and Propagation*, Vol. 2008, 1–7, 2008.
13. Peng, L. and C.-L. Ruan, "UWB band-notched monopole antenna design using electromagnetic-bandgap structures," *IEEE Trans. Microwave Theo. and Tech.*, Vol. 59, No. 4, 1074–1081, 2011.
14. Nikolaou, S., N. D. Kingsley, G. E. Ponchak, J. Papapolymerou, and M. M. Tentzeris, "UWB elliptical monopoles with a reconfigurable band notch using MEMS switches actuated without bias lines," *IEEE Trans. Ant. and Propag.*, Vol. 57, No. 8, 2242–2251, 2009.

15. Zhou, Z. L., L. Li, and J. S. Hong, "Compact UWB printed monopole antenna with dual narrow band notches for WiMAX/WLAN bands," *Electronic Lett.*, Vol. 47, No. 20, 1111–1112, 2011.
16. Tilanthe, P., P. C. Sharma, and T. K. Bandopadhyay, "A Compact UWB antenna with dual band rejection," *Progress In Electromagnetics Research B*, Vol. 35, 389-405, 2011.
17. Hong, Z., Y.-C. Jiao, B. Yang, and W. Zhang, "A dual band-notched antenna for ultra-wideband applications," *Proceedings of 2011 IEEE Int. Conf. on Microwave Technology and Comput. Electromag., ICMTCE*, Beijing, China, May 2011.
18. Zhang, W., Y.-C. Jiao, B. Yang, and Z. Hong, "CPW-fed ultrawideband antenna with 3.5/5.5 GHz dual band-notched characteristics," *Proceedings of 2011 IEEE Int. Conf. on Microwave Technology and Comput. Electromag., ICMTCE*, Beijing, China, May 2011.
19. Li, L., Z.-L. Zhou, J.-S. Hong, and B.-Z. Wang, "Compact dual-band-notched UWB planar monopole antenna with modified SRR," *Electronic Lett.*, Vol. 47, No. 17, 950–951, 2011.
20. Liu, C.-Y., T. Jiang, and Y.-S. Li, "A compact wide slot antenna with dual bandnotch characteristic for ultra wideband applications," *Journal of Microwaves, Optoelectronics and Electromagnetic Applications*, Vol. 10, No.1, 55–64, June 2011.
21. *IE3D User's Manual*, Release 12.3, Zeland Software, Inc., Fremont, CA, 2007.

The Antenna Feed Structure with the Wide Impedance Bandwidth

Sinhyung Jeon, **Yang Liu**, **Jaeseok Lee**, **Hyunmin Jang**, **and Hyeongdong Kim**
Hanyang University, Republic of Korea

Abstract— A simple but efficient feed structure for achieving a wide impedance bandwidth is proposed. The feed structure operating as a parallel resonance circuit can provide controllable resonance additionally in the conventional PIFA. It was verified that the modified PIFA incorporated with the proposed feed fully covers Long Term Evolution (LTE) 13, Global System for Mobile Communications (GSM) 850 and 900 bands under VSWR 3 : 1 with good radiation patterns. The average realized antenna efficiency over the LTE13, GSM850 and GSM900 bands are about 55%. In addition, good radiation patterns are obtained for mobile services at the desired frequency bands.

1. INTRODUCTION

A demand for compact mobile antennas with a wide impedance bandwidth and high radiation efficiency has been continuously increasing. However, it is difficult to enlarge the impedance bandwidth in the small antenna because the impedance bandwidth of the small antenna is proportional to its physical volume [1]. Because the same difficulties exist in getting a wide bandwidth of a typical internal antenna of mobile phones, planar inverted-F antenna (PIFA), various configurations of internal antennas have been introduced in order enhance the operating bandwidth. Various configurations of internal antennas have been introduced in order to enhance the operating bandwidth [2–4]. These antenna configurations are complicate and typically require additional volume, especially when they are applied to the lower frequency bands (e.g., LTE13/GSM850/GSM900). Thus, a simple handset antenna structure for a wide impedance bandwidth characteristic in the lower frequency bands remains challengeable task to antenna designers.

In this paper, a new internal antenna for mobile handsets is proposed, which can provide a very wide impedance bandwidth covering the LTE13 (746 MHz–787 MHz), GSM850 (824 MHz–894 MHz), GSM900 (880 MHz–960 MHz) bands. The proposed antenna is realized by simply adding a branch line in the feed structure of the conventional PIFA. An improvement in impedance bandwidth performance has been verified through numerical simulations and experimental results.

2. THEORY DESCRIPTION AND ANTENNA DESIGN

The geometry of the proposed antenna is shown in Fig. 1. The proposed antenna consists of an antenna element, a feed line, a short line, a ground plane and a branch line structure ( ). The

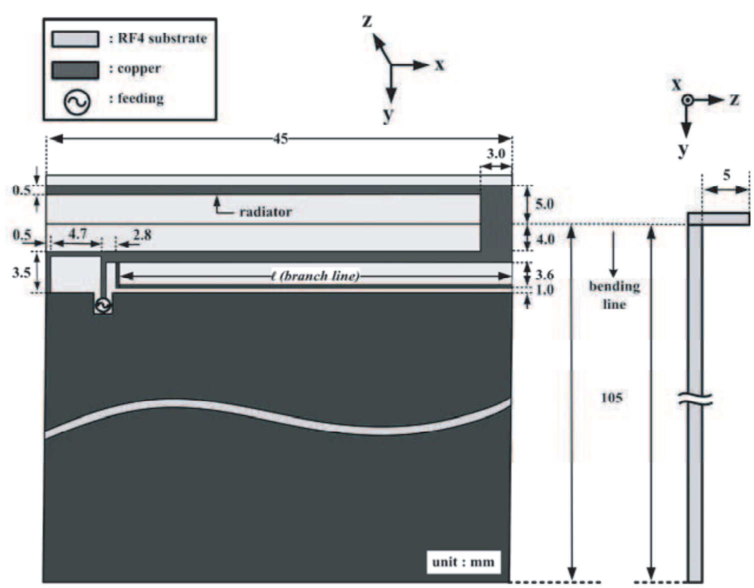

Figure 1: The geometry of the proposed antenna.

copper pattern of size 45 mm × 95 mm for the ground plane were printed on an FR4 printed circuit board (PCB) with 1.6 mm thickness ($\varepsilon_r = 4.7$, $\tan\delta = 0.025$). The occupied antenna space is 45 mm × 10 mm × 5 mm. The antenna element operates as a series resonance mode at 740 MHz. In the first radiation mode, a radiator is excited by a current loop formed by the feed line and shorting pin like a conventional PIFA. However, the impedance bandwidth of the PIFA generally remains narrow. In order to enhance the impedance bandwidth, a branch line is added in the conventional PIFA as shown in Fig. 1. The feed structure with a branch line can be modeled as added shunt capacitance to the feed structure of the conventional PIFA. This branch line have an the electrical length less than a quarter wavelength ($\lambda/4$) in operating frequency, which is not intended to contribute the radiation and provide capacitance to its feed structure. The following Equation (1) is used to approximately predict capacitance provided by a branch line [6]:

$$Y_b = jB = j\frac{1}{Z_o}\cot\,\beta\ell, \tag{1}$$

where Z_o is the characteristic impedance of the transmission line formed by the branch line and the ground, is the length of the branch line and is the propagation constant. The current loop formed by the shorting pin and shunt capacitance generates the parallel resonance mode at the operating frequency. The radiator is additionally excited by such a parallel resonance mode of a current loop. Thus, extra radiation mode is generated near the first radiation mode, and dual resonances are obtained. As a result, the antenna with an additional branch line in its feed structure provides wider impedance bandwidth characteristic compared with the typical PIFA. The extra radiation frequency of the proposed antenna can be controlled by capacitance produced by a branch line. In order to verify the enhanced impedance bandwidth by the proposed antenna with a branch line, a comparative analysis on both a reference antenna and the proposed antenna are conducted by the

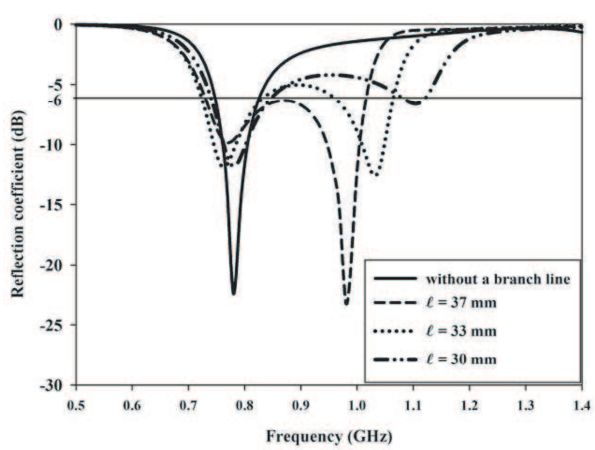

Figure 2: Simulated return loss characteristics for various length of the branch line (ℓ).

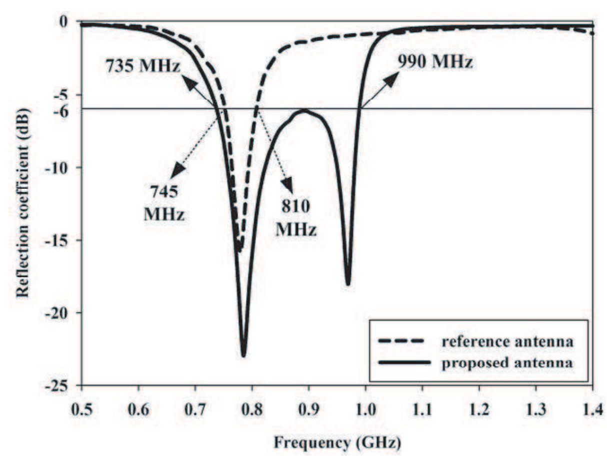

Figure 3: Measured return loss characteristics of the reference and the proposed antennas.

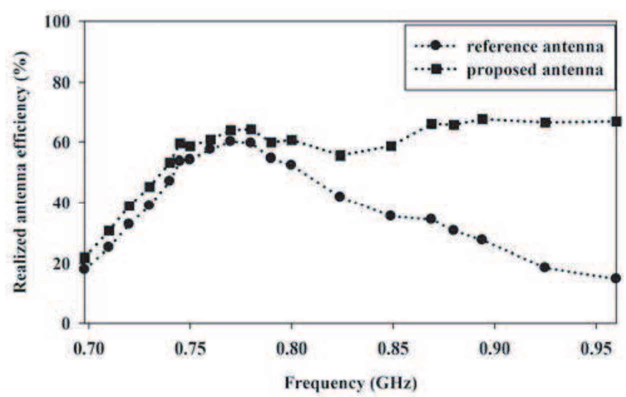

Figure 4: Radiation efficiency of the proposed antenna.

EM simulation. The proposed antenna was designed and analyzed using SEMCAD X by SPEAG commercial software [5]. Fig. 2 shows the simulated return loss characteristics of the reference antenna and proposed antenna for various capacitance. Even when is changed, the identical fundamental resonance frequency is observed, which corresponds to the fundamental resonance mode of the radiator. In case of the reference PIFA, there is no additional radiation mode. Note that only the fundamental radiation mode of the PIFA is operating with a narrow bandwidth at LTE13 band. It is clearly observed that the additional radiation mode along with the fundamental radiation mode is generated by adding a branch line in the feed structure of the conventional PIFA. When the is decreased, the additional radiation mode is lowered. However fundamental radiation mode at LTE13 band did not significantly affect. The additional radiation mode of the proposed antenna can be easily controlled by simply adjusting the capacitance provided by a branch line. Compared with the reference antenna the impedance bandwidth of the proposed antenna is enhanced approximately three times at a VSWR < 3.

3. MEASURED RESULTS AND DISCUSSION

The reference antenna and the proposed antenna were fabricated and measured. Fig. 3 depicts the measured return loss characteristics of two antennas. The simulated and measured results strongly resemble each other. The measured impedance bandwidth of the proposed antenna with the criteria of a voltage standing wave ratio (VSWR) = 3 is 255 MHz (735 MHz–990 MHz) while the reference antenna is 55 MHz (745 MHz–800 MHz). The measured impedance bandwidth of the proposed antenna compared with the reference antenna is enhanced approximately four times. The impedance bandwidth of the proposed antenna is sufficient for LTE13, GSM850, GSM900 band applications. Fig. 4 shows the measured realized antenna efficiency of the reference PIFA and the proposed antenna. In case of the proposed PIFA antenna, the average efficiency over the LTE13 bands is about 61%, and that over the GSM850/900 bands is about 63%. For reference antenna, 56% of the average efficiency is obtained over the LTE13 band; however, the low efficiency ($\approx 29\%$) over the GSM850/900 bands is achieved due to the narrow impedance bandwidth characteristic of the reference PIFA. From the results, good performance for mobile handset antennas is believed to be achieved. Fig. 5 plots the measured far-field radiation patterns at 780 MHz and 960 MHz, respectively. The measured radiation patterns in each x-z plane (E-theta) of 780 MHz and 960 MHz are sufficiently omnidirectional, which are suitable for mobile services.

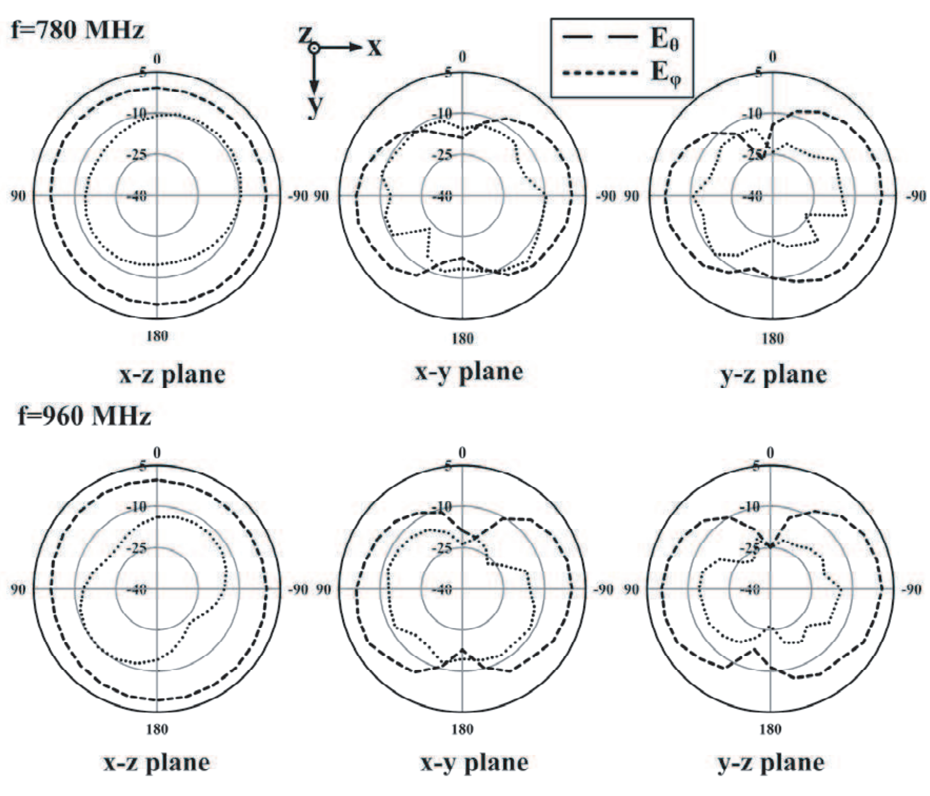

Figure 5: Measured radiation pattern at 780 MHz and 960 MHz.

4. CONCLUSIONS

We proposed a new antenna design, which can achieve a wide impedance bandwidth in the low frequency bands. The antenna performances of the reference PIFA and the proposed antenna such as impedance bandwidth and realized antenna efficiency are compared and analyzed. The proposed antenna results in a successful improvement of the impedance bandwidth, which was observed to expand to 255 MHz. It is a sufficient bandwidth to cover the LTE13, GSM850, GSM 900 applications. In addition, good radiation pattern and realized antenna efficiency are achieved for a mobile handset of lower frequency bands.

ACKNOWLEDGMENT

This work was supported by the National Research Foundation of Korea (NRF) grant funded by the Korea government (MEST) (No. 2011-0015540).

REFERENCES

1. McLean, J. S., "A re-examination of the fundamental limits on the radiation Q of electrically small antenna," *IEEE Trans. Antennas Propag.*, Vol. 44, No. 5, 672–676, 1996.
2. Xin, Y. and H. S. Tan, "New compact six-band internal antenna," *IEEE Antennas Wireless Propag. Lett.*, Vol. 3, No. 1, 295–297, 2004.
3. Choi, H., S. Jeon, S. Kim, and H. Kim, "Controlling resonance frequencies in antennas to achieve wideband operation," *Electron. Lett.,* Vol. 45, No. 14, 716–717, 2009.
4. Lui, G. K. H. and R. D. Murch, "Compact dual-frequency PIFA designs using LC resonators," *IEEE Trans. Antennas Propag.,* Vol. 49, No. 7, 1016–1019, 2001.
5. "Schmid & partner engineering AG (SPEAG)," SPEAG SEMCAD X, available at http://www.speag.com.
6. Pozar, D. M., *Microwave Engineering*, Wiley, New York, 2004.

A New CPW-Fed C-slot Based Printed Antenna for Dual Band WLAN Applications

Jawad K. Ali[1], **Ali J. Salim**[1], **Zaid A. Abed AL-Hussain**[2], **and Hussam Alsaedi**[1]

[1]Department of Electrical and Electronic Engineering
University of Technology, Baghdad, Iraq
[2]Department of Electrical Engineering, College of Engineering
Al-Mustansiriya University, Baghdad, Iraq

Abstract— The C shaped structures and alike have been widely used in numerous antenna designs for various applications. In this paper, a printed slot antenna has been introduced as a candidate for use in the dual band wireless communication applications. The antenna slot structure is to be composed of two or more C shaped slots with different lengths combined together to form a single slot structure. The antenna has been fed with 50 Ohms CPW, and the slot structure is to be etched on the ground plane. Performance evaluation of the proposed antenna design has been carried out using a method of moments based EM simulator, IE3D. Simulation results show very interesting results. The antenna with two C-slot structure offers a dual band resonant behavior meeting the requirements of the 2.4/5.2 GHz WLAN. The resulting percentage impedance bandwidths of the modeled antenna at the center frequencies of 2.51 GHz and 5.21 GHz are 22.70 (2.29 GHz to 2.86 GHz), and 4.80 (5.11 GHz to 5.36 GHz) respectively. In addition, the antenna with three C-slot structure possesses a dual frequency resonant behavior covering the 2.45/5.8 GHz WLAN applications. The resulting percentage impedance bandwidths at the center frequencies of 2.45 GHz and 5.71 GHz are 11.80 (2.32 GHz to 2.61 GHz), and 7.2 (5.53 GHz to 5.94 GHz) respectively. Parametric study has been carried out to explore the effects of antenna parameters on its performance. Besides the satisfactory radiation characteristics, the simple structure of the proposed antenna makes it an attractive choice for antenna designers.

1. INTRODUCTION

There has been an ever increasing demand for antennas which can operate at different frequencies as a result of the rapid development of the wireless communication systems. An additional challenge; these antennas have to meet the requirements of these systems to be compact and with multi-band behavior.

The C-based structures have, in different ways, attracted antenna designers to construct antennas for various wireless applications [1–7]. These antennas cover a wide spectrum ranging from multiband [1], dual band [2–4], to impedance enhancement of single resonant applications [5–7]. Regarding antennas for dual-band WLAN applications, many variants of C-shaped structure have been reported in the literature [2–4]. A dual inverted C-shaped slot antenna has been proposed in [2] to cover dual band WLAN. In [3], a printed two C-shaped monopole antenna has been presented for 2.4/5.2 GHz WLAN applications. The C-shaped structure has been used as a ground plane of an L-shaped monopole antenna designed for dual band WLAN, as reported in [4]. However, different slot based structures have been proposed to design antennas for dual-band WLAN applications [8–13].

Based on a former work [7], a CPW fed slot antenna has been introduced in this paper, as a candidate for use in dual band WLAN applications. The proposed antenna slot structure is in the form of a C-shape. Antennas with two and three slot structures with different scales have been demonstrated to achieve the task.

2. THE ANTENNA STRUCTURE

The motivation of the proposed antenna slot structure has arisen from the work of Tsai and York [7], where a single and multiple C-slot antenna structures have been proposed as a means to enhance the impedance bandwidth of a CPW fed slot antenna. Instead of using composite slots with similar scale, as in [7], the antenna slot structures, proposed in this paper, are composed of slots with different scales to provide the required multi-resonant behaviour. Figure 1 shows the geometries of two proposed structures; one is with two slots, while the other has three slots.

The dielectric substrate is supposed to be the FR4 with a relative dielectric constant of 4.4 and thickness of 1.6 mm. A 50 Ω CPW is used to feed the slot antenna. The resulting CPW has a width of about 3.0 mm is placed on the centreline of the slot structure (y-axis).

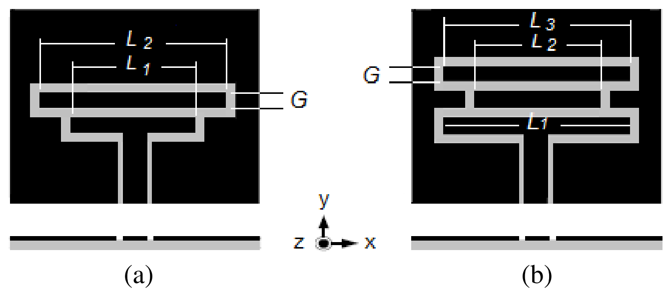

Figure 1: The geometries of the proposed antennas with: (a) two, and (b) three composite C-slot structures.

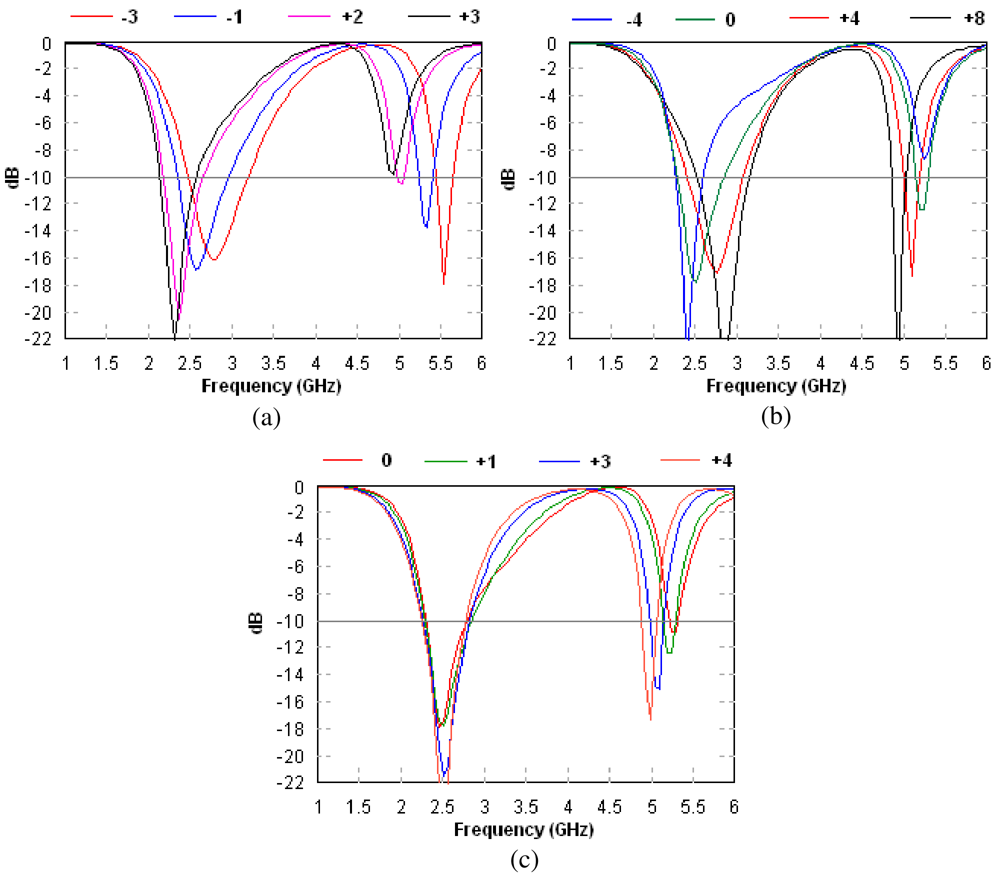

Figure 2: Return loss responses of Ant. I with: (a) L_2, (b) L_1, and (c) G as the parameters.

3. THE ANTENNA DESIGN

Two sets of CPW fed slot antennas, based on the structures depicted in Figures 1(a) and (b), have been designed to resonate a lower frequency of 2.4 GHz. The first set is consist of antennas with two composite C-slots, Figure 1(a), while the other set is with three composite C-slots, Figure 1(b). These antennas have been modeled and analyzed using the method of moments (MoM) based electromagnetic (EM) simulator IE3D [14].

Observing the influence of the various parameters on the antenna performance, it has been found that the dominant factors in the antenna are the slot side lengths L_1 and L_2 of the first antenna structure, L_1, L_2, and L_3, for the second antenna, and the gap width G for both antenna slot structures. In this work, the gap width has been kept the same, $G = G_1 = G_2$, for the antenna geometry depicted in Figure 1(a), and $G = G_1 = G_2 = G_3$, for the proposed antenna shown in Figure 1(b). The slot width, T, has been taken equal to G. Initial antenna designs, based on the structures depicted in Figures 1(a) and (b), have been modeled for such a task. These antennas have been referred to as Ant. I, and Ant. II respectively, and they will be used as references in

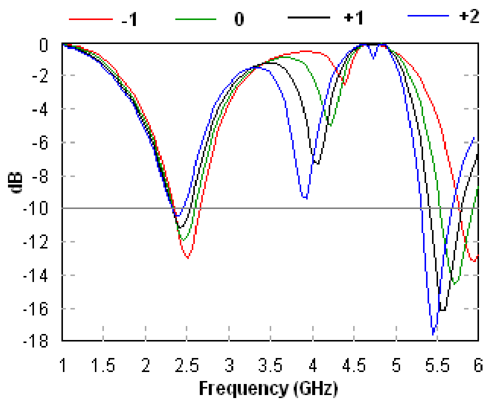

Figure 3: Return loss responses of Ant. II with the gap width G as the parameters.

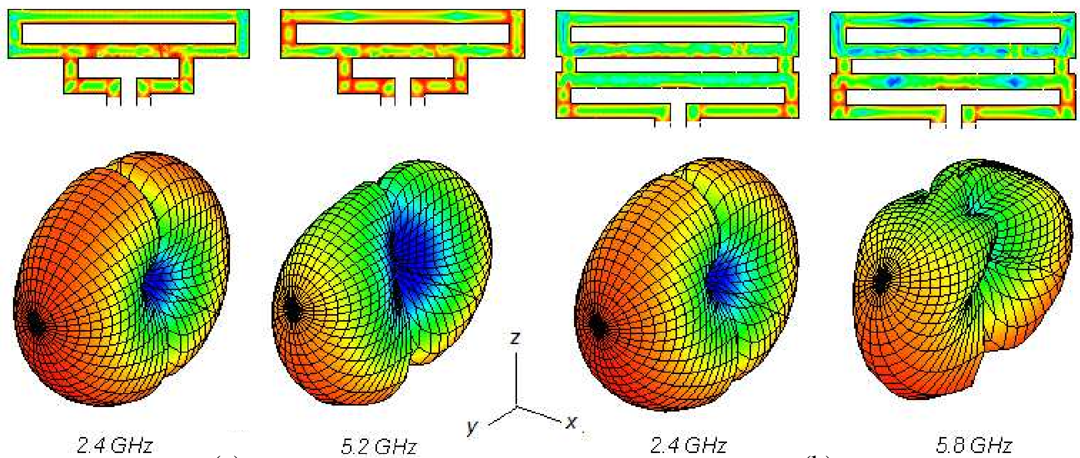

Figure 4: Simulated surface current distributions and the 3D electric field radiation patterns at the corresponding resonances for: (a) Ant. I, and (b) Ant. II.

the related parametric studies to be performed later. Table 1 summarizes the dimensions of these antennas when resonating at 2.4 GHz.

4. PERFORMANCE EVALUATION

A slot antenna with structure depicted in Figure 1(a) has been designed, using the said substrate, to resonate at lower frequency of 2.4 GHz. With these parameters, the antenna exhibits a dual band response, centered near the 2.4 and 5.2 GHz WLAN bands. A parametric study has been carried out to demonstrate the effects of various antenna parameters on its performance, as shown in Figure 2, where the values of L_1, L_2, and Ghave been varied, in mm, with respect to those presented in Table 1, for Ant. I. Figure 2(a) demonstrates the effects of varying the slot length L_2 on the antenna return loss response. Increasing this length causes both the lower and the upper resonant frequencies to be decreased, while approximately maintaining the same frequency ratio f_{0U}/f_{0L}. However, the lower resonant bandwidth is significantly increased with the larger values of L_2, while the upper resonant bandwidth is almost kept unchanged.

On other hand, the variation of the slot length L_1 has an interesting impact on the antenna return loss response, as shown in Figure 2(b). The increase of this length makes the lower and the upper resonant frequencies approaching each other; if the lower frequency is increased the upper frequency will be decreased, and vice versa. This supports the findings reported in [7] where single resonance has been excited, when this length has been increased such that it equals L_2. In this case, the proposed antenna offers different ratios of f_{0U}/f_{0L}, making it suitable for use in many dual band communication applications. The effect of varying the gap width G is shown in Figure 2(c). The lower resonant frequency has almost not affected, while the upper resonant decreases as G has been increased. For a value of $G = 3.6$ mm, the resulting percentage impedance bandwidths of the modeled antenna at the center frequencies of 2.51 GHz and 5.21 GHz are 22.70 (2.29 GHz to

Table 1: Summary of Ant. I and Ant. II dimensions, in mm, as depicted in Figures 1(a) and 1(b).

Ant. I	L_1	L_2	T	$G = G_1 = G_2$	
	20.88	40.82	2.57	2.57	
Ant. II	L_1	L_2	L_3	T	$G = G_1 = G_2 = G_3$
	43.60	41.20	43.60	2.90	2.90

2.86 GHz), and 4.80 (5.11 GHz to 5.36 GHz) respectively.

Due to the limited space, similar parametric study of Ant. II, depicted in Table 1, cannot be provided here. Instead, only the effect of varying the slot gap width G on the antenna return loss has been presented in Figure 3. Many observations can be extracted here. In comparison with Ant. I, Ant. II offers triple band response; with slight modification this might fit triple band WiMAX impedance bandwidth requirements. However, the lower and the upper resonant frequencies and the corresponding bandwidths fit the 2.4/5.8 GHz WLAN bands. The variations of G slightly affect the position of the lower resonant frequency, but the corresponding bandwidths are noticeably increased with the decrement of G, providing an interesting tuning range. For a value of $G = 2.9$ mm, the resulting percentage impedance bandwidths of the modeled antenna at the center frequencies of 2.45 GHz and 5.71 GHz are 11.80 (2.32 GHz to 2.61 GHz), and 7.2 (5.53 GHz to 5.94 GHz) respectively.

Figure 4 summarizes the simulated surface current density on the slot structures of the two antennas at the related resonances together with the corresponding 3D radiation patterns. The resulting values of the antenna gains for the lower and the upper bands are 1.92 and 3.12 dB, for Ant. I and 1.78 and 3.49 dB, for Ant. II respectively.

5. CONCLUSION

In this paper, CPW fed slot antennas with two and three C-slot structures have been presented as candidate for use in dual band WLAN applications. The proposed antennas have been analyzed using a method of moments based EM simulator, IE3D. The conducted parametric studies show that antenna with two C-slot structure fits the 2.4/5.2 GHz WLAN bands, while the antenna with three C-slot structure successfully meet the requirements of 2.4/2.8 GHz WLAN. In addition, this antenna offers triple band resonant behavior; with careful tuning it can meet the triple band WiMAX applications. Furthermore, both antennas possess dual band and triple band behaviors with different resonant frequency ratios; making them suitable for use in a wide variety of dual band and triple band wireless applications. It is hopeful that, the simple structure of the presented antennas besides the degrees of freedom, their corresponding designs offer, will make the proposed antennas an attractive choice for the antenna designers.

REFERENCES

1. Tlili, B., "Design of double C-slot microstrip patch antenna for WiMax application," *Proceedings of the 2010 IEEE International Symposium on Antennas and Propagation Society*, Toronto, ON, Jul. 11–17, 2010.
2. Xi, D., L. H. Wen, Y. Z. Yin, Z. Zhang, and Y. N. Mo, "A compact dual inverted C-shaped slots antenna for WLAN applications," *Progress In Electromagnetics Research Letters*, Vol. 17, 115–123, 2010.
3. Luo, Q., H. M. Salgado, and J. R. Pereira, "Compact printed monopole antenna array for dual-band WLAN application," *Proceedings of the International Conference on Computer as a Tool*, Lisbon, Apr. 27–29, 2011.
4. Tsai, C.-J., C.-H. Lin, W.-C. Chen, C.-L. Lu, and J.-K. Guo, "A compact dual-band antenna with a C-shaped ground plane for WLAN applications," *Proceedings of the IEEE Cross Strait Quad-regional Radio Science and Wireless Technology Conference*, Harbin, Jul. 26–30, 2011.
5. Chen, R. H. and Y.-C. Lin, "Miniaturized design of microstrip-fed slot antennas loaded with C-shaped rings," *IEEE Antennas and Wireless Propag. Letts.*, Vol. 10, 203–206, 2011.
6. Su, S.-W., T.-C. Hong, and F.-S. Chang, "Very compact coupled fed loop antenna for 2.4-GHz WLAN applications," *Microwave and Opt. Tech. Lett.*, Vol. 52, No. 8, 1883–1887, 2010.
7. Tsai, H. S. and R. A. York, "Applications of planar multiple-slot antennas for impedance control, and analysis using FDTD with Berenger's PML method," *Proceedings of the IEEE AP-Symposium Digest*, Newport Beach, CA, 1995.

8. Lee, K. F., K. M. Lu, K. M. Ma, and S. L. S. Yang, "On the use of U-slots in the design of dual-and triple-band patch antennas," *IEEE Antennas and Propag. Magazine*, Vol. 53, No. 3, 60–74, 2011.
9. Wei, Y., Y. Yin, Y. Yang, S. Jing, and W. Hu, "Compact dual-band antenna with modified open U-shaped slot for WLAN applications," *Proceedings of the 2011 IEEE International Conference on Microwave Technology and Computational Electromagnetics, ICMTCE*, Beijing, May 22–25, 2011.
10. Gai, S., Y.-C. Jiao, Y.-B. Yang, C.-Y. Li, and J.-G. Gong, "Design of a novel microstrip-fed dual-band slot antenna for WLAN applications," *Progress In Electromagnetics Research Letters*, Vol. 13, 75–81, 2010.
11. Huang, C.-Y. and E.-Z. Yu, "A slot-monopole antenna for dual-band WLAN applications," *IEEE Antennas and Wireless Propag. Letts.*, Vol. 10, 500–502, 2011.
12. Chang, M.-C. and W.-C. Weng, "A dual-band printed dipole slot antenna for 2.4/5.2 GHz WLAN applications," *Proceedings of the 2011 IEEE International Symposium on Antennas and Propagation Society*, Spokane, WA, Jul. 3–8, 2011.
13. Mahmoud, N. M. and R. Baktur, "A dual band microstrip-fed slot antenna," *IEEE Trans. Ant. and Propag.*, Vol. 59, No. 5, 1720–1724, 2011.
14. *IE3D User's Manual, Release*, 12.3, Zeland Software, Inc., Fremont, CA, 2007.

Analysis and Simulation of Electric Field Intensity from a Half-wave Dipole Antenna in Open Area Test Site

I. A. Wibowo, M. Z. Mohd Jenu, and A. Kazemipour
Center for Electromagnetic Compatibility, Faculty of Electrical and Electronic Engineering
Universiti Tun Hussein Onn Malaysia, 86400 Parit Raja, Batu Pahat, Johor, Malaysia

Abstract— Accurate measurement of electric field intensity is important in electromagnetic compatibility (EMC) field where the measured electric field emitted by an electrical or electronic product determines whether the product complies with regulation. To have valid measurement, the antennas used in the measurement must be calibrated accordingly. Both the measurement and calibration have to be done in a test site. Although there have been various alternative test sites available nowadays such as the anechoic chamber, legislative body such as the International Electrotechnical Commission (IEC) requires an open-area test site (OATS) as the reference for radiated emission measurement and antenna calibration. Therefore it is very important to understand the propagation mechanism in the OATS in order to design, evaluate and operate the OATS. This paper discusses the modeling and simulation of propagation mechanism in the OATS, starting with the basic propagation equation as a foundation, and the derivation of the electric field propagation model in an ideal OATS. The model uses a half wave dipole antenna as the transmitter. Simulations of the radiation of electromagnetic wave from a half-wave dipole antenna in the range of 30–1000 MHz have been performed in CST Microwave Studio® simulation software. The results of the calculation using the model were compared to the simulation. The average deviation was used to compare the result of the calculation using the theoretical model and the result of the simulation. The importance of height scanning of the receiving antenna was also elaborated. The results have proven that the theoretical model and the simulation are consistent and therefore the simulation validates the model.

1. INTRODUCTION

An open area test site (OATS) is a flat, outdoor open area, with conductive ground plane, free from overhead wires and nearby reflecting structures. The equipment under test (EUT) is placed on a non-metallic turntable and the electric field is measured for various orientations using an antenna. An ideal OATS has infinite ground plane made of perfect electric conductor [1, 2].

The knowledge on the propagation mechanism in the OATS is important to design, evaluate and operate the OATS. Therefore, this paper contributes to the understanding of the propagation mechanism by deriving the electric field propagation model in an ideal OATS and creating simulations to be compared with the theoretical model.

2. PROPAGATION OVER INFINITE GROUND PLANE

The electric field intensity at distance R from a non-isotropic transmitter is given by

$$E = \frac{\sqrt{30 P_t g_t}}{R} \tag{1}$$

where P_t is the input power to the transmitter (W) and g_t is the gain of the transmitter [3–6].

If an infinite ground plane exists below the antennas, then the electric field intensity at the receiving antenna becomes the resultant between the electric field intensities due to direct and reflected waveforms as follows:

$$\mathbf{E} = \mathbf{E}_d + \mathbf{E}_r \tag{2}$$

where $\mathbf{E}_d$ is the component of electric field intensity due to direct waveform and $\mathbf{E}_r$ is the component of electric field intensity due to reflected waveform.

The electric field intensity due to reflected waveform can be analysed using mirror image of the transmitting antenna as shown in Figure 1 [7].

For sinusoidal waveform the electric field intensity becomes

$$E = \sqrt{30 P_t g_t} \left(\frac{e^{-j\beta d_d}}{d_d} + \frac{\Gamma e^{-j\beta d_r}}{d_r} \right) \tag{3}$$

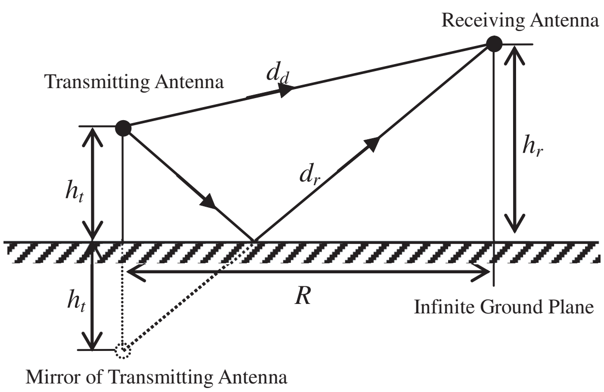

Figure 1: Geometry of electric field propagation over infinite ground plane.

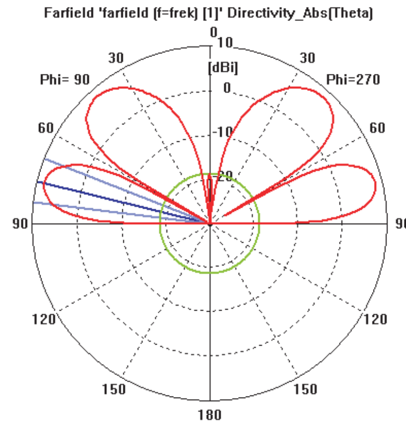

Figure 2: Radiation pattern of the half wave dipole over infinite ground plane.

Table 1: Height of receiving antenna versus electric field intensity.

RX height (m)	E (dBV/m)	
	Calculated	Simulated
1	12.15	11.82
1.5	4.94	6.01
2	0.91	0.18
2.5	8.40	8.40
3	10.02	10.09
3.5	9.81	9.66
4	8.79	8.42

where $d_d = \sqrt{R^2 + (h_t - h_r)^2}$, $d_r = \sqrt{R^2 + (h_t + h_r)^2}$, $\Gamma = e^{j\Phi}$ is the reflection coefficient, Φ is the phase shift due to the reflection and $\beta = 2\pi/\lambda$ is the free space wavenumber.

If the ground plane is a perfect electric conductor, the magnitude of the reflection coefficient is unity while its phase is shifted by 180° therefore Equation (3) becomes

$$E = \sqrt{30P_t g_t}\left(\frac{e^{-j\beta d_d}}{d_d} - \frac{e^{-j\beta d_r}}{d_r}\right) \tag{4}$$

3. SIMULATION RESULTS

The average deviation as given in the following formula will be used to compare the result of the calculation using the theoretical model and the result of the simulation.

$$D_{av} = \frac{\sum |d_n|}{n} \tag{5}$$

where $|d_n|$is the absolute value of the deviation and n is the total number of data.

Simulations of the radiation of electromagnetic wave from a half-wave dipole antenna in the range of 30–1000 MHz have been performed in CST Microwave Studio®. The simulations were done for horizontal polarization only. In this simulation an infinite perfect electric conductor ground plane was included by setting the boundary condition at the ground plane to be electric ($E = 0$).

Due to effect of the ground plane the radiation pattern of the antenna have been changed into several lobes as shown in Figure 2.

A probe situated at the receiver was height scanned from 1 m to 4 m with 0.5 m increment. It was aimed to obtain the maximum electric field intensity. The simulation was done in the frequency of 300 MHz. The results were recorded in Table 1. The values obtained in the simulation were then compared to the calculated electric field intensity from Equation (4). The results in Table 1 are be visualized in a graph as illustrated in Figure 3.

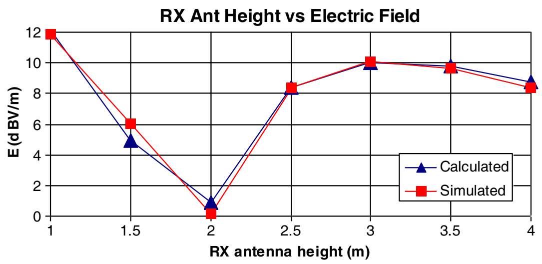

Figure 3: Height of the receiving antenna versus electric field strength.

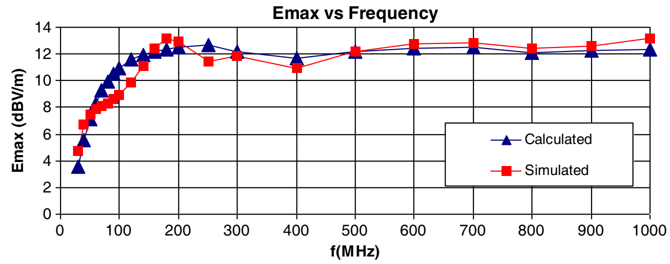

Figure 4: Maximum Electric Field Intensity at 30–1000 MHz.

Table 2: Maximum electric field intensity at various frequencies.

f (MHz)	RX height (m)	$E_{\max}$ (dBV/m) Calculated	$E_{\max}$ (dBV/m) Simulated
30	2.9	3.54	4.75
40	2.9	5.59	6.75
50	2.8	7.13	7.46
60	2.7	8.32	7.83
70	2.6	9.25	8.1
80	2.5	9.97	8.3
90	2.4	10.52	8.58
100	2.2	10.96	8.92
120	1.9	11.57	9.86
140	1.7	11.95	11.09
160	1.5	12.20	12.39

f (MHz)	RX height (m)	$E_{\max}$ (dBV/m) Calculated	$E_{\max}$ (dBV/m) Simulated
180	1.3	12.36	13.14
200	1.2	12.48	12.9
250	1.0	12.64	11.46
300	1.0	12.15	11.82
400	2.1	11.64	10.9
500	1.6	12.16	12.19
600	1.3	12.39	12.75
700	1.1	12.50	12.81
800	1.0	12.06	12.44
900	1.4	12.22	12.61
1000	1.3	12.32	13.15

As seen in Table 1 and Figure 3, the values of the simulated results are quite close to the calculated results. This is proven by the calculation of the average deviation which results 0.39 dBV/m.

To validate the model further, simulations were done in the whole frequency range at the calculated height obtained from Equation (3). The results are listed in Table 2 and visualized in a graph as illustrated in Figure 4.

Again, to compare the theory and simulation the average deviation was calculated. The result is 0.84 dBV/m. This indicates that the theoretical model and the simulation are consistent.

4. CONCLUSIONS

The electric field intensity at a distance from a transmitter is frequency independent. When a ground plane exists the electric field intensity becomes frequency dependent due to the reflection by the ground plane. The ground plane alters the radiation pattern of the transmit antenna. In EMC application, height scanning of the receiver is very important, because the maximum electric field intensity at different frequency is obtained at different receiver height. The electric field propagation model is valid as it has been proven conforms to the result of the simulations.

ACKNOWLEDGMENT

The authors thank EMC Center Universiti Tun Hussein Onn Malaysia Johor for providing facilities to do this research work.

REFERENCES

1. CISPR 16-1-4, *Specification for Radio Disturbance and Immunity Measuring Apparatus and Method*, Edition 2.1, The International Electrotechnical Commission, 2008.
2. ANSI C63.4, *American National Standard for Methods of Measurement of Radio-noise Emissions from Low-voltage Electrical and Electronic Equipment in the Range of 9 kHz to 40 GHz*, American National Standards Institute, New York, 2003.

3. Liao, S. Y., "Measurements and computations of electric field intensity and power density," *IEEE Transactions on Instrumentation and Measurement*, Vol. 26, No. 1, 53–57, 1977.
4. Frazier, W. E., *Handbook of Radio Wave Propagation Loss, Part I*, US Department of Commerce, 1984.
5. Friis, H. T., "A note on a simple transmission formula," *Proceedings of the I.R.E. and Waves and Electrons*, 254–256, 1946.
6. Popović, Z. and B. Popović, *Introductory Electromagnetics*, Prentice Hall, Upper Saddle River, 2000.
7. Balanis, C. A., *Antenna Theory Analysis and Design*, 2nd Edition, Wiley, New York, 1997.

Impact of Spacing and Number of Elements on Array Factor

S. F. Maharimi[1], **M. F. Abdul Malek**[2], **M. F. Jamlos**[1], **S. C. Neoh**[3], **and M. Jusoh**[1]

[1]School of Computer & Communication Engineering, University Malaysia Perlis, Malaysia
[2]School of Electrical System Engineering, University Malaysia Perlis, Malaysia
[3]School of Microelectronic Engineering, University Malaysia Perlis, Malaysia

Abstract— The impact of spacing and number of elements in terms of gain and half power beam-width (HPBW) are shown in this paper. The antenna's gain is depending on two parameters which are number of elements and element spacing. These measurements were measured by array factor's algorithm. The algorithm has been designed to operate with 2, 3, 4 and 10 number of elements at the each specific spacing. The particular spacing are 0.1λ, 0.25λ, 0.5λ and 0.75λ. It is observed that the HPBW and number of side lobes is increased as spacing of elements are increases. And the gain is maintains in the same condition.

1. INTRODUCTION

The capability of an antenna to increase the quality of the performance is depends on their parameters such as number of elements, spacing between elements, phase and amplitude excitation. The main parameters for linear array antenna are the number of elements and spacing elements which must be taken into consideration. Hence, these parameters are used to determine the antenna performance on the gain and HPBW.

The array factor is fundamental of the antenna parameters. This paper described the impact of the spacing and the number of elements on gain and HPBW through array factor algorithm for linear array antenna and simulated using MATLAB software as illustrated.

2. ARRAY FACTOR

The array factor depends on the number of elements, the element spacing, amplitude and the phase of the applied signal to each element [1]. The antenna array can aligned either z-axis or x and y-axis. A uniform array is defined by uniformly spaces identical elements of equal magnitude with linearly progressive phase from element to element [2]. The radiation pattern of the array excluding the element pattern is referred to as the array factor. A general form for along the z-axis for linear array is given by [3].

$$AF = 1 + e^{j(kd\cos\theta+\delta)} + e^{j2(kd\cos\theta+\delta)} + \ldots + e^{j(N-1)(kd\cos\theta+\delta)} \tag{1}$$

where $k = \frac{2\pi}{\lambda}$, N is the number of elements.

The N-elements linear array can be designed to radiate in either broadside array where radiation perpendicular to array orientation the z-axis or end fire array will radiate in the same direction as the array orientation in the y-axis [2]. The array factor of N-elements can be written as [3]:

$$AF(\theta) = \sum\nolimits_{i=1}^{N} e^{j(n-1)(kd\cos\theta+\delta)} \tag{2}$$

The term of $kd\cos\theta + \delta$ can be written as ψ, so the array factor becomes

$$AF(\theta) = \sum\nolimits_{i=1}^{N} e^{j(n-1)\psi} \tag{3}$$

Refer to (2) the notation of θ is the angle between the array axis and the vector from the origin to the observation point [3]. According to broadside array, the phase shift of δ is equal to zero ($\delta = 0$) such that all element current are in phase.

2.1. Equal and Unequal Spacing N-element Linear Array Antenna

Linear array antenna has two spacing technique elements either equal spacing between elements or unequal spacing elements. The number of elements depends on the designer to put how many in the antenna design. This section described the theory of the N-number elements in equal and unequal spacing in linear array arrangement.

2.1.1. Equal Spacing N-element Linear Array

For equal spacing between elements, the distance for each element to element is equal in lambda. Figure 1 below show the linear array for equal spacing elements. This arrangement is also called uniform linear array [5].

2.1.2. Unequal Spacing N-element Linear Array

The distances for unequal spacing linear array of an antenna with N-element are nonuniform in z-axis arrangement. Their configuration can be rearranged either in symmetrical or asymmetrical arrangement [5, 6, 8].

Figure 2 illustrates the unequal spacing of *d1* till *d5* in an arrangement of an antenna in the linear array for 6-elements as an example [5, 6].

Figure 3 illustrates the arrangement of linear array antenna in the symmetrical condition. A symmetrical arrangement could be described that the position of the element number of 1, 2, and 3 in both sides of positive and negative are equal [6–8].

3. SIMULATION OF N-ELEMENT FOR 0.1λ, 0.25λ, 0.5λ, 0.75λ SPACING ELEMENTS OF LINEAR ARRAY ANTENNA

This section described the simulation method using MATLAB Software where the array factor was used as the algorithms for evaluate the HPBW and gain to achieve better performance in antenna design.

The simulation started with 2, 3, 4 and 10 elements in linear array antenna with spacing elements of 0.1λ, 0.25λ, 0.5λ, and 0.75λ as shown in Figures 4, 5, 6 and 7. From the results, the antenna's gain is measured by array factor algorithm.

The gain is rising according to the number of elements. The shape of the graph for the array factor changed when the spacing elements increased. Referring to the result obtained by difference

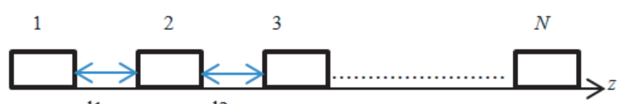

Figure 1: Linear array antenna for equal spacing.

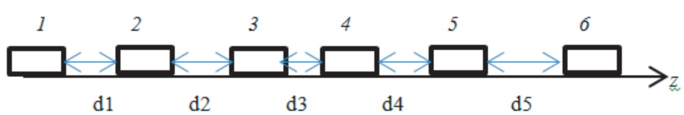

Figure 2: Linear array for unequal spacing in asymmetric array arrangement.

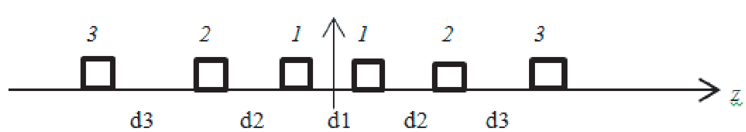

Figure 3: Linear array for unequal spacing symmetrical array arrangement.

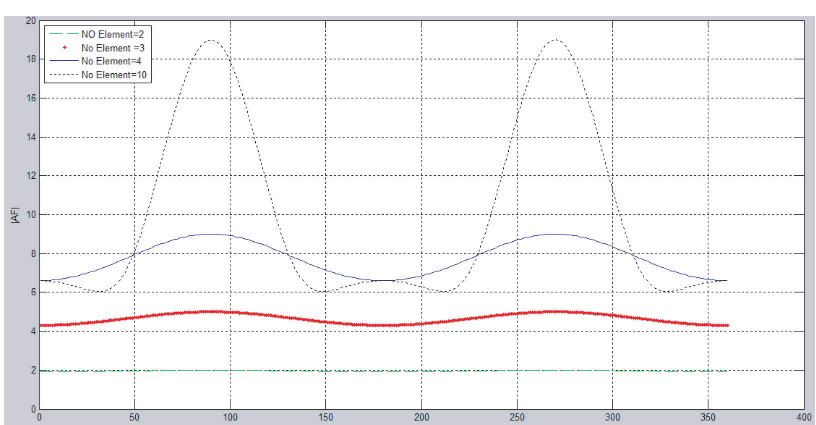

Figure 4: Array factor for 0.1λ spacing elements.

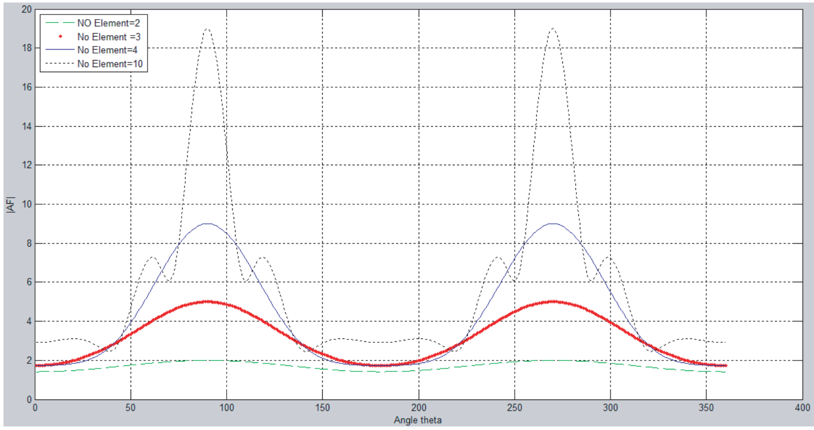

Figure 5: Array factor for 0.25λ spacing elements.

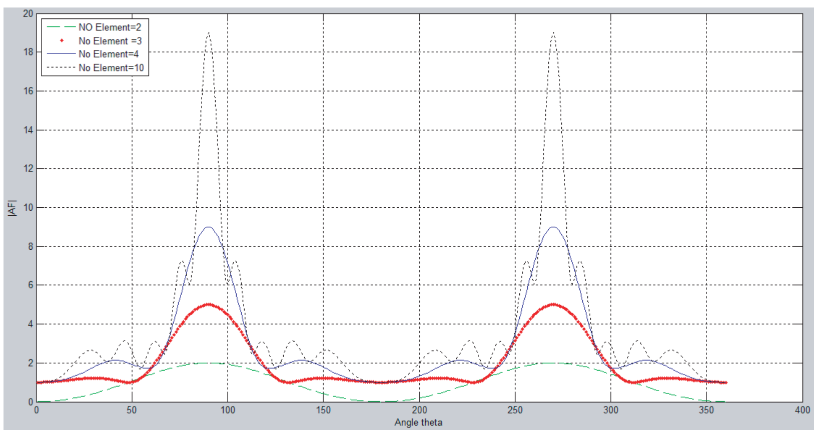

Figure 6: Array factor for 0.5λ spacing elements.

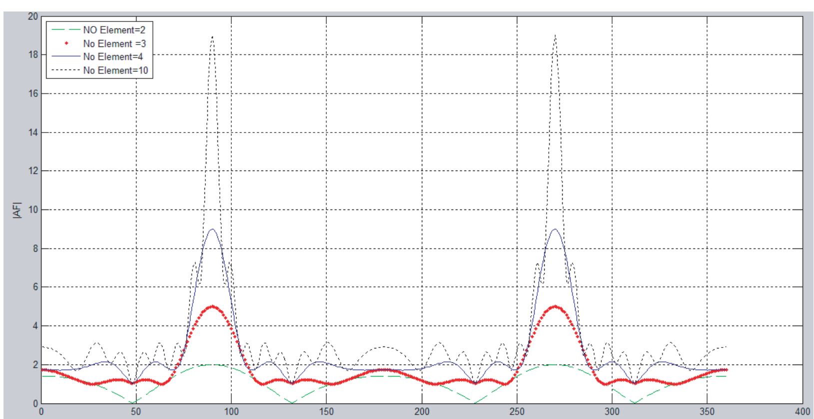

Figure 7: Array factor for 0.75λ spacing elements.

number elements, although the gain become increasing according to the number element but their gain was maintains when the spacing element is increasing towards to the lambda. Whole gain for these different spacing elements is not changed but their HPBW reduce when the spacing element is increase. The each element's gain is not change though the spacing element has increase.

Comparing all the result in Figures 4, 5, 6 and 7, the number of ripples or side lobes strictly increased when the spacing elements increased. The width of the main lobe decreased when the number of elements and spacing elements were increased. From the results observation, the increasing number of elements and spacing elements have affected on their radiation pattern.

Table 1: HPBW and gain for $N = 2$, 3, 4, and 10 at 0.1λ, 0.25λ, 0.5λ and 0.75λ spacing elements.

	0.1λ		0.25λ		$0.5\ \lambda$		$0.75\ \lambda$	
Element	HPBW	Gain (dB)	HPBW	Gain (dB)	HPBW	Gain (dB)	HPBW	Gain (dB)
2	90.83°	2	89.8°	2	83.77°	2	52.57°	2
3	87.39°	5	70°	5	42°	5	27.64°	5
4	85.44°	9	62°	9	29.76°	9	19.63°	9
10	53.37°	19	23.62°	19	10.29°	19	6.8°	19

4. CONCLUSIONS

As a conclusion from the results obtained, HPBW was increasing according to the number and spacing elements and when the gain was increasing according to the number elements. The result achieved a good performance in the antenna design at the highest gain of 19 dB at spacing element is equal to 0.1λ. Furthermore, increasing the spacing elements in the gain is unsuitable for application seeking to improve system performance when degradation is mainly caused by interference or jamming.

ACKNOWLEDGMENT

The authors would like to thank everyone for their helps and support especially to Embedded Computing team members and University Malaysia Perlis. Special thanks to the Ministry of Higher Education in Malaysia for their financial support.

REFERENCES

1. The Basics of Antenna Arrays notes, 2010, Available: http://www.orbanmicrowave.com.
2. Antenna Arrays notes, 2009, Available: http://www.ece.msstate.edu/˜donohoe/ece4990notes 6.pdf
3. Zooghby, A. E., *Smart Antenna Engineering*, Artech House, Inc., U.S., 2005.
4. Gross, F., *Smart Antenna for Wireless Communication with Matlab*, The McGraw-Hill Companies Inc., U.S., 2005.
5. Jin, N. and Y. Rahmat-Samii, "Advances in particle swarm optimization for antenna design: Real-number, binary number, single-objective and multiobjective implementations," *IEEE Transaction on Antenna Propagation*, Vol. 53, 556–567, Mar. 2007.
6. Tan, M. N. Md, S. K. A. Rahim, M. T. Ali, and T. A. Rahman, "Smart antenna; weight calculation and side lobe reduction by unequal spacing technique," *IEEE International FR and Microwave Conference Proceedings*, 441–445, Kuala Lumpur, Malaysia, Dec. 2008,
7. Tan, M. N. Md, T. A. Rahman, S. K. A. Rahim, M. T. Ali, and M. F. Jamlos, "Elements reduction using unequel spacing technique for linear array antenna," *PIERS Conference Proceedings*, 568–572, Xi'an, China, Mar. 2010, .
8. Balanis, C. A., *Antenna Theory*, Canada, A John Wiley & Sons, Inc., U.S, 2005.

Analysis of Multi Turn 4-Arm Archimedean Spiral Antenna with Varying Spacing between Arms

Ashutosh Baheti[1], **Ali M. Mehrabani**[2], **and Lotfollah Shafai**[2]

[1]The LNM Institute of Information Technology, Jaipur, India
[2]The University of Manitoba, Winnipeg, Manitoba, Canada

Abstract— For so long spiral antennas has its applications in Aerospace, Missile systems, GPS navigations Systems etc. Multi turn four arm spiral Antenna array has gained its utility in Radar systems and in mode forming systems for angle of arrival estimation. This paper investigates the effects on the electromagnetic characteristics like Impedance, Circular polarization gain, Axial ratio, Radiation pattern, S-parameter etc. of Multi turn four arm Archimedean spiral antenna array owing to the changes in the spacing between the arms and number of turns on the dielectric substrate. Results show that the change in spacing with change in number of turns has much influence on the input Impedance, RHCP gain and Multiband properties.

1. INTRODUCTION

Planar Archimedean spiral antenna has been widely used with its low profile, light weight, wide bandwidth [1], high efficiency and circular polarization for airborne applications [2], satellite communications, wireless communications [3], UWB communications [4], radio navigations, biological medicine [5], Radar, early warning, and direction finding systems. The Archimedean one is not a true frequency independent antenna (the conductor's width is constant). Spiral antennas radiate bi-directionally, which is, for most applications undesired. To radiate unidirectionally, Archimedean spiral antennas are usually backed by a conducting plane [6], a conducting cavity or an absorbing cavity [7]. Previous work in this area has primarily focused on the operation of the antenna without dielectric backing. When backed by a dielectric substrate, multiple turns lying in the active region (antenna radiates from a region where the circumference of the spiral equals one wavelength is called the active region of the spiral) [8] effects the RHCP gain, multiband properties etc. and antenna array approach allows for pattern control and higher gains, but the wideband characteristics of the frequency independent element are lost in the array environment. Inter-element spacing usually limits array bandwidth to a value much less than a frequency independent element can achieve outside an array [9]. In this paper the effects of electromagnetic properties of Multi turn 4 Arm planar Archimedean spiral antenna array operating at 1 GHz–2.5 GHz, owing to the change in number of turns and spacing between two arms are investigated respectively. Section 1 describes the background of the antenna and contents of paper. Section 2 describes the Antenna geometry and Operation used for the design. Section 3 describes the simulation results and discussions. Conclusions are discussed in Section 4.

2. ANTENNA GEOMETRY & OPERATION

The Archimedean spiral antenna as shown below in Fig. 1 is composed of four symmetric arms fed by SMA ports of port impedance 200 Ω. The antenna is backed by a dielectric constant of $\epsilon_r = 2.5$ and height of substrate as 1.57 mm. The equations can be formulated for four arm spiral over a

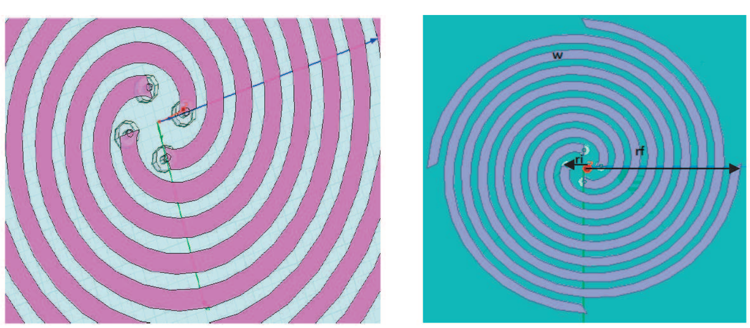

Figure 1: Antenna geometry and physical dimensions.

substrate using basic key equation $r_f - r_i = a\varphi$ [10] where a = flare rate of spiral = 3.1987 mm/rad which is kept constant for the entire geometry, r_f = outer radius and r_i = inner radius. The inner and outer radii denote the maximum and minimum frequencies of operation of spirals. The range of operation is further degraded incurring losses due to the Dielectrics. In this paper number of turns is varied keeping the geometry and flare rate as the same. When the width of microstrip line increases from 1 mm to 5 mm, spacing between arms is reduces proportionally. The equations are modified for four arm geometry for N number of turns is [8, 9]

$$r_f - r_i = Na(\varphi_f - \varphi_i) \tag{1}$$

$$\varphi_f - \varphi_i = 2\pi \tag{2}$$

$$f_{high_{sub}} = \frac{c}{2\pi r_i \sqrt{\epsilon_{r_{eff}}}} \tag{3}$$

$$f_{low_{sub}} = \frac{c}{2\pi r_f \sqrt{\epsilon_{r_{eff}}}} \tag{4}$$

where N = number of turns, a = flare rate, φ = angle, $f_{high_{sub}}$ = Maximum frequency corresponding to r_i on substrate, $f_{low_{sub}}$ = Minimum frequency corresponding to r_f on substrate, $\epsilon_{r_{eff}}$ = Effective dielectric constant of microstrip. The behavior of change in spacing between two arms with change in number of turns is studied. For 1 turn the $r_i = 0.6$ cm, $r_f = 3$ cm, $N = 1$ and $a = 3.9187$ mm/rad. For 2 turn, the $r_i = 0.6$ cm, $r_f = 5.4$ cm, $N = 2$ and $a = 3.9187$ mm/rad.

3. SIMULATION RESULTS & DISCUSSIONS

3.1. *Z*-parameter & Impedance

The impedance of spiral antenna is of concern, the erratic behavior at the upper and lower frequencies, a band of nearly constant impedance of 188 Ω is seen in case of single spiral in free space by booker's relation [11]. The impedance of antenna is due to the integrated effect of microstrip width as seen from Equations (5) & (6), due to mutual coupling between the arms, which is taken into account by Equation (7) and heavy substrate losses & dielectric constant effect impedance too. From the equations it is seen that width of arm increases, the impedance of antenna reduces and vice versa. In Fig. 2(a), for 1 turn the impedance reduces as width of microstrip line increases. As we move further in Fig. 2(b) for 2 turns we see many resonating frequencies and impedance reduces with increase in width of microstrip line or less spacing between arms.

The impedance Z_c due to microstrip line width is also a function of the ratio of the height to the width W/H of the transmission line, and also has separate solutions depending on the value of W/H [12].

$$\text{When } \left(\frac{W}{H}\right) < 1 \qquad Z_c = \frac{60}{\sqrt{\epsilon_{eff}}} \ln\left(8\frac{H}{W} + 0.25\frac{W}{H}\right)\ \Omega \tag{5}$$

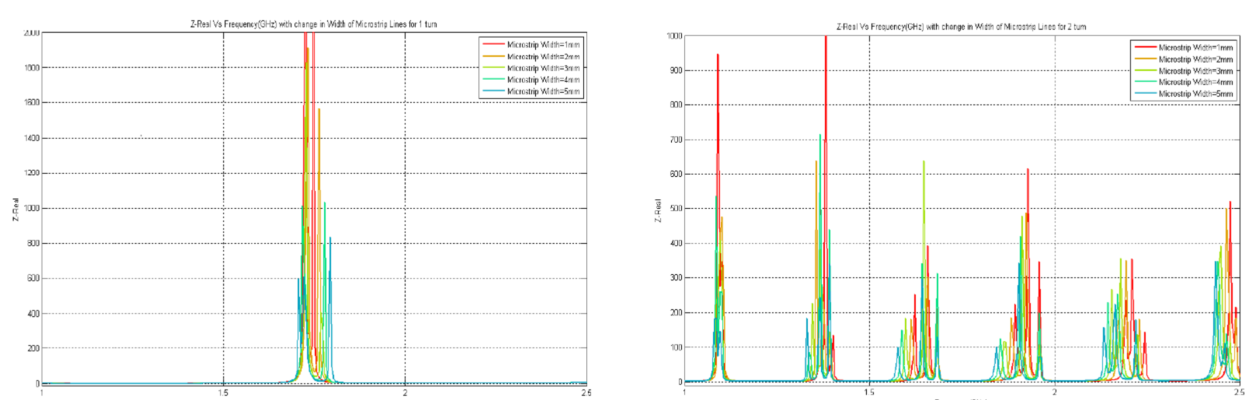

(a) 1 turn (b) 2 turn

Figure 2: Variation of *Z*-real (in Ω) with varying width of Microstrip line for 1 turn and 2 turns respectively with frequency (GHz).

$$\text{When } \left(\frac{W}{H}\right) > 1 \qquad Z_c = \frac{120\pi}{\sqrt{\epsilon_{eff}}\left[\frac{W}{H} + 1.393 + \frac{2}{3}\ln\left(8\frac{W}{H} + 1.444\right)\right]}\,\Omega \tag{6}$$

The impedance of antenna calculated from the above equations does not consider the effect of coupling which is calculated by the scattering parameter matrix of all the four arms in simulation tool [13] and Z-real (in Ω) is calculated by keeping $Z_o = 200\,\Omega$ as constant port impedance.

$$Z_{real} = \sqrt{Z_0}(1-S)^{-1}(1+S)\sqrt{Z_0} \tag{7}$$

where S is the nxn generalized S-matrix consisting of S_{11}, S_{12}, S_{13} and S_{14} for Z_{11}, I is the identity matrix and Z_0 is a diagonal matrix having the impedance of each port assigned as a diagonal value [14]. The huge difference between the impedance of antenna for two different turns is due to the mutual coupling of 2 turn which reduces the Impedance drastically from 1 turn to 2 turn as shown in Fig. 2(a) and Fig. 2(b). The result shows that choosing more microstrip width reduces the impedance of antenna.

3.2. Scattering Parameter

Looking at S_{11} of Figs. 3(a) and 3(b) of 1 turn and 2 turns respectively, it can be contributed that scattering parameters do not indicate too much about the coupling as individual arms are taken into consideration for s-parameter but the S-matrix describes what fraction of power associated with a given field excitation, is transmitted or reflected at each port. If we look at Fig. 3(a) of 1 turn, it can be stated that the maximum width has reasonably good matching and as width reduces matching becomes poor but as number of turns increases as shown in Fig. 3(b), it becomes difficult to acknowledge previous consideration as the S-parameter does not include coupling effect and thus impedance, as shown above in Z-parameter section, plays a significant role in determining which microstrip width or spacing between arms to be chosen, to have less reflection and a desired matching. S-parameter only takes self resonances of each arm into consideration and not coupling between the arms. As far as the S-parameter is concerned they are good to judge the matching of the antenna array with its four arms and due to its periodicity and symmetric design, matching condition will remain the same for every arm.

3.3. RHCP Gain

The Archimedean spiral antennas radiate circularly polarized (CP) wave and its radiation mechanism is first reported by Kaiser [1]. The antenna is radiated in Mode-1, and as the spiral winds outwards from the center, there exists some region for each frequency (wavelength) where the currents add constructively and produce radiation. Spiral Antennas with more arms are used to radiate in multiple modes or to suppress unwanted modes of propagation. The extra arms aid the pattern symmetry because that suppresses the radiation of higher order modes that distort the radiation pattern. We increase the number of arms to suppress higher modes of radiation through the phase cancellation produced by the feed network [14]. The Fig. 4(a) shows that for 1 turn the gain achieved is around 6–7 dB which is constant for most of frequencies and is almost the same

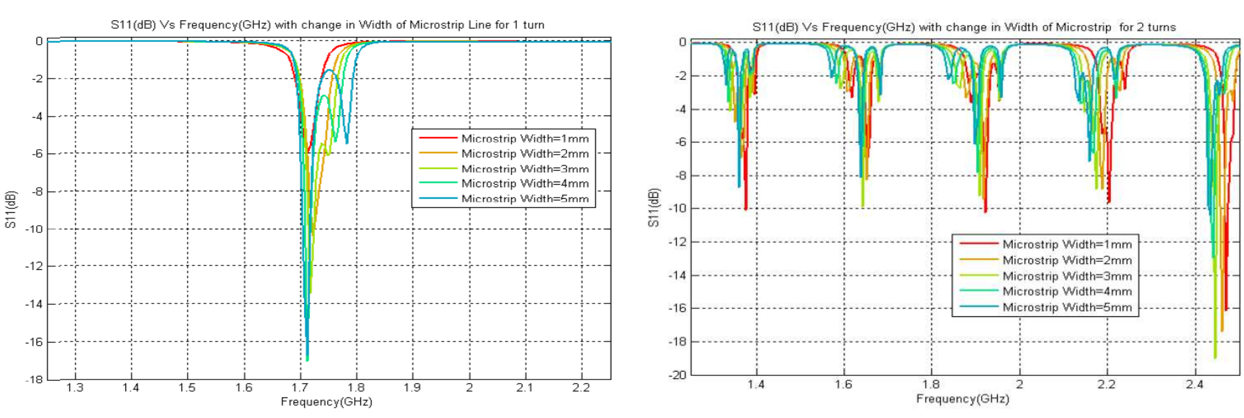

(a) 1 turn (b) 2 turn

Figure 3: Variation of S-parameter (dB) with varying width of Microstrip line of 1 turn and 2 turns respectively with frequency (GHz).

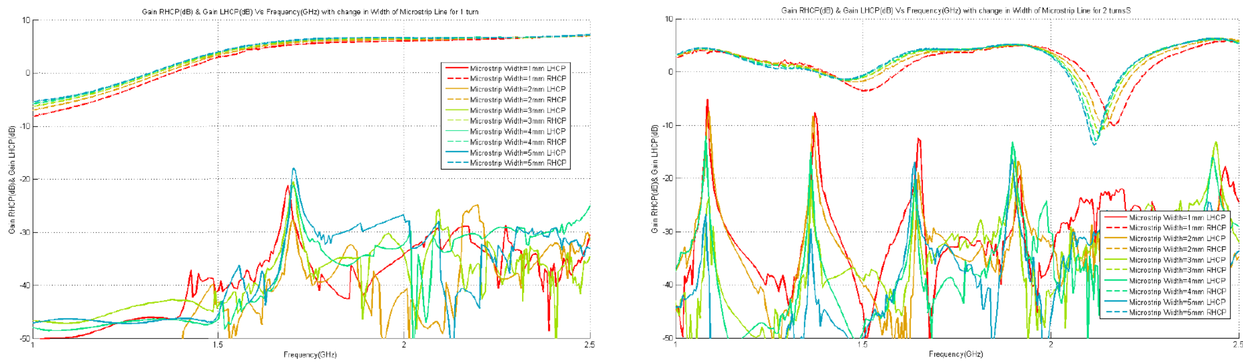

(a) 1 turn

(b) 2 turn

Figure 4: Variation of RHCP & LHCP gain (dB) with varying width of microstrip for 1 turn and 2 turns with frequency (GHz) respectively.

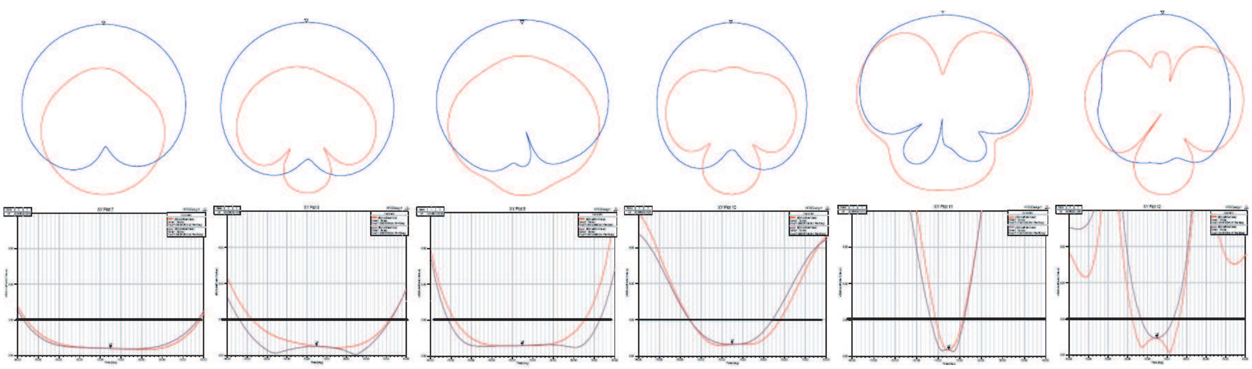

Freq: 1.0853GHz	1.3662GHz	1.6421 GHz	1.9080 GHz	2.1739 GHz	2.4448 GHz
Gain: 4.3572dB	1.4639 dB	3.6857 dB	5.1392 dB	-3.8179dB	6.2469 dB
AR: 0.5974 dB	0.7404 dB	0.8736 dB	0.9492 dB	0.5473 dB	1.3983 dB
CP: -14.5974 dB	-17.1974 dB	-19.5704 dB	-12.2401 dB	-4.6787 dB	-8.8503 dB

Figure 5: 2 turn 3 mm microstrip width showing Row_1 — Radiation Pattern (Blue line: RHCP Gain, Red line: LHCP Gain), Row_2 — axial ratio (line showing 3 dB axial ratio), Row_3 — Resonating Frequency, Row_4 — Maximum RHCP Gain, Row_5 — Axial Ratio ($\Theta = 0°$), Row_6 — Cross Polarization.

for all the width of microstrip lines, while Fig. 4(b) shows that for 2 turns the antenna is showing a good coherence with 6–7 dB of gain at few frequencies and is even negative at some frequencies. Since antenna is Right hand circular polarized, the cross polarization is highly negative as LHCP gain is very low as shown in Figs. 4(a) & 4(b).

To illustrate more on radiation pattern and 3 dB axial ratio an example of 3 mm Microstrip width for 2 turns on the resonating frequencies is shown in Fig. 5.

The above data in Fig. 5 shows that as the frequency increases the radiation pattern becomes narrow & beamwidth also narrows down, as seen in 3 dB axial ratio curve which indicates it starts radiating higher order modes and also very small cross polarization makes this antenna highly right hand circularly polarized.

3.4. Axial Ratio

The tighter wrap of spiral near the outer diameter reduces the change to produce a lower axial ratio design. An outer circumference of 1.17λ is sufficient for 6 dB axial ratio design [14]. As shown in Fig. 6(a) for 1 turn the axial ratio is below 1 dB, which makes this antenna highly circular polarized, but with width there is no much variation all have good coherence with low axial ratio and high circular polarization. But in the case of 2 turns, as shown in Fig. 6(b) the axial ratio for smaller width of microstrip line are more than 3 dB but for microstrip width of 5 mm we still have respectable circular polarization. Increase in the number of turns increases the length of arms but smaller active region of antenna degrades the axial ratio and thus no more circular polarization is achievable.

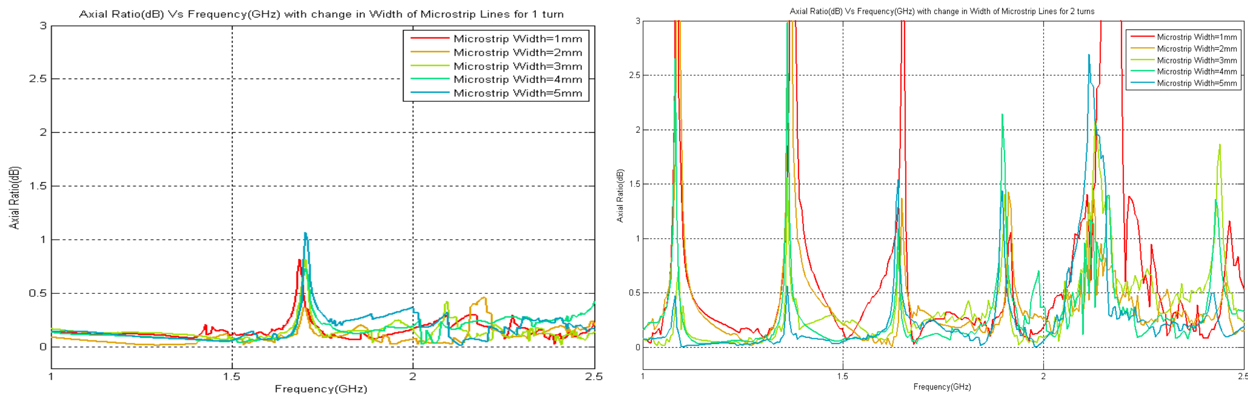

(a) 1 turn (b) 2 turn

Figure 6: Variation of axial ratio (dB) with varying microstrip width for 1 turn and 2 turns with frequency (GHz) respectively.

4. CONCLUSION

This study shows that impedance is critical factor for spiral antennas and can be worked upon in order to reduce it by using wideband matching circuits. The change in width and increase in number of turns shows that there is no reasonable width change effect on RHCP Gain but has effect on Axial ratio, Impedance, so choosing more width of microstrip line helps in better coupling, good matching with 200 Ω of port impedance, lower axial ratio and high circular polarization.

REFERENCES

1. Kaiser, J. A., "The Archimedean two-wire spiral antenna," *IRE Trans. Antennas and Propagation*, Vol. 8, No. 3, 312–323, 1986.
2. Schreider, L., X. Begaud, M. Soiron, and B. Perpere, "Design of a broadband Archimedean spiral antenna above a thin modified electromagnetic band gap substrate," *Antennas & Propagation Conference*, 1–4, Paris, France, Nov. 2006.
3. Khalid, A., M. A. Haron, A. Baharudin, and A. Sulaiman, "Design of a spiral antenna for Wi-Fi applications," *IEEE International RF and Microwave Conference Proceedings*, 431–435, Malaysia, Dec. 2–4, 2008.
4. Powell, J. and A. Chandrakasan, "Spiral slot patch antenna and circular disc monopole antenna for 3.1–10.6 GHz ultra wideband communication," *International Symposium Antennas and Propagation*, Aug. 2004.
5. Kwak, S. L., K. Chang, and Y. J. Yoon, "Small spiral antenna for wideband capsule endoscope," *Electronics Letters*, Vol. 42, No. 23, 9, Nov. 2006.
6. Nakano, H., K. Nogami, S. Arai, S. Mimaki, and J. Yamauchi, "A spiral antenna backed by a conducting plane reflector," *IEEE Transaction Antennas & Propagation*, Vol. 34, No. 6, 725–796, Jun. 1986.
7. Corzine, R. G. and J. A. Morkel, *Four-arm Spiral Antennas*, Artech House, Norwood, MA, 1990.
8. Caswell, E. D., "Design and analysis of star spiral with application to wideband arrays with variable element sizes," Ch. 1, Dissertation, http://scholar.lib.vt.edu/theses/available/etd-01082002-073223/unrestricted/Caswell_etd_Ch1.pdf.
9. Caswell, E. D., "Design and analysis of star spiral with application to wideband arrays with variable element sizes," Ch. 2, Dissertation, http://scholar.lib.vt.edu/theses/available/etd-01082002-073223/unrestricted/Caswell_etd_Ch2.pdf.
10. Changjie, S., W. Guobin, Z. Hu, and X. Ma, "Design and simulation of planar archimedean spiral antenna," *PIERS Proceedings*, 821–824, Xi'an, China, Mar. 22–26, 2010.
11. Booker, H. G., "Slot aerials and their relation to complementary wire aerials (Babinet's principle)," *J. Inst. Electr. Eng.*, Vol. 93, 620–626, 2010.
12. Bahl, I. J. and D. K. Trivedi, "A designer's guide to microstrip line," *Microwaves*, 174–182, May 1977.
13. High Frequency Structure Simulator (HFSS) Help Menu.
14. Milligan, T. A., *Modern Antenna Design*, 2nd Edition, 522–542, Jul. 11, 2005.

Compatibility between Cognitive Radio and the Terrestrial Digital Broadcasting Services in the Digital Dividend Band

W. A. Hassan and T. A. Rahman
Wireless Communication Center, University Technology Malaysia (UTM), Malaysia

Abstract— The switching from analogue to digital broadcasting created newly freed spectrum in the band 470–862 MHz called Digital Dividend band. The sub-band 470–790 MHz is reserved for terrestrial digital broadcasting; however, the band is not fully utilized in many countries and the sharing of it is needed. The cognitive radio system gives the opportunity to share the licensed spectrum without causing interference to the primary service. In this paper, an overview of the compatibility between the cognitive radio system and the terrestrial digital broadcasting in the band 470–790 MHz is conducted. This is done based on the studies, methodologies, results and recommendations conducted by the European Conference of Postal and Telecommunication administration in 2011. Our study investigates the new proposed sensing methodologies for cognitive radio system. The study shows that sensing method is not efficient as a stand-alone technique for the compatibility between cognitive radio system and digital broadcasting systems, whereas the geolocation database is the current most efficient technique.

1. INTRODUCTION

The introduction of the digital broadcasting with high spectral efficiency forced the analogue broadcasting to be phased out. The efficient spectrum usage by the digital broadcasting service creates freed spectrum in the UHF band, which is called the Digital Dividend Spectrum (DDS). The DDS is the main interest of most of the wireless communication systems for its favorable propagation characteristics and consider as a cost effective solution. The sub-band 470–790 MHz is occupied by the terrestrial digital broadcasting in region 1, 2 and 3 [1], but considered as not fully utilized [1]. Many broadcasting users have an alternative broadcasting reception platform such as satellite and cable [1]. Some countries such as Germany, Belgium and Luxemburg have less than 10% of terrestrial broadcasting service [1]. Because of the low spectrum utilization in the sub-band 470–790 MHz, the sharing of it is needed with other communication services for its favorable characteristics such as propagation and penetration. Especially for services that need to accommodate the higher number of users such as mobile and broadband services. The cognitive radio system (CRS) is the proposed technology that can share the spectrum dynamically and operates in the unused frequencies in the digital broadcasting licensed spectrum called TV White Space (TVWS). A recent study [2] conducted by the European Conference of Postal and Telecommunication (CEPT) to investigate the requirements of the CRS operation in the TVWS to ensure the protection of the primary service that already reserve the band. The study investigates three types of spectrum sharing techniques; (i) power sensing, (ii) beacon and (iii) geolocation database.

Our paper investigates the protection of the digital broadcasting service from the CRS emissions using sensing technique. This is done by analyzing the new proposed methodologies published by study [2].

2. SYSTEM PARAMETERS AND ASSUMPTIONS

Since no CRS parameters are currently available, the Long Term Evolution (LTE) parameters will be used as a CRS, since the CRS is expected to be used for broadband using the OFDM modulation for high data rate [2]. Meanwhile, the Digital Video Broadcasting-Terrestrial (DVB-T) will represent the terrestrial digital broadcasting along with its deployment requirement and protection criteria. These parameters are tabulated in Table 1.

3. METHODOLGY

The study [2] have proposed two new methodologies to calculate the required sensing parameters for CRS system; firstly, a methodology to calculate the detection threshold for DVB-T transmission, secondly, a methodology to find the required emission limits (in band and out of band) for the CRS in order not to affect the broadcasting service.

Table 1: The CRS and DVB-T parameters in rural and urban deployment.

	CRS (BS)		CRS (M)	DVB-T (BS)		DVB-T (Receiver)	
Parameter	Rural	Urban	Rural/Urban	Rural	Urban	Rural	Urban
Pt (dBm)	48	24	23	74.6	63.6	----	
Frequency (MHz)	650						
Frequency edge separation (MHz)	33						
$\mathbf{E\_med_{plan}}$	----			56.64		----	
Height (m)	30	23.5	1.5	200	100	10	
Gain (dBi)	15		2.15	0		14.5	
Propagation model	Free space						
Body Loss (dB)	----	3		----			
PR (0)	----			----		27	
ACLR (dB)	45		36	----			
ACS ($\mathbf{\Delta f = 33}$) (dB)	----		----	----		−50	
ACS ($\mathbf{\Delta f = 0}$) (dB)	----		----	----		60	

3.1. Detection Threshold Methodology

The decision of operating the CRS in the TVWS will be based on the detection threshold value. Each DVB-T planning deployment has its own detection value. The sensed power Ps (dBm) is:

$$P_S = E_S - 20\log(f_S) - 77.2 - G_S - L_{pol} - L_{body} \tag{1}$$

where E_S (dBμV/m) is the sense median electric field strength, f_S (MHz) is the sensed frequency, G_S (dBi) is CRS antenna gain, L_{pol} (dB) is the polarization loss. In case of mobile CRS (M-CRS) the Body loss *L_body* (dB) will be considered.

In order to find the P_S, the E_S is needed, and can be calculated as:

$$E_S = Emed - \mu_{sense}\,\sigma_{sense} \tag{2}$$

$$Emed = Emed_{plan} - \Delta H_{\text{DVB-T\_CRS}} \tag{3}$$

where *Emed* (dBμV/m) is DVB-T median electric field strength received by the DVB-T receiver, $\mu_{sense}\ \sigma_{sense}$ (dB) is the shadowing margin related to the variation of the sensed signal. $Emed_{plan}$ (dBμV/m) is the planned median electric field strength for s specified deployment, $\Delta H_{\text{DVB-T\_CRS}}$ (m) is the height loss based on the [3].

3.2. The CRS Emission Limits for the Broadcasting Protection Methodology

In order to protect the broadcasting service from the CRS emission, the CRS need to calculate its own in band power (PIB) in dBm and the out of band power (POOB) in dBm. These two parameters are calculated as:

$$\begin{aligned}\text{PIB} \;=\;& P_{\text{DVB-T\_min}}(fs) + \sigma\mu_{\text{DVB-T}} - \text{PR}(0) - 3 + \text{ASC}_{\text{DVB-T}}(f_{\text{CRS}} - f_{\text{DVB-T}}) \\ & -q\sqrt{\sigma^2_{\text{DVB-T}} + \sigma^2_{\text{CRS}}} - \text{MI} - \text{SM} + Dir + Pol - Gi + Lf + Pl(d_{\text{CR-BS}})\end{aligned} \tag{4}$$

where $P_{\text{DVB-T\_min}}$ (dBm) is the DVB-T minimum transmitted power at frequency f_S, $\mu\sigma_{\text{DVB-T}}$ (dB) is the shadowing margin related to the variation of the DVB-T transmitted signal, $\sigma_{\text{DVB-T}}$ (dB) is the standard deviation of the shadowing between the DVB-T transmitter and receiver, PR(0) (dB) is the protection ratio for the DVB-T receiver in co channel based on the values of [4], ACS (f_{CRS}–$f_{\text{DVB-T}}$) (dB) is the adjacent channel selectivity for the DVB-T receiver for the frequency offset (f_{CRS}–$f_{\text{DVB-T}}$), σ_{CRS} (dB) is the standard deviation of the shadowing between the CRS transmitter and receiver (dB), q (dB) is the Gaussian confidence factor related to the target location percentage where protection to be calculated. MI (dB) is the multiple interference margin, SM (dB) is the safety margin, *Dir* (dB) is the DVB-T receiver antenna directivity discrimination, *Pol* (dB) is the DVB-T receiver polarization, *Lf* (dB) is the feeder loss of the DVB-T receiver.

Based on the PIB calculation, the POOB can be calculated as:

$$\mathrm{POOB} = \mathrm{PIB} - \mathrm{ACLR}_{\mathrm{CRS}} \tag{5}$$

3.3. The Clutter Loss

An addition to the study [2] methodology is the clutter loss CL (dB) based on the ITU-R 452-14 [5], the cluster loss will clearly show the different environments effect on the compatibility results for rural and urban environments.

4. SHARING SCENARIO FOR THE PROTECTION OF DVB-T SERVICE FROM THE CRS

Figure 1 shows the possible interference scenario that the CRS may cause. In the figure, the CRS is allocated in area 2 and operating in an unused frequency (F2), which is adjacent to a used frequency (F1). The DVB-T service is deployed in area1 and operating in the frequency F1. The sharing scenario is assumed to be deployed in rural and urban environments to analyze the difference in DVB-T deployment planning. The investigation will assess the emission limit of the CRS verses the separation distance (D1) between the mobile (M-CRS) and the DVB-T receiver.

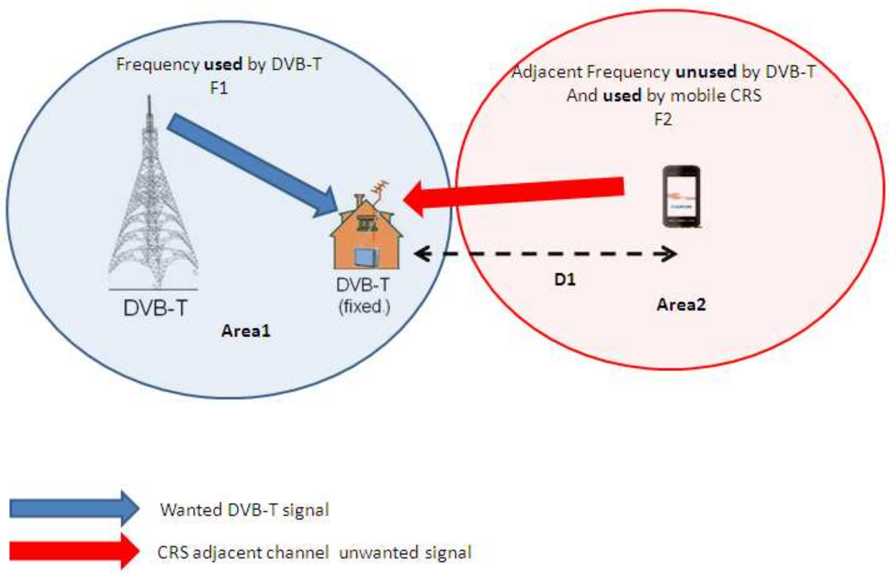

Figure 1: The compatibility scenario between the DVB-T operating in F1 and deployed in area1 and the M-CRS operating in an unused frequency F2 and deployed in area 2.

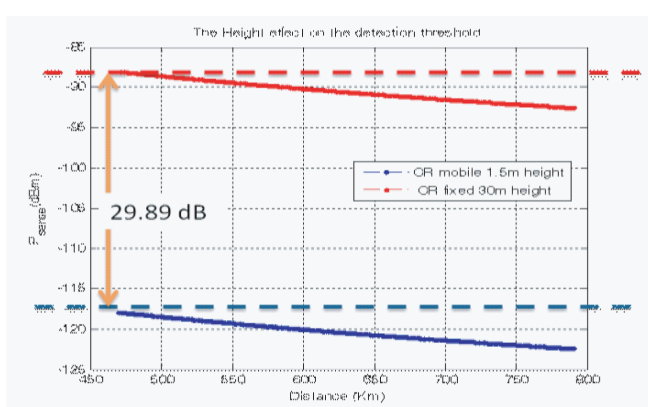

Figure 2: The sensing detection threshold as a function of operating frequency from 470 MHz to 790 MHz.

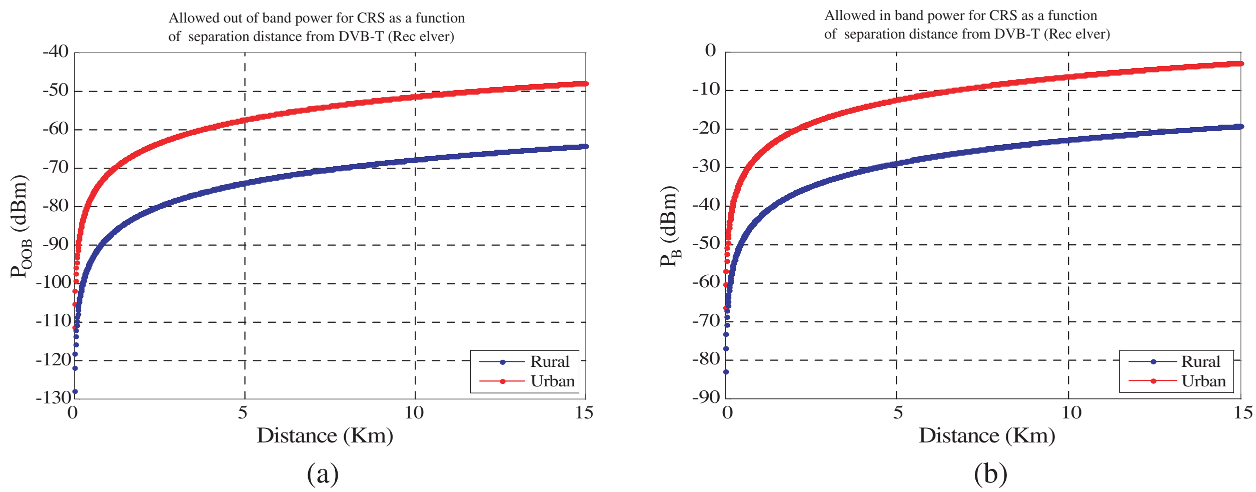

Figure 3: The (a) in band power PIB and (b) out of band power POOB for the CRS in order not to affect the DVB-T reception as a function of distance in rural and urban environments with frequency edge separation of 33 MHz.

5. RESULTS AND DISCUSSION

5.1. Detection Threshold (DT)

In Figure 2, the DVB-T detection threshold level is investigated for different CRS height (i.e., fixed CRS (F-CRS) reception with 30 m height and mobile CRS reception with 1.5 m height) in the frequency band 470–790 MHz. The figure shows that the sensing threshold depends on following: (i) the type of the deployment of the DVB-T, (ii) the environments and (iii) the operating frequency.

Base on the above figure, it can be concluded that the sensing threshold can be improved based on the CRS and DVB-T height difference. The F-CRS reception has 29.89 dB higher sensing levels than the M-CRS. The values of the detection threshold range from −88.05 dBm to −92.56 dBm for F-CRS reception and −117.9 to −122.4 dBm for M-CRS reception in the frequency range 470–790 MHz. These values seem extremely challenging to the current technologies in order to detect them.

5.2. CR Emission Limits

Figure 3 show the required PIB and POOB limits for CRS operation. The values are functions of distance between the DVB-T receiver and the M-CRS. Figure 3 shows the low values for the CRS emission even with a frequency edge separation of 33 MHz. In the distance range from 0 to 15 Km, the PIB values ranges from (−76.86/66.47) to (−19.37/ − 2.94) dBm and POOB values ranges from (−121.9/ − 111.5) to (−47.95/ − 64.37) dBm in rural and urban deployment. These low values will be hard to be used in practical operation. The differences in these values are because the protection ratio (PR) in urban area is lower than PR in rural area. These values show that the environment deployment does not affect the emission limit calculation.

6. CONCLUSIONS

The CRS sensing technique is investigated for the compatibility between the CRS and DVB-T system in the band 470–790 MHz. The study analyzes the current sensing proposed methodology. Based on the results, the sensing technique is considered not efficient, firstly, because the detection threshold depends on the planning of the DVB-T system, and these values are challenging to current technologies. Secondly, the low emission levels for the CRS to operate are considered not practical. Finally, in order to CRS to establish its own calculation to find the allowable emission limits, it requires knowledge of the distance and its pathless, the terrain shape and clutter path and finally the DVB-T receiver antenna discrimination. These parameters require a database to store their values. Therefore, currently the geolocation data base technique is considered as the most efficient technique for the CRS system to share the unused spectrum.

REFERENCES

1. Modlic, B., G. Sisul, and M. Cvitkovic, "Digital dividend — Opportunities for new mobile services," *51st International Symposium ELMAR*, 1–8, Zadar, Croatia, Sep. 28–30, 2009.

2. ECC Report 159, "Technical and operational requirement for the possible operation cognitive radio system in the white space of the frequency band 470–790 MHz," *ECC*, Cardiff, 2011.
3. ITU-R P.1546-4, "Method for point-to-area predictions for terrestrial services in the frequency range 30 MHz to 3 000 MHz ," *ITU*, Oct. 2009, Acess Date: Nov. 15, 2011, available from www.itu.com.
4. RRC-06, "Final acts of the regional radiocommunication conference for planning of the digital terrestrial broadcasting service in parts of regions 1 and 3, in the frequency bands 174–230 MHz and 470–862 MHz (RRC-06)," *ITU*, Geneva, 2006, Acess Date: Nov. 15, 2011, available from www.itu.com.
5. ITU-R P.452-14, "Prediction procedure for the evaluation of interference between stations on the surface of the Earth at frequencies above about 0.1 GHz," *ITU*, Oct. 2009, Acess Date: Nov. 15, 2011, available from www.itu.com.

The Digital Dividend Spectrum in Asia

W. A. Hassan, Y. Abdulrahman, and T. A. Rahman
Wireless Communication Center, University Technology Malaysia (UTM), Malaysia

Abstract— The introduction of the digital broadcasting with high spectral efficiency forced the analogue terrestrial broadcasting to be phased out. The efficient spectrum usage by the digital broadcasting creates a freed spectrum in the Ultra High Frequency (UHF) band, which is called Digital Dividend Spectrum (DDS). In 2008, the European Communication Office (ERO) proposed the first frequency channel assignment (FCA) for mobile service operating in the DDS band for region 1. The second FCA was proposed by the Asian Pacific Telecommunity (APT) in 2010 for region 3. Because of the late submission of the APT FCA, some countries in region 3 follow the European FCA, the other the follows the APT FCA. Clearly, region 3 will not have a harmonized FAC, although the APT channel assignment approach is more favorable than European FAC. The study is conduced to review the non harmonized DDS issues in Asia. The study recommends the administration of region 3 to take a cooperative step in order to benefit maximally from the DDS.

1. INTRODUCTION

The world is witnessing the transitions from analogue to digital broadcasting in the Ultra High Frequency (UHF) band below 1 GHz, which has led to the creation of the Digital Dividend spectrum (DDS) band. A wide range of researches were conducted to investigate the preferred frequency channel assignment (FCA) for the mobile service in the DDS. Currently, there are two FAC proposals submitted to the International Telecommunication Union (ITU): (**i**) the European Harmonized FAC submitted by the European Conference for Postal and Telecommunity (CEPT) in 2008 for region 1 (Europe, Africa) [1] and (**ii**) the Asian Pacific Telecommunity (APT) FAC proposal for region 3 submitted in 2010 [2]. Due to early submission of the CEPT proposal, some countries in region 3 adopted the European FAC proposal such as Malaysia [3], while others adopted the APT proposal. This will create a non-harmonized spectrum in the near future leading to an inefficient use of the new DDS. The main aim of the paper is to emphasize the expected non harmonized DDS problem in region 3.

2. ASIA (REGION 3)

2.1. The Digital Broadcasting Standards in Region 3

Region 3 countries differ in digital broadcasting standards. Some follow European standard, while others follow region 2. China and Korea have their own standard. These differences would lead to incompatibility between varied broadcasting services in region 3 countries. Some countries are ready to migrate to digital broadcasting such as Japan, Korea, Singapore, while others, such as Malaysia and Indonesia, are still in trial stages. This implies that the transition to digital broadcasting will be based on a country-by-country basis in region 3 [4].

Different administration research groups and studies have published reports and studies regarding the DDS band in region 3 [2, 4–7]. These studies had concluded that region 3 will not have a harmonized DDS. For instance, some countries will use the region 1 FCA, while others will follow the APT FCA. The studies also highlighted that the DDS allocations are different in region 3 countries. These differences are due to the fact region 3 have different broadcasting services. Unlike region 1 that has only one broadcasting system, which is the DVB and uses the European FAC.

Indonesia is considered as one of the region 3 countries that have issues in the analogue to digital broadcasting migration plan. Its plan consists of three phases, (i) the analogue broadcasting operation, followed by (ii) a simulcast phase (i.e., both digital and analogue broadcasting uses the DDS band) and finally, (iii) the digital switch over phase, where the band will be used for both mobile and broadcasting services. The final stage should have been reached after the year 2015. However, according to GSMA workshop conducted in London in 2010, regarding the spectrum in Indonesia, the migration from analogue to digital broadcasting has not yet commenced [7]. This implies that Indonesia will not benefit from the DDS until the country starts the first migration stage that should be in 2015 according to the GE-06. Additionally, this will affect the transition from analogue to digital broadcasting of neighboring countries, such as Singapore. This is due to sensitivity of digital broadcasting to interference from high transmitted power by the analogue broadcasting radiation.

2.2. APT FCA

The APT Wireless Form (AWF) had conducted studies on the band 698–806 MHz, and the outcomes were the FCA in 2008 as a first response from APT to the WRC-07 agenda 1.17. In 2010, the AWF-8 had conducted a consensus regarding the basic FCA for the proposed 698–806 MHz band. At the end of 2010, the AWF-9 had conducted further discussions regarding the studies that were submitted as contributions from different countries. The reports of the studies were used to deliver the first harmonized FCA draft of the region 3. Two approaches were presented for the Frequency Division Duplex (FDD) and Time Division Duplex (TDD) modes, as briefly described in the following subsections.

2.2.1. FDD Mode

As shown in Figure 1 the FDD spectrum allocation contains 2×45 MHz block band for Uplink (UL) and Downlink (DL) communication. The spectrum block allocation has a duplex gap of 10 MHz wide (748–758 MHz). The UL guard band is 5 MHz (698–703 MHz) wide and DL guard band is 3 MHz (806–803 MHz) wide.

2.2.2. TDD Mode

Figure 2 shows the APT approach for the TDD arrangement. The TDD approach had a 4 MHz guard band (694–698 MHz), an internal guard-band of 5 MHz at the lower edge (698 MHz) and 3 MHz at the upper edge (806 MHz).

The DDS bandwidth is 90 MHz, and its allocation is between 698 to 806 MHz (simply denoted as 700 MHz band). These two facts make the band more favorable in terms of propagation characteristics compared to the 800 MHz (i.e., 790–862 MHz) band, as will be shown in Section 3.

3. COMPARISON BETWEEN THE ASIAN AND THE EUROPEAN FREQUENCY CHANNEL ASSIGNMENTS

Based on the presented FAC, Table 1 shows the comparison between different frequency assignments for the Asian and European countries.

Cleary, Table 1 shows that the APT FAC approach is more favorable due to the following reasons: **i)** higher band availabilities. **ii)** The band location (i.e., 700 MHz) is more efficient than the 800 MHz in terms of propagation and CAPEX, as shown in Table 2, based on BBC R&D.

The European harmonized FCA has an advantage over the APT FCA as it will be used by all the members union. In other words, the harmonization is achieved because all region 1 countries use one digital broadcasting standard (i.e., DVB-T) and the CEPT FAC. This will maximize the DDS usage efficiency.

4. THE MALAYSIN DDS AS A PROPOSED CASE STUDY

Currently, in Malaysia the band 790–862 MHz is occupied by fixed, mobile and broadcasting services. The DDS band in Malaysia is shown in Figure 3. The 790–824 MHz and 832–869 MHz bands are allocated for either UL or DL transmission. This shows that there are 34 MHz and 37 MHz frequency portions; whereas the duplex gap is 8 MHz. The limitations of the Malaysian DDS are

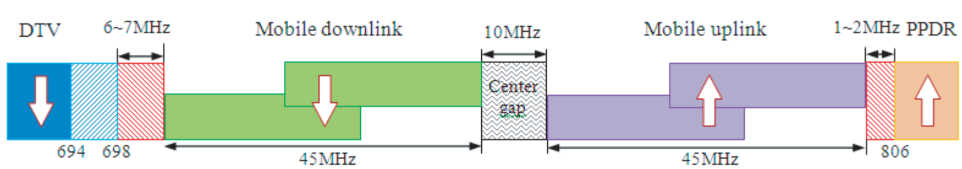

Figure 1: The APT harmonized FAC, FDD mode [4].

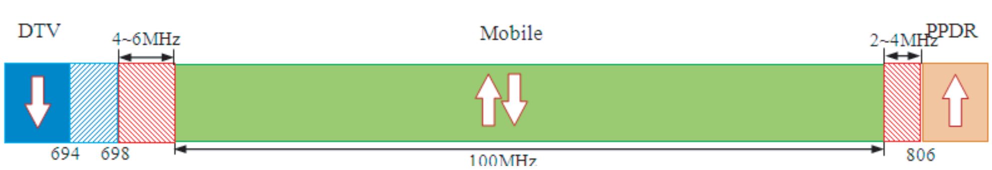

Figure 2: The APT harmonized FAC, TDD mode [4]

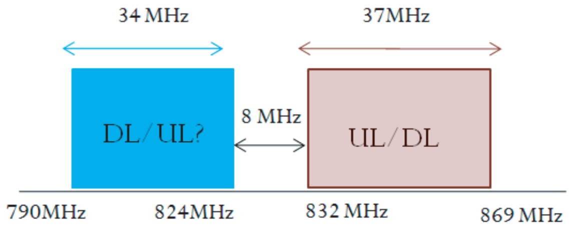

Figure 3: The current Malaysian FAC in the band 790–869 MHz [19].

Table 1: Comparison between the Region 1 and region 3 channel allocation.

Parameters (MHz)		CEPT	APT
FDD			
UL Freq		832–862 (30)	694–739 (45)
DL Freq		791–821 (30)	749–794 (45)
Available BW		60	90
Duplex Gap		11	10
UL Guard band		0	5
DL Guard band		3	1
Channels	1.4	~ 21	32
	3	10	15
	5	6	~ 7
	10	3	~ 4
	15	2	3
	20	1	~ 2
	100	X	X
TDD			
Allocation		798–862	698–806
Bandwidth		59 (option 5)	96
Duplex Band		5	5
UL Guard band		0	3
DL Guard band		1	4
Channels	1.4	~ 42	~ 68
	3	~ 19	32
	5	~ 11	~ 19
	10	~ 5	~ 9
	15	~ 3	~ 6
	20	~ 2	~ 4
	100	X	X

as follows: (i) The duplex gap is 8 MHz. According to a current study [8] the duplex gap needs to be greater than 10 MHz in the 800 MHz band. (ii) In case Malaysia willing to adopt the Long Term Evolution- Advanced (LTE-A) as a mobile service, this will indicate that the Malaysian DDS is reversed duplex direction (i.e., upper part of the spectrum is UL and the lower part is DL), as shown in Figure 8. If this is bound to happen, then there would be no guard band between the mobile services and other services that are in the lower frequencies than the 790 MHz. According to the same study [8], the compliance is not impossible with a guard band of zero MHz.

Clearly, more studies and investigation are required in the Malaysian DDS for efficient use of the spectrum. The harmonization with neighboring countries is also required to be investigated. In Malaysia, one of the neighboring counties (Singapore) is ready to migrate to the digital broadcasting while Indonesia did not start its first migration phase. For maximum benefit of the DDS, Cooperation steps are required between the neighboring countries.

Table 2: Comparison between the 700 MHz and 800 MHz bands.

	700 MHz band	800 MHz band
No of BSs	$\approx$ 1 to 2	$\approx$ 3 to 5
Coverage (Km)	$\approx$ 10 to 11	$\approx$ 8 to 9
CAPEX	$\approx$ 100%	$\approx$ 120%

5. CONCLUSIONS

The Asian DDS is critically investigated. Different DDS proposals have been overviewed. The capabilities and limitations of each proposal were highlighted in details. The comparison shows that the former approach is more favorable than the latter. Many countries are still in the trial stage of the migration from analogue to digital broadcasting, especially in region 3, where Indonesia is given as a good example. This will delay the creation of the DDS in Asia. Finally Malaysian DDS was proposed as a case study. The capabilities and limitations of the Malaysian DDS allocation were also discussed. The Asian countries need to cooperate by reaching a fair solution in adopting a harmonized DDS FAC, if not this will result in serious limitations in DDS utilization.

REFERENCES

1. CEPT Report 30, "The identification of common and minimal (least restrictive) technical conditions for 790–862 MHz for the digital dividend in the European Union," *European Conference of Postal and Telecommunications (CEPT)*, 2009, Available from: http://www.erodocdb.dk/doks/doccategoryECC.aspx?doccatid=16.
2. "Draft report on the technical analysis of the FDD and TDD channel arrangement in the UHF band of Region 3," Republic of Korea, (APT), 2010.
3. "Draft reviewed spectrum plan," Cyberjaya, MCMC, 2010.
4. "Harmonised frequency arrangement for the band 689–806 MHz," APT, Seoul, ITU, 2010.
5. Setiawan, D., D. Gunawan, and D. Sirat, "Interference analysis of guard band and geographical separation between DVB-T and E-UTRA in digital dividend UHF band," *Icici-bme: International Conference on Instrumentation, Communication, Information Technology, and Biomedical Engineering*, 254–259, 2009.
6. Sirat, D., D. Setiawan, and M. F. Mirza, "A basic framework analysis on the needs of radio frequency spectrum allocation at ultra high frequency (UHF) band for digital terrestrial TV broadcasting in indonesia," *Second International Conference on Computer Engineering and Applications (ICCEA)*, 73–77, Bali Island IEEE, March 19–21, 2010.
7. Setiawan, D., *Overview of the Spectrum Issues in Indonesia*, London, 2010.
8. Karimi, H. R. F., M. Lapierre, and E. G. Fournier, "European harmonized technical conditions and band plans for broadband wireless access in the 790–862 MHz digital dividend spectrum," *2010 IEEE Symposium on New Frontiers in Dynamic Spectrum*, 1–9, Singapore, IEEE, April 6–9, 2010.

Analytical Unit Pulse Propagation in an Active Single Resonance Lorentzian Medium

Ali Abdolali, **Maziar Hedayati**, **and Shahram Hedayati**
Department of Electrical Engineering, Iran University of Science and Technology, Iran

Abstract— In a causally dispersive medium the signal arrival appears in the dynamical field evolution as an increase in the field amplitude from that of the precursor fields to that of the steady-state signal. The classical theory of Sommerfeld and Brillouin of pulse propagation in a Lorentz medium is reexamined. While many rigorous studies of wave propagation in passive Lorentzian media have been performed, the corresponding problem in active media has remained theoretically unexplored. We use analytical approximations for describe the correct saddle-point. In this method used the refractive index for the determination of the response of an active Lorentzian medium. In this paper illustrated that do not exist distance saddle points and then the near saddle points used for the determination of the response of an active Lorentzian medium to a step modulated pulse. There are Two types of wave dispersion, (Temporal dispersion and Spatial dispersion). Here used the time dispersion and surveyed in the frequency domain.

1. INTRODUCTION

Wave propagation through a linear, temporally dispersive medium has been a complex and sometimes controversial research topic since the 19th century. Hamilton did the first study on the dispersive medium in the 1839 which the time that Group velocity is introduce. Subsequently, Rayleigh describe the difference between Group velocity and phase velocity. Classical Lorentz models, Debye and Drude has been the turning point feature in speech the liner Nonconductor medium. Sommerfeld and Brillouin were among the early researchers studying the wave propagation in linear, homogeneous, isotropic, causally dispersive media. With Sommerfeld's proof within the classical Maxwell-Lorentz theory that an electromagnetic signal could not propagate faster than the vacuum speed of light in a Lorentz model dielectric, Brillouin then introduced the signal and energy velocities within that medium as a replacement for the group velocity This theory is valuable because it provides analytic expressions for the dynamics of pulses under mature dispersion conditions in a medium that accurately models several real lossy dispersive materials [1]. Their study led to the discovery of two Precursor signal. In the classical theory of dispersive pulse propagation. Both a high-frequency (above resonance) Sommerfeld precursor and a low-frequency (below resonance) Brillouin precursor are present in the propagated field structure when the input pulse is ultra wideband. That's the approach the refractive index were replaced with Mac Lauren series of refraction depending on the frequency. The result was a simple phrase that was associated with complex frequency, distance and time. At after time Handelsman and Bleistein removed the shortcoming of this method byuniform asymptotic approach. But Einstein did the newest method for describing propagation wave in this media [2]. In this paper we consider the propagation of wave in an active Lorentzian medium. Recently, there has been experimental observation of superluminal velocities in active media. This paper is organized as follows. In Section 2, we present the active Lorentzian medium, which is a model for an inverted two level atomic medium. In Section 3, presented we achieve saddle points by analytical method. Section 4 includes the asymptotic analysis of the wave propagation in an active Lorentzian medium.

2. THE COMPLEX INDEX OF REFRACTION FOR THE ACTIVE LORENTZIAN AND THE LOCATIONS OF BRANCH POINT LOCATION

The analysis is presented here. The analysis is presented for the case of a single-resonance Lorentz model dielectric with dielectric permittivity

$$\frac{\varepsilon(\omega)}{\varepsilon_0} = 1 + \frac{b^2}{\omega^2 - \omega_0^2 + 2i\delta\omega} \tag{1}$$

where ω_0 is the undammed resonance frequency,

$$b^2 = \frac{2\pi N|f|\theta^2}{m} \tag{2}$$

where ω_0 is the frequency difference between the two levels ω_p is the plasma frequency with number density N of Lorentz oscillators, me the mass of an electron, f and e, are the oscillator strength, electron charge and δ is the line width of the resonance. With relative magnetic permeability $\mu = \mu_0$, the complex index of refraction is given by

$$n(\omega) = \sqrt{\epsilon(\omega)/\epsilon_0} = \sqrt{1 + \frac{b^2}{\omega^2 - \omega_0^2 + 2i\delta\omega}} \tag{3}$$

Based on these inequalities an arbitrary set of the parameters for the active Lorentzian medium is chosen as, $\omega_0 = 4.0 \times 10^{15}$ Hz, $b = 1.0 \times 10^{15}$ Hz, $\delta = 0.2 \times 10^{15}$ Hz.

Figure 1 shows the plot of the real and imaginary part of the refractive index of the medium in active and passive case and Fig. 2 the imaginary of them. The branch point locations are given by

$$\begin{aligned} \omega'_{\pm} &= \pm\sqrt{\omega_1^2 - \delta^2} - \delta i \\ \omega_{\pm} &= \pm\sqrt{\omega_0^2 - \delta^2} - \delta i \end{aligned} \tag{4}$$

where $\omega_1^2 = \omega_0^2 - b^2$.

The branch lines chosen here consists of the line segments $\omega'_+\omega_+$ and $\omega'_-\omega_-$ as shown in Fig. 3. We can analyze $n(\omega)$ in the complex w-plane expect in the $\omega'_+\omega_+$, $\omega'_-\omega_-$.

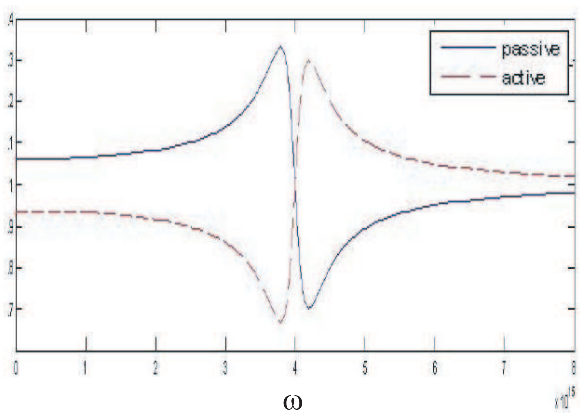

Figure 1: The real part of the refractive index for passive and active media.

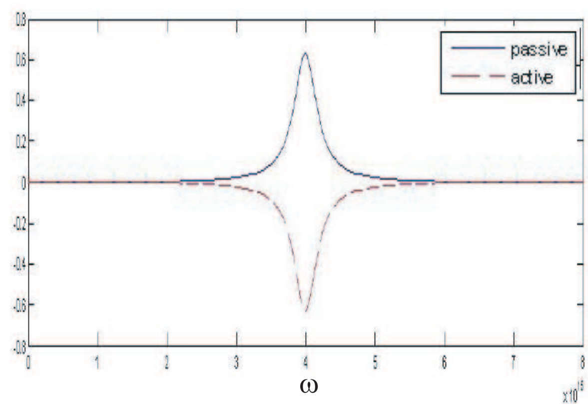

Figure 2: The imaginary part of the refractive index for passive and active media.

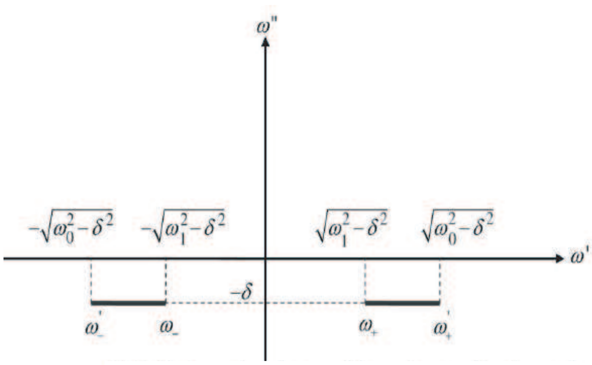

Figure 3: Branch points and branch cuts for the active single resonance Lorentzian medium.

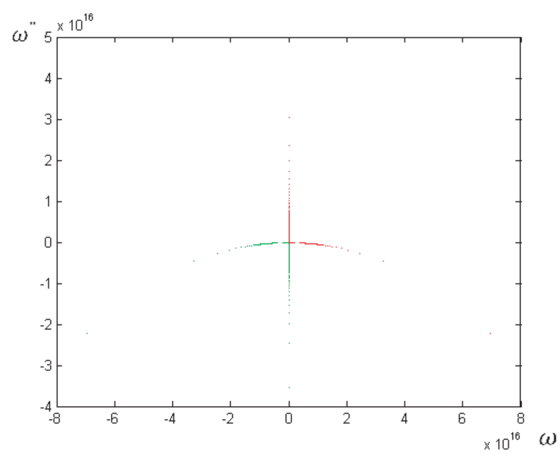

Figure 4: A general picture of the two distance saddle points path.

3. ANALYSIS OF THE PHASE FUNCTION AND ITS SADDLE POINTS

For achieve the response of wave that propagating in the dispersive media we must solve this integration [3]

$$A(Z,t) = \frac{1}{2\pi} \oint \tilde{f}(\omega) \exp\left[i(k(\omega)Z - \omega t)\right] \quad Z > 0 \tag{5}$$

where $\tilde{f}(\omega)$ is the is the Laplace transform of the initial time behavior of the wave at the plane boundary $z = 0$, In preparation for the asymptotic analysis in a temporally dispersive medium, it is necessary first to determine the location of saddle point. If $\varphi(\omega, \theta)$ is the complex phase function which is defined as follows

$$\Phi(\omega, \theta) = i\omega[n(\omega) - \theta]$$

To obtain the asymptotic expansion of the propagated field $A(z, t)$ we must study the behavior of $\varphi(\omega,\theta)$ in the saddle points. The condition that $\varphi(\omega,\theta)$ be in the saddle point

$$n(\omega) + \omega n'(\omega) - \theta = 0 \tag{6}$$

The roots of this equation then give the desired saddle-point locations. So

$$\left(\frac{\omega^2 - \omega_1^2 + 2j\delta\omega}{\omega^2 - \omega_0^2 + 2j\delta\omega}\right) - \frac{b^2\omega(\omega + i\delta)}{\left(\omega^2 - \omega_0^2 + 2j\delta\omega\right)^2} = \theta\left(\frac{\omega^2 - \omega_1^2 + 2j\delta\omega}{\omega^2 - \omega_0^2 + 2j\delta\omega}\right)^2 \tag{7}$$

where

$$\omega_1^2 = \omega_0^2 - b^2$$

We can the roots of this equation to be calculated numerically the and gain the saddle point but we use the analytical method and with good approximation for this work. The degree of this equation is eight so we have eight root but the four of this them is acceptable.

3.1. High-frequency Approximation

To solve the Eight-degree equation use of both high and low frequency approximation

$$\frac{1}{\theta^2(\omega^2 - \omega_0^2 + 2\delta i\omega)}\left[\omega^2 - \omega_1^2 + 2\delta i\omega - \frac{b^2\omega(\omega + \delta i)}{\omega^2 - \omega_0^2 + 2\delta i\omega}\right]^2 = \omega^2 - \omega_1^2 + 2\delta i\omega$$

therefore to achieve the distant saddle points we use the bellow approximation

$$\begin{gathered}\frac{b^2\omega(\omega + i\delta)}{\left(\omega^2 - \omega_0^2 + 2j\delta\omega\right)^2} \simeq b^2\left(1 - \frac{\delta i}{\omega} + O\left(\frac{1}{\omega^2}\right)\right) \\ \omega^3 + 2\delta i\omega^2 - \left(\omega_0^2 - \frac{b^2\theta^2}{\theta^2 - 1}\right)\omega - \frac{2i\delta b^2}{\theta^2 - 1} = 0\end{gathered} \tag{8}$$

3.2. Low-frequency Approximation

To obtain description of the near saddle point locations, We use the Equation (7) with eight degree which may be rewritten as that used Taylor expansion

$$\begin{aligned}\theta^2\left(\omega^2 - \omega_0^2 + 2j\delta\omega\right) \; = \; & \omega^2 - \omega_1^2 + 2j\delta\omega - 2b^2\frac{\omega(\omega + \delta i)}{\omega^2 - \omega_0^2 + 2j\delta\omega} \\ & + b^4\frac{\omega^2(\omega + \delta i)^2}{(\omega^2 - \omega_1^2 + 2j\delta\omega)(\omega^2 - \omega_0^2 + 2j\delta\omega)}\end{aligned} \tag{9}$$

If $|\omega| \ll |\omega_0$

$$\frac{\omega^2(\omega + \delta i)^2}{\left(\omega^2 - \omega_0^2 + 2j\delta\omega\right)^2\left(\omega^2 - \omega_1^2 + 2j\delta\omega\right)} \cong -\frac{\omega^2}{\omega_1^2\omega_0^4}\left[-\delta^2 + 2\delta\omega i - \frac{2\delta^3 i}{\omega_0^2\omega_1^2}\left(2\omega_1^2 + \omega_0^2\right)\omega\right]$$

And

$$\frac{\omega(\omega + \delta i)}{\omega^2 - \omega_o^2 + 2j\delta\omega} \cong -\frac{1}{\omega_0^2}\left[\delta i\omega + \left(1 - \frac{2\delta^2}{\omega_0^2}\right)\omega^2 + \frac{\delta i}{\omega_0^2}\left(3 - 4\frac{\delta^2}{\omega_0^2}\right)\omega^3\right]$$

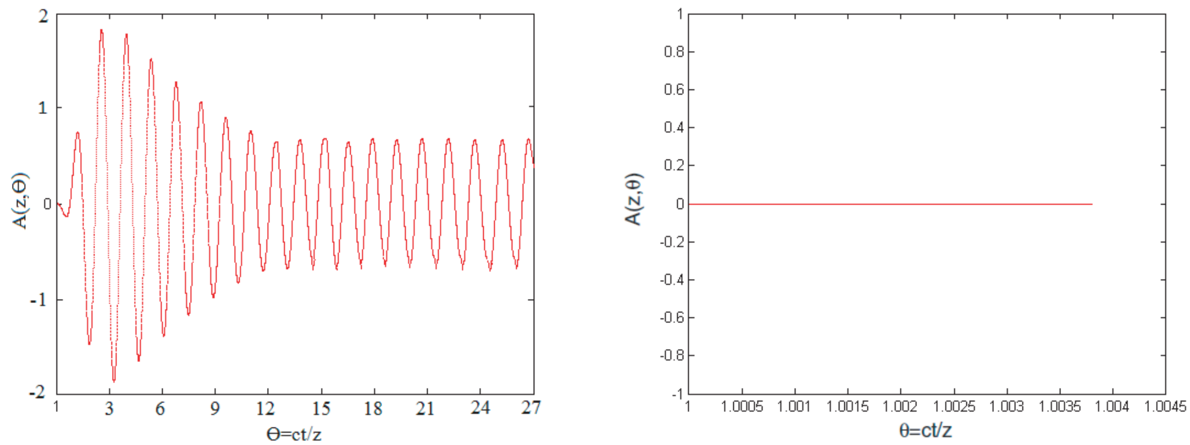

(a) (b)

Figure 5: Total sampled field at 1 μm inside the active media for (a) $1.0038 < \theta < 10$; (b) $1 < \theta < 1.0038$.

By replacing this approximation and if $\delta \ll b$, ω_0, Equation (8) simplified

$$\begin{aligned}
&\omega^2 + 2\delta i \frac{\theta^2 - \theta_0^2 - \frac{2b^2}{\omega_0^2}}{\theta^2 - \theta_0^2 - \frac{3b^2}{\omega_0^2}\alpha}\omega - \frac{\omega_0^2\left(\theta^2 - \theta_0^2\right)}{\theta^2 - \theta_0^2 - \frac{3b^2}{\omega_0^2}\alpha} = 0 \\
&\alpha = 1 - \frac{\delta^2}{3\omega_0^2\omega_1^2}(4\omega_1^2 - b^2)
\end{aligned} \tag{10}$$

With solving the equation obtained the near saddle points.

$$\begin{aligned}
&\omega_{sp_N}^{\pm} \cong \pm\psi(\theta) - 2j\delta\zeta(\theta)\psi(\theta) = \left[\frac{\omega_0^2(\theta^2 - \theta_0^2)}{\theta^2 - \theta_0^2 - \frac{3b^2}{\omega_0^2}\alpha} - \delta^2\left(\frac{\theta^2 - \theta_0^2 - \frac{2b^2}{\omega_0^2}}{\theta^2 - \theta_0^2 - \frac{3b^2}{\omega_0^2}\alpha}\right)^2\right]^{1/2} \\
&\zeta(\theta) = \frac{3}{2}\frac{\theta^2 - \theta_0^2 - \frac{2b^2}{\omega_0^2}}{2\theta^2 - \theta_0^2 - \frac{3b^2}{\omega_0^2}\alpha}
\end{aligned} \tag{11}$$

Fig. 4 shows a general picture of the two near saddle points path that we achieve by analytical method.

4. ASYMPTOTIC CALCULATION OF THE FIELD $A(Z, \theta)$

After obtaining the dynamics of saddle points and surviving of the topography of the phase function $\Phi(\omega, \theta)$ it is now possible to calculate $A(z, \theta)$. For our modulated unit step function we use the method that mentioned in [4]. Fig. 5 shows the analytical evaluated propagated pulse for $1 < \theta < 1.0038$ and $1.0038 < \theta < 10$. The values of ω_0, δ and b used here are $\omega_0 = 4.0 \times 10^{15}$ Hz, $b = 1.0 \times 10^{15}$ Hz, $\delta = 0.1 \times 10^{15}$ and $\omega_c = 1.0 \times 10^{15}$ Hz.

In the active medium against the passive medium when time increase, the response of the unit pulse is not damped and dominate of the wave remain Constance.

5. CONCLUSION

We use analytical approximations for describe the correct saddle-point. In this method, we used the refractive index for the determination of the response of an active Lorentzian medium and we illustrated that do not exist distance saddle points and then the near saddle points used for the determination of the response of an active Lorentzian medium to a step modulated pulse

REFERENCES

1. Wait, J. R., "Propagation of pulses in dispersive media," *Radio Sci. D*, Vol. 69, 1387–1401, 1965.

2. Loudon, R., "The propagation of electromagnetic energy through an absorbing dielectric," *J. Phys. A*, Vol. 3, 233–245, 1970.
3. Chu, S. and S. Wong, "Linear pulse propagation in an absorbing medium," *Phys. Rev. Lett.*, Vol. 48, 738–741, 1982.
4. Oughstun, K. E. and G. C. Sherman, "Comparison of the signal velocity of a pulse with the energy velocity of a time-harmonic field in Lorentz media," *Proceedings of the International Union of Radio Science 1980 International Symposium on Electromagnetic Waves*, Paper 113, C/1–C/5, International Union of Radio Science, Munich, Federal Republic of Germany, 1980.

System Power Integrity Impact by Package Power/Ground Balls Assignment

C. H. Lin[1], **H. Y. Wang**[1], **and C. C. Wang**[2]

[1]Department of Electronic Engineering
National Kaohsiung University of Applied Sciences Kaohsiung, Taiwan
[2]R & D Electrical Laborary, Advanced Semiconductor Engineering, Inc., Taiwan

Abstract— Power integrity is one of the important issues of system design in present-day. Power and current levels are expected to increase with a corresponding to decrease in the voltage and increment of I/O number. Based on these factors, system designer has a novel challenge on power delivery network. Therefore, to design a power delivery network (PDN) becomes a major research topic. The impact by power/ground ball assignment has been discussed in this paper. The power/ground ball is often used as a link between the package and printed circuit board (PCB). The resonance between the full planes will impact power stability. And it relates to the system power distribution from the voltage regulator module (VRM) to IC. In this investigation, the power signal propagation noise for different power/ground balls assignment has been pointed out. For power/ground balls assignment, the preferred design is a power ball in the vicinity of a ground ball. But it is not always feasible for practical designs. When considering the PDN design, power/ground balls position is the key point for complete power delivery. That the power/ground balls position will affect the power delivery is demonstration. In this research, the VRM delivers energy to inner IC from PCB through power/ground balls to the package. The assignment of the power/ground balls at several places with different parasitic effects has been investigated for the impact of power integrity. The proposed arrangement of power/ground balls position is presented. The parasitic effects for different conditions of system design are extracted for comparison. The simulation results confirm with our theoretical analysis.

1. INTRODUCTION

The shrinking of the device feature sizes and the increasing complexity of ICs require higher operating frequencies with faster clock rates. The ball grid array (BGA) package becomes an important technology to shorten propagation delay of signal. The package is the interconnection between one die circuitry and another die or the printed circuit board (PCB) [2]. Its electrical function includes signal transmission and power delivery, known as signal and power integrity. For the high-pin-count package, signal integrity and power integrity have become the critical challenges that must be treated carefully at the system level considering the parasitic effects of package and board [3]. The induced effects include ringing, crosstalk, ground bounce and other related issues. As devices scale and more transistors are integrated into a single IC continuously, power and current levels are expected to increase with a corresponding decrease in the voltage [4]. It increases the importance of power integrity design. The ability to supply clean power to the transistor circuits becomes very critical. The design of power delivery network (PDN) received much attention.

Simultaneous switching noise (SSN) is major issue for power integrity. The interconnections have resistance and inductance in them, are used to establish this connection. The current flowing through these paths creates both a DC drop and time-varying fluctuation of the voltage across the power and ground terminals of the IC [5]. The voltage fluctuation across the power supply of the IC is called power supply noise, or simultaneous switching noise, since it occurs only during the switching of the transistors. This issue can be improved by adding the decoupling capacitor. When the VRM is unable to respond because of high output impedance, the current should be supplied by an alternative source for maintaining the voltage. In other words, when the output impedance of the VRM exceeds the desired impedance, then an alternative method is necessary to pull down the impedance [5]. Decoupling capacitors perform this function. However, since ESL and ESR parasites of the decoupling capacitor affect high frequency response, the power supply noise will be resolved by more layer power/ground plane of package and PCB.

In this paper, the power integrity effect resulted from the power/ground balls assignment is studied. In the BGA package, most of the balls will be used as signal I/O. The number of power/ground balls is limited. In the system design, the issue of signal integrity has received much attention. Little attention has been paid to the issue of power integrity. Therefore, for worst PDN case, only one available pair of power/ground balls is discussed in this paper. The power integrity effect is investigated by virtue of PDN equivalent circuit.

2. THE TEST STRUCTURE

The BGA package of 4 cm × 4 cm is electrically mounted on a test PCB of 10 cm × 8 cm through solder balls of 561 µm diameter, as shown in Fig. 1(a). Fig. 1(b) shows the cross section of the test sample. The BGA package consists of four copper layers with a total substrate thickness of 420 µm. The inner two layers are ground and power layers with 180 µm spacing [1]. A twolayer PCB with substrate thickness 700 µm includes the power and ground planes. Figs. 1(c) and (d) show the top view and bottom view of the BGA package. As shown by the short dot dash lines of Fig. 1(d), the power balls are connected with power plane through vias in BGA package. Other balls are connected with ground plane through vias in BGA package. The power plane of BGA package conducts with power plane of PCB by power balls and vias in PCB. The ground plane of BGA package conducts with ground plane of PCB by ground balls, as shown in Fig. 1(b). Using the test sample with 81 solder balls connected between BGA package and the PCB, SI-Wave simulations are performed.

The Port 1 and Port 2 are used as the input and output ports, respectively, as shown in Fig. 1(c). The simulation result of the integrated structure with multiple power/ground balls connection in

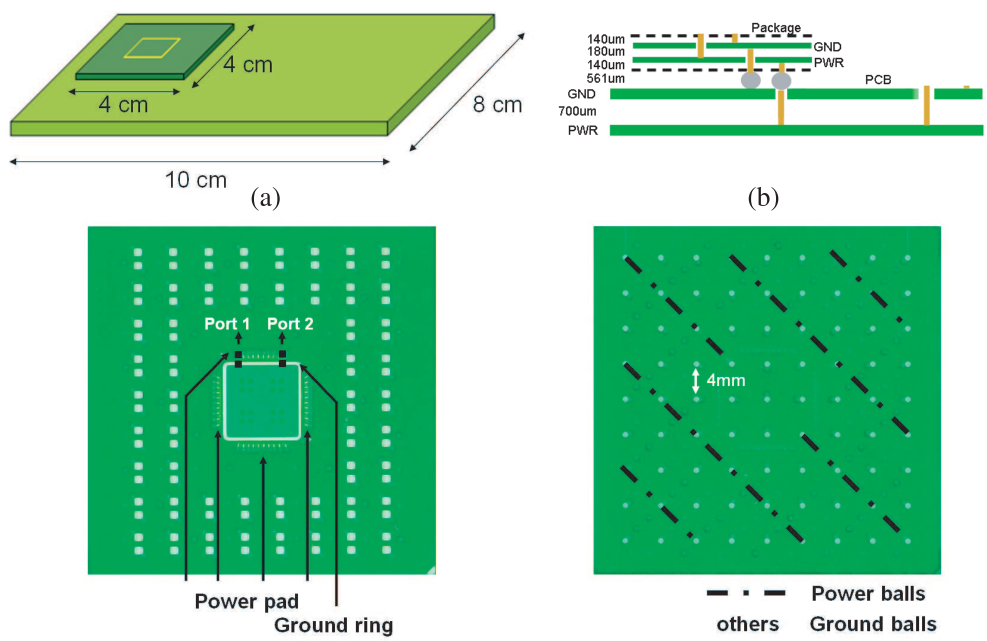

Figure 1: (a) BGA package attached on the PCB. (b) Cross section of the test sample. (c) Top view of the BGA package. (d) Bottom view of the BGA package.

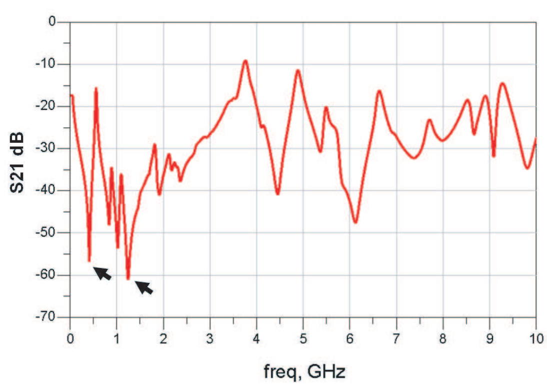

Figure 2: Simulation result of Package on PCB.

Fig. 1 is shown in Fig. 2. There are two cavity resonators in the test sample. One is formed by the power/ground planes on the package substrate. And the other is formed by the power/ground planes on the PCB. It can be observed that the simulated result of combined structure contains both PCB and package characteristics. In the resonant circuit capacitance and inductance change with frequency The inductance interacts with the capacitance of the capacitor, causing it to resonate. The electrolytic capacitors are capacitive below the resonant frequency as (1) and become inductive above the resonant frequency. The interaction between the IC and package can cause a large anti-resonance in the impedance profile of IC. Large voltage fluctuations can occur if the operating frequency of the chip coincides with the chip-package anti-resonance frequency [5].

$$f = \frac{1}{2\pi\sqrt{LC}} \tag{1}$$

3. PRACTICAL DESIGN AND SIMULATION RESULT

The impact of power instability can be improved by power/ground balls assignment in system since the reduction of parasitic effects. The path distance from VRM to IC must be decreased to reduce resistance and inductance. The power/ground balls assignments have been discussed for three different cases below.

The first case considers setting the measured port1 as the VRM in the lower-right position of PCB. Port2 is set as the power port of IC. Power/ground balls are assigned in the four corners of package between the package and PCB in turn. Let the power balls is close to the ground ball as shown in Fig. 3(a) The four equivalent inductance data can be obtained from simulation result, as shown in Table 1. The better power/ground balls position is on lower-right, because the distance is shortest between port1 and power/ground balls.

For power/ground balls assignment, the preferred design is a power ball in the vicinity of a ground ball. But it is not always feasible for practical designs. The noise will be increase by longer distance between the power ball and ground ball. For the second case in Fig. 3(b), the power ball and ground ball with identical distance and different position is considered. The three equivalent inductance data can be obtained from simulation result, as shown in Table 2. For the same distance

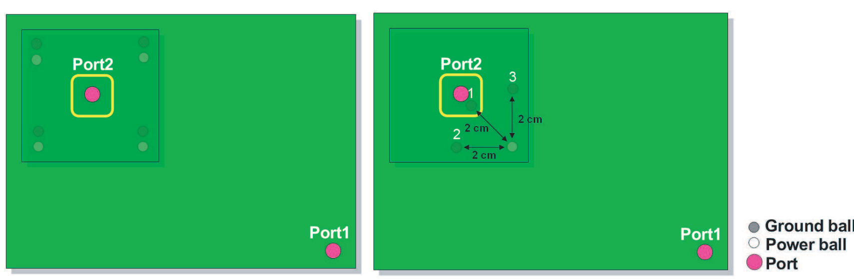

(a) (b)

Figure 3: (a) Power/ground balls assignment in four corners. (b) Power/ground balls assignment on same distance.

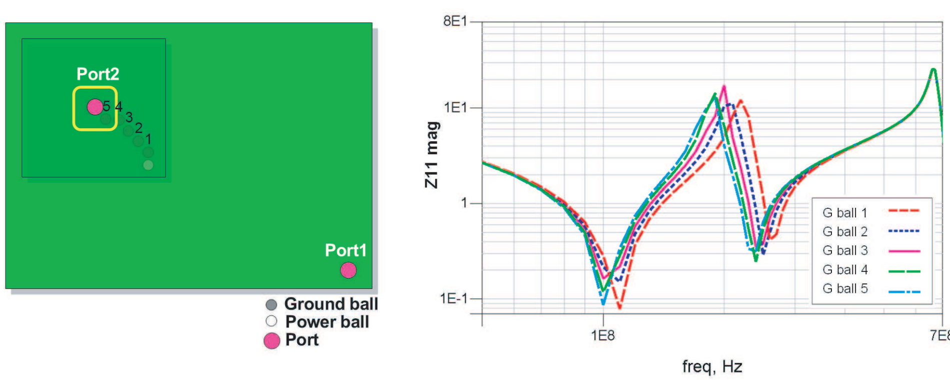

(a) (b)

Figure 4: (a) Ground ball positions. (b) Simulated Z_{11} for ground ball positions.

Table 1: The data of balls position in four corners.

Location	R	L	C
Upper left	0.090 Ω	6.809 nH	1.193 nF
Upper right	0.081 Ω	6.001 nH	1.171 nF
Lower left	0.083 Ω	6.157 nH	1.175 nF
Lower right	0.081 Ω	5.893 nH	1.163 nF

Table 2: The data of balls on same distance position.

Location	R	L	C
G ball 1	0.094 Ω	7.167 nH	1.193 nF
G ball 2	0.105 Ω	7.611 nH	1.195 nF
G ball 3	0.104 Ω	7.515 nH	1.193 nF

Table 3: Parasitic data for different ground ball positions.

Location	R	L	C
G ball 1	0.081 Ω	5.893 nH	1.163 nF
G ball 2	0.087 Ω	6.415 nH	1.173 nF
G ball 3	0.092 Ω	6.783 nH	1.181 nF
G ball 4	0.094 Ω	7.028 nH	1.187 nF
G ball 5	0.094 Ω	7.167 nH	1.193 nF

between the power ball and ground balls, the shortest current path is the ground ball in the vicinity of port2.

For the third case, the power ball position is fixed and different locations of ground balls are considered, as shown in Fig. 4(a). The five equivalent inductance data can be obtained from simulation result, as shown in Table 3. Their system impedances Z_{11} are given in Fig. 4(b). The ground ball location must be near power ball to reach shortest current path and reduce parasitic inductance.

4. CONCLUSIONS

The various power/ground balls assignments causing system power integrity impacts have been studied in this paper. To enhance power integrity, the best arrangement of power/ground balls location is both power and ground balls in the vicinity of VRM for reducing current path. If ground ball is not in the vicinity of power ball, the power ball should be close to VRM and ground ball should be designed to reach shortest current path for reducing parasitic inductance in the system.

REFERENCES

1. Wang, T. K., S. T. Chen, C. W. Tsai, S. M. Wu, J. L. Drewniak, and T. L. Wu, "Modeling noise coupling between package and PCB power/ground planes with an efficient 2-d FDTD/lumped element method," *IEEE Transactions on Advanced Packaging*, Vol. 30, No. 4, November 2007.
2. Wei, X. C., S. M., and E.-P. Li, "Integral-equation equivalent-circuit method for modeling of noise coupling in multilayered power distribution networks," *IEEE Transactions on Microwave Theory and Techniques*, Vol. 58, No. 3, March 2010.
3. Chen, J. and L. He, "Efficient in-package decoupling capacitor optimization for I/O power integrity," *IEEE Transactions on Computer-aided Design of Integrated Circuits and Systems*, Vol. 26, No. 4, April 2007.
4. Bharath, K., E. Engin, M. Swaminathan, K. Uriu, and T. Yamada, "Efficient modeling of package power delivery networks with fringing fields and gap coupling in mixed signal systems," *Proc. of 15th IEEE EPEP*, 59–62, October 2006.
5. Swaminathan, M. and A. E. Engin, *Power Integrity Modeling and Design for Semiconductor and Systems*, Prentice-Hall, Englewood Cliffs, NJ, 2007.

Applicational Effects of an Atmospheric Pressure Plasma Device

Zhu-Wen Zhou[1], **Yan-Fen Huang**[2], **Si-Ze Yang**[3], **and De-Yong Xiong**[1]

[1]Institute of Applied Physics, Guizhou Normal College, Guiyang 550018, China
[2]School of Chemistry and Biology, Guizhou Normal College, Guiyang 550018, China
[3]Institute of Physics, Chinese Academy of Sciences, Beijing 100080, China

Abstract— We designed a atmospheric pressure plasma equipment, eggplant seeds were treated using the equipment with different voltage from 4420 to 6800 V. The results showed that the effects of different voltage plasma treatments on the seeds germination were not the same. The plant height, the plant extent, the root length, the root extent and the single fruit weight of the eight treatments from 4420 to 6800 V were increased distinctly. The eggplant yields of eight different voltage plasma treatments were increased than of the control (CK), the fruit yields of voltage treatments ($5440 \sim 6460$ V) were better than of other voltages, the effects of fifth (5780 V) and sixth (6120 V) plasma treatments were best in most test indexes. The reasons may be that the treated seeds had been in different physical surroundings, the equipment is a dielectric barrier discharge (DPD), it creates a typical glow discharge free from filament and arc plasma, the macro-temperature of the plasma is nearly at room temperature, and plasma discharge gas pressure is atmospheric pressure. As the seeds were passed through the plasma on the carrier, the seeds were treated with uniform plasma discharge and were not burned. Test data were consistent with the similar estimating statistical analysis.

1. INTRODUCTION

Applications of physical technology in agriculture are more and more popular, but most of them are radiations and irradiations with γ-ray, ^{60}Co-ray, laser, electric and magnetic field [1–13], cells of plant seeds are damaged by radiations. Plasma has been used in industry for applications, few experimental studies have been carried out for seed mutation induced by atmospheric plasma. We used a atmospheric plasma discharge equipment [14, 15] to study the mutations of plant seeds. The set is atmospheric dielectric barrier discharge (DPD) with two parallel high voltage electrodes. A mass of electrons bomb plant seeds and bring much ozone, the ozone can kill bacterium and virus, and also plant seeds are radiated by ultraviolet-ray, plant seeds are mutated by the many factors. We tested with eggplant seeds, to study the effects of atmospheric pressure plasma on the seeds germination, seedling growth, yield and quality, in order to find the methods of improving the eggplant seeds.

2. MATERIALS AND METHODS

2.1. Eggplant Seed Treatment and Test Field

We tested with eggplant seeds. These seeds were counted and treated with eight plasma voltage treatments: 4420 V, 4760 V, 5100 V, 5440 V, 5780 V, 6120 V, 6460 V, and 6800 V for 6 s, respectively, and one untreated CK (0 V). The plasma experiment carried out at Plasma Lab. of Institute of Physics of Chinese Academy of Sciences. The seedlings were grown in the greenhouse before being transplanted into the field. The field tests were carried out at Horticulture Research Institute of Guizhou Academy of Agricultural Sciences in Feb.–Sept. 2008. The test field total area was 667 m^2, according to factorial randomized complete block design, unit plot size area was 11.2 m^2 (1.4 m $\times$ 8 m). The eggplant seedlings were transplanted at a 100 cm plant spacing and a 50 cm narrow row spacing and 60 cm wide row spacing, and each treatment was repeated two times.

2.2. Plasma Experiment Device and Experimental Process

The plasma experiment device is shown in Fig. 1, it is two parallel containers made of quartz, the thickness of quartz is 1 mm, the length is 15 cm, the width is 5 cm, the space of dielectrics is 10 mm. there are some liquid of potassium chloride in two containers, two inner copper rings dipped in the liquid are two electrodes connected to AC high voltage power supply (30 kV, $8 \sim 30$ kHz).

As compact joined between the liquid of potassium chloride and dielectrics, both cool quartz dielectrics and uniform plasma discharge. In our experiment, put uniformly the eggplant seeds on a speed evenly moving carrier, turned on high voltage power supply to discharge, the seeds passed through the plasma, treatment time was controlled by the speed of the carrier. There were eight different voltage treatments with the same treatment time 6 seconds.

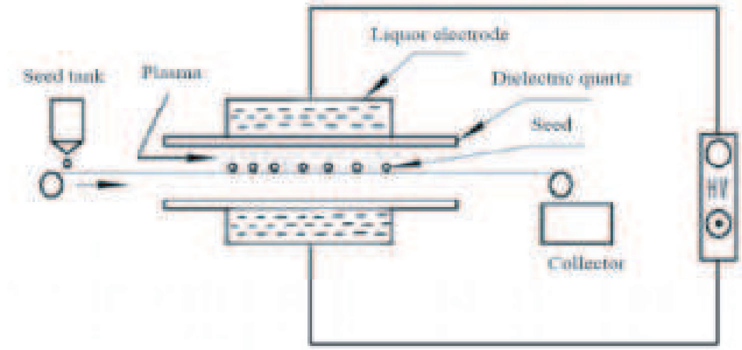

Figure 1: Schematic diagram of the atmospheric plasma dielectric barrier discharge (DBD).

Table 1: Change of botanic properties of the eggplants treated by different voltage.

Treat group	Treat voltage [V]	Plant height [cm]	Plant extent [cm × cm]	Cyanosis incidence [%]	Root length [cm]	Root extent [cm × cm]	Fruit length [cm]	Fruit diameter [cm]	Fruit weight [g]	Fruit yield per [667 m^2/kg]
CK	0	103	70 × 80	26.56	17.3	25.838.3	21.6	5.2	155	3210
1	4420	108	75 × 80	15.63	19.3	29.539.3	22.8	5.2	160	3308
2	4760	110	75 × 85	6.25	18.7	31.340.1	22.4	5.4	170	3415
3	5100	110	73 × 80	7.81	19.4	31.843.0	22.7	5.3	180	3452
4	5440	110	70 × 85	17.19	18.9	33.241.5	24.3	5.3	185	3510
5	5780	110	75 × 85	7.81	19.4	32.638.9	23.8	5.5	195	3582
6	6120	105	72 × 83	7.81	20.2	30.444.0	23.5	5.4	190	3563
7	6460	107	70 × 82	10.94	19.9	32.443.4	23.0	5.4	180	3532
8	6800	104	75 × 84	17.19	19.2	30.346.1	22.5	5.3	170	3428

3. RESULTS AND DISCUSSION

3.1. Change of Botanic Properties of the Eggplant

We designed a atmospheric pressure plasma equipment. The seeds were treated using the device with different voltage from 4420 to 6800 V. The results showed that the effects of different voltage plasma treatments on the seeds germination were not the same. The plant height, the plant extent, the root length, the root extent and the single fruit weight of the eight treatments from 4420 to 6800 V were increased distinctly (Tab. 1). In additionanti-cyanosis of eight treatments were better than the untreated, as well as anti-virus except fourth and eighth treatment.

The eggplant yields (kg/667 m^2) of eight different voltage plasma treatments were increased, the fourth (5440 V), the fifth (5780 V), sixth (6120 V) and seventh (6460 V) treatments were better (yield: 3510 kg, 3582 kg, 3563 kg, and 3532 kg) than other voltages, in most indexes of our tests, the effects of fifth (5780 V) and sixth (6120 V) plasma treatments were best. By used different voltage (4420 $\sim$ 6800 V) plasma treating the eggplant seeds, the fruit weight, length, diameter and yield of eggplant were all better than the untreated (CK) in our experiments, the reasons may be that the treated seeds had been in different physical surroundings, the atmospheric pressure plasma equipment is a dielectric barrier discharge (DPD), it creates a typical glow discharge free from filament and arc plasma [16], the macro-temperature of the plasma is nearly at room temperature, and plasma discharge gas pressure is atmospheric pressure. As the seeds were passed through the plasma on the carrier, the seeds were treated with uniform plasma discharge and were not burned.

3.2. Irradiation Intensity of Violet Blue Light and Homogeneous Discharge Region

In Fig. 2 there were eight different discharge processes with eight different voltages, intensity of violet blue light (350 $\sim$ 500 nm) gradually increase with voltage adding. The discharges were not uniform and the powers were lower in low voltages (4420 $\sim$ 5440 V), there were nearly uniform discharges under the plasma voltages (5440 $\sim$ 6800 V), but the discharge powers were higher in high voltages (6460 $\sim$ 6800 V). In Fig. 3, there were eight violet blue light intensities under different

Figure 2: Eight different discharge processes with eight different voltages (4420 ∼ 6800 V), intensity of violet blue light gradually increased with adding voltage. In Figures (a)–(d) the discharges were not uniform and the powers were lower with low voltages 4420 ∼ 5440 V, there were nearly uniform discharges under the plasma voltages (5780 ∼ 6800 V) in Figures (e)–(h), but the discharge powers were higher in high voltages (6460, 6800 V) in Figures (g) and (h).

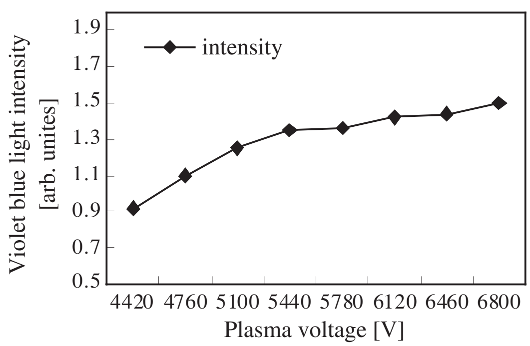

Figure 3: The violet blue light intensity versus different plasma voltage.

plasma discharge voltages, it showed that there was a approximate step of light intensity unchanged in voltages 5440 ∼ 6120 V, it relate with the homogeneous discharge regions in Figs. 2(d), (e), (f), these regions were in general agreement with the uniform discharges (5440 ∼ 6800 V).

4. SUMMARY

The fruit yields in 5440 V ∼ 6460 V voltage ranges were better than other voltages, the effects of fifth (5780 V) and sixth (6120 V) plasma treatments were best in most test indexes. It is due to the energy of the electron and the active air particles in the plasma increasing with atmospheric plasma voltage adding, more electric charges are produced per unit time and cannot be neutralized at once, which can strengthen the reaction between the air particles and seeds. The active air particles and ultraviolet radiation can penetrate into the capsule of the seedsaccelerate to decompose the inner nutriment of the seeds, reduce relative penetrability of cell velum, improve the activities of the root of the eggplant seedling. Lower voltages (4420 ∼ 5100 V) cannot penetrate into the seeds capsule and higher voltages ($>$ 6460 V) maybe burnt the inner cells of the seeds. So that the eggplant yields increase and the most the botanic properties of the eggplants are improved.

ACKNOWLEDGMENT

The project supported by the Nature Science Foundation of Guizhou Province Science & Technology Bureau under Grant No. J20082101 and the Science Foundation of the Bureau of Education in Guizhou Province under Grant No. 2010053.

REFERENCES

1. Li, H. Z. and J. Pang, *Agriculture & Technology*, Vol. 23, No. 2, 47–49, 2003.
2. Li, J. W., Z. K. Sun, S. Yang, et al., *China Vegetables*, Vol. 2, 22–24, 1997.
3. Wang, Y. H., L. B. Han, S. X. Yin, et al., *Chinese Journal of Grassland*, Vol. 28, No. 1, 54, 2006.
4. Lin, R. R., *Journal of Fujian Agricultural University*, Vol. 28, No. 4, 509–512, 1999.
5. Xiao, W., Y. L. Wang, and Z. Q. Guan, *Biomagnetism*, Vol. 4, No. 2, 7–10, 2004.
6. Wu, X. H., W. M. Sun, and H. Y. Zhang, *Heilongjiang Agricultural Sciences*, Vol. 2, 44, 2005.
7. Rajput, M. A. and M. J. Qureshi, *Sabrao Newsletter*, Vol. 5, No. 1, 39–42, 1973.
8. Carstensen, E. L., *Journal of Electrostatics*, Vol. 39, No. 3, 157–174, 1997.
9. Souza, T. A., L. E. Porras, and F. R. Casate, *Horticult Abs*, Vol. 70, No. 8, 6892, 1999.
10. Thimmaiah, S. K., P. Mahadevu, and K. N. Srinivasappa, *Journal of Nuclear Agriculture and Biology*, Vol. 27, No. 2, 1998, 142–145.
11. Garcia, R. F. and P. L. Arza, *Bioelectromagnetics*, Vol. 22, No. 8, 589–595, 2001.
12. Xia, L. H., Y. L. Yi, X. Y. Liu, et al., *Journal of Shenyang Agriculture University*, Vol. 30, No. 1, 24–26, 1999.
13. Chen, J. G. and S. H. Li, *Journal of Nuclear Agriculture*, Vol. 9, No. 1, 1995, 7–12.
14. Wang, M., Q. Y. Chen, S. Z. Yang, et al., *ACTA Agricultural Boreali-Sinica*, Vol. 22, No. 6, 2007, 108–113.
15. Wang, M., S. Z.Yang, Q. Y. Chen, et al., *Transactions of the CSAE*, Vol. 23, No. 2, 195, 2007.
16. Chen, G. L., S. H. Fan, C. L. Li, et al., *Chinese Physics Letters*, Vol. 22, No. 8, 2005, 1980–1983.
17. Johnson, R. A., *Probability and Statistics for Engineers*, 7th Edition, Electronic Industry Publishing Company, Beijing, 2005.
18. Goldstein, M. L., S. A. Morris, and G. G. Yen, *Europe Physics Journal*, Vol. B41, 255, 2004.

Terahertz Emission by Atom in Multicolor Laser Field in Ionization-free Regime

A. V. Andreev[1], **S. Yu. Stremoukhov**[1,2], **and O. A. Shoutova**[2]

[1]Physical Department, M. V. Lomonosov Moscow State University
119992 Leninskie Gory, 1, Build. 2, Moscow, Russia
[2]International Laser Center, M. V. Lomonosov Moscow State University
119992 Leninskie Gory, 1, Build. 62, Moscow, Russia

Abstract— Here we present the result of theoretical investigations of a single atom interaction with a multicolor laser field formed by an arbitrary number of the components with an arbitrary orientation of polarization vectors. The developed theory is non-perturbative and valid in the whole sub-relativistic region of the laser field strength. It results in a new mechanism of a nonlinear atomic response which is mainly due to the light-induced anisotropy of an electron wave function but not by electron transitions between the free atom eigenstates. For example, the terahertz (THz) emission in ionization-free regime is interpreted without exploiting the plasma nonlinearities (usually the four-wave mixing rectification process). The numerical experiment simulates an Argon atom interaction with the fundamental and the second harmonic of Ti:Sapphire laser. It is shown that the spectral width and efficiency of the THz emission depend nonlinearly on the parameters of the multicolor laser field.

1. INTRODUCTION

Frequency mixing a laser's fundamental and second harmonic fields in atomic gases generates a directional electrical current for which the magnitude and polarity depend upon the relative phase between the two fields [1, 2]. In the case of ultrafast lasers, this process can generate electromagnetic radiation at THz frequencies. Although such THz generation has been observed in semiconductors [3] and air [4], the THz generation mechanism is not well understood and the THz yield has not been optimized. Initially, THz generation in gases was understood on a phenomenological basis to involve a four-wave mixing process in plasma [5]. Here we present a new mechanism of the THz generation, which is based not on the four-wave mixing process in plasma, but on the intra-atomic non-linearities. We apply the non-perturbative theory for explanation of this mechanism. This theory was firstly presented in [6], developed in [7] and used to explain such experimentally observed features of interaction as the cut-off frequency saturation [8], the dipole selection rules breaking [9] etc. The main steps of the theory are presented below.

2. THEORETICAL BACKGROUND

Our non-perturbative theory is based on the consequent expansion of the wave-function $\psi(\vec{r}, t)$ of the time-dependent Schrödinger equation

$$i\hbar\frac{\partial\psi(\vec{r},t)}{\partial t} = \left[\frac{1}{2m}\left(\vec{p}-\frac{q}{c}\vec{A}\left(t\right)\right)^2 + U\left(\vec{r}\right)\right]\psi(\vec{r},t)$$

through the wave-function of the free atom boundary value problem and the wave-function of "an atom in the external field" boundary value problem [7]. This consequent expansion enables us, on the one hand, to take into account the difference between the symmetry of the "atom+field" problem and the symmetry of the free atom, and on the other hand, permits us to avoid the calculation of the matrix element $\int \varphi_n^*(\vec{r},t)\partial\varphi_m(\vec{r},t)/\partial t dV$ which appear because the time derivatives $\partial\varphi_n(\vec{r},t)/\partial t$ are not the eigenfunctions of "an atom in the external field" boundary value problem and, therefore, they are not orthogonal to the eigenfunctions $\varphi_n(\vec{r},t)$. Making this transformations we obtain the following set of differential equations for probability amplitudes of discrete and continuum states

$$i\hbar\frac{da_n}{dt} = \sum_{m,k} V_{nk}^{-1} E_k V_{km} a_m. \tag{1}$$

The system of Equation (1) contains an infinite number of equations because the basis of discrete and continuum states of any hydrogen-like atom is infinite. That is why it is important for numerical solving of the (1) to limit its value. We suggest a method of the limitation of the number of the system (1) equations [7].

The results of the solution of the system (1) are used to calculate the total atomic current $J(\vec{r}, t)$. The vector potential spectrum of the atomic response field in the far-field range is proportional to the spectrum of the atomic current density (see [10]). The partial matrix elements for $J(\vec{r}, t)$ have the form:

$$\begin{aligned}
&\left\langle n_1 l_1 m_1 \left| \vec{J} \right| n_2 l_2 m_2 \right\rangle \\
= \; & 4\pi q i^{l_2 - l_1 + 1} \sqrt{(2l_1+1)(2l_2+1)} \sum_{n_3 l_3} \sum_{n_4 l_4} \left(\omega_{n_3 l_3} - \omega_{n_4 l_4}\right)(2l_3+1)(2l_4+1) \\
& \cdot \sum_{l=|l_1-l_3|}^{l_1+l_3} \sum_{l'=|l_2-l_4|}^{l_2+l_4} \sqrt{(2l+1)(2l'+1)} \left\langle n_1 l_1 \left\| j_l \right\| n_3 l_3 \right\rangle \left\langle n_3 l_3 \left\| r \right\| n_4 l_4 \right\rangle \left\langle n_4 l_4 \left\| j_{l'} \right\| n_2 l_2 \right\rangle \\
& \cdot \begin{pmatrix} l_1 & l & l_3 \\ 0 & 0 & 0 \end{pmatrix} \begin{pmatrix} l_3 & 1 & l_4 \\ 0 & 0 & 0 \end{pmatrix} \begin{pmatrix} l_4 & l' & l_2 \\ 0 & 0 & 0 \end{pmatrix} \\
& \sum_{m=-1}^{+1} \sum_{m_3=-l_3}^{l_3} (-1)^{l'-m_2+m_3} Y_{l(m_3-m_1)}(\vec{e})\, \vec{n}^{(m)} Y_{l'(m_3-m_2-m)}(\vec{e}) \\
& \cdot \begin{pmatrix} l_1 & l & l_3 \\ -m_1 & m_1-m_3 & m_3 \end{pmatrix} \begin{pmatrix} l_3 & 1 & l_4 \\ -m_3 & m & m_3-m \end{pmatrix} \begin{pmatrix} l_4 & l' & l_2 \\ m_3-m & m_2-m_3+m & -m_2 \end{pmatrix}, \qquad (2)
\end{aligned}$$

where $j_l = j_l(qA(t)r/\hbar c$, $\omega_{nl} = E_{nl}/\hbar$ and E_{nl} is the energy eigenvalues for the free atom problem.

Thus, the mathematical formalism of this section provides us with a possibility to calculate the angular-frequency spectrum (AFS) of the atomic response for the case of arbitrary mutual orientation of the atomic angular momentum and the laser field polarization vector. As it follows from (2), the polarization of the AFS components depends on both the angular momentum direction and the polarization of the incident field. In the non-polarized ensemble of atoms the response field polarization depends only on the polarization state of the laser field.

3. NUMERICAL RESULTS

We use our theoretical approach to describe the interaction of an Argon atom ($I_p = 15.76\,\text{eV}$) with a two-color laser field formed by the fundamental and the second harmonics of the Ti:Sapphire laser. The Argon model contains 13 discrete states which cover 96.5% of the ionization potential of an Argon atom. This number of discrete states is enough to describe the interaction of an Argon atom with the laser field the intensity of which is less than $I < 6.77 \times 10^{12}\,\text{W/cm}^2$. We have assumed that the seven parameters of the external field: the amplitudes and the durations of pulses (the first 4), the delay time (the 5th), and the angle between their polarizations (the 6th), chirp of the components (the 7th), may vary within the wide ranges.

In our researches we have calculated, discussed and illustrated the influence of the parameters (1–7) on the emission spectra. Here we demonstrate only the influence of variation of the angle between their polarizations. Fig. 1(a) represents the dependence of the THz-signal output on the angle mentioned above for the laser pulses with the parameters $I_{01} = 6.77 * 10^{12} \frac{\text{W}}{\text{cm}^2}, I_{02} =$

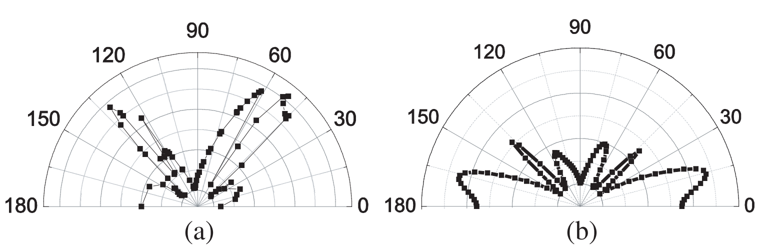

Figure 1: The THz-signal output dependence on the angle between the polarizations of the two-color field components calculated for the laser pulse's parameters (a) $I_{01} = 6.77 * 10^{12} \frac{\text{W}}{\text{cm}^2}, I_{02} = 6.77 * 10^{12} \frac{\text{W}}{\text{cm}^2}$, $\tau_1 = \tau_2 = 4.25\,\text{fs}$ and (b) $I_{01} = 6.77 * 10^{12} \frac{\text{W}}{\text{cm}^2}, I_{02} = 1.37 * 10^{12} \frac{\text{W}}{\text{cm}^2}$, $\tau_1 = 50\,\text{fs}$, $\tau_2 = 35.5\,\text{fs}$.

$6.77 * 10^{12} \frac{\mathrm{W}}{\mathrm{cm}^2}$, $\tau_1 = \tau_2 = 4.25\,\mathrm{fs}$ and the delay time 0 fs. Fig. 1(b) represents the dependence of THz-signal output on the angle for the laser pulses with the parameters $I_{01} = 6.77 * 10^{12} \frac{\mathrm{W}}{\mathrm{cm}^2}$, $I_{02} = 1.37 * 10^{12} \frac{\mathrm{W}}{\mathrm{cm}^2}$, $\tau_1 = 50\,\mathrm{fs}$, $\tau_2 = 35.5\,\mathrm{fs}$ and the delay time 0 fs. The THz-signal output is determined as the total signal registered at the frequency of 1 THz. The most remarkable feature of this curve is its non-monotonic behavior. It can be seen that the slight variation in the angle may lead to a considerable enhance in the efficiency of the THz-signal generation.

Thus, the presented results of computer simulations clearly demonstrate that the variation of the mutual polarizations and the temporal profiles of the two-color field pulses is an effective instrument to modify the nonlinear atomic response spectra in a strongly controllable way.

4. CONCLUSIONS

The numerical results demonstrate that in the two-color scheme the THz signal should be detected in the ionization-free regime. The THz generation efficiency non-monotonically depends on the parameters of the two-color laser field.

ACKNOWLEDGMENT

This study was financially supported in part by the RFBR (grant No. 12-02-00969).

REFERENCES

1. Yin, Y. Y., C. Chan, D. S. Elliott, and A. V. Smith, "Asymmetric photoelectron angular distribution from interfering photoionization processes," *Phys. Rev. Lett.*, Vol. 73, 2353–2356, 1992.
2. Schumacher, D. W., F. Weihe, H. G. Muller, and P. H. Bucksbaum, "Phase dependence of intense field ionization: A study using two colours," *Phys. Rev. Lett.*, Vol. 73, 1344–1347, 1994.
3. Cote, D., J. M. Fraser, M. DeCamp, P. H. Bucksbaum, and H. M. van Driel, "THz emission from coherently controlled photocurrents in GaAs," *Appl. Phys. Lett.*, Vol. 75, 3959–3961, 1999.
4. Cook, D. J. and R. M. Hochstrasser, "Intense terahertz pulses by four-wave rectification in air," *Opt. Lett.*, Vol. 25, 1210–1212, 2000.
5. Kim, K. Y., A. J. Taylor, J. H. Glownia, and G. Rodriguez, "Coherent control of terahertz supercontinuum generation in ultrafast laser-gas interactions," *Nat. Phot.*, Vol. 2, 605–609, 2008.
6. Andreev, A. V., "Self-consistent equations for the interaction of an atom with an electromagnetic field of arbitrary intensity," *JETP*, Vol. 89, 421, 1999.
7. Andreev, A. V., S. Yu. Stremoukhov, and O. A. Shoutova, "Nonlinear optical response of an atom in the field of femtosecond laser pulses with near-atomic intensity," *JETP Letters*, Vol. 93, No. 8, 476–486, 2011.
8. Ganeev, R. A., M. Baba, M. Suzuki, and H. Kuroda, "High-order harmonic generation from silver plasma," *Phys. Lett. A*, Vol. 339, 103, 2005.
9. Nandor, M. J., M. A. Walker, and L. D. Van Woerkom, "Angular distributions of high-intensity ATI and the onset of the plateau," *J. Phys. B*, Vol. 31, 4617, 1998.
10. Bethe, H. and E. Salpeter, *Quantum Mechanics of One- and Two-Electron Atoms*, Academic Press Inc., Berlin, 1957.

Simultaneous Measurement of Stress, Temperature and Refractive Index Using an PMFBG Cascaded with an LPG

Jiang-Chiou Mau[1], **Pei-Ping Wu**[2], **Ming-Yue Fu**[3], **and Wen-Fung Liu**[2]

[1]Ph.D. Program in Electrical and Communications Engineering
Feng-Chia University, Taichung, Taiwan, R.O.C.
[2]Department of Electrical Engineering, Feng-Chia University, Taichung 40724, Taiwan, R.O.C.
[3]Department of Avionics Engineering, Air Force Academy, Kaohsiung, Taiwan, R.O.C.

Abstract— This study proposes a new fiber sensor based on the cascaded different types of fiber gratings for applying in the simultaneous measurement of stress, temperature, and refractive index. The fiber sensor is composed of a concatenated the fiber Bragg grating fabricated in polarization maintaining fiber (PMFBG) and the long period fiber grating (LPG) fabricated in photosensitive fibers. The sensing mechanism is based on the variation both of the power in the reflection wavelength and the Bragg wavelength corresponding to the Bragg peaks to be located on the positive or negative slope of the loss peak of LPG. Thus, it can be used for detecting the changes of stress, refractive index, and temperature simultaneously by monitoring the wavelength shift and power variation of PMFBG.

1. INTRODUCTION

Optical fiber sensors have been used for a wide range of applications in recent years due to their intrinsic outstanding characteristics such as light weight, small size, and immunity against electromagnetic interference, etc. Thus, fiber optical sensors for practical application are attractive and growing fast for their development By using the different optical properties of the FBG and LPG, the strain, temperature, and refractive index can be measured simultaneously [1–7]. When a fiber Bragg grating is fabricated in a polarization maintaining fiber (PMF), due to the different reflective index corresponding to the fast-axis and slow-axis mode of the fiber, there are two reflective peaks at the reflection spectrum for the applications of fiber sensors [8].

In this paper, we demonstrate experimentally that a PMFBG in series with a LPG to measure three physical parameters of stress, temperature, and refractive index simultaneously. The sensing mechanism is based on the variation both of the power in the reflection wavelength and the Bragg wavelength corresponding to the Bragg peaks to be located on the positive or negative slope of the loss-dip of LPG. This scheme may provide another simple method for a wide range of sensing applications

2. BASIC PRINCIPLES

In this study, the sensing head (PMFBG-LPG) includes a PMFBG to be cascaded with an LPG. The LPG is fabricated by using a 248 nm KrF excimer laser to exposure on photosensitive fibers (Fibercore PS-1250/1500) by the amplitude-mask writing technique with the periods of 380 μm. The PMFBG is fabricated on hydrogen-loaded PMF (Nufern PM1550-HP, panda fiber) by using the phase mask writing technique with the periods of 1.0741 μm. The length both of the LPG and PMFBG of 2 cm and the separation of 1 cm between these two gratings are shown in Fig. 1.

Because of the birefringence characteristics of PMFs with different refractive indexes for the slow and fast axes, the FBG fabricated in the PMFs shows two different reflection grating wavelengths

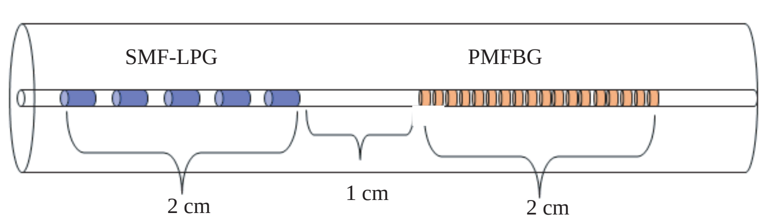

Figure 1: Schematic diagram of a PMFBG connected in series with a LPG for the mode coupling..

corresponding to the fast and slow axes. Moreover the light speed along the slow axis is lower than the fast axis, thus the refractive index of the slow axis is higher than that of the fast axis. The reflection peak at the longer Bragg wavelength belongs to the slow-axis grating (effective mode index n_{slow}) and the shorter peak wavelength belongs to the fast-axis grating (effective mode index n_{fast}) as shown in Eq. (1) :

$$\lambda_F = 2n_{\mathit{eff}}^F \Lambda, \quad \lambda_S = 2n_{\mathit{eff}}^S \Lambda \tag{1}$$

where λ_F and λ_S are the Bragg wavelength corresponding to the fast-axis and slow-axis mode respectively and Λ is the grating period.

For the LPG, owing to the phase-matching condition the fundamental core modes are coupled to the cladding modes to generate several loss dips in the transmission spectrum. When the specific resonant wavelength of input light source passes through the LPG in the core mode, it will be coupled to co-propagating cladding mode to result in the power loss. The resonant wavelength can be expressed as follows:

$$\lambda_m = \left(n_{\mathit{eff},core} - n_{\mathit{eff},cladding}^m\right)\Lambda, \tag{2}$$

where Λ is the grating period, and $n_{\mathit{eff},core}$ is the effective core index , and $n_{\mathit{eff},cladding}^m$ is the m-th effective cladding-mode index. The parameters both $n_{\mathit{eff},core}$ and $n_{\mathit{eff},cladding}^m$ are dependent on the resonant wavelength λ_m, which is strongly influenced by the surrounding refractive index.

Therefore, the stress, temperature, and index can be simultaneously obtained by means of the measurement of the Bragg wavelength shift ($\Delta\lambda$) of fast axis and the Bragg-wavelength reflective power change of both slow and fast axes (ΔR_S, ΔR_F) on the slope region of the loss dip of LPG to be expressed as the following matrix:

$$\begin{bmatrix} \Delta\lambda \\ \Delta R_F \\ \Delta R_S \end{bmatrix} = \begin{bmatrix} M_{11} & M_{12} & M_{13} \\ M_{21} & M_{22} & M_{23} \\ M_{31} & M_{32} & M_{33} \end{bmatrix} \begin{bmatrix} \Delta S \\ \Delta T \\ \Delta n \end{bmatrix} \tag{3}$$

where ΔS is the variation of stress, ΔT is the variation of temperature, Δn is the index variation. The coefficients of $M_{11} \sim M_{33}$ can be determined by the Bragg wavelength shift and the Bragg-wavelength reflective power variation of PMFBG in the separated experiment by applying various stress, temperature, and indexes into the sensor head.

3. EXPERIMENTAL RESULTS

The experimental setup is shown in Fig. 2. The sensing head is connected in series with a broadband light source and an optical spectrum analyzer for monitoring the variation of grating spectra. For the measurement of index, the sensor is placed on the wafer and dropping the refractive index oil. For the measurement of temperature, the chamber temperature can be controlled by varying the heating electrical power of the oven. Moreover, the stress variation can be obtained by changing the different weights applying in the sensing head. From the original transmission spectra of the PMFBG-LPG, two Bragg loss dips due to the birefringence of PMF are located at the positive slope of LPG with the wavelengths of 1540.66 nm and 1541.1 nm, respectively.

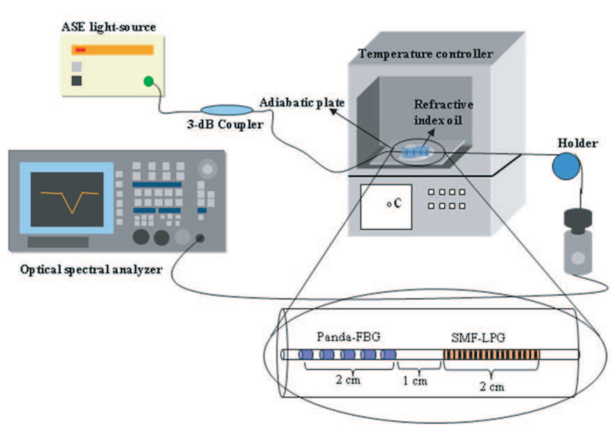

Figure 2: The experimental set-up of measuring the stress, temperature, and index.

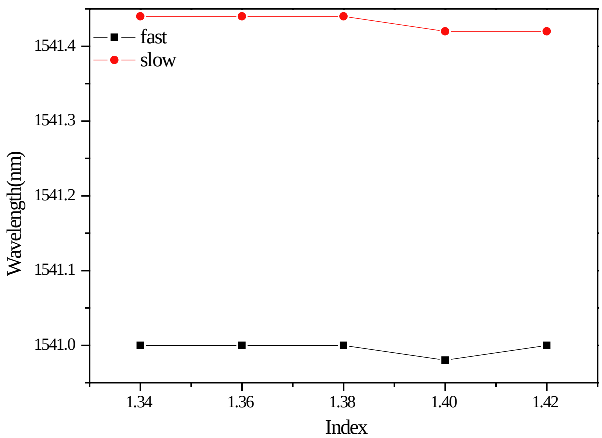

Figure 3: The reflection wavelength shift versus index increment from 1.34 to 1.42.

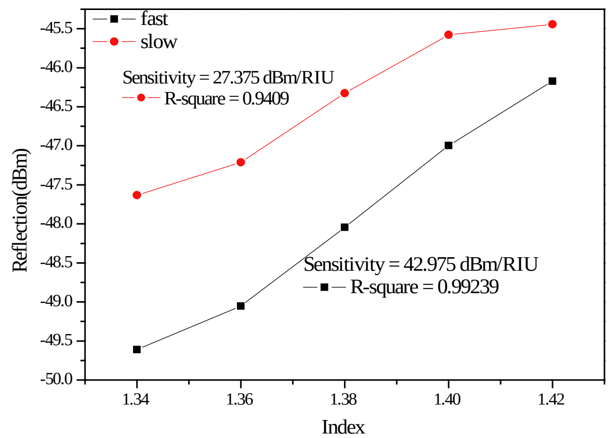

Figure 4: The reflection intensity versus refractive index increment from 1.34 to 1.42.

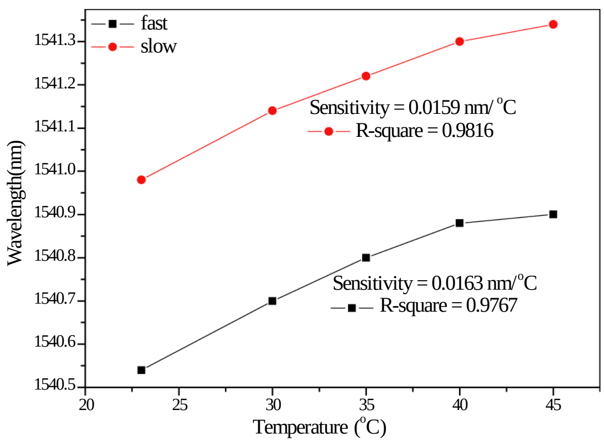

Figure 5: The reflection wavelength shift versus temperature increment from 23 °C to 45 °C.

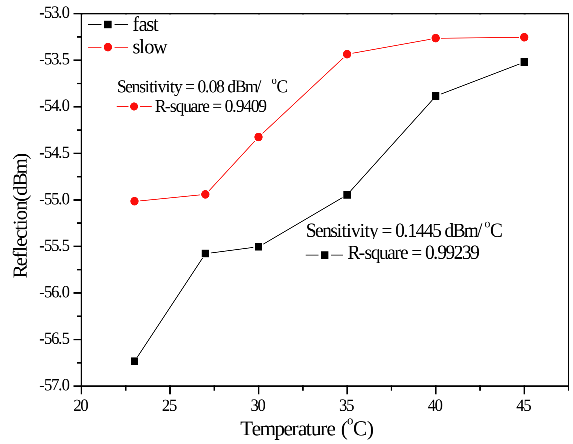

Figure 6: The reflection intensity versus temperature increment from 23 °C to 45 °C.

In the index-measured experiment, the index surrounding the sensing head is changed by dropping the different-index oils on the surface of the grating in the index range from 1.34 to 1.42. The Bragg wavelengths of PMFBG almost keep a constant as shown in Fig. 3. However, due to the loss-dip wavelength shift of LPG to be red shift, the Bragg reflective power of PMFBG is increased in the range of index from 1.34 to 1.42. The sensitivities both of R_F and R_S are 42.975 and 27.375 dBm per unit index as shown in Fig. 4.

For the temperature measurement, as the temperature is changed from 23 °C to 45 °C, the loss dip of LPG is blue shift and the wavelengths of PMFBG are red shift. The sensitivities both of 0.0163 nm/°C and 0.1445 dBm/°C for the fast axis are obtained as shown in Fig. 5 and the sensitivities both of 0.0159 nm/°C and 0.08 dBm/°C for the slow axis are obtained as shown in Fig. 6.

For measuring the effect of stress, 0, 23.96, 47.92, 63.90, and 71.88 MPa are applied in the sensor head in keeping the constant both of index and temperature. The different levels of stress cause the variation both of the grating center-wavelength and the reflective power of PMFBG. The grating wavelength in the fast axis (λ_F) is shifted from 1540.66 to 1542 nm with the sensitivity of 0.01864 nm/MPa and the grating wavelength in the slow axis (λ_S) is shifted from 1541.1 to 1542.42 nm with the sensitivity of 0.01836 nm/MPa as shown in Fig. 7. Besides, due to the PMFBG to be located at the positive slope of LPG, the reflective power is increased when the grating wavelength of PMFBG is shifted toward longer wavelength. The R_F is varied from −52.39 dBm to −51.173 dBm, and R_S is varied from −50.203 dBm to −49.293 dBm, corresponding to the sensitivities of 0.01992 and 0.1266 dBm/MPa as shown in Fig. 8.

Because the fiber Bragg grating is not sensitive to the external refractive index, therefore, the

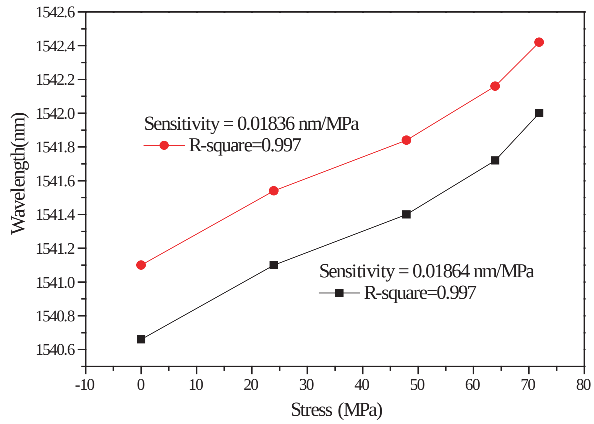

Figure 7: The reflection wavelength shift versus stress increment from 0 to 71.88 MPa.

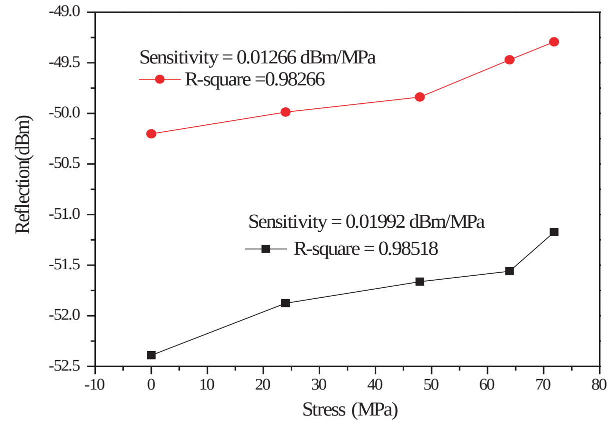

Figure 8: The reflection intensity versus stress increment from 0 to 71.88 MPa.

Bragg wavelength shift on the fastaxis and slowaxis is almost zero. For measuring the stress and temperature experiments, the wavelength sensitivity of fastaxis is higher than that of slowaxis. However, when we series_the fiber grating for the refractive index, temperature, and stress experiments by measuring reflected energy, all sensitivities of the fastaxes are larger than that of slowaxes.

According to the above experimental results, the three unknown parameters (ΔS, ΔT and ΔN) in the transfer matrix of Eq. (4) can be obtained from the given Bragg wavelength shift of the fast axis and the given reflective power variations of both fast and slow axes of the PMFBG.

$$\begin{bmatrix} \Delta\lambda \\ \Delta R_F \\ \Delta R_S \end{bmatrix} = \begin{bmatrix} 0.01864 & 0.0163 & 0 \\ 0.01992 & 0.1445 & 42.975 \\ 0.01266 & 0.08 & 27.375 \end{bmatrix} \begin{bmatrix} \Delta S \\ \Delta T \\ \Delta index \end{bmatrix}, \tag{4}$$

4. CONCLUSIONS

This study demonstrates that a new fiber sensor based on a PM-FBG cascaded with a LPG can be applied in the simultaneous measurement of stress, temperature, and refractive index. By the transfer matrix, the measured the Bragg wavelength shift and Bragg reflective power variation of PMFBG can be used for obtaining the variation in stress, refractive index, and temperature. The proposed scheme of concatenating a PMFBG and a LPG is a highly promising and simple design for a wide range of sensing applications.

In the future, we expected that the fabrication process can be optimized for improving the sensitivity and repeatability.

REFERENCES

1. Wang, Y. W. Jin, and D. N. Wang, "Unique temperature sensing characteristics of CO_2-laser-notched long-period fiber gratings," *Optics and Lasers in Engineering*, Vol. 47, 1044–1048, 2009.
2. Zhu, T., Y. J. Rao, J. L. Wang, and Y. Song, "A highly sensitive fiber-optic refractive index sensor based on an edge-written long-period fiber grating," *IEEE Photonics Technology Letters*, Vol. 19, No. 24, 1946–1948, 2007.
3. Zhuo, Z. C. and B. S. Ham, "A temperature-insensitive strain sensor using a fiber Bragg grating," *Optical Fiber Technology*, Vol. 15, 442–444, 2009.
4. Shu, X. W., B. A. L. Gwandu, Y. Liu, L. Zhang, and I. Bennion, "Sampled fiber Bragg grating for simultaneous refractive-index and temperature measurement," *Optics Letters*, Vol. 26, No. 11, 774–776, 2001.
5. Ye, C. C., S. W. James, and R. P. Tatam, "Simultaneous temperature and bend sensing with long-period fiber gratings," *Optics Letters*, Vol. 25, No. 14, 1007–1009, 2000.
6. Song, M., S. B. Lee, S. S. Choi, and B. Lee, "Simultaneous measurement of temperature and strain using two fiber Bragg gratings embedded in a glass tube," *Optical Fiber Technology*, Vol. 3, 194–196, 1997.

7. Lee, S. M., S. S. Saini, and M. Y. Jeong, "Simultaneous measurement of refractive index, temperature, and strain using etched-core fiber Bragg grating sensors," *IEEE Phtonics Technology Letters*, Vol. 22, No. 19, 1431–1433, 2010.
8. Chen, G., L. Liu, H. Jia, J. Yu, L. Xu, and W. Wang, "Simultaneous strain and temperature measurements with fiber Bragg grating written in novel Hi-Bi optical fiber", *IEEE Photon. Technol. Lett.*, Vol. 16, No. 1, 221–223, 2004.

QoS-based Genetic Expression Programming Prediction Scheme in the EPONs

I-Shyan Hwang[1,2], **Jhong-Yue Lee**[2], **and Andrew Tanny Liem**[2]

[1]Department of Information Communication, Yuan-Ze University, Chung-Li 32003, Taiwan
[2]Department of Computer Science and Engineering, Yuan-Ze University, Chung-Li 32003, Taiwan

Abstract— Ethernet Passive Optical Network (EPON) have been widely considered as one of the candidates to resolve the last mile problem in the next generation broadband access networks due to its simplicity, cost-effectiveness and high data rate. As a time-division multiplexing PON (TDM-PON) technology, the transmission of EPON is shared among multiple subscribers. Therefore, the traffic prediction in the Dynamic Bandwidth Allocation (DBA) plays an important role in the EPON system to boost the Triple-Play-Services (data, video, voice) Quality-of-Service (QoS). However, nowadays, most literatures predict the unexpected incoming packet by adopting credit-prediction and linear-prediction scheme. In this paper, we propose an evolutionary algorithm Genetic Expression Programming (GEP) prediction to solve the queue variation during waiting times as well as reducing the packet delay. We set the predictor in GEP based on cycle time, waiting time, bandwidth request and the mean bandwidth history request in every cycle time. Simulation results show that GEP prediction in DBA can avoid longer packet delay, reduce queue length, enhance QoS and effectively reduce high priority traffic delay and network performance degradation. Furthermore, we showed that our proposed prediction scheme can improve IPACT and has better system performance than well-known scheduling algorithm DBAM in terms of system throughput, queue length, end-to-end delay and jitter.

1. INTRODUCTION

The growth of Internet traffic such as IP telephony, video-on-demand, interactive gaming or two-way video conferencing in the residential and small business area has played an essential role in the evolution of broadband access networks [1]. This new technology required inexpensive, simple, scalable and capable for delivering Triple-Play-Services to an end user over a single network. Ethernet Passive Optical Networks (EPONs) that represent the convergence between Ethernet and Fiber infrastructure, appear to be the best solutions for the next-generation access network [2]. EPON provides bi-directional transmissions. In the downstream transmission, OLT has the entire channel bandwidth to broadcast the control messages and the data packets through a $1 : N$ passive splitter to each ONU. In the upstream transmission, a PON is a multipoint to point network, where all ONUs share the common transmission channel towards the OLT, and only a single ONU can upstream data in the transmission time slot to avoid data collisions [3]. To emphasize, any data collision will cause a longer end-to-end delay and degrade the system performance. Therefore, a proficient bandwidth allocation algorithm has become a prominent concern in EPON research, especially with the huge bandwidth demands and critical applications.

Bandwidth allocation schemes can be divided into two categories: *fixed bandwidth allocation* (FBA) [4] and *dynamic bandwidth allocation* (DBA) [5–8] schemes. In the FBA scheme, the OLT pre-allocates the fixed time slot regardless of the actual traffic arrival of each ONU, thus the upstream channel will be occupied although there is no frame to transmit. This can result in long delays for all Ethernet frames buffered in the other ONUs. Conversely, the DBA assigns the bandwidth dynamically based on the queue state information received from ONUs. However, in the traditional DBA scheme, the OLT will begin bandwidth allocation after collecting all REPORT messages which result in the *waiting time problem.* The waiting time at each ONU is the time between sending REPORT message and sending the buffered frames, which potentially leads to longer delays. As a result, when OLT grants the requested bandwidth to ONUs, a predict credit will add in the requirement of each ONU. Thus the incoming traffic during the waiting time is expected to be transmitted within the current time slot. Recently, exhaustive queue size prediction mechanisms have been proposed (which are credit-based [5], linear-based [6], proportion-based [7], waited-based [4], QoS-based [8]). These traffic prediction schemes are unable to provide feasible solutions for differentiated services (DiffServ) and also unable to address the queue size inconsistency problem. To address this problem, in this paper we proposed a prediction scheme technique by using Genetic Expression Programming (GEP) [9] for the creation of network traffic prediction.

The predictors in GEP are set based on the traits of ONUs such as: cycle time, waiting time, bandwidth request and history mean bandwidth request in every cycle time. In the GEP the individuals are encoded as linear strings of fixed length which are afterwards expressed as nonlinear expression trees (ETs) of different sizes and shapes. In this paper we integrate the GEP with IPACT referred as IPACT_GEP and compared it with DBAM [4]. Simulation results show that IPACT incorporated with GEP can improve overall system performances in terms of queue length, end-to-end delay, jitter, and system throughput.

2. PROPOSED GENETIC EXPRESSION PROGRAMMING PREDICTION

We implemented GEP as an extension of the traffic prediction mechanism for DBA. Our experiments studied the influence of the number of genes on the capability of the algorithms to evolve good solutions.

$$T = f(predictor) \tag{1}$$

where T is the target set which is the mean queue length of each ONUs based on network traffic from 10% to 100% (randomly selected information from $5 * 10^4$ data) and the predictor set are the traits of ONUs such as: cycle time, waiting time, bandwidth request, history mean bandwidth request in every cycle time, and the common basic parameters to both GEP and GP were kept equally as those used by Koza [10–12]. Thus, a set of 2000 random fitness cases chosen from the target value was used; and a very simple function set, composed only of the seven arithmetic operators $F = \{+, -, *, /, \exp(x), \mathrm{sqrt}(x), \mathrm{pi}\}$ was used. Additionally, for random numerical constants, we see that is not crucial for the evolution of perfect solutions problems. Nonetheless, evolution still goes efficiently if integer constants are used, hence one can illustrate the role random constants play and how they are integrated with Automatically Defined Functions by choosing real random constants. Therefore, real random constants are chosen from the interval $[-10, 10]$ with the mutation rate of random constant is 0.01. The fitness function used to evaluate the performance of each evolved program is based on the mean square error (Equation (2)) and explores the idea of a selection range and a precision. The selection range is used as a limit for selection to operate.

$$Variance = \sum_{N=1}^{N} (P_i - T_i)^2 \tag{2}$$

$$fitness = \frac{1}{1 + \frac{Variance}{N}}. \tag{3}$$

where P_i is the predicted value for the row i and T_i is the actual target value; N is the number of rows in the training data set. All fitness functions compute fitness scores that range from 0.0 to 1.0. A fitness of 0.0 means the model is poorly fitted or it is worthless or not viable. A fitness score of 1.0 means the model fits the data perfectly. Thus, for a perfect fit, the variance value term is zero and fitness is equal to 1.0. In our experiments we use a selection range of 100 and a precision of 0.01. The algorithms use a population size of 60, gene head length of 8, mutation rate of 0.0044, IS and RIS transposition rates of 0.1, and two-point and one-point recombination rates of 0.3; recombination and gene transposition rates are 0.1 each, and the linking function is addition. The parameters used per run and our experimental results are summarized in Table 1 and Table 2 respectively.

3. PERFORMANCE EVALUATION

In this section, we present the results of simulation experiments conducted to evaluate the system throughput, queue length, end-to-end delay and jitter of the IPACT_GEP compared to the DBAM [4]. The system model is set up in the OPNET simulator with one OLT and 32 ONU. The downstream and upstream channels are both 1 Gb/s. The distance from an ONU to the OLT is assumed to range from 10 to 20 km and each ONU has a finite buffer of 10 MB. For system operation parameter, the cycle time is set to 1 ms, the guard time is 5 µs and the DBA computation time is 10 µs in the evaluation. For the traffic model considered here, an extensive study shows that most network traffic can be characterized by self-similarity and long-range dependence (LRD). This model is utilized to generate highly bursty BE and AF traffic classes with the Hurst parameter of 0.7, and packet sizes are uniformly distributed between 64 and 1518 bytes. On the other hand, high-priority traffic (e.g., voice applications) is modeled using a Poisson distribution and packet size is fixed to 70 bytes [13]. The proportion of the Constant Bit Rate traffic (CBR) such as Expedited

Table 1: General settings.

Parameter	Value	Parameter	Value
Population size	60	IS transposition rate	0.1
Number of genes	4	Two-point recombination rate	0.3
Genes head length	8	One-point recombination rate	0.3
Genes length	33	Random constant per gene	10
Maximum number of generations	2000	Random constants data type	real
Generations without improvement	200	Random constants range	$-10 \sim 10$
V-fold cross-validation	10	Random constants Mutation rate	0.01
Mutation rate	0.044	Number of fitness cases	200
Inversion rate	0.1	Capture target interval time	1 ms
RIS transposition rate	0.1		0.1

Table 2: GEP results.

Parameter \ Class	IPACT
EF Generations	1623
AF Generations	1839
BF Generations	1689
EF Variance	49773.86
AF Variance	213630.58
BE Variance	214495.57
EF Mean APE	2.80%
AF Mean APE	6.01%
BE Mean APE	5.86%

Forwarding (EF) is 20% and the Variable Bit Rate (VBR) such as Assured Forwarding (AF) and Best Efforts (BE) are 40% respectively.

3.1. Waste Bandwidth Improvement

Figure 1 compares the Bandwidth waste vs. traffic load among the IPACT with/without GEP and DBAM. The improve percentage can be calculated as follow:

$$\frac{\left(W^T_{Origin} - W^T_{after}\right)}{W^T_{Origin}}, \tag{4}$$

where $T \in$ {IPACT with GEP}. The IPACT has the worst throughput because the idle period problem will reduce whole passive optical network resource and poor bandwidth allocation mechanism will lead in lowering system throughput. On the other hand, DBAM has better system performance by add some waited-based prediction to face the packet arrival in the waiting time problem. The propose GEP prediction mechanism not only can improve the throughput performance in Fixed-IPACT but also in DBAM because of GEP can offer a better prediction mechanism then DBAM.

3.2. Average End-to-End Delay and Queue-Length

Figure 2 and Figure 3 compared average packet end-to-end delay and queue length among IPACT, IPACT_GEP and DBAM. The simulation result shows the IPACT_GEP has a lowest end-to-end delay and queue length especially in the heavy traffic load. The reason is that as the network load is high, the IPACT_GEP can still guarantee the whole traffic class to transmit more packets which are leading to a lower average end-to-end packet delay and queue length.

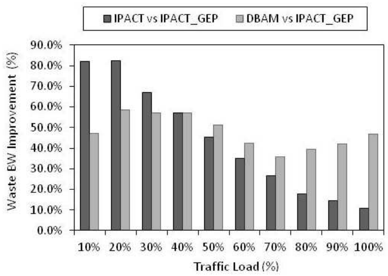

Figure 1: Waste bandwidth improvement (%).

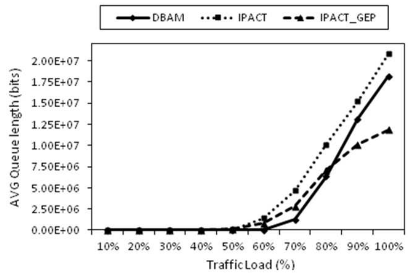

Figure 2: Average queue length (bits).

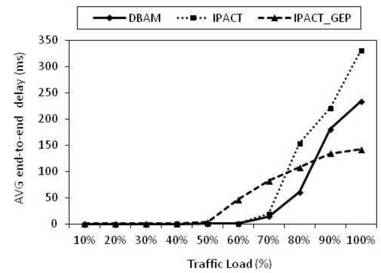

Figure 3: Average end-to-end delay (ms).

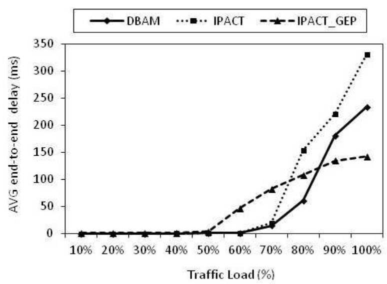

Figure 4: EF end-to-end delay (ms).

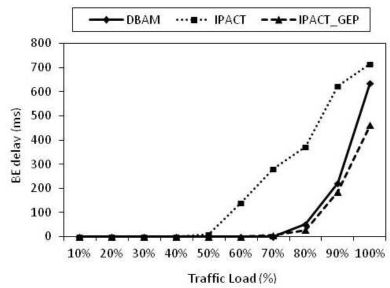

Figure 5: BE end-to-end delay (ms).

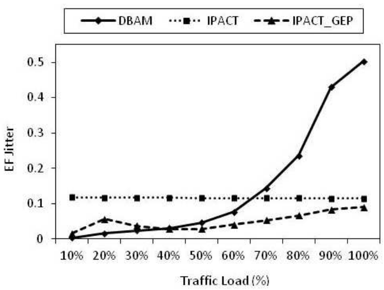

Figure 6: EF jitter.

3.3. EF and BE End-to-end Delay

Figure 4 and Figure 5 compared average EF and BE end-to-end delay packet delay among IPACT, IPACT_GEP and DBAM. The simulation result shows the IPACT_GEP has a lowest EF end-to-end delay, particularly when the traffic load exceeds 80%. The reason is that the IPACT_GEP can still accurately predict the CBR traffic class and VBR traffic class without scarifying the low priority traffic which is leading to a lower EF and BE end-to-end packet delay. On the other hand, the DBAM can guarantee the CBR traffic but can not guarantee VBR traffic because of the waited-based prediction mechanism. Additionally, the IPACT_GEP meets the ITU-T recommendation G.114 that specifies the delay for EF traffic in the access network is 1.5 ms [14].

3.4. Jitter

Figure 5 compares the jitter performance of IPACT, IPACT_GEP and DBAM for EF traffic class versus the traffic loads. The delay variance is calculated as , where represents the delay time of EF packet i and N is the total number of received EF packets. Simulation result shows that the jitter for EF traffic is increasing as the traffic load increase. The IPACT can guarantee a stable but higher jitter because of the fixed window size and cycle time. The waited-base DBAM can not predict the variable bit rate traffic which leads to an inconsistent cycle time that causing the poor jitter performance especially in heavy traffic load. The IPACT_GEP can achieve a stable and lower jitter because of maintaining a stable cycle time

4. CONCLUSION

In this study, the crucial issues that can improve the performance in EPON are discussed and evaluated specifically. The IPACT_GEP prediction scheme resolves the waiting time problem in the traditional DBA and enhances the system performance, reduce end-to-end packet delay and improve the bandwidth utilization. Additionally, the GEP mechanism considers the prediction for differential traffic characteristic and allocates bandwidth for differential traffic adaptively. Simulation results show that the throughput of artificial neural network programming prediction is better than non-predict and linear programming prediction mechanism, especially in throughput performance. Furthermore, the proposed GEP prediction scheme can support better QoS, the average end-to-end delay and lower bandwidth waste of each ONU than IPACT and DBAM

REFERENCES

1. Dhaini, A. R., H. Pin-Han, and S. Gangxiang, "Toward green next-generation passive optical networks," *IEEE Communications Magazine*, Vol. 49, No. 11, 94–101, Nov. 2011.
2. Aurzada, F., M. Scheutzow, M. Reisslein, N. Ghazisaidi, and M. Maier, "Capacity and delay analysis of next-generation passive optical networks (NG-PONs)," *IEEE Transactions on Communications*, Vol. 59, No. 5, 1378–1388, May 2011.
3. IEEE Draft P802.3ah/D1.0TM, Media Access Control Parameters, Physical Layers and Management Parameters for Subscriber Access Networks, Aug. 2002.
4. Luo, Y. and N. Ansari, "Bandwidth allocation for multiservice access on EPON," *IEEE Communications Magazine*, Vol. 43, No. 2, S16–S21, Feb. 2005.
5. Sue, C. C. and H. W. Cheng, "A fitting report position scheme for the gated ipact dynamic bandwidth algorithm in EPONs," *IEEE/ACM Transactions on Networking*, Vol. 18, No. 2, 624–637, Apr. 2010.
6. Hwang, I. S., Z. D. Shyu, L. Y. Ke, and C. C. Chang, "A novel early DBA mechanism with prediction-based fair excessive bandwidth allocation scheme in EPON," *Computer Communications*, Vol. 31, No. 9, 1814–1823, Jun. 2008.
7. Zheng, J., "Efficient bandwidth allocation algorithm for ethernet passive optical networks," *IEEE Proceedings Communications*, Vol. 153, No. 3, 464–468, Jun. 2006.
8. Chen, J., B. Chen, and L. Wosinska, "Joint bandwidth scheduling to support differentiated services and multiple service providers in 1 G and 10 G EPONs," *IEEE/OSA Journal of Optical Communications and Networking*, Vol. 1, No. 4, 343–351, Sep. 2009.
9. Karakasis, V. K. and A. Stafylopatis, "Efficient evolution of accurate classification rules using a combination of gene expression programming and clonal selection," *IEEE Transactions on Evolutionary Computation*, Vol. 12, No. 6, 662–678, 2008.
10. Mitchell, M., *An Introduction to Genetic Algorithm*, MIT Press, Cambridge, MA, 1996.
11. Koza, J. R., *Genetic Programming: On the Programming of Computers by Means of Natural Selection*, MIT Press, Cambridge, MA, 1992.
12. Koza, J. R., *Genetic Programming II: Automatic Discovery of Reusable Programs*, MIT Press, Cambridge, MA, 1994.
13. Grossman, D., "New Terminology and clarifications for diffserv," IETF RFC 3260, Apr. 2002.
14. ITU-T Recommendation G.114, "One-way transmission time," in Series G: Transmission Systems and Media, Digital Systems and Networks, Telecommunication Standardization Sector of ITU, May 2000.

Performance and Confidentiality Comparison of Different Hybrid SAC/OCDMA-WDM Overlay Schemes

Isaac A. M. Ashour[1], **Sahbudin Shaari**[1], **Hossam M. H. Shalaby**[2], **and P Susthitha Menon**[1]

[1]Institute of Microengineering and Nanoelectronics (IMEN), Universiti Kebangsaan Malaysia
43600 UKM Bangi, Selangor, Malaysia
[2]Department of Electronics and Communications Engineering
School of Electronics, Communications, and Computer Engineering
Egypt-Japan University of Science and Technology (E-JUST), Alexandria 21934, Egypt

Abstract— Code pulses of a spectral amplitude coding/optical code division multiple-access (SAC/OCDMA) system are overlaid onto a multichannel wavelength division multiplexing (WDM) system. Modified quadratic congruence (MQC) codes are developed as the signature codes for the SAC/OCDMA system. The developed code is to avoid the overlapping between signals of both systems with no use of notch filters. In addition, performance and confidentiality results of this scheme are compared to our previous hybrid SAC/OCDMA-WDM overlay scheme which utilizes normal MQC codes with notch filters. The system performance and data confidentiality are evaluated in terms of bit-error rate (BER) and eye diagrams. The eavesdropper's interceptor that is based on a simple energy detector can scan all corresponding SAC/OCDMA wavelengths to detect an entire coded signal of an authorized user. Our results indicate that the performance and confidentiality have inverse relationship between the two hybrid systems. For a first hybrid scheme that does not adopt notch filters, the BER performance, when a data rate is 622 Mbps, for OCDMA users is about 10^{-15} at 4 dB of an optical attenuator, and BER for eavesdropper detection values vary from 10^{-6} to 10^{-15} due to different overlapping effects between WDM interferes and OCDMA pulses. On the second hand for a hybrid scheme that contains notch filters, the BER performance for OCDMA users is about 10^{-12} at 4 dB of an optical attenuator, and for eavesdropper detection values are mostly about 10^{-2}. However, it is concluded that an eavesdropper faces immunity from SAC/OCDMA system in both cases because WDM channels act as a partial masking over encoded signals in a hybrid scheme. Furthermore, the tradeoff between the performance and confidentiality for authorized SAC/OCDMA users is considered.

1. INTRODUCTION

The main Optical CDMA and WDM systems have been of widespread implementation for local and metro access network. This is because OCDMA systems provide users both simultaneous and asynchronous access to networks with high security [1, 2], and WDM systems provide a relatively high transmission capacity [13]. In addition, OCDMA can be overlaid onto existing WDM networks in order to enhance the network security [3, 4]. It has been shown that modified quadratic congruence (MQC) code is an effective code for spectral amplitude coding/optical CDMA (SAC/OCDMA) [5]. This code can reduce the effects of both phase induced intensity noise (PIIN) and multiple access interference (MAI).

Recently, each WDM channel can employ the same set of SAC/OCDMA systems [6, 7]. In [8, 9], a hybrid WDM-OCDMA scheme has been demonstrated using spectrally phase-encoded OCDMA channels. In [10–12], we have also demonstrated in-band transmission of both SAC/OCDMA and WDM signals using MQC codes.

In this paper, we develop a new MQC code for simultaneous transmission of several OCDMA channels and WDM channels on the same spectral band without spectrum overlapping. In addition, we apply the eavesdropper's technique, used in [10], for comparison of performance and confidentiality between this scheme and our previous scheme [10, 11] in terms of both bit-error rate (BER) performance and eye diagrams.

The remainder of this paper is organized as follows. In Section 2, the development of our new MQC code is presented for the proposed system. Different hybrid schemes designs and simulations are demonstrated in Section 3. Section 4 is devoted for our results and discussions. Finally the conclusion of the paper is provided in Section 5.

2. NEW MQC CODE DEVELOPMENT

A new MQC code for simultaneous transmission of both SAC-OCDMA and WDM channels without spectrum overlapping is to be developed. The MQC code that is mentioned in [5] has code families

Table 1: MQC binary sequences, S with $p = 3$ and $N = 12$; and the corresponding wavelengths.

N	C_1	C_2	C_3	C_4	C_5	C_6	C_7	C_8	C_9	C_{10}	C_{11}	C_{12}
Wavelength (nm)	1549	1549.2	1549.4	1549.6	1549.8	1550	1550.2	1550.4	1550.6	1550.8	1551	1551.2
Code sequences of S matrix	1	0	0	0	1	0	0	1	0	0	0	1
	0	1	0	0	0	1	0	0	1	0	0	1
	0	0	1	1	0	0	1	0	0	0	0	1
	0	1	0	0	1	0	1	0	0	1	0	0
	0	0	1	0	0	1	0	1	0	1	0	0
	1	0	0	1	0	0	0	0	1	1	0	0
	0	1	0	1	0	0	0	1	0	0	1	0
	0	0	1	0	1	0	0	0	1	0	1	0
	1	0	0	0	0	1	1	0	0	0	1	0

$(N, w, \lambda) = (p^2 + p, p + 1, 1)$, with p a prime number. Here, $N = p^2 + p$ is the code length, $w = p + 1$ is the code weight, and $\lambda = 1$ is the cross-correlation. This code allows $K = p^2$ simultaneous users. Table 1 shows some binary code sequences, S, for parameters $p = 3$ and $N = 12$; and the corresponding wavelengths.

A new binary MQC sequences, Q, is generated based on the old binary MQC sequences, S, by using a shifting technique. This technique can be done by a multiplication of S and an A_x matrix, as defined below. A basic matrix A_1 is given by a 3×4 matrix:

$$A_1 = \begin{bmatrix} 1000 \\ 0100 \\ 0010 \end{bmatrix}_{3\times 4} \tag{1}$$

The matrix A_x is defined as

$$A_x = \begin{bmatrix} A_1 & 0 & \dots & \dots & 0 \\ 0 & A_1 & 0 & \dots & 0 \\ 0 & 0 & \ddots & \dots & \dots \\ \vdots & \vdots & \dots & \ddots & \dots \\ 0 & 0 & \dots & 0 & A_1 \end{bmatrix}_{N\times(N+x)} \tag{2}$$

where $x = \frac{N-(N \bmod 3)}{3}$ represents the number of A_1 matrices in A_x and the zeros in A_x are of dimension 3×4. If S matrix has size $K\times N$, then the size of A_x is $N\times M$ where $M = N + \frac{N-(N \bmod 3)}{3}$. The result is a new binary code sequences, Q, with a size of $K \times M$. We notice that the number of columns of Q increases by one for each old three columns with consideration of integer number. In our proposed system, we assume that the bandwidth of a WDM channel, B_w equals that of a chip of MQC code of SAC/OCDMA, B_c. That is, $B_w = B_c = 0.2\,\text{nm}$. The WDM channels are allocated at every 100 GHz (or equivalently 0.8 nm in wavelength). Therefore, for each 3 elements of MQC chip, there is 1 channel of WDM system. This method can also be applied on any code of SAC/OCDMA. In this paper, we present as an example; MQC code sequences with $p = 5$ and $K = 25$, so the size of S is 25×30. Hence, the size of A_x 30×40 and the size of $Q = S \times A_x$ is 25×40. This leads to having 10 locations for WDM channels as shown in Table 2. This technique is important to avoid the direct spectrum overlapping between the signals from both subsystems, which improves the performance compared to that of our previous systems [10, 11].

3. DIFFERENT HYBRID SCHEMES DESIGN AND SIMULATION

In a hybrid scheme as shown in Fig. 1, broadband OCDMA signals and narrow band WDM signals are combined together in one system. We have two techniques to reduce the overlapping between these signals. The first technique that mentioned in [10, 11] utilizes notch filters at the receiver side. The second one that was introduced in the above section does not need notch filters. The two

Table 2: MQC binary sequences with shifting process, Q with $p = 3$, $x = 4$ and $M = 16$.

N	C_1	C_2	C_3	W_1	C_4	C_5	C_6	W_2	- - -	C_{28}	C_{29}	C_{30}	W_{10}
λ (nm)	1546.0	1546.2	1546.4	1546.6	1546.8	1547.0	1547.2	1547.4	- - -	1553.2	1553.4	1553.6	1553.8
Code sequences of Q matrix	1	0	0	0	0	0	0	0	- - -	1	0	0	0
	0	1	0	0	0	0	0	0	- - -	0	1	0	0
	0	1	0	0	0	0	0	0	- - -	1	0	0	0
	0	0	1	0	0	0	0	0	- - -	1	0	0	0
	0	0	0	0	1	0	0	0	- - -	0	1	0	0
	0	0	1	0	0	0	0	0	- - -	0	0	0	0

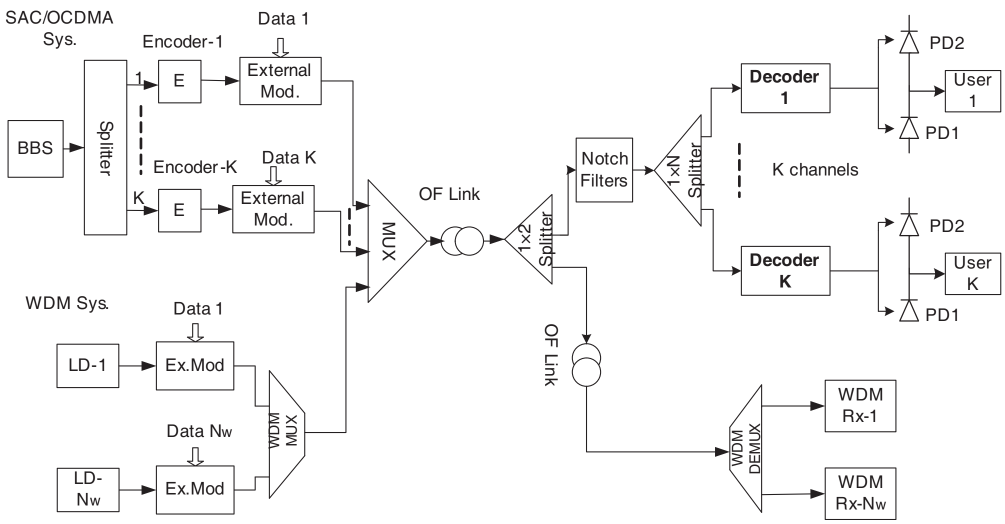

Figure 1: A hybrid system block-diagram.

Table 3: Typical parameters used for simulation.

Broadband source transmitted power for SAC/OCDMA	16 dBm
Laser source transmitted power for WDM	1 dBm
Data bit rates for SAC/OCDMA and WDM, respectively	622 Mbps and 2.5 Gbps
Bandwidth of encoder/decoder filters	25 GHz
Fiber link attenuation	0.2 dB/km
Fiber dispersion	17 ps/nm-km
Dispersion slope	0.075 ps/$\sqrt{}$km
External modulator extinction	30 dB
Dark current	5 nA
Thermal noise coefficient of the photodetector for SAC/OCDMA and WDM, respectively	1×10^{-22} W/Hz and 1.8×10^{-22} W/Hz
Number of SAC/OCDMA users	25
Number of WDM users	8

different schemes have been simulated for performance comparison. The MQC code for 25 users used in the simulation is (N, 6, 1), while used WDM channels are eight with 100 GHz frequency spacing. The typical system parameters, considered for the simulation, are illustrated in Table 3.

For data confidentiality comparison, an eavesdropper's code interceptor that is based on scanning all corresponding wavelengths used by SAC/OCDMA users is used in the simulation. This technique of an eavesdropper basically depends on a classical detection theory [14]. The eavesdropper can tap a codeword of the OCDMA system to detect whether the energy of a single pulse is available or not. An optical matched filter and a photodiode can perform this detection. After some calculations by a smart eavesdropper, the data for an authorized user will be read. The receiver structure of an eavesdropper is shown in Fig. 2. However, due to WDM signals that perform a partial masking over OCDMA pulses, the eavesdropper faces challenges to distinguish between the 0's and 1's pulses of a SAC/OCDMA code, and hence, he or she will take more time to detect the entire code and to read the authorized data.

4. RESULTS AND DISCUSSION

The bit-error rate (BER) performances for both hybrid systems are evaluated and plotted in Figs. 3 and 4. Fig. 3 shows the BER for an OCDMA user with various optical attenuator values for both hybrid schemes. The BER for the hybrid scheme that without notch. This is expected because the effect of overlapping is more in the former case. For example, at 4 dB of an optical attenuator, the BER performance for OCDMA users are about 10^{-12} and 10^{-15} for the first and second schemes,

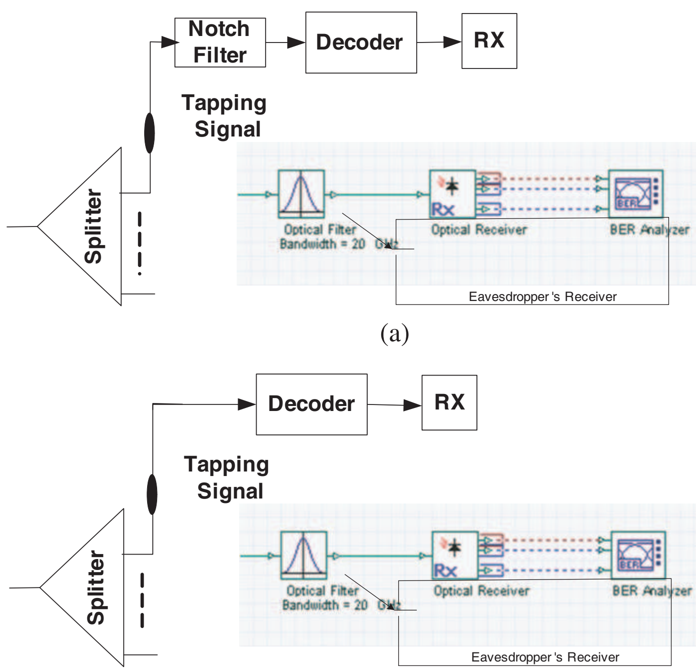

(b)

Figure 2: Eavesdropper's technique at: (a) an OCDMA receiver has notch filters; (b) an OCDMA receiver has no notch filters.

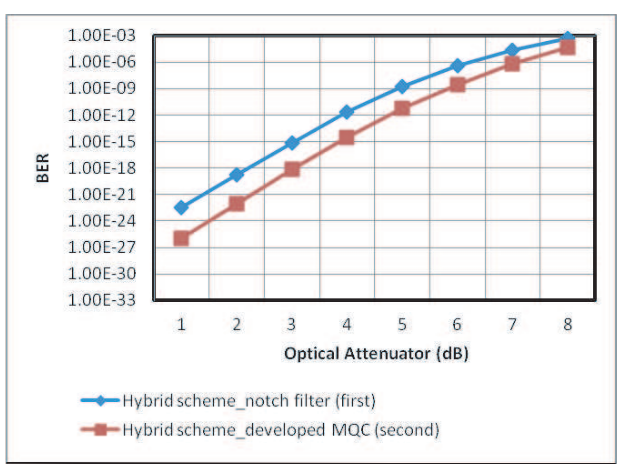

Figure 3: BER versus optical attenuator values for OCDMA user for both hybrid schemes.

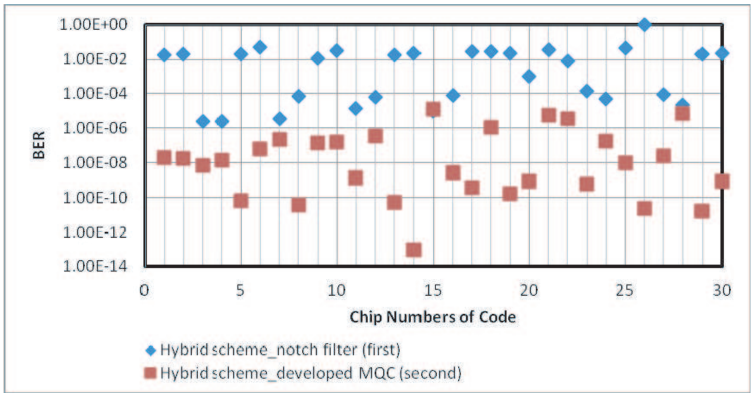

Figure 4: BER versus chip numbers of MQC codes for eavesdropper's interceptor for both hybrid schemes.

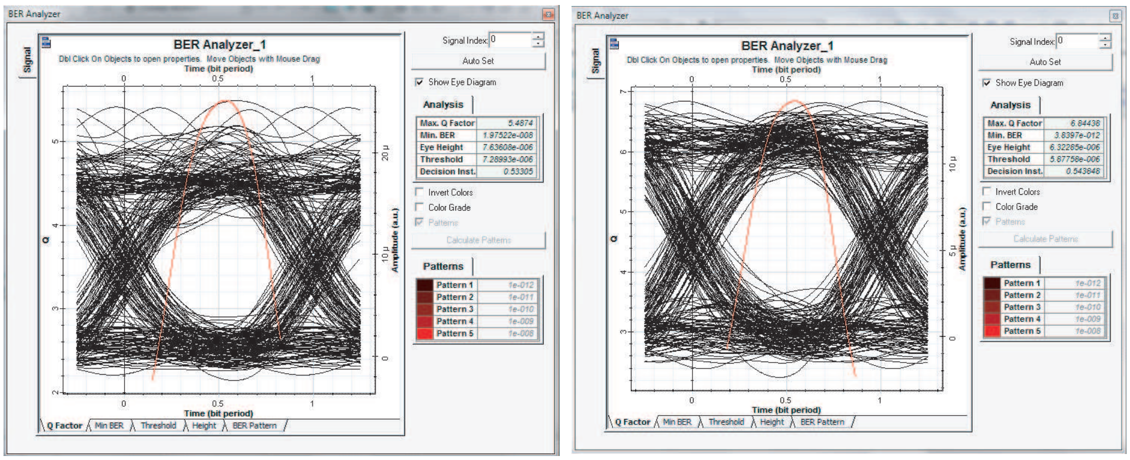

(a) (b)

Figure 5: Eye diagrams for a WDM user at 4 dB optical attenuator: (a) Hybrid scheme_notch filter (first); (b) Hybrid scheme_developed MQC (second).

respectively. Fig. 4 also shows the BER but for an eavesdropper's interceptor for both hybrid schemes with versus chip numbers of MQC codes. At the first scheme, the BER for eavesdropper detection values are mostly about 10^{-2}, while at the second scheme the BER values vary from 10^{-6} to 10^{-15} due to different overlapping effects between WDM interferes and OCDMA pulses. These results indicate that the data confidentiality for the first hybrid scheme is better than that for the second one. Hence, the performance and confidentiality have inverse relationship between the two hybrid systems.

The eye diagrams for evaluating the performance of WDM systems under both hybrid schemes are shown in Fig. 5. These diagrams are obtained at 12 dB optical attenuator and 2.5 Gbps data rates. The BER is found to be 1.9×10^{-8} for first scheme setup as in Fig. 3(a) and 3.8×10^{-12} for second scheme setup as in Fig. 3(b). It is obvious that the performance relationship of WDM systems under the two schemes is as mentioned above for OCDMA system.

5. CONCLUSIONS

The separation process between WDM and SAC/OCDMA systems has been presented by developing a new MQC code. In addition, BER performance and confidentiality results of this scheme have been compared to hybrid SAC/OCDMA-WDM overlay scheme which utilizes normal MQC codes with notch filters. Our results indicate that the performance and confidentiality have inverse relationship between the two hybrid schemes. It is also concluded that an eavesdropper faces immunity from SAC/OCDMA system in both cases because WDM channels act as a partial masking over encoded signals in a hybrid scheme. Furthermore, the tradeoff between the performance and confidentiality for authorized SAC/OCDMA users is considered.

ACKNOWLEDGMENT

We would like to acknowledge Universiti Kebangsaan Malaysia for sponsoring this project under grant no. UKM-OUP-NBT-27-119/2011. We also would like to thank the management of UKM for the fellowship grant "ZAMALAH".

REFERENCES

1. Salehi, J. A., "Code division multiple access techniques in optical fiber network — Part I: Fundamental principles," *IEEE Trans. Commun.*, Vol. 37, 824–833, Aug. 1989.
2. Salehi, J. A. and C. A. Brackett, "Code division multiple access techniques in optical fiber network — Part II: System performance analysis," *IEEE Trans. Commun.*, Vol. 37, 834–842, Aug. 1989.
3. Wu, B. B., P. R. Prucnal, and E. E. Narimanov, "Secure transmission over an existing public WDM lightwave network," *IEEE Photonic Tech. L.*, Vol. 18, No. 17, 1870–1872, 2006.
4. Wu, B. B. and E. E. Narimanov, "A method for secure communications over a public fiber-optical network," *Opt. Express*, Vol. 14, No. 9, 3738–3751, 2006.
5. Wei, Z., H. M. H. Shalaby, and H. G. Shiraz, "Modified quadratic congruence codes for fiber Bragg-grating-based spectral amplitude coding optical CDMA systems," *J. Lightwave Technol.*, Vol. 19, No. 9, 1274–1281, 2001.
6. Yang, C. C., "Hybrid wavelength-division-multiplexing/spectral-amplitude-coding optical CDMA system," *IEEE Photonic Tech L.*, Vol. 17, No. 6, 1343–1345, 2005.
7. Huang, J., Y. Chang, and C. Hsu, "Hybrid WDM and optical CDMA implemented over waveguide-grating-based fiber-to-the-home networks," *Opt. Fiber Technol.*, Vol. 13, No. 3, 215–225, 2007.
8. Galli, S., R. Menendez, P. Toliver, T. Banwell, J. Jackel, J. Young, and S. Etemad, "Experimental results on the simultaneous transmission of two 2.5 Gbps optical-CDMA channels and a 10 Gbps OOK channel within the same WDM window," *Proc. IEEE Optical Fiber Communication (OFC)*, Vol. 3, 29–31, Anaheim, CA, Mar. 6–11, 2005.
9. Galli, S., R. Menendez, P. Toliver, T. Banwell, J. Jackel, J. Young, and S. Etemad, "Novel results on the coexistence of spectrally phase encoded OCDMA and DWDM," submitted to ICC'05, Sep. 2004.
10. Ashour, I. A., S. Shaari, H. M. Shalaby, and P. S. Menon, "Investigation of in-band transmission of both spectral amplitude coding/optical code division multiple-access and wavelength division multiplexing signals," *SPIE Opt. Eng*, Vol. 50, No. 6, 1–7, Jun. 2011.
11. Ashour, I. A., S. Shaari, H. M. Shalaby, and P. S. Menon, "Simulation of MQC code of SAC/optical CDMA and WDM hybrid overlay system," *Proc. IEEE Conf. International Conference on Modeling, Simulation and Applied Optimization (ICMSAO 2011)*, 1–4, Kuala Lumpor, Malaysia, 2011.
12. Ashour, I. A., S. Shaari, H. M. Shalaby, P. S. Menon, and H. A. Bakarman, "Hybrid SAC/optical CDMA-WDM overlay system for enhancing network security," *Proc. IEEE Conf. International Conference on Photonics (ICP2010)*, 1–4, Langkawi, Malaysia, 2010.
13. Agrawal, G. P., *Fiber-Optic Communications Systems*, 3rd Ed., John Wiley & Sons, New York, 2002.
14. Shake, T. H., "Security performance of optical CDMA against eavesdropping," *J. Lightwave Technol.*, Vol. 23, No. 2, 655–670, 2005.

2D Fiberoptic Metal Profile Detector

Wei-Shu Hua[1], **Joshua Hooks**[2], **Nicholas Erwin**[2], **Wen-Jong Wu**[1],
Feng-Ju Hsieh[2], **and Wei-Chih Wang**[2,3,4]

[1]Department of Engineering Science and Ocean Engineering, National Taiwan University, Taiwan
[2]Department of Mechanical Engineering, University of Washington, Seattle, WA, USA
[3]Department of Electrical Engineering, University of Washington, Seattle, WA, USA
[4]Medical Device Innovation Center, National Cheng Kung University, Taiwan

Abstract— Metal detector systems are widely using in current daily life. Nowadays, metal detectors operate on three basic technologies: very low frequency (VLF), pulse induction (PI), and beat-frequency oscillation (BFO). They are commonplace in libraries, airports, military camp, prisons, stores and shops. However, these devices share the common disadvantages of not being able to detect the profile of metal object. To resolve these problems, we recently developed a compact metal detector capable of differentiate metal of different shapes and geometry using a fiber-optic magnetostriction sensor. The basic concept of the metal detection is based on monitoring strain-induced optical path length change in the interferometer stems from the magnetic field induces magnetostriction effect on the ferromagnetic material which is coated on optic-fiber. Metal detection is made possible by disrupting the magnetic flux density present on the magnetostrictive sensor. In this paper, we will present our approach and the latest result of 2D metal profile measurement.

1. INTRODUCTION

Metal detector systems are widely used in our everyday lives, such as walk-through metal detectors in an airport or handheld metal detection devices at a concert or sporting event, etc.. In general, metal detector technology is a huge part of our daily lives, with a range of uses which spans from leisure to work to safety. They are commonplace in airports security, libraries, prisons, stores, armed forces, shops and government buildings. Currently metal detectors can be categorized into three basic technologies: very low frequency (VLF), pulse induction (PI), and beat-frequency oscillation (BFO) [1–3]. These conventional metal detector systems share common disadvantages of not being able to detect the profile of a metal object, being relatively bulky in size, and not being resistant to RF interference caused by the surrounding electronics devices. In this paper, our research will concentrate on developing a novel compact metal detector system that overcomes aforementioned shortcomings. As we have previously published [4], our metal detector system is integrated fiber-optic Mach-Zehnder interferometer with the novel magnetostrictive material. The main concept of our metal detector is the use a simple DC magnetic field scheme with the magnetostrictive material as the sensing device. The overall main structure consists of fiber-optic Mach-Zehnder interferometers. Therefore, our metal sensor can be regarded as a novel metal detector system.

For our detector, a fiber-optic magnetic field sensor uses the change in length of a magnetostrictive element in the presence of a magnetic field to change the optical path length of a fiber optic magnetic sensor. Therefore, our metal detection is made possible by monitoring strain-induced optical path length change in the interferometer which stems from the magnetostrition effect induced by magnetic field. Previous studies of our magnetostrictive material (WC-WSJOSH-2) coated on to fibers proves this concept is successful for metal detection [5]. Also, our previous experimental results show that our metal detector can identify the general geometrical shape of a rod rectangular bar, wrench and steel plate with two holes [6, 7]. In the present study, we report the latest results of the magnetostriction applications in clamp metal profile sensing.

2. POLYMERIC FIBEROPTIC MAGNETOSTRICTIVE METAL DETECTION SYSTEM

The fiber-optic sensor is coated with magnetostrictive material and embedded in composite resin. Numerous fiber-optic magnetic field sensors have been developed. Yariv and Winsor [8] proposed a now common configuration which uses a magnetostrictive film coating an optic fiber. This sensor is in the form of two Mach-Zehnder fiber-optic interferometers immersed in a magnetic field. The magnetic field leads to the magnetostrictive film to deform, straining the optic fiber. This causes a change in the length of the optical path. An interferometer is used to measure the phase changes. Our research on metal detector system will concentrate on this technique; please refer to our previous experiments [4, 5] for greater detail. In this paper, the metal detector utilizes a single mode fiber with the ferromagnetic polymer coating applied directly onto the cladding of the sensing arm. Measurement of the intensity of the resulting strain on the magnetostrictive material is based on the magnetic field induced phase shift in the interferometer given by [8]. In this paper, the structure of magnetostrictive metal sensor is shown in Figure 1(a). We use the different layout and geometry that we reported previously [6]. In this case, the sensing fiber is bent into a circle shape in order to reduce the detector size (30 cm long and 1.5 mm thick, see Figure 1(b)), and the magnetostrictive material is manipulated during fabrication to increase its sensitivity.

3. EXPERIMENTAL PROCEDURES

The overall metal detector system is based on Mach-Zehnder fiberoptic interferometer, the aforementioned sensing element consisting of magnetostrictive material associated with an optical fiber of an interferometer arm is the defining component for detecting changes in magnetic fields. When a change in the magnetic field occurs it causes longitudinal dimension changes in the magnetostrictive material. These changes induce a strain in the optical fiber. This strain causes a phase shift in the optically propagating beam in the fiber which is detectable by interferometry. The overall experimental setup for the magnetostrictive metal detector system is shown in Figure 2. For experimental components chosen and set up procedure, please refer to our previous publications [4, 5] for greater detail.

In this paper, the metal object is mounting on homemade wooded track stage (Figure 3). For complex metal measurement, the clamp metal object (Figure 4) was attached on the underside of the cart, parallel to the metal sensor. When a metal object is directly above the transformer, a localized magnetic disturbance is created. This disturbance results in a phase shift that is observed in the output interferometer. Similar to the previous metal detector setup [6], a constant DC magnetic field is applied to the metal sensor, with a Hall Effect sensor positioned directly above for a reference signal (~ 1 cm above the autotransformer). Table 1 provides details on the actual size and position of the metal object. The space between the metal object and the sensor is 1 cm.

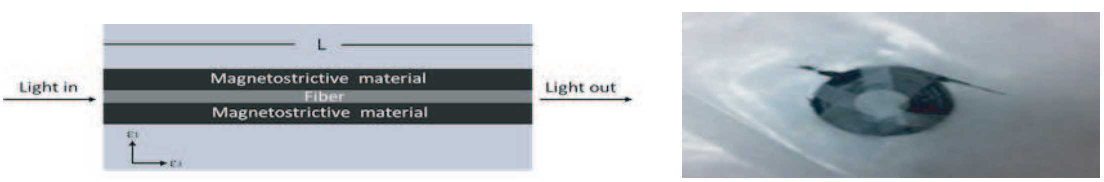

(a) (b)

Figure 1: Configuration of metal sensor. (a) The structure of magnetostrictive metal sensor. (b) The photo of magnetostrictive metal sensor (WC-WSJOSHNICK-1).

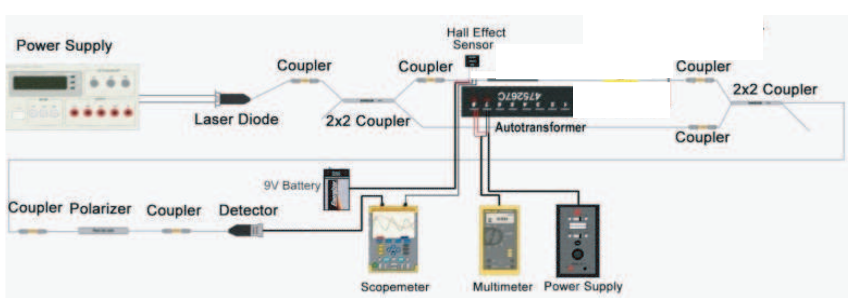

Figure 2: Scheme of polymeric fiber-optic magnetostrictive metal detector system.

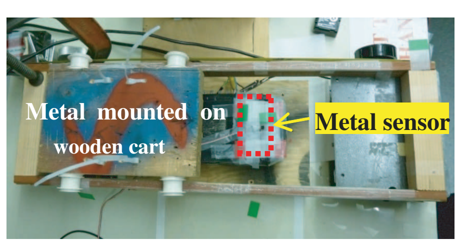

Figure 3: Configuration of wooden track stage.

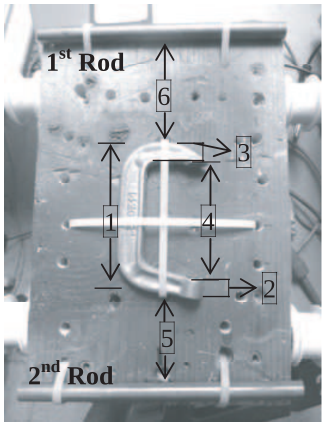

Figure 4: Configuration of clamp metal object.

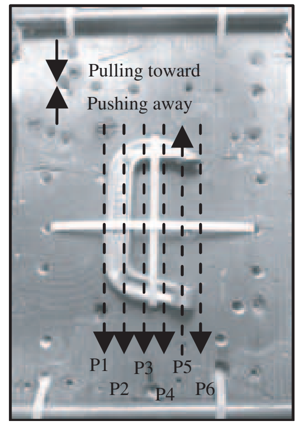

Figure 5: The movement direction of wooden cart with metal object.

Table 1: The dimensions of investigated samples.

Investigated samples	Position	Distance
Rod	1st Rod	0.9 cm
	2nd Rod	0.9 cm
Clamp	Clamp's arm (1)	8.5 cm
	Clamp south (2)	1.3 cm
	Clamp north (3)	1.3 cm
Gap	Distance middle (4)	6.7 cm
	Distance south (5)	5 cm
	Distance north (6)	6.5 cm

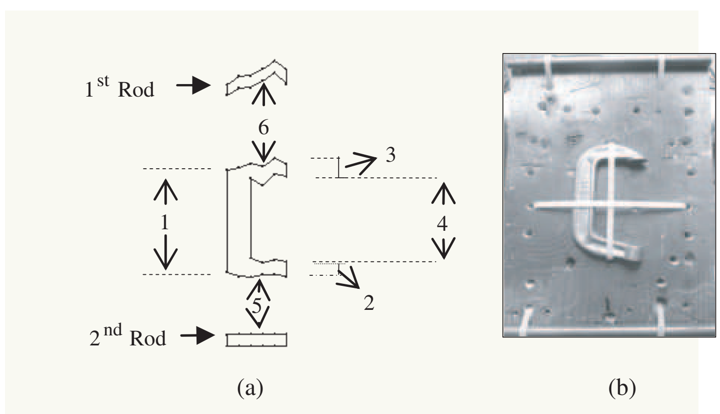

Figure 6: Plots of output mapping result from magnetostrictive metal sensor with C clamp. (a) Mapping metal's outline. (b) Actual investigated metals.

The cart was moved back and forth by hand, striving for a constant speed. For metal's profile mapping, the cart with clamp metal was being shifted toward right direction with 1 cm by each measurement. Figure 5 shows the movement direction of wooden cart with metal object. This experimental design was not only able to detect the presence of metal objects, but was also capable of mapping metal shapes. By mounting metal objects on a wooden cart and moving the cart over the metal sensor, it becomes possible to attempt numerous metal detection trials. Finally, we use the results of these trials to determine the shape and size of the metal object. The resulting signals from both the metal sensor are shown in Figure 6 and Table 2.

Table 2: The calculation result of investigated samples.

Investigated samples	Actual size (cm)	P1	P2	P3	P4	P5	P6
1st Rod	0.9	0.86	1	1	1	1	1.24
2nd Rod	0.9	0.98	1	1	1	1	1
Clamp's arm (1)	8.5	8.59	9.16	N\A	N\A	N\A	N\A
Clamp south (2)	1.3	N\A	N\A	1.6	1	1.24	1.24
Clamp north (3)	1.3	N\A	N\A	1.24	1.6	1.33	1.04
Distance middle (4)	6.7	N\A	N\A	6.72	6.48	7.2	7.2
Distance south (5)	5	5.25	4.86	4.8	5.04	5.04	4.86
Distance north (6)	6.5	6.33	6.72	6.42	7.2	7.2	6.72
D istance between two rods	20.4	19.74	20.33	21.2	21.4	20.25	20.53

4. RESULTS & DISCUSSION

For the metal detector testing, a DC magnetic field was fixed at 500 gauss (corresponding input DC voltage of 4V from the autotransformer). Our previous publication [7] details how the fiber sensor successfully detects a steel wrench and steel plate. The results from [7] show that the magnetostrictive metal sensor can roughly distinguish the metal's profile. In this paper, we also discuss the broadened application of the sensor: the ability to create a 2D outline of an object. The metal object used for testing was an irregularly shaped metal clamp (Figure 4(a)). In publication [7], it was proved that the size of the metal object could be calculated based on the period of time it was detected and the velocity of the object being detected Because our sensor was 1 cm in diameter and the metal object was approximately 5 cm in width, the object was scanned in five segments. Using the resultant output signals and velocities from each segment, we could calculate the size of the metal object; the results are shown in Table 2. According to the calculated results, we could plot the metal object's outline using AutoCAD (Figure 6).

Based on Figure 6, it shows that the metal sensor (WC-WSJOSHNICK-1) is capable of determining the metal's irregular shape. Due to the limitation of sensor size and sensor detection area, we could only detect the rough shape of the metal. From Table 2, we can clear see that the values calculated were very close to the actual dimensions of the metal object. These errors could be due to a number of factors. First, the biggest error probably came from the calculation of velocity. The velocity was calculated with a camera that shot 30 frames per second. An even faster camera would give an even more precise measurement of velocity. The method used currently assumes that the velocity is constant. However, in testing the velocity is not a constant which creates another source of error.

5. CONCLUSIONS

Magnetostrictive sensor technology continues to mature and will provide important capabilities to growing commercial sensor marketplaces in the years ahead. In this paper, we presented a polymeric magnetostrictive metal detector system using a magneostrictive material (WC-WSJOSHNICK-1). The results from the fiber-optic system show that it can roughly identify irregular metal shapes. Our sensors have been notably successful in detecting the general shape of the metal objects. We further improved the sensor's capability by using the metal sensor to create a 2D outline of the metal object. However, we are striving to improve the sensitivity of metal detection using the fiber-optic magnetostriction metal detector system described herein. It is our future work that the sensitivity can be improved to the level where we can identify metals of different permeability and also increase the accuracy of width detection of the metals. The final goal of this sensor is to identify and calculate the shape of more complicated metal objects and to develop a novel 3D metal detector system.

ACKNOWLEDGMENT

This research was supported by the National Institutes of Health (NIH) under grant R01 EB007636-01A2.

REFERENCES

1. http://electronics.howstuffworks.com/gadgets/other-gadgets/metal-detector2.htm.
2. http://engnet.anu.edu.au/DEpeople/Salman.Durrani/_teaching/TA5.pdf.
3. http://www.hobby-hour.com/electronics/metal_ detectors.php.
4. Hua, W.-S., J. R. Hooks, W.-J. Wu, and W.-C. Wang, "Development of a novel polymeric fiberoptic magnetostrictive metal detector," *Proceedings of SPIE NDE Health Monitoring and Diagnostics, (SPIE 2010)*, San Diego, California, USA, Mar. 10–13, 2010.
5. Hua, W.-S., J. R. Hooks, W.-J. Wu, and W.-C. Wang, "Development of a polymer based fiberoptic magnetostrictive metal detector system," *Proceedings of International Symposium on Optomechatronic Technologies, (ISOT 2010)*, Toronto, Ontario, Canada, Oct. 25–27, 2010.
6. Hua, W.-S., J. R. Hooks, N. A. Erwin, W.-J. Wu, and W.-C. Wang, "Fiberoptic metal detector capable of profile detection," *Proceedings of SPIE NDE Health Monitoring and Diagnostics, (SPIE 2011)*, San Diego, California, USA, Mar. 6–10, 2011.
7. Hua, W.-S., J. R. Hooks, N. A. Erwin, W.-J. Wu, and W.-C. Wang, "A polymeric fiberoptic metal sensor capable of profile detection," *Proceedings of 22th International Conference on Adaptive Structures and Technologies (ICAST 2011)*, Corfu, Greece, Oct. 10–12, 2011.
8. Yariv, A. and H. V. Winsor, "Proposal for detection of magnetic fields through magnetostrictive perturbation of optical fibers," *Optical Letters*, Vol. 5, No. 3, 87–89, 1980.

Gain Flattening in Erbium Doped Fiber Amplifiers by Use of a Coaxial Fiber

Jyoti Anand[1], **Jagneet Kaur Anand**[1], **and Enakshi K. Sharma**[2]

[1]Department of Electronics, Keshav Mahavidyalaya, University of Delhi, India
[2]Department of Electronic Science, University of Delhi South Campus, New Delhi 110021, India

Abstract— We propose the use of a band reject filter in coaxial fiber configuration for gain flattening in Erbium doped fiber (EDF) amplifiers. The band reject filter can be used as a gain flattening filter at the end of an EDF or alternatively, an erbium doped coaxial fiber with doping only in the inner core region (rod) can be used for inherent gain flattening. This results in inherent gain flattening as well as increase in the average gain across the 1530 to 1560 nm band as in the case of long period grating in erbium doped fibers.

1. INTRODUCTION

In this paper, we propose the use of a coaxial fiber configuration [1] for gain flattening in erbium doped fiber amplifiers. Although the use of an Erbium doped coaxial fiber for inherent gain flattening has also been proposed earlier [2], it assumes the selective excitation of only the LP_{01} supermode in the coaxial fiber, whereas, for the reported parameters, the fiber supports three symmetric modes (the LP_{01}, LP_{02} and LP_{03} supermodes). We also considered a similar coaxial fiber which supports LP_{01} and LP_{02} supermode and have shown that if such a coaxial fiber is spliced to a single mode fiber at the input end in an actual transmission system, in general both the supermodes get excited. When the output of the coaxial fiber is spliced to another single mode fiber, the amplified signal power coupled into it can be a very sensitive function of the length of coaxial fiber used due to the two mode interference, especially around the phase matching wavelength [3]. If the phase matching wavelength is chosen around 1510 or 1560 nm, the power spectrum becomes insensitive to the coaxial EDF length in the entire C band of operation but no inherent gain flattening is seen.

In coaxial fibers (Fig. 1), the rod and tube form two independent waveguides, each supporting only one azimuthally symmetric mode. The two individual waveguides can be chosen to be synchronous at a phase matching wavelength $\lambda = \lambda_{ph}$. When the rod and tube waveguides are close, the rod and tube waveguide modes get evanescently coupled. In a WDM system the input single mode fiber excites the rod waveguide mode and the power oscillates between the rod and the tube waveguides as it propagates along the coaxial fiber; finally, the power in the rod waveguide is coupled out into the output fiber. At phase matching wavelength the entire power oscillates between the rod and the tube. However, away from phase matching wavelength on either side, the fraction of power oscillating is less. Hence, this combination with the coaxial fiber of appropriate length acts as a band reject filter at the phase matching wavelength. The fiber parameters are chosen such that the phase matching wavelength coincides with the peak of EDF spectrum, i.e., typically around 1530 nm. This property can be employed for gain flattening at the end of an EDF. Alternatively, an erbium doped coaxial fiber with doping only in the inner core region (rod) can be used for inherent gain flattening. For such a configuration, the power at the phase matching wavelength couples back and forth between the inner doped core (which has amplification) and the outer undoped core as it propagates along the length of doped coaxial fiber. When a large number of wavelengths propagate through the EDF, the population inversion is reduced due to stimulated emission at each wavelength. The coaxial fiber couples in and out the wavelength corresponding to the gain peak which reduces the corresponding stimulated emissions around 1530 nm and hence, the population inversion is available to other wavelengths. This results in inherent gain flattening as well as increase in the average gain across the 1530 to 1560 nm band as in the case of long period grating in erbium doped fibers [4].

2. COUPLED MODE ANALYSIS FOR COAXIAL FIBERS WITH GAIN

Various numerical methods have been suggested in literature [5, 6] to characterize the complete coaxial fiber in terms of its supermodes and their propagation characteristics. To get a better insight into the propagation characteristics of the coaxial fiber we have used coupled mode analysis [7].

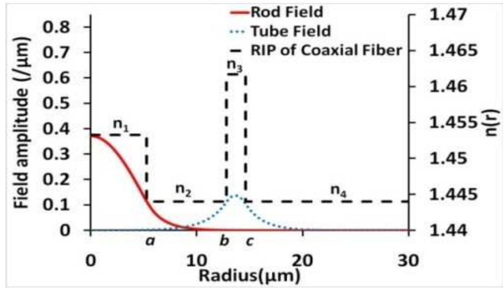

Figure 1: Refractive index profile of coaxial fiber along with the rod and tube field profiles.

The total field of the coaxial fiber can be written as the superposition of the fields of the inner rod, $\psi_1(r)$ and outer tube, $\psi_2(r)$ waveguides as

$$\Psi(r, z) = a(z)\,\psi_1(r) + b(z)\psi_2(r) \tag{1}$$

where amplitudes $a(z)$ and $b(z)$ are functions of z. Using the conventional 'slowly varying' coupled mode theory one obtains the solutions in the form of two supermodes of the coaxial waveguide:

$$\Psi_{s,a}(r, z) = \psi_{s,a}(r)\, e^{-j\beta_{s,a} z} \tag{2}$$

with the field profiles given by

$$\psi_{s,a}(r) = \frac{1}{\sqrt{1+\bar{b}_{s,a}^2}}\left[\psi_1(r) + \bar{b}_{s,a}\psi_2(r)\right] = \frac{1}{\sqrt{1+\bar{a}_{s,a}^2}}\left[\bar{a}_{s,a}\psi_1(r) + \psi_2(r)\right] \tag{3}$$

where $\bar{b}$ and $\bar{a}$ are given by

$$\bar{b}_s = \frac{\beta_s - \beta_1}{\kappa_{12}}, \quad \bar{a}_s = \frac{\beta_s - \beta_2}{\kappa_{21}}, \quad \bar{b}_a = \frac{\beta_a - \beta_1}{\kappa_{12}}, \quad \bar{a}_a = \frac{\beta_a - \beta_2}{\kappa_{21}} \tag{4}$$

with β_1 and β_2 being the propagation constants of the individual rod and tube waveguides and β_s and β_a the propagation constants of the two supermodes. An EDF in coaxial configuration would exhibit gain. We have considered the fiber doped with erbium ions in the inner core (rod), i.e., over a region $0 < r < a$. Hence, the propagation constant of the rod of the coaxial fiber would be complex, i.e., $\beta_1 = \beta_1 + j\gamma_1$, where γ_1 is the corresponding gain coefficient of the rod briefly discussed in the next section. The propagation constants of the two supermodes are given by

$$\beta_{s,a} = \frac{1}{2}(\beta_1+\beta_2) + j\frac{\gamma_1}{2} \pm \frac{1}{2}\sqrt{(\beta_1 + j\gamma_1 - \beta_2) + 4\kappa^2} = \frac{1}{2}(\beta_1+\beta_2) + j\frac{\gamma_1}{2} \pm \frac{1}{2}(p + jq) \tag{5}$$

with $\kappa = (\sqrt{\kappa_{12}\kappa_{21}})$, κ_{12} and κ_{21} representing the strength of interaction between the two waveguides defined as

$$\kappa_{12} = \frac{k_0}{2}\left(n_1^2 - n_2^2\right)\int_0^a \psi_1\psi_2 r dr \qquad \kappa_{21} = \frac{k_0}{2}\left(n_3^2 - n_2^2\right)\int_b^c \psi_1\psi_2 r dr \tag{6}$$

Hence

$$\beta_{s,a} = \left(\frac{\beta_1+\beta_2}{2}\right) \pm \frac{p}{2} + j\left(\frac{\gamma_1}{2} \pm \frac{q}{2}\right) \tag{7}$$

where $\frac{p}{2}$ and $\frac{q}{2}$ are given by

$$\frac{p}{2} = \frac{1}{\sqrt{2}}\Delta^{1/2}\left[\sqrt{1 + \frac{(\beta_1-\beta_2)^2\gamma_1^2}{4\Delta^2}} + 1\right]^{1/2}, \qquad \frac{q}{2} = \frac{1}{\sqrt{2}}\Delta^{1/2}\left[\sqrt{1 + \frac{(\beta_1-\beta_2)^2\gamma_1^2}{4\Delta^2}} - 1\right]^{1/2} \tag{8}$$

with

$$\Delta = \left(\frac{\beta_1-\beta_2}{2}\right)^2 + \left(\kappa^2 - \frac{\gamma_1^2}{4}\right). \tag{9}$$

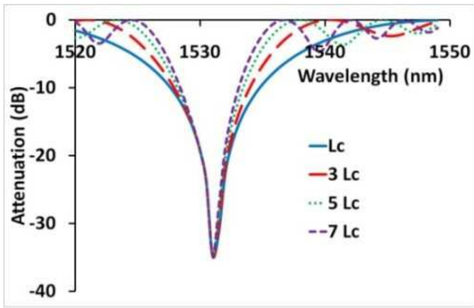

(a)

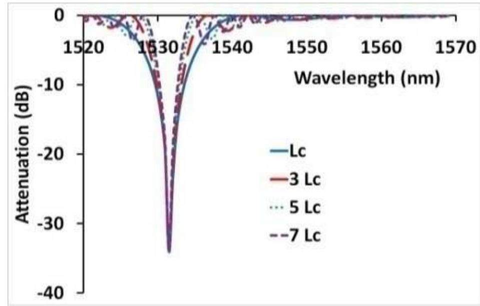

(b)

Figure 2: Output spectrum for different lengths for two different inter waveguide separation for a fiber with $n_2 = 1.4440236$, $\Delta_1 = 0.00643$, $\Delta_3 = 0.01232$ and (a) $a = 5.25\,\mu\text{m}$, $b = 15\,\mu\text{m}$, $c = 16.8\,\mu\text{m}$ and $L_c = 3.1\,\text{cm}$ (b) $a = 5.22\,\mu\text{m}$, $b = 16\,\mu\text{m}$, $c = 17.8\,\mu\text{m}$ and $L_c = 5.5\,\text{cm}$.

Then propagation constants of the two supermodes LP_{01} and LP_{02} of the coaxial EDF are given by $\gamma_{s,a} = \frac{\gamma_1}{2} \pm \frac{q}{2}$. At $\lambda = \lambda_{ph}$, $q = 0$ and hence $\gamma_{s,a} = \frac{\gamma_1}{2}$, i.e., both the supermodes have the same gain coefficient.

If we consider a coaxial fiber without erbium doping, i.e., no gain is present ($\gamma_1 = 0$) and we excite the coaxial fiber from a single mode fiber (same as the rod waveguide) spliced at the input end, both the supermodes get excited with excitation coefficients $a_1 = (1 + \bar{b}_s^2)^{-1/2}$ and $a_2 = (1 + \bar{b}_a^2)^{-1/2}$. After a propagation length z_L, the power coupled into a similar single mode output fiber (assuming unit input power) is given by

$$P_{out} = 1 - \frac{\kappa^2}{\frac{1}{4}\Delta\beta^2 + \kappa^2} \sin^2\left[\left(\frac{1}{4}\Delta\beta^2 + \kappa^2\right)^{\frac{1}{2}} z_L\right] \tag{10}$$

where $\Delta\beta = \beta_1 - \beta_2$. At $\lambda = \lambda_{ph}$, $\Delta\beta = 0$ and no output power is obtained for $z_L = (2n+1)L_c$ where $L_c = \frac{\pi}{2\kappa}$ is the coupling length and the output spectrum is shown in Fig. 2. The resonance dip becomes sharper as length increases in odd multiples of L_c as depicted in Fig. 2; however, side lobes start appearing.

3. EDF IN COAXIAL CONFIGURATION

For an EDF in coaxial fiber configuration, we consider the fiber doped with erbium ions in the inner core (rod), i.e., over a region $0 < r < a$. Following the analysis in [8], for a 980 nm pump, the gain coefficient of the LP_{01} mode of the rod is given by

$$\gamma_1(\lambda, z) = \frac{1}{2}\left[\int_0^a \{\sigma_e(\lambda) N_2(r, z) - \sigma_a(\lambda) N_1(rz)\}\psi_1^2(r)\, r dr\right] \tag{11}$$

where σ_a and σ_e are the wavelength dependent absorption and emission cross-sections and N_2 and N_1 are the steady state population density in the upper and lower state respectively; and ψ_1 is the inner rod field.

As the power propagates in the coaxial fiber it oscillates back and forth between the rod and the tube wavelength around $\lambda = \lambda ph$. The power coupled to the output single mode fiber (P_{out}) is given by

$$P_{out} = \left[a_1^2 A_1^2(z_L) + a_2^2 A_2^2(z_L) + 2A_1(z_L) A_2(z_L)\, a_1 a_2 \{\cos(\phi_s - \phi_a)\}\right] \tag{12}$$

where the amplitudes $A_{1,2}$ take into account the gain/loss in the coaxial fiber and $\phi_{s,a}$ represent the accumulated phase and are given by

$$A_{1,2}(z) = a_{1,2} e^{\gamma_{s,a}(\lambda,0)\Delta z} e^{\gamma_{s,a}(\lambda,\Delta z)\Delta z} e^{\gamma_{s,a}(\lambda,2\Delta z)\Delta z} \ldots e^{\gamma_{s,a}(\lambda,z)\Delta z} \tag{13}$$

$$\phi_{s,a} = \beta_{s,a}(\lambda, 0)\Delta z + \beta_{s,a}(\lambda, \Delta z)\Delta z + \beta_{s,a}(\lambda, 2\Delta z)\Delta z + \ldots + \beta_{s,a}(\lambda, z)\Delta z \tag{14}$$

The given length z_L of the coaxial EDF has been divided into small segments of length Δz and propagation is considered in terms of local gain/loss and propagation through each segment.

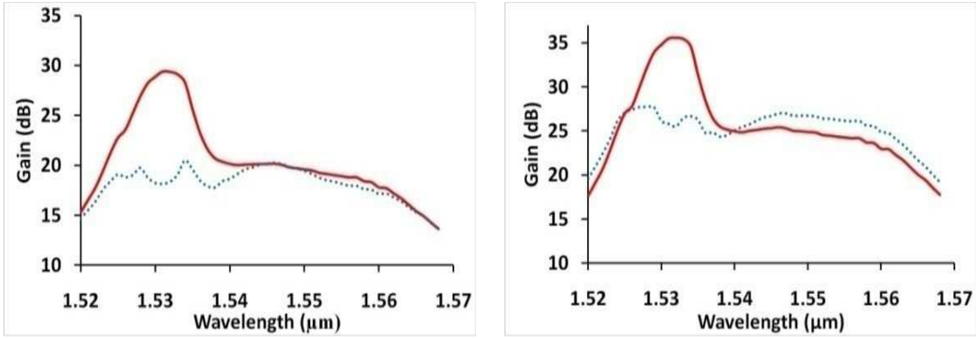

Figure 3: Comparison of the gain spectra of the EDF with simultaneous propagation of 50 different wavelengths each carrying 1 μW power (solid line) with (a) external coaxial fiber gain flattening filter of length ~ 3.7 cm (dotted line) (b) EDF in coaxial configuration of length ~ 3.66 m (dotted line).

4. DESIGN OF AN EFFICIENT GAIN FLATTENING MODULE

The band reject filter described in Section 2 with $\lambda_{ph} = 1530$ nm can be used at the end of an amplifying EDF to reject the excess gain around 1530 nm region. The parameters of the coaxial fiber can be tailored to give an appropriate attenuation and bandwidth. Fig. 3(a) shows the flattened gain spectrum obtained by using a coaxial fiber of ~ 3.7 cm length at the end of a single core EDF of length 3 m (dotted line). It shows a ± 1.36 dB flat gain over a band of 40 nm ranging from 1525 nm to 1565 nm. In comparison the gain variation obtained in single core fiber of same length is ± 4.68 dB in the same range. Alternately, an erbium doped coaxial fiber with doping only in the rod can be used for inherent gain flattening. For such a configuration, the power at λ_{ph} chosen to correspond to gain peak, couples back and forth between the rod (which has amplification) and the tube as it propagates along the length of doped coaxial fiber. When a large number of wavelengths propagate through the EDF, the population inversion is reduced due to stimulated emission at each wavelength. The coaxial fiber couples in and out the wavelength corresponding to the gain peak (1530 nm) which reduces the corresponding stimulated emissions around 1530 nm and hence, the population inversion is available to other wavelengths. This results in inherent gain flattening as well as increase in the average gain across the 1540–1560 nm band as shown in Fig. 3(b), in the case of long period grating written in erbium doped fibers. Fig. 3(b) shows the flattened gain spectrum by using a coaxial fiber of ~ 3.66 m length after a length of 1 m of single core EDF (dotted line). It shows a gain flattening of ± 1.68 dB over a band of 40 nm ranging from 1525 nm to 1565 nm. In comparison the gain variation obtained in single core fiber of same length is ± 5.36 dB in the same range.

5. CONCLUSIONS

The parameters of a coaxial fiber can be tailored to give an appropriate attenuation and bandwidth for use as a gain flattening filter. The excess gain around 1530 nm can be reduced by terminating it with an external coaxial fiber gain flattening filter. Alternatively, EDF itself can be used in coaxial configuration for inherent gain flattening. The latter gives gain enhancement in 1540–1560 nm region along with gain flattening in 1525–1565 nm region.

ACKNOWLEDGMENT

The authors would like to acknowledge the financial support from University Grants Commission, India for their research work.

REFERENCES

1. Boucouvalas, A. C., "Coaxial optical fiber coupling," *J. Lightwave Technol.*, Vol. 3, 1151–1158, 1985.
2. Thyagarajan, K. and J. Kaur, "A novel design of intrinsically gain flattened erbium doped fiber," *Opt. Comm.*, Vol. 183, 407–413, 2000.
3. Anand, J., J. K. Anand, and E. K. Sharma, "Study of the amplification characteristics of a coaxial EDF with varying coupling conditions," *Optics & Laser Tech.*, Vol. 44, No. 3, 688–695, 2012.

4. Singh, R., Sunanda, and E. K. Sharma, "Gain flattening with long period gratings in erbium doped fibers," *Optics Commun.*, Vol. 240, 123–132, 2004.
5. Boucouvalas, A. C. and X. Qian, "Mode dispersion and delay characteristics of optical waveguides using equivalent T-L circuits," *IEEE J. Quantum Electron.*, Vol. 41, 951–957, 2005.
6. Morishita, K., " Numerical analysis of pulse Broadening in graded index optical fibers," *IEEE Trans. Microwave Th. and Tech.*, Vol. 29, 348–352, 1981.
7. Ghatak, A. K. and K. Thyagarajan, *Introduction to Fiber Optics*, Cambridge University Press, 1999.
8. Pedersen, B., "Small signal erbium-doped fiber amplifiers pumped at 980 nm: a design study," *Optical and Quantum Electron.*, Vol. 26, S273–S284, 1994.

A Proposed Method for Sensitivity Analysis of Log-periodic Dipole Antenna Array-type Optical Electric Field Sensor

S. Tsujino[1], **H. Sugama**[2], **A. Tsuchiya**[1,2], **K. Miyamoto**[1], **N. Hidaka**[2], **and O. Hashimoto**[1]

[1]Aoyama Gakuin University, Japan
[2]Kanagawa Industrial Technology Center, Japan

Abstract— This paper reports on a study of the characteristics of a high sensitivity and wide band (1.8 GHz to 6.0 GHz) log-periodic dipole antenna array-type optical electric field sensor (LPDA-type OEFS). In this paper, we propose an analysis method of the sensitivity characteristic of LPDA-type OEFS using an electromagnetic field simulator and a computer program which calculates the operation of multiple electrode OEFS. One conclusion reached by this study was that the calculated result corresponded to the measured one. In addition, we investigated the directional pattern by our proposed method.

1. INTRODUCTION

Recently, the growth of information technology has spurred the development of many new technologies including wireless LAN, WiMAX and UWB. To employ these technologies effectively, it is necessary to accurately characterize their electromagnetic field intensity. An accurate characterization is often not realizable because conventional measurement techniques that use coaxial cables often interfere with the subject field during the measurement process. It is possible, however, to utilize an optical electric field sensor (OEFS) based instrument with optical fiber to precisely measure the electromagnetic field.

The OEFS, which is made of dielectric materials (except for its antenna elements), creates less interference with electromagnetic fields than antennas made of metal. The OEFS is able to measure electric field strength and frequency using Pockels effect. Thus, we have proposed a log-periodic dipole antenna array-type OEFS (LPDA-type OEFS) with high sensitivity and wide band characteristics [1]. The minimum detectable electric field strength is 40 dBμV/m at 2.0 GHz and 60 dBμV/m at 6.0 GHz. The operating frequency range is from 1.8 GHz to 6.0 GHz. A schematic and photograph of the LPDA-type OEFS are shown in Fig. 1. The OEFS has a compact size of $107 \times 70 \times 15$ mm. One problem is that it takes half a year to fabricate a prototype of the OEFS. Thus, characterization by simulation is needed. However, it is difficult to evaluate the sensitivity characteristic of LPDA-type OEFS by an electromagnetic field simulator because the OEFS has an optical modulator having micro and multiple electrodes. In this paper, we propose an analysis method of the sensitivity characteristic for LPDA-type OEFS using an electromagnetic field simulator and a computer program which calculates the operation of OEFS having multiple electrodes. In addition, we investigated the directional pattern by our proposed method.

2. ANALYTICAL METHOD

2.1. Calculation of Phase Shift of Lightwave

We couldn't simulate the optical modulation of LPDA-type OEFS by the electromagnetic field simulator. However, we are able to analyze the sensitivity characteristic to calculate the phase shift

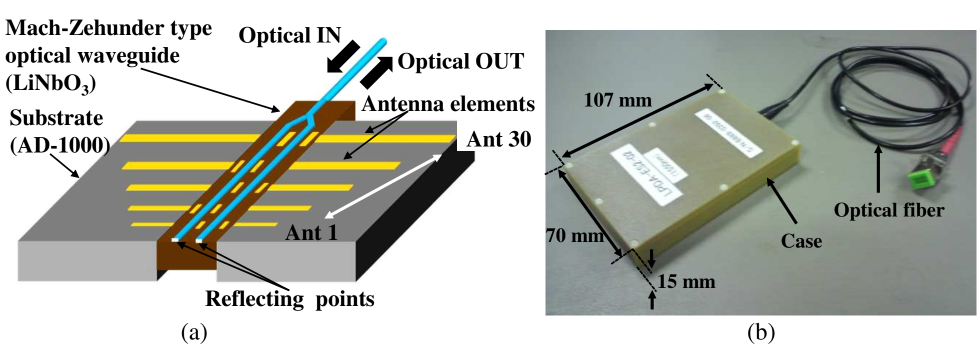

Figure 1: Schematic and photograph of LPDA-type OEFS. (a) Schematic. (b) Photograph.

of lightwave. The phase shift is proportional to the output light intensity of the optical modulator. As a result, we made a computer program which calculated the phase shift of lightwave. The program was written in a LabVIEW program [2].

When an electric wave is impressed at antenna elements, the impressed voltage between the n-th electrodes V_n is given by

$$V_n = V_{mn} \sin(\omega t - \phi_{mn}) \tag{1}$$

where, V_{mn}, ϕ_{mn} and ω are amplitude, phase of the impressed voltage of the n-th electrodes, and angular frequency of the receiving electric wave. The phase of lightwave in optical waveguide φ_n is given by

$$\varphi_n = \sin\{\omega(t - T_n) - \phi_{mn}\} \tag{2}$$

where, T_n is the time passing from the n-th antenna element to the reflecting points. In the case of a pair of the antenna elements, output light intensity I_{out} [3] is given by

$$I_{out} = \frac{I_{in}}{2}\left\{1 + \cos\left(\pi\frac{V_n}{V_\pi} + \Phi\right)\right\} \tag{3}$$

where, I_{in}, V_π and Φ are input light intensity, the half-wave voltage and the optical bias angle. Here, V_π is given by

$$V_\pi = \frac{\pi d}{k_0 L_n r_{33} n_e^3} \tag{4}$$

where,

$$k_0 = \frac{2\pi}{\lambda_0}, \tag{5}$$

d, λ_0 ($= 1.55\,\mu\text{m}$), r_{33} ($= 30.8$) and n_e ($= 2.15$) are the length of electrode spacing, wave length of light source, electro-optical constant and refractive index of $LiNbO_3$. When the optical bias angle Φ is $-\pi/2$ for maximizing modulation efficiency, Eq. (3) is given by

$$I_{out} = \frac{I_{in}}{2}\left\{1 + \cos\left(\Delta\delta_n - \frac{\pi}{2}\right)\right\} \tag{6}$$

where,

$$\Delta\delta_n = 2\frac{r_{33} n_e^3 \pi}{d\lambda_0} L_n V_{mn} \sin\{\omega(t - T_n) - \phi_{mn}\}, \tag{7}$$

$\Delta\delta_n$ is the phase shift from a pair of the antenna elements. By applying Eq. (7) to the n-pairs of antenna elements, the total amount of phase shift from all antenna elements is calculated. The total amount of phase shift δ_n is given by

$$\delta_n = 2\frac{r_{33} n_e^3 \pi}{d\lambda_0} \sum_{n=1}^{N} \left[L_n V_{mn} \sin\{\omega(t - T_n) - \phi_{mn}\}\right] \tag{8}$$

When LPDA-type OEFS has reflective optical waveguide and light phase-inverted structure, Eq. (8) is given by

$$\begin{aligned} \delta_n \;=\; & 2\frac{r_{33} n_e^3 \pi}{d\lambda_0}\left(\sum_{n=1}^{N}\left[(-1)^n \cdot L_n V_{mn} \sin\{\omega(t - T_n) - \phi_{mn}\}\right]\right. \\ & \left. + \sum_{n=1}^{N}\left[(-1)^n \cdot L_n V_{mn} \sin\{\omega(t + T_n) - \phi_{mn}\}\right]\right) \end{aligned} \tag{9}$$

Thus, Eq. (9) enables the analysis of sensitivity characteristic of LPDA-type OEFS.

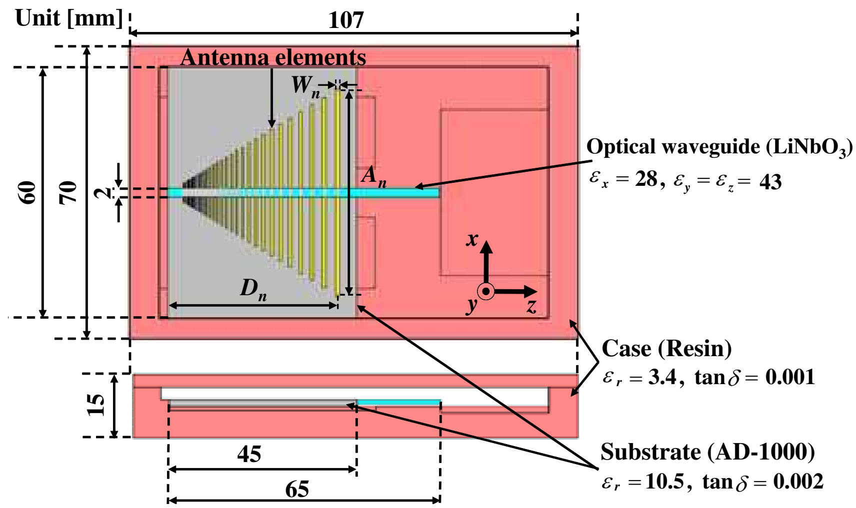

Figure 2: Analytical model of LPDA-type OEFS in the case.

Table 1: Specifications for LPDA-type OEFS.

	$n = 1$	$n = 30$
Distance from the n-th antenna element to the reflecting points D_n [mm]	3.76	40.00
Antenna length A_n [mm]	4.62	49.18
Antenna width W_n [mm]	0.09	1.00
Electrode length L_n [mm]	0.25	2.67
Capacitance C_n [pF]	0.15	1.60

2.2. Analytical Model

Figure 2 shows the analytical model of LPDA-type OEFS in the case where it consists of a resin. Table 1 shows the specifications for LPDA-type OEFS. D_n, A_n, W_n, L_n and C_n are the distance from the n-th antenna element to the reflecting points, the length, the width, the electrode length, and the capacitance of the n-th antenna element. When the ordinal number of the antenna elements n is one, it shows the shortest antenna element. 30 pairs of antenna elements with a thickness of 0.018 mm are arranged on substrate (Arlon AD-1000) with a thickness of 1.6 mm. The lengths of elements are half wave and vary log-periodically from 4.62 mm to 49.18 mm. Optical waveguide is positioned in the center of the OEFS. The waveguide consists of a $LiNbO_3$ with a thickness of 1 mm.

The capacitance C_n was used in the simulation instead of the electrodes because they were sufficiently short [4]. The capacitance per unit length of electrode C_0 on $LiNbO_3$ is about 0.6 pF/mm at a distance of electrodes $d = 15\,\mu\text{m}$. The capacitance C_n is given by

$$C_n = C_0 \cdot L_n \tag{10}$$

2.3. Electromagnetic Field Simulation

The sensitivity characteristic and the directional pattern of LPDA-type OEFS were calculated by using CST MW-Studio [5] and Eq. (9). We analyzed the amplitude and phase characteristics of the modulation voltage V_n between electrodes by incidenting the plane wave of excitation source. In this paper, the angle of plane wave was shifted every 10 degrees from 0 degree to 360 degrees.

3. RESULTS AND DISCUSSION

Figure 3 shows the calculated and measured results of sensitivity characteristics in the front of OEFS. The results of sensitivity characteristic set 0 dB as a maximum value. The calculated result having the ripple of 3 dB on average decreased with an increase in frequency from 1.8 GHz to

3.8 GHz. The measured result denoted the same tendency as the calculated one. The calculated result has the ripple of 4–15 dB from 3.8 GHz to 6.0 GHz. There was a difference of 11 dB between the calculated and measured results at 4.6 GHz. However, the ripple of the calculated result had the same behavior as that of the measured one. Thus, the calculated result corresponded to the measured one.

Figure 4 shows the calculated and measured results of the directional pattern at 1.8 GHz in (a) horizontal plane and (b) vertical plane. The results of directional pattern set 0 dB as a maximum value. The calculated result of directional pattern at 1.8 GHz in horizontal plane corresponded to the measured result from −90 degrees to 70 degrees. There was a difference of more than 15 dB between the calculated and measured results in 100 degrees and −100 degrees. However, the behavior of calculated result was similar to that of measured one. The calculated result of directional pattern at 1.8 GHz in vertical plane corresponded to the measured one from −120 degrees to 110 degrees. There was a difference of 4.4 dB at a maximum between the calculated and measured results in −180 degrees and 180 degrees.

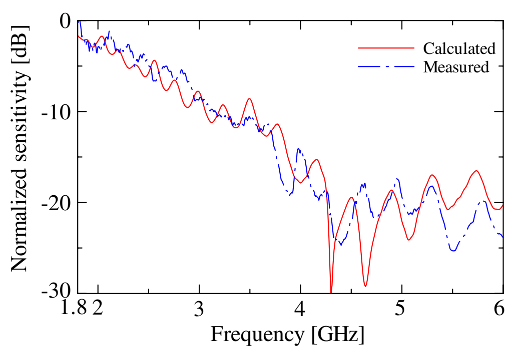

Figure 3: Normalized sensitivity characteristics.

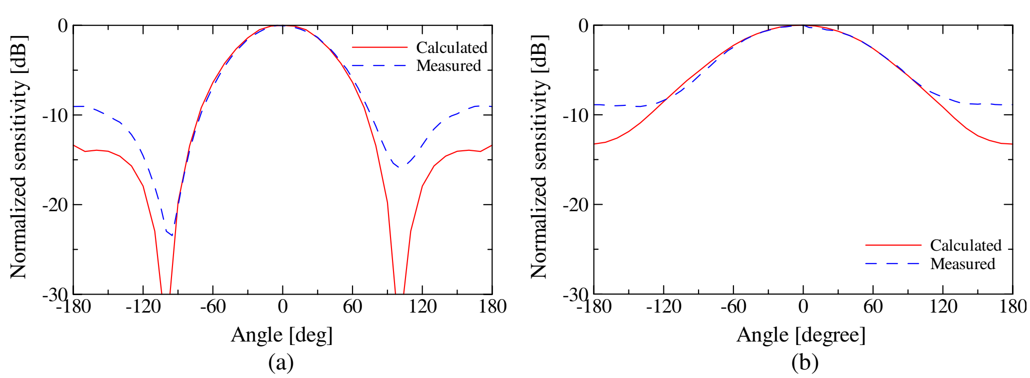

Figure 4: Directional pattern at 1.8 GHz. (a) Horizontal plane and (b) vertical plane.

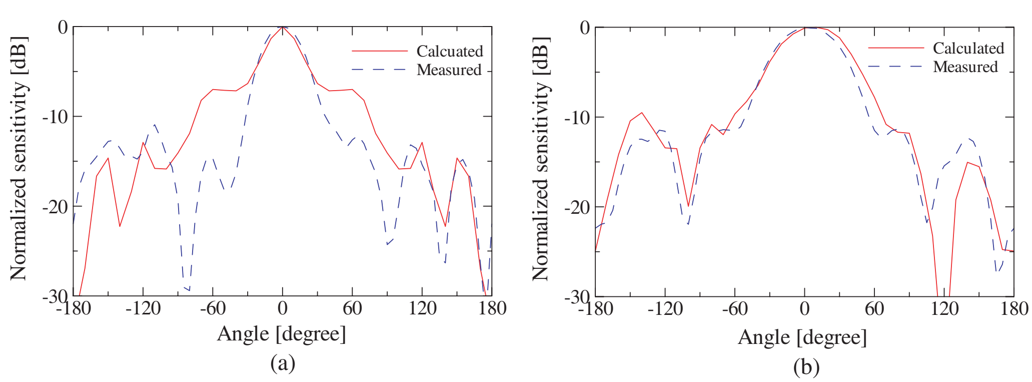

Figure 5: Directional pattern at 6.0 GHz. (a) Horizontal plane and (b) vertical plane.

Figure 5 shows the calculated and measured results of the directional pattern at 6.0 GHz in (a) horizontal plane and (b) vertical plane. The calculated result of directional pattern at 6.0 GHz in horizontal plane corresponded to the measured one from −30 degrees to 30 degrees and from 120 degrees to 180 degrees. There was a difference of 17 dB at a maximum in −80 degrees between the calculated and measured results. However, the behavior of calculated results was similar to that of measured ones. There was a difference of more than 15 dB at a maximum in 120 degrees between the calculated and measured results of directional pattern at 6.0 GHz in vertical plane. However, the calculated result corresponded to the measured one.

Differences between calculated and measured results are confirmed from the above results. It is assumed that the analytical model didn't include the wire bonding by which a antenna element and a electrode connected in order to reduce analysis time. However, the proposed method provided evidence of its effectiveness because the trend of calculated results corresponded to measured ones.

4. CONCLUSION

In this paper, an analysis method for LPDA-type OEFS which calculates phase shift of lightwave using analyzed modulation voltage by microwave was proposed. The sensitivity characteristic and directional pattern of LPDA-type OEFS were calculated using this proposed method. The calculated result of sensitivity characteristic corresponded to the measured one. And the calculated results of directional patterns corresponded to the measured ones in main lobe. Thus, the proposed method provided evidence of its effectiveness.

ACKNOWLEDGMENT

This work was supported by Japan and a Grant-in-Aid for The Private School High-tech Research Center Program of the Ministry of Education, Culture, Sports, Science, and Technology, Japan.

REFERENCES

1. Hidaka, N., K. Kobayashi, H. Sugama, R. Usui, Y. Tanabe, and O. Hashimoto, "Log-periodic dipole antenna array-type optical electric field sensor," *IEICE Trans. Electron.*, Vol. E88-C, No. 1, 98–104, Jan. 2005.
2. National Instruments, LabVIEW 2011, http://www.ni.com/labview/.
3. Nishihara, H., M. Haruna, and T. Suhara, "Control by electro-optic effect," *Optical Integrated Circuit*, 107–117, Ohmsya, Tokyo, 1985.
4. Tajima, K., R. Kobayashi, N. Kuwabara, and M. Tokuda, "Development of optical isotropic E-field sensor operating more than 10 GHz using Mach-Zehnder interferometers," *IEICE Trans. Electron.*, Vol. E85-C, No. 4, 961–968, Apr. 2002.
5. Computer Simulation Technology (CST), Micro Wave Studio 2011, http://www.cst.com/.

Design of Undersampled Digitally Heterodyned SFGPR with Variable Sampling Frequency

D. Adirosi[1], **G. Alberti**[2], **and G. Galiero**[2]

[1]Thales Alenia Space Italia, Italy
[2]Consortium for Research on Advanced Remote Sensing Systems — CO.RI.S.T.A, Italy

Abstract— In this paper the design of an innovative architecture of an undersampled digitally heterodyned stepped frequency GPR is presented. The whole set of parameters characterising the performances of the SFGPR is optimised by means of a "brute force" approach by using the software tools previously developed in a high level language. The results of the simulations performed as well as the key aspects of the design are presented.

1. INTRODUCTION

It is well known that the capability of electromagnetic waves to propagate beyond the physical discontinuities of propagation media makes it possible to exploit them to investigate internal features of dielectric bodies. From this property, an endless number of practical applications have been arisen, ranging from medical prospecting to detection of mines, nondestructive testing of industrial items and GPR applications.

In [1] a new architecture of an Undersampled Digitally Heterodyned SFGPR with variable sampling frequency was presented. The key aspects and the advantages of the new architecture were presented and discussed: signal generation by means of DAC; undersampling of the echoes by means of a large bandwidth ADC with a planned step by step varying sampling frequency; digital quadrature demodulation of the undersampled echoes.

In this paper a preliminary design of a SFPGR based on the previously proposed architecture is shown. The whole set of parameters characterising the performances of a GPR (step frequency, first frequency to generate, number of steps, ...) is optimised by means of a "brute force" approach by using the software tools previously developed in a high level language (LabView$^{\mathrm{TM}}$).

The results of the simulations of the whole post-processing chain, from the undersampling of the step frequencies to their quadrature demodulation and processing to synthesize simulated target, are shown to fix the performances achievable with the chosen set of parameters.

2. PROPOSED ARCHITECTURE

The choice of a stepped frequency GPR (SFGPR) has been adopted for this design because it has several advantages with respect to the traditional impulsive GPR systems spacing from the larger dynamic range to greater signal to noise ratio attainable due to the narrow band of the receiver. The choice of an heterodyne architecture for the proposed design allows to reduce both its weight and power consumption.

An heterodyne GPR detects targets by performing a downconversion of the received signal to a constant intermediate frequency (IF). Because this IF is greater than 0 Hz, this architecture alleviates the problems related to flicker noise and DC values drift with the temperature typical of homodyne receivers. The problems related to the IQ demodulation (errors due to phase and amplitude gain imbalances of the quadrature mixer) can be solved if it is performed in the digital domain instead of the analog one by acquiring directly the IF signal. Undersampling is the optimum choice that allow to solve both the problems: the downconversion of the signal is performed automatically (as result of the sampling process) and the signal is sampled optimally without the need to oversample it (in fact the frequencies of the tones transmitted are in the order of 100 MHz–400 MHz that would require a sampling frequency of 250 MHz–1 GHz, well above the few kHz needed to acquire the transmitted bandwidth according to the Nyquist criteria for bandlimited signals). Once acquired the echoes are digitally downconverted (quadrature downconversion) to determine their phase.

A brief description of the main blocks of the SFGPR presented in [1] and showed in Figure 1 is given below:

Transmitting Chain (Tx Chain): the output a Direct Digital Signal generator (DDS) is low pass filtered and amplified prior to be sent to the transmitting antenna.

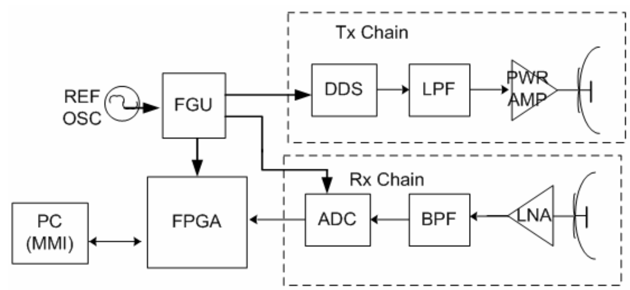

Figure 1: SFGPR architecture presented in this paper.

Receiving Chain (Rx Chain): the received signal is amplified by an Low Noise Amplifier (LNA) and provided to a large band ADC; the signal is undersampled with sampling frequencies provided by the FGU.

Frequency Generation Unit (FGU): aim of this unit is to generate all the frequencies employed in the SFPGR from a very low phase noise master oscillator: DDS and ADC clocks, FPGA reference clock.

The main advantages of the presented architecture are:

- Absence of a synchronism chain, generally used in SFGPR to get a phase reference of the transmitted signal [3].
- Simplified RF front end: both Tx and Rx chains are substantially constituted by an amplifier and a filter; this is allowed by the undersampling of the received echoes.
- Simplified Frequency Generation Unit.
- Substantial reduction of the power consumption and weight due to the great simplification brought in the RF front end.

In [2] the proposed SFGPR architecture was analysed for what concerns the aliased images. The necessity of the analysis performed was due to the wide bandwidth needed to be generated to achieve high resolution. The mentioned intrinsic advantages achievable by moving GPR complexities from the analogue domain into the digital one have the side effect to potentially "move" aliased images into the useful intermediate frequency band if a suitable frequency plan was not performed in advance. The analysis showed that a successful result is achievable with the aid of ad hoc software tools and that the characteristics of the filtering to be performed both in the analogue domain (anti-aliasing LPF at DDS output) and in the digital one (LPF at the quadrature downconversion output) were easily achievable: results showed that the digital transition bandwidth can be increased from 0.5 MHz to 1.5 MHz.

The achievement of the mentioned goals had been possible by moving SFGPR complexities from the analogue domain into the digital one. In the next paragraph the design of the SFGPR's subsystems is presented and described in detail.

3. SFGPR DESIGN

The control of the overall SFPGR is performed by a PC where a Man Machine Interface (MMI) allows the user both to control the GPR functionalities and to receive the data to be processed.

3.1. Tx Chain

The DDS of the transmitting chain (Figure 1) is clocked by a high sampling frequency generated by the FGU.

Its value is high enough to allow the generations of all the sinusoidal tones inside the band of interest by means of proper DDS registers programming by the digital section of the radar.

To allow the use of the greater part of the Nyquist band, the DDS performs also the SINC compensation. The value chosen for the clock frequency is 1200 MHz; the band of frequencies to be generated is: 100 MHz–450 MHz.

At the output of the DDS there is an antialias low pass filter to attenuate the generated image frequencies. The out of band attenuation required for this filter depends on the dynamic range of the GPR and on the partition of the attenuation made on this filter and on the ADC antialias filter. As explained later, the ADC to be used in this design is a 10 ENOB, for this reason the overall out of band attenuation to be partitioned between the two mentioned filters is at least 65 dB.

The power amplifier at the end of the Tx chain set the power of the signal to be transmitted in order to obtain, among the other contributions, the required maximum penetration depth and dynamic range (DR) of the GPR.

3.2. Rx Chain

The first element of the Rx chain is the LNA (Figure 1) that substantially sets the noise level of the receiver. Besides it and the other amplifiers, not shown in Figure 1 for sake of simplicity, set the maximum level of the signal to be acquired to 0.5 dB less than the maximum acceptable level at the input of the ADC. Before it there is a band pass filter to avoid aliasing and to reduce the level of out of band frequencies as explained in the previous paragraph.

The ADC of this design undersamples the signal transmitted by the GPR and reflected by targets. This choice eliminates the need of a mixer, with the relative LO signal generation, and greatly simplifies the synchronization chain mentioned in previous paragraphs; in fact instead to have an heterodyne receiver with IF at a fixed value, established by the LO offset frequency, the ADC samples directly the radiofrequency signal in input to the Rx chain. This have the net effect to greatly simplify the RF section of the GPR at the cost of an increased complexity of the digital section. This increased complexity can be easily handled by means of modern FPGA without increasing neither the budget of the radar nor its power consumption; on the contrary this choice allows to save both of them.

Because whatever sampling frequency value should be chosen it is not sufficiently high to acquire all the band transmitted by the GPR without introducing errors, it is mandatory to change its value on a steps' group basis. The result of this way to proceed is to have digital signals whose IF value changes step by step and that, as described in the following, it shall be taken into account in the digital section of the GPR by varying the frequency of the numeric oscillator of the digital IQ demodulator to be implemented.

After a market survey as ADC candidate has been chosen the AD9211 by Analog Devices. It is a 10 bit ADC characterised by an input bandwidth of 700 MHz and an aperture uncertainty of 0.2 ps rms. Other possible candidates were both the AD9445 (14 bits resolution) and AD9446 (16 bits) both with input bandwidth greater than 500 MHz and with an aperture uncertainty of 60 ps rms. As it will be explained in the FGU paragraph, to guarantee a dynamic of 60 dB, the jitter (rms value) of the sampling frequency should be less than 350 fs, with this value the aperture uncertainty of the AD9211 does not alter the target dynamic achievable. The main aim of the design of the GPR prototype presented in this paper is to demonstrate the validity of the new architecture rather than pushing too much on the GPR performances and for this reason the performances achievable with the AD9211 are more than satisfactory. Anyway by choosing one of the other two ADCs indicated before, a trade-off process should be started by taking into account that an higher dynamic is achievable by using ADCs with higher number of bit but the sampling frequency jitter to be guaranteed in this case it has to be decisively lower.

An important subsystem of the digital section is the synchronism detector circuit described in [1]. This detector circuit is needed in that the sampling frequencies are different between them (on a step by step basis) and they are not integer multiple of the FPGA reference clock frequency; so it is necessary a circuit that determine when both are phase aligned. It has been designed by starting from phase detector circuits of digital PLLs [4] and adapted to the needs of the presented design.

3.3. Digital Section

The samples acquired by the ADC are transferred to the FPGA to be stored and transferred to the control PC for further processing (in this initial design the digital downconversion is performed on the PC for sake of simplicity in that aim of this design is to start immediately with on field tests).

The number of samples to be acquired for each frequency step, as showed by the tuning performed by means of software simulations, is in the order of 1000. To keep the "digital section — Pc" interface as simple as possible the RS232@54kbaud is used; this requires about 6 seconds to transfer the samples acquired in each complete frequency swept. The same sw tool used to perform the simulations is adopted to perform the quadrature downconversion in the digital domain; the local oscillator of this downconverter is chosen according to the frequency of the transmitted signal and to the planned sampling frequency; its phase takes into account the possibility of spectral inversion of undersampled signals also.

The main tasks to be performed by the FPGA are:

Table 1: SFPGR values for frequency generation main parameters.

PARAMETER	VALUE
F_DDS	1200 MHz
F_Start	100 MHz
Step Frequency	14 MHz
Number of Steps	21
Sampling Frequencies	44 MHz/58 MHz

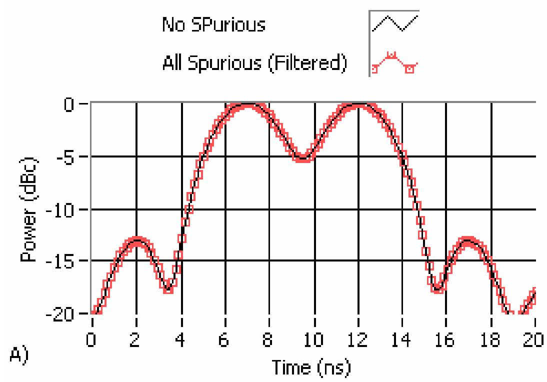

Figure 2: Simulated targets without taking into account any spurious frequency (reference line) and by filtering all of them.

- Generation of the timing signals (e.g., start generation for the DDS, start acquisition signal to the ADC and so on).
- Synchronism circuit (mentioned previously).
- Interface to/from MMI to receive commands and configuration parameters and to provide acquired data.

3.4. FGU

As reported in the previous section this unit has the task to generate the frequencies reported below with low jitter values:

- Sampling Frequency for the DDS (1200 MHz).
- Sampling frequency (variable) for the ADC: 42 MHz and 58 MHz digitally programmable.
- Reference frequency for the synchronism circuit and for the clock tree generation inside the FPGA.

3.5. SFGPR Performances

In order to give an estimate of the GPR performances achievable, a ground with a relative dielectric constant of 9 is considered. In this hypothesis and with the values shown in Table 1, the unambiguous range is about 3.6 m and the depth resolution expected is about 17 cm. The values showed in Table 1 are the set to be taken into account for the development of the presented SFGPR and they constitute the result of the trial and error process performed.

Figure 2 shows the results obtained from one of the simulations performed: it was obtained by simulating two targets with the same relative amplitude and at a "temporal distance" of, respectively, 7 ns and 12 ns. The characteristics of the digital LPF considered for the simulations are: Elliptic Filter type of 4th order; CutOff Freq 500 kHz; in band ripple 0.5 dB and out of band attenuation 40 dB. In Figure 2 two plots are reported to show the effectiveness of the filtering performed on the "spurious" signals.

4. CONCLUSIONS

This paper presented the design of a new SFGPR architecture based on the analysis and architecture previously proposed [1–3]. The details and the simulations results of the proposed design have been shown. These results show that the proposed SFGPR performs as foreseen.

REFERENCES

1. Adirosi, D., G. Alberti, and G. Galiero, "Undersampled digitally heterodyned SFGPR with variable sampling frequency," *PIERS Proceedings*, 325–328, Marrakesh, Morocco, Mar. 20–23, 2011.
2. Adirosi, D., G. Alberti, and G. Galiero, "'Spurious' analysis of a wide bandwidth undersampled digitally heterodyned SFGPR," *Proc. 6th International Workshop on Advanced Ground Penetrating Radar, IWAGPR 2011*, Aachen, Germany, Jun. 2011.
3. Alberti, G., L. Ciofaniello, G. Galiero, R. Persico, and M. Sacchettino, "An Italian experience on stepped frequency GPR," *PIERS Proceedings*, PISA, Italy, Mar. 2004,
4. Best, R. E., *Phase-locked Loops: Design, Simulation and Applications*, McGraw-Hill Professional, 2007

Checking of Combustion Chamber of Rocket Using ECT with AMR Sensor

D. F. He[1], **M. Shiwa**[1], **J. Takatsubo**[2], **and S. Moriya**[3]

[1]National Institute for Materials Science, Sengen 1-2-1, Tsukuba 305-0047, Japan
[2]Advanced Industrial Science and Technology, 1-2-1 Namiki, Tsukuba 305-8564, Japan
[3]Japan Aerospace Exploration Agency, Sengen 2-1-1, Tsukuba 305-8505, Japan

Abstract— Eddy current testing (ECT) system with high sensitive AMR sensor was developed. The magnetic field resolution of the AMR sensor was about 12 $\mathrm{pT}/\sqrt{\mathrm{Hz}}$ at the frequencies above 1 kHz. A 20 turn circular coil with the diameter of 3 mm was used to produce the excitation field. A chamber type specimen made of copper alloy was prepared to simulate the cooling grooves of the combustion chamber of liquid rocket. Artificial defects with the left wall thickness of 0 mm, 0.2 mm, 0.4 mm, 0.6 mm. were made in the bottom of the cooling grooves. The width of the defects was 0.2 mm and the lengths of the defects were 3 mm, 5 mm and 10 mm respectively. The AMR sensor was located inside of the chamber and close to the inner surface of the chamber. The scanning was realized by rotating the chamber with a motor. To reduce the influence of lift off variance during scanning, a dual frequency excitation method was used. For the higher frequency (20 kHz) eddy-current signal, due to the smaller penetration depth, it only measured the surface condition and the variance of the lift off; for the lower frequency (2 kHz) eddy-current signal, due to the bigger penetration depth, it also measured the defect signals except of the surface condition and the lift of variance. By subtracting the eddy-current signals of the two frequencies and choosing a proper subtraction factor, the influence of the lift-off variance could be reduced. Using our dual frequency ECT system, all the artificial defects could be successfully detected and the influence of lift-off variance could also be reduced well.

1. INTRODUCTION

The combustion chamber of liquid fuel rocket is made of Cu-Cr-Zr copper alloy. Inside of the combustion chamber is the ultra high temperature gas of about 3000 K. Cooling grooves are made in the wall of the combustion chamber and liquid hydrogen (20 K) flow in them for the cooling. Due to the big thermal gradient, small cracks are easily generated in the wall of the combustion chamber. For the recycling and safety checking, nondestructive testing of the combustion chamber is necessary. The aim of this research project is to develop a high sensitive ECT (eddy current testing) system to detect the small cracks in the copper alloy wall of combustion chamber We once developed high sensitive AMR (anisotropic magneto resistive) sensor and used it in ECT system [1]. With the AMR-based ECT system, we successfully detected the artificial defects in aluminum plate [2] and copper alloy plate [3, 4], in which grooves and artificial defects were made to simulate the wall of the combustion chamber of liquid fuel rocket.

In this report, we will illustrate the experiments and the results of the checking of a chamber type specimen made of Cu-Cr-Zr copper alloy The scanning was realized by rotating the chamber. To reduce the influence of the variance of lift off during scanning, dual frequency excitation method was developed.

2. EXPERIMENTAL SETUP

Figure 1 shows the schematic block diagram of the experimental setup of ECT with AMR sensor. AMR sensor of HMC1001 was used [5]. The coil was used to produce the AC magnetic field. Two lock-in amplifiers and two frequencies were used in this ECT system. The penetration depth can be estimated by formula $\delta = 1/\sqrt{\pi f \mu \sigma}$, where δ is the penetration depth, f is the frequency, μ is the permeability of the material and σ is the conductivity. For high frequency f_2, the penetration depth is small, surface condition and lift off have big influence to the output of V_2. For low frequency f_1, the penetration depth is big. Both the inside and surface properties of the material can be detected. If we subtract the output of V_1 and V_2, it is possible to reduce the influence of the variance of lift off.

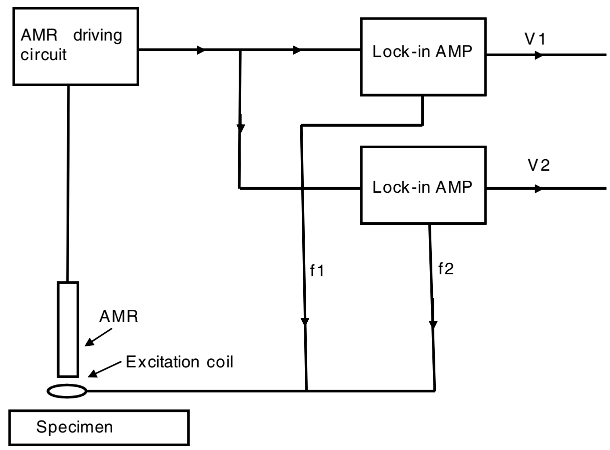

Figure 1: Schematic block diagram of ECT system with AMR sensor.

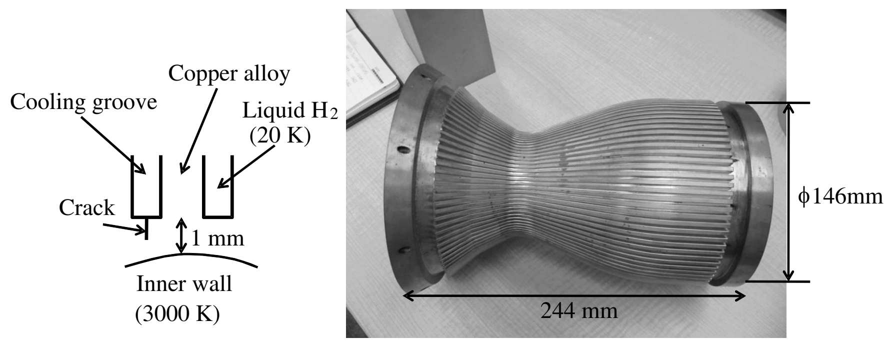

Figure 2: Chamber type specimen to simulate the combustion chamber of liquid rocket.

3. EXPERIMENT AND RESULTS

A chamber type specimen made of copper alloy was fabricated to simulate the combustion chamber of liquid rocket. Figure 2 shows it. Grooves were made on it to simulate the cooling grooves of the combustion chamber. From the bottom of the grooves, the wall thickness was about 1 mm. 12 artificial slits with different length and depth were made under the bottom of some grooves to simulate the defects. The width of the slits was about 0.2 mm. The lengths were 2 mm, 5 mm, and 10 mm; and the left thickness of the wall at the positions of the slits were 0 mm (through), 0.2 mm, 0.4 mm, and 0.6 mm.

The conductivity of the copper alloy is about 5.8×10^6 S/m. According to the thickness of the chamber (1 mm), the low excitation frequency f_1 of 2 kHz was used. The corresponding penetration depth was about 1.5 mm. 20 kHz was used as the high excitation frequency and the penetration depth was about 0.5 mm. The excitation coil was a 20 turn circular coil with the diameter of about 3 mm. The AMR sensor was located inside the chamber and was kept static. The chamber was rotated by a stepping motor for the scanning. The rotating speed was about 60 degree/second.

Figure 3 shows the scanning results for the slits with the left thickness of 0 mm (though) and 0.2 mm. For slits with the left thickness of 0 mm, it was observed by the low excitation frequency and the high excitation frequency. For the slits with the left thickness of 0.2 mm, the signals became smaller when using high excitation frequency. During the scanning, the variance of the lift off was about 0.2 mm, which caused the non-flatness of the output. After the subtraction of the outputs of low frequency and high frequency, and choosing proper subtraction factor, it became flat. This proved that the dual frequency method was effective to reduce the influence of the variance of lift off.

Figure 4 shows the scanning results for the slits with the left thickness of 0.4 mm and 0.6 mm. For the high excitation frequency, due to the small penetration depth, no slit signals could be observed. After the subtraction of the outputs of low frequency and high frequency, the line became flat. This also proved that the dual frequency method was effective to reduce the influence of the variance of lift off.

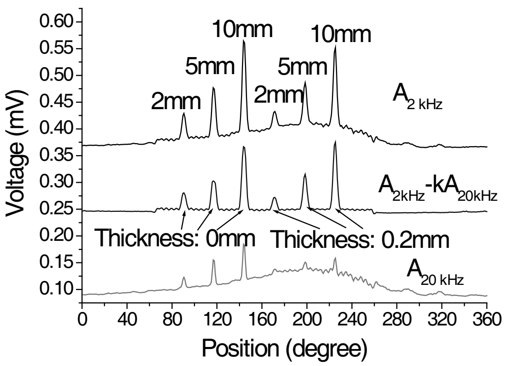

Figure 3: Scanning results for the slits with the left thickness of 0 mm (though) and 0.2 mm.

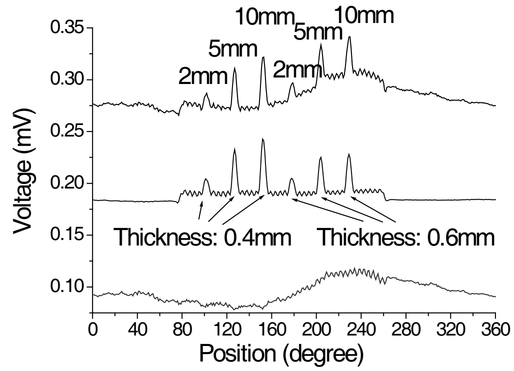

Figure 4: Scanning results for the slits with the left thickness of 0.4 mm and 0.6 mm.

4. SUMMARY

Using dual frequency excitation method, the lift-off effect could be reduced. All the slit defects could be successfully detected and the signal-to-noise ratio was good. The experimental results proved that ECT method can be used to detect the defect in the combustion chamber of liquid rocket.

REFERENCES

1. He, D. F., M. Tachiki, and H. Itozaki, "Highly sensitive anisotropic magnetoresistance magnetometer for Eddy-current nondestructive evaluation," *Rev. Sci. Instru.*, Vol. 80, 036102, 2009.
2. He, D. F., M. Shiwa, H. Yamawaki, M. Tachiki, H. Itozaki, S. Moria, T. Masuoka, and I. Uetake, "Basic examination for the defect detection of combustion chambers using ECT with an AMR sensor," *Journal of JSNDI*, Vol. 59, No. 10, 510514, 2010.
3. He, D. F., M. Shiwa, J. P. Jia, et al., "Multi-frequency ECT with AMR sensor," *NDT & E International*, Vol. 44, No. 5, 438–441, 2011.
4. He, D. F., M. Shiwa, J. Takatsubo, and S. Moriya, "Checking of combustion chamber of rocket using ECT with AMR sensor," *PIERS Proceedings*, 540–542, Marrakesh, Morocco, Mar. 20–23, 2011.
5. Data sheet of HMC1001, Honeywell, http://www.ssec.honeywell.com/magnetic/products.html.

SWB: An Analysis and Visualization Tool for COSMO SkyMed

V. A. Loré[1], **G. Milillo**[2], **P. Milillo**[3], **A. Valentino**[1], **and G. Franceschetti**[4]

[1]INNOVA Consorzio per L'informatica e la Telematica s.r.l., Italy
[2]Agenzia Spaziale Italiana (ASI), Italy
[3]Facoltà di Scienze Matematiche, Fisiche e Naturali Dipartimento Interateneo di Fisica
Università Degli Studi di Bari, Italy
[4]Dipartimento di Ingegneria Elettronica e delle Telecomunicazioni
Università di Napoli "Federico II", Italy

Abstract— With the increase of the availability of high quality data for Earth Observation (EO), and SAR in particular, it is even more important to have advanced applications that can exploit this great amount of data. Also it is important to have software (SW) tools that allow scientists and engineers to process and analyze data, and to develop innovative applications.

"SAR WorkBench" (SWB) is a SW for the fast visualization/browsing, analysis and post processing of multi-mission EO data. It was developed in the framework of one of the Italian Space Agency (ASI) projects for COSMO SkyMed data exploitation and has, among others, some features that are very peculiar like the Quality Analysis ones. SWB has a modular architecture and it is extendible via plug-ins. It can be programmed in an high level programming language, close to the ones scientists are used to, and do not requires expensive SW licenses.

In this paper, it is presented an overview of the SW and its architecture and some examples of data analysis performed with SWB.

1. INTRODUCTION

In recent years there has been a significant increase in the availability of data for Earth Observation (EO) and SAR in particular. The availability of high quality and low cost data will be further increased with the launch of ESA SENTINEL missions. It is important, therefore, to have advanced applications that can take advantage of this great amount of data and also have software (SW) tools that enable scientists and engineers to process and analyze data, and to develop new and innovative applications.

The panorama of scientific SW for EO (commercial and not) had a great evolution in recent times as well, and it is in this context that the "SAR WorkBench" (SWB) SW is placed.

It was initially developed in the framework of one of the Italian Space Agency (ASI) projects (ASI contract n.I/038/07/1 "ASI-GRID") to overcome a lack of specific SW tools for COSMO SkyMed (CSK) data in early stages of the mission, when other SW on the market were still not ready to provide and adequate support. SWB is an application for the analysis and post processing of multi-mission SAR data (but also supports non SAR EO data). It is modular and has a plug-in architecture. Core modules provide functionalities for ingestion/data exchange, Quality Analysis (QA) and basic data processing. SWB also provides a powerful viewer for fast visualization and browsing of large sized EO products.

Currently exists a base set of plug-ins that provide specific capabilities (such as CSK RAW data analysis) or allow SWB to interface external packages. As an example, it is already available a plug-in that enables SWB to exploit some of the powerful processing capabilities of Orfeo ToolBox (http://orfeo-toolbox.org). New extension modules for interferometry and polarimetry are planned.

One of the key features of SWB is that it is highly programmable. It can be extended writing new plug-ins in a high level programming language (www.python.org) that has very good extensions for scientific programming (www.scipy.org). The resulting environment is very close to what scientists are used to but it do not requires expensive SW licenses.

2. SWB OVERVIEW

SWB is a desktop application for the management of multi-mission SAR data. It is modular and has a plug-in architecture that makes it very flexible. The main modules include: the Graphical User Interface (GUI), ingestion/data exchange, Quality Analysis (QA) and data processing.

The GUI component is mainly a multi-mission data viewer that includes facilities and graphical interfaces for controlling other modules. It currently supports a large number of SAR missions: COSMO-SkyMed, TerraSAR-X, Radarsat 1/2, PALSAR, ERS 1/2, ENVISAT, etc.. It can also handle optical and multi-spectral data such as the ones from ENVISAT/MERIS sensor and ALOS/AVNIR-2. The viewer has been designed to be extremely user-friendly. It provides a dataset browser, that lists the open products, a main visualization area, a metadata viewer and a panel indicating the geographical location of the image on a map. Through the GUI interface the user can access the other modules available in SWB.

Besides allowing access to multi-mission data, the "ingestion and data exchange" sub-system also enables the user to export data into standard graphic formats (GeoTIFF, JPEG, PNG) compatible with wide spread software tools and in formats specific for the main GIS and EO applications (NetCDF, etc.). This is fundamental for the integration of SWB into scientific and production environments.

The Quality Analysis (see Section 6) component includes tools for measurement of Impulse Response Function (IRF) parameters and for radiometric analysis. Also a specific extension module has been developed for the analysis of CSK Level 0 data.

The data processing modules include a set of tools, also accessible via command line, for basic data manipulation (cropping, data type conversion, raster algebra, filtering, re-sampling, etc.) and also tools that are specific for SAR data processing (complex data re-sampling and detection, speckle filtering, geo-coding and ortho-rectification, etc.). It is important to stress that data processing modules, and the underlying infrastructure, are designed to handle data products that are potentially very large sized. They have built-in streaming capabilities and are able to perform (from file to file) processing, splitting the data into chunks in order to reduce memory requirements.

SWB provides the base infrastructure for data access and a simple extension mechanism. Extensions can be written using an high level programming language, Python (www.python.org), that provides an environment suitable for fast prototyping (see www.scipy.org) that is very similar to wide spread commercial ones like IDL™ and Matlab®. In this framework, it is quite simple to call external programs and also integrate external tools and scientific libraries, e.g., written in C/C++ and FORTRAN. Being the entire framework based on a *open source* SW stack the user do not need to buy expensive SW licenses in order to write its own extensions.

3. QUALITATIVE ANALYSIS AND INTERPRETATION OF THE AMPLITUDE SIGNAL

The SAR is an active sensor and use a coherent, polarized and monochromatic radiation in microwave band for imaging (X band for CSK). The information in the data is relative to how the targets react to the specific wavelength and polarization used. For SAR data interpretation [1] it is important to take into account both scattering phenomena and distortions due to acquisition geometry. For example the layover effect gives a horizontal "laid-over" visual image of any vertical target.

Sometimes the interpretation of SAR data is not obvious [1, 2] so the user needs to perform a qualitative and visual analysis of the imaged scene. This kind of analysis consists in individualizing specific targets on the scene and interpreting the data and the connected phenomena taking into account the satellite configuration and acquisition characteristics. Maps or optical images are often used for comparison and guidance.

SWB has been used to analyze images in various contexts, with specific attention to human interest areas, such as metropolitan and agricultural areas, ports and coasts. In this case SWB revealed to be very handy thanks to its fast browsing and viewing capabilities. The qualitative analysis has been carried out using standard CSK products delivered by the CSK C-UGS (Civilian User Ground Segment) of Matera (Italy).

The data set used for the analysis includes SCS (Single-look Complex Slant), DGM (Detected Ground Multilook), GEC (Geocoded Ellipsoid Corrected) and GTC (Geocoded Terrain Corrected) products acquired in Stripmap and Enhanced Spotlight acquisition modes. Fig. 2 shows an example of the layover effect on a SAR image of New York. Skyscrapers appear to be in a horizontal position. The high resolution of CSK and the strong targets' response to the sensor allow the naked eye to count the floors of each building.

4. CHANGE DETECTION ANALYSIS

Storing co-registering images, acquired at different times, in the different channels of an RGB image (with opportune combination) produces a, so called, multi-temporal RGB product. This kind of product can be used to detect changes in the imaged area. The targets or areas in which scattering does not vary have the same value in each colour channel and hence are visualized in gray tones. Regions in which scattering changes between acquisitions result to be colored in different

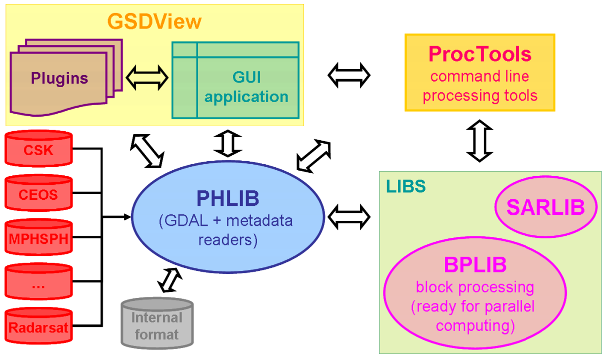

Figure 1: High level SWB architecture.

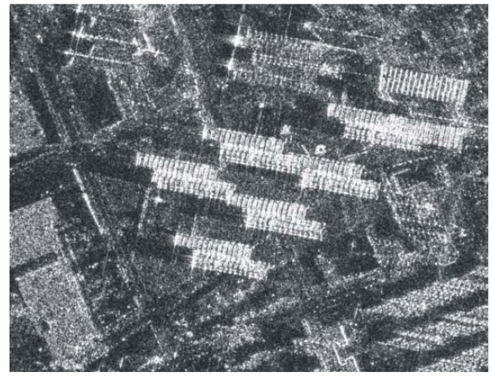

Figure 2: Skyscrapers in New York city.

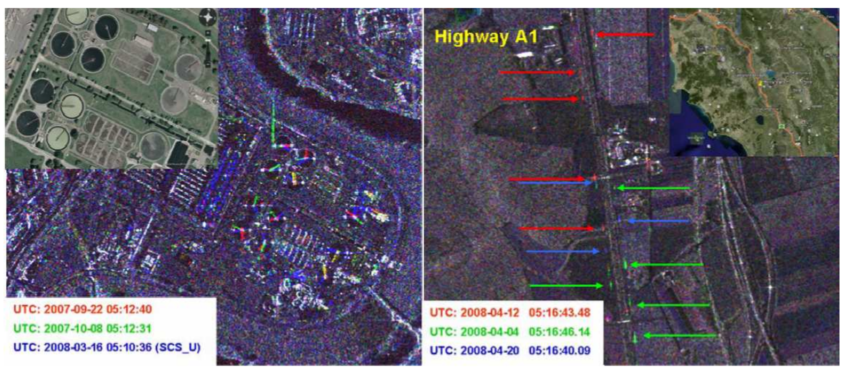

(a) (b)

Figure 3: (a) Purification plant, (b) A1 highway in Tuscany — Italy.

fashions (non-grey). Such products can be easily generated, in many variants, by SWB starting from co-registered products.

The high resolution of the CSK sensor makes it possible to appreciate a large number of details and, in many cases, "to guess" the nature and shape of the target visualized even if it has a relatively reduced size.

In the left hand side of Fig. 3, it is showed an example of visual change detection performed using a multi-temporal RGB image. The picture also include the corresponding optical image. It is the image of a purification plant near the urban area of Rome. It is made up of a set of circular structures, each of which has a rotating arm. The arms were in different positions at the times in which the three images used to produce the RGB were acquired and this is evident by the three colored lines in the cistern circle.

5. MOVING TARGET EXAMPLES

The same kind of products described in the previous section can also be used for a visual moving target detection [3]. Results shown in this section have been obtained using three stripmap images in repeat-pass interferometric configuration of an area between Tuscany and Umbria (Italy).

The motion of a target in the satellite across-track direction causes an additional (linear) phase term in the signal history and hence a displacement of the target in azimuth direction in the focused SAR image [4]. The entity of the displacement can be expressed as follows:

$$\Delta_{AZ} = -R \cdot \frac{v_{LOS}}{v_{SAT}} \tag{1}$$

being R the slant range, v_{LOS} component of the motion vector into the line-of-sight direction of the sensor and v_{SAT} is the sensor velocity.

The along track motion causes de-focusing of the target. A moving vehicle appears in a high resolution multi-temporal RGB image like a small patch with a dominant color (red, green or blue) near (it can be outside) the road path.

The right hand side of Fig. 3 shows the A1 highway (in Tuscany — Italy) and various moving targets for each of the three images used. In this case the possibility, provided by SWB, to display geographic and image coordinates of the cursor position allowed an easy calculation of the v_{LOS} and, projecting in ground along the road path, to perform an approximated estimation of the actual vehicle velocity.

6. SAR DATA QUALITY ANALYSIS

SWB provides a quality analysis tool (see Fig. 4), mainly targeted to engineers and scientists. It can be used to measure a wide set of quality parameters on the SAR image including statistic ones, parameters related to the IRF (geometric resolution, PSLR, SSLR, ISLR and IRF shape), to the image geometry (geo-location accuracy, etc.) and radiometry. Also it is possible to perform the spectral analysis of an image portion. This kind of functions can be very useful for in the development phase of a new processing algorithms to track down bugs in the code and to perform the tuning of various processing parameters.

7. SWB AND SAR INTERFEROMETRY

Although SWB currently does not have an integrated interferometric tool for co-registration (that is a core step of the interferometric processing chain) other basic steps, like interferogram formation, complex multi loocking and phase extraction, are already available in SWB libraries together to visualization capabilities. This allow SWB to be an efficient helper tool to monitor the development of interferometric SW chains. An example of SWB use in this context is provided in [5, 6].

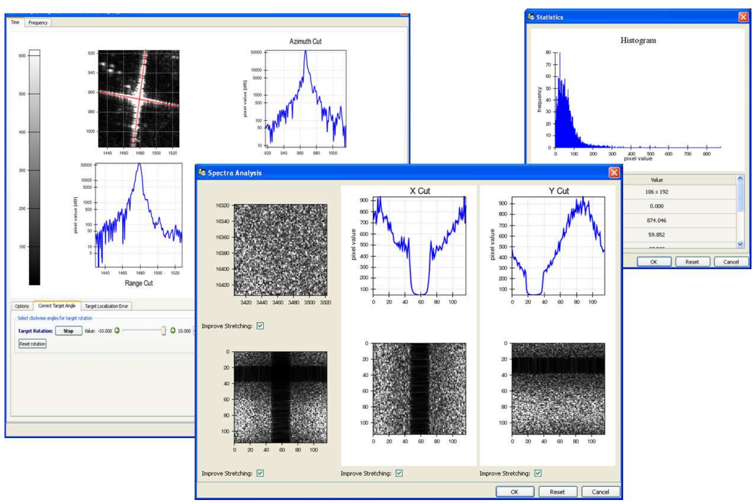

Figure 4: Quality analysis tool of SWB.

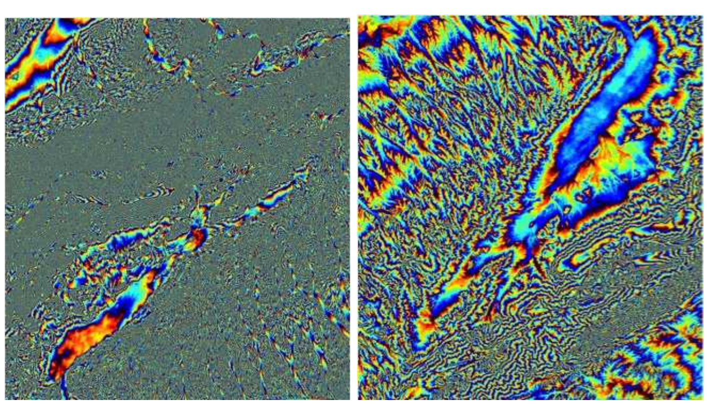

(a) (b)

Figure 5: DORIS processed COSMO-SkyMed SAR data of the Abruzzo area. (a) Right descending pair, (b) Right ascending.

SWB in conjunction with an interferometric SW like DORIS [7] becomes a powerful analysis tool able to fully exploit the great capabilities of the DORIS processor (see Fig. 5).

8. CONCLUSION

Although not feature complete like some other similar SW (commercial and free) SWB have proved to be very useful in many contexts. Beyond features directly available in it, some of which very peculiar like the QA, it is considered very important the possibility of SWB to integrate with existing production and experimental environments thanks to its data exchange capabilities and programmability. New features planned for SWB include a better support for applications in the field of SAR interferometry and polarimety.

REFERENCES

1. Ulaby, F. T., R. K. Moore, and K. Fung, *Microwave Remote Sensing Active and Passive: Volume 3, "From Theory to Application"*, Addison-Wesley, 1986.
2. Lillesadn, T. M. and R. W. Kiefer, *Remote Sensing and Image Interpretation*, 2nd Edition, Wiley, 2004.
3. Hinz, S., F. Meyer, A. Laika, and R. Bamler, "Spaceborne traffic monitoring with dual channel synthetic aperture radar — Theory and experiments," *Proceedings CVPR'05*, 57–65, San Diego, California, Jun. 2005.
4. Curlander, J. C. and R. N. McDonough, *Synthetic Aperture Radar: Systems and Signal Processing*, Wiley-Interscience, New York, 1991.
5. Milillo, P., *Elaborazione ed Analisi di DEM Interferometrici a Partire da Dati Satellitari SAR Della Missione Italiana COSMO-SkyMed*, Università Degli Studi di Bari "Aldo Moro", Tesi di Laurea in Fisica, 2010.
6. Brizio, F., N. Stella, G. Milillo, and P. Milillo, "Interferometric and radargrammetic DEM form COSMO-SkyMed dataset: Result and validation," *16th KA and Broadband Communications, Navigation and Earth Observation Conference*, Milan, 2010.
7. Kampes, B. M., R. F. Hanssen, and Z. Perski, "Radar interferometry with public domain tools," *Third International Workshop on ERS SAR Interferometry, 'FRINGE03'*, 6, Frascati, Italy, Dec. 1–5, 2003.

High-gain and Light-weight Antenna for Radar System Using a Horn Covered with Curved Woodpile EBG

S. Kampeephat, P. Krachodnok, and R. Wongsan
School of Telecommunication Engineering, Institute of Engineering
Suranaree University of Technology, Nakhon Ratchasima, Thailand

Abstract— A high-gain and light-weight antenna using a horn covered with curved woodpile Electromagnetic Band Gap (EBG) is presented. The proposed antenna has the advantages of high gain, low profile, and low cost for fabrication. Moreover, it provides the moderately light weight compare to the other antennas in radar system at present. Because of, it can use the small mechanism system to rotate its antenna, as in the past. A Computer Simulation Technology (CST) software has been used to compute the return loss, VSWR, radiation pattern, beamwidth (-3 dB), and gain of the antenna. The bandwidth, at S_{11} (-10 dB), is between 8 to 12 GHz with a gain more than 20 dB.

1. INTRODUCTION

The horns are widely used as antennas at UHF and microwave frequency, above 300 MHz [1]. They are used as feeders for larger antenna structures, as standard calibration antennas to measure the gain of other antennas, and as directive antennas [2]. Their widespread applicability stems from their simplicity in construction, ease of excitation, versatility, large gain, and preferred overall performance [3]. In this paper, we extend the idea of planar EBG resonator to a curved form to realize an EBG antenna. Similar configurations using metallic elements for EBG structures have been studied and tested at microwave frequency [4, 5]. However, metallic elements are not preferred at radar frequency due to their conduction losses by a small skin depth. In this paper, we design and simulate a curved woodpile EBG based on low loss alumina materials at 10 GHz, and demonstrate its use in a horn antenna for Short RangeRadar (SRR).

At first, the general approach will be presented which is including the configurations of a horn antenna and a curved woodpile EBG structures as shown in Section 2. In Section 3, we apply this approach into the results and discussion. Finally, the conclusions are given in Section 4.

2. HORN ANTENNA AND EBG CONFIGURATIONS

A horn antenna may be considered as a transformer from the impedance of a transmission line to the impedance of free space, 377 Ω. A common microwave transmission line is waveguide, a hollow pipe carrying an electromagnetic wave. The horn antenna consists of a flaring metal waveguide shaped like a horn to direct the radio waves as shown in Fig. 1. The design of a horn antenna is initiated by determining its aperture dimension as follow [3] The simulated result shows that the gain at 10 GHz is 14 dB.

We apply a similar geometry as in the planar woodpile structure [6] to design the curved woodpile EBG made of alumina rods ($\varepsilon_r = 8.4$, $\tan\delta = 0.002$) The parameters for the curved woodpile EBG are the filament thickness or diameter (w), the inner (R_1) and outer (R_2) radii, the height (h), the number of radial filaments (N_{rad}), and the number of rings (N_{ring}) of the curved, as shown in Table 1. Fig. 2 shows geometry of the curved woodpile EBG.

Table 1: The design parameters of the curved woodpile EBG.

Woodpile EBG parameters	Size
filament thickness or diameter (w)	0.133λ
inner radii (R_1)	12λ
outer radii (R_2)	12.27λ
height (h)	2.66λ
number of radial filaments (N_{rad})	9
number of rings (N_{ring})	2

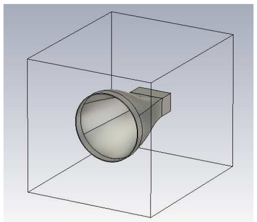

Figure 1: A horn antenna.

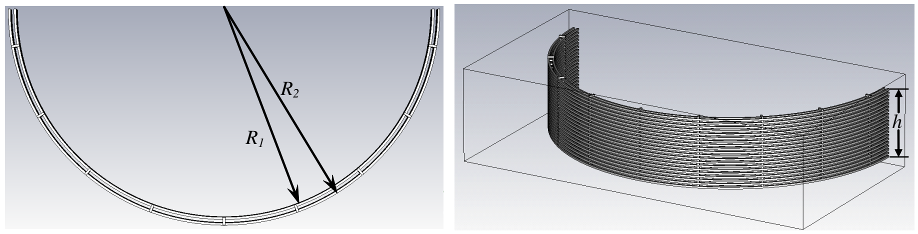

Figure 2: The geometry of the curved woodpile EBG.

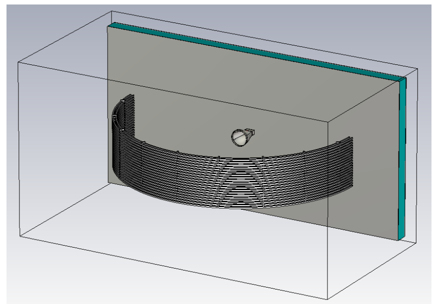

Figure 3: A horn covered with curved woodpile EBG.

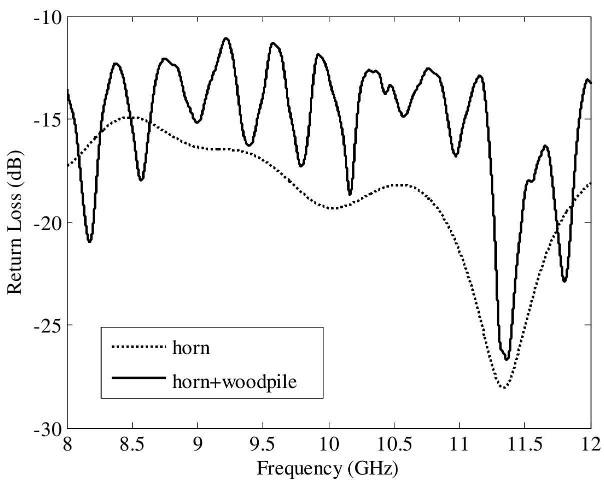

Figure 4: The return loss.

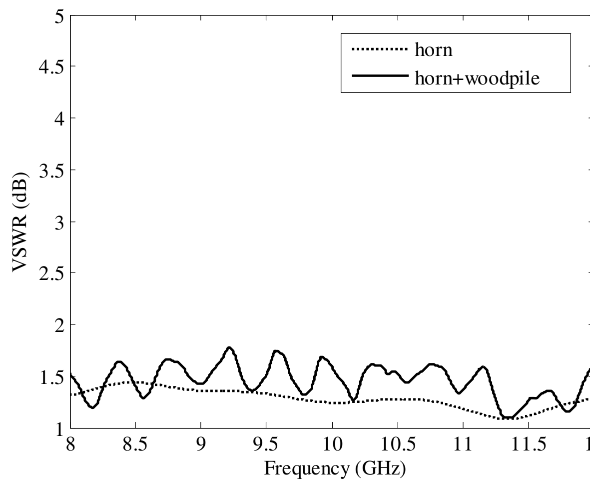

Figure 5: The VSWR.

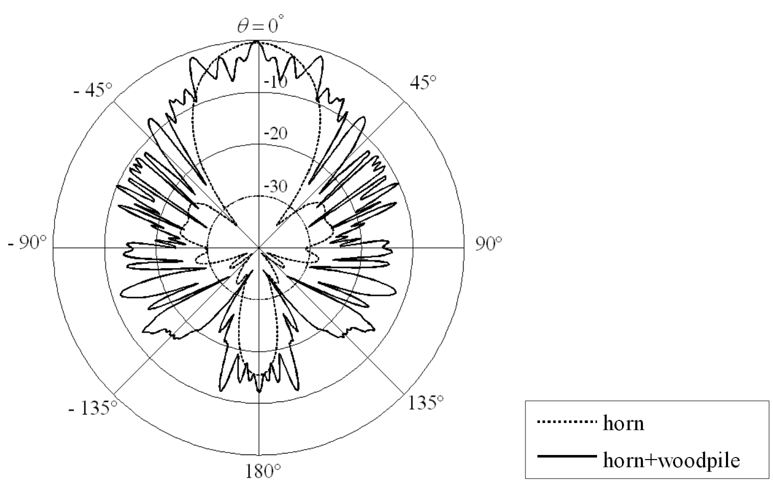

Figure 6: The azimuth pattern.

3. RESULTS AND DISCUSSION

The configuration of the model is shown in Fig. 3. It consists of a horn antenna, curved woodpile EBG of alumina rods, and FR4 reflector. From Fig. 4, it can be clearly seen that the S_{11} are lower than -10 dB, which are between 8 to 12 GHz. Fig. 5 shows the VSWR that is lower than 1.8. It found that a curved woodpile EBG has low effect of S_{11} and VSWR. The azimuth pattern of the proposed antenna at the center frequency band of 10 GHz has narrow beamwidth (-3 dB) of 3.7 degree, as shown in Fig. 6. The simulated result shows that the gain at 10 GHz is 20.47 dB.

4. CONCLUSIONS

In this paper, we present the design of a horn covered with the curved woodpile EBG covering the 8 to 12 GHz frequency spectrum. It has been shown that this design produces high gain, low profile, and low cost for fabrication. Moreover, it provides the moderately light weight compared to the other antennas in radar system at present. Therefore, this proposed antenna accords to the requirements and appropriate for the radar system.

REFERENCES

1. Bevilaqua, P., "Horn antenna — Intro.," Retrieved Nov. 11, 2010, Antenna-theory.com website.
2. Poole, I., "Horn antenna," Adrio Communications Ltd., Retrieved Nov. 11, 2010, Radio-Electronics.com website.
3. Constantine, A. B., *Antenna Theory*, Wiley-Interscience, 2005.
4. Palikaras, G. K., A. P. Feresidis, and J. C. Vardaxoglou, "Cylindrical EBG surfaces foromni-directional wireless LAN antennas," *IEEE International Symposium on Antennasand Propagation*, Vol. 4B, 339–342, Jul. 2005,
5. Chreim, H., E. Pointereau, B. Jecko, and P. Dufrane, "Omnidirectional electromagneticband gap antenna for base station application," *IEEE Antennas and Wireless Propagation Letters*, Vol. 6, 499-502, 2007.
6. Yoonjae, L., H. Yang, and C. G. Parini., "High-gain omni-directional antenna using a freeformed cylindrical cavity for high data-rate short range communications at millimetre-wave bands," *3rd European Conference Antennas and Propagation*, London, 2828–2831, Mar. 2009.

Gain Improvement of Curved Strip Dipole Using EBG Resonator

N. Fhafhiem, P. Krachodnok, and R. Wongsan
School of Telecommunication Engineering, Suranaree University of Technology
Nakhonratchasima 30000, Thailand

Abstract— In this work, the electromagnetic band gap (EBG) and metallic reflector plane are used for cavity wall of a curved strip dipole. The reflection phase of cavity walls is important for the cavity height (h) calculation, which has an effect on the antenna characteristic. The simulation results found that the cavity height of 0.63λ is most direction gain of 9.3 dB. The HPBW in E- and H-plane are 59.1° and 71.4°, respectively. Moreover, the patterns have low side lobe, so we can estimate that the structure volume is well designed. The proposed antenna covers bandwidth of 2.2 GHz–2.85 GHz that suitable for wireless communication and RFID system.

1. INTRODUCTION

With the rapid development of the wireless communication, the antenna is an important to develop the radio identification (RFID) technology. This technology can be used for example in identification objects in warehousing supply chain management, service logistics, control, and author automation process. The RFID system consists of the radio frequency transponder (tag), interrogator (reader), and data processing system, which the communication between the tag and the reader is achieved by modulated back scattering of the reader's carrier wave signal. The antenna is designed for the RFID system which have different requirement for diverse applications. To design the antenna's reader the traditional antenna type can be designed by the classic theory of microstrip antenna [1, 2]. Because the RFID reader at 2.45 GHz is applied for the electronic toll collection on expressway, the antenna design has been sufficient gain, coverage aboard area, and high power handing. The curved strip dipole antenna has some qualifications that are pertinent point, its beamwidth is wide and its shape could be change easy [3]. However, the curved strip dipole antenna has low gain. This argues, if we can design the antenna to work well due to bad weather on motorway such as fog and heavy raining,it will have more efficiency for field radiating. In previous paper [4], we proposed a short-end curved strip dipole antenna on conductor plane for 2.45 GHz that the HPBW is wider than straight dipole, which is necessary for the structure that requires the simple in concept, simple feeder, and used for microwave frequency. Moreover, there are many papers that presented radiating antenna with cavity wall which is composed of electromagnetic band gap (EBG) and frequency selective surface (FSS) [5, 6]. The cavity wall has a positively effect on direction, improving the antenna gain. In this paper, the EBG and conductor plane are used for cavity wall of a curved strip dipole antenna. The proposed antenna designed from extremely attractive solutions for check point at the high-way that collect fees from many cars at 2.45 GHz is presented.

2. ANTENNA DESCRIPTION AND DESIGN GEOMETRY

The geometry of the curved strip dipole using EBG resonator with detailed dimensions is illustrated in Fig. 1. The curved strip dipole antenna is designed to resonate around 2.45 GHz, which is the microwave frequency used in RFID transportation application. The radiating is constructed of metal plate (a 1-mm thick perfect conductor plate). It is mounted over an inexpensive polyvinyl chloride (PVC) with the dielectric constant of 3.14. The thickness and the wide (w_2) of PVC are 1-mm and 30-mm, respectively. The parameters of the antenna consists of the total length and the wide of the curved strip dipole expressed by L_d and w_1, respectively, and the radius of the curved is a. The half wavelength of the curved strip dipole is $L_d = \pi a$. Furthermore, the analysis model of the cavity wall consists of the metallic EBG and a conductor ground plane. The structure of EBG has five metallic elements and uses a 9.3-mm rod thickness. The rod width (W) is 9.3-mm and the gap (g) width is 22-mm, which the EBG structure geometry is summarized in Table 1. Besides, the overall dimensions of PEC ground plane is the overall size of EBG. Finally, the curved strip dipole antenna is placed between the EBG and the conductor plane with cavity height (h_2) of 76.8-mm, which is shown in Fig. 2.

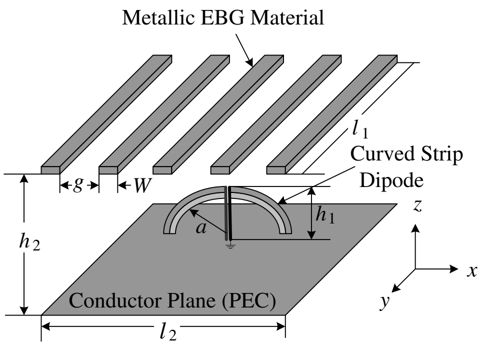

Figure 1: Configuration of the curved strip dipole using EBG resonator.

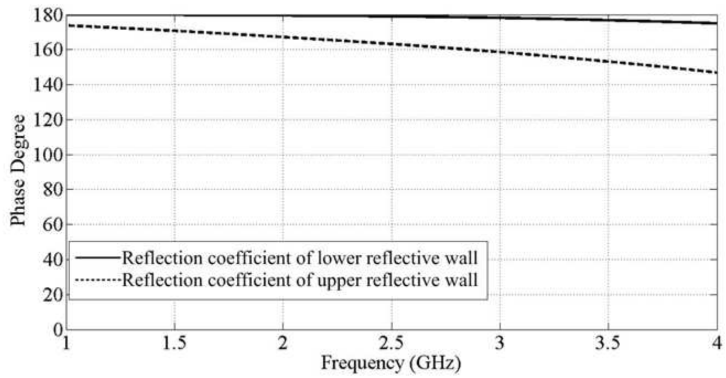

Figure 2: The reflection coefficient.

Table 1: The data of the curved strip dipole using EBG resonator.

Parameter	Size (λ)
w_1	0.082λ
w_2	0.25λ
L_d	0.425λ
a	0.159λ
W	0.075λ
g	0.179λ
$h1$	0.248λ
$h2$	0.627λ
l_1	1.141λ
l_2	1.164λ

3. NUMERICAL SIMULATIONS RESULTS

The objective of this paper is to increased directive gain of the curved strip dipole for application in RFID technology at 2.45 GHz. From optimized analysis, the good matching of this antenna could be obtained. As the resulting, the curved strip dipole antenna has a low gain of 1.5 dB and the HPBW in E-plane is 95.3°. It has omnidirectional radiation pattern, so the power may be loss to unnecessary place.In order to solve such problems, the cavity wall is used for improve the gain of the curved strip dipole antenna. The first step consists in designing an EBG with a resonant frequency corresponding to the microwave band around 2.45 GHz. Fig. 2 is illustrated the reflection coefficient phase of the upper and lower reflective wall by using the periodic boundary condition [7]. The cavity height has a relations with reflection coefficient of cavity wall, where is based on the following reaction (1)

$$h = \frac{c}{2f}\left[\frac{\phi_{PEC} + \phi_{EBG}}{360^o}\right] \tag{1}$$

where, the variables c, f, ϕ_{PEC}, and ϕ_{EBG} are the speed of light, resonant frequency, and the reflection coefficient phase of PEC and EBG, respectively. Because the combination of phase should be $2n\pi$, so the cavity height could be obtained. Fig. 3 shows the height variations versus the frequency. It appears that a cavity height of 56.8-mm is proper resonant frequency which complies with the requirements of RFID reader for ETC.

We can calculate the h parameter is 56.8-mm because the upper and the lower reflective wall are simulated separately by using the periodic boundary condition. Fig. 4 shows the return loss at $h = 56.8$-mm, which is mismatch between the curved strip dipole antenna and the cavity. In case of the specialty dipole, the effect of reflection coefficient phase is not only in almost feed center but also in two arms of dipole, the h parameter is adjusted the gain as shown in Table 2. The cavity height of 76.8-mm has the most directive gain of 9.3 dB. In Fig. 4, we found that the proposed

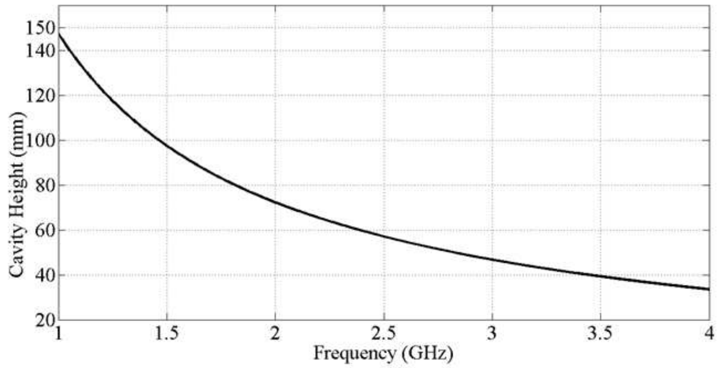

Figure 3: Calculation of cavity height.

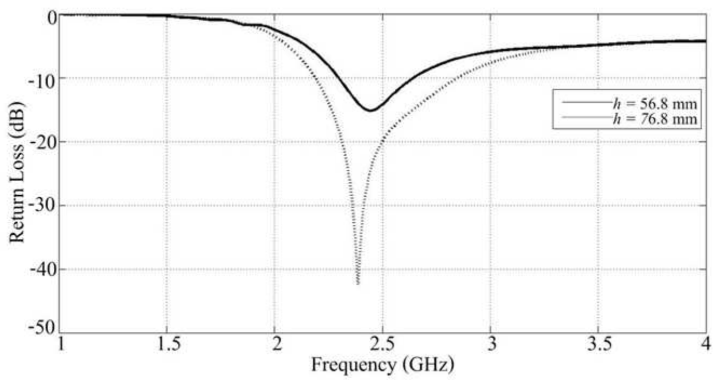

Figure 4: Return loss.

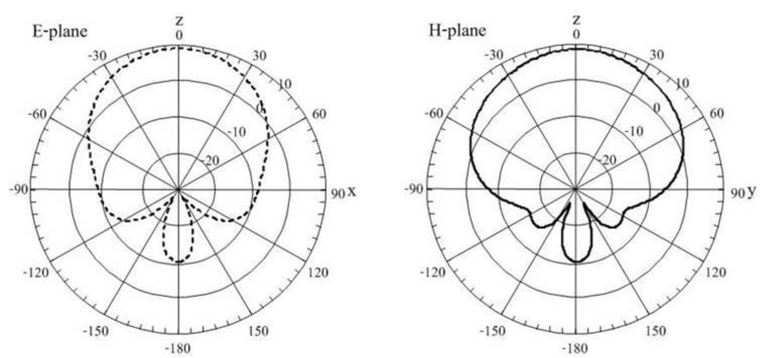

Figure 5: Radiation pattern.

Table 2: The optimizing of cavity height.

h (mm)	Gain (dB)	HPBW (degree)	
		E-plane	H-plane
56.8	7.6	77.1	104.8
61.8	8.13	72.7	91.1
66.8	8.6	67.8	80.9
71.8	9.1	62.8	74.1
76.8	9.3	59.1	71.4
81.8	9.2	57.1	71.3

antenna still exhibits a return loss batter than -10 dB in resonant frequency band. The E- and H-plane radiation patterns at 2.45 GHz are shown in Fig. 5, which is directive. The patterns have low side lobe, so we can estimate that the structure volume is will dimensioned.

4. CONCLUSION

The simulation results of curved strip dipole by using the cavity wall for improve the gain have been presented in this paper. It is utilized to place at the RFID reader for checkpoint at high-way that collects fees from many cars at 2.45 GHz. Then the modeling software (CST Microwave Studio), it is successful to improve the gain of 9.3 dB because of the qualifications of cavity wall. The PEC redirects half of the radiation into the opposite direction. In addition, the EBG wall increases the gain and redirects the radiation too, as far as the radiation can be radiate to the user's zone. Moreover, it has been structure uncomplicated and inexpensive that demand on equipment for wireless communication system. The band of frequency is covered 2.2–2.58 GHz in microwave frequency band.

ACKNOWLEDGMENT

The authors gratefully financial support for this research project from the Telecommunications Research and Industrial and Development Institute (TRIDI), National Telecommunications Commission (NTC) Fund, Thailand.

REFERENCES

1. Xianming, Q. and N. Yang, "2.45 GHz circularly polarized RFID reader antenna," *The Ninth International Conference ICCS*, 1189–1192, Krakow, Poland, Jun. 2004.
2. Lei, C., S. Yan, and H. Yang, "Study and design of modified fractal antenna for RFID application," *ISECS International Colloguium*, 8–11, Vancouver, Canada, Aug. 2009.
3. Fhafhiem, N., K. Piyaporn, and W. Rangsan, "High directive gain antenna using shorted-end curved strip dipole on electromagnetic band gap," *PIERS Proceedings*, 840–844, Xi'an, China, Mar. 22–26, 2010.
4. Fhafhiem, N., K. Piyaporn, and W. Rangsan, "A shorted-end curved strip dipole on dielectric and conducting plane for wireless LANs," *The International Symposium on Antenna and Propagation*, 835–838, Bangkok, Thailand, Oct. 2009.
5. Rodes, E., M. Diblanc, E. Arnaud, T. Monediereand, and B. Jecko, "Dual-band EBG resonator antenna using a single-layer FSS," *IEEE Antenna and Wireless Propagation Letter*, Vol. 6, 368–371, 2007.
6. Hajj, M., E. Rodesand, and T. Monediere, "Dual-band EBG sectoral antenna using a single-layer FSS for UMTS application," *IEEE Antenna and Wireless Propagation Letter*, Vol. 6, 368–371, 2007.
7. Fan, Y. and Y. Rahmat-Samii, *Electromagnetic Band Gap Structure in Antenna Engineering*, USA Cambridge University Press, New York, 2009.

A New Feed for Reflector Based 100 Ω Impulse Radiating Antenna

Dhiraj K. Singh[1], **D. C. Pande**[1], **and A. Bhattacharya**[2]

[1]Electronics & Radar Development Establishment, Bangalore, India
[2]Indian institute of Technology, Kharagpur, West Bengal, India

Abstract— Improvement in the feeding structure of the reflector based impulse-radiating antenna (IRA) is attempted to reduce the input impedance of the conventional 200 Ω-conical plate-fed IRA. A novel feeding structure known as asymptotic conical dipole (ACD) was designed to get 100 Ω input impedance for reflector IRA. ACD-fed IRA has been analyzed using the Finite Difference Time Domain (FDTD) method and the result obtained shows better gain than a conventional conical taper-fed IRA. Moreover, a half ACD-fed IRA can give an input impedance of nearly 50 Ω which can be readily used with most of the single ended instrumentation without using a 50–200 Ω BALUN as commonly done with IRA.

1. INTRODUCTION

Impulse Radiating antennas are gaining lots of attention for ultra wide band Radar Applications due to their large instantaneous bandwidth and pulse fidelity. The spherical wave that propagates through the transmission line feed is converted to the plane wave by the parabolic reflector. One of the commonly used IRA consists of a parabolic reflector fed by a conical transverse electromagnetic (TEM) transmission line. The popularly known Impulse Radiating Antennas had [1–6] been designed for 200 Ω input impedance wherein the conical plate transmission line feed used is of 400 Ω as shown in Fig. 1.

Typically in an IRA two 400 Ω conical plate lines are connected in parallel at the feed point to get 200 Ω input impedance. The reason for choosing a 400 Ω line is to get a smaller cone angle for the transmission line thereby reducing the aperture blockage and, in turn, a better antenna gain. Most of the pulse generators have an unbalanced coaxial output with a 50 Ω source resistance. To Connect 50 Ω voltage source to the 200 Ω input of IRA, a 50 Ω to 200 Ω Balun is used. The commonly used Balun [10] for IRA consists of two 100 Ω coaxial cable connected in parallel at source end and in series at IRA feed end as shown in Fig. 2. The 100 Ω cables like RG-213 and its equivalents are not commonly available, hence it limits the wide use of the IRA for different applications.

This paper describes a novel design of feed transmission line of 200 Ω to get a 100 Ω IRA without sacrificing the gain of the 200 Ω Antenna. In Section 2 of the paper, the design formulas for this novel feed are presented. The time domain analysis of IRA with novel feed arm and comparison with conventional conical arm is discussed in Section 3. Discussion on the simulation results and Conclusion is presented in Section 4 and Section 5 respectively.

2. FEEDING DIPOLE DESIGN

Two Asymptotic conical dipoles of 200 Ω impedance have been designed and connected in parallel at the feed point to get a 100 Ω IRA. Equivalent charge method [9] has been used to generate the

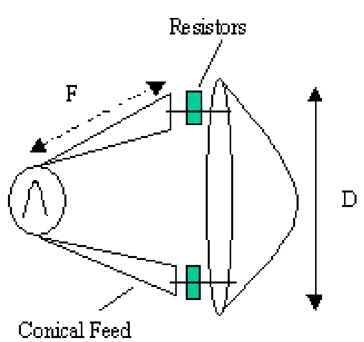

Figure 1: Schematic of conventional IRA.

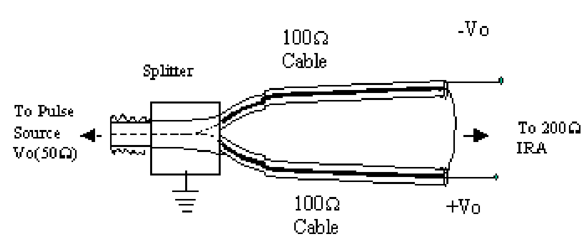

Figure 2: Schematic of 50–200 Ω Balun.

profile of the feeding dipole. In Equivalent Charge Method a hypothetical static charge distribution is defined with the total charge being set equal to zero. This distribution is usually taken to be rotationally symmetric about a particular axis (z-axis) with opposite charge reflected about the apex on the symmetry plane (x-y plane). Two equipotential surfaces of equal and opposite potentials are thus generated, which define two separate closed volumes. Both of these surfaces can be realized by perfect conductors with appropriate total surface charge such that the potential distribution external to the surface remains unchanged.

Let the equivalent line charge $\lambda(z)$ on the z-axis is given by

$$\lambda(z) = \begin{cases} \lambda_0 & \text{for} \quad 0 < \ z \leq z_0 \\ -\lambda_0 & \text{for} \quad 0 > z \geq -z_0 \\ 0 & \text{for} \quad z = 0 \text{ and } |z| > z_0 \end{cases}$$

Potential distribution due to this equivalent charge distribution, at any point $P(r, \varphi, z)$ in cylindrical coordinate is

$$\phi = \frac{\lambda_0}{4\pi\varepsilon_0} \ln \left\{ \frac{\left[z + \sqrt{z^2 + r^2}\right]}{\left[z + z_o + \sqrt{(z + z_o)^2 + r^2}\right] \left[z - z_o + \sqrt{(z - z_o)^2 + r^2}\right]} \right\} \tag{1}$$

Now, two equipotential biconical Surface is defined as shown in Fig. 4. so that surface potential function for an infinite biconical structure is given by

$$\varphi = \frac{1}{4\pi\varepsilon_0} \left(\int_0^{\infty} \frac{\lambda(z')dz'}{\left[(z - z')^2 + \psi^2\right]^{1/2}} + \int_{-\infty}^{0} \frac{\lambda(z')dz'}{\left[(z - z')^2 + \psi^2\right]^{1/2}} \right) \tag{2}$$

After simplification the surface potential at any one surface can be written as,

$$\phi_S = \frac{\lambda_0}{2\pi\varepsilon_0} \ln \left[\cot\left(\frac{\theta_0}{2}\right) \right] \tag{3}$$

where,

$$\Theta_0 \ = \ \tan\left(\frac{\theta_0}{2}\right) \tag{4}$$

Equating Eqs. (1) & (2) the contour of the equipotential surface (shown in Fig. 4. which is asymptotic to the bicone at the origin) can be defined as,

$$\Theta_o^{-2} = \frac{\left[z + \sqrt{z^2 + r^2}\right]^2}{\left[z + z_o + \sqrt{(z + z_o)^2 + r^2}\right] \left[z - z_o + \sqrt{(z - z_o)^2 + r^2}\right]} \tag{5}$$

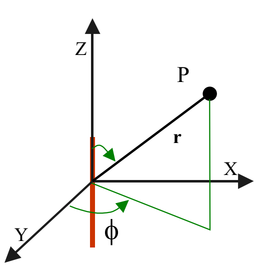

Figure 3: Charge distribution.

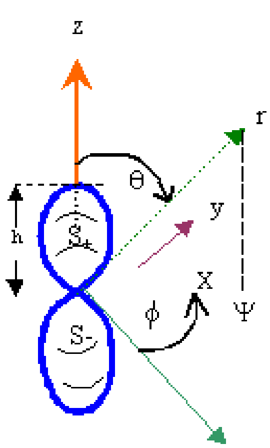

Figure 4: Feed arm geometry.

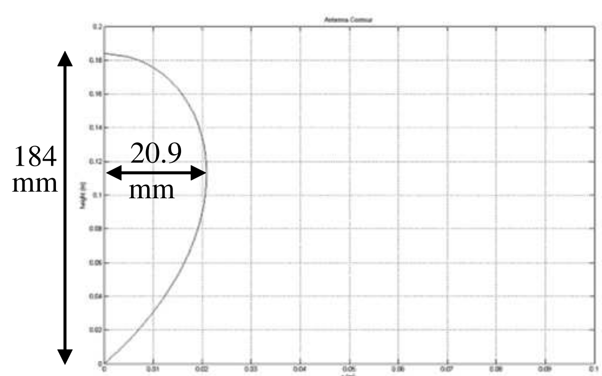

Figure 5: Half Contour of ACD.

So, Θ_0 is a constant determined by desired asymptotic impedance given by any infinite biconical surface [9]. For each value of z between zero and the antenna height h, there exists a unique value for the element radius r. Eq. (5) was solved numerically using Newton-Raphson method to get the contour of asymptotic element as shown in Fig. 5. The mirror image of this profile together with the original gives the complete ACD surface.

3. ANTENNA DESIGN AND ANALYSIS

A Reflector based IRA was designed using 46 cm diameter parabolic reflector with focal length 18.4 cm as shown in Fig. 6. The feed arm for the IRA was designed using the contour obtained in Fig. 5. These two 200 Ω asymptotic conical dipole connected in parallel at the input of the IRA gives 100 Ω input impedance for the new IRA. Feed arms are placed at ±30 degree from the vertical axis. For the conventional conical feed, approximately 40° flare angle is necessary to achieve an impedance of 100 Ω. This results in the maximum width of arms to be 134 mm whereas the maximum width of the ACD-fed arm is 41.8 mm occurring at a height of 11.2 mm (Fig. 7). Thus for the same value of impedance, the aperture blockage is higher for the conventional fed arm as compared to that of an ACD-fed arm. Moreover, conical arms become bulky for a smaller diameter paraboloid and puts extra weight on the antenna. Various parameters for antenna design are listed in Table 1. Solid model of new IRA with support structure is shown in Fig. 8.

ACD-fed IRA has been analyzed in time domain using finite difference time domain solver XFDTD (v7.1). The excitation signal used for simulation of the antenna was Gaussian pulse waveform of pulse width of 100 ps. Fig. 9 shows antenna gain at bore sight versus frequency. It shows comparable gain for the new 100 Ω IRA as obtained by the conventional 200 Ω IRA. The new IRA response is flatter at higher frequencies and the peak gain of 28 dB is achieved at the highest frequency of the simulation.

The real and imaginary parts of input impedance against frequency is plotted in Fig. 10. The input impedance profile variation is acceptable for the frequency range. The return loss of the designed antenna is under −10 dB for a range of frequency from 500 MHz to 15 GHz as shown in Fig. 11.

The excitation pulse used for the time domain analysis shown in Fig. 12. is Gaussian in nature. The time domain characteristics of the farzone radiated field observed at bore sight of the antenna is shown in Fig. 13. The radiated far field consists [2, 3] of prepulse of duration in orders of 2 F/c, a main impulse, which is time derivative of the input excitation pulse and post pulse mainly due to edge diffraction. The fractional bandwidth of the newly designed ACD IRA is 187% and is

Table 1: IRA parameters.

Parameter	Value
Diameter	460 mm
Focal length (F)	184 mm
$f_a = F/d$	0.4
Input Impedance (Z_{in})	100 Ω
Length of feed arm	184 mm

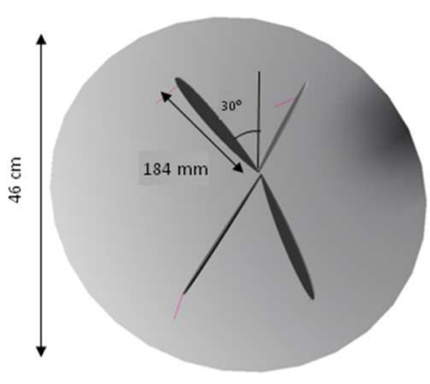

Figure 6: The ACD feed antenna.

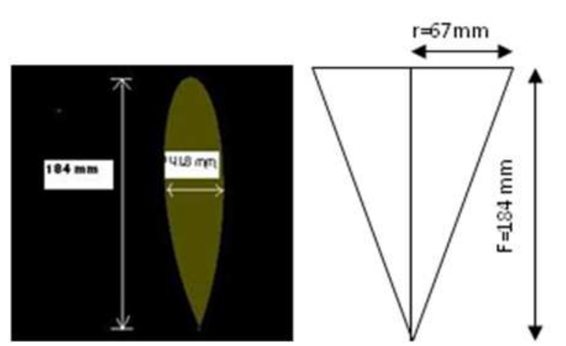

(a) ACD Feed arm (b) Conventional Feed arm

Figure 7: Comparison of the antenna arms.

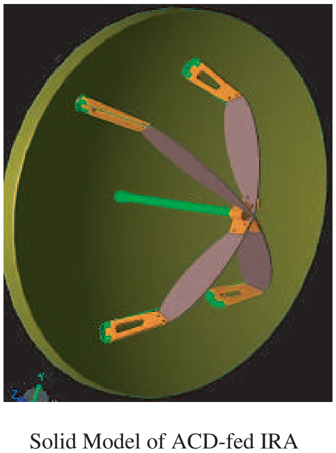

Figure 8: Solid model of ACD-fed IRA.

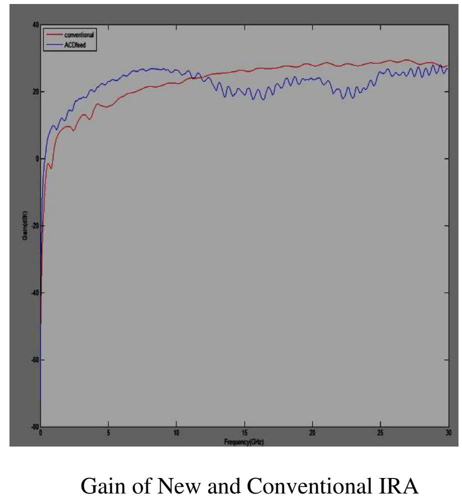

Figure 9: Gain of new and conventional IRA.

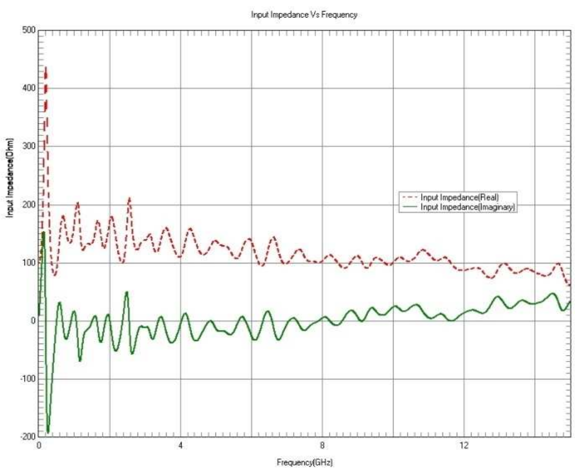

Figure 10: Input impedance (Ω) vs frequency (GHz).

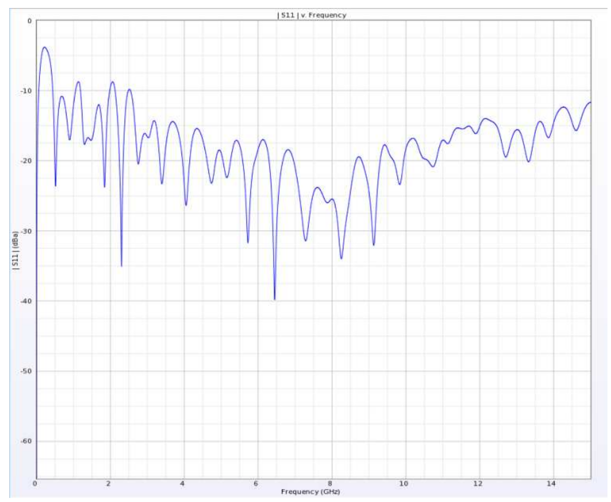

Figure 11: Return loss (dB) vs frequency (GHz).

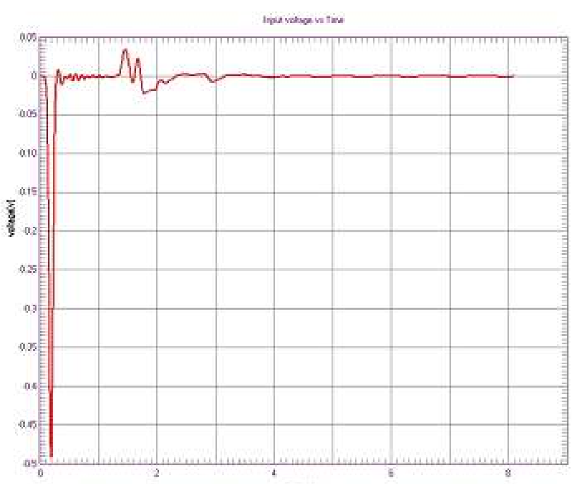

Figure 12: Excitation gaussian pulse (V) versus time (ns).

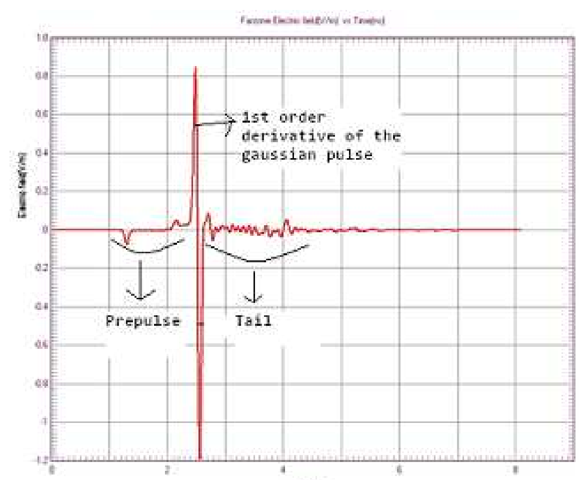

Figure 13: Farzone electric field (V/m) versus time (ns).

calculated using

$$\frac{2\left(f_h - f_l\right)}{f_h + f_l} \times 100 \tag{6}$$

where f_h & f_l are higher and lower cutoff frequency respectively.

4. DISCUSSION

The premise behind choosing 400 Ω Conical TEM line in the conventional IRA was to have smaller cone angle leading to small form factor and hence minimum aperture blockage. ACD has been used in this work as feed, which allows achieving smaller impedance value with smaller cone angle and smaller form factor. IRA with ACD-fed allows us to reduce the impedance to 100 Ω without either any reduction in gain or any increment in the aperture blockage. The Gain of an ACD-fed IRA is higher than conical feed IRA when compared higher when compared at corresponding frequencies. The requirement of 50–200 Ω Balun in the conventional IRA restricts its wide application because of non-availability of 100 Ω cables readily. This novel design can be used with differential source, also the half ACD-fed IRA can be readily used with single ended 50 Ω pulse generators and other measurement instrumentations.

5. CONCLUSION

The novel scheme of ACD-fed IRA is shown to give comparable or better performance than conical-fed IRA in terms of gain, Impedance and time domain response. The proposed feed eliminates the need of baluns and can be directly connected to either single ended or differential sources.

REFERENCES

1. DuHamel, R. H., et al., "Frequency independent conical feeds for lens and reflectors," *Proc. IEEE Int. Antennas Propagation Symp. Dig.*, Vol. 6, 414–418, Sep. 1968.
2. Baum, C. E., "Radiation of impulse-like transient fields," Sensor and Simulation Note#321, Nov. 25, 1989.
3. Baum, C. E. and E. G. Farr, "Impulse radiating antennas," *Ultra-wideband Short Pulse Electromagnetics*, 139–147, H. L. Bertoni, et al., Eds., Plenum Press, NY, 1993.
4. Baum, C. E., "Configuration of TEM feed for IRA," Sensor and Simulation Note 327, Apr. 27, 1991.
5. Farr, E., "Optimizing the feed impedance of impulse radiating antenna, Part I: Reflector IRA," Sensor and Simulation Notes 354, Jan. 1993.
6. Farr, E., "Development of a reflector IRA and a solid dielectric lens IRA," Sensor and Simulation Note 396, Apr. 1996.
7. Manteghi, M. and Y. Rahamat-Sammii, "A novel Vivaldi fed reflector impulse radiating antenna (IRA)," *Proc. IEEE Int. Symp. Antennas and Propagation*, 549–552, Washington, DC, Jul. 3–8, 2005.
8. Manteghi, M. and Y. Rahamat-Sammii, "On the characterization of a reflector impulse radiating antenna (IRA): Full-wave analysis and measurement results," *IEEE Trans. Antennas and Propagation*, Vol. 54, No. 3, 812–822, Mar. 2006.
9. Baum, C. E., et al., "Sensors for electromagnetic pulse measurements both inside and away from nuclear source regions," *IEEE Tran. Antennas and Propagation*, Vol. 26, 22–35, Jan. 1978.
10. Bowen, L. H., et al., " A high voltage Cable feed impulse radiating antenna," *Ultrawideband Short Pulse Electromagnetics*, Vol. 8, 9–16, Baum, et al., Eds., Springer, 2007.
11. Giri, D. V., "Peak power gain in time domain of impulse radiating antenna (IRAs)," Sensor and Simulation Notes 546, Oct. 2009.
12. Singh, D. K. and D. C. Pande, "Time domain characterization of asymptotic conical monopole," *Ultrawideband Short Pulse Electromagnetics*, Vol. 9, 113–120, F. Sabath, et al., Springer, 2010.

A Dielectric Loaded HMSIW *H*-plane Horn Antenna

S. A. Razavi and M. H. Neshati
Department of Electrical Engineering, Ferdowsi University of Mashhad, Iran

Abstract— A half mode substrate integrated waveguide (HMSIW) H-plane horn antenna with a dielectric load is proposed in this paper. A coaxial line is used as the feed in order to avoid parasitic radiation and high conductor loss. The proposed antenna is simulated with HFSS software and its radiation properties are investigated. Results illustrate that the proposed antenna has marrow beamwidth in both E-plane and H-plane. A 1×4 array of the dielectric loaded antenna is also designed in order to investigate the usefulness of the presented antenna in an array. The antenna is designed for around 28 GHz and all the simulations are done with HFSS software.

1. INTRODUCTION

Recently the substrate integrated waveguide (SIW) technology has been widely used in the implementation of microwave devices and antennas [1–9]. Horn antenna is one of the antennas implemented by this technology. Based on the authors' knowledge, there are few works on SIW horn antennas and no work is done on half mode substrate integrated waveguide (HSIW) horn antennas. In [10] an integrated H-plane horn antenna is proposed. In [11] a dielectric load is added to SIW H-plane horn antenna in order to have narrow beamwidths in both E-plane and H-plane. In [12] a broadside horn antenna is implemented by SIW technology.

When only the mode TE_{10} is propagating in SIW waveguide, the maximum value of E-field is located at the vertical center plane along the propagating direction and the center plane can be considered as an equivalent magnetic wall. As a result, the HMSIW can be simply achieved by dividing the SIW into two equal parts. But in horn antennas, in addition to TE_{10} mode the higher order modes are slightly exist (the effect of higher order modes is more intensive if the length of the horn is chosen improperly) so the above approximation (consideration of center plane as an equivalent magnetic wall) is not yet valid and the antenna's performance will be considerably degraded if it is divided into two parts from the center line.

In this paper, a new HMSIW horn antenna is introduced in which, field distribution is approximately half of the corresponding one in SIW horn antenna. The proposed antenna is fed by a coaxial feed line unlike the previous works on HMSIW components witch are fed by micr ostrip line. But, this kind of feeding suffers from parasitic radiation (witch may degrade the radiation pattern of the horn antenna in E-plane) and high conductor loss in high frequencies, and so a coaxial line is used as the feed in order to avoid these imperfections. A dielectric load is also added to the proposed antenna in order to have narrower beam width in both E-plane and H-plane. The proposed antenna is simulated with HFSS software and its radiation properties are investigated. Simulation results confirm that the proposed antenna has marrow beam width in both E-plane and H-plane. A 1×4 array of the dielectric loaded antenna is also designed and simulated in order to investigate the usefulness of the presented antenna in an array. The antenna is designed for about 28 GHz and all the simulations are done with HFSS software.

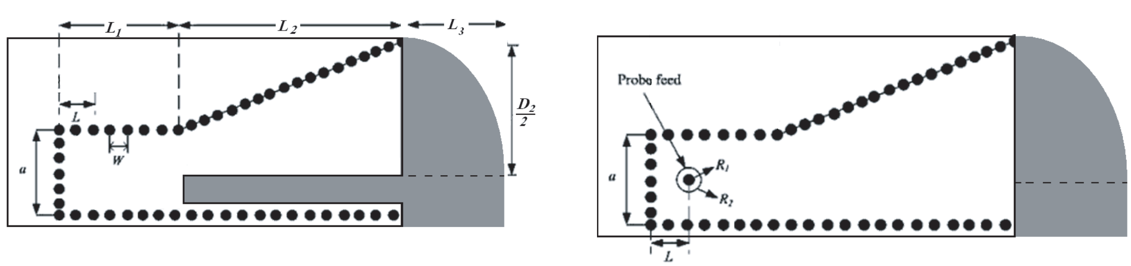

(a) (b)

Figure 1: Geometry of dielectric loaded HMSIW horn antenna. (a) Front view. (b) Back view. $W = 1$ mm, $L = 1.8$ mm, $a = 5$ mm, $D_2 = 14$ mm, $L_1 = 7$ mm, $L_2 = 10$ mm, $L_3 = 9.5$ mm, $R_1 = 0.216$ mm, $R_2 = 0.5$ mm, $h = 1$ mm.

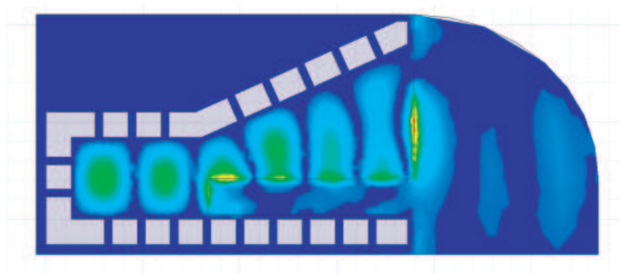

Figure 2: Field distribution in the proposed dielectric loaded HMSIW horn antenna.

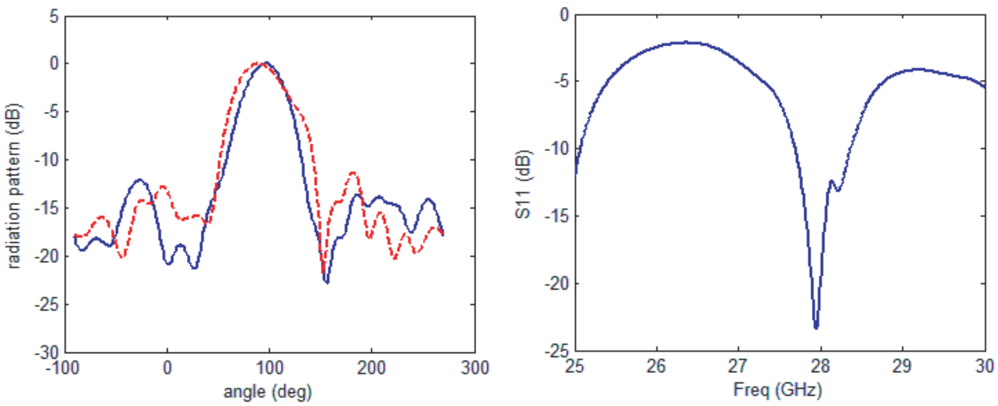

(a) (b)

Figure 3: Radiation properties of the proposed dielectric loaded HMSIW horn antenna. (a) Normalized radiation pattern in E-plane and H-plane. (b) Return loss.

2. ANTENNA CONFIGURATION

The geometry of proposed antenna is illustrated in Fig. 1. In this scheme the half dielectric loaded sectoral horn is integrated to a rectangular waveguide by a single substrate using SIW technology and fed by a $50\,\Omega$ coaxial line. The width a, the thickness b, working frequency f and dielectric constant ε_r are chosen so that only TE_{10} mode propagates in the waveguide. The spacing between the centers of two neighbor vias W and the radius of each via R should satisfy the design rules of SIW proposed in [9] and [13]. Based on the above considerations, the parameters a, b, W, R, f and ε_r are chosen 5 mm, 2.5 mm, 1 mm, 0.4 mm, 28 GHz and 4.8 respectively. In the simulation process, the rectangular vias are used. The spacing between two neighbor rectangular vias is chosen 0.4 mm (which is determined by W and R values: W-2R). The aperture length $D_2/2$ is also 7 mm. The length L_2 affects both the quadratic phase error on the aperture and the higher order mode excitation in the horn [11]. The length of 10 mm is determined for L_2 to get the acceptable quadratic phase error and single mode on the aperture. The dielectric load contains a rectangular load and a quarter of elliptic load. The length of the dielectric slab L_3 is directly proportional to the antenna gain however it should be properly chosen since the improper choice for L_3 may result in beam width increment in H-plane. Based in this consideration, the length of 9.5 mm is determined for the dielectric load. The parameter h, the height of the probe feed, affects the insertion loss at the working frequency. By the full wave optimization, the value of 1 mm is determined to obtain minimum insertion loss at 28 GHz. The SIW horn shown in Fig. 1 is simulated and its results are presented in next part.

3. SIMULATION RESULTS

3.1. Single Antenna

The proposed antenna is simulated and its performance is investigated. In Fig. 2 the field distribution of the proposed antenna is depicted. It can be observed that the proposed antenna is a half mode SIW horn antenna in witch the field distribution is approximately half of that in the SIW horn antenna. Return loss and radiation patterns of the antenna are shown in Fig. 3. Results

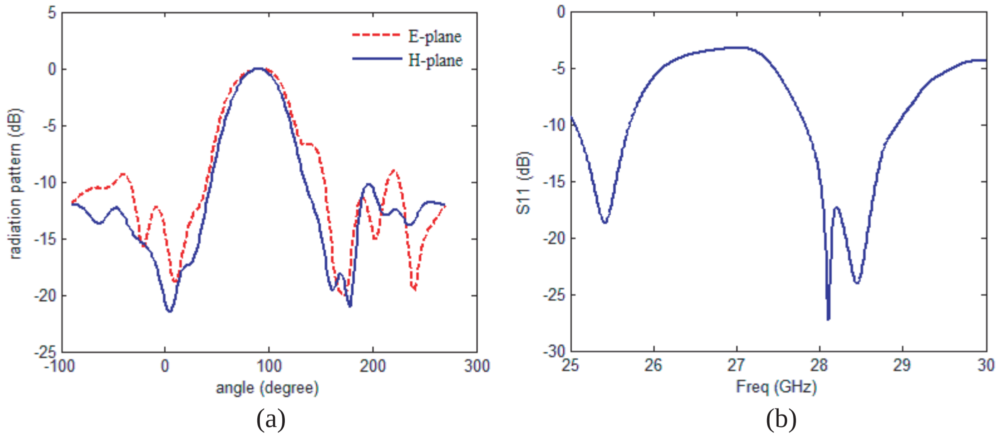

Figure 4: Radiation properties of the small aperture dielectric loaded HMSIW horn antenna. (a) Normalized radiation pattern in E-plane and H-plane. (b) Return loss.

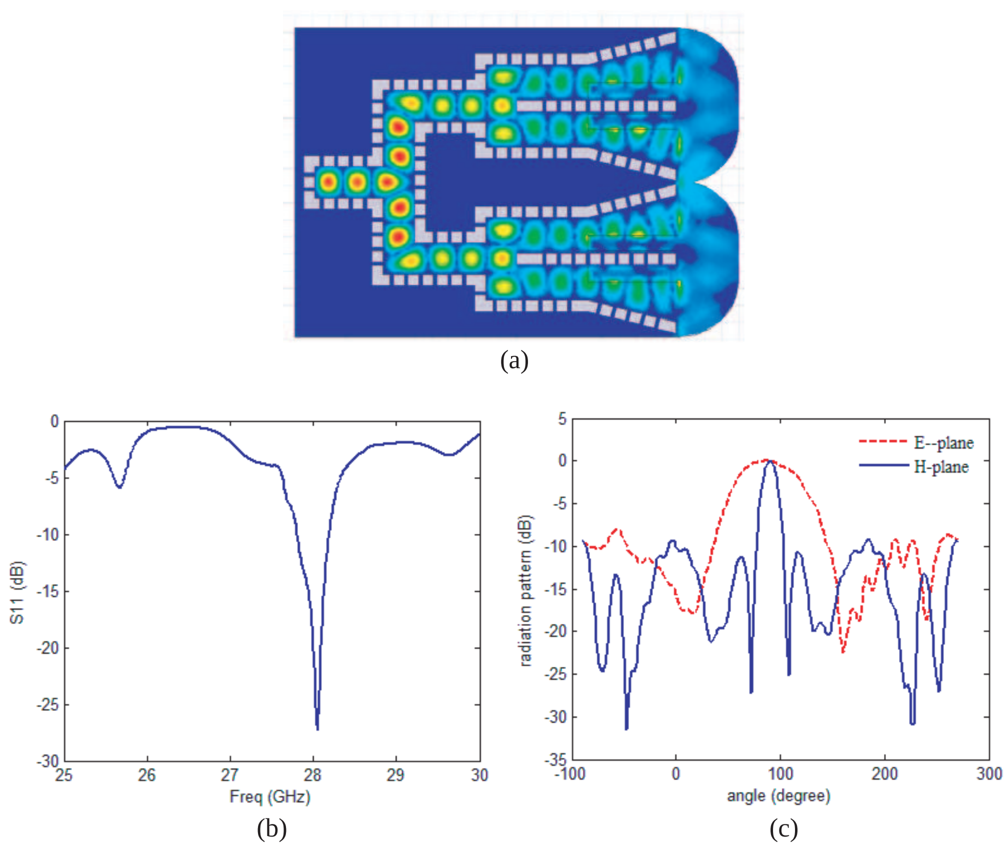

Figure 5: Simulation results of the designed array. (a) Configuration of array and its field distribution. (b) Return loss. (c) Normalized radiation pattern in E-plane and H-plane.

illustrate that the performance of the proposed antenna is similar to those of a dielectric loaded SIW horn antenna, while it has a different configuration with reduction in size.

3.2. Antenna Array

In order to construct the H-plane array of the proposed antenna, the aperture of each element in H-plane should be within one wavelength. So, to use the proposed antenna in an array, the size of its aperture $D_2/2$ is reduced to 5 mm which is smaller than one wavelength. The length of the dielectric slab L_3 is also chosen as 7 mm for the shortened aperture antenna. This small aperture is simulated and its simulation results are plotted in Fig. 4. Comparison of Fig. 4(b) with Fig. 3(b) shows that the impedance bandwidth is increased for the small aperture antenna. A 1×4 array of the proposed antenna is designed and simulated. The configuration of the designed array and its simulation results are depicted in Fig. 5.

4. CONCLUSIONS

In this paper a dielectric loaded coaxial fed HMSIW H-plane horn antenna is presented. Through proper choosing of the geometrical parameters, the performance similar to a dielectric loaded SIW horn antenna could be obtained while the proposed antenna introduces a different configuration with reduction in size. In addition, the structure of the proposed antenna is very suitable in an array.

REFERENCES

1. Luo, G. Q., Z. F. Hu, L. Y. Yu, and L. L. Sun, "Development of low profile cavity backed crossed slot antennas for planar integration," *IEEE Trans. Antennas Propag.*, Vol. 57, No. 10, 2972–2979, 2009.
2. Cheng, Y. J., W. Hong, and K. Wu, "Design of a monopulse antenna using a dual v-type linearly tapered slot antenna (DVLSA)," *IEEE Trans. Antennas Propag.*, Vol. 56, No. 9, 2903–2909, 2010.
3. Cheng, Y. J., W. Hong, and K. Wu, "Millimeter-wave half mode substrate integrated waveguide frequency scanning antenna with quadri-polarization," *IEEE Trans. Antennas Propag.*, Vol. 58, No. 6, 1848–1855, 2010.
4. Dong, Y. D. and T. Itoh, "Composite right/left-handed substrate integrated waveguide leaky-wave antennas," *Proceeding of European Microwave Conference*, 276–279, Rome, Italy, September 2009,
5. Liu, B., W. Hong, Y. Q. Wang, Q. H. Lai, and K. Wu, "Half mode substrate integrated waveguide (HMSIW) 3-dB coupler," *IEEE Microw. Wireless Compon. Lett.*, Vol. 17, No. 1, 22–24, 2007.
6. Cheng, Y., W. Hong and K. Wu, "Half mode substrate integrated waveguide (HMSIW) directional filter," *IEEE Microw. Wireless Compon. Lett.*, Vol. 17, No. 7, 504–506, 2007.
7. Wang, Y., W. Hong, Y. Dong, B. Liu, H. J. Tang, J. chen, X. Yin, and K. Wu, "Half mode substrate integrated waveguide (HMSIW) band pass filter," *IEEE Microw. Wireless Compon. Lett.*, Vol. 17, No. 4, 265–267, 2007.
8. Liu, B., W. Hong, Z. Kuai. X. Yin, G. Luo, J. Chen, H. Tang, and K. Wu, "Substrate integrated waveguide (SIW) monopoulse slot antenna array," *IEEE Trans. Antennas Propag.*, Vol. 57, No. 1, 275–279, 2009.
9. Yan, L., W. Hong, G. Hua, J. Chen, K. Wu, and T. J. Cui, "Simulation and experiment on SIW slot array antennas," *IEEE Microw. Wireless Compon. Lett.*, Vol. 14, No. 9, 446–448, 2004.
10. Li, Z. L. and K.Wu, "A new approach to integrated horn antennas," *Proceedings of International of Symposium on Antenna Technology and Applied Electromagnetics*, 535–538, July 2004.
11. Wang, H., D. Fang, B. Zhang, and W. Che, "Dielectric loaded substrate integrated waveguide (SIW) H-plane horn antennas," *IEEE Trans. Antennas Propag.*, Vol. 58, No. 3, 640–647, 2010.
12. Wong, M., A. R. Sebak and T. A. Denidni, "A broadside substrate integrated horn antenna," *Proceedings of International Symposium, AP-S,* 2008.
13. Deslandes, D. and K. Wu, "Accurate modeling, wave mechanisms, and design considerations of substrate integrated waveguide," *IEEE Trans. Microw. Theory Tech.*, Vol. 54, No. 6, 2516–2526, 2006.

On the Radiation Fields of the Hyperbolic Helical Antenna

S. Adeniyi Adekola[1, 2], **A. Ike Mowete**[1], **and A. Ayotunde Ayorinde**[1]

[1]Department of Electrical and Electronics Engineering
Faculty of Engineering, University of Lagos, Lagos, Nigeria
[2]Department of Electrical and Electronics Engineering
Niger Delta University, Wilberforce Island, Yenegoa, Nigeria

Abstract— Cylindrical helical antenna structures of various cross-sections have received extensive analytical attention in the open literature, starting with the 1947 contributions of Kraus [2], through those of Wong and Loh [4], to Adekola et al. [3, 6], to mention a few. One geometry that has yet, to the best of our knowledge, to be treated is that of the helix, wound on a hyperbolic cylinder, which is the focus of this presentation. Utilizing the circuit-geometric approach offered by the method of moments, the paper models the hyperbolic helical antenna as a configuration of two thin-wire elements, one or both of which may be excited. Analysis followed that described elsewhere [3], and the computational results obtained for the configuration in which only one of the two elements has a delta-gap excitation suggest that the hyperbolic helical antenna of this type should be particularly suitable for applications requiring multi-lobed radiation patterns.

1. INTRODUCTION

Ever since the discovery of the circular-cylindrical helical antenna by Kraus [2], cylindrical helical antennas of other cross-sections have continued to receive attention from the global research community. Notable contributions include those of Jones [5], who experimentally investigated the performance characteristics of the rectangular helix, Knudsen [1], who provided a rigorous analysis of the square helix, and Wong and Loh [4] with focus on the rigorous analysis of the elliptical helix problem; and more recently, the specialized method of moments solution given by Adekola et al. [3, 6]. A careful search of the literature suggests that the electromagnetic fields radiated by the interesting configuration of the helix wound on a hyperbolic cylinder(consisting of two distinct arms; one being a mirror reflection of the other), has yet to receive either analytical or experimental investigative attention.

This paper examines the hyperbolic helix problem, and models it in terms of a two-element configuration, in which either element or both elements may be excited; though in the analysis presented, one element is excited at its geometrical centre while the other element is considered a parasitic. The antenna is modelled as an electrically thin radiator and the versatile method of moments is employed for the determination of the current distributions along the helical arms, as well as the associated far-zone fields. Current profiles on both helical elements as well as the radiated electromagnetic fields are computed and graphically illustrated. And the preliminary numerical results presented here indicate that the antenna could be useful for multi-lobed radiation applications.

2. THEORY

From Fig. 1, which depicts the cross section of a full hyperbolic helix, the geometry may be parametrically described by the following equations:

$$x = \pm a \cosh t \tag{1a}$$

and

$$y = b \sinh t \tag{1b}$$

where a and b represent the semi-axes, and the plus/minus sign indicates that the full hyperbola has two branches, which are open-ended.

Clearly, the element of arc length along the hyperbola symbolized here by, ds admits representation in the form

$$ds = \sqrt{dx^2 + dy^2} = b\sqrt{1 + \kappa^2 \sinh^2 t}\, dt \tag{2}$$

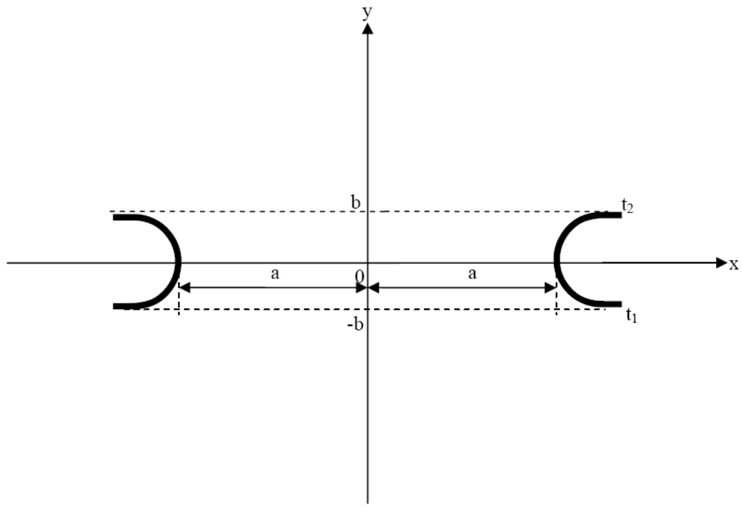

Figure 1: Cross section of the hyperbolic helix located on the x-y plane.

provided that $\kappa = 1+\frac{a^2}{b^2}$. When use is made of the fact that $dz = ds\tan\alpha = b\tan\alpha\sqrt{1+\kappa^2\sinh^2 t}dt$, we find that

$$z = b\tan\alpha\int_{t_1}^{t_2}\sqrt{1+\kappa^2\sinh^2 t}dt = b\tan\alpha\,\Omega(\kappa,t) \tag{3a}$$

where

$$\Omega(\kappa,t) = \int_{t_1}^{t_2}\sqrt{1+\kappa^2\sinh^2 t}dt \tag{3b}$$

whilst arc length (denoted by ℓ) along the helical wire takes the representation

$$\ell = b\sec\alpha\,\Omega(\kappa,t) \tag{4}$$

It is then easy to see that

$$\begin{aligned} x &= \pm a\cosh t \\ y &= b\sinh t \qquad t_1 \le t \le t_2 \\ z &= b\tan\alpha\,\Omega(\kappa,t) \end{aligned} \tag{5}$$

which expressions enable us to write the position vector from the origin of the coordinate system origin to any feed point on the hyperbolic helix as:

$$\bar{r}' = \pm a\cosh t\ \hat{a}_x + b\sinh t\ \hat{a}_y + b\tan\alpha\,\Omega(\kappa,t)\ \hat{a}_z \tag{6}$$

For the thin-wire, vector magnetic potential for the hyperbolic helix is given by

$$\bar{A} = \frac{\mu_o}{4\pi}\int_{t_1}^{t_2}\hat{a}_t' I(t)\frac{e^{-jk_oR}}{R}dt \tag{7}$$

in which

$$\hat{a}_t' = \frac{\pm a\sinh t\ \hat{a}_x + b\cosh t\ \hat{a}_y + b\tan\alpha\,\Omega'(\kappa,t)\ \hat{a}_z}{\sqrt{a^2\sinh^2 t + b^2\cosh^2 t + b^2\tan^2\alpha\,[\Omega'(\kappa,t)]^2}} \tag{8}$$

In the far-field where

$$R = r - \bar{r}'\cdot\hat{a}_r \tag{9}$$

with $\hat{a}_r = \cos\varphi \sin\theta\, \hat{a}_x + \sin\varphi \sin\theta\, \hat{a}_y + \cos\theta\, \hat{a}_z$ and $\bar{r}'$ is as defined by Equation (6), we find that

$$R = r - [\pm a \cosh t \cos\varphi \sin\theta + b \sinh t\ \sin\varphi \sin\theta + b \tan\alpha \cos\theta\, \Omega(\kappa, t)] \tag{10}$$

Hence:

$$\begin{aligned}\bar{A} \ &= \ \frac{\mu_o e^{-jk_o r}}{4\pi\, r} \int\limits_{t_1}^{t_2} \left[\frac{\pm a \sinh t\ \hat{a}_x + b \cosh t\ \hat{a}_y + b \tan\alpha\, \Omega'(\kappa, t)\ \hat{a}_z}{\sqrt{a^2 \sinh^2 t + b^2 \cosh^2 t + b^2 \tan^2 \alpha\, [\Omega'(\kappa, t)]^2}} \right] I(t) \\ &\quad \times \exp\left[jk_o(\pm a \cosh t \cos\varphi \sin\theta + b \sinh t \sin\varphi \sin\theta + b \tan\alpha\ \cos\theta\, \Omega(\kappa, t)) \right]\end{aligned} \tag{11}$$

It then follows that

$$\begin{aligned}E_\theta \ &= \ \frac{j\omega\mu_o e^{-jk_o r}}{4\pi\, r} \int\limits_{t_1}^{t_2} \left[\frac{\pm a \sinh t\ \cos\theta \cos\phi + b \cosh t \cos\theta \sin\phi - b \tan\alpha \sin\theta\, \Omega'(\kappa, t)\ \hat{a}_z}{\sqrt{a^2 \sinh^2 t + b^2 \cosh^2 t + b^2 \tan^2 \alpha\, [\Omega'(\kappa, t)]^2}} \right] I(t) \\ &\quad \times \exp\left[jk_o(\pm a \cosh t \cos\phi \sin\theta + b \sinh t \sin\phi \sin\theta + b \tan\alpha\ \cos\theta\, \Omega(\kappa, t)) \right]\end{aligned} \tag{12a}$$

and

$$\begin{aligned}E_\phi \ &= \ \frac{-j\omega\mu_o e^{-jk_o r}}{4\pi\, r} \int\limits_{t_1}^{t_2} \left[\frac{\pm a \sinh t \sin\phi + b \cosh t \cos\phi}{\sqrt{a^2 \sinh^2 t + b^2 \cosh^2 t + b^2 \tan^2 \alpha\, [\Omega'(\kappa, t)]^2}} \right] I(t) \\ &\quad \times \exp\left[jk_o(\pm a \cosh t \cos\phi \sin\theta + b \sinh t \sin\phi \sin\theta + b \tan\alpha\ \cos\theta\, \Omega(\kappa, t)) \right]\end{aligned} \tag{12b}$$

An approximate solution for the unknown current distribution in these expressions is provided by the method of moments as described by Adekola et al. (2011), through the matrix equation

$$\begin{bmatrix} [V_m^i] \\ [V_m^j] \end{bmatrix} = \begin{bmatrix} [Z_{mn}^{ii}] & [Z_{mn}^{ij}] \\ [Z_{mn}^{ji}] & [Z_{mn}^{jj}] \end{bmatrix} \begin{bmatrix} [I_n^i] \\ [I_n^j] \end{bmatrix} \tag{13}$$

3. COMPUTATIONAL RESULTS AND DISCUSSIONS

Numerical results were generated for the particular case in which the helical arm on the left is excited at its geometrical centre by a 1 V delta-gap generator, while the right-arm helix is treated as parasitic. The operating frequency is fixed at 3 GHz, and ratio b/a ranges from 1/4 to 1.

The current distributions obtained for both the excited and parasitic hyperbolic helical arms are displayed in Figs. 2(a) and 2(b), respectively. It is observed that the peaks of the current curves occur at the geometrical centre of the excited helical arm except when a equals b which corresponds to the rectangular hyperbola helix.

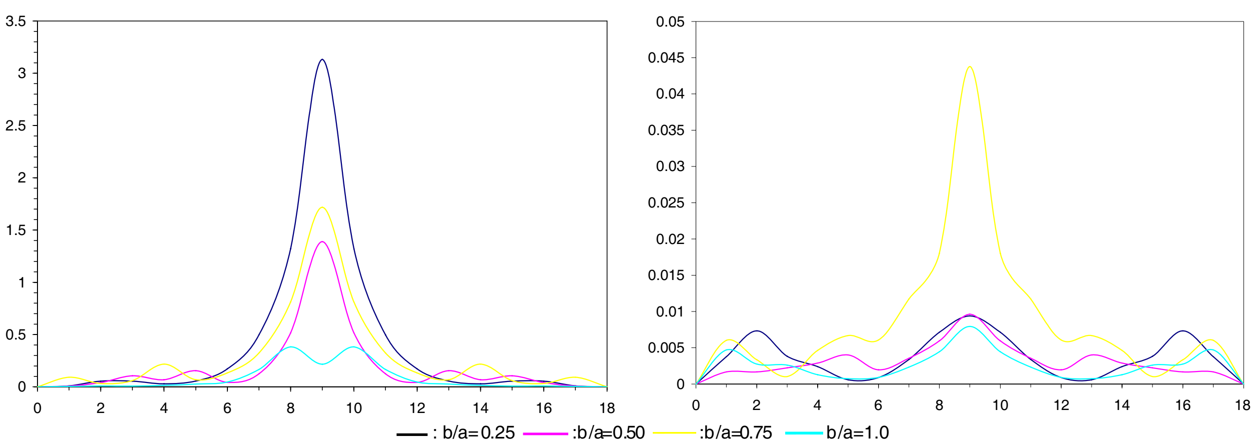

(a) (b)

Figure 2: (a) Current distributions on the excited hyperbolic helical arm. (b) Current distributions on the parasitic hyperbolic helical arm.

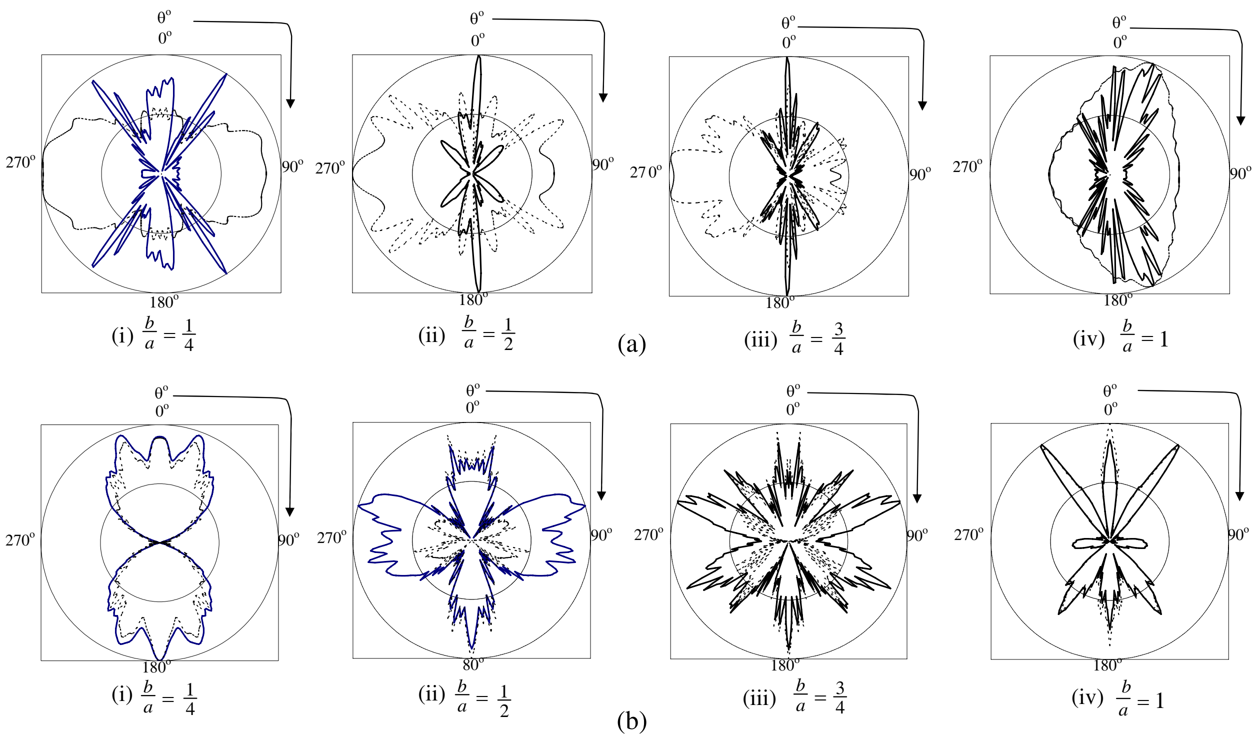

Figure 3: (a) The electric field components on the $\varphi = 0°$ plane: - - -: E_φ — E_θ when b/a varies from 0.25 to 1.0. (b) The electric field components on the $\theta = 90°$ plane: - - -: E_φ —: E_θ when b/a varies from 0.25 to 1.0.

However, the maxima of the current profiles are noticed at the centre of the parasitic hyperbolic helix for all the ratios b/a considered. For the case $b/a = 1/4$, the current distribution decays smoothly in exponential form to zero towards the open ends of the excited helical arm, while for the other ratios b/a, the current undulates along the arm and die out at the arm ends. Conversely, the currents on the parasitic helical arm undulate for all the ratios of b/a investigated. As expected, the current magnitude of the excited helical arm far exceeds that of the parasitic element.

The electric field components are computed both in the vertical plane ($\varphi = 0°$) and the horizontal plane ($\theta = 90°$). Vertical plane patterns are shown in Fig. 3(a), and the horizontal plane patterns are depicted in Fig. 3(b). Clearly, both patterns are characterized by several lobes which suggest the suitability of the antennas for applications requiring multi = lobed radiation patterns.

4. CLOSURE

This paper has described, for first time, to the best of our knowledge, a moment-method analysis of the hyperbolic helical antenna, with the primary focus on the radiation fields of the antenna. The results obtained point to possible uses of the antenna for applications requiring multi-lobed radiation. It may be remarked that for the case considered, only one of the helical arms is excited at its centre while the other arm is considered as parasitic. Effects of feeding the two helical arms simultaneously at their centres and also at the ends should be of interest, and are presently being investigated.

REFERENCES

1. Knudsen, H. L., "Radiation field of a square helical beam antenna," *Jour. Appl. Phys.*, Vol. 23, No. 4, 483–491, 1952.
2. Kraus, J. D., "Helical beam antenna," *Electronics*, 109–111, 1947.
3. Adekola, S. A., A. I. Mowete, and A. A. Ayorinde, "Compact theory of the broadband elliptical helical antenna," *European Journal of Scientific Research*, Vol. 31, No. 3, 446–490, 2009.
4. Wong, J. Y. and S. C. Loh, "Radiation field of an elliptical helical antenna," *IRE Trans. Ant. & Prop.*, Vol. 7, 46–52, Jan. 1959.
5. Jones, G. C., "An experimental design study of some S- and X-band helical aerial systems," *IEE Journal*, 764–771, Nov. 1956.
6. Adekola, S. A., A. I. Mowete, and A. A. Ayorinde, "Performance characteristics of a dual-sense helical-beam antenna," *PIERS Proceedings*, 569–572, Marrakesh, Morocco, Mar. 20–23, 2011.

Analysis of a Circular-loop Zigzag Thin-wire Antenna

S. A. Adekola[1,2], A. Ike Mowete[1], and H. A. Muhammed[1]

[1] Department of Electrical and Electronics Engineering, Faculty of Engineering
University of Lagos, Lagos, Nigeria
[2]Department of Electrical and Electronics Engineering, Niger Delta University
Wilberforce Island, Yenegoa, Nigeria

Abstract— In this presentation, we develop an analytical model, using the electric field integral equation (EFIE) approach, for a folded zigzag thin-wire antenna, with the geometry of a circular-loop. Following a treatment described elsewhere [1], for the bi-elliptical toroidal helical antenna, the kernel of the integral expression for the magnetic vector potential for the problem is derived in a matrix format, through which distinct contributions to the radiation field by the circular-loop geometry and the zigzag emerge.

The computational results obtained for some input characteristics and the far-zone fields, for an assumed uniform current distribution, indicate that choice of number of zigzag sections provides the important possibilities of varying antenna's electrical length and controlling pattern directivity. Similar conclusions were arrived at by Zainud-Deen et al. [2], who investigated the performance features of zigzag antennas for portable radio equipment.

1. INTRODUCTION

In the open literature, various treatments of zigzag antennas were presented [2–4]. Employing numerical technique for determination of current distribution by method of moment, the near and far-fields patterns as well as the input impedance were determined for a portable radio equipment [2] whilst constant gain was shown to exist over the communication satellite frequency band of 2.27–12.25 GHz when used as a feed element in a paraboloidal reflector antenna [3].

The treatments given in [2–4] relate to linear antennas designed to operate as wideband antennas by folding them into zigzags form with logarithmic dependence between the zigzag sections which are then referred to as algorithmic antennas. However, in this presentation the zigzag antenna is folded to form a loop having a uniform zigzag length around the circumference as shown in Figure 1. The antenna so form have an imaginary loop of radius b that run midway between the highest and the lowest point of the zigzag section. The maximum length measured from the loop axis and the highest or lowest point of the zigzag section is termed d. By employing the magnetic vector potential (VMP) approach for a thin-wire antenna in which the current distribution is assumed to be constraint along the axis of the antenna, the far-field radiation characteristics are determined by employing the appropriate amplitude and phase approximation of $\bar{R}$ appearing in the Green's function. The expressions for the electric fields is shown to be constituted of contributions from the fields due to that of circular loop and of the zigzag sections after the integrand of the integration are cast into a matrix forms as established elsewhere [1]. Other associated parameters such as poynting vector and radiation resistance for different zigzag length and section number were determined numerically. Comparisons were made with that of a circular loop in all cases.

The numerical results obtained when $b = 0.2\lambda$ are graphically displayed in which the normalized electric field patterns for all cases of zigzag lengths and sections have similar pattern to that of a circular loop of comparable dimension. However, the radiation resistances show remarkable difference to that of a loop. The resistances are fairly uniform over a wide range of frequencies.

2. THEORY

Figure 1 shows a circular zigzag loop antenna oriented in horizontal position with the centre coincident with the origin of a Cartesian coordinate. An elemental source of length dl' is situated at point $p(x', y', z')$ a distance $\bar{r}'$ from centre while the point $p(x, y, z)$, a distance $\bar{r}$ from the centre of the antenna is the observation point or field point in which the field is sort out. The field and source point are related to each other by $\bar{R}$, being the separation between the field and source points.

Close observation of Figure 1 shows that source point can be described by

$$\bar{r}' = \hat{x}\left(b + d\cos N\phi'\right)\cos\phi' + \hat{y}\left(b + d\cos N\phi'\right)\sin\phi' \tag{1}$$

where N is the number of zigzag segment and b and d as already defined.

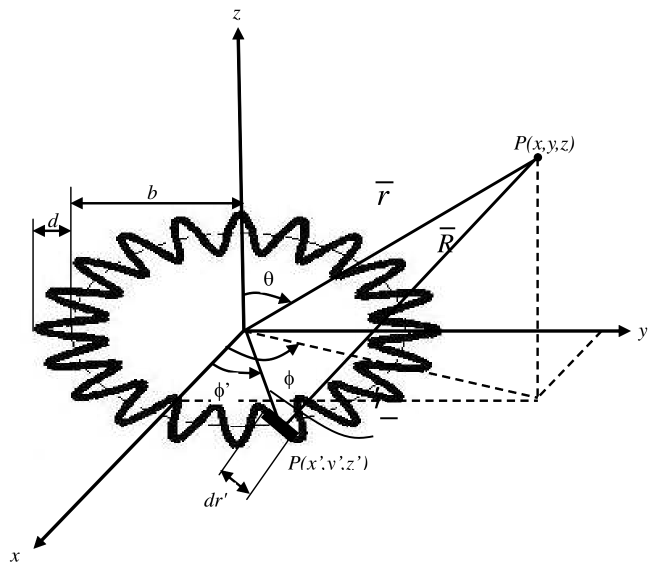

Figure 1: The geometry of a Circular-loop Zigzag Thin-wire Antenna presented in a spherical coordinate system.

Employing the VMP for thin wire in which the current is constraint to flow along the axis of the antenna gives

$$\bar{A}\left(r\right)=\frac{\mu}{4\pi}\int_{l}^{l'}I\left(l'\right)\frac{e^{-jkR}}{R}dr' \tag{2}$$

where $\bar{A}(r)$ is the vector magnetic potential, $I(l')$ is the current distribution along the axis of the antenna, μ is the permeability of the material, k is the propagation constant, dr' is the small elemental length of the wire as shown in Figure 1 and R is the separation between the source point and the field point as shown in Figure 1. The prime coordinate depicts the source point while the unprimed the field point.

By differentiating Eq. (1) with respect to ϕ', the small elemental length appearing in Eq. (2) can be obtained as

$$dr'=\left\{-\hat{x}\left(X'\sin\phi'+Y'\cos\phi'\right)+\hat{y}\left(X'\cos\phi'-Y'\sin\phi'\right)\right\}d\phi' \tag{3}$$

where

$$X'=b+d\cos N\phi' \tag{3a}$$

and

$$Y'=dN\sin N\phi' \tag{3b}$$

Substituting Eq. (3) into Eq. (2) and noting the x-, y- and z-components of the VMP magnetic potential are

$$A_x=-\frac{\mu}{4\pi}\int_0^{2\pi}I\left(\phi'\right)\left(X'\sin\phi'+Y'\cos\phi'\right)\frac{e^{-jkR}}{R}d\phi' \tag{4a}$$

$$A_y=\frac{\mu}{4\pi}\int_0^{2\pi}I\left(\phi'\right)\left(X'\cos\phi'-Y'\sin\phi'\right)\frac{e^{-jkR}}{R}d\phi' \tag{4b}$$

$$A_z=0 \tag{4c}$$

Applying the Cartesian to spherical transformation to Eqs. (4a)–(4c) result in

$$A_r=\sin\theta\frac{\mu}{4\pi}\int_0^{2\pi}I\left(\phi'\right)\left\{X'\sin\left(\phi-\phi'\right)-Y'\cos\left(\phi-\phi'\right)\right\}\frac{e^{-jkR}}{R}d\phi' \tag{5a}$$

$$A_\theta=\cos\theta\frac{\mu}{4\pi}\int_0^{2\pi}I\left(\phi'\right)\left\{X'\sin\left(\phi-\phi'\right)-Y'\cos\left(\phi-\phi'\right)\right\}\frac{e^{-jkR}}{R}d\phi' \tag{5b}$$

$$A_\phi=\frac{\mu}{4\pi}\int_0^{2\pi}I\left(\phi'\right)\left\{X'\cos\left(\phi-\phi'\right)+Y'\sin\left(\phi-\phi'\right)\right\}\frac{e^{-jkR}}{R}d\phi' \tag{5c}$$

Substituting Eqs. (3a) and (3b) into Eqs. (5a)–(5c), and then expanding, rearranging and recasting the result expressions into matrices form as established elsewhere [1], results in the following compact matrix formatted expressions

$$A_r = \sin\theta \frac{\mu}{4\pi}\int_0^{2\pi} I(\phi')\left\{ b\begin{bmatrix}0\\1\end{bmatrix}^T - d\begin{bmatrix}N\\-1\end{bmatrix}^T\begin{bmatrix}\sin N\phi' & 0\\ 0 & \cos N\phi'\end{bmatrix}\right\}\begin{bmatrix}\cos(\phi-\phi')\\ \sin(\phi-\phi')\end{bmatrix}\frac{e^{-jkR}}{R}d\phi' \quad (6a)$$

$$A_\theta = \cos\theta \frac{\mu}{4\pi}\int_0^{2\pi} I(\phi')\left\{ b\begin{bmatrix}0\\1\end{bmatrix}^T - d\begin{bmatrix}N\\-1\end{bmatrix}^T\begin{bmatrix}\sin N\phi' & 0\\ 0 & \cos N\phi'\end{bmatrix}\right\}\begin{bmatrix}\cos(\phi-\phi')\\ \sin(\phi-\phi')\end{bmatrix}\frac{e^{-jkR}}{R}d\phi' \quad (6b)$$

$$A_\phi = \frac{\mu}{4\pi}\int_0^{2\pi} I(\phi')\left\{ b\begin{bmatrix}1\\0\end{bmatrix}^T + d\begin{bmatrix}1\\N\end{bmatrix}^T\begin{bmatrix}\cos N\phi' & 0\\ 0 & \sin N\phi'\end{bmatrix}\right\}\begin{bmatrix}\cos(\phi-\phi')\\ \sin(\phi-\phi')\end{bmatrix}\frac{e^{-jkR}}{R}d\phi' \quad (6c)$$

3. THE FAR FIELD DISTANCE BETWEEN THE SOURCE AND FIELD POINTS

From Figure 1, the distance between the source point and the field point can be expressed as

$$|R| \approx r - \hat{r}\cdot r' \quad (7)$$

where $\hat{r} = \hat{x}\sin\theta\cos\phi + \hat{y}\sin\theta\sin\phi + \hat{z}\cos\theta$ and r' is given in Eq. (1).

Upon substitution of the above expressions, Eq. (7) simplifies to

$$|R| \approx r - \left(b + d\cos N\phi'\right)\sin\theta\cos\left(\phi-\phi'\right) \quad (7a)$$

And for the phase term appearing in the denominator, Eq. (7) becomes

$$|R| \approx r \quad (7b)$$

The electric fields and the VMPs in the far-field are related by the equation

$$\bar{E} \approx -j\omega\left(\bar{A} - \hat{r}\cdot\bar{A}\right) \quad (8)$$

The components of the electric fields is easily deduce when Eqs. (6a)–(6c) are substituted into Eq. (8) yielding

$$E_r \approx 0 \quad (9a)$$

$$\begin{aligned} E_\theta &= -j\omega\mu\frac{e^{-jkr}}{4\pi r}\cos\theta\int_0^{2\pi} I(\phi')\left\{ b\begin{bmatrix}0\\1\end{bmatrix}^T - d\begin{bmatrix}N\\-1\end{bmatrix}^T\begin{bmatrix}\sin N\phi' & 0\\ 0 & \cos N\phi'\end{bmatrix}\right\}\begin{bmatrix}\cos(\phi-\phi')\\ \sin(\phi-\phi')\end{bmatrix}\\ &\quad\times\exp\left\{jk\left(b+d\cos N\phi'\right)\sin\theta\cos\left(\phi-\phi'\right)\right\}d\phi' \end{aligned} \quad (9b)$$

$$\begin{aligned} E_\phi &= -j\omega\mu\frac{e^{-jkr}}{4\pi r}\int_0^{2\pi} I(\phi')\left\{ b\begin{bmatrix}1\\0\end{bmatrix}^T + d\begin{bmatrix}1\\N\end{bmatrix}^T\begin{bmatrix}\cos N\phi' & 0\\ 0 & \sin N\phi'\end{bmatrix}\right\}\begin{bmatrix}\cos(\phi-\phi')\\ \sin(\phi-\phi')\end{bmatrix}\\ &\quad\times\exp\left\{jk\left(b+d\cos N\phi'\right)\sin\theta\cos\left(\phi-\phi'\right)\right\}d\phi' \end{aligned} \quad (9c)$$

4. METHOD OF SOLUTION

Observation of Eqs. (9a)–(9c) showed that all the parameters in the expressions can be completely defined as they pertain to the physical geometry of the antenna except the current distribution $I(\phi')$. In this problem we are proposing the use of a uniform current distribution of the form

$$I(\phi') = I_o e^{j\omega t} \quad (10)$$

where I_o is a constant complex quantity. Meanwhile, for simplicity the $e^{j\omega t}$ is assumed but suppress throughout the problem paper. The fields radiated by the antenna are thus obtained by substituting

Eq. (10) into Eqs. (9b) and (9c). These simplify to

$$\begin{aligned} E_\theta \;=\; & -jk\eta C I_o \frac{e^{-jkr}}{4\pi r}\cos\theta \frac{1}{2\pi}\int_0^{2\pi}\left\{\begin{bmatrix}0\\1\end{bmatrix}^T - \xi\begin{bmatrix}N\\-1\end{bmatrix}^T\begin{bmatrix}\sin N\phi' & 0\\0 & \cos N\phi'\end{bmatrix}\right\}\begin{bmatrix}\cos(\phi-\phi')\\ \sin(\phi-\phi')\end{bmatrix} \\ & \times \exp\left\{jk\left(b+d\cos N\phi'\right)\sin\theta\cos\left(\phi-\phi'\right)\right\}d\phi' \qquad (11a) \\ E_\phi \;=\; & -jk\eta C I_o \frac{e^{-jkr}}{4\pi r}\frac{1}{2\pi}\int_0^{2\pi}\left\{\begin{bmatrix}1\\0\end{bmatrix}^T + \xi\begin{bmatrix}1\\N\end{bmatrix}^T\begin{bmatrix}\cos N\phi' & 0\\0 & \sin N\phi'\end{bmatrix}\right\}\begin{bmatrix}\cos(\phi-\phi')\\ \sin(\phi-\phi')\end{bmatrix} \\ & \times \exp\left\{jk\left(b+d\cos N\phi'\right)\sin\theta\cos\left(\phi-\phi'\right)\right\}d\phi' \qquad (11b) \end{aligned}$$

In which the relationship $\omega\mu = k\eta$ is utilized and that η $(= 120\pi)$ is the intrinsic impedance of the free space and C $(= 2\pi b)$ is the circumference of the circular imaginary loop of radius b as stated earlier. The quantity ξ $(= d/b)$ is define as the ratio of the maximum zigzag length to that of the loop.

Equations (11a) and (11b) can be recast into the form

$$E_\theta = -jk\eta C I_o \frac{e^{-jkr}}{4\pi r}\left\{F_\theta^{lp}(\theta,\phi) - \xi F_\theta^{zz}(\theta,\phi)\right\} \qquad (12a)$$

or

$$E_\theta = -jk\eta C I_o \frac{e^{-jkr}}{4\pi r} F_\theta(\theta,\phi) \qquad (12b)$$

where

$$F_\theta(\theta,\phi) = F_\theta^{lp}(\theta,\phi) - \xi F_\theta^{zz}(\theta,\phi) \qquad (12c)$$

Provided that

$$\begin{aligned} F_\theta^{lp}(\theta,\phi) \;=\; & \cos\theta\frac{1}{2\pi}\int_0^{2\pi}\begin{bmatrix}0\\1\end{bmatrix}^T\begin{bmatrix}\cos(\phi-\phi')\\ \sin(\phi-\phi')\end{bmatrix} \\ & \times \exp\left\{jk\left(b+d\cos N\phi'\right)\sin\theta\cos\left(\phi-\phi'\right)\right\}d\phi' \qquad (13a) \end{aligned}$$

and

$$\begin{aligned} F_\theta^{zz}(\theta,\phi) \;=\; & \cos\theta\frac{1}{2\pi}\int_0^{2\pi}\begin{bmatrix}N\\-1\end{bmatrix}^T\begin{bmatrix}\sin N\phi' & 0\\0 & \cos N\phi'\end{bmatrix}\begin{bmatrix}\cos(\phi-\phi')\\ \sin(\phi-\phi')\end{bmatrix} \\ & \times \exp\left\{jk\left(b+d\cos N\phi'\right)\sin\theta\cos\left(\phi-\phi'\right)\right\}d\phi' \qquad (13b) \end{aligned}$$

Hence,

$$\left|F_\theta(\theta,\phi)\right| = \left|F_\theta^{lp}(\theta,\phi) - \xi F_\theta^{zz}(\theta,\phi)\right| \qquad (14)$$

Similarly, from Eq. (11b)

$$E_\phi = -jk\eta C I_o \frac{e^{-jkr}}{4\pi r}\left\{F_\phi^{lp}(\theta,\phi) + \xi F_\phi^{zz}(\theta,\phi)\right\} \qquad (15a)$$

or

$$E_\phi = -jk\eta C I_o \frac{e^{-jkr}}{4\pi r} F_\phi(\theta,\phi) \qquad (15b)$$

where

$$F_\phi(\theta,\phi) = F_\phi^{lp}(\theta,\phi) + \xi F_\phi^{zz}(\theta,\phi) \qquad (15c)$$

Provided also that

$$\begin{aligned} F_\phi^{lp}(\theta,\phi) \;=\; & \frac{1}{2\pi}\int_0^{2\pi}\begin{bmatrix}1\\0\end{bmatrix}^T\begin{bmatrix}\cos(\phi-\phi')\\ \sin(\phi-\phi')\end{bmatrix} \\ & \times \exp\left\{jk\left(b+d\cos N\phi'\right)\sin\theta\cos\left(\phi-\phi'\right)\right\}d\phi' \qquad (16a) \end{aligned}$$

and

$$\begin{aligned} F_\phi^{zz}(\theta,\phi) &= \frac{1}{2\pi}\int_0^{2\pi}\begin{bmatrix}1\\N\end{bmatrix}^T\begin{bmatrix}\cos N\phi' & 0\\ 0 & \sin N\phi'\end{bmatrix}\begin{bmatrix}\cos(\phi-\phi')\\ \sin(\phi-\phi')\end{bmatrix} \\ &\times\exp\left\{jk\left(b+d\cos N\phi'\right)\sin\theta\cos\left(\phi-\phi'\right)\right\}d\phi' \end{aligned} \quad (16b)$$

Hence, Eq. (15c)

$$|F_\phi(\theta,\phi)| = \left|F_\phi^{lp}(\theta,\phi)+\xi F_\phi^{zz}(\theta,\phi)\right| \quad (17)$$

Since the electric field radiation in the far field is related to magnetic field by the expressions [5]

$$\bar{H} = \frac{\hat{r}}{\eta}\times\bar{E} \quad (18)$$

where the parameters appearing in Eq. (18) are already defined in the literature, the corresponding magnetic fields when Eqs. (12b) and (15b) are utilized in Eq. (18) yields

$$H_\phi = -jkCI_o\frac{e^{-jkr}}{4\pi r}F_\theta(\theta,\phi) \quad (19a)$$

$$H_\theta = jkCI_o\frac{e^{-jkr}}{4\pi r}F_\phi(\theta,\phi) \quad (19b)$$

5. NUMERICAL EVALUATION OF SOME ANTENNA PARAMETERS

The primary parameters required to evaluate the circular zigzag antenna parameters are obtained in Eqs. (12b), (15b), (19a) and (19b) based on the assumption of a uniform current distribution as stated earlier. With these developments, radial outward flow of complex power can be deduced from the well known expression of the poynting vector expressed as [6]

$$P_r = \frac{1}{2}\left[E_\theta(\theta,\phi)H_\phi^*(\theta,\phi)-E_\phi(\theta,\phi)H_\theta^*(\theta,\phi)\right] \quad (20)$$

where the asterisk symbols (*) denote complex conjugate and P_r is the power radiated per unit area.

Upon substitution of Eqs. (12b), (15b), (19a) and (19b) into Eq. (20), the power radiated per unit area becomes

$$P_r = \kappa\left[|F_\theta(\theta,\phi)|^2+|F_\phi(\theta,\phi)|^2\right] \quad (21)$$

where $\kappa = \frac{\eta k^2C^2I_o^2}{32\pi^2r^2}$ as defined in Adekola, S. A. [7].

The total radiated power is obtained by integrating power per unit area obtained in Eq. (21) over large sphere of radius r and is given as

$$W_T = \int_0^{2\pi}\int_0^{\pi}P_r r^2\sin\theta d\theta d\phi \quad (22)$$

or

$$W_T = \kappa r^2\int_0^{2\pi}\int_0^{\pi}\left[|F_\theta(\theta,\phi)|^2+|F_\phi(\theta,\phi)|^2\right]\sin\theta d\theta d\phi \quad (23)$$

As stated elsewhere [8], the radiation resistance is related to the total radiated power by expression

$$R_r(kb) = \frac{2W_T}{I_o^2} \quad (24)$$

Substituting Eq. (23) into Eq. (24) and simplifying yields

$$R_r(kb) = 30\pi(kb)^2\int_0^{2\pi}\int_0^{\pi}\left[|F_\theta(\theta,\phi)|^2+|F_\phi(\theta,\phi)|^2\right]\sin\theta d\theta d\phi \quad (25)$$

where $\kappa r^2 = 15\pi(kb)^2I_o^2$.

6. RESULTS AND DISCUSSIONS

Two sets of results are shown here, namely: the radiation patterns and the radiation resistance for three different zigzag number, N and length b. For the purpose of comparison, the figures also include that of a circular loop also of radius b ($when\ d = \xi = 0$) in which deviation from it is considered. For instant, Figures 2, 3 and 4 show that the fields have generally the same field pattern as that of a circular loop but with slightly different directivity which increases with the zigzag length. Figures 5, 6 and 7 compares the radiation resistance of the different configurations of the antenna with that of loop as in the previous cases as a function of the electrical length C_λ $(= 2\pi b/\lambda)$. As the number of zigzag length and section is increased, the radiation resistances remain fairly uniform over significant range of frequencies. For example, in respective of the number of zigzag section, the radiation resistance for $N = 10$, 15 and 20 has the centre values of approximately 1,600 Ω, 1,500 Ω and 1,200 Ω with approx. variation of ±480 Ω, ±380 Ω and ±200 Ω when $\xi = 0.1$, 0.3, and 0.5, respectively. The results correspond to a frequency ratio of 2.33 : 1, 3.67 : 1, 3.67 : 1 for $N = 10$, and 2.33 : 1, 5.67 : 1, 5.00 : 1 for $N = 15$ for which lower band of $C_\lambda = 2.0$ is observed to be same for all values of zigzag section N.

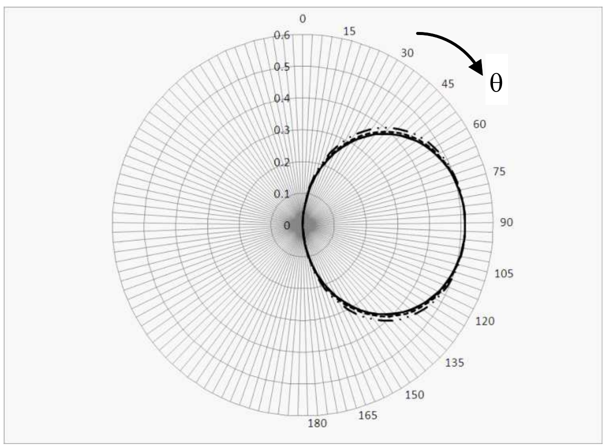

Figure 2: The radiation pattern computed from Eq. (17) for $|F_\phi(\theta, \phi)|$ when $b = 0.2\lambda$ and $\xi = 0.0$ (loop) —, $\xi = 0.1$ – –, $\xi = 0.3$ - - -, $\xi = 0.5$ – · · – and $N = 10$.

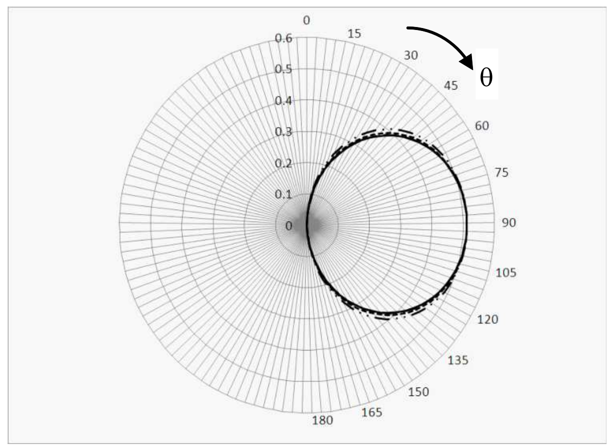

Figure 3: The radiation pattern computed from Eq. (17) for $|F_\phi(\theta, \phi)|$ when $b = 0.2\lambda$ and $\xi = 0.0$ (loop) —, $\xi = 0.1$ – –, $\xi = 0.3$ - - -, $\xi = 0.5$ – · · – and $N = 15$.

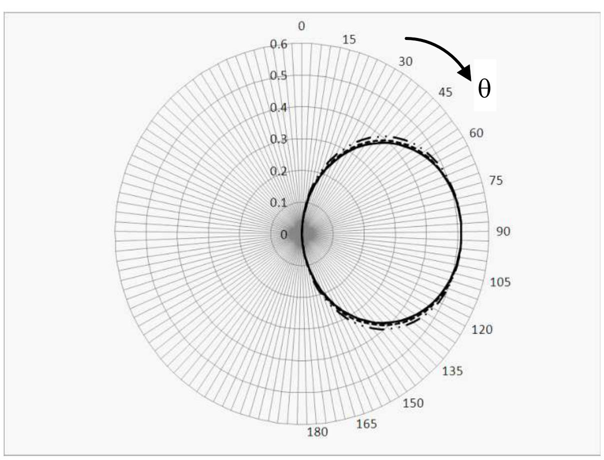

Figure 4: The radiation pattern computed from Eq. (17) for $|F_\phi(\theta, \phi)|$ when $b = 0.2\lambda$ and $\xi = 0.0$ (loop) —, $\xi = 0.1$ – –, $\xi = 0.3$ - - -, $\xi = 0.5$ – · · – and $N = 20$.

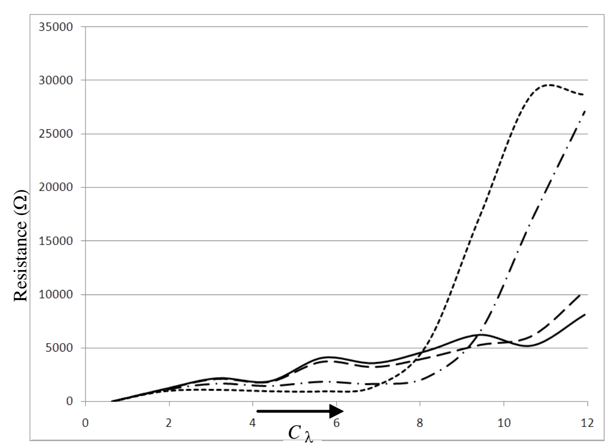

Figure 5: The radiation resistance computed from Eq. (24) when $b = 0.2\lambda$ and $\xi = 0.0$ (loop) —, $\xi = 0.1$ – –, $\xi = 0.3$ - · · -, $\xi = 0.5$ - - - and $N = 10$.

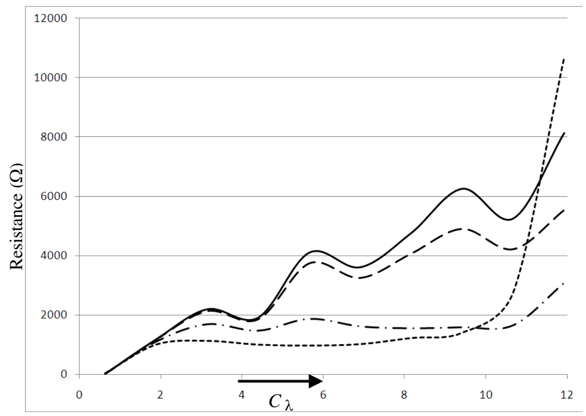

Figure 6: The radiation resistance computed from Eq. (24) when $b = 0.2\lambda$ and $\xi = 0.0$ (loop) —, $\xi = 0.1$ – –, $\xi = 0.3$ - · -, $\xi = 0.5$ - - - and $N = 15$.

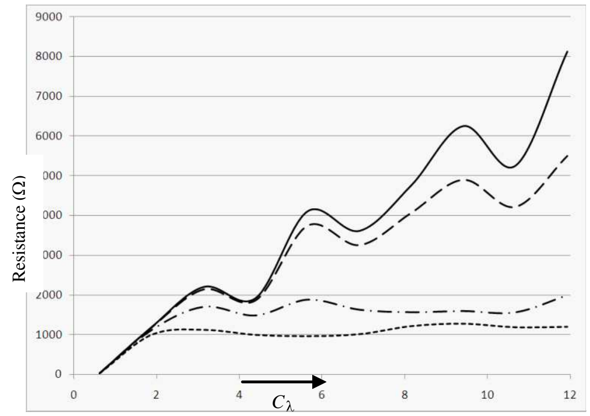

Figure 7: The radiation resistance computed from Eq. (24) when $b = 0.2\lambda$ and $\xi = 0.0$ (loop) —, $\xi = 0.1$ – –, $\xi = 0.3$ - · -, $\xi = 0.5$ - - - and $N = 20$.

7. CONCLUSION

A new wideband antenna referred to as Circular-loop Zigzag Thin-wire Antenna, is proposed and its characteristics were determined. The electric fields obtained are composed of the fields due to contributions from the circular loop geometry and the zigzag section. The results of the fields are compared with that of a circular loop and were discovered to have a striking resemblance for all the values of zigzag length and section investigated. However, slight variations in the directivity are noticeable such that there is relative widening of the pattern as one increase the zigzag length. We find also that for the radiation resistance a uniform behavior over a range of frequencies is obtainable, a finding that make the antenna a suitable choice for wideband application.

REFERENCES

1. Adekola, S. A., A. I. Mowete, and H. A. Muhammed, "A matrix-vector-potential analysis of the bi-elliptical toroidal helical antenna," *PIERS Proceedings*, 825–829, Marrakesh, Morocco, Mar. 20–23, 2011.
2. Zainud-Deen, S. H., K. H. Awadalla, A. L. Bahnacy, and H. A. Sharshar, "Performance analysis of zigzag antenna for portable radio equipment," *Antennas and Propagation Society International Symposium*, Vol. 1, 442–447, 1997.
3. Nakano, H., S. Yokota, H. Mimaki, and J. Yamauchi, "Backfire mode zigzag antenna," *IEEE Electronics Letters*, Vol. 29, No. 22, 1905–1906, 1993.
4. Nakano, H., H. Tagami, and J. Yamauchi, "Numerical analysis of an axial-mode zigzag antenna" *IEEE Electronics Letters*, Vol. 21, No. 14, 606–608, 1985.
5. Balanis, C., *Antenna Theory Analysis and Design*, 3rd Edition, 125, A John Wiley & Sons Inc. Publication, 2005.
6. Jordan, E. C. and K. G. Balmain, *Electromagnetic Waves and Radiating Systems*, 2nd Edition, 172, Printice-Hall Inc. Publication, 1968.
7. Adekola, S. A., "On the excitation of a circular loop antenna by travelling-and standing-wave current distributions," *International Journal of Electronics*, 1362–3060, Vol. 54, No. 6, 705–732, 1983.
8. Wolff, E. A., *Antenna Analysis*, Vol. 75, 14, John Wiley and Sons Inc. Publication, 1966.

On the Insulated Dipole Antenna in a Dissipative Non-conducting Medium

A. I. Mowete[1] and A. Ogunsola[2]

[1]Department of Electrical and Electronics Engineering, Faculty of Engineering
University of Lagos, Lagos, Nigeria
[2]Parsons Group International, Rail Transit Division, London, United Kingdom

Abstract— Using the quasi-static model earlier described elsewhere [1], this paper investigates the characteristics features of the fields radiated in the ambient medium, by the insulated thin-wire antenna, located in a dissipative dielectric medium. Accordingly, the dielectric insulation carried by the thin-wire dipole antenna is modeled by a volumetrically distributed polarization current, related to the distribution of current along the axis of the bare antenna, through the equation of continuity. Approximate expressions are subsequently derived for the axial and radial components of electric field intensity in the region occupied by the dielectric insulation, through which the fields in the ambient medium are characterized. As a test for the validity of the analytical results, computational results obtained from the expressions, for the case of the symmetric insulated antenna (half-wave dipole in an air-filled glass tube) are compared with those reported by Atlamazoglou and Uzonoglu [2], and the similarities in these results suggest that the quasi-static model may be suitable for use as proposed by the paper.

1. INTRODUCTION

When part or all of a wire antenna is insulated by a dielectric layer, the antenna's radiation efficiency is known to significantly improve [2]. And in addition to this desirable property, the insulated wire antenna has quite a few others [1, 3], which commend it for use in applications including geophysical explorations and microwave hyperthermia, where it is required to ensure that the conductor does not make contact with the ambient medium. One application that typifies the analytical problem posed by applications of the type mentioned in the foregoing is the interstitial or invasive hyperthermia application, for which a large percentage of the heating is localized within the antenna's near field; and as has been pointed out [2], this field is more difficult to model than the near field. Previous analytical efforts include those described in the open literature by Atlamazoglou and Uzonoglu [2], King et al. [4], and Casey and Bansal [3]. This paper presents an analytical model similar to that proposed in [2], where a model developed by Richmond and Newman [5], was adapted for use, in a Galerkin Moment-Method approach. Here the quasi-static model proposed by [1] is utilized for characterizing the field within the dielectric insulation; the results are then extended into the ambient medium through the boundary conditions on the axial and radial components of the field in the dielectric layer. Computational results obtained for the 'symmetrically insulated' dipole antenna compare favorably with those reported in [2], to suggest that this simplified approach should prove useful in a more rigorous analysis.

2. THEORY

Following the quasi-static theory described elsewhere [1, 6], the field in the dielectric region of the coated wire antenna described by the illustration of Figure 1 has the two components given as

$$E_\rho = \frac{1}{4\pi\varepsilon_d}\int\limits_{wire}\frac{\sigma(z')\rho dz'}{(z'^2+\rho^2)^{3/2}} \tag{1}$$

$$E_z = \frac{-1}{4\pi\varepsilon_d}\int\limits_{wire}\frac{\sigma(z')z' dz'}{(z'^2+\rho^2)^{3/2}} \tag{2}$$

These field components, as described in [6], are restricted to the region occupied by the dielectric insulation: and they are due to the quasi-static charge distribution symbolized in (1) by $\sigma(z')$, which in turn, derives from the current distribution carried by the bare (thin) wire antenna structure, through the equation of continuity. When numerical results for the fields are available, the

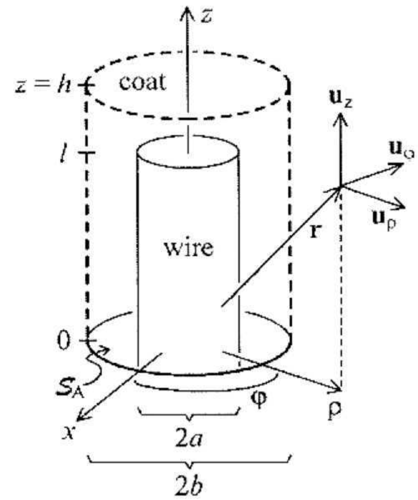

Figure 1: Coated thin-wire antenna.

corresponding components of the fields in the ambient medium are specified by boundary conditions as:

$$E(\text{Insulation})_z = E(\text{ambient})_z \tag{3}$$

$$\varepsilon_d E(\text{Insulation})_\rho = \varepsilon_{amb} E(\text{ambient})_\rho \tag{4}$$

where ε_d and ε_{amb} denote the dielectric constants of the insulation and ambient medium, respectively. In the moment-method approach utilized here, the piece-wise linear functions, whose nth member is described by (5) are employed as basis and testing functions;

$$T_n(z) = \begin{cases} \frac{z - z_{2n-1}}{z_{2n+1} - z_{2n-1}}, & z_{2n-1} \le z \le z_{2n+1} \\ \frac{z_{2n+3} - z}{z_{2n+3} - z_{2n+1}} & z_{2n+1} \le z \le z_{2n+3} \end{cases}; \tag{5}$$

3. COMPUTATIONAL RESULTS AND DISCUSSIONS

Analytical expressions for the field components specified by (1) and (2) can be shown to have nth components given by:

$$\begin{aligned} E_{zn} = & \frac{-1}{j\omega 4\pi\varepsilon_d}\left[\frac{1}{z_{2n+1} - z_{2n-1}}\left\{\frac{1}{\left(z_{2n+1}^2 - \rho^2\right)^{1/2}} - \frac{1}{\left(z_{2n-1}^2 - \rho^2\right)^{1/2}}\right\}\right. \\ & \left. - \frac{1}{z_{2n+3} - z_{2n-1}}\left\{\frac{1}{\left(z_{2n+3}^2 - \rho^2\right)^{1/2}} - \frac{1}{\left(z_{2n-1}^2 - \rho^2\right)^{1/2}}\right\}\right] \end{aligned} \tag{6}$$

$$\begin{aligned} E_{\rho n} = & \frac{-1}{j\omega 4\pi\varepsilon_d \rho^2}\left[\frac{1}{z_{2n+1} - z_{2n-1}}\left\{\frac{z_{2n+1}}{\left(z_{2n+1}^2 - \rho^2\right)^{1/2}} - \frac{z_{2n-1}}{\left(z_{2n-1}^2 - \rho^2\right)^{1/2}}\right\}\right. \\ & \left. - \frac{1}{z_{2n+3} - z_{2n+1}}\left\{\frac{z_{2n+3}}{\left(z_{2n+3}^2 - \rho^2\right)^{1/2}} - \frac{z_{2n+1}}{\left(z_{2n+1}^2 - \rho^2\right)^{1/2}}\right\}\right] \end{aligned} \tag{7}$$

For numerical values, we utilized (3), (4), and (5), for the insulated wire antenna (half-wave dipole) and ambient medium specified by the following parameters [2]: Conductor inner radius = 0.47 mm; half-length of dipole = 3.1 cm; frequency of operation; $\varepsilon_d = 1.373$; thickness of insulating shell = 0.33 mm; and for the ambient medium (described by [2] as having the 'electrical properties of the human brain tissue'), we used $\varepsilon_{amb} = (34.42 - j15.49)$ [7]. The results obtained are displayed in Figures (2a) and (2b) for E_z and E_ρ, respectively.

And as can be seen from the illustrations, the curves follow the general pattern as those displayed as Figure (3) in [2], for the same insulated dipole. We find that in the ambient medium, and for the case of the axial component, the values obtained here are comparable with those reported in [2],

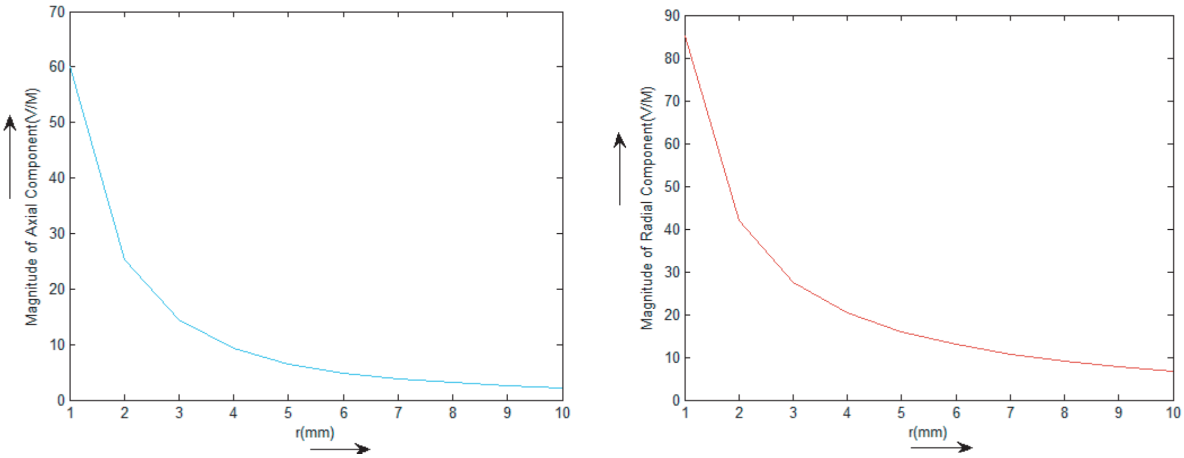

(a) (b)

Figure 2: Magnitude of electric field intensity in the ambient medium. (a) Axial component. (b) Radial component.

numerical values obtained here for the radial component are in general, larger than corresponding values in [2]. Several factors may have contributed to this, the most critical of them being the choice of relative permittivity for the ambient. The other possibilities of course include the nature of the approximations inherent in both analytical models, with particular reference to how they account for the dependence with 'r', of the radial component in the ambient medium.

4. CONCLUSION

We have in this presentation, described a model for the insulated dipole antenna in a dissipative dielectric medium, using the quasi-static theory earlier proposed elsewhere [1, 6]. For the dielectric insulation, a Schelkunnuff's volume equivalent current was utilized as model, and by suggesting that the associated field is a function of current distributed along the axis of the wire, a model emerged for the field within the dielectric medium as being due to an equivalent static charge distribution, related to the afore mentioned current distribution, through the equation of continuity. The analytical results were then extended into the ambient medium, through the simple expedient of imposing boundary conditions on the axial and radial components of the fields in region occupied by the dielectric insulation. Computational results obtained for the symmetrically insulated half-wave dipole described in [2], suggest that the model should prove useful in a more rigorous development that we plan to explore.

REFERENCES

1. Mowete, A. I., A. Ogunsola, and L. Sandrolini, "A quasi-static theory for dielectric-coated thin-wire antenna structures," *Progress In Electromagnetics Research Letters*, Vol. 20, 45–54, 2011.
2. Atlamazoglou, P. E. and N. K. Uzonoglu, "A Galerkin moment method for the analysis of an insulated antenna in a dissipative dielectric medium," *IEEE Transactions on Microwave Theory and Techniques*, Vol. 46, No. 7, 988–997, 1998.
3. Casey, J. P. and R. Bansal, "The near field of an insulated dipole in a dissipative dielectric medium," *IEEE Transactions on Microwave Theory and Techniques*, Vol. 34, 459–463, 1986.
4. King, R. W. P., B. S. Trembly, and J. W. Strohbhen, "The electromagnetic field of an insulated antenna in a conducting or dielectric medium," *IEEE Transactions on Microwave Theory and Techniques*, Vol. 31, 574–583, 1983.
5. Richmond, J. H. and E. H. Newman,"Dielectric coated wire antenna," *Radio Science*, Vol. 11, 13–20, 1976.
6. Adekola, S. A., A. I. Mowete, and A. Ogunsola, "On the problem of dielectric coated wire antenna," *PIERS Proceedings*, 431–437, Moscow, Russia, Aug. 18–21, 2009.
7. Charles, P. and E. Postow, *Handbook of Biological Effects of Electromagnetic Fields*, CRC Press, 1996.

A Planar Resonator Antenna Using Folded Dipole with Reflective Walls

S. A-Sa, **P. Krachodnok**, **and R. Wongsan**
School of Telecommunication Engineering, Suranaree University of Technology
Nakhon Ratchasima 30000, Thailand

Abstract— A resonator antenna using a planar folded dipole with reflective walls is presented. A planar antenna comprising two back-to-back folded dipoles printed on a dielectric substrate and separated by a narrow rectangular ground plane is operated resonance frequency at 5.8 GHz. A highly directive radiation pattern is created due to the angle-dependent attenuation of the resonator antenna coupling to free space. The complete reflection phase for reflective walls is investigated through cavity height calculation. The simulation results found that the cavity height of 0.58α is most direction gain of 12.97 dB. Effect of reflective walls height on the performance of the proposed antenna is also studied.

1. INTRODUCTION

Antennas having a highly directive radiation pattern can cover a large area and very attractive for applications in wireless communications. For this purpose,several promising antenna designssuch as the cylindrical patch array antenna [1, 2] and the planar back-to-back dipole antenna [3–7] have recently been reported. However, the construction cost of the former design using cylindrical patch radiators is usually high,because the patch radiators need to be made conformal to a cylindrical ground surface.As mentioned above, for the paper design, the dipole antenna can easily be fabricated by printing or etching on a planar dielectric substrate, leading to a low fabrication cost for the antenna.On the other hand, the half-wave folded dipole antenna has low gain [8–12].

In this paper, we propose the planar resonator antenna using the folded dipole and reflective walls. The antennas main characteristics, namely its gain and radiation pattern will be determined by the properties of the reflective walls. However, efficient of these antenna can seem in term of gain versus compactness.In fact, for gain greater than 12.97 dB which is effect of reflective walls on the performance antenna is presented.

Parameters	Size (λ)
w	0.348λ
L	1.315λ
l	0.305λ
W_g	0.096λ
W_a	0.096λ
t	1.5
s	1.5
g	1
d_1	32.5
d_2	19.7

Table 1: Design parameters of folded dipole antenna.

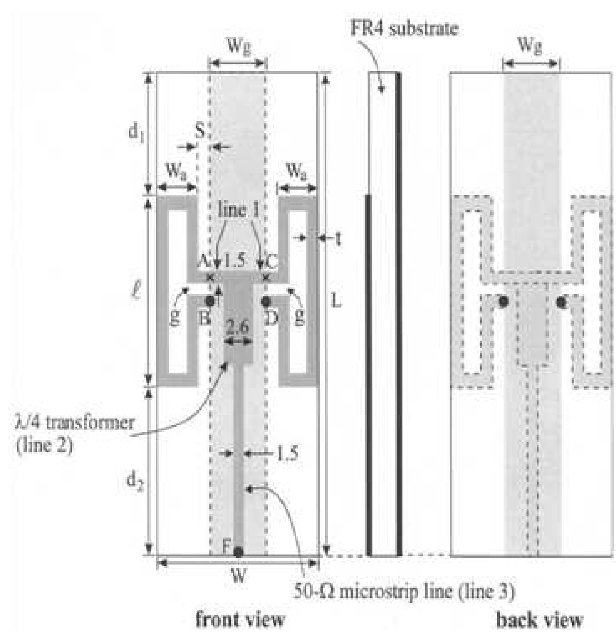

Figure 1: Geometry of the folded dipoleantenna.

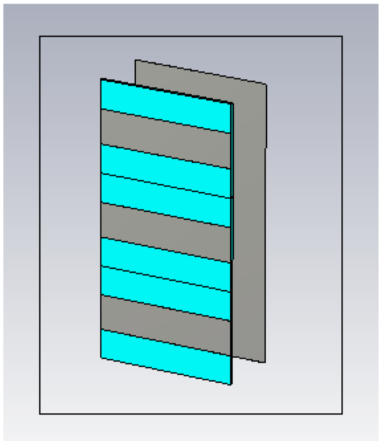

Figure 2: The reflective walls.

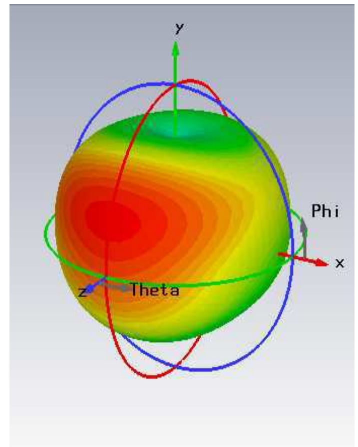

Figure 3: The radiation pattern of the folded dipole.

Table 2: The optimizing of cavity height.

h (mm)	Gain (dB)
10.0	6.886
20.0	7.386
30.0	12.97

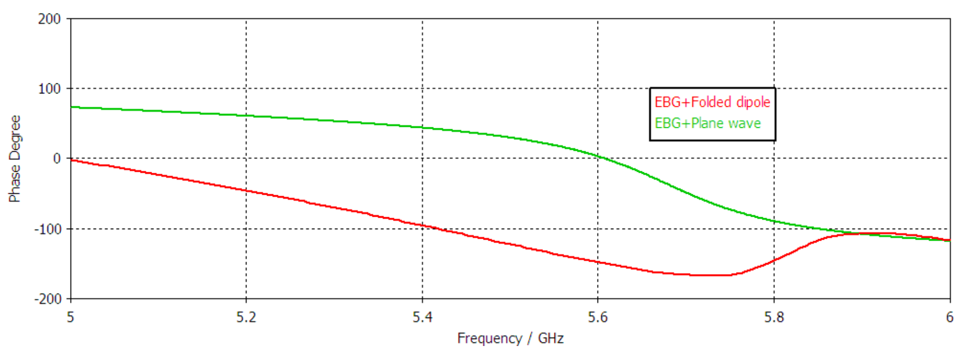

Figure 4: The reflection coefficient phase of upper reflective wall using folded dipole and plane wave.

2. ANTENNA DESIGN

A resonator antenna consists of a planar folded dipole and two reflective walls.We apply a similar geometry as in the planar folded dipole structure [13], for the design of a resonator antenna at 5.8 GHz. The folded dipole antenna,as shown in Fig. 1, is printed on FR4 substrate with the dielectric constant of 4.5 and the thickness of 1.6 mm, respectively. The optimizing of parameter is illustrated in Table 1. The analysis model of reflective walls structure is illustrated in Fig. 2. The upper reflective wall is printed on FR4 substrate with the width (w) and length (L). Concerning the Partially Reflecting Surface (PRS), the structure has three metallic elements, the metallic line and the wide are68 mmand 16.8 mm, respectively, interspaced by 30.8 mm. The lower reflective wall is a metallic sheet with the dimension of 68×16.8 mm.

3. SIMULATION RESULTS

The simulated results,as shown in Fig. 3, show that the gain of the folded dipole at 5.8 GHz is 5.691 dB and its radiation pattern is bidirectional. A mechanism to enhance the directivity of radiating sources is to enclose its inside a cavity formed between an optimally design reflective wall and a ground plane. The configuration of the model is shown in Fig. 2, the folded dipole is placed between the upper reflective walland a ground plane.Because of the folded dipole, the metamaterial reflective wall modifies the resonant condition of the cavity as shown in Fig. 4, increasing the resonantfrequency. Table 2 and Fig. 5 shown the optimizing of cavity height to resonance at the

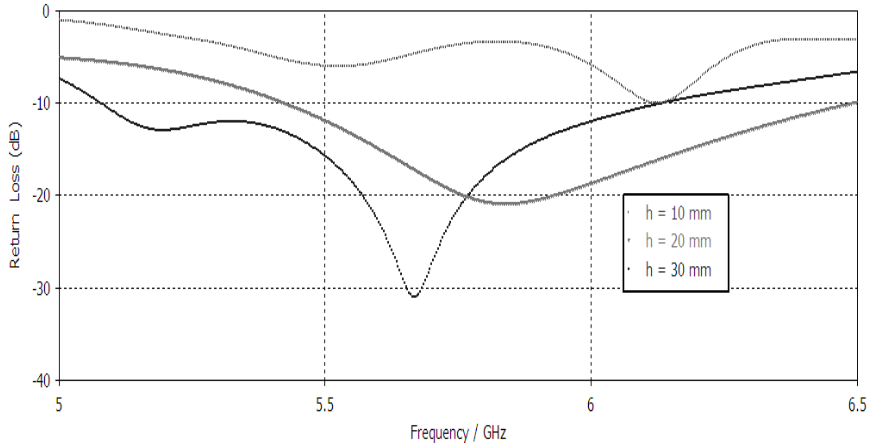

Figure 5: The return loss.

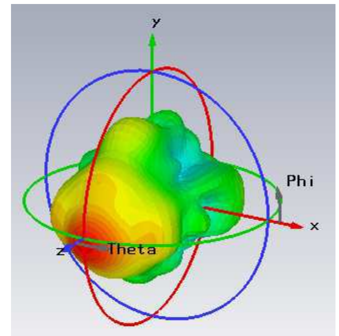

Figure 6: The radiation pattern of the proposed antenna.

center frequency, it can be clearly seen that the S_{11} are lower than -10 dB at 5.8 GHz. The bandwidth is covered between 5.07–6.13 GHz. The cavity height has effect of directive gain. The simulated result shows that the gain at 5.8 GHz is 12.97 dB at the height of 30 mm.

4. CONCLUSION

This papers presented the design of planar resonator antenna at 5.8 GHz with modeling software (CST Microwave Studio), it is successful to improve the gain of 12.97 dB because of the qualifications of reflective walls. Therefore, the proposed antenna has high gain which demands on equipment for wireless communication system.

REFERENCES

1. Audenaerde, K. R., S. Sabo, and J. Y. Lee, 'Microstrip antenna," U.S. Patent 6 166 702, Dec. 26, 2000.
2. Herscovici, N., Z. Sipus, and P.-S. Kildal, "The cylindrical omnidirectionalpatch antenna," *IEEE Trans. Antennas Propagat.*, Vol. 49, 1746–1753, Dec. 2001.
3. Lam, T. H., M. J. Milicic, Jr., and D. M. Pritchett, "Dipole antenna havingco-axial radiators and feed," U.S. Patent 5 387 919, Feb. 7, 1995.
4. Koscica, T. E. and B. J. Liban, "Simplified stacked dipole antenna," U.S. Patent 6 014 112, Jan. 11, 2000.
5. Zhu, L., Y. Guo, and X. Chen, "High efficiency feed network for antennas," U.S. Patent 6 377 227 B1, Apr. 23, 2002.
6. Le Balier, J., A. Le Bayon, and D. Nedelec, "Vertical polarization antenna," U.S. Patent 6 529 171 B1, Mar. 4, 2003.
7. Wong, K. L., *Planar Antennas for Wireless Communications*, 219, NewYork, Wiley, 2003.
8. Stutzman, W. L. and G. A. Thiele, *Antenna Theory and Design*, 2nd Edition, Ch. 5, Wiley, New York, 1998.
9. Van Beurden, M. C., A. B. Smolders, M. E. J. Jeuken, G. H. C. van Werkhoven, and E. W. Kolk, "Analysis of wide-band infinite phased arraysof printed folded dipoles embedded in metallic boxes," *IEE Trans. Antennas Propagat.*, Vol. 50, 1266–1273, Sep. 2002.
10. Buxton, C. G., W. L. Stutzman, R. R. Nealy, and A. M. Orndorff, "The folded dipole: A self-balancing antenna," *Microwave Opt. Technol. Lett.*, Vol. 29, 155–160, May 2001.
11. McNamara, D. A. and L. Botha, "On the functioning of folded dipoleantennas on conducting masts," *IEEE Trans. Veh. Technol.*, Vol. 42, 393–398, Nov. 1993.
12. Tanaka, T., S. Hayashida, H. Morishita, Y. Koyanagi, and K. Fujimoto, "Built-in folded dipole antenna for handsets," *IEEE Antennas Propagat. Soc. Int. Symp. Dig.*, Vol. 1, 451–454, 2003.
13. Hsiao, R. and K.-L. Wong, "Omnidirectional planar folded dipole antenna," *IEEE Trans. Antennas Propagat.*, Vol. 52, 1898–1902, Jul. 2004.

Reduction of EMI due to Antenna Radiation inside Complex PCB

Cheng-Wei Chen[2], Dau-Chyrh Chang[1], Hsiao-Bin Liang[2], Chi-Hsiung Wang[2], and Tsan-Hung Wu[2]

[1]Oriental Institute of Technology, Taiwan
[2]Climax Technology Co., Ltd., Taiwan

Abstract— In this paper, a reflector is adopted for modifying the radiation pattern of an on-board PIFA to reduce the EMI effect due to complex PCB environment, which degrades the performance of the PIFA, inside a wireless product. The measured results of TRP/TIS (total radiation power/total isotropic sensitivity) for GSM module paneling in a wireless home security system verifies the improvement of this proposed solution. The EM simulation tool, GEMS [1], is applied to design and analyze the performance of antennas and 3D EM environment in this work.

1. INTRODUCTION

For the PCB (printed circuit board) of a wireless product, there are always several wireless solutions on it due to the need of versatile application. For examples, ISM band (868/433 MHz), GSM, WiFi, Zigbee, Z-wave and so on. In addition to those HW (hardware) devices, brilliant ID (industrial design) and ME (mechanical) design make EM environment complex for PCB, which complicate and limit the performance of internal antennas. In this paper, we demonstrate that a GSM antenna designing internally inside the case of a wireless home security product has better performance after a copper strip is properly attached inside the case. The copper strip modifies the radiation pattern of GSM antenna, and further decreases the reflected EM wave by complex PCB environment from GSM antenna itself. That is, a simple reflection plane forming by copper strip reduces EMI (electromagnetic interference) for the GSM antenna [2, 3].

This internal GSM antenna is designed in form of on-board PIFA (printed inverted-F antenna) structure with the PCB of 2-layer FR4, 4.4 dielectric constant and 1.6 mm thickness [4–8], which can operate the frequency ranges of E-GSM 900 (880 MHz $\sim$ 960 MHz) and DCS 1800 (1710 MHz $\sim$ 1880 MHz) bandwidth. The passive performances (radiation efficiency, peak gain and pattern) and active performances (TRP/TIS, total radiation power/total isotropic sensitivity) of this GSM PIFA cooperating in a wireless home security product are measured by fast antenna measurement system, SATIMO. The details will be presented and discussed in the following sections.

2. DESIGN OF ON-BOARD GSM PIFA

In this work, a wireless module is designed for upgrading a wired home security system toward wireless system. For the purpose of easy-to-install for customers, an on-board GSM PIFA is designed and implemented on the RF module. The picture of wireless home security product, which is composed of RF module plugging into a wired home security deck, is shown in Fig. 1. The dimension of GSM PIFA is described in Fig. 2. In order to deal with the EMI problem, a copper strip is attached on the case to modify the radiation pattern, which is shown in the left down side of Fig. 1.

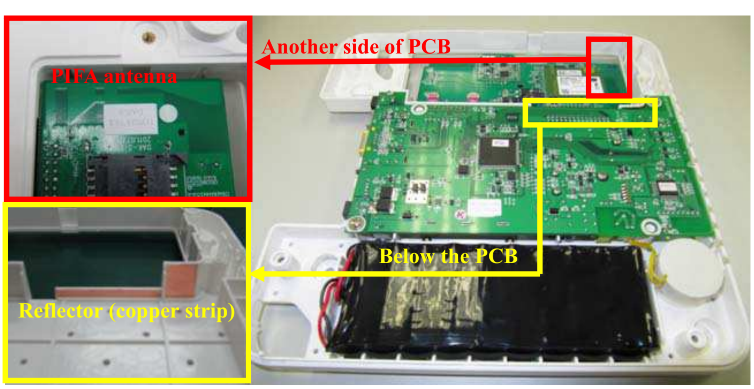

Figure 1: The GSM PIFA in a wireless home security product.

3. MEASUREMENT AND DISCUSSION

The measured return loss, radiation efficiency, peak gain, XY-cut 2D pattern, XZ-cut 2D pattern and YZ-cut 2D pattern of on-board GSM PIFA with/without copper strip are shown in Fig. 3,

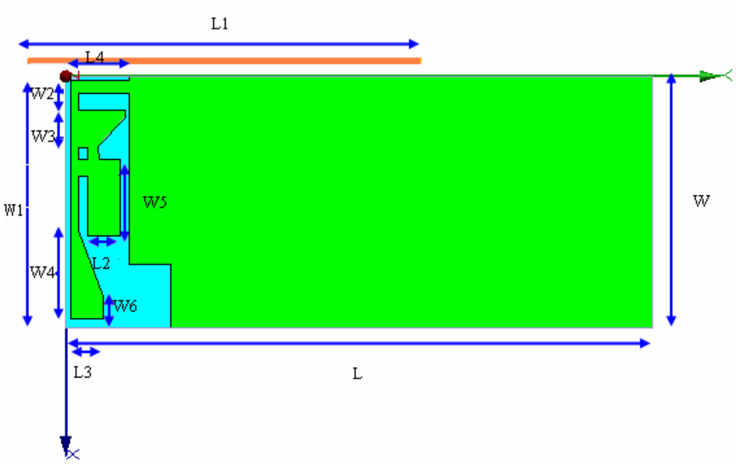

Name	W	W1	W2	W3	W4	W5	W6	L	L1	L2	L3	L4	H
Size	60	57	7	9	21	18	6	140	100	8	5	14	1.6
Unit	mm	mm	mm	mm	mm	mm	mm	mm	mm	mm	mm	mm	mm

Note: L1 is the length of copper strip.

Figure 2: The dimension of on-board GSM PIFA.

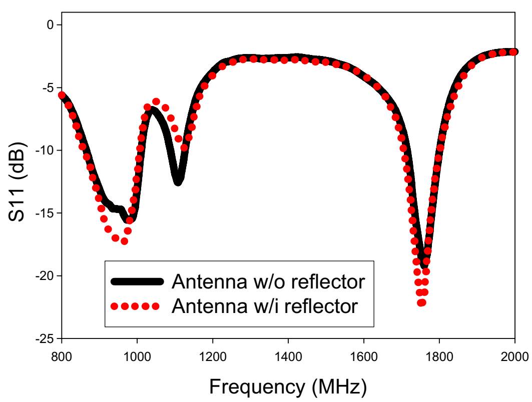

Figure 3: Measured S-parameter of on-board GSM PIFA.

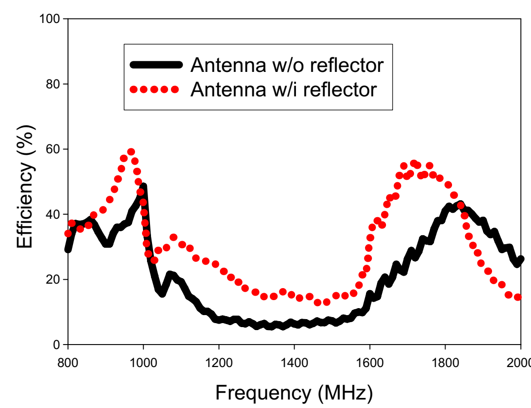

Figure 4: Measured radiation efficiency of on-board GSM PIFA.

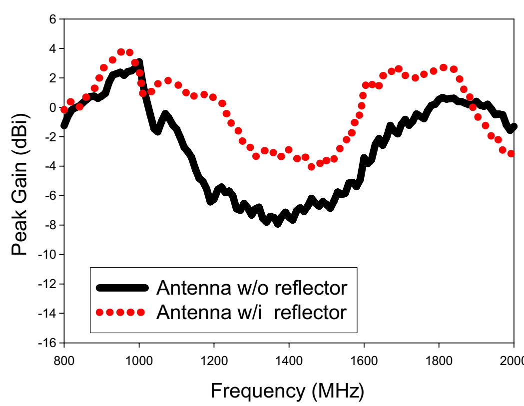

Figure 5: Measured peak gain of on-board GSM PIFA.

Fig. 4, Fig. 5, Fig. 6, Fig. 7 and Fig. 8, respectively. From those measured results, it can be observed that the GSM PIFA with/without copper strip performs almost the same return loss (S_{11}) but different radiation efficiency, peak gain and radiation pattern. Furthermore, the TRP/TIS showing in Fig. 9 and Fig. 10 reveal that the GSM PIFA with copper strip has much more compromised active results (TRP $\geqq$ 27 dBm and TIS $\geqq$ 100 dBm for E-GSM 900, TRP $\geqq$ 24 dBm and TIS $\geqq$ 100 dBm for DCS 1800) than that without copper strip, especially for TIS [9]. This is because the copper strip serves as a reflector for modifying the radiation pattern of GSM PIFA while the distant between copper strip and antenna is properly decided ($\sim \lambda/8$). Then the radiation pattern is concentrated in front of the reflector, isolating the EMI noise from PCB and eliminating EM wave

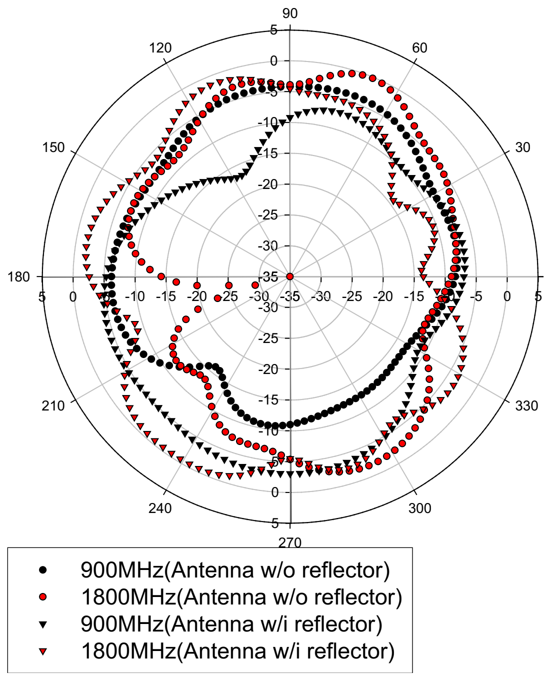

Figure 6: Measured XY-cut 2D pattern of on-board GSM PIFA.

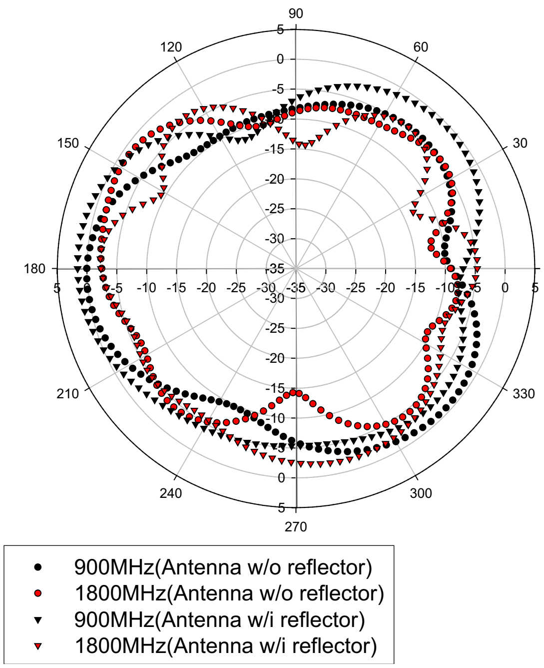

Figure 7: Measured XZ-cut 2D pattern of on-board GSM PIFA.

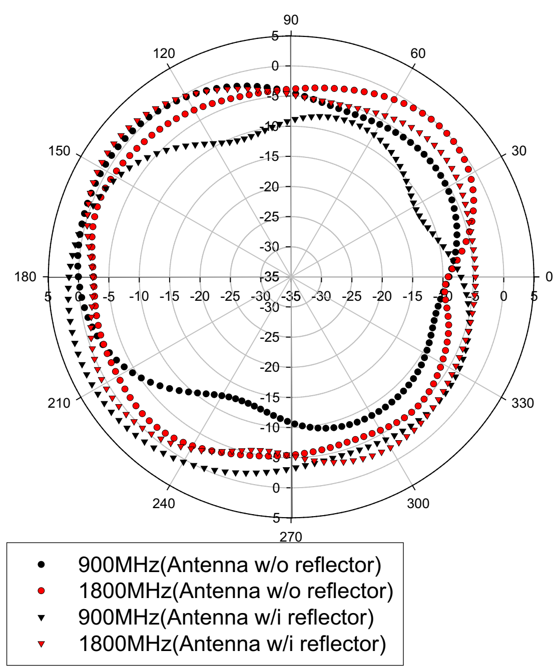

Figure 8: Measured YZ-cut 2D pattern of on-board GSM PIFA.

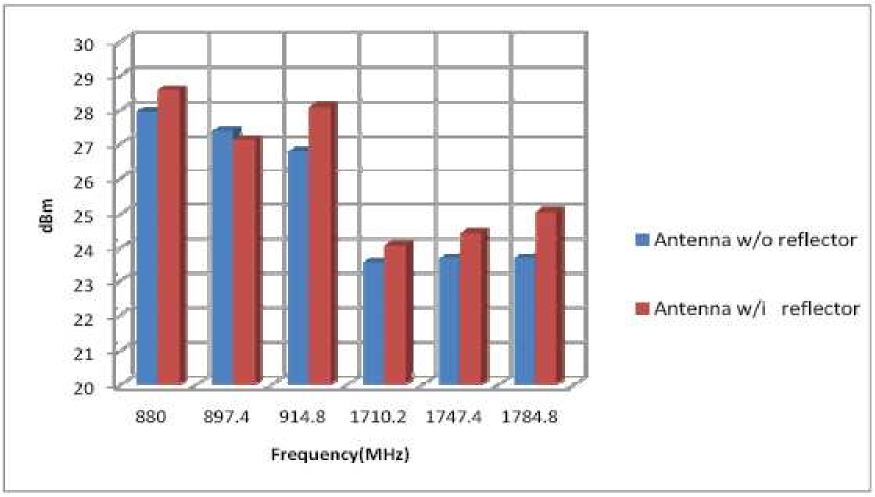

Figure 9: Measured TRP of the wireless home security product.

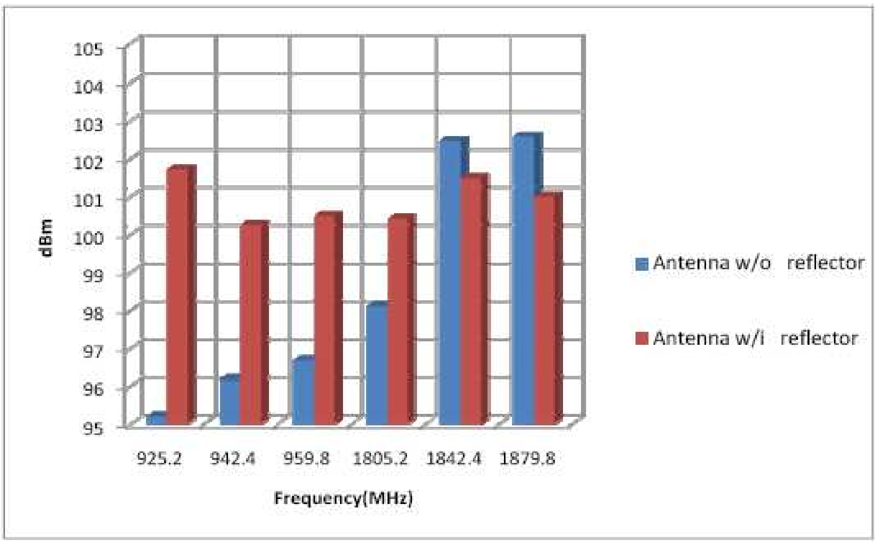

Figure 10: Measured TIS of the wireless home security product.

power reflected by complex PCB environment behind the reflector. This is the reason why the TIS can be substantially improved in E-GSM 900 band. Furthermore, TRP is generally enhanced during the frequency band of E-GSM 900 and DCS 1800.

4. CONCLUSION

The comprehensive measurement and comparison of on-board GSM PIFA with and without copper strip are presented. The passive measured results of GSM PIFA present that the radiation efficiency and peak gain can be obviously enhanced while the copper strip, i.e., reflector, is attached. Furthermore, the active measurement also verifies that the communication quality of this GSM-based wireless home system product is effectively improved while the reflector is attached. Those experiments reveal that the reflector made by a simple copper strip make great improvement in GSM wireless communication quality due to the isolation of EMI noise from PCB and modification of antenna pattern.

REFERENCES

1. GEMS, 3-D High Performance parallel EM simulation Software, www.2comu.com.
2. Wu, C.-F., "MC control and prevention," 2008.
3. Chen, Y.-Z. and R.-Y. Gu, "The study of measurement theorem and prevention over electromagnetic interference environment and RF noise," Da-Yeh University, 2005.

4. Lee, W.-S. and Y.-S. Chen, "900/1800 MHz dual-band ceramic chip antenna bandwidth improvement and equivalent circuit simulation and analysis," National Cheng Kung University, 2005.
5. Hung, W.-L., Design and study of small PIFA structures," 18–32, June 2007.
6. Chang, Y.-H., "Design of compact printed dual-band and ultra-wideband monopole antenna," 26–33, July 2008.
7. Lai, K.-C., "Design and measurement of ultra wide band antenna," 21–37, July 2008.
8. Chen, W.-S., "Studies of dual-band and broadband printed slot antennas," 57–69, January 2001.
9. Alpaslan, A., "Global test specification for terminals for performance measurements-performance TST-radiated performance VF_Ant_Req_V2.2," Vodafone Global.

Fast Adaptive Least Mean Square Algorithm

S. Maity, S. Dasgupta, and B. Gupta
Department of Electronics and Tele-Communication Engineering, Jadavpur University, Kolkata, India

Abstract— Least Mean Square (LMS) algorithm is probably the most widely used learning algorithm for its robustness, simplicity, low computational cost. Most of the adaptive learning algorithms including LMS suffer from its initial convergence rate when the no of input elements (N) is too large. In this paper, we use a modified form of LMS algorithm having an adaptive step size (μ) such that it will give a fast convergence irrespective of the no of input elements (N) with a typical limiting error of 10^{-10}.

1. INTRODUCTION

Adaptive algorithms such as Least Mean Square (LMS), Normalized LMS (NLMS), Recursive Least square (RLS), Differential Steepest Descent (DSD), Accelerated Gradient Approach etc., take many iterations to give satisfactory result when the number of input elements (N) is too large, because they suffer from slow initial convergence. Variable length LMS [1, 2] is also introduced to improve the initial convergence for $N = 2^p$ where p is any positive real integer. Our contribution in this paper is to get the desired output signal $\{d(n)\}$ within a very few iterations irrespective of N using variable step size (μ) [3]. Mean Square Error (MSE) is used to compute the step size. This algorithm can be used in adaptive beam forming systems to steer the beam of the resulting antenna or in any adaptive signal processing system. We can use this proposed algorithm for weight adjustment of any antenna or a system where the weights have to be found very fast.

2. LMS ALGORITHM AND NOTATION

Let the input vector $X(n) = [X_1(n), X_2(n), X_3(n) \ldots X_N(n)]$ and weight vector $W(n) = [W_1(n), W_2(n), W_3(n) \ldots W_N(n)]$ produce the signal $f(n) = W(n)X(n)^T$ as shown in Fig. 1. The weight vector $W(n)$ in computed iteratively using error signal $e(n)$ and noise signal $N'(n)$ as

$$\begin{cases} W(n+1) = W(n) + \Delta W(n) \\ \Delta W(n) = \mu e(n) X(n) \\ e(n) = d(n) - Y(n) \\ Y(n) = f(n) + \sum\limits_{M} N'(n) \end{cases} \tag{1}$$

where μ is learning rate, $Y(n)$ and $d(n)$ are output and desired signal respectively Equation (1) is convergent for $0 < \mu < 2/\lambda_{\max}$, where $\lambda_{\max}$ is the largest eigen-value of the input correlation matrix [3].

3. NEW ADAPTIVE ALGORITHM

In Variable Length LMS (VL-LMS) kth stage is implemented by merging two stages of $(k-1)$th stage such that $\mu_{k-1} > \mu_k$ [1]. But choose of $N = 2^p$ limits its applicability. In this algorithm to get the faster convergence rate we propose step size

$$\mu = A/g(N) \tag{2}$$

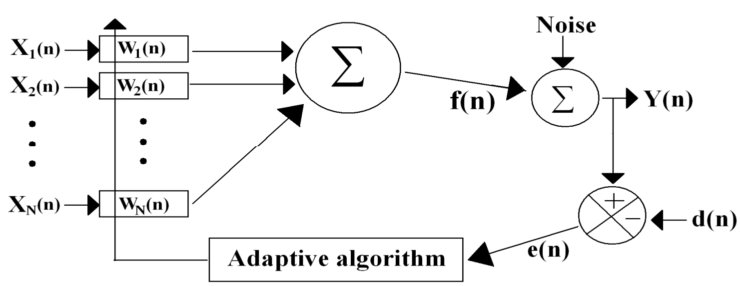

Figure 1: Block diagram of adaptive LMS algorithm.

where A is a constant and $g(N)$ is a polynomial of N of degree 1. We update $\mu(n)$ depending on the value of MSE as:

$$\begin{cases} \mu(n) = \mu(n-1) - \Delta\mu; & \text{for } MSE(n) > MSE(n-1) \\ \mu(n) = \mu(n-1) + \Delta\mu & \text{otherwise} \end{cases} \tag{3}$$

Same thing is also valid for $\sqrt{MSE}$ case.

3.1. Proposed Algorithm

1. Initialize randomly $X(n)$ and initialize desired output $d(n)$
2. Initialize $W(n) = 0$
3. Compute output $Y(n)$ and error $e(n)$
4. Update μ using (1)
5. Assign $\Delta\mu = \mu$
6. While ($MSE >$ limiting error)
   a. Compute $\Delta W(n)$
   b. Update $W(n)$
   c. Compute error $e(n)$ and MSE
   d. Update μ

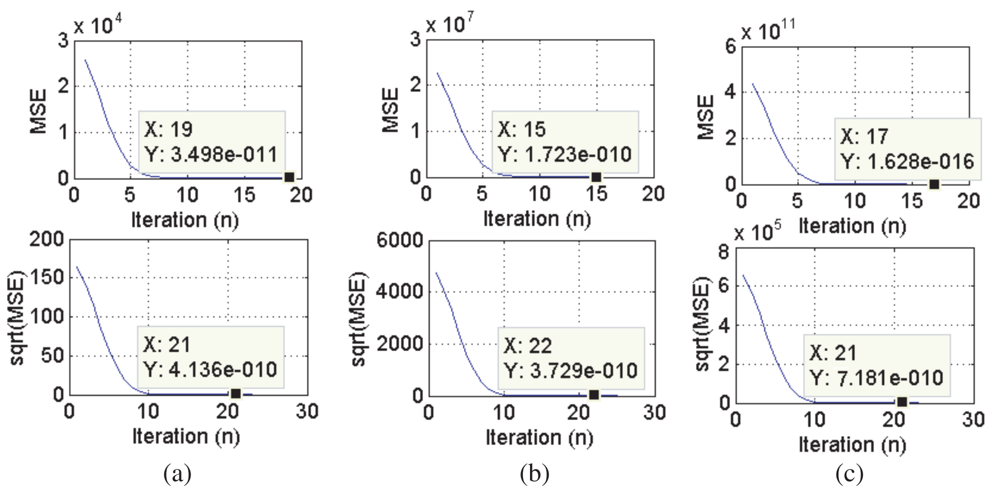

Figure 2: Error as a function of iteration for (a) $N = 247$, (b) $N = 7131$, (c) $N = 10^6$.

Table 1: comparison of MSE and $\sqrt{MSE}$ case.

No of input (N)	$MSE < 10^{-10}$	$\sqrt{MSE} < 10^{-10}$
12	77	21
64	68	24
247	21	23
1729	19	27
6825	16	26
23456	16	21
10^6	17	24
4×10^6	17	28

Table 2: Comparison of various existing algorithms and new algorithm.

Value of Mean Square Error $= E\{e(n)^2\}$ for $N = 32$					
***i*th Iteration**	***LMS* [1]**	***NLMS* [1]**	***VL-LMS* [1]**	***MSE as limit***	**$\sqrt{MSE}$ *as limit***
3	3.25	3.25	1	214	14.63
8	2.125	2.125	0.8875	0.704	0.839
12	2.016	2.016	0.8341	4.1×10^{-9}	2.8×10^{-2}
20	1.062	1.362	0.60625	8.92×10^{-9}	8.2×10^{-11}
50	0.6625	0.6625	0.4375	3.1×10^{6}	0
75	0.4375	0.4375	0.0381	4.9×10^{6}	0
80	0.325	0.325	0.0325	6.1×10^{-11}	0
250	3.25×10^{-3}	1.56×10^{-3}	4.375×10^{-4}	0	0
350	5.5×10^{-4}	4.23×10^{-4}	3.81×10^{-4}	0	0
380	3.81×10^{-4}	3.81×10^{-4}	3.81×10^{-4}	0	0
600	3.81×10^{-4}	3.81×10^{-4}	3.81×10^{-4}	0	0

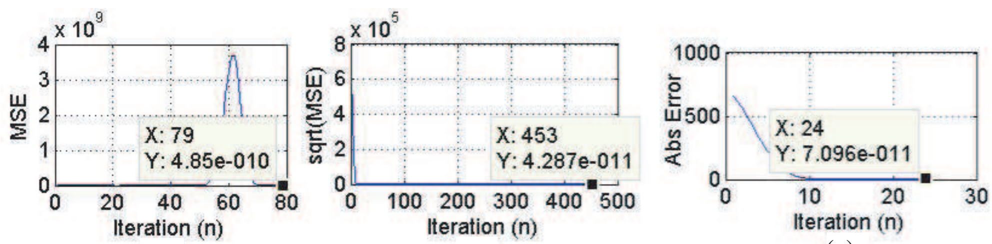

Figure 3: Plot of error vs iteration for (a) $N = 32$, (b) $N = 12345$, (c) $N = 10^6$.

4. RESULTS

To get fast convergence we found that $g(N) = N$ and $A = 0.1$ give satisfactory results than other form of polynomial. The limiting error is set to 10^{-10} using long format in MATLAB [4]. We have used MSE and $\sqrt{MSE}$ to compare it with limiting error and also to update the step size (μ). The results are shown in Fig. 2 and tabulated in Table 1.

5. CONCLUSION

In Multi Split LMS (MS LMS) [2] or VL-LMS [1], $N = 2^p$ where p is any positive integer and N is also small. The system takes a long time to give the desired result for large N [1–3]. We have simulated up to $N = 4 \times 10^6$. In our algorithm N drives the step size (μ) in such a way that we get the desired result within very few iteration irrespective of N. Due to memory limitation we could not simulate this when N exceeds 4×10^6 but it will give the same faster convergence if we are able to make these simulations possible by providing sufficient memory for the case when N is greater than 4×10^6.

The starting error for MSE case is much larger than $\sqrt{MSE}$ case. Not only that, when N is small (probably $N < 200$) generally we get a spike having large amplitude in the MSE case as shown in Fig. 3(a). For medium N (probably $N < 500$) we may get that type of spike but ultimately we get the convergence very fast compared to VL-LMS, MS-LMS, RLS etc. Besides that, when N is large generally there is a possibility to get slow convergence for $\sqrt{MSE}$ case as shown in Fig. 3(b) but no of iteration $n \leq 500$ for any value of N. To solve this problem, $\sqrt{MSE}$ and MSE cases can be efficiently utilized as:

$$\begin{cases} \text{error} = \sqrt{MSE} & \text{for } N < 1000 \\ \text{error} = MSE & \text{otherwise} \end{cases} \tag{4}$$

In this new algorithm there is no constraint in choosing the value of N in contrast to the other methods such as VL-LMS, MS-LMS etc., the values of N can be an arbitrary number (even or odd) which is a salient feature of the proposed new algorithm.

Table 2 compares the approximated values of MSE obtained by using various existing algorithms [1] and the new algorithm. From Table 2 it is readily seen that for $N = 32$, LMS, NLMS, VL-LMS converge after 380th iteration but MSE and $\sqrt{\text{MSE}}$ take 80 and 20 no of iterations respectively. If we use the same algorithm by replacing $MSE = abs\{e(n)\}$ then it will be a new algorithm (different from LMS algorithm) which results in very fast convergence irrespective of the no of input elements (N) as shown in Fig. 3(c). Earlier works have been reported by taking limiting error in the order of 10^{-4} or 10^{-5}. But, here 10^{-10} is taken as limiting error. Hence our algorithm gives fast convergence for any positive real values of N.

REFERENCES

1. Nascimento, V. H., "Improving the initial convergence of adaptive filters: Variable-length LMS algorithm," *IEEE DSP, 14th International Conf. 2002*, Vol. 2, 667–670, 2002.
2. Souza, R. D., L. S. Resende, and M. G. Bellanger, "A justification for the improving performance of the multi-split LMS algorithm," *IEEE International Conf. on Acoustics, Speech, and Signal Processing*, Vol. 6, VI-89–92, 2003.
3. Haykin, S., *Adaptive Filter Theory*, Prentice Hall, 2002.
4. MATLAB-2010a, User's Reference, 2010.

Nonlinear Effects of Electromagnetic TM Wave Propagation in Anisotropic Layer with Kerr Nonlinearity

Yu. G. Smirnov and D. V. Valovik
Penza State University, 40 Krasnay Street, Penza 440026, Russia

Abstract— The problem of electromagnetic TM wave propagation through a layer with Kerr nonlinearity is considered. The layer is located between two half-spaces with constant permittivities. This electromagnetic problem is reduced to the nonlinear boundary eigenvalue problem for ordinary differential equations. It is necessary to find eigenvalues of the problem (propagation constants of an electromagnetic wave). The dispersion equation (DE) for the eigenvalues is derived. The DE is applied to nonlinear media simulating nonlinear metamaterials. Comparison with a linear case is made. In the nonlinear problem new propagating waves are discovered. Numerical results are presented.

1. INTRODUCTION

Problems of electromagnetic wave propagation in nonlinear waveguide structures are intensively investigated during several decades. Phenomena of electromagnetic wave propagation in nonlinear media have original importance and also find a lot of applications, for example, in plasma physics, microelectronics, optics, laser technology [1, 2].

2. STATEMENT OF THE PROBLEM

Let us consider electromagnetic wave propagation through a homogeneous anisotropic nonmagnetic dielectric layer. The layer is located between two half-spaces: $x < 0$ and $x > h$ in Cartesian coordinate system $Oxyz$. The half-spaces are filled with isotropic nonmagnetic media without any sources and characterized by permittivities ε_1 and ε_3, respectively. Assume that everywhere $\mu = \mu_0$ is the permeability of free space (see Figure 1).

The electromagnetic field ($\mathbf{E}$, $\mathbf{H}$) depends on time harmonically with circular frequency ω and satisfies the Maxwell equations

$$\mathrm{rot}\mathbf{H} = -i\omega\varepsilon\mathbf{E}, \quad \mathrm{rot}\mathbf{E} = i\omega\mu\mathbf{H}, \tag{1}$$

the continuity condition for the tangential field components on the media interfaces $x = 0$, $x = h$ and the radiation condition at infinity: the electromagnetic field exponentially decays as $|x| \to \infty$ in the domains $x < 0$ and $x > h$; where $\mathbf{E}$ and $\mathbf{H}$ are complex amplitudes.

The permittivity inside the layer is described by the diagonal 3×3-tensor $\hat{\varepsilon}$, where only diagonal elements ε_{xx}, ε_{yy}, and ε_{zz} are not equal to zero: $\varepsilon_{xx} = \varepsilon_{2x} + b|E_x|^2 + a|E_z|^2$, $\varepsilon_{zz} = \varepsilon_{2z} + a|E_x|^2 + b|E_z|^2$; and a, b, ε_1, ε_2, ε_3 are real numbers. It does not matter what a form ε_{yy} has. Since ε_{yy} is not contained in the equations below for the TM case. It should be noticed that $\hat{\varepsilon}$ describes tensor Kerr nonlinearity. When $a = b$ we obtain scalar Kerr nonlinearity. Chosen nonlinearity satisfies the condition $\frac{\partial \varepsilon xx}{\partial E_z^2} = \frac{\partial \varepsilon zz}{\partial E_x^2}$. This equation is satisfied by almost every known nonlinear Kerr mechanism, such as electronic distortion, molecular orientation, electrostriction, and Kerr nonlinearities described within the uniaxial approximation is said in the paper [3]. The case when $\varepsilon_{2x} = \varepsilon_{2z}$ is studied in [4].

The solutions to the Maxwell equations are sought in the entire space.

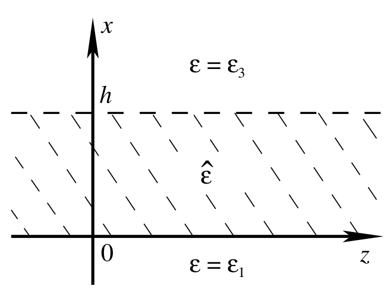

Figure 1. The geometry of the problem.

3. TM-WAVES

Let us consider TM waves $\mathbf{E} = (E_x, 0, E_z)^T$, $\mathbf{H} = (0, H_y, 0)^T$ and E_x, E_z, H_y are functions of three spatial variables. It is easy to show that the components of the fields do not depend on y. Waves propagating along medium interface z depend on z harmonically. This means that the fields components have the form $E_x = E_x(x)e^{i\gamma z}$, $E_z = E_z(x)e^{i\gamma z}$, $H_y = H_y(x)e^{i\gamma z}$, where γ is the spectral parameter of the problem (propagation constant).

So we can derive from system (1) [5]

$$\gamma(iE_x(x))' - E_z''(x) = \omega^2\mu\varepsilon_{zz}E_z(x), \quad \gamma^2(iE_x(x)) - \gamma E_z'(x) = \omega^2\mu\varepsilon_{xx}(iE_x(x)). \tag{2}$$

Let us denote by $k_0^2 := \omega^2\mu_0\varepsilon_0$ and perform the normalization according to the formulas $\tilde{x} = k_0 x$, $\frac{d}{dx} = k_0\frac{d}{d\tilde{x}}$, $\tilde{\gamma} = \frac{\gamma}{k_0}$, $\tilde{\varepsilon}_j = \frac{\varepsilon_j}{\varepsilon_0}$ $(j = 1,\ 2,\ 3)$, $\tilde{a} = \frac{a}{\varepsilon_0}$, $\tilde{b} = \frac{b}{\varepsilon_0}$. Denoting by $Z(\tilde{x}) := E_z$, $X(\tilde{x}) := iE_x$ and omitting the tilde symbol, from system (2) we obtain

$$-Z'' + \gamma X' = \varepsilon_{zz}Z, \quad -Z' + \gamma X = \gamma^{-1}\varepsilon_{xx}X. \tag{3}$$

It is necessary to find eigenvalues γ of the problem that correspond to surface waves propagating along boundaries of the layer $0 < x < h$. We seek the real values of the spectral parameter γ such that real solutions $X(x)$ and $Z(x)$ to system (3) exist[1].

Functions X, Z are supposed to be sufficiently smooth due to physical nature of the problem

$$X(x) \in C\left(-\infty,\ 0\right] \cap C[0,h] \cap C\left[h,\ +\infty\right) \cap C^1\left(-\infty,\ 0\right] \cap C^1[0,h] \cap C^1\left[h,\ +\infty\right);$$
$$Z(x) \in C(-\infty,+\infty) \cap C^1\left(-\infty,\ 0\right] \cap C^1[0,h] \cap C^1\left[h,\ +\infty\right) \cap C^2(-\infty,0) \cap C^2(0,h) \cap C^2(h,+\infty).$$

4. DIFFERENTIAL EQUATIONS OF THE PROBLEM

For $x < 0$, in accordance with the condition at infinity we get from (3)

$$X(x) = Ae^{x\sqrt{\gamma^2-\varepsilon_1}}, \quad Z(x) = A\gamma^{-1}\sqrt{\gamma^2-\varepsilon_1}e^{x\sqrt{\gamma^2-\varepsilon_1}}. \tag{4}$$

For $x > h$, in accordance with the condition at infinity we get from (3)

$$X(x) = Be^{-(x-h)\sqrt{\gamma^2-\varepsilon_3}}, \quad Z(x) = -B\gamma^{-1}\sqrt{\gamma^2-\varepsilon_3}e^{-(x-h)\sqrt{\gamma^2-\varepsilon_3}} \tag{5}$$

We assume that $\gamma^2 > \varepsilon_1$, $\gamma^2 > \varepsilon_3$ otherwise it will be impossible to satisfy the radiation condition. The constant A is defined from the transmission conditions and B is supposed to be known (initial condition).

Inside the layer $0 < x < h$ system (3) can be rewritten in the normal form

$$\begin{cases} \dfrac{dX}{dx} = \dfrac{2a}{\gamma}\dfrac{\varepsilon_{2x} - \gamma^2 + bX^2 + aZ^2}{\varepsilon_{2x} + 3bX^2 + aZ^2}X^2Z + \gamma\dfrac{\varepsilon_{2z} + aX^2 + bZ^2}{\varepsilon_{2x} + 3bX^2 + aZ^2}Z, \\ \dfrac{dZ}{dx} = -\gamma^{-1}\left[\varepsilon_{2x} - \gamma^2 + bX^2 + aZ^2\right]X. \end{cases} \tag{6}$$

System (6) has the first integral. It can be written in the following form

$$\begin{aligned} C \ = \ & b^2X^6 + 2abX^4Z^2 + a^2X^2Z^4 + \frac{1}{2}\left(4\varepsilon_{2x} - 3\gamma^2\right)bX^4 + \left(2\varepsilon_{2x} - \gamma^2\right)aX^2Z^2 + \frac{1}{2}\gamma^2bZ^4 \\ & +\gamma^2\left(\varepsilon_{2x} - \gamma^2\right)X^2 + \left(\varepsilon_{2x} - \gamma^2\right)^2X^2 + \gamma^2\varepsilon_{2z}Z^2, \end{aligned} \tag{7}$$

where C is the constant of integration.

[1]Indeed, in this case $|\mathbf{E}|^2$ does not depend on z. Since $\mathbf{E} = (E_x(x)e^{i\gamma z}, 0, E_z(x)e^{i\gamma z}) = e^{i\gamma z}(E_x, 0, E_z)$; therefore, $|\mathbf{E}| = |e^{i\gamma z}| \cdot \sqrt{|E_x|^2 + |E_z|^2}$. It is known that $|e^{i\gamma z}| = 1$ as $\Im\gamma = 0$. Let $\gamma = \gamma' + i\gamma''$. Then, we obtain $|e^{i\gamma z}| = |e^{i\gamma' z}| \cdot |e^{-\gamma'' z}| = e^{-\gamma'' z}$. If $\gamma'' \neq 0$, then $e^{-\gamma'' z}$ is a function on z. In this case the components E_x and E_z depend on z, but it contradicts to the choice of $E_x(x)$ and $E_z(x)$. So we can consider only real values of γ.

5. TRANSMISSION CONDITIONS

Tangential components of electromagnetic field are known to be continuous at media interfaces. In this case the tangential components are H_y and E_z. It is known that normal components of electromagnetic field have a finite jump at the interface. In this case the normal component is E_x. It is also known that εE_x is continuous at the interface. From these conditions we obtain the transmission conditions for functions X, Z: $[\varepsilon X]_{x=0} = 0$, $[\varepsilon X]_{x=h} = 0$, $[Z]_{x=0} = 0$, $[Z]_{x=h} = 0$, where $[f]_{x=x_0} = \lim\limits_{x\to x_0-0} f(x) - \lim\limits_{x\to x_0+0} f(x)$ denotes a jump of the function f at the interface.

Let us denote by $X_0 := X(0+0)$, $X_h := X(h-0)$, $Z_0 := Z(0+0)$, and $Z_h := Z(h-0)$ boundary values of required functions X and Z at the interface inside the layer. From (4), (5) we obtain $X(0-0) = A$, $X(h+0) = B$, $Z(0-0) = A\gamma^{-1}\sqrt{\gamma^2 - \varepsilon_1}$, and $Z(h+0) = -B\gamma^{-1}\sqrt{\gamma^2 - \varepsilon_3}$. From transmission conditions we obtain $Z_0 = A\gamma^{-1}\sqrt{\gamma^2 - \varepsilon_1}$, $Z_h = -B\gamma^{-1}\sqrt{\gamma^2 - \varepsilon_3}$. The value X_h is defined from the cubic equation $[\varepsilon_{2x} + bX_h^2 + aZ_h^2]X_h = \varepsilon_3 B$.

Using first integral (7) at $x = h$, we find the value $C_h^X := C|_{x=h}$ from the equation

$$\begin{aligned} C_h^X \;=\; & b^2X_h^6 + 2abX_h^4Z_h^2 + a^2X_h^2Z_h^4 + 2^{-1}\left(4\varepsilon_{2x} - 3\gamma^2\right)bX_h^4 + \left(2\varepsilon_{2x} - \gamma^2\right)aX_h^2Z_h^2 \\ & + 2^{-1}\gamma^2 bZ_h^4 + \gamma^2\left(\varepsilon_{2x} - \gamma^2\right)X_h^2 + \left(\varepsilon_{2x} - \gamma^2\right)^2 X_h^2 + \gamma^2\varepsilon_{2z}Z_h^2. \end{aligned}$$

In order to find the values X_0 and Z_0 it is necessary to solve the following system

$$\begin{cases} \varepsilon_1 A = \left[\varepsilon_{2x} + bX_0^2 + aZ_0^2\right]X_0, \\ C_h^X = b^2X_0^6 + 2abX_0^4Z_0^2 + a^2X_0^2Z_0^4 + 2^{-1}\left(4\varepsilon_{2x} - 3\gamma^2\right)bX_0^4 + \left(2\varepsilon_{2x} - \gamma^2\right)aX_0^2Z_0^2 \\ \qquad + 2^{-1}\gamma^2 bZ_0^4 + \gamma^2\left(\varepsilon_{2x} - \gamma^2\right)X_0^2 + \left(\varepsilon_{2x} - \gamma^2\right)^2 X_0^2 + \gamma^2\varepsilon_{2z}Z_0^2. \end{cases}$$

6. DISPERSION EQUATION

Introduce the new variables $\tau(x) = \frac{\varepsilon_{2x} + bX^2(x) + aZ^2(x)}{\gamma^2}$, $\eta(x) = \gamma\frac{X(x)}{Z(x)}\tau(x)$. Using new variables rewrite system (6)

$$\begin{cases} \dfrac{d\tau}{dx} = 2\dfrac{\tau\eta\left(\gamma^2\tau - \varepsilon_{2x}\right)}{b\eta^2 + a\gamma^2\tau^2} \times \dfrac{\left(b\eta^2 + a\gamma^2\tau^2\right)\left(b\varepsilon_{2z} - a\gamma^2\tau(\tau-1)\right) + \left(a\eta^2 + b\gamma^2\tau^2\right)\left(\gamma^2\tau - \varepsilon_{2x}\right)}{\gamma^2\tau\left(b\eta^2 + a\gamma^2\tau^2\right) + 2b\eta^2\left(\gamma^2\tau - \varepsilon_{2x}\right)}, \\ \dfrac{d\eta}{dx} = \dfrac{\tau - 1}{\tau}\eta^2 + \varepsilon_{2z} + \left(\gamma^2\tau - \varepsilon_{2x}\right)\dfrac{a\eta^2 + b\gamma^2\tau^2}{b\eta^2 + a\gamma^2\tau^2}, \end{cases} \tag{8}$$

and Equation (7)

$$\begin{aligned} & \frac{\gamma^2\tau - \varepsilon_{2x}}{b\eta^2 + a\gamma^2\tau^2}\left[\eta^2\left((\gamma^2\tau - \varepsilon_{2x})^2 + \varepsilon_{2x}(\varepsilon_{2x} - \gamma^2)\right) + \gamma^4\varepsilon_{2z}\tau^2\right] \\ & + \frac{(\gamma^2\tau - \varepsilon_{2x})^2}{2(b\eta^2 + a\gamma^2\tau^2)^2}\left[(4\varepsilon_{2x} - 3\gamma^2)b\eta^4 + 2(2\varepsilon_{2x} - \gamma^2)a\gamma^2\tau^2\eta^2 + \gamma^6 b\tau^4\right] = C, \end{aligned} \tag{9}$$

where constant C is equal to the constant C in (7).

It is clear that $\eta(0) = \gamma\frac{X(0)}{Z(0)}\tau(0)$, $\eta(h) = \gamma\frac{X(h)}{Z(h)}\tau(h)$. Taking into account that $\gamma^2X(x)\tau(x) = \varepsilon X(x)$ it is easy to obtain that $\eta(0) = \varepsilon_1(\gamma^2 - \varepsilon_1)^{-1/2} > 0$, $\eta(h) = -\varepsilon_3(\gamma^2 - \varepsilon_3)^{-1/2} < 0$.

It is easy to see that the right-hand side of the second equation of system (8) is strictly positive if $\gamma^2 < \varepsilon_{2x}$, $a > 0$, $b > 0$, $\varepsilon_{2z} > 0$. This means that the function $\eta(x)$ monotonically increases on interval $(0,\ h)$. Taking into account $\eta(0)$ and $\eta(h)$ we obtain that the function $\eta(x)$ can not be differentiable on the entire interval $(0, h)$. This means that the function $\eta(x)$ has a break point. It is natural to suppose that the function $\eta(x)$ on interval $(0, h)$ has several break points x_0, x_1, $\ldots$, x_N. The properties of function $\eta(x)$ imply $\eta(x_i - 0) = +\infty$, $\eta(x_i + 0) = -\infty$, where $i = \overline{0, N}$.

Let $\frac{1}{w} := \frac{\tau-1}{\tau}\eta^2 + \varepsilon_{2z} + (\gamma^2\tau - \varepsilon_{2x})\frac{a\eta^2 + b\gamma^2\tau^2}{b\eta^2 + a\gamma^2\tau^2}$, where $w = w(\eta)$; $\tau = \tau(\eta)$ is expressed from the first integral. Taking into account our hypothesis we will seek to the solutions on each (semi)interval $[0\ ,x_0)$, $(x_0,\ x_1)$, $\ldots$, $(x_N\ ,h]$. Introduce the notation $T := \int_{-\infty}^{+\infty} w d\eta$. It can be proved that $0 < x_{i+1} - x_i = T < h$, where $i = \overline{0, N-1}$. This implies the convergence of the improper integral.

Finally we obtain

$$-\int_{\eta(h)}^{\eta(0)} w d\eta + (N+1)T = h, \quad \eta(0) = \varepsilon_1(\gamma^2 - \varepsilon_1)^{-1/2}, \quad \eta(h) = -\varepsilon_3(\gamma^2 - \varepsilon_3)^{-1/2}. \tag{10}$$

Expression (10) is the DE, which holds for any finite h. Let γ be a solution of DE (10) and an eigenvalue of the problem. Then, there are eigenfunctions X and Z, which correspond to the eigenvalue γ. The eigenfunction Z has $N+1$ zeros on the interval $(0, h)$.

It can be proved that the DE which holds for any real ε_{2x}, ε_{2z}, a, b has the form

$$-\int_{\eta(h)}^{\eta(0)} w d\eta \pm (N+1)T = h, \quad \eta(0) = \varepsilon_1\left(\gamma^2 - \varepsilon_1\right)^{-1/2}, \quad \eta(h) = -\varepsilon_3\left(\gamma^2 - \varepsilon_3\right)^{-1/2}. \tag{11}$$

It is necessary to stress that in (11) the value γ^2 can be greater than ε_{2x}.

Expression (11) is the DE, which holds for any finite h. It should be noticed that for every number $N+1$ it is necessary to solve two DEs: for $N+1$ and for $-(N+1)$.

Note 1. If there is a certain value γ_*^2, such that some of the integrals in DEs (10) or (11) diverge at certain inner points this simply means that the value γ_*^2 is not a solution of chosen DE and the value γ_*^2 is not an eigenvalue of the problem.

Note 2. It is necessary to emphasize that this boundary eigenvalue (transmission) problem essentially depends on the initial condition Z_h. The transmission problem for a linear layer does not depend on the initial condition.

Note 3. It is possible to pass to the limit in DEs (10) or (11) when $a = b$ as $a \to 0$. Classic DE for a linear layer results from this passage to the limit (see [4, 6, 7]).

7. NUMERICAL RESULTS

Dispersion curves (DC) calculated from Equation (11) are shown in Figures 2, 4.

In Figure 2, $\gamma(h)$ is plotted. The first few DCs are shown. Solid curves for the nonlinear case (solutions of Equation (11)); dashed curves for the linear case. The following parameters are used for both cases: $\varepsilon_1 = 1.44$, $\varepsilon_2 = 9$, $\varepsilon_3 = 1$, and for the nonlinear case $a = 0.1$, and $E_z^{(h)} = 1$. Dashed lines are described by formulas: $h^* = 3.206$ (thickness of the layer), $\gamma = 1.2$ (lower bound for γ), $\gamma = 3$ (upper bound for γ in the linear case).

As it is known and it is shown in Figure 2, the line $\gamma = 3$ is an asymptote for DCs in the linear case. It should be noticed that in the linear case there are no DCs in the region $\gamma^2 \geq \varepsilon_2$. It can be proved that function $h \equiv h(\gamma)$ defined from Equation (11) is continuous at the neighborhood $\gamma^2 = \varepsilon_2$ when $a \neq 0$ (see Figure 2). This is the important distinction between linear and nonlinear cases.

In Figure 2 for $h = 3.206$ in the case of a linear layer there are 3 eigenvalues (black dots where the line $h = 3.206$ intersects DCs). These eigenvalues correspond to 3 eigenmodes. In the case of a nonlinear layer in Figure 2 are shown 5 eigenvalues (uncolored dots). These eigenvalues correspond to 5 eigenmodes.

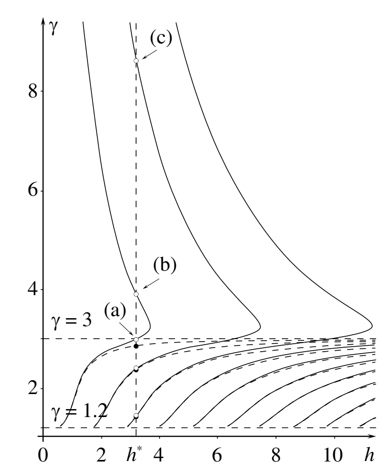

Figure 2.

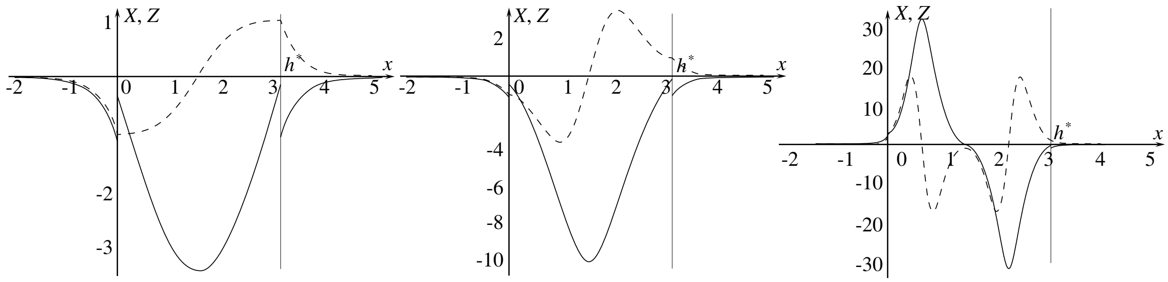

(a) (b) (c)

Figure 3.

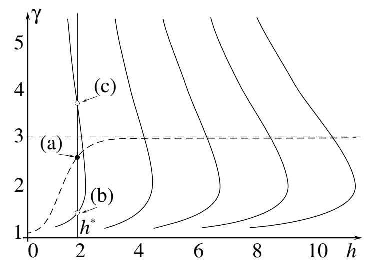

Figure 4.

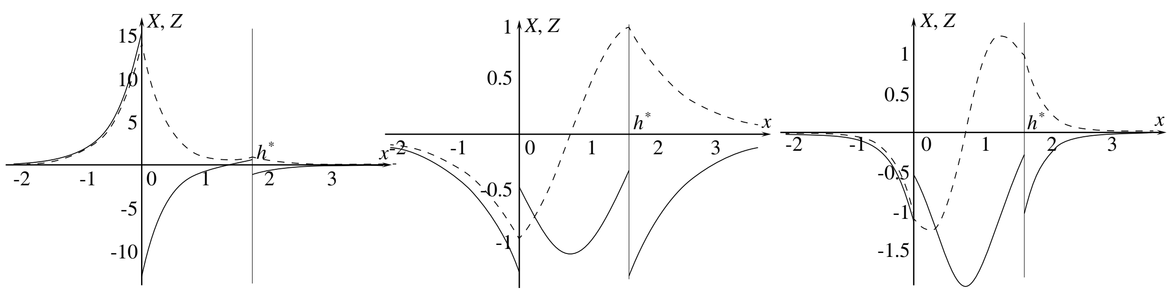

(a) (b) (c)

Figure 5.

It is easy to see in Figure 6 that the less nonlinearity coefficient a is the more stretched DCs in the nonlinear case. The maximum points of the curves $h(\gamma)$ (in Figure 6 they are marked by asterisks) move to the right. The parts of the DCs that locate below the maximum points asymptotically tend to the DCs for the linear case as $a \to 0$.

In Figure 3, eigenfunctions (fields) for the nonlinear problem are shown. Solid curves for X; dashed curves for Z. The same parameters as in Figure 2 are used. For (a): $\gamma = 2.994$; for (b): $\gamma = 3.892$: for (c): $\gamma = 8.657$, and $h = 3.206$ is used for all three cases. The eigenvalues are marked in Figure 2.

It should be noticed that in the case of Kerr nonlinearity in a layer and TE waves there are strong constraints on the value a depending on the value ε_2 (for details see [8]). It is naturally to suppose that there are some constraints in the case under consideration (see also [9, 10]).

As far as we know experiments to observe the new nonlinear eigenmodes were not carried out. So the question if the modes corresponding to the new eigenvalues exist (in an experiment) stays open!

In Figure 4 $\gamma(h)$ is plotted. The first few DCs are shown. Solid curves for the nonlinear case (solutions of Equation (11)); dashed curve for the linear case. The following parameters are used for both cases: $\varepsilon_1 = 1$, $\varepsilon_2 = -1.5$, $\varepsilon_3 = 1$, and for the nonlinear case $a = 5.2$, and $E_z^{(h)} = 1$. The line $h^* = 1.71$ is a thickness of the layer, $\gamma = 1$ is a lower bound for γ, $\gamma = 3$ is an upper bound for γ in the linear case.

In Figure 5 eigenfunctions (fields) for the nonlinear problem are shown (solid curves for X; dashed curves for Z). The same parameters as in Figure 4 are used. For (a): $\gamma = 2.620$, $a = 0$; for (b): $\gamma = 1.565$; for (c): $\gamma = 3.481$, and $h = 1.71$ is used for all three cases. The eigenvalues are marked in Figure 4.

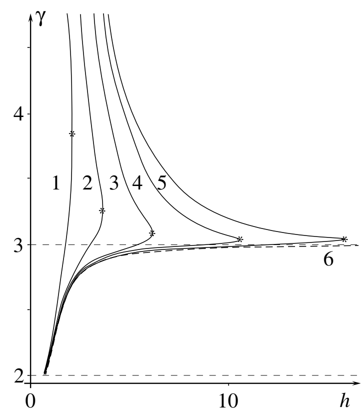

Figure 6.

In Figure 6 $\gamma(h)$ is plotted for different values a: $1-a=1$; $2-a=0.1$; $3-a=0.01$; $4-a=0.001$; $5-a=0.0001$; $6-a=0$ (linear case). The following parameters are used for both cases: $\varepsilon_1=4$, $\varepsilon_2=9$, $\varepsilon_3=1$, and for the nonlinear case $E_z^{(h)}=1$. Dashed lines are described by formulas: $\gamma=2$ (lower bound for γ), $\gamma=3$ (upper bound for γ in the case of linear medium in the layer). Curves (solid) 1–5 are solutions of Equation (11), and curve 6 (dashed) is the DC for the linear case.

ACKNOWLEDGMENT

This study was supported by the Russian Federation President Grant, project No. MK-2074.2011.1 and the Russian Foundation for Basic Research, project No. 11-07-00330-A.

REFERENCES

1. Akhmediev, N. N. and A. Ankevich, *Solitons, Nonlinear Pulses and Beams*, Chapman and Hall, London, 1997.
2. Boardman, A. D., et al., "Third-order nonlinear electromagnetics TE and TM guided waves," *Nonlinear Surface Electromagnetic Phenomena*, edited by H.-E. Ponath and G. I. stegeman, Elsevier Science Publishers B.V., 1991.
3. Joseph, R. I. and D. N. Christodoulides, *Opt. Lett.*, Vol. 12, 826, 1987.
4. Valovik, D. V. and Y. G. Smirnov, *J. Comm. Tech. Electron.*, Vol. 54, 411, 2009.
5. Eleonskii, P. N., L. G. Oganes'yants, and V. P. Silin, *Soviet Physics JETP*, Vol. 35, 44, 1972.
6. Valovik, D. V. and Y. G. Smirnov, *J. Comm. Tech. Electron.*, Vol. 53, 934, 2008.
7. Valovik, D. V. and Y. G. Smirnov, *Comp. Maths. Math. Phys.*, Vol. 48, 2186, 2008.
8. Valovik, D. V., *J. Comm. Tech. Electron.*, Vol. 56, 587, 2011.
9. Valovik, D. V. and Y. G. Smirnov, *J. Comm. Tech. Electron.*, Vol. 56, 309, 2011.
10. Valovik, D. V., *J. Comm. Tech. Electron.*, Vol. 56, 1329, 2011.

Electromagnetic TM Wave Propagation through a Nonlinear Metamaterial Layer with Arbitrary Nonlinearity

D. V. Valovik
Penza State University, 40 Krasnay Street, Penza 440026, Russia

Abstract— Propagation of TM wave through a nonlinear layer is considered. The problem for Maxwell's equations is reduced to a nonlinear boundary eigenvalue problem. Dispersion equation (DE) for propagation constants is derived. The DE can be used for analytical and numerical study of the problem. Some numerical results are also presented.

1. INTRODUCTION

Problems of electromagnetic waves propagation in nonlinear waveguide structures are intensively investigated during last decades. The article [1] is the first one, where the problems of electromagnetic waves propagation in a layer and a circular cylindrical waveguide with Kerr nonlinearities are considered in strict electromagnetic statement. At least from 1970-th till now these problems attract attention (for bibliography see [2–5]). The problems of propagation TE and TM waves in layers with Kerr nonlinearity have been solved in [2, 3], respectively. Then, in [6] the problem of TE wave propagation in a metamaterial layer with Kerr nonlinearity is considered and many numerical results are also presented. The articles [3–8] are devoted to the studies of TM waves in nonlinear layers also for nonlinear metamaterials.

2. MAXWELL EQUATIONS AND STATEMENT OF THE PROBLEM

Let us consider electromagnetic waves propagating through a homogeneous isotropic nonmagnetic dielectric layer. The layer is located between two half-spaces: $x < 0$ and $x > h$ in Cartesian coordinate system $Oxyz$. The half-spaces are filled with isotropic nonmagnetic media without any sources and characterized by permittivities $\varepsilon_1 \geq \varepsilon_0$ and $\varepsilon_3 \geq \varepsilon_0$, respectively, where ε_0 is the permittivity of free space. Assume that everywhere $\mu = \mu_0$ is the permeability of free space.

Electromagnetic field harmonically depends on time [1]: $\tilde{\mathbf{E}}(x, y, z, t) = \mathbf{E}_+ \cos\omega t + \mathbf{E}_- \sin\omega t$, $\tilde{\mathbf{H}}(x, y, z, t) = \mathbf{H}_+ \cos\omega t + \mathbf{H}_- \sin\omega t$, where ω is the circular frequency; $\mathbf{E}_+$, $\mathbf{E}_-$, $\mathbf{H}_+$, $\mathbf{H}_-$ are real functions of three spatial variables. Below the time multipliers are omitted. Expressions $\mathbf{E} = \mathbf{E}_+ + i\mathbf{E}_-$, $\mathbf{H} = \mathbf{H}_+ + i\mathbf{H}_-$ are complex amplitudes and $\mathbf{E} = (E_x, E_y, E_z)^T$, $\mathbf{H} = (H_x, H_y, H_z)^T$.

Electromagnetic field $(\mathbf{E}, \mathbf{H})$ satisfies Maxwell equations

$$\operatorname{rot}\mathbf{H} = -i\omega\tilde{\varepsilon}\mathbf{E}, \quad \operatorname{rot}\mathbf{E} = i\omega\mu\mathbf{H},$$

the continuity condition for the tangential field components on the media interfaces $x = 0$, $x = h$ and the radiation condition at infinity: the electromagnetic field exponentially decays as $|x| \to \infty$ in the domains $x < 0$ and $x > h$.

The permittivity inside the layer is described by the diagonal tensor

$$\tilde{\varepsilon} = \begin{pmatrix} \varepsilon_{xx} & 0 & 0 \\ 0 & \varepsilon_{yy} & 0 \\ 0 & 0 & \varepsilon_{zz} \end{pmatrix},$$

where $\varepsilon_{xx} = \varepsilon_f + \varepsilon_0 f\left(|E_x|^2, |E_z|^2\right)$, $\varepsilon_{zz} = \varepsilon_g + \varepsilon_0 g\left(|E_x|^2, |E_z|^2\right)$.

In the case of TM waves it does not matter what a form ε_{yy} has. As for TM waves the value ε_{yy} is not contained in the equations below.

It is assumed that $\varepsilon_f > \max(\varepsilon_1, \varepsilon_3)$, $\varepsilon_g > \max(\varepsilon_1, \varepsilon_3)$ are constants parts of the permittivity $\tilde{\varepsilon}$. The functions f, g are analytical[1] and such that the relation $\frac{\partial f}{\partial\left(|E_z|^2\right)} = \frac{\partial g}{\partial\left(|E_x|^2\right)}$ is satisfied (this relation yields the total differential equation) [4].

The solutions to the Maxwell equations are sought in the entire space.

[1]Everywhere below when we consider an analytical function we mean that it is the analytical function of real variable.

3. TM WAVE

Let us consider TM wave: $\mathbf{E}=(E_x,0,E_z)^T$, $\mathbf{H}=(0,H_y,0)^T$, where $E_x=E_x(x,y,z)$, $E_z=E_z(x,y,z)$, and $H_y=H_y(x,y,z)$. It is easy to prove that components of the electromagnetic field do not depend on y. Waves propagating along medium interface z depend on z harmonically. This means that the fields components have the form $E_x=E_x(x)e^{i\gamma z}$, $E_z=E_z(x)e^{i\gamma z}$, $H_y=H_y(x)e^{i\gamma z}$, where γ is the propagation constant (the spectral parameter of the problem).

Substitute the latter into the Maxwell equations, normalize according to the formulae $\tilde{x}=k_0x$, $\frac{d}{dx}=k_0\frac{d}{d\tilde{x}}$, $\tilde{\gamma}=\frac{\gamma}{k_0}$, $\tilde{\varepsilon}_i=\frac{\varepsilon_i}{\varepsilon_0}$ $(i=1,2)$, $\tilde{\varepsilon}_f=\frac{\varepsilon_f}{\varepsilon_0}$, $\tilde{\varepsilon}_g=\frac{\varepsilon_g}{\varepsilon_0}$, where $k_0^2:=\omega^2\mu_0\varepsilon_0$, denote by $Z(\tilde{x}):=E_z$, $X(\tilde{x}):=iE_x$ and omit the tilde symbol, we obtain

$$-\frac{d^2Z}{dx^2}+\gamma\frac{dX}{dx}=\varepsilon_{zz}Z,\quad -\frac{dZ}{dx}+\gamma X=\frac{1}{\gamma}\varepsilon_{xx}X. \tag{1}$$

It is necessary to find eigenvalues γ of the problem that correspond to surface waves propagating along boundaries of the layer $0<x<h$, i.e., the eigenvalues corresponding to the eigenmodes of the structure. We seek the real values of spectral parameter γ such that real solutions $X(x)$ and $Z(x)$ to system (1) exist[2]. Also we assume that $\max(\varepsilon_1,\varepsilon_3)<\gamma^2<\varepsilon_f$. This two-sided inequality naturally appears for an analogous problem in a layer with constant permittivity tensor.

Also we assume that functions X and Z are sufficiently smooth

$$X(x)\in C\,(-\infty,\ 0]\cap C[0,h]\cap C\,[h,\ +\infty)\cap C^1\,(-\infty,\ 0]\cap C^1[0,h]\cap C^1\,[h,\ +\infty)\,;$$
$$Z(x)\in C(-\infty,+\infty)\cap C^1\,(-\infty,\ 0]\cap C^1[0,h]\cap C^1\,[h,\ +\infty)\cap C^2(-\infty,0)\cap C^2(0,h)\cap C^2(h,+\infty).$$

Physical nature of the problem implies these conditions.

It is clear that system (1) is an autonomous one. System (1) can be rewritten in a normal form (it will be done below). This system in the normal form can be considered as a dynamical system with analytical with respect to X and Z right-hand sides (of course, in the domain where these right-hand sides are analytical with respect to X and Z). It is known [9] that the solution X and Z of such a system are analytical functions with respect to independent variable as well.

System (1) is the system for the anisotropic layer. Systems for the half-spaces can be easily obtained from system (1). For this purpose in system (1) it is necessary to put $\varepsilon_{xx}=\varepsilon_{zz}=\varepsilon$, where ε is the permittivity of the isotropic half-space.

4. SOLVING THE SYSTEM OF DIFFERENTIAL EQUATIONS

In the half-spaces $x<0$ and $x>h$ the permittivity $\tilde{\varepsilon}$ is a constant: ε_1 or ε_3 respectively. Taking it into account for system (1) in both cases one obtains systems of linear differential equations.

In the domains $x<0$ and $x>h$ solutions of system (1) are

$$X(x)=A\exp\left(x\sqrt{\gamma^2-\varepsilon_1}\right),\qquad Z(x)=\gamma^{-1}\sqrt{\gamma^2-\varepsilon_1}A\exp\left(x\sqrt{\gamma^2-\varepsilon_1}\right), \tag{2}$$

$$X(x)=B\exp\left(-(x-h)\sqrt{\gamma^2-\varepsilon_3}\right),\quad Z(x)=-\gamma^{-1}\sqrt{\gamma^2-\varepsilon_3}B\exp\left(-(x-h)\sqrt{\gamma^2-\varepsilon_3}\right), \tag{3}$$

respectively, where condition at infinity is taken into account; and $\gamma^2-\varepsilon_1>0$, $\gamma^2-\varepsilon_3>0$. Constants A and B in (2) and (3) are defined by transmission conditions and initial conditions.

Inside the layer $0<x<h$ system (1) takes the form

$$-\frac{d^2Z}{dx^2}+\gamma\frac{dX}{dx}=(\varepsilon_g+g)Z,\quad -\frac{dZ}{dx}+\gamma X=\frac{1}{\gamma}(\varepsilon_f+f)X, \tag{4}$$

further the arguments of the functions f and g are omitted (if there is no misunderstanding).

System (4) can be rewritten in the form

$$\frac{dX}{dx}=\frac{\gamma^2(\varepsilon_g+g)+2(\varepsilon_f-\gamma^2+f)X^2f'_v}{\gamma\left(2X^2f'_u+\varepsilon_f+f\right)}Z,\quad \frac{dZ}{dx}=\frac{1}{\gamma}(\gamma^2-\varepsilon_f-f)X, \tag{5}$$

[2]In this case $|\mathbf{E}|^2$ does not depend on z. Since $\mathbf{E}=(E_x(x)e^{i\gamma z},0,E_z(x)e^{i\gamma z})=e^{i\gamma z}(E_x,0,E_z)$; therefore, $|\mathbf{E}|=|e^{i\gamma z}|\cdot\sqrt{E_x^2+E_z^2}$. It is known that $|e^{i\gamma z}|=1$ as $\mathrm{Im}\gamma=0$. Let $\gamma=\gamma'+i\gamma''$. Then, we obtain $|e^{i\gamma z}|=|e^{i\gamma' z}|\cdot|e^{-\gamma'' z}|=e^{-\gamma'' z}$. If $\gamma''\neq 0$, then $e^{-\gamma'' z}$ is a function on z. In this case the components E_x, E_z depend on z, but it contradicts to the choice of $E_x(x)$ and $E_z(x)$. So we can consider only real values of γ.

where $f'_u := \left.\frac{\partial f(u,Z^2)}{\partial u}\right|_{u=X^2}$, $f'_v := \left.\frac{\partial f(X^2,v)}{\partial v}\right|_{v=Z^2}$ (further these derivatives are understood in this sense, while the other sense will not be pointed out).

Dividing the first equation in system (5) to the second one we obtain the ordinary differential equation

$$\left(2X^2 f'_u + \varepsilon_f + f\right)\frac{dX}{dZ} = \frac{\gamma^2(\varepsilon_g + g)Z + 2(\varepsilon_f - \gamma^2 + f)X^2 Z f'_v}{(\gamma^2 - \varepsilon_f - f)X}. \tag{6}$$

Equation (6) can be integrated (the equation can be transformed into a total differential equation) and the integral has the form

$$X^2\left(\varepsilon_f - \gamma^2 + f\right)^2 + \gamma^2\left(\left(\varepsilon_f - \gamma^2\right)X^2 + \varepsilon_g Z^2\right) + \gamma^2 G \equiv C, \tag{7}$$

where $G = G\left(X^2, Z^2\right) \equiv \int g\left(X^2, s\right) ds\big|_{s=Z^2}$ and C is a constant of integration.

5. TRANSMISSION CONDITIONS

Tangential components of an electromagnetic field are known to be continuous at media interfaces. In this case the tangential components are H_y and E_z. Normal components of an electromagnetic field are known to have a finite jump at media interfaces. In this case the normal component is E_x. It is also known that εE_x is continuous at media interfaces. From these conditions we obtain conjugation condition for functions X and Z

$$[\varepsilon X]_{x=0} = 0, \ \ [\varepsilon X]_{x=h} = 0, \ \ [Z]_{x=0} = 0, \ \ [Z]_{x=h} = 0, \tag{8}$$

where $[f]_{x=x_0} = \lim\limits_{x\to x_0-0} f(x) - \lim\limits_{x\to x_0+0} f(x)$.

Denote by $X_0 := X(0+0)$, $X_h := X(h-0)$, $Z_0 := Z(0+0)$, $Z_h := Z(h-0)$. Formulae (8) imply that $Z_0 = Z(0-0)$, $Z_h = Z(h+0)$. The constant $Z(h+0)$ is supposed to be known (initial condition). So we obtain that $A = \frac{\gamma}{\sqrt{\gamma^2-\varepsilon_1}}Z_0$, $B = \frac{\gamma}{\sqrt{\gamma^2-\varepsilon_3}}Z_h$.

Then for $x = h$ we obtain from (8) the equation on X_h

$$-Z_h\gamma\varepsilon_3(\gamma^2 - \varepsilon_3)^{-1/2} = \left(\varepsilon_f + f(X_h^2, Z_h^2)\right)X_h. \tag{9}$$

If $Z_h > 0$ (we assume it), then, as it is easy to see from (9), $X_h < 0$ (if $\varepsilon_{xx} > 0$).

Denote by $f_h := f(X_h^2, Z_h^2)$ and $G_h := G(X_h^2, Z_h^2)$. Then, using first integral (7), substituting $x = h$, we find the value $C_h := C|_{x=h}$:

$$C_h = X_h^2\left(\varepsilon_f - \gamma^2 + f_h\right)^2 + \gamma^2\left(\left(\varepsilon_f - \gamma^2\right)X_h^2 + \varepsilon_g Z_h^2\right) + G_h. \tag{10}$$

In order to find the values X_0 and Z_0 it is necessary to solve the following system:

$$\begin{cases} \frac{\gamma\varepsilon_1}{\sqrt{\gamma^2-\varepsilon_1}}Z_0 = \left(\varepsilon_f + f_0\right)X_0; \\ \left(\varepsilon_f - \gamma^2 + f_0\right)^2 X_0^2 + \gamma^2\left(\left(\varepsilon_f - \gamma^2\right)X_0^2 + \varepsilon_g Z_0^2\right) + G_0 = C_h, \end{cases} \tag{11}$$

where $f_0 = f\left(X_0^2, Z_0^2\right)$ and $G_0 = G\left(X_0^2, Z_0^2\right)$.

System (11) is obtained by using formula (6) at $x = 0$ and first integral (5) at $x = 0$.

It is easy to see from the second equation of system (11) that the values X_0 and Z_0 can have arbitrary signs. At the same time from the first equation of system (11) we can see that X_0 and Z_0 must be positive or negative simultaneously (here the condition $\varepsilon_{xx} > 0$ is used).

6. DISPERSION EQUATION

Introduce the new variable η instead of X: $X(x) = \eta(x)Z(x)$. Perhaps in every particular case it is better to choose new variables in another way. We also assume that here and further $f \equiv f\left(\eta^2 Z^2, Z^2\right)$, $g \equiv g\left(\eta^2 Z^2, Z^2\right)$. Using this new notation system (2) takes the form

$$\frac{dZ}{dx} = \gamma^{-1}\left(\gamma^2 - \varepsilon_f - f\right)\eta Z, \quad \frac{d\eta}{dx} = \gamma^{-1}\left(\chi + (\varepsilon_f - \gamma^2 + f)\eta^2\right). \tag{12}$$

where $\chi = \frac{\gamma^2(\varepsilon_g+g)+2(\varepsilon_f-\gamma^2+f)\eta^2 Z^2 f'_v}{(2\eta^2 Z^2 f'_u+\varepsilon_f+f)}$; here and further $f'_u = \left.\frac{\partial f(u,v)}{\partial u}\right|_{(\eta^2Z^2,Z^2)}$, $f'_v = \left.\frac{\partial f(u,v)}{\partial v}\right|_{(\eta^2Z^2,Z^2)}$.

First integral (6) takes the form

$$Z^2\left[(\varepsilon_f-\gamma^2+f)^2\eta^2+\gamma^2\left(\varepsilon_g+(\varepsilon_f-\gamma^2)\eta^2\right)\right]+G\left(\eta^2Z^2,Z^2\right)\equiv C. \tag{13}$$

Equation (13), in general, is a transcendental equation with respect to X, η. Its solution with respect to a certain variable (X or η) can be analytically expressed only in exceptional cases.

The functions f and g are assumed such that the right-hand side of the second equation in system (12) is positive. On the face of it, this condition seems too rigid. However it is not so. For example, if f and g are polynomials with positive coefficients, then this condition is satisfied. It is necessary to remember that the condition $\frac{\partial f}{\partial\left(|E_z|^2\right)}=\frac{\partial g}{\partial\left(|E_x|^2\right)}$ constrains the forms of the polynomials f and g.

Now it is possible to find the signs of the values $\eta(0)$ and $\eta(h)$. One can see from system (10) that the values X_0 and Z_0 either positive or negative simultaneously. At the same time, from formula (8) it is clear that the values X_h and Z_h have opposite signs. Taking it into account we obtain

$$\eta(0)=\frac{X_0}{Z_0}>0 \quad\text{and}\quad \eta(h)=\frac{X_h}{Z_h}<0 \tag{14}$$

and here X_0 and Z_0 can be found from system (10).

So the right-hand side of the second equation in system (12) is strictly positive. This means that the function $\eta(x)$ strictly increases on interval $(0,h)$. Taking into account (14) we obtain that the function $\eta(x)$ can not be differentiable on the entire interval $(0,h)$. This means that the function $\eta(x)$ has a break point.

Since the solutions X and Z of system (2) are analytical functions; therefore, the function η has only discontinuities of the second kind. And the points where the function Z vanishes are these discontinuities. Let the function η have a discontinuity at the point $x^*\in(0,h)$. It is obvious that in this case $\eta\left(x^*-0\right)\to+\infty$ and $\eta\left(x^*+0\right)\to-\infty$.

It is natural to suppose that the function $\eta(x)$ on interval $(0,h)$ has several break points $x_0,\ x_1,\ \dots,\ x_N$. The properties of function $\eta(x)$ imply $\eta(x_i-0)=+\infty$, $\eta(x_i+0)=-\infty$, where $i=\overline{0,N}$. Denote by $w:=\gamma\left(\chi+(\varepsilon_f-\gamma^2+f)\eta^2\right)^{-1}$, where $w=w(\eta)$; $Z=Z(\eta)$ is expressed from first integral (13); and χ is defined earlier.

One can prove that the DE has the form

$$-\int_{\eta(h)}^{\eta(0)}wd\eta+(N+1)T=h, \tag{15}$$

where $\eta(0)$, $\eta(h)$ are defined by formulas (14), $T:=\int_{-\infty}^{+\infty}wd\eta$.

Expression (15) is the DE, which holds for any finite h. Let γ be a solution of DE (15) and an eigenvalue of the problem. Then, there are eigenfunctions X and Z, which correspond to the eigenvalue γ. The eigenfunction Z has $N+1$ zeros on the interval $(0,h)$.

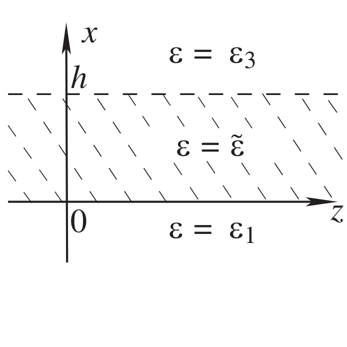

Figure 1: The geometry of the problem.

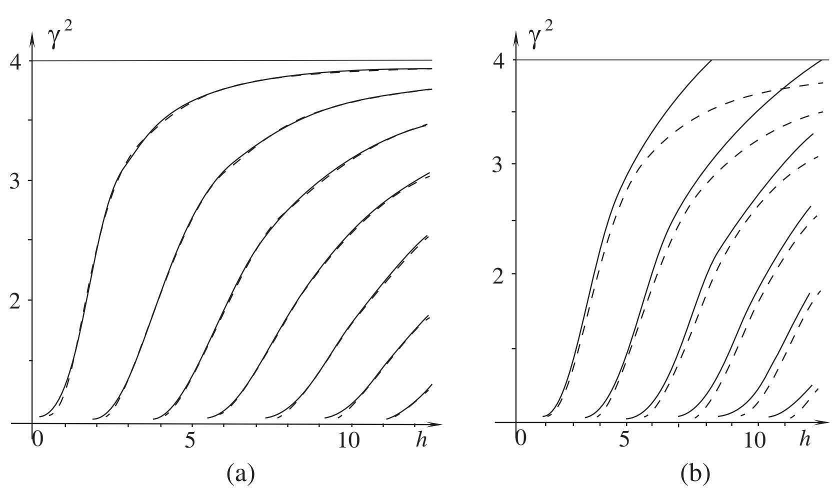

Figure 2: (a) $-\alpha=0.000001$, $\beta=0.001$; (b) $\alpha=0.1$, $\beta=0.01$.

As the left-hand side of the DE does not depend on h so it is easy to calculate with the DE.

Notice that improper integrals in DE (15) converge.

DE (15) can be generalized for the case when all used parameters such as ε_{xx}, ε_{zz} can possess arbitrary real values. The generalized DE has the form $-\int_{\eta(h)}^{\eta(0)} w d\eta + kT = h$, where $k = \pm 1, \pm 2, \ldots, \pm(N+1)$ (see also [10]).

Note 1. If there is a certain value γ_*^2, such that some of the integrals in DEs (15) diverge at a certain inner points, then this simply means that the value γ_*^2 is not a solution of chosen DE and the value γ_*^2 is not an eigenvalue of the problem.

Note 2. It is necessary to emphasize that this boundary eigenvalue problem essentially depends on the initial condition Z_h. The transmission problem for a linear layer does not depend on the initial condition. If the nonlinearity function is a specific one, then in some cases it will be possible to normalize the Maxwell equations in such way that the transmission problem does not depend on initial condition Z_h explicitly (it is possible for example for Kerr nonlinearity in layers and in circle cylindrical waveguides). Stress the fact once more that the opportunity of such normalization is an exceptional case. What is more, in spite of the fact that this normalization is possible in certain cases it does not mean that the normalized transmission problem is independent of the initial condition. In this case one of the problem's parameter depends on the initial conditions.

7. NUMERICAL RESULTS

In the Fig. 2 the behavior of dispersion curves (DC) is shown. For both cases the following functions and parameters $f = g = \frac{\alpha(X^2+Z^2)}{1+\beta(X^2+Z^2)}$, $\varepsilon_1 = \varepsilon_3 = 1$, $\varepsilon_f = \varepsilon_g = 4$, $Z_h = 1$ are used. The dashed curves are DCs for the linear layer (when $f \equiv 0$ and $g \equiv 0$), the lines $\gamma^2 = 4$ are asymptotes for DCs in the linear case, solid curves are DCs for the nonlinear case (solutions of DE (15)). For comparison with the TE wave case see [11].

ACKNOWLEDGMENT

This study was supported by the Russian Federation President Grant, project No. MK–2074.2011.1 and the Russian Foundation for Basic Research, project No. 11–07–00330–A. I also should like to thank Yu. G. Smirnov for his valuable advice.

REFERENCES

1. Eleonskii, P. N., L. G. Oganes'ants, and V. P. Silin, "Cylindrical nonlinear waveguides," *Sov. Phys. JETP*, Vol. 35, No. 1, 44–47, 1972.
2. Shürmann, H. W., V. S. Serov, and Yu. V. Shestopalov, "TE-polarized waves guided by a lossless nonlinear three-layer structure," *Physical Review E*, Vol. 58, No. 1, 1040–1050, 1998.
3. Valovik, D. V. and Yu. G. Smirnov, "Calculation of the propagation constants of TM electromagnetic waves in a nonlinear layer," *Journal of Communications Technology and Electronics*, Vol. 53, No. 8, 883–889, 2008.
4. Joseph, R. I. and D. N. Christodoulides, "Exact field decomposition for TM waves in nonlinear media," *Optics Letters*, Vol. 12, No. 10, 826–828, 1987.
5. Leung, K. M., "Scattering of transverse-magnetic waves with a nonlinear film: Formal field solutions solutions in quadratures," *Physical Review B*, Vol. 44, No. 10, 5007–5012, 1991.
6. Valovik, D. V., "Propagation of electromagnetic waves in a nonlinear metamaterial layer," *Journal of Communications Technology and Electronics*, Vol. 56, No. 5, 544–556, 2011.
7. Valovik, D. V. and Yu. G. Smirnov, "Calculation of the propagation constants and fields of polarized electromagnetic TM waves in a nonlinear anysotropic layer," *Journal of Communications Technology and Electronics*, Vol. 54, No. 4, 391–398, 2009.
8. Valovik, D. V. and Yu. G. Smirnov, "Nonlinear effects in the problem of propagation of TM electromagnetic waves in a Kerr nonlinear layer," *Journal of Communications Technology and Electronics*, Vol. 56, No. 3, 283–288, 2011.
9. Bautin, N. N. and E. A. Leontovich, "Methods of qualititive investigating dynamical systems in a plane," Moscow, Nauka, 1990, in Russian.
10. Valovik, D. V., "Propagation of TE-waves through a nonlinear metamaterial layer with arbitrary nonlinearity," *PIERS Online*, Vol. 7, No. 8, 721–725, 2011.
11. Valovik, D. V., "Propagation of electromagnetic TE waves in a nonlinear medium with saturation," *Journal of Communications Technology and Electronics*, Vol. 56, No. 11, 1311–1316, 2011.

Wave Equation in the Electromagnetic Field with Velocity Curl

Zi-Hua Weng
School of Physics and Mechanical & Electrical Engineering
Xiamen University, Xiamen 361005, China

Abstract— The paper studies the wave equation of the electromagnetic field in the presence of the gravitational field and the velocity curl. With the algebra of octonions, it is found that there exist some weightlessness states in the two fields, and the amplitudes of the waves will increase or decrease steadily. The study claims that the field potential has an influence on the gravitational strength, the electromagnetic strength, and the weightlessness state, and impacts finally the wave feature related to the rotational charged object.

1. INTRODUCTION

The validity of the wave equation is confined merely to one special status that there exists only the electromagnetic field up to now. The people doubt whether the wave equation of the electromagnetic field is still correct or not in the presence of the gravitational field and the velocity curl. The existing theories do not explain why the wave equation should keep unchanged for the rotational charged objects, and then do not offer relevant compelling reasons.

The algebra of quaternions was invented by W. R. Hamilton [1], subsequently the quaternion was first used by J. C. Maxwell [2] to describe electromagnetic fields in 1861. The quaternion space for the gravitational field is independent of that for the electromagnetic field [3]. Those two quaternion spaces can be combined together to become an octonion space, which was invented by A. Cayley [4] etc. Further the radius vector in the octonion space can be combined with the integral of the field potential to become the compounding physical quantity, which can be used to rephrase the wave feature of the electromagnetic field and of the gravitational field simultaneously.

In terms of the algebra of octonions, the study deduces the field equation and the wave equation of the electromagnetic field and the gravitational field, and claims that the electromagnetic wave and the gravitational wave are the transverse waves in a vacuum. The field potential will impact the weightlessness state [5] as well as the wave radiation, and the fluctuation of field potential may cause the field strength to deviate from the velocity curl slightly and frequently.

2. GRAVITATIONAL FIELD

The wave feature of gravitational field can be depicted by the quaternion. In the quaternion space for the gravitational field, the coordinate is r_i, the basis vector is $\mathbb{E}_g = (1, \mathbf{i}_1, \mathbf{i}_2, \mathbf{i}_3)$. The radius vector is $\mathbb{R}_g = \Sigma(r_i \mathbf{i}_i)$, the velocity is $\mathbb{V}_g = \Sigma(v_i \mathbf{i}_i)$. The gravitational potential is $\mathbb{A}_g = \Sigma(a_i \mathbf{i}_i)$, the gravitational strength is $\mathbb{B}_g = \Sigma(b_i \mathbf{i}_i) = \lozenge \circ \mathbb{A}_g$, which covers two components, $\mathbf{b} = \nabla \times \mathbf{a}$, and $\mathbf{g}/v_0 = \partial_0 \mathbf{a} + \nabla a_0$, with $\mathbf{a} = \Sigma(a_j \mathbf{i}_j)$. Herein the $\circ$ denotes the octonion multiplication, the operator $\lozenge = \Sigma(\mathbf{i}_i \partial_i)$, and $\nabla = \Sigma(\mathbf{i}_j \partial_j)$, with $\partial_i = \partial/\partial r_i$. $\mathbf{i}_0 = 1$. $r_0 = v_0 t$, v_0 is the speed of light, and t denotes the time. $i = 0, 1, 2, 3$. $j = 1, 2, 3$.

The integral of the gravitational potential, $\mathbb{X}_g = \Sigma(x_i \mathbf{i}_i)$, can combine with the $\mathbb{R}_g$ to become the compounding radius vector $\bar{\mathbb{R}}_g = \mathbb{R}_g + k_{rx} \mathbb{X}_g = \Sigma(\bar{r}_i \mathbf{i}_i)$. And the velocity $\mathbb{V}_g$ and the gravitational potential $\mathbb{A}_g$ can combine together to become the compounding velocity $\bar{\mathbb{V}}_g = \mathbb{V}_g + k_{rx} \mathbb{A}_g = \Sigma(\bar{v}_i \mathbf{i}_i)$, or the compounding potential $\bar{\mathbb{A}}_g = \mathbb{A}_g + (1/k_{rx}) \mathbb{V}_g = \Sigma(\bar{a}_i \mathbf{i}_i)$. Similarly the velocity curl, $\mathbb{U}_g = \lozenge \circ \mathbb{V}_g = \Sigma(u_i \mathbf{i}_i)$, and the strength $\mathbb{B}_g$ can combine together to become the compounding strength $\bar{\mathbb{B}}_g = \mathbb{B}_g + (1/k_{rx}) \mathbb{U}_g = \Sigma(\bar{b}_i \mathbf{i}_i)$. The gauge equation is $\bar{b}_0 = \partial_0 \bar{a}_0 + \nabla \cdot \bar{\mathbf{a}} = 0$, with $\bar{\mathbf{a}} = \Sigma(\bar{a}_j \mathbf{i}_j)$.

2.1. Field Equation

The source density, $\bar{\mathbb{S}}_g = m \bar{\mathbb{V}}_g$, of gravitational field is defined from the $\bar{\mathbb{B}}_g$,

$$\left(\bar{\mathbb{B}}_g/v_0 + \lozenge\right)^* \circ \bar{\mathbb{B}}_g = -\mu \bar{\mathbb{S}} = -\mu_g \bar{\mathbb{S}}_g + \bar{\mathbb{B}}_g^* \circ \bar{\mathbb{B}}_g/v_0, \tag{1}$$

where m is the mass density. μ and $\mu_g = 4\pi G/v_0^2$ are the coefficients, with G being the gravitational constant. And $\bar{\mathbb{B}}_g^* \circ \bar{\mathbb{B}}_g/(2\mu_g)$ is the field energy density of gravitational field with the velocity curl. $*$ denotes the octonion conjugate.

Further, the above can be separated into

$$\nabla \cdot \bar{\mathbf{b}} = 0, \quad \partial_0 \bar{\mathbf{b}} + \nabla^* \times \bar{\mathbf{g}}/v_0 = 0, \tag{2}$$

$$\nabla^* \cdot \bar{\mathbf{g}} = -m/\varepsilon_g, \quad \partial_0 \bar{\mathbf{g}}/v_0 + \nabla^* \times \bar{\mathbf{b}} = -\mu_g \bar{\mathbf{s}}, \tag{3}$$

where $\varepsilon_g = 1/(\mu_g v_0 \bar{v}_0)$. $\bar{\mathbf{s}} = \Sigma(\bar{s}_j \mathbf{i}_j)$. $\bar{s}_i = m\bar{v}_i$. $\bar{\mathbf{g}}/v_0 = \partial_0 \bar{\mathbf{a}} + \nabla \bar{a}_0$, $\bar{\mathbf{b}} = \nabla \times \bar{\mathbf{a}}$.

The above states that the compounding radius vector $\mathbb{R}_g$ can be considered as the radius vector in the quaternion compounding space, which is one kind of function space with the quaternion basis vector $\mathbb{E}_g$. And the Newton's law of gravitation in the quaternion compounding space is similar to that in the classical gravitational theory [6].

2.2. Wave Equation

In a vacuum space far away from the gravitational sources, there exist the $\bar{s}_0 = 0$ and the $\bar{\mathbf{s}} = 0$, and then the gravitational field equation is reduced to, $\lozenge^* \circ \mathbb{B}_g = 0$. Proceeding with the operator ∂_0 and ∇, the wave equation about the components of field strength are obtained from the field equation Eqs. (2) and (3) directly,

$$(\Sigma \partial_i^2) \bar{\mathbf{g}} = 0, \quad (\Sigma \partial_i^2) \bar{\mathbf{b}} = 0. \tag{4}$$

The above is the Laplace equation in the Euclid space, meanwhile it is the wave equation in the quaternion space. And the two components of gravitational strength, $\bar{\mathbf{b}}$ and $\bar{\mathbf{g}}$, are both possessed of wave features, although their wave impact may be too tiny to be detected at present.

2.3. Transverse Wave

In the quaternion compounding space, for the gravitational wave with the angular frequency ω, the gravitational strength should be a harmonic function $\cos \omega t$. In order to operate handily and cover more physics contents, it is convenient to substitute the function $\exp(-i\omega t)$ for the $\cos \omega t$.

The gravitational strength $\bar{\mathbf{g}}$ and $\bar{\mathbf{b}}$ can be written as follows,

$$\bar{\mathbf{g}} = \bar{\mathbf{g}}(\bar{r}) \exp(-i\omega t), \quad \bar{\mathbf{b}} = \bar{\mathbf{b}}(\bar{r}) \exp(-i\omega t), \tag{5}$$

combining this with Eq. (4), gives

$$\left\{-(\omega/v_0)^2 + \Sigma \partial_j^2\right\} \bar{\mathbf{g}}(\bar{r}) = 0, \quad \left\{-(\omega/v_0)^2 + \Sigma \partial_j^2\right\} \bar{\mathbf{b}}(\bar{r}) = 0. \tag{6}$$

Analyzing the field equation finds that the amplitude of gravitational strength will be increased steadily or deceased continuously. And the field strength should be one hyperbolic cosine, $\cos(i\alpha)$. It will substitute the function $\exp(-i\mathbf{i}\alpha)$ for the $\cos(i\alpha)$. Herein the wave vector $\mathbf{k} = \Sigma(\mathbf{i}_j k_j)$, the vector radius $\bar{\mathbf{r}} = \Sigma(\mathbf{i}_j \bar{r}_j)$, and $i\alpha$ is an imaginary angle. $\alpha = -\Sigma(k_j \bar{r}_j)$, k_j is the coefficient.

And then the gravitational strength $\bar{\mathbf{g}}(\bar{r})$ and $\bar{\mathbf{b}}(\bar{r})$ are

$$\bar{\mathbf{g}}(\bar{r}) = \bar{\mathbf{g}}_0 \circ \exp(-i\mathbf{i}\alpha), \quad \bar{\mathbf{b}}(\bar{r}) = \bar{\mathbf{b}}_0 \circ \exp(-i\mathbf{i}\alpha), \tag{7}$$

where $\bar{\mathbf{g}}_0$ and $\bar{\mathbf{b}}_0$ are constant vectors. $\exp\{\mathbf{i}(a + ib)\} = \cos(a + ib) + \mathbf{i} \sin(a + ib)$. a and b are all real. i is the imaginary unit, with $i^2 = -1$. $\mathbf{i}$ is the quaternion unit, with $\mathbf{i} \circ \mathbf{i} = -1$.

Substituting the above in Eq. (6), the result is, $-(\omega/v_0)^2 + \Sigma k_j^2 = 0$. From the field equations, $\nabla \cdot \bar{\mathbf{g}} = 0$ and $\nabla \cdot \bar{\mathbf{b}} = 0$, we obtain

$$\mathbf{k} \cdot \bar{\mathbf{g}}_0 = 0, \quad \mathbf{k} \cdot \bar{\mathbf{g}}_0' = 0, \quad \mathbf{k} \cdot \bar{\mathbf{b}}_0 = 0, \quad \mathbf{k} \cdot \bar{\mathbf{b}}_0' = 0, \tag{8}$$

where $\bar{\mathbf{g}}_0' = \bar{\mathbf{g}}_0 \circ \mathbf{i}$ and $\bar{\mathbf{b}}_0' = \bar{\mathbf{b}}_0 \circ \mathbf{i}$ are two new kinds of gravitational waves.

The above states that the gravitational waves are transverse waves in a vacuum, including the wave components, $\bar{\mathbf{g}}_0$ and $\bar{\mathbf{b}}_0$, as well as two new wave components, $\bar{\mathbf{g}}_0'$ and $\bar{\mathbf{b}}_0'$. And the amplitudes of the $\bar{\mathbf{g}}_0'$ and $\bar{\mathbf{b}}_0'$ equal to that of the $\bar{\mathbf{g}}_0$ and $\bar{\mathbf{b}}_0$ respectively.

The field equations, $\nabla \times \bar{\mathbf{g}} = \partial \bar{\mathbf{b}}/\partial t$ and $\nabla \cdot \bar{\mathbf{g}} = 0$, can be written as, $\nabla \circ \bar{\mathbf{g}} = \partial \bar{\mathbf{b}}/\partial t$. Expanding the $\exp(-i\mathbf{i}\alpha)$, and considering the α is a variable, the above deduces

$$\mathbf{k} \times \bar{\mathbf{g}}_0' + \omega \bar{\mathbf{b}}_0 = 0, \quad \mathbf{k} \times \bar{\mathbf{g}}_0 - \omega \bar{\mathbf{b}}_0' = 0. \tag{9}$$

In the same way, from the field equations, $v_0^2 \nabla \times \bar{\mathbf{b}} = \partial \bar{\mathbf{g}}/\partial t$ and $\nabla \cdot \bar{\mathbf{b}} = 0$, we get

$$\mathbf{k} \times \bar{\mathbf{b}}_0' + \omega \bar{\mathbf{g}}_0/v_0^2 = 0, \quad \mathbf{k} \times \bar{\mathbf{b}}_0 - \omega \bar{\mathbf{g}}_0'/v_0^2 = 0. \tag{10}$$

Table 1: The octonion multiplication table.

	1	$\mathbf{i}_1$	$\mathbf{i}_2$	$\mathbf{i}_3$	$\mathbf{I}_0$	$\mathbf{I}_1$	$\mathbf{I}_2$	$\mathbf{I}_3$
1	1	$\mathbf{i}_1$	$\mathbf{i}_2$	$\mathbf{i}_3$	$\mathbf{I}_0$	$\mathbf{I}_1$	$\mathbf{I}_2$	$\mathbf{I}_3$
$\mathbf{i}_1$	$\mathbf{i}_1$	-1	$\mathbf{i}_3$	$-\mathbf{i}_2$	$\mathbf{I}_1$	$-\mathbf{I}_0$	$-\mathbf{I}_3$	$\mathbf{I}_2$
$\mathbf{i}_2$	$\mathbf{i}_2$	$-\mathbf{i}_3$	-1	$\mathbf{i}_1$	$\mathbf{I}_2$	$\mathbf{I}_3$	$-\mathbf{I}_0$	$-\mathbf{I}_1$
$\mathbf{i}_3$	$\mathbf{i}_3$	$\mathbf{i}_2$	$-\mathbf{i}_1$	-1	$\mathbf{I}_3$	$-\mathbf{I}_2$	$\mathbf{I}_1$	$-\mathbf{I}_0$
$\mathbf{I}_0$	$\mathbf{I}_0$	$-\mathbf{I}_1$	$-\mathbf{I}_2$	$-\mathbf{I}_3$	-1	$\mathbf{i}_1$	$\mathbf{i}_2$	$\mathbf{i}_3$
$\mathbf{I}_1$	$\mathbf{I}_1$	$\mathbf{I}_0$	$-\mathbf{I}_3$	$\mathbf{I}_2$	$-\mathbf{i}_1$	-1	$-\mathbf{i}_3$	$\mathbf{i}_2$
$\mathbf{I}_2$	$\mathbf{I}_2$	$\mathbf{I}_3$	$\mathbf{I}_0$	$-\mathbf{I}_1$	$-\mathbf{i}_2$	$\mathbf{i}_3$	-1	$-\mathbf{i}_1$
$\mathbf{I}_3$	$\mathbf{I}_3$	$-\mathbf{I}_2$	$\mathbf{I}_1$	$\mathbf{I}_0$	$-\mathbf{i}_3$	$-\mathbf{i}_2$	$\mathbf{i}_1$	-1

The above means that the $\bar{\mathbf{g}}$ and $\bar{\mathbf{b}}$ can not be determined at the same time. When $\bar{v}_i = 0$, the rotational object stays on the weightlessness state, and there is not the gravitational wave, that is, the $\bar{\mathbf{g}} = 0$, $\bar{\mathbf{b}} = 0$, $\bar{\mathbf{g}} \circ \mathbf{i} = 0$, and $\bar{\mathbf{b}} \circ \mathbf{i} = 0$. In case $\bar{v}_i \neq 0$, the rotational object does not stay on the weightlessness state, and there exist the gravitational waves in a vacuum, that is, the $\bar{\mathbf{g}} \neq 0$, $\bar{\mathbf{b}} \neq 0$, $\bar{\mathbf{g}} \circ \mathbf{i} \neq 0$, and $\bar{\mathbf{b}} \circ \mathbf{i} \neq 0$. In some cases the rotational object may stay on some movement states, including the $\bar{\mathbf{g}} = 0$ and $\bar{\mathbf{b}} \neq 0$, or the $\bar{\mathbf{g}} \neq 0$ and $\bar{\mathbf{b}} = 0$ etc.

3. ELECTROMAGNETIC FIELD

The wave feature of gravitational field and electromagnetic field can be described simultaneously by the octonion space, which consists of two orthogonal quaternion spaces. In the quaternion space for the electromagnetic field, the basis vector is $\mathbb{E}_e = (\mathbf{I}_0, \mathbf{I}_1, \mathbf{I}_2, \mathbf{I}_3)$, the radius vector is $\mathbb{R}_e = \Sigma(R_i \mathbf{I}_i)$, the velocity is $\mathbb{V}_e = \Sigma(V_i \mathbf{I}_i)$. The electromagnetic potential is $\mathbb{A}_e = \Sigma(A_i \mathbf{I}_i)$, the electromagnetic strength is $\mathbb{B}_e = \Sigma(B_i \mathbf{I}_i) = \lozenge \circ \mathbb{A}_e$, which covers two components, $\mathbf{B} = \nabla \times \mathbf{A}$, and $\mathbf{E}/v_0 = \partial_0 \mathbf{A} + \nabla \circ \mathbf{A}_0$, with $\mathbf{A} = \Sigma(A_j \mathbf{I}_j)$ and $\mathbf{A}_0 = A_0 \mathbf{I}_0$. Herein the $\mathbb{E}_e$ is independent of the $\mathbb{E}_g$, with $\mathbb{E}_e = \mathbb{E}_g \circ \mathbf{I}_0$.

In the octonion space, the octonion basis vector is $\mathbb{E} = (\mathbf{i}_0, \mathbf{i}_1, \mathbf{i}_2, \mathbf{i}_3, \mathbf{I}_0, \mathbf{I}_1, \mathbf{I}_2, \mathbf{I}_3)$, the radius vector is $\mathbb{R} = \mathbb{R}_g + k_{eg}\mathbb{R}_e$, the velocity is $\mathbb{V} = \mathbb{V}_g + k_{eg}\mathbb{V}_e$. The field potential is $\mathbb{A} = \mathbb{A}_g + k_{eg}\mathbb{A}_e$, the field strength is $\mathbb{B} = \lozenge \circ \mathbb{A} = \mathbb{B}_g + k_{eg}\mathbb{B}_e$, with the k_{eg} being a coefficient.

The integral of field potential, $\mathbb{X} = \Sigma(x_i \mathbf{i}_i + k_{eg} X_i \mathbf{I}_i)$, can combine with the $\mathbb{R}$ to become the compounding radius vector $\bar{\mathbb{R}} = \mathbb{R} + k_{rx}\mathbb{X} = \Sigma(\bar{r}_i \mathbf{i}_i + k_{eg}\bar{R}_i \mathbf{I}_i)$. The velocity $\mathbb{V}$ and the field potential $\mathbb{A}$ can combine together to become the compounding velocity $\bar{\mathbb{V}} = \mathbb{V} + k_{rx}\mathbb{A} = \Sigma(\bar{v}_i \mathbf{i}_i + k_{eg}\bar{V}_i \mathbf{I}_i)$, or the compounding potential $\bar{\mathbb{A}} = \mathbb{A} + (1/k_{rx})\mathbb{V} = \Sigma(\bar{a}_i \mathbf{i}_i + k_{eg}\bar{A}_i \mathbf{I}_i)$. The velocity curl, $\mathbb{U} = \lozenge \circ \mathbb{V} = \Sigma(u_i \mathbf{i}_i + k_{eg} U_i \mathbf{I}_i)$, and the field strength $\mathbb{B}$ can combine together to become the compounding strength $\bar{\mathbb{B}} = \mathbb{B} + (1/k_{rx})\mathbb{U} = \Sigma(\bar{b}_i \mathbf{i}_i + k_{eg}\bar{B}_i \mathbf{I}_i)$. The gauge equation is $\bar{B}_0 \mathbf{I}_0 = \partial_0 \bar{\mathbf{A}}_0 + \nabla \cdot \bar{\mathbf{A}} = 0$, with $\bar{\mathbf{A}} = \Sigma(\bar{A}_j \mathbf{I}_j)$ and $\bar{\mathbf{A}}_0 = \bar{A}_0 \mathbf{I}_0$. $\bar{\mathbb{A}}_e = \Sigma(\bar{A}_i \mathbf{I}_i)$, $\bar{\mathbb{B}}_e = \Sigma(\bar{B}_i \mathbf{I}_i) = \lozenge \circ \bar{\mathbb{A}}_e$.

3.1. Field Equation

The compounding source $\bar{\mathbb{S}}$ is devised to describe the electromagnetic source, $\bar{\mathbb{S}}_e = q\bar{\mathbb{V}}_e$, and the gravitational source $\bar{\mathbb{S}}_g$ simultaneously, and is defined from the compounding strength $\bar{\mathbb{B}}$,

$$(\bar{\mathbb{B}}/v_0 + \lozenge)^* \circ \bar{\mathbb{B}} = -\mu\bar{\mathbb{S}} = -(\mu_g \bar{\mathbb{S}}_g + k_{eg}\mu_e \bar{\mathbb{S}}_e) + \bar{\mathbb{B}}^* \circ \bar{\mathbb{B}}/v_0, \tag{11}$$

where μ_e is the electromagnetic constant, with $k_{eg}^2 = \mu_g/\mu_e$. And $\bar{\mathbb{B}}_e^* \circ \bar{\mathbb{B}}_e/(2\mu_e)$ is the field energy density of electromagnetic field with the velocity curl. q is the electric charge density.

According to the basis vectors, the above can be decomposed further as follows,

$$\lozenge^* \circ \bar{\mathbb{B}}_g = -\mu_g \bar{\mathbb{S}}_g, \quad \lozenge^* \circ \bar{\mathbb{B}}_e = -\mu_e \bar{\mathbb{S}}_e, \tag{12}$$

where the former equation is similar to Eq. (1) and is suitable for the gravitational field, while the latter equation is for the electromagnetic field.

Further, the latter equation in the above can be rewritten as follows

$$\nabla \cdot \overline{\mathbf{B}} = 0, \quad \partial_0 \overline{\mathbf{B}} + \nabla^* \times \overline{\mathbf{E}}/v_0 = 0, \tag{13}$$

$$\nabla^* \cdot \overline{\mathbf{E}} = -q\boldsymbol{I}_0/\varepsilon_e, \quad \partial_0 \overline{\mathbf{E}}/v_0 + \nabla^* \times \overline{\mathbf{B}} = -\mu_e \overline{\mathbf{S}}, \tag{14}$$

where $\varepsilon_e = 1/(\mu_e \bar{V}_0 v_0)$. $\bar{\mathbf{B}} = \nabla \times \bar{\mathbf{A}}$, $\bar{\mathbf{E}}/v_0 = \partial_0 \bar{\mathbf{A}} + \nabla \circ \bar{\mathbf{A}}_0$. $\bar{\mathbf{S}} = \Sigma(\bar{S}_j \mathbf{I}_j)$, $\bar{\mathbf{S}}_0 = \bar{S}_0 \mathbf{I}_0$, $\bar{S}_i = q\bar{V}_i$.

The above means that the compounding radius vector $\mathbb{R}$ can be considered as the radius vector in the octonion compounding space, which is one kind of function space with the octonion basis vector $\mathbb{E}$. And that the Maxwell's electromagnetic equations in the octonion compounding space are similar to that in the classical electromagnetic theory [7].

3.2. Wave Equation

In a vacuum far away from the electromagnetic sources, there exist the $\bar{\mathbf{S}}_0 = 0$ and the $\bar{\mathbf{S}} = 0$, and then the electromagnetic field equation can be reduced to, $\lozenge^* \circ \mathbb{B}_e = 0$. Proceeding with the operator ∂_0 and ∇, we can obtain the wave equation about the components of field strength from Maxwell equation directly,

$$(\Sigma\partial_i^2)\bar{\mathbf{E}} = 0, \ (\Sigma\partial_i^2)\bar{\mathbf{B}} = 0. \tag{15}$$

The above is the Laplace equation in the Euclid space, meanwhile it is the wave equation in the octonion space. And two strength components of the electromagnetic field, $\bar{\mathbf{E}}$ and $\bar{\mathbf{B}}$, are both possessed of wave features, and can be detected indirectly at present.

3.3. Transverse Wave

In the octonion compounding space, for the electromagnetic wave with the angular frequency ω, the field strength should be a harmonic function, $\cos\omega t$, and can be chosen as $\exp(-i\omega t)$.

The electromagnetic strength $\bar{\mathbf{E}}$ and $\bar{\mathbf{B}}$ can be written as follows,

$$\bar{\mathbf{E}} = \bar{\mathbf{E}}(\bar{r})\exp(-i\omega t), \quad \bar{\mathbf{B}} = \bar{\mathbf{B}}(\bar{r})\exp(-i\omega t), \tag{16}$$

substituting the above in Eq. (15),

$$\left\{-(\omega/v_0)^2 + \Sigma\partial_j^2\right\}\bar{\mathbf{E}}(\bar{r}) = 0, \quad \left\{-(\omega/v_0)^2 + \Sigma\partial_j^2\right\}\bar{\mathbf{B}}(\bar{r}) = 0. \tag{17}$$

Analyzing the field equation finds that the amplitude of the electromagnetic strength will be increased steadily or deceased continuously. So the field strength is the hyperbolic cosine $\cos(i\alpha)$, and can be replaced by $\exp(-i\mathbf{I}\alpha)$. Herein the wave vector $\mathbf{K} = \Sigma(\mathbf{I}_j K_j)$, $i\alpha$ is an imaginary angle. $\alpha = -\Sigma(K_j \bar{r}_j)$, K_j is the coefficient.

And then, the field strength $\bar{\mathbf{E}}(\bar{r})$ and $\bar{\mathbf{B}}(\bar{r})$ are

$$\bar{\mathbf{E}}(\bar{r}) = \bar{\mathbf{E}}_0 \circ \exp(-i\mathbf{I}\alpha), \quad \bar{\mathbf{B}}(\bar{r}) = \bar{\mathbf{B}}_0 \circ \exp(-i\mathbf{I}\alpha), \tag{18}$$

where $\bar{\mathbf{E}}_0$ and $\bar{\mathbf{B}}_0$ both are the constant vectors. $\exp\{\mathbf{I}(a+ib)\} = \cos(a+ib) + \mathbf{I}\sin(a+ib)$. a and b are all real. i is the imaginary unit, with $i^2 = -1$. $\mathbf{I}$ is the octonion unit, with $\mathbf{I} \circ \mathbf{I} = -1$.

Further substituting Eq. (18) in Eq. (17), we have the result, $-(\omega/v_0)^2 + \Sigma K_j^2 = 0$. From the field equations $\nabla \cdot \bar{\mathbf{E}} = 0$ and $\nabla \cdot \bar{\mathbf{B}} = 0$, we obtain

$$\mathbf{K} \cdot \bar{\mathbf{E}}_0 = 0, \quad \mathbf{K} \cdot \bar{\mathbf{E}}'_0 = 0, \quad \mathbf{K} \cdot \bar{\mathbf{B}}_0 = 0, \quad \mathbf{K} \cdot \bar{\mathbf{B}}'_0 = 0, \tag{19}$$

where $\bar{\mathbf{E}}'_0 = \bar{\mathbf{E}}_0 \circ \mathbf{I}$ and $\bar{\mathbf{B}}'_0 = \bar{\mathbf{B}}_0 \circ \mathbf{I}$ are two new kinds of electromagnetic waves.

The above states that the electromagnetic waves are the transverse waves in a vacuum, including the waves components, $\bar{\mathbf{E}}_0$ and $\bar{\mathbf{B}}_0$, as well as two new wave components, $\bar{\mathbf{E}}'_0$ and $\bar{\mathbf{B}}'_0$. Moreover the amplitudes of wave components, $\bar{\mathbf{E}}'_0$ and $\bar{\mathbf{B}}'_0$, equal to that of $\bar{\mathbf{E}}_0$ and $\bar{\mathbf{B}}_0$ respectively.

The field equations, $\nabla \times \bar{\mathbf{E}} = \partial\bar{\mathbf{B}}/\partial t$ and $\nabla \cdot \bar{\mathbf{E}} = 0$, can be incorporated into, $\nabla \circ \bar{\mathbf{E}} = \partial\bar{\mathbf{B}}/\partial t$. Expanding the $\exp(-i\mathbf{I}\alpha)$, and considering the α may be any value, the above yields

$$\mathbf{K} \times \bar{\mathbf{E}}'_0 + \omega\bar{\mathbf{B}}_0 = 0, \quad \mathbf{K} \times \bar{\mathbf{E}}_0 - \omega\bar{\mathbf{B}}'_0 = 0. \tag{20}$$

In the same way, from the field equations, $v_0^2 \nabla \times \bar{\mathbf{B}} = \partial\bar{\mathbf{E}}/\partial t$ and $\nabla \cdot \bar{\mathbf{B}} = 0$, we have

$$\mathbf{K} \times \bar{\mathbf{B}}'_0 + \omega\bar{\mathbf{E}}_0/v_0^2 = 0, \quad \mathbf{K} \times \bar{\mathbf{B}}_0 - \omega\bar{\mathbf{E}}'_0/v_0^2 = 0. \tag{21}$$

The above means that the $\bar{\mathbf{E}}$ and $\bar{\mathbf{B}}$ can not be determined simultaneously. When $\bar{V}_i = 0$, the rotational charged object stays on the weightlessness state, and there is not the electromagnetic wave, that is, the $\bar{\mathbf{E}} = 0$, $\bar{\mathbf{B}} = 0$, $\bar{\mathbf{E}} \circ \mathbf{I} = 0$, and $\bar{\mathbf{B}} \circ \mathbf{I} = 0$. In case $\bar{V}_i \neq 0$, the rotational charged object does not stay on the weightlessness state, and there exist the electromagnetic waves in a vacuum, that is, the $\bar{\mathbf{E}} \neq 0$, $\bar{\mathbf{B}} \neq 0$, $\bar{\mathbf{E}} \circ \mathbf{I} \neq 0$, and $\bar{\mathbf{B}} \circ \mathbf{I} \neq 0$. In some cases the rotational charged object may stay on some states, including the $\bar{\mathbf{E}} = 0$ and $\bar{\mathbf{B}} \neq 0$, or the $\bar{\mathbf{E}} \neq 0$ and $\bar{\mathbf{B}} = 0$ etc.

Table 2: The operator and multiplication of the physical quantity in the octonion space.

definition	meaning
$\nabla \cdot \mathbf{a}$	$-(\partial_1 a_1 + \partial_2 a_2 + \partial_3 a_3)$
$\nabla \times \mathbf{a}$	$\mathbf{i}_1(\partial_2 a_3 - \partial_3 a_2) + \mathbf{i}_2(\partial_3 a_1 - \partial_1 a_3) + \mathbf{i}_3(\partial_1 a_2 - \partial_2 a_1)$
∇a_0	$\mathbf{i}_1 \partial_1 a_0 + \mathbf{i}_2 \partial_2 a_0 + \mathbf{i}_3 \partial_3 a_0$
$\partial_0 \mathbf{a}$	$\mathbf{i}_1 \partial_0 a_1 + \mathbf{i}_2 \partial_0 a_2 + \mathbf{i}_3 \partial_0 a_3$
$\nabla \cdot \mathbf{A}$	$-(\partial_1 A_1 + \partial_2 A_2 + \partial_3 A_3)\mathbf{I}_0$
$\nabla \times \mathbf{A}$	$-\mathbf{I}_1(\partial_2 A_3 - \partial_3 A_2) - \mathbf{I}_2(\partial_3 A_1 - \partial_1 A_3) - \mathbf{I}_3(\partial_1 A_2 - \partial_2 A_1)$
$\nabla \circ \mathbf{A}_0$	$\mathbf{I}_1 \partial_1 A_0 + \mathbf{I}_2 \partial_2 A_0 + \mathbf{I}_3 \partial_3 A_0$
$\partial_0 \mathbf{A}$	$\mathbf{I}_1 \partial_0 A_1 + \mathbf{I}_2 \partial_0 A_2 + \mathbf{I}_3 \partial_0 A_3$

4. CONCLUSIONS

In the quaternion compounding space, the gravitational potential affects the gravitational waves, $\bar{\mathbf{g}}$, $\bar{\mathbf{b}}$, $\bar{\mathbf{g}} \circ \mathbf{i}$, and $\bar{\mathbf{b}} \circ \mathbf{i}$ in a vacuum. When the rotational object is on weightlessness state, there is not the gravitational wave radiation. In case the rotational object does not stay on the weightlessness state, there exists the gravitational wave radiation. The $\bar{\mathbf{g}}$ and the $\bar{\mathbf{b}}$ can be transformed into each other, and it causes the fluctuation of the $\mathbf{g}$ and of the $\mathbf{b}$, therefore the motion of the rotational object will depart from the anticipation of the Newton's law of gravitation.

In the octonion compounding space, the electromagnetic potential impacts the electromagnetic waves, $\bar{\mathbf{E}}$, $\bar{\mathbf{B}}$, $\bar{\mathbf{E}} \circ \mathbf{I}$, and $\bar{\mathbf{B}} \circ \mathbf{I}$ in a vacuum. When the rotational charged object is on weightlessness state, and there is not the electromagnetic wave radiation. In case the rotational charged object does not stay on the weightlessness state, there exists the electromagnetic wave radiation. The $\bar{\mathbf{E}}$ and $\bar{\mathbf{B}}$ can be transformed into each other, and it causes the undulation of the $\mathbf{E}$ and $\mathbf{B}$, and the motion of rotational charged object may deviate from the expectation of the Coulomb's law.

It should be noted that the study for the influences of the field potential to the electromagnetic wave equation of the rotational charged object examined only some simple cases in the presence of the gravitational field and the velocity curl. Despite its preliminary characteristics, this study can clearly indicate that the field potential impacts the wave equation and the weightlessness state etc. For the future studies, the research will focus on some predictions about the fluctuation of the electromagnetic wave of the rotational charged objects.

ACKNOWLEDGMENT

This project was supported partially by the National Natural Science Foundation of China under grant number 60677039.

REFERENCES

1. Hamilton, W. R., *Elements of Quaternions*, Longmans, Green & Co., London, 1866.
2. Maxwell, J. C., *A Treatise on Electricity and Magnetism*, Dover Publications Inc., New York, 1954.
3. Weng, Z.-H., "Electromagnetic field equation described with the octonions," *Modern Physics*, Vol. 1, No. 1, 17–22, 2011, in Chinese.
4. Cayley, A., *The Collected Mathematical Papers*, Johnson Reprint Co., New York, 1963.
5. Weng, Z.-H., "Velocity curl and spin in electromagnetic fields," *PIERS Proceedings*, 352–356, Marrakesh, Morocco, March 20–23, 2011.
6. Newton, I., *The Mathematical Principles of Natural Philosophy*, Dawsons of Pall Mall, London, 1968.
7. Gogberashvili, M., "Octonionic electrodynamics," *Journal of Physics A*, Vol. 39, No. 22, 7099–7104, 2006.

Optical Neural Router Consisting of Acousto-optic Waveguide-type Switches for Adaptive Network

N. Goto[1] **and Y. Miyazaki**[2]

[1]University of Tokushima, Japan
[2]Aichi University of Technology, Japan

Abstract— In this paper, optical neural router consisting of acousto-optic waveguide-type switching devices is proposed and studied. As an algorithm to obtain the shortest path between routers, we propose a method using neural learning. In this proposed device, switching of optical input signal is carried out by controlling surface acoustic waves. Switching characteristics are numerically simulated using FDTD method for an incident Gaussian beam. In this analysis, total analysis space is divided into small subdomains and each subdomain is calculated successively to simulate optical pulse propagation in long distance of hundreds times as long as wavelength.

1. INTRODUCTION

In packet transmission through broadband networks, the transmission efficiency decreases for heavy traffic if route selection in each router is not properly carried out [1]. We propose an adaptive system using optical neural routers for suitable route selection [2, 3].

As an algorithm to obtain the shortest path between routers, we propose a method using neural learning. There are dynamic routing and static routing in conventional routing in the Internet. The dynamic routing exchanges routing information which may not be necessarily efficient. Memories and processing time increase when the control becomes complicated. On the contrary, the static routing is not necessarily efficient because the routing tables have to be updated when the network configuration is changed or a trouble occurs in the network.

In this paper, we propose a method using neural learning as an algorithm to find the shortest route. We consider a router consisting of neuro devices and formularize it considering router performance and transmission speed [4, 5]. Output packets from the router are determined by controlling the neuro devices to minimize the time-of-arrival of the packets. Since the neural network learns change of transmission capacity, flexible route selection can be expected in an emergency. Optimum route selection algorithm considering various factors such as transmission time can be realized by varying coupling weights among neurons.

We discuss optical neuro router consisting of multi-layered structure of acousto-optic (AO) waveguide-type neuro switching devices. In the AO neuro device, transmission route is controlled by applying r.f. electric signals for surface acoustic waves (SAWs) which have been determined by learning. The AO switching device for optical neuro router is analyzed by FDTD method [6, 7]. In this analysis, total analysis space is divided into small subdomains and each subdomain is calculated successively to simulate optical pulse propagation along hundreds times as long as wavelength.

The multi-layered configuration of the optical neuro devices controlled by r.f. electric signals obtained from learning gives fundamentals for optical neuro routers.

2. NETWORK WITH ROUTERS USING OPTICAL NEURO DEVICES

A lot of time and communication are required to comprehend whole of a complex network. We divide a network into small networks containing routers, and derive the shortest route in each small networks. An observation station of router is located in each network to comprehend the whole of its belonging small network and to derive the shortest routes, as shown in Fig. 1(a).

We propose a basic model for deriving the shortest routes by using neural network. By regarding circuit network routers as neuro-type routers, we formulate the arrival time of packets considering router performance and transmission rate. We assume a layered structure for the circuit network. Flexible route selection is expected in case of emergency because learning of change of communication rate is adopted in neural networks.

We discuss derivation of the shortest routes using neural networks. We consider a neuro-type router consisting of mutually connected circuit network as shown in Fig. 1(b). An input packet passes router $R_i^{(s)}$, $(i = 1, 2, \ldots, m)$ at step s $(s = 1, 2, \ldots)$. The sum of input packets and the sum of output packets in router $R_i^{(s)}$ at step s are $x_j^{(s)}, (j \neq i)$ and $x_i'^{(s+1)}$, respectively, which usually

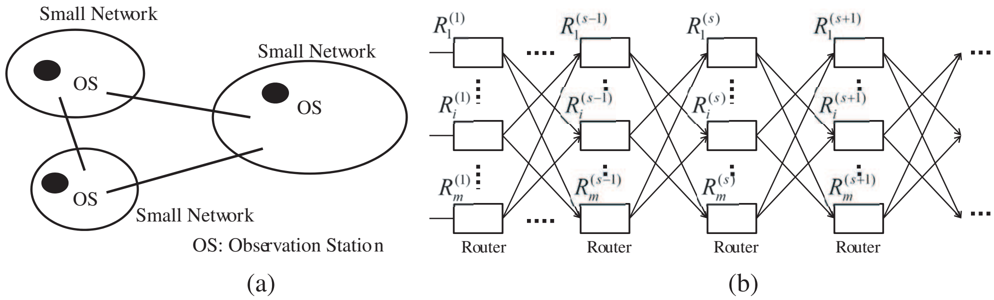

Figure 1: (a) Observation station of networks and (b) architecture of network with neuro-type routers.

have 0 or 1. The connection weight from router $R_j^{(s)}$ at step s to router $R_i^{(s)}$ at step $s+1$ is $w_{ji}^{(s)}$. Router $R_i^{(s)}$ has a threshold value θ_i. Thus, the sum $x_i^{(s)}$ of the input packets in router $R_i^{(s)}$ at step s is given by

$$x_i^{(s)} = \sum_{j=1}^{m} w_{ji}^{(s-1)} x_j'^{(s-1)} - \theta_i. \tag{1}$$

Then, the sum $x_i^{(s+1)}$ of the input packets in router $R_i^{(s+1)}$ at step $s+1$ is given by

$$x_i^{(s+1)} = f\left(\sum_{\substack{j=1\\(i\neq j)}}^{n} w_{ji}^{(s)} x_j'^{(s)} - \theta_i \right), \tag{2}$$

where the input-output function f is a nonlinear function such as sigmoid function.

Next, we derive transmission time of a packet transmitted from router $R_i^{(s)}$ at step s. The transmission rate $C_i^{(s)}$ from router $R_i^{(s)}$ at step s is given by $C_i^{(s)} = K_i^{(s)} x_i^{(s)}$, where $K_i^{(s)}$ is proportional constants. Using the total transmission length $l_i^{(s)}$ from router $R_i^{(s)}$ to the next router, the transmission time $\tau_i^{(s)}$ is given by $\tau_i^{(s)} = l_i^{(s)}/C_i^{(s)}$. Processing time $P_i^{(s)}$ in router $R_i^{(s)}$ at step s is assumed to be given as a function of $R_i^{(s)}$ as $P_i^{(s)} = g(R_i^{(s)})$.

The transmission time T from each router to the next router at step n is given by

$$T = \sum_{i=1}^{m} \left(\tau_i^{(n)} + P_i^{(n)} \right). \tag{3}$$

Output packets are determined to minimize T. Under the above conditions, optimum connection weight $w_{ji}^{(s)}$ $(i, j = 1, 2, \ldots, m)$ is found. The performance of router $R_i^{(s)}$ for achieving objective transmission time is also determined.

The algorithm to find shortest route is as follows: (1) At $s = 0$, initialize $x_i^{(s)}$, (2) update connection weights, (3) find j using transition probability matrix P_{ij}, (4) calculate $x_j^{(s+1)}$ using input-output function, (5) if $x_j^{(s+1)}$ changes, set all of $x_k^{(s+1)}$ having $P_{i,k\neq j} > 0$ to be zero, and (6) set $s = s+1$ and return to procedure (2).

3. PRINCIPLE OF ROUTERS USING OPTICAL NEURO DEVICES

In adaptive Y-branch router in neuro-type router structure, packets in the network are relayed at multiple routers as shown in Fig. 2(a). Control signals in the routers using optical neuro devices are determined to minimize the packet arrival time by learning as a routing algorithm. We consider a Y-branch device having one input port and two output ports. When the stage number S is $S_{\max}$, the number of the output ports is $2^{S_{\max}}$. In the ith router R_i, the 2^S ports correspond to binary number representation as shown in Fig. 2(b). The output port number n is written as

$$n = a_{S_{\max}-1}^{(i)} 2^{S_{\max}-1} + a_{S_{\max}-2}^{(i)} 2^{S_{\max}-2} + \ldots + a_1^{(i)} 2^1 + a_0^{(i)} 2^0, \tag{4}$$

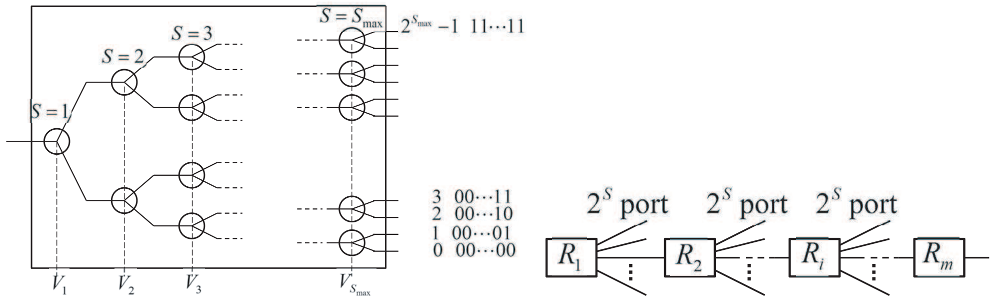

Figure 2: (a) Optical neuro router consisting of multi-stage Y-branch and (b) network with mulitple routers.

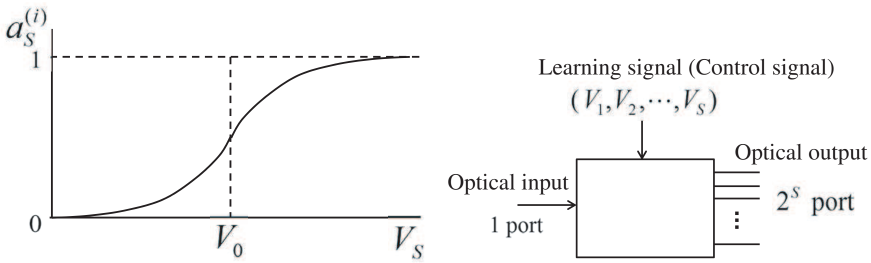

Figure 3: (a) Relation of control signal V_S and $a_S^{(i)}$ and (b) a model of optical neuro router.

where $a_S^{(i)} = 0, 1$. At the branch in Sth stage, the output $a_S^{(i)}$ has a neuro characteristic. As shown in Fig. 3(a), the control signal $V_S^{(i)}$ at Sth stage in ith router is given by

$$a_S^{(i)} = \frac{1}{1 + e^{-\alpha(V_S^{(i)} - V_0)}}, \tag{5}$$

where $a_S^{(i)} = 1$ for $V_S^{(i)} \gg V_0$ and $a_S^{(i)} = 0$ for $V_S^{(i)} \ll V_0$. The control signal $V_S^{(i)}$ is determined by learning statistical amount of network transmission efficiency. We consider the processing and transmission time between router k and router l to be T_{kl}. Objective evaluation amount to minimize T_{kl} is used in learning, and $V_S^{(i)}$ is given by

$$\min_{V_S^{(i)}} \left\{ \sum_{k,l} T_{kl} \right\} \tag{6}$$

The output port for optical input at one port is determined by the control signal $V_S^{(i)}$ ($S = 1, 2, \ldots, S_{\max}$). In the whole routers as shown in Fig. 3(b), we have

$$(a_{S-1}, a_{S-2}, \ldots, a_1, a_0) = f(V_{S-1}, V_{S-2}, \ldots, V_1, V_0), \tag{7}$$

where f is the decision function as given by Eq. (5).

4. MODEL OF OPTICAL AO NEURO DEVICE

The basic structure of a collinear AO device is shown in Fig. 4(a). On a $-Z$-cut $LiNbO_3$ substrate, an embedded rib waveguide is formed by proton exchange (PE) as waveguide 1. On this waveguide, a rib waveguide is formed from TiO_2 to serve as waveguide 2. Since the PE region of waveguide 1 has a trapping effect on SAWs, optical waveguide 1 and its cladding region with a width of Wa functions as a SAW waveguide. The interaction region with length l_{SW} is a laminate of two rib optical waveguides. Coupling between two fundamental modes, even and odd modes, in the coupled waveguide is induced by the AO interaction.

In this paper, a device consisting of a two-dimensional waveguide as shown in Fig. 4(b) is analyzed. For an optical wavelength of $\lambda = 1.55\,\mu$m, it is assumed that the refractive indices are

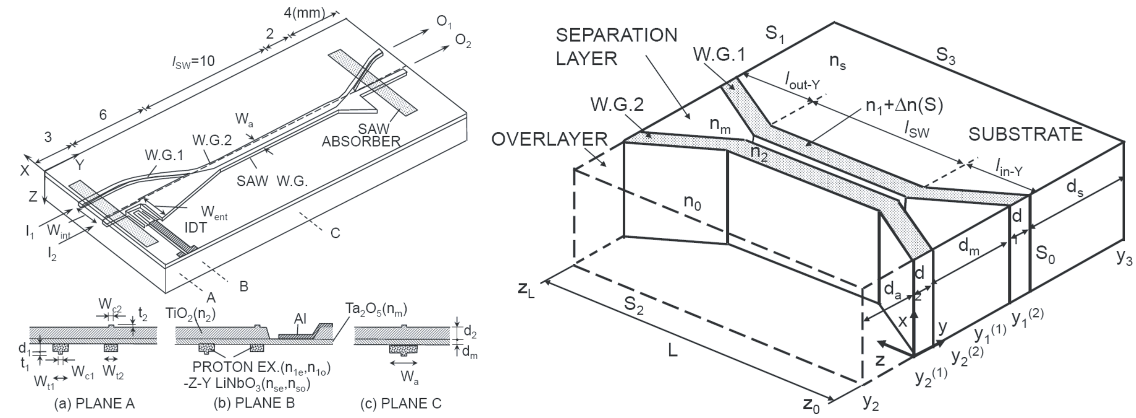

(a) (b)

Figure 4: (a) Collinear AO device and (b) a two-dimensional model for FDTD analysis.

$n_s = n_0 = 2.135$, $n_1 = n_2 = 2.211$, and $n_m = 2.063$. The device in Fig. 4(a) operates for the TM wave whereas the analysis is carried out for the TE wave. For efficient AO interaction, the effect of the AO coupling must be concentrated in only one of the waveguides. Therefore, the analysis here assumes that the SAW-generated periodic refractive indices change only in waveguide 1.

5. FDTD ANALYSIS OF SWITCHING OF OPTICAL NEURO AO DEVICE

From the stability condition, we analyzed with $\Delta s = 0.05\,\mu\text{m}$ and $\Delta t = 0.1\,\text{fs}$. By discretization of Maxwell's equations, the electromagnetic field $E_x(y, z, t)$ can be computed as $E_x(i, j, n)$:

$$\begin{aligned} E_x(i,j,n) &= E_x(i,j,n-1) + \frac{\Delta t}{\varepsilon(i,j,n-1)\Delta s} \\ &\quad \cdot[H_z(i,j,n-1) - H_z(i-1,j,n-1) - H_y(i,j,n-1) + H_y(i-1,j,n-1)] \quad (8) \\ H_y(i,j,n) &= H_y(i,j,n-1) - \frac{\Delta t}{\mu\Delta s}[E_x(i,j+1,n-1) - E_x(i,j,n-1)] \quad (9) \\ H_z(i,j,n) &= H_z(i,j,n-1) + \frac{\Delta t}{\mu\Delta s}[E_x(i+1,j,n-1) - E_x(i,j,n-1)]. \quad (10) \end{aligned}$$

The incident wave in the discrete form is given by

$$E_x(i,j,n) = E_0(i)f(j,n)\sin(\omega n\Delta t - \beta j\Delta s), \quad H_y(i,j,n) = H_0(i)f(j,n)\sin(\omega n\Delta t - \beta j\Delta s), \quad (11)$$

where $f(t)$ denotes the envelope of an optical incident packet. The incident wave is excited in the incident plane S_0. Mur's second-order absorbing boundary condition is used at S_1, S_2, and S_3.

If there exists a SAW satisfying the phase match condition and the power, then mode conversion occurs between the even and odd modes. We assume the variation of the refractive index of the medium $\Delta n(S) = \Delta n_0 \cos(Kz)$ to the medium in waveguide 1, where S is the SAW strain and K is the SAW propagation constant. When the substrate is $LiNbO_3$, $\Delta n \approx 2 \times 10^{-4}$ is expected for $10\,\mu\text{m}\times 100\,\mu\text{m}$ cross section of acoustic wave of 10 mW.

First, we assume $\Delta n_0 = 0.01$ to confirm switching along the whole AO device. The switching depends on the shift of K from the Bragg condition $\Delta K = K - (\beta_E - \beta_O)$, where β_E and β_O are the propagation constants of optical even and odd modes, respectively. When $\Delta K = 0$, 100% mode conversion is obtained for $l_{SW} = 250\,\mu\text{m}$ as shown in Fig. 5(a). The outputs depends on ΔK as shown in Fig. 5(b).

Next, we discuss segmentation of FDTD analysis media to confirm mode conversion of an optical pulse with $\Delta n_0 = 5 \times 10^{-4}$. The interaction region is divided into segments of length ΔZ as shown in Fig. 6(a). We consider a short optical pulse within $\Delta Z/2$. The optical pulse propagation in $z_1^{(i)} \le z \le z_3^{(i)}$ is analyzed. After the tail end of the optical pulse passes the center $z = z_2^{(i)}$, the analysis is continued in the next region $z_1^{(i+1)} \le z \le z_3^{(i+1)}$. In this process, the optical pulse located in $z_2^{(i)} \le z \le z_3^{(i)}$ is copied to $z_1^{(i+1)} \le z \le z_2^{(i+1)}$ spatially corresponding to the same medium. We assume $\Delta Z = 300\,\mu\text{m}$. When an even mode is incident, the optical fields at $t = 10\,\text{ps}$ and 380 ps

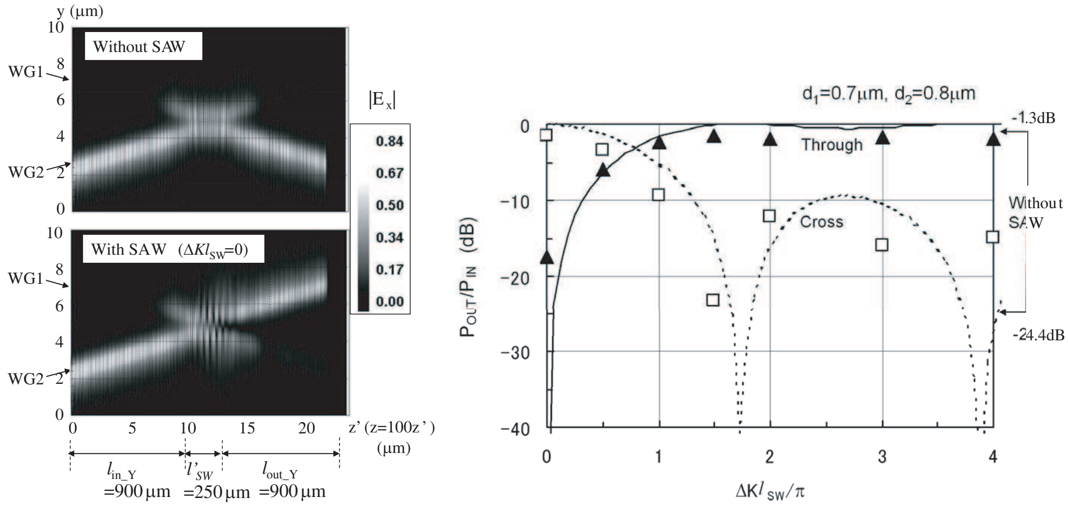

(a) (b)

Figure 5: (a) Optical switching by SAW of $\Delta n_0 = 0.01$, and (b) dependence of switched outputs on ΔK.

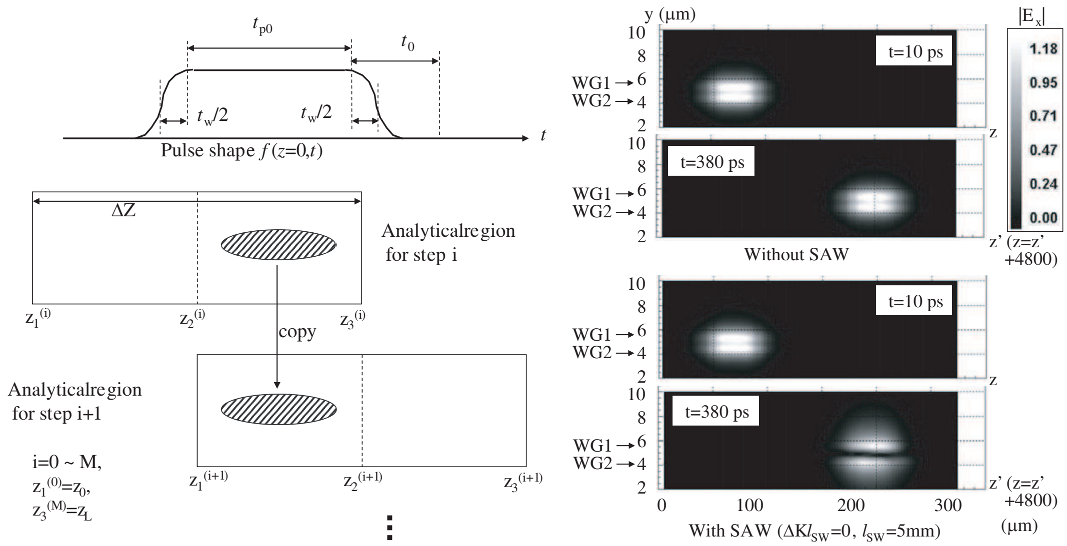

(a) (b)

Figure 6: (a) Segmented FDTD analysis model of $\Delta n_0 = 5 \times 10^{-4}$ used in pulse propagation and (b) top view of optical pulse propagation without and with SAW of $\Delta K = 0$.

are shown in Fig. 6(b). Almost complete mode conversion is performed with $l_{SW} = 5\,\text{mm}$, which corresponds to $t = 380\,\text{ps}$.

6. CONCLUSION

Optical neuro routers in multi-stage structure consisting of waveguide-type optical neuro switching devices were proposed. As an algorithm to find shortest routes, neural learning method was proposed. A waveguide-type collinear AO device was considered as the optical neuro switching device. Fundamental switching characteristics using the collinear AO device were analyzed by FDTD analysis. We will investigate the detail algorithm to derive shortest routes in future.

REFERENCES

1. Li, S. and Y. Miyazaki, "A fair and wasteless channel assignment protocol for optical dual bus networks," *IEICE Trans. Commun.*, Vol. E78-B, No. 4, 539–545, 1995.
2. Huan, X.-M. and Y. Miyazaki, "A class of semi-orthogonally associative memories neural network model," *IEICE Trans. Inf. & Syst.*, Vol. J77-D-II, No. 1, 228–235, 1994.
3. Huan, X.-M. and Y. Miyazaki, "Connected associative memory neural network with dynamical threshold function," *IEICE Trans. Inf. & Syst.*, Vol. E75-D, No. 1, 170–179, 1992.

4. Minamoto, J. and Y. Miyazaki, "Thin film waveguide type optical neural devices by controlled index distribution," *Optoelectronics Conf., Chiba*, 16D2-17, 222–223, 1992.
5. Miyazaki, Y. and J. Minamoto, "Index distribution of optical neural computing devices using graded index waveguide," *Optoelectronics — Devices and Technologies*, Vol. 8, No. 1, 99–110, 1993.
6. Goto, N. and Y. Miyazaki, "FDTD analysis of wavelength-selective optical switch using collinear acoustooptic interaction for WDM routing," *IEICE Trans. Electron.*, Vol. J86-C, No. 12, 1272–1281, 2003.
7. Goto, N. and Y. Miyazaki, "Dynamic characteristics analysis of wavelength-division-multipl exing guided-wave separation switch using acoustooptic effect," *Jpn. J. Appl. Phys.*, Vol. 42, Part 1, No. 5B, 3041–3047, 2003.

Spatial Sampling Characteristics of Beam Wave Eigen Functions Representation for Optical CT

Yasumitsu Miyazaki
Department of Media Informatics, Aichi University of Technology
50-2 Manori, Nishihasama-cho, Gamagori 443-0047, Japan

Abstract— For medical image diagnosis assisted by computers, computer tomography technologies using X-ray, optic and electromagnetic beam waves as incident waves have been rapidly developed. Incident beam waves scan in transverse cross sections of biological organs to get interior medical image information. Wave CT technologies are developed by inverse Fourier transforms for beam wave attenuations along beam propagation axises. Beam transverse scanning is based on spatial sampling theorem for transversely scanning of incident beam waves. Similar principle in space as sampling theorem in time is expressed by eigen function expansions of beam fields.

In spatial case, electric field may be expressed as super-position of local field sampling data, using local eigen functions with spatial unit element distances. In free space, asymptotic Hermite Gaussian functions for rectangular coordinates can show local beam eigen functions.

Based on spatial sampling theorem, precise image reconstruction theory of electromagnetic CT method is shown, discussing scattering and mode couplings in virtual waveguide arrays.

1. INTRODUCTION

Medical image diagnosis using computer system is rapidly developed in recent years, and computer aided image diagnosis and measurement are used in wide fields of societies including usual lives and industrial activities [1–3]. In computer tomography technology, received detected waves are mainly concerned with local absorption characteristics of propagation media and disturbed by scattering characteristics [4–6].

Incident waves are scanned along transverse direction of measured media cross-sections and have parameters of incident angles. Scanning incident waves have transversely small field distributions for scanning directions vertical to beam propagation direction. Transverse beam scannings for spatial information of measured media depend on spatial sampling theorem, considering transversely local field distribution of lower and higher beam waves [7, 8].

In this paper, generalizing of sampling theorem in time domain, basic theory of spatial sampling theorem for CT technology using beam wave eigen function systems, is discussed. For the spatial sampling theorem of CT method, asymptotic Hermite Gaussian functions expressed in rectangular coordinates are discussed for local beam eigen functions in virtual waveguide array with unit element spatial distances. For inhomogeneous target media, scattering fields disturb CT information depending on attenuation characteristics. Fundamental theory of electromagnetic waves for CT imaging is shown by electromagnetic boundary value problem, considering interaction fields of scattering and attenuation. Statistical theory of electromagnetic wave is described for electromagnetic wave propagation, attenuation and scattering in random inhomogeneous biological media. Precise image reconstruction theory of electromagnetic CT method is discussed, based on scatterings and mode couplings in inhomogeneous guided modes in virtual waveguide array consisting of random biomedical media.

2. PROJECTION CHARACTERISTICS OF EM FIELDS IN RANDOM MEDIA

Figure 1 shows transmitted and scattered laser beam waves in bio-medical media for CAD and optical scattering filter system. Propagation and scattering of electromagnetic waves in CT, are studied by the Maxwell's wave equation and integral field equation, as in Fig. 2.

Here, complex dielectric constants of bio-medical materials are $\varepsilon^*(\mathbf{r}) = \varepsilon + \sigma/(j\omega)$. Incident waves are linear polarization with z direction and t direction of propagation, vertical to z axis and transverse s direction. Time factor is $e^{j\omega t}$ and electric fields satisfy the following wave equation with $\varepsilon^* = \varepsilon_1^* + \Delta\varepsilon^*(\mathbf{r})$ and $\Delta\varepsilon^* = \varepsilon_1^*\Delta\eta$ in random media.

$$\nabla \times \nabla \times \mathbf{E} - \mu\varepsilon^*\omega^2\mathbf{E} = 0 \tag{1}$$

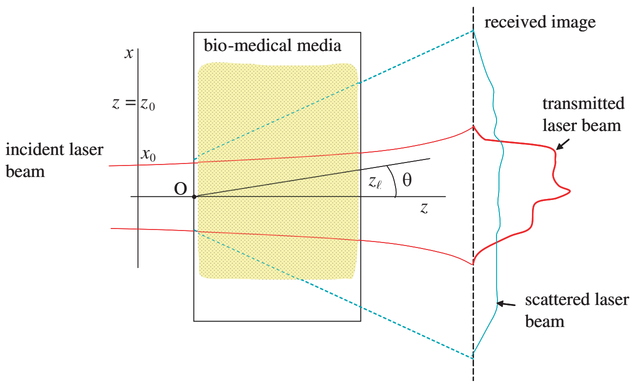

Figure 1: Transmitted and scattered laser beam waves in bio-medical media.

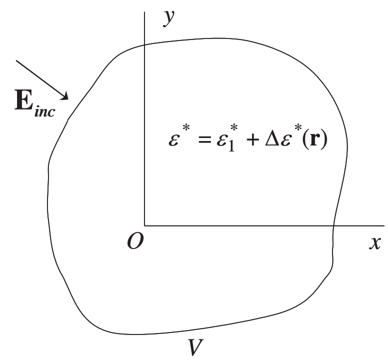

Figure 2: Propagation and scattering of electromagnetic wave in CT.

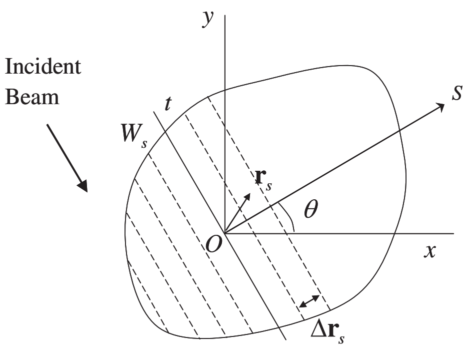

Figure 3: Projection coordinates (s, t) for spatial.

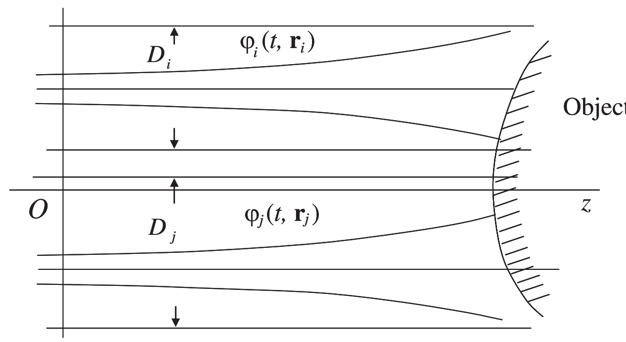

Figure 4: Global field and local beam field in sub-domain.

Incident beam waves $\mathbf{E}_{inc}$ are shown as

$$\mathbf{E}_{inc}(\mathbf{r}) = \mathbf{E}_0(\mathbf{r})\, e^{-j\beta\cdot\mathbf{r}-j\varphi(\mathbf{r})} \tag{2}$$

Using Green dyadic $\mathbf{\Gamma}(\mathbf{r}, \mathbf{r}', \omega)$ in free space, satisfying

$$\nabla\times\nabla\times\mathbf{\Gamma}\left(\mathbf{r}, \mathbf{r}'\right) - \beta^2\mathbf{\Gamma}\left(\mathbf{r}, \mathbf{r}'\right) = \mathbf{I}\delta\left(\mathbf{r}, \mathbf{r}'\right) \tag{3}$$

where $\beta^2 = \omega^2\varepsilon_1^*\mu$, total electric fields are

$$\mathbf{E} = \mathbf{E}_{inc} + \int \mathbf{\Gamma}\cdot\mathbf{F}dv' \tag{4}$$

where

$$\mathbf{F} = \mu\varepsilon_1^*\sum\int\omega^2\Delta\eta\left(\omega'\right)\mathbf{E}\left(\omega-\omega'\right)d\omega'$$

In Eq. (4), the second terms show reflected and scattered fields. Magnetic fields are

$$\mathbf{H} = \mathbf{H}_{inc} - \frac{1}{j\omega\mu}\int\nabla\times\mathbf{\Gamma}\cdot\mathbf{F}dv \tag{5}$$

When incident beam waves are transversely compact for the transverse s direction, and scanned along the s direction, local sub-domains with propagation axis of t direction may be considered as in Fig. 3. Measured regions can be divided into small sub-domains D_i ($i = 1, 2, \ldots, N$) with propagation t direction, as shown in Fig. 4.

3. SPATIAL SAMPLING THEOREM AND WAVE EIGEN FUNCTIONS

In the time domain, sampling theorem shows for temporal function $x(t)$ with limited spectrum characteristics of $|f| \leq W$,

$$x(t) = \sum_{i=-\infty}^{\infty} x\left(\frac{i}{2W}\right)\varphi_i\left(t-\frac{i}{2W}\right) \tag{6}$$

where

$$\varphi_i\left(t-\frac{i}{2W}\right)=\frac{\sin 2\pi W\left(t-i\Delta t\right)}{2\pi W\left(t-i\Delta t\right)},\quad \Delta t=\frac{1}{2W} \tag{7}$$

Sampling width $\Delta t=\frac{1}{2W}$, and i covers all region of $(-\infty,\infty)$.

Sampling theorem in space shows for the electric field $\mathbf{E}$ is given by

$$\mathbf{E}\left(\mathbf{r}\right)=\sum_{\bar{s}=-\infty}^{\infty}E^{(s)}\left(\mathbf{r}_s\right)\mathbf{\Psi}\left(\mathbf{r}-\bar{s}\Delta\mathbf{r}_s\right) \tag{8}$$

using local function $\mathbf{\Psi}\left(\mathbf{r}\right)$ for sampling distance $\Delta\mathbf{r}_s$, where $\mathbf{r}_s=\mathbf{r}-\bar{s}\Delta\mathbf{r}_s$ and discrete parameter $\bar{s}$. The local functions may be eigen functions with t propagation direction and transversely compact distribution.

Spatial sampling theorem for electromagnetic fields in random media can be discussed for sub-domains corresponding to virtual waveguide arrays with propagation t direction and s direction as in Figs. 3 and 4. Sampling coordinates (s,t) are rotated from physical coordinates (x,y) with rotation angle θ.

Total fields in random media are given by integral equations of Eq. (4) using Green's dyadic, when the incident wave is $\mathbf{E}_{inc}$. Transmitted fields can be studied by superposition of local fields with sampling distances $\Delta\mathbf{r}_s$, if total domain is divided into sub-domains corresponding to virtual waveguide W_s of $\bar{s}$ index.

These virtual waveguides W_s construct waveguide array with same parallel propagation axis t. In each virtual waveguide, field can be represented by compact local functions. Following spatial sampling theorem, incident electric field $\mathbf{E}_{inc}$ can be written, using local functions $\mathbf{\Psi}\left(\mathbf{r}\right)$ of waveguide modes and $s\mathbf{r}_{s0}=\mathbf{r}-\bar{s}\Delta\mathbf{r}_s$

$$\mathbf{E}_{inc}=\sum_{s=1}^{m}\mathbf{E}_{inc}^{(s)}\mathbf{\Psi}\left(\mathbf{r}-\bar{s}\Delta\mathbf{r}_s\right) \tag{9}$$

where corresponding amplitude in each waveguide is $\mathbf{E}_{inc}^{(s)}$, and $\mathbf{r}_{s0}$ is unit vector of s direction.

4. BEAM EIGEN FUNCTION SYSTEM AND BOUNDARY VALUE PROBLEM

At incident input, beam eigen functions have constant phase values in the t propagation axis, and local functions can be easily determined. However, in general space of propagation $t>0$, phase parameters have functions of projection coordinates (t,s), depending t coordinates as in Fig. 5. Scattering and transmission of beam wave $\mathbf{E}^{(s)}(\mathbf{r},\omega)$ at interface in Fig. 6 can be asymptotically studied for incident $s=i$ and reflection $s=r$.

Beam wave fields in free space (I) are shown, in case of z propagation, using spectrum function $\hat{\mathbf{E}}(\beta_x,\beta_y)$ with wave spectrum β_x,β_y for x,y direction.

$$\mathbf{E}^{(s)}\left(\mathbf{r},\omega\right)=E_0\int_{-\infty}^{\infty}\int_{-\infty}^{\infty}e^{-j\beta_x x-j\beta_y y-j\sqrt{\beta^2-\beta_x^2-\beta_y^2}z}\hat{\mathbf{E}}^{(s)}\left(\beta_x,\beta_y\right)d\beta_x d\beta_y \tag{10}$$

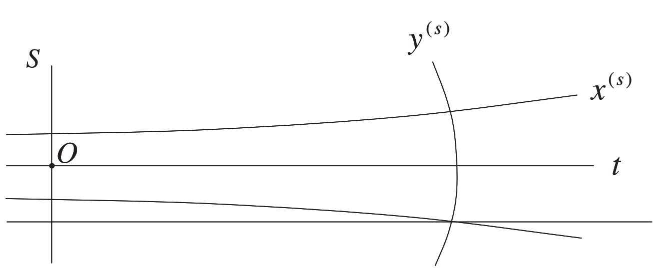

Figure 5: Beam coordinates $(x^{(s)},y^{(s)})$ for incident beam wave scanning.

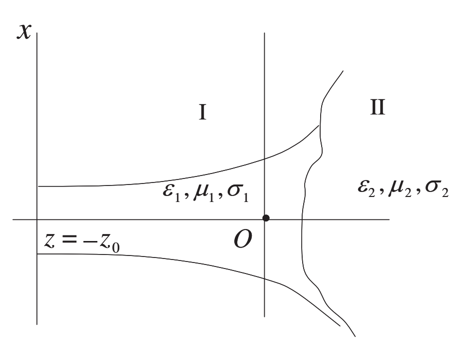

Figure 6: Reflection, scattering and transmission of optical beam waves.

Here, spectrum function of integrand can be expanded as Hermite-Gaussian system for y polarization and $i = x, y$

$$\hat{\mathbf{E}}^{(s)}(\beta_x, \beta_y) = \mathbf{i}_y \hat{\psi}_x(\beta_x)\hat{\psi}_y(\beta_y), \quad \hat{\psi}_x^{(s)}(\beta_x) = \sum_m a_{mx}^{(s)} \hat{\phi}_m(\beta_x), \quad \hat{\psi}_y^{(s)}(\beta_y) = \sum_n a_{ny}^{(s)} \hat{\phi}_n(\beta_y),$$
$$\hat{\phi}_n(\beta_i) = e^{-\frac{1}{2}\frac{\beta_i^2}{\alpha_i^2}} H_n\left(\frac{\beta_i}{\alpha_i}\right) \frac{1}{\sqrt{\alpha_i \left(2^n n! \sqrt{\pi}\right)^{1/2}}}, \quad \int_{-\infty}^{\infty} \hat{\phi}_n \hat{\phi}_{n'} d\beta_i = \delta_{nn'} \tag{11}$$

Here, transverse spectrum β_x and β_y are small, compared with β, and

$$-j\sqrt{\beta^2 - \beta_x^2 - \beta_y^2} = -j\beta\left(1 - \frac{\beta_x^2}{2\beta^2} - \frac{\beta_y^2}{2\beta^2}\right) - j\left(-\frac{1}{8}\frac{\beta_x^4}{2\beta^3} - \frac{1}{8}\frac{\beta_y^4}{2\beta^3}\right) \tag{12}$$

Hence, incident beam wave in free space can be expressed by Hermite-Gaussian mode system, using beam focusing parameter α_s, as

$$\mathbf{E}^{(s)}(\mathbf{r}_t, z) = \sum \mathbf{a}_{mn}^{(s)} \phi_m \phi_n e^{-j\beta_{mn}(x,y,z)z}, \quad \mathbf{E}(\mathbf{r}_t, z) = \sum_s \mathbf{E}^{(s)}(\mathbf{r}_t, z) \tag{13}$$

where $\mathbf{r}_t + z\mathbf{i}_z$ corresponds to $\mathbf{r} - \bar{s}\Delta\mathbf{r}_s$.

5. SPATIAL SAMPLING THEOREM USING BEAM WAVE EIGEN FUNCTION SYSTEM

When incident wave is the fundamental beam mode for z propagation, in two dimensional space (x, z)

$$\mathbf{E}^{(i)} = E_0 \mathbf{i}_y e^{-j\beta(z+z_i)} \frac{1}{\sqrt{1 - j\zeta}} e^{-\frac{a_i^2 (x - x_i)^2}{2(1 - j\zeta)}} \tag{14}$$

Here, $\zeta = \frac{(z+z_i)}{\beta} a_i^2$ and beam spot size $w_i = \frac{1}{a_i}$.

In case of two dimensional space (s, t) for t propagation, the fundamental mode is

$$E(s, t) = \frac{A}{\sqrt{1 - j\zeta}} e^{-j\beta t} e^{-\frac{s^2}{s_0^2(1 - j\zeta)}} = A\left(\frac{s_0}{s_b}\right)^{1/2} e^{-j\beta t} e^{-\frac{s^2}{s_b^2}} e^{j\phi_b} \tag{15}$$

Here, $\zeta = \frac{2t}{\beta s_0^2}$, $\alpha^2 = a^2 = \frac{2}{s_0^2}$, $s_b = s_0\sqrt{1 + \zeta^2}$ and $\phi_b = \tan^{-1}\zeta - \frac{s^2}{s_b^2}\zeta$.

When beam coordinates $(x^{(s)}, y^{(s)})$ corresponding to amplitude factor and phase factor s_b, ϕ_b are defined, beam eigen functions are, for higher modes, using Hermite functions H_m and spectrum functions

$$\hat{\phi}_m = C_m e^{-\frac{1}{2}\frac{\beta_s^2}{\alpha_s^2}} H_m\left(\frac{\beta_s}{\alpha_s}\right),$$
$$\Psi\left(x^{(s)}, y^{(s)}\right) = C_m H_m\left(\frac{y^{(s)}}{s_b}\right) e^{-\frac{y^{(s)2}}{s_b^2}} e^{j(m\tan^{-1}\zeta + j\phi_b)} = C_m H_m\left(\frac{y^{(s)}}{s_b}\right) e^{-\frac{y^{(s)2}}{s_b^2}} e^{j\phi_{b,m}} \tag{16}$$

Here, $\phi_{b,m} = \phi_b + m\tan^{-1}\zeta$.

Comparing with fundamental mode, phase factors of higher modes depend on propagation axis t and coordinate $x^{(s)}$. For small ζ, $\zeta \ll 1$, projection coordinates (s, t) coincide beam coordinates $(x^{(s)}, y^{(s)})$. Beam eigen functions are effective functions for local functions.

Beam eigen functions have asymptotic characteristics of harmonic oscillation function, for large s, $y^{(s)}$, as

$$H_m\left(\frac{y^{(s)}}{s_b}\right) \cong 2^{\frac{m+1}{2}} m^{\frac{m}{2}} e^{-\frac{m}{2}} e^{\frac{1}{2}\frac{y^{(s)2}}{s_b^2}} \cos\left(\sqrt{2m+1}\,\frac{y^{(s)}}{s_b} - \frac{m\pi}{2}\right) \tag{17}$$

Hence, spatial sampling width $|\Delta\mathbf{r}_s|$ is $y^{(s)} = \frac{\pi}{2}s_b$. The maximum mode index is given by maximum spatial frequency M of fields.

6. MODE COUPLINGS AMONG WAVEGUIDES AND IMAGE RECONSTRUCTION OF CT

Among virtual waveguide arrays, rectangular and projection coordinates, (x, y) and (s, t) are related as

$$\begin{pmatrix} x \\ y \end{pmatrix} = \begin{pmatrix} \cos\theta & -\sin\theta \\ \sin\theta & \cos\theta \end{pmatrix} \begin{pmatrix} s \\ t \end{pmatrix} \tag{18}$$

In virtual waveguide W_s, each field is expanded as, using spatial sampling characteristic and eigen functions $\{\mathbf{\Phi}_m^{(s)}\}$.

$$\mathbf{E}^{(s)} = \sum_{m=0}^{\infty} a_m^{(s)}(t)\,\mathbf{\Phi}_m^{(s)}(\mathbf{r}_t), \qquad \int \mathbf{\Phi}_m^{(s)}(\mathbf{r}_t)\,\mathbf{\Phi}_n^{*(s)}(\mathbf{r}_t) d^2\mathbf{r}_t^{(s)} = \delta_{mn} \tag{19}$$

Transmission equation is shown as

$$\frac{d\mathbf{A}}{dt} = -\mathbf{\Gamma I A} - j\mathbf{CA} \tag{20}$$

where amplitudes, and attenuation constants and phase constants of the m mode in W_s waveguide are $a_m^{(s)}$, $\alpha_m^{(s)}$ and $\beta_m^{(s)}$, and $\mathbf{A}(t)$, $A_i(t) = \alpha_m^{(s)}$, $\mathbf{\Gamma}(t)$, $\Gamma_i(t) = \alpha_m^{(s)} + j\beta_m^{(s)}$, $\mathbf{C}(t)$, $C_{ij} = C_{mn}^{(ss')}$. If $\mathbf{A}_0 = \mathbf{A}(0)$, we have

$$\mathbf{A} = \mathbf{A}_0 e^{-\int_0^\ell (\mathbf{\Gamma I} + j\mathbf{C})dt} \tag{21}$$

Hence, if the second terms of right hand side in Eq. (20) is expressed as f, intensities of the modes in waveguide W_s for waveguide length ℓ_s,

$$\left|a_m^{(s)}(\ell_s)\right|^2 = e^{-\int_0^{\ell_s} \gamma_m^{(s)}(t)dt} \tag{22}$$

where

$$\gamma_m^{(s)}(t) = 2\alpha_m^{(s)}(t) + \sum_{n,m=0}^{\infty} \sum_{s,s'=0}^{S} \sum_{\substack{u = s, s' \\ v, v' = n, m}} f\left(\alpha_v^{(u)}(t), \beta_v^{(u)}(t), C_{v,v'}^{(u,u')}(t)\right) \tag{23}$$

In Eq. (23), the first term shows attenuation effects, and the second term shows multiple reflections and scatterings that have not been enough discussed and precisely shown in this paper, using spatial sampling theorem for image reconstruction of CT. $|a_m^{(s)}(t)|^2$ are projection field data measured at received output. Extending integral region $[0, \ell_s]$ to $[-\infty, \infty]$

$$\begin{aligned} \Gamma_m(\omega) &= \int_{-\infty}^{\infty} \left\{-\log\left|a_m^{(s)}(t)\right|^2\right\} e^{-j\omega s} ds = \iint_{-\infty}^{\infty} \gamma_m^{(s)}(t)\,dt e^{-j\omega s} ds \\ &= \int_{-\infty}^{\infty}\int_{-\infty}^{\infty} \gamma_m(x, y)\, e^{-j\omega(x\cos\theta + y\sin\theta)} dxdy \end{aligned} \tag{24}$$

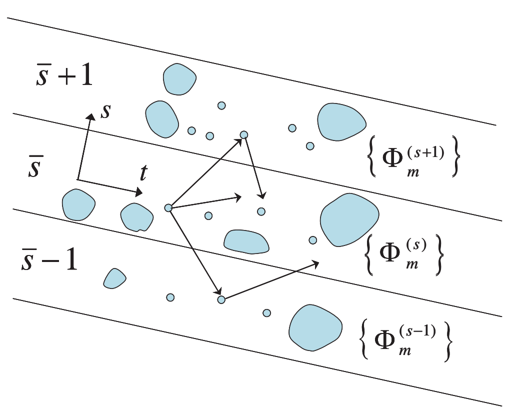

Figure 7: Multiple scatterings and mode coupling in random virtual coupling.

and using $\omega\cos\theta = \zeta$ and $\omega\sin\theta = \eta$,

$$\gamma_m(x,y) = \frac{1}{(2\pi)^2}\iint \Gamma_m(\zeta,\eta)\, e^{j\zeta x + j\eta y} d\zeta d\eta \tag{25}$$

From measured data $|a_m^{(s)}|^2$ in virtual waveguide, their Fourier transform $\Gamma_m(\omega)$ and inverse Fourier transform lead to $\gamma_m(x,y)$. From $\gamma_m(x,y)$, filtering scattered terms, we have exact absorption characteristics that yield precise image reconstruction.

7. CONCLUSION

Spatial sampling theorem is discussed using local wave eigen functions that satisfy Maxwell's equation and wave field equations. Local wave eigen functions are shown by using asymptotic Hermite-Gaussian eigen functions satisfying field equations in free space. Based on spatial sampling theorem, using local eigen functions, image reconstruction theory is shown by mode couplings among virtual random waveguides.

REFERENCES

1. Aichinger, H., et al., *Radiation Exposure and Image Quality in X-ray Diagnosis Radiology*, Springer-Verlag, 2004.
2. Miyazaki, Y., "Light scattering of laser beams by random micro-inhomogeneities in glasses and polymers," *Jpn. Jour. Appl. Phys.*, Vol. 13, No. 8, 1238–1248, 1974.
3. Sato, T., Y. Miyazaki, M. Hayakawa, and M. Koshiba, "Recent trend of electromagnetic theory in advanced technology and society," *IEE J. Trans. FM*, Vol. 126, No. 1, 5–7, 2006.
4. Miyazaki, Y., "Electromagnetic characteristics of grid structures for scattering fields of nanometer electromagnetic waves and X-rays," *PIERS Proceedings*, 643–647, Tokyo, Japan, August 2–5, 2006.
5. Miyazaki, Y., "Spatial filtering characteristics of transmitted and scattered nano-meter electromagnetic waves and X-rays in bio-medical media by waveguide-type grids," *PIERS Proceedings*, 1729–1735, Beijing, China, March 26–30, 2007.
6. Miyazaki, Y. and K. Kouno, "FDTD analysis of spatial filtering of scattered waves for optical CT of medical diagnosis," *IEE J. Trans. FM*, Vol. 129, No. 10, 693–698, 2009.
7. Miyazaki, Y., "Partially coherent optical wave in random gradient fibers," *Opt. and Quantum Electron.*, Vol. 9, 153–165, 1977.
8. Miyazaki, Y., "Image reconstruction theory of electromagnetic wave CT for scattering and absorption," *Proc. of ISMOT 2011*, 4, Electromagnetic Theory, Embedded Systems, Prague, Czech Republic, EU, 2011.

Axisymmetric Electric and Magnetic Field Calculations with Zonal Harmonic Expansion

F. Glück[1, 2]

[1]Karlsruhe Institute of Technology, IEKP, Karlsruhe 76021, P. O. Box 3640, Germany
[2]KFKI, RMKI, H-1525 Budapest, P. O. Box 49, Hungary

Abstract— The zonal harmonic expansion method is a special version of the spherical harmonic method, applied for axisymmetric systems. It can be 100–1000 times faster than the more widely known elliptic integral method and is more general than the similar radial series expansion. It has not only high speed, but also high accuracy, which makes the method especially appropriate for trajectory calculations of charged particles. Due to these properties, no interpolation is necessary when the electric and magnetic field during particle trajectories is computed with the aid of the zonal harmonic method.

The zonal harmonic field series formulas are convergent at field points within the central and remote regions, which have spherical boundaries, and their center, the source point, can be arbitrarily chosen on the symmetry axis. The rate of convergence of the field series depends on the distance of the field and the source point; smaller distance for central field points and larger distance for remote field points correspond to higher convergence rate. For a given field point, one can improve the convergence properties of the zonal harmonic method by optimal choice of the field expansion method (central or remote), of the source point, and of the source representation method. The zonal harmonic method is applicable also for special three-dimensional magnetic systems, whose components (coils or magnetic materials) are axially symmetric in their own local coordinate systems.

1. INTRODUCTION

Electric and magnetic field calculation is important in many areas of physics: electron and ion optics, charged particle beams, charged particle traps, electron microscopy, electron spectroscopy, plasma and ion sources, electron guns, superconducting and air coils, etc.. A special kind of electron and ion energy spectroscopy is realized by the MAC-E filter spectrometers, where integral energy spectrum is measured by the combination of electrostatic retardation and magnetic adiabatic collimation [1–3].

We present in our paper the zonal harmonic expansion method for electric and magnetic field caclulations: explanation of the central and remote convergence regions, and electric potential and field formulas for general axisymmetric electric systems (Section 2), magnetic field formulas for general axisymmetric magnetic systems (Section 3), considerations about the practical application of the method (Section 4), and conclusions (Section 5).

2. ELECTRIC FIELD CALCULATION

The electric potential of an arbitrary electric system in a source-free region (vacuum) can be generally written as an expansion of the spherical harmonics, which are proportional to the associated Legendre polynomials $P_n^m(\cos\theta)$. In the special case of axially symmetric electric systems, the absence of the azimuthal dependence reduces the problem to the simpler zonal harmonic expansion. Defining an arbitrary reference point S on the symmetry axis (we shall call it a source point), the central and remote solid zonal harmonics are the functions $\rho^n P_n(\cos\theta)$ and $\rho^{-(n+1)} P_n(\cos\theta)$, where ρ is the distance between the source point and the field point, θ denotes the angle between the symmetry axis and the line connecting the source and field points (Fig. 1), and $P_n(\cos\theta)$ is the Legendre polynomial of order n. Within a spherical region inside the electrodes (central region), with the source point as the center of the sphere, the electric potential and field can be expanded by central zonal harmonics:

$$\Phi(z,r) = \sum_{n=0}^{\infty} \Phi_n^{cen} \left(\frac{\rho}{\rho_{cen}}\right)^n P_n(u), \tag{1}$$

$$E_z(z,r) = -\frac{1}{\rho_{cen}} \sum_{n=0}^{\infty} \Phi_{n+1}^{cen} \cdot (n+1) \left(\frac{\rho}{\rho_{cen}}\right)^n P_n(u), \tag{2}$$

$$E_r(z,r) = \frac{s}{\rho_{cen}} \sum_{n=0}^{\infty} \Phi_{n+1}^{cen} \left(\frac{\rho}{\rho_{cen}}\right)^n P_n'(u). \tag{3}$$

Here $P_n'(u) = dP_n(u)/du$ denotes the first derivative of the Legendre polynomial of order n. The radius of the sphere (ρ_{cen}: central convergence radius) is the minimal distance between the source point and the electrodes (see Fig. 1). The parameters ρ, u and s can be written as: $\rho = \sqrt{(z-z_0)^2 + r^2}$, $u = \cos\theta = (z-z_0)/\rho$, $s = \sin\theta = \sqrt{1-u^2} = r/\rho$.

In order to compute the $P_n(u)$ and $P_n'(u)$ values for very high indices n, one can use the recurrence relations A.11 and A.12 of Ref. [4].

The central electric source constants Φ_n^{cen} represent the electric field sources (electric charges and dipoles) inside the central region. They depend on the electric sources (electric system geometry, electrode potentials, dielectric permittivities), and on the given source point: $\Phi_n^{cen} = \Phi_n^{cen}(z_0)$. In general, the Φ_n^{cen} source constants are proportional to the higher derivatives of the on-axis potential function $\Phi_0(z)$ at the source point $S(z_0, 0)$ (see Section 2.1 in Ref. [4]).

The well-known radial series expansion [6] is a special case of the more general central zonal harmonic expansion. Namely, in the case of the radial series expansion the field point and the source point have the same axial coordinate values: $z = z_0$. Changing the coordinate z of the field point, one needs different source constants for the radial series expansion, since for this calculation method the field and source points should have the same axial coordinate values. In the case of the zonal harmonic expansion, this complication is not present: one can use the same central source constants for all field points which are inside the convergence sphere with radius ρ_{cen} and center $(z_0, 0)$.

Defining the remote convergence radius ρ_{rem} by the maximal distance between the source point and the electrodes, within the remote region outside the electrodes (at field points $\rho > \rho_{rem}$) the potential can be expanded in remote zonal harmonics:

$$\Phi(z,r) = \sum_{n=0}^{\infty} \Phi_n^{rem} \left(\frac{\rho_{rem}}{\rho}\right)^{n+1} P_n(u), \tag{4}$$

$$E_z(z,r) = \frac{1}{\rho_{rem}} \sum_{n=1}^{\infty} \Phi_{n-1}^{rem} \cdot n \left(\frac{\rho_{rem}}{\rho}\right)^{n+1} P_n(u), \tag{5}$$

$$E_r(z,r) = \frac{s}{\rho_{rem}} \sum_{n=1}^{\infty} \Phi_{n-1}^{rem} \left(\frac{\rho_{rem}}{\rho}\right)^{n+1} P_n'(u). \tag{6}$$

The coefficients Φ_n^{rem} ($n = 0, 1, \ldots$) are the remote electric source constants: they represent the electric field sources (charges) in the remote region. They depend on the electric sources and on the given source point: $\Phi_n^{rem} = \Phi_n^{rem}(z_0)$. The remote zonal harmonic expansions correspond to the

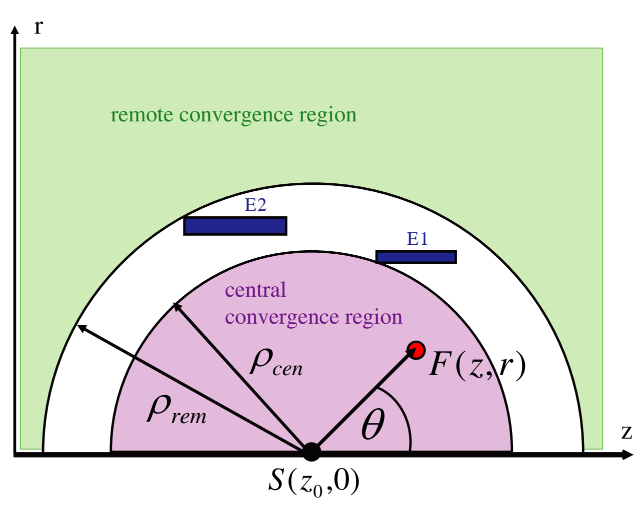

Figure 1: Electrodes E1 and E2, with field point F and source point S, and with the central ($\rho < \rho_{cen}$) and remote ($\rho > \rho_{rem}$) convergence regions.

multipole expansion of the electric potential and field, for axisymmetric systems. The first term in each expansion corresponds to the charge, the second to dipole, the third to quadrupole, etc.. The remote source constants Φ_n^{rem} are proportional to the axisymmetric multipole electric moments.

These central and remote expansion series are convergent only for $\rho < \rho_{cen}$ and $\rho > \rho_{rem}$, respectively. Let us define the convergence ratio $\mathcal{R}_c = \rho/\rho_{cen}$ for the central expansion and $\mathcal{R}_c = \rho_{rem}/\rho$ for the remote one. The rate of convergence is fast if the convergence ratio is small, and slow if $\mathcal{R}_c$ is close to 1; for $\mathcal{R}_c > 1$ the series are divergent.

The central and remote electric source constants for a charged ring, a general axisymmetric electrode and an axisymmetric dielectric can be found in Sections 3, 4 and 5 of Ref. [4].

3. MAGNETIC FIELD CALCULATION

Replacing the electrodes in Fig. 1 by coils, we get an example for an axisymmetric magnetic system. Inside the central convergence region $\rho < \rho_{cen}$, the magnetic field components B_z and B_r can be expressed by the following zonal harmonic expansion:

$$B_z = \sum_{n=0}^{\infty} B_n^{cen} \left(\frac{\rho}{\rho_{cen}}\right)^n P_n(u), \tag{7}$$

$$B_r = -s \sum_{n=1}^{\infty} \frac{B_n^{cen}}{n+1} \left(\frac{\rho}{\rho_{cen}}\right)^n P_n'(u). \tag{8}$$

The central magnetic source constants B_n^{cen} represent inside the central region the magnetic field sources (coils and magnetic materials). They depend on the magnetic sources and on the given source point: $B_n^{cen} = B_n^{cen}(z_0)$; In general, they are proportional to the higher derivatives of the on-axis magnetic field function $B_0(z)$ at the source point z_0 (see Section 2.1 in Ref. [5]).

In the remote region $\rho > \rho_{rem}$, the magnetic field can be written with the following remote zonal expansion formulas:

$$B_z = \sum_{n=2}^{\infty} B_n^{rem} \left(\frac{\rho_{rem}}{\rho}\right)^{n+1} P_n(u), \tag{9}$$

$$B_r = s \sum_{n=2}^{\infty} \frac{B_n^{rem}}{n} \left(\frac{\rho_{rem}}{\rho}\right)^{n+1} P_n'(u), \tag{10}$$

The coefficients B_n^{rem} ($n = 2, 3, \ldots$) are the remote source constants: they represent in the remote region the magnetic field sources (coils and magnetic materials). They depend on the magnetic sources and on the given source point: $B_n^{rem} = B_n^{rem}(z_0)$; The remote zonal harmonic expansions correspond to the multipole expansion of magnetic field for axisymmetric systems: the first term in each equation corresponds to the magnetic dipole, the second to the quadrupole, etc.. The remote source constants B_n^{rem} are proportional to the multipole magnetic moments.

The central and remote magnetic source constants for a circular current loop, a general axisymmetric coil, and a general axisymmetric magnetic material can be found in Sections 3, 4 and 5 of Ref. [5], respectively.

4. THE ZONAL HARMONIC EXPANSION IN PRACTICE

In order to use the zonal harmonic expansion for practical field calculations, the first step is to obtain the sources of the fields. In the case of electric field, one has to compute the charge density distribution on the surface of the electrodes and dielectrics, and the volume charge density in the dielectrics. The most natural method for this purpose is BEM, but in principle one could also use FDM or FEM. In the case of coils and permanent magnets the current densities and the magnetization is known. The magnetization of magnetic materials can be computed using some appropriate integral equation or finite element method.

The second step is the definition of the source points. They should be chosen in such a way that the central zonal harmonic expansion is convergent within a large region inside the system. The optimal distance between two neighboring central source points should be a few times smaller than the central convergence radius at these points; otherwise, it could happen that the central zonal method is not convergent at some points near the axis. In the case of a three-dimensional coil system, where each coil is axisymmetric within a local coordinate system (symmetry group), the central source points should be defined in each symmetry group. The remote source points are then defined at the center of each symmetry group.

After the source points have been defined, the code should compute the source constants at all these points. The maximal source constant index $n_{\max}$ should be chosen a few hundred or 1000, depending on the requirements of the convergence ratio and of the accuracy of the field computation. The source constant computation time is proportional to $n_{\max}$, but this is typically only a minute or less, and the source constants have to be calculated only once for a fixed magnetic system configuration. In addition to the source constants, also the convergence radii for all source points have to be computed. At the end, the source points, convergence radii and source constants for all symmetry groups are saved to the hard disk, so that they could be used for field computation later.

In the beginning of a field calculation, the source points, convergence radii and source constants have to be read from the hard disk into the main memory. In order to compute the electric or magnetic field at an arbitrary field point, the computer program first has to search for the best source point, i.e., that source point for which the convergence ratio $\mathcal{R}_c = \rho/\rho_{cen}$ or $\mathcal{R}_c = \rho_{rem}/\rho$ is minimal. If the neither the central nor the remote zonal harmonic expansion is convergent for the best source point ($\mathcal{R}_c > 1$), or the convergence is too slow (e.g., $\mathcal{R}_c > 0.98$), the elliptic integral or some other method has to be used for the field calculation.

At the end of this section, we compare the computational speed of the zonal harmonic method with the elliptic integral calculation in the case of a practically interesting problem. With our notebook (multiplication time: 0.5 ns) we have made a computation for the electric potential of the KATRIN main spectrometer [3]. The charge density calculation with BEM and with a discretization of 1800 subelements took about 20 seconds, the central source constant computation time with 600 source points and with $n_{\max} = 500$ was 40 seconds. Then, using the elliptic integrals (summing over all subelements), the computation time for the potential at a point near the middle of the spectrometer was 7 ms. With the zonal harmonic expansion method, the computation time values for the potential and field components at points with convergence ratios of 0.5, 0.8 and 0.9 were 2 µs, 6 µs and 14 µs, respectively. This example illustrates that for electric field and potential calculations the zonal harmonic expansion method is by several orders of magnitude faster than the elliptic integral method.

5. CONCLUSION

The zonal harmonic electric and magnetic field calculation method has several important advantages. First, the field and source equations are separated: during the source constant computations one has to use only the source point and source parameters (geometry, currents, magnetization), but not the field point parameters; and during the field computation the source constants contain already the whole information about the magnetic sources. As an important consequence, the field calculation with the zonal harmonic method is much faster (in some cases even 1000 times) than with the widely known elliptic integral method. Second, the zonal harmonic method has not only high speed, but also high accuracy, which makes the method especially appropriate for trajectory calculations of charged particles. Due to these properties, no interpolation is necessary when the electric and magnetic field during particle trajectories is computed with the aid of the zonal harmonic method. Third, it is more general and for practical applications more advantageous than the radial series expansion method, which is more widely known in the electron optics literature than the zonal harmonic method. In addition, the zonal harmonic field series formulas are relatively easy to differentiate and integrate, in contrast to the elliptic integral formulas. Furthemore, the low-order source constants can be helpful for system design optimization; for example, vanishing low-order central source constants imply a homogenous magnetic field near the central source point.

We wrote several FORTRAN and C codes for electric and magnetic field calculations of axially symmetric electrodes and coils. These codes have been used for electromagnetic design studies and/or trajectory calculations connected with the aSPECT proton spectrometer [1], the WITCH ion spectrometer [2], and various axisymmetric electrode systems of the KATRIN experiment [3] (see the homepages [7, 8] for many diploma theses and dissertations of KATRIN). Based upon our C codes, further electric and magnetic field simulation C and C++ codes have been written by various students at the University of Münster, at MIT, and at KIT. The zonal harmonic method presented in this paper has been included into the C++ simulation package KASSIOPEIA of the KATRIN experiment.

ACKNOWLEDGMENT

I would like to thank Profs. W. Heil, E. Otten and G. Drexlin for the possibility of long stays at the University of Mainz and at KIT (former University of Karlsruhe and Forschungszentrum Karlsruhe), supported by the German Federal Ministry of Education and Research (BMBF) under Contract Nos. 05CK1UM1/5, 05A08VK2 and 05CK5VKA/5.

REFERENCES

1. Glück, F., et al., "The neutron decay retardation spectrometer aSPECT: Electromagnetic design and systematic effects," *Eur. Phys. J. A*, Vol. 23, 135, 2005.
2. Beck, M., et al., "WITCH: A recoil spectrometer for weak interaction and nuclear physics studies," *Nucl. Instrum. Methods A*, Vol. 503, 567, 2003.
3. Angrik, J., et al., "KATRIN design report 2004," *Wissenschaftliche Berichte FZKA 7090*, KATRIN Collaboration, http://bibliothek.fzk.de/zb/berichte/FZKA7090.pdf.
4. Glück, F., "Axisymmetric electric field calculation with zonal harmonic expansion," *Progress In Electromagnetics Research B*, Vol. 32, 319–350, 2011.
5. Hawkes, P. W. and E. Kasper, *Principles of Electron Optics*, Vol. 1, Academic Press, Harcourt Brace Jovanovich, 1989.
6. Glück, F., "Axisymmetric magnetic field calculation with zonal harmonic expansion," *Progress In Electromagnetics Research B*, Vol. 32, 351–388, 2011.
7. KATRIN homepage, Talks and Publications, Diploma and Phd Theses, http://www-ik.fzk.de/ katrin/publications/thesis.html.
8. Westfälische Wilhelms-Universität Münster, Institut für Kernphysik, AG Prof. Dr. C. Weinheimer, http://www.uni-muenster.de/Physik.KP/AGWeinheimer/Arbeiten-de.html.

Dispersion Characteristics of Hyperbolic Waveguide for Weak-guidance

D. Kumar, **K. H. Mak**, **and H. Y. Wong**
Multimedia University, Malaysia

Abstract— This paper presents results on the electromagnetic wave propagation in a new type of dielectric optical waveguide of hyperbolic cross-section. The theoretical analysis essentially requires the use of an elliptic coordinate system. The Mathieu and modified Mathieu functions arise naturally in the representation of the electromagnetic field within a hyperbolic waveguide. Field components in the different sections of the guide are deduced, and the eigenvalue equation for the system is derived. The small difference in the refractive index classifies this as a case of weak guidance.

1. INTRODUCTION

The purpose of this communication is to obtain the characteristic dispersion equation of a hyperbolic waveguide. Nearly half a century has elapsed since Watkins [1] wrote his classic work on topics in electromagnetic theory dealing with periodic transmission systems. Watkins himself cited the works of Brillouin [2], Kornhauser [3], Mathers and Kino [4] as references.

The elliptic coordinate system [5] in Figure 1 is typically used in the analysis of optical waveguides with elliptic cross section, where the triplet (ξ, η, z) represents the radial, angular and axial coordinates, respectively. A structure of *hyperbolic* cross-section is a natural extension to the study of elliptic waveguides since the coordinate system used possesses both radial and angular symmetries. A special case has already been considered by Deepak et al. [6] in their detailed treatment of a similar waveguide with helical winding.

2. MATHEMATICAL PRELIMINARIES

The cross section of a simple hyperbolic waveguide is shown in Figure 2. For an elliptic waveguide, the core-cladding cross-sectional boundary is represented by a curve of constant $\xi = \xi_0$, i.e., an ellipse. Conversely, the boundary for a hyperbolic waveguide is the hyperbola $\eta = \eta_0$.

In Cartesian coordinates, the equation for this hyperbola can be written as

$$\frac{x^2}{q^2 \cos^2 \eta} - \frac{y^2}{q^2 \sin^2 \eta} = 1, \tag{1}$$

where $\pm q$ are the locations of the foci and $2q \cos \eta$ is the separation of the vertices along the x-axis. The core-cladding refractive indices are n_1 and n_2, respectively. We consider the case of a weakly-guiding, step-index waveguide, where the ratio $(n_1 - n_2)/n_1$ is positive, but much smaller than 1.

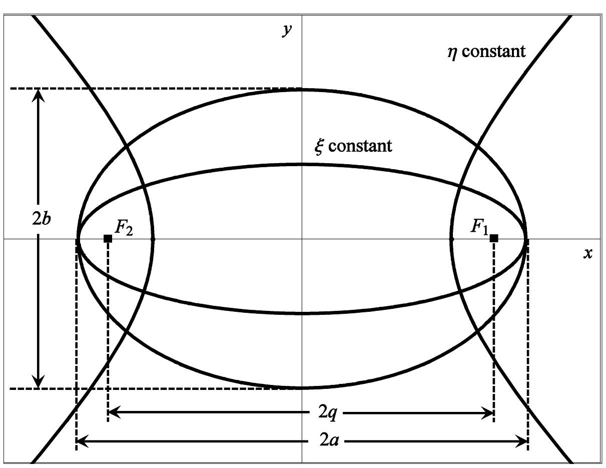

Figure 1: Elliptic coordinate system.

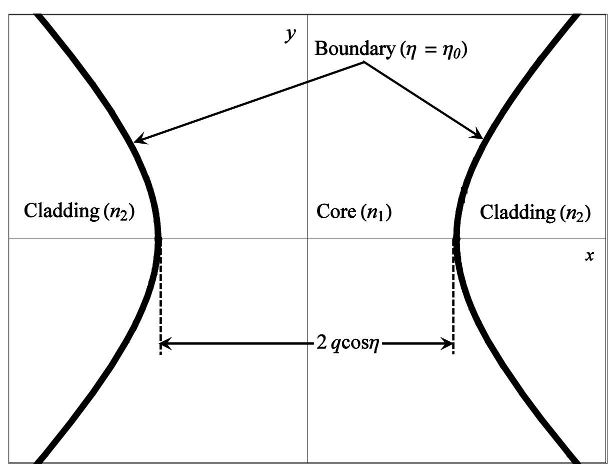

Figure 2: Cross-sectional view of hyperbolic waveguide.

The appropriate expressions are derived for the field components [7,8] E_{z1}, H_{z1}, E_{z2} and H_{z2} of the axial electric and magnetic fields, respectively. We also write the expressions for the tangential (elliptic radial) electric field components $E_{\xi 1}$, $H_{\xi 1}$, $E_{\xi 2}$ and $H_{\xi 2}$. In this notation, the subscripts "1" and "2" refer to the core and cladding regions of the guide, respectively.

3. ELECTROMAGNETIC FIELD COMPONENTS AT THE BOUNDARY

Since the hyperbola is symmetrical with respect to both the x-axis and y-axis, it is sufficient to consider the part of the structure in the first quadrant only: $\eta_0 < \eta < \pi/2$ represents the core region and $0 < \eta < \eta_0$ the cladding region. The field components in both regions are presented in the following sections (the reader may refer to the Appendix for notation used in relation to Mathieu functions.)

3.1. Even Modes

In the core region ($\eta_0 < \eta < \pi/2$),

$$E_{z1} = K\,Se_\nu(\xi,\gamma_1^2)se_\nu(\eta_0,\gamma_1^2), \tag{2a}$$
$$H_{z1} = L\,Ce_\nu(\xi,\gamma_1^2)ce_\nu(\eta_0,\gamma_1^2). \tag{2b}$$

In the cladding region ($0 < \eta < \eta_0$),

$$E_{z2} = M\,Gek_\nu(\xi,-\gamma_2^2)se_\nu(\eta_0,-\gamma_2^2), \tag{3a}$$
$$H_{z2} = N\,Fek_\nu(\xi,-\gamma_2^2)ce_\nu(\eta_0,-\gamma_2^2). \tag{3b}$$

3.2. Odd Modes

In the core region ($\eta_0 < \eta < \pi/2$),

$$E_{z1} = KCe_\nu(\xi,\gamma_1^2)ce_\nu(\eta_0,\gamma_1^2), \tag{4a}$$
$$H_{z1} = LSe_\nu(\xi,\gamma_1^2)se_\nu(\eta_0,\gamma_1^2). \tag{4b}$$

In the cladding region ($0 < \eta < \eta_0$),

$$E_{z2} = MFek_\nu(\xi,-\gamma_2^2)ce_\nu(\eta_0,-\gamma_2^2), \tag{5a}$$
$$H_{z2} = NGek_\nu(\xi,-\gamma_2^2)se_\nu(\eta_0,-\gamma_2^2). \tag{5b}$$

In Eqs. (2)–(5), K, L, M and N are arbitrary constants to be determined from the boundary conditions. The tangential field components can be obtained by converting Maxwell's equations into elliptic coordinates:

$$\begin{aligned} E_{\xi 1} &= \frac{i}{\omega n_1^2\varepsilon_0 ql}L\cdot Ce_\nu(\xi,\gamma_1^2)ce'_\nu(\eta_0,\gamma_1^2) \\ &\quad+\frac{i\beta}{\omega n_1^2\varepsilon_0 u^2 ql}\left[\beta L\cdot Ce_\nu(\xi,\gamma_1^2)ce'_\nu(\eta_0,\gamma_1^2)+\omega n_1^2\varepsilon_0 K\cdot Se'_\nu(\xi,\gamma_1^2)se_\nu(\eta_0,\gamma_1^2)\right], \end{aligned} \tag{6a}$$

$$\begin{aligned} H_{\xi 1} &= \frac{-i}{\omega\mu_0 ql}K\cdot Se_\nu(\xi,\gamma_1^2)se'_\nu(\eta_0,\gamma_1^2) \\ &\quad-\frac{i\beta}{\omega\mu_0 u^2 ql}\left[\beta K\cdot Se_\nu(\xi,\gamma_1^2)se'_\nu(\eta_0,\gamma_1^2)-\omega\mu_0 L\cdot Ce'_\nu(\xi,\gamma_1^2)ce_\nu(\eta_0,\gamma_1^2)\right], \end{aligned} \tag{6b}$$

$$\begin{aligned} E_{\xi 2} &= \frac{i}{\omega n_2^2\varepsilon_0 ql}N\cdot Fek_\nu(\xi,-\gamma_2^2)ce'_\nu(\eta_0,-\gamma_2^2) \\ &\quad-\frac{i\beta}{\omega n_2^2\varepsilon_0 w^2 ql}\left[\beta N\cdot Fek_\nu(\xi,-\gamma_2^2).ce'_\nu(\eta_0,-\gamma_2^2)+\omega n_2^2\varepsilon_0 M\cdot Gek'_\nu(\xi,-\gamma_2^2)se_\nu(\eta_0,-\gamma_2^2)\right], \end{aligned} \tag{7a}$$

$$\begin{aligned} H_{\xi 2} &= \frac{-i}{\omega\mu_0 ql}M\cdot Gek_\nu(\xi,-\gamma_2^2)se'_\nu(\eta_0,-\gamma_2^2) \\ &\quad+\frac{i\beta}{\omega\mu_0 w^2 ql}\left[\beta M\cdot Gek_\nu(\xi,-\gamma_2^2)se'_\nu(\eta_0,-\gamma_2^2)-\omega\mu_0 N\cdot Fek'_\nu(\xi,-\gamma_2^2)ce_\nu(\eta_0,-\gamma_2^2)\right], \end{aligned} \tag{7b}$$

where $u^2 = k^2n_1^2-\beta^2$, $-w^2 = k^2n_2^2-\beta^2$, $l = (\cosh^2\xi-\cos 2\eta)^{1/2}$, $\gamma_1 = uq/2$ and $\gamma_2 = wq/2$.

4. THE EIGENVALUE EQUATION

The tangential components of the electric and the magnetic fields must satisfy the following equations at the boundary $\eta = \eta_0$:

$$E_{z1} = E_{z2}, \quad H_{z1} = H_{z2}, \quad E_{\xi 1} = E_{\xi 2}, \quad H_{\xi 1} = H_{\xi 2}. \tag{8}$$

Applying the above boundary conditions, we obtain the homogeneous system of equations

$$KCe_\nu(\xi,\gamma_1^2)ce_\nu(\eta_0,\gamma_1^2) - MFek_\nu(\xi,-\gamma_2^2)ce_\nu(\eta_0,-\gamma_2^2) = 0, \tag{9a}$$

$$LSe_\nu(\xi,\gamma_1^2)se_\nu(\eta_0,\gamma_1^2) - NGek_\nu(\xi,-\gamma_2^2)se_\nu(\eta_0,-\gamma_2^2) = 0, \tag{9b}$$

$$\begin{aligned}
&K\frac{i\beta}{u^2 ql}Se'_\nu(\xi,\gamma_1^2)se_\nu(\eta_0,\gamma_1^2)\\
&+L\left[\frac{i}{\omega n_1^2\varepsilon_0 ql}Ce_\nu(\xi,\gamma_1^2)ce'_\nu(\eta_0,\gamma_1^2) + \frac{i\beta^2}{\omega n_1^2\varepsilon_0 u^2 ql}Ce_\nu(\xi,\gamma_1^2)ce'_\nu(\eta_0,\gamma_1^2)\right]\\
&+M\frac{i\beta}{\omega w^2 ql}Gek'_\nu(\xi,-\gamma_2^2)se_\nu(\eta_0,-\gamma_2^2)\\
&+N\left[\frac{i\beta^2}{\omega n_2^2\varepsilon_0 w^2 ql}Fek_\nu(\xi,-\gamma_2^2)ce'_\nu(\eta_0,-\gamma_2^2) - \frac{i}{\omega n_2^2\varepsilon_0 ql}Fek_\nu(\xi,-\gamma_2^2)ce'_\nu(\eta_0,-\gamma_2^2)\right] = 0.
\end{aligned} \tag{9c}$$

$$\begin{aligned}
&K\left[\frac{-i}{\omega\mu_0 ql}Se_\nu(\xi,\gamma_1^2)se'_\nu(\eta_0,\gamma_1^2) - \frac{i\beta^2}{\omega\mu_0 u^2 ql}Se_\nu(\xi,\gamma_1^2)se'_\nu(\eta_0,\gamma_1^2)\right]\\
&+L\frac{i\beta}{u^2 ql}Ce'_\nu(\xi,\gamma_1^2)ce_\nu(\eta_0,\gamma_1^2)\\
&+M\left[\frac{i}{\omega\mu_0 ql}Gek_\nu(\xi,-\gamma_2^2)se'_\nu(\eta_0,-\gamma_2^2) - \frac{i\beta^2}{\omega\mu_0 w^2 ql}Gek_\nu(\xi,-\gamma_2^2)se'_\nu(\eta_0,-\gamma_2^2)\right]\\
&+N\frac{i\beta}{w^2 ql}Fek'_\nu(\xi,-\gamma_2^2)ce_\nu(\eta_0,-\gamma_2^2) = 0.
\end{aligned} \tag{9d}$$

Eliminating the constants K, L, M and N from this system yields the following 4×4 determinant:

$$\begin{vmatrix}
Ce_\nu(\xi,\gamma_1^2)ce_\nu(\eta_0,\gamma_1^2) & 0 & -Fek_\nu(\xi,-\gamma_2^2)ce_\nu(\eta_0,-\gamma_2^2) & 0\\
0 & Se_\nu(\xi,\gamma_1^2)se_\nu(\eta_0,\gamma_1^2) & 0 & -Gek_\nu(\xi,-\gamma_2^2)se_\nu(\eta_0,-\gamma_2^2)\\
\frac{i\beta}{u^2 ql}Se'_\nu(\xi,\gamma_1^2)se_\nu(\eta_0,\gamma_1^2) & \left(\frac{i}{\omega n_1^2\varepsilon_0 ql}\left(1+\frac{\beta^2}{u^2}\right)\cdot Ce_\nu(\xi,\gamma_1^2)ce'_\nu(\eta_0,\gamma_1^2)\right) & \frac{i\beta}{\omega w^2 ql}Gek'_\nu(\xi,-\gamma_2^2)se_\nu(\eta_0,-\gamma_2^2) & \left(\frac{-i\beta^2}{\omega n_2^2\varepsilon_0 w^2 ql}\left(1-\frac{\beta^2}{w^2}\right)\cdot Fek_\nu(\xi,-\gamma_2^2)ce'_\nu(\eta_0,-\gamma_2^2)\right)\\
\left(\frac{-i}{\omega\mu_0 ql}\left(1+\frac{\beta^2}{u^2}\right)\cdot Se_\nu(\xi,\gamma_1^2)se'_\nu(\eta_0,\gamma_1^2)\right) & \frac{i\beta}{u^2 ql}Ce'_\nu(\xi,\gamma_1^2)ce_\nu(\eta_0,\gamma_1^2) & \left(\frac{i}{\omega\mu_0 ql}\left(1-\frac{\beta^2}{w^2}\right)\cdot Gek_\nu(\xi,-\gamma_2^2)se'_\nu(\eta_0,-\gamma_2^2)\right) & \frac{i\beta}{w^2 ql}Fek'_\nu(\xi,-\gamma_2^2)ce_\nu(\eta_0,-\gamma_2^2)
\end{vmatrix}$$

$$= 0 \tag{10}$$

Its resulting expansion provides the waveguide eigenvalue equation:

$$\begin{aligned}
&\frac{-\beta^2}{(2\pi/\lambda)cw^4}Ce_\nu(\xi,\gamma_1^2)Se_\nu(\xi,\gamma_1^2)Gek'_\nu(\xi,-\gamma_2^2)Fek'_\nu(\xi,-\gamma_2^2)\\
&ce_\nu(\eta_0,\gamma_1^2)se_\nu(\eta_0,\gamma_1^2)se_\nu(\eta_0,-\gamma_2^2)ce_\nu(\eta_0,-\gamma_2^2)\\
-&\frac{1}{(2\pi/\lambda)^2 n_2^2}Ce_\nu(\xi,\gamma_1^2)Se_\nu(\xi,\gamma_1^2)Gek_\nu(\xi,-\gamma_2^2)Fek_\nu(\xi,-\gamma_2^2)\\
&ce_\nu(\eta_0,\gamma_1^2)se_\nu(\eta_0,\gamma_1^2)se'_\nu(\eta_0,-\gamma_2^2)ce'_\nu(\eta_0,-\gamma_2^2)
\end{aligned}$$

$$
\begin{aligned}
&- \frac{\beta^4}{(2\pi/\lambda)^2 n_2^2 w^4} Ce_\nu(\xi,\gamma_1^2) Se_\nu(\xi,\gamma_1^2) Gek_\nu(\xi,-\gamma_2^2) Fek_\nu(\xi,-\gamma_2^2)\\
&\quad ce_\nu(\eta_0,\gamma_1^2) se_\nu(\eta_0,\gamma_1^2) se'_\nu(\eta_0,-\gamma_2^2) ce'_\nu(\eta_0,-\gamma_2^2)\\
&+ \frac{1}{(2\pi/\lambda)^2 n_1^2} Ce_\nu(\xi,\gamma_1^2) Se_\nu(\xi,\gamma_1^2) Gek_\nu(\xi,-\gamma_2^2) Gek_\nu(\xi,-\gamma_2^2)\\
&\quad ce_\nu(\eta_0,\gamma_1^2) se_\nu(\eta_0,-\gamma_2^2) se'_\nu(\eta_0,-\gamma_2^2) ce'_\nu(\eta_0,\gamma_1^2)\\
&+ \frac{\beta^2}{(2\pi/\lambda)^2 n_1^2} Ce_\nu(\xi,\gamma_1^2) Ce_\nu(\xi,\gamma_1^2) Gek_\nu(\xi,-\gamma_2^2) Gek_\nu(\xi,-\gamma_2^2)\\
&\quad ce_\nu(\eta_0,\gamma_1^2) se_\nu(\eta_0,-\gamma_2^2) ce'_\nu(\eta_0,\gamma_1^2) se'_\nu(\eta_0,-\gamma_2^2) \left[1/u^2 - 1/w^2\right]\\
&- \frac{\beta^4}{(2\pi/\lambda)^2 n_1^2 u^2 w^2} Ce_\nu(\xi,\gamma_1^2) Ce_\nu(\xi,\gamma_1^2) Gek_\nu(\xi,-\gamma_2^2) Gek_\nu(\xi,-\gamma_2^2)\\
&\quad ce_\nu(\eta_0,\gamma_1^2) se_\nu(\eta_0,-\gamma_2^2) ce'_\nu(\eta_0,\gamma_1^2) se'_\nu(\eta_0,-\gamma_2^2)\\
&- \frac{\beta^2}{(2\pi/\lambda) c u^2 w^2} Ce_\nu(\xi,\gamma_1^2) Ce'_\nu(\xi,\gamma_1^2) Gek_\nu(\xi,-\gamma_2^2) Gek'_\nu(\xi,-\gamma_2^2)\\
&\quad ce_\nu(\eta_0,\gamma_1^2) se_\nu(\eta_0,-\gamma_2^2) se_\nu(\eta_0,-\gamma_2^2) ce_\nu(\eta_0,\gamma_1^2)\\
&- \frac{\beta^2}{u^2 w^2} Fek_\nu(\xi,-\gamma_2^2) Se_\nu(\xi,\gamma_1^2) Se'_\nu(\xi,\gamma_1^2) Fek'_\nu(\xi,-\gamma_2^2)\\
&\quad ce_\nu(\eta_0,-\gamma_2^2) se_\nu(\eta_0,\gamma_1^2) se_\nu(\eta_0,\gamma_1^2) ce_\nu(\eta_0,-\gamma_2^2)\\
&+ \frac{\beta^2}{(2\pi/\lambda)^2 n_2^2} Fek_\nu(\xi,-\gamma_2^2) Fek_\nu(\xi,-\gamma_2^2) Se_\nu(\xi,\gamma_1^2) Se_\nu(\xi,\gamma_1^2)\\
&\quad ce_\nu(\eta_0,-\gamma_2^2) se_\nu(\eta_0,\gamma_1^2) se'_\nu(\eta_0,\gamma_1^2) ce'_\nu(\eta_0,-\gamma_2^2) \left[1/u^2 - 1/w^2\right]\\
&+ \frac{1}{(2\pi/\lambda)^2 n_2^2} Fek_\nu(\xi,-\gamma_2^2) Fek_\nu(\xi,-\gamma_2^2) Se_\nu(\xi,\gamma_1^2) Se_\nu(\xi,\gamma_1^2)\\
&\quad ce_\nu(\eta_0,-\gamma_2^2) se_\nu(\eta_0,\gamma_1^2) se'_\nu(\eta_0,\gamma_1^2) ce'_\nu(\eta_0,-\gamma_2^2)\\
&- \frac{\beta^4}{(2\pi/\lambda)^2 n_2^2 u^2 w^2} Fek_\nu(\xi,-\gamma_2^2) Fek_\nu(\xi,-\gamma_2^2) Se_\nu(\xi,\gamma_1^2) Se_\nu(\xi,\gamma_1^2)\\
&\quad ce_\nu(\eta_0,-\gamma_2^2) se_\nu(\eta_0,\gamma_1^2) ce'_\nu(\eta_0,-\gamma_2^2) se'_\nu(\eta_0,\gamma_1^2)\\
&- \frac{\beta^4}{u^4} Fek_\nu(\xi,-\gamma_2^2) Gek_\nu(\xi,-\gamma_2^2) Se'_\nu(\xi,\gamma_1^2) Ce'_\nu(\xi,\gamma_1^2)\\
&\quad ce_\nu(\eta_0,-\gamma_2^2) se_\nu(\eta_0,-\gamma_2^2) se_\nu(\eta_0,\gamma_1^2) ce_\nu(\eta_0,\gamma_1^2)\\
&- \frac{1}{(2\pi/\lambda)^2 n_1^2} Fek_\nu(\xi,-\gamma_2^2) Gek_\nu(\xi,-\gamma_2^2) Se_\nu(\xi,\gamma_1^2) Ce_\nu(\xi,\gamma_1^2)\\
&\quad ce_\nu(\eta_0,-\gamma_2^2) se_\nu(\eta_0,-\gamma_2^2) se'_\nu(\eta_0,\gamma_1^2) ce'_\nu(\eta_0,\gamma_1^2)\\
&- \frac{2\beta^2}{(2\pi/\lambda)^2 n_1^2 u^2} Fek_\nu(\xi,-\gamma_2^2) Gek_\nu(\xi,-\gamma_2^2) Se_\nu(\xi,\gamma_1^2) Ce_\nu(\xi,\gamma_1^2)\\
&\quad ce_\nu(\eta_0,-\gamma_2^2) se_\nu(\eta_0,-\gamma_2^2) se'_\nu(\eta_0,\gamma_1^2) ce'_\nu(\eta_0,\gamma_1^2)\\
&- \frac{\beta^4}{(2\pi/\lambda)^2 n_1^2 u^4} Fek_\nu(\xi,-\gamma_2^2) Gek_\nu(\xi,-\gamma_2^2) Se_\nu(\xi,\gamma_1^2) Ce_\nu(\xi,\gamma_1^2)\\
&\quad ce_\nu(\eta_0,-\gamma_2^2) se_\nu(\eta_0,-\gamma_2^2) se'_\nu(\eta_0,\gamma_1^2) ce'_\nu(\eta_0,\gamma_1^2) = 0
\end{aligned}
\tag{11}
$$

5. CONCLUSIONS

The characteristic equation (11) constitutes the central new idea of this investigation on the hyperbolic waveguide, which is a complex structure to study analytically. It is of interest to see that the method used is able to make an appreciable simplification of this highly complicated problem. This is also a starting point for numerical computations which the authors intend to submit in future communication.

APPENDIX

Table 1 summarizes the various types of Mathieu functions used in this paper.

Table 1: Mathieu function notation.

$ce_\nu(\eta_0, \gamma_1^2)$ $se_\nu(\eta_0, \gamma_1^2)$	Mathieu functions of the first kind.
$ce_\nu(\eta_0, -\gamma_2^2)$ $se_\nu(\eta_0, -\gamma_2^2)$	Mathieu functions of the second kind.
$Ce_\nu(\xi, \gamma_1^2)$ $Se_\nu(\xi, \gamma_1^2)$	Modified Mathieu functions of the first kind.
$Gek_\nu(\xi, -\gamma_2^2)$ $Fek_\nu(\xi, -\gamma_2^2)$	Modified Mathieu functions of the second kind.

REFERENCES

1. Watkins, D. A., *Topics in Electromagnetic Theory*, Wiley, New York, 1958.
2. Brillouin, L., *Wave Propagation in Periodic Structures*, Dover Publications, Inc., New York, 1953.
3. Kornhauser, E. T., "Radiation field of helical antennas with sinusoidal current," *J. Appl. Phy.*, Vol. 22, 887–891, 1951.
4. Mathers, G. W. C. and G. S. Kino, "Some properties of a sheath helix with a center conductor or external shield," Report No. 65, Electronics Research Laboratory, Stanford University, Stanford, California, 1953.
5. Verma, K. K. and D. Kumar, *The Elements of Vector Calculus*, AITBS Publisher and Distributor, New Delhi, India, 2005.
6. Kumar, D., P. K. Choudhury, and F. Abd-Rahman, "Towards the characteristic dispersion relation for step-index hyperbolic waveguide with conducting helical winding," *Progress In Electromagnetic Research*, Vol. 71, 251–275, 2007.
7. Kumar, D. and O. N. Singh, II, "Modal characteristic equation and dispersion curves for an elliptical step-index fiber with a conducting helical winding on the core-cladding boundary — An analytical study," *IEEE J. of Lightwave Tech.*, Vol. 20, No. 8, 1416–1424, 2002.
8. Kumar, D. and O. N. Singh, II, "Some special cases of propagation characteristics of an elliptical step-index fiber with a conducting helical winding on the core-cladding boundary — An analytical treatment," *Optik*, Vol. 112, No. 12, 561–566, 2001.

Design of 120 GHz, 1 MW Gyrotron for Plasma Fusion Application

Anil Kumar, **Nitin Kumar**, **Udaybir Singh**, **R. Bhattacharya**, **Narendra K. Singh**, **Hasina Khatun**, **M. K. Alaria**, **and A. K. Sinha**
Central Electronics Engineering Research Institute (CEERI, CSIR)
Pilani, Rajasthan-333031, India

Abstract— In this article a complete design of the gyrotron is presented. Considering the goal of 1 MW power and 120 GHz frequency, first the mode selection and the interaction cavity design are performed. The high order asymmetric mode $TE_{22,6}$ is selected as the operating mode by using the mode selection code GCOMS. The interaction cavity geometry is calculated on the basis of selected operating mode and Particle-in-Cell (PIC) code is used for the beam-wave interaction computation and power and frequency growth estimation. The electron beam source (generally called Magnetron Injection Gun, MIG) is designed by using the EGUN and TRACK codes. The spent electron beam energy is collected at the specially designed cylindrical waveguide type of structure called collector. For the 120 GHz gyrotron, single stage depressed collector is designed to improve the efficiency considering the maximum beam spread at the collector wall. Finally, the RF window is designed for the effective transmission of the generated RF power. The overall design data shows the 1 MW power generation at 120 GHz frequency.

1. INTRODUCTION

The gyrotron is a high power, high frequency millimeter wave source based on the phenomenon called Cyclotron Resonance Maser (CRM) instability [1]. The device generates the coherent millimeter and sub-millimeter wave radiation up to megawatt power level by the interaction between the relativistic gyrating electron beam and the RF [2]. The device shows various potential applications at different frequencies and power levels in the field of plasma diagnostics, material processing, THz spectroscopy, high density communication, weather monitoring, security etc. [3, 4]. The development of the device was initiated by the plasma fusion community to fulfill the requirement of a high power, high frequency radiation source required in the Electron Cyclotron Resonance Heating (ECRH) in the magnetically confined plasma fusion. At present, the gyrotron is a signature device in the field of ECRH [5]. The millimeter wave radiation of 120 GHz frequency with 1 MW or more RF power is used in the TOKAMAK system for plasma fusion applications. Considering the importance of this frequency for the Indian plasma fusion system, an activity related to the development of the high power, high frequency gyrotron is initiated. The design task for 120 GHz gyrotron has been completed and reported in this article. The design study of various parts including electron beam source, magnet system, mode selection, interaction cavity, beam dumping system and RF window, is presented in the upcoming sections. Various commercial as well as in-house developed computer codes are used in the designing and discussed in the successive sections.

2. INTERACTION CAVITY DESIGN

The first step in the gyrotron designing is the mode selection. The theory of the mode selection is quit mature and on the basis of the developed theory and various mode selection parameters, a computer code GCOMS is developed. GCOMS [6, 7]. Various high order modes, like, $TE_{22,6}$, $TE_{28,4}$, $TE_{28,6}$, $TE_{24,6}$, etc, are analyzed considering the start oscillation current and ohmic wall loss as minimum as possible because of high output power (> 1 MW). The mode selection parameters like space charge effect, start oscillation current, coupling coefficient, etc are also analyzed for these modes. Finally, $TE_{22,6}$ mode is selected as the operating mode (Fig. 1). The co-rotating electric field of first radial maxima of the operating mode is selected as the electron beam launching position for better beam-wave coupling. The optimized interaction cavity geometry is given in Table 1.

On the basis of the calculated interaction cavity geometrical parameters, the cold cavity analysis is performed by using the Particle-in-Cell (PIC) code MAGIC. The electron beam consist all the initially estimated parameters is launched at the first radial maxima ($R_b = 9.25$ mm) of the operating mode in the interaction cavity during the simulations. Further, the beam parameters are optimized by PIC code to obtain the maximum interaction efficiency. Finally optimized electron beam parameters are shown in Table 2. Figs. 2 and 3 show the frequency and power growth with respect to the time. 1.2 MW of output power is achieved at 120.36 GHz frequency with 37.5% efficiency.

Table 1: Interaction cavity parameters.

Middle section length (L)	15 mm
Input taper length (L_1)	12 mm
Output taper length (L_2)	20 mm
Cavity radius (R_c)	18.2 mm
Input taper angle (θ_1)	2.8°
Output taper angle (θ_2)	2.8°
Operating mode	$TE_{22,6}$
Quality factor (Q)	700

Table 2: Optimized electron beam parameters.

Beam voltage (V_b)	80 kV
Beam current (I_b)	40 A
Cavity magnetic field (B_0)	4.82 T
Beam radius (R_b)	9.25 mm
Velocity ratio of electron beam (α)	1.35–1.4

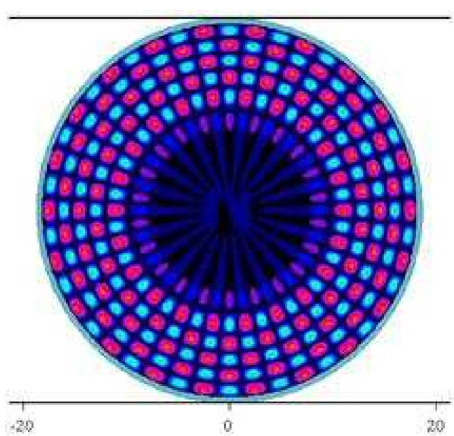

Figure 1: Electric field profile for the operating mode.

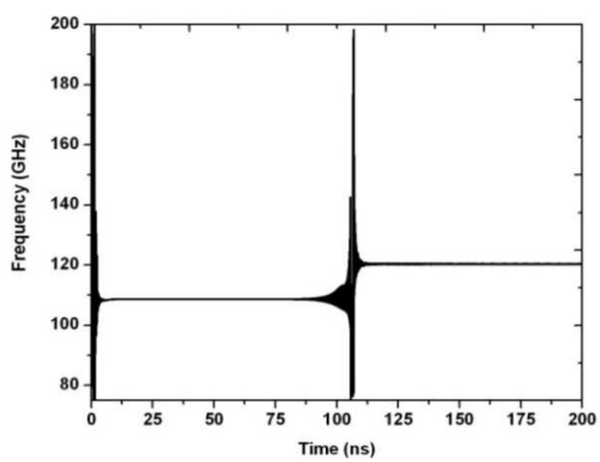

Figure 2: Frequency growth with time.

3. MAGNETRON INJECTION GUN

On the basis of the cavity simulation results, a 3.2 MW triode type electron gun having the beam voltage (V_0) = 80 kV, the beam current (I_0) = 40 A and the transverse to axial velocity ratio of the gyrating beam (α) = 1.4 is designed. The triode type MIG is chosen because of its additional control on the electron beam properties. The initial gun parameters are obtained from the analytical trade-off equations [8]. Optimization of the MIG geometry is performed by using the commercially available code EGUN and in-house developed code MIGANS [9]. The main goals of the MIG designing are the launching of electron beam at particular radial position (decided in cavity design, R_b = 9.25 mm) with minimum velocity spread ($\delta\beta_{\perp\,\max} < 5\%$) and an optimum velocity ratio ($1.2 < \alpha < 1.5$). Considering these goals, the geometry of cathode (emitter) and anodes, gap between cathode and anodes, slant angle, slant length, magnetic field profile, magnetic field at cathode center, modulating anode voltage, etc are optimized. Fig. 4 shows the electron trajectory simulation results and magnetic field profile for the optimized MIG parameters using EGUN code.

4. DESIGN OF BEAM DUMPING SYSTEM AND RF WINDOW

Single stage depressed collector is designed for the 120 GHz gyrotron to enhance the overall efficiency of gyrotron and to minimize the thermal loading on the collector wall. The use of the depressed collector enhances the overall tube efficiency up to around 50% [10]. On the basis of previous experience of un-depressed collector designing [11], the design process is started considering two goals: maximum beam spreading at collector wall and maximum collector efficiency. EGUN trajectory code is used for the trajectory analysis. Extra three collector magnet coils are used to spread out the electron beam at the collector surface. The position of magnet coils and number of turns are optimized for efficient beam spreading at the collector wall and summarized in Table 3. Fig. 5 shows the optimized collector geometry with the electron beam spreading. The spreading is almost uniform with 281 mm of spread length. For this spread length the calculated heat flux is 0.48 kW/cm^2, which is under the technical limit of heat flux for OFHC copper (1 kW/cm^2). 32 beamlets are used in the EGUN simulations. The depressed potential of 45 kV is optimized consid-

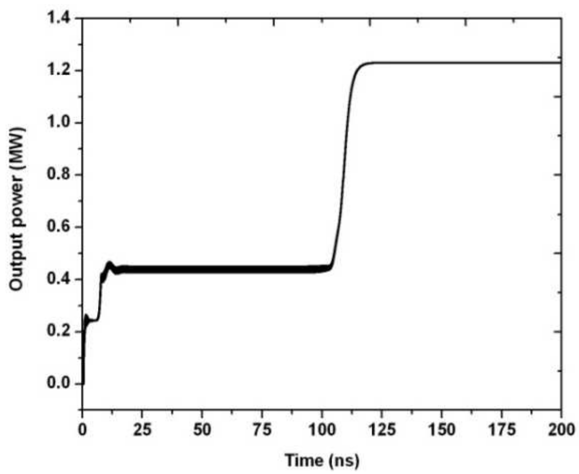

Figure 3: Power growth with time.

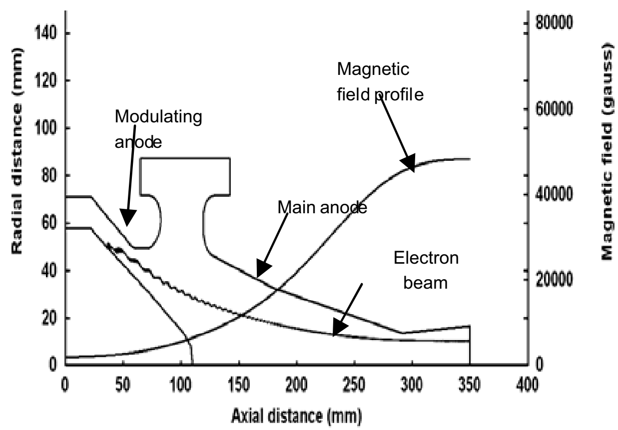

Figure 4: MIG with electrode geometry, beam profile and magnetic field.

Table 3: The collector magnet coils data.

	Position Axial	Radial	Ampere turns
Magnet A	1054 mm	180 mm	285
Magnet B	1194 mm	180 mm	300
Magnet C	1312 mm	180 mm	300

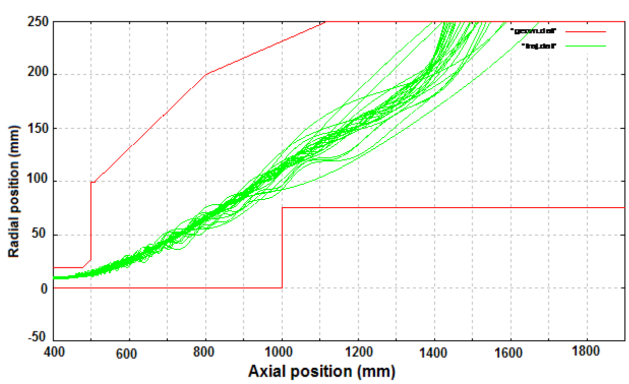

Figure 5: Collector geometry with the beam spreading.

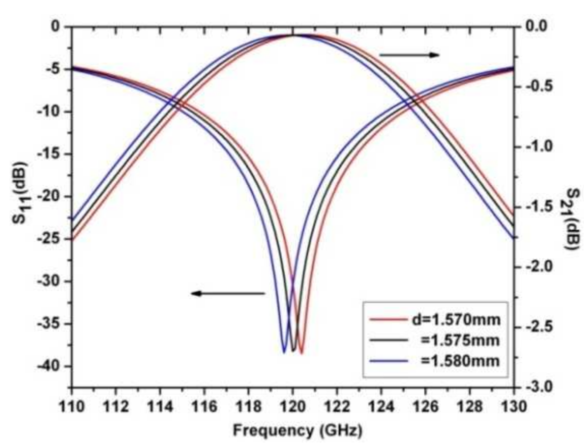

Figure 6: S_{11} and S_{21} with respect to the frequency for CVD diamond window.

ering the maximum collector efficiency. The collector efficiency is calculated by using the beamlets data of current and potential obtained by EGUN output file. The calculated collector efficiency is 58% which enhance the total tube efficiency up to 50% (considering the 5–8% RF loss in the generated power at cavity).

The RF window is a very critical part of any vacuum tube as it separate the ultrahigh vacuum environment inside the tube ($> 10^{-7}$ torr) from the external system located in the normal pressure environment. The window material must be very good in case of mechanical strength and pressure gradient due to the separation of two very opposite environments. Among various window materials, CVD diamond is selected as it shows remarkable mechanical and electrical properties [2]. The disk thickness (d) is estimated by $d = N\lambda/(2\varepsilon_r^{'1/2})$, where N is an integer; λ is the free space wavelength and $\varepsilon_r^{'}$ is the permittivity. Finally, the S matrix analysis is performed for the calculated disk thickness of 1.575 mm by using the computer tool CST-MS. Fig. 6 shows the reflection characteristic of CVD diamond window used in the 120 GHz gyrotron.

5. CONCLUSION

The design of 120 GHz, 1 MW gyrotron operating at $TE_{22,6}$ mode is presented. The design study shows more than 1 MW output power with 38.5% interaction efficiency and around 50% total tube efficiency (including depressed collector efficiency).

ACKNOWLEDGMENT

The authors are pleased to acknowledge the support of Dr. Chandra Shekhar, Director, CEERI Pilani and Dr. S. N. Joshi, National Coordinator of Gyrotron project. The authors also wish to thank to the team members of gyrotron for helpful discussions. Thanks are also due to CSIR for funding this project and awarding the Senior Research Fellowship (SRF) to the corresponding author.

REFERENCES

1. Flyagin, V. A., A. V. Gaponov, I. Petelin, and V. K. Yulpatov, "The gyrotron," *IEEE Trans. on Microwave Theory and Techniques*, Vol. 25, 514–521, 1977.
2. Thumm, M., "State-of-the-art of high power gyro-devices and free electron masers update 2010," *KIT Scientific Report 7575*, KIT Scientific Publication, Karlsruhe, Germany, 2011.
3. Kumar, N., U. Singh, T. P. Singh, and A. K. Sinha, "A review on the applications of high power, high frequency microwave source — Gyrotron," *J. of Fusion Energy*, Vol. 30, 257–276, 2011.
4. Gaponov-Grekhov, A. V. and V. L. Granatstein, *Application of High Power Microwaves*, Artech House Publication, London, 1994.
5. Thumm, M., "High power gyro-devices for plasma heating and other applications," *Int. J. Infrared Millim. Waves*, Vol. 26, 483–503, Apr. 2005.
6. Kumar, N., U. Singh, A. Kumar, H. Khatun, T. P. Singh, and A. K. Sinha, "Design of 35 GHz gyrotron for material processing applications," *Progress In Electromagnetic Research B*, Vol. 27, 273–288, 2011.
7. Kumar, N., U. Singh, A. Kumar, and A. K. Sinha, "Design and misalignment analysis of 140 GHz, 1.5 MW gyrotron interaction cavity for plasma heating applications," *J. of Fusion Energy*, Vol. 30, 169–175, 2011.
8. Singh, U., A. Bera, R. R. Rao, and A. K. Sinha, "Synthesized parameters of MIG for 200 kW, 42 GHz gyrotron," *J. of Infrared, Millimeter, and Terahertz Waves*, Vol. 31, 533–541, 2009.
9. Singh, U., A. Bera, N. Kumar, and A. K. Sinha, "Numerical simulation of MIG for 200 kW, 42 GHz gyrotron," *Int. J. of Infrared and Millimeter Waves*, Vol. 31, 708–713, 2010.
10. Read, M. E., W. G. Lawson, A. J. Dudas, and A. Singh, "Depressed collectors for high-power Gyrotrons," *IEEE Tr. Electron Devices*, Vol. 37, 1579–1589, 1990.
11. Kumar, A., U. K. Goswami, S. Poonia, U. Singh, N. Kumar, M. K. Alaria, A. Bera, H. Khatun, and A. K. Sinha, "Integrated design of undepressed collector for low power gyrotron," *J. Infrared Milli. Terahz. Waves*, Vol. 32, 733–741, 2011.

Investigation of a Disc-Loaded Gyro-TWT Using Particle-In-Cell Simulation

R. K. Singh[1], **Ashutosh**[2], **and P. K. Jain**[2]

[1]Bharat Sanchar Nigam Limited, Ludhiana, India
[2]Center of Research in Microwave Tubes, Department of Electronics Engineering
Institute of Technology, Banaras Hindu University, Varanasi, India

Abstract— Beam-wave interaction behavior of a disc-loaded gyro-TWT amplifier has been investigated using PIC simulation with the help of a commercially available tool MAGIC. Here, a second-harmonic 91.4 GHz single-stage disc-loaded gyro-TWT operating in the TE_{02} mode has been simulated. Beam absent analysis has been presented for the device operation in the desired mode and frequency using eigenmode solver. Beam present analysis has also been demonstrated which yields an output power of 235 kW at 91.4 GHz with input power 450 W along with approximately 10% efficiency.

1. INTRODUCTION

Among the gyrotron devices, the gyro-TWT has the potential as a high power wideband amplifier in the millimeter and sub-millimeter wave range [1]. Gyro-TWTs find its applications in myriad of areas, such as, high-resolution radars and high-information-density communication systems, high-gradient linear colliders, atmospheric sensing, etc., lead its intensive research and development all around [2–4]. Gyro-TWTs incorporate interaction between RF electromagnetic waves and space charge cyclotron waves on the gyrating (periodic) electron beam in a smooth wall interaction structure supporting a fast waveguide mode.

A large number of literatures have been published to demonstrate the design and analysis for the gyro-devices using linear and nonlinear approaches. Nonlinear theory for a gyro-TWT employing cylindrical structures has been presented in various works but is having restrictions in one way or other. Some of them are valid only for gyro-TWT employing only cylindrical shape of interaction structures and the mode of operation is restricted to TE_{mn} modes [5, 6]. The approach for non-linear analysis has been extended for a disc-loaded gyro-TWT that is expected to provide wide device bandwidths and high gain. The beam-wave interaction mechanism in a disc-loaded gyro-TWT amplifier has been investigated using PIC simulation with the help of a commercially available tool MAGIC [7]. MAGIC is an electromagnetic PIC code, i.e., a finite-difference time-domain code for the processes that involve interactions between space charge and EM fields. It simulates the interaction between charged particles and EM fields as they evolve in time and space from some defined initial configuration [7]. The beam absent and present cases have been taken for the investigation.

2. PIC SIMULATION

In order to study the beam-wave interaction mechanism in a gyro-TWT employing a disc-loaded cylindrical waveguide structure, firstly, the structure is simulated in beam absent case to identify the desired mode of operation at desired frequency. Secondly, beam present case is undertaken and simulated. Disc-loaded waveguide structure used in the simulation is shown in Fig. 1. The design parameters have been selected for a second harmonic 91.4 GHz disc-loaded gyro-TWT excited in TE_{02} mode [6]. Beam voltage and beam current is 100 kV and 25 A respectively. Axial DC magnetic field is 1.78 Tesla and pitch factor 1.2 is considered. Wall radius (r_w) is 5.07 mm and beam guiding center radius is 2.079 mm. Disc parameters; disc-hole radius, disc-periodicity and disc-thickness, are $0.6r_w$, $0.4r_w$, and $0.1r_w$ respectively.

2.1. Beam Absent Simulation

In the absence of beam, the behavior of disc-loaded gyro-TWT for the desired operating mode and frequency is firstly observed. The contours of electric and magnetic fields in the transverse plane of disc-loaded waveguide indicate that the desired TE_{02} mode is propagating in the structure (Figs. 2(a) and (b)). The vector plot (Fig. 2(c)) for the electric field orientation in a disc-loaded waveguide also confirms the presence of TE_{02} mode in device. Here, it is clear from Fig. 2 that the radial variation is two and azimuthal variation is zero.

2.2. Beam Present Simulation

A gyro-magnetic beam with a current of 25 Amp is introduced at the left end of the confining interaction structure. The guiding center radius is 2.078 mm. The gyro emission produces a beam center axis parallel to the externally applied magnetic field. Particles (electrons) are emitted from a circle on the surface, which must be conformal with a spatial coordinate. The guiding center and beam axes must be normal to the surface. Eight beamlets are considered in the present simulation due to time and computer hardware limitations, however larger number of beamlets, usually, 32 or 62 in number should be taken for better simulation results. The number of particles in the beam annulus is roughly the number of cells around the annulus emission zone. MAGIC code determines the cell resolution on the emission surface and then creates the number of emission sites that will provide a smooth distribution of density around the annulus of emission. All the beamlets in waveguide before and after interaction are shown in Fig. 3. Additionally, the phase of all particles is shown in Fig. 4 at a simulation time 110 ns after the beam-wave interaction. It is clear that bunch formed in all the beamlets have constant phase relationship with each other.

The azimuthal bunching mechanism in a disc-loaded gyro-TWT at different time intervals is shown in Fig. 4. Initially, electrons are uniformly distributed and they start to bunch as they drift along the interaction region. Once the electrons are bunched, they may give up energy to an electric field which reverses its direction in each half cycle of the cyclotron frequency in synchronism with the Larmor gyration of the electrons. This makes possible is amplification of an electromagnetic wave at the cyclotron frequency. Zoomed beamlets at the output port of the disc-loaded gyro-TWT at 110 ns in transverse momentum space are shown in Fig. 5.

Figure 6(a) shows the frequency spectrum of azimuthal electric field which is obtained from Fourier transform of the electric field. Obviously, it is characterized by a single-frequency component, peaked at 91.4 GHz. This validates the frequency of operation of the gyro-TWT. The growth

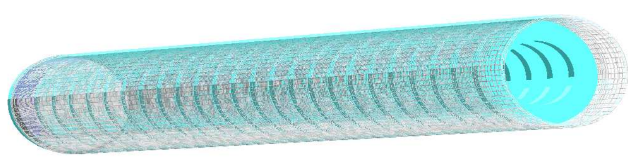

Figure 1: 3-D view of disc-loaded circular interaction structure used in simulation.

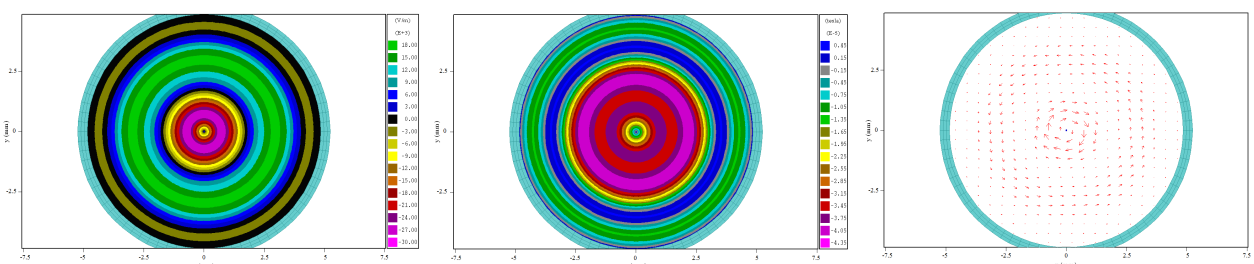

(a) (b) (c)

Figure 2: Contour plot of (a) electric field and (b) magnetic field and (c) vector plot of electric field, in transverse plane of a disc-loaded gyro-TWT.

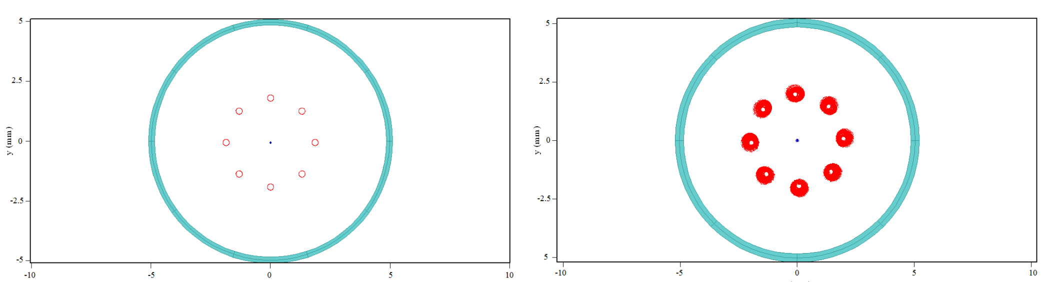

(a) (b)

Figure 3: Cross section of all beamlets in waveguide (a) before interaction and (b) after interaction.

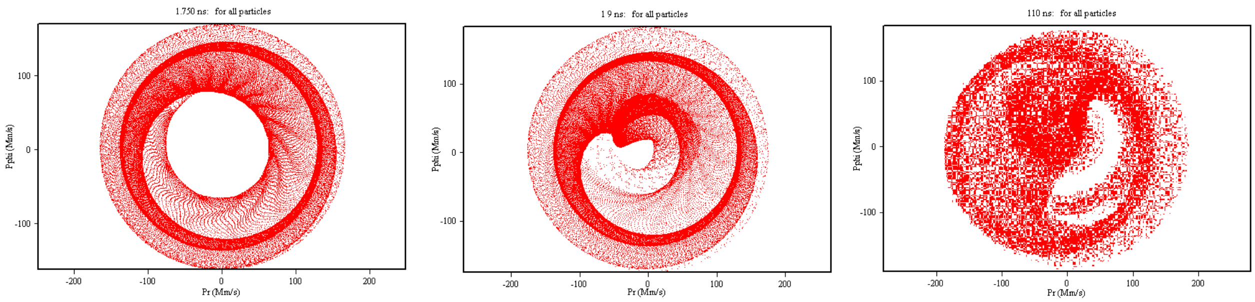

(a) (b) (c)

Figure 4: Phase of all particles showing bunching mechanism in the Larmor orbit at (a) $t = 1.75\,\text{ns}$, (b) $t = 19\,\text{ns}$, and (c) $t = 110\,\text{ns}$.

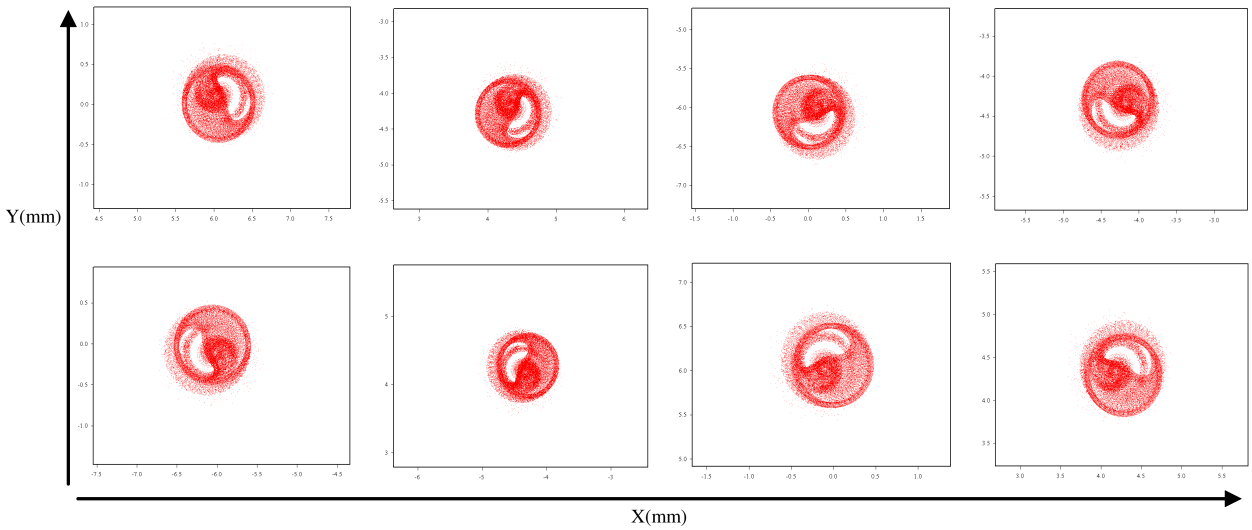

Figure 5: Beamlets observed at the output port (end of RF interaction structure) of the disc-loaded gyro-TWT at 110 ns in transverse momentum space.

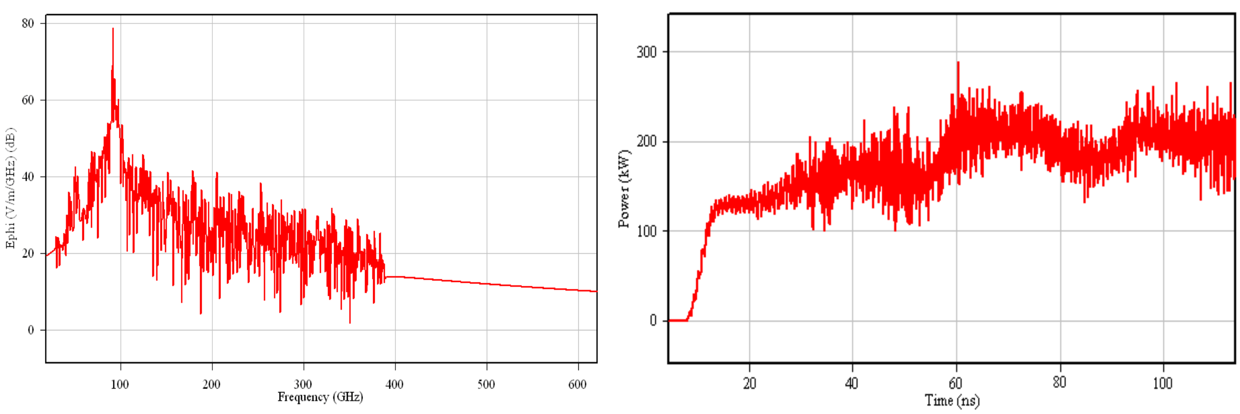

(a) (b)

Figure 6: (a) Frequency spectrum of the azimuthal electric field, (b) RF output power versus time plot at the output end of disc-loaded circular interaction structure used in the gyro-TWT.

of RF output power with time is shown in Fig. 6(b). The simulation results show that the output power is 235 kW for the disc-loaded gyro-TWT amplifier for the taken set of design parameters. In this plot, the fluctuations are also visible. By increasing the duration of simulation run and by taking more number of beamlets, it would be possible to get more stable output power. But due to the limitations of the available hardware resources, it could not be extended here beyond a certain limit.

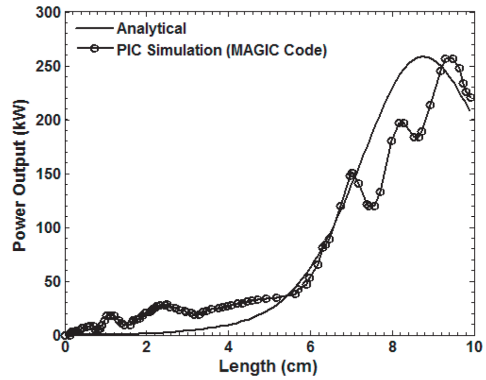

Figure 7: Spatial growth of output power in a disc-loaded gyro-TWT.

The growth of output power versus the axial position of disc-loaded interaction structure of the gyro-TWT is shown in Fig. 7 for both obtained through the large signal analysis [6] as well as PIC simulation using MAGIC code. It can be seen from the above plot that there is a reasonable match between the large signal analysis and PIC simulation results. There is a local variation in simulation plot compared to analytical one for which the several reasons are attributed. One of the major constraints is mesh resolution and size of the time step which should be carefully and wisely taken. The mesh size should be taken in such a way that courant criterion must be fulfilled [7]. Also, particles which travel more than one cell size in one time step will decouple in particle integer and coordinate space. In some outer boundaries, the time step must be less than the cell width divided by the phase velocity. During our PIC simulation, the velocity-spread consideration has not been involved and also the thermal effects have not been demonstrated.

3. CONCLUSIONS

Beam-wave interaction in a disc-loaded gyro-TWT amplifier has been investigated using PIC simulation with the help of a commercially available tool MAGIC. For this purpose, typically a 91.4 GHz single-stage second-harmonic disc-loaded gyro-TWT operating in the TE_{02} mode has been selected for investigation. Simulations have been performed in both the electron beam absent (cold) as well as electron beam present (hot) cases. In order to ensure the device operation at the desired mode and frequency, beam absent eigenmode simulation has been performed. Further, for the beam present simulation, the electrons has been considered as uniformly distributed in azimuthal direction in the form of gyrating beamlets and their evolution along the interaction length in the presence of RF has been observed in time domain. Electrons start to bunch as they drift along the interaction region. Once the electrons are bunched, they transfer their energy to electric field which reverses its direction in each half cycle of the cyclotron frequency in synchronism with the Larmor gyration of the electrons. This makes possible amplification of an electromagnetic wave at the cyclotron frequency. The Fourier transform of time varying field conformed the exact frequency of operation in beam present case. Bunching phenomena in phase plot is explicitly observed along interaction length. PIC simulation demonstrates a disc-loaded gyro-TWT of high output power and wideband along with appreciable gain. For this typically selected disc-loaded gyro-TWT, the saturated RF output power of 235 kW at 91.4 GHz with input power 450 W with approximately 10% efficiency has been obtained. Spatial power growth results obtained through PIC simulation has been also validated with the non-linear analytical values and found in fair agreement.

REFERENCES

1. Parker, R. K., R. H. Abrams, Jr., B. G. Danly, and B. Levush, "Vacuum electronics," *IEEE Trans. Microwave Theory Tech.*, Vol. 50, No. 3, 835–845, Mar. 2002.
2. Furuno, D. S., D. B. McDermott, C. S. Kou, N. C. Luhmann, Jr., and P. Vitello, "Theoretical and experimental investigation of a high-harmonic gyro-travelling-wave tube amplifier," *Phys. Rev. Lett.*, Vol. 62, 1314–1317, 1989.
3. Granatstein, V. L., R. K. Parker, and C. M. Armstrong, "Vacuum electronics at the dawn of the twenty-first century," *Proc. IEEE*, Vol. 187, 702–716, 1999.
4. Basu, B. N., *Electromagnetic Theory and Applications in Beam-wave Electronics*, World Scientific, Singapore, 1996.

5. Chu, K. R., A. T. Drobot, H. H. Szu, and P. Sprangle, "Theory and simulation of gyrotron travelling-wave amplifier operating at cyclotron harmonics," *IEEE Trans. Microwave Theory Tech.*, Vol. 28, 313–317, 1980.
6. Wang, Q. S., C. S. Kou, D. B. McDermott, A. T. Lin, K. R. Chu, and N. C. Luhmann, Jr., "High-power harmonic gyro-TWT — Part II: Nonlinear theory and design," *IEEE Trans. Plasma Sci.*, Vol. 20, No. 3, 163–169, 1992.
7. *Magic Help Manual*, Larry Ludeking, ATK Mission Systems, Newington, Virginia, Jan. 2007.

Design of Higher Harmonic Interaction Cavity for 0.3 THz Gyrotron

Anil Kumar[1,2], **Nitin Kumar**[1], **Hasina Khatun**[1], **Udaybir Singh**[1],
V. Vyas[2], **and A. K. Sinha**[1]

[1]Gyrotron Laboratory, Microwave Tube Division
CSIR-Central Electronics Engineering Research Institute (CEERI)
Pilani, Rajasthan 333031, India
[2]Department of Physics, Banasthali University, Banasthali, Rajasthan 304022, India

Abstract— The design of weakly tapered interaction cavity for 0.3 THz, 3 kW gyrotron operating at the second harmonic is presented in this paper. The symmetric low order mode $TE_{0,6}$ is selected as the operating mode. The interaction cavity geometry and beam parameters are optimized for the operating mode by using the Particle-in-Cell (PIC) electromagnetic simulation approach. The operating mode is selected by using the code GCOMS, in which various mode selection parameters and start oscillation current are calculated. Further, the power and frequency estimation are performed to finalize the cavity and electron beam parameters.

1. INTRODUCTION

The research in the field of THz radiation (300 GHz–3 THz) is getting big thrust due to the several remarkable and innovative applications in the field of fundamental material research, medical science, security, sensing, etc.. There is a lack of efficient sources, detectors, transmission systems, etc., in the THz band, also called THz gap [1, 2]. Several applications, like NMR spectroscopy, material processing, etc., required high power (from tens of watt to few kW) in the THz band. The gyrotron is a perfect device as a radiation source to fulfill the demand of high power at THz band [3, 4]. The required magnetic field in the gyrotron operation directly depends on the frequency and inversely on the harmonic. In THz band, the magnetic field becomes very large at the fundamental harmonic operation of the device, so the higher harmonic operation ($s = 2$) is selected to reduce the magnetic field in the design of 0.3 THz gyrotron. The gyrotron is designed for the RF power more than 1 kW which is required in several applications like the high frequency ceramic sintering, high resolution spectroscopy, etc. [5]. The mode competition becomes severe at higher harmonic operation as the fundamental harmonic ($s = 1$) mode also compete due to the lower start oscillation current. A careful investigation of the start oscillation current and coupling coefficient is performed for several modes to avoid the high mode competition. The symmetric low order mode $TE_{0,6}$ is selected as the operating mode. The interaction cavity geometry and beam parameters are optimized for the operating mode. The beam-wave interaction simulations are performed for the higher harmonic operation by using the Particle-in-Cell code MAGIC. The results confirm more than 3 kW of power at 300 GHz frequency at second harmonic. In this article the design of the interaction cavity and beam-wave interaction computation for 0.3 THz, 3 kW CW gyrotron is presented. The design goals of the gyrotron are summarized in Table 1.

2. COLD CAVITY AND BEAM-WAVE INTERACTION ANALYSIS

The geometrical parameters of the interaction cavity are decided on the basis of the operating mode. The operating mode selection depends on various parameters, like, space charge effect, ohmic wall loss, coupling factor between electron beam and RF, etc.. It is found that the $TE_{0,6}$ mode is an appropriate choice as a most favorable operating mode for the 300 GHz, 3 kW gyrotron operating at second harmonic operation [6]. Beam-wave interaction simulations are carried out in PIC simulator MAGIC [7]. The code has been used successfully in the beam-wave interaction computation

Table 1: Design goals of 0.3 THz gyrotron.

Frequency (f)	300 GHz
Output power (P_{out})	≈ 3.0 kW
Efficiency (η)	$\geq 10\%$,without energy recovery
Ohmic wall loss	< 2 kW/cm^2
Voltage Depression (V_d)	$< 10\%$ of V_b

for low power as well as high power fusion gyrotron [8]. An initial estimation of the electron beam parameters, like, beam voltage, beam current, electron velocity ratio and magnetic field are carried out by using the normalized parameters (F, μ, Δ). Finally, calculated and optimized cavity geometrical parameters and electron beam parameters are summarized in Table 2. Figs. 1–3 show the results of beam-wave interaction simulations. Fig. 1 shows the contour plot of electric field intensity at the cross sectional top view of interaction cavity Fig. 2 shows the RF power growth with respect to time with 15% of interaction efficiency. The power growth becomes stable around 20 ns. Fig. 3 shows the frequency spectrum (gain versus frequency) and maximum gain is achieved at the frequency 301.89 GHz.

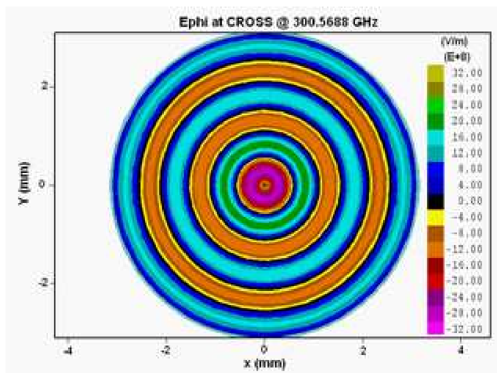

Figure 1: Contour plot of electric field at the cross sectional top view of interaction cavity.

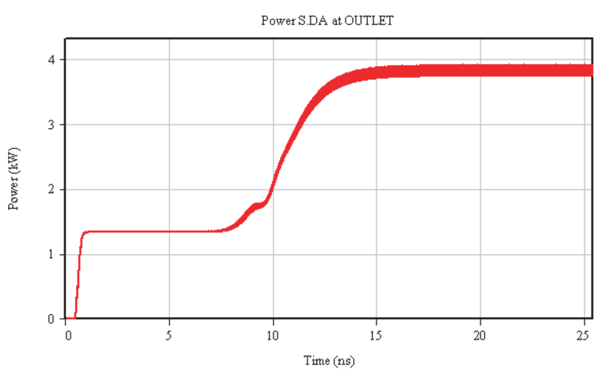

Figure 2: Power growth with respect to time for second harmonic operation.

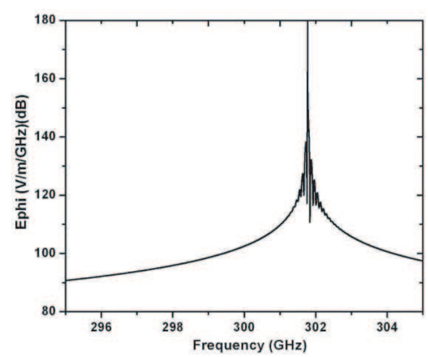

Figure 3: Frequency spectrum in the interaction cavity for second harmonic.

Table 2: Final optimized cold cavity design parameters and electron beam parameters of interaction cavity.

Cavity Radius (R_c)	3.12 mm
Middle section length (L)	9.00 mm
Input taper length (L_1)	6.00 mm
Output taper length (L_2)	12.00 mm
Input taper angle (θ_1)	2.8°
Output taper angle(θ_2)	5.0°
Diffractive Q value	1547
Beam current (I_b)	1.3 A
Beam voltage (V_b)	20 kV
Velocity ratio (α)	1.3
Cavity center magnetic field (B_0)	5.58 T
Beam launching position (R_b)	0.486 mm

3. CONCLUSION

The presented design of a 0.3 THz gyrotron interaction cavity shows the feasibility of 3 kW of output power. Symmetric mode $TE_{0,6}$ is selected as the operating mode for second harmonic operation. To check the stability of the operating mode, the eigenmode and cold cavity analysis are carried out. Around 3.5 kW output power is achieved at 301.89 GHz frequency. The beam parameters are optimized considering around 15% interaction efficiency as $V_b = 20\,\mathrm{kV}$, $I_b = 1.3\,\mathrm{A}$, $B_0 = 5.58\,\mathrm{T}$ and $\alpha = 1.3$, respectively.

ACKNOWLEDGMENT

The authors are pleased to acknowledge the support of Dr. Chandra Shekhar, Director, CEERI Pilani and Dr. SN Joshi, National Coordinator of Gyrotron. The authors also wish to thank the team members of gyrotron for helpful discussions. Thanks are also due to Council of Scientific and Industrial Research (CSIR) for awarding the Senior Research Fellowship to Mr. Anil Kumar.

REFERENCES

1. Thumm, M., "State-of-the-art of high power gyro-devices and free electron masers update 2010," KIT Scientific Report 7575, KIT Scientific Publication 2011, Karlsruhe, Germany.
2. Kumar, N., U. Singh, T. P. Singh, and A. K. Sinha, "A review on the applications of high power, high frequency microwave source — Gyrotron," *J. of Fusion Energy*, Vol. 30, 257–276, 2011.
3. Idehara, T., I. Ogawa, T. Saito, S. Mitsudo, Y. Tatematsu, L. A. H. Mori, and S. Kobayashi, "Development of THz gyrotrons and application to high power THz technologies," *Terahertz Science and Technology*, Vol. 1, 100–106, 2008.
4. Danly, B. G. and R. J. Temkin, "Generalized nonlinear harmonic gyrotron theory," *Physics of Fluids*, Vol. 29, 561–567, 1985.
5. Mitsudo, S., H. Hoshizuki, T. Idehara, and T. Saito, "Development of material processing system by using, a 300 GHz CW gyrotron," *IOP Journal of Physics: Conference Series*, Vol. 51, 549–552, 2006.
6. Lei, W., M. Li, L. Song, and Z. Yang, "RF cavity simulation of 0.3 THz 400 W gyrotron oscillator," *IRMMW-THz*, California, USA, 2008.
7. Kumar, A., N. Kuamr, U. Singh, H. Khatun, V. Vyas, and A. K Sinha, "Design of interaction cavity of a 170-GHz, 1-MW gyrotron for ECRH application," *Vacuum*, Vol. 86, 184–188, 2011.
8. MAGIC User Mannual: 2007 version of Magic 3D, ATK Mission Research, Washington.

Study of Stagger-tuning in the Gyroklystrons

M. S. Chauhan and P. K. Jain
Center of Research in Microwave Tubes, Department of Electronics Engineering
Institute of Technology, Banaras Hindu University, Varanasi-221005, India

Abstract— In present paper, the detailed study of stagger tuning has been carried out for multicavity gyroklystrons. The present analysis is based on the point-gap model for gyroklystrons in which the size of the cavities assumed much smaller than the drift sections. Therefore, we can assume that the effect of electron ballistic phase bunching took place only in the long drift sections whereas the electron energy modulation taking place in the short cavities. These assumptions help us to obtain the necessary equations for studying the effect of stagger tuning in gyroklystrons. The results obtained here for two and three cavity gyroklystrons clearly demonstrate the bandwidth enhancement, decrease in gain and overall increase in gain-bandwidth product due to stagger tuning.

1. INTRODUCTION

The gyroklystron is a fast-wave electron-beam device which combines the multi-cavity klystron configuration with the cyclotron resonance maser instability energy extraction mechanism of gyrotron. The operation is similar to conventional klystron except that electron bunching occurs in the transverse direction rather than in axial direction and the overmoded cavities are utilized. This scheme makes them to be used at higher frequencies with larger cavity dimensions. There are numerous applications of gyroklystrons, like radars, linear colliers, plasma heating, spectroscopy, etc. Like klystrons, gyroklystrons are also capable of producing high gain, high power amplification even in the millimeter wave frequency range however with limited bandwidth. Stagger tuning of RF cavities techniques as successfully applied in conventional klystrons to increase the device bandwidth can also be applied for gyroklystron [1, 2].

The basic concept involves in increasing the bandwidth of gyroklystron is slightly detuning the resonant frequencies of gyroklystron cavities. This method is known as the stagger tuning and widely used in the conventional multicavity klystrons for the enhancement of bandwidth. However, this increase in bandwidth is at the cost of decrease in gain. The aim of the present paper is to study the some tradeoff in gain and bandwidth for the multicavity stagger-tuned gyroklystrons.

2. ANALYSIS

The equations of motion for weakly relativistic electrons in each cavity of gyroklystron, under the assumption of no space charge effect and zero velocity spread can be described by the following two interdependent expressions in terms of momentum (p), phase (ϑ) and distance (ζ) in normalized form as [3]:

$$\frac{dp}{d\zeta} = p^{n-1}\mathrm{Re}\left(Ff(\zeta)e^{in\vartheta}\right) \tag{1}$$

$$\frac{d\vartheta}{d\zeta} - \Delta + 1 - p^2 = p^{n-2}\mathrm{Re}(iFf(\zeta)e^{in\vartheta}) \tag{2}$$

Here, $p = p_\perp/p_{\perp 0}$ is the normalized electron momentum, $\vartheta = (\omega_i/n_i)\,t - \theta$ is the difference between the electron phase θ and the phase of the resonator field, $\zeta = \left(\beta_{\perp 0}^2/2\beta_{z0}\right)(\omega_0 z/c)$ is the normalized axial coordinate, $\Delta = \left(2/\beta_{\perp 0}^2\right)(1 - n\omega_{c0}/\omega)$ is the frequency detuning parameter and $F = \left(E_0\beta_{\perp 0}^{n-4}/B_0 c\right)\left(n^{n-1}/2^{n-1}n!\right)J_{m\pm n}(k_\perp r_b)$ is the normalized field amplitude.

The susceptibility χ is the quantity which determines the interaction of electron beam with the cavity mode and it is defined as [4]

$$\chi = \frac{-i\sigma}{\omega} \tag{3}$$

where σ is the medium conductivity. This susceptibility can be calculated after solving Equations (1) and (2) as [4]

$$\chi = -\frac{2i}{F}\int_0^\mu f^*\left(\frac{1}{2\pi}\int_0^{2\pi}(pe^{-i\vartheta})^n d\vartheta_0\right)d\zeta \tag{4}$$

Here, μ is the normalized length of the cavity and ϑ_0 is the initial phase of the electrons equally distributed at the entrance of the first cavity from 0 to 2π.

The balanced equation used here for obtaining the amplitude and phase of the cavity field as $F = |F_1|e^{i\psi_1}$ for the input cavity are:

$$|F_1|^2 = \frac{A^2}{(1 - I_{01}\chi'')^2 + (\delta_1 + I_{01}\chi')^2} \quad \text{and} \quad \tan\psi_1 = \frac{\delta_1 + I_{01}\chi'}{1 - I_{01}\chi''} \tag{5}$$

where χ' and χ'' are the real and imaginary part of the susceptibility. A^2 is the intensity of the signal in the input cavity which is related to the driver power as

$$A^2 = 4I_{01}\frac{P_{dr}Q_{1,T}}{P_{b\perp}Q_{cpl}} \tag{6}$$

Here I_{01} is the normalized beam current parameter for the input cavity, $Q_{1,T}$ is the total quality factor and Q_{cpl} is the coupling quality factor of the input cavity. P_{dr} is the driver power and $P_{b\perp}$ is the electron beam power associated with the electron gyration.

For other cavities these equation can be written as

$$I_0\chi'' = 1 \quad \text{and} \quad I_0\chi' = -\delta \tag{7}$$

Here δ is the normalized detuning between the operating frequency and the cold cavity frequency, $\delta = (\omega - \omega_s)/(\omega/2Q)$. Here Q is the loaded quality factor of the cavity.

With the help of the above balance equation, the gain of the gyroklystron can be simply written as

$$G\,(\mathrm{dB}) = 10\log\left(\frac{|F_N|^2}{A^2}\right) \tag{8}$$

For the case of multicavity gyroklystrons, it is better to write this ratio of field intensities as the products of ratios characterizing the gain in each stage

$$\frac{|F_N|^2}{|F_{N-1}|^2}\frac{|F_{N-1}|^2}{|F_{N-2}|^2}\cdots\frac{|F_1|^2}{A^2} \tag{9}$$

Here each ratio in the above chain can be expressed in terms of the balance equations discussed in Equation (7). Since we are studying the stagger tuning in which δ_i can be different for each cavity. So, we can calculate the bandwidth in terms of normalized frequency detuning.

2.1. Two-cavity Gyroklystron

The gain of two cavity gyroklystron for studying the effect of frequency detuning on the gain can be expressed as [3, 4]

$$G = G^{(const.)} - G^{(var.)} \tag{10}$$

Here the first term,

$$G^{(const.)} = 20\log\left\{\frac{2I_{02}\mu_{dr}}{(1 + I_{01})(1 + I_{02})}\right\} \tag{11}$$

is independent of frequency detuning, while the second term is the variable part of the gain and it depends on frequency detuning.

$$G^{var} = 10\log\left\{\frac{q^2}{4J_1^2(q)}\frac{\left[(1 + I_{01})^2 + \delta_1^2\right]\left[(1 + I_{02})^2 + \delta_2^2\right]}{(1 + I_{01})^2(1 + I_{02})^2}\right\} \tag{12}$$

The expressions for $G^{(const.)}$ and G^{var} are normalized in such a way that when bunching parameter $q \to 0$ and frequency detuning in both the cavities is zero, the variable term vanishes.

To simplify further, let us assume that both cavities have equal quality factor and also the normalized current parameter in both the cavities is same. Also, by defining some of the parameters like mean frequency of two cavities, $\omega_0 = (\omega_1 + \omega_2)/2$, the stagger tuning parameter, $\xi = 2Q(\omega_2 - \omega_1)/$

$\omega_0 (1 + I_0)$ and detuning of signal frequency with respect to ω_0, $\delta = (\omega_s - \omega_1)/(\omega_0/2Q)(1 + I_0)$ we can write the small signal gain as

$$G_{SS}^{(var.)} = 10 \log \left\{ \left[1 + (\delta - \xi/2)^2\right] \left[1 + (\delta + \xi/2)^2\right] \right\} \tag{13}$$

After analyzing the above equation at its extremum points, we find that the variable gain has a local maximum at $\delta = 0$ and two symmetric minima at $\delta = \pm\sqrt{\bar{\xi} - 1}$ where $\bar{\xi} = \xi^2/4$.

The bandwidth of the gyroklystron can be determined by using Equation (12) and can be written as

$$BW(\xi) = \left[\bar{\xi} - 1 + \sqrt{2(1 + \xi^2)}\right]^{\frac{1}{2}} (1 + I_0)/Q \tag{14}$$

For $\bar{\xi} \leq 1$, and

$$BW(\xi) = \left[\bar{\xi} - 1 + 2\sqrt{\bar{\xi}}\right]^{\frac{1}{2}} (1 + I_0)/Q \tag{15}$$

for $\bar{\xi} \geq 1$. The maximum value of $\bar{\xi}$ obtained is $3 + \sqrt{8}$ that corresponding to maximum bandwidth.

The ratio of the gain-bandwidth product in the presence of stagger tuning to that its absence is given by

$$\Phi = \frac{BW(\xi) G(\xi)}{BW_0 G_0} = \frac{BW(\xi)}{BW_0}\left[1 - \frac{\Delta G}{G_0}\right] \tag{16}$$

where, $\Delta G = 20 \log\left(1 + \bar{\xi}\right)$ is the gain at $\delta = 0$ and $G_0 = G^{const.}$.

2.2. Three-cavity Gyroklystron

Using the same approach as we did for the two cavity gyroklystron the gain of a three cavity gyroklystron can be expressed as

$$G_{ss} = G_{ss}^{(const.)} - G_{ss}^{(var.)} \tag{17}$$

where,

$$G_{ss}^{(const.)} = 20 \log \left\{ \frac{4 I_{02} I_{03} \mu_{dr}^2}{(1 + I_{01})(1 + I_{02})(1 + I_{03})} \right\} \tag{18}$$

and

$$G_{ss}^{(var.)} = 10 \log \left\{ \left(1 + \bar{Q}\delta^2\right) \left[\left(1 + \delta^2 + \xi^2\right)^2 - 4\xi^2\delta^2\right] \right\} \tag{19}$$

where, $\bar{Q} = (1 + I_0)^2 \tilde{Q}/(1 + \tilde{Q} I_0)^2$ where, $\tilde{Q} = Q_1/Q_2 = Q_1/Q_3$. Q_1, Q_2 and Q_3 are the quality factor of first, second and third cavity respectively. Now as we did for the two cavity gyroklystron, the Equation (19) has been solved at its extremum points to obtain the value of ξ^2 for getting the bandwidth of three cavity gyroklystron. The maximum value of ξ^2 is obtained 36.8 at $\bar{Q} = 1/4$. The bandwidth and the gain bandwidth product of the three cavity gyroklystron can be easily obtained by using the same equation as we used for the two cavity gyroklystron.

3. RESULTS AND DISCUSSION

To get the gain and bandwidth relation for two cavity gyroklystron the Equation (13) has been solved at its extremum which gives us the value for detuning parameter for maximum and minimum gain. These obtained values of detuning parameter are further used in calculating the bandwidth of the two cavity gyroklystron by making use of Equations (14) and (15). The same technique is also used for three cavity stagger tuned gyroklystron. In Figure 1 the variable part of small-signal gain for two cavity stagger-tuned gyroklystron has been plotted as the function of frequency detuning for various values of stagger-tuning parameter. In Figure 2 the normalized bandwidth has been plotted for two cavity stagger-tuned gyroklystron as the function of stagger-tuning parameter. For the case of two cavity stagger tuned gyroklystron we have obtained maximum 5 times increase in bandwidth as compared to the two cavity gyroklystron with no stagger tuning ($\xi = 0$). The gain degradation for two cavity stagger-tuned gyroklystron is obtained around 17 dB as shown in Figure 3. In Figure 4 the normalized gain-bandwidth product is obtained nearly two times larger as compared to the two cavity 30 dB gain gyroklystron without stagger tuning.

In Figure 5 the variable part of small-signal gain for three cavity stagger-tuned gyroklystron has been plotted as the function of frequency detuning for various values of stagger-tuning parameter.

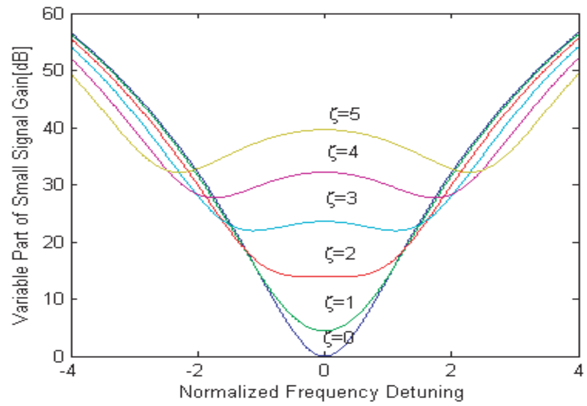

Figure 1: Variable part of small signal gain in the two-cavity stagger-tuned gyroklystron.

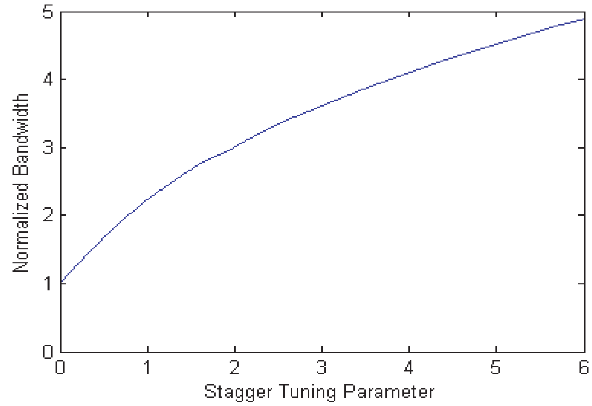

Figure 2: Normalized bandwidth for two-cavity stagger-tuned gyroklystron.

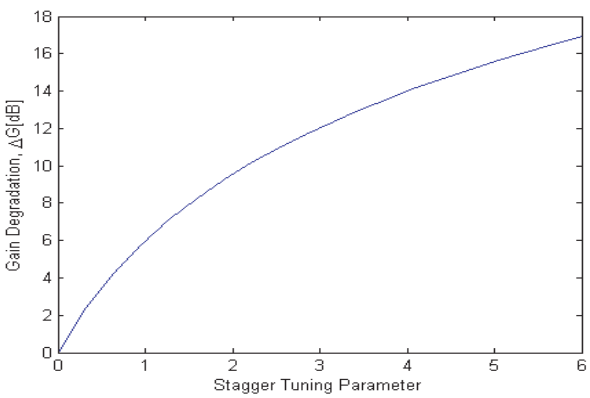

Figure 3: Gain-degradation for two cavity stagger-tuned gyroklystron.

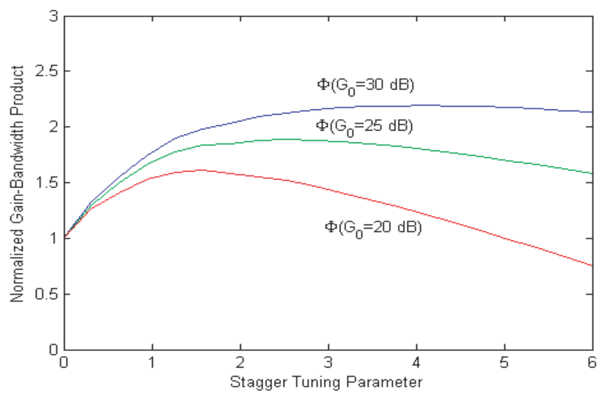

Figure 4: Normalized gain-bandwidth product for two-cavity stagger-tuned gyroklystron.

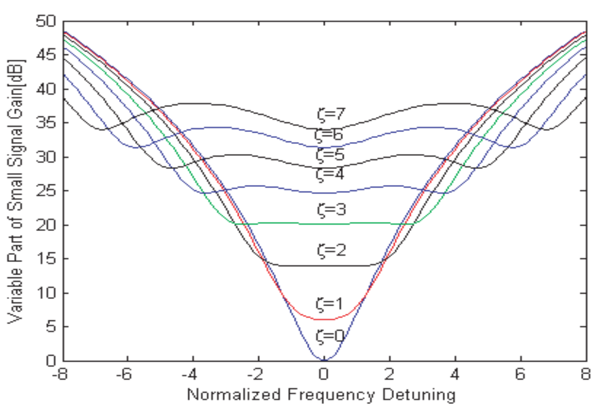

Figure 5: Variable part of small signal-gain in the stagger-tuned three cavity gyroklystron.

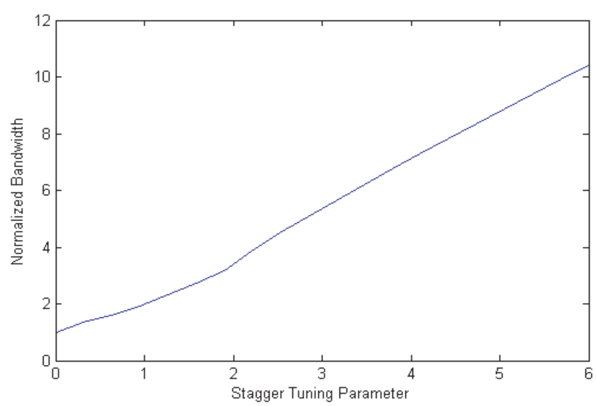

Figure 6: Normalized bandwidth, for three-cavity stagger-tuned gyroklystron.

In Figure 6 the normalized bandwidth has been plotted for three cavity stagger-tuned gyroklystron as the function of stagger-tuning parameter. The results obtained for three-cavity stagger tuned gyroklystron shows nearly 10 times more bandwidth as compared to the three cavity gyroklystron without stagger tuning ($\xi = 0$). The gain degradation for three cavity stagger-tuned gyroklystron is obtained around 32 dB as shown in Figure 7. The results obtained here are also used to calculate the bandwidth of a two cavity 35 GHz gyroklystron [5]. The specification of this gyroklystron are beam voltage = 70 kV, beam current = 8.2 A, α = 1.43 and beam radius = 2.6 mm. Both the cavities are operated at TE_{011} mode with input cavity quality factor = 188 and output cavity quality factor = 191. We have obtained the normalized current for the output cavity = 0.18 and the device bandwidth = 0.39%. The reported bandwidth is 0.36% [5].

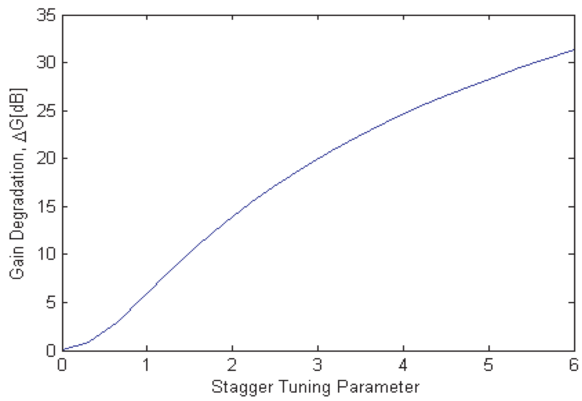

Figure 7: Gain-degradation for two-cavity stagger-tuned gyroklystron.

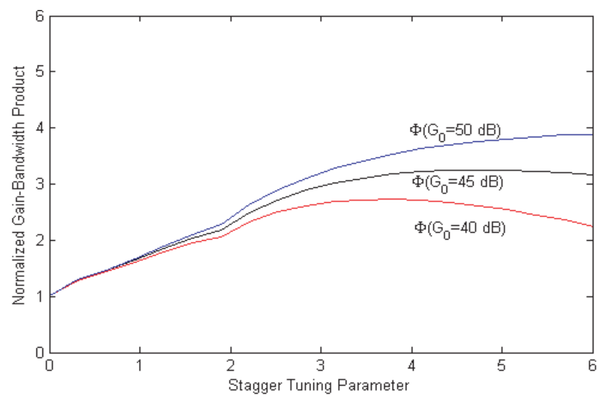

Figure 8: Normalized gain-bandwidth product for two cavity stagger-tuned gyroklystron.

4. CONCLUSION

The study of stagger-tuning has been carried out for the two and three-cavity gyroklystron operating at the fundamental harmonic. The influence of stagger-tuning parameter on gain and bandwidth has been presented for both the cases. The results obtained here show that in case of a stagger-tuned two-cavity gyroklystron, the bandwidth can be increased nearly 5 times as compared to without stagger tuning with the degradation in gain around 17 dB. In case of three-cavity stagger-tuned gyroklystron, bandwidth is two times larger as compared to the two cavity stagger-tuned gyroklystron with the degradation in gain around 32 dB. The stagger tuning of the gyroklystron, improves device bandwidth with decrease in gain. Moreover, it is interesting to notice that the overall increase in the gain-bandwidth product of the device is observed. Therefore, the stagger tuning technique, like in klystrons, can be used for the performance improvement of gyroklystrons.

REFERENCES

1. Gold, S. H. and G. S. Nusinovich, "Review of high-power microwave source research," *Review of Scientific Instruments*, Vol. 68, No. 11, 3945–3974, 1997.
2. Granatstein, V. L. and W. Lawson, "Gyro-amplifiers as candidate RF drivers for TeV linear colliders," *IEEE Trans. Plasma Sci.*, Vol. 24, No. 3, 648–665, 1996.
3. Nusinovich, G. S., B. G. Danly, and B. Levush, "Gain and bandwidth in stagger-tuned gyroklystrons," *Physics of Plasmas*, Vol. 4, No. 2, 469–478, 1997.
4. Nusinovich, G. S., *Introduction to the Physics of Gyrotrons,* The Johns Hopkins University Press, Baltimore, Maryland, 2004.
5. Choi, J. J, A. H McCurdy, F. N. Wood, R. H. Kyser, J. P. Calame, K. T. Nguyen, B. G. Danly, T. M. Antonsen, B. Levush, and R. K. Parker, "Experimental investigation of a high power, two-cavity, 35 GHz gyroklystron amplifier," *IEEE Trans. Plasma Sci.*, Vol. 26, No. 3, 416–425, 1998.

Power and Frequency Estimation for 0.67 THz Gyrotron for Radioactive Material Detection

Nitin Kumar, **Udaybir Singh**, **Anil Kumar**, **Hasina Khatun**, **and A. K. Sinha**
Central Electronics Engineering Research Institute (CEERI, CSIR)
Pilani, Rajasthan 333031, India

Abstract— In this article, the results of beam-wave interaction and power and efficiency growth for 670 GHz, 300 kW gyrotron are presented. The beam parameters and the interaction cavity geometry calculations are performed for the selected operating mode $TE_{25,10}$. The detail of mode selection process is also presented. The mode competition is studied in terms of the start oscillation current and coupling coefficient. $TE_{22,11}$ and $TE_{25,10}$ are found as the most competing modes to the operating mode. The magnetic field at the cavity center is calculated directly from the frequency and detuned up to an optimum value to achieve the maximum efficiency. MAGIC code is used in the power and frequency calculations. The electron beam is launched at the first co-rotating maxima of the operating mode during the MAGIC simulations to obtain maximum beam-wave interaction efficiency. The results show more than 300 kW power at 670 GHz frequency at $TE_{25,10}$ mode.

1. INTRODUCTION

Terahertz radiation (300 GHz–3 THz) is emerging as a thrust research area due to its various remarkable applications described in detail in review articles by *P. H. Siegel* [1] and *T. Idehara* et al. [2]. A new application of terahertz radiation for the detection of concealed radioactive materials is proposed by *Granatstein* and *Nusinovich* at 670 GHz frequency [3–5] and by *Choi* at 400 GHz frequency [6]. The detection of radioactive materials is based on the phenomena of air breakdown by focused terahertz radiation. In the presence of radioactive material in a container, the density of electrons increases several folds in air and initiate the breakdown in the presence of electromagnetic radiation of terahertz frequency region, which is not possible in the absence of extra electrons produced by some radioactive material. A detail calculation and physics of this phenomenon is described in Ref. [3]. The results presented in Refs. [3–5] show the frequency of 670 GHz with 200–300 kW power and few μs pulse length is suitable for the radioactive material detection application.

Gyrotron has been established as a powerful source of millimeter and terahertz radiation. The gyrotrons as the source of millimeter wave (~ 1 MW power) are used widely in the plasma fusion research [7]. The gyrotrons of terahertz frequency range and moderate power level (tens of watts to few kilowatts) are used in DNP/ NMR spectroscopy and developed by several research groups around the globe [2, 7]. Theses gyrotrons operate at higher harmonics to reduce the magnetic field at cavity center ($B = f\gamma/28\,\mathrm{s}$). Present status of the design and development technology for gyrotron shows the capability to generate high power radiation in terahertz band. Considering the power requirement at 670 GHz frequency for the radioactive material detection application, the work on the development of 670 GHz gyrotron is started recently at University of Maryland [5]. As the required power level is quite high in case of gyrotrons for radioactive material detection compared to the gyrotrons used in spectroscopic applications, thus fundamental harmonic operation is suitable as the efficiency decreases for higher harmonics. Another problem for the higher harmonic operation for 670 GHz gyrotron is the high mode competition as the higher order mode is required to keep the ohmic wall loss minimum.

In this article, the results of power and frequency growths for 670 GHz gyrotron are presented. This feasibility study for the RF power generation around 300 kW at 670 GHz frequency using $TE_{25,10}$ mode is carried out for the simple cylindrical open resonator cavity. $TE_{25,10}$ is a popular mode in the gyrotron community and has been used in the designing of high power, high frequency fusion gyrotrons. Here, in case of 670 GHz gyrotron with the output power around 300 kW, $TE_{25,10}$ mode is analyzed again in terms of mode selection parameters, like, space charge effect, ohmic wall loading, start oscillation current, etc., by using in-house developed code GCOMS [8, 9]. Particle-in-Cell (PIC) numerical approach is used in the beam-wave interaction simulations. Parametric analysis is also performed considering the power and efficiency as main parameters. The design goals for the 670 GHz gyrotron are summarized in Table 1.

Table 1: Design goals of gyrotron.

Frequency	670 GHz
Power	≈ 300 kW
Efficiency	$> 30\%$*
Beam Voltage	65–74 kV
Velocity ratio (α)	1.25–1.4

*Without depressed collector

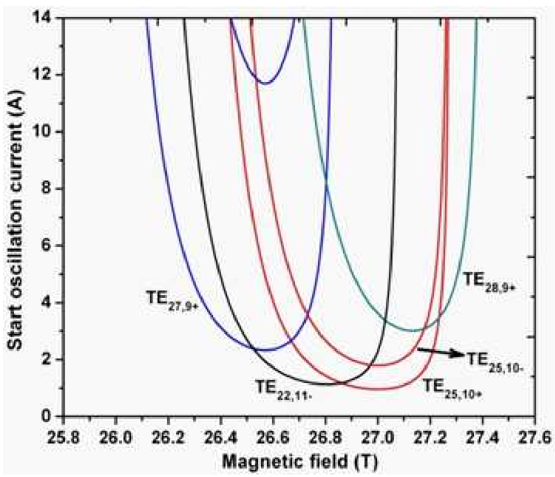

Figure 1: Start oscillation current curves with respect to magnetic field.

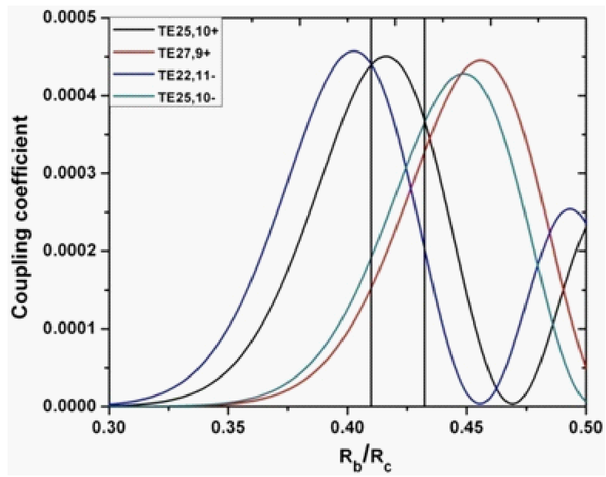

Figure 2: Coupling coefficient with respect to the ratio of beam radius to cavity radius.

2. MODE SELECTION AND ESTIMATION OF POWER AND FREQUENCY GROWTH

High order modes are suitable for 670 GHz gyrotron due to the requirement of high RF power (≈ 300 kW). Various mode selection parameters like ohmic wall loading, voltage depression, limiting current, etc., are calculated for several higher order modes by using the GCOMS. The mode competition in terms of start oscillation current and coupling coefficient is analyzed for the high order modes. Finally $TE_{25,10}$ is selected as the operating mode. The electron beam is launched at the first radial maxima of co-rotating electric field of the selected operating mode for the maximum beam-wave coupling. The start oscillation current curves for the operating mode and its neighboring competing modes are shown in Fig. 1. Figure shows $TE_{22,11}$ and $TE_{25,10}$ are the most competing modes to the operating mode (-ve sign represents the counter-rotating electric field). Further, Fig. 2 shows the most strength coupling position for various modes including the operating mode. It is clear from the Fig. 2 that the sufficient space (represented by two black vertical line) exist in the beam launching position where other competing modes do not show maximum coupling strength. The interaction cavity geometrical parameters are summarized in Table 2.

On the basis of initially designed interaction cavity, the electron beam parameters are optimized considering 300 kW RF power at 670 GHz frequency as the main parameter. Particle-in-Cell code MAGIC is used for the simulations of power and frequency growth. PIC code has been used successfully in the interaction cavity designing and power growth estimation for gyro-amplifiers and fusion gyrotrons such as 140 GHz gyrotron, 170 GHz gyrotron, etc. [10, 11]. Simple cylindrical interaction cavity consisting an input taper section, a straight middle section and an output taper section is made with very fine meshing in the PIC code. The gyrating electron beam (perpendicular to axial velocity ratio of electrons, $\alpha = 1.3$) is launched at the co-rotating electric field of first radial maxima (1.88 mm) of the selected operating mode. The electron beam transports along the cavity length under the influence of very high magnetic field ($B_0 = 26.34$ T) and transfer a fraction of its perpendicular kinetic energy to the RF at the middle section. Figs. 3 and 4 show the typical plots of frequency and power growths with respect to time. The growths become stable at 100 ns. Results show 310 kW RF power at the frequency of 670.15 GHz. The beam current (I_b) and beam voltage (V_b) are optimized as 14 A and 70 kV, respectively.

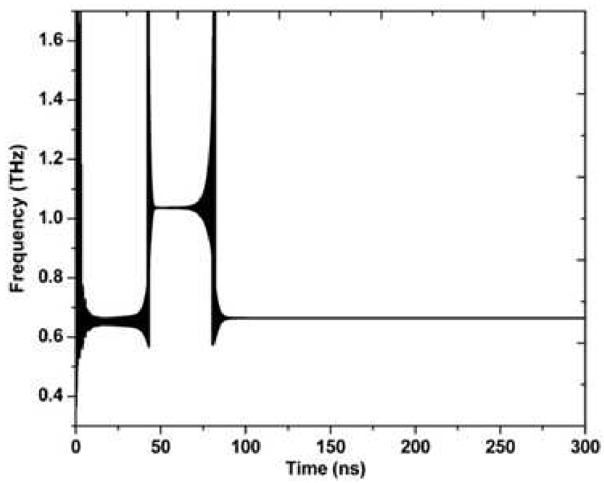

Figure 3: Frequency growth with respect to time ($I_b = 14\,\mathrm{A}$, $V_b = 70\,\mathrm{kV}$, $B_0 = 26.34\,\mathrm{T}$).

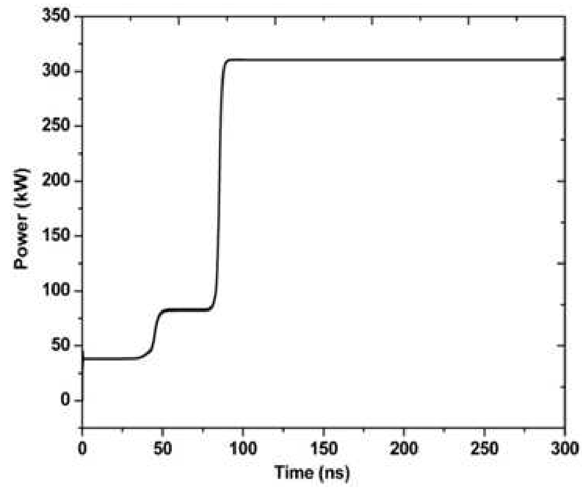

Figure 4: Powergrowth with respect to time ($I_b = 14\,\mathrm{A}$, $V_b = 70\,\mathrm{kV}$, $B_0 = 26.34\,\mathrm{T}$).

Table 2: Interaction cavity geometrical parameters.

Middle section length (L)	4.5 mm
Cavity radius (R_c)	4.5 mm
Input taper angle (θ_1)	4°
Output taper angle (θ_2)	4°
Input taper length (L_1)	4 mm
Output taper length (L_2)	4 mm

3. CONCLUSION

The results presented in the article shows more than 300 kW RF power at $TE_{25,10}$ mode for 670 GHz gyrotron used in the detection of concealed radioactive material. A preliminary design of simple cylindrical interaction cavity is also presented. The beam-wave interaction simulations are performed for the first harmonic to avoid the high mode competition. The power and frequency growths become stable around 100 ns. The results show more than 300 kW power at 670 GHz frequency.

ACKNOWLEDGMENT

The authors are pleased to acknowledge the support of Dr. Chandra Shekhar, Director, CEERI Pilani and Dr. SN Joshi, National Coordinator of Gyrotron project. The authors also wish to thank to the team members of gyrotron for helpful discussions. Thanks are also due to Council of Scientific and Industrial Research (CSIR) for awarding the Senior Research Fellowship to Mr. Nitin Kumar.

REFERENCES

1. Siegel, P. H., "Terahertz technology," *IEEE Tr. on Microwave Theory and Techniques*, Vol. 50, 910, 2002.
2. Idehara, T., T. Saito, I. Ogawa, S. Mitsudo, Y. Tatematsu, and S. Sabchevski, "The potential of the gyrotrons for development of the sub-terahertz and the terahertz frequency range — A review of novel and prospective applications," *Thin Solid Films*, Vol. 517, 1503, 2008.
3. Granatstein, V. L. and G. S. Nusinovich, "Detecting excess ionizing radiation by electromagnetic breakdown of air," *J. of Applied Physics*, Vol. 108, 063304, 2010.
4. Nusinovich, G. S., et al., "Development of THz gyrotrons with pulse solenoids for detecting concealed radioactive materials," *IEEE-IVEC*, Montrey, USA, 2010.
5. Nusinovich, G. S., et al., "Development of THz-range gyrotrons for detection of concealed radioactive materials," *J. Infrared Millimeter Terahz Waves*, Vol. 32, 380, 2011.

6. Choi, E. M., "Design study of a 0.4 THz 100 kW pulsed gyrotron," *IEEE-IVEC*, Bangalore, India, 2011.
7. Kumar, N., U. Singh, T. P. Singh, and A. K. Sinha, "A review on the applications of high power, high frequency source-gyrotron," *J. of Fusion Energy*, Vol. 30, 257, 2011.
8. Kumar, N., U. Singh, A. Kumar, H. Khatun, T. P. Singh, and A. K. Sinha, "Numerical analysis of interaction cavity for 1.5 MW/127.5 GHz gyrotron," *J. of Fusion Energy*, Vol. 30, 1, 2011.
9. Kumar, N., U. Singh, T. P. Singh, and A. K. Sinha, "Design of 95 GHz, 2 MW gyrotron for communication and security applications," *J. Infrared Millimeter Terahz Waves*, Vol. 32, 186, 2011.
10. Kumar, N., U. Singh, A. Kumar, and A. K. Sinha, "Design and misalignment analysis of 140 GHz, 1.5 MW gyrotron interaction cavity for plasma heating applications," *J. of Fusion Energy*, Vol. 30, 169, 2011.
11. Kumar, A., N. Kumar, U. Singh, H. Khatun, V. Vayas, and A. K. Sinha, "Design of interaction cavity of a 170-GHz, 1-MW gyrotron for ECRH application," *Vacuum*, Jun. 2011.

Swarm Optimization of Raised Cosine Non-linear Cylindrical Waveguide Taper for High-power Applications

Rajeev Sharma[1], **Smrity Dwivedi**[2], **R. P. Gupta**[3], **and P. K. Jain**[2]

[1]Department of Scicence & Technology, TDT Division, New Delhi, India
[2]Department of Electronics Engineering, Institute of Technology
Banaras Hindu University, Varanasi, India
[3]Department of Electronics & Communication, Jaipur National University, Jaipur, India

Abstract— A non-linear cylindrical waveguide taper with given end diameter and length is designed for a raised cosine shape profile. Nonlinear taper has been analyzed for the transmission and reflection coefficient using mode matching technique. This taper design has been optimized further using artificial neural network technique for the maximum power transmission and minimum mode conversion in the desired mode of operation and operating frequency. Scattering parameters are calculated in terms of design parameters of taper and then the optimized for both the transmission (S_{21}) and reflection (S_{11}) coefficients using particle swarm optimization technique for best fitness value, which is found to be $> 97\%$ and $< 2\%$, respectively in a typical design case of TE_{03} mode cylindrical waveguide taper with modified raised cosine shape profile. Final optimized nonlinear taper has been also simulated using commercial simulation code 'CST Microwave Studio'. Simulated values for the reflection and transmission coefficients for the optimum design have been found in close agreement with the analytical results.

1. INTRODUCTION

The requirement of non-linear taper arises at the output stage of high-power microwave/millimeter wave active devices, e.g., klystron, gyrotron, accelerator or any other system and act as the RF interface line between the device and system with maximum power transfer and minimum mode conversion [1–5]. The presence of a taper section inevitably introduces unwanted parasitic modes. In the present paper, a non-linear cylindrical waveguide taper excited in the TE mode for its application in high-power CW gyrotron as a output taper connected at the end of RF interaction cavity has been analyzed using mode matching technique and optimized using an ANN technique [4, 5]. For the non-linear taper raised cosine profile has been taken since this function provides uniform contour at both the ends. This profile provides good impedance matching, low reflection as well as low mode conversion for a relatively smaller taper length.

The mode matching technique involves matching of the total modal field at each junction between uniform sections so that conservation of power is maintained [3]. From this process, the amplitudes of the separate modes at the output of a junction have been deduced in terms of the amplitudes of the mode spectrum at the input junction. Each junction along the length has its own scattering matrix. The matrices for all junctions have been be cascaded and an overall scattering matrix for the total taper length has been formed. The coefficients of the overall scattering matrix contain the input reflection coefficient (S_{11}) and the output transmission coefficient (S_{21}). Then the optimization of taper has been performed by optimizing the coefficients of the S-parameter using particle swarm optimization (PSO) tool, which is used to solve nonlinear function and optimizes multi variables at a time, for a given operating frequency and mode. PSO has been used here to achieve optimized tradeoff between matching of desired resonant frequency and minimizing the reflections in the desired mode of operation. The optimized taper is also simulated using commercial tool 'CST Microwave Studio' and simulated values are found in close agreement with the analytical result.

2. SCATTERING MATRIX FORMULATION OF CYLINDRICAL WAVEGUIDE TAPER

Mode matching technique is applied for the formulation of scattering matrix for cylindrical waveguide taper [3]. The nonlinear taper is divided into large number of step discontinuity maintaining the same axis. Waveguide with arbitrary radius but the common area between the two guides must be identical to the cross section of the smaller waveguide. As the electromagnetic fields defined left of the junctions and right of the junctions as the sum of normal modes of respective waveguides. The electric E and magnetic H field expressions at the left (subscript L) and right (subscript R) of the junction, considering M modes in left side of junction and N modes in right side of junction, can be written as [3]:

For left side of the junction:

$$E_L \textit{ or } H_L = \sum\nolimits_{m=1}^{M}[A_m \exp\{-\gamma_m z\} + B_m \exp\{-\gamma_m z\}]e_{Lm} \tag{1}$$

$$E_R \textit{ or } H_R = \sum\nolimits_{n=1}^{N}[C_n \exp\{-\gamma_n z\} + D_n \exp\{-\gamma_n z\}]e_{Rn} \tag{2}$$

Here, the numbers of modes M and N have to be chosen large for the convergence. e_{xy} and h_{xy} represent the normalized vector functions for the yth mode on the x side of the junction.

In the circular waveguide, eigenmodes for the TE_{mn} mode can be calculated on either side of junction using the relation

$$\begin{aligned} e_{mn} &= (\sqrt{\epsilon_m}/\sqrt{\pi}(\gamma_{mn}'^2 - m^2)J_m\{\gamma_{mn}'\}) \\ &\times \Big[(m/r)\sin(m\theta)\, J'_m\{\gamma_{mn}' r/a\}\hat{r} + (\gamma_{mn}'/a)\cos(m\theta)\, J'_m\{\gamma_{mn}' r/a\}\hat{\theta}\Big]. \end{aligned} \tag{3}$$

For $m = 0$, $\epsilon_m = 1$ and for $m \neq 0$, $\epsilon_m = 2$. Also,

$$h_{mn} = z \times e_{mn}.$$

For both side of junctions, the normalization of e_{Lm} and h_{Lm} enables to write

$$\int_{SL} (e_{Lm} \times h_{Lm}) \cdot ds = R_{mm}, \tag{4}$$

and from the orthogonality of waveguide mode, when $m \neq n$, matching Equation (4) equals to zero. Matching the electric field and magnetic fields over the common apertures between the two regions, one can write:

$$E_L = E_R \text{ inside } S_{L,} \Rightarrow E_L \times h_{Rm} = E_R \times h_{Rn} \text{ inside } S_L$$

or, one can modify Equation (4) as

$$\int_{SL} (E_L \times h_{Rn}) \cdot ds = \int_{SR} (E_R \times h_{Rn}) \cdot ds.$$

Since, electric field is null on the metal surface, making up the surface S_R and S_L, the integral limit on the right hand side may be modified:

$$\int_{SL} (E_L \times h_{Rn}) \cdot ds = \int_{SL} (E_R \times h_{Rn}) \cdot ds. \tag{5}$$

Using the properties

$$\sum_{m=1}^{M} (A_m + B_m)P_{mn} = (C_n + D_n)Q_{nn}, \tag{6}$$

where

$$P_{mn} = \int_{SL} (e_{Lm} \times h_{Rn}) \cdot ds, \quad \text{and} \quad Q_{nn} = \int_{SR} (e_{Rn} \times h_{Rn}) \cdot ds.$$

The other boundary condition required is the continuity of magnetic field intensity:

$$H_L = H_R \text{ within } S_L.$$

Following a similar line of reasoning

$$\int_{SL} (e_{Lm} \times H_L) \cdot ds = \int_{SL} (e_{Lm} \times H_R) \cdot ds \Rightarrow R_{mm}(A_m - B_m) = \sum_{n=1}^{N} P_{mn}(c_n - D_n), \tag{7}$$

where

$$R_{mm} = \int_{SL} (e_{Lm} \times h_{Lm}) \cdot ds.$$

Equations (6) and (7) may be rearranged into a more compact matrix form, giving:

$$(A + B)[P] = (C + D)[Q] \tag{8}$$

$$(A - B)[R] = (D - C)[P]^T. \tag{9}$$

These two Equations (8) and (9) are simplified into a scattering matrix relating the normalized output vector B and D to the normalized input vector A and B. The S_{11} and S_{21} coefficients of the matrix are thus obtained in terms of $[P]$, $[P]^T$, $[R]$, and $[Q]$ as:

$$[S_{11}] = \left[\sqrt{R}\right]\left([R] + [P]^T[P]\right)^{-1}\left([R] - [P]^T[P]\right)\left[\sqrt{R}\right]^{-1}, \tag{10}$$

$$[S_{21}] = 2\left[\sqrt{Q}\right]\left([Q] + [P][P]^T\right)[P]\left[\sqrt{R}\right]^{-1}. \tag{11}$$

This is the calculation for a single junction. As the cascading of small sections discussed previously, one can get the scattering matrix of the overall taper. Here, we require only the transmitted power for a given incident at input to the output in desired mode. So, calculation for transmission coefficient S_{21} is sufficient for the analysis. The cascading equation for two junctions a and b can be written as:

$$[S_{21}^c] = \left[S_{21}^b\right]\left[[I] - [S_{22}^a]\left[S_{11}^b\right]\right]^{-1}\left[S_{21}^b\right]. \tag{12}$$

3. RAISED COSINE SHAPE PROFILE

Keeping the basic raised cosine nature and arbitrary profile equation, a modified arbitrary profile taper with input radius (a_1), output radius (a_2) and length (L) can be taken as:

$$a(z) = ((a_2 - a_1)/2)\lfloor -1 + 2(z/L)^s + (1/\pi)\sin(\pi(-1 + 2(z/L)^s))\rfloor + ((a_2 - a_1)/2) \tag{13}$$

Here, S is the shape factor and keeping all parameters constant one can generate any possible shape by varying $S = 0$ to 100.

4. PARAMETER SELECTION IN PSO

In the standard particle swarm optimization (PSO), instead of using generic operators, each particle adjusts its mission according to its own mission experience (local best) as well its companion's mission experience. Each particle is treated as a point in a D-dimensional space $[X]$.

The ith particle is represented as $X_i = (x_{i1}, x_{i2}, x_{i3}, \ldots, x_{iD})$. The best previous position giving best fitness value of ith particle is recorded as $P_i = (p_{i1}, p_{i2}, p_{i3}, \ldots, p_{iD})$. The velocity of ith particle is represented as $V_i = (v_{i1}, v_{i2}, v_{i3}, \ldots, v_{iD})$. The index of best particle among the population is denoted by g. The velocity and position of each particle are updated according to following relation [5]:

$$v_{id} = w^* v_{id} + c_1^* \,\mathrm{rand}(\,)^* \frac{(p_{id} - x_{id})}{\Delta t} + c_2^* \,\mathrm{Rand}(\,)^* \frac{(p_{gd} - x_{id})}{\Delta t}, \quad x_{id} = x_{id} + v_{id} \tag{14}$$

Here, w = inertia factor, c_1 = self-confidence, c_2 = swarm confidence, $\frac{(p_{id} - x_{id})}{\Delta t}$ = particle memory influence, $\frac{(p_{gd} - x_{id})}{\Delta t}$ = swarm influence, and rand ( ) and Rand ( ) are two random function in the range [0, 1].

5. BASIC NUMERICAL COMPUTATION AND OPTIMIZATION

For circular waveguide operating TE mode, first for each section and for each mode Eigenvalue γ_n as the roots of Bessel functions, self coupling power coefficient (R_{ii}) of the left hand side of junction, self coupling power coefficient (Q_{jj}) of the right hand side of junction, and cross coupling coefficient (P_{ij}) are computed. Modes are added till converging results which is used for the scattering coefficients for that single junction. Secondly, repeating the steps scattering matrix of second section is computer. Third, the overall matrix is obtained by cascading these two sections. Process is repeated till all sub-sections are cascaded to form the overall scattering matrix of the total taper length. Finally the aperture modal coefficient $[D]$ and input reflection coefficient $[B]$ is computed to get S_{21}.

Inertia factor, is dependent on iteration w using (16), (17), iterated from 0.4 to 0.9. c_1 and c_2 values remain constant throughout the optimization and taken between 1.5 to 2. Here, we are kept them equal and value is 1.5. Tolerance will come in action when S_{21} calculation in the two consecutive iterations has such less difference that the process undergoes saturation and taken out of the loop. Tolerance (stopping criteria) is taken as $10^{-6}\,\%$. Particle swarm optimization technique involves a swarm size, each particle has provided the five parameters values or position randomly in their range and each having variation or velocity (change in position in unit time) within the range using analysis technique transmission coefficient for desired mode is calculated for whole swarm. Swarm size is taken as 20. Selection of maximum S_{21} out of the swarm size and corresponding particle's design parameters are considered as *gbest*. Each particle has its own S_{21} and in consecutive iterations the design parameters corresponding to the higher S_{21} for each particle gives *pbest*. This *gbest* and *pbest* along with the PSO parameters gives the update in variation or velocity and thus update in value or position after each iteration. This process goes on upto the desired iteration or at some stopping criteria.

The taper design expression (15) consists of four parameters, i.e., length of taper, input radius, output radius and shape factor and from design point of view, we need the fifth parameter, number of sub-sections. A typical example case of output taper for the 42 GHz, 200 kW, CW gyrotron under development is taken. For this nonlinear cylindrical taper TE_{03} mode operation input radius = 13.99 mm, output radius = 42.5 mm, length = 350 mm, number of sections = 350 have been selected as input constraints. Here, keeping these dimension as constant, it has been found that for every time we are using same optimization steps, one get different set of design parameters giving maximum S_{21} because of random nature involve in the process. It is found that variation of shape factor is critical parameter and affects most the mode conversion issue.

At instant of the position matrix 20×1, result converges which is the optimum shape factor $S = 0.5331$. Figure 1 is showing the variation range of shape factor considered and optimum taper profile obtained by using particle swarm optimization. Figure 2 show the improvement of transmission coefficient S_{21} and reflection S_{11} with increase in number of iterations. It is found that ~ 100 iteration is sufficient for obtaining the converging result.

6. RESULTS AND CONCLUSION

A cylindrical nonlinear taper with raised cosine shape profile has been designed using modal matching method. For a typical parameter set taken as the input, particle swarm optimization technique described in the previous section has been applied and the optimum profile obtained with the shape factor $S = 0.5331$ giving the $S_{21} = 98.90\%$ at frequency 42 GHz (Figure 2).

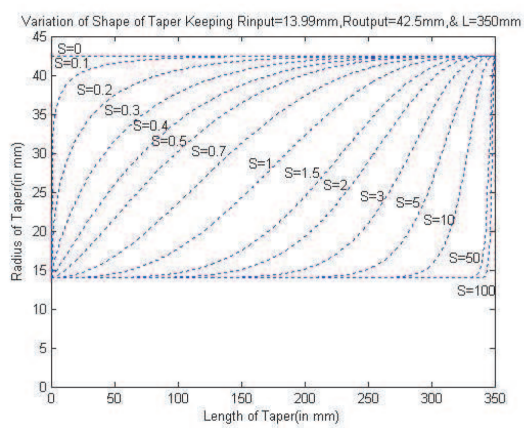

Figure 1: Raised cosine nonlinear taper shape profile with the variation of its shape factor.

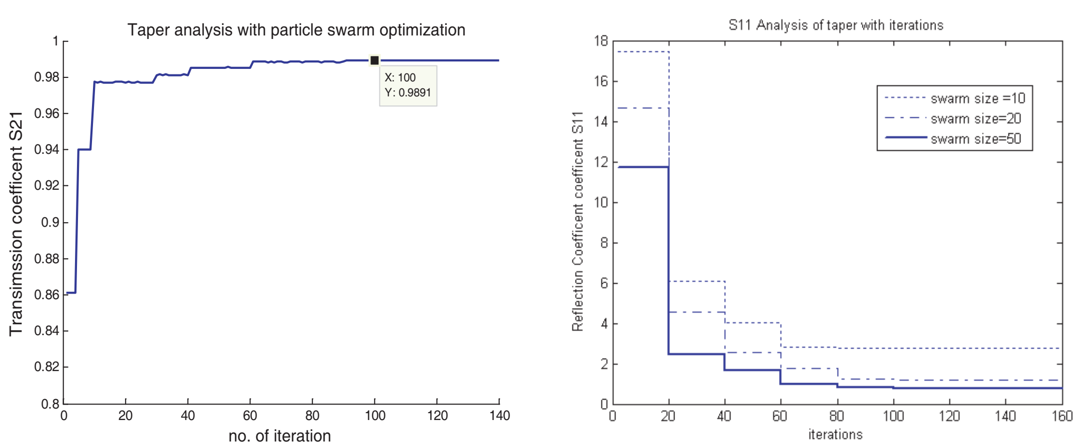

Figure 2: PSO result of nonlinear taper with iteration: transmission coefficient S_{21} and Reflection coefficient S_{11}.

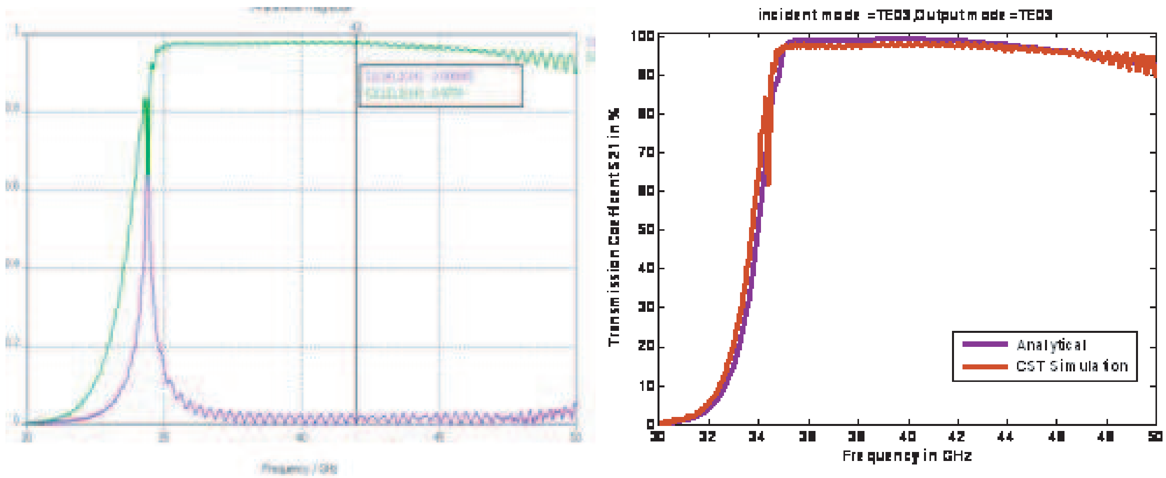

(a) (b)

Figure 3: The S Parameter plots of PSO optimized taper in (a) CST Microwave Studio, (b) comparison with the analytical values.

Table 1: Transmission coefficient of different modes of PSO optimized taper.

Transmitted Coefficient S_{21}	
Mode Number	% Power
TE_{01}	0.039
TE_{02}	0.730
$\boldsymbol{TE_{03}}$	**98.90**
TE_{04}	0.199
TE_{05}	0.000
TE_{06}	0.000
TE_{07}	0.000

Table 2: Comparison of results with two different approaches.

Approach	$\boldsymbol{S_{11}}$	$\boldsymbol{S_{21}}$ **in** $\boldsymbol{TE_{03}}$ **mode**
Analytical	0.67%	98.90%
Simulation	2.22%	96.61%

A non-linear cylindrical waveguide taper design has been presented using mode matching technique. A raised cosine shape profile taper is selected for a typical case of TE_{03} mode of operation with a fixed input, output radii and taper length. Particle swarm optimization technique has been applied to optimize the taper design for the maximum transmission and minimum mode conversion at the desired mode of operation for best fitness value. For the typical test case taken, the reflection (S_{11}) and transmission (S_{21}) have been achieved as 0.67% and 98.90%, respectively. This design has been also validated using commercial simulation code 'Microwave Studio' and the results are found in good agreement with the analytical values.

REFERENCES

1. Flugel, H. and E. Kuhn, "Computer aided analysis and design of circular waveguide tapers," *IEEE Trans. Microwave Theo. & Tech.*, Vol. 36, 332–336, 1988.
2. Huting, W. A. and K. J. Webb, "Numerical analysis of rectangular and circular waveguide tapers," *IEEE Trans. on Magnetics*, Vol. 25, 3095–3097, 1989.
3. Hoppe, D. J., "Modal analysis applied to circular, rectangular, and coaxial waveguides," TDA Progress Report, NASA, July–September 1988.
4. Bogdashov, A. A. and Y. V. Rodin, "Mode converter synthesis by the particle swarm optimization," *Int. J. Infrared Millimeter Waves*, Vol. 28, 627–638, 2007.
5. Chauhan, N., A. Mittal, D. Wagner, M. V. Kartikeyan, and M. K. Thumm, "Design and optimization of non-linear tapers using particle swarm optimization," *Int. J. Infrared and Millimeter Waves*, Vol. 29, 792–798, 2008.

Eigenmode Analysis of Metal Photonic Band Gap Cavity for Gyrotron Operating in Higher Order Mode

Ashutosh and P. K. Jain
Center of Research in Microwave Tubes, Department of Electronics Engineering
Institute of Technology, Banaras Hindu University, Varanasi, India

Abstract— In the present paper, a systematic analysis has been presented for designing a PBG cavity operating in a higher order mode. In particular, a 35 GHz photonic band gap cavity has been designed for TE_{341} mode of operation and eigenmode analysis has been presented to ensure the device operation in desired mode with all possible mode competition. Two dimensional structure of triangular lattice has been used for modelling of PBG cavity. In order to obtain the structure band gap information, dispersion characteristics has been calculated using standard Yee cell based finite difference time domain (FDTD) method. With the global band gap, mode map has been calculated to demonstrate the occurrence of all possible modes in the PBG cavity. The usefulness of mode map has been illustrated to design the RF cavity using PBG structure replacing the conventional tapered wall cylindrical waveguide cavity used in gyro devices to achieve the single mode operation.

1. INTRODUCTION

Photonic band gap (PBG) structures have proven wider research interest due to its fascinating frequency and mode selective property for the propagation of the electromagnetic wave through it. Thus, promising performances are achieved in the devices utilizing PBG structures [1]. PBG structures are periodic structures using dielectric or metallic inclusions or sometimes combination of both. The propagation of electromagnetic waves is restricted in the forbidden region, which is known as photonic or electromagnetic band gap. On the other hand, in the allowed region, waves propagate without any attenuation. The PBG structures have potential application in microwave, millimeter-wave and infrared devices, such as, antennas, waveguides, filters, resonators, planar reflectors, integrated circuits, etc. [1–3]. Moreover, PBG structures find their use in the communication purpose such as in optical fibers, lasers etc. PBG structures are also successfully implemented in gyro-devices, high gradient accelerators, backward wave oscillators (BWO) and, traveling wave tube (TWT) amplifiers [3–6]. Dielectric PBG structures have found various applications even though metal photonic band gap (MPBG) structures are more suitable for certain applications specifically in vacuum electron beam devices. The dielectric materials exhibit the problem of breakdown and charging which limits the application in vacuum electronic devices [2, 6]. On the contrary, such phenomena do not take place in MPBG structures due to their excellence conductibility. Their nearly perfect reflector property minimizes absorption related problems. The operating temperature of vacuum electron beam devices is too high to sustain the device using dielectric PBG structure with sufficient mechanical strength. MPBG structures fulfill these requirements.

Gyrotron is an attractive electron beam device providing high power microwave and millimeter waves with good efficiency. In order to increase the structure dimension and reduce the DC magnetic field requirements, gyrotrons are often operated at the higher order modes. However, higher order mode operation causes overmoding of RF cavity due to the increase in density of nearby modes [3]. Such, mode competition problems can be reduced by using PBG structures.

In this paper, the design and simulation of MPBG cavity operating in a higher order TE_{341} mode is presented. Dispersion characteristics of the two dimensional PBG structure of triangular lattice is calculated using standard Yee's cell based finite difference time domain (FDTD) method for the TE mode of propagation. FDTD is used due to its various advantages over the other existing methods. The global band gap diagram of the structure has been calculated for the different value of rod radius to lattice constant ratio. Using this global band gap diagram and waveguide concept for operating frequency, mode spectrum is observed for all possible modes in the cavity. A proper design point is chosen for the PBG cavity to operate in a higher order mode with reduced mode competition. The designed PBG cavity is simulated using high frequency structure simulator (HFSS) for eigenmode analysis. The confinement of desired TE_{341} mode at 35 GHz operating frequency is observed. Eigenmode analysis is performed in a range of frequency to investigate all possible modes existing in the cavity. Comparison of transverse dimension of the PBG cavity and conventional cavity is also demonstrated.

2. PBG STRUCTURE MODEL

A triangular lattice PBG structure, which provides better azimuthal symmetry, is chosen for the realization of the gyrotron RF interaction cavity. The triangular lattice and its reciprocal lattice are shown in Figs. 1(a) and 1(b), where r is the metal rod radius and a is the lattice periodicity. The irreducible Brillouin zone is shown by shaded portion, where Γ, X and M are symmetry points. Eigen values along the sides (Γ-X, X-M, and M-Γ) of Brillouin zone are determined to yield the dispersion diagram. The cross section of PBG cavity is shown in Fig. 1(c) where R is the defect radius, which is created by removing some finite number of rods at the centre. This defect serves as RF interaction structure of the desired resonant frequency. Structures dimension is adjusted in such a way that the resonant frequencies of desired mode must be in the bandgap and possibly all other competing modes lying in the pass band of the lattice.

3. ANALYTICAL APPROACH

3.1. Dispersion Curve

Photonic band structure or dispersion curve of metal PBG structure has been calculated using finite difference time domain method (FDTD) based on rectangular Yee cell with a modified unit cell [7, 8]. FDTD method involves several fundamental steps as the spatial definition of the system with an appropriate distribution of physical parameter, proper termination of the calculation domain, i.e., the boundary conditions, electromagnetic fields calculation at each spatial discretization point and timestep, an exciting source and final post processing to calculate the band structure [8]. In a two-dimensional (2D) case, time-dependent Maxwell's equations can be discretized in space and time which gives updating field equations for TE mode case and can be given as:

$$E_x^{n+1}(i,j)=\left(\frac{2\varepsilon(i,j)-\Delta t\sigma(i,j)}{2\varepsilon(i,j)+\Delta t\sigma(i,j)}\right)\times E_x^n(i,j)+\left(\frac{2\Delta t}{2\varepsilon(i,j)+\Delta t\sigma(i,j)}\right)\times\frac{H_z^{n+\frac{1}{2}}(i,j)-H_z^{n+\frac{1}{2}}(i,j-1)}{\Delta y} \quad (1)$$

$$E_y^{n+1}(i,j)=\left(\frac{2\varepsilon(i,j)-\Delta t\sigma(i,j)}{2\varepsilon(i,j)+\Delta t\sigma(i,j)}\right)\times E_y^n(i,j)-\left(\frac{2\Delta t}{2\varepsilon(i,j)+\Delta t\sigma(i,j)}\right)\times\frac{H_z^{n+\frac{1}{2}}(i,j)-H_z^{n+\frac{1}{2}}(i-1,j)}{\Delta x} \quad (2)$$

$$E_z^{n+\frac{1}{2}}(i,j)=H_z^{n-\frac{1}{2}}(i,j)+\left(\frac{\Delta t}{\mu(i,j)}\right)\times\left(\frac{E_x^n(i,j+I)-E_x^n(i,j)}{\Delta y}-\frac{E_y^n(i+1,j)-E_y^n(i,j)}{\Delta x}\right) \quad (3)$$

Here, ε and μ are the permittivity and permeability of the medium. i and j are the grid point in the discretized space. A modified unit cell is descretized with uniform grids with Δx and Δy length of each cell in x and y direction [7]. The time t is also discretized with time increment Δt and n is an integer denoting time instant. The time evolution of the fields can be obtained by these time-stepping equations with a specified initial field distribution in the computation domain. Stability limit is also determined by choosing a suitable time step Δt. The field has to satisfy the Bloch theory which results the periodic boundary condition as:

$$E(j,N) = E(j,1)\times\exp\{-ia(k_x+\sqrt{3}k_y)/2\} \quad (4)$$

$$E(N,j) = E(1,j)\times\exp\{-iak_x\} \quad (5)$$

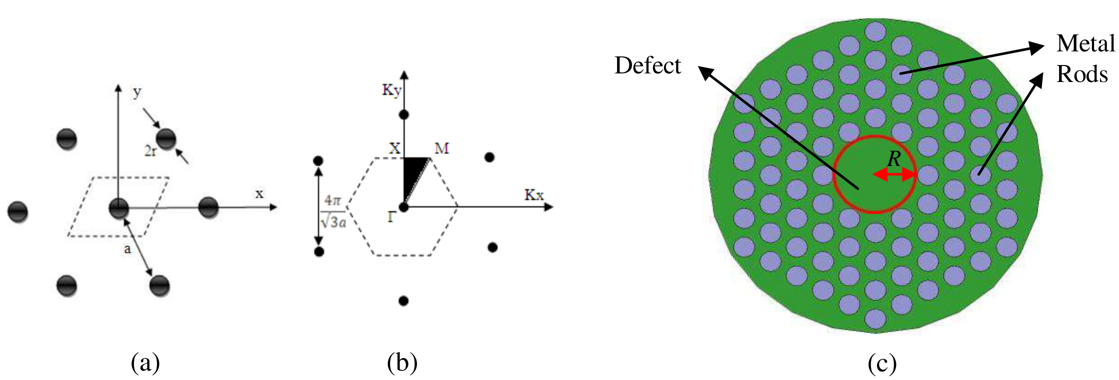

Figure 1: (a) Metal PBG of triangular lattice. (b) Reciprocal lattice and irreducible Brillouin zone (shaded portion). (c) Cross section of PBG cavity made from triangular lattice of metal (copper) rods.

where, N denotes number of grid points. kx and ky are the wave vector in the x and y direction respectively with proper sign convention. The field values at several discretization point is recorded to detect all the possible transmission modes and Fourier transform of these fields yields the frequency spectra. The peaks of the spectral distribution correspond the location of the eigen frequencies of the structure and hence dispersion diagram has been obtained [9].

3.2. Mode Spectrum in PBG Cavity

Gyrotron oscillator involves interaction between the gyrating electron beam and RF wave supporting by the structure in TE mode so only TE mode has been considered for further observation. The operating frequency is close to cut-off of the interaction structure, therefore defect radius of PBG cavity can be approximated as similar to the cylindrical waveguide by the following equation [10],

$$R = \frac{cx_{m,n}}{2\pi f_r} \tag{6}$$

where, c is velocity of light, f_r is resonant frequency of interaction structure and $x_{m,n}$ is zeros of Bessel function derivative $j'_{n(x)}$.

Calculating approximate PBG cavity radius created by 7 rods removal in terms of r and a, the normalized frequency ($f = af_r/c$) of particular mode can be obtained with the following relation

$$x_{m,n} = (\sqrt{3} - r/a)2\pi f \tag{7}$$

This equation yields the mode spectrum in the PBG cavity.

4. RESULTS AND DISCUSSION

4.1. Photonic Band Structure

The unit cell of triangular lattice is meshed with 30×26 uniform rectangular grids For the ratio r/a is 0.2, the calculated dispersion diagram with only few lowest eigenmodes are shown in Fig. 2(a) for the TE mode. This band structure is in close agreement with the result obtained through non orthogonal (NFDTD) analysis by Qiu et al. [9]. For a range of r/a, the global band gap is observed and is demonstrated in global band gap diagram (Fig. 2(b)). In the global band gap diagram, no global bad gap exists before r/a equal to 0.2. The lowest global band gap occurs between the second and third modes of the dispersion diagram which occurs at $r/a \geq 0.35$. Second global TE band gap occurs between the third and fourth modes, having lower ratios of r/a than those for the lowest global TE band gap. A third global band gap region occurs for $r/a \geq 0.35$ and normalised frequency ≥ 1.6. This global band gap of higher normalized frequency can be used to design the PBG cavity operating in a higher order mode.

4.2. Mode Map Calculation in the Global Band Gap

Using the higher order global band gap region of normalized frequency ≥ 1.6 (Fig. 2(b)) and the resonant frequency of the cavity with the relation given in Equation (7), mode spectrum in the

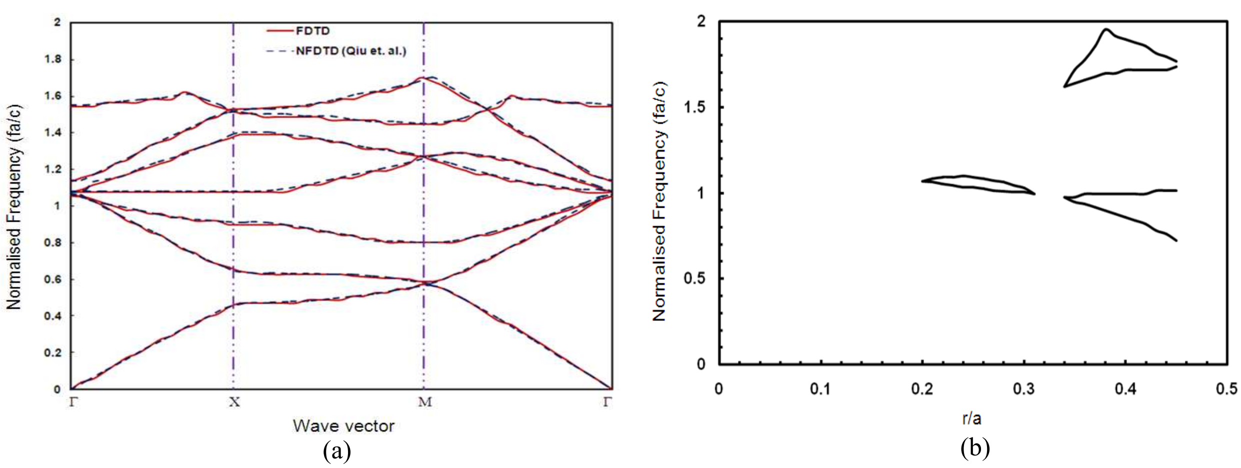

Figure 2: (a) Band structure of the 2-D metallic triangular lattice for TE mode of operation ($r/a = 0.2$) and (b) its global band gap diagram.

PBG cavity is calculated. This plot illustrates occurrence of all possible TE modes confined in the PBG cavity in accordance with global band gap of structure. Shaded portion demonstrates almost single mode of operation with TE_{341} mode around the ratio r/a 0.34.

4.3. PBG Cavity Design and Simulation

For the PBG cavity design, ratio r/a and normalised frequency is chosen 0.345 and 1.670 respectively from mode map for the TE_{341} mode. The axial length of the cavity is taken 8 wavelengths. For 35 GHz resonant frequency, rod radius is 4.9 mm and lattice constant is 14.3 mm. The designed cavity is simulated in 33–36 GHz range of frequency using eigenmode solver of high frequency structure simulator (HFSS). A well confined TE_{341} mode at 34.1 GHz is found which electric field

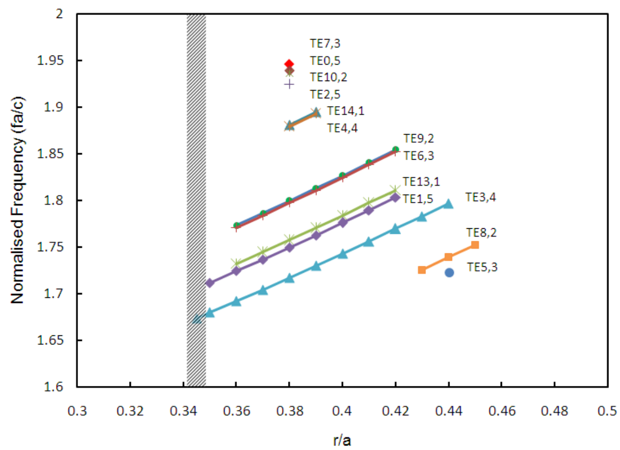

Figure 3: Mode map of PBG cavity formed by removing 7 rods (shaded portion is used for cavity design).

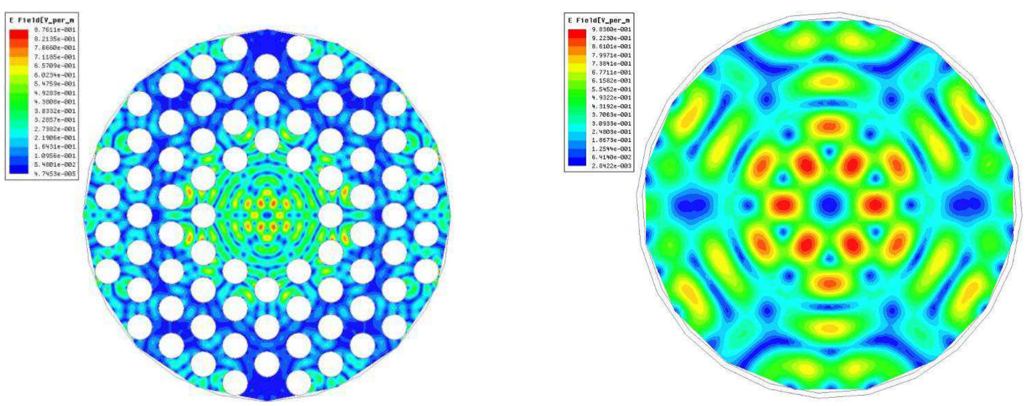

(a) (b)

Figure 4: Electric field of TE_{341} mode in (a) PBG cavity and (b) cylindrical cavity using HFSS.

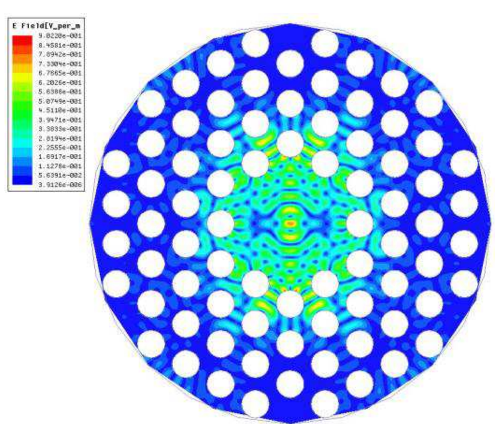

Figure 5: Electric field intensity in PBG cavity for TE_{151} mode obtained from HFSS.

distribution is shown in Fig. 4(a). The difference in the resonance frequency is observed in simulation compared with the calculated value since the field slightly penetrates into the rod region and radius considered analytically is smaller than actual one. The analogous TE_{341} mode in cylindrical cavity at same 35 GHz resonant frequency is shown in Fig. 4(b). The radius of cylindrical cavity is 19.9 mm and of PBG cavity is 71.7 mm. Hence transverse dimension of PBG cavity is quite larger than conventional cylindrical cavity. In simulation, only nearby TE_{151} mode at 34.8 GHz is observed (Fig. 5). The observed Ohmic Q-factor from the simulation for TE_{341} mode is 13778.

5. CONCLUSION

In this paper, a 35 GHz photonic band gap cavity made of triangular lattice of metallic rods has been designed and simulated. The PBG cavity is designed with proper selection of the periodic structure dimension in such a way that least nearby mode appears for the fundamental mode of operation. Dispersion curve obtained from FDTD method shows good agreement with that obtained by NFDTD method. Complete global band gap information is observed with the help of global band gap diagram. Mode map is an important figure to demonstrate the occurrence of all possible modes in the global band gap for the PBG cavity. This helps to choose design parameter of PBG cavity to operate possibly in single mode. A well confined TE_{341}-like mode is observed at 34.1 GHz resonant frequency in the PBG cavity. The difference in resonant frequency is noticed which is due to the fields slightly penetrate into the rods region and radius consider in design is somewhat smaller than the actual one. Only nearby TE_{151} competing mode is found confined in the PBG cavity. The transverse dimension of PBG cavity is much larger compared to conventional cylindrical cavity.

REFERENCES

1. Joannopoulos, J. D., R. D. Meade, and J. N. Winn, *Photonic Crystals: Molding the Flow of Light*, Princeton University Press, Princeton, NJ, 1995.
2. Ozbay, E., B. Temelkuran, M. Sigalas, G. Tuttle, C. M. Soukoulis, and K. M. Ho, "Defect structures in metallic photonic crystals," *Appl. Phys. Lett.*, Vol. 69, No. 25, 3797–3799, December 1996.
3. Sirigiri, J. R., K. E. Kreischer, J. Macuhzak, I. Mastovsky, M. A. Shapiro, and R. J. Temkin, "Photonic band gap resonator gyrotron," *Phys. Rev. Lett.,* Vol. 86, 5628–5631, 2001.
4. Jang, K.-H., S.-G. Jeon, J.-I. Kim, J.-H. Won, J.-K. So, S.-H. Bak, A. Srivastava, S.-S. Jung, and G.-S. Parkb, "High order mode oscillation in a terahertz photonic-band-gap multibeam reflex klystron," *Appl. Phys. Lett.,* Vol. 93, 211104, November 2008.
5. Smirnova, E. I., A. S. Kesar, I. Mastovsky, M. A. Shapiro, and R. J. Temkin, "Demonstration of a 17-GHz, high-gradient accelerator with a photonic-band-gap structure," *Phys. Review Lett.*, Vol. 95, 074801, September 2005.
6. Gao, X., Z. Yang, Y. Xu, L. Qi, D. Li, Z. Shi, F. Lan, and Z. Liang, "Dispersion characteristic of a slow wave structure with metal photonic band gap cells," *Nuclear Instruments and Methods in Physics Research A*, Vol. 592, 292–296, May 2008.
7. Umenyi, A. V., K. Miura, and O. Hanaizumi, "Modified finite-difference time-domain method for triangular lattice photonic crystals," *Journal of Lightwave Technology*, Vol. 27, No. 22, 4995–5001, 2009.
8. Elsherbeni, A. Z. and V. Demir, *The Finite Difference Time Domain Method for Electromagnetics with MATLAB Simulations*, Scitech Publishing Inc., Raleigh, 2009.
9. Qiu, M. and S. He, "A nonorthogonal finite-difference time-domain method for computing the band structure of a two-dimensional photonic crystal with dielectric and metallic inclusion," *J. Appl. Phys.*, Vol. 87, No. 12, 8268–8275, June 2000.
10. Liu, C., Y. Luo, C. Tang, and P. Liu, "Electromagnetic mode analysis on photonic band gap resonant cavity in a Gyrotron," *Int. Journal. of Electronics*, Vol. 97, No. 2, 207–216, 2010.

A Triple-bandgap Uni-planar EBG Structure for Antenna Applications

Huynh Nguyen Bao Phuong[1], **Dao Ngoc Chien**[1], **and Tran Minh Tuan**[2]

[1]School of Electronics and Telecommunications, Hanoi University of Technology
No. 1 Dai Co Viet Road, Hanoi, Vietnam
[2]National Institute of Information and Communications Strategy
No. 115 Tran Duy Hung Road, Hanoi, Vietnam

Abstract— A triple-band electromagnetic bandgap (EBG) structure for antenna applications is presented in this paper. The idea proposed in this the paper is etching several properly shapes in the metal surface of the uni-planar compact EBG (UC-EBG) cell to introduce three bandgaps separately. These bandgaps are represented by three different equivalent circuits, from which the resonant frequencies can be estimated. An in-house developed computational code based on FDTD method was used to analysis the dispersion properties of the structure. Formulas for investigating the central frequencies of the three bandgaps are also presented corresponding to the equivalent circuits. An array with size of 4×5 of EBG cell was numerically simulated and experimentally measured to verify the accuracy of the bandgaps.

1. INTRODUCTION

EBG structures are periodical cell composed of metallic or dielectric elements. Unique feature of EBG structures is to create the forbidden band of frequencies in which surface waves cannot propagate. When the antenna operates in the frequency band of this prohibition, it will improve significantly enhanced features, such as increasing the antenna gain and reducing the back radiation.

There have been many proposed EBG structures with applications in different frequency bands. Overall, there are two types of EBG is very widely used today is mushroom-type EBG [1] and uni-planar EBG [2]. These structures are more compact size compare to the other EBG structure, such as the dielectric rods and holes. Besides miniaturization the EBG structure by modifying the vias or the shape of patch [3–6], the researchers also are developing multi-band EBG structure for antenna applications. There have been many studies on multi-band EBG structure. However, most of which are dual-band EBG structure [7–9]. There are very few studies proposed triple-band EBG-band [10, 11]. These models mainly use metal plates with grounding vias that makes it difficult for manufacturing. Thus, a challenge was set for researchers to generate the uni-planar EBG structure with multi-band.

In this paper, we propose a triple-bandgap uni-planar EBG structure, which can be considered as kind of distorted uni-planar compact EBG. By etching the square split rings and L-shaped on the patch of the structure, it has created the equivalent elements L, C. As the results, three complete bandgaps are created, including the frequency bands from 3.125 to 4.65 GHz (39.2%), from 4.936 to 5.285 GHz (6.83%), and from 6 to 7.42 GHz (21.16%). The structure is applicable to suppression of the surface wave propagating in all directions and can be used for multi-band applications such as dual/triple antennas. The dispersion properties of the proposed EBG structure are evaluated by simulations and experiments.

2. EBG STRUCTURE DESIGN AND ANALYSIS

An EBG structure can be described as a lumped element circuit with distributed capacitors and inductor. This electrical LC-circuit forms frequency selective surface impedance. From the UC-EBG as shown in Figure 1(a), the gaps between the conductor edges of two adjacent cells introduce equivalent capacitance C. In addition, the narrow strips, connected the two patches, introduce equivalent inductance L. Thus, it can be described using the equivalent LC circuit, as shown in Figure 1(a). The center frequency f_C of the bandgap is defined as follows [12]:

$$f_c = \frac{1}{2\pi\sqrt{LC}} \tag{1}$$

The establishments of the bandgaps depend on the creation of components capacitors and inductors. These elements can be combined together into the equivalent circuit to determine the

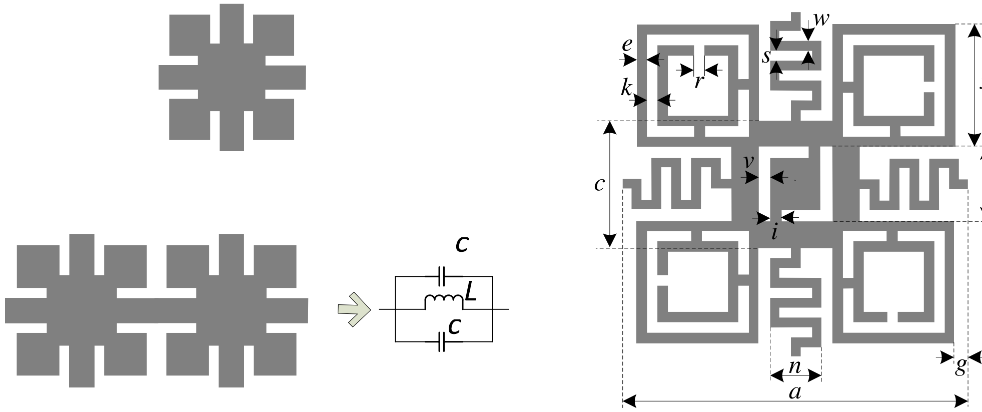

(a) (b)

Figure 1: (a) Conventional UC-EBG structure. (b) Novel triple-bandgap EBG structure.

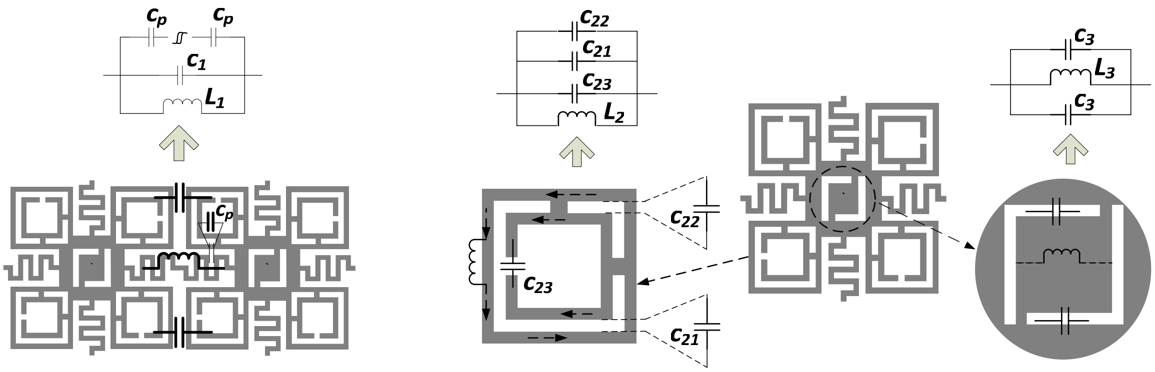

(a) (b)

Figure 2: Equivalent circuit of the triple-bandgap UC-EBG. (a) The first bandgap. (b) The second and the third bandgap.

corresponding center frequency of the bandgap. In the proposed structure, these bandgaps can be represented by three different equivalent circuits.

From the conventional UC-EBG structure as shown in Figure 1(a), the straight lines are transformed into the meandered lines for connecting two adjacent cells. These lines introduce the equivalent inductances, while the gaps between the conductor edges of two contiguous lattices introduce the equivalent capacitance C_1. In this design, parasitical capacitances C_P, which are produced by zigzags of the meandered lines, will allow to increase the total capacitance of the equivalent circuit, and hence move down the first bandgap of the structure lower frequency region. This bandgap is formed similar as the principle of conventional UC-EBG. The other bandgaps are created by introducing more equivalent capacitance C and inductance L in the proposed structure.

The equivalent circuit is described in Figure 2(a). The frequency of the first bandgap can be determined as follows:

$$f_{c1} = \frac{1}{2\pi\sqrt{L_1\left[C_1 + \left(\frac{1}{C_p} + \ldots + \frac{1}{C_p}\right)\right]}} = \frac{1}{2\pi\sqrt{L_1\left(C_1 + \frac{2n}{C_p}\right)}} \tag{2}$$

Note that n denoted the number steps of the meandered line. In the proposed EBG structure, the value of n is 4.

In four pad corners, square split ring resonators (SSRR) are embedded to obtain the second bandgap. The total capacitance with SSRR consists of two parts, in which one part is the coupling capacitance C_C between the outer and the inner rings, and the other one is produced by the electric charges accumulates at the split (r).

In Figure 2(b), the equivalent capacitances C_{21} and C_{22} engendered by the voltage gradients between SRR gap (k). Moreover, the split of the inner ring with gap r is introduced the equivalent capacitance C_{23}. The electric current, which is denoted by dashed arrows, flowing along the core (width e) will form the equivalent inductance L_2. The coupling capacitance C_C can be estimated by the following equation [13]:

$$C_C = \left[0.06 + 3.5 \times 10^{-5}(r_{out}) + r_{in}\right] \tag{3}$$

Then the coupling capacitance shoud be divided into four equal counter parts named C_0 for SRR four sides [14], thus:

$$C_0 = \frac{1}{4}[0.06 + 3.5 \times 10^{-5}(r_{out} + r_{in})] \tag{3a}$$

Here r_{out} and r_{in} represent the radius of the outer and the inner circumcircle of the SRR ring.

It is vital to estimate the capacitances at the inner split, but it is difficult because of the intense electromagnetic brink effects. So they are estimated as the following approaches:

$$C_{inner\ split} = 3\varepsilon_0\mu/r \tag{3b}$$

Note that, ε_0 is the permittivity in vacuum.

The equivalent capacitances of the SRR in the proposed EBG structure are estimated as follows:

$$C_{21} = 3C_0; \quad C_{22} = C_0 \text{ and } C_{22} = C_{inner\ split} \tag{3c}$$

Thus, the central frequency of the second bandgap of the equivalent circuit shown in Fig. 3(b):

$$f_{c2} = \frac{1}{2\pi\sqrt{L_2(C_{22} + C_{21} + C_{22})}} \tag{3d}$$

At last, two L-shaped slots are etching symmetry at the central pad of the structure. The slot width v introduces equivalent capacitance C_3 and the square pad connecting two slots can be resulted in equivalent inductance L_3. As a result, it can be described by another equivalent circuit that defines the third bandgap independently with the other bandgaps.

$$f_{c3} = \frac{1}{2\pi\sqrt{L_3(2C_3)}} \tag{4}$$

3. RESULTS AND DISCUSION

3.1. Surface Wave Bandgap

The proposed EBG structure is showed in the Figure 1(b), which is printed on a FR4 dielectric slab with dielectric constant of 4.4 and thickness of 1.6 mm. The periodic spacing $a = 12$ mm is chosen, the length of conductor edges is $x = 4.2$ mm and the gap g between conductor edges of two adjacent cells is 0.5 mm. The SRR include the outer and inner rings, which have the same width $e = 0.3$ mm, was connected by two strip lines with width $k = 0.35$ mm. The split of the inner ring is $r = 0.35$ mm, which is similar to the gap k between the rings and the width v of two slots etched in the center pad. The other parameters are chosen as follows: $b = 2.6$ mm, $c = 4.3$ mm, $l = 1.5$ mm, $s = 0.35$ mm, $w = 0.35$ mm, $i = 0.35$ mm.

In the FDTD simulation, we are trying to identify the eigen-frequencies for specific wave numbers (k_x, k_y). The FDTD simulation is repeated for thirty different combinations of k_x and k_y in the horizontal axis of the Brillouin triangle, and the resonant frequencies of surface waves are extracted and plotted in Figure 3. Each point in the modal diagram represents a certain surface wave mode. Connecting the modes with similar field distributions together, we obtain dispersion curves of the EBG structures. The first mode starts at zero frequency and the eigen-frequency increases with the wave number. When it reaches a turning point at 3.125 GHz, it decreases as the wave number is further increased.

It is also noticed that the field for the first mode is TM dominant. The second mode starts to appear at frequency higher than 4.65 GHz. It is clear that no eigen-mode exists in the frequency range from 3.125 GHz to 4.65 GHz. Thus, this frequency region is defined as a surface wave band gap. No surface waves can propagate in the EBG structure inside this frequency band gap. Here the second mode is TE1 mode. Two remainder bandgaps are determined by the higher TE modes. The second bandgap spans from 4.936 to 5.285 GHz with central frequency of 5.11 GHz. Finally, it is observed that the third bandgap is centered at 6.71 GHz with a bandwidth spreading from 6 to 7.42 GHz.

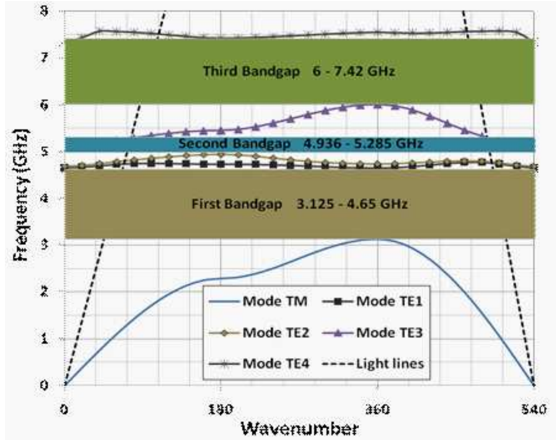

Figure 3: Dispersion diagram of triple-bandgap EBG structure.

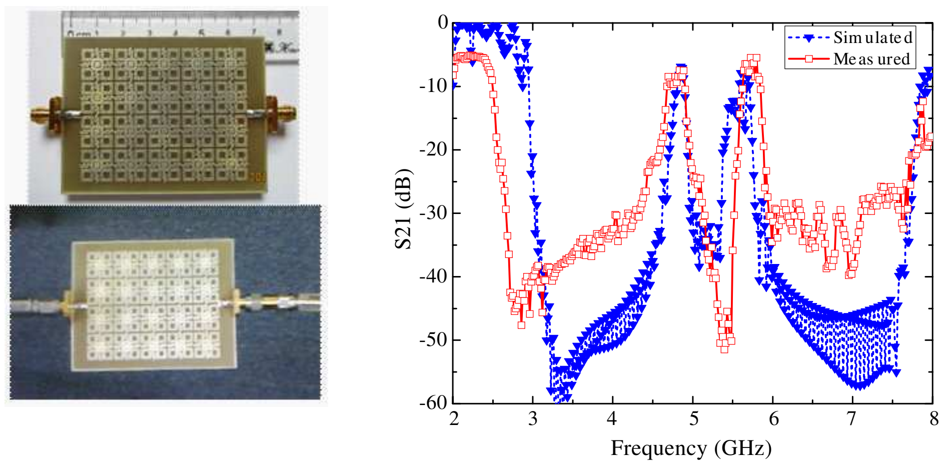

(a) (b)

Figure 4: (a) Photograph of a 4×5 proposed EBG array, (b) simulated and measured of a 4×5 EBG patches array of the proposed EBG structure.

Table 1: Frequency bands of the proposed EBG structure.

Results of methods	**Range of frequencies**		
	Fist Bandgap [GHz]	**Second Bandgap [GHz]**	**Third Bandgap [GHz]**
Dispersion Diagram	3.125–4.625	4.936–5.285	6–7.42
S_{21} simulated	2.98–4.695	4.94–5.38	5.76–7.78
S_{21} measured	2.56–4.58	4.975–5.57	5.9–7.81

3.2. Experimental Result

To verify the accuracy of the bandgap, a different simulation method is used [15]. A 4×5 lattice of the EBG cell, which is mounted on a grounded dielectric slab, is connected with $50\,\Omega$ microstrip lines at both ends. This array acts as a filter in which the transmission coefficient S_{21} of the structure used to determine the frequency ranges of the bandgap. The bandgap bandwidth defined with S_{21} is below $-20\,\text{dB}$. The top side and the measurement setup of the structure are shown in Figure 4(a).

The experimentally measured of coefficient S_{21} of the array is performed by Anritsu 37369D network analyzer. As can be observed from Table 1, the simulation results by means of dispersion diagram and transmission coefficient S_{21} is consistent each other. Experimental measured coefficient S_{21} is similar to simulation result. The results of transmission coefficient S_{21} is shown in Figure 4(b).

4. CONCLUSION

A triple-bandgap UC-EBG structure has proposed in this paper. The complete triple-bandgap has been created by simply distorting the conventional UC-EBG. The band-stop properties of the structure have investigated by using the in-house developed computational tool based on the FDTD method. The bandwidths of the bandgaps are determined simultaneously from the dispersion diagram and transmission coefficients S_{21}. Experimental measurement of a 4×5 array of EBG cell is consistent with simulation results. Thus, EBG structure is promising for use with the planar antennas operating at multiple frequency bands.

REFERENCES

1. Sievenpiper, D., L. J. Zhang, R. F. J. Broas, N. G. Alexopolous, and E. Yablonovitch, "High-impedance electromagnetic surface with a forbidden frequency band," *IEEE Trans. Microw. Theory Tech.*, Vol. 47, No. 11, 2059–2074, Nov. 1999.
2. Yang, F. R., K. P. Ma, Y. X. Qian, and T. Itoh, "A uniplanar compact photonic-bandgap (UC-PBG) structure and its applications for microwave circuit," *IEEE Trans. Microw. Theory Tech.*, Vol. 47, No. 8, 150–1514, Aug. 1999.
3. Fu, Y., N. Yuan, and G. Zhang, "Compact high-impedance surfaces incorporated with interdigital structure," *Electron. Lett.*, Vol. 40, No. 5, 31–311, Mar. 2004.
4. Yang, L., M. Y. Fan, F. L. Chen, J. Z. She, and Z. H. Feng, "A novel compact electromagnetic-bandgap (EBG) structure and its applications for microwave circuits," *IEEE Trans. Microw. Theory Tech.*, Vol. 53, No. 1, 183–190, Jan. 2005.
5. Rajo-Iglesias, E., L. Inclan-Sanchez, J. L. Vazquez-Roy, and E. Garcia-Muoz, "Size reduction of mushroom-type EBG surfaces by using edge-located vias," *IEEE Microw. Wireless Compon. Lett.*, Vol. 17, No. 9, 67–672, Sep. 2007.
6. Hosseinipanah, M. and Q. Wu, "Miniaturised high-impedance surface with high angular stability of esonant frequency," *Electron. Lett.*, Vol. 45, No. 24, 1204–1206, Nov. 2009.
7. Wang, W., X. Cao, R. Wang, and J. Ma, "A small dual-band EBG structure for microwave," *International Conference on Microwave and Millimeter Wave Technology (ICMMT'08)*, Apr. 21–24, 2008.
8. Zhang, L.-J., C.-H. Liang, L. Liang, and L. Chen, "A novel design approach for dual-band electromagnetic band-gap structure," *Progress In Electromagnetics Research M*, Vol. 4, 81–91, 2008.
9. Ayop, O., M. Kamal, A. Rahim, and T. Masri, "Dual band electromagnetic band gap (EBG) structure," *Asia Pacific Conference on Applies Electromagnetic Proceedings (APACE'07)*, Melaka, Malaysia, Dec. 4–6, 2007.
10. Peng, L., C. L. Ruan, and Z. Q. Li, "A novel compact and polarization-dependent mushroom-type EBG using CSRR for dual/triple-band applications," *IEEE Microw. Wireless Compon. Lett.*, Vol. 20, No. 9, 489–491, Sep. 2010.
11. Bao, X. L. and M. J. Ammann, "Design of compact multi-band EBG structures," *The Second European Conference on Antenna and Propagation*, 2007.
12. Sievenpiper, D., L. J. Zhang, R. F. J. Broas, N. G. Alexopolous, and E. Yablonovitch, "High-impedance electromagnetic surface with a forbidden frequency band," *IEEE Trans. Microw. Theory Tech.*, Vol. 47, No. 11, 2059–2074, Nov. 1999.
13. Wu, Q., M. F. Wu, F. Y. Meng, J. Wu, and L. W. Li, "Modeling the effects of an individual SRR by equivalent circuit method," *IEEE AP-S International Symposium and USNC/URSI National Radio Science Meeting*, 2005.
14. Wu, M. F., F. Y. Meng, and Q. Wu, "A compact equivalent circuit model for the SRR structure in metamaterials," *Proceeding of Asia-Pacific Microwaves Conference (APMC'08)*, Dec. 4–7, 2005.
15. Lin, B. Q., F. Li, and H. M. Zhang, "A novel planar spiral EBG structure with improved compact characteristics," *Asia-Pacific Microwaves Conference (APMC'08)*, Dec. 16–20, 2008.

A Terahertz Meta Surface Filter Employing Sub-wavelength Metallic Apertures on a Thin Substrate

S. Hussain, D. Kim, and J. H. Jang
School of Information and Communication
WCU Department of Nano-Bio Materials and Electronics
Gwangju Institute of Science and Technology, Gwangju, South Korea

Abstract— In this paper, the design and simulation of a single layer meta-surface filter, having the simple geometry, has been demonstrated. The filter is made up of sub-wavelength metallic slot apertures which are periodic in a two dimensions, essentially forming a meta-surface. The filter is realized by fabricating the apertures using micro structured gold film on an ultra-thin silicon nitride substrate. Since, the substrate thickness is much smaller than the free space wavelength of the incident electromagnetic wave so there are no unwanted Fabry-Perot resonances which are inescapable in thick substrates. Ultra-thin substrate also facilitates achieving higher transmitted amplitude because of extremely low dielectric loss. The design of the filter was analyzed using finite element method (FEM) and was optimized for attaining the better out of band attenuation. Insertion loss of less than 0.5 dB has been achieved in the numerical simulation at the resonant frequency of the 1 THz.

1. INTRODUCTION

Frequency Selective Surfaces (FSS) have been analyzed and designed in detail in the past because of their potential application as absorbers, antenna radomes, filters and polarizers [1–7]. Frequency selective surfaces may be realized by a two dimensional array of metallic patches or its complement metallic apertures, as stated by the Babinet's principal, fabricated on the substrate. Incident electromagnetic wave on these FSS gets reflected or transmitted, for the patches and apertures respectively, in the resonant region of the unit cell. Single or multiple metallic layers of these structures may be used to construct FSS in order to get the desired spectral response. Such structures have been investigated in detail in antenna theory for over a long time. Various numerical simulators based on Method of Moments (MoM), Finite Element Method (FEM), Finite Domain Time Difference (FDTD) are available not to verify the theoretical design for FSS only but also to optimize it to achieve desired specifications as well [8].

More recently, Terahertz frequency band has acquired the attention of researchers because of its potential applications in medical, security and communication system. More efforts are being put to fill this band which was not possible in the past due to technology limitations. These structures, described above to construct FSS, are easy to fabricate in microwave frequencies because of significantly large dimensions of a unit cell. However, in terahertz frequency band, the size of elements in the FSS is of the order of micrometers, making these structures much more difficult to fabricate in the past. Advances in fabrication technology over the last few years have allowed construction of periodic structures with unit cell sizes less than one micrometer. Construction of FSS filters for the terahertz, and even for optical frequency band is no longer difficult to fabricate. Technology advancement has opened a gateway for the researcher to design, analyze and characterize these FSS even at the optical frequencies.

Free standing slot apertures are not possible to fabricate in terahertz frequencies because of mechanical issues associated with it. In this paper, we have proposed a simple design of single layer of slot shaped apertures perforated in gold film fabricated on ultra-thin silicon nitride membrane, having a thickness of 1um, in order to avoid the major disadvantages associated with the thick substrate. Thin silicon nitride membrane is supported by a thick silicon frame to make it able to sustain external stresses. Using thick substrates, it is very hard to eliminate the effect of Fabry-Perot Resonances [9]. Moreover, dielectric loss, associated with thickness [10], becomes larger which contributes to the insertion loss of the FSS. Since power is very precious at higher frequencies especially in terahertz, where devices like amplifiers are not readily available, proposed design finds its applications into ultra-low loss filters, absorbers and polarizers, etc..

2. DESIGN

The design of a free standing rectangular aperture, commonly known as "slot antenna", is simple. Where, the larger dimension of the aperture is equal to $\lambda_0/2$ and λ_0 is the free space wavelength of the incident field. Design of the metallic aperture unit cell was complicated by the thickness of the substrate. Resonant frequency is inversely proportional to the thickness of the substrate which gets saturated after the certain thickness of substrate [11]. However, resonant frequency is much sensitive to the thinner substrate. Because of the higher dielectric constant of the silicon nitride membrane (i.e., $\varepsilon_r = 7.5$), aperture dimensions and unit cell size is reduced. Larger dimension L_{slot} is recalculated by using the following equation.

$$L_{slot} = \frac{\lambda_0}{2\sqrt{\epsilon_{eff}}} \tag{1}$$

where, ε_{eff} is the effective dielectric permittivity, and may be approximated by using the following equation at the interface between air ($\varepsilon_r = 1$) and dielectric (silicon nitride, $\varepsilon_r = 7.5$).

$$\epsilon_{eff} = \frac{1+\epsilon_r}{2} \tag{2}$$

By using the above equations, initial value for the length of slot aperture, L_{slot} was found to be 73 µm. While the other dimension of the slot W_{slot} was set to 8 µm.

3. SIMULATION

Numerical simulation for the meta-surface was performed using a commercial simulation engine Ansoft HFSS v13. The said simulator solves the given 3D electromagnetic problem using Finite Element Method (FEM).

Simulation model included the unit cell fabricated on an ultra-thin silicon nitride membrane of 1 µm thickness and bounded by a parallel plate waveguide with PEC and PMC boundary conditions assigned to the sides. Such boundary conditions in the simulation depict the behavior of infinite array of the unit cell in this case. This was done to realize the practical scenario in which there would be a hundreds of metallic apertures excited by the THz radiation incident on them.

Two wave ports, on either sides of the model, were assigned to calculate the transmitted component. Wave ports are assigned on the interface to provide a window that couples the model device to the external world. Simulator engine assumes that each wave port is connected to a semi-infinitely long waveguide that has the same cross-section and material properties as the port.

In a numerical simulation based on FEM, transmission characteristic for different thicknesses of the bared silicon nitride substrate was calculated to verify that there exists no resonance at the resonant frequency for the thickness of 1 µm and results are plotted in Figure 2(a). The design of the meta-surface was optimized to achieve the desired frequency response, the optimization variables were the dimensions $L_{unit\ cell}$ and $W_{unit\ cell}$ of the unit cell and the length of the slot aperture, L_{slot} while keeping all other geometrical dimensions constant. This optimization process countenanced to obtain a filter that satisfied the design specifications. The dimensions of the optimized filter

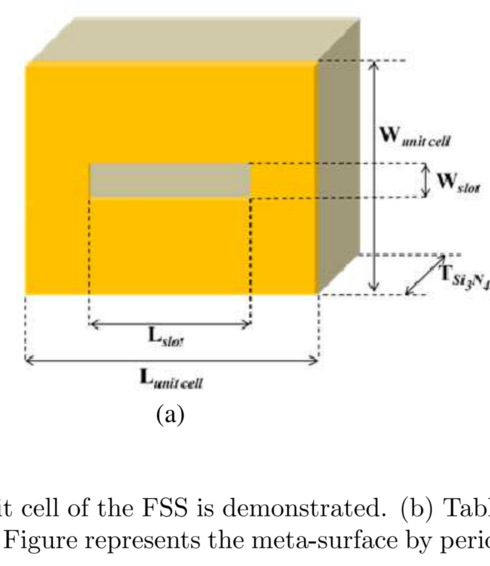

(a)

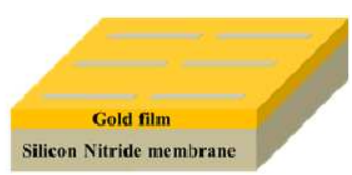

(c)

Variable	Dimensions (um)
L_{slot}	123
W_{slot}	8
$L_{unit\ cell}$	160
$W_{unit\ cell}$	120
$T_{Si_3N_4}$	1
T_{Gold}	0.5

(b)

Figure 1: (a) Unit cell of the FSS is demonstrated. (b) Table illustrates the dimensions of different variables shown in (a). (c) Figure represents the meta-surface by periodically repeating the unit cell in two dimensions.

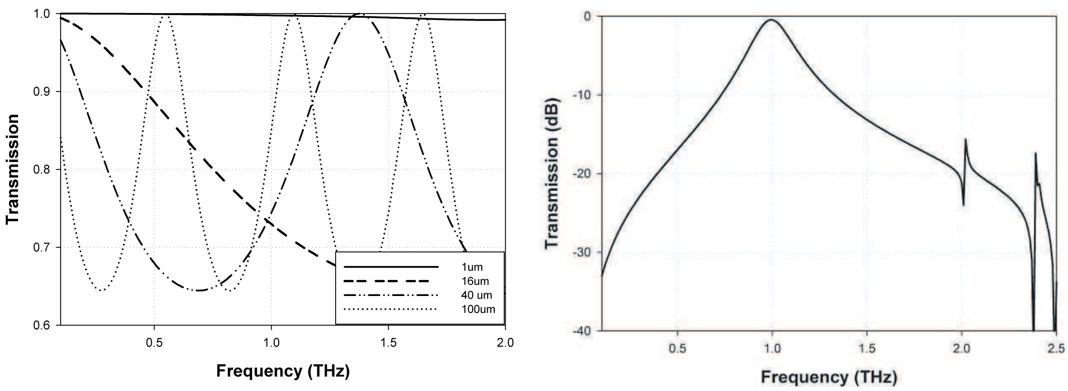

(a) (b)

Figure 2: (a) Simulated results for the transmission through the Si_3N_4 substrate for different thickness values. (b) Simulated results for transmission characteristic of the designed meta-surface.

resulted: $L_{slot} = 123\,\mu\text{m}$, $L_{unit\ cell} = 160\,\mu\text{m}$ and $W_{unit\ cell} = 120\,\mu\text{m}$ keeping aperture width and metal thickness constant. Simulation was performed for a wide frequency range from 0.1 THz to 2.5 THz and insertion loss of less than 0.5 dB is obtained as depicted in Figure 2(b). Spikes in the spectral response beyond 2 THz, in Figure 2(b), are due to the higher modes generated in the parallel plate waveguide.

4. CONCLUSION

A meta-surface has been designed and simulated to work as a band pass filter with a resonance frequency at 1 THz. Meta-surface was constructed using a two dimensional array of slot shaped apertures perforated into thin gold film which is deposited on an ultra-thin silicon nitride membrane of 1um in thickness. Initial values for the geometry of unit cell were calculated theoretically and then optimized using numerical simulation based on Finite Element Method (FEM). Simulated results depicted the minimum insertion loss of better than 0.5 dB in the pass band with no Fabry-Perot Resonance observed because of using electrically thin silicon nitride membrane in the simulation. The device based on this simulation would be fabricated and the measured results will be published in future.

ACKNOWLEDGMENT

This work was partially supported by the World Class University (WCU) program at GIST through a grant provided by the Ministry of Education, Science and Technology (MEST) of Korea (Project No. R31-10026).

REFERENCES

1. Pozar, D. M. and R. Pous, "A frequency selective surface using aperture coupled microstrip patches," *Antennas and Propagation Society International Symposium*, Vol. 1, 96–99, 1990.
2. Mosallaei, H. and K. Sarabandi, "A one-layer ultra-thin meta-surface absorber," *Antennas and Propagation Soceity*, Vol. 1B, No. 5, 615–618, 2005.
3. Biber, S., et al., "Design and testing of frequency-selective surfaces on silicon substrates for submillimeter-wave applications," *IEEE Transactions on Antennas and Propagation*, Vol. 54, No. 9, 2638–2645, 2006.
4. Kim, D. H. and J. I. Choi, "Design of a multiband frequency selective surface," *ETRI Journal*, Vol. 28, No. 4, 506–508, 2006.
5. Debus, C. and P. H. Bolivar, "Frequency selective surfaces for high sensitivity terahertz sensing," *Applied Physics Letters*, Vol. 91, No. 18, 184102-1–184102-3, 2007.
6. Sarabandi, K. and N. Behdad, "A frequency selective surface with miniaturized elements," *IEEE Transactions on Antennas and Propagation*, Vol. 55, No. 5, 1239–1245, 2007.
7. Zhang, J.-C., Y.-Z. Yin, and J.-P. Ma, "Design of narrow band-pass frequency selective surfaces for millimeter wave applications," *Progress In Electromagnetics Research*, Vol. 96, 287–298, 2009.

8. Jeffery, A. R., "Frequency selective surfaces with multiple periodic elements," Ph.D. Dissertations, University of Texas at Dallas, December 1997.
9. Lee, J. W., et al., "Terahertz transparency at Fabry-Perot resonances of periodic slit arrays in a metal plate: Experiment and theory," *Optics Express*, Vol. 14, No. 26, 12637–12643, 2006.
10. Kang, J. H., et al., "Substrate effect on aperture resonances in a thin metal film," *Optics Express*, Vol. 17, No. 18, 15652–15658, 2009.
11. Park, H. R. and D. S. Kim, "Resonance behavior of single ultrathin slot antennas on finite dielectric substrates," *Applied Physics Letters*, Vol. 96, No. 21, 211109-1–211109-3, 2010.

A Broadband Photolithographic Polariser for Millimetre Wave Applications

G. Pisano, M. W. Ng, V. Haynes, and B. Maffei
Jodrell Bank Centre for Astrophysics, School of Physics and Astronomy
The University of Manchester, United Kingdom

Abstract— Circular polarisers are used to convert linear- into circular-polarisation, and vice versa. This is achieved by introducing a phase-shift of 90° between two orthogonal polarisations passing through the device. These devices can be designed using slabs of birefringent material with the appropriate thicknesses (Quarter-Wave Plates). An interesting alternative solution consists of designing planar metallic grids with sub-wavelength geometries that exhibits different behaviour along two orthogonal axes. In this work we present a broadband dielectrically embedded quasi-optical polariser built using photolithographic techniques. The device was experimentally tested using a Vector Network Analyser working in W-band (75–110 GHz). The presented results are in excellent agreement with finite-element analysis simulations: across a 30% bandwidth the transmission along the two axes and the very flat differential phase-shift are respectively: $T_C = 0.92$, $T_L = 0.95$ and $\Delta\varphi_{LC} = 89.3 \pm 1.5°$.

1. INTRODUCTION

Circular polarisers are devices that can convert linear polarisations into circular polarisations, and viceversa. These devices can be used for example in antenna systems to let the receiver/transmitter be-sensitive-to/irradiate circularly polarised signals still using normal orthomode transducers in front of their detectors/sources. The simplest way to build a millimetre wave polariser is by using birefringent materials. For example, a slab of sapphire cut with the ordinary and the extraordinary birefringent axes along its surface and its thickness tuned to provide a differential phase-shift of 90° between the two orthogonal axes. However, the high costs and the limited dimensions of the commercially available birefringent materials have driven to alternative solutions based on metamaterials. These materials can be designed using sub-wavelength periodic metallic structures. The development of Frequency Selective Structures (FSSs), started many decades ago, aimed to the realisation of filters working in spectral regions where the required natural materials where not available. At that time using the same techniques low frequency polarisers have been built using different recipes: Shatrow[1] and Lerner [2].

The realisation of these devices is based on accurate photolithographic techniques that allowed recently to build a photolithographic Half-Wave Plate (HWP) working in W-band [3]. This first device was based on an air-gap solution where the different grids were kept at specific distances by means of thin metallic spacers. However, these structures are inherently very delicate and more robust solutions are highly desirable. A first attempt to solve the problem has been to embedd the HWP grids into a dielectric material [4] in the way millimetre wave mesh filter are commonly realised [5]. The recipe used in this case was still of the Shatrow type, so requiring many grids with the associated uncertainties in the overall performance. We present here a quasi-optical polariser (a Quarter-Wave Plate) realised dielectrically embedding the grids and using a Lerner type recipe that allows reduction of the number of grids by a factor 2 and that exhibits excellent performance.

2. CONCEPT

The polariser design suggested in [1] by Shatrow consisted of two orthogonal stacks of capacitive and inductive grids independently interacting with two orthogonal polarisations. The two stack of grids provide phase-shifts with opposite signs and are almost transparent for the orthogonal polarisation. The device is designed with a certain number of grids and distances able to provide a differential phase-shift between the two orthogonal polarisations close to 90° across a wide band. A photolithographic W-band HWP was realised more recently using a Shatrow type design [3]: in spite of the good performance achieved, this type of air-gap devices are very delicate expecially in cases where large diameters are required. A dielectrically embedded design still using a Shatrow type recipe was presented later [4]: the big number of grids, equal to 12, was probably responsible for the measured phase errors of the order of 20–30°.

The polariser design presented in this work is based on a Lerner type recipe [2]. Here the capacitive and inductive geometries are realised on the same grid, so reducing the total number of grids by a factor two compared to the Shatrow types. A sketch of a single cell is highlighted in Fig. 1. Radiation polarised along the capacitive 'C-axis' will interact with the parallel dashed copper lines, that in transmission line terms can be represented with capacitive lumped admittances. The orthogonal polarisation, along the inductive 'L-axis', will interact with continuous parellel copper lines, that can be represented with inductive lumped impedances. The opposite behaviours of the capacitive and inductive axes is reflected in the phase shift that they introduce on the two polarisations having opposite signs.

Cascading more of the above grids, and keeping their axes aligned, it is possible to design devices exhibiting cumulative differential phase-shifts close to 90° over wide bandwidths. In addition, across the same bandwidth the other requirement is to keep the trasmissions high along both axes. This is not a simple task considering that the device will be embedded into a dielectric material (polypropilene in our case) that will inherently introduce reflections at its surfaces. However, optimising the grid geometry parameters and tuning the grid distances it is possible to keep the intensity tranmsission above 90% over 30% bandwidths without using anti-reflection coatings.

3. MODELING

Frequency Selective Surfaces can be modelled using transmission line circuits where the grids are represented by shunted lumped element admittances [6]. There is plenty of literature providing the analytical expressions for calculating the grid admittances for a wide variety of different geometries. Unfortunately, transmission line codes based on these expressions in many cases can provide only first order approximations and in addition, when the quantity of interest is the phase, their results can be very inaccurate.

A more accurate method to model FSS is to de-embeed the grid admittances using Finite Element Analysis (FEA) commercial software, such as Ansoft HFSS [7]. The same transmission line codes used before can be fed now by much more realistic and accurate numerical admittances. The new codes can be very accurate and the resulting phase errors can be reduced down to a few degrees. These codes, that can be written with any programming language, allow very fast computation and the possibility to optimise a complex device spanning over the many different geometrical parameters. Once obtained an appropriate 'recipe' that meets the requirements, a final FEA fine-tuning of the whole device is required to reduce the phase error below 1°.

The polariser presented here is designed to work in W-band (75–110 GHz). In order to achieve differential phase-shift of the order of 90° the minimum number of grids resulted to be equal to three. A sketch of the equivalent transmission lines used to model the device is reported in Fig. 2. A final recipe was found running an optimisation targeted to achieve axis transmissions greater

Figure 1: Lerner type geometry adopted for the polariser design.

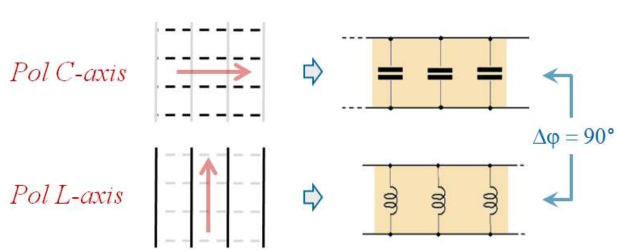

Figure 2: Transmission line equivalent circuits for the polariser C- and L-axes.

than 90% and differential phase-shift within $90 \pm 1^\circ$ across a 30% bandwidth. The simulated axes transmission, phase-shifts and differential phase-shift are reported respectively in Figs. 4, 5 and 6. We note the flatness of the phase across the band.

4. MANUFACTURE AND EXPERIMENTAL TESTS

The polariser was manufactured using photolithographic techniques. Three thin polypropylene substrates were coated with a thin film of copper using evaporation methods. They were then wet etched in order to achieve the required metallic geometry shown in Fig. 1. The three grid-substrates were then interspaced with plain polypropylene substrates with thicknesses dictated by the optimised recipe obtained from the modelling discussed above. Particular attention was paid to guarantee the proper alignment of the grids in order to avoid the emergence of cross-polarisation effects in the final device. The stack of grids and substrates was then mechanically pressed and heated to the polypropylene bonding temperature inside a vacuum oven. A polariser prototype is shown in Fig. 3 together with some of the grid geometry details.

The RF characterisation of the polariser was carried out using a Rohde and Schwarz ZVA40 Vector Network Analyser equipped with two WR10 heads. The VNA waveguide ports were connected to corrugated horns in order to generate gaussian beams and be able to test the polariser in free space. Eccosorb panels were used all around the optical setup to minimise the spurious reflections and standing-waves. The polariser was tested by sending linearly polarised radiation along

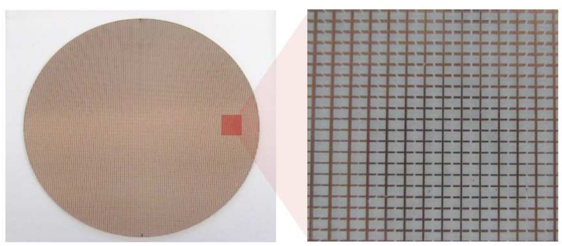

Figure 3: W-band polariser prototype (20 cm diameter and 2 mm thickness) and grid details.

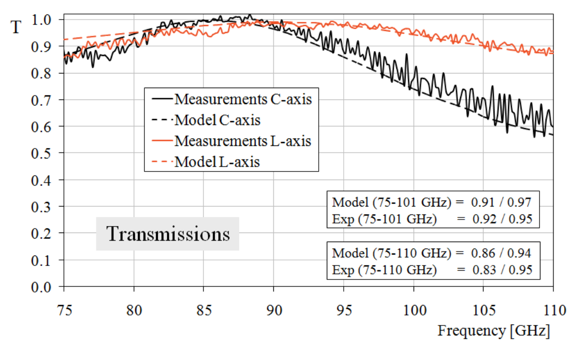

Figure 4: Polariser transmissions along the axes: simulations and measurements.

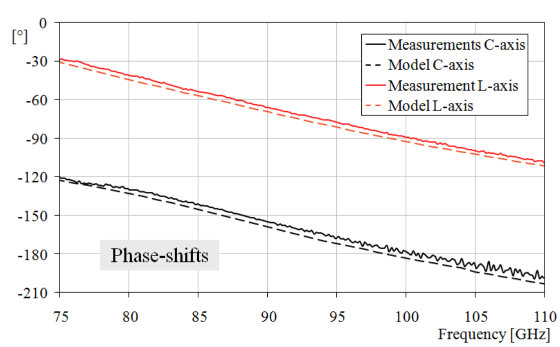

Figure 5: Polariser transmission phase-shifts along the axes: simulations and measurements.

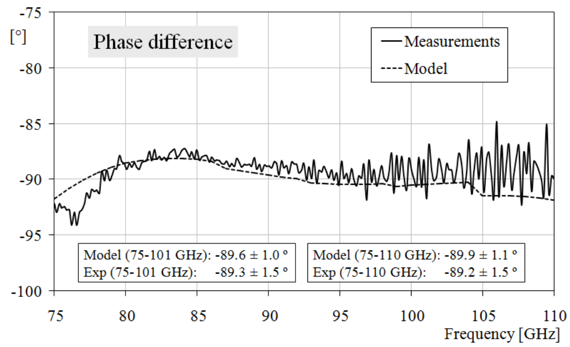

Figure 6: Polariser differential phase-shifts simulations and measurements.

the C- and L-axes and measuring the transmitted complex field in terms of S_{21}. The measured transmission intensities are reported and compared with the modelling results in Fig. 4. From the arguments of the complex transmissions it was possible to extract the phase-shifts introduced by the two axes, plotted and compared with the simulations in Fig. 5. Finally, the overall differential phase-shift introduced by the polariser, obtained by subtracting the phase-shifts along its axes, is compared with the modelling results in Fig. 6. It is clear from Figs. 4, 5 and 6 the very good agreement between simulations and experimental data and the excellent performance of the polariser in terms of differential phase shift. In summary, across a 30% bandwidth, specifically between 75 and 101 GHz, the axes transmissions and differential phase-shift are respectively: $T_C = 0.92$, $T_L = 0.95$ and $\Delta\varphi_{LC} = 89.3 \pm 1.5°$.

5. CONCLUSIONS

A W-band quasi-optical polariser based on a Lerner type design has been manufactured using photolithographic techniques. The experimental measurements, carried out using a Vector Network Analyser, showed excellent agreement with the finite element analysis simulations. Averaged across a 30% bandwidth (75–101 GHz) the polariser transmissions along the axes and their differential phase-shift were respectively: $T_C = 0.92$, $T_L = 0.95$ and $\Delta\varphi_{LC} = 89.3 \pm 1.5°$.

ACKNOWLEDGMENT

This work was supported by the UK Engineering and Physical Sciences Research Council (EPSRC), grant EP/H021299/1, for the "Development of new planar retarding surfaces for mm- and sub-mm wave applications".

REFERENCES

1. Shatrow, A. D., A. D. Chuprin, and A. N. Sivov, "Constructing the phase converters consisting of arbitrary number of translucent surfaces," *IEEE Trans. Antennas Propag.*, Vol. 43, No. 1, 1995.
2. Lerner, D. S., "A wave polarization converter for circular polarization," *IEEE Trans. Antennas Propag.*, Vol. 15, 3–7, 1964.
3. Pisano, G., G. Savini, P. Ade, and V. Haynes, "A metal-mesh achromatic half-wave plate for use at submillimetre wavelengths," *Applied Optics*, Vol. 47, No. 33, 6251–6256, 2008.
4. Zhang, J., P. A. R. Ade, P. Mauskopf, G. Savini, L. Moncelsi, and N. Whitehouse, "Polypropylene embedded metal mesh broadband achromatic half-wave plate for millimeter wavelengths," *Applied Optics*, Vol. 50, No. 21, 3750–20757, 2011.
5. Ade, P. A. R., G. Pisano, C. E. Tucker, and S. O. Weaver "A review of metal mesh filters," *Proc. SPIE*, Vol. 6275, U2750, 2006.
6. Marcuvitz, N., *Waveguide Handbook*, M.I.T. Rad. Lab. Ser., Mc.Graw-Hill, 1951.
7. Ansoft HFSS website: http://www.ansoft.com/.

Design and Characterization of a Dielectric Q-plate for Millimetre-wave Photon Orbital Angular Momentum Applications

S. Maccalli[1], **G. Pisano**[1], **M. W. R. Ng**[1],
B. Maffei[1], **Malcolm Gray**[1], **and S. Colafrancesco**[2]

[1]School of Physics and Astronomy, The University of Manchester, Manchester, UK
[2]School of Physics, University of the Witwatersrand, Johannesburg, South Africa

Abstract— We present the design, fabrication and beam pattern characterization of a nylon-made q-plate that generates ±2 charged OAM states at millimetre wavelengths. This q-plate is optimized to work around 100 GHz but the same design can be scaled to work at other frequencies in the millimetre-wave range. The simple manufacturing method used here allows a cheap and fast q-plate production. The designed plate can create a point defect on the phase front structure of a fundamental Gaussian beam with the associated optical vortex and annular intensity pattern. The q-plate has been experimentally characterized using a millimetre-wave Vector Network Analyzer and beam scanning test set-up.

1. INTRODUCTION

Recent years have seen a growing interest in the research field of optical beams with complex wave front structures. This new area of research began when it was discovered that the angular momentum of a photon is not just limited to its intrinsic angular momentum: the usual *Spin Angular Momentum* (SAM) associated with circular polarization of the field. These new-style beams (also called optical vortices) carry an additional and different form of angular momentum: the so-called *Orbital Angular Momentum* (OAM) [1].

An optical vortex is a point defect where the value of the phase is not defined, since the value of the field is zero. This causes the wave front of the defect to have an helical structure around the propagation axis [2]. The OAM is the consequence of the phase-front being no longer parallel to the transverse plane. The total phase shift around the axis of the vortex is a multiple l of 2π, where l is defined as the topological charge and can have any integer value from $-\infty$ to $+\infty$, with the positive and negative sign determining clockwise or anticlockwise direction. Since the Poynting vector is defined to be perpendicular to the equiphase wave front, in waves with optical vortices it spirals around the beam propagation axis [1].

OAM eigenstates have an azimuthal phase dependence of the form $\exp(il\varphi)$ giving rise to the intertwined helical phase fronts. Photons of such a beam carry an OAM equal to $l\hbar$ [1]. Optical vortices have applications in disparate fields such as: non-contact manipulation of matter, laser trapping and tweezers, sub-wavelength resolution nano-optics, biological cell handling, microfluidics, nanofabrication, atom trapping, control of Bose-Einstein condensates, astronomical observations and quantum informatics [3].

The most commonly used form to represent the field's amplitude of these beams carrying OAM is given, in cylindrical coordinates, by the Laguerre-Gaussian (L-G) modes:

$$u_p^l(r,\varphi,z) \propto e^{-\frac{ikr^2}{2R}} e^{-\frac{r^2}{w^2}} e^{-i(2p+l+1)\Psi} e^{-il\varphi} (-1)^p \left(\frac{2r^2}{w^2}\right)^{1/2} L_p^l\left(\frac{2r^2}{w^2}\right) \tag{1}$$

where r is the distance from the optical axis of the beam, φ is the azimuthal angle, z is the distance from the beam waist w_0 along the optical axis, $L_p^l(x)$ are the generalized Laguerre polynomials, $w(z)$ is the beam radius, $R(z)$ is the wavefront radius of curvature and Ψ is the Gouy phase, i.e., the additional longitudinal phase delay [4]. The L-G modes (1) properly represent both the characteristic far field annular intensity pattern and the azimuthal phase dependence [1], and are solutions of the paraxial wave equation.

Beams with helical wave fronts can be produced by lasers operating in Laguerre-Gaussian regime or with devices such as cylindrical lenses [1, 6], computer-generated holograms [6], spiral phase-plates [7, 8], q-plates or, in the radio domain, with special configurations of antennas/horns [9]. Our aim is to develop new q-plates to efficiently manipulate OAM states in the millimeter-wave region.

2. Q-PLATES

In order to transform a constant phase wave front into one with azimuthal dependence it is necessary to design a device that acts differently across its surface and specifically that introduces different phase shifts depending only on the azimuthal angle φ. It is well known that a circularly polarized beam passing through an HWP will emerge with opposite circular polarization and with a phase shift equal to twice the angle between the HWP birefringence axis and the electric field direction when entering the HWP. While an homogeneous HWP introduces the same phase shift across its surface, an inhomogeneous HWP with the birefringent axis changing direction across its surface would introduce different localized phase-shifts. In order to create OAM states it is possible to design an inhomogeneous HWP with the axis direction only dependent on the azimuthal angle φ: a q-plate.

The overall pattern of a q-plate will define which Δl will be added into the incoming circularly polarized beam, that may or may not possess OAM already. This is due to the SAM changing sign, as the plate locally acts as a HWP, and its momentum difference being totally or partially transformed into OAM, depending on the plate design [10]. Note that being the SAM and OAM changes related, the polarization sign of the incoming beam controls the helicity sign of the output wave front [10].

Natural birefringent crystals have their birefringent axis fixed in direction and cannot be used to design q-plates. However, these plates can be realized using artificial birefringent materials where the local orientation of the axis, parallel to the surface, can be designed in the desired direction [10]. Using this technique, we have produced a q-plate for millimetre wave applications using the design parameters $q = 1$, $\alpha_0 = \pi/2$ defined and discussed in [10]. With this q-plate, a circularly polarized beam will be transformed into one with opposite circular polarization and in addition it will have acquired a phase factor $\exp(il\varphi)$ with helicity $l = 2$, i.e., an helical wavefront with orbital angular momentum $2\hbar$ per photon. The exchange in angular momentum (SAM), from $-\hbar$ to $+\hbar$ or vice versa, provides the $2\hbar$ of momentum that is transferred to the photons.

3. Q-PLATES DESIGN AND MANUFACTURE

As mentioned above, a q-plate can be imagined as an inhomogeneous birefringent plate where the ordinary and extraordinary axes, lying on the plate surface, change their orientation across it. The usual way to generate birefringent materials starting from normal dielectrics is to cut sub-wavelength parallel grooves across it. Light crossing these materials will experience different refractive indices depending on its polarization being parallel or perpendicular to the grooves. This difference will also create differential phase-shifts that can be quantified using Finite-Element analysis software, such as Ansoft HFSS [11]. With this technique it is possible to design quasi-optical retarders starting from dielectric slabs and machining parallel grooves with appropriate geometries across their surfaces. The differential phase-shift introduced by the device will depend on the grooves depth and width. The device will be inherently narrow-band being the desired phase-shift achieved at a specific frequency (and its harmonics).

It is possible to adopt the above technique to manufacture q-plates. Using the design parameters discussed in the previous section, we have realized a q-plate optimized to work at 100 GHz. This $l = \pm 2$ q-plate is equivalent to an Half-Wave Plate with variable birefringent axes orientations: across the plate they follow directions parallel and perpendicular to concentric rings. In practice, this implies cutting circular concentric grooves, as shown in Fig. 1. The q-plate disc is 1 cm thick and has a diameter of 11 cm. The dielectric material used is Nylon, with a refractive index $n = 1.73$

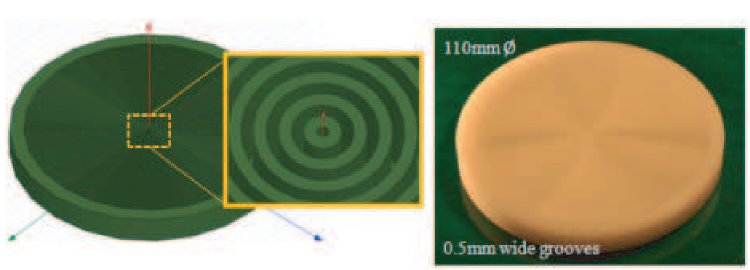

Figure 1: Q-plate CAD model and manufactured prototype.

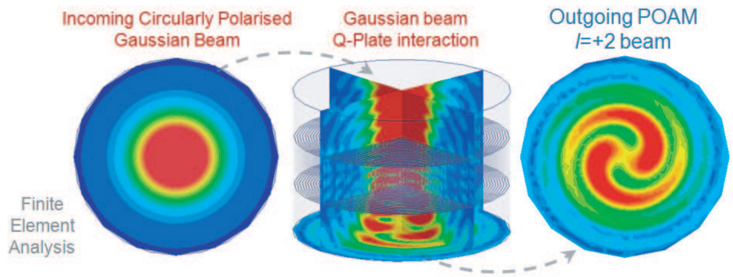

Figure 2: Finite-Element simulations of the q-plate.

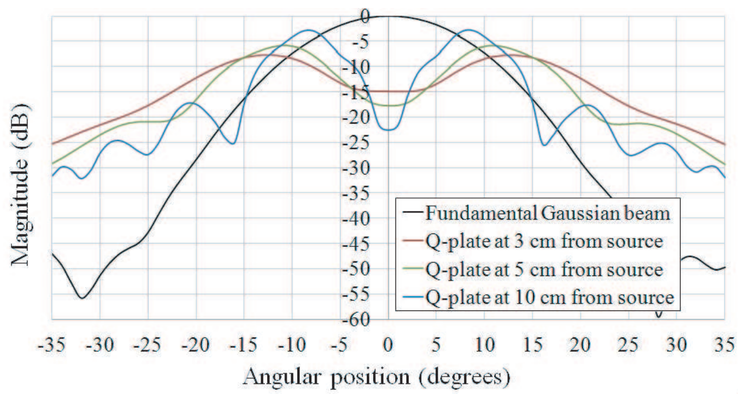

Figure 3: Beam profile HFSS simulations: the fundamental Gaussian beam taken as a reference is compared with the same beam going through the q-plate positioned at 3, 5 and 10 cm from the horn antenna aperture.

at 100 GHz and room temperature [12]. The artificial birefringent material was optimized using 3D electromagnetic field Finite-Element analysis software [11]: the grooves have a width $w_g = 0.5$ mm and a depth $d_g = 8.2$ mm required to achieve the π phase-shift at 100 GHz. Unfortunately, commercially available milling tools of such width cannot reach the required depth and, in order to keep low manufacturing costs, we decided to cut half-depth grooves on both sides of the disc, keeping the same overall phase-shift effects.

It was not possible to simulate the whole q-plate using Finite-Element analysis: the q-plate model, tens of wavelengths in size, creates a huge tetrahedral mesh at the computational limits of present PCs. However, it was possible to simulate the central part of it, as shown in Fig. 2, to verify the transformation of an incoming 100 GHz circularly polarized Gaussian beam into a beam with $l = \pm 2$ charged OAM. Simulated beam profiles obtained changing the distance between a Gaussian beam source and the q-plate are reported in Fig. 3 together with the original fundamental Gaussian beam.

4. Q-PLATE CHARACTERIZATION

The q-plate was characterized using a Rohde & Schwarz Vector Network Analyzer (VNA) equipped with W-band heads (75–110 GHz). The VNA produces and detects linearly polarized radiation propagating in rectangular waveguides. Therefore, in order to generate the circular polarised Gaussian beam required by the q-plate, a rectangular-to-circular waveguide transition, a waveguide polariser and a corrugated horn were added on the VNA transmitter. The receiver head, positioned in the far field of the source, was equipped with another corrugated horn and another transition. In order to perform beam pattern measurements, a rotary stage was used to rotate both the VNA transmitter and the q-plate around the horn phase centre. The rotating system could cover an off-axis angle of $+/-35^\circ$ in order to scan the main beam. The zero position corresponded to the situation where the source and the q-plate were aligned with the receiver. In order to minimize reflections of diffracted radiation outside the optical path, pyramidal Eccosorb was used to cover the metallic surfaces surrounding the optical path.

The VNA allows the measurement of the complex scattering S-parameters of the system. Both beam intensity and phase profiles could be reconstructed as a function of the off-axis angle. Measurements were recorded across the whole W-band although only the 100 GHz frequency, for which

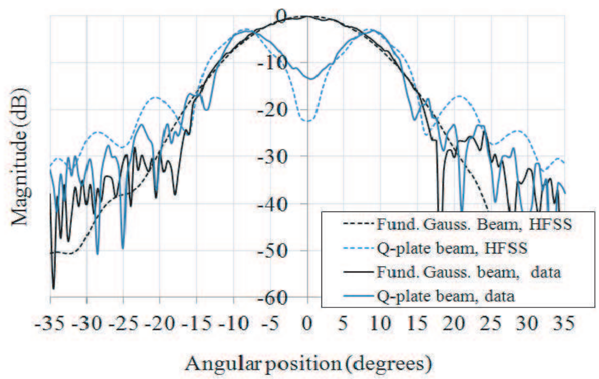

Figure 4: Model (dashed lines) and experimental data (solid lines) of the original Gaussian beam and the beam after passing through the q-plate placed at 10 cm from the source.

the q-plate is designed, was analysed. Beam measurements were initially taken without the q-plate to characterize the reference Gaussian beam that had an equivalent beam waist radius of about 5.5 mm. The q-plate was then inserted at a fixed distance (10 cm) from the source and the beam characterized again. Fig. 4 shows the comparison between the experimental and the modelled results both for the reference Gaussian beam and for the beam passing through the q-plate. The transmission magnitude, calculated from the S_{12} parameter, is reported as a function of the off-axis angle at the fixed frequency of 100 GHz. The data are normalized to the central value of the beam without q-plate. The characteristic central null and the annular shape are visible in the intensity profile, in good agreement with the modelled beam.

5. CONCLUSION

We designed, manufactured and tested a dielectric q-plate, optimized to work around 100 GHz. The q-plate was realized using a dielectric slab that was machined with sub-wavelength grooves on its surfaces. The very simple pattern of the grooves, concentric rings, was designed to imprint $l = \pm 2$ orbital angular momentum states on circularly polarized Gaussian beams. The modelling was performed using electromagnetic Finite-Element analysis software (HFSS) and the measurements carried out using a millimetre wave Vector Network Analyzer. The good agreement between the experimental and the modelling results proved the possibility to generate millimetre wave OAM states with q-plates that can be manufactured very cheaply and within very short timescales. On the modelling side, it will be possible to improve the results performing more accurate simulations, now limited only by the computational power of the PC used.

REFERENCES

1. Allen, L., et al., *Phys. Rev. A*, Vol. 45, No. 11, 8185–8189, 1992.
2. Marcuse, D., *Light Transmission Optics*, Van Nostrand, New York, 1972.
3. Andrews, D. L., *Structured Light and Its Applications: An Introduction to Phase-structured Beams and Nanoscale Optical Forces*, Elsevier, 2008.
4. Vaziri, A., et al., *Phys. Rev. Lett.*, Vol. 91, No. 22, 227902-1–4, 2003.
5. Beijersbergen, M. W., et al., *Optics Communications*, Vol. 96, 123–132, 1993.
6. Heckenberg, N. R., et al., *Optics Letters*, Vol. 17, No. 3, 221–223, 1992.
7. Beijersbergen, M. W., et al., *Optics Communications*, Vol. 112, No. 5–6, 321–327, 1994.
8. Turnbull, G. A., et al., *Optics Communications*, Vol. 127, No. 4–6, 183–188, 1996.
9. Thidé, et al., *Phys. Rev. Lett.*, Vol. 99, No. 8, 087701-1–4, 2007.
10. Marrucci, L., et al., *Phys. Rev. Lett.*, Vol. 96, No. 16, 163905-1–4, 2006.
11. Ansoft HFSS website: www.ansoft.com.
12. Lamb, J. W., *International Journal of Infrared and Millimeter Waves*, Vol. 17, No. 19, 1997–2034, 1996.

Dog Bone Triplet Metamaterial Wave Plate

I. Mohamed, G. Pisano, M. W. Ng, V. Haynes, and B. Maffei
Jodrell Bank Centre for Astrophysics, School of Physics and Astronomy
The University of Manchester, United Kingdom

Abstract— Metamaterials are artificially made sub-wavelength structures arranged in periodic arrays. They can be designed to interact with electromagnetic radiation in many different and interesting ways such as allowing radiation to experience a negative refractive index (NRI). We have used this technique to design and build a quasi-optical Half Wave Plate (HWP) that exhibits a large birefringence by virtue of having a positive refractive index in one axis and a NRI in the other. Previous implementations of such NRI-HWP have been narrow band ($\sim$ 1–3%) due to the inherent reliance on needing a resonance to create the NRI region. We manufacture a W-band prototype of a novel HWP that uses the Pancharatnam method to extend the bandwidth (up to more than twice) of a usual NRI-HWP. Our simulated and experimentally obtained results despite their differences show that a broadening of a flat region of the phase difference is possible even with the initially steep gradient for a single plate.

1. INTRODUCTION

Electromagnetic metamaterials are artificially created sub-wavelength structures and are known for their use in creating a negative refractive index (NRI), an effect first demonstrated in 2000 [1].

Wave plates are used to alter the polarisation of radiation passing through them. Rotating HWPs are used to rotate linear polarisations at twice their mechanical rotation speed. Conventionally made from birefringent materials such as sapphire or quartz, wave plates can also be constructed out of metal mesh grids [2]. Such constructions are advantageous due to the costs and limited dimensions of the available birefringent materials at these frequencies and the ability to scale the designs to work at other frequencies. Their use is becoming increasingly important in Cosmic Microwave Background Radiation experiments where the detection of the weak B-mode polarisation is the current goal in observational cosmology.

The phase difference, $\Delta\phi$, between the two polarisations of radiation of frequency, f, after passing through a wave plate of thickness, d, is given by

$$\Delta\phi = \frac{2\pi df}{c_0} \cdot \Delta n \tag{1}$$

where c_0 is the speed of light in a vacuum and Δn is the difference in the refractive indices of the birefringent materials two orthogonal axes. By designing a metamaterial with a geometry that has a NRI along one axis and a positive index along the other we are able to create a wave plate with very high birefringence: this allows the creation of relatively thin wave plates.

Previous implementations [3, 4] of metamaterial wave plates that have used NRI were narrow band in nature due to the NRI region only occurring in the narrow resonance band and the high gradient of the phase difference in this band.

In this paper we seek to show how the functional bandwidth can be increased by utilisation of the Pancharatnam method [5] that has been successfully used in the past with birefringent materials [6].

2. CELL GEOMETRY AND DESIGN

Metal mesh structures can be modelled by isolating a single cell that is in practice reproduced periodically in a two-dimensional array. The electromagnetic properties of the cell can be optimised using finite element analysis software, such as HFSS [7], imposing periodic boundary conditions around it. To create the required 180° phase difference we based our design on a dog bone geometry (also referred to as "I" or "H" in the literature). The metal grid is made of a 2 μm thick evaporated copper layer, supported by a polypropylene ($\epsilon = 2.2$) substrate. The HWP unit cell consists of a triplet of dog bones, with only the middle one embedded in the substrate. All the dimensions are given in the caption to Figure 1. The cell dimensions were optimised at 92.5 GHz, the centre of the W-band, in order to have transmissions and differential phase-shift along the axes respectively satisfying: $|S_{21}^{x,y}|^2 \geq 0.8$ and $\Delta\phi = \arg(S_{21}^x) - \arg(S_{21}^y) = -180°$.

The transmission properties of the optimised unit cell are shown in Figure 2. Around 92.5 GHz the gradient of the phase difference is very steep. The spectral region where the phase difference is within $-180^\circ \pm 3^\circ$ is extremely narrow, providing an operational fractional bandwidth of only 0.3% (92.8–93.1 GHz). In this region the transmissions in the x- and y-axes have mean values of 0.81 and 0.84 respectively. The refractive indices along the x- and y-axes are shown in Figure 3. These were calculated starting from the HFSS reflection and transmission coefficients and adopting the extraction methods discussed in [8, 9]. The refractive index, being a property of a bulk material, can only truly be defined for a set of regularly cascaded metamaterials. As each of our plates is only a single cell thick we have taken the effective thickness to be equal to the physical thickness to provide an indicative value of the refractive index. The true refractive index values would be smaller in magnitude as the effective thickness extends beyond the substrate surface to where the reflected radiation has a planar wave front. We see that a NRI band exists for x-polarized radiation above 89.6 GHz whilst in the y-axis the refractive index is constant.

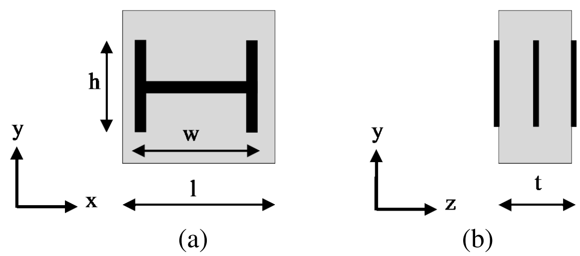

Figure 1: (a) Face on view of a unit cell. (b) Side on view of the dog bone triplet cell. The dimensions are: $h = 300\,\mu\text{m}$, $w = 556\,\mu\text{m}$, $l = 591\,\mu\text{m}$ and $t = 260\,\mu\text{m}$. The copper is 35 μm wide and 2 μm thick.

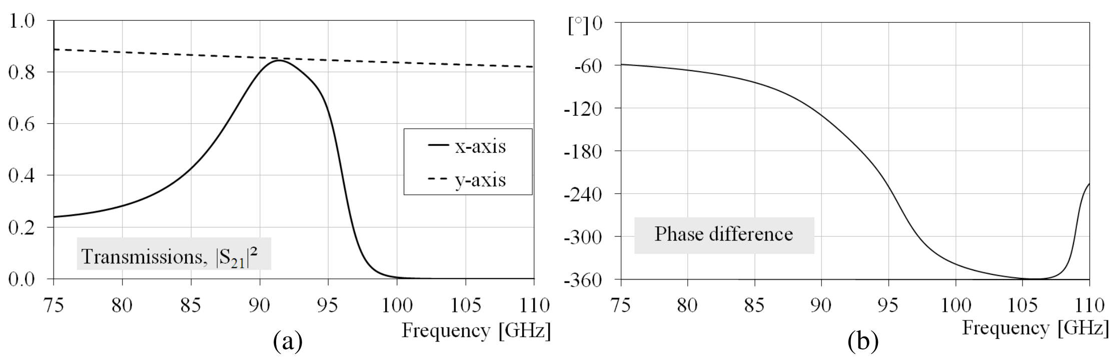

Figure 2: (a) Transmissions along the x and y axes of the one Dog Bone Triplet (DBT) cell. (b) Phase difference between the x and y axes produced by a single DBT unit cell.

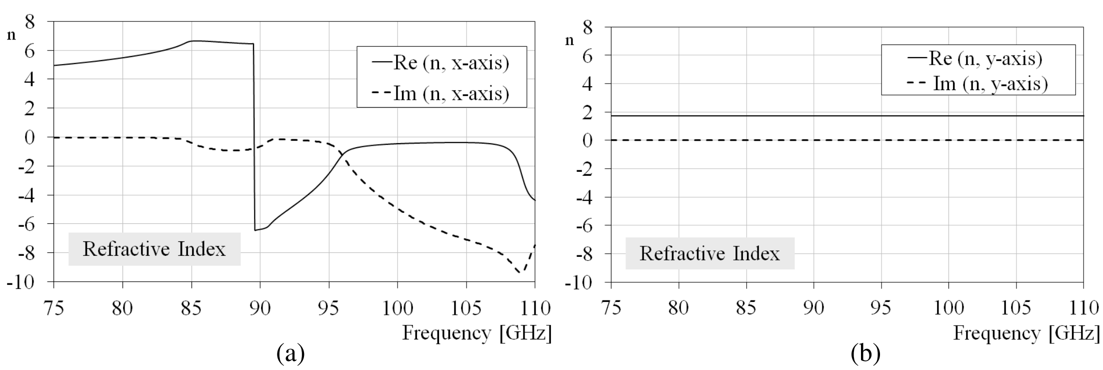

Figure 3: (a) Refractive index of the dog bone triplet along the x-axis. (b) Refractive index along the y-axis..

3. MODELING

Whilst modeling of a single cell's transmission spectra in HFSS can be carried out comfortably, modelling of a cascaded set of cells is a very CPU and memory intensive process. In addition, the Pancharatnam recipes that we want to adopt are based on stacks of rotated plates. Given the geometry of the cell, when rotated it would not be possible to make use of the periodic boundary conditions provided by HFSS. In this case we turned to transmission line modeling which can produce accurate results provided the cells are far enough such that inter-cell interactions can be considered negligible. The S-parameters for a single cell are converted into the ABCD (Transmission) parameters [10] and the air gaps between the cells are represented using the propagation matrices for a transmission line. The Pancharatnam method was then implemented as had been done in previous papers [6] using three plates. The distance and angle between the successive plates was optimised to get the broadest possible bandwidth where the phase difference was flat and the transmission on both axes were as high and equal to each other as possible.

The resultant values came to be 1.3 mm for the air gaps and angles of 30°, −29° and 30° for the plates with respect to the final HWP equivalent fast axis. This increased the bandwidth from 0.3%, for the single plate, to 6.6%, between 88.8 GHz and 94.9 GHz. This shows that despite the phase difference's initially steep gradient for a single cell, marked improvements can be achieved using the Pancharatnam method: a bandwidth more than a factor 20 wider. The transmissions in this region vary between 0.36 and 0.72 in the x-axis and 0.36 and 0.73 in the y-axis, with the two axes showing similar transmission values to each other. The simulated transmission and phase differences of this HWP are shown as dashed lines together with experimental data in Figure 4.

4. MEASUREMENTS

To create the dog bone triplets, the single dog bone grids were made using photolithographic techniques. The plate required three grids to be made and layered atop one another with the appropriate thickness of polypropylene sheets between them. Three of these plates were made and mounted onto aluminium rings that acted as support and provided the necessary air gaps.

Measurements were taken using a Rhode & Schwarz ZVA40 vector network analyser connected to two WR10 heads and corrugated horns to provide Gaussian shaped beams of W-band radiation. Eccosorb was used to cover the surfaces in the setup to reduce unwanted reflections. The transmission measurements along the two axes were taken individually and compared to the simulated data.

The experimentally obtained transmissions and phase differences are shown as solid lines in Figure 4. Compared to the simulated transmission data, the measured transmission data shows a small red shift in frequency but otherwise the two show comparable concurrence. The phase difference also shows good correlation below 87 GHz. This, unfortunately, does not continue such that it reaches −180°. Instead, a flattening of the phase difference at −150° is achieved between 87 GHz to 93.5 GHz providing a flat region of bandwidth 7.2% in size. The difference between the simulation and experimental data is due to fabrication errors in the grids. Simulations have indeed showed that minor deviations in the air gap thicknesses and the plates' rotations would not impact on the HWP's ability to produce a phase difference that reached −180°. On the other hand, the comparison of the model and the measured data of the individual plates showed that two of them

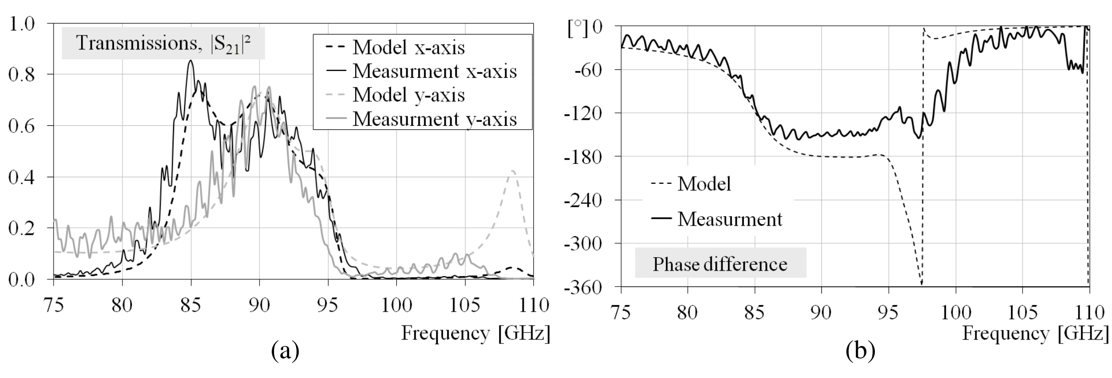

Figure 4: (a) The transmission on the x and y axes of the simulated and manufactured HWP. (b) The phase difference.

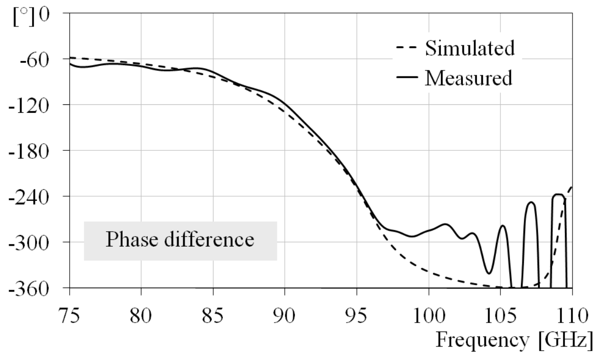

Figure 5: The measured and simulated phase difference for the best performing plate.

suffered from deviations above 85 GHz in their phase difference. For example at 93 GHz where the expected phase difference is $-181°$ these two plates had phase differences of $-164°$ and $-124°$. The best performing plate achieved $-176°$ and its measured phase difference is shown in Figure 5. It is interesting to note that the average of these values equals $-155°$, close to the measured value of the flat region of the final HWP. In all of the plates, above $\sim$ 95 GHz, the measured phase difference ceases to decrease and instead flattens out. This could explain the lack of the dip the measured phase difference makes above 95 GHz in the full HWP.

So whilst the experimental results do not exactly match the simulations for manufacturing reasons, it can be seen that a broadening of a flat region in the phase difference can be achieved using the Pancharatnam method, even with highly birefringent wave plates.

5. CONCLUSIONS

We have created a novel HWP that utilises a highly birefringent metamaterial plate with refractive indices of different signs in each axis and cascaded three of them using the Pancharatnam method to increase their bandwidth. The simulated data showed an increase in bandwidth from 0.3% (92.8–93.1 GHz) for a single plate to 6.6% (88.8–94.9 GHz) for the whole device: about a factor 20 wider. The experimentally measured data shows a flattening in the phase difference at 150° between 87 GHz to 93.5 GHz. Whilst not a good match with the simulation this does show that in principle this method can achieve a flattening of the phase difference even with highly birefringent wave plates. An attempt to account for the differences between the simulation and experiment was made by studying the transmissions of the individual plates. It is found that the likely cause for the discrepancy in the final HWP's performance is due to fabrication errors in the individual grids themselves. Future HWP prototypes will be manufactured using grids selected on their performance in order to achieve the predicted results. Even better performances could in principle be achieved by designing single NRI plates with broader bandwidths, i.e., with geometries showing gentler phase difference slopes.

ACKNOWLEDGMENT

The first author is funded by a studentship from the Science and Technology Facilities Council (STFC).

REFERENCES

1. Smith, D. R., W. J. Padilla, D. C. Vier, S. C. Nemat-Nasser, and S. Schultz, "Composite medium with simultaneously negative permeability and permittivity," *Phys. Rev. Lett.*, Vol. 84, No. 18, 4184–4187, 2000.
2. Pisano, G., G. Savini, P. A. R. Ade, and V. Haynes, "Metal-mesh achromatic half-wave plate for use at submillimeter wavelengths," *Appl. Opt.*, Vol. 47, No. 33, 6251–6256, 2008.
3. Imhof, C. and R. Zengerle, "Strong birefringence in left-handed metallic metamaterials," *Opt. Comm.*, Vol. 280, No. 1, 213–216, 2007.
4. Weis, P., O. Paul, C. Imhof, R. Beigang, and M. Rahm, "Strongly birefringent metamaterials as negative index terahertz wave plates," *App. Phys. Lett.*, Vol. 95, No. 17, 171104, 2009.
5. Pancharatnam, S., "Achromatic combinations of birefringent plates, Part II: An achromatic quarter-wave plate," *Proc. Indian Acad. Sci., Sec. A*, Vol. 41, No. 4, 137–144.

6. Pisano, G., G. Savini, P. A. R. Ade, V. Haynes, and W. K. Gear, "Achromatic half-wave plate for submillimeter instruments in cosmic microwave background astronomy: experimental characterization," *App. Opt.*, Vol. 45, No. 27, 6982–6989, 2006.
7. Ansoft HFSS version 13: http://www.ansoft.com
8. Smith, D. R., S. Schultz, P. Markoš, and C. M. Soukoulis, "Determination of effective permittivity and permeability of metamaterials from reflection and transmission coefficients," *Phys. Rev. B*, Vol. 65, No. 19, 195104, 2002.
9. Chen, X., T. M. Grzegorczyk, B.-I. Wu, J. Pacheco, and J. A. Kong, "Robust method to retrieve the constitutive effective parameters of metamaterials," *Phys. Rev. E*, Vol. 70, No. 1, 016608, 2004.
10. Pozar, D. M., *Microwave Engineering*, 2nd Edition, John Wiley & Sons, 1998.

Millimetre Waves Photolithographic Polariser Beam Impact

B. Maffei, G. Pisano, M. W. Ng, V. Haynes, and F. Ozturk
Jodrell Bank Centre for Astrophysics, School of Physics and Astronomy
The University of Manchester, UK

Abstract— Quasi-optical polarisers can be used to create circularly polarised beams from linearly polarised fields. These devices can be designed using planar metallic grids with sub-wavelength structures that behave differently along two orthogonal axes. On the one hand, their design is usually based on transmission-line codes that implicitly assume plane waves and normal incidence conditions. On the other hand, in real practical situations, these devices are used with Gaussian beams. In this work, we experimentally study the effects of a dielectrically embedded polariser made with photolithographic techniques on the Gaussian beam of a horn. The impact of the polariser on the beam is measured using a W-band (75–110 GHz) Vector Network Analyser.

1. INTRODUCTION

Polarimeters often include polarisation modulators. For general antenna applications one might want to modify the polarisation status of the transmitter, or of the receiver, such as rotating the linear polarisation with a Half Wave Plate modulator (HWP) or transforming a linearly polarised wave into a circular polarised wave or vice-versa with a Quarter Wave Plate (QWP). One important application is in astronomical instrumentation where an array of polarimeters can be used in conjunction with a modulator that will modify the polarisation of the astronomical source under study. So far, modulators operated in the millimetre wave domain were based on birefringent material. However, in the last few years similar modulators have been developed based on metallic mesh grid technology [1, 2]. We present the work performed to characterise the impact on a horn beam shape due to a millimetre wave photolithographic QWP located in front of the horn aperture. The development of this new QWP is described in a companion article [2] presented at the same PIERS conference.

2. EXPERIMENTAL SET-UP

The beam of a horn is usually characterised by a minimum of four angular beam response cuts, three co-polarisation cuts: the E-cut (for which the angle between the E-field and the vertical line is $\phi = 0$ deg and the cut will be performed along a horizontal axis), the H-cut ($\phi = 90$ deg), the diagonal cut ($\phi = 45$ deg) and the cross-polarisation cut for $\phi = 45$ deg. For our purpose, two circularly-symmetric corrugated horns, for which the beam pattern showing a low level of cross-polarisation has been well-characterised and modelled [3], have been used in conjunction with a Vector Network Analyser (Rhode and Schwarz ZVNA-40 with W-band extensions) in order to assess the impact on the E, H and diagonal cuts due to the QWP located in between the horns. For a far-field horn beam pattern measurement, the horns are mounted on each of the VNA heads separated by at least the far-field distance (22 cm for this instance but horn separation is about 50 cm in our set-up). The VNA output waveguide is rectangular, setting the direction of the E-field. The horn is matched through a rectangular to circular transition. One horn is left still, while the horn under test is being rotated (angle θ — see Figure 1) around its phase centre. This measurement has been repeated in an identical way for each of the cuts that are presented in this paper.

The QWP is located 5 cm in front of the aperture of the horn being rotated. The QWP can be rotated around its optical axis, changing its orientation with respect to the E-field emitted by the horn. The inductive (L-axis) and capacitive (C-axis) axes [2] can be aligned respectively to the incoming E-field direction (Figures 1 and 2).

While the VNA W-band extensions have the full bandwidth 75–110 GHz, the corrugated horns that have been used in our measurement system have a cut-on frequency of 83 GHz. Moreover the QWP has a transmission optimised for frequencies up to 100 GHz [2]. Therefore beams amplitude and phase have been characterised across the band 83–110 GHz, but expecting to have the best results across 83–100 GHz as for frequencies above 100 GHz the standing waves due to higher QWP reflections will not only affect the beam amplitude but mainly the phase measurements.

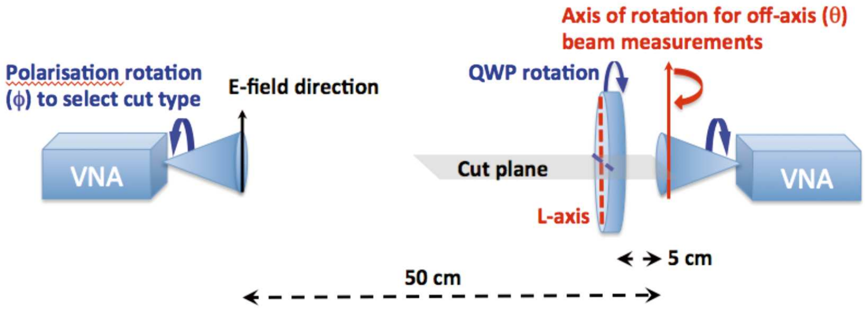

Figure 1: Beam pattern measurement set-up. Two identical corrugated horns are connected to the VNA (75–110 GHz). The QWP is located in between the horn apertures in order to measure the free-space S-parameters. The system under test (QWP + horn) is rotated around the horn phase centre.

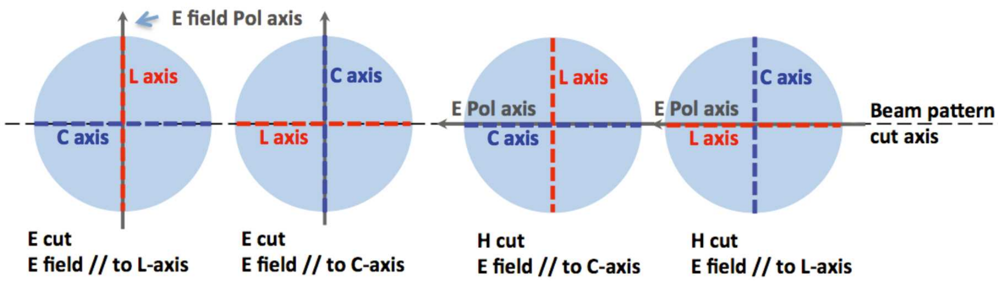

Figure 2: Orientation of the QWP for the beam pattern measurements. The QWP axes are aligned relatively to the E-field direction in order to measure the impact of the QWP on the various beam-cuts.

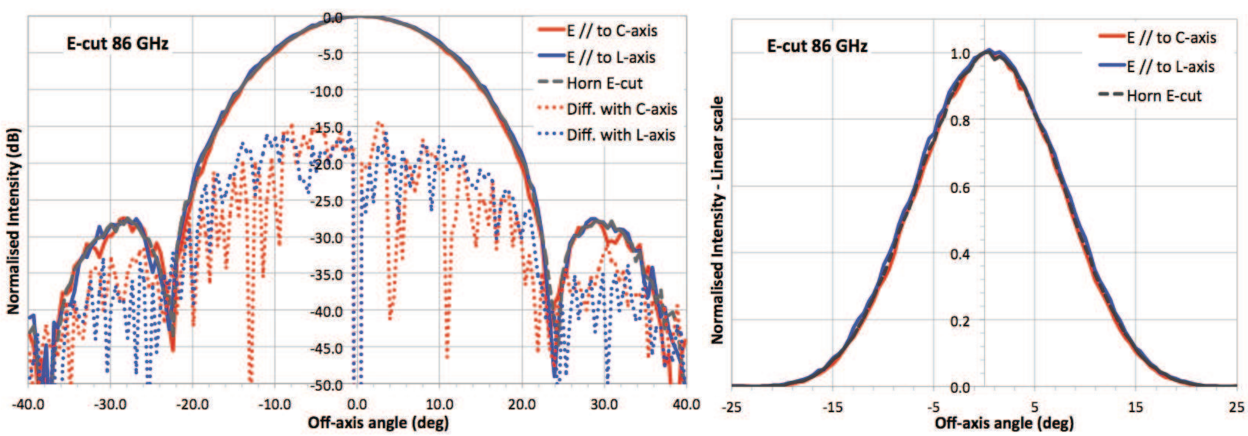

(a) (b)

Figure 3: E-cut beam intensity patterns versus off-axis angle θ at a frequency of 86 GHz. (a) dB scale. (b) linear scale. For the horn only (dashed black), with the QWP and the horn when the C-axis (red) or L-axis (blue) is aligned parallel to the linearly polarised E-field. The differences between the horn beam pattern and the C-axis beam pattern (red dashed) or L-axis beam pattern (blue dashed) are also plotted.

3. EXPERIMENTAL RESULTS

3.1. Beam Intensity Shape

Sub-sets of beam amplitude measurements are shown in Figures 3, 4 and 5. These represent the characterisation of E-cut beams performed on the horn only and on the horn with the QWP located in front of its aperture when the linearly polarised E-field of the horn is either parallel to the QWP L-axis or C-axis. Identical measurements have been performed for H and diagonal beam cuts. The figures show the beam intensity measurements in dB and linear scales. The dB scale also shows the difference between the beam with and without the QWP normalised to the maximum defined as:

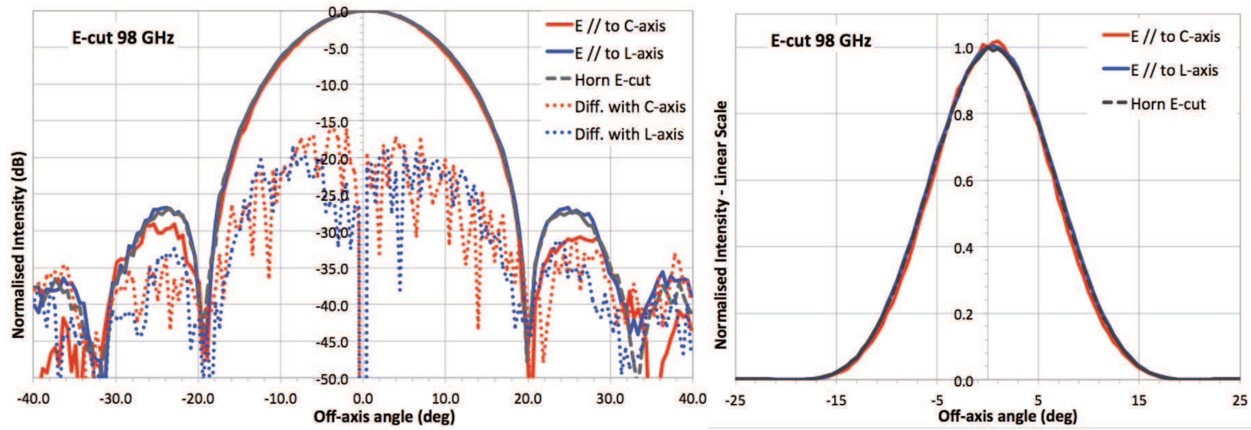

(a) (b)

Figure 4: Similar to Figure 3 but for a frequency of 98 GHz.

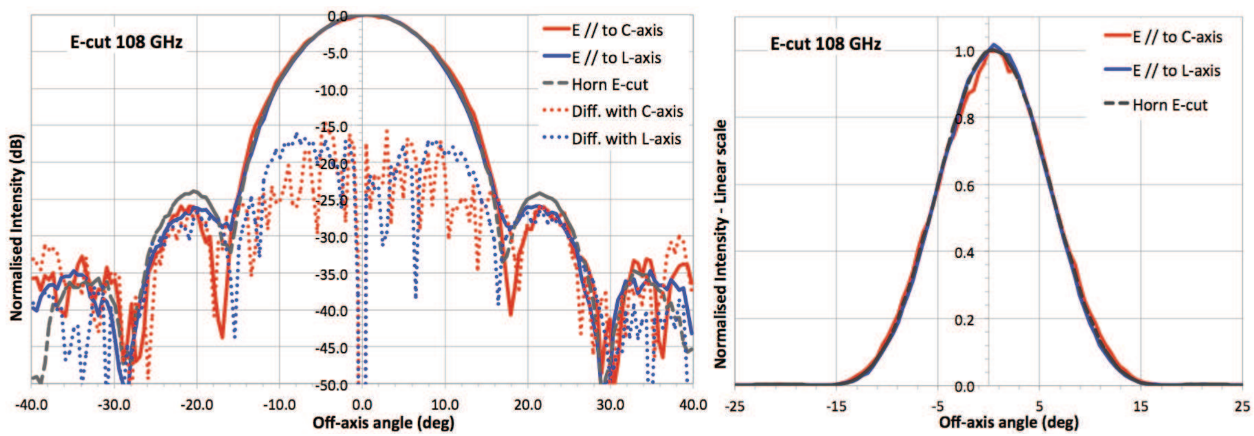

(a) (b)

Figure 5: Similar to Figure 3 but for a frequency of 108 GHz.

Table 1: Average QWP differential phase-shift across the main beam.

	$\boldsymbol{H}$-cut	$\boldsymbol{E}$-cut
85 GHz averaged for $\boldsymbol{-19^\circ \leq \theta = 19^\circ}$	$-85.7 \pm 1.7^\circ$	$-88.0 \pm 1.0^\circ$
98 GHz averaged for $\boldsymbol{-15^\circ \leq \theta = 15^\circ}$	$-89.0 \pm 2.0^\circ$	$-88.3 \pm 1.5^\circ$

Difference (dB) $= 10 \log \left(\frac{|I_{QWP}(\theta) - I_{Horn}(\theta)|}{I_{Horn}(\theta=0)} \right)$ where I(θ) is the intensity of the beam at an off-axis angle θ.

These sets of data are normalised and do not show the losses due to the QWP, which has an average transmission of $TC = 0.92$ and $TL = 0.95$ for each axis across the band 75–101 GHz [2], but present the impact on the beam shape for three spot frequencies across the measured bandwidth.

We can see that even at frequencies higher than 100 GHz below which the QWP is optimised, the impact on the beam is lower than 15 dB (corresponding to a maximum variation of 3%) according to the definition of the difference we have adopted. This value includes the effect of standing waves between the QWP and the horn that can be seen more clearly in Figure 5 right: the red curve (E-field parallel to C-axis) is showing a structure for $|\theta| < 5$ deg which is probably due to these standing waves (QWP transmission of about 0.6 at 108 GHz). Standing wave reduction through time domain analysis is being investigated in order to reduce these effects.

3.2. Phase Difference Across Beam

Analysis of the phase variation has also been performed from the beam phase measurements. Figure 6 gives the E-cut phase variation with the off-axis angle θ at the horn phase centre for a

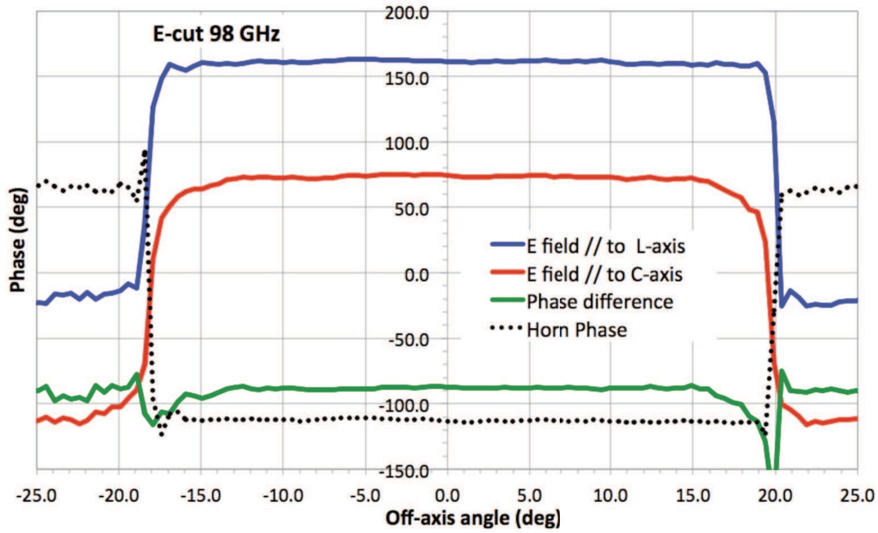

Figure 6: Off-axis phase E-cut beam patterns at 98 GHz. Dotted black: Horn only. Phase pattern of horn + QWP with L-axis (blue) or C-axis (red) aligned along E-field. Green: differential phase-shift between L and C axes.

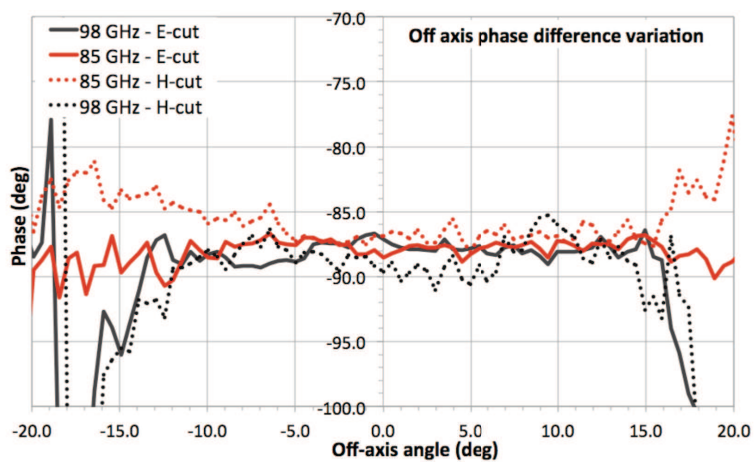

Figure 7: E and H cuts differential phase-shift for two frequencies.

frequency of 98 GHz. The dotted black line is the phase measurement for the horn only while the red and blue are the same measurements but with the QWP located in front of the horn aperture with either its C-axis or L-axis respectively aligned with the linearly polarised E-field of the horn. While Figure 6 from [2] gives the on-axis differential phase-shifts measurement across the whole W-band, the green line of Figure 6 in the present paper represents the off-axis phase difference between the C-axis and the L-axis phase measurements for one frequency (98 GHz).

Through the same analysis, Figure 7 gives the off-axis differential QWP phase-shift for both E and H cuts and for two frequencies, 85 and 98 GHz. The differential phase-shift has to be compared to the average experimental value of $89.3 \pm 1.5°$ across the spectral band 75–101 GHz [2]. Averaged across the major part of the main beam, the plots of Figure 7 lead to the values presented in Table 1.

4. CONCLUSION

The impact of the addition of a recently developed millimetre wave photolithographic Quarter Wave Plate on the beam pattern of corrugated horn has been measured both in amplitude and phase. We have found that the introduced systematic effect is very low across the measured 17% bandwidth (84–100 GHz) with a low frequency limit set by our test equipment. We would expect similar low systematic effects down to 75 GHz. The maximum intensity beam pattern difference with the beam of a corrugated horn normalised the on-axis maximum is less than 3% across the measured spectral band. The differential phase-shift introduced between the inductive and capacitive axes of this QWP is about 88 degrees with a variation across the main beam limited to about $+/-2$ degrees.

ACKNOWLEDGMENT

This work was supported by both the UK Engineering and Physical Sciences Research Council (EPSRC) and the Science and Technology Facilities Council (STFC).

REFERENCES

1. Pisano, G., et al., "A metal-mesh achromatic half-wave plate for use at submillimetre wavelengths," *Applied Optics*, Vol. 47, No. 33, 6251–6256, 2008.
2. Pisano, G., et al., "A broadband photolithographic polariser for millimetre wave applications," *PIERS Proceedings*, Kuala Lumpur, Malaysia, 2012.
3. Maffei, B., et al., in Preparation.

Maxwell's Transfer Functions

M. J. Underhill
Underhill Research Ltd., UK

Abstract— For antennas and propagation we require the total transfer function between the transmitter and the receiver over the operating band of frequencies. The classical EM equations need to be transformed into transfer functions conveniently defined by time and spatial domain Laplace Transforms. Transfer functions equations can define all the parameters of an antenna such as, near field stored energy and fields, coupling to other antennas and surfaces, and far-field array patterns.

1. INTRODUCTION

In free space as they stand, Maxwell's equations are not causal. There are no explicit sources and sinks and no 'time-line' showing progressive decay or building up of the fields represented in the equations. However spatial and time domain Laplace Transforms may be applied to Maxwell's equations to make good these deficiencies. Observed physics demands that we also include two (newly discovered?) sets of physical laws, those of 'Electro-Magnetic (EM) Coupling' and of 'Process Capture' [2]. Coupling is defined between two points in space for any physical parameters, in this case for EM fields etc.. Essentially it is a more representative replacement for the dyadic Green's function often used to solve Maxwell's equations. These (new) laws define the *near-field ether* that is induced by any antenna or physical object. The local ether is defined by local values of ε and μ. Amongst other things Process Capture defines the spatial *region* or *frame* in which any particular coupling factor is dominant. (Frames for different or partially coupled processes may be overlapping). When this is done we arrive at Maxwell's Transfer Functions.

The route to the transfer functions is through the "Physical EM (PEM) Model of Electromagnetism" put forward at PIERS 2011 in Marrakesh [1]. This model is based on multiple filamentary transmission lines in space carrying electric and magnetic displacement currents. Such a representation removes any need for any arbitrary and artificial gauge, such as the Lorenz gauge. Electro-Magnetic Coupling defines the profile of the 'evanescent wave', local ether, and the stored energy that surrounds any current. It is found (initially experimentally) to be inversely proportional to the square root of frequency. This finding is a major link between electromagnetics and quantum theory and the rest of physics [1, 2]. Another outcome is that it explains why 'small' antennas do not scale with frequency but with the square root of frequency. Small antennas cannot therefore be scale modelled. All these factors are compatible with the proposed set of EM transfer functions equations. It means that the proposed equations are inextricably well linked to the rest of physics [1].

"Maxwell's Equations" were created about six years after his death by FitzGerald, Heaviside, and Lodge — Along with key contributions from Hertz [3]. That is why Maxwell's name is given to the proposed set of equations, "Maxwell's Transfer Functions"— MTFs.

2. THE CLASSICAL MAXWELL EQUATIONS

Equations (1) to (6) are the classical differential form of Maxwell's Equations with some small additions and alterations made to ensure better compliance with observed physics. For example, the magnetic charge and displacement current, ρ_M and J_E are taken to be non-zero. Real (surface) currents J_R are combined with the electric displacement current J_E in Equation (4). We have also included the magnetic surface current J_{MS} in Equation (3) to facilitate the analysis of ferrite rod antennas. All field symbols implicitly include the phase factor, $e^{-j\omega t+\phi}$ where the phase shift ϕ has specific values for each field at each point in space. The classical equations then are:

$$\mathrm{div}D = \nabla \cdot D = \rho_E \tag{1}$$
$$\mathrm{div}B = \nabla \cdot B = \rho_M \tag{2}$$
$$-\mathrm{curl}E = -\nabla \times E = \frac{\partial B}{\partial t} + J_M \tag{3}$$
$$\mathrm{curl}H = -\nabla \times H = \frac{\partial D}{\partial t} + J_R + J_E \tag{4}$$

$$D = \varepsilon E \text{ where } \quad \varepsilon > \varepsilon_0 \text{ generally in the near-field} \tag{5}$$
$$B = \mu H \text{ where } \quad \mu > \mu_0 \text{ generally in the near-field} \tag{6}$$

It is important to note that the inequalities in the 'constitutive relations' of Equations (5) and (6) are what are found in practice in the near-field of an antenna. This is the consequence of the existence of the 'local ether' that surrounds any antenna or physical object [1].

Also note in Equation (3) that the quantity $\partial B/\partial t$ is, and effectively defines, a magnetic displacement current. Similarly in Equation (4) note that the quantity $\partial D/\partial t$ is, and effectively defines, an electric displacement current.

3. REDEFINITION OF FIELDS FOR PARTITIONING OF MAXWELL'S EQUATIONS

It is convenient to partition and factorise Maxwell's equations to deliver separate travelling wave and evanescent wave solutions [1]. We redefine the four fields, E/jk and H/jk as vector potentials, and D and B as vector charges. For a travelling wave in homogenous space away from any physical objects we observe that E and D are aligned, as are H and B, and these pairs are at right angles to each other. This gives rise to the classical Poynting vector as $P_z = E_x \times H_y$ where P_z is a vector representing power flow (density) in the z wave direction. These are the directions assigned to the vector potentials and vector charges. The displacement currents are 'bi-vectors'. One of the bi-vector directions is the (two-way) axis of flow of the current. This is also aligned with the power flow direction. For electric displacement current the second bi-vector direction is the (alignment) direction of the E field. These new definitions of the symbols leave the Maxwell equations, as in expressed in Equations (1) to (6), unchanged in appearance.

Note that field directions (polarisations) and the power flow direction in space in practice all vary slowly and never abruptly. This fact is exploited in the PEM model based on filamentary transmission lines in space [1].

We can now extend the properties of the classical Poynting Vector to define local stored energy and local spatial Q in the near-field region. The in-phase component of the Poynting vector $\Re[E\times H]$ is the transported energy density. The quadrature component $\Im[E\times H]$ is the stored energy density which defines the extent of the 'near-field'. The stored energy $\Im[E \times H]$ is also $= D \cdot E + H \cdot B$. The Local Q is defined as the ratio of stored energy density to transported energy density:

$$Q_{local} = \frac{\Im[E \times H]}{\Re[E \times H]} \tag{7}$$

The above redefinition of the symbols without apparently altering Maxwell's equations is what allows the solutions to be factorised into traveling and evanescent wave parts as presented in Reference [1].

4. CAUSAL EM EQUATIONS AS A CONSEQUENCE OF EM COUPLING

It is the EM coupling factor κ (kappa) that allows Maxwell's equations to be transformed into 'causal' equations where sources create fields and fields supply energy to sinks. A transmitting antenna is a source and a receiving antenna is a sink. As in circuit theory the coupling factor κ is defined to be dimensionless. It represent a phase shift ϕ proportional to time delay, and an attenuation that has been discovered to be inversely proportional to distance r times the square root of frequency f [2]. For units of metres and with the best measured estimate so far of $f_c = 14\,\text{MHz}$ we find:

$$\kappa = \frac{1}{2\pi}\left(\frac{f_c}{f}\right)^{1/2}\frac{1}{r}e^{-j\phi} \tag{8}$$

This is the coupling factor that is the main determinant of the properties of antennas as sources and sinks.

For reasonably uniform local space anywhere away from the surface of the antenna we find that the asymptotic causal coupling between the fields in Maxwell's equation is not the 100% that has implicitly been assumed since the equations were originally constructed. In fact a value of around $\kappa_0 = 1/2\pi$ is what has been found experimentally. Thus experimental measurement validates any theory that predicts $\kappa_0 = 1/2\pi$.

Some of the supporting evidence in addition to evidence in Reference [2] are the findings: (a) that small tuned loop size scales inversely as the square root of frequency, (b) that the small tuned loop asymptotic antenna Q is about $248 = (2\pi)^3$ and (c) small tuned loops can easily have measured efficiencies of $> 90\%$, as predicted by (c) and by observation that high power small tuned loops do not overheat and self-destruct as they would if they were inefficient.

A consequence of a coupling factor that is less than one is that sink strength is always less than source strength. This means that Maxwell's equations are not reversible and should really be expressed as causal (cause and effect) transfer functions. We find that only the constitutive relations in Equations (5) and (6) need to be made into two pairs of unidirectional causal equations as given in Equations (9a) to (10b). This enforces causality into all the Maxwell equations. The 'becomes equal to' sign ':=' is unidirectional and is used in Equations (9) and (10).

$$D := \kappa\varepsilon E, \tag{9a}$$

$$E := \kappa\frac{D}{\varepsilon} \tag{9b}$$

$$B := \kappa\mu H, \tag{10a}$$

$$H := \kappa\frac{B}{\mu} \tag{10b}$$

5. IMPOSITION OF CONSERVATION OF ENERGY ON MAXWELL'S EQUATIONS

The physics requirement of *conservation of energy* imposes further changes on the formulation of Maxwell's equations. The div and curl operators, $\nabla\cdot$ and $\nabla\times$, have to be redefined. The RSS rule has to be applied to its components. Also the Phasor RSS addition rule has to be imposed on the additions in Maxwell's equations that relate to D, B, the displacement currents and spatial charges. RSS stands for 'Root Sum of the Squares'. The Phasor RSS rule combines the components taking relative phases into account. To indicate this we replace addition signs by the (proposed) RSS addition sign '$\oplus$'. RSS Integrals are required to combine components of D and B. The conventional (scalar addition) rules are used for the additions of potentials and for E or H. We therefore conclude that E and H are essentially potentials and are fundamentally different from D and B. As an example we redefine the div operator as the square root of the Laplacian:

$$(\nabla\cdot) = (\nabla^2)^{1/2} = \left[\left(\frac{\partial}{\partial x}\right)^2 + \left(\frac{\partial}{\partial y}\right)^2 + \left(\frac{\partial}{\partial z}\right)^2\right]^{1/2} \tag{11}$$

Phasor RSS addition is more complicated because the components are assumed to have different phases so that reinforcement or cancellation of components can occur. We have to consider solutions to Maxwell's Equations where the parameters are not fields but power and stored energy. To do this we can combine solutions for E and D for electric waves and their energy, and solutions for H and B for magnetic waves and their energy. Towards the far field away from an antenna the energy progressively converts in a balance of electric and magnetic energy. For a plane wave this should correspond to $E/H = Z_0 = 120\pi = 377\,\text{ohms}$. The RSS symbol also flags up the problem of combining waves from different sources. This problem is addressed automatically in the transmission line PEM model [1], the associated paper [4] and in Section 7 below.

6. THE CAUSAL MAXWELL'S EQUATIONS

Putting $\kappa = \kappa_0 = 1/2\pi$, we can now set out the causal Maxwell equations as:

$$\text{div}D = \nabla\cdot D = \rho_E \tag{12}$$

$$\text{div}B = \nabla\cdot B = \rho_M \tag{13}$$

$$-\text{curl}E = -\nabla\times E = \frac{\partial B}{\partial t} \oplus J_M \tag{14}$$

$$\text{curl}H = -\nabla\times H = \frac{\partial D}{\partial t} \oplus J_R \oplus J_E \tag{15}$$

$$D := \kappa_0\varepsilon E \tag{16a}$$

$$E := \kappa_0\frac{D}{\varepsilon} \tag{16b}$$

$$B := \kappa_0 \mu H \tag{17a}$$
$$H := \kappa_0 \frac{B}{\mu} \tag{17b}$$

In the all the Equations (12) to (17b) the sources are on the right and the sinks are on the left. Like the original Maxwell equations these equations describe the physics of what is happening at a single point in space. In this case sources and sinks are all at the same point. We can therefore see that the field pairs are not 100% coupled. In fact, as mentioned. we find by measurement and deduction that the coupling is $\kappa_0 = 1/2\pi$. This is an important discovery and obviously has far-reaching consequences.

7. MAXWELL'S TRANSFER FUNCTIONS

To obtain Maxwell's Transfer functions we can convert the coupling factor κ to represent the coupling between any two points in space. The coupling factor κ becomes a dyadic. We can then for example compute the capacitance C and inductance L between two small wires at two different points in space. The wires can represent parts of an antenna or filaments of displacement current in space [1]. We then have the two impedances, $1/j\omega C$ and $j\omega L$, and these are current to voltage transfer functions. We also have the two admittances, $j\omega$C and $1/j\omega L$, and these are voltage to current transfer functions.

It is easier to solve Maxwell's equations if they are first factorised into traveling wave and evanescent wave parts [1]. This implies establishing local cylindrical coordinates with the z-axis along the direction of power flow and at right angles to the direction of power flow. We can then set out the partitioned equations as follows with the equation number suffixes z and r, representing the components for the traveling and evanescent waves respectively. In this case, we remove all the external sources J and ρ, we replace $\partial/\partial x$ etc. by propagation constants jk_x etc.. Note that then Equations (18) and (19) become equivalent:

$$\mathrm{div} D = \nabla \cdot D = j\left(k_z^2 + k_r^2\right)^{1/2} D = 0 \tag{18}$$
$$\mathrm{div} B = \nabla \cdot B = j\left(k_z^2 + k_r^2\right)^{1/2} B = 0 \tag{19}$$
$$\mathrm{curl} E_x = \frac{\partial E_x}{\partial y} = jkE_x \quad \text{and} \quad \frac{\partial B_y}{\partial t} = j\omega B_y = j\kappa\mu H_y \text{ to give} : -jk\delta E_x = j\kappa\mu H_y \tag{20}$$
$$\mathrm{curl} H_y = \frac{\partial E_x}{\partial y} = jkE_x \quad \text{and} \quad \frac{\partial B_y}{\partial t} = j\omega B_y = j\kappa\mu H_y \text{ to give} : \; -jk\delta E_x = j\kappa\mu H_y \tag{21}$$
$$\delta D_x := \kappa\varepsilon E_x \oplus \tag{22a}$$
$$\delta E_x := \kappa \frac{D_x}{\varepsilon} \tag{22b}$$
$$\delta B_y := \kappa\mu H_y \oplus \tag{23a}$$
$$\delta H_y := \kappa_0 \frac{B_y}{\mu} \tag{23b}$$

Equations (19) to (23) are Maxwell's Transfer Functions in terms of impedances and admittances. The sinks are on the left and sources on the right. The δ sign shows that these equations can be integrated to sum all the contributions to the parameter on the left. The coupling κ is now a dyadic and therefore a function of the distance between two relevant points in space. The $\oplus$ sign warns where *RSS integration* should be used. (RSS integration is the square root of the integral of the quantity squared. Phasor RSS integration takes phase into account also.)

For these we find *four loosely coupled* ($\kappa_0 = 1/2\pi$) *travelling wave equations* for E, D, H, and B of the form:

$$\frac{\partial^2 X}{\partial z^2} = -\varepsilon\mu \frac{\partial^2 X}{\partial t^2} \quad \text{all four equations having velocity,} \quad c_{EM} = 1/\sqrt{\varepsilon\mu} \tag{24}$$

The partial coupling of $1/2\pi$ means that the initial impedance E/H close to an electric or magnetic field source can be one of the two values respectively $2\pi Z_0 = 2400$ or $Z_0/2\pi = 60$. Beyond the

Goubau Distance $r_G = (14/f_{\mathrm{MHz}})^{1/2}$ the impedance rapidly approaches $Z_0 = 120\pi = 377$ ohms in both cases. The *evanescent wave profile* solution of the Maxwell (Transfer Function) Equations are then derived by applying Equation (8). We then obtain the profile for vector potentials such as E and H [1]:

$$X = \left[1 - e^{-\left(\frac{1}{r}\right)\left(\frac{f_c}{f}\right)^{1/2}}\right] e^{-j\phi} \tag{25}$$

where $f_c = 14$ MHz, and ϕ_r is the (4-valued) phase along a standing wave.

REFERENCES

1. Underhill, M. J., "A physical model of electro-magnetism for a theory of everything," *PIERS Online*, Vol. 7, No. 2, 196–200, 2011.
2. Underhill, M. J., "The phase noise spectrum and structure of photons?," *Proc. 16th EFTF-2010*, 8, Noordwijk, Netherlands, Apr. 13–16, 2010.
3. Hunt, B., *The Maxwellians*, Cornell University Press, 1991, ISBN 0-8014-8234-8.
4. Underhill, M. J., "Novel analytic EM modelling of antennas and fields," submitted for publication.

Novel Analytic EM Modelling of Antennas and Fields

M. J. Underhill
Underhill Research Ltd., UK

Abstract— The Physical EM model presented at Piers 2011in Marrakesh is the basis for an analytic EM and antenna modelling method that requires no matrix inversion. 'Analytic Region Modelling' is therefore very fast and efficient and scalable to problems of high complexity. A Mathcad implementation of the methodology is presented with some illustrative examples.

1. INTRODUCTION

1.1. Summary of Method

Analytic Region Modelling is based on two newly observed physical laws, 'process capture' and 'electro-magnetic (EM) coupling' [1]. These laws define 'process regions' in space, in which only one physical or electromagnetic process is dominant. The third law that is strictly obeyed (by the new laws) is 'energy conservation'. This is particularly useful for establishing the overlapping boundaries between process regions where the processes are partially coupled progressively through space.

The Physical EM model presented at Piers 2011 in Marrakesh [1] leads to analytic formulas for the various possible EM processes that can take place in a process region. It also is used to establish the impedances and excitation currents and potentials at every point on the antenna conductors. This is done analytically with no matrix inversion, thus removing any need for Method of Moment (MoM) or Finite Element (FE) computation. Because no matrix inversion is required, 'Analytic Region Modelling (ARM)' is therefore very fast and efficient and scalable to problems of high complexity.

We can also include the classical antennas far-field (interference) pattern formation formulas, if desired with any lossy ground effects (within the Goubau Height) as illustrated in the examples below.

1.2. The Local Ether Four Transmission Line Model of EM

The Physical EM Model (PEM) in [1] is an underlying basis for ARM. It is a two low-pass and high-pass pairs of co-located transmission lines in a 'local ether'. One LP/HP pair represents conventional and electric displacement current, with electric vector potential. The other represents magnetic displacement current and magnetic vector potential. The local ether is the region of the stored energy of an antenna. The local ether is a new definition of the near field region.

Importantly this transmission line model is also usable for the antenna conductor surfaces. Surface and wire impedances are thereby established.

1.3. Process Capture

'Process capture' is a fundamental law originally seen in small tuned loop antennas for the various radiation and loss resistances [2]. We then deduce that overlapping distributed processes combine at any co-local point according to the RSS (Root-Sum-of-the-Squares) law. The strongest process 'captures' and suppresses the weaker ones. Over a short (coupling) distance the suppression is progressive.

1.4. Analytic Process Regions

Process Capture allows 'process regions' to be defined in each of which there is only one dominant process and in which the local ether properties of permittivity, permeability, velocity and acceleration are well defined. The process region is thus a relativistic 'frame', but with the advantage that the bounded volume and position of the frame can be defined in space [1]. (If the frame has no acceleration and is uniform over a sufficient size, the Michelson-Morley experiment holds only within the confines of the frame. In the overlap region of two frames having different accelerations the Michelson-Morley Doppler shifts are predicted not to cancel perfectly.) Process regions are relevant to all of physics.

1.5. Process Region Boundaries

There is power flow density continuity across the region boundaries. This links across the region boundaries from one region to another. At the region RSS process combining has to be used. Any losses are in general considered to be distributed, so power loss is a gradient and does not negate power continuity.

1.6. Electro-Magnetic Coupling

'EM coupling' is the process that until now has been omitted from Maxwell's equations. Both the Physical Electro-Magnetic (PEM) model [1] and Maxwell's Transfer Functions (MTFs) make good this omission. Additional self-stable evanescent wave solutions become possible requiring no external boundary conditions or external boundary surfaces. The self-coupling replaces the need for an external boundary condition. Thus EM coupling is useful for finding the stored energy and surface wave profile formulas, for use in analytic region modelling (ARM).

In fairly uniform space the coupling between fields (as in Maxwell's Transfer Functions) is $\kappa_{11} = \kappa_0 = 1/2\pi$.

The EM coupling factor κ (kappa) is found by experiment to be proportional to the inverse square root of the frequency. This means that antennas do not 'scale' perfectly in practice. Scale modelling is not always effective. This effect is most obvious in the estimation and measurement of the near-field. The far field is much less affected. This $1/\sqrt{f}$ scaling is incorporated in ARM particularly for modelling fields, stored energy and power flow in the near field region.

There is a critical (Goubau) radial distance r_G from a (wire) source at which the stored energy density starts to decay rapidly. With distance from source r in units of metres we find that at the critical frequency f_c of approximately 14 MHz r_{GW} is one metre. For an extended surface source as associated with a surface wave the critical distance r_{GS} is larger by a value about π, but to be confirmed by further experiments (on antenna to ground absorption height). We therefore have:

$$r_{Gw} = \left(\frac{f_c}{f}\right)^{1/2} = \left(\frac{14}{f_{\mathrm{MHz}}}\right)^{1/2} \tag{1}$$

$$r_{GS} = \pi r_{GW} = \pi \left(\frac{f_c}{f}\right)^{1/2} = \left(\frac{140}{f_{\mathrm{MHz}}}\right)^{1/2} \tag{2}$$

Coupling κ_{11} is also the evanescent standing wave profile. The standing wave phase factor is e^{-jkr} so that for a wire:

$$\kappa_{11} = \frac{1}{2\pi}\left[1 - e^{\frac{-1}{r}\left(\frac{f_c}{f}\right)^{1/2}}\right] e^{-jkr} \text{ where } k = 2\pi/\lambda, \text{ and } e^{-jkr} = \cos kr – j \sin kr \text{ (de Moivre's Theorem)} \tag{3}$$

An evanescent wave is a standing wave in the direction(s) at right angles to the direction of power flow. A standing wave is most realistically represented by an in-phase and quadrature component as shown in Equation (3). We find that these should be considered as separate entities as explained in [1, 4]. Note how the phase of the in-phase component $\cos kr$ is zero for the first quarter wavelength then it switches rapidly to π for the next half wavelength and thereafter it switches adding π radians of phase shift every additional half wave of distance r. The quadrature component $\sin kr$ switches phase at the quarter wave points between the $\cos kr$ switching points.

In free-space formula (1) confirms that the co-local ($r = 0$) electro-magnetic (EM) coupling between the fields H and D/ε, and between H and B/μ is not 100% but is $\kappa = 1/2\pi$. (The value $1/2\pi$ was first mooted in 2002 in reference [3] with respect to the coupling of fields into field sensors and to the need for calibration in situ.) This means that Process Regions of different processes can overlap, and the transfer of one process to another is progressive in the direction of power flow. Thus the positions of the process boundaries are not the same for transmission and reception by the antenna. There is 'hysteresis'. ARM propagation formulas take care of this.

Partial EM coupling also means that magnetic and electric antenna modes can exist in the same volume with coupling arguably somewhere between $1/(2\pi)^2$ and $1/(2\pi)^4$. This is low but non-zero coupling.

1.7. The Theory of Transmission and Reception for ARM

A displacement current in an in-phase potential will radiate power so that the current attenuates away from the source of the current. A displacement current in an out-of-phase potential will receive power, and the current increases in the direction towards the sink of the current. With these definitions the power transmitted or received at any point on an antenna surface may be calculated. Note that there can be conversion between electric and magnetic quantities and they must be taken into account both separately and together. All this is fully computable analytically.

1.8. Direct Theory of Reception

Antenna 'aperture' for signals received by a wire (dipole) antenna is orders of magnitude greater than the wire area presented to the signal flux. Thus an antenna acts as a lens wherever an antenna has an RF aperture greater than its physical aperture. The antenna modifies ε and μ and creates a 'local ether' around the antenna with a refractive index greater than one. It has an evanescent wave profile as found by application of the coupling profile Equation (3) above. The power flow lines for reception may then be found directly and analytically from the profiles.

1.9. Stored Energy in Space

The stored energy is the product of the displacement current and the quadrature potential. The stored energy of standing waves can be obtained by separation into forward and reflected waves. This is computable analytically within the near-field region, as are the following:

1.10. Stored Energy Capacity, Local Q and Antenna Q

The local Q is the stored energy in a small volume divided by the transported energy flowing through that volume. The local Q is the *stored energy capacity*. The antenna Q is 2π times the total stored energy of an antenna divided by the transmitted or received energy per cycle.

1.11. Multi-mode Antennas

For analytic modelling of antennas usually one transmission line per antenna element is sufficient. Multi-mode antennas such as the loop-monopole usually require additional transmission lines for each operative mode. The various transmission lines are partially coupled. This is all computable analytically.

1.12. Analytic Region Modelling

With the above definitions, three dimensional analytic expressions for all physical quantities surrounding an antenna, over a surface, in a waveguide, etc. may be obtained. The physical quantities can include, all fields, potentials, displacement currents, power flow (Poynting) vectors, spatial impedances and Qs, etc. Process capture allows finite regions to be represented in compact form with very few terms. No matrix inversion is required. The accuracy of the model in given cases may be considerably improved by a few practical measurements to calibrate the model.

2. IMPLEMENTATION OF ANALYTIC REGION MODELLING

ARM models the physics of antennas and propagation. The space containing the antennas and the propagation paths is divided into overlapping regions. Because of process capture the physical process in each region can be represented by a simple analytic formula.

Mathcad is chosen for implementing the formulas of ARM. It is not the only possible choice. But it is preferred for its visual layout of formulas and good 3D and 2D plotting capabilities. Rotation of 3D antenna plots is a particularly useful facility. Three Mathcad examples of ARM are now given.

3. AR MODELLING OF THE STRING-ARROW MODEL OF A PHOTON

In reference [4] a photon in free space is shown to be a cylindrical 'arrow', travelling at the speed of light, of radius $= (f_c/f)^{1/2}$ where f_c obtained from Goubau single wire non-radiating transmission line and surface wave measurements as $\sim 14\,\text{MHz}$. The photon length is $c/2\delta f$ where $2\delta f$ is the photon line bandwidth. The cross–section of the photon is similar to the distribution of energy that surrounds the Goubau line. It is a number of interlaced layers of two complementary types e.g., $\cos(kr)$ and $\sin(kr)$ of radial distance r. The edge of the energy distribution of the photon is sharp and possibly it is this that makes the photon stable and non-dissipative.

Figure 1 is an ARM representation of the cross section of the energy of a photon or on a Goubau single wire transmission line. For a visible photon the radius of the string arrow profile is about 300 wavelengths corresponding to $4 \times 300 = 1200$ layers interlaced at quarter wavelength intervals. A plot of this rather than the 16 or so layers in figure 1 would require the change of only one parameter in the analytic formula.

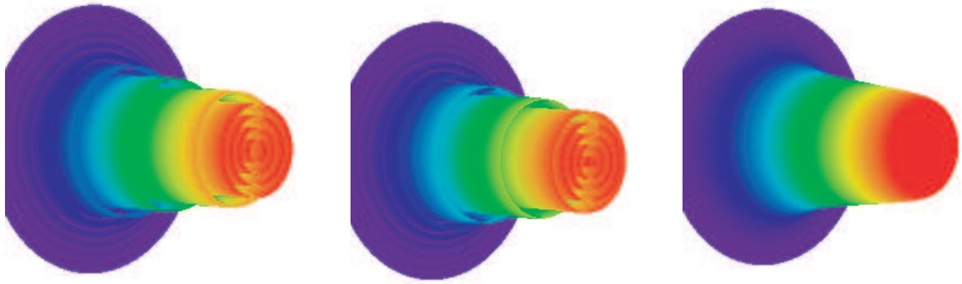

(a) (b) (c)

Figure 1: Representation of Goubau line or photon layer magnitudes. Red is maximum to the right and blue is minimum to the left. (a) is for 'sine' layers. (b) is for 'cosine' layer. (c) is magnitude of total energy.

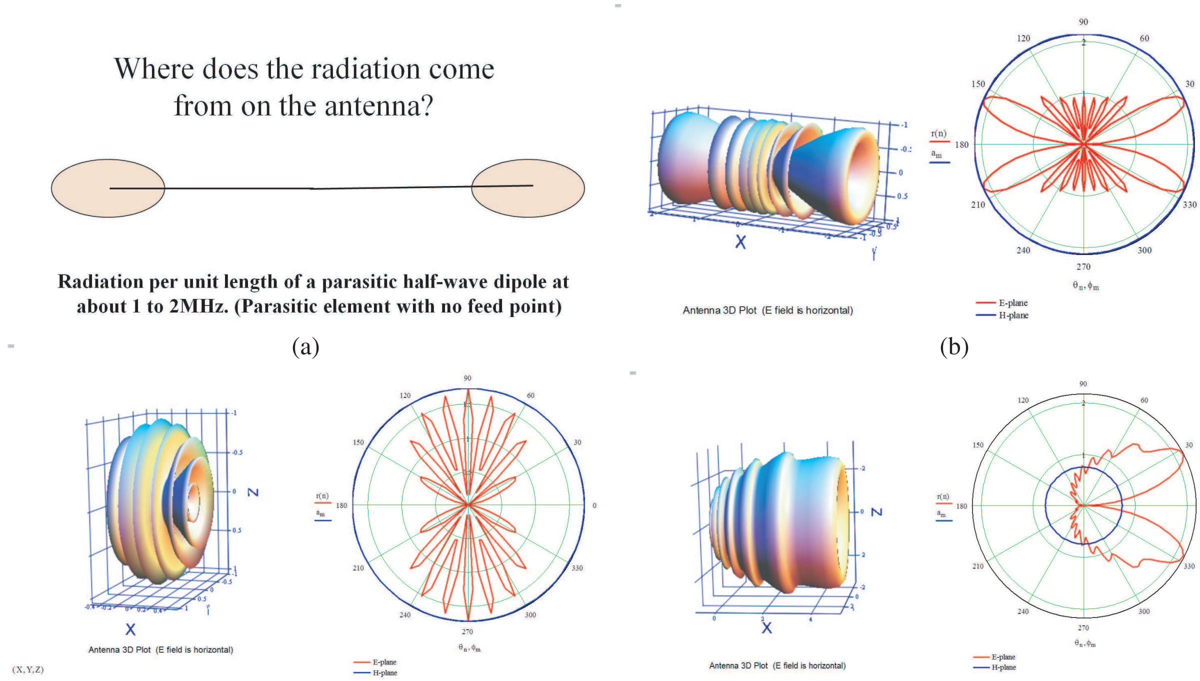

(a) (b) (c) (d)

Figure 2: (a) Radiation from the antenna ends. (b) 4.5λ wire antenna pattern using the Kraus/Balanis formula. (c) An ARM pattern of 4.5λ top left. (d) End-fed 4.5λ travelling wave wire at low frequency.

The plots in Figure 1 are Mathcad 3D plots in cylindrical coordinates rotated so that the structure may be seen. The plots represent the in-phase, quadrature and magnitude parts of Equation (3) respectively. This example shows that once the analytic formulas are known the pictorial representation may be chosen as desired.

4. AR MODELLING OF ANTENNA PATTERNS

Figure 2 shows ARM can combine two or more antenna radiation modes for a simple antenna and how the plots compare with the classical idealised plots.

5. ARM OF EFFECT OF GROUND LOSS ON LOW HEIGHT ANTENNA PATTERNS

In Figure 3 the assumption is that the loss for a low angle (to the horizon) signal is $x/\sin\theta = x\text{Cosec}\theta$ in dBs. It is proportional to the path length in the shaded area below the Goubau height in Figure 3. It is actually independent of the Goubau height and exact profile of loss. These can be derived from Equation (3) if desired.

The maximum ground loss figure of 24 dB was chosen because it is within the region of measured loss differences between two loop 82 m perimeter horizontal loop antennas, one at 2 m height and one at 15 m height, for NVIS (vertical) signals at 3.7 MHz over (wet) clay soil.

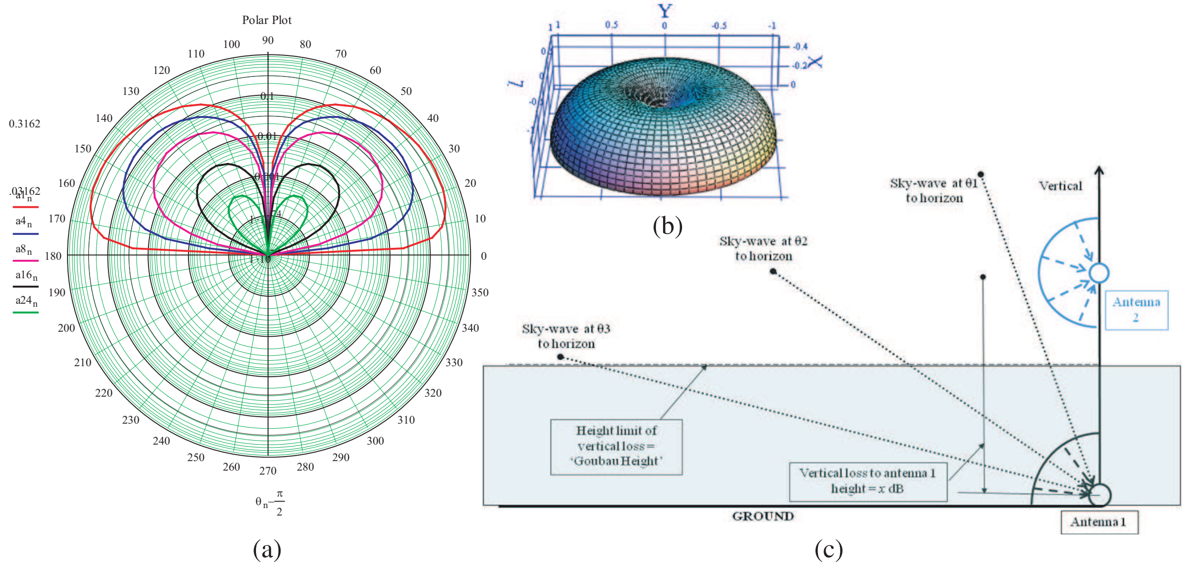

Figure 3: (c) Ground Loss Scenario for small antenna. (b) Pattern of short vertical whip or small horizontal (tuned) loop over perfect ground. (a) Far-field Radiation Pattern for total vertical path coupled ground loss values between 1dB (outer red plot) and 24 dB (inner green plot).

6. CONCLUSION

'Process capture' means that the number of significant modes and processes for any antenna or array even including environmental and propagation is quite small, showing that 'Analytic Region Modelling' (ARM) is easily extensible to compute and simulate complex EM scenarios. Thus ARM could well be the future of most, if not all, Antennas, Propagation and EM modelling.

REFERENCES

1. Underhill, M. J., "A physical model of electro-magnetism for a theory of everything," *PIERS Online*, Vol. 7, No. 2, 196–200, 2011.
2. Underhill, M. J. and M. Harper, "Simple circuit model of small tuned loop antenna including observable environmental effects," *IEE Electronics Letters*, Vol. 38, No. 18, 1006–1008, 2002.
3. Underhill, M. J. and M. Harper, "Small antenna input impedances that contradict the chu-wheeler Q criterion," *Electronics Letters*, Vol. 39, No. 11, May 23, 2003.
4. Underhill, M. J., "The phase noise spectrum and structure of photons?" *Proc. 16th EFTF-2010*, 8 pages, Noordwijk, Netherlands, April 13–16, 2010.

A New View of Spectral Analysis of Linear Systems

J. Heredia and E. Gago-Ribas
Electrical Engineering Department, University of Oviedo, Spain

Abstract— There are many scientific and technological areas where Signals & Systems Theory (SST) plays a fundamental role. There are also many references which treat this field, especially in connection with communication and circuit theory and with the important application concerning discrete signals and systems. While the usual point of view is valid for practical purposes, it uses to avoid many concepts which become fundamental in the generalization of the analysis of physical problems: a general representation different from the usual time-frequency domains, the description in terms of vector spaces and the algebra associated, the description of the Dirac delta and other generalized signals in terms of the distributions theory, etc. The most important aim of obtaining a Generalized Signals & Systems Theory (GSST) is to connect the usual Signals & Systems Theory with important mathematical representations that lead to obtain more general representations that may be rigorously applied to model general physical problems (EM radiation and scattering problems in our particular case). This generalization is based on defining any problem under the theory of infinite dimensional spaces of signals and systems and the subsequent representations based on the GSST scheme.

A particularly important analysis under the GSST is the so called *Generalized Spectral Analysis.* The description of this particular generalization will be the main goal of the present paper and can be summarized as follows. Once the infinite dimensional vector space algebra is defined — distance, vector spaces, norm and scalar product — each signal can be described as a *generalized linear combination*. By choosing a set of basis functions, it is possible to reconstruct the signal in terms of the generalized linear combination with the basis functions weighted by a set of coefficients which are obtained through the minimization of the *distance* between the original signal and this generalized linear combination. Usually, each coefficient is obtained as the projection of the signal over each element of the base if the set of infinite basis functions is orthogonal with respect to the scalar product. Different convergence criteria usually appear from this particular analysis.

From this point of view, a *generalized transformation* can be defined when dealing with a generalized set of basis functions; its particularization to specific sets become specific transforms; for instance, if exponentials with imaginary arguments are chosen as the set of basis functions in the continuous variable signal space, the generalized transform becomes the well known Fourier transform. These functions are eigenfunctions of any linear invariant system and their corresponding eigenvalues — spectrum of the system — are the Fourier transform of the impulse response. The generalization of these concepts for linear non invariant systems where the sets of basis functions are not eigenfunctions of the systems together with the definition of a generalized transform leads to the concept of a generalized spectral analysis which widely open the scope of the traditional spectral analysis specially when dealing with time-space physical problems, usually invariant in time domain but non invariant in space. The complete description of this generalization will be provided in the present paper.

1. INTRODUCTION

Signals and Systems Theory (SST) plays a fundamental role in the educational and professional background of electrical engineering as well as in other scientific areas. Many authors present this theory following a similar scheme, [1–3] for instance. However, there are many important concepts avoided in these references and go over the physical or mathematical interpretation associated to them. This lead to many conceptual problems, such as the definition of many distributions as the Dirac delta — which is essential for the right understanding of the SST —, the analysis in time-frequency domains only or simply the study of linear invariant systems, leaving out many important linear non invariant systems.

The final aim of our work is to develop a Generalized Signals and Systems Theory (GSST) where the representation and interpretation of any physical problem can be studied as a particular case under the framework of infinite dimensional vector spaces together with the theory of distributions. This procedure makes possible to generalize the important concepts associated to transformations and spectral analysis of systems leading to a *generalized transform* (GT) and a *generalized spectral analysis of systems* (GSAS) which include the spectral analysis of linear invariant and non-invariant

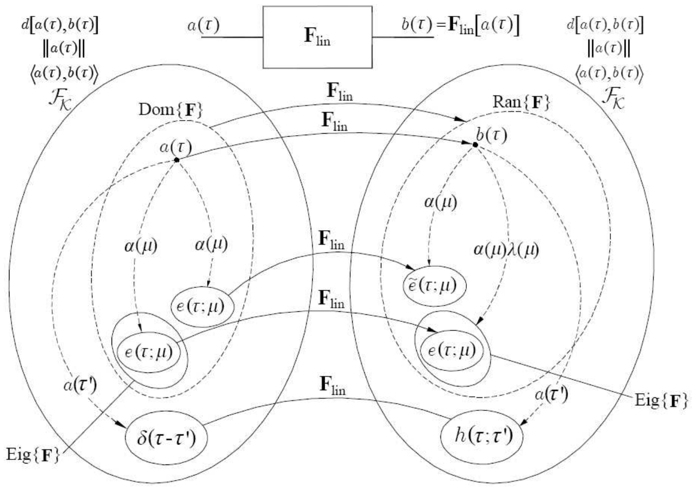

Figure 1: Summary of the GSST scheme which supports the generalized spectral analysis. Dashed lines identify generalized linear combination operators with coefficients those crossed by the lines.

systems under any kind of transformation. Their description will be the main purpose of the current paper.

This scheme is being used nowadays in both undergraduate and postgraduate courses, not only to present the basic SST but also to introduce important concepts in electromagnetic theory such as the integral representations of Maxwell equations as well as a generalized version of the Green's function theory. Also, many research activities are directly involved with this scheme, especially those involving Rigged Hilbert Spaces (RHS) [4], and the continuation of real time-space radiation/scattering EM problems to their complex time-space version [5]. A summary of the GT and the GSAS based on the GSST will be presented in next sections, avoiding most of the mathematical developments and focusing only in the most important concepts associated to the scheme.

2. SUMMARY OF THE GSST

The proposed GSST scheme may be summarized as follows; Fig. 1 shows the schematic representation of this theory. In order to facilitate the well understanding of this scheme, only the most important mathematical concepts will be included. An exhausted development of the theory may be found in [6–9].

2.1. Initial Algebraic Definitions

The first step for the construction of the theory is to consider an initial vector space of signals $\mathcal{F}_{\mathcal{K}}$ which elements are denoted by $a(\tau)$, and where internal and external compositions laws are required. The independent variable may represent either discrete or continuous variable ($\tau \equiv n \in \mathbb{Z}$, $\tau \equiv x \in \mathbb{R}$); in practical cases, x may be time, space, or any other physical magnitude. As a future aim, it is intended that τ may be a complex variable. The dimension of the space may be finite, or infinite — numerable or continuous —, but the usual case in practical problems corresponds to an infinite continuous variable, which requires introducing some important remarks which make the differences to the regular finite dimensional case. Carrying out the definition of the distance $d(\circ, \circ)$, norm $\|\circ\|$ — which usually measures the energy of the signals — and scalar product $\langle \circ, \circ \rangle$, the algebraic structure of the space is completed. These definitions determine not only the way of measuring within the space, but also have influence in the definition of certain important distributions such as the Dirac delta.

The way used to identify subsets within the space is through the definition of a new parameter μ. It can identify finite, infinite-countable or infinite-continuous subsets of functions which will be denoted by $u(\tau; \mu)$. It is important to remark that μ is initially an *identification* parameter and in later stages usually corresponds to the so-called *spectral variable*, so the initial meaning gets easily lost. This fact is emphasized by the use of the semicolon instead of the typical comma which denotes two variable functions although the final set of functions may be interpreted as discrete-type or continuous-type surfaces.

2.2. Linear Combinations and Generalized Transforms

Using the composition laws required in a vector space, any element $a(\tau) \in \mathcal{F}_{\mathcal{K}}$ may be represented in terms of a generalized linear combination — represented by a general operator $\mathbf{LC}_{(\mu)}$ — of a set of basis functions $e(\tau;\mu) \in \mathcal{F}_{\mathcal{K}}$ weighted by a set of coefficients $\alpha(\mu)$, Fig. 1. The generalized analysis of $\alpha(\mu)$ requires the study of the distance, which leads to the following set of equations:

$$a(\tau) = \mathbf{LC}_{(\mu)} \left[\alpha(\mu) e(\tau;\mu)\right], \tag{1}$$

$$d\left\{a(\tau), \mathbf{LC}_{(\mu)} \left[\alpha(\mu) e(\tau;\mu)\right]\right\} \rightarrow 0 \Rightarrow \alpha(\mu). \tag{2}$$

The pair of Eqs. (1)–(2) describes a *generalized transform*, where $\alpha(\mu)$ is the direct transform of $a(\tau)$ in the base $e(\tau;\mu)$ and $a(\tau)$ is the inverse transform of $\alpha(\mu)$ in the same base. The general representation in (1)–(2) takes into account that the operator $\mathbf{LC}_{(\mu)}$ may describe both discrete sums either continuous integrals (Riemann or Lebesgue), and also functional representations connected to the theory of distributions.

2.3. Real Domain Characterization of Systems

If the set of basis functions chosen are $e(\tau;\mu) = e(\tau;\tau') = \delta(\tau - \tau')$, it is possible to represent the output of any linear system described by an operator $\mathbf{F_{lin}}$ as,

$$a(\tau) = \mathbf{LC}_{(\tau')} \left[a(\tau')\delta(\tau - \tau')\right], \tag{3}$$

$$b(\tau) = \mathbf{F_{lin}}[a(\tau)] = \mathbf{LC}_{(\tau')} \left[a(\tau')\mathbf{F_{lin}}[\delta(\tau - \tau')]\right] = \mathbf{LC}_{(\tau')} \left[a(\tau')h(\tau;\tau')\right]. \tag{4}$$

The set of functions $h(\tau;\tau') = \mathbf{F_{lin}}\left[\delta(\tau - \tau')\right]$ are denoted as the *set of impulse responses* of the system and the $\mathbf{LC}_{(\tau')}$ operator in (3)–(4) must be interpreted under the *theory of distributions* if the real variable is continuous ($\tau \equiv x \in \mathbb{R}$). In this case, (3)–(4) can be seen as a particular case of (1)–(2) being the spectral variable $\mu \equiv \tau'$. The relation between ordinary functions and distributions are currently investigated under the RHS Theory [4].

2.4. Spectral Domain Characterization of Systems

The transformation of $a(\tau)$ represented as in Eq. (1) may be described in terms of the transformation of the set of basis functions through the system as,

$$b(\tau) = \mathbf{F_{lin}}\left[a(\tau)\right] = \mathbf{F_{lin}}\left\{\mathbf{LC}_{(\mu)}\left[\alpha(\mu)e(\tau;\mu)\right]\right\} = \mathbf{LC}_{(\mu)}\left\{\alpha(\mu)\mathbf{F_{lin}}\left[e(\tau;\mu)\right]\right\}, \tag{5}$$

When the set of basis functions belongs to the subspace of eigenfunctions of the operator $\mathbf{F_{lin}}$, Eq. (5) reduces to,

$$e(\tau;\mu) \in \mathrm{Eig}\left\{\mathbf{F_{lin}}\right\} \rightarrow b(\tau) = \mathbf{LC}_{(\mu)}\left\{\alpha(\mu)\lambda(\mu)e(\tau;\mu)\right\}, \tag{6}$$

where the coefficients $\lambda(\mu)$ are the eigenvalues associated to each function $e(\tau;\mu)$. For instance, the set $e(\tau;\mu) = e(x;\xi) = e^{j\xi x}$ used in the Fourier transform are always eigenfunctions of any linear invariant system and then Eq. (6) describes the usually called *spectral representation* of a system; notice that the Fourier transform basis functions are not eigenfunctions of a linear non invariant system. Thus, if $e(\tau;\mu) \notin \mathrm{Eig}\left\{\mathbf{F_{lin}}\right\}$, a *generalized spectral analysis* may be defined [8, 9].

3. GENERALIZED SPECTRAL ANALYSIS

The usual spectral analysis is performed under the study of the eigenvalues of a system, $\lambda(\mu)$. In this case, the output signal in the $e(\tau;\mu)$-spectral domain reduces to the product $\alpha(\mu)\lambda(\mu)$. When the basis functions do not belong to the subspace of eigenfunctions of the operator $\mathbf{F_{lin}}$ (for instance, when the system is not invariant under Fourier analysis or the spectral analysis is performed under other transformation different from the Fourier one) a *generalized spectral analysis* is required. This analysis will not be in terms of eigenvalues but in terms of a set of functions depending on the system and the $e(\tau;\mu)$-transform under analysis. This set of functions will be denoted by $H(\mu;\mu')$ which means the transformation of the set of impulse responses $h(\tau;\tau')$, first with respect to the real variable τ and then with respect the *parameterization* variable τ'. The output signal in the spectral domain will be determined as follows,

$$\beta(\mu) = K\mathbf{LC}_{(\mu')}\left\{\alpha(\mu')H_*(\mu;\mu')\right\}, \text{ where} \tag{7}$$

$$H(\mu;\mu') = \mathbf{T}_\tau\left[\mathbf{T}_{\tau'}\left[h(\tau;\tau')\right]\right] \tag{8}$$

Table 1: Particularization of the generalized spectral analysis for some usual transforms.

	Linear System	Linear Invariant System
Fourier Transform	$G(\xi)=\frac{1}{2\pi}\int_{\xi'=-\infty}^{\infty}F(\xi')H(\xi;-\xi')d\xi'$	$G(\xi)=F(\xi)H(\xi)$
Hilbert Transform	$G(x')=\int_{y'=-\infty}^{\infty}F(y')H(x';y')dy'$	$G(x')=F(x')*h(x')=f(x')*H(x')$
Bessel Transform (order ν)	$G_\nu(\xi)=\int_{\xi'=0}^{\infty}F(\xi')H_\nu(\xi;\xi')d\xi'$	No expression
Fourier Series Expansion	$b(m)=X_0\sum_{m'=-\infty}^{\infty}a(m')h(m;-m')$	$b(m)=a(m)H(m)$

and the subscript * denoting that the set of functions $H(\mu;\mu')$ will depend on the set of basis functions which specify the transform. Table 1 shows some particular results for different transforms. Actually, the general expression of $H_*(\mu;\mu')$ is given by,

$$H_*(\mu;\mu')=\mathbf{LC}_{(\varpi)}\left[H(\mu;\varpi)\mathbf{LC}_{(\tau')}e(\tau';\varpi)e(\tau';\mu')\right]. \tag{9}$$

By direct comparison of the real and spectral domain representations of the output signal, Eqs. (4) and (7), it can be noticed that there is a formal relationship of the expressions in those domains; in both cases, the output signal depends on the input in the corresponding domain and a set of functions depending on the system and, in the case of the spectral domain, also on the $e(\tau;\mu)$-transformation under analysis,

$$b(\tau)=\mathbf{LC}_{(\tau')}\left[a(\tau')h(\tau;\tau')\right] \quad\leftrightarrow\quad \beta(\mu)=K\mathbf{LC}_{(\mu')}\left\{\alpha(\mu')H_*(\mu;\mu')\right\} \tag{10}$$

If the basis functions are eigenfunctions of the system, $H_*(\mu;\mu')$ becomes as in (11), reducing to the usual analysis.

$$H_*(\mu;\mu')=\frac{1}{K}\lambda(\mu')\delta(\mu-\mu'), \tag{11}$$

4. CONCLUSION

This paper presents a brief summary of a Generalized Spectral Analysis based on a Generalized Signals and Systems Theory scheme. This analysis takes into account linear invariant and non invariant systems — in both continuous and discrete variables — under any kind of transformation. This is especially important because many physical problems — for instance, those concerning spatial domain, such as the radiation and scattering of EM waves, and others in time, such as modulations — are non invariant. A very important particular case of this generalization connects directly with the Green's functions theory and is also being important to understand the relation between functions and distributions through the RHS theory. More details about GSAS may be found in [9].

ACKNOWLEDGMENT

This work has been supported by the Ministerio de Ciencia e Innovacion of Spain /FEDER under project TEC2011-24492, by the Gobierno del Principado de Asturias (PCTI) FEDER-FSE under project PC10-06 and by Severo Ochoa program under grant BP10-139.

REFERENCES

1. Oppenheim, A. V., A. S. Willsky, and I. T. Young, *Signals and systems*, 2nd Edition, Prentice-Hall International, 1997.
2. Lindner, D. K., *Introduction to Signals and Systems*, McGraw-Hill, 1999.
3. Skinner, R. and J. A. Weil, "An introduction to generalized functions and their application to static electromagnetic point dipoles, including hyperfine interactions," *American Journal of Physics*, Vol. 57, No. 9, 777–791, Sep. 1989.
4. De la Madrid, R., "Rigged hilbert space approach to the schröedinger equation," *Journal of Physics A: Mathematical and General*, Vol. 35, 319–342, 2002.
5. Gago-Ribas, E., M. J. González, and C. Dehesa, "Challenges and perspectives of complex spaces and complex signal theory analysis in electromagnetics: First steps," *Electromagnetic in a Complex World: Challenges and Perspectives, Springer-Verlang (Springer Proceedings in Physics)*, Vol. 96, 175–188, USA, 2003.

6. Gago-Ribas, E. and A. Serroukh, "A generalized signals and systems theory scheme and its applications in the description of electromagnetic problems," *PIERS Proceedings*, 370–374, Moscow, Russia, Aug. 18–21, 2009.
7. Gago-Ribas, E., "A scheme to generalize signal theory and its application to electromagnetics," *IEEE International Symposium on Antennas* & *Propagation and URSI Meeting*, Ref. 978-1-4244-3647-7/09, Charleston, SC, USA, Jun. 2009.
8. Varona de Miguel, F. and E. Gago-Ribas, "About real and fourier-spectral characterization of general linear systems," *International Conference on Engineering and Mathematics, ENMA 2008 Proceedings*, 269–276, Bilbao, Spain, Jul. 2008.
9. Heredia Juesas, J., "Generalización de la teoría de señales y sistemas para el análisis de sistemas lineales no invariantes," *Master Thesis in Information Technologies and Communication in Mobile Networks (TICRM)*, EPSIG, University of Oviedo, Jul. 2010.

Complex Parameterization of the Lossy Transmission Line Theory

E. Gago-Ribas and M. Carril-Campa
Electrical Engineering Department, University of Oviedo, Spain

Abstract— The usual transmission line theory (TLT) found in the specialized literature often deals with its analysis for the ideal case (lossless case) or the low losses approximation, the last one obtained from a mathematical point of view. The present paper deals with a rigorous methodology that lets to address the TLT for the general lossy case in a very understanding and visual way. This methodology is based on analyzing the theory from the point of view of performing a rigorous analysis of the complex transformations (complex parameterization of the lossy transmission line theory, CTLT) which define the mathematical parameters involved in the physical description of the behavior of a transmission line with losses under time harmonic regime. From this point of view, the usual lossless case becomes a particularization of the general results in the CTLT analysis; by the way, the low losses approximation may be fully understood under this generalization as well as other interesting particular cases such as the non dispersive lossy case. One of the main important properties associated to the CTLT comes from the fact that they may be graphically represented by analytical curves which, in many cases, correspond to very interesting mathematical curves running from basic circumferences to Cassini ovals, for instance. This leads to a set of graphs that may be summarized as follows: (1) "Universal" characterizations of the behavior of both the basic parameters (characteristic impedance and propagation constant) as well as the wave parameters (impedance, admittance and reflection coefficient) involved in the transmission line theory, with all the parameterizations described by well-known analytical curves, and (2) Graphical parameterizations of losses and important physical interpretations directly induced by the geometrical properties of these curves, many of them not easily available from the usual mathematical approach. The large number of physical interpretations appearing from the graphical analysis may be exemplified by the following examples: (i) the usual Smith Chart becomes a particular case (when losses become null) of a Generalized Smith Chart. In fact, the new Generalized Smith Chart is only one of the several complex parameterizations that will be presented in the paper; (ii) the description of all the possible values of the characteristic impedance and propagation constant in terms of losses and the subsequent identification of all the transmission lines with a fixed value of a basic parameter (for instance, all the transmission lines with the phase of the characteristic impedance fixed to a specific value); (iii) from the practical and designing points of view it is possible to determine whether a solution is possible or not given some specific design constraints and, in case a solution is indeed possible, describing the range of transmission-line-wave-parameter values associated to such solution and the understanding of which parameters are susceptible of variation to resolve possible design errors, allowing optimization approaches to their solution. All these aspects are particularly relevant, both from the educational point of view, and from the standpoint of TL's based circuit design. Also, the difficulty of resolving some of the equations associated to the lossy TLT can be substantially reduced by using the geometrical properties associated to the CTLT methodology. In this sense, the paper will emphasize the concepts and physical interpretations that can be extracted from this methodology. This fully analytical methodology has also been implemented into a software tool that will be introduced also in the present paper.

1. INTRODUCTION

The literature covering the transmission line theory (TLT) and waveguides deals often with its analysis for the ideal case without losses, addressed if at all, using a low losses approximation, the latter without a rigorous analysis of its real meaning, see for example, [1–3]. Not addressing rigorously the TL theory for the general lossy case may be due probably to the fact that transmission systems require losses as low as possible to minimize its effects in the process of signal propagation. While this is true, a rigorous analysis of the general case with losses reveals that both the ideal lossless case as well as the low-losses regime (defined under the usual conditions $R \ll \omega L$ and $G \ll \omega C$) are better explained and justified as special cases of the general case. In this sense, the general analysis allows for the parameterization of the effect of losses in the behavior of the parameters which determine the final solution to a TL problem with specific boundary conditions. As an example, it may be advanced that among all the parameters involved, the most critical one in the final behavior of a lossy TL is the phase of the characteristic impedance. In fact, the generalization of the Smith chart to the lossy line will depend precisely on this parameter.

Furthermore, the previously mentioned parameterization can also predict the ultimate behavior of the problem and even detect physical phenomena associated with losses that may be of great practical interest. All these aspects are particularly relevant, both from the educational point of view, and from the standpoint of TL's based circuit design. One of the difficulties associated with studying the theory of TL's from the general viewpoint is the complexity in analyzing the equations describing the model. This complexity can be substantially avoided by using the complex analysis presented in this paper (CTLT), providing also with general graphical descriptions that are capable of be 'physically' interpreted and also that can be used to obtain final solutions by using visual geometrical procedures.

2. SUMMARY OF THE CTLT

Based on the well-known general scheme presented in Fig. 1, the most important parameters — both the *basic* and the *wave parameters* — will be summarized in the present section. All the results that will be presented in this paper have been obtained analytically; the corresponding analyses will be avoided due to space restrictions but most of them can be found in [4]. All the complex analyses concerning these parameters will be based on the knowledge of R, L, G and C. Tables 1–2 summarize the most important expressions of the well-known *basic and wave parameters* together with some important *generalization parameters* (r, g and c) which let to clearly separate the effects due to the losses in the conductors and the losses in the dielectrics. Also, the *normalizations* described in these tables become fundamental to determine *universal curves* describing the behavior for a complete set of TL's; for instance, any TL that satisfies the condition $c =$ cte. will be described by the same complex curve in a particular complex plane. With these general considerations in mind, it is possible to obtain the so-called *complex analysis* which must be understood as the analysis of any quantity on its own complex plane.

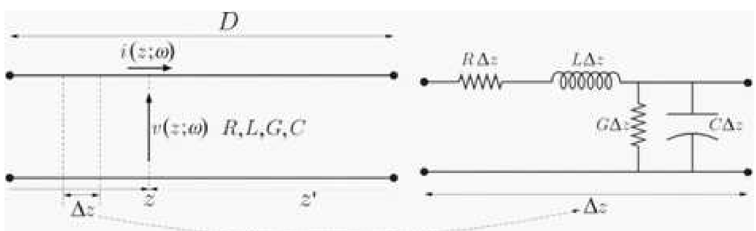

Figure 1: General scheme representing the usual equivalent circuit per unit length of a lossy transmission line.

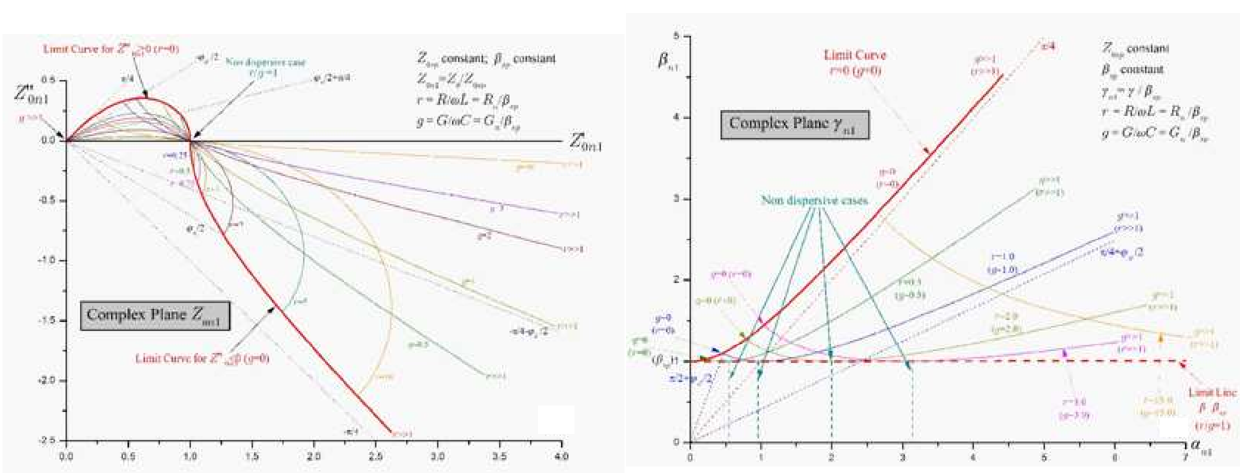

(a) (b)

Figure 2: Frequency parameterizations of the complex planes Z_{0n1} and γ_{n1} in terms of r and g.

Table 1: Definition and normalizations of the basic parameters in the CTLT.

<table>
<tr><td colspan="3">Basic TL Parameters</td></tr>
<tr><td colspan="2">$Z_0 = \sqrt{(R + j\omega L)/(G + j\omega C)}$</td><td>Characteristic impedance (complex)</td></tr>
<tr><td colspan="2">$Z_{0sp} = \sqrt{L/C}\ (R = G = 0)$</td><td>Lossless characteristic impedance (real)</td></tr>
<tr><td colspan="2">$Z_{0n1} = Z_0/Z_{0sp}$</td><td>1st normalized characteristic impedance</td></tr>
<tr><td colspan="2">$Z_{0n2} = Z_0/\lvert Z_0\rvert$</td><td>2nd normalized characteristic impedance</td></tr>
<tr><td colspan="2">$\gamma = \sqrt{(R + j\omega L)(G + j\omega C)} = \alpha + j\beta$</td><td>Propagation constant (complex)</td></tr>
<tr><td colspan="2">$\{{}^{\alpha}_{\beta}\} = \frac{1}{\sqrt{2}}\sqrt{\sqrt{(R^2 + \omega^2 L^2)(G^2 + \omega^2 C^2)} \pm (RG - \omega^2 LC)}$</td><td>Attenuation and phase constants</td></tr>
<tr><td colspan="2">$\gamma_{bp} = \alpha_{bp} + j\beta_{bp} = [R/2Z_{0sp} + GZ_{0sp}/2] + j\omega\sqrt{LC}$</td><td>Propagation constant (low losses approximation)</td></tr>
<tr><td colspan="2">$\gamma_{sp} = j\beta_{sp} = j\omega\sqrt{LC}\ (R = G = 0)$</td><td>Lossless propagation constant (purely imaginary)</td></tr>
<tr><td colspan="2">$\gamma_{n1} = \gamma/\beta_{sp}$</td><td>1st normalized propagation constant</td></tr>
<tr><td colspan="2">$\gamma_{n2} = \gamma/\alpha_{bp}$</td><td>2nd normalized propagation constant</td></tr>
<tr><td colspan="3">Generalization parameters</td></tr>
<tr><td>$r = \frac{R}{\omega L}$</td><td>$g = \frac{G}{\omega C}$</td><td>$c = \frac{r}{g} = \frac{R/L}{G/C} = \frac{1}{Z_{0sp}^2}\frac{R}{G}$</td></tr>
</table>

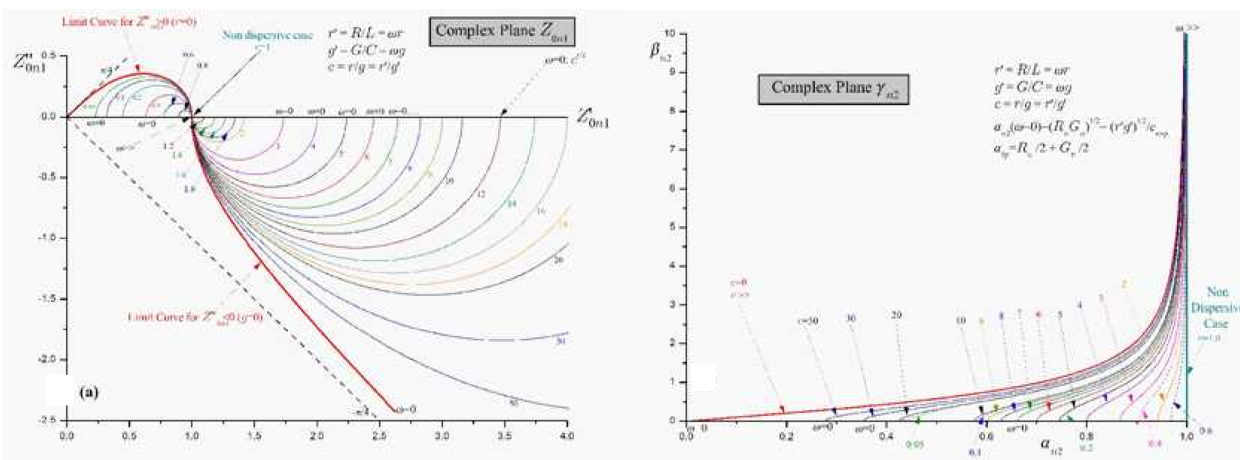

(a) (b)

Figure 3: Frequency parameterizations of the complex planes Z_{0n1} and γ_{n2} in terms of c.

2.1. Basic TL Parameters

Table 1 summarizes the most important expressions, generalization parameters and normalizations concerning the analysis of the basic parameters in the CTLT. The complex analysis of the basic parameters may be summarized as follows (recalling that all the analytical expressions may be found in [4]).

2.1.1. Fixed Frequency Analyses

these analyses are of special interest because they allow to understand the physical behavior of the TL with respect to the lossless case. The analytical curves obtained from this analyses are shown in Fig. 2 by considering the normalized complex planes Z_{0n1} and γ_{n1} parameterized in terms of r and g.

2.1.2. Frequency Analyses

In this case, the universal curves are obtained by considering the normalized planes Z_{0n1} and γ_{n2} as shown in Fig. 3 — notice that the last one has to be normalized with respect to the attenuation constant under low-losses approximation — and the parameterizations are performed in terms of c. For instance, the value $c = r/g = 1$ identifies the non-dispersive case (lossy TL's with characteristic impedance and phase constant equal to those in the ideal lossless case).

2.2. Wave Parameters

Based on the behavior of the basic parameters, it is possible to study the relationships among wave parameters seen as complex transformations. This will result in the parameterization of certain curves of interest in the wave parameters complex planes; for instance, the usual Smith chart, [5], is simply the transformation of the curves $\mathrm{Re}\{Z_n\} = \mathrm{cte} = a \in [0, \infty)$ and $\mathrm{Im}\{Z_n\} = \mathrm{cte} = b \in (-\infty, \infty)$ into the complex ρ-plane for the lossless case. The parameterization of these curves in the ρ-plane is given by functions that depend on $\rho' = \mathrm{Re}\{\rho\}$, $\rho'' = \mathrm{Im}\{\rho\}$, and the constants a and b. These curves may be represented by using the notation $h_{Za}(\rho', \rho''; a)$ and $h_{Zb}(\rho', \rho''; b)$. The generalization of this procedure applied to the lossy case leads to the results summarized in Table 2. Note that all the parameterizations in Table 2 are described by analytical circumferences. As an example, we can highlight the parameterization that leads to the *Generalized Smith chart*, [6], described by the following pair of equations,

$$Z_n' = a : h_{Za}(\rho', \rho''; a) \to \left(\rho' - \tfrac{a}{a+c_0}\right)^2 + \left(\rho'' + \tfrac{s_0}{a+c_0}\right)^2 = \left(\tfrac{1}{a+c_0}\right)^2, \tag{1}$$

$$Z_n'' = b : h_{Zb}(\rho', \rho''; b) \to \left(\rho' - \tfrac{b}{b+s_0}\right)^2 + \left(\rho'' - \tfrac{c_0}{b+s_0}\right)^2 = \left(\tfrac{1}{b+s_0}\right)^2. \tag{2}$$

Notice that all the curves depend on the phase of Z_0. Fig. 4 shows an example for all the TL's with $\varphi_{Z0} = 20°$.

3. AN EXAMPLE OF THE APPLICATION OF THE CTLT

Using the graphical parameterizations arising from the CTLT, it is possible to *geometrically* analyze a large number of interesting problems. One of these examples is summarized in this section. The problem consists on studying analytically which are the possible values of the reflection coefficient at the load, ρ_L, when the losses on the dielectrics and/or the conductors vary. Fig. 5 shows the particular example of the geometrical location of ρ_L when the losses in the dielectric -represented by parameter g-increases (this study implies that parameter $r = 0$). The scheme shows how the values of ρ_L may be analytically obtained by a geometrical construction which implies the *generalized Smith chart* among other parameterizations summarized in Table 2. The analytical curves obtained from the geometrical construction are not included here due to size restrictions but they can be obtained from the authors and some publications under preparation. Notice also that the physical implications of losses just become evident from this point of view.

Table 2: Definition and normalizations of the wave parameters in the CTLT.

$\varphi_{Z_0} \in \left(\frac{-\pi}{4}, \frac{\pi}{4}\right)$	$c_0 = \cos(\varphi_{Z_0})$	$s_0 = \sin(\varphi_{Z_0})$
Normalized impedance plane	Normalized admittance plane	Reflection coefficient plane
$Z_n = \frac{Z}{\lvert Z_0\rvert} = e^{j\varphi_{Z_0}} \frac{1+\rho}{1-\rho}$	$Y_n = \frac{Y}{\lvert Y_0\rvert} = e^{-j\varphi_{Z_0}} \frac{1-\rho}{1+\rho}$	ρ
$Z_n' = a \in [0, \infty)$	$g_{Z_a}(Y_n', Y_n''; a; s_0, c_0)$	$h_{Z_a}(\rho', \rho''; a; s_0, c_0)$
$Z_n'' = b \in (-\infty, \infty)$	$g_{Z_b}(Y_n', Y_n''; b; s_0, c_0)$	$h_{Z_b}(\rho', \rho''; b; s_0, c_0)$
$\lvert Z_n\rvert = m \in [0, \infty)$	$g_{Z_m}(Y_n', Y_n''; m; s_0, c_0)$	$h_{Z_m}(\rho', \rho''; m; s_0, c_0)$
$\varphi_{Z_n} = p \in [-\pi/2, \pi/2]$	$g_{Z_p}(Y_n', Y_n''; p; s_0, c_0)$	$h_{Z_m}(\rho', \rho''; p; s_0, c_0)$
$f_{Y_a}(Z_n', Z_n''; a; s_0, c_0)$	$Y_n' = a \in [0, \infty)$	$h_{Y_a}(\rho', \rho''; a; s_0, c_0)$
$f_{Y_b}(Z_n', Z_n''; b; s_0, c_0)$	$Y_n'' = b \in (-\infty, \infty)$	$h_{Y_b}(\rho', \rho''; b; s_0, c_0)$
$f_{Y_m}(Z_n', Z_n''; m; s_0, c_0)$	$\lvert Y_n\rvert = m \in [0, \infty)$	$h_{Y_m}(\rho', \rho''; m; s_0, c_0)$
$f_{Y_p}(Z_n', Z_n''; p; s_0, c_0)$	$\varphi_{Y_n} = p \in [-\pi/2, \pi/2]$	$h_{Y_p}(\rho', \rho''; p; s_0, c_0)$
$f_{\rho_a}(Z_n', Z_n''; a; s_0, c_0)$	$g_{\rho_a}(Y_n', Y_n''; a; s_0, c_0)$	$\rho' = a \in \left[\frac{-1}{c_0}, \frac{1}{c_0}\right]$
$f_{\rho_b}(Z_n', Z_n''; b; s_0, c_0)$	$g_{\rho_b}(Y_n', Y_n''; b; s_0, c_0)$	$\rho'' = b \in \left[\frac{-c_0}{1-s_0}, \frac{c_0}{1+s_0}\right]$
$f_{\rho_m}(Z_n', Z_n''; m; s_0, c_0)$	$g_{\rho_m}(Y_n', Y_n''; m; s_0, c_0)$	$\lvert\rho\rvert = m \in \left[0, \frac{c_0}{1 \mp s_0 \mathrm{sgn}(\varphi_{Z_0})}\right]$
$f_{\rho_p}(Z_n', Z_n''; p; s_0, c_0)$	$g_{\rho_p}(Y_n', Y_n''; p; s_0, c_0)$	$\varphi_\rho = p \in (-\pi, \pi]$

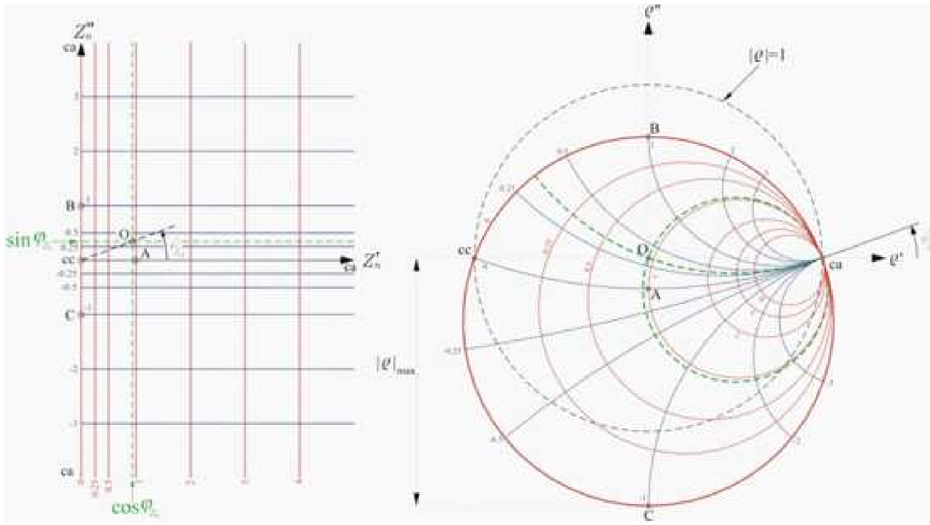

Figure 4: Generalized Smith chart for lossy TL's with $\varphi_{Z0} = 20°$. This complex parameterization corresponds to the one summarized in the shaded cells of Table 2.

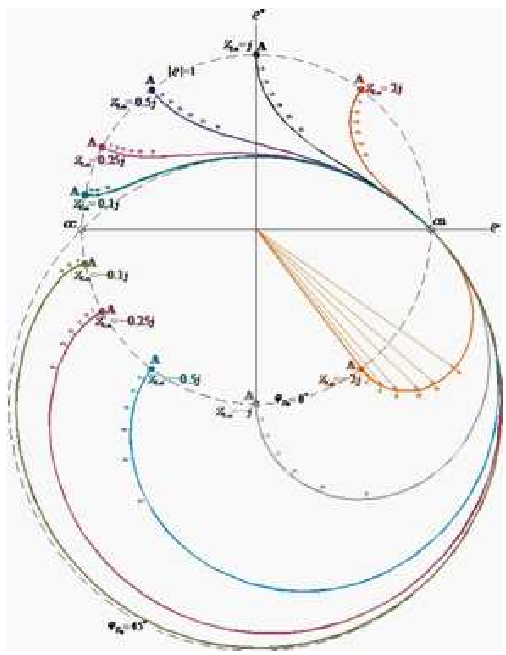

Figure 5: Geometrical parameterization of ρ_L with $r = 0$ and varying g.

4. CONCLUSIONS

The complex analysis methodology outlined in this paper allows a clear and intuitive way to generalize the analysis of the lossy TL's. The most important aspects to detach can be summarized as follows: (i) the graphical-analytical parameterizations under the CTLT, (ii) the possibility of obtaining analytical solutions by geometrical means, and (iii) the physical prediction capabilities associated to the CTLT and their application in the design of high-frequency circuits, for instance. Finally, it is important to remark that the CTLT is currently being completed by analyzing new problems, identifying mathematical explicit curves associated to the actual ones and its possible extension to real guided-wave problems.

ACKNOWLEDGMENT

This work has been supported by the Ministerio de Ciencia e Innovacion of Spain/FEDER under project TEC2011-24492 and by the Gobierno del Principado de Asturias (PCTI) FEDER-FSE under project PC10-06.

REFERENCES

1. Cheng, D. K., *Field and Wave Electromagnetics*, Addison-Wesley Publishing Company, 1989.
2. Pozar, D. M., *Microwave Engineering*, Addison-Wesley Publishing Company, 1990.
3. Collin, R. E., *Foundations for Microwave Engineering*, McGraw-Hill International Editions, 1992.
4. Gago-Ribas, E., *Complex Transmission Line Analysis Handbook*, Vol GWI of the *Electromagnetics & Signal Theory Notebooks Series*, GR Editores, Leon, Spain, 2001 (www.greditores.com).
5. Smith, P. H., "An improved transmission-line calculator," *Electronics*, Vol. 17, 130, January 1944.
6. Gago-Ribas, E., C. D. Martinez, and M. J. G. Morales, "Complex analysis of the lossy-transmission line theory: A generalized Smith Chart", *Turkish Journal of Electrical Engineering & Computer Sciences*, Vol. 14, No. 1, 173–194, Elektrik, Special Issue on *Electrical and Computer Engineering Education in the 21st Century*, Issues, Perspectives and Challenges, Turkey, 2006.

Channel Base Current Effects on the Magnetic Flux Density Waveshape Associated with Vertical Lightning Channel

M. Izadi, M. Z. A Ab Kadir, C. Gomes, and W. F. Wan Ahmad
Centre of Excellence on Lightning Protection (CELP), Faculty of Engineering
Universiti Putra Malaysia, UPM, Serdang, Selangor 43400, Malaysia

Abstract— The electromagnetic fields due to lightning channel are considered as effective factors to induce voltage on the power systems. The shape of electromagnetic wave associated with lightning channel depends highly on return stroke current wave shape and the parameters of lightning channel and its geometry. This paper considered on the relation between channel base current parameters based on Heidler function as a realistic current function and the wave shapes of magnetic flux density. Furthermore, some general functions were proposed by considering their effects The results showed that the proposed equations are in very good agreement with the calculated values using direct methods They could also predict the magnetic flux wave shapes versus different channel base current parameters under similar geometrical and lightning channel conditions. The estimated magnetic flux density waveshapes can be applied to Rachidi model for evaluation of the induced voltage due to indirect strike.

1. INTRODUCTION

The indirect effect of lightning on the power lines can be contemplated as an appealing issue on insulation level of power systems. In a situation when lightning strikes the ground surface [1]or any tall objective case [2], the electromagnetic fields generated by lightning channel will be propagated on the air by the speed of light. Therefore, by coupling between electromagnetic fields and power systems, the induced voltage will be created [3, 4] Accordingly, the electromagnetic fields associated with lightning channel would be an interesting objective for predicting and protecting the lightning induced voltages. Several methods are considered for the calculation of electromagnetic fields due to lightning channel in the time [5] and Fourier domains [1], but in all of them the channel current is the source of field. The channel current can be categorized into two parts: the channel base current and the current along lightning channel. The first part can be simulated by channel base current functions. The most important channel base current functions can be expressed by the Bruce and Golde function [6], the Pierce and Cianos function [7] and Heidler function [8] Whereas, the current along lightning channel can be predicted by four important current models as follows [9]: the Gas-Dynamic models, the Current distributed models, the Electromagnetic models and the Engineering models Therefore, the electromagnetic fields due to lightning channel are directly related to the channel base current function and current models. Moreover, in order to propose the general equations for the prediction of the magnetic flux density waveshapes versus channel base current parameters changes, the relation between parameters of magnetic flux density waves shape and the parameters of channel base current function should be considered. The predicted magnetic flux density waveshape can be applied into the Rachidi's coupling model [10] for the estimation of lightning induced voltage (will not be considered in this study). This study focuses on the Hiedler current function as a realistic channel base current function. The Modified Transmission Line Exponential decay model (MTLE) as a branch of engineering models [1] is applied in the present study as well The basic assumptions in this study are expressed, i.e., the lightning channel is perpendicular on the ground surface, the ground conductivity is infinity and the observation point is located above the ground surface

2. RETURN STROKE CURRENT

Several functions are taken into account for the channel base current. The widely used functions can be expressed by the Bruce and Golde [6] function, Pierce and Cianos [7] function and the Heidler function [8]. The Bruce and Golde function and the Pierce and Cianos function have an issue of accuracy due to the derivative of current with respect to time, i.e., non-zero value at time equal to zero although this factor (di/dt) is very much affected in calculating the electromagnetic fields. It should be noted that, the Heidler current function has been extended into two current functions proposed by Diendorfer-Uman [11] and Nucci [12], respectively. However the focus of

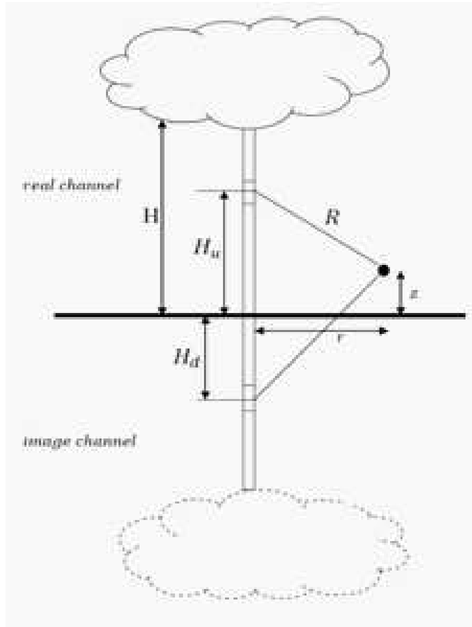

Figure 1: The geometry of lightning channel.

this study is on using the original Heidler current function as expressed by Equation (1) where $\eta = \exp[-(\Gamma_1/\Gamma_2)(n\frac{\Gamma_2}{\Gamma_1})^{\frac{1}{n}}]$.

$$I\left(0,t\right)=\frac{I_0}{\eta}\frac{\left(\frac{t}{\Gamma_1}\right)^n}{1+\left(\frac{t}{\Gamma_1}\right)^n}\exp\left(\frac{-t}{\Gamma_2}\right) \tag{1}$$

In addition, different engineering current models are considered on the current wave shape along lightning channel. The engineering current models can be classified into two parts: the current generation models (CG) and the current propagation models (CP) [13] In the current generation models, it is assumed that the source of current travels upward along lightning channel and the downward current is injected along lightning channel. Whilst in the current propagation models, the source of current and the lightning channel are assumed to be at the channel base on the ground surface resembling a transmission line In this study, the MTLE current model based on CP current group is used as presented by Equation (2) where z' is the temporary charge height along lightning channel; $I(z',t)$ is the return stroke current at height of z' along the lightning channel; $I(0,t)$ is the return stroke current at channel base; v is the return stroke current velocity; c is the speed in open space; λ is a constant factor that is typically 2000 m [1].

$$i(z',t) = i(0,t - z'/v)\exp(-z'/\lambda) \tag{2}$$

3. LIGHTNING ELECTROMAGNETIC FIELD

The electromagnetic fields due to lightning channel can be estimated by the dipole method. The electromagnetic field's components associated with a vertical lighting channel based on geometry of problem from Figure 1 can be obtained from Equations (3), (4) and (5) [14] for vertical and horizontal electric fields and magnetic flux density, respectively where $R = \sqrt{r^2{+}(z{-}z')^2}E_z(r,z,t)$ is vertical electric field, $E_r(r,z,t)$ is the horizontal electric field, $B_\varphi(r,z,t)$ is the magnetic flux density, z is height of observation point, z' is the vertical space variable, $\varepsilon_0{=}\ 8.85{\times}10^{-12}$, $\mu_0 = 4\pi \times 10^{-7}$, $\beta = v/c$, $\chi = \sqrt{\frac{1}{1-\beta^2}}$, $A1 = \sqrt{(\beta ct - z)^2 + (\frac{r}{\chi})^2}$, $A2 = \sqrt{(\beta ct + z)^2 + (\frac{r}{\chi})^2}$, $H_u = \beta\chi^2\{-(\beta z - ct) - A1\}$, $H_d = -\beta\chi^2\{-(\beta z + ct) + A2\}$. This study assumes that the ground conductivity is perfect. It is important to mentioned, all electromagnetic fields in the time less than $R(z'=0)/c$ are equal to zero [5]

$$E_z(r,z,t) = \left(\frac{1}{4\pi\varepsilon_0}\right)\int_{H_d}^{H_u}\left(\frac{2(z-z')^2-r^2}{R^5}\int_0^t i\left(z',\tau-\frac{R}{c}\right)d\tau + \frac{2(z-z')^2-r^2}{cR^4} i\left(z',t-\frac{R}{c}\right) - \frac{r^2}{c^2R^3}\frac{\partial i\left(z',t-\frac{R}{c}\right)}{\partial t}\right)dz' \quad (3)$$

$$E_r(r,z,t) = \left(\frac{1}{4\pi\varepsilon_0}\right)\int_{H_d}^{H_u}\left(\frac{3r(z-z')}{R^5}\int_0^t i\left(z',\tau-\frac{R}{c}\right)d\tau + \frac{3r(z-z')}{cR^4} i\left(z',t-\frac{R}{c}\right) - \frac{r(z-z')}{c^2R^3}\frac{\partial i\left(z',t-\frac{R}{c}\right)}{\partial t}\right)dz' \quad (4)$$

$$B_\varphi(r,z,t) = \left(\frac{\mu_0}{4\pi}\right)\int_{H_d}^{H_u}\left(\frac{r}{R^3} i\left(z',t-\frac{R}{c}\right) + \frac{r}{cR^2}\frac{\partial i\left(z',t-\frac{R}{c}\right)}{\partial t}\right)dz' \quad (5)$$

4. MAGNETIC FIELD BEHAVIOR AGAINST CURRENT FUNCTION PARAMETERS

The magnetic flux density wave shape can be characterized using four important parameters such as: $B_{\max}$, $t_{\max}$, $t_{50\%-50\%}$, $t_{10\%-90\%}$ as shown in Figure 2 where $B_{\max}$, $t_{\max}$ consider the maximum value of magnetic flux density and the relevant time, respectively; $t_{50\%-50\%}$ expresses the time period between two point with $\frac{B_{\max}}{2}$ value on the magnetic flux density wave shape and $t_{10\%-90\%}$ considers on the time period between two points with values of $0.1B_{\max}$ and $0.9B_{\max}$ on the magnetic flux density wave shape [15]. Note that, the current parameters in Figure 2 are obtained from Table 1 [8, 16] and return stroke current velocity is set on the 1×10^8 m/s, while the observation point is located at ground surface with 100 m distance from lightning channel and the MTLE model with $\lambda = 1500$ m is used for current model.

The behavior of magnetic flux density parameters versus Γ_1 changes (in the return stroke current function) is investigated and the results are tabulated in Table 2 while the current parameters are obtained from Table 1 (excluded Γ_1) and the channel and the observation point parameters are set

Table 1: Return stroke current parameters based on Heidler function.

I_0 (kA)	Γ_1 (µs)	Γ_1 (µs)
11	0.072	30

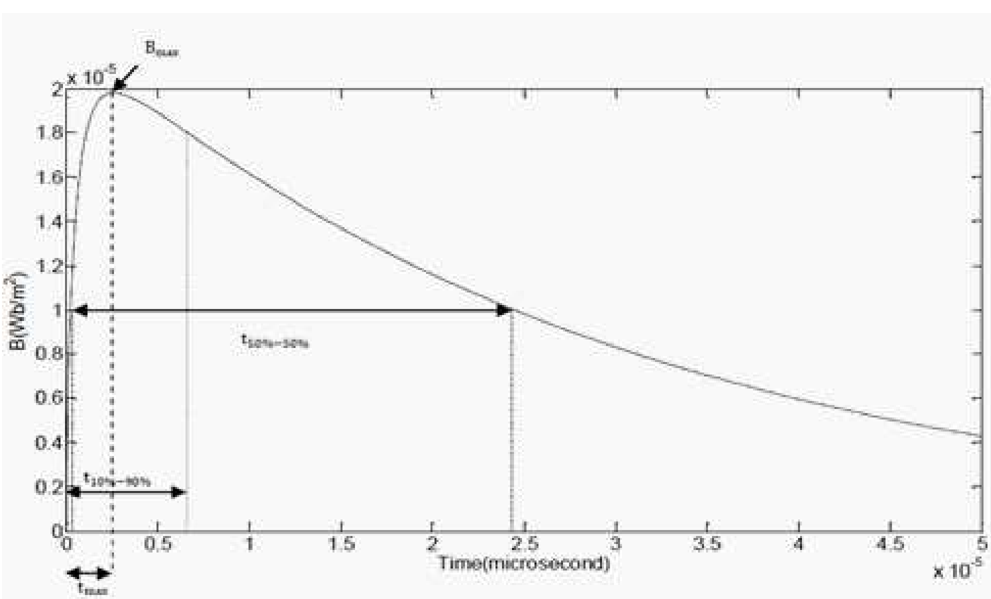

Figure 2: Characterization of magnetic flux density wave shape.

Table 2: The proposed fitness functions for Γ_1 changes in current function.

Fitness function	P_1	P_2	P_3	P_4	P_5
$B_{\max} = P_1 \times \Gamma_1^{P_2}$	3.31×10^{-5}	0.03107	-	-	-
$t_{\max} = P_1\Gamma_1^4 + P_2\Gamma_1^3 + P_3\Gamma_1^2 + P_4\Gamma_1 + P_5$	4.288×10^{18}	-1.225×10^{13}	1.126×10^{7}	-1.145	2.693×10^{-6}
$t_{50\%-50\%} = P_1\Gamma_1^3 + P_2\Gamma_1^2 + P_3\Gamma_1 + P_4$	-8.88×10^{12}	1.577×10^{7}	-4.212	2.477×10^{-5}	-
$t_{10\%-90\%} = P_1\Gamma_1^4 + P_2\Gamma_1^3 + P_3\Gamma_1^2 + P_4\Gamma_1 + P_5$	3.533×10^{18}	-9.839×10^{12}	9.031×10^{6}	-1.988	1.109×10^{-6}

Table 3: The proposed fitness functions for Γ_2 changes in current function.

Fitness function	P_1	P_2	P_3	P_4
$B_{\max} = P_1\Gamma_2^3 + P_2\Gamma_2^2 + P_3\Gamma_2 + P_4$	1.683×10^{7}	-2675	0.1468	1.738×10^{-5}
$t_{\max} = P_1 \times \Gamma_2^{P_2}$	0.0001071	0.3576	-	-
$t_{50\%-50\%} = P_1\Gamma_2 + P_2$	0.7271	2.498×10^{-6}	-	-
$t_{10\%-90\%} = P_1\Gamma_2^2 + P_2\Gamma_2 + P_3$	-133.5	0.01639	6.047×10^{-7}	-

Table 4: The proposed fitness function for I_0 changes in current function.

Fitness function	P_1	P_2
$B_{\max} = P_1 I_0 + P_2$	1.801×10^{-9}	-1.113×10^{-9}

with similar condition as in Figure 2 Therefore, the general functions that took into account the variations of those four important parameters of the magnetic flux wave and Γ_1 are proposed and listed in Table 2, together with the value of coefficients for each general functions derived.

On the other hand, the effect Γ_2 on the parameters of magnetic flux density wave shape can be considered using Table 3 whereby when the current parameters (excluded Γ_2) are applied from Table 1 other channel and observation point parameters will be similar to the plot in Figure 2.

In addition, effects of I_0 parameter on the magnetic flux density parameters are also considered in this study. Therefore, the fitness function and related constant coefficients for I_0 that affect on the $B_{\max}$ values are indicated in Table 4. It shows that the fitness function of $B_{\max}$ versus I_0 changes has a linear trend.

The proposed fitness functions can easily predict the magnetic flux density wave shapes versus different channel base current parameters. Also, the results illustrated that all current parameters are affected on the maximum value of magnetic flux density. The reflection on different magnetic flux density wave shapes due to different channel base current parameters can be valuable information for electrical power designers in checking insulation coordination of power lines under different current conditions in order to set an appropriate protection level for the line. Note that, the magnetic flux density obtained can easily be used for the estimation of lightning induced voltage on the lines using Rachidi model [10].

5. CONCLUSION

In this study, the most important channel base current functions and different engineering current models were considered. The magnetic flux density wave shape was characterized and the channel base current parameters that affect on the magnetic flux density wave shape were investigated with the use of the Heidler current function and MTLE current model. The results demonstrated a good conformity between the proposed fitness functions and the calculated values for the fast determination of magnetic flux density wave shapes and lightning induced voltages using Rachidi model against different current parameters.

REFERENCES

1. Nucci, C. A., "Lightning-induced voltages on overhead power lines. Part I: Return stroke current models with specified channel-base current for the evaluation of the return stroke

electromagnetic fields," *Electra*, Vol. 161, 75–102, 1995.

2. Mossadeghi, A., A. Shoory, and F. Rachidi, "Lightning electromagnetic fields at very closed distances assosiated with lightning strikes to the Gaisberg tower," *Journal of Geophysical Research*, Vol. 115, 2010.
3. Borghetti, A., A. Morched, F. Napolitano, C. Nucci, and M. Paolone, "Lightning-induced overvoltages transferred through distribution power transformers," *IEEE Transactions on Power Delivery*, Vol. 24, No. 1, 360–372, 2009.
4. Nucci, C. A., "Lightning-induced voltages on overhead power lines. Part II: Coupling models for the evaluation of the induced voltages," *Electra*, Vol. 162, 121–145, 1995.
5. Izadi, M., M. Z. A. Ab Kadir, C. Gomes, and W. F. W. Ahmad, "An analytical second-FDTD method for evaluation of electric and magnetic fields at intermediate distances from lightning channel," *Progress In Electromagnetics Research*, Vol. 110, 329–352, 2010.
6. Bruce, C. and R. Golde, *The Lightning Discharge*, Vol. 2, 88, Inst. Elect. Eng.-Pt., 1941.
7. Pierce, E., "Triggered lightning and some unsuspected lightning hazards (Lightning triggered by man and lightning hazards)," *ONR Naval Res. Rev.*, Vol. 25, No. 3, 1972.
8. Heidler, F., "Analytische Blitzstromfunktion zur LEMP-Berechnung," *18th ICLP 1985*, 63–66, Munich, Germany, 1985.
9. Delfino, F., R. Procopio, and M. Rossi, "Lightning channel-base current identification as solution of a volterra-like integral equation," *Open Atmospheric Science Journal*, Vol. 2, 160–165, 2008.
10. Rachidi, F., "Formulation of the field-to-transmission line coupling equations interms of magnetic excitation field," *IEEE Transactions on Electromagnetic Compatibility*, Vol. 35, No. 3, 404–407, 1993.
11. Diendorfer, G. and M. Uman, "An improved return stroke model with specified channel-base current," *Journal of Geophysical Research-Atmospheres*, Vol. 95, 13, 621–13, 644, 1990.
12. Nucci, C., G. Dindorfer, M. Uman, F. Rachidi, and C. Mazzetti, "Lightning return-stroke models with channel-base specified current: A review and comparison," *Journal of Geophysical Research*, Vol. 95, No. D12, 20395–20408, 1990.
13. Cooray, V., *The Lightning Flash*, Vol. 34, IET, 2003.
14. Izadi, M. and M. Z. A. Kadir, "New algorithm for evaluation of electric fields due to indirect lightning strike," *Computer Modeling in Engineering & Sciences*, Vol. 67, 1–12, 2010.
15. Jerauld, J., M. Uman, V. Rakov, K. Rambo, et al., "Electric and magnetic fields and field derivatives from lightning stepped leaders and first return strokes measured at distances from 100 to 1000 m," *J. Geophys. Res.*, Vol. 113, 2008.
16. Rakov, V. and M. Uman, "Review and evaluation of lightning return stroke models including some aspects of their application," *IEEE Transactions on Electromagnetic Compatibility*, Vol. 40, No. 4, 403–426, 1998.

Optical Classification and the Absorption Character of Inland Entrophic Water in China

Yunmei Li[1], **Qiao Wang**[2], **Heng Lu**[1], **Jiazhu Huang**[1], **Chuanqing Wu**[2], **and Li Zhu**[2]

[1]Key Laboratory of Virtual Geographic Environment, Nanjing Normal University
Ministry of Education, Nanjing 210046, China
[2]Satellite Environment Application Center
Ministry of Environmental Protection, Beijing 100029, China

Abstract— Optical property of inland eutrophic water varies spatially and temporally corresponding to change of concentrations of water components. The same water type classified by optical property may have uniform character which may make water components deriving algorithm simpler and accuracy. Our purpose of this study is to elaborate water type classification scheme for inland eutrophic waters according above water reflectance, and compare the difference of absorption properties between different water types. Field measurements were carried out in August 2006, November 2006, 2007 and 2008, April, June, July and September 2009 in Taihu Lake, Chaohu Lake, Dianchi Lake and Sanxia Gorges Reservoir (China). The waters were classified into six optical water types (type A, B, C, D, E and F) by comparing peak and trough of remote sensing reflectance (R_{rs}) between 500–750 nm. All of the samples in Dianchi Lake belong to type A water, while other water bodies have several types at the same time. When parameterized a_{CDOM} and a_{NAP} by power function, the slope of CDOM S_{CDOM} could be clustered into two groups, i.e., one group for type A and one for type B, C, D, E and F; there is no significant difference of S_{NAP} between different water types. Absorption coefficients of phytoplankton were calculated by absorption coefficient of 440 nm and 675 nm using quadratic function and the coefficients varied in different water types.

1. INTRODUCTION

Nowadays, the reflectance spectrum is widely used for evaluating water quality, such as estimating chlorophyll, suspended matter, Secchi depth, and turbidity of the water. Numerous models on water components inversing have been put forward for different regions. Different models are necessary because remote sensing algorithms have local and seasonal characteristics, and the algorithms, developed for certain water bodies cannot be used for other waters [6]. Optical property of inland eutrophic water is complex because it is strongly affected by terrigenous inputs. That also makes the relationship between remote sensing information and water component concentration such as chlorophyll a concentration, CDOM, etc. uncertainty in different water bodies, and sometime even in the same water body. If inland eutrophic waters can be identified to some typical water types and these types have approximately stability optical properties, then more stable correlation between remote sensing information and optical constituents can be built. This will be significant for increasing evaluation accuracy of water components. In this paper, we investigated four different eutrophic water bodies in China, i.e., Taihu Lake, Chaohu Lake, Dianchi Lake and Sanxia Gorges Reservoir. Our purpose is to elaborate water type classification scheme for inland eutrophic waters by above water reflectance, and compare their absorption properties hoping that we can develop water constituents' deriving algorithm based on the classification in future.

2. MATERIAL AND METHODS

2.1. Study Area

In situ investigations were conducted in four eutrophic water bodies of China, i.e., Taihu Lake, Chaohu Lake, Dianchi Lake and Sanxia Gorges Reservoir. Both Taihu Lake and Chaohu Lake are among five major freshwater lakes located in east of China. Taihu Lake has a water area of 2338 km^2 and an average depth of about 1.9 m located between 30°56′–31°33′N and 119°53′–120°36′E; Chaohu Lake is deeper and smaller than Taihu Lake with average depth of 3 m and water area of 760 km^2 located between 30°28′–31°43′N and 117°16′–117°51′E. Dianchi Lake is the sixth freshwater lake located in west-east of China (24°40′–25°02′N and 102°36′–102°47′E). It has an average depth of 5.12 m and a water area of 294 km^2. Since 1980s, with rapid developing economy, water eutrophication has becoming a serious environmental problem in these three lakes with annually blooming algae. After the building of Sanxia Dam in 2006, water quality has been arousing attention with algal blooming in recent years. The Dam transferred about 640 km length of Yangzhi River to a huge gorge which may bring out new ecological problem. So that the water environment of these four eutrophic waters have been becoming the focus of much attention in China.

2.2. In Situ Measurements

The in situ experiments were conducted on August 16–17, 2006, October 24–November 4, 2006, November 8–21, 2007, November 10–21, 2008, April 17–28, 2009 for Taihu Lake (usually more than 60 sample stations were measured, but just 15 sample stations of Meiliang Bay in north part of Taihu Lake were measured in August 2006), June 13–16 for Chaohu Lake (32 sample stations), September 19–20 for Dianchi Lake (25 sample stations) and July 22–24 for Sanxia Gorges Reservoir (25 sample stations). At last, the total of 333 samples were used in this paper eliminating those presented the same reflectance spectra as plant because of thick alga floating.

Water samples and reflectance measurements were collected between 10:00 and 14:00 h local time and when wind speed was lower than 5 m/s. Surface water samples (2.5 L) were collected at a depth of 0.5 m below the surface immediately after reflectance measurement. Then the samples were stored in a cooler with ice in the dark, and taken back to the laboratory for analyzing concentration and absorption coefficient at the end of the day.

3. RESULTS

3.1. R_{rs} Character of Different Classes

The waters were classified into 6 types according to measured R_{rs}. The four inland waters have different types (Table 1).

3.2. Absorption Character of Different Classes

Remote sensing reflectance of water surface is strongly influenced by absorption and back scattering of water body [4, 7]. So that absorption properties of water components are greater contributors to surface reflectance. Water absorption is generally subdivided into four additive components [1, 2, 8, 9], i.e., absorption coefficients of pure water (a_w), CDOM (a_{CDOM}), phytoplankton (a_{ph}), NAP (a_{NAP}) and particulate (a_p).

Contributions of pure water, non-pigment, phytoplankton and CDOM to water absorption are shown in Figure 1. In type A, phytoplankton is always dominant factor of absorption, then the non-algal particulate. The latter has greatest contribution from 400 nm to 550 nm in type B, C, D, E and F waters.

3.3. Absorption Coefficients Parameterization for Different Classes

3.3.1. CDOM Absorption Coefficients Parameterization

CDOM absorption coefficient can be parameterized by formula (1).

$$a_{\mathrm{CDOM}}(\lambda) = a_{\mathrm{CDOM}}(\lambda_0) \exp[S_{\mathrm{CDOM}}(\lambda_0 - \lambda)] \tag{1}$$

where $a_{\mathrm{CDOM}}(\lambda)$ is the CDOM absorption coefficient at wavelength λ (m^{-1}); λ_0 is the reference wavelength (nm), often 440 nm; S_{CDOM} is the spectral slope of the $a_{\mathrm{CDOM}}(\lambda)$ spectrum (nm^{-1}), and the mean values in type A, B, C, D, E and F are $(0.0109 \pm 0.0004)\,\mathrm{nm}^{-1}$, $(0.0155 \pm 0.0013)\,\mathrm{nm}^{-1}$,

Table 1: Proportion of water classification in different water bodies/%.

Water body / Water type	Dianchi Lake (Sep. 2009)	Chaohu Lake (Jun. 2009)	Taihu Lake (Aug. 2006)	Taihu Lake (Nov. 2006)	Taihu Lake (Nov. 2007)	Taihu Lake (Nov. 2008)	Taihu Lake (Apr. 2009)	Sanxia Gouges Reservoir (Jul. 2009)
A	100	23	92	20	10	6	6	0
B	0	26	0	3	0	6	0	0
C	0	32	0	55	42	38	40	17
D	0	19	8	14	38	28	16	0
E	0	0	0	8	10	21	34	37
F	0	0	0	0	0	1	4	46

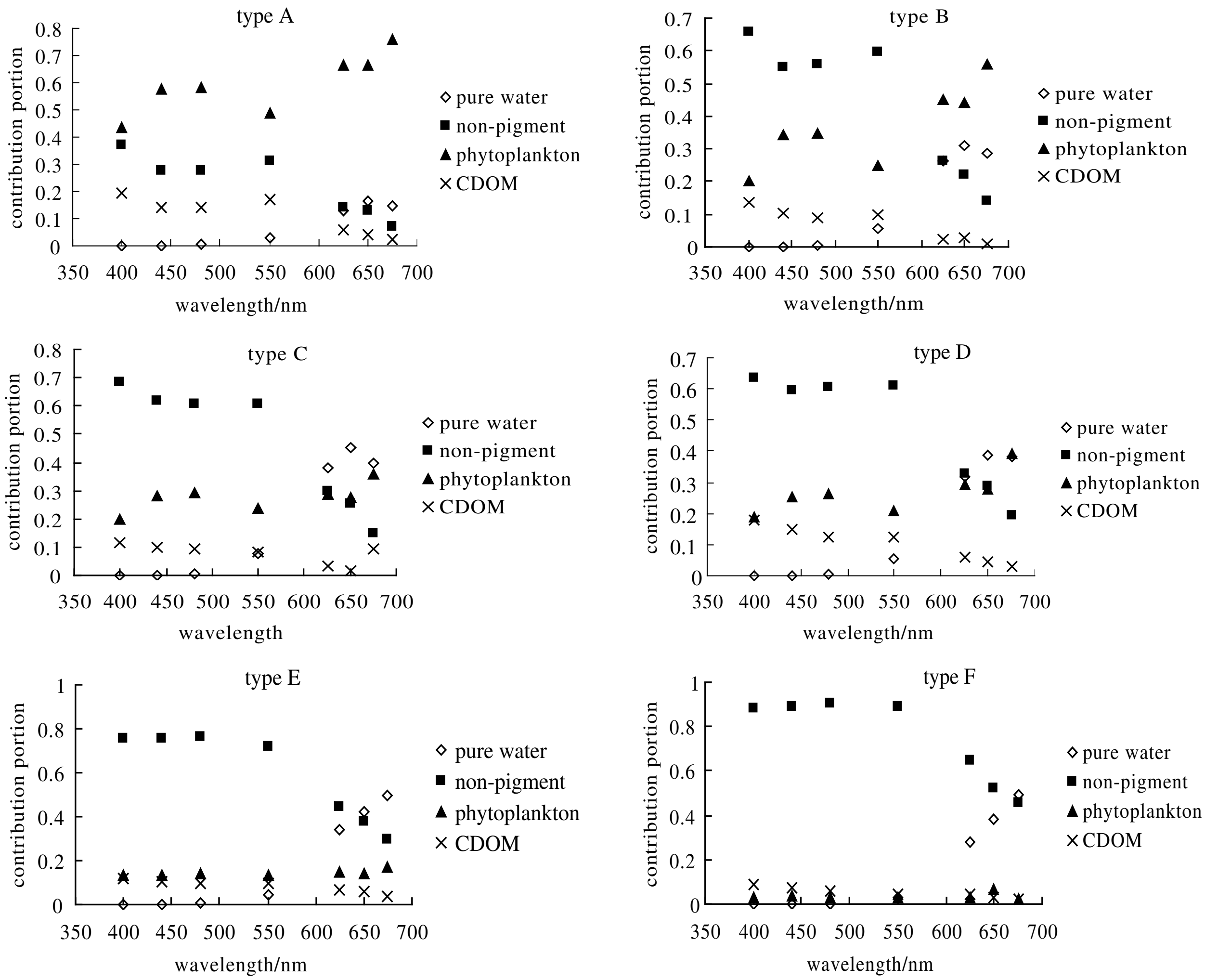

Figure 1: Absorption contributions of pure water, CDOM, NAP and phytoplankton in different water types.

$(0.0143 \pm 0.0003)\,\text{nm}^{-1}$, $(0.0146 \pm 0.0007)\,\text{nm}^{-1}$, $(0.0128 \pm 0.0007)\,\text{nm}^{-1}$ and $(0.0151 \pm 0.0010)\,\text{nm}^{-1}$, respectively.

3.3.2. Non-pigment Particulate Absorption Coefficient Parameterization

The NAP absorption spectra are similar to those of CDOM, which suggests that these two components may share some common chromophores [1]. The following expression is often fitted to the $a_{\text{NAP}}(\lambda)$ spectra:

$$a_{\text{NAP}}(\lambda) = a_{\text{NAP}}(\lambda_0) \exp[S_{\text{NAP}}(\lambda_0 - \lambda)] \tag{2}$$

where $a_{\text{NAP}}(\lambda)$ is the NAP absorption coefficient at wavelength λ (m^{-1}); λ_0 is the reference wavelength (nm), often 440 nm; and S_{NAP} is the spectral slope of the $a_{\text{NAP}}(\lambda)$ spectrum (nm^{-1}).

The S_{NAP} mean values in type A, B, C, D, E and F are $(0.0111 \pm 0.0003)\,\text{nm}^{-1}$, $(0.0112 \pm 0.0001)\,\text{nm}^{-1}$, $(0.0110 \pm 0.0001)\,\text{nm}^{-1}$, $(0.0112 \pm 0.0001)\,\text{nm}^{-1}$, $(0.0114 \pm 0.0001)\,\text{nm}^{-1}$ and $(0.0118 \pm 0.0003)\,\text{nm}^{-1}$, respectively, taking 440 nm as reference wavelength.

3.3.3. Pigment Absorption Coefficient Parameterization

Phytoplankton absorption characteristics are affected by many factors, such as algae species, pigment cell cyst, and growth cycle [3]. By comparing the different algorithms, it indicates that quadratic model is more suitable for these eutrophic waters. Self-relationships between $a_{ph}(\lambda)$ ($\lambda \in [400, 700]$) and $a_{ph}(400)$, $a_{ph}(440)$, $a_{ph}(480)$, $a_{ph}(550)$, $a_{ph}(625)$ and $a_{ph}(675)$ were detected thereafter. Both $a_{ph}(440)$ and $a_{ph}(675)$ have strong relationship with other wavelengths, but usually $a_{ph}(440)$ has stronger relationship than $a_{ph}(675)$ at 570 nm and below. So that when wavelength $<=$ 570 nm, we use $a_{ph}(440)$ to build quadratic model for simulating phytoplankton absorption coefficient of other wavelength, while when wavelength > 570 nm, $a_{ph}(675)$ was used to model $a_{ph}(\lambda)$.

4. CONCLUSION

We classified Taihu Lake, Chaohu Lake, Dianchi Lake and Sanxia Gorges Reservoir water into six water types by comparing peak and trough between 500–750 nm. The different water bodies belong to different water types, and most water bodies have several types, i.e., three water types were observed in Sanxia Gorges Reservoir, four types were found in Chaohu Lake, and two types in August 2006 in Meiliang Bay of Taihu Lake were classified while the whole lake had four types in Novermber 2006.

Type A, B, C and D have two peaks at 540–590 nm and 690–720 nm. Type A has deepest trough at 650–690 nm with highest mean concentration of chlorophyll a. With increasing concentration of total suspended matter and decreasing concentration of chlorophyll a, R_{rs} of type E and F get the maxima at near 590 nm, and decline fast after 690 nm. The variance of a_{ph} of different water type is larger than other absorption coefficient.

When parameterize a_{CDOM} and a_{NAP}, S_{CDOM} can be clustered into two groups, i.e., one group for type A and one for type B, C, D, E and F; while $0.11\,\mathrm{m}^{-1}$ can be the same value S_{NAP} for all water types. Absorption coefficients of phytoplankton can be calculated by absorption coefficient of 440 nm and 675 nm using quadratic function.

ACKNOWLEDGMENT

This research was supported by National Natural Science Foundation of China (No. 40971215), National Science, Technology Support Project of China (No. 2008BAC34B05). We thank L. Wu, X. Wang, K. Shi, R. Xia, Y. Yang, X. Jin, Y. F. Wang, H. Zhang, Y. F. Xu, X. Xu and Z. H. Liu for their participation in the field experiments.

REFERENCES

1. Babin, M., D. Stramski, G. M. Ferrari, H. Claustre, A. Bricaud, G. Obolensky, and N. Hoepffner, "Variations in the light absorption coefficients of phytoplankton, nonalgal particles, and dissolved organic matter in coastal waters around Europe," *Journal of Geophysical Research*, Vol. 108, No. C7, 3211, doi: 10.1029/2001JC000882, 2003.
2. Belzile, C., W. F. Vincent, C. Howard-Williams, I. Hawes, M. R. James, M. Kumagai, and C. S. Roesler, "Relationships between spectral optical properties and optically active substances in a clear oligotrophic lake," *Water Resource Research*, Vol. 40, 1–12, 2004.
3. Ciotti, A. M. and A. Bricaud, "Retrievals of a size parameter for phytoplankton and spectral light absorption by colored detrital matter from water-leaving radiances at SeaWiFS channels in a continental shelf region off Brazil," *Limnology Oceanograph: Methods*, Vol. 4, 237–253, 2006.
4. Gordon, H. R., O. B. Brown, R. H. Evans, J. W. Brown, R. C. Smith, K. S. Baker, and D. K. Clark, "A semi-analytic radiance model of ocean color," *Journal of Geophysical Research*, Vol. D93, 10909–10924, 1988.
5. Kirk, J. T. O., "Spectral absorption properties of natural waters: contribution of the soluble and particulate fraction to light absorption in some inland waters of south-eastern Australia," *Australian Journal of Marine and Freshwater Research*, Vol. 31, No. 3, 287–296, 1980.
6. Kutser, T., A. Herlevi, K. Kallio, and H. Arst, "A hyperspectral model for interpretation of passive optical remote sensing data for turbid lakes," *Science of the Total Environment*, Vol. 268, 47–58, 2001, doi: 10.1016/S0048-9697(00)00682-3.
7. Morel, A. and B. Gentili, "Diffuse reflectance of oceanic waters. II. Bidirectional aspects," *Applied Optics*, Vol. 32, 6864–6879, 1993.
8. Prieur, L. and S. Sathyendranath, "An optical classification of coastal and oceanic water based on the specific absorption curves of phytoplankton pigments, dissolved organic matter, and other particulate materials," *Limnology and Oceanography*, Vol. 26, 671–689, 1981.
9. Roesler, C. S., M. J. Perry, and K. L. Carder, "Modeling in situ phytoplankton absorption from total absorption spectra in productive inland marine waters," *Limnology and Oceanography*, Vol. 34, No. 8, 1510–1523, 1989.

Automatic Detection Algorithms for Oil Spill from Multisar Data

Maged Marghany and Mazlan Hashim
Institute for Science and Technology Geospatial (INSTeG)
Universiti Teknologi Malaysia, 81310 UTM, Skudai, Johore Bahru, Malaysia

Abstract— The main objective of this work is to develop comparative automatic detection procedures for oil spill pixels in multimode (Standard beam S2, Wide beam W1 and fine beam F1) RADARSAT-1 SAR satellite data that were acquired in the Malacca Straits using two algorithms namely, post supervised classification, and neural network (NN) for oil spill detection. The results show that NN is the best indicator for oil spill detection as it can discriminate oil spill from its surrounding such as look-alikes, sea surface and land. The receiver operator characteristic (ROC) is used to determine the accuracy of oil spill detection from RADARSAT-1 SAR data. In conclusion, that NN algorithm is an appropriate algorithm for oil spill automatic detection and W1 beam mode is appropriate for oil spill and look-alikes discrimination and detection.

1. INTRODUCTION

Synthetic aperture radar (SAR) has been recognised as a powerful tool for oil spill detection. SAR data have unique features as compared to optical satellite sensors which makes the satellite particularly valuable for spill monitoring [1, 9, 13]. These features are involved with several parameters: operating frequency, band resolution, incidence angle and polarisation [10, 12]. A dark oil spill spot on the ocean can be viewed every 1 to 3 days by virtue of the variable RADARSAT-1 SAR beam modes and their variable incidence angles, which are considered the most advantageous parameters of RADARSAT-1 SAR data [5, 12, 20]. The contribution of this work concerns with comparison between Mahalanobis classifier, and artificial intelligence techniques. In fact, previous work have implemented post classification techniques [4, 16, 18] or artificial neural net work [19, 20–22, 24] without comparing with other techniques.

2. COMPARATIVE ALGORITHMS

2.1. Mahalanobis Classification

Mahalanobis classification procedures were adopted. This algorithm is based on a correlation between variables by which different patterns can be identified and analyzed. It is a useful way of determining similarity of an unknown sample set to a known one. It differs from Euclidean distance in that it takes into account the correlation of the data set and is scale-invariant, i.e., not dependent on the scale of measurement [5]. Formally, the Mahalanobis distant of a multivariate vector is given as:

$$D_{M_{(v)}} = \sqrt{(v-\mu)^T S^{-1}(v-\mu)}. \tag{1}$$

where $V = (v_1, v_2, v_3, \dots, v_n)^t$ from group of values with mean $\mu = (\mu_1, \mu_2, \mu_3, \dots, \mu_n)^t$ and S, is covariance matrix. In order to apply Mahalanobis classification procedures to different remote sensing data, let v be the feature vector for the unknown input, and let M_1, M_2 be the two classes: oil spill, and look-alike. Then the error in matching v against M_j is given by $[v - M_j]$, the Euclidean distance. A minimum-error classifier computes $[v - m_j]$ for $j = 1$ to 2 and chooses the class for which this error is minimum.

2.2. AI Techniques for Oil Spill Automatic Detection

Following, Hect-Nielsen [6] and Topouzelis et al. [22] the ANN's and the pattern recognition (PR) technique, feed forward network with back-propagation algorithm are used in this study for both static and dynamic security assessment. For this application, a multi-layer feed forward network with error back-propagation has been employed [2, 21]. The major steps in the training algorithm are: Feed forward calculations, propagating error from output layer to input layer and weight updating in hidden and output layers [20, 5]. Forward pass phase calculations are shown by the following equations between input (i) and hidden (j) [14, 22].

$$\theta_j = \frac{1}{1 + e^{(\sum_j w_{ij}\theta_i + \theta_j)}}. \tag{2}$$

$$\theta_k = \frac{1}{1 + e^{(\sum_k w_{jk}\theta_j + \theta_k)}}. \tag{3}$$

where θ_j is the output of node j, θ_i is the output of node i, θ_k is the output of node w_{jk} is the weight connected between node i and j, and θ_j is the bias of node j, θ_k is the bias of node k. In backward pass phase, error propagated backward through the network from output layer to input layer as represented in Equation (2). Following Topouzelis et al. [22]. The weights are modified to minimize mean square error (MSE).

$$MSE = \frac{1}{n} \sum\nolimits_{i=1}^{n} \sum\nolimits_{j=a}^{m} (d_{ij} - y_{ij})^2. \tag{4}$$

where d_{ij} is the jth desired output for the ith training pattern, and y_{ij} is the corresponding actual output. More details of the mathematical procedure are available in Michael [14]. Finally, the receiver-operator-characteristics (ROC) curve and error standard deviation are used to determine the accuracy level of each algorithm has been used in this study. In addition, ROC and error standard deviation was used to determine the accuracy of feature detections in RADARSAT-1 SAR data. These methods have been described [12].

3. RESULTS AND DISCUSSION

The output results of Mahalanobis classification with different RADARSAT-1 SAR mode data are shown in Figure 1. Initial results indicate obvious discriminations between oil spill, look-alikes and low wind zone. Figure 1(a) and Figure 1(c) show that the oil spill has a large contrast to the gray-values of surrounding pixels. In fact, the surrounding areas are homogenous, with a constant gray-level. It is the most powerful classification methods when accurate training data is provided and one of the major widely used algorithms [4, 24].

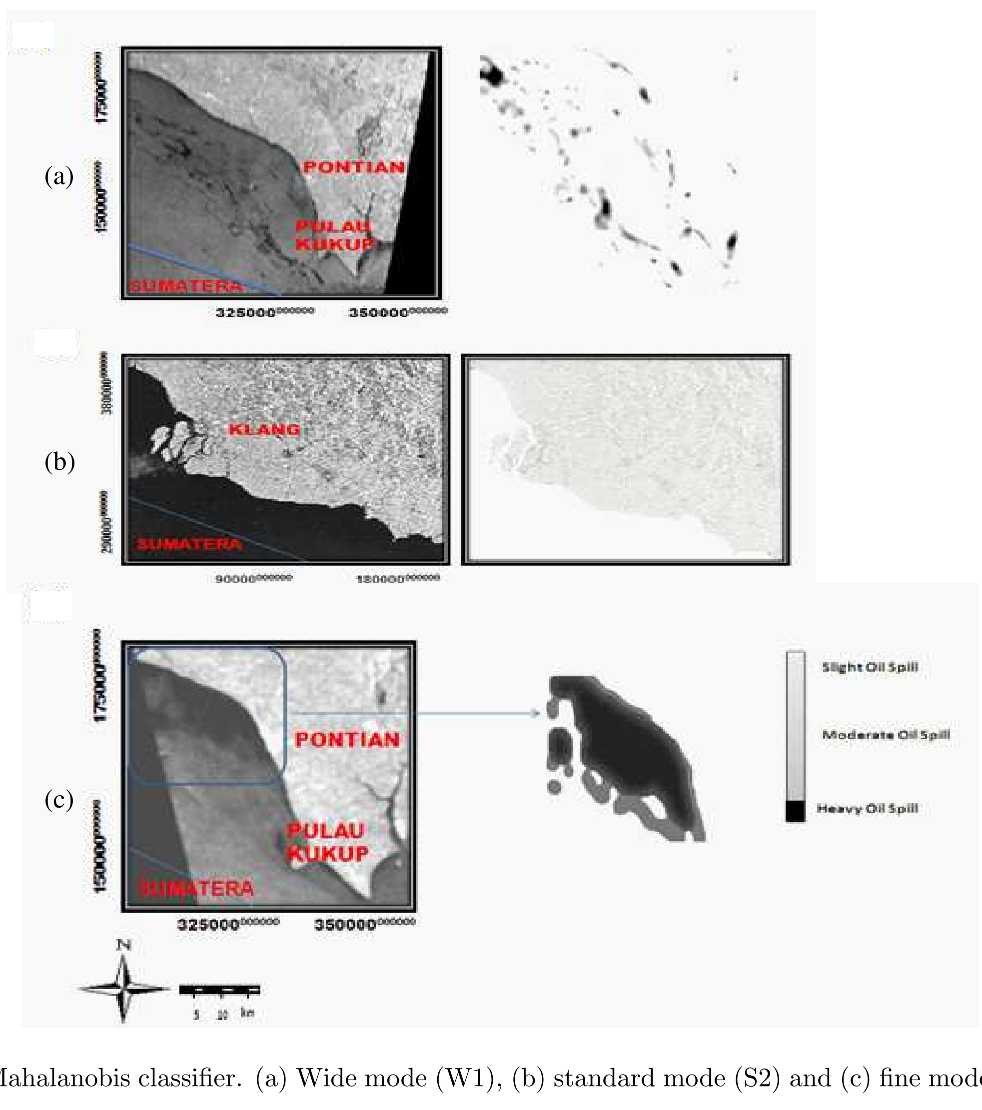

Figure 1: Mahalanobis classifier. (a) Wide mode (W1), (b) standard mode (S2) and (c) fine mode (F1) data.

It is clear that neural network algorithm is able to isolate oil spill dark pixels from the surrounding environment. In other words, look-alikes, low wind zone, sea surface roughness, and land are marked by white colour while oil spill pixels are marked all black. Figure 2(b) does not show any class presence or existence of oil spill event. Further, Figure 2 shows the results of the Artificial Neural Net work, where 99% of the oil spills in the test set were correctly classified. Three scenes by the leave-one-out method presented an exact classification of 99% for oil spills (an approach based on multilayer perceptron (MLP) neural network with two hidden layers). The net is trained using the back-propagation algorithm to minimize the error function. 99% of oil spills are automatically detected using the leave-one-out method. This study agrees with study of Topouzelis et al. [22].

The receiver-operator characteristics (ROC) curve in Figure 3 indicates significant difference in the discriminated between oil spill, look-alikes and sea surface roughness pixels. In terms of ROC area, oil spill has an area difference of 20% and 35% for look-alike and 30% for sea roughness and a ρ value below 0.005 which confirms the study of Marghany et al. [10, 11]. This suggests that Mahalanobis classifier and neural net works are good methods to discriminate region of oil slicks from surrounding water features.

Figure 4 shows that W1 mode data has lower persentage value of standard error of 15 percent in comparison to F1 and S2 mode data. This means that W1 mode perform better detection of oil spills than F1and S2 modes. In fact, the W1 mode showed steeper incident angle of 30° than the S1 and S2 modes. The offshore wind speed during the W1 mode overpass was 4.11 m/s, whereas the offshore wind speed was 7 m/s during the S2 mode overpass. Wind speeds below 6 m/s are appropriate for detection of oil spill in SAR data [19]. Therefore, applications requiring imaging of ocean surface, steep incidence angles are preferable as there is a greater contrast of backscatter manifested at the ocean surface [10, 11].

This study does not agree with Fiscella et al. [4] and Marghany and Mazlan [13]. In fact, the Mahalanobis classifier provides classification pattern of oil spill where the slight oil spill can distin-

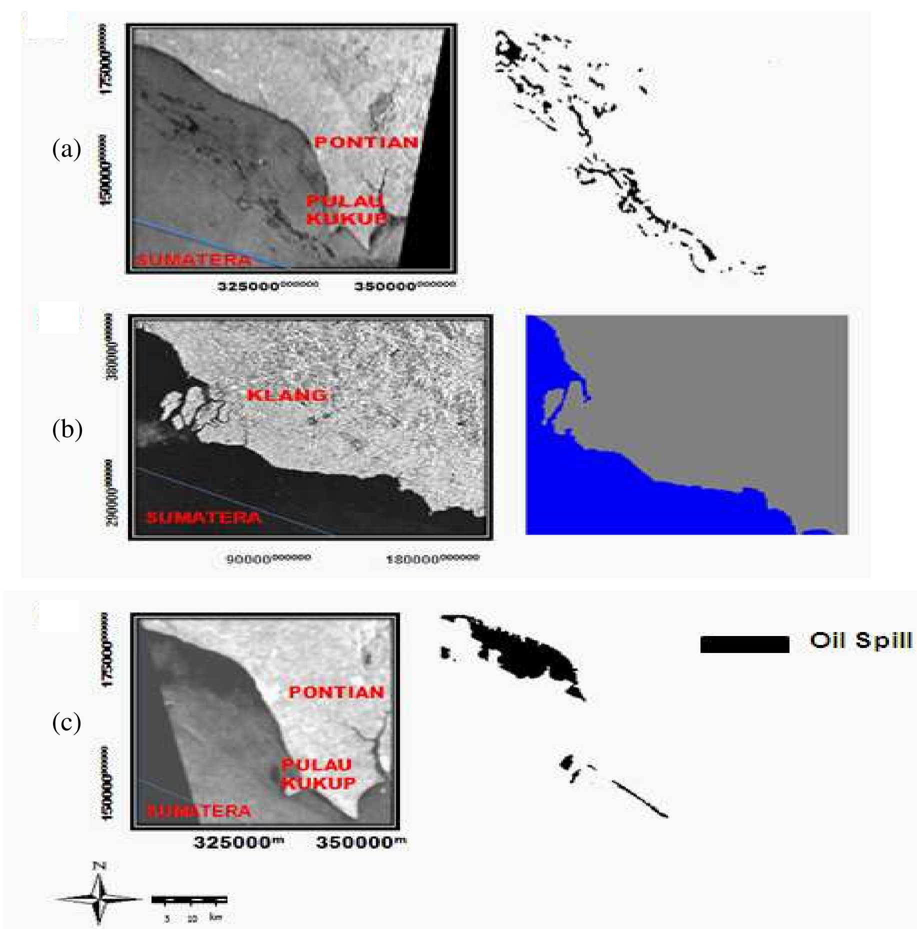

Figure 2: Neural network for automatic detection of oil spill from (a) W1, (b) S2, and (c) F1 mode data.

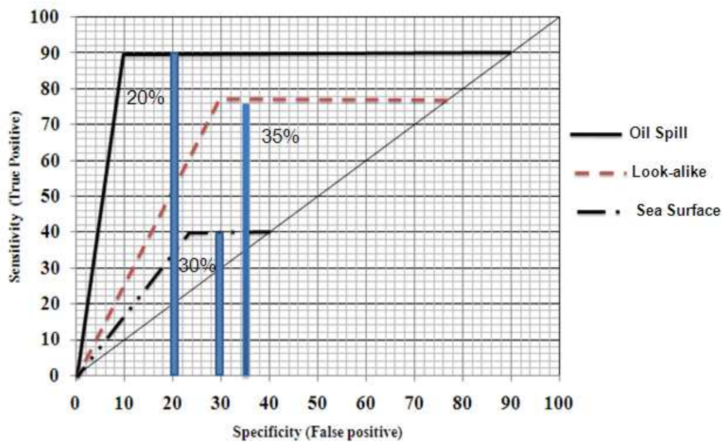

Figure 3: ROC for oil spill discrimination from look-alikes and sea surface roughness.

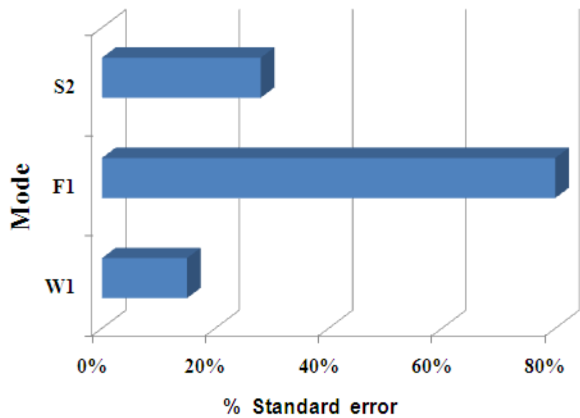

Figure 4: % standared error for different modes.

guish from medium and heavy oil spill pixels. Nevertheless, this study is consistent with Topouzelis et al. [20–22]. In consequence, the ANN extracted oil spill pixels automatically from surrounding pixels without using thresholding technique or different segemntation algorithm [13, 18, 19].

4. CONCLUSIONS

This study used two methods of post supervised classification (Mahalanobis Classification), and neural network (NN) for oil spill automatic detection. The study shows in terms of ROC area, it could be inferred that oil spill, look-alikes and sea surface roughness were perfectly discriminated, as provided by area difference of 20% for oil spill, 35% look–alikes and 30% for sea roughness. In conclusion, the ANN algorithms is an appropriate algorithm for oil spill detection and while the W1 mode is appropriate for oil spill and look-alikes discrimination and detection using RADARSAT-1 SAR data.

REFERENCES

1. Adam, J. A., "Specialties: Solar wings, oil spill avoidance, on-line patterns," *IEEE Spect.*, Vol. 32, 87–95, 1995.
2. Aggoune, M. E., L. E. Atlas, D. A. Cohn, M. A. El-Sharkawi, and R. J. Marks, "Artificial neural networks for power system static security assessment," *IEEE Int. Sym. on Cir. and Syst.*, Portland, Oregon, 490–494, 1989.
3. Brekke, C. and A. Solberg, "Oil spill detection by satellite remote sensing," *Rem. Sens. of Env.*, Vol. 95, 1–13, 2005.
4. Fiscella, B., A. Giancaspro, F. Nirchio, P. Pavese, and P. Trivero, "Oil spill detection using marine SAR images," *Int. J. of Rem. Sens.*, Vol. 21, No. 18, 3561–3566, 2000.

5. Frate, F. D., A. Petrocchi, J. Lichtenegger, and G. Calabresi, "Neural networks for oil spill detection using ERS-SAR data," *IEEE Tran. on Geos. and Rem. Sens.*, Vol. 38, No. 5, 2282–2287, 2000.
6. Hect-Nielsen, R., "Theory of the back propagation neural network," *Proc. of the Int. Joint Conf. on Neu. Net*, Vol. 1, 593–611, IEEE Press, New York, June 1989.
7. Marghany, M. and H. Mazlan, "Simulation of oil slick trajectory movements from the RADARSAT-1 SAR," *Asi. J. of Geo.*, Vol. 5, 17–27, 2005.
8. Marghany, M., "RADARSAT automatic algorithms for detecting coastal oil spill pollution," *Int. J. of App. Ear. Obs. and Geo.*, Vol. 3, 191–196, 2001.
9. Marghany, M., "RADARSAT for oil spill trajectory model," *Env. Mod. & Sof.*, Vol. 19, 473–483, 2004.
10. Marghany, M., A. P. Cracknell, and M. Hashim, "Modification of fractal algorithm for oil spill detection from RADARSAT-1 SAR data," *Int. J. of App. Ear. Obs. and Geo.*, Vol. 11, 96–102, 2009.
11. Marghany, M., A. P. Cracknell, and M. Hashim, "Comparison between Radarsat-1 SAR different data modes for oil spill detection by a fractal box counting algorithm," *Int. J. of Dig. Ear.*, Vol. 2, No. 3, 237–256, 2009.
12. Marghany, M., M. Hashim, and A. P. Cracknell, "Fractal dimension algorithm for detecting oil spills using RADARSAT-1 SAR," *ICCSA*, Gervasi O. and Gavrilova M. (Eds.), Part I, 1054–1062, Springer-Verlag Berlin Heidelberg, 2007.
13. Marghany, M. and M. Hashim, "Texture entropy algorithm for automatic detection of oil spill from RADARSAT-1 SAR data," *Int. J. of the Phy. Sci.*, Vol. 5, No. 9, 1475–1480, 2010.
14. Michael, N., *Artificial Intelligence: A Guide to Intelligent Systems*, 2nd Editon, Addison Wesley, Harlow, England, 2005.
15. Migliaccio, M., A. Gambardella, and M. Tranfaglia, "SAR polarimetry to observe oil spills," *IEEE Tran. on Geos. and Rem. Sens.*, Vol. 45, No. 2, 506–511, 2007.
16. Mohamed, I. S., A. M. Salleh, and L. C. Tze, "Detection of oil spills in malaysian waters from RADARSAT synthetic aperture radar data and prediction of oil spill movement," *Proc. of 19th Asi. Conf. on Rem. Sen.*, Hong Kong, China, November 23–27, 1999; *Asian Remote Sensing Society*, Vol. 2, 980–987, Japan, 1999.
17. Provost, F. and T. Fawcett, "Robust classification for imprecise environments," *Mach. Lear.*, Vol. 42, 203–231, 2001.
18. Samad, R. and S. B. Mansor, "Detection of oil spill pollution using RADARSAT SAR imagery," *CD Proc. of 23rd Asi. Conf. on Rem. Sens. Birendra International Convention Centre in Kathmandu*, Nepal, November 25–29, 2002.
19. Solberg, A. H. S., G. Storvik, R. Solberg, and E. Volden, "Automatic detection of oil spills in ERS SAR images," *IEEE Tran. on Geos. and Rem. Sens.*, Vol. 37, No. 4, 1916–1924, 1999.
20. Topouzelis, K., V. Karathanassi, P. Pavlakis, and D. Rokos, "Potentiality of feed-forward neural networks for classifying dark formations to oil spills and look-alikes," *Geo. Int.*, Vol. 24, No. 3, 179–19, 2009.
21. Topouzelis, K., V. Karathanassi, P. Pavlakis, and D. Rokos, "Detection and discrimination between oil spills and look-alike phenomena through neural networks," *ISPRS J. Photo. Rem. Sens.*, Vol. 62, 264–270, 2007.
22. Topouzelis, K. N., "Oil spill detection by SAR images: Dark formation detection, feature extraction and classification algorithms," *Sens.*, Vol. 8, 6642–6659, 2008.
23. Trivero, P., B. Fiscella, and P. Pavese, "Sea surface slicks measured by SAR," *Nuo. Cim.*, Vol. 24C, 99–111, 2001.
24. Trivero, P., B. Fiscella, F. Gomez, and P. Pavese, "SAR detection and characterization of sea surface slicks," *Int. J. Rem. Sen.*, Vol. 19, 543–548, 1998.

3-D Coastal Water Front Visualization Using RADARSAT-1 SAR Satellite Data

Maged Marghany and Mazlan Hashim
Institute for Science and Technology Geospatial (INSTeG)
Universiti Teknologi Malaysia, 81310 UTM, Skudai, Johor Bahru, Malaysia

Abstract— This paper presents work done to utilize RADARSAT-1 SAR data to reconstruct 3-D of coastal water front. Three algorithms of velocity bunching, Volterra and fuzzy B-spline are used to reconstruct 3-D coastal front. The velocity bunching algorithm modeled significant wave height, Volterra algorithm simulated coastal current movement while fuzzy B-spline implemented the significant wave height to reconstruct 3-D coastal front. The study shows the significant wave height varied between 0.7 m to 1.3 m across the front. The front is dominated by strong tidal current that ranged between 0.9 m/s to 1.5 m/s. This front occurred in water depth of 20 m. Additionally, fuzzy B-spline reconstructed 3-D front with smooth graphic feature. Indeed, fuzzy B-spline tracked the smooth and rough surface. Finally, fuzzy B-spline algorithm can keep track of uncertainty with representing spatially clustered gradient of flow points across the front. In conclusion, the fuzzy B-spline algorithm can be used for 3-D front reconstruction with integration of velocity bunching and Volterra algorithm.

1. INTRODUCTION

3D reconstruction of natural phenomena plays tremendous role to understand a complex system such as the dynamic processes of coastal waters [1–6, 24]. SAR images can sometimes be used to interpret frontal dynamics, including growth and decay of meanders [9, 17–19]. Recently, Jiang et al. [8] exploited various remote sensing data. Satellite images obtained from the Advanced Very High Resolution Radiometer (AVHRR), the Moderate Resolution Imaging Spectroradiometer (MODIS), the Sea-viewing Wide Field-of-view Sensor (SeaWiFS) and RADARSAT-1 SAR S1 mode data to study coastal water plume and front which is also captured in S1 mode data [9, 12]. In this paper, we address how 3D front can be reconstructed from single SAR data (namely the RADARSAT-1 SAR) using integration of Volterra kernel [7], velocity bunching [20–23] and Fuzzy B-spline models [16–18].

2. 3-D FRONT RECONSTRUCTION PROCEDURES

There are three algorithms involved for 3-D front reconstruction; velocity bunching, Volterra and Fuzzy B-spline. Significant wave heights are simulated from RADARSAT-1 SAR image by using velocity bunching model. Fuzzy B-spline used significant wave height information to reconstruct 3-D front. Moreover, front flow pattern is modeled by Volterra model.

2.1. Velocity Bunching Model

The velocity bunching modulation transfer function (MTF) is the dominant component of the linear MTF for the ocean waves with an azimuth wave number (k_x). According to Alpers et al. [2] and Vachon et al. [13, 20–24], the velocity bunching can contribute to linear MTF based on the following equation

$$M_v = \frac{R}{V}\omega\left[\frac{k_x}{k}\sin\theta + i\cos\theta\right] \tag{1}$$

where R/V is the scene range to platform velocity ratio, which is 111 s in the case of RADARSAT-1 SAR image data, θ is RADARSAT-1 SAR image incidence angel (35°–49°) and ω is wave spectra frequency which equals to 2Π/K. According to Vachon et al. [22] the significant wave height H_s can be obtained:

$$H_s = 0.6(\rho_{\zeta\zeta})^{0.5}\left[\frac{1+\theta^2/4}{R/V}\right]T_0 \tag{2}$$

where θ is the RADARSAT-1SAR incidence angle and Equation (4) is used to estimate the significant wave height which is based on the standard deviation of the azimuth shift σ.

2.2. Volterra Model

In refereeing to Ingland and Garello [7], Volterra series can be used to model nonlinear imaging mechanisms of surface current gradients by RADARSAT-1 SAR image. As result of that Volterra linear kernel is contained most of RADARSAT-1 SAR energy which used to simulate current flow along range direction. In reference to Ingland and Garello [7], the inverse filter $G(v_x, v_y)$ is used since the kernel $H_{1y}(v_x, v_y)$ has a zero for (v_x, v_y) which indicates the mean current velocity should have a constant offset [7, 15, 24]. The inverse filter $G(v_x, v_y)$ can be given as

$$G(v_x, v_y) = \begin{cases} [H_{1y}(v_x, v_y)]^{-1} & \text{If} \quad (v_x, v_y) \neq 0, \\ 0 & \quad\quad \text{otherwise} \end{cases} \tag{3}$$

The range current velocity [23] $U_y(0, y)$ can be estimated by

$$U_y(0, y) = I_{RADARSAT\text{-}1\ SAR} \cdot G(v_x, v_y) \tag{4}$$

where $I_{RADARSAT\text{-}1\ SAR}$ is the frequency domain of RADARSAT-1 SAR image acquired by applying 2-D Fourier transform on RADARSAT-1 SAR image.

2.3. Fuzzy B-splines Method

Fuzzy B-spline concept has adopted from Anile et al. [2] and Anile [1] which shows excellent 3-D reconstruction stated by Marghany et al. [17]. Considering significant wave height modeled by using velocity bunching and radar backscatter cross section across front, fuzzy numbers are created. Let us consider a function $f : h \to h$, of N [10] fuzzy variables $h_1, h_2, \ldots, h_n$. Where h_n is the global minimum and maximum values of significant wave heights. Additionally, the following must hold for each pair of confidence interval which define a number: $\mu \succ \mu' \Rightarrow h \succ h'$. The construction begins with the same preprocessing to compress the measured significant wave height values into an uniformly spaced grid of cells. Then, a membership function is defined for each pixel which incorporates the degrees of certainty of radar cross backscatter. The 0 value suits to minimum knowledge of significant wave heights, and 1 to the maximum of significant wave height. A fuzzy number is then prearranged in the confidence interval set, each one related to an assumption level μ [0, 1].

3. RESULTS AND DISCUSSION

The RADARSAT-1 F1 mode backscatter cross-section of front (Figure 1) has a maximum value of −21.25 dB. It is known the maximum backscatter value of 0.33 dB is found across the brightness frontal line. Moreover, the variation of radar backscatter cross-section is due to the current boundary gradient. According to Vogelzang et al. [23], ocean current boundaries are often accompanied by the changes in the surface roughness that can be detected by SAR. These interactions can cause an increase in the surface roughness and radar backscatter [13, 17].

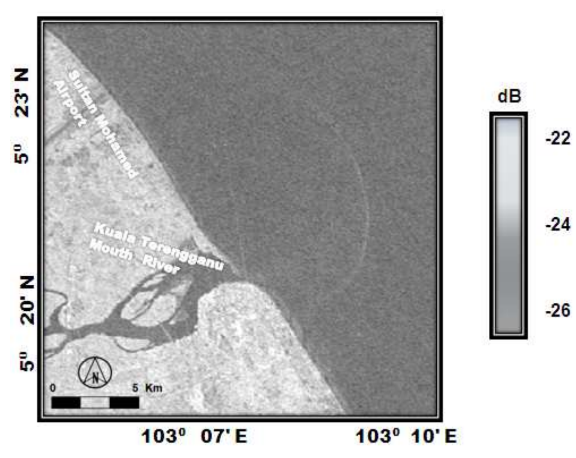

Figure 1: Backscatter variations in F1 mode data.

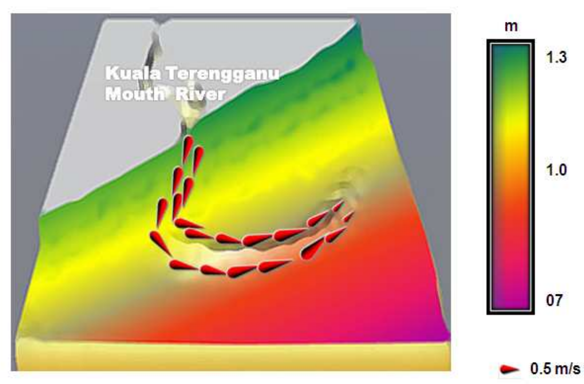

Figure 2: 3-D front reconstruction with significant wave height (Hs) and surface current variations (Uy).

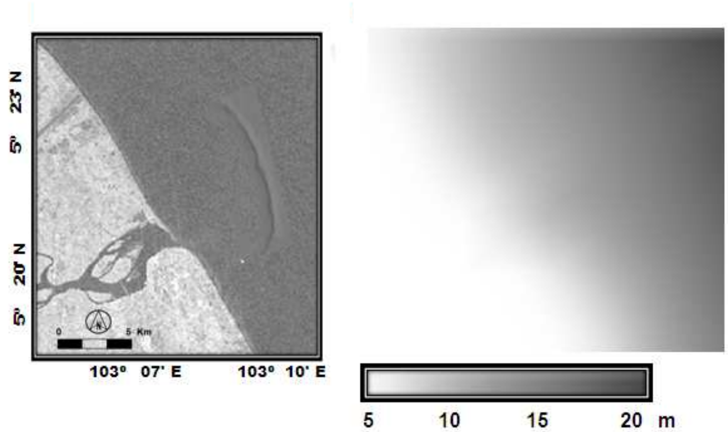

(a) (b)

Figure 3: F1 mode data for (a) 3-D front and (b) coastal bathymetry.

Figure 2 shows 3-D front reconstruction with significant wave heights, and current variations cross front. Figure 3 shows that significant wave variation cross front with maximum significant wave height of 1.2 m and gradient current of 0.9 m/s. Clearly, 3-D front coincides with water depth range between 10 to 20 m (Figure 3). This indicates shallow water where the strong tidal stream (Figure 2) that causes vertical mixing.

The visualization of 3-D front is sharp with the RADARSAT-1 SAR C_{HH} band because of each operations on a fuzzy number becomes a sequence of corresponding operations on the respective μ and μ'-levels, and the multiple occurrences of the same fuzzy parameters evaluated as a result of the function on fuzzy variables [2, 17]. In fact, the fuzzy B-spline depicts optimize a locally triangulation between two different points [1, 4, 11, 14]. This corresponds to the feature of deterministic strategies of finding only sub-optimal solutions usually which overcomes uncertainties. In this context, the spatial cluster of gradient flow at each triangulation points can simulated (Figure 3). Consequently, triangle-based criteria follow the rule of maximization or minimization, respectively, of the angles of each triangle [14] which prefers short triangles with obtuse angles. Further, edge-based criteria prefer edges are closely related. This study confirms the previous studies of Anile et al. [2]; Fuchs et al. [14]; Marghany et al. [17]. Indeed, these studies have agreed that fuzzy B-spline algorithm is an accurate tool for 3-D surface reconstruction from 2-D data.

4. CONCLUSION

In this study, three algorithms of velocity bunching, Volterra and fuzzy B-spline are involved to reconstruct 3-D coastal front. The velocity bunching algorithm modeled significant wave height, Volterra algorithm simulated coastal current movement while fuzzy B-spline implemented the significant wave height to reconstruct 3-D coastal front. The study shows fuzzy B-spline reconstructed 3-D front with smooth graphic feature. In conclusion, the fuzzy B-spline algorithm can be used for 3-D front reconstruction with integration of velocity bunching and Volterra algorithm.

REFERENCES

1. Adeyemo, J. and O. Fred, "Optimizing planting areas using differential evolution (DE) and linear programming (LP)," *International Journal of Physical Sciences*, Vol. 4, No. 4, 212–220, 2009.
2. Alpers, W. R., D. B. Ross, and C. L. Rufenach, "On the detectability of ocean surface waves by real and synthetic aperture radar," *J. Geophysical Research*, Vol. 86, 6481–6498, 1981.
3. Anile, A. M., "Report on the activity of the fuzzy soft computing group," 10, Technical Report, Dept. of Mathematics, University of Catania, March 1997.
4. Anile, A. M., S. Deodato, and G. Privitera, "Implementing fuzzy arithmetic," *Fuzzy Sets and Systems*, Vol. 72, 1995.
5. Bowden, K. F., *Physical Oceanography of Coastal Waters*, Ellis Horwood Ltd., England, 1983.
6. Guillermo, D. L. T., G. M. Soto-Zarazúa Ramón, G. Guevara-González, and E. Rico-García, "Bayesian networks for defining relationships among climate factors," *International Journal of the Physical Sciences*, Vol. 6, No. 18, 4412–4418, 2011.

7. Inglada, J. and R. Garello, "Depth estimation and 3D topography reconstruction from SAR images showing underwater bottom topography signatures," *Proceedings of IGARSS'99*, 1999.
8. Jiang, L., X. H. Yang, and V. Klemas, "Remote sensing for the identification of coastal plumes: Case studies of Delaware Bay," *International Journal of Remote Sensing*, Vol. 30, No. 8, 2033–2048, 2009.
9. Johannessen, J. A., R. A. Shuchman, G. Digranes, D. R. Lyzenga, C. Wackerman, O. M. Johannessen, and P. W. Vachon, "Coastal ocean fronts and eddies imaged with ERS 1 synthetic aperture radar," *J. Geophysical Research*, Vol. 101, No. C3, 6651–6667, 1996.
10. Hassasi, N. and R. Saneifard, "A novel algorithm for solving fuzzy differential inclusions based on reachable set," *International Journal of the Physical Sciences*, Vol. 6, No. 9, 4712–4716, 2011.
11. Khadijeh, M., H. Motameni, and R. Enayatifar, "New method for edge detection and de noising via fuzzy cellular automata," *International Journal of Physical Sciences*, Vol. 6, No. 13, 3175–3180, 2011.
12. Klemas, V., "Remote sensing of coastal plumes and ocean fronts: Overview and case study," *Journal of Coastal Research*, 2011, in Press.
13. Krogstad, H. E. and H. Schyberg, "On Hasselman's nonlinear ocean — SAR transformation," *Proc. of IGARSS'91*, 841–849, Espo, Finland, June 3–6, 1991.
14. Fuchs, H., Z. M. Kedem, and S. P. Uselton, "Optimal surface reconstruction from planar contours," *Commun. of the ACM*, Vol. 20, 693–702, 1997.
15. Majid, K. and M. A. Gondal, "An efficient two step Laplace decomposition algorithm for singular Volterra integral equations," *International Journal of the Physical Sciences*, Vol. 6, No. 20, 4717–4720, 2011.
16. Marghany, M., "Velocity bunching model for modelling wave spectra along east coast of Malaysia," *J. Indian Society of Remote Sensing*, Vol. 32, No. 2, 185–198, 2004.
17. Marghany, M., H. Mazlan, and A. P. Cracknell, "3-D visualizations of coastal bathymetry by utilization of airborne TOPSAR polarized data," *Int. J. of Dig. Ear.*, Vol. 3, No. 2, 187–206, 2010.
18. Marghany, M. and H. Mazlan, "Simulation of sea surface current velocity from synthetic aperture radar (SAR) data," *International Journal of the Physical Sciences*, Vol. 5, No. 12, 1915–1925, 2010.
19. Robinson, I. S., *Satellite Oceanography: An Introduction for Oceanographers and Remote-sensing Scientists*, Johan Wiley & Sons, New York, 1994.
20. Vachon, P. W., H. E. Krogstad, and J. S. Paterson, "Airborne and spaceborne synthetic aperture radar observations of ocean waves," *Atmosphere-Ocean*, Vol. 32, No. 10, 83–112, 1994.
21. Vachon, P. W., A. K. Liu, and F. C. Jackson, "Near-shore wave evolution observed by airborne SAR during SWADE," *Atmosphere-Ocean*, Vol. 2, 363–381, 1995.
22. Vachon, P. W., J. W. M. Campbell, and F. W. Dobson, "Comparison of ERS and RADARSAT SARS for wind and wave measurement," *Paper Presented at third ERS Symp.*, ESA, Florence, Italy, March 2–18, 1997.
23. Vogelzang, J., G. J. Wensink, C. J. Calkoen, and M. W. A. van der Kooij, "Mapping submarine sand waves with multiband imaging radar, 2, Experimental results and model comparison," *J. Geophysical Research*, Vol. 102, 1183–1192, 1997.
24. Zaki, M. S., "On asymptotic behaviour of a second order delay differential equation," *International Journal of Physical Sciences*, Vol. 2, No. 7, 185–187, 2007.

Digital Elevation Model of Spit Using Dinsar of Radarsat-1 Fine Mode Data

Maged Marghany and Mazlan Hashim
Institute for Science and Technology Geospatial (INSTeG)
Universiti Teknologi Malaysia, 81310 UTM, Skudai, Johor Bahru, Malaysia

Abstract— This work presents a new approach for 3-D object simulation using Differential synthetic aperture interferometry (DInSAR). In doing so, new approach of using fuzzy B-spline algorithm is implemented with phase unwrapping technique. Consequently, fuzzy B-spline is used to eliminate the phase decorrelation impact from the interferograms. The study shows the performance of DInSAR method using fuzzy B-spline is better than DInSAR technique which is validated by a lower range of error (0.02 ± 0.21 m) with 90% confidence intervals. In conclusion, integration of fuzzy B-spline with phase unwrapping produce accurate 3-D coastal geomorphology reconstruction.

1. INTRODUCTION

Interferometric synthetic aperture radar (InSAR or IfSAR), is a geodetic technique uses two or more single look complex synthetic aperture radar (SAR) images to produce maps of surface deformation or digital elevation [1–4]. Further, the precision DEMs with of a couple of ten meters can produce from InSAR technique compared to conventional remote sensing methods. Even so, alternative datasets must acquire at high latitudes or in areas of rundown coverage [6]. However, the baseline decorrelation and temporal decorrelation make InSAR measurements unfeasible [5–11]. In this context, Gens [12] reported the length of the baseline designates the sensitivity to height changes and sum of baseline decorrelation. According to Roa et al. [7], uncertainties could arise in DEM because of limitation InSAR repeat passes. In addition, the interaction of the radar signal with troposphere can also induce decorrelation. This is explained in several studies [3, 8, 15].

A constant phase difference between the two images caused by the horizontally homogeneous atmosphere was over the length scale of an interferogram and vertically over that of the topography. The atmosphere, however, is laterally heterogeneous on length scales both larger and smaller than typical deformation signals [9]. In other cases the atmospheric phase delay, however, is caused by vertical inhomogeneity at low altitudes and this may result in fringes appearing to correspond with the topography. Under this circumstance, this spurious signal can appear entirely isolated from the surface features of the image, since the phase difference is measured other points in the interferogram, would not contribute to the signal [3]. This can reduce seriously the low signal-to-noise ratio (SNR) which restricted to perform phase unwrapping. Accordingly, the phases of weak signals are not reliable. According to Yang et al. [11], the correlation map can be used to measure the intensity of the noise in some sense. It may be overrated because of an inadequate number of samples allied with a small window [9]. Weights are initiated to the correlation coefficients according to the amplitudes of the complex signals to estimate accurate reliability [11]. The main contribution of this study is to implement fuzzy B-spline with DInSAR technique. Three hypotheses examined are: (i) Fuzzy B-spline which is based on triangle-based criteria and edge- based criteria can be used as filtering technique to reduce noise before phase unwrapping; (ii) 3-D topography reconstruction can be produced using satisfactory phase unwrapping by involving the fuzzy B-spline algorithm; and (iii) high accuracy of deformation rate can be estimated by using the new technique.

2. DINSAR DATA PROCESSING

The DInSAR technique measures the block displacement of land surface caused by subsidence, earthquake, glacier movement, and volcano inflation to cm or even mm accuracy [10]. According to Lee [9], the surface displacement can estimate using the acquisition times of two SAR images S_1 and S_2. The component of surface displacement thus, in the radar-look direction, contributes to further interferometric phase (φ) as

$$\phi = \frac{4\pi}{\lambda}(\Delta R + \zeta) \tag{1}$$

where ΔR is the slant range difference from satellite to target respectively at different time, λ is the RADARSAT-1 SAR fine mode wavelength which is about 5.6 cm for CHH-band. In practice, zero-baseline, repeat-pass InSAR configuration is hardly achievable for either spaceborne or airborne SAR. Therefore, a method to remove the topographic phase as well as the system geometric phase in a non-zero baseline interferogram is needed. The three-pass approach has the advantage in that all data is kept within the SAR data geometry while DEM method can produce errors by misregistration between SAR data and cartographic DEM [9, 20]. However, this is not practical and it is difficult to achieve from the system design for a repeat-pass interferometer. From Equation (1) the displacement sensitivity of DInSAR is given as

$$\frac{\partial \phi_d}{\partial \zeta} = \frac{4\pi}{\lambda} \tag{2}$$

The phase difference and correlation coefficient of master and slave complex amplitude patches can express as fuzzy B-spline by

$$Sp, q = \frac{\sum\limits_{i=0}^{M}\sum\limits_{j=0}^{O} \phi' C_{ij}\beta_{i,4}(p)\beta_{j,4}(q)\gamma(j,k)}{\sum\limits_{m=0}^{M}\sum\limits_{l=0}^{O} \beta_{m,4}(p)\beta_{l,4}(q)\gamma(j,k)} = \sum_{i=0}^{M}\sum_{j=0}^{O} \phi' C_{ij} S_{ij}(p,q) \tag{3}$$

$\beta_{i,4}(p)$ and $\beta_{j,4}(q)$ are two bases B-spline functions, and $\{C_{ij}S_{ij}\}$ is the bidirectionally control nets with the curve points $S(p,q)$ that are affected by $\{w_e(j,k)\}$. According to Yang et al. [9], the weighted square error is defined as:

$$w_e(j,k) = \sum_{y=-1}^{I}\sum_{x=-1}^{I} \gamma(j+y,k+x)|a_I(j,k)x + b_I(j,k)y + c_I(j,k) - s_I(j+y,k+x)| \tag{4}$$

where $\gamma(j,k)$ is the degree of the coherence, s_I and $I = (s, M)$ are donated both pixels' locations at j, k in slave and Master images while y, x donated the relative co-ordinates of adjacent pixel from j, k and $x, y \in \{-1, 0, 1\}$. Finally, $a_I(j,k)$, $b_I(j,k)$ and $c_I(j,k)$ is the complex coefficients [15].

3. RESULTS AND DISCUSSION

Figure 1 shows the combination between coherence and the phase of the interferogram produced from the RADARSAT-1 SAR F1 mode tandem pair of December 23, 2003, and March 26, 2005.

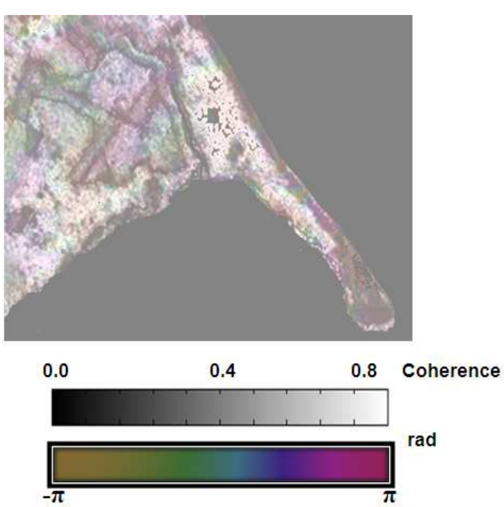

Figure 1: Combination between coherence and phase of the interferogram produced from the RADARSAT-1 SAR F1 mode tandem pair of December 23, 1999, and March 26, 2004.

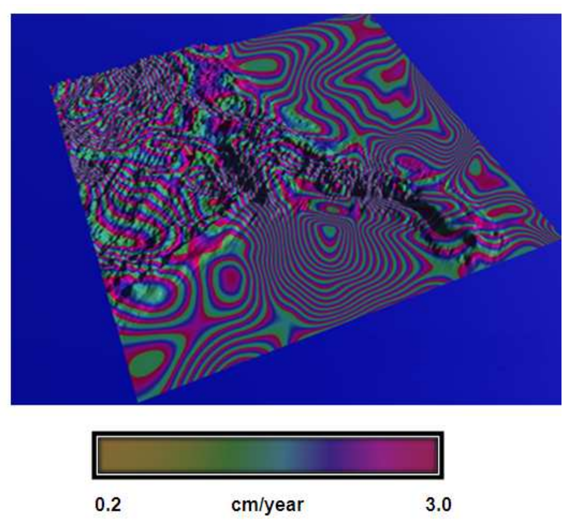

Figure 2: 3-D fringes of deformation phase produced from fuzzy B-spline of DInSAR.

It in interest to find the interferogram fringes are corresponding with the high coherence area of 1, e.g., urban and sandy areas. In contrast, vegetation area and water zone of value less than 0.2 are coincided with absent of interferogram fringe absents. This occurs because of decorrelation. In fact, the baseline decorrelation and temporal decorrelation make InSAR measurements unfeasible.

The topographic phase of Figure 3 was modulated into deformation of the interferomateric phase of 3 November, 1999, 23 December, 2003 and March 26, 2005 to investigate deformation of coastline geomorphology. This can be seen along the spit. The 3-D fringes are indicating the actual pattern of deformation along the coastline specially the spit area (Figure 2). It is interesting to find that the coastal geomorphology patterns have been exposed to tremendous changes since 1999 to 2005 (Figure 2). In addition, fuzzy B-spline able to produce fringe pattern in coastal water. It may be these fringe patterns represent the direction of wave, current and wave-current interaction. It is interesting to find that fuzzy B-spline can produce solid interferomatery and ocean dynamic interferometry. In addition, Parviz [21] proposed new method name by **Liqui-InSAR** on aquatic bodies in different locations all around the globe "the project C1P.8242" under the ESA affiliated European Space Research Institute (ESRIN). Further, Parviz [21] can generate fringe patterns on the water bodies with the temporal baseline of maximum 16 seconds. Nevertheless, fuzzy B-spline generates DInSAR fringe patterns with a long temporal baseline. Moreover, the continues fringe pattern from the land ocean show that the wide fringe patterns occurred on water body. This could due to coastal hydrodynamic interaction between coastline, water flow from the mouth river and ocean motion.

Figure 3 represents 3-D spit reconstruction using fuzzy B-spline with the maximum spit's elevation is 3 m with gentle slope of 0.86 m. Table 1 represents the bias (averages mean the standard error, 90 and 95% confidence intervals, respectively. Evidently, the DInSAR using fuzzy B-spline performance has bias of −0.05 m, lower than ground measurements and the DInSAR method. Therefore, fuzzy B-spline has a standard error of mean of ±0.034 m, lower than ground measurements and the DInSAR method. Overall performances of DInSAR method using fuzzy B-spline is better than DInSAR technique which is validated by a lower range of error (0.02 ± 0.21 m) with 90% confidence intervals.

Further, it can be noticed that fuzzy B-spline preserves detailed edges with discernible fringes. Typically, in computer graphics, two objective quality definitions for fuzzy B-spline were used: triangle-based criteria and edge-based criteria. Triangle-based criteria follow the rule of maximiza-

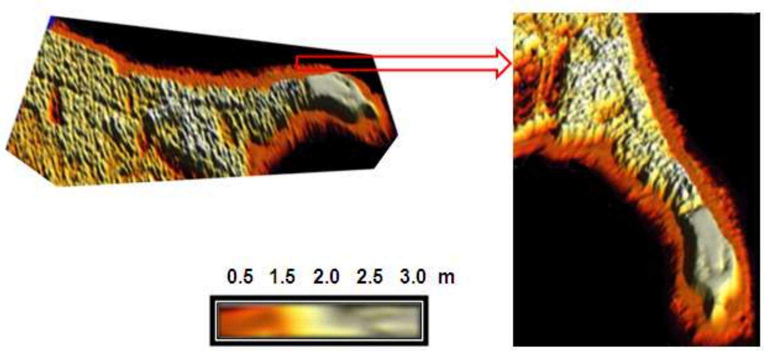

Figure 3: 3-D reconstruction of Spit using fuzzy B-spline algorithm of DInSAR.

Table 1: Statistical comparison between DInSAR and DInSAR-Fuzzy B-spline techniques.

Statistical Parameters	**DInSAR techniques**			
	DInSAR		**DInSAR-Fuzzy B-spline**	
Bias	2.5		−0.05	
Standard error of the mean	1.5		0.034	
90% (90% confidence interval)	Lower	Upper	Lower	Upper
	1.2	2.6	0.02	0.16
'95% (95% confidence interval)	0.98	2.35	0.03	0.21

tion or minimization, respectively, of the angles of each triangle. The so-called max-min angle criterion prefers short triangles with obtuse angles. Indeed, Figure 5 shows smooth interferogram, in terms of spatial resolution maintenance, and noise reduction, compared to conventional methods [2, 5, 8, 10]. This result agrees confirms the studies of Anile et al. [13]; Marghany et al. [14]; Marghany and Mazlan [15].

4. CONCLUSIONS

This work has established the 3-D spit reconstruction from DInSAR using three C-band SAR images acquired by RADARSAT-1 SAR F1 mode data. The fuzzy B-spline algorithm used to reconstruct fringe pattern, and 3-D from decorrelate unwrap phase. The fringe pattern shows the deformation of 0.4 cm along spit and 1.4 cm in urban area. In addition, the maximum 3-D spit elevation is 3 m with the standard error of mean of ± 0.034 m. In conclusion, the integration between the conventional DInSAR method and the FBSs could be an excellent tool for 3-D coastal geomorphology reconstruction from SAR data the under circumstance of temporal decorrelation.

REFERENCES

1. Massonnet, D. and K. L. Feigl, "Radar interferometry and its application to changes in the earth's surface," *Rev. Geophys.*, Vol. 36, 441–500, 1998.
2. Burgmann, R., P. A. Rosen, and E. J. Fielding, "Synthetic aperture radar interferometry to measure Earth's surface topography and its deformation," *Ann. Rev. of Earth and Plan. Sci.*, Vol. 28, 169–209, 2000.
3. Hanssen, R. F., *Radar Interferometry: Data Interpretation and Error Analysis*, Kluwer Academic, Dordrecht, Boston, 2001.
4. Zebker, H. A., P. A. Rosen, and S. Hensley, "Atmospheric effects in inteferometric synthetic aperture radar surface deformation and topographic maps," *J. Geophys. Res.*, Vol. 102, 7547–7563, 1997.
5. Askne, J., M. Santoro, G. Smith, and J. E. S. Fransson, "Multitemporal repeat-pass SAR interferometry of boreal forests," *IEEE Trans. Geosci. Remote Sens.*, Vol. 41, 1540–1550, 2003.
6. Nizalapur, V., R. Madugundu, and C. Shekhar Jha, "Coherence-based land cover classification in forested areas of Chattisgarh, Central India, using environmental satellite — Advanced synthetic aperture radar data," *J. Appl. Remote Sens.*, Vol. 5, 059501-1–059501-6, 2011.
7. Rao, K. S., H. K. Al Jassar, S. Phalke, Y. S. Rao, J. P. Muller, and Z. Li, "A study on the applicability of repeat pass SAR interferometry for generating DEMs over several Indian test sites," *Int. J. Remote Sens.*, Vol. 27, 595–616, 2006.
8. Rao, K. S. and H. K. Al Jassar, "Error analysis in the digital elevation model of Kuwait desert derived from repeat pass synthetic aperture radar interferometry," *J. Appl. Remote Sens.*, Vol. 4, 1–24, 2010.
9. Lee, H., "Interferometric synthetic aperture radar coherence imagery for land surface change detection," Ph.D theses, University of London, 2001.
10. Luo, X., F. Huang, and G. Liu, "Extraction co-seismic deformation of bam earthquake with differential SAR interferometry," *J. New Zea. Inst. of Surv.*, Vol. 296, 20–23, 2006.
11. Yang, J., T. Xiong, and Y. Peng, "A fuzzy approach to filtering interferometric SAR data," *Int. J. Remote Sens.*, Vol. 28, 1375–1382, 2007.
12. Gens, R., "The influence of input parameters on SAR interferometric processing and its implication on the calibration of SAR interferometric data," *Int. J. Remote Sens.*, Vol. 2, 11767–1771, 2000.
13. Anile, A. M., B. Falcidieno, G. Gallo, M. Spagnuolo, and S. Spinello, "Modeling uncertain data with fuzzy B-splines," *Fuzzy Sets and Syst.*, Vol. 113, 397–410, 2000.
14. Marghany, M., M. Hashim, and A. P. Cracknell, "3-D visualizations of coastal bathymetry by utilization of airborne TOPSAR polarized data," *Int. J. of Dig. Earth*, Vol. 3, 187–206, 2010.
15. Marghany, M. and M. Hashim, "Differential synthetic aperture radar interferometry (DInSAR) for 3D coastal geomorphology reconstruction," *IJCSNS Int. J. of Comp. Sci. and Network Secu.*, Vol. 9, 59–63, 2009.
16. Marghany, M. and M. Hashim, "Different polarised topographic synthetic aperture radar (TOPSAR) bands for shoreline change mapping," *Int. J. Phys. Sci.*, Vol. 5, 1883–1889, 2010.

17. Marghany, M., Z. Sabu, and M. Hashim, "Mapping coastal geomorphology changes using synthetic aperture radar data," *Int. J. Phys. Sci.*, Vol. 5, 1890–1896, 2010.
18. Marghany, M. and M. Hashim, "Velocity bunching and Canny algorithms for modelling shoreline change rate from synthetic aperture radar (SAR)," *Int. J. Phys. Sci.*, Vol. 5, 1908–1914, 2010.
19. RADARSAT International, "RADARSAT application," [online] available from http:\www.rsi.ca [Accessed 8 June 2011].
20. Zebker, H. A., C. L. Werner, P. A. Rosen, and S. Hensley, "Accuracy of topographic maps derived from ERS-1 interferometric radar," *IEEE Geosci. Remote Sens.*, Vol. 2, 823–836, 1994.
21. Parviz, T., "Liqui-InSAR [online]," [online] available from http://parviztarikhi.wordpress.com/what%E2%80%99s-new. [Accessed 16 March 2012], 2012.

Design of Reconfigurable Slot Antenna for Diverse Frequency Wireless Applications

C. Sulakshana and L. Anjaneyulu
Department of ECE, NIT Warangal, India

Abstract— This paper deals with design and simulation analysis of a novel and compact reconfigurable CPW fed slot antenna with frequency diversity. The basic antenna consists of CPW fed slot antenna which operates at 5.8 GHz. The frequency reconfigurability is obtained by connecting three slots through switches in basic antenna by using PIN diodes or RF MEMS. By controlling the switches the antenna can be operated at six different frequencies namely 5.65 GHz, 5.3 GHz, 4.42 GHz, 4.35 GHz, 3.95 GHz, and 3.22 GHz which are suitable Wi-Fi, WiMAX, and WLAN, RFID and other C-band applications. The compact aperture area of the antenna is $35\,\mathrm{mm} \times 30\,\mathrm{mm} \times 1.5\,\mathrm{mm}$ and it is designed on a low cost FR4 substrate whose dielectric constant $\varepsilon_r = 4.3$. The effect of antenna length, size, substrate, thickness, shape has been evaluated and obtained good and acceptable 2D Radiation Pattern in elevation plane, gain, and efficiency. Method of Moments based IE3D software has been used for simulations and the results are presented.

1. INTRODUCTION

Antennas that can intentionally and reversibly change the distribution or character of their performance-governing electromagnetic fields are said to be reconfigurable antennas. These antennas effectively allow the antenna volume to be reused as an antenna in a different form and this helps in miniaturizing the entire device size [1]. Now a day's radioelectronic systems employ multiple antenna systems. Intelligent smart or adaptive antennas are the most suitable for today's wireless communication systems especially third and fourth generation systems. Instead of having multiple antennas switched into multiple transceivers covering different frequency range, a single multi-band tunable antenna set would provide reduction in size and minimize product complexity. The idea of reconfigurable antennae is gaining great attention. As more wireless services are becoming more common, the available radio spectrum is decreasing. Hence, it is not practical to dedicate one antenna to each service; many of these services are ON at a time, while others may be required to be available all the time. Many services means many antennas, and many standards means that more antennas are needed in conventional case of multiple antennas while reconfigurable antennas use a single antenna [2]. Reconfigurable Antennas commonly adapts their properties to achieve selectivity in frequency, bandwidth, radiation pattern and polarization. These antennas are capable of multi-band operation, adaptive beamforming, jamming/interference mitigation, polarization diversity, low observability, and direction of arrival estimation [3].

Reconfigurable patch antennas are considered as promising paradigm for generating several antenna modes using a single reconfigurable structure. The attraction of reconfigurable antennas leads its introduction to applications such as military, besides commercial applications. Reconfiguration of an antenna can be achieved through an intentional dynamic redistribution of the currents of the antenna's aperture. These changes are enabled through various mechanisms such as switching, material tuning, and structural modifications [4]. The switching technology can be implemented using PIN diodes, FETs which are classified as solid state switches. Recently due to many attractive features of RF-MEMS over solid state switches, such as lower power consumption, on resistance, insertion loss, parasitic capacitance and manufacturing cost, higher isolation, and better intermodulation due to their linearity, RF MEMS switches are used in common.

Recently, the Co-Planar Waveguide (CPW)-fed antenna has been used as an alternative to conventional antennae for different wireless communication systems due to its many attractive features [5]. Miniaturization always indicates scientific progress. So efforts are always directed towards reducing the size of the antenna. Another major drawback that prevails in the present antenna systems is the frequency of operation. It is very important that the frequency of operation of the antenna falls in the specific area of application.

The proposed reconfigurable antenna attempts to address these problems. In this paper, a brief description of frequency reconfigurable antenna which includes antenna design and geometrical layout is presented in Section 2 and finally the simulation results of return loss, radiation pattern are discussed in Section 3. Simulations are carried out using Zeland's 'Method of Moments' based commercial IE3D (Integral Equation 3-Dimensional simulator). IE3D simulator is preferred than other RF CAD tools because of its high efficiency, high accuracy and low cost with windows based graphic interface that allows interactive construction of 3D and multilayer metallic structures as a set of polygons.

2. STRUCTURE AND DESIGN OF PROPOSED RECONFIGURABLE ANTENNA

The geometrical configuration of the proposed reconfigurable CPW fed patch antenna is shown in Fig. 1. The designed antenna is etched on a single layer of FR4 dielectric substrate which is $35 \times 30\,\mathrm{mm}^2$ in dimension. The antenna is symmetrical with respect to the longitudinal direction, whose main structure is a T-shaped slot with Co-planar waveguide (CPW) feed line.The geometrical parameters are adjusted carefully and finally the antenna dimensions are obtained as $L_1 = 30\,\mathrm{mm}$, $L_2 = 2\,\mathrm{mm}$, $L_3 = 1.5\,\mathrm{mm}$, $L_4 = 5\,\mathrm{mm}$, L_5=0.5 mm, L_6=6 mm, $W_1 = 15.3\,\mathrm{mm}$, $W_2 = 3.6\,\mathrm{mm}$, $W_3 = 10\,\mathrm{mm}$, $W_4 = 6\,\mathrm{mm}$, $\varepsilon_r = 4.3$. The gap spacing between ground plane and CPW feed line is $g = 0.4\,\mathrm{mm}$. The thickness of the substrate is $h = 1.5\,\mathrm{mm}$.

Three switches are introduced in the structure namely S_1, S_2 and S_3 which are connected between four slots. Keeping switches in the structure means placing connection. In order to obtain frequency diversity, the three switches are made ON and OFF in eight (2^n where $n = 3$) different combinations.

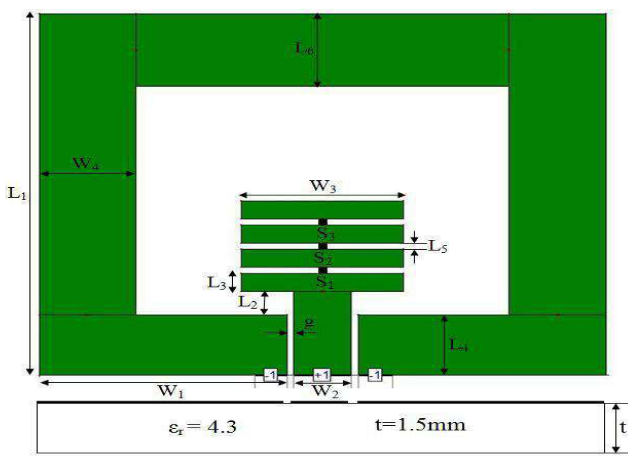

Figure 1: Geometry of the proposed reconfigurable antenna.

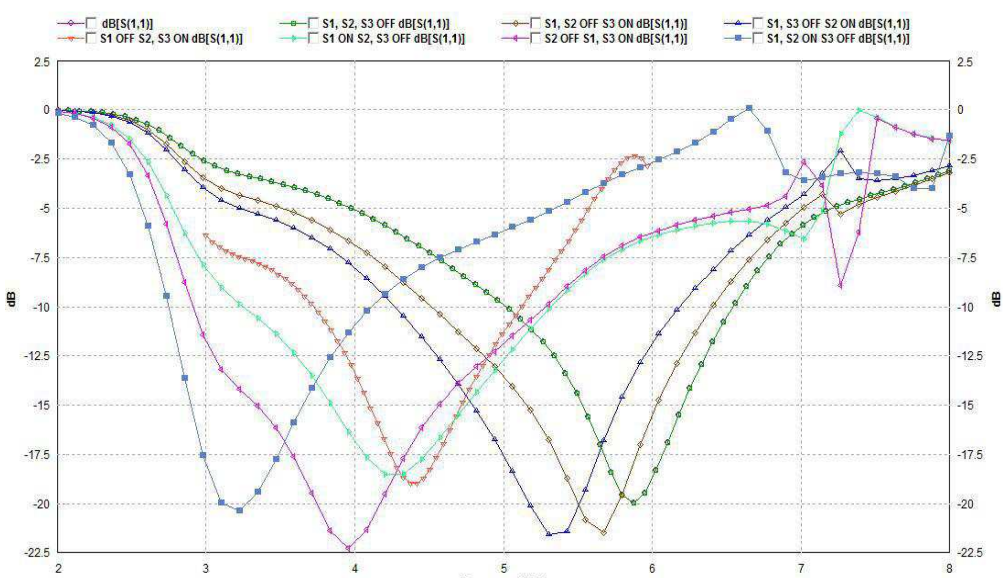

Figure 2: Comparison of return losses for various switch configurations.

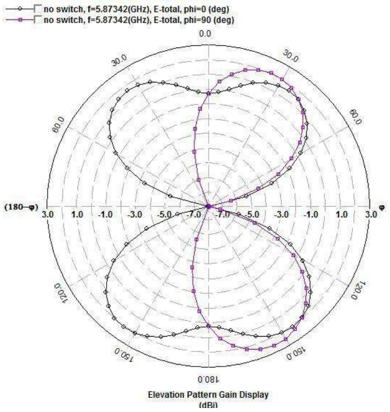

Figure 3: 2D elevation pattern at 5.8 GHz.

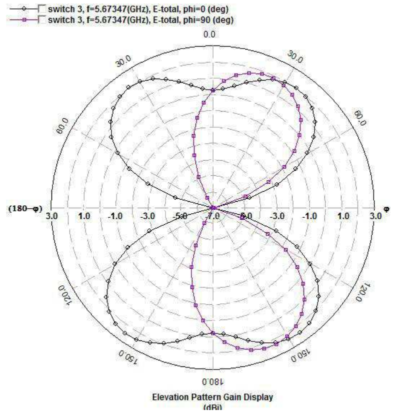

Figure 4: 2D elevation pattern at 5.6 GHz.

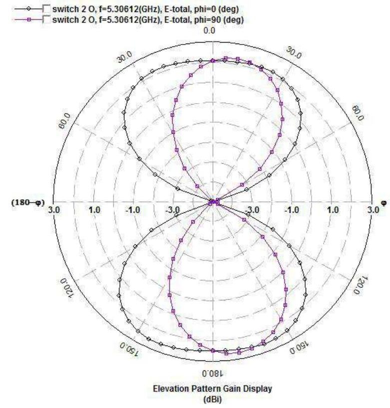

Figure 5: 2D Elevation Pattern at 5.3 GHz.

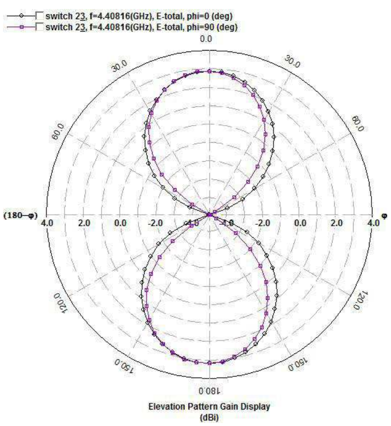

Figure 6: 2D Elevation Pattern at 4.41 GHz.

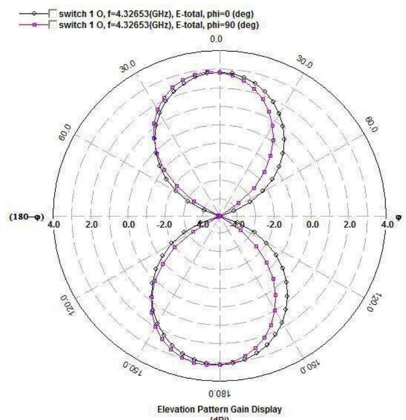

Figure 7: 2D Elevation Pattern at 4.32 GHz.

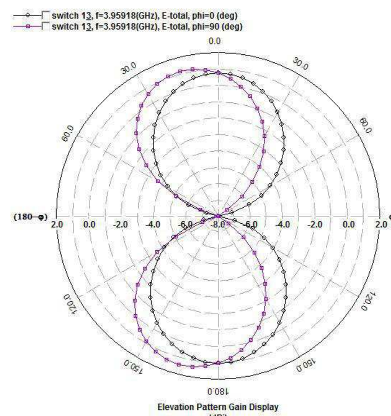

Figure 8: 2D Elevation Pattern at 3.9 GHz.

3. INFERENCES FROM SIMULATED RESULTS AND DISCUSSIONS

To investigate the performance of the proposed antenna configurations in terms of achieving the required results, a commercially available Moment Method based CAD tool-IE3D, was used for required numerical analysis and obtaining the proper geometrical parameters as shown in Fig. 1.

The return loss for various switch configurations is compared in Fig. 2. The individual radiation pattern which gives E_φ polarization pattern in the elevation cuts (y-z plane and x-z plane) for the antenna at different operating frequencies for different modes is also shown in Figs. 3–9. It is observed from Fig. 2 that a return loss of −20 dB at 5.8 GHz with −10 dB band width of 1.52 GHz is obtained when all switches are OFF. This antenna is suitable for RFID/IEEE 802.11a WLAN (5.725 GHz–5.875 GHz). Applications. It depicts the return loss of −21.36 dB at 5.65 GHz with −10 dB band width of 1.88 GHz is obtained when S_1, S_2 OFF and S_3 ON. This antenna is suitable for WLAN application. When S_1, S_3 OFF and S_2 ON, a return loss of −21.55 dB at 5.3 GHz with −10 dB band width of 1.91 GHz is obtained and is suitable for WLAN application. It also shows a −19.5 dB return loss at 4.42 GHz with −10 dB band width of 1.39 GHz with S_1, OFF, S_2, S_3 ON. This antenna is suitable for C-band application. When switch S_1 ON and S_2, S_3 are in OFF condition, a return loss of −18.5 dB at 4.35 GHz with band width of 2.07 GHz is obtained. Return losses of −22.26 dB and −20.34 dB at 3.95 GHz and 3.22 GHz with −10 dB band width of 2.36 GHz and 1.35 GHz are obtained when switches S_1, S_3 are in ON and S_2 in OFF condition; and S_1, S_2 ON and S_3 are in OFF condition respectively. In all the modes desired antenna gain which is above 2 dBi and efficiency above 70% is obtained from simulation. The results are shown in Table 1.

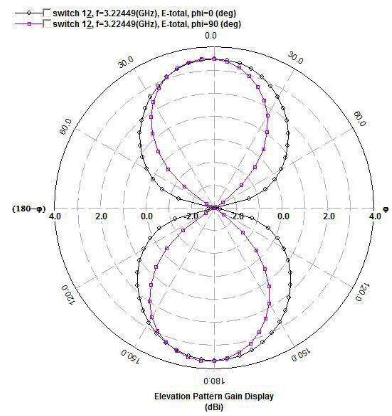

Figure 9: 2D Elevation Pattern at 3.22 GHz.

Table 1: Results.

Antenna Parameters	**Case 1**	**Case 2**	**Case 3**	**Case 4**	**Case 5**	**Case 6**	**Case 7**
Return Loss	−19.9 dB	−21.4 dB	−21.5 dB	−19.5 dB	−18.5 dB	−22.3 dB	−20.3 dB
Operating Frequency	5.8 GHz	5.65 GHz	5.39 GHz	4.42 GHz	4.35 GHz	3.9 GHz	3.22 GHz
Bandwidth	1.53 GHz	1.88 GHz	1.91 GHz	1.4 GHz	2.07 GHz	2.36 GHz	1.35 GHz
Antenna Gain	2.75 dBi	2.72 dBi	2.65 dBi	5.29 dBi	3.12 dBi	2.1 dBi	3.64 dBi
Radiating Efficiency	70%	70%	71%	100%	70%	70%	93%
Application	RFID	WLAN	WLAN	C- Band Application			

4. CONCLUSION

In this paper, a novel reconfigurable CPW fed slot antenna with frequency diversity is presented. This antenna is compact in comparison to existing antennas. It operates at the frequency bands 5.8 GHz, 5.65 GHz, 5.39 GHz, 4.42 GHz, 4.35 GHz, 3.95 GHz, 3.22 GHz which are all found suitable for wireless communication applications such as WLAN, WiMAX, RFID, and typical C-band applications. When all switches are turned ON a dual band characteristic with return loss of −16.72 dB at 6.68 GHz and −17.39 dB at 7.29 GHz; −10 dB band width of 408 MHz and 225 MHz are obtained. In this case, cross polarization is greater than co-polarization. This mode is not suitable for any practical application and hence not reported. The designed antenna meets the desired antenna gain and efficiency at different operating frequency bands.

REFERENCES

1. Zhang, J., A. Wang, and P. Wang, " A survey on reconfigurable antennas," *Proceedings of Int. Conf. on Microwave and Millimeter Wave Technology*, Vol. 3, 1156–1159, Apr. 2008.
2. Yashchyshyn, Y. M., "Reconfigurable antennas," *Proceedings of 18th International Conference on Microwave Radar and Wireless Communications MIKON*, 1–9, 2010.
3. Chen, K.-H., S.-J. Wu, C.-H. Kang, and C.-K. Chan, "A frequency reconfigurable slot antenna using PIN diodes," *Proceedings of Asia Pacific Microwave Conference*, 1930–1933, 2009.
4. Chiu, C.-Y. and R. D. Murch, "Reconfigurable multi slot multi-port antennas using RF MEMS switches for handheld devices," *Proceedings of Asia-Pacific Microwave Conference*, 999–1002, 2010.
5. Simons, R. N., *Coplanar Waveguide Circuits, Components and Systems*, John Wiley & Sons Inc., 2001.

A Single Feed Circularly Polarized Wallis Sieve Fractal Microstrip Antenna

V. Venkateshwar Reddy and N. V. S. N. Sarma
National Institute of Technology, Warangal, India

Abstract— A new type of compact circularly polarized single feed microstrip antenna is presented. In order to achieve the specified characteristics Wallis sieve fractal geometry is employed. Simulated results indicate that the proposed antenna gives a very good circular polarization with minimum axial ratio very close to 0 dB at the center frequency of 2430 MHz and impedance bandwidth (at 10 dB reference) of 4.25%. The antenna provides almost constant gain of about 3.2 dBi over the frequency band of operation. This antenna can be used in WLAN, Bluetooth and WiMAX, Wi-Fi etc at ISM band. The antenna can also be used for multiband opearation.

1. INTRODUCTION

Microstrip patch antennas are small size, low profile antennas. Circularly polarized microstrip antennas find applications in different fields like WLAN, GPS, Mobile satellite, RFID applications etc. It is required to design antennas with compact size without degradation in gain of the antenna in the said applications. The circular polarization can be obtained by exciting two near degenerate modes which are orthogonal to each other. The conventional method of getting circular polarization is by the use of nearly square patch or square patch with diagonal slot. Those methods give 6 dB axial ratio bandwidth not more than 1%. There are many methods reported in the literature with single feed circularly polarized antennas using square patch. The first single feed CP antennas are reported by P. C. Sharma and K. C. Gupta [2] using square patch with truncated corners and square patch with inclined slot. But the obtained 6 dB axial ratio bandwidth is only 0.831% and 1.134% respectively with those antennas. M. L. Wong et al. [3] presented a different method to get circular polarization mainly aiming for compact size by incorporating slots and adding tails to the square patch. But with that method the impedance and 3 dB axial ratio bandwidths are 1.61% and 0.381% respectively. J. S. Rowand and C. Y. Ai [4] have proposed a compact design of single feed circular polarized antenna by cutting a crossed slot on the circular patch backed by square shaped ground plane with crossed slot. But the peak gain is very low which is in the order of 1.8 dBi and 3 dB axial ratio bandwidth is around 0.9%. M. Elsdon et al. [5] have published work on a single feed star loaded patch antenna for circular polarization with 3 dB axial ratio bandwidth at 2.4 GHz around 1.1%. The input impedance of the patch varies from 245 ohms to 705 ohms. Wen-Shyang Chen et al. [6] have presented a novel compact circularly polarized square microstrip antenna. The gain variation with that antenna is only 1.4 dBi to 3.5 dBi. Kin-Lu Wong and Jian-Yi Wu [7] have proposed a single feed circularly polarized microstrip antenna by providing two pairs of narrow slits in the x and y directions of the square patch. It is not clear whether the methods mentioned above give 0 dB axial ratio at the center frequency.

However there is a need to design a circularly polarized antenna which provides 0 dB axial ratio at the center frequency and should give at least 3 dB axial ratio bandwidth of 1%. Further the antenna should be perfectly matched to the line. In the present paper a novel technique is used to get circular polarization by the use of fractal antenna which not only has all the above qualities but also compact in size.

2. ANTENNA GEOMETRY

The proposed wallis sieve fractal antenna to be operated at 2.5 GHz can be realized by introducing slots on the square patch with size $6 \times 6\,\text{mm}^2$ in iteration 1, $6 \times 6\,\text{mm}^2$ and $2 \times 2\,\text{mm}^2$ slots in iteration 2. The generation of the fractal Antennas is shown in Figures 1–4. Two cases have been considered in this paper: first one is linearly polarized wallis sieve fractal antenna and the second one is circularly polarized antenna. The size of the patch is 36×36 and is printed on RT Duroid substrate of thickness 1.6 mm with relative permittivity of 2.75. The antennas are simulated using Zeland IE3D electromagnetic simulator. For linearly polarized case the antennas are with transmission line feeding at point $(-18, 0)$ and keeping electrical length constant in both sides. In this case the behavior of the antenna for three iterations is studied. The geometries of the antenna are shown in Figures 1–4. The resonant frequency of the antenna is changed from 2493 MHz to

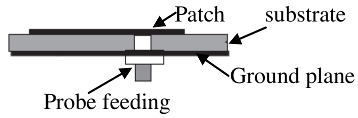

Figure 1: Basic microstrip antenna side view.

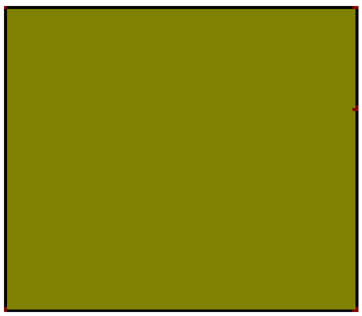

Figure 2: Iteration 0 antenna.

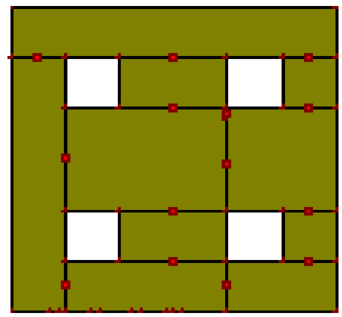

Figure 3: Iteration 1 antenna.

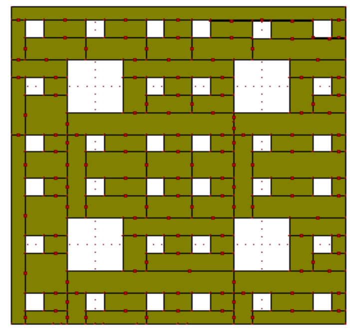

Figure 4: Iteration 2 antenna.

2374 MHz when the iteration is changed from zero to two as shown in Figure 4. The resonant frequencies for the different cases are given in Table 1. All the antennas are of $36 \times 36\,\mathrm{mm}^2$ size.

A square patch antenna with same size operates at a frequency of about 2493 MHz. By introducing slots on the iteration 0 antenna at four corners the resonant frequency can be altered in iteration 1, and for iteration 2. This is very useful in designing circularly polarized antenna with probe feeding.

The proposed antenna with iteration 2 gives axial ratio at the center frequency very close to 0 dB, the 3 dB axial ratio bandwidth of about 2% and 10 dB impedance bandwidth of 4.25%. Circularly polarized wave can be obtained by simply changing the probe feeding point to the point (−8.5, 3.6). Right hand circularly polarized wave and left hand circularly polarized wave can be obtained by simply changing the feed point to the opposite direction of the same point. The variation of impedance, return loss and axial ratio, VSWR with frequency are shown in Figures 5–8 respectively.

2.1. Iteration 0 Antenna

This antenna is generally a microstrip patch antenna with size $36 \times 36\,\mathrm{mm}^2$, feeding line is a microstrip line with size $9 \times 0.8\,\mathrm{mm}^2$. A simple microstrip patch antenna is known as the iteration 0 of wallis sieve fractal. For iteration zero the basic formulas for determining the length and width of a microstrip patch antenna are used. These formulas as in [1] are given below for ready reference.

$$W = \frac{c}{2f_0}\frac{1}{\sqrt{\varepsilon_r + 1}} \tag{1}$$

$$L = \frac{c}{2f_0}\frac{1}{\sqrt{\varepsilon_{eff}}} - 2\Delta L \tag{2}$$

$$\Delta L = 0.412h\frac{(\varepsilon_{eff} + 3)(\frac{w}{h} + 0.264)}{(\varepsilon_{eff} - 0.258)(\frac{w}{h} + 0.8)} \tag{3}$$

$$\Delta L = 0.412h\frac{(\varepsilon_{eff} + 3)(\frac{w}{h} + 0.264)}{(\varepsilon_{eff} - 0.258)(\frac{w}{h} + 0.8)} \tag{4}$$

where W is the width, L is the length, ΔL is the length reduced from the antenna to reduce fringing effects, and ε_{eff} is the effective dielectric constant. Using the above equations and calculating at an operating frequency of 2.493 GHz the length and width turned out to be $36\,\mathrm{mm} \times 36\,\mathrm{mm}$ as indicated in Figure 2.

2.2. Iteration 1 Antenna

This antenna is normally a microstrip patch antenna with size $36 \times 36\,\mathrm{mm}^2$ and having four slots with dimension $6 \times 6\,\mathrm{mm}^2$, feeding line is a microstrip line with size $9 \times 0.8\,\mathrm{mm}^2$ as appeared in Figure 3.

2.3. Iteration 2 Antenna

The antenna designed is a microstrip patch antenna with size $36 \times 36\,\mathrm{mm}^2$ and having four bigger slots with dimension $6 \times 6\,\mathrm{mm}^2$ and smaller slots with dimension $2 \times 2\,\mathrm{mm}^2$, feeding line is a microstrip line with size $9 \times 0.8\,\mathrm{mm}^2$ as shown in Figure 4.

2.4. CP Antenna

This antenna is formally a microstrip patch antenna with size $36 \times 36\,\mathrm{mm}^2$ and having four bigger slots with dimension $6 \times 6\,\mathrm{mm}^2$ and smaller slots with dimension $2 \times 2\,\mathrm{mm}^2$, fed with probe feeding at point $(-8.5, 3.6)$ as depicted in Figure 4. The same antenna can be used for multiband operation by changing the substrate relative permittivity to 4.7.

3. RESULTS AND DISCUSSION

All the discussed antennas are simulated using Zeland IE3D electromagnetic simulator. It is observed from Figure 5 that as the iteration increases the resonant frequency is being shifted towards left. Simulation results of CP antenna are shown in Figures 6–9, it can be seen in Figure 8 that axial ratio is 0 dB at resonant frequency. The presented antenna can be used for multiband operation

Table 1: Resonance frequencies of the proposed antenna for different cases in linear polarization.

Antenna	Iteration	fo (MHz)	Return loss (dB)
Antenna 1	Zero	2493	−23
Antenna 2	One	2420	−24
Antenna 3	Two	2374	−26

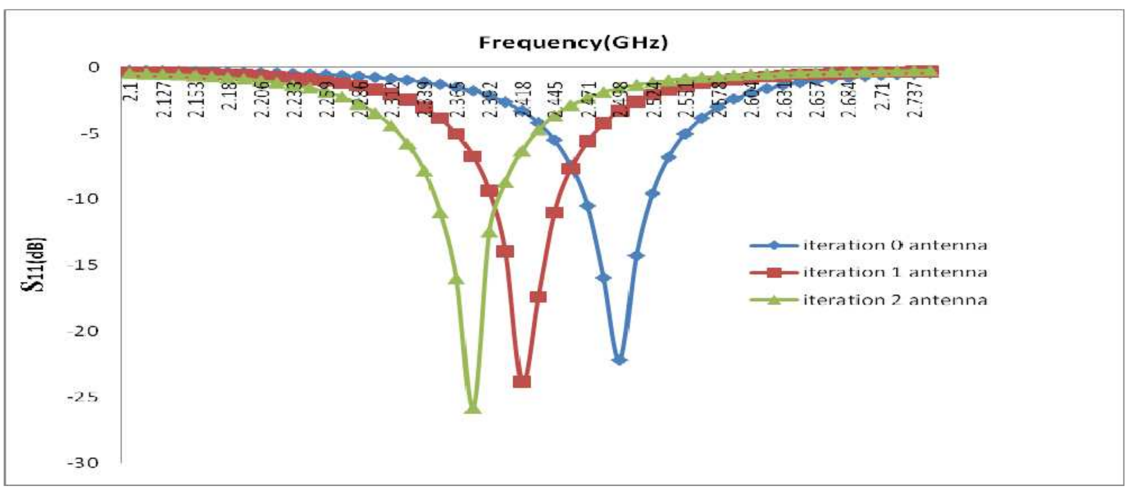

Figure 5: S_{11} Characteristics of linearly polarized Wallis sieve fractal microstrip antenna.

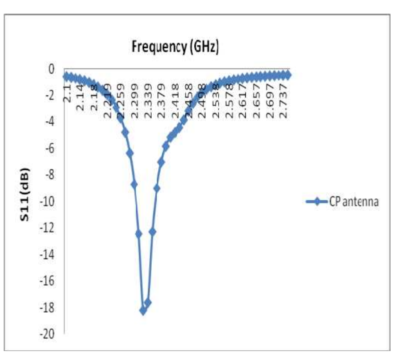

Figure 6: S_{11} characteristics of CP antenna.

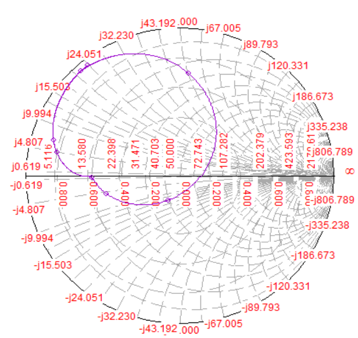

Figure 7: Variation of input impedance with frequency of CP antenna.

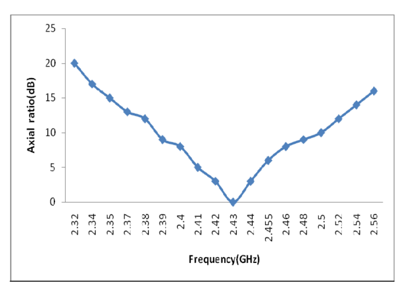

Figure 8: Axial ratio vs frequency.

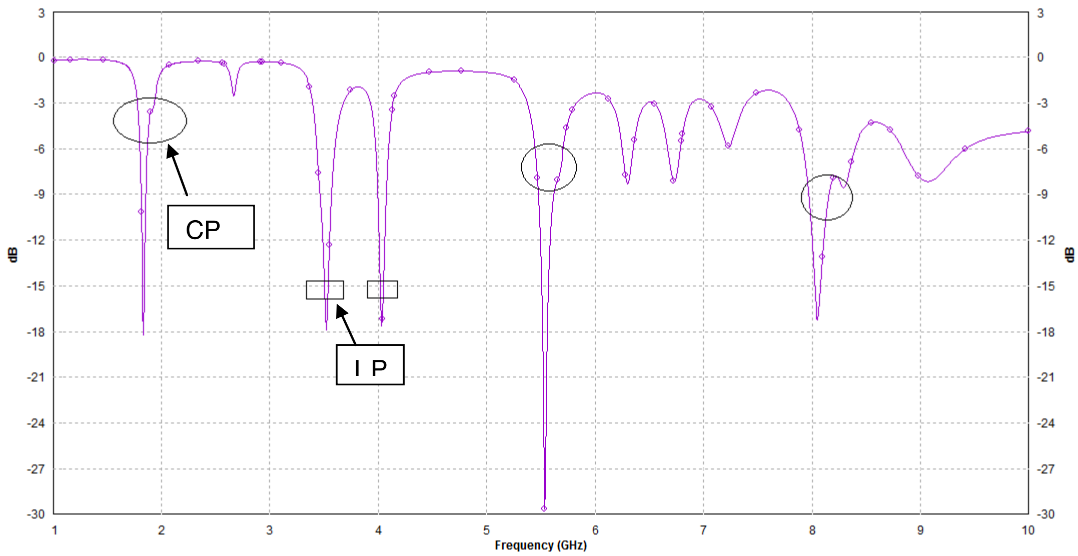

Figure 9: Return loss of multiband antenna, after changing CP antenna relative permittivity to 4.7.

and has the nature of giving linear polarization at certain resonant frequencies, circular polarization at other frequencies when changing the relative permittivity of substrate to 4.7. The multiband antenna is operating at 1.9 GHz, 3.5 GHz, 4 GHz, 5.6 GHz, 6.3 GHz, 6.7 GHz, 7.2 GHz, 8.2 GHz, and 9.1 GHz respectively. In the multiband operation case antenna is giving linear polarization at 3.5 GHz, 4 GHz, 6.3 GHz, 6.7 GHz, 7.2 GHz, and 9.1 GHz whereas it is giving circular polarization at 1.9 GHz, 5.6 GHz, and 8.2 GHz.

4. CONCLUSION

A compact circularly polarized fractal microstrip antenna is presented. The antenna provides axial ratio very close to 0 dB at the center frequency and operates over a band width of 2% (3 dB AR bandwidth) and 10 dB impedance bandwidth of 4.25%. It is established that by using a fractal wallis sieve geometry, it is simple and easy to design circularly polarized antenna.

REFERENCES

1. Constantine, A. B., *Antenna Theory Analysis and Design*, 3rd Edtion, John Wiley & Sons Inc., 1997.
2. Sharma, P. C. and K. C. Gupta, "Analysis and optimized design of single feed circularly polarized microstrip antennas," *IEEE Transactions on Antennas and Propagation*, Vol. 3l, 949–955, Nov. 1983.
3. Wong, M. L., H. Wong, and K. M. Luk, "Small circularly polarized patch antenna," *Electronics Letters*, Vol. 41, No. 16, Aug. 7–8, 2005.
4. Row, J. S. and C. Y. Ai, "Compact design of single-feed circularly polarized microstrip antenna," *Electronic Letters*, Vol. 40, No. 18, 1093–1094, Sep. 2, 2004.
5. Elsdon, M., A. Sambell, S. C. Gao, and Y. Qin, "Compact circular polarized patch antenna with relaxed manufacturing tolerance and improved axial ratio bandwidth," *Electronics Letters*, Vol. 39, No. 18, 1296–1298, Sep. 2003.
6. Chen, W.-S., C.-K. Wu, and K.-L. Wong, "Novel compact circularly polarized square microstrip antenna," *IEEE Transactions on Antennas and Propagation*, Vol. 49, No. 3, 340–342, Mar. 2001.
7. Wong, K. L. and J. Y. Wu, "Single feed circularly polarized square microstrip antenna," *Electronics Letters*, Vol. 33, No. 22, 1833–1834, Oct. 1997.
8. Borja, C. and J. Romeu, "On the behavior of Koch island fractal boundary microstrip patch antenna," *IEEE Transactions on Antennas and Propagation*, Vol. 51, No. 6, 128l–l29l, Jun. 2003.

Flat Lens Based on Aperture-coupled-patch FSS with Four-pole Resonance Behavior

Yu Wang, Hiroyuki Deguchi, and Mikio Tsuji
Department of Electronics, Doshisha University, Kyotanabe, Kyoto 610-0321, Japan

Abstract— A 24-GHz flat lens antenna based on aperture-coupled microstrip patch element with four-pole resonance behavior is discussed in this paper. A novel and simple structure of multiple-layered frequency selective surface (FSS) element is proposed for lens antenna use. Features of design are discussed, and results for transmission coefficient magnitude and phase against frequency are presented. The principle of design is explained and the measurement result for the radiation patterns are also shown in this paper to confirm the theory.

1. INTRODUCTION

Reflectors and lens are the most commonly used high-gain antenna in many applications [1] They can transform the spherical wave illuminated from a primary source (such as horn) into plane wave. Although reflectors are very efficient radiators, high surface accuracy is required. The traditional lens is similar to the lens used in optical fields. However, with the development of the PCB technology, flat lens with advantages of easier fabrication, thinner structure and lower profile are more possible to implement and can be a better alternative for the traditional ones. In this paper, flat lens are discussed and designed. The concept of flat printed lens can be described as follows. An inhomogeneous array of printed conducting elements serves as a filter to the incident wave and exhibits total transmission at the resonance points. Inhomogeneous array is desired here for compensating the phase-delay so that spherical wave can be transformed into plane wave.

A lot of reports about the research on flat lens antenna have been presented before. Some structures have been proposed in these reports to control the phase shift, such as patches with delay lines [2–4], multiple layered FSS [5], and coupled resonance element [6, 7]. In order to obtain multiple poles in pass-band, a kind of element combining slots with aperture-coupled patches was also presented previously [7].

In this paper, a kind of aperture-coupled patches element for a 24-GHz lens antenna use is proposed. A four-pole characteristic in pass-band can be obtained in this design. The details of design and results will be explained in the later section.

2. DESIGN PRINCIPLE

Figure 1 shows the typical system of flat lens antenna. As shown in Fig. 1, lens is a device that transforms the spherical wave out of primary source into plane wave after the incident wave transmitted through the lens surface. In Fig. 1, Ri is the distance between phase center of primary source and i'th cell on the lens surface. F is the focal distance which is decided for edge level less than -15 dB. The aperture-coupled patch array is called by "Antenna-Filter-Antenna (AFA)" array in some papers, because the single cell of such array can be regarded as an aperture-coupled patch antenna.

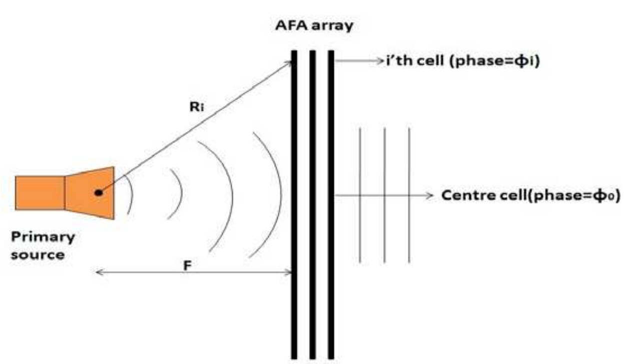

Figure 1: Lens antenna.

In order to transform the incident wave, the phase differences between each cell on the lens need to be compensated. The desired compensating phase of each cell can be obtained by Equation (1) [6]:

$$\varphi_i = \frac{2\pi}{\lambda_0}(R_i - F) \pm 2\pi N + \varphi_0 \tag{1}$$

Here, φ_0 is the phase of central cell on the lens, φ_i is the desired phase of i'th cell, N is a integer number chosen here just to make sure that $0 < \varphi_i \leq 2\pi$.

A novel structure of aperture-coupled element is proposed in this paper for lens use, shown as Fig. 2. The proposed element consists of three layers of metal surface and two layers of substrate. Both of the two outside metal surfaces are made of four identical microstrip lines in the vertical and horizontal direction respectively, and the inside surface is made of four identical slots etched on a metal plane. The parameter 'a' in Fig. 2 is a scale parameter which is introduced to control the phase of FSS.

The frequency response of the proposed structure is shown in Fig. 3. It can be observed from Fig. 3 that a four-pole pass-band is obtained by using the proposed structure. The first and second resonance points are generated by the coupled patches, and the third one is generated by the inside slots. As for the fourth resonance point, it is a similar phenomenon to Fabry-Perot (FP) resonance which is decided by the thickness and permittivity of substrate.

In order to compensate the phase differences between each region on lens, the unit cell should be ranged in an inhomogeneous array. The scale parameter 'a' which is marked in Fig. 1 can be used to control the transmission phase of each unit cell. When 'a' changes, the transmission phase will shift equably in the frequency band, which is shown in Fig. 4.

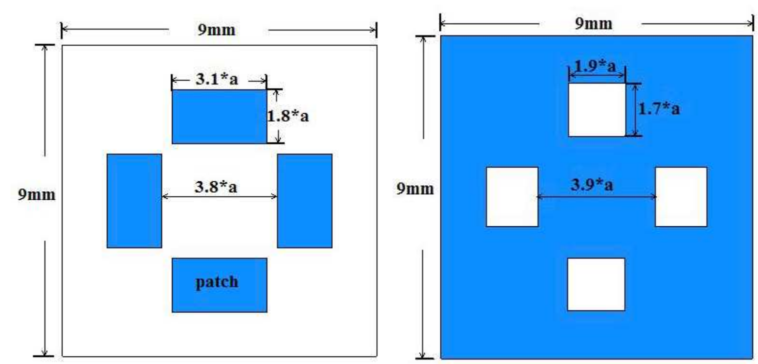

(a) Coupled patches (b) Inside slots

Figure 2: Geometry of proposed FSS element.

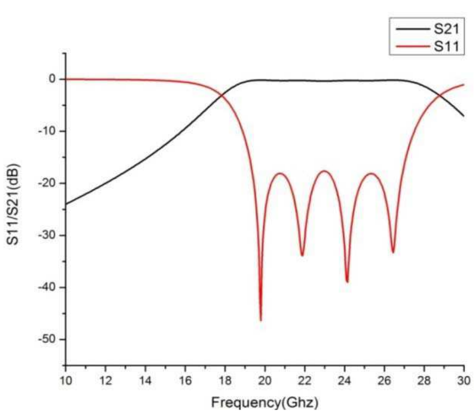

Figure 3: Frequency response of proposed structure ($a = 1.08$).

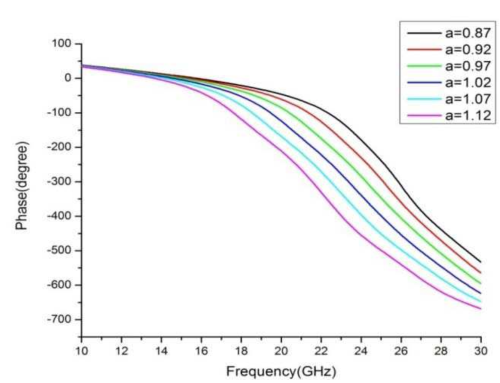

Figure 4: Transmission phase shift against scale parameter 'a'.

3. RESULTS FOR LENS ANTENNA

A 15×15 array which consists of the proposed element is used here to make up the lens antenna working at 24 GHz, which is illustrated in Fig. 5. The total thickness of the lens is 2 mm, and the electrical parameter of substrate is: $\varepsilon_r = 2.8$, $\tan\delta = 0.003$. The focal distance F which is marked in Fig. 1 is 108.2 mm for edge level less than -15 dB. Then the desired phase of each cell can be calculated by using Equation (1). The scale parameter 'a' is chosen from 0.87 to 1.13 for S_{21} larger than -1 dB and S_{11} less than -10 dB at 24 GHz. The phase shift at 24 GHz ranges from -178.6 degrees to -467.2 degrees when the scale 'a' changes from 0.87 to 1.13.

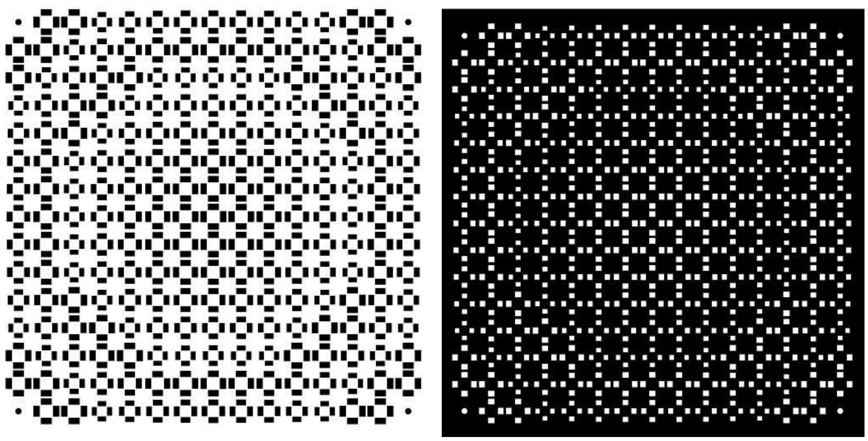

(a) Coupled patches array (b) Inside slots array

Figure 5: Designed flat lens antenna (size: $135\,\text{mm} \times 135\,\text{mm}$).

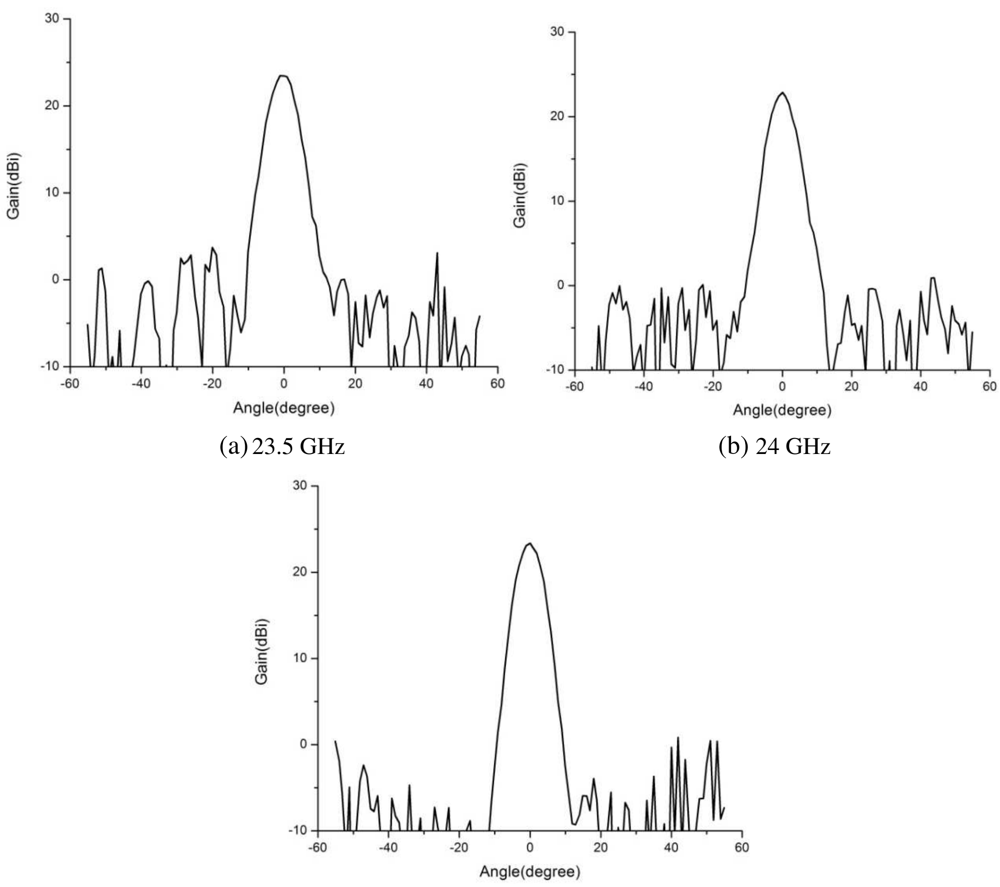

(a) 23.5 GHz (b) 24 GHz

(c) 24.5 GHz

Figure 6: Measured radiation patterns.

The measured results are shown in Fig. 6. The gain of the standard horn which is used as the primary source is 15.7 dBi, 15.9 dBi and 16.1 dBi at 23.5 GHz, 24 GHz and 24.5 GHz respectively. After equipping the lens, the gain is increased to be 23.4 dBi, 22.8 dBi and 23.3 dBi at these three frequency points. These results confirm the guess that the spherical wave front is transformed into plane wave front so that the gain is enhanced.

4. CONCLUSION

A novel and simple aperture-coupled patch element with four-pole pass-band is proposed in this paper. Ranging such proposed element in an inhomogeneous array can make up a lens antenna. The detail design principle is explained and the results for the proposed FSS and lens antenna are shown as well. More details will be explained in the presentation.

ACKNOWLEDGMENT

This work was supported in part by a Grant-in-air for Scientific Research (c) (23560421) from Japan Society for the Promotion of Science.

REFERENCES

1. Gao, Y. J. and S. K. Barton, "Flat printed lens and reflector antennas," *Ninth International Conference on Antennas and Propagation*, Vol. 1, 253–256, 1995.
2. Popovic, D. and Z. Popovic, "Multibeam antennas with polarization and angle diversity," *IEEE Trans. Antennas Propagat.*, Vol. 50, No. 5, 651–657, 2002.
3. White, D. T., J. P. Ebling, and G. Rebeiz, "A wide-scan printed planar K-band microwave lens," *IEEE Antennas Propagat. Symp. Digest*, Vol. 4A, 313–316, 2005.
4. McGrath, D. T., "Planar three-dimentional constrained lenses," *IEEE Trans. Antennas Propagat.*, Vol. 34, No. 1, 46–50, 1986.
5. Pozar, D. M., "Flat lens antenna concept using aperture coupled microstrip patches," *Electronic Letters*, Vol. 32, No. 23, 2109–2111, 1996.
6. Datthanasombat, S., A. Prata, L. R. Amaro, J. A. Harrell, S. Spitz, and J. Perret, "Layered lens antennas," *IEEE Antennas Propagat. Symp. Digest*, Vol. 2, 777–780, 2001.
7. Shibayama, R., H. Deguchi, and M. Tsuji. "Flat thin polarizer-lens based on multiple resonance behavior," *IEEE Antennas Propagat. Symp. Digest*, 1–4, 2010.

Analysis on Physical and Electromagnetic Parameter of a Concentric Split Ring Square Reflectarray Element

S. H. Yusop[1], N. Misran[1,2], M. T. Islam[2], and M. Y. Ismail[3]

[1]Department of Electrical, Electronic and System Engineering
Universiti Kebangsaan Malaysia, Bangi, Selangor 43600, Malaysia
[2]Institute of Space Science (ANGKASA)
Universiti Kebangsaan Malaysia, Bangi, Selangor 43600, Malaysia
[3]Communication Engineering Department, Faculty of Electrical and Electronics Engineering
Universiti Tun Hussein Onn Malaysia (UTHM), Batu Pahat, Johor 86400, Malaysia

Abstract— A series of characterization studies of physical and electromagnetic parameters has been carried out and presented in this paper. This study is focused in improving the performance of the bandwidth of reflectarray antenna element. The physical parameter is considering investigation on a variation of gap sizes of the element while for electromagnetic parameters is considering investigation on a variation of substrate thickness and its permittivity. Figure of Merit used in this paper is the phase range and phase slope to analyze the practicality of the element and the bandwidth performance. The FoM is according to the analysis from reflection phase and return loss versus frequency responses graph. The element is designed using computer software CST Microstripes namely concentric split ring square element. This element is the combination of a conventional annular ring and a novel square ring element, with the introduction of a gap into the element at TE direction. As the results, both physical and electromagnetic parameters are affects the performance of both phase range and phase slope of the element.

1. INTRODUCTION

High gain antenna is an inevitable requirement for most communication systems applications, especially for long distance communication [1]. Typically, high gain antenna used is a parabolic reflector antenna where it has a very good performance in term of a wide frequency range, simple geometry and mature design methodology. However, this type of antenna has some difficulties in mounting to some applications besides of high cost development due to its bulky size, large in mass and curvy reflector structure. Therefore, the reflectarray antenna has emerged around 1960s to improve this problem by introducing the flat reflective surface, which still retains the ability to operate as a high gain antenna [2]. This antenna consists of the order of microstrip elements arranged in the configuration array and printed on a grounded substrate material. A feed antenna is placed in the right distance in front of the reflector surface [3].

The key of the reflectarray antenna to perform as the parabolic reflector antenna is to ensure the reflection of each element is able to reflect the incident energy with a modified phase to form the planar phase front [4]. Reflectarray antenna has advantages of simple flat reflector structure, light in mass, low manufacturing cost and easy mountable to most of communication application especially in satellite applications. It only suffers one disadvantage of its narrow bandwidth which mainly caused by two factors which is its microstrip reflector element and unequal distance between the antenna feed to the antenna surface [5]. Recently, it is observed the limited bandwidth performance is also much impressed of the substrate material properties such as thickness, permittivity and loss tangent [6].

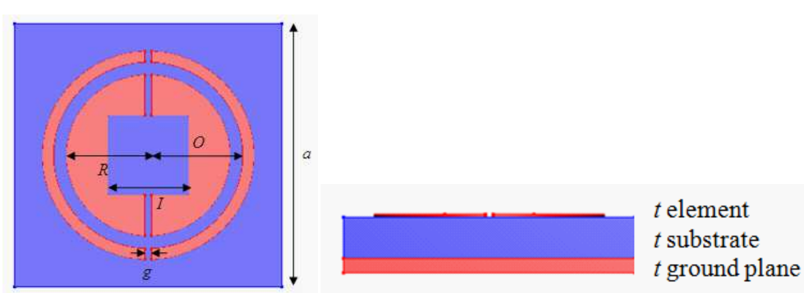

(a) (b)

Figure 1: Configuration of a concentric split ring square reflectarray element. (a) Top-view. (b) Side-view.

This paper presents the investigation on the physical interpretation and electromagnetic parameters affects to the element performance in term of phase range and phase slope. The objective is to increase the phase range and reduce the phase slope. Phase range is the stability of the reflection phase when the element size is changed which the higher value gives more stability. While, the small phase gradient improves the bandwidth performance according to the definition of a small phase gradient gives the expansion of bandwidth [3]. The optimum phase range is observed to be larger than 300° while the phase slope is less than 0.3°/μm. Besides that, return loss is also observed not to be more than 3 dB to respect the reflector concept of antenna [7, 8].

2. METHODOLOGY

The element developed in this study is a combination of a conventional annular ring and the novel single square element with the gap introduction in the element at TE direction, as shown in Figure 1. Single layer structure is used instead of multilayer configuration since it is less costly and simple in design geometry [9].

Referring to Figure 1, I is defined as the length of the square hole, R is the square ring radius and O is the outer ring radius. Meanwhile, g is the gap, a is the periodicity of unit element and t is the thickness value of reflectarray antenna elements. This element is designed and analyzed using computer software tool CST Microstripes. Dual element combination is intended to achieve dual frequency operation, while the introduction of the gap is to improve the bandwidth performance of the reflectarray antenna [10]. This paper is investigating the physical and electromagnetic parameter including the gap sizes, substrate thickness and substrate permittivity.

In order to investigate the gap sizes variation, the value is analyzed at $g = 0.14$ mm, $g = 0.28$ mm and $g = 0.56$ mm. The value is selected referring to studies in [10]. This paper is to configure out which size of gap is suitable for a concentric split ring square element. To study gap variation value, the periodicity is fixed at 10 mm, substrate permittivity at 3.54 and substrate thickness at 1.524 mm. While for investigation on thickness of substrate material variation, the thickness of the element and ground plane is set at $t = 0.1$ mm and $t = 0.5$ mm, respectively. The value of the substrate thickness is determined and analyzed at three values of $t = 0.764$ mm, $t = 1.524$ mm and $t = 3.044$ mm. These values are chosen based on the RF35 thickness provided by the manufacturer which is available in the lab. To study substrate thickness variation value, the gap is fixed at 0.28 mm, the periodicity is fixed at 10 mm and the substrate permittivity at 3.54.

As stated in [11], dielectric of substrate material is one of the factors which affect the bandwidth performance, which is said as the bandwidth of the reflectarray antenna can be increased by using a suitable dielectric material. Generally, bandwidth performance is inversely proportional with dielectric permittivity, as the higher value of dielectric degrades the bandwidth performance [11]. This paper presented investigation on substrate permittivity at fixed value of $\varepsilon_r = 1.5$, $\varepsilon_r = 3.54$ and $\varepsilon_r = 10$. The values of this study are randomly selected using RF35 material. To study substrate permittivity variation value, the gap is fixed at 0.28 mm, the periodicity is fixed at 10 mm and the substrate thickness is fixed at 1.524.

For all these analysis of physical and electromagnetic parameter, the outer ring radius is fixed at the value of 3.56 mm, outer ring width at 0.4 mm, square length at 3.06 mm, square ring radius at 3.06 mm and substrate loss tangent at 0.0018. The parameter studied in this paper is referring to the graph of reflection phase versus frequency responses. The phase range and phase slope performance is observed to be larger than 300° and lower than 0.3°/μm, respectively. In this study, radiation pattern, antenna gain or antenna loss is not analysed since this paper focused on the initial performance of a novel unit cell element instead of a whole antenna.

3. RESULTS AND DISCUSSIONS

Figure 2 shows the analysis results of the gap sizes for a concentric split ring square reflectarray element. Referring to Figure 2, the larger size of gap, $g = 0.56$ mm shows a smooth phase curve with a less steep phase slope that will provide improvements to the bandwidth.

Return loss shown in Figure 2(b) is the lowest with the value of 0.47 dB only for larger size of gap, in line with the less slope phase curve. While, return loss value is increasing for the smaller gap size as $g = 0.28$ mm, return loss is observed at 0.65 dB and for $g = 0.14$ mm, return loss is 0.8 dB. The larger value of return loss will degrade the reflection performance, which leads to the smaller bandwidth [6]. The smaller gap size is also results in difficulties of fabrication process. However, the phase range is reduced for larger gap size compared to the smaller gap size, where the larger phase range is a needed in practicality of a reflectarray element. Therefore, $g = 0.28$ mm was

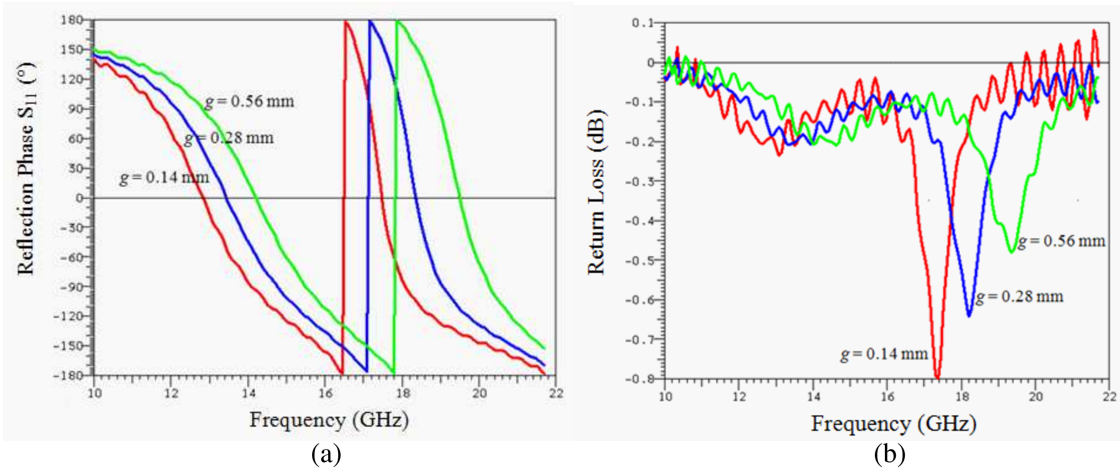

Figure 2: Frequency responses of a concentric split ring square element for gap analysis.

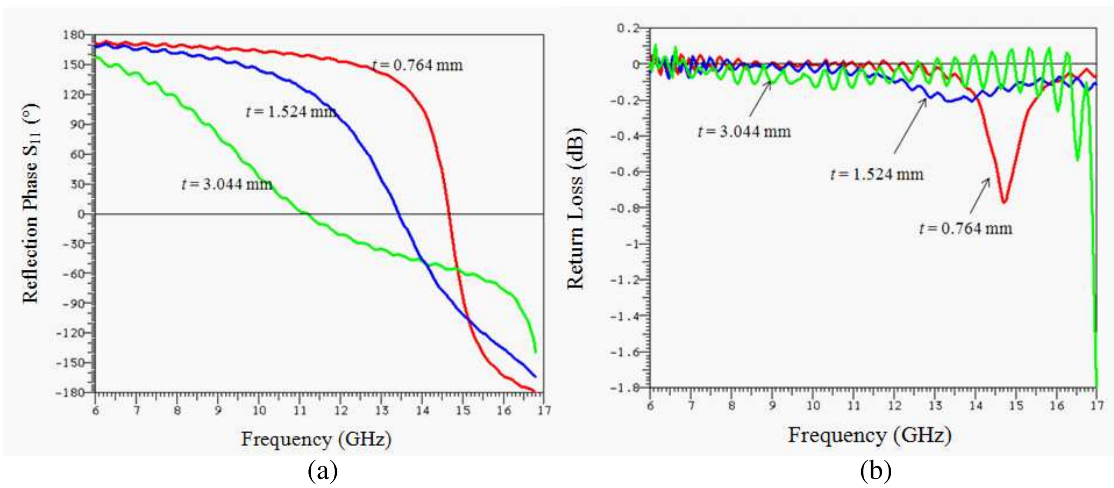

Figure 3: Frequency responses of a concentric split ring square element for substrate thickness analysis.

Table 1: Gap size analysis.

g (mm)	Frequency (GHz)	Return Loss (dB)
0.14	17.5	0.80
0.28	18.3	0.65
0.56	19.5	0.47

chosen as the gap size since it provides optimum performance for both phase range and phase slope. Table 1 summarizes the analysis of variation gap sizes observed at second resonant frequency.

Figure 3 shows the analysis results of the substrate thickness for a concentric split ring square reflectarray element. Referring to Figure 3, the thicker substrate produces a lower resonant frequency while the thinner substrate operates at higher resonant frequency.

Figure 3 shows three thickness value that have been analysed and it is shown that the thicker substrate gives the less steep phase slope which provides improvements in bandwidth performance. However, the phase range is also reduced due to the high loss in the substrate. It is observed that the thinner substrate, $t = 0.764$ mm will result in sudden changes to the phase around the resonant 14.7 GHz and slow around the element size is too small and too large. This abrupt changes cause the distribution phase becomes very sensitive to fabrication errors. Thus, substrate thickness $t = 1.524$ mm was chosen as the optimum thickness at both phase range and phase slope performance. The return loss is observed at the value of 0.2 dB. This value is small and respects the reflector concept of reflectarray antenna. Table 2 summarizes the analysis for substrate thickness studies.

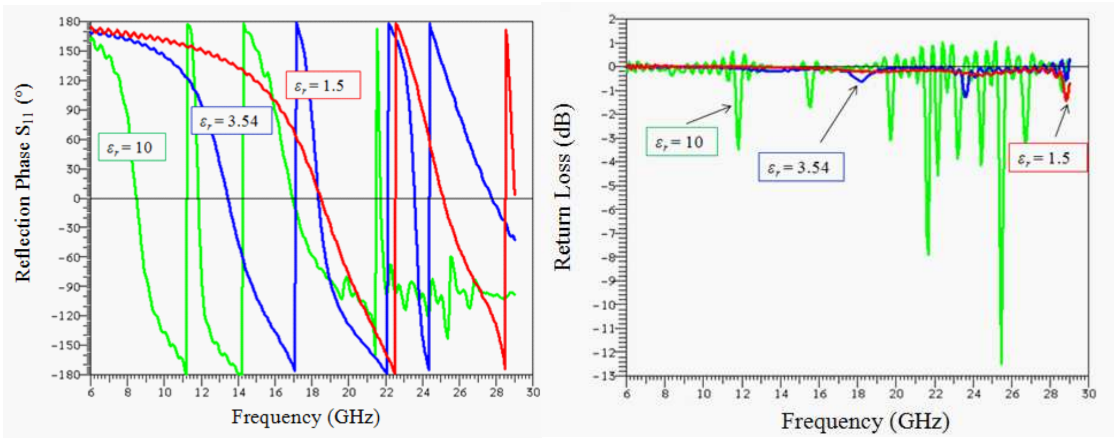

(a) (b)

Figure 4: Frequency responses of a concentric split ring square element for substrate permittivity analysis.

Table 2: Substrate thickness analysis.

t (mm)	Frequency (GHz)	Return Loss (dB)
0.764	14.6	0.8
1.524	13.5	0.2
3.044	11.1	0.1

Table 3: Substrate thickness analysis.

ε_r	Frequency (GHz)	Return Loss (dB)
1.5	18.6	< 1
3.54	13.5	< 1
10	8.6	4

Figure 4 shows the analysis results of the substrate permittivity for a concentric split ring square reflectarray element. It is shown in Figure 4 that the substrate with high permittivity ($\varepsilon_r = 10$) produce a high gradient phase and reduce its bandwidth performance. This high permittivity leads to more reflection in microwave energy which causes high reflection loss. This can be proved from Figure 4 where $\varepsilon_r = 10$ gives the highest reflection loss of up to 4 dB at second resonant frequency compared to the lower permittivity which have smaller value of reflection loss which less than 1 dB. This high loss will degrade the reflector performance of the reflectarray antenna element.

However, the smaller value of permittivity leads to phase error where the maximum phase error occurs because of inability to give a phase range of 360°. Therefore $\varepsilon_r = 3.54$ was chosen as the nominal permittivity for giving optimum performance of large phase range ($> 300°$) and phase slope ($< 0.3°$ µm), with return loss value less than 1 dB. Table 3 summarizes the analysis on permittivity changes of substrate material.

4. CONCLUSIONS

Analysis physical and electromagnetic parameters of a reflectarray antenna element namely concentric split ring square have been carried out in this paper. The result shows that a right design and parameterization procedure will improve the bandwidth performance and practicality factor in term of phase slope and phase range. Analysis carried out shows the suitable gap size is $g = 0.28$ mm, thickness of a suitable substrate for the antenna element developed is $t = 1.524$ mm while its permittivity $\varepsilon_r = 3.54$ for a concentric split ring square reflectarray element.

ACKNOWLEDGMENT

The authors would like to thank the MOSTI Secretariat, Ministry of Science, Technology and Innovation of Malaysia, Science fund: 01-01-02-SF0608, for sponsoring this work.

REFERENCES

1. Huang, J. and J. A. Encinar, *Reflectarray Antennas*, John Wiley and Sons, New Jersey, 2008.
2. Huang, J., "Analysis of a microstrip reflectarray antenna for microspacecraft applications," *Spacecraft Telecommunications Equipment Section TDA Progress Report*, 42–120, 1995.
3. Pozar, D. M., S. D. Targonski, and H. D. Syrigos, "Design of millimeter wave microstrip reflectarrays," *IEE Trans. Antennas and Propag.*, Vol. 45, 287–295, 1997.
4. Han, C. M., "Dual-band reflectarrays using microstrip ring elements and their applications with various feeding arrangements," Ph.D. Dissertation, Texas A&M University, Texas, 2006.
5. Sze, K. Y. and L. Shafal, "Analysis of phase variation due to varying patch length in a microstrip reflectarray," *IEEE Antennas and Propagation Society International Symposium*, Vol. 2, 1134–1137, 1998.
6. Ismail, M. Y., M. Inam, and A. M. A. Zaidi, "Reflectivity of reflectarrays based on dielectric substrates," *American J. of Engineering and Applied Sciences*, Vol. 3, No. 1, 180–185, 2010.
7. Misran, N., R. Cahill, and V. F. Fusco, "Design optimisation of ring elements for broadband reflectarray antennas," *Proceeding IEEE Microwaves Antennas and Propagation*, 2003.
8. Misran, N., R. Cahill, and V. F. Fusco, "Performance of a broadband ring element reflectarray," *IEEE Student Colloquium*, The Queen's University Belfast, Ireland, 2003.
9. Abbosh, A., "Design of dual-band microstrip reflectarray using single layer multiresonance double cross elements," *Progress In Electromagnetics Research Letters*, Vol. 13, 67–74, 2010.
10. Misran, N., "Design optimisation of ring elements for broadband reflectarray antennas," Ph.D. Thesis, Queen's Belfast University, UK, 2004.
11. Ismail, M. Y. and M. Inam, "Numerical analysis and equivalent circuit modeling for loss quantification of reflectarrays using different substrate materials," *IEEE International Conference on Antennas, Propagation and Systems (INAS 2009)*, Johor, Malaysia, 2009.

A Novel Design of Dual-feed Single-element Antenna for 4G MIMO Terminals

Nguyen Khac Kiem, **Dang Nhu Dinh**, **Hoang The Viet**, **and Dao Ngoc Chien**
School of Electronics and Telecommunications, Hanoi University of Science and Technology
No. 1 Dai Co Viet Road, Hanoi, Vietnam

Abstract— A novel design of dual-feed single-element antenna for 4G multiple input-multiple output (MIMO) terminals is proposed and analyzed in this paper. The antenna consists of a radiating patch which is fed by two input ports. The proposed antenna is a promising candidate for MIMO systems. With the presence of the crossover, the signal from the left port will excite for the right part of antenna and vice versa. The antenna shows high performance such as good isolation less than −15 dB GHz, return loss less than −10 dB in the frequency band ranging from 1.92 GHz to 2.17 GHz, covering the UMTS IMT band for 3G/4G wireless communications.

1. INTRODUCTION

In recent years, the growing demand for wireless multimedia applications has motivated the development of broadband wireless-access technologies. The IEEE 802.16m and 3GPP LTE-Advanced are the two evolving standards targeting 4G wireless systems. In the standards, MIMO antenna technologies play an essential role in meeting the 4G requirements. The application of MIMO technologies is one of the most crucial distinctions between 3G and 4G. A large family of MIMO techniques has been developed for various links and with various amounts of available channel state information in both IEEE 802.16e/m and 3GPP LTE/LTE-Advanced [1–3]. Due to limited spectrum resources, MIMO techniques are paramount for achieving the minimum target cell spectral efficiency, peak spectral efficiency and cell edge user spectral efficiency defined by the ITU [4]. Therefore, a lot of researches has been made in the design of MIMO antennas [5–7]. In this paper, we propose a model of MIMO antenna with a new feeding structure. The proposed antenna is designed operating in the UMTS IMT frequency band. The resonant frequency of antenna can be controlled by adjusting the length of the radiating patch of antenna. Due to the radiating patch is fed by two input ports, two different modes are excited. Each mode will produces separate radiation pattern; therefore, the diversity for the antenna was achieved. In this model, the crossover is connected to the radiating patch to form MIMO antenna as a novel cross-fed method. Details of the proposed antennas are described and studied.

2. ANTENNA DESIGN

2.1. Structure of Antenna

Our proposed MIMO antenna is shown in Fig. 1. The antenna has an area of $64.2 \times 88.4\,\mathrm{mm}^2$ and is printed on a low-cost FR4 substrate with a relative permittivity of 4.4, thickness of 1.6 mm and loss tangent of 0.02. In order to produce a compact antenna, we use the planar-monopole technology

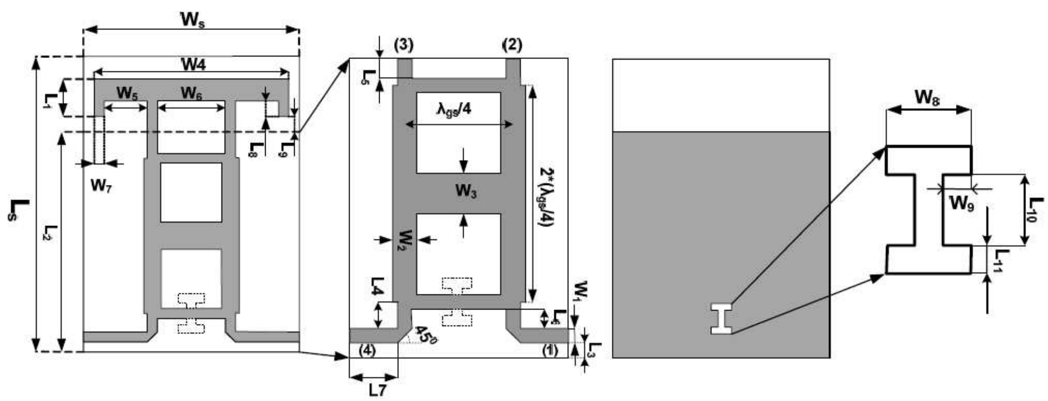

(a) (b)

Figure 1: Configuration of proposed antenna: (a) top view, (b) bottom view.

to achieve a compact antenna size for applications in small wireless devices. The antenna consists of a radiating patch with two broken lines at two ends. To achieve good impedance matching, the distance between the radiator patch and the ground plane (L_9) is set to 5 mm, the length of the radiating patch (W_4) is set to 57.8 mm and the width of the feed line (W_1) is set to 3 mm. In addition, a crossover is embedded as feeding part of the antenna. With the presence of the crossover, the signal from the left port will excite for the right part of antenna and vice versa. The dimensions of the antenna are optimized using computer simulation with detailed values listed in Table 1.

3. DESIGN OF ANTENNA

This section is aim to analyze in detail the design process of the here proposed antenna in the two following steps: firstly, the crossover is designed to operate in the band of UMTS IMT, the second work is the design of radiating patch of antenna, and the crossover connected to the radiating patch to form MIMO antenna with novel cross-fed method.

Firstly, the crossover coupler was designed, as shown in Fig. 1(a). The crossover is a symmetrical four port network with two inputs and two outputs. Theoretically, the conventional crossover can be achieved by connecting two 90° hybrids; therefore, this crossover is designed by the two 50 Ohm parallel arms and the middle of the structure is placed by a single 25 Ohm line. The perfect design of crossover is accomplished if the adjacent ports are isolated. It means that when one input, i.e., port 1 is fed, the electric current flowing through crossover coupler will go out via port 3 and vice verse [8, 9]. Practical results, however, showed that it is difficult to achieve the desired requirements in all of frequency band of UMTS system with the conventional crossover, as shown in Fig. 2. Because the structure of crossover includes some bends; therefore, the signal will be changed phase and magnitude when passing this bends. To overcome this limitation, a novel crossover with I-shaped Defected Ground Structure (DGS), Fig. 1(b), is introduced as the effective solution [10, 11]. The I-shaped DGS acts as a LC filter to collect energy, so when port (1) is fed, the signal will be cancelled at port (4) and vice versa, as plotted in Fig. 3. The adjusting of the dimensions of I-shaped DGS will affect the operation of S-parameters. From Fig. 4 it can be seen that S-parameters achieve the optimum values at $W_8 = 6$ mm, $W_9 = 2$ mm, $L_{10} = 5$ mm and $L_{11} = 2$ mm.

The work is the design of radiating patch of antenna with the connected crossover. The idea is

Table 1: Optimized parameters of antenna (mm).

W_s	W_1	W_2	W_3	W_4	W_5
64.2	3	5.1	8.2	57.8	12.8
W_6	W_7	W_8	W_9	h	$\lambda_{gs}/4$
20.2	3	6	2	1.6	23.2
L_1	L_2	L_3	L_4	L_5	L_6
11.2	65.4	3	5.51	5.98	4
L_7	L_8	L_9	L_{10}	L_{11}	L_s
19	4.6	5	5	2	88.4

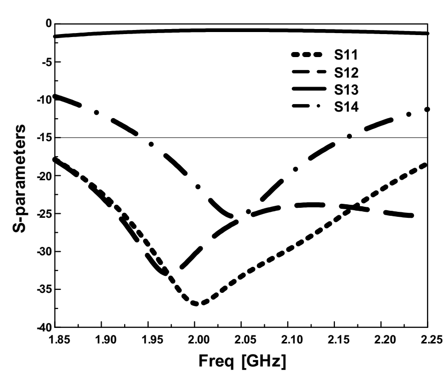

Figure 2: S-parameters of conventional crossover.

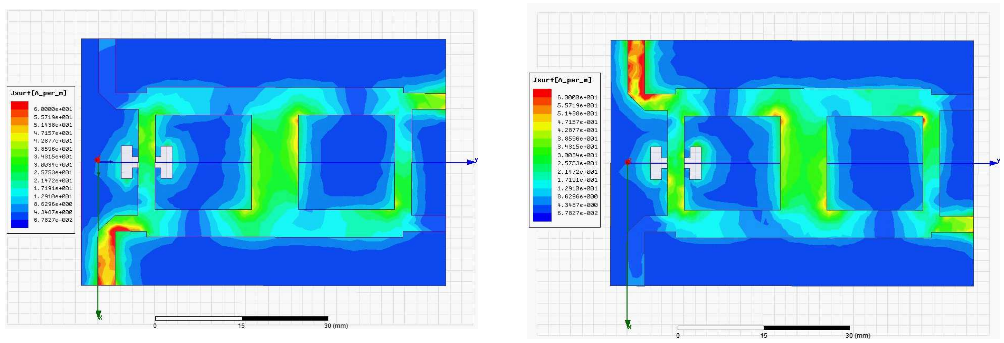

Figure 3: Surface current distributions at 2.05 GHz.

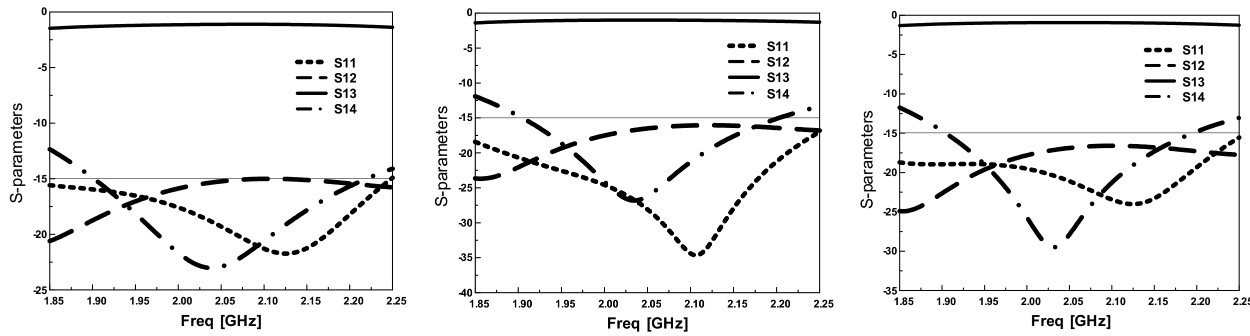

(a) (b) (c)

Figure 4: S-parameters of novel crossover after adjusting the dimensions of the I-shaped DGS. (a) $W_8 = 10\,\text{mm}$, $W_9 = 4\,\text{mm}$, $L_{10} = 5\,\text{mm}$, $L_{11} = 2\,\text{mm}$. (b) $W_8 = 6\,\text{mm}$, $W_9 = 1\,\text{mm}$, $L_{10} = 5\,\text{mm}$, $L_{11} = 2\,\text{mm}$. (c) $W_8 = 6\,\text{mm}$, $W_9 = 2\,\text{mm}$, $L_{10} = 5\,\text{mm}$, $L_{11} = 2\,\text{mm}$.

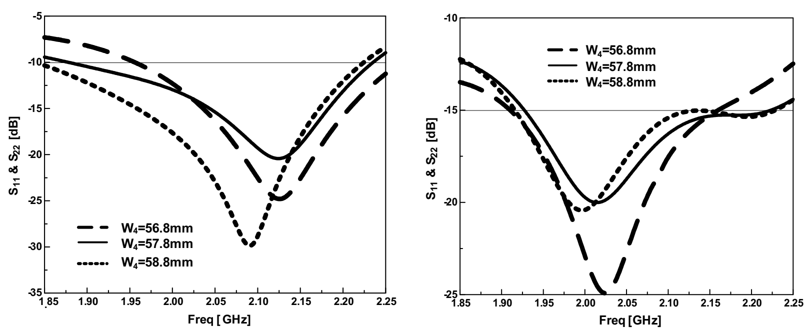

(a) (b)

Figure 5: (a) Return Loss and (b) S_{12} & S_{21} of antenna after adjusting the length of radiating patch.

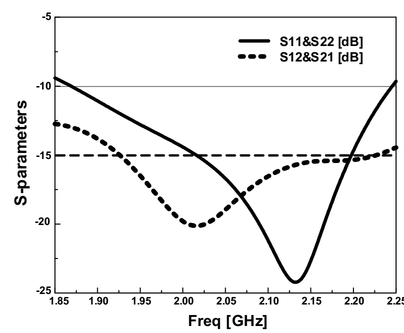

Figure 6: S-parameters of proposed antenna diagram.

to use isolated mode antenna technology — "iMAT" [12] as mean of reducing dimension of antenna and mutual coupling between ports. With the radiating patch of antenna is fed at two different locations, two different modes are excited, which are independent of each other. Each mode will produces separate radiation pattern, the diversity for the antenna was achieved. Thanks to this characteristic, the antenna is a promising candidate for MIMO system. With our proposed antenna, the length of radiating patch determines the resonant frequency of antenna, simultaneously also influences the isolation of two ports. In order to get a graph with the resonant frequency at 2.05 GHz, the length of radiating patch (W_4) is set to approximately 57 mm. Fig. 5 show the results of various S-parameters simulations and the optimum results are expressed in Fig. 5(c). The antenna can work well in the band covering from 1.92 GHz to 2.17 GHz, defined as return loss (S_{11} & S_{22}) less than $-10\,\text{dB}$, and the transmission coefficients of two ports are much below the threshold ($-15\,\text{dB}$) with $W_4 = 57.8\,\text{mm}$. Moreover, the antenna consists of a radiating patch with two broken lines at two ends which significantly reduce antenna size. Therefore the total dimension

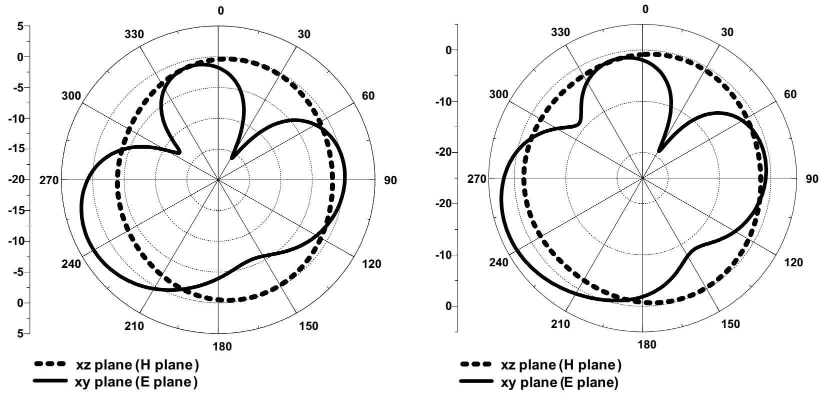

(a) 1.92 GHz (b) 2.05 GHz

Figure 7: Simulated radiation pattern of proposed antenna.

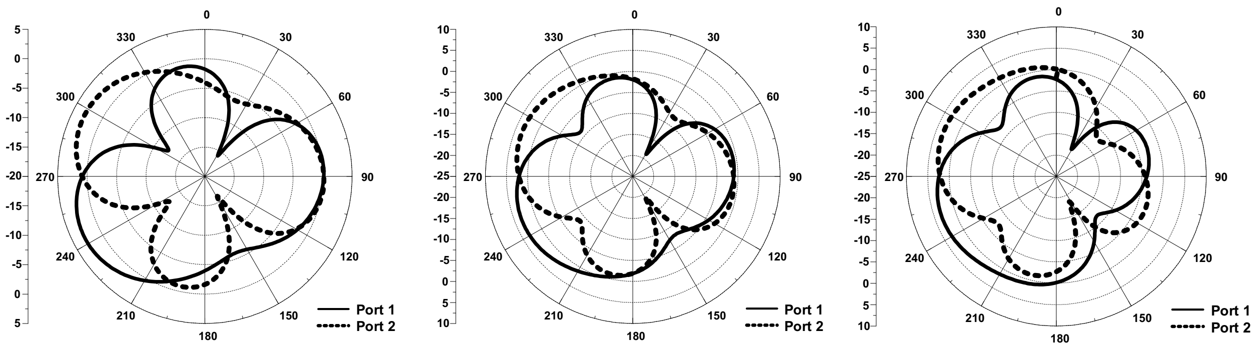

(a) 1.92 GHz (b) 2.05 GHz (c) 2.17 GHz

Figure 8: Radiation pattern of proposed antenna in x-y plane (E plane).

of antenna is 88.4×64.2 mm, allowing the antenna to be integrated into electronic devices, e.g., PDA, laptop.

4. RESULTS AND DISCUSSIONS

Figure 6 shows the simulated S-parameters of the proposed antenna. The antenna maintained the band performance from 1.87 GHz to 2.25 GHz with return loss less than -10 dB, covering the entire UMTS IMT frequency band. In addition the transmission coefficients of two MIMO models are below the threshold (-15 dB) for all the operating frequency bands. This indicates that the MIMO model can work well in the UMTS IMT band. The simulated radiation patterns in the E (x-y) and the H (x-z) planes at 1.92 and 2.05 GHz are shown in Figs. 7(a)–(b), respectively. The antenna displays good omni-directional radiation patterns in the H-plane. Finally the simulated radiation patterns in the E (x-y) planes at 1.92, 2.05 and 2.17 GHz when the antenna is fed each port in turn are shown Fig. 8. The far-field pattern differences due to separate port excitation are generally expected to provide an improvement in signal independence by sampling different spatial channels. The iMAT approach relies on the electromagnetic modal distribution to achieve isolation, and therefore the frequency at which the modes are supported results in improved isolation as well as high-radiation efficiency as resonance is approached.

5. CONCLUSION

In this paper, a dual-feed, single element antenna for 4G MIMO terminals has been proposed. Based on the isolated mode antenna technology, MIMO configuration is achieved with good properties, i.e., high isolation and compact size. Moreover the crossover is connected to the radiating patch to form MIMO antenna with novel cross-fed method. This antenna can operate in the UMTS IMT band spreading from 1.92 GHz to 2.17 GHz frequency band. Simulated results show great performance of the proposed antenna. Due to the total dimension of antenna is 88.4×64.2 mm, the antenna can be integrated into electronic devices, e.g., PDA, laptop.

REFERENCES

1. ITU-R Rec. M.1457-8, "Detailed specifications of the radio interfaces of international mobile telecommunications-2000 (IMT-2000)," May 2009.
2. ITU-R SG WP 5D, "Acknowledgment of Candidate submission from IEEE under step 3 of the IMT-advanced process (IEEE technology)," Doc. IMT-ADV/4-E, Oct. 23, 2009.
3. ITU-R SG WP 5D, "Acknowledgment of Candidate sub-mission from 3GPP proponent (3GPP organization partners of ARIB, ATIS, CCSA, ETSI, TTA and TTC) under step 3 of the IMT-advanced process (3GPP technology)," Doc. IMT-ADV/8-E, Oct. 23, 2009.
4. ITU-R Rep. M.2134, "Requirements related to technical system performance for IMT-advanced radio interface(s)," Nov. 2008.
5. Kulkarni, A. N. and S. K. Sharma, "A compact multiband antenna with MIMO implementation for USB size 4G LTE wireless devices," *2011 IEEE International Symposium on Antennas and Propagation (APSURSI)*, 2215–2218, Jul. 2011.
6. Sharawi, M. S., Y. S. Faouri, and S. S. Iqbal, "Design and fabrication of a dual electrically small MIMO antenna system for 4G terminals," *Microwave Conference (GeMIC)*, 1–4, Mar. 2011.
7. Chung, J.-Y., T. Yang, J. Lee, and J. Jeong, "Low correlation MIMO antenna for LTE 700 MHz band," *2011 IEEE International Symposium on Antennas and Propagation (APSURSI)*, 2202–2204, Jul. 2011.
8. Abdallah, A. S., "Printed circuit switched-beam smart antenna system using 4×4 butler matrix beamforming network at the band (11.25–12.85) GHz," *IJACT: International Journal of Advancements in Computing Technology*, Vol. 1, No. 1, 70–77, 2009.
9. Zheng, S., W. S. Chan, S. H. Leung, and Q. Xue, "Broadband butler matrix with flat coupling," *Electron Letters*, Vol. 43, No. 10, 576–577, May 2007.
10. Maddah-Ali, M. and K. Forooraghi, "A compact butler matrix for WLAN application," *Microwave and Optical Technology Letters*, Vol. 52, No. 10, 2294–2298, Oct. 2010.
11. Vidhya, K. and T. Jayanthy, "Design of microstrip hairpin band pass filter using defected ground structure and open stubs," *International Conference on Information and Electronics Engineering IPCSIT*, Vol. 6, 268–272, Singapore, Sep. 2010.
12. Caimi, F. M. and M. Mongomery, "Dual feed, single element antenna for WiMAX MIMO application," *International Journal of Antennas and Propagation*, Vol. 2008, Article ID 219838, 5 pages, 2008.

Circularly Polarized Multiband Microstrip Antenna Using the Combination of Novel Fractals

Homayoon Oraizi and Shahram Hedayati
Electrical Engineering Department, Iran University of Science and Technology, Tehran, Iran

Abstract— In this paper, by computer simulation, it is demonstrated that multiband operation with circular polarization of radiation may be achieved by the combination of square and Giusepe Peano fractal geometries realized on a two layer microstrip antenna. The antenna feed is designed by an electromagnetic coupling system. The proposed antenna configuration also achieves some degree of miniaturization, which makes it suitable for wireless applications. The antenna characteristics, such as return loss, axial ratio and radiation patterns achieved by the proposed structure attest to its effectiveness as a mobile radiator.

1. INTRODUCTION

If the antenna dimensions are smaller than a quarter wave length, they become impractical. However, the utilization of fractal geometries may makes the effective electrical length of antennas longer and actually make them multiband. Consequently, a self-similar geometry which includes several copies of itself with different proportional sizes inside its structure, has an inherent frequency independent characteristics or at least a multi-frequency property [1–3]. The property of self-similarity of fractal geometries is used to achieve multiband operations [4]. Utilization of fractal geometries is one of the best methods for their miniaturization. Since the fractal structures are generated by a recursive process, they can produce a very long length or a wide surface area in a limited space [5–10].

In this paper, a multiband antenna is introduced using the novel square and Giusepe Peano fractals. It is designed for operation in the following bands: Global positioning system L_1 (GPS 1.575 GHz); Hiper-Lan2 (High Performance Radio Local Area Network Type2) in the band 2.12–2.32 GHz; IEEE802.11b/g in the band from 2.4 to 2.484 GHz, which is one of the WLAN bands and IMT advanced system or forth generation (4G) mobile communication system in the band 4.6–5.2 GHz. We investigate the miniaturization and multibanding properties of the square fractal microstrip patch antenna. We also study the radiation properties of the combination of square and Peano fractals for the microstrip patch antenna with electromagnetically coupled feed systems. The miniaturization, multibanding and circular polarization of the proposed fractal antenna is verified by the simulation results.

2. SQUARE FRACTAL MICROSTRIP PATCH ANTENNA

Consider the square fractal geometry in Fig. 1, where the initiator, first and second iterations are shown. We compare the radiation properties of the initiator and first iteration, where the parameters are selected as $a = 2.3$ mm and $k_2 = k_1 = 2.5$ for the resonance frequency of about

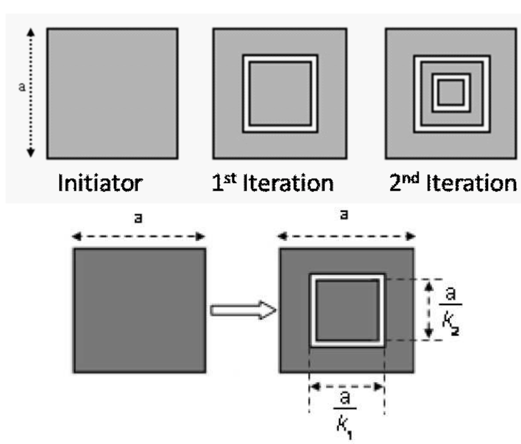

Figure 1: Configuration of the square fractal geometry.

2.45 GHz. We select the substrate FR4 with dielectric constant $\varepsilon_r = 4.4$, height $h = 1.6$ mm and loss tangent $\tan\delta = 0.02$.

We use the HFSS12 software for the computer simulation. The antenna feed is designed through an electromagnetic coupling system. The width of feed line is designed for 50 Ω by the TXLINE software.

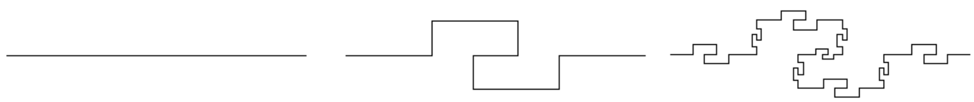

Figure 2: Initiator and generator of the Giusepe Peano fractal.

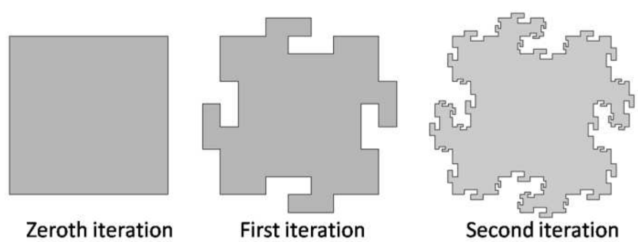

Figure 3: Implementation of the Peano fractal to the edges of square patch up to the second iteration.

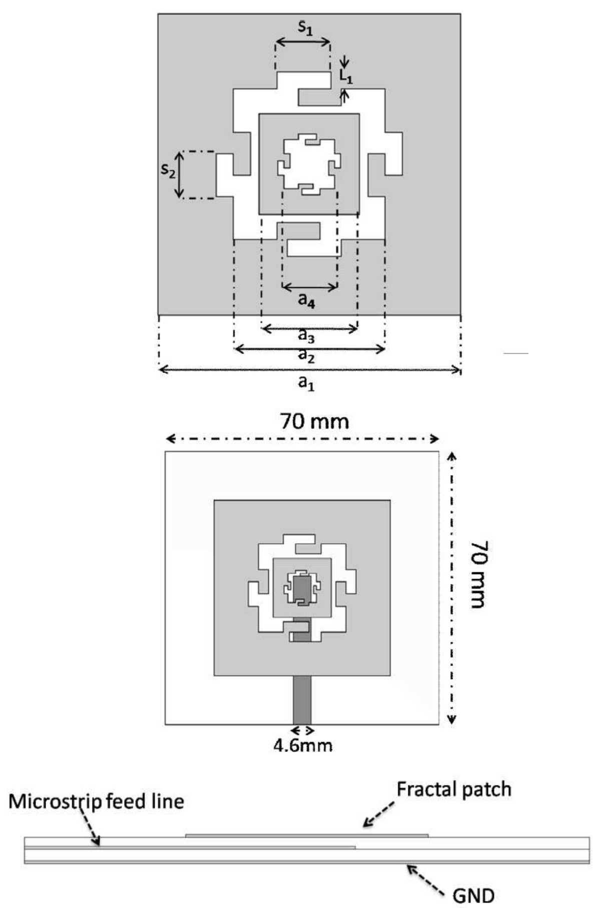

Figure 4: The proposed combination of square and Giusepe Peano fractal.

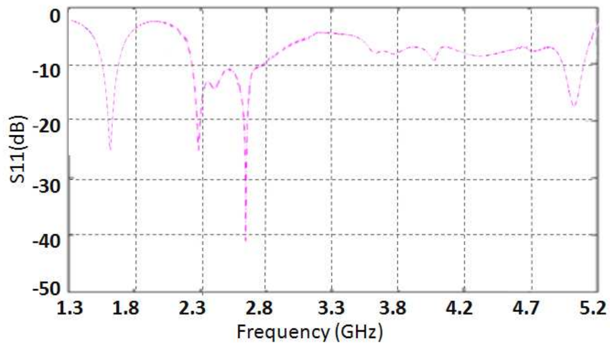

Figure 5: Reflection coefficient at the antenna feed point across the whole frequency band.

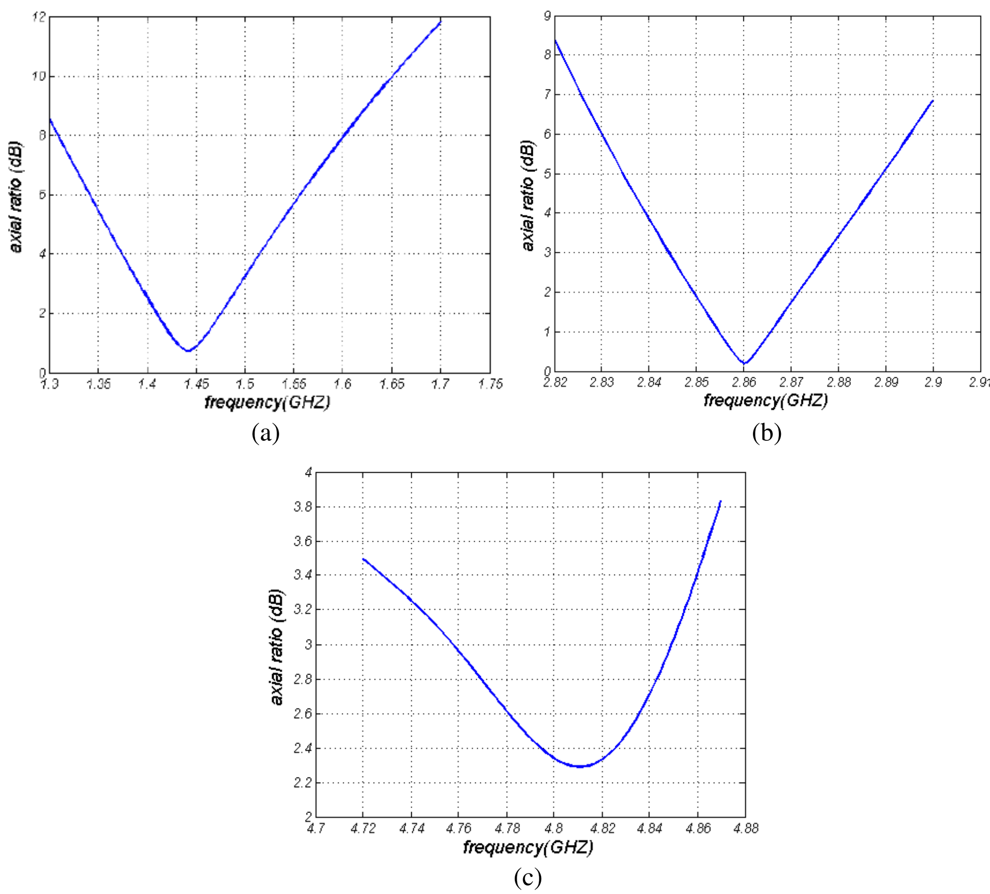

Figure 6: Axial ratio of the antenna at three frequency bands a) 1.5 GHz; b) 2.5 GHZ; c)4.9 GHz.

3. COMBINATION OF THE SQUARE AND GIUSEPE PEANO FRACTALS

Consider the initiator and generator of the Peano fractal as shown in Fig. 2. Application of such a fractal generation to the edges of square patch up to the second iteration is drawn in Fig. 3. Such a fractal structure up to the first iteration is shown in Fig. 4. It consists of two layers. The lower substrate is Rogers RT/Duroid 5880 (with $\varepsilon_r = 2.2$, $h = 1.524$ mm and $\tan\delta = 0.0009$) and the upper substrate is FR4 (with $\varepsilon_r = 4.4$, $h = 1$ mm and $\tan\delta = 0.02$). The feeding system is by electromagnetic coupling through a microstrip line on the lower substrate and the fractal patch is placed on the upper one.

For the generation of circular polarization, a perturbation of electrical length is produced on the two perpendicular edges of the square patch, which are in the form of Giusepe Peano fractals. The aim is to excite two orthogonal modes with a phase difference of 90°. The perturbations on the lengths of fractal edges on the outer square, namely S_1, S_2 and L_1 and those on the inner square, namely S_1/k_1, S_2/k_1 and L_1/k_1, are made for the generation of circular polarization in the first and also second and third bands, respectively. These parameters are optimized for the achievement of axial ratio AR < 3 dB. The other parameters of structure are optimized for the desired impedance matching. The first and second resonance frequencies determine the length of outer and inner square sides (a_1 and a_3), respectively. The optimized values of parameters are given below:

$$\begin{aligned} a_1 &= 30\,\text{mm}, \quad a_2 = 15\,\text{mm}, \quad a_3 = 10\,\text{mm}, \\ a_4 &= 5\,\text{mm}, \quad s_1 = 4.3\,\text{mm}, \quad s_2 = 3.9\,\text{mm}, \quad L_1 = 1.7\,\text{mm} \end{aligned}$$

The size of the inner fractal teeth are one third (0.33) that of the outer one. The width and length of the feed line are 3.4 mm and 38 mm, respectively.

The simulation results are compared in the following figures. The reflection coefficient (as S_{11}) at the antenna feed point across the whole frequency band is drawn in Fig. 5. Observe that the resonance frequency of the first iteration fractal antenna is actually 200 MHz lower than that of the corresponding simple square patch. Consequently, it is shown that some antenna miniaturization is achievable by the proposed fractal antenna. The bandwidth at the first resonance frequency (1.5 GHz) is 40 MHz, that at the second one (2.5 GHz) is 900 MHz and that at the third one (4.9 GHz) is 310 MHz. The circular polarization of radiation pattern is obtained by different lengths of teeth on the perpendicular sides of the square fractal (namely S_1 and S_2 in Fig. 4), which produce two orthogonal modes with 90° phase difference. The axial ratio of the antenna is drawn in Fig. 5. The bandwidth of circular polarizations at the first, second and third bands are 30, 40 and 50 MHz, respectively. The measurement of radiation patterns in the E- and H-planes for the first, second and third bands are drawn in Fig. 7. The gain of the fractal antenna versus frequency across the operating bands is drawn in Fig.8, which is quite good.

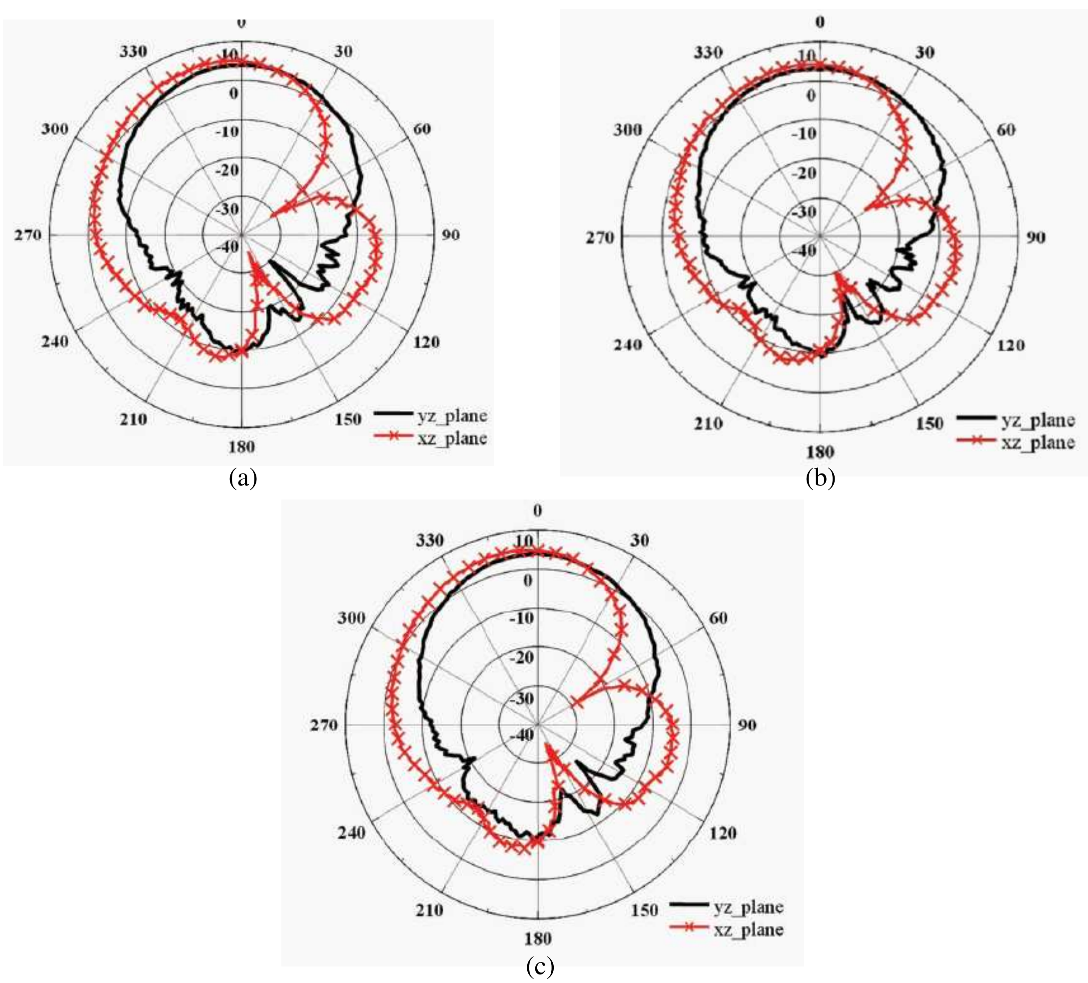

Figure 7: Radiation patterns in the E- and H-planes at three frequency bands a) 1.5 GHz; b) 2.5 GHZ; c) 4.9 GHz.

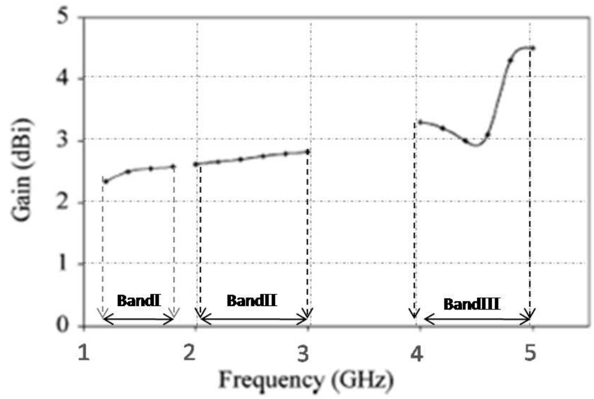

Figure 8: The gain of the fractal antenna versus frequency in all application bands.

4. CONCLUSION

In this paper, a microstrip antenna is proposed as a combination of square and Giusepe Peano fractals, which may produce three distinct frequency bands of operation with circular polarization. The antenna achieves some degree of miniaturization. Simulation results of the proposed antenna for the return loss, axial ratio and radiation patterns attest to the effectiveness and suitability of the proposed fractal antenna for wireless applications. The Giusepe Peano fractal geometry proposed for the microstrip antenna produces radiation characteristics with lower number of iterations than those obtained by other fractals with higher number of iterations, and also achieves better antenna miniaturization.

REFERENCES

1. Garg, R., P. Bhartia, I. Bahl, and A. Ittipiboon, *Microstrip Antenna Design Handbook*, Artech House, Norwood, 2001.
2. Wong, K. L., *Compact and Broadband Microstrip Antennas*, John Wiley & Sons, New York, 2002.
3. Lu, J. H., "Single-feed dual-frequency rectangular microstrip antenna with pair of step-slots," *Electronics Letters*, Vol. 35, 354–355, 1999.
4. Krishna, D. D., M. Gopikrishna, C. K. Aanandan, P. Mohanan, and K. Vasudevan, "Compactdual band slot loaded circular microstrip antenna with a superstrate," *Progress In Electromagnetics Research*, Vol. 83, 245–255, 2008.
5. Bhalla, R. and L. Shafai, "Broadband patch antenna with a circular arc shaped slot," *IEEE AP-S Int. Symposium* Vol. 1, 394–397, 2002.
6. Bhalla, R. and L. Shafai, "Resonance behavior of single U-slot microstrip patch antenna," *Microwave and Optical Technology Letters*, Vol. 32, 333–335, 2002.
7. Tada, S., R. Chayono, Y. Shinohe, Y. Kimura, and M. Haneishi, "Radiation properties of modified fractal microstrip antennas," *IEICE Transactions on Communications*, Vol. 89, 1519–1531, 2006.
8. Edwards, T. C., *Foundations for Microstrip Circuit Design*, John Wiley & Sons, Chichester, 1983.
9. Werner, D. H. and R. Mittra, *Frontiers in Electromagnetics*, 48–81, IEEE Press, Piscataway, NJ, 2000.
10. Gianvittori, J. P. and Y. Rahmat-Samii, "Fractal antenna: A novel antenna miniaturization technique ,and apllications," *IEEE Antenna and Propagation Mag.*, Vol. 44, No. 1, 20–36, Feb. 2002.

An Equivalent Circuit of Microstrip Slot Coupled Rectangular Dielectric Resonator Antenna

M. F. Ain[1], **Y. M. Qasaymeh**[1], **Z. A. Ahmad**[2], **M. A. Zakariya**[1], **and Ubaid Ullah**[1]

[1]School of Electrical and Electronic Engineering
University Sains Malaysia, Pulau Pinang, Malaysia
[2]School of Materials and Mineral Resources Engineering
University Sains Malaysia, Pulau Pinang, Malaysia

Abstract— In this paper, an approximate model of the rectangular dielectric resonator antenna fed by microstrip slot coupled is presented. The equivalent model will be based on the input impedance of the antenna sub-elements. Since the antenna sub-elements impedances are functions of relative dimensions, the resonant frequency can be predicted using this model. The validity of the modeling is supported by comparing the values of the return losses measured of antenna geometry using computer simulation technology (CST) against those obtained by proposed model using Agilent advanced design system (ADS).

1. INTRODUCTION

Since the dielectric resonator antenna (DRA) was introduced by Long et al. in 1983 [1], over the past few years, considerable attention has been directed towards the development of analysis techniques capable of dealing with these antennas. These antennas show the benefits of light weight, small size, low cost, ease of excitation and the deficiency of conduction losses in the resonator [2]. Moreover, various antenna features such as input impedance, bandwidth, and radiation patterns can be easily regulated by varying the antenna specifications and feed mechanism.

Normally, the dimensions of the individual DRs are determined using the equations in [3, 4]. In this paper, a simple approximate model based on the input impedance of the antenna is presented. The equivalent circuit of the structure is given and calculations for the determining its elements impedance are outlined. The approach is particularly useful for fast evaluation of the rectangular DRA fed by microstrip slot coupled resonant frequency.

2. MODELING

In most designs, the dimensions of the rectangular DRA determined by using the Equation (1) stated in [4] by an iterative manner:

$$\varepsilon_r k_o^2 = k_x^2 + k_y^2 + k_z^2 \tag{1}$$

where: $k_o = \frac{2\pi}{\lambda_o} = \frac{2\pi f_o}{c}$, is the free-space wave number, $k_x = \frac{m\pi}{a}$, propagation number in X direction, $k_y = \frac{n\pi}{b}$, propagation number in Y direction.

The aim of analyzing the input impedance of the proposed antenna is to ensure the dimensions of the DR at a certain frequency. The first step used in the experiment was to model the DR with a RLC network. The formulas used to represent a resonator as parallel resonant circuit can be found in [5], when the resonator is coupled to the excitation source.

$$R_r = \frac{2n^2 z_0 s_{11}}{1 - s_{11}}, \tag{2a}$$

$$C_r = \frac{Q_0}{\omega_0 R_r}, \tag{2b}$$

$$L_r = \frac{1}{C_r \omega_0}. \tag{2c}$$

It was mentioned in [5] that the value of R_r can be chosen since the value of R_r plays an important role in determining the values of C_r and L_r. Thus, finding a suitable value of R_r in order to obtain reasonable C_r and L_r values is a complicated process. Agilent advanced design system (ADS) program was used to build the model and extract the optimum values of RLC at a specific resonant

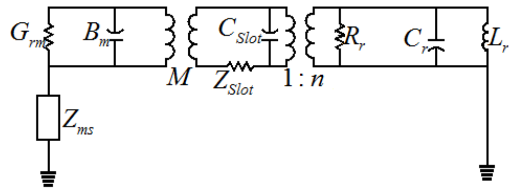

Figure 1: Equivalent circuit of microstrip slot coupled DR.

frequency, while a Matlab® program was developed to analyze values of RLC which related to DR at that resonant frequency. The factor n in Equation (2a) represents the coupling between the DR and excitation source which plays an important role to determine R_r and, later on, $C_r L_r$.

The second step is to find the input impedance of the slot. From transmission line theory, the slot impedance Z_s is given by:

$$Z_{slot} = Z_c \frac{2R}{1-R}$$

where R is the voltage reflection coefficient.

But when the transmission line is terminated by a stub length $\lambda_g/4$ (i.e., antinode), one simple computes the input impedance under the infinite line assumption and this result is added as series reactance, $X = -jZ_c \cot(\beta_f L_t)$ and thus the total impedance is:

$$Z_{Slot} + X \tag{3}$$

where: Z_c is the characteristic impedance of the transmission line [6]. Z_{Slot} can be calculated using the program in [7].

The third step was to find the input impedance of the microstrip line. At the antinodes points, the input impedance is high resistance, hence the line acts as a parallel resonant circuit. As demonstrated in [8], the input admittance Y_m is equal to $G_{rm} + jB_m$ where G_{rm} is the equivalent radiation conductance and B_m is the susceptance of the fringing field capacitance of the microstrip. The expressions of G_{rm} and B_m are:

$$G_{rm} = \frac{160\pi^2 h^2}{Z_{cm}^2 \lambda_0^2 \varepsilon_{cm}}, \tag{4a}$$

$$B_m = \omega C_l, \quad C_l = \frac{l_{eq} C \sqrt{\varepsilon_{cm}}}{Z_{cm}} \tag{4b}$$

where: h Substrate height, Z_{cm} Characteristic impedance of the microstrip, ε_{cm} Effective dielectric constant, l_{eq}, Equivalent extra length of microstrip, C Velocity of light.

The last step was to transform the impedance of the slot along the microstrip line. The mutual inductance between the microstrip and the slot is:

$$M = (\mu_0 W_s/2\pi) \ln(\sec\theta_0), \quad \theta_0 = \arctan(L_s/2h) \tag{5}$$

Since every antenna impedance function has an equivalent circuit in Darlington form, Figure 1 shows the equivalent input impedance circuit of a single DR microstrip slot coupled presented in Darlington form.

3. RESULTS AND DISCUSSIONS

First Antenna was modeled into its equivalent model in ADS and then antenna geometry was built in CST in as in Figure 2. Using the dimensions and relative permitivities stated on Figure 3, the equivalent impedance circuit over a substrate of permittivity equals to 3.38 with the dimensions of the slot to be 8 mm in length, 1 mm in width, the impedances of the microstrip, slot and coupling between them can be calculated using Equations (3), (4a) (4b) and (5) mentioned in Section 2. The DR RLC network, representing the DR, can be tuned with the help of ADS to make the antenna resonate at a certain frequency. Since the value of R_r plays a role in determining C_r and L_r, 55 Ohm was chosen because reasonable and realistic C_r and L_r values could be achieved. Then, by solving Equations (1) the dimensions of the DRA were found to be 8 mm (width), 14 mm (length),

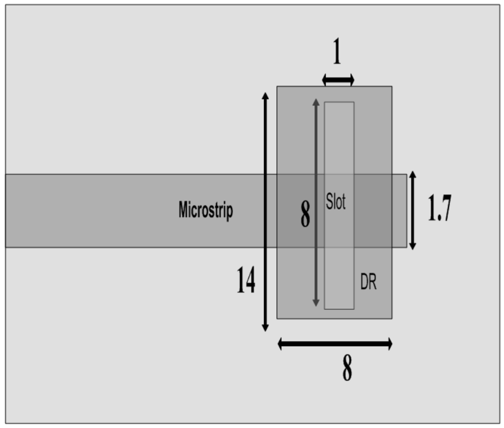

Figure 2: The dimensions of the antenna (DR height = 8) [all dimensions in mm].

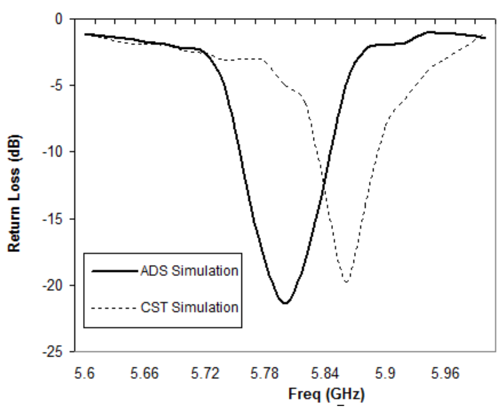

Figure 3: Simulated Return loss in ADS model and antenna in CST.

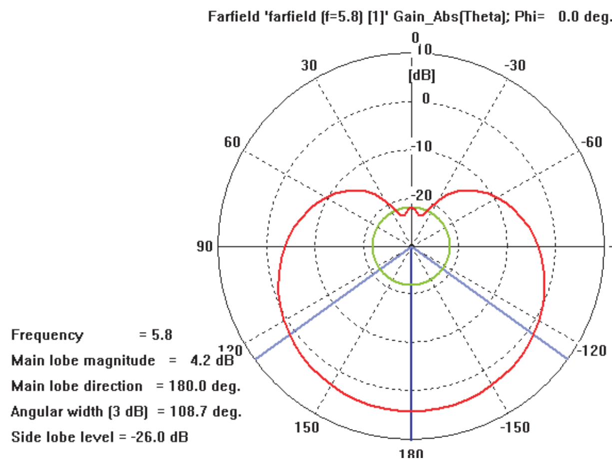

Figure 4: Simulated E-plane radiation pattern of antenna in CST.

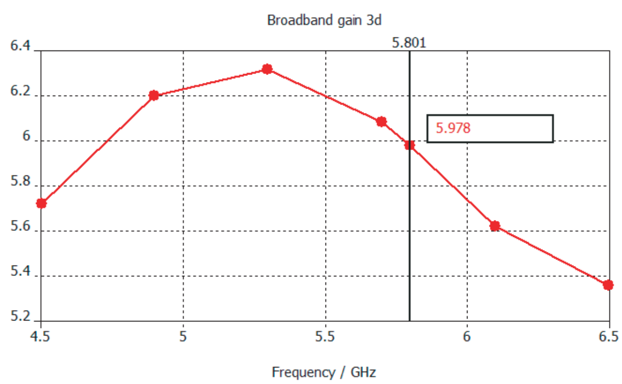

Figure 5: Simulated gain of antenna in CST.

and 8 mm (height), then the values of R, L and C calculated using Equations (2a), (2b) and (2c). As stated earlier the validity of the proposed model judged by comparing the resonant frequency from antenna geometry using CST and antenna equivalent model using ADS, Figure 4 shows the return loss for model and structure. A good agreement between both results was achieved.

The validity of the modeling is judged by comparing the values of the return losses obtained using computer simulation technology (CST) against those obtained theoretically. The ADS simulation and CST simulation results for the input return loss are given in Figure 3. The minimum ADS simulated input return loss frequency could be fine tuned to 5.79 GHz equals to -21.4 dB with a bandwidth of 80 MHz and impedance of 52.23–j4.55 Ω. The minimum CST simulated inputs return loss is 5.85 GHz of -19.8 dB and a bandwidth of 60 MHz and impedance of 51.23+j3 Ω.

The E-plane simulated radiation pattern of the antenna in CST is shown in Figure 4. The antenna main loop direction was 180° with main loop magnitude of 4.2 dB and a HPBW of 108.7°. The simulated H-plane main loop direction was 155° with a main loop magnitude of 6 dB and HPBW of 73.3°.

Figure 5 shows the simulated gain of the antenna in CST. The maximum gain a long operation band was at 5.3 GHz with 6.3 dBi. The gain of antenna at 5.8 GHz was about 6 dBi.

4. CONCLUSION

In this paper, a model of rectangular DRA fed by microstrip slot coupled is presented. This model represents a validity of resonant frequency of microstrip slot coupled feeding Dr. Reasonable agreement between simulation and theoretically data was obtained.

ACKNOWLEDGMENT

The authors gratefully acknowledge that this work was financially supported by theUSM Short Term Grant under project No. 304/PBAHAN/6039035 and the USMResearch University (RU) Grant under project No. 1001/PELECT/814117.

REFERENCES

1. Long, S. A., M. W. McAllister, and L. C. Shen, "The resonant cylindnical dielectric cavity antenna," *IEEE Trans. Antennas Propagat.*, Vol. 31, 406–412, May 1983.
2. Luk, K. M. and K. W. Leung, *Dielectric Resonator Antennas*, Research Studies Press, Hertfordshire, UK, 2003.
3. Ittipiboon, A., R. K. Mongia, Y. M. M. Antar, P. Bhartia, and M. Cuhaci, "Aperture fed rectangular and triangular dielectric resonators for use as magnetic dipole antennas," *Electronics Letters*, Vol. 29, No. 23, 2001–2002, Nov. 11, 1993.
4. Ittipiboon, A., et al., "Aperture fed rectangular and triangulardielectric resonators for use as magnetic dipole antennas," *Electronics Letters*, Vol. 29, No. 23, 2001–2002, 1993.
5. Collin, R. E., *Foundations for Microwave Engineering*, 2nd Edition, 514–515, McGraw-Hill, 1992.
6. Junker, G. P., A. A, Kishk, and A. W. Glisson, "Input impedance of aperture-coupled dielectric resonator antennas," *IEEE Transactions on Antennas and Propagation*, Vol. 44, No. 5, 600, May 1996.
7. Mirshekar-Syahkal, D., *Spectral Domain Method for Microwave Integrated Circuits*, John Wiley and Sons, New York, 1990.
8. Akhavan, H. G. and D. Mirshekar-Syahkal, "Approximate model for microstrip fed slot antennas," *Electronics Letters*, Vol. 30, No. 23, 1902–1903, Nov. 10, 1994.

Low Cost, Efficient, High Gain and Wideband Microstrip Antenna Fed Yagi Array in Fabry-Perot Cavity

Avinash Ramnath Vaidya[1], **Rajiv Kumar Gupta**[2], **Sanjeev Kumar Mishra**[1], **and Jayanta Mukherjee**[1]

[1]Department of Electrical Engineering, IIT Bombay, Powai, Mumbai 400076, India
[2]Department of Electronics and Communication Engineering
Terna Engineering College, Nerul, New Mumbai 400706, India

Abstract— This article proposes an efficient, high gain and wideband antenna. Gain and bandwidth improvement using Fabry-Perot Cavity is demonstrated. The structure consists of Yagi array placed in $1.0\lambda_0$ Fabry-Perot Cavity (FPC) resonator. The structure is fed by a microstrip antenna that acts as a driven element, ground plane as a reflector and three metal patches above it act as directors. Gain as well as impedance and gain bandwidth is improved by fabricating third director on a FR4 superstrate. Bandwidth improvement is due to two near resonant frequencies and gain improvement is due to FPC formed by FR4 superstrate, which acts as PRS placed at about $1.0\lambda_0$ above the ground plane. Superstrate enhances the gain due to its phase smoothening effect and decreases the resonance frequency of third director fabricated on it. It results in two near resonance frequencies that leads to an improvement in impedance as well as gain bandwidth. The elements in the antenna are excited in space using a single feed microstrip patch. The array is easy to fabricate since the feed-lines network is completely avoided and air substrate is used, which results in good efficiency. Antenna offers 7.6% impedance bandwidth and maximum gain of 14.6 dBi with 3 dB gain bandwidth of 10.8%. Radiation patterns are symmetrical in broadside direction with little variation. SLL is less than -20 dB and F/B is about 20 dB with -26 dB cross polarization. The structure offers more than 90% antenna efficiency. The proposed structure can be packaged inside an application platform.

1. INTRODUCTION

Microstrip antennas (MSA) offer many attractive features such as low weight, small size, ease of fabrication, ease of integration with microwave integrated circuits and can be made conformal to host surface. However MSA suffers from low gain, narrow bandwidth, low efficiency and low power handling capability. Various broadband techniques have been reported using electromagnetic coupling or stacking the patches [1].

Gain enhancement techniques based on Fabry-Perot Cavity (FPC) has been considered to increase broad side directivity. A partially reflecting sheet (PRS) formed by single or multiple dielectric layers or a periodic screen at integral multiple of $\lambda/2$ above a ground plane is used to increase directivity. The gain of PRS antenna depends on the reflection coefficient of PRS and feed antenna [2–5]. High gain antenna using parasitic patches on a superstrate has been reported. The antenna offers high efficiency, low SLL and avoids feed network [6, 7]. However, these antennas have narrow bandwidth. The technique for improving the gain and bandwidth by arranging parasitic elements above the feeding MSA is investigated [8–11].

Planar Yagi array with MSA as driven antenna, ground plane as reflector and parasitic patches as directors have been reported [12–17]. The working of antenna is based on a conventional Yagi-Uda dipole array in which the electromagnetic energy couples from the driven dipole to the parasitic dipoles through space and is then reradiated to form a directional beam. In a microstrip Yagi array, however, the electromagnetic energy couples from the driven patch to the parasitic patches through space as well as by surface waves in the substrate. The antenna provides 14 dBi gain but 4–5 dB F/B lobe ratios [13]. Gain of about 10 dBi with improved 15 dB F/B lobe ratio has been reported [14]. Use of director elements in a three-layer stacked microstrip Yagi array can minimize the surface waves and result in a gain of 10 dBi or higher without the need for a high-permittivity dielectric layer [15]. Multilayer stacked dipole and patch Yagi antennas have been reported [16, 17]. The structure is a resonant mode antenna unlike the Yagi antenna, which is a traveling-wave antenna. Further substrate thickness can be adjusted to achieve an optimized bandwidth performance [16].

This article deals with the metal plated microstrip Yagi antenna which consists of ground plane as reflector, MSA as driven element and three directors. High efficiency is achieved using air as a dielectric. The patches are shorted at the centre by a copper rod. Bandwidth and gain is improved by fabricating the third director on a low cost, easily available FR4 superstrate. The following sections deal with the antenna geometry, design theory, simulation and experimental results. Radiation patterns and impedance variations of antenna structures on finite ground plane are also described.

2. ANTENNA GEOMETRY AND DESIGN THEORY

The geometry of two antenna structures is shown in Fig. 1. Initially, metal plated Yagi array fed by MSA as shown in Fig. 1(a) is designed. The structure is referred as Ant-1. Metal plate of 0.5 mm thickness is used for MSA, which acts as driven element, three director elements, and a reflector ground plane. The MSA radiates and electromagnetic energy couples to parasitic elements through space. The separation between the elements and dimensions of elements determine the phase and amplitude of coupling between the elements and hence, the gain of antenna. The amplitude and phase of current induced in parasitic elements also depend on the dimension and separation between parasitic elements. The length of first director element is less than the driven MSA element and length of director decreases progressively to ensure that the radiations from different elements are in phase in broadside direction. Voltage is zero at the centre of each patch; therefore the patches are shorted at the centre by a metal rod of 2 mm diameter without affecting the antenna performance. In Ant-2 structure, shown in Fig. 1(b), third director is fabricated on FR4 dielectric, which decreases its resonance frequency, therefore enhances impedance bandwidth due to two near resonance frequencies [1]. Gain improvement is due to one wavelength FPC resonator effect where FR4 superstrate acts as PRS placed at about $1.0\lambda_0$ from ground [7, 8].

The Ant-2 structure consists of a ground plane and a partially reflecting surface, which is excited by a MSA fed Yagi array. It results in multiple reflections between PRS and ground plane. A broadside directive radiation pattern results when the distance between the ground plane and PRS causes the waves emanating from PRS in phase in normal direction. If reflection coefficient of the PRS is $\rho e^{j\psi}$ and $f(\alpha)$ is the normalized field pattern of feed antenna, then normalized electric field E and power S at an angle α to the normal are given by [2]

$$|E| = \sqrt{\frac{1-\rho^2}{1+\rho^2-2\rho\cos\phi}}f(\alpha) \quad \text{and} \quad S = \frac{1-\rho^2}{1+\rho^2-2\rho\cos\phi}f^2(\alpha) \tag{1}$$

where, ϕ is the phase difference between waves emanating from PRS. For the waves emanating from PRS to be in phase in normal direction, resonant distance L_r between ground plane and PRS is given by [2]

$$L_r = \left(\frac{\psi_0}{360} - 0.5\right)\frac{\lambda}{2} + N\frac{\lambda}{2} \tag{2}$$

where ψ_0 is phase angle of reflection coefficient of the PRS in degree and $N = 0$, 1, 2, 3 etc..

Radiation pattern of such structures depend on two frequency sensitive processes — one is the interference of waves reflected from PRS and other is the resonant interaction of waves with metallic patches [6].

3. ANALYSIS ON INFINITE GROUND PLANE

Initially, a metal plated MSA on an infinite ground plane with spacing $h_r = 2$ mm is designed to operate over 5.725–5.875 GHz ISM band. MSA provides gain of 9.5 dBi. Then metallic parasitic

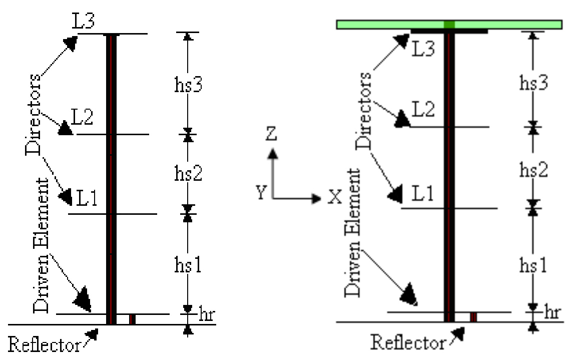

(a) Ant-1 (b) Ant-2

Figure 1: Geometry of antenna structures.

patches are placed above MSA. The impedance becomes capacitive when a first director is placed above MSA. The return loss increases and impedance bandwidth decreases with the addition of a director patch. There is strong coupling between the driven and director patch as indicated by the impedance variation plot on the Smith chart. The capacitive impedance decreases and impedance bandwidth increases with addition of another director. Capacitive impedance further decreases and bandwidth improves with addition of third director. Dimensions and spacing between first director and other directors and MSA are optimized to obtain maximum gain and VSWR < 2 over 5.725–5.875 GHz. Impedance variation of MSA and structures with one, two and three directors is shown in Fig. 2. The field distribution in x-z plane at 5.8 GHz in Fig. 3 shows the coupling of fields between directors and between MSA and first director. The radiation is mainly due to E_x fields and the fields are nearly in phase above the third directors, which increases the effective aperture area, resulting in gain improvement.

Gain variation of these structures is shown in Fig. 4. The metal plated Yagi array antenna structure on infinite ground plane 'Ant-1' offers 3.6% bandwidth, maximum gain of 13.0 dBi with 1 dB and 3 dB gain bandwidths for VSWR $<$ 2 of 4.5% and 8.2% respectively. The optimum dimensions for this structure are $L_1 = 0.35\lambda_0$, $L_2 = 0.29\lambda_0$, $L_3 = 0.27\lambda_0$, $h_{s1} = 0.37\lambda_0$, $h_{s2} = 0.29\lambda_0$ and $h_{s3} = 0.37\lambda_0$ respectively, where λ_0 is the free space wavelength at central operating frequency of 5.8 GHz.

In configuration 'Ant-2' shown in Fig. 1(b), the third director is fabricated at the bottom of 1.59 mm thick FR4 superstrate so that superstrate acts as a radom. Relative permittivity and loss tangent of FR4 superstrate are 4.4 and 0.02 respectively. Besides impedance bandwidth enhancement, FR4 superstrate also enhances the gain of antenna. Gain improvement is due to FR4 superstrate acting as PRS placed at about $1.0\lambda_0(h_r + h_{s1} + h_{s2} + h_{s3})$ from ground plane. The superstrate affects the phase and amplitude distribution of fields. The phase distributions of the

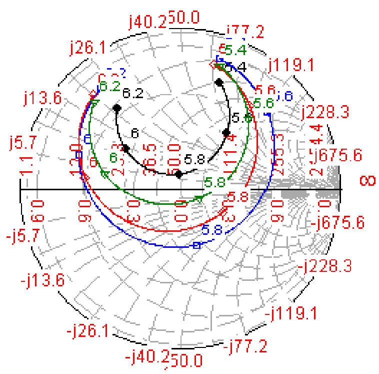

(—MSA, — MSA with one, — MSA with two and — MSA with three directors)

Figure 2: Impedance variations vs. frequency for Ant-1.

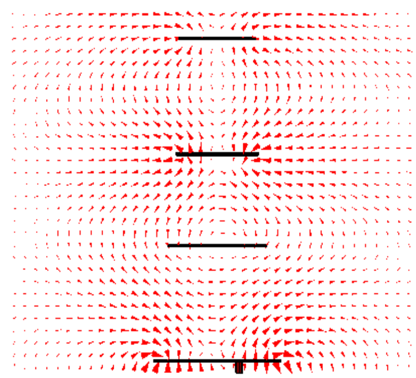

Figure 3: Electric field distribution in x-z plane in metal plated Yagi array.

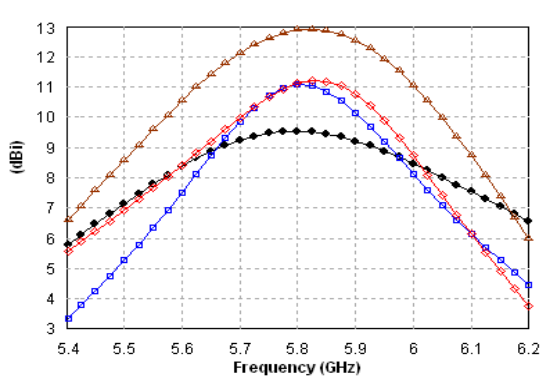

(—MSA, —MSA with one, — MSA with two and — MSA with three directors)

Figure 4: Gain variations vs. frequency.

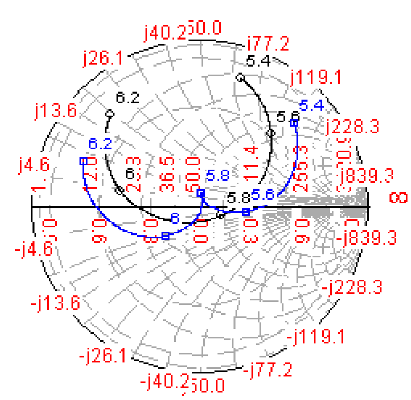

(— Ant-1, —Ant-2)

Figure 5: Impedance variations vs. frequency.

fields with a superstrate are observed to be more uniform than the one without superstrate. The superstrate has a focusing or phase smoothening effect and thus increases the effective aperture area, resulting in gain improvement [7, 8]. The input impedance variation of two structures Ant-1 and Ant-2 are shown in Fig. 5. Antenna structure, 'Ant-2' offers 7.8% impedance bandwidth, maximum gain of 14.6 dBi with 1 dB and 3 dB gain bandwidths of 7.3% and 10.2% respectively.

4. ANTENNA REALIZATION ON FINITE GROUND-DESIGN, FABRICATION AND RESULTS

The structures are redesigned on finite ground plane of size $1.5\lambda_0 \times 1.5\lambda_0$. The metal plated Yagi array antenna structure in first configuration, 'Ant-1' offers 3.3% impedance bandwidth and maximum gain of 13.5 dBi with 3 dB gain bandwidth of 7.8%. Antenna structure in second configuration, 'Ant-2' offers 7.6% impedance bandwidth and maximum gain of 14.6 dBi with 3 dB gain bandwidth

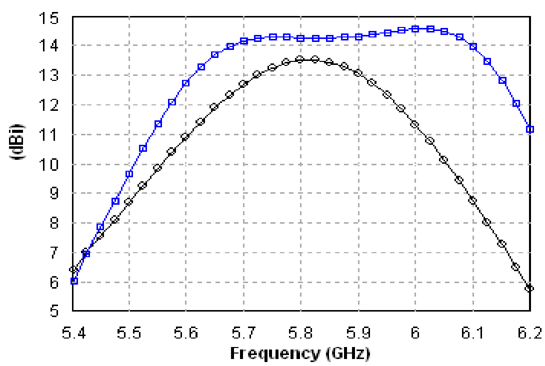

(Ant-1, Ant-2)

Figure 6: Gain vs. frequency on finite ground.

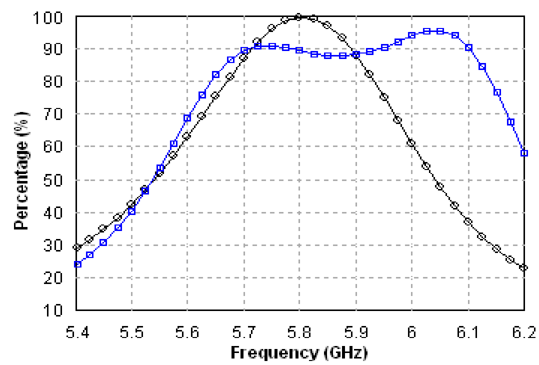

(Ant-1, Ant-2)

Figure 7: Antenna efficiency vs. frequency on finite ground.

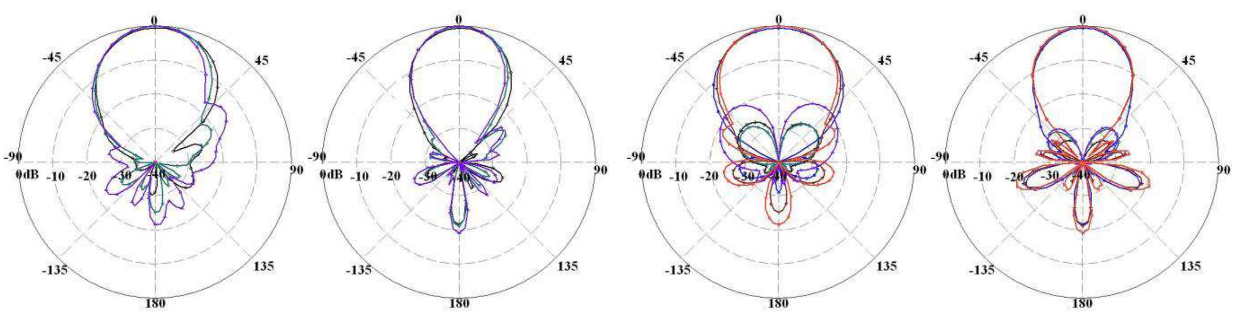

(i) Ant-1 (ii) Ant-2

(a) H-plane radiation patterns (E_θ, E_Φ at 5.6 GHz, E_θ, E_Φ at 5.8 GHz, E_θ, E_Φ at 6.0 GHz)

(i) Ant-1 (ii) Ant-2

(b) E- plane radiation patterns (E_θ, E_Φ at 5.6 GHz, E_θ, E_Φ at 5.8 GHz, E_θ, E_Φ at 6.0 GHz)

Figure 8: Radiation patterns on finite ground.

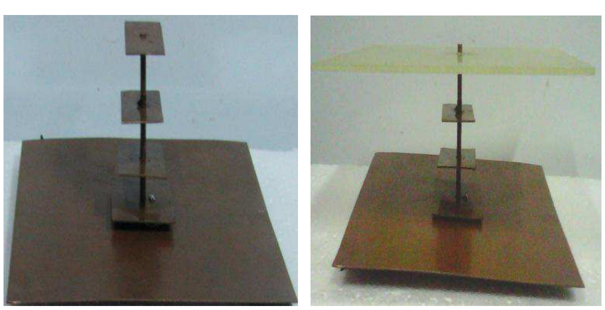

(a) Ant-1 (b) Ant-2

Figure 9: Fabricated antenna structures.

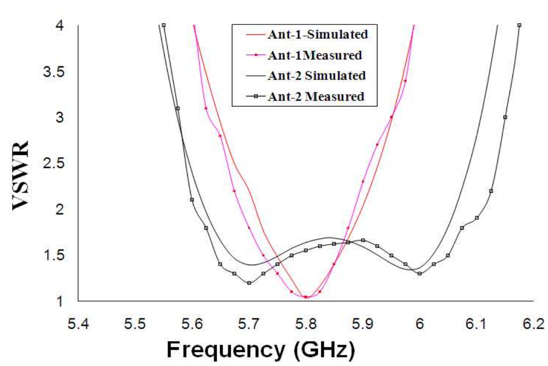

Figure 10: VSWR vs. frequency.

of 10.8%. Gain variations of two structures on finite ground are shown in Fig. 6. It is observed that gain increases slightly with finite ground and HPBW decreases in 'Ant-1' structure. It is due to constructive interference between radiated and reflected waves at particular dimensions of finite ground. Both structures offer more than 90% antenna efficiency as shown in Fig. 7. Radiation patterns on finite ground are shown in Fig. 8. Radiation patterns are symmetrical in broadside direction. There is little variation in radiation patterns. SLL is less than −20 dB and F/B is about 20 dB with −26 dB cross polarization. Fabricated antenna structures are shown in Fig. 9. The measured VSWR plots of the two antenna structures are shown in Fig. 10. Measured VSWR bandwidths of 'Ant-1' and 'Ant-2' are 3.4% and 8.8% respectively.

5. CONCLUSION

An efficient, high gain, wide band, easy-to-fabricate MSA driven Yagi array having low SLL and high F/B is proposed. The antenna is placed in a FPC to enhance impedance and gain bandwidths. Superstrate enhances the gain due to its phase smoothening effect and decreases the resonance frequency of third director fabricated on it. It results in two near resonance frequencies that leads to an improvement in impedance as well as gain bandwidth. The proposed structure is suitable for satellite as well as terrestrial communications and can be embedded into the host vehicle.

REFERENCES

1. Kumar, G. and K. P. Ray, *Broadband Microstrip Antennas*, Artech House, Norwood, MA, 2003.
2. Trentini, G. V., "Partially reflecting sheet arrays," *IRE Trans. Antennas Propag.*, Vol. 4, 666–671, 1956.
3. Feresidis, A. P. and J. C. Vardaxoglou, "High gain planar antenna using optimized partially reflective surfaces," *IEE Proc. Microw. Antennas Propag*, Vol. 148, 45–350, 2001.
4. Gardelli, R., M. Albani, and F. Capolino, "Array thinning by using antennas in a Fabry-Perot cavity for gain enhancement," *IEEE Trans. Antennas Propag.*, Vol. 54, 1979–1990, 2006.
5. Djordjevi, A. R. and A. G. Zaji, "Optimization of resonant cavity antenna," *European Conference on Antennas and Propagation*, 2006.
6. Parker, E. A., "The gentleman's guide to frequency selective surfaces," *17th Q. M. W. Antenna Symposium*, London, Apr. 1991.
7. Gupta, R. K. and J. Mukherjee, "Low cost efficient high gain antenna using array of parasitic patches on a superstrate layer," *Microw. Opt. Technol. Lett.*, Vol. 51, 733–739, 2009.
8. Gupta, R. K. and J. Mukherjee, "Effect of superstrate material on a high gain antenna using array of parasitic patches," *Microw. Opt. Technol. Lett.*, Vol. 52, 82–88, 2010.
9. Ge, Z.-C., W.-X. Zhang, Z.-G. Liu, and Y.-Y. Gu, "Broadband and High gain printed antennas constructed from Fabry-Perot resonator structure using EBG or FSS cover," *Microw. Opt. Technol. Lett.*, Vol. 48, 1272–1274, 2006.
10. Legay, H. and L. Shafai, "A new stacked microstrip antenna with large bandwidth and high gain," *Proc. IEEE AP-S Int. Symp.*, 948–951, 1993.
11. Egashira, S. and E. Nishiyama, "Stacked microstrip antenna with wide bandwidth and high gain," *IEEE Trans. Antennas Propag.*, Vol. 44, 1533–1534, 1996.
12. Lee, R. Q. and K. F. Lee, "Experimental study of two layer electromagnetically coupled rectangular patch antenna," *IEEE Trans. Antennas Propag.*, Vol. 38, 1298–1302, 1990.
13. Haung, J. and A. C. Densmore, "Microstrip Yagi array antenna for mobile satellite vehicle applications," *IEEE Trans. Antennas Propag.*, Vol. 37, 1024–1030, 1991.
14. DeJean, G. R. and M. M. Tentzeris, "A new high gain microstrip Yagi array antenna with a high front to back (F/B) ratio for WLAN and millimeter wave applications," *IEEE Trans. Antennas Propag.*, Vol. 55, 298–304, 2007.
15. Hoofer, A., "Analysis of a 'Yagi-like' printed stacked dipole array for high gain applications," *Microw. Opt. Technol. Lett.*, Vol. 17, 317–321, 1998.
16. Kramer, O., T. Djerafi, and K. Wu, "Vertically multilayer stacked Yagi antenna with single and dual polarization," *IEEE Trans. Antennas Propag.*, Vol. 58, 1022–1030, 2010.
17. Nessel, J. A., A. Zaman, R. Q. Lee, and K. Lambert, "Demonstration of a X-band multilayer Yagi-like microstrip patch antenna with high directivity and large bandwidth," *Proc. IEEE AP-S Int. Symp.*, 227–230, 2005.
18. IE3D release 12.0, Zeland software Inc., Fremont, CA, USA, 2006.

Parallel Metal Plated U-shape Ultra-wide Band Antenna with WLAN Band-notched Characteristics

Sanjeev Kumar Mishra[1], **Rajiv Kumar Gupta**[2], **Avinash R. Vaidya**[1], **and Jayanta Mukherjee**[1]

[1]Department of Electrical Engineering
Indian Institute of Technology (IIT), Bombay, Mumbai-400076, India
[2]Department of Electronics and Telecommunication Engineering
Terna Engineering College, Mumbai-400706, India

Abstract— In this article, a parallel metal plated ultra-wideband (UWB) antenna with band stop characteristics is proposed. The proposed antenna is a simple U-shaped monopole structure where a rectangular strip is placed on both sides at the top of semi annular ring monopole structure. The band-rejection characteristic is achieved by introducing a $\lambda/4$ open stub in the microstrip feeding line to prevent interference due to WLAN (wireless local area network) systems operating within ultra-wideband. To achieve the desired UWB response with WLAN band notched characteristics, the dimensions of rectangular strip, length and width of stub, and the gap between the ground plane and the radiating structure are optimized. Frequency rejection characteristics depend on the dimension of stub and can be fine controlled using other parameters. The proposed antenna is simulated, fabricated and tested. The antenna structure is designed using 0.5 mm thick copper metal plate for ground plane and radiating structure and 0.6 mm thick foam dielectric is placed between them. The relative permittivity (ε_r) 1.06 and loss tangent ($\tan\delta$) of foam are 1.06 and 0.0 respectively. The antenna structure is fed through a 50 Ω microstrip line using a SMA connector. The results show that the $S_{11} \leq -10$ dB from 3.09–11.1 GHz except 4.4–6.4 GHz frequency band. The proposed antenna provides more than 95% antenna efficiency and gain varies from 3–6 dB over the 3.09–11.1 GHz range except in 4.4–6.4 GHz notched band. The structure exhibits nearly omnidirectional radiation patterns, stable gain, and small group delay variation over the desired bands.

1. INTRODUCTION

This UWB technology has received an impetus and attracted academia and industrial attention in the wireless world ever since FCC released a 10 dB bandwidth of 7.5 GHz (3.1–10.6 GHz) with an effective isotropic radiated power (EIRP) spectral density of −41.3 dBm/MHz. UWB systems have been allocated frequency band of 3.1–10.6 GHz for the merits of high transmission rate, high capacity, and low power consumption for indoor communication applications. UWB systems also find applications in imaging radar, remote sensing and localization [1, 2]. Planar monopole antennas exhibit a relatively wide impedance bandwidth, good radiation pattern characteristics, high radiation efficiency and polarization purity [2–4], however these antennas are three dimensional in geometry as radiating structure is placed perpendicular to ground plane. These antennas occupy large space which comes as an obtrusion in mobile applications. The printed monopole antenna is a good candidate for UWB applications because of its ease of fabrication, low profile and lightweight but radiation pattern of these antennas varies over the UWB frequency range. Beside this, narrow-band wireless communication systems such as wireless local-area network (WLAN) IEEE802.11a and HIPERLAN/2 WLAN which operate in the 5.15–5.825 GHz band cause interference and affect UWB performance. Therefore, it is desirable to design the UWB antenna with band-notch characteristics. UWB antennas with band-notched characteristics have been proposed [5–13]. Band rejection characteristics are achieved by cutting a slot or a slit in radiating patch. Parasitic strips near the radiating patch or a stub is also used to achieve band notched characteristics. These UWB antennas with filtering property at WLAN band have been proposed not only to mitigate the potential interferences but also to eliminate the requirement of a band stop filter in the system. However, these antenna structures have large ground plane and are not suitable for compact UWB system.

This article proposes a compact parallel metal plated U-shaped UWB monopole antenna with WLAN band-notched characteristics. The band-notched characteristics are achieved by a $\lambda/4$ open stub in the feed line. The notch frequency can be tuned by changing the total width and length of the stub. The proposed antenna provides $S_{11} \leq 10$ dB from 3.09–11.1 GHz except over 4.4–6.4 GHz band. The following sections deal with antenna geometry, design theory, simulation and measured results. The effect of length and width of stub and gap between radiating plane and ground plane on return loss are also discussed. Simulation of structure is carried out using IE3D software [14].

2. ANTENNA GEOMETRY AND DESIGN THEORY

The geometry of proposed antenna is shown in Figure 1. Initially a circular monopole antenna of radius 'R' is designed and optimized to achieve the desired UWB response. A circular slot of radius 'r' is cut at the centre of the circular monopole resulting in annular ring monopole antenna. Thereafter a semi annular ring is designed and a rectangular strip is placed on both sides at the top of semi annular ring monopole resulting in a U-shaped monopole antenna [2]. Thereafter band-notched characteristics are obtained by introducing a $\lambda/4$ open stub in the microstrip feed line. The antenna is designed using 0.5 mm copper metal plates with 0.6 mm thick foam substrate having relative permittivity (ε_r) 1.06 and loss tangent ($\tan\delta$) 0.0. By introducing a $\lambda/4$ open stub in the microstrip feed line, a frequency band notch is introduced. The U shape radiating structure is optimized to obtain UWB bandwidth. The structure has two distinct resonant mode which results in omnidirectional radiation pattern with low cross polar component over UWB frequency range [2].

To achieve the desired UWB response with WLAN band notched characteristics, the dimensions of stub, length and width of ground plane, and the gap between the radiating patch and the ground plane are optimized. The dimensions of the proposed antenna are $W_g = 27.8$ mm, $L_g = 12.7$ mm, $R = 10.2$ mm, $r = 4$ mm, $W = 6.2$ mm, $L = 10.2$ mm, $W_f = 2.4$ mm, $g = 0$ mm, $w = 13.9$ mm, $l = 0.1$ mm. The key design parameters, which influence the performances of the proposed antenna, are (i) g — the gap between radiating patch and ground patch, (ii) w and l — the width and length of stub. The dimensions of quarter-wave resonating stub at central band-notched frequency can be postulated [8] as

$$f_{notch} = \frac{c}{4w\sqrt{\varepsilon_{eff}}} \tag{1}$$

$$\varepsilon_{eff} = \frac{(\varepsilon_r+1)}{2} + \frac{(\varepsilon_r-1)}{2}\left(\sqrt{1+\frac{12H}{W_g}}\right)^{-1} \tag{2}$$

where, w is the length and l is the width of the stub, ε_{eff} is the effective dielectric constant, ε_r is the relative dielectric constant, H is the substrate height, and c is the speed of the light.

3. SIMULATION RESULTS AND DISCUSSION

The performance of the proposed UWB antenna with WLAN band rejection depends on number of parameters such as gap (g) between radiating patch and ground plane, width (l) and length (w) of stub, width (W) and length (L) of rectangular strip over semicircular annular ring and inner (r) and outer radius (R) of semi-annular ring. Beside this, antenna performance also depends on size and shape of the ground plane. Width of the ground plane should be approximately same as that of the radiating patch to reduce cross polar component [2], however, width of the ground plane is

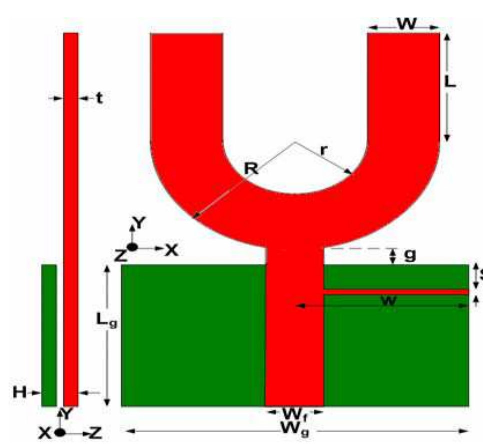

(a) Side view (b) Front view

Figure 1: Geometry of the proposed parallel metal plated WLAN band notched UWB antenna.

taken such that it can accommodate $\lambda/4$ open stub in the microstrip feed line. Length of the ground plane should be as small as possible as transmission losses and antenna size increases with increase in ground plane length. Ground plane length is optimized to provide UWB impedance bandwidth. The parameters which have significant effect on UWB with WLAN band notched performance are discussed below.

The gap between the radiating patch and the ground plane affects the band dispensation because it acts as a matching network. The return loss of the UWB antenna at different gap 'g' is shown in Figure 2. The optimum UWB impedance bandwidth with WLAN band notched characteristic is obtained at $g = 0$ mm. The central band rejection frequency can be tuned by changing the dimensions of w and l. It also affects the frequency rejection bandwidth. The central band rejection frequency increases with decrease in w and rejection bandwidth decreases with decrease l. These two parameters can be tuned separately to fine tune the notched band. The simulated return loss for different w and l is shown in Figure 3 and Figure 4 respectively.

The surface current distributions at 3.5, 5.5 and 9.5 GHz are shown in Figure 5. The current distributions in pass band at 3.5 and 9.5 GHz shows that a little current from feed line does flow in the stub, But as its length is about 0.16λ at 3.5 GHz it does not radiates efficiently and affect radiation pattern, however at 9.5 GHz, the stub length is about 0.43λ and therefore it radiates and affects radiation pattern especially increases cross polar component. Reflections due to open stub not only affect the impedance but also induce surface current in the ground plane which in turn affect radiation pattern of the structure. However, in stop band at 5.5 GHz the current mainly flows in the stub as shown in Figure 5(b) which acts as short circuit resonator. There is little current in the radiating patch and therefore it does not radiate. Also at 5.5 GHz ground plane has considerable surface current which causes the antenna to be non-responsive at that frequency. Further destructive interference between radiating patch and ground plane excited surface currents results in decrease in antenna efficiency and gain in stop band.

The antenna efficiency and gain of the proposed antenna shown in Figure 6 and Figure 7 respectively, shows a sharp decrease in gain and efficiency at WLAN notched band. The proposed antenna provides more than 95% antenna efficiency and gain varies from 3–6 dB over the 3.09–11.1 GHz range except in 4.4–6.4 GHz notched band. Radiation efficiency, a measure of power radiated to input power and antenna efficiency, a measure of power radiated to incident power are

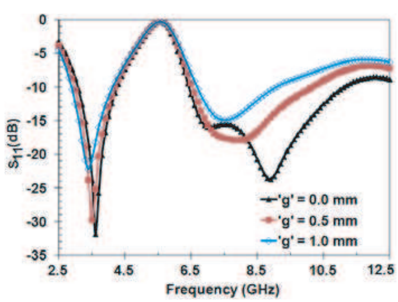

Figure 2: Simulated S_{11} Vs frequency for different gap 'g'.

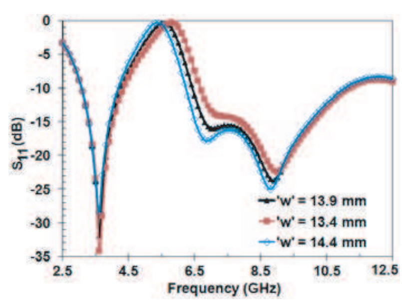

Figure 3: Simulated S_{11} Vs frequency for different stub length 'w'.

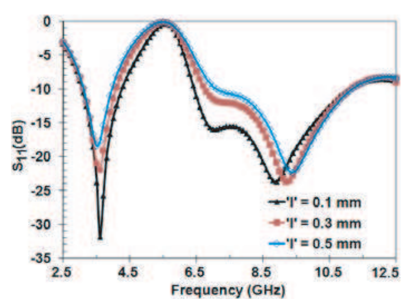

Figure 4: Simulated S_{11} Vs frequency for different stub width 'l'.

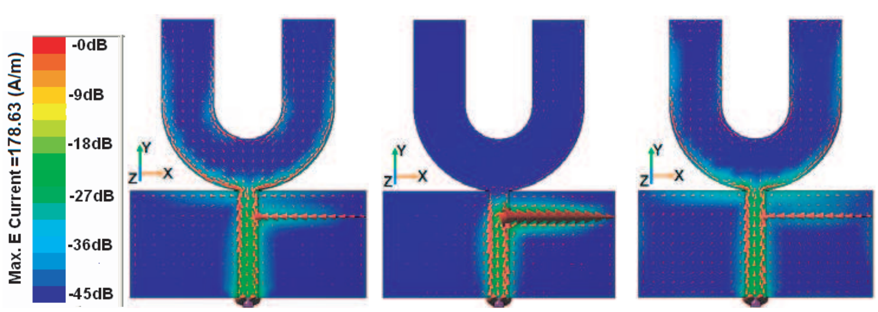

(a) 3.5 GHz (b) 5.5 GHz (c) 9.5 GHz

Figure 5: Current distributions at 3.5 GHz, 5.5 GHz and 9.5 GHz.

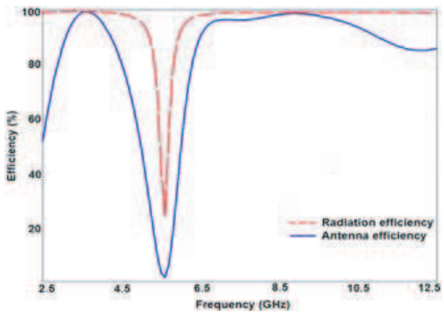

Figure 6: Antenna efficiency Vs frequency of proposed antenna.

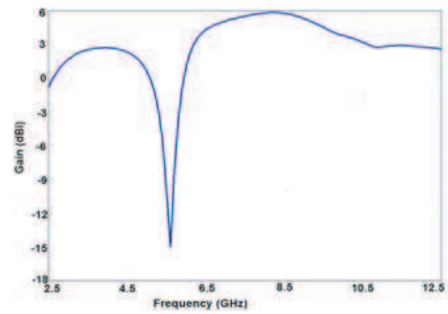

Figure 7: Gain vs. frequency of proposed antenna.

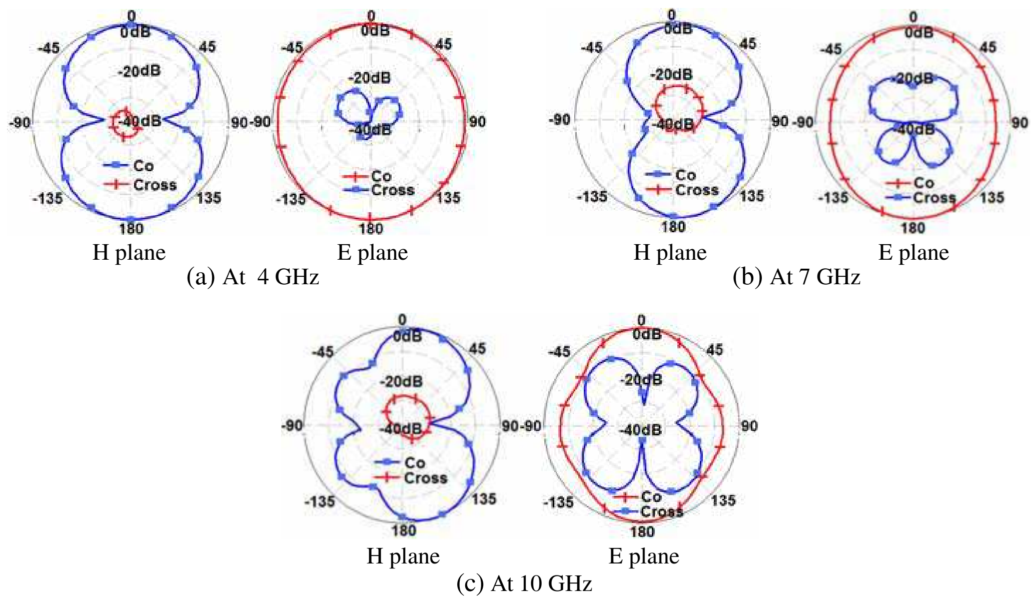

Figure 8: Radiation patterns of proposed antenna.

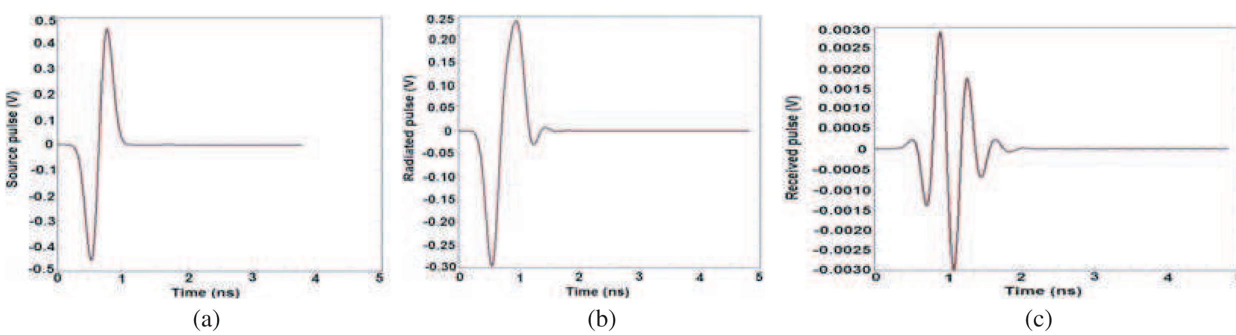

Figure 9: (a) Excited Gaussian source pulse, (b) radiated pulse and (c) received pulse at the receiving antenna.

shown in Figure 6. Radiation efficiency considers only conducting and dielectric losses whereas reflection losses also included in antenna efficiency [14]. The simulated radiation patterns at 4, 7 and 10 GHz are shown in Figure 8. The radiation patterns are observed to be nearly figure of eight pattern in $\Phi = 90^\circ$ plane and omnidirectional in $\Phi = 0^\circ$ plane.

Using MDSPICE, IE3D [14], the time domain characteristics viz. group delay and magnitude of transfer function of the proposed antenna are obtained. Two identical antennas are placed at 0.3 m in the face-to-face orientations. Figures 9 (a), (b) and (c) show excited Gaussian source pulse, radiated pulse and the received pulse at the receiving antenna respectively. The magnitude of the transfer function has little variation and constant group delay over the operating bands except over

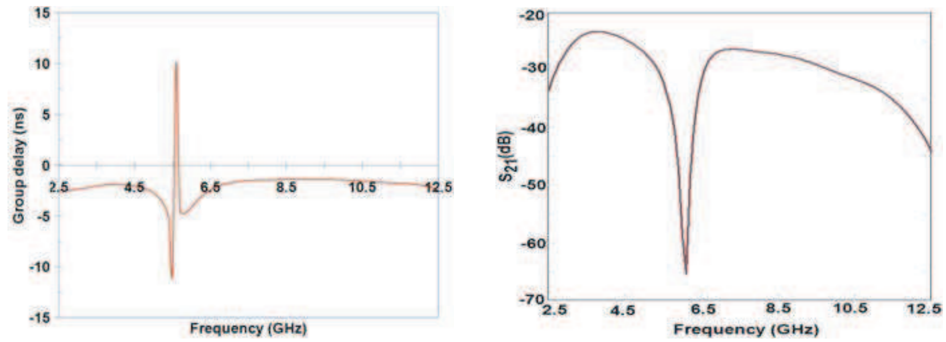

(a) (b)

Figure 10: (a) Group delay, (b) transfer function of the proposed antenna.

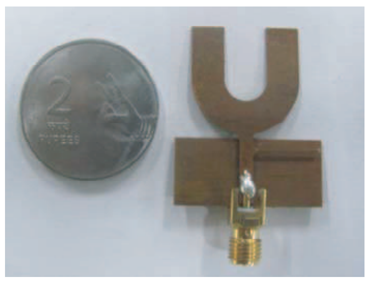

Figure 11: Photograph of the proposed UWB antenna with WLAN band notch.

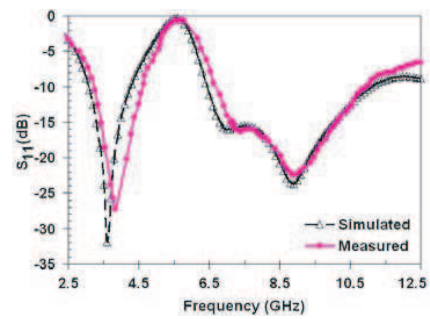

Figure 12: Measured and simulated S_{11} of the proposed antenna.

the notched band, as shown in Figure 10. Therefore, the proposed antenna is capable of offering good pulse handling capability as demanded by modern UWB communication systems.

4. FABRIACATION AND MEASURED RESULTS

The antenna structure is fabricated and tested. The fabricated antenna structure is shown in Figure 11. The simulated and measured return loss using the Agilent 8722ET VNA of the proposed structure is shown in Figure 12. The measured result reasonably agrees with simulated result. The variation in measured return loss can be attributed to inaccuracy in dimensions of radiating patch and ground plane as metal plated antenna has to be mechanically fabricated, impedance mismatch due to feed tip of SMA connector and increase in ground plane dimensions due to SMA connector.

5. CONCLUSION

To minimize the potential interferences between the UWB system and the WLAN system, a compact microstrip line fed U-shaped metal plated monopole UWB antenna with WLAN band rejection has been proposed and discussed. The results indicate that by simply adjusting the length and width of stub, the desired band-notched frequency can be controlled. The proposed antenna provides more than 95% antenna efficiency and gain varies from 3–6 dB over the 3.1–11.1 GHz range except in 4.4–6.4 GHz notched band. The radiation patterns are nearly omnidirectional over UWB range except in the notched band. One drawback of this antenna is mechanical fabrication which may cause inaccuracy in dimensions and performance degradation.

ACKNOWLEDGMENT

This work was supported in part by the Department of Science and Technology, India. The authors thank the efforts of the team of IDEMI, Bombay for fabrication of the structure.

REFERENCES

1. First Report and Order, "Revision of part 15 of the commission's rule regarding UWB transmission system FCC 02–48," Federal Communications Commission, 2002.

2. Mishra, S. K., R. K. Gupta, and J. Mukherjee, "Parallel metal plated tuning fork shaped omnidirectional monopole antenna for UWB application," *Microwave Opt. Technol. Lett.*, Vol. 53, No 3, 601–604, March 2011.
3. Kumar, G. and K. P. Ray, *Broadband Microstrip Antennas*, Artech house, Norwood, MA, 2003.
4. Agrawall, N., G. Kumar, and K. Ray, "Wide-band planar monopole antennas," *IEEE Trans. Antennas Propag.*, Vol. 46, 294–295, 1998.
5. Wong, K. L., Y. W. Chi, C. M. Su, and F. S. Chang, "Band-notched ultra-wideband circular-disk monopole antenna with an arc-shaped slot," *Microwave Opt. Technol. Lett.*, Vol. 45, 188–191, 2005.
6. Yuan, T., C. W. Qiu, L. W. Li, M. S. Leong, and Q. Zhang, "Elliptically shaped ultra-wideband patch antenna with band-notch features," *Microwave Opt. Technol. Lett.*, Vol. 50, 36–738, 2008.
7. Li, P., L. Ma, and J.-S. Li, "A Hexagonal ultrawideband antenna with notched band," *Microw. Opt. Technol. Lett.*, Vol. 51, 2917–2921, 2009.
8. Mishra, S. K., R. K. Gupta, and J. Mukherjee, "A simple U-shaped printed ultra-wideband antenna with WLAN band rejection," *Microwave Opt. Technol. Lett.*, Vol. 53, No. 7, 1645–1649, July 2011.
9. Chen, Y. L., C.-L. Ruan, and L. Peng, "A novel ultra-wideband bow-tie slot antenna in wireless communication systems," *Progress In Electromagnetics Research Letters*, Vol. 1, 101–108, 2008.
10. Lin, Y. C. and K. J. Hung, "Compact ultra-wideband rectangular aperture antenna and band-notched designs," *IEEE Trans. Antennas Propag.*, Vol. 5, 3075–30814, 2006.
11. Cho, Y. J., K. H. Kim, D. H. Choi, S.-S. Lee, and S. O. Park, "A miniature UWB planar monopole antenna with 5-GHz band-rejection filter and the time-domain characteristics," *IEEE Trans. Antennas Propag.*, Vol. 54, 1453–1460, 2006.
12. Peng, L., C.-L. Ruan, Y.-L. Chen, and G.-M. Zhang, "A novel band-notched elliptical ring monopole antenna with a coplanar parasitic elliptical patch for UWB applications," *Journal of Electromagnetic Waves and Applications*, Vol. 22, No. 4, 517–528, 2008.
13. Gao, G.-P., M. Li, S.-F. Niu, X.-J. Li, B.-N. Li, and J.-S. Zhang, "Study of a novel wideband circular slot antenna having frequency band-notched function," *Progress In Electromagnetics Research*, Vol. 96, 141–154, 2009.
14. IE3D Release 14, Zeland Software Inc., Fremont, CA, USA, 2008.

Necessity of Quantitative Based Thermographic Inspection of Electrical Equipments

A. S. Nazmul Huda, Soib Bin Taib, and Dahaman Bin Ishak
School of Electrical and Electronic Engineering, Universiti Sains Malaysia
Nibong Tebal 14300, Pulau Pinang, Malaysia

Abstract— The paper discusses the necessity of automatic quantitative based infrared thermographic inspection of electrical equipments and also limitations of qualitative based temperature measurement. Infrared (IR) inspection is a non-touching and non-invasive diagnosis system. Power system consists of both indoor and outdoor electrical equipments such as circuit breaker, bushing, current transformer, different connectors, insulator, potential transformer, lighting arrester, capacitor, transformer and bus-bar etc can cause faults when the internal temperature within equipments reached the abnormality. Various reasons including contact problem, unbalanced current distribution, cracks in insulators, defective relays or terminal blocks etc produce unwanted heat within electrical equipments due to these abnormal behaviour. Thermographic inspection uses an IR camera for capturing and analyzing the thermal profile of faulty electrical equipment. Analysis of temperature distribution profile of target equipment can be performed by qualitatively or quantitatively. Qualitative based measurement is based on only image processing where the abnormal region is detected by the comparative evaluation between reference and hot spot temperature of the target equipment. But IR inspection in an uncovered environment can be strongly influenced by different environmental parameters such as ambient temperature, reflected or background temperature, wind speed, relative humidity of the object and precipitation etc. For this reasons accurate evaluation of equipment health can be interrupted and this can lead the inspection to the erroneous conclusion. So, the aim of this paper is to present the review of these effects on the IR temperature inspection and proposed an advanced quantitative based intelligent diagnosis system combining image processing and artificial neutral network.

1. INTRODUCTION

Infrared (IR) thermography is seen as a most effective faults diagnosis technology of electrical equipments. It is a two dimensional predictive and cost reducing reliable defects detection system where heat related problems within electrical equipments are found and fixed before eventual failure. The principle of IR thermography is based on the thermal radiation laws [1]. In the earth, all objects above absolute zero temperature (-273°C or $0\,\mathrm{k}$) emits infrared radiated energy and this energy is used to measure the temperature of the objects [2]. The more infrared energy it emits, the more heat the object. Temperature is the most critical parameter for getting information about electrical equipment health. Due to electrical resistance, current flowing through an electrical system produces heat in limit. All electrical equipments have expected useful life given by manufacturers. With time the equipments begin to deteriorate gradually until eventual failure [3]. Fault occurs when the current is diverted from its intended path and more heat is generated in which it exceeds its reliability. IR thermography is conducted by a special type of thermal camera that senses the emission of infrared radiation from object and produces a visual image of temperature distribution profile of equipment surface. Thus the effect of heat within different areas in the electrical equipment, i.e., thermal abnormalities can easily be identified using thermography.

Thermographic inspection can be performed by qualitatively or quantitatively. But the qualitative inspection of outdoor power equipments in open environment can be affected by different environmental parameters such as sun heat, humidity, wind speed, solar reflection and precipitation etc. These factors reduce the success of inspection to a considerable level. An intelligent quantitative based thermography combining advanced thermal image processing and artificial neural network considering all external effects is necessary for obtaining more accuracy and reliability in inspection. The main aims of this paper are to describe the effects of environmental factors on qualitative based thermography and propose an intelligent inspection system.

2. QUALITATIVE-BASED THERMOGRAPHY

Qualitative based thermography is based on comparative temperature analysis between hotspots and reference spot and thermal image processing. This technology is simply called ΔT factor analysis [4]. After capturing thermal images of electrical equipments, the hotspot and reference areas are identified visually by analyzing colour map. The hotspots support maximum temperature of faulty equipment part and reference is the minimum temperature of same type or same repeated part of equipment. For identify the hotspots clearly, i.e., thermal abnormal position image processing is done. Thresholding and watershed transform are very common image processing techniques used in thermography [5, 6]. Then difference between hotspot and reference temperature is determined as ΔT factor which is used as the decision making parameter about fault condition. Fig. 1 shows the basic block diagram of qualitative based thermography. The main drawback of qualitative based thermography is that various influential factors including environmental and emissivity parameters affect the temperature measurement. Thus performance decreases to low level and misguides the faults classification system.

3. EFFECT OF ENVIRONMENTAL FACTORS

The effects of environmental factors depend on the weather condition, image capturing time, place, season and also material surface properties. There are two types of effects. Due to some effects measurement temperature tends to increase and for some reasons temperature will increase depending on the surrounding conditions. To measure the accurate temperature of object surface, all kinds of effects should be considered. Some common effects are described as follows.

3.1. Effect of Sun Heat

Externally temperature rise more than normal loading heating is strongly related with the sun heat. Intensity of heat depends on geographic location, sun angle of exposure of light, time of day, duration of sunshine season. On the other hand solar position depends on time, solar declination and latitude. Since the orbit of earth is not perfectly circular but slightly elliptical and so that solar heating on a specific surface varies with the changing of seasons and unequal periods of daylight [7]. In a day, heat from solar radiation is maximum at noon and diminishes at zero at sun-set. Actually the changing of sun heat from zero to maximum and then zero again can be described as sine wave [8]. Also the horizontal orientation of surface receives more heat than vertical surface. Another thing is the surface colour of electrical equipment enclosure that has a little influence on external temperature rise comparing with internal heat generation. But dark coloured paints absorbs more sun heat than light coloured and resulting higher temperature rise above actual reading. Metallic and reflecting paints also absorb heat both from low and high temperature sources [9]. So, there is a questionable difference between the measurement during

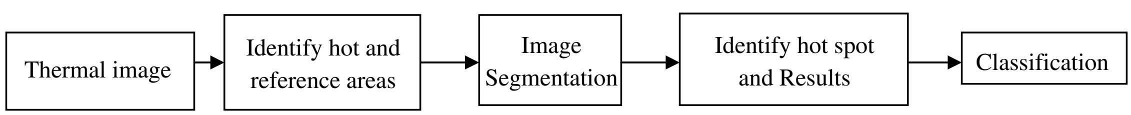

Figure 1: Block diagram of qualitative based thermography.

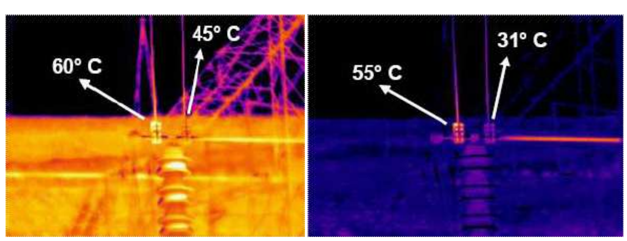

(a) (b)

Figure 2: Infrared image at (a) day (b) night.

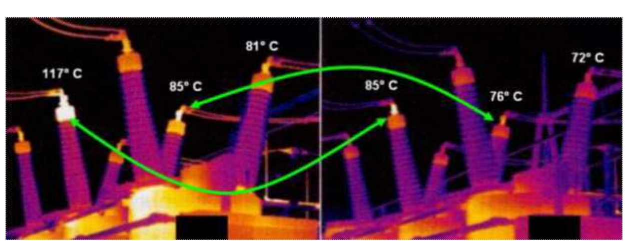

Figure 3: Effect of wind on infrared temperature measurement.

day and night. Fig. 2 presents the same thermal image capturing at daytime and night [11].

3.2. Wind Speed

Wind speed can make effective change to the accuracy of temperature measurement. Low wind speed changes temperature dramatically. If wind speed is high, then due to convection radiation from surface is resisted also. Actually there is an exponential relationship between hotspot temperature change and wind speed [10]. Fig. 3 shows the effect of wind on measurement [11]. In normal condition the temperature of insulator defects was 117,85 and 81. But due to considerable wind influence the temperatures changed to 85,75 and 72 respectively.

3.3. Relative Humidity

Relative humidity is the amount of water in the air at any particular temperature relative to the saturation level. It has minimal effect on object temperature measurement [12, 13] and increases with the object temperature. Due to fog and rain, humidity crosses the saturation level and decreases the actual surface temperature. Fig. 4 shows the effect of rain on thermal image [11]. The color of connector has been totally changed after raining.

3.4. Reflected Temperature

Reflected temperature can change the actual temperature of object. If the background has more emissivity than the target object. Then thermographer will see the background more hotter than the target. In case of the target object has more emissivity than background, then target object will be more hotter than background. On the other hand, if the same emissivity and reflectivity of target object and background, then both will show same temperature.

4. INTELLIGENT QUANTITATIVE THERMOGRAPHY

An intelligent system combining advanced thermal image processing and artificial neural network can be used to improve the inspection results and classify faults automatically. Wind speed, intensity of sun heat, humidity will be measured by weather meter. Then all the values of different environmental factors and thermogram with proper emissivity and distance from object to camera settings are the inputs of artificial neural network. Output will be the temperature considering these effects. Hybrid multilayered perceptron (HMLP) network [14, 15] is dedicated in the proposed method. It has three layers, i.e., input layer, output layer and hidden layer and layers are connected with each other by weights and bias values. HMLP is trained using modified recursive prediction

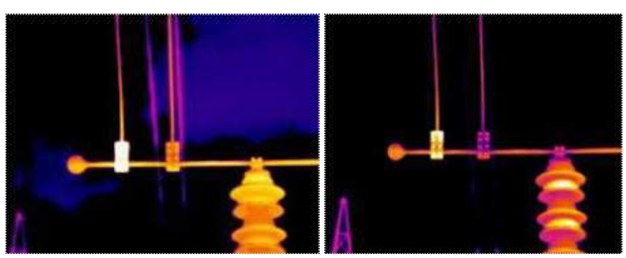

(a) (b)

Figure 4: Thermal image (a) before raining (b) after raining.

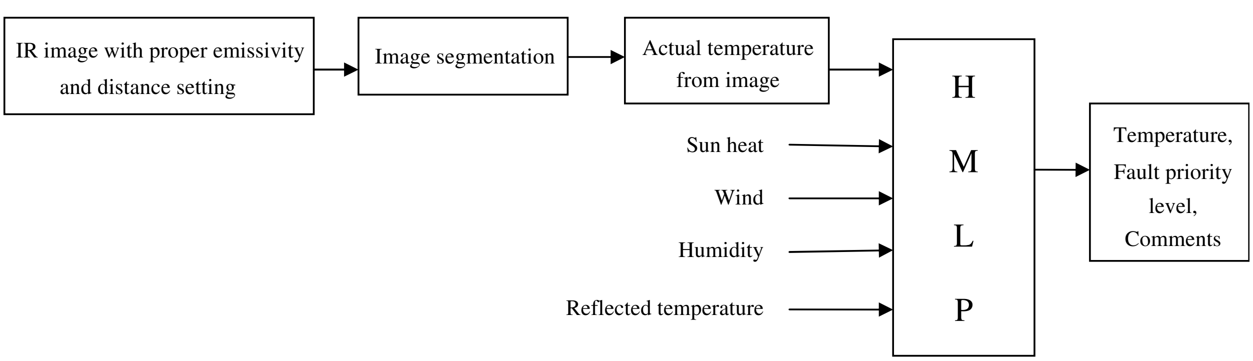

Figure 5: Basic structure of quantitative based diagnosis.

error(MRPE) algorithm will be used as the classification system of faults. Fig. 5 presents basic structure of quantitative based diagnosis is given as follows.

5. CONCLUSIONS

In this paper the effects of environmental factors on infrared temperature measurement are reviewed from the previous experiments. Also an intelligent quantitative based automatic inspection system has been proposed for better result. Infrared thermography is assumed as a safe, reliable and accurate condition monitoring and predictive diagnosis system. But due to some limitations and lack of expert thermographer, it seems sometimes difficult to obtain actual results. Using quantitative based intelligent automatic diagnosis system will overcome these problems. In future, infrared thermography will be used at every power plant as the common and most important tool of electrical equipment diagnosis system.

ACKNOWLEDGMENT

The work was supported by Fundamental Research Grant Scheme (FRGS), Universiti Sains Malaysia.

REFERENCES

1. Wild, D., "Application of infrared thermography in civil engineering," *Proc. of Estonian Science and Engineering*, 436–444, 2007.
2. Lizak, F. and M. Kolcun, "Improving reliability and decreasing losses of electrical system with infrared thermography," *Acta Electritechnica et Information*, Vol. 8, No. 1, 60–63, 2008.
3. "Improving electrical system reliability with infrared thermography," website: www.infraredelectrical.com/index.htm
4. Jadin, M. S., S. Taib, S. Kabir, and M. A. B. Yousuf, "Image processing methods for evaluating infrared thermographic image of electrical equipments," *PIERS Proceedings*, 1299–1302, Marrakesh, Morocco, Mar. 20–23, 2011.
5. Chou, Y. and L. Yao, "Automatic diagnosis system of electrical equipment using infrared thermography," *Proc. of International Conference of Soft Computing and Pattern Recognition*, 155–160, 2009.
6. Jadin, M. S., S. Taib and S. Kabir, "Thermal imaging for qualitative-based measurements of thermal anomalies in electrical equipments," *IEEE Conf. EEPC*, Saudi Arab, Jun. 24–26, 2011.
7. Bortani, E. C., G. S. Bastos, E. S. Souza, M. A. C. Craveiro, and L. Santos, "Development of an acclimatized chamber for IR based diagnostic research," *Int. Conference on Quantitative Infrared Thermography*, Quebec, Canada, Sept. 27–30, 2010.
8. Bolleni, N. K., "Environmental effects on subsurface defect detection in concrete structures using infrared thermography," M.Sc. Thesis, University of Missouri, Columbia, 2009.
9. Castenmiller, C. J. J., "Surface temperature of a wooden window frames under the influence of solar radiation," *TNO Building and Construction*, Delft, The Netherlands.
10. Madding, R. P. and B. R. Lyon, "Wind effects on electrical hotspots," *Infrared Training Center*, North Billerica, MA, 2009.
11. Bortani, E. C. and L. Santos, "Development of models to exact ambient variables influence from outdoor thermographic inspections," *10th International Conference on Quantitative Infrared Thermography*, Quebec, Canada, Sept. 27–30, 2010.
12. Baranski, M. and A. Polak, "Thermographic diagnosis of electrical machines," *XIX International Conference on Electrical Machines*, Rome, 2010.
13. Minkina, W. and S. Dudziz, *Infrared Thermography Errors and Uncertainties*, John Wiley & Sons Ltd., United Kingdom, 2009.
14. Al-Batah, M. S., N. A. M. Isa, K. Z. Zamli, and K. A. M. Azizli, "Modified ecurcive least square to train hybrid multilayered perceptron (HMLP) network," *Applied Soft Computing (Elsevier)*, Vol. 10, No. 1, Jan. 2010.
15. Joret, A., N. A. M. Isa, K. Z. Zamli, K. A. M. Azizli, and M. S. Al-Batah," Classifying the shape of the aggregate using hybrid multilayered network," *9th WSEAS International Conference on Systems*, 497–514, Voliambmeni, Athens, Greece, 2005.

Analysis and Prediction of Temperature of Electrical Equipment for Infrared Diagnosis Considering Emissivity and Object to Camera Distance Setting Effect

A. S. Nazmul Huda, Soib Bin Taib, and Dahaman Bin Ishak
School of Electrical and Electronic Engineering, Universiti Sains Malaysia
Nibong Tebal, Pulau Pinang 14300, Malaysia

Abstract— The paper presents the analysis and predictive model of infrared (IR) temperature with different emissivity and object to camera distance settings effect for obtaining accurate assessment of electrical equipment temperature using IR thermographic inspection. In recent years, IR thermography technology has gained more popularity than other fault diagnosis system of electrical equipments due to its non-contact and non-destructive properties. Abnormal behaviour of electrical equipment is occurred when current is diverted from its intended path due to overloading, load imbalance, corrosion and contact problems etc.. As a result internal heat will begin to rise continuously until eventual failure. IR inspection is such a fast, reliable inspection system without interrupting the running operation of power system where fault diagnosis is performed through the analysis of thermal image captured by IR camera. Usually the emissivity values of camera are pre-defined by the thermal camera manufacturer. But emissivity value can be changed by object surface properties, angle of view and object to camera distance. So, incorrect emissivity settings can cause erroneous diagnosis of equipment and also interrupt actual abnormalities classifications to take automatic recommended actions. For conducting experiments, at first both effects were determined from the comparative evaluation of temperature measurement between thermocouple thermometer and infrared camera capturing pictures at different emissivities at a specific object to camera distance where the actual one implies the closest value to one another. For indirect measurement of IR temperature, the relationship between IR and thermocouple temperature for any given emissivity and distance was established. Furthermore prediction model of IR temperature and measurement error were also developed using response surface methodology. Experimental results conducted on 320 thermal images show that error of temperature measurement can be more than 15% for incorrect emissivity and distance settings. The comparison between predicted and experimental values describes that prediction model approach is appropriate.

1. INTRODUCTION

Each material at temperature above absolute zero ($-273°$C), emits energy in the form of electromagnetic radiation and this energy is radiated at different wavelengths across the electromagnetic spectrum [1]. Infrared (IR) technology is nothing but measuring IR radiation from the material and taking a thermal picture of temperature distribution of electrical equipment surface using an infrared camera [2]. All electrical equipments show an increase in temperature than normal when malfunctioning. Thermographic inspections allow the visualization of heat and diagnosis the faulty equipment without interrupting running system. This system detects only faulty equipments and thus reduces repair time, maintenance costs [3]. It is a non-touching and non-destructive diagnosis system [4]. But infrared radiation measured by camera is not only the function of surface temperature of object but also depends on its emissivity and reflectivity. Again in case of indoor power equipments, as the equipments are close, thermographers can easily find the proper thermal image which describes the faults properties clearly. But temperature measurement of outdoor power equipments can also be affected by the distance between object and camera [5]. To insure the actual heating condition measurement of equipment, these effects must be considered. A survey is conducted in this paper of outdoor equipment 'insulators' with considering images at different emissivities and object to camera distance settings. The main objectives of this paper are to establish a general equation of IR temperature, measurement error of insulators and relationship between IR temperature and thermocouple temperature using response surface methodology.

2. CAUSES OF EMISSIVITY AND DISTANCE VARIATIONS EFFECTS ON MEASUREMENT

Accurate setting of surface emissivity is necessary for getting the true condition of electrical equipments. Emissivity depends on surface condition, size or shape of the object, viewing angle and also with temperature and spectral wavelength nature of object [6]. A blackbody is an ideal imaginary perfect emitter of thermal radiation having no capacity of reflecting radiation, i.e., absorbs entire thermal radiant energy at all possible wavelengths and angle of incidences. So, the emissivity of blackbody is always one. In order to avoid reflection of the thermal imaging camera, viewing angle is important. The wavelength at which the peak energy emittance occurs becomes shorter as temperature increases. Rough or oxidized metal surface has higher emissivity than a polished surface [7]. The emissivity of polished metal strongly depends on the chosen wavelength range and on the polishing process. Objects with very low emissivities (below 0.2) can be difficult to be captured for the IRT applications. Low emissivity objects like polished metals may create problem in quantitative analysis of infrared thermal imaging, since small variation of emissivity value will lead to large variation in the measured temperature.

If camera is placed at very far away from object, energy within target starts to spread into surroundings. This dilutes hotspot temperature due to cool surroundings [5]. But if the ambient and hotspot temperature are same, then it does not change in temperature even at far distance. Again sometimes identifying the location of hotspots is difficult due to image capturing from far away. So there must be maintained a distance criteria between object and camera.

3. EXPERIMENTAL RESULTS

The thermal images of insulators are captured keeping distances $(1, 3, 5, 10\,\mathrm{m})$ between infrared camera and equipment setting different emissivities using Fluke TI 25 thermal imaging camera. A portable compact size K-type thermocouple thermometer is also used to measure the temperature of hotspots. Desired actual temperature is found by comparing temperature between thermocouple and IR camera which is the closest value to each other [8]. Variations of IR temperature (T_{ir}) with thermocouple temperatures (T_c), emissivity values (ε), distances (d) and percentage error(a) vs. emissivity graphs are plotted respectively in Fig. 1. For each insulator there is a gradual decrease of IR temperature with increasing emissivity values. When emissivity values are set at different values from 1.0 to 0.75, IR temperatures, thermocouple temperature. For 90 cases, the errors are less than 5%, for 220 cases errors are from 5% to 15% and for 10 cases errors are above 15%. Generally equipments with high temperature are affected more by emissivity effects than low temperature equipments. From the lowest error point, there is a rapid increase of errors in both directions with different emissivity settings.

4. IR TEMPERATURE AND MEASUREMENT ERROR PREDICTION MODEL

Response surface methodology is an important statistical and mathematical technique used to model and analyze of problems in which a response of interest is influenced by different variables and aim is to optimize response [9]. All regression terms, i.e., linear, linear with square, linear with interaction and full quadratic model were examined to get the suited values. But the best fitted regression model of IR temperature and measurement error were established through linear with interaction regression considering confidence level 95%. Where values for IR temperature and error are 98.8% and 54.5% respectively. Statistical analysis results using MINITAB 14 are presented in Table 1 as follows.

The regression model equations for IR temperature for any given thermocouple temperature,

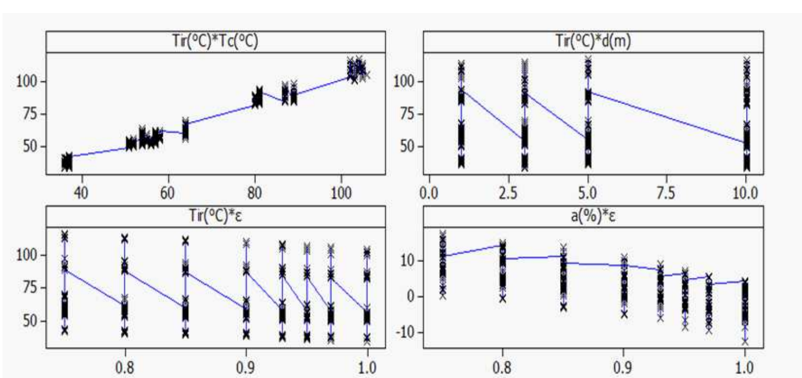

Figure 1: Scatter plots of IR temp vs Thermocouple temp, distance, emissivity and measurement error vs emissivity.

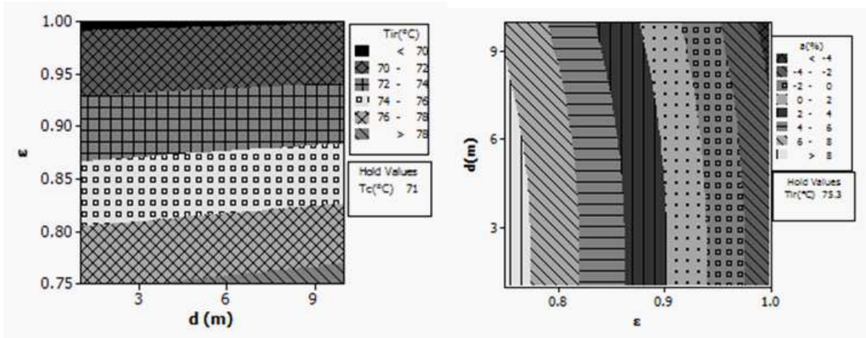

(a) (b)

Figure 2: Contour plots of (a) IR temperature vs emissivity, distance, (b) measurement error vs emissivity, distance.

Table 1: Statistical analysis results.

IR temperature T_{ir} (°C)					Measurement Error a (%)				
Response Surface Regression:					**Response Surface Regression:**				
T_{ir} **(°C) versus** T_c **(°C),** d**,** ε					a **(%) versus** T_{ir} **(°C),** d **(m),** ε				
The analysis was done using uncoded units.					The analysis was done using uncoded units				
Estimated Regression Coefficients for T_{ir} (°C)					Estimated Regression Coefficients for a (%)				
Term	Coef	SE Coef	T	P	Term	Coef	SE Coef	T	P
Constant	6.81505	5.34077	1.276	0.203	Constant	62.2800	8.35426	7.455	0.000
T_c (°C)	1.33435	0.07345	18.166	0.000	T_{ir}(°C)	−0.2323	0.10801	−2.151	0.032
d	−0.40244	0.46697	−0.862	0.389	d (m)	−0.8470	0.75779	−1.118	0.265
ε	−5.44489	5.91489	−0.921	0.358	ε	−63.0763	9.19572	−6.859	0.000
T_c(°C) $* d$	0.01028	0.00199	5.162	0.000	T_{ir} (°C) $* d$ (m)	0.0124	0.00292	4.255	0.000
T_c(°C) $* \varepsilon$	−0.37225	0.08118	−4.585	0.000	T_{ir} (°C) $* \varepsilon$	0.2216	0.11990	1.849	0.065
$d * \varepsilon$	−0.30128	0.50145	−0.601	0.548	d(m) $* \varepsilon$	−0.0985	0.79528	−0.124	0.901
$S = 2.441$	$R - Sq = 98.8\%$		$R - Sq(adj) = 98.8\%$		$S = 3.848$	$R - Sq = 55.3\%$		$R - Sq(adj) = 54.5$	

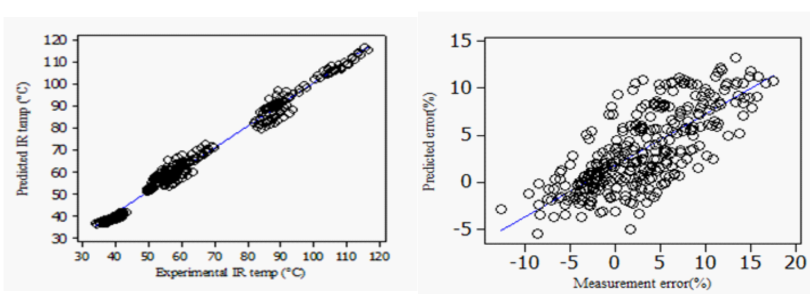

(a) (b)

Figure 3: Scatter plots of (a) predicted vs experimental IR temperature ($R^2 = 98.8\%$), (b) predicted vs experimental error ($R^2 = 54.5\%$).

distance and emissivity value is as follows.

$$T_{ir} = 6.81505 + 1.33435T_c - 0.40244d - 5.44489\varepsilon + 0.01028 * T_c * d - 0.37225 * T_c * \varepsilon \quad (1)$$

Again, regression model equations for measurement error for any given IR temperature, distance and emissivity value can also be expressed as

$$a = 62.28 - 0.2323T_{ir} - 63.0763\varepsilon - 0.8470d + 0.0124 * T_{ir} * d + 0.2216 * T_{ir} * \varepsilon \quad (2)$$

where, $33.80°\text{C} < T_{ir} < 116.80°\text{C}$, $0.75 < \varepsilon < 1.00$ and $1\,\text{m} < d < 10\,\text{m}$.

Generally, R^2 measures the percentage of fluctuation between measured response and predicted response that is explained by regression equations [10]. When R^2 approaches 1, the better the response model fits the actual data [11, 12]. The coefficient of a variable is a constant which represents the change of dependent variables as a function of that variable. The 'SE coef' stands for standard error of coefficient used to generate confidence intervals. The 'T' describes test statistics used in null hypothesis tests and it is given as the ratio of 'coef' to 'SE coef'. The 'P' value is the probability of describing the correlation between the terms of regression equation and response. The $P < 0.05$ means that the estimated value is statistically significant [13]. The contour plots of IR temperature and measurement error as a function of emissivity and distance are shown in Fig. 2 respectively. Fig. 3 presents the plots of predicted vs experimental IR temperature and predicted vs experimental error using Equations (1) and (2) respectively.

5. CONCLUSION

In this paper, the analysis and modeling of IR temperature and measurement error for finding the emissivity setting effect on qualitative based infrared temperature measurement were successfully performed using response surface methodology. It is concluded that there is a remarkable effect of emissivity and image capturing distance from object on temperature measurements. In most cases, correct emissivity values vary from 0.75 to 1.0 and emissivity effect is higher for high temperature electrical equipment. Predictive models will help to measure indirectly IR temperature and measurement error. In future, an intelligent system will be developed considering all environmental effects for more meaningful conclusion of measurement.

ACKNOWLEDGMENT

The work was supported by Fundamental Research Grant Scheme (FRGS), Universiti Sains Malaysia.

REFERENCES

1. Garnaik, S. P., "Infrared thermography: A versatile technology for condition monitoring and energy conversion," http://www.reliabilityweb.com.
2. Lizak, F. and M. Kolcun, "Improving reliability and decreasing losses of electrical system with infrared thermography," *Acta Electritechnica et Information*, Vol. 8, No. 1, 60–63, 2008.
3. Wild, D., "Application of infrared thermography in civil engineering," *Proc. of Estonian Science and Engineering*, 436–444, 2007.
4. Chunli, F., S. Fengrui, and Y. Li, "Investigation of nondestructive evaluation of pipelines using infrared thermography," *IEEE Int. Conf. Terahertz Electronics*, Vol. 2, 339–340, Sep. 19–23, 2005.
5. Madding, R. P., "Common misconceptions infrared thermography condition based maintenance applications," *Infrared Training Center*, North Billerica, MA, 2002.
6. Walsh, R. A., *Electromechanical Handbook*, 3rd Edition, McGraw-HILL, 2000.
7. Wenzel, D., A. Bernal, D. Burris, and A. M Dalton, "Thermal energy emission diagnostics enhancement to the advanced power supply test system," *IEEE System Readiness Conference*, 1998.
8. Neto, E. T. W., E. G. da Costa, and M. J. A. Maia, "Influence of emissivity and distance in high voltage equipments thermal imaging," *IEEE PES Transmission and Distribution Conference and Exposition*, Latin America, Venezuela, 2006.
9. Bradley, N., "The response surface methodology," M.Sc. Thesis, Department of Mathematical Sciences, Indiana University of South Bend, 2007.
10. Suhail, A. H., N. Ismail, S. V. Wong, and N. A. A. Jalil, "Workpiece surface temperature for in process using response surface methodology," *Journal of Applied Sciences*, 308–315, 2011.
11. Jayswal, S. C. and M. Taufik, "Modeling and analysis of surface roughness and geometrical error using taguchi and response surface methodology," *International Journal of Engineering Science and Technology*, Vol. 3, No. 7, Jul. 2011.
12. Montgomery, D. C., *Design and Analysis of Experiments*, John Willey & Sons, New Delhi, 2001.
13. Korbahti, F and M. A. Rauf, "Application of response surface analysis to the photolytic degradation of basic red 2 dye," *Che. Eng. Journal*, Vol. 138, 166–171, 2008.

On the Construction of Dirac's Delta Functions from Poisson's and Maxwell's Equations

A. R. Baghai-Wadji[1,2]

[1]School of Electrical and Computer Engineering, RMIT University, Australia
[2]Center for Electromagnetic Simulation CEMS, Beijing Institute of Technology, China

Abstract— A procedure, having its genesis in partial differential equations arising in mathematical physics, has been introduced to construct 1D- and 2D Dirac's delta functions. Assuming a line charge sandwiched between two parallel infinite ground planes, the associated electric potential response (Green's function) has been constructed, and subsequently employed to obtain a convergent series representation for the Dirac's delta function $\delta(x - x')$. It has been formally established that the derived expression is a genuine generalized function. The insight gained from this exercise suggests a systematic approach for the regularization of singular surface integrals arising in the Method-of-Moments applications. In particular, the application of the proposed technique makes obsolete the customary *ad hoc* introduction of exponentially ϵ-damped terms for regularizing divergent series; problem-tailored exponentially-damped terms appear in the proposed theory "naturally". To further illuminate the structure of the damped exponential terms, inhomogeneous and anisotropic dielectric materials have been examined next. Finally, a problem in 3D has been considered to derive a convergent series representation for $\delta(x - x', y - y')$. The proposed method promises to regularize divergent series by following a sophisticated recipe, and thus, it contributes to the solution of the summability and integrability issues encountered in a myriad of applications in accelerated computational Electromagnetics. A relationship has been established between the methodology in this paper and Leibniz's Law of ontological identity.

1. INTRODUCTION

A field theoretic concept for constructing one- and two dimensional Dirac's delta functions, originating from Poisson's equations, has been introduced. Given a boundary value problem with an isolated line charge excitation, problem's scalar-valued Green's function has been constructed first. The Green's function is then used to establish a series expansion for the Dirac's delta function. It is shown that a plethora of problem-specific representations for the Dirac's delta functions $\delta(x-x')$ and $\delta(x - x', y - y')$ can be obtained, by considering boundary value problems as consistent models for physically realizable systems. Formal proofs have been provided to establish the fact that the derived series expansions are genuine generalized functions. The new representations can be used for a systematic regularization of singular surface integrals appearing in the Method of Moments (MoM) applications. The customary arbitrary introduction of ϵ-damped exponential terms in divergent series and integrals has been made redundant, and instead, replaced by a transparent systematic physics-based fundamental reasoning. The method promises to become an algorithmically sound way of regularizing divergent series and integrals — it can be viewed as a sophisticated methodology for ensuring the summability and integrability of divergent series and integrals appearing in Electromagnetic (EM) simulations. In addition to practical applications in accelerated EM computing, the underlying ideas have also been interpreted from a philosophical stand point, by alluding to Leibniz's Law of ontological identity, correlation and causation. Furthermore, it is hoped that the method reveals strategies for generating equivalent relations; a strategy the utility of which was impressively demonstrated by masters of the trade such as Leonhard Euler. It is also hoped that the proposed method will contribute to the popularization of the theory of generalized functions in the computational EM community by making generalized functions computable.

The current work should be profitably read and interpreted in conjunction with author's earlier works [1–3], in which integral representations were constructed for $\delta(x-x')$ and $\delta(x-x', y-y')$. The exposition complements previously published analyses by deriving series expansions. The interplay of the integral- and series representations is hoped to shed light onto the ways how summability and integrability manifest themselves in the resulting expressions, straightforwardly and effortlessly.

2. 2D POISSON EQUATION

2.1. Simulation Domain and Coordinates

Let the x-axis run horizontally from left to right. Let the y-axis point into the surface. Let the z-axis run vertically upwards. Assume no variation with respect to the y-axis ($\partial/\partial y \equiv 0$). Let $\mathcal{D}$

denote the strip defined by $-L/2 \leq x \leq L/2$ and $-\infty < z < \infty$. Furthermore, let $\mathcal{D}^+$ and $\mathcal{D}^-$ denote the semi-strips $-L/2 \leq x \leq L/2$ and $z > 0$, and $-L/2 \leq x \leq L/2$ and $z < 0$, respectively.

2.2. Boundary- and Interface Conditions

The electric potential $\varphi(x,z)$ is assumed to be subject to the boundary conditions $\varphi(-L/2,z) = 0$ and $\varphi(L/2,z) = 0$ (assumption of two ground plates at $x = -L/2$ and $x = L/2$). Furthermore, $\varphi(x,z)$ is required to vanish for $|z| \to \infty$. In addition, the fields are subject to (real or fictitious) interface conditions at $z = 0$. The latter conditions will be made precise as we proceed further.

2.3. Source Function

Consider the line charge $\rho(x) = \rho_0\delta(x - x')$, located at $z = 0$, with ρ_0 a constant, and $-L/2 < x' < L/2$. (The line charge can be placed as close to the ground planes as desired, however, the condition $-L/2 < x' < L/2$ prevents the line charge from being located on the ground planes.)

2.4. Problem I: Free-space

The first boundary value problem to be analysed is the simplest possible. Let the entire simulation domain $\mathcal{D}$ be free space (electrically characterized by ε_0).

2.4.1. Field Analysis

Since $\rho(-L/2) = \rho(L/2) = 0$, the charge distribution function $\rho(x)$ can be expanded in terms of the complete set of orthonormal functions[1]:

$$\left\{ s_n(x) = \sqrt{\frac{2}{L}} \sin n\pi \left(\frac{x}{L} + \frac{1}{2}\right) \middle| n \in N \right\} \quad \text{with} \quad \langle s_m(x)|s_n(x)\rangle = \delta_{mn} \quad \text{and} \quad m,n \in N \tag{1}$$

In (1) the usual bracket $\langle|\rangle$ notation and the Kronecker symbol δ_{mn} have been used. Thus,

$$\rho_0\delta(x - x') = \sum_n \rho_n s_n(x). \tag{2}$$

Projecting both sides onto $s_m(x)$ we obtain:

$$\langle s_m(x)|\rho_0\delta(x - x')\rangle = \sum_n \rho_n \langle s_m(x)|s_n(x)\rangle \quad \Rightarrow \quad \rho_0 s_m(x') = \sum_n \rho_n \delta_{mn} = \rho_m \tag{3}$$

In the above transition we used the sifting property of the delta function, and the orthonormality condition in (1). Changing indices; i.e., $\rho_n = \rho_0 s_n(x')$, and substituting ρ_n into (2) leads to:

$$\delta(x - x') = \sum_n s_n(x)s_n(x'). \tag{4}$$

This is the celebrated completeness relation for the set of functions $\{s_n(x)|n \in N\}$. The LHS is a generalized function having the RHS as its divergent series expansion. The goal is to establish a convergent series representation for $\delta(x - x')$, which "naturally" embeds $\delta(x - x')$ into the space of the solutions in our problem, and can be conveniently employed in numerical calculations.

2.4.2. Potential Function

Denoting the field variables in $\mathcal{D}^+$ by the superscript $+$, the Laplace equation reads:

$$\varphi^+_{xx}(x,z) + \varphi^+_{zz}(x,z) = 0 \tag{5}$$

Substituting a variable-separated solution Ansatz of the form $\varphi^+_n(x,z) \propto s_n(x)e^{\gamma_n z}$ into (5), for non-trivial solutions, we obtain $\gamma_n^2 = (n\pi/L)^2$, or, equivalently, $\gamma_n^{\pm} = \pm\gamma_n$, with $\gamma_n = n\pi/L$. Thus:

$$\varphi^+_n(x,z) = A^+_n s_n(x)e^{-\gamma_n z} + B^+_n s_n(x)e^{\gamma_n z} \quad \Rightarrow \quad \varphi^+_n(x,z) = A^+_n s_n(x)e^{-\gamma_n z}, \tag{6}$$

where the boundary condition $\lim_{z\to\infty} \varphi^+_n(x,z) \to 0$ has been imposed.

Similarly, denoting the variables in $\mathcal{D}^-$ by the superscript $-$, and using $\lim_{z\to-\infty} \varphi^-_n(x,z) \to 0$:

$$\varphi^-_n(x,z) = A^-_n s_n(x)e^{\gamma_n z} + B^-_n s_n(x)e^{-\gamma_n z} \quad \Rightarrow \quad \varphi^-_n(x,z) = A^-_n s_n(x)e^{\gamma_n z} \tag{7}$$

[1] The expression for the completeness condition of the functions $s_n(x)$ will be established momentarily.

2.4.3. Interface Conditions

The interface condition for the electric potential: From $\varphi^+(x,0^+) = \varphi^-(x,0^-)$ it follows that:

$$\varphi_n^+(x,0^+) = \varphi_n^-(x,0^-) \quad \Rightarrow \quad A_n^+ = A_n^- = A_n \quad \Rightarrow \quad \varphi_n^{\pm}(x,z) = A_n s_n(x) e^{\mp\gamma_n z} \tag{8}$$

The interface condition for the "normal" z-components of the dielectric displacement:

$$D_3^+(x,0^+) - D_3^-(x,0^-) = \rho(x) \quad \Rightarrow \quad D_{3,n}^+(x,0^+) - D_{3,n}^-(x,0^-) = \rho_n(x) \tag{9}$$

With $D_{3,n}(x,z) = -\varepsilon_0 \partial\varphi_n(x,z)/\partial_z$ for the n^{th} Fourier terms of the components of the dielectric displacements $D_{3,n}^+(x,z)$ and $D_{3,n}^-(x,z)$ in the z-direction we obtain:

$$D_{3,n}^{\pm}(x,z) = \pm\varepsilon_0\gamma_n A_n s_n(x) e^{\mp\gamma_n z} \tag{10}$$

Substituting (10) into (9) results in the expression for A_n and thus:

$$A_n = \frac{\rho_0}{2\varepsilon_0\gamma_n} s_n(x') \quad \Rightarrow \quad D_3^{\pm}(x,z) = \pm\frac{\rho_0}{2}\sum_n s_n(x') s_n(x) e^{\mp\gamma_n z} \tag{11}$$

In particular for $D_3^+(x,\epsilon)$ and $D_3^-(x,-\epsilon)$, with $\epsilon > 0$ we have

$$D_3^{\pm}(x,\pm\epsilon) = \pm\frac{\rho_0}{2}\sum_n s_n(x) s_n(x') e^{-\gamma_n\epsilon} \tag{12}$$

Back-substituting (12) into the interface condition for $D_3(x,z)$ results in:

$$\lim_{\epsilon\to 0}\left[D_3^+(x,\epsilon) - D_3^-(x,-\epsilon)\right] = \rho(x) \quad \Rightarrow \quad \lim_{\epsilon\to 0}\sum_n s_n(x) s_n(x') e^{-\gamma_n\epsilon} = \delta(x-x') \tag{13}$$

Or, more explicitly,

$$\delta(x-x') = \lim_{\epsilon\to 0}\frac{2}{L}\sum_{n=1}^{\infty}\sin\left[n\pi\left(\frac{x}{L}+\frac{1}{2}\right)\right]\sin\left[n\pi\left(\frac{x'}{L}+\frac{1}{2}\right)\right]e^{-\gamma_n\epsilon} \tag{14}$$

Theorem: The expression at the RHS of (14) is a valid representation for $\delta(x-x')$.

Proof: Expressing $\sin(\cdot)$ in terms of $\exp(\pm j(\cdot))$ and absorbing the term $\exp(-n\pi\varepsilon/L)$ lead to:

$$\delta(x-x') \overset{?}{=} -\frac{1}{2L}\lim_{\epsilon\to 0}\left\{\sum_{n=1}^{\infty}q_1^n - \sum_{n=1}^{\infty}q_2^n - \sum_{n=1}^{\infty}q_3^n + \sum_{n=1}^{\infty}q_4^n\right\} \tag{15}$$

$$q_1 = e^{j\pi(\frac{x+x'}{L}+1)-\frac{\epsilon\pi}{L}}, \quad q_2 = e^{-j\pi\frac{x-x'}{L}-\frac{\epsilon\pi}{L}}, \quad q_3 = e^{j\pi\frac{x-x'}{L}-\frac{\epsilon\pi}{L}}, \quad q_4 = e^{-j\pi(\frac{x+x'}{L}+1)-\frac{\epsilon\pi}{L}}$$

Since $|q_i| = e^{-\pi\epsilon/L} < 1$, $S_i = \sum\limits_{n=0}^{\infty} q_i^n = 1/(1-q_i)$, with $i = 1,2,3,4$. Thus,

$$S_1 = \frac{e^{\frac{\epsilon\pi}{L}}}{e^{\frac{\epsilon\pi}{L}} + e^{j\pi\frac{x+x'}{L}}}, \quad S_2 = \frac{e^{\frac{\epsilon\pi}{L}}}{e^{\frac{\epsilon\pi}{L}} - e^{-j\pi\frac{x-x'}{L}}}, \quad S_3 = \frac{e^{\frac{\epsilon\pi}{L}}}{e^{\frac{\epsilon\pi}{L}} - e^{j\pi\frac{x-x'}{L}}}, \quad S_4 = \frac{e^{\frac{\epsilon\pi}{L}}}{e^{\frac{\epsilon\pi}{L}} + e^{-j\pi\frac{x+x'}{L}}}$$

$$\delta(x-x') \overset{?}{=} -\frac{1}{2L}\lim_{\epsilon\to 0}\left\{S_1 + S_4 - (S_2+S_3)\right\}, \tag{16}$$

and consequently, after some manipulations:

$$\delta(x-x') \overset{?}{=} -\frac{1}{2L}\lim_{\epsilon\to 0}\sinh\left(\frac{\pi\epsilon}{L}\right)\left[\frac{1}{\cosh\frac{\pi\epsilon}{L}+\cos\frac{\pi(x+x')}{L}} - \frac{1}{\cosh\frac{\pi\epsilon}{L}-\cos\frac{\pi(x-x')}{L}}\right] \tag{17}$$

Note that letting the summation index start from $n = 0$ rather than $n = 1$ has no implication to the RHS in (15). At the limit $\epsilon \to 0$ the ϵ-terms in (17), can be safely approximated by their respective Taylor series expansions for small arguments; i.e., $\sinh(\pi\epsilon/L) \approx \pi\epsilon/L$ and $\cosh(\pi\epsilon/L) \approx 1 + \pi^2\epsilon^2/(2L^2)$. The treatment of the $(x+x')$- and $(x-x')$-terms is, however, more delicate. In view of the fact that we are interested in examining whether or not the RHS of (17) is a valid representation for $\delta(x-x')$, consider the important case of $x \approx x'$; i.e., $0 \le |x-x'| \ll L$ subject to the constraints $-L/2 \le x \le L/2$ (the observation point can assume any position between the ground plates — including the plates) and $-L/2 < x' < L/2$ (the source point can assume any position between the ground plates - excluding the plates). Thus, $0 \le |x+x'| < L$.[2] On the other hand, $|x-x'| \ll L$ implies $\cos[\pi(x-x')/L] \approx 1 - \pi^2(x-x')^2/(2L^2)$. In general, however, a similar expansion for $\cos[\pi(x+x')/L]$ is not valid, since it is only guaranteed that $|x+x'| < L$ (rather than $|x+x'| \ll L$), except possibly the case $x \approx x' \approx 0$, where the expansion $\cos[\pi(x+x')/L] \approx 1 - \pi^2(x+x')^2/(2L^2)$ holds valid. Summarising the results obtained so far, we have:

$$\delta(x-x') \overset{?}{=} -\frac{1}{2L}\lim_{\epsilon\to 0}\frac{\pi\epsilon}{L}\left[\frac{1}{1+\frac{1}{2}\left(\pi\frac{\epsilon}{L}\right)^2+\cos\frac{\pi(x+x')}{L}} - \frac{1}{1+\frac{1}{2}\left(\pi\frac{\epsilon}{L}\right)^2-1+\frac{1}{2}\left(\pi\frac{x-x'}{L}\right)^2}\right] \tag{18}$$

From $0 \le |x+x'| < L$ and thus $0 \le \pi|x+x'|/L < \pi$ the relationships $-1 < \cos[\pi(x+x')/L] \le 1$ follow. Consequently, $0 < 1+\cos[\pi(x+x')/L] \le 2$. In particular, consider the strict inequality $1+\cos[\pi(x+x')/L] > 0$, implying $\lim_{\epsilon\to 0}\{1+(\pi\epsilon/2L)^2+\cos[\pi(x+x')/L]\} > 0$. Thus the denominator of the first fraction in (18) is always positive (irrespective of how small, it never vanishes). Therefore, the first term in the bracket in (18) multiplied by $\pi\epsilon/L$ vanishes in the limit $\epsilon \to 0$. Considering this fact and simplifying the second fraction leads to

$$\delta(x-x') \overset{?}{=} -\frac{1}{2L}\lim_{\epsilon\to 0}\frac{\pi\epsilon}{L}\left[-\frac{\frac{2L^2}{\pi^2}}{\epsilon^2+(x-x')^2}\right] \quad \Rightarrow \quad \delta(x-x') = \frac{1}{\pi}\lim_{\epsilon\to 0}\frac{\epsilon}{\epsilon^2+(x-x')^2} \tag{19}$$

The last expression is a well-known representation for the Dirac's delta function; a fact which has justified the removal of the question mark on the equality sign. This completes the proof.[3] $\square$

2.5. Problem II: Inhomogeneous Dielectric Junction

To gain further insight into the structure of series representations for the δ-function, consider the same geometry as in the foregoing problem, except the condition that the dielectric material in region $z < 0$ is diagonally anisotropic, and characterized by non-zero, positive permittivity constants ε_{ii} $(i, = 1, 2, 3)$. Maintaining the assumption of a 2D analysis $(\partial_y \equiv 0)$, and following a similar line of argument, a comparatively tedious, but straightforward calculation, results in:

$$\delta(x-x') \overset{?}{=} \lim_{\epsilon\to 0}\left\{\frac{\sqrt{\varepsilon_{33}}}{\sqrt{\varepsilon_{11}}+\sqrt{\varepsilon_{33}}}\sum_{n=1}^{\infty}s_n(x)s_n(x')e^{-\frac{n\pi}{L}\epsilon} + \frac{\sqrt{\varepsilon_{11}}}{\sqrt{\varepsilon_{11}}+\sqrt{\varepsilon_{33}}}\sum_{n=1}^{\infty}s_n(x)s_n(x')e^{-\sqrt{\frac{\varepsilon_{11}}{\varepsilon_{33}}}\frac{n\pi}{L}\epsilon}\right\} \tag{20}$$

A further lengthy calculation, similar to the one in Problem I, shows that in the limit $\epsilon \to 0$, each of the sums in (20) individually adds up to $\delta(x-x')$. Thus, factoring out $\delta(x-x')$ and adding the resulting two terms establishes the equality in (20). $\square$

3. DIRAC'S DELTA FUNCTION IN TWO DIMENSIONS

Considering the domain $[-L_1/2, L_1/2] \times [-L_2/2, L_2/2]$, and following a similar procedure, leads to:

$$\begin{aligned}\delta(x-x', y-y') \;=\; &\frac{4}{L_1L_2}\lim_{\epsilon\to 0}\sum_{m=1}^{\infty}\sum_{n=1}^{\infty}\sin\left[m\pi\left(\frac{x}{L_1}+\frac{1}{2}\right)\right]\sin\left[m\pi\left(\frac{x'}{L_1}+\frac{1}{2}\right)\right]\\ &\times\sin\left[n\pi\left(\frac{y}{L_2}+\frac{1}{2}\right)\right]\sin\left[n\pi\left(\frac{y'}{L_2}+\frac{1}{2}\right)\right]\times e^{-\sqrt{\left(\frac{m\pi}{L_1}\right)^2+\left(\frac{n\pi}{L_2}\right)^2}\epsilon}\end{aligned} \tag{21}$$

[2] As it is shown in the paragraphs between the Eqs. (18) and (19), the imposition of the condition $0 \le |x+x'| < L$ rather than $0 \le |x+x'| \le L$ is fundamental to our arguments.

[3] The main point in the above argument is the property that the denominator of the first fraction in (17) can never vanish. The examination of the following particular case may further illuminate this property: Let the source point be located at the $x' = -L/2+\eta$, with η being an arbitrarily small but finite positive number. Let the observation point be located at $x = -L/2$. Thus $x+x' = -L+\eta$ with $\eta > 0$. (It should be reiterated that the condition $\eta > 0$ prohibits the line charge source from coinciding with the ground plate at $-L/2$.) Thus, $\cos[\pi(x+x')/L] > -1$. An equally critical case occurs when $x' = L/2-\eta$, with $\eta > 0$, and $x = L/2$. Thus, $x+x' = L-\eta$ with $\eta > 0$; once again implying the condition $\cos[\pi(x+x')/L] > -1$. Therefore, as long as the line charge does not coincides with any of the ground plates, a condition implied by the physical realizability, the denominator of the first fraction in (17) is a positive real number, irrespective of how small.

This result makes explicit the ϵ-decay behavior of the exponential functions in the double series expansion of $\delta(x-x', y-y')$. It remains a challenge to show that (21) is equivalent with the following identity, which was established in [3] following an alternative path of argument:

$$\delta(x-x', y-y') = \frac{1}{2\pi} \lim_{\epsilon \to 0} \frac{\epsilon}{\left[(x-x')^2 + (y-y')^2 + \epsilon^2\right]^{3/2}} \tag{22}$$

4. CONCLUSION

A novel physics-inspired approach has been developed for deriving series expansions for the Dirac's delta function in 1D and 2D. The work supplements author's earlier works in which integral counterparts were utilized. Throughout the discussion Poisson's equation was employed; extension to Maxwell's electrodynamic equations, or for this matter, to any of the linear partial differential equations (PDEs) in mathematical physics, should be immediate [3]. The method (tacitly) employed the eigenpairs of the algebraic system of equations corresponding to the underlying PDEs. An important feature of the proposed technique is its utility for fully coupled EM fields in anisotropic or bi-anisotropic media, where the eigenpairs are obtainable in numerical form only. This ability should be pointed out emphatically. Since the derived delta functions are, by construction, embedded in the space of field solutions, they are optimally matched to the associated problems, when regularizing the arising singular integrals. Details remain to be demonstrated elsewhere.

The following ontological and epistemological remarks maybe worth mentioning. The roles of the source (delta function) and the associated response (Green's function) were reversed in the arguments: The derivative of the response was used to construct an expression for the cause, establishing a connection with Leibniz's Law of ontological identity. Introducing $\alpha = \sqrt{\varepsilon_{11}}$, $\beta = \sqrt{\varepsilon_{33}}$, $\hat{x} = x/L$, and $\hat{z} = z/L$, the results can be stated abstractly, allowing their utility to tackle problems of varied origins. The ideas in this paper advocate the pursuit of "physical mathematics" in conjunction with conventional "mathematical physics": At any given time in history of science, governing equations are viewed as our best models for "reality". Thus, any computational scheme, derived from the governing equations, promises to provide the optimum technique for solving contemporary boundary value problems. This *plaidoyer* for physical mathematics, as a discipline, concludes the paper. With profound admiration, this work is devoted to Leonhard Euler.

ACKNOWLEDGMENT

This project has been carried out under an Australian Research Counsel (ARC) Linkage Grant: LP0775463. Generous support granted by EPCOS AG (Munich) and EPCOS Pty (Singapore) are gratefully appreciated.

REFERENCES

1. Baghai-Wadji, A. R., "Zooming into the near field: A novel formulation of the BEM as applied to EMC modelling and simulation problems," *APEMC 2010*, Beijing, China, May 2010 (invited).
2. Baghai-Wadji, A. R., "Near-field phenomena in EMC applications," *Electromagnetic Compatibility Symposium Melbourne*, 1–16, Australia, Sep. 2010.
3. Baghai-Wadji, A. R., "On the construction of physics-inspired integral representations for the dirac delta function in EMC applications," *APEMC*, Jeju Island, Korea, May 16–19, 2011 (invited).

On the Construction of a Hierarchy of Lower Dimensional Auxiliary Boundary Value Problems for Solving Real-life Problems in Engineering Applications

A. J. Smith and A. Baghai-Wadji
School of Electrical and Computer Engineering, RMIT University, Australia

Abstract— Solving two- and three-dimensional Boundary Value Problems (BVPs) in engineering can be computationally very demanding. The primary ideas in this contribution are centered about designing tailored basis- and weighting functions for Galerkin-type methods, simultaneously reducing the order of the complexity of the problem (Model Order Reduction, MOR), based on physical considerations. The concept involves the following steps: (i) Given a higher (two or three) dimensional BVP, construct a hierarchy of lower dimensional (one or two) related auxiliary problems. (ii) Examine the hermiticity property of the differential operators involved in the auxiliary problems. (iii) In case the auxiliary operators are already hermitian, no change is necessary; otherwise modify the operators adequately so that they become hermitian. (iv) Determine the positive eigenvalues and the corresponding orthogonal eigenvectors of the (modified) auxiliary problems. (v) The tensor-product of the derived eigenfunctions, corresponding to one-dimensional operators, results in a set of higher-dimensional analysis functions. To demonstrate the versatility of the method, quantum dot and quantum wire structures, under realistic conditions, have been analyzed, and the numerical results are compared against available data in literature.

1. INTRODUCTION

Quantum wires (QWs) and quantum dots (QDs) represent the fundamental building blocks that makeup nano-scale and small-scale electronic devices. Nano-structures, due to their highly desirable physical characteristics, are prime candidates for future electronic devices [1].

The development of high performance computational models for describing the physical characteristics in such structures and devices is of critical importance. To date, there have been many modelling techniques employed to simulate and predict the quantum confinement characteristics. Some of the most prominent methods include: finite element method [2], finite difference method [3], transfer matrix method [4], boundary element method [5], and spectral techniques [6]. Each of the aforementioned methods suffers from one or more of the following limitations or computational bottlenecks, which are addressed in this paper: the requirement for a dense discretization of the simulation domain; incorporation of artificial absorbing boundary conditions; tedious treatment of strong or hyper-strong singularities; laborious handling of the large number of boundary conditions (especially when the quantum structures are geometrically and functionally too complex and require a three dimensional analysis).

In our earlier work [7], a Galerkin-type method was used to calculated the quantum confinement properties of an isotropic QW structure. Two simpler (auxiliary) QW problems were constructed which closely mimicked the problem of interest (target problem), but were easier to solve. The solutions to the auxiliary problems served as trial solutions for the target problem. Figure 1 shows a schematic of the hierarchy of auxiliary problems that are used to solve the target problem. The dashed frame refers to the isotropic QW problems that were solved in reference [7]; with Q_{2D}^{aux} denoting an asymmetrical, periodic QW problem, $Q_{1D,2}^{aux}$ referring to a simple finite well problem, $Q_{1D,1}^{aux}$ representing the harmonic oscillator problem, and Q_{1D}^{aux} (periodic) denoting a fundamental periodic problem. The problem denoted P_{2D} is the anisotropic QW structure of interest, and is the focus of this paper. Following the procedure used to solve Q_{2D}^{aux} [7], the solutions of Q_{2D}^{aux} will be used as trial functions to solve P_{2D}. Furthermore, to demonstrate the validity of the proposed method, various QW problems from literature have been considered. The Brillouin band diagrams and total energy values, which have been calculated in literature, are reproduced here using the proposed method; excellent agreement has been achieved.

This paper is organized as followed: In Section 2, the problem of interest is defined, where Section 3 explains the procedure on how the QW problem is solved. Section 4 gives a brief overview of the calculated results of the proposed method; the computed results are compared against pre-calculated data available in literature. Section 5 concludes the paper.

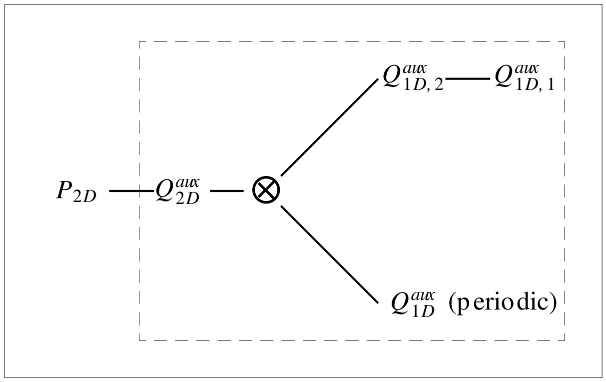

Figure 1: A schematic showing the connection between the target problem (P_{2D}), the hierarchy of auxiliary problem, Q^{aux}_{2D}, and its constituent auxiliary problems $Q^{aux}_{1D,2}$, $Q^{aux}_{1D,1}$ and Q^{aux}_{1D} (periodic). To solve the isotropic QW problem (Q^{aux}_{2D}), the tensor product of the eigenfunctions in $Q^{aux}_{1D,2}$ and Q^{aux}_{1D} (periodic) have been utilized. P_{2D} is the anisotropic QW problem of interest, which is the focus of this paper. P_{2D} utilizes the computed eigenfunctions associated with Q^{aux}_{2D}. While it has not been included in the figure, it should be obvious that the solution to P_{2D} can itself serve to tackle related P_{3D} problems.

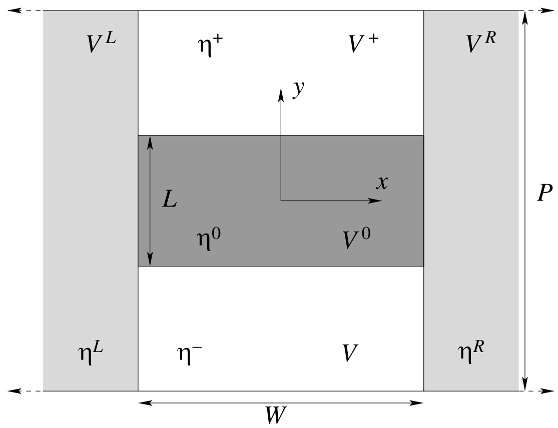

Figure 2: A sketch of the "fundamental cell" of an inhomogeneous and fully-anisotropic QW. Along the x-direction, as indicated by the arrows, the structure extends indefinitely, while along the y-direction, the fundamental cell is repeated periodically.

2. STATEMENT OF THE PROBLEM

Consider the two dimensional structure depicted in Figure 2, which shows the fundamental cell of a P-periodic (in the y-direction), fully anisotropic QW. The channel having an aperture length W is characterized by the potential- function $V(x, y)$ and inverse effective mass tensor $\boldsymbol{\eta}(x, y)$ ($\boldsymbol{\eta}(x, y) = \mathbf{M}^{-1}(x, y)$). Within the channel, there is no potential or effective mass variation along the x-direction. Constant values outside the channel characterize the potential function and effective mass tensor. The wavefunctions and energy values describing the behavior of an electron, traveling through such a QW structure, are governed by the position-dependent effective mass Schrödinger equation:

$$-\frac{\hbar^2}{2m_0}\nabla^T_{xy}\boldsymbol{\eta}(x, y)\nabla_{xy}\psi(x, y) + V(x, y)\psi(x, y) = E\psi(x, y) \tag{1}$$

Here, the superscript T stands for transposition, $\hbar$ is the reduced Planck constant and m_0 is the electron rest mass.

3. PROPOSED SOLUTION PROCEDURE

Introducing the scaled variables, $\hat{x} = x/P$, $\hat{y} = y/P$, the scaled wavefunction $\hat{\psi}(\hat{x}, \hat{y})$, defined as $\hat{\psi}(\hat{x}, \hat{y}) = \psi(x, y)$, and the scaled inverse effective mass tensor $\hat{\boldsymbol{\eta}}(\hat{x}, \hat{y})$, defined as $\hat{\boldsymbol{\eta}}(\hat{x}, \hat{y}) = \boldsymbol{\eta}(x, y)$, Eq. (1) can be written in the following non-dimensional form

$$-\frac{1}{4\pi^2}\nabla^T_{\hat{x}\hat{y}}\begin{bmatrix}\hat{\eta}_{11}(\hat{x},\hat{y}) & \hat{\eta}_{12}(\hat{x},\hat{y})\\ \hat{\eta}_{21}(\hat{x},\hat{y}) & \hat{\eta}_{22}(\hat{x},\hat{y})\end{bmatrix}\nabla_{\hat{x}\hat{y}}\hat{\psi}(\hat{x},\hat{y})+\hat{V}(\hat{x},\hat{y})\hat{\psi}(\hat{x},\hat{y})=\hat{E}\hat{\psi}(\hat{x},\hat{y}), \tag{2}$$

where $\hat{\boldsymbol{\eta}}(\hat{x},\hat{y})$ has been written component-wise. Furthermore, $\hat{V}(\hat{x},\hat{y}) = V(x,y)/E_0$ and $\hat{E} = E/E_0$ with $E_0 = (\pi\hbar/m_0P)^2$.

To solve this equation, a set of eigenpairs from a suitably constructed, problem-specific auxiliary problem is required. The auxiliary problem should be chosen such that it is considerably simpler to solve than Eq. (2), but retains as many of the features of the original QW structure as possible.

3.1. Auxiliary Problem

The auxiliary problem is chosen by assuming the particle's mass to be constant throughout the entire domain, while still being subject to the potential $\hat{V}(\hat{x},\hat{y})$. Under these conditions, Eq. (2) transforms into

$$-\frac{1}{4\pi^2}\nabla^T_{\hat{x}\hat{y}}\begin{bmatrix}1 & 0\\ 0 & 1\end{bmatrix}\nabla_{\hat{x}\hat{y}}\hat{\psi}^a(\hat{x},\hat{y})+\hat{V}(\hat{x},\hat{y})\hat{\psi}^a(\hat{x},\hat{y})=\hat{E}^a\hat{\psi}^a(\hat{x},\hat{y}). \tag{3}$$

Here, the superscript a has been introduced to explicitly denote the solutions which belong to the auxiliary problem. As shown in our earlier work [7], the eigenfunctions corresponding to the auxiliary problem can be expressed as a linear superposition of tensor products of two one-dimensional functions; i.e.,

$$\hat{\psi}^a_m(\hat{x},\hat{y})=\sum_{r,s}\beta^m_{rs}\hat{A}_r(\hat{x})\hat{B}_s(\hat{y}). \tag{4}$$

Here, $\hat{A}_r(\hat{x})$ correspond to the solutions of $Q^{aux}_{1D,2}$ and $\hat{B}_s(\hat{y})$ are the solutions to Q^{aux}_{1D} (periodic). The coefficients β^m_{rs} are *a priori* unknown. The index m corresponds to the eigenmode of the auxiliary problem, hence, $m \in \{0,1,2,\ldots,M\}$, with M being some chosen upper limit.

3.2. Target Problem

Exploiting the orthonormality of the solutions to the auxiliary problem, the solutions of Eq. (2) can be expressed in terms of a linear superposition of these functions;

$$\hat{\psi}(\hat{x},\hat{y})=\sum_m \alpha_m\hat{\psi}^a_m(\hat{x},\hat{y}), \tag{5}$$

where α_m are *a priori* unknown.

Applying Galerkin's method to the target problem, Eq. (5) is substituted into Eq. (2) as a trial solution, and tested by the complex conjugate of the $\bar{m}^{th}$ eigenfunction, $\hat{\psi}^{a*}_{\bar{m}}(\hat{x},\hat{y})$. The resulting equation is then integrated over the fundamental cell. Next, using Galerkin's method on the auxiliary problem, the mth solution of Eq. (3) is chosen and multiplied by a weighting function, $\hat{\psi}^*(\hat{x},\hat{y})$. Eq. (5) is substituted in place of the weighting function (with the running index denoted by $\bar{m}$) and integrated over the domain of the fundamental cell. Next, taking the difference between the integrated target and auxiliary equations, the following equation is obtained:

$$\begin{aligned}&-\frac{1}{4\pi^2}\sum_m\alpha_m\Big\{\left\langle\hat{\psi}^a_{\bar{m}}\left|\partial_{\hat{x}}\hat{\eta}_{11}\partial_{\hat{x}}\right|\hat{\psi}^a_m\right\rangle+\left\langle\hat{\psi}^a_{\bar{m}}\left|\partial_{\hat{x}}\hat{\eta}_{12}\partial_{\hat{y}}\right|\hat{\psi}^a_m\right\rangle+\left\langle\hat{\psi}^a_{\bar{m}}\left|\partial_{\hat{y}}\hat{\eta}_{21}\partial_{\hat{x}}\right|\hat{\psi}^a_m\right\rangle\\ &+\left\langle\hat{\psi}^a_{\bar{m}}\left|\partial_{\hat{y}}\hat{\eta}_{22}\partial_{\hat{y}}\right|\hat{\psi}^a_m\right\rangle-\left\langle\hat{\psi}^a_{\bar{m}}\left|\partial_{\hat{x}\hat{x}}\right|\hat{\psi}^a_m\right\rangle-\left\langle\hat{\psi}^a_{\bar{m}}\left|\partial_{\hat{y}\hat{y}}\right|\hat{\psi}^a_m\right\rangle\Big\}=\sum_m\alpha_m(\hat{E}-\hat{E}^a_m)\left\langle\hat{\psi}^a_{\bar{m}}\,|\,\hat{\psi}^a_m\right\rangle\end{aligned} \tag{6}$$

The influence of the potential function $\hat{V}(\hat{x},\hat{y})$ has manifested itself in the calculation of the eigenpairs $\hat{\psi}^a_m(\hat{x},\hat{y}) \leftrightarrow \hat{E}^a_m$, and thus plays its role in Eq. (6) implicitly. Varying $\bar{m}$ in the range $\{0,1,\ldots,M\}$, Eq. (6) results in an eigenvalue problem for the determination of $\hat{E}$ and α_m (and thus ultimately $\hat{\psi}(\hat{x},\hat{y})$).

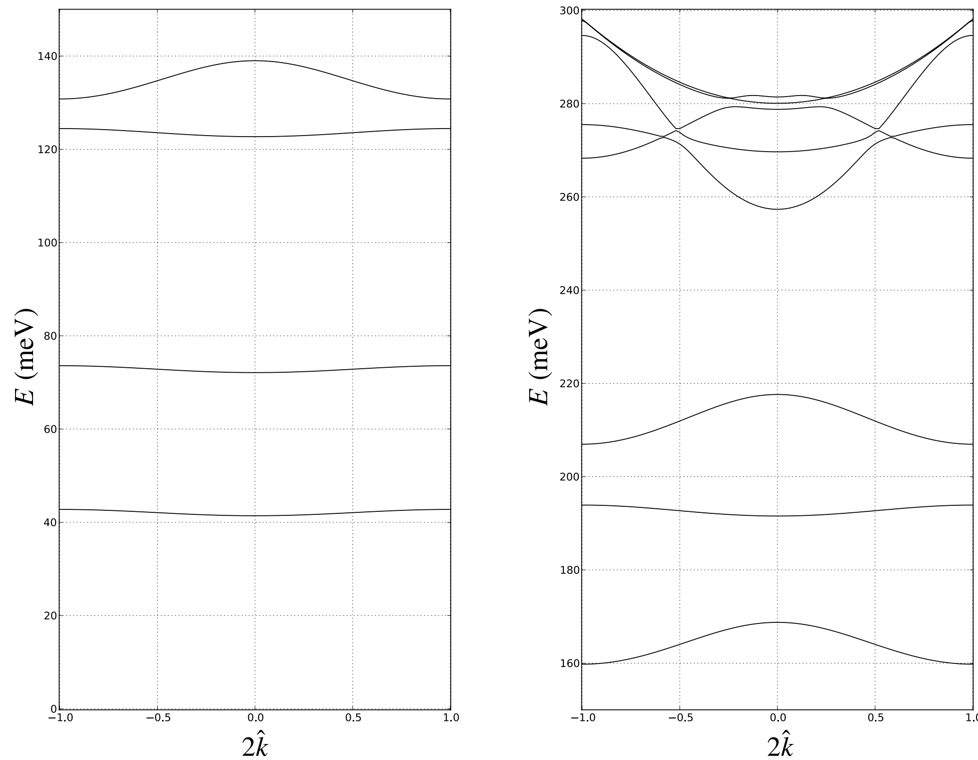

(a) $0 < E < 150$ (b) $150 < E < 300$

Figure 3: The energy dispersion diagram for a conduction electron in a GaAs/$Ga_{0.63}Al_{0.37}As$ periodic QW.

Table 1: Bound Energy Levels of a conduction electron in a GaAs/$Ga_{0.63}Al_{0.37}As$ Single QWW.

Cross-Section $L_x \times L_y (nm)^2$	Proposed Method (meV)	Gangopadhyay (meV)	Shertzer (meV)
5×5	155.27	155.2	155.3
5×10	111.13	111.2	111.1
10×10	63.473	63.47	63.5
	155.23	...	155.2

4. RESULTS AND DISCUSSION

To validate the proposed method set out in Section 3, the solutions of two QW problems, which have been treated elsewhere, are reproduced here using the proposed method.

The first QW problem is the infinite array of quantum wire wells, shown in reference [8]. The QW structure can be obtained from Figure 2 by setting $V^l = V^R = V^+ = V^- = 276\,\text{meV}$, $V^0 = 0\,\text{meV}$, $\eta^l = \eta^R = \eta^+ = \eta^- = 1/0.0858$, $\eta^0 = 1/0.0665$, $P = 15\,\text{nm}$, $W = 20\,\text{nm}$ and $L = 10\,\text{nm}$. The potential and effective mass values set for this structure characterize a conduction electron, propagating along a $Ga_{0.63}Al_{0.37}As$ QW. The energy dispersion diagram, calculated using the proposed method, is shown in Figure 3. Here, an electron propagating along the y-direction is considered. The dispersion diagram constructed is in excellent agreement with the dispersion diagram obtained by Pokatilov et al. in reference [8].

Next, consider the QW structure depicted in Figure 4. The lengths L_x and L_y characterize the dimensions of the QW cross-section, where the barrier material extends indefinitely for $|x| \to \infty$ and $|y| \to \infty$. The energy eigenstates are calculated for a conduction electron, bound within the QW. The material composition of this QW is the same as the previous structure. Here, $V = 0$ and $\eta = 1/0.0665$ inside the well, and $V = 276\,\text{meV}$ and $\eta = 1/0.0858$ outside the well.

Table 1 shows the calculated energy eigenstates for the $Ga_{0.63}Al_{0.37}As$ QW, using the proposed method, along with the results obtained by a spectral method using Fourier expansion terms [9] and the finite element method [10]. As it is shown, the bound energy states were calculated for

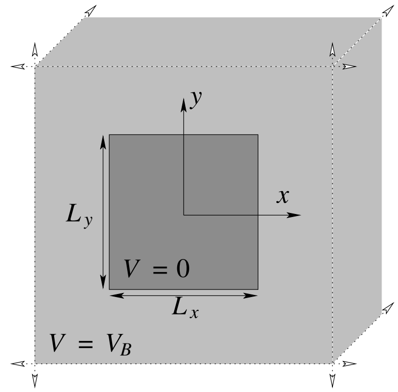

Figure 4: A diagram of a single quantum wire well (QWW). The QWW is contained within a finite potential.

different cross-sectional areas. The calculated energy eigenvalues, using the proposed method, are in excellent agreement with those obtained by the other two methods.

5. CONCLUSION

A method has been proposed to solve the position-dependent effective mass Schrödinger equation for anisotropic QW structures. The method employs a hierarchy of auxiliary problems, which are fundamentally simpler and thus easier to solve than the target problem. Using entire-domain basis functions, all interface conditions have been naturally met, which has made the enforcement of interface conditions totally redundant. The validity of the proposed technique was shown by considering two types of QW problems, which are considered in literature.

ACKNOWLEDGMENT

This project has been carried out under an Australian Research Council (ARC) linkage Grant: LP0775463. Generous support granted by EPCOS AG (Munich, Germany) and EPCOS Pty (Singapore) are gratefully appreciated.

REFERENCES

1. Li, Y., F. Qian, and C. M. Lieber, "Nanowire electronic and optoelectronic devices," *Materials Today*, Vol. 9, No. 10, 18–27, 2006.
2. Nakamura, K., A. Shimizu, M. Koshiba, and K. Hayata, "Finite-element analysis of quantum wells of arbitrary potential profiles," *IEEE J. Quantum Electron.*, Vol. 25, No. 5, 889–895, 1989.
3. Bouazra, A., S. A.-B. Nasrallah, A. Poncet, and M. Said, "Numerical simulation of a coupling effect on electronic states in quantum dots," *Superlattices and Microstructures*, Vol. 48, No. 1, 1–8, 2010.
4. Deo, P. S. and A. M. Jayannavar, "Quantum transport in a two-dimensional modulated channel," *Physica B*, Vol. 228, No. 3–4, 353–362, 1996.
5. Knipp, P. A. and T. L. Reinecke, "Boundary-element method for the calculation of electronic states in semiconductor nanostructures," *Phys. Rev. B*, Vol. 54, No. 3, 1880–1891, 1996.
6. Lee, L. and Q. H. Liu, "An efficient 3D spectral-element method for Schrödinger equation in nanodevices simulation," *IEEE Trans. Computer-Aided Design of Integrated Circuits and Systems*, Vol. 24, No. 12, 1848–1858, 2005.
7. Smith, A. J. and A. Baghai-Wadji, "Ab-initio modelling of asymmetrical finite-barrier quantum wire structures," *2011 IEEE MTT-S International Microwave Symposium Digest (MTT)*, 1–4, Baltimore, USA, June 2011.
8. Pokatilov, E. P., V. A. Fonoberov, S. N. Balaban, and V. M. Fomin, "Electron states in rectangular quantum well wires (single wires, finite and infinite lattices)," *J. Phys.: Condens. Matter*, Vol. 12, No. 42, 9037–9052, 2000.
9. Gangopadhyay, S. and B. R. Nag, "Energy eigenvalues in square and rectangular quantum wires with finite Barrier potential," *Phys. Stat. Sol. (b)*, Vol. 195, No. 1, 123–128, 1996.
10. Shertzer, J. and L. R. Ram-Mohan, "Removal of accidental degeneracies in semiconductor quantum wires," *Phys. Rev. B*, Vol. 41, No. 14, 9994–9999, 1990.

On the Construction of Distributed Elementary Source Self-regularized Dyadic Green's Functions

H. A. Vagh and A. R. Baghai-Wadji
School of Electrical and Computer Engineering, RMIT University, Australia

Abstract— Elastodynamic simulation of complex structures built from rectangular/hexahedron building blocks are considered. For the purpose of the analysis, the structures are decomposed into the constituent fundamental rectangular- and hexahedron building blocks. The individual building blocks are excited time-harmonically by the members of a complete set of distributed elementary source, thus resulting in a number of the corresponding dyadic Green's functions. Thus derived Green's functions are by construction regularized; they are devoid of singularities, prompting the notion of distributed-source self-regularized Green's functions. The constructed Green's functions are then reduced onto the bounding surfaces of the building blocks, and stored for frequent future usage, substantially reducing the simulation time for the given composed structure. Key steps of the method have been discussed in applying the proposed technique to micro-acoustic device subsections involving isotropic and anisotropic materials.

1. INTRODUCTION

Simulation of the massloading effect continues to be of great interest and paramount significance in micro-acoustic devices community. The massloading effect is a major higher-order effect. It is a phenomenon which is understood as altering the acoustic impedance of propagating surface- or bulk waves by the mass- and the elasticity property of metallic electrodes. Thereby, waves propagating along the substrate surface, or within the substrate volume, interact electrically and acoustically with electrodes which are deposited in large numbers on the plane surface of a piezoelectric substrate, prior to getting scattered into various types of coupled surface- and bulk waves. Examples for the piezoelectric commonly substrates are $LiNbO_3$, $LiTaO_3$ or Quartz, which typically support several hundreds to a few thousands metallic electrodes made of, in majority of cases, aluminium or, in some cases, of much heavier gold. The massloading effect may decisively deteriorate the device performance or be exploited advantageously in signal forming, shaping and processing devices. The massloading effect is accounted for by solving a boundary value problem subject to fairly complex boundary conditions. A routine complexity analysis would reveal that in modern devices the number of unknowns in computations may easily exceed tens of millions. Traditional simulation packages based on the almighty Finite Element Method (FEM) and the elegant Boundary Element Method (BEM) or a hybridization of both, are quite general tools in terms of the geometry of electrodes, the substrate and their material constitutions [1–4]. These methods, however, lack a most desirable property; i.e., the flexibility in producing pre-calculated data, so that they can be stored in libraries for frequent future usage in device design cycles. Ordinarily, pre-calculating data is regarded to be particularly challenging as the mechanical stress distributions on the bounding surfaces of the metallic electrodes are not only dependent on various topological- and material parameters, but are also strongly frequency dependent. The ability of pre-calculating of such primary data and storing them for future use, is an important feature of this work.

2. ON THE NOTION OF SELF-REGULARIZED DYADIC GREEN'S FUNCTION TECHNIQUE

The proposed method of Self-regularized Dyadic Green's functions may conceptually be viewed as a sophisticated process. To ease the discussion, here purely mechanical problems are considered, assuming that the electrodes and all the other sub-structures are mechanically excited by sources which oscillate time-harmonically according to $\exp(-j\omega t)$ at a given frequency ω.

The method is based on the concept of divide and rule. To begin with, the geometry of the test structure is partitioned into adequate number of fundamental building blocks. Subsequently, for each constituent building block, the complete set of the Distributed-Elementary-Source (DES) Self-regularized (SR) Dyadic Green's Functions (DGFs), abbreviated as $\mathcal{GF}s$, are constructed. Thereby, the interaction between two acoustic partitions manifests itself through an energy exchange in such a way that the boundary- and interface conditions are satisfied. The resulting easy-to-use recipe is elaborated further, by developing the tools that are core to the proposed $\mathcal{GF}$s method. They are described after considering the involved Boundary Value Problems (BVPs).

2.1. BVP with Neumann Boundary Conditions

The equation of motion for an elastodynamic problem is given by:

$$\underline{\underline{\nabla}}^t \mathbf{T} = -\rho_I \omega^2 \mathbf{u}, \quad \text{in} \quad \Omega \tag{1}$$

In case of inhomogeneous Neumann boundary condition, the stress over test boundary reads:

$$\boldsymbol{\tau}_3|_{TestBoundary} = F \tag{2}$$

The outward unit vector normal to the test boundary has been assumed to be in the $z-$direction (subindex 3).

2.2. BVP with Interface Condition

Consider two partitions occupying the volumina, Ω_a and Ω_b, representing one electrode and the substrate hexahedron, respectively, having a common interface. Additionally, assume that the block "a" is subject to external forces at the "north" boundary. Thus the BVP characterizing the "ab"-composed structure is given by:

$$\underline{\underline{\nabla}}^t \mathbf{T}_a = -\rho \omega^2 \mathbf{u}_a, \quad \text{in} \quad \Omega_a \tag{3a}$$

and

$$\underline{\underline{\nabla}}^t \mathbf{T}_b = -\rho \omega^2 \mathbf{u}_b, \quad \text{in} \quad \Omega_b. \tag{3b}$$

The governing Eqs. (3) are subject to the boundary condition

$$\boldsymbol{\tau}_3^a|_{TestBoundary} = \mathbf{F}, \tag{4}$$

and the stress- and displacement conditions

$$\boldsymbol{\tau}_3^a|_{Interface} = \boldsymbol{\tau}_3^b|_{Interface} \tag{5a}$$

and

$$\mathbf{u}_a|_{interface} = \mathbf{u}_b|_{Interface}. \tag{5b}$$

At the interface between "a" and "b", equivalent forces shall be introduced to partition the blocks for independent analysis utilizing the precalculated and stored dyadic Green's functions, which characterize "a" and "b". In the present analysis, the boundary sections, other than the interface- and the test boundary, are assumed to be stress-free.

3. PROPOSED SOLUTION

3.1. Basic Tools

A standard Galerkin scheme is followed to solve the BVP given by Eqs. (1) and (2) for the test cuboid. The orthonormalized Legendre polynomials $b_l(x), b_m(y)$ and $b_n(z)$ over the interval $[-1, 1]$ are employed to form a set of 3D $B_j(x, y, z)$ basis functions: $B_j(x, y, z) = B_{l\odot m\odot n}(x, y, z) = b_l(x)b_m(y)b_n(z)$, with $l = 0, \dots, L$; $m = 0, \dots, M$; $n = 0, \dots, N$, and $j = 0, \dots, L \times M \times N$. Thereby, the ith component of the displacement vector $\mathbf{u}$ can approximately be expressed in terms of a linear superposition of the constructed basis functions $B_j(x, y, z)$:

$$u_i(x, y, z) \approx \sum_{j=0}^{L\times M\times N} u_j^{(i)} B_j(x, y, z), \tag{6}$$

where, $i = 1, 2, 3$. Similarly, the force function $F(x, y)$, can be approximated by

$$F(x, y) \approx \sum_{k=0}^{L\times M} \alpha_k B_k(x, y). \tag{7}$$

A standard Galerkin scheme results in the system of coupled algebraic equations for determination of expansion coefficients of the displacements, and thus the solution of the underlying BVP.

The implementation of the Galerkin scheme is straightforward. However, for varying source functions one needs to solve the system of equation anew, a process, which can be exhaustive computationally. This bottleneck can be remedied by utilizing the pre-calculated and stored Green's Functions. to this end successive application of the forces, and solving the resulting system of equations, as described above, results in the associated displacement components, and thus to the required Green's functions, which will be collectively denoted by $\mathcal{GF}$s. The computed information defining $\mathcal{GF}$s is then stored for frequent future usage. Since any displacement distribution in response to an arbitrary excitation function can be modeled by the pre-computed Green's functions, the displacement functions can be represented as:

$$u_i(x,y,z) \approx \sum_{j=0}^{L\times M\times N} \alpha_j^{(i)} \mathcal{GF}_j^{(i)}(x,y,z), \quad i=1,2,3 \tag{8}$$

However, storing entire-domain solutions in their original form, as they stand, requires excessive amounts of storage space, rendering the retrieval of data an exceedingly slow process. Instead the calculated $\mathcal{GF}$s and their derivatives are evaluated (collapsed) on the boundary, collectively leading tot he content of problem's LIBRARY. The information in the LIBRARY enables both 2D and 3D device modeling and simulation. In applications only those encoded $\mathcal{GF}$s are retrieved and copied into the WORKING MEMORY which are unconditionally necessary for modeling a given building blocks.

3.2. Sufficiency Principle

Assume that the generated LIBRARY contains all the tabulated $\mathcal{GF}$s required to solve a given time-harmonic BVP associated with a given building block, with prescribed material properties and prescribed accuracy. Upon changing the applied force vector, the stored information about the Green's functions fully suffices to solve the new BVP with agreed accuracy.

3.3. The Principle of Exhaustion

In Subsection 3.1 it was pointed out that the $\mathcal{GF}$s have been collapsed onto the boundary prior to being stored in the LIBRARY. Despite this significant data compression, it can be shown that the compressed data exhausts the entire information about any physically realizable boundary conditions [5]. The latter property justifies the notion of Exhaustion principle.

3.4. Application of the Sufficiency- and Exhaustion Principles

In order to elucidate the interface conditions in the test structure, the solution of a comparatively easier problem, i.e., the Dirichlet boundary condition is explained first. As it turns out, solving interface problem is conceptually a minor modification of solving the Dirichlet boundary condition. Consider the equation of motion

$$\underline{\underline{\nabla}}^t \mathbf{T} = -\rho\omega^2 \mathbf{u}, \quad \text{in} \quad \Omega, \tag{9}$$

and the inhomogeneous Dirichlet boundary condition, with $\mathbf{U}$ being a known function, defined on the test boundary Γ:

$$\mathbf{u}|_{TestBoundary} = \mathbf{U} \tag{10}$$

It should be noted that while the displacement on Γ is known upon assumption, the stress on Γ is *a priori* unknown. Assume that each of the three component of the unknown stress distribution on the boundary can be synthesized using $\mathcal{N}_0$ appropriately chosen orthonormal basis functions, weighted by $\mathcal{N}_0$ expansion coefficients $c_0, c_1, \ldots, c_N$. Excite the (Ω,Γ)-medium by the force (basis) function $b_n(s)$, acting on Γ. The Green's Function evaluated on the boundary Γ, i.e., $G_n(s)$, has been, however, pre-calculated and thus can be copied from the LIBRARY into the WORKING MEMORY. By saying that the Green's functions $G_n(s) = \sum_{i=0}^{N} g_{ni} b_i(s)$ are stored in the LIBRARY, it is meant that merely the coefficients $g_{ni}, i \in \mathcal{N}_0$ have been stored in the LIBRARY. A further realization is that $G_n(s)$ is, upon construction, the displacement functions $u_n(s)$, evaluated on the boundary. Obviously, in virtue of linearity, exciting the medium by $c_n b_n(s)$, the corresponding displacement on Γ is $c_n G_n(s)$. Retrieving $G_n(s)$ for $n = 0, \ldots, N$ from the LIBRARY, multiplying by $c_0, \ldots, c_N$, and adding, we obtain the displacement on Γ:

$$u(s)|_\Gamma = \sum_{n=0}^{N} c_n G_n(s) \tag{11}$$

Thus the computational task is reduced to the determination of the unknowns c_n, with $n \in \mathcal{N}_0$. In view of the fact that the displacement on Γ is a given function; i.e., $U(s)$, set $\sum_{n=0}^{N} c_n G_n(s) = U(s)$. Taking into account the relationship $G_n(s) = \sum_{i=0}^{N} g_{ni} b_i(s)$ leads to:

$$\sum_{n=0}^{N} c_n \sum_{i=0}^{N} g_{ni} b_i(s) = U(s) \tag{12}$$

On the other hand since $U(s)$ is known, $U(s) = \sum_{k=0}^{N} \alpha_k b_k(s)$, where α_k are known. Substituting the latter equation into Eq. (12); multiplying both the sides by $b_j(s)$ and integrating over Γ and using orthonormality condition for the basis functions results in

$$\sum_{n=0}^{N} c_n \sum_{i=0}^{N} g_{ni} \delta_{ij} = \alpha_j, \tag{13}$$

or, equivalently in:

$$\sum_{n=0}^{N} c_n g_{nj} = \alpha_j \tag{14}$$

Proceeding similarly with the remaining basis functions, $\mathcal{N}_0$ equations are obtained for the determination of $\mathcal{N}_0$ unknowns c_n. Thus, with the available coefficient matrix $[g_{nj}]$ and, consequently, its inverse $[g_{nj}]^{-1}$ the expansion coefficients c_n can be determined:

$$[c_n] = [g_{nj}]^{-1}[\alpha_j] \tag{15}$$

Remark: In order to simplify the foregoing discussion, two tacital assumptions were made: (1) The force- and displacement functions were assumed to be scalar. (2) The support of the basis functions were taken to comprise the entire boundary Γ. These two constrains can easily be relaxed, refer to [5] for details.

In summary, to obtain the solution for the BVPs with interface conditions proceed the following easy-to-use recipe: Copy the Distributed-Elementary-Source Self-regularized Dyadic Green's Functions ($\mathcal{GF}$s) from the LIBRARY into the WORKING MEMORY individually for each building blocks. Utilize the $\mathcal{GF}$s employing the Sufficiency- and Exhaustion Principles, to match the solutions at the interfaces.

4. RESULTS

Figures 1 and 2 show the results for the elastodynamic simulation of given 2- and 3D structures. In both cases the structures were partitioned into fundamental building blocks. For example,

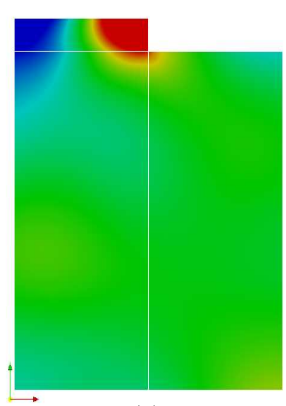

(a)

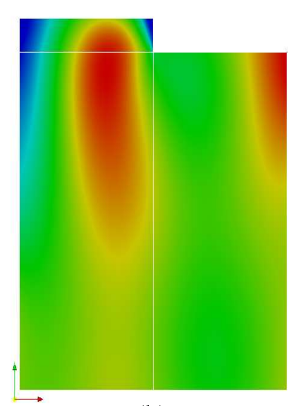

(b)

Figure 1: (a) Displacements $u_1(x, z)$ and (b) $u_3(x, z)$ in response to the constant force ($0.7\,\mathrm{N/m^2}$) acting at 'north' boundary of the electrode (upper-left rectangular block in each subfigure). The operating frequency is $\omega = 1.1\,\mathrm{GHz}$. The 2D substrate is assumed to be anisotropic.

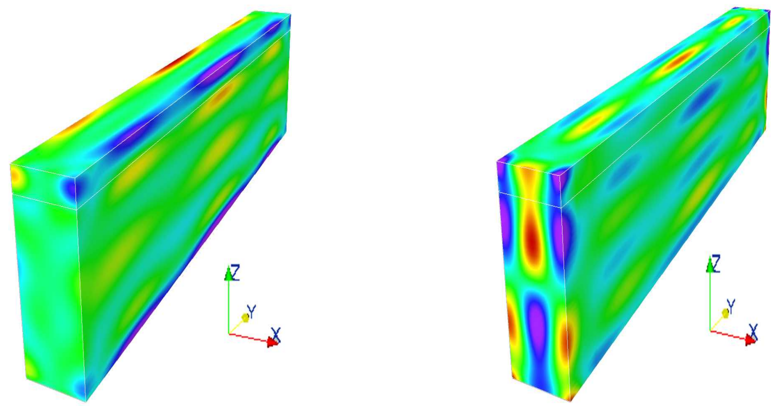

(a) (b)

Figure 2: (a) Displacements $u_1(x, y, z)$ and (b) $u_3(x, y, z)$ in response to the constant force ($0.5\,\mathrm{N/m^2}$) acting at the 'north' boundary of the electrode. The operating frequency is $\omega = 2.1\,\mathrm{GHz}$.

considering the entire metallic-electrode as one building block, the respective $\mathcal{GF}$s were derived and stored. These stored information was then retrieved and utilized in order to simulate the entire composed structure. In the case of 2D simulation the number of unknowns were reduced to only 60 with 10 basis functions in each direction. This is basically where the strength of the proposed method resides.

5. CONCLUSION

The Distributed-Elementary-Source Self-regularized Dyadic Green's function method possesses distinct advantages over the traditional methods such as FEM and BEM. Each type of the boundary condition (Dirichlet, Neumann and Interface condition) could be easily addressed by merely loading an insignificant amount of data into the Working Memory. The postprocessing step is simplified and merely involves the construction of the system matrix for the determination of the expansion coefficients of the field variables on the interface. Using Sufficiency- and Exhaustion principles it was demonstrated how anisotropic composed structures can be analyzed.

ACKNOWLEDGMENT

This project has been carried out under an Australian Research Counsel (ARC) Linkage Grant: LP0775463. Generous support granted by EPCOS AG (Munich) and EPCOS Pty (Singapore) are gratefully appreciated.

REFERENCES

1. Benjeddou, A., "Advances in piezoelectric finite element modeling of adaptive structural elements: A survey," *Computers and Structures*, Vol. 76, 347–363, 2000.
2. Baghai-Wadji, A. R., "Theory and applications of Green's functions," *International Journal of High Speed Electronics and Systems*, Vol. 10, No. 4, 949–1015, 2000.
3. Lerch, R., "Simulation of piezoelectric devices by two- and three-dimentional finite element," *IEEE Transactions on Ultrasonics, Ferroelectrics, and Frequency Control*, Vol. 37, No. 2, 233–247, 1990.
4. Ventura, P. and W. Steichen, "FEM/BEM analysis of a generalized periodic array," *IEEE Transactions on Ultrasonics, Ferroelectrics, and Frequency Control*, Vol. 54, No. 10, 2052, 2007.
5. Vagh, H. A. and A. R. Baghai-Wadji, "Distributed-elementary-source self-regularized dyadic Green's functions for modeling the massloading effect in acoustic devices: 2D isotropic problems," *Engineering Analysis with Boundary Elements*, Vol. 36, No. 5, 665–674, 2012.

Numerical Experiments for Radial Dynamics and Opacity Effect in Argon Plasma Focus

Z. Ali[1,2], **J. Ali**[1], **S. H. Saw**[3,5], **and S. Lee**[4,5]

[1]Institute of Advanced Photonics Science, Nanotechnology Research Alliance
Universiti Teknologi Malaysia (UTM), Johor Bahru 81310, Malaysia
[2]Karachi Institute of Power Engineering, P. O. Box 3183, Karachi, Pakistan
[3]INTI University College, Nilai 71800, Malaysia
[4]Nanyang Technological University, National Institute of Education, Singapore
[5]Institute for Plasma Focus Studies, 32 Oakpark Drive, Chadstone VIC3148, Australia

Abstract— A z-pinch in its simplest form is a column of plasma in which current (J) is driven in the axial direction (z) by an electric power source producing an azimuthal (θ) direction magnetic field (B) that tends to confine plasma by ($J \times B$) force. One application of this configuration is Plasma Focus. Dense plasma focus (DPF) is essentially a pulsed electric gas discharge between coaxially arranged electrodes. DPF devices belong to the family of dynamic Z-pinches which are self-constricted plasma configurations. The Lee model code was developed to simulate the plasma dynamics in a DPF. The model incorporates the energy and mass balances equivalent, at least in the gross sense, with radiation-coupled dynamics to all the processes which are not even specifically modeled. It is a well known fact that radiation loss is an inevitable phenomenon in the final stage of pinch compression. The most obvious one is that of a focus or a Z-pinch. Plasma self-absorption is an important factor during the pinch compression. In this paper the effect of self absorption of line radiation was investigated in argon plasma by a series of numerical experiment considering both aspects, i.e., by including and excluding the self absorption term in Lee code. The results were compared for various parameters, i.e., Radial trajectories, pinch duration, pinch current, line radiation yield while changing pressure. The effect of radiation self absorption was observed in last few fractions of seconds (200–300 ns). Considering self absorption, the compression shows a value of radius of about 0.2 mm while a collapse (radiative collapse) was observed otherwise. The results illustrated that the radiation cooling becomes significant when the plasma is dense and turn to be opaque for radiation. Hence in real case we do not see a radiative collapse in argon PF as self absorption plays in real experiments. The results of pinch duration and pinch current also indicated that self absorption is essentially enhancing the pinch in terms of stability.

1. INTRODUCTION

A z-pinch in its simplest form is a column of plasma in which current (J) is driven in the axial direction (z) by a pulsed electric power source producing an azimuthal (θ) direction magnetic field (B) that tends to confine plasma by ($J \times B$) force. Dense plasma focus (DPF) is essentially a pulsed electric gas discharge between coaxially arranged electrodes. DPF devices belong to the family of dynamic Z-pinches which are self-constricted plasma configurations. Radiation collapse is known as a phenomenon of a sudden decrease in plasma temperature caused by an increase of radiation loss. It is a well known fact that radiation loss is an inevitable phenomenon in the final stage of pinch compression. The most obvious one is that of a focus or a Z-pinch.

Lee has proposed that current-stepping technique can significantly reduce the plasma pinch ratio. Therefore, this technique can enhance the pinch compression to a significant level which can play important role while designing high intensity soft x-ray sources using argon or xenon plasma [1]. Saw has developed current-stepped pinches [2] to confirm the predictions of the numerical experiments. Jalil et al has developed the model to explore the effects of radiation loss and elongation on the compression dynamics in a small size plasma focus [3]. Plasma focus machines have been studied as intense source of various radiations like soft x-rays (SXRs), electrons, neutrons etc. with potential applications [4, 5]. Whilst many recent experiments have concentrated efforts on low energy devices [4, 5] with a view of operating these as repetitively pulsed sources, other experiments have looked at x-ray pulses from larger plasma focus devices [6] extending to the megajoule regime. Numerical experiments simulating x-ray pulses from plasma focus devices are gaining more interest in the public domain. A comparison was made for the case of the NX2 machine [4], showing good agreement between computed and measured SXR yield (Ysxr) as a function of pressure [7, 8]. This gives confidence that the Lee model code gives realistic results in the computation of Ysxr.

Here, we report on a series of numerical experiments to explain the dynamics of self absorption during the slow compression phase occurring in the last fractions of seconds of pinch. The X-ray radiation properties of plasma are dependent on the plasma temperature, ionization states and density. Recently Ar has been considered for micro-machining due to the harder characteristic line radiation [9].

2. SELF ABSORPTION AND RADIATIVE COLLAPSE IN LEE MODEL

The Lee Model code incorporates radiation dynamics [10] using the following equation:

$$\frac{dr_p}{dt} = \frac{-\frac{r_p}{\gamma I}\frac{dI}{dt} - \frac{1}{\gamma+1}\frac{\gamma_p}{z_f}\frac{dz_f}{dt} + \frac{4\pi(\gamma-1)}{\mu\gamma z_f}\frac{r_p}{f_c^2 I^2}}{\frac{\gamma-1}{\gamma}} \tag{1}$$

where r_p is piston radius γ is specific heat z_f focus length while f_c is current factor and I is discharge current.

The volumetric plasma self-absorption correction factor A is obtained in the following manner [10–12]:

$$A_1 = (1 + 10^{-14} n_i Z)\Big/ T^{35} \tag{2}$$

$$A_2 = 1/AB_1 \tag{3}$$

$$A = A_2^{(1+M)} \tag{4}$$

where M is photonic excitation number given by

$$M = 1.66 \times 10^{-15} r_p Z_n^{0.5} n_i \Big/ (ZT^{1.5}) \tag{5}$$

Transition from volumetric to surface emission occurs when the absorption correction factor goes from 1 (no absorption) down to $1/e$ ($e = 2.718$) when the emission becomes surface-like given by the expression:

$$\frac{dQ}{dt} = -\text{const} \times Z^{0.5} Z_n^{3.5} \, (r_p) \; z_f T^4 \tag{6}$$

where the constant const is taken as 4.62×10^{-16} to conform with numerical experimental observations that this value enables the smoothest transition, in general, in terms of power values from volumetric to surface emission. Where necessary another fine adjustment is made at the transition point adjusting the constant so that the surface emission power becomes the same value as the absorption corrected volumetric emission power at the transition point. Beyond the transition point (with A less than $1/e$) radiation emission power is taken to be the surface emission power [10, 11].

3. NUMERICAL EXPERIMENTS WITH ARGON FILLED NX2 PLASMA FOCUS

NX2 Plasma Focus was configured with Argon as filling gas at voltage of 11 kV and the tube and model parameters used for configuration are:

Table 1: Configuration Parameters for PF.

Electrical Bank Parameters	**Lo**	**Co**	**ro**	
	20 nH	28 µF	2.3 mΩ	
Geometrical Tube Parameters	**b**	**a**	**zo**	
	4.1 cm	1.9 cm	5 cm	
Model Parameters	**massf**	**currf**	**massfr**	**currfr**
	0.0635	0.	0.16	0.

A series of Numerical experiments had been performed after configuring the machine for both the cases, i.e., including the self absorption term and without accounting for it into the code. The radial trajectories were plotted against time at various pressures ranging from 0.1–2.0 Torr with a step of 0.1 Torr. Finally the results were compared for both the cases as shown in figure.

4. RESULTS & DISCUSSION

4.1. Radial Dynamics

Starting from Figs. 1 & 2 showing the radial position of piston and shock as well as focus length at 0.5 torr the radial shock of about 18 mm is driven to the axis by magnetic piston and hits after 120 ns. After hitting the axis of anode, a reflected shock (RS) moves out and hits the incoming magnetic piston after about 20 ns. At this point the plasma column initiates to be compressed and radiation emit out from the pinch making it cool. But to notice the effect of radiation cooling there should be equilibrium between energy gain by Joule Heating and energy loss due to Bremstrahlung and Line radiation emission. The situation is same for both cases when the numerical experiment was done with and without including the term of self absorption.

Figures 3 & 4 at 1.0 torr is radiative collapse of the pinch as the radial shock of about 18 mm is driven to the axis by magnetic piston and hits after 155 ns at this pressure. After hitting the axis, the reflected shock (RS) hits the incoming magnetic piston after about 25 ns. Here the pinch shows clear signs of radiative collapse; and we can see the difference that without including self absorption the pinch collapses earlier than the case when Self Absorption is considered in the calculation. When self absorption was not included the radial shock collapse in shorter time in only a few ns to the radius of 0.1 mm set as cut-off in the model as the pressure increased, while the pinch duration and focus length has increased when radiation absorbed for instance after hitting the shock pinch duration is observed as 24 ns, 35 ns and 41 ns for pressures 1.0, 1.5 and 2.0 Torr respectively. In this case the pinch doesn't collapse but attains a minimum radius (See Figs. 5, 6, 7 & 8). It suggests that the pinch radius collapses less when self absorption is taken into account.

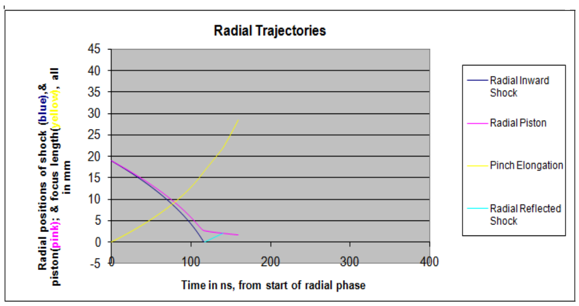

Figure 1: At 0.5 torr without self absorption.

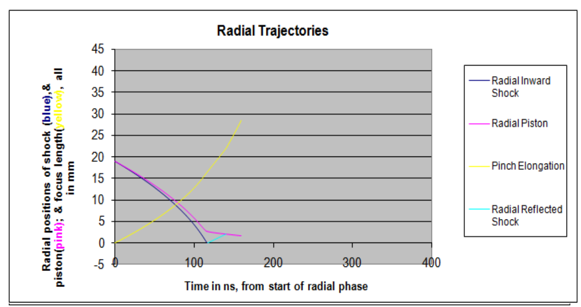

Figure 2: At 0.5 torr with self absorption.

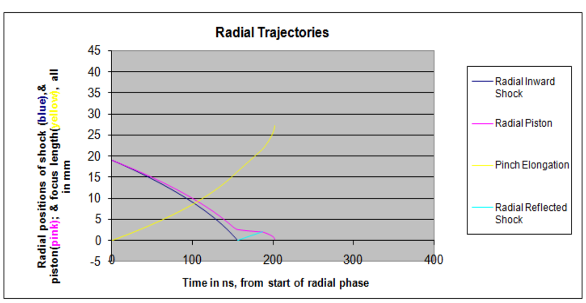

Figure 3: At 1.0 torr without self absorption.

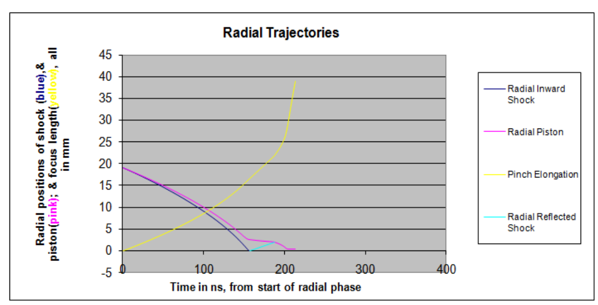

Figure 4: At 1.0 torr with self absorption.

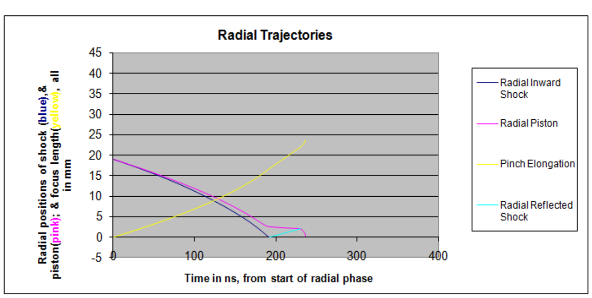

Figure 5: At 1.5 torr without self absorption.

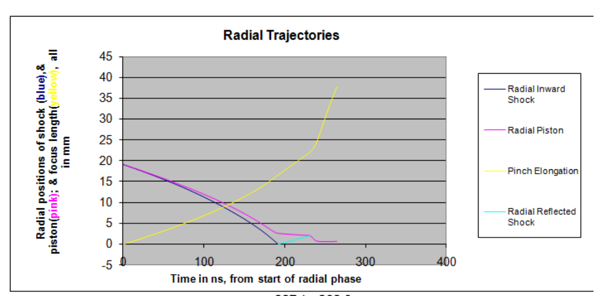

Figure 6: At 1.5 torr with self absorption.

This is because the self-absorption reduces the amount of radiation loss from the plasma.

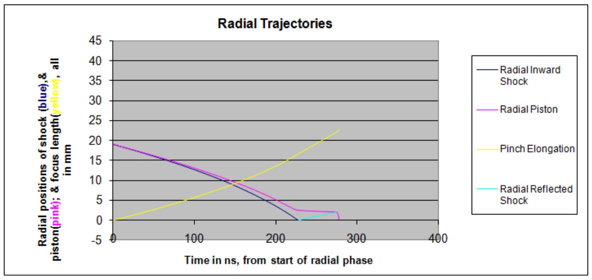

Figure 7: At 2.0 torr without self absorption.

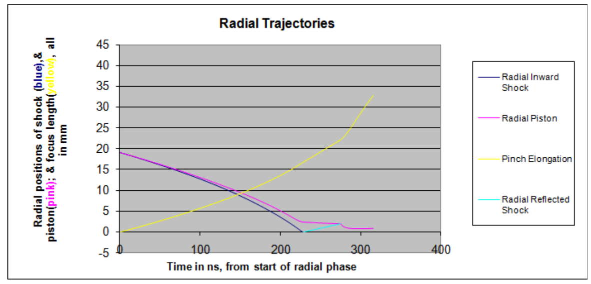

Figure 8: At 2.0 torr without self absorption.

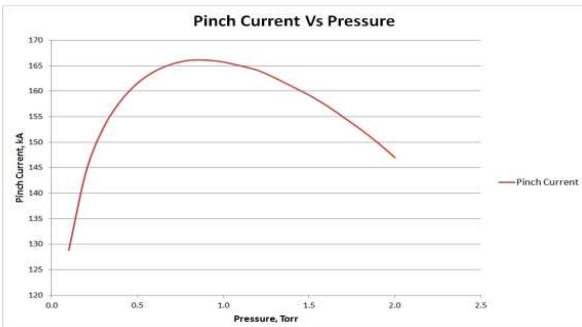

Figure 9: Pinch current vs pressure.

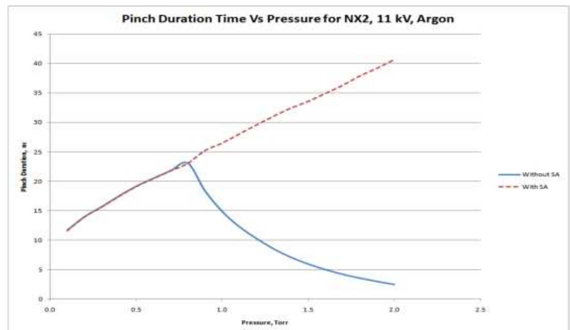

Figure 10: Pinch duration vs pressure.

4.2. Pinch Current & Pinch Duration

It is also notable in Fig. 9 that as the pressure was increased pinch current first increases upto 166 kA and then after 1.0 Torr it reduces gradually until 2.0 Torr where it is at its minimum value of 147 kA. At that point pinch radius collapses to 0 in case of no self absorption while it collapses and maintains to 0.1 mm if self absorption is considered in play as an evidence that radiation self absorption retards pinch collapse and gives a denser and hot pinch with high yield of radiation

Observing Fig. 10 it is apparent that pinch duration is decreasing as we increased the pressure in case of no absorption and it continues increasing while there is absorption. This indicates that due to higher pressure the density of plasma column increases which in turn causes the radiation to be absorbed due to opacity of the column and hence delaying the pinch collapse.

5. CONCLUSIONS

The self absorption effect of line radiation was determined in argon plasma by changing the pressure of gas in steps. After comparing the results of Numerical Experiment considering both aspects, i.e., by including and excluding the self absorption term in Lee code, the effect of radiation self absorption was observed in the slow compression phase. Considering self absorption, the compression shows a value of radius of about 0.2 mm while without including this term of self absorption a collapse (radiative collapse) was observed due to radiative cooling. This comparison indicates that the radiation cooling becomes significant when the plasma is dense enough to become opaque for radiation. The same effect was corroborated further in the pinch duration in both the cases. Hence in argon numerical experiments indicate that radiative collapse does occur (Figs. 4, 6, 8) but not as severely as the case when we neglect self absorption (Figs. 3, 5, 7) The consideration of self absorption is playing a significant role in this case leading to realistic results. Otherwise the radiative collapse may become overestimated by excluding the power absorbing in the plasma due to reabsorbed radiation.

ACKNOWLEDGMENT

We are deeply indebted to Dr. Lee Sing for his assistance in providing the understanding of code and Universiti Teknologi Malaysia for its generous support.

REFERENCES

1. Lee, S., "A current-stepping technique to enhance pinch compression," *Journal of Physics D: App. Phys.*, Vol. 17, No. 4, 733, 1984.
2. Saw, S. H., S. Lee, and C. S. Wong, "A current-stepping technique to enhance pinch compression — An experimental study," *AIP Conf. Proc.*, Vol. 195, No. 1, 500–506, 1989.
3. Ali, J., *Development and Studies of a Small Plasma Focus*, Universiti Teknologi Malaysia, Skudai, 1990.
4. Lee, S., et al., "High rep rate high performance plasma focus as a powerful radiation source," *IEEE Trans. on Plasma Sci.*, Vol. 4, No. 26, 1119–1126, 1998.
5. Bogolyubov, E. P., et al., "A powerful soft X-ray source for X-ray lithography based on plasma focusing," *Physica Scripta*, Vol. 57, No. 4, 488, 1998.
6. Filippov, N. V., et al., "Filippov type plasma focus as intense source of hard X-rays $E_x \sim$ 50 keV) plasma science," *IEEE Transactions*, Vol. 24, No. 4, 1215–1223, 1996.
7. Lee, S., et al., "Soft x-ray yield from NX2 plasma focus," *Journal of Applied Physics*, Vol. 106, No. 2, 2009.
8. Haines, M. G., "The Joule heating of a stable pinched plasma," *Proceedings of the Physical Society*, Vol. 76, No. 2, 250, 1960.
9. Gribkov, V. A., et al., "Operation of NX2 dense plasma focus device with argon filling as a possible radiation source for micro-machining," *IEEE Trans. on Plas. Sci.*, Vol. 30, No. 3, 1331–1338, 2002.
10. *Plasma Focus*, 2010 Updated: 19 October 2010, [cited 2011 4 Oct 2011]; Available from: http://www.intimal.edu.my/school/fas/UFLF/
11. Khattak, N. A. D., *Plasmafocus.net*, 2007, [cited 2009 7 October]; Available from: http://www.plasmafocus.net/IPFS/modelpackage/File3Appendix.pdf.
12. Robson, A., "Lower hybrid ddrift instability and radiative collapse of a dense z pinch," *Phys. Fluids B*, Vol. 3, No. 6, 1461, 1991.

Microwave Characterization of Expanded Graphite/Phenolic Resin Composite for Strategic Applications

Jyoti Prasad Gogoi and Nidhi Saxena Bhattacharyya
Microwave Engineering Laboratory, Department of Physics
Tezpur University, Tezpur-784028, India

Abstract— Light weight expanded graphite (EG) flakes are synthesized from natural graphite flakes of size $\sim 2\,\mu\text{m}$ employing chemical oxidation and thermal treatment method. Scanning electron microscope investigation shows that EG flakes consist of numerous graphite sheets of nanometers thickness and micrometer in diameter. EG flakes are mechanically mixed with novolac phenolic resin (NPR) in different weight ratios (30 wt%, 40 wt% & 50 wt%) and compressed with thermal treatment to develop expanded graphite/novolac phenolic resin (EG/NPR) composites. Nicolson–Ross method is used to determined the complex permittivity ($\varepsilon_r = \varepsilon_r' - j\varepsilon_r''$) of the developed composites using Agilent E8362C vector network analyzer. A high value of dielectric loss tangent ($\varepsilon_r''/\varepsilon_r'$) > 1 has been observed for the three compositions in the entire X band. Shielding effectiveness of developed composites of thickness 3.7 mm measured in the frequency range of 8 to 12 GHz shows a maximum value of -48 dB for 50 wt% EG/NPR composites. The material production is simple and cost effective, and the absorbing material is light weight and thus, is beneficial for installation in some strategic components.

1. INTRODUCTION

Detection avoidance through camouflage or signature reduction is an important aspect of the modern warfare. The detectability of a target is measured in terms of the radar cross section (RCS). The RCS is a property of the targets size, shape and the material from which it is fabricated and is ratio of the incident to reflected power. Radar absorbing materials (RAM) have been widely used to prevent or minimize electromagnetic reflections from large structures such as aircraft, ships and tanks and to cover the walls of anechoic chambers [1, 2]. RAMs are fabricated in the form of sheets that consist of insulating polymer with magnetic or dielectric loss materials such as ferrite, permalloy, carbon black, and short carbon fiber [3, 4]. Electromagnetic wave absorption characteristic of material depends on its dielectric properties (complex permittivity, $\varepsilon_r = \varepsilon_r' - j\varepsilon_r''$), magnetic properties (complex permeability, $\mu_r = \mu_r' - j\mu_r''$), thickness and operating frequency range. Polymer nanocomposites with carbon nanotubes (CNTs) have received widest attention in RAM or EMI shielding application due to their good mechanical, electrical, and thermal properties [5]. However, mass scale production and applications cost effectiveness and processing ease are issues which has to be considered. Another promising composite reinforcement is expanded graphite flakes, with the characteristics of very low density, good electrical, thermal and mechanical properties [6]. Expanded graphite/novolac phenolic resin (EG/NPR) composites have been reported to have good electrical conductivity, thermal stability and mechanical strength [7]. In the present investigation, microwave characterization and shielding effectiveness measurement of EG/NPR composites have been conducted with different weight ratios over the frequency range 8 to 12 GHz with a view to develop light weight, cost effective alternate microwave absorbing material.

2. EXPERIMENTAL

2.1. Preparation of Expanded Graphite

Chemical oxidation and thermal treatment method are employed to synthesize expanded graphite (EG) flakes from natural graphite (NG) flakes of size $\sim 2\,\mu\text{m}$ [7]. NG flakes are were dried at 75°C in vacuum oven for 8 h to remove the moisture content and then mixed with saturated acid consisting of sulfuric acid and concentrated nitric acid in a volume ratio $3:1$ for 12 hours to form graphite intercalated compound (GIC). These chemically treated flakes are then thoroughly rinsed with water until the pH level of the solution reach 7 (neutral) and dried at 60°C in vacuum oven for 5 hours. GIC was suddenly exposed to high temperature in a muffle furnace maintained at temperature 800–900°C to form EG.

2.2. Preparation of Composites

The polymer matrix binder used for composite preparation is novolac phenolic resin (NPR) in powder form due to their good heat resistance, electrical insulation, dimensional stability, flame and chemical resistance as well as cost effective [8]. EG/NPR composites of size 10.38 mm × 22.94 mm × 3.7 mm were prepared by compression molding technique with varying the ratio of resin and expanded graphite for X band EMI shielding characterization. The EG and resin powder was mix uniformly with the help of mixture and grinder to obtain uniform EG/resin compound. The mixture was poured in a cavity of three-piece die-mould which was placed on the hot plate of a hydraulic press. At temperature between 95–100°C, pressure was applied slowly on the die mould and then kept for isothermal heating at 150°C for 2 hours.

2.3. Analysis and Characterization Techniques

Surface morphology of the materials is studied by Scanning electron microscope (SEM), model (JEOL JSM-6390LV). Microwave characterization of the composites is performed using Agilent 8722ES vector network over the X-band.

2.4. Complex Permittivty Measurement

Complex permittivity ($\varepsilon_r = \varepsilon_r' - j\varepsilon_r''$), of the polymer composites are determined using Nicolson-Ross method using Agilent 8722ES vector network analyzer [9]. The specimens are machined into rectangular shape of thickness 3.7 mm and inserted into rectangular flange of thickness 5.4 mm for X band calibration using Agilent X11644A calibration kit. The measurements are carried out to measure the electromagnetic shielding effectiveness in terms of S_{11} (reflected/incident) and S_{21} (transmitted/incident) values. The reflection coefficient Γ is given as

$$\Gamma = \frac{Z - Z_0}{Z + Z_0} = \frac{\sqrt{\frac{\mu_r}{\varepsilon_r}} - 1}{\sqrt{\frac{\mu_r}{\varepsilon_r}} + 1} \tag{1}$$

the transmission coefficient for finite distance (d) is given as

$$\begin{aligned}
T &= \exp\left[-j\left(\frac{\omega}{c}\right)\sqrt{\mu_r \epsilon_r} d\right] && (2)\\
S_{21}(\omega) &= \frac{(1-\Gamma^2)T}{1-\Gamma^2 T^2} && (3)\\
S_{11}(\omega) &= \frac{(1-T^2)\Gamma}{1-\Gamma^2 T^2} && (4)\\
V_1 &= S_{21} + S_{11} && (5)\\
V_2 &= S_{21} - S_{11} && (6)\\
X &= \frac{1 - V_1 V_2}{V_1 - V_2} && (7)\\
\Gamma &= X \pm \sqrt{X^2 - 1} && (8)\\
|\Gamma| &\leq 1 && (9)
\end{aligned}$$

Expression (9) is the criteria of the computation. Also, transmission coefficient (T) can be written as [14]

$$\begin{aligned}
T &= \frac{V_1 - \Gamma}{1 - V_1 \Gamma} && (10)\\
\frac{\mu_r}{\varepsilon_r} &= \left(\frac{1+\Gamma}{1-\Gamma}\right)^2 = c_1 && (11)\\
\mu_r \epsilon_r &= -\left[\frac{c}{\omega d}\ln\left(\frac{1}{T}\right)\right]^2 = c_2 && (12)\\
\epsilon_r &= \sqrt{\frac{c_2}{c_1}} && (13)
\end{aligned}$$

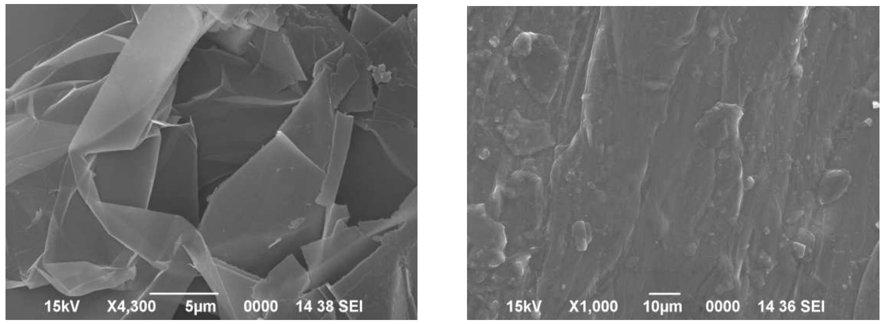

Figure 1: SEM micrograph of (a) EG and (b) fractured EG/NPR composite.

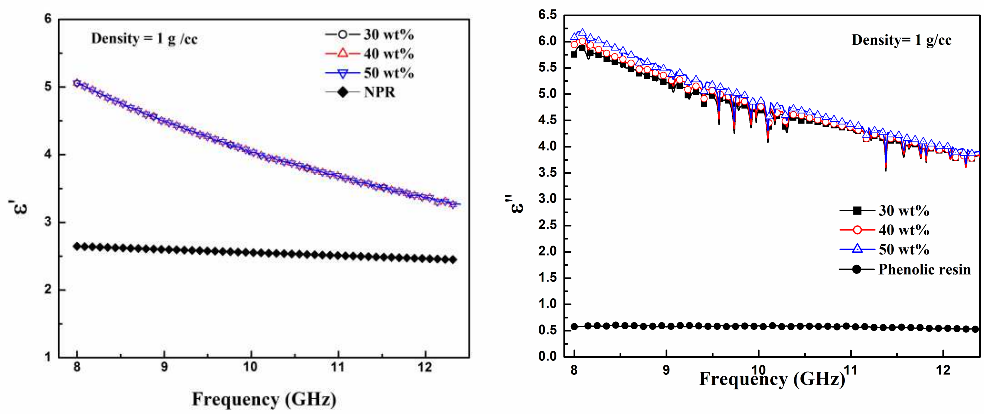

(a) (b)

Figure 2: Complex permittivity of EG/NPR composite (a) real part & (b) imaginary part.

3. RESULTS AND DISCUSSION

3.1. SEM Analysis

SEM micrograph (Figure 1(a)) shows that EG flakes consist of numerous graphite sheets of nanometers thickness and micrometer in diameter. This structure endows EG with high surface area. Figure 1(b) shows the uniform distribution of EG inside the bulk of novolac phenolic resin composite.

3.2. Complex Permittivty Measurement

Figures 2(a) and 2(b) show the frequency dependence of the real part (ε_r') and imaginary part (ε_r'') of relative complex permittivity of EG/NPR composites in the frequency range 8 to 12 GHz. Composite with 50 wt% of EG loading shows decline in the values of ε_r' and ε_r'' from 5 to 3.5 and from 6.2 to 3.9, respectively, as the frequency is swept from 8 to 12 GHz. The other two composites of 30 wt% & 40 wt% EG loading also show similar trends. ε_r' values do not show much variation, however, a noticeable decrease in ε_r'' values with decrease in EG content are observed. The EG/NPR composites contains NPR as insulating section and EG as conducting section, with EG encapsulated within the polymer. The insulating sections acts like a high resistive path for flow of free electrons, however some electrons may still conduct by tunneling effect [10]. Within the composite system, there could be two paths of electromagnetic propagation as shown in Figure 5(c). In one path line of electric flux can pass from EG flakes-polymer-EG flakes and in the other path through direct contact between the EG flakes. This is in analogy to reference [11] where M. Matsumoto and Y. Miyata have discussed a model for metal-polymer composite, with filler conductivity of $\sim 10^4$ S/cm. The second path of conduction, however, will be more effective for higher filler concentration which increases the interaction between the fillers. As EG conductivity is quite high as compared to polymer, increasing EG content increases the effective conductivity which in turn increases the loss factor ε_r''. In the same reference, the modeling done for higher concentration metal particles embedded in polymer matrix showed a decreasing trend for real and imaginary part of permittivity with frequency, as is observed in EG/NPR composite system. Figure 3 shows the dielectric loss tangent of the composites. A high value $(\varepsilon_r''/\varepsilon_r') > 1$ has been observed for the three compositions

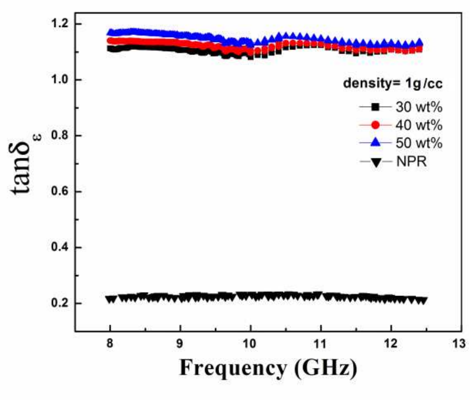

Figure 3: Dielectric loss tangent of EG/NPR composite.

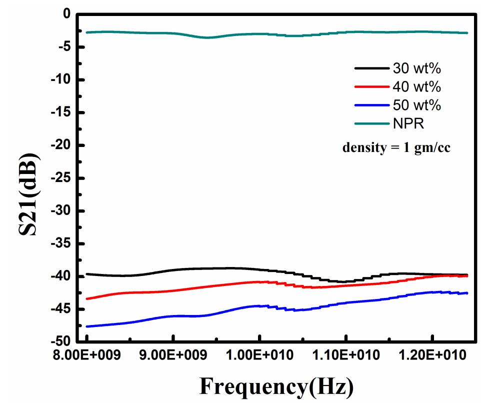

Figure 4: S_{21} parameters of EG/NPR composites.

in the entire X band. The composition with 50 wt%, 40 wt% and 30 wt% EG show dielectric loss of 1.21, 1.19 and 1.17 respectively, over the entire X band. Dielectric loss greater than unity suggest that the material has high dissipation factor rather than storage capacity.

3.3. Insertion Loss Measurement

The insertion loss (IL) of the developed composite of thickness 3.7 mm are measured using Agilent X11644A calibration kit and Agilent 8722ES vector network analyzer in the frequency range 8 to 12 GHz using the concept of Shielding effectiveness (SE). Mathematically

$$\mathrm{SE}\ (\mathrm{dB}) = 10\log(P_i/P_t)$$

where P_i, is the incident power density of incident electromagnetic wave and P_t, the transmitted power density of the same electromagnetic wave after passing through the shielding material. In the present work, measured (S_{21}) values are reported as *IL* values. Pure NPR shows small *IL* values of about -2 dB over the entire X band, but with incorporation of EG in the composites, *IL* values enhances from -40 dB to -48 dB for 30 wt% to 50 wt% of EG/NPR composites respectively, as shown in Figure 4. This increase of *IL* values is due to increase of dielectric loss tangent with increasing EG percentages. Also, the *IL* values of the composites are almost constant over the entire X band with slightly reducing towards the upper frequency range. Thus, the developed composites have potential for broadband microwave absorber applications.

4. CONCLUSION

Expanded graphite flakes are successfully synthesized from natural graphite flakes by chemical oxidation and thermal treatment method. Complex permittivity and dielectric loss tangent values show that the developed composites are lossy in nature. IL of 30 wt%, 40 wt% & 50 wt% EG/NPR composites are measures in the X band and show that the values of IL increases with increase in EG percentages in the composites. An IL value of about ~ -48 dB is achieved for 50 wt% EG/NPR composites almost over the entire X-band. The material production is simple and cost effective, and the absorbing material is light weight, this is beneficial for installation in some strategic components.

ACKNOWLEDGMENT

The authors would like to sincerely thank Department of Information Technology, New Delhi for providing financial support.

REFERENCES

1. Knott E. F., J. F. Shaeffer, and M. T. Tuley, *Radar Cross Section*, Artech House, New York, 1993.
2. Petrov, V. M. and V. V. Gagulin, "Microwave absorbing materials," *J. Inorg. Mater.*, Vol. 37, 93–98, 2001.
3. Elimat, Z. M., "AC electrical conductivity of poly (methyl methacrylate)/carbon black composite," *J. Phys. D*, Vol. 39, 2824–2828, 2006.

4. Chung, D. D. L., "Electromagnetic interference shielding effectiveness of carbon materials," *Carbon*, Vol. 39, 279–285, 2001.
5. Grimes, C. A., E. C. Dickey, C. Mungle, K. G. Ong, and D. Qian, "Effect of purification of the electrical conductivity and complex permittivity of multiwall carbon nanotubes," *J. Appl. Phys.*, Vol. 90, 4134–4137, 2001.
6. Debelak, B. and K. Lafdi, "Use of expanded graphite filler to enhance polymer physical properties," *Carbon*, Vol. 45, 1727–1734, 2007.
7. Dhakate, S. R., S. Sharma, M. Borah, R. B. Mathur, and T. L. Dhami, "Development and characterization of expanded graphite-based nanocomposite as bipolar plate for polymer electrolyte membrane fuel cells (PEMFCs)," *Energy & Fuels*, Vol. 22, 3329–3334, India, 2008.
8. Knop, A. and I. A. Pilot, *Phenolic Resin*, Springer Verlag, Berlin, 1985.
9. Nicolson, A. M. and G. F. Ross, "Measurement of the intrinsic properties of materials by time-domain techniques," *IEEE Trans. Instrum. Meas.*, Vol. 19, 377–382, 1970.
10. Wenge, Z., S. C. Wongand, and H. J. Sue, "Transport behavior of PMMA/expanded graphite nanocomposites," *Polymer*, Vol. 43, 6767–6773, 2002.
11. Matsumoto, M. and Y. Miyata, "Complex permittivity based on equivalent circuit model for polymer/metal composite frequency dependence of permittivity as function of concentration," *IEEE Trans. Dielectr Electr. Insul.*, Vol. 6, 27–34, 1999.

Kalman Filter for ABR Signal Analysis

M. Hafizi Omar, **Sh-Hussain Salleh**, **Ting Chee Ming**,
R. Ariffi Suraya, **Kamarulafizam**, **and Tan Tian Swee**
Center for Biomedical Engineering (CBE), Transportation Research Alliance (TRA)
Universiti Teknologi Malaysia, Skudai, Johor 81310, Malaysia

Abstract— Auditory brainstem response (ABR) is an electrophysiological response in the electroencephalogram (EEG) reading which generated by the brainstem in response to auditory stimulus. ABR is very useful in determination of hearing threshold especially for uncooperative subject's and newborn infants. However, due to several factors, particularly on the technical aspects, including noise interference and other brain activities, the screening consumes a large portion of time to obtain the meaningful result. Conventional method to retrieve the underlying wave V using averaging technique requires more trials. Because of this, screening cannot be performed in a large scale. Based on this issue, this paper purposes a method for ABR denoising and detection of wave V by using Kalman Filter. This technique estimates the potential being analyzed sequentially by referring the previous sweeps information. By implementing this technique, the unwanted signal can be filtered out from every sweeps of ABR recorded. The system has been tested on 20 normal adult subjects with no history of hearing impairment. The ABR signal is collected using high accuracy biosignal data acquisition and processing system (high-end 24 bit biosignal amplifier, gUSBamp, gTec, Austria). From the analyzed result, wave V can be detected by less number of sweeps and still preserving the morphology of ABR signal. This approach shows better capability of estimating ABR signal by detecting wave V in minimum number of sweeps compared to conventional averaging technique. Therefore, our results show that the time of recording can be reduced for each screening.

1. INTRODUCTION

Auditory brainstem response (ABR) is an electrophysiological response in the electroencephalogram (EEG) reading which generated by the brainstem in response to auditory stimulus. The ABR signal consists of very low amplitude of signal (nano volts) [15]. The behavior of the ABR signal itself causes difficulties in acquiring the signals, which the signal easily distorted by another spontaneous brain activity and random muscle artifacts. Other electroencephalograph (EEG) signal also is observed to have higher amplitude than ABR signal, which will cause the signal obscured inside it. From revision on the ABR, the suitability on application of each technique in the signal-processing actually depends on the match between method and signal. Therefore, the successful implementation of any signal-processing techniques is strongly depended on the knowledge about the characteristics of the signal.

In newborn hearing screening, there are two objective methods implement, either Transient Otoacoustic Emission [3] or Auditory Brainstem Response. By following the evolution from time to time of the effectiveness of each method, it is observed ABR gives promising results than TOAE in terms of the specificity and low number of follow-up rate [1, 2, 9, 12]. The statement is supported by lot of evidence that shows the significant of ABR method in hearing screening. By referring to [3, 6, 11], shows that the ABR method gives better performance rather than the TOAE method. However, the weakness of this method significantly can be seen on the allocation of time to record data. The regular procedure in acquiring the ABR signal is by providing stimuli on the auditory sensor [5] to ensure that the auditory brainstem will response consistently with similar signals and different from other signals. This will induce the auditory nerves to evoke potential consistently rather than other kinds of brain signals. The conventional averaging techniques are used to retrieve the underlying clean ABR signal by averaging at assumed randomly distributed noises. However, these drawbacks can be overcome with the implementation signal processing techniques that are appropriate for this ABR signal. There are various method been implemented in ABR signal processing, especially instantaneous energy [4, 13], and time-frequency scale analysis (including wavelet) [7, 8]. Our approach is implementing Kalman filter technique for fast ABR screening. This method estimates each trial/sweeps to get significant result in less number of sweeps. In the ABR signal, wave V is the indicator to ensure the subject ear response to the audio stimulation at a specific range of time [4, 9, 10].

2. METHODOLOGY

In this study, universal biosignal acquisition system from Guger Technology (G-tec) system is used to record the EEG signals. It comes in a package which consists of Programmable Attenuator Headphone buffer (g-PAH), USB Biosignal Amplifier, Multimode Trigger Conditioner Box (g-TRIGbox), and Biosignal Analysis Software. The tools are adjusted in terms of connection and arrangement, particularly for ABR recording purpose. The g-tec Biosignal Analysis is comprised with MATLAB software as signal processing tools.

Figure 1 shows the diagram of the hardware system setup. It consists of gTec USBamp, a biosignal amplifier and data acquisition machine; gPAH, a programmable attenuator; trigger box, headphone, laptop, sound card (second computer to play the stimulus) and active electrodes.

Audio chirps stimulus is given to subject by using second computer to ensure no interruption on

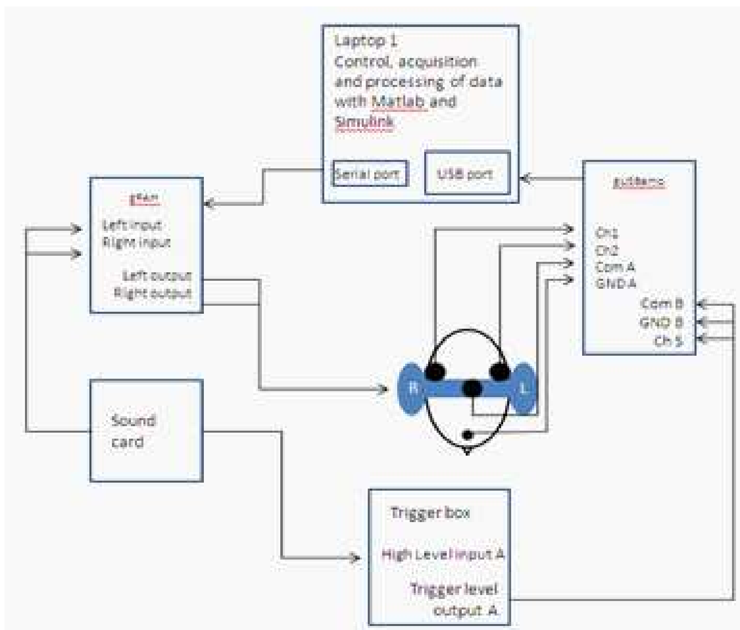

Figure 1: Diagram of hardware system setup.

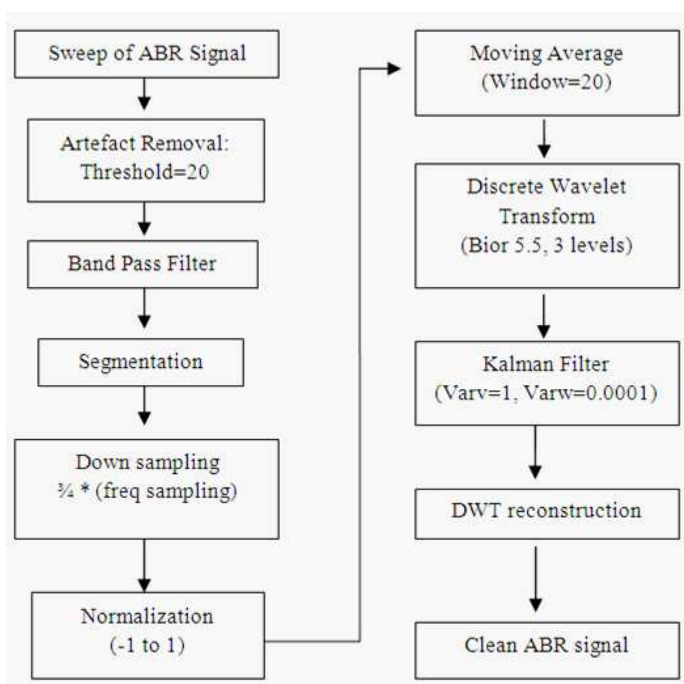

Figure 2: ABR signal processing procedure.

the stimulus signal itself, while the another computer will record and process the ABR signal. From this part, trigger box is connected in parallel with programmable attenuator (G-Pah). Trigger box function to produce trigger signal from the stimulus chirps for framing and windowing purposes. It indicates the reference point to the EEG signal based on triggered detection from the stimulus given. The recorded signals captured were transferred to G-tec USBamp for signal conditioning and amplification process before transferred to the computer.

The recorded signal was filtered at bandwidth ranges from 100 Hz–1500 kHz. The rising chirp's stimulus rate was played at 20 chirps per second and the ABR signal was sampled at 19.2 kHz with 24 bit resolution. The stimulus intensity levels used in the experiments are 30 to 60 dBnHL with 10 dB increment. However, this research is focuses on 40 dBnHL by following mostly screening program that applied intensity level among that value. The signals were recorded, cut into frames in synchronous manner, saved and averaged after 2000 frames is completed. The artifact rejection is set to 20 μV to remove artifacts, mostly from EMG, and subject's movement. The active electrode is used to acquire signal from subjects scalp. Figure 3 shows the electrodes configuration used in the experiments. The positive electrode (channel 1 and 2) was connected to both mastoid (right and left), the negative electrode (reference) was connected to vertex and ground electrode were connected to forehead. Even the connection for positive electrode on both mastoids, the recording still run for single side stimulus sound to subject's ear, and process the signal of the related side of stimulus sound given.

Figure 2 shows the overall system of ABR signal processing technique. However, the main focus on this research is on the implementation of Kalman filter technique through this process. In this research Bior 5.5 wavelet is used as a feature to reduce number of samples in Kalman filter. The theory is based on [14].

3. RESULT AND DISCUSSION

The results of ABR trials and their corresponding average are indicated by light dark-blue lines in Figure 3 and Figure 4. Those signal recorded from 40 dB stimulus intensity. Wave V threshold is obtained by the location of the maximum amplitude (peak amplitude), single sweep tracing and morphology of the ABR shape.

By referring to the result from both methods, it is shown that Kalman filter technique gives a better representation in each sweeps. Even though the number of sweeps has been reduced to 500, wave V still can be traced (on normal subjects). The situation not occurs to Moving Averaging method, where the wave V is invisible (buried in noise) even sweeps number has reduced to 500.

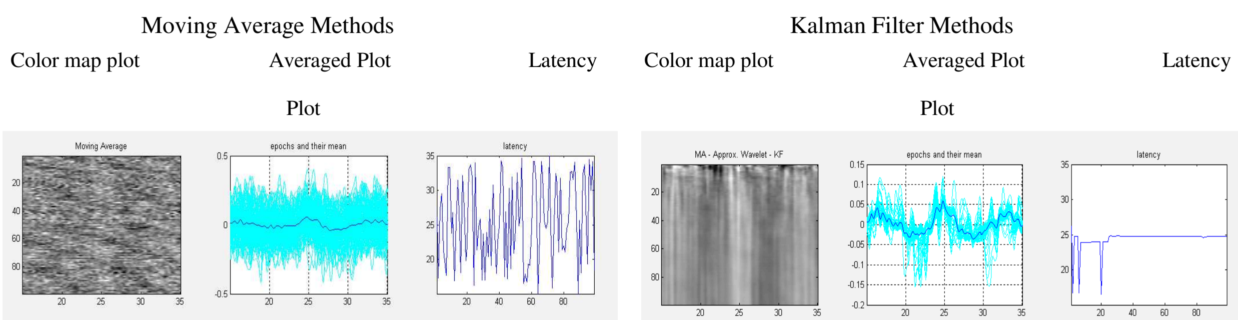

Figure 3: Comparison of 2000 sweeps recorded ABR signal's.

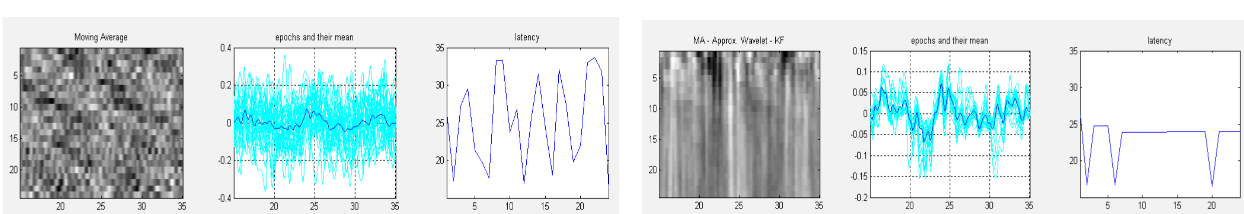

Figure 4: Comparison of 500 sweeps recorded ABR signal's.

4. CONCLUSION

This paper proposed Kalman Filtering method for wave V detection in the ABR signal. From the result, it is shown that better detection of wave V is obtained using Kalman Filter with the reduced number of sweeps.

REFERENCES

1. Abdullah, H., et al., "Newborn hearing screening: Experience in a Malaysian hospital," *Singapore Med. J.*, Vol. 1, No. 47, 60–64, 2006.
2. Abdullah, A., M. Y. Hazim, A. Almyzan, A. G. Jamilah, S. Roslin, M. T. Ann, L. Borhan, A. Sani, L. Saim, and N. Y. Boo, "Newborn hearing screening: Experience in a Malaysian hospital," *Singapore Med. J.*, Vol. 1, No. 47, 60–64, 2006.
3. Ahmad, D. A., "A study of outcome of newborn hearing screening programme in HUSM from January 2003 to December 2007," *Malaysian Journal of Medical Sciences*, Vol. 16, No. 3, 69, 2009.
4. Arooj, A., M. R. Muhamed, et al., "Use of instantaneous energy of ABR signals for fast detection of wave V," *J. Biomedical Science and Engineering*, Vol. 3, 816–821, 2010.
5. Barbara, S., A. R. T. Herman, and J. M Josepth, "Automated infant hearing screening using the ABR: Development and validation," *American Journal of Audiology*, Vol. 4, No. 2, 1995.
6. Benito-Orejas, J. I., B. Ramirez, et al., "Comparison of two-step transient evoked otoacoustic emissions (TEOAE) and automated auditory brainstem response (AABR) for universal newborn hearing screening programs," *International Journal of Pediatric Otorhinolaryngology*, Vol. 72, 1193–1201, 2008.
7. Bradley, A. P. and W. J. Wilson, "On wavelet analysis of auditory evoked potentials," *Clinical Neurophisiology*, Vol. 115, 1114–1128, 2004.
8. Causevic, E., R. E. Morley, et al., "Fast wavelet estimation of weak biosignals," *IEEE Transactions on Biomedical Engineering*, Vol. 52, No. 6, 1021–1032, 2005.
9. Corona-Strauss, F. I., W. Delb, et al., "The johor screening scheme: Is an area-wide newborn hearing screening possible in malaysia," *Third International Conference on International Information Hiding and Multimedia Signal Processing*, Vol. 2, 213–216, Kaohsiung, Taiwan, IEEE, 2007.
10. Farah, I., W. D. Corona-Strauss, M. Bloching, and D. J. Strauss, "On the single sweep processing of auditory brainstem responses: Click vs. chirp stimulations and active vs. passive electrodes," *30th Annual International IEEE EMBS Conference*, 4166–4169, Vancouver, British Columbia, Canada, IEEE, 2008.
11. Geal-Dor, M., C. Adelman, et al., "Comparison of two hearing screening programs in the same population OAE screening in newborns and behavioral screening when infants," *International Journal of Pediatric Otorhinolaryngology* Vol. 74, No. 12, 1351–1355, 2010.
12. Hayes, D., "Screening methods: Current status," *Mental Retardation and Developmental Disabilities Research Review*, Wiley InterScience, Vol. 9, 65–72, 2003.
13. Rushaidin, M. M., S.-H. Salleh, T. T. Swee, J. M. Najeb, and A. Arooj, "Wave V detection using instantaneous energy of auditory brainstem response signal," *American Journal of Applied Sciences*, Vol. 6, No. 9, 1669–1674, 2009.
14. Mohseni, H. R., K. Nazarpour, et al., "The application of particle filters in single trial event-related potential estimation," *Physiological Measurement*, Vol. 30, 1101–1116, 2009.
15. Usakli, A. B., "Improvement of EEG signal acquisition: An electrical aspect for state of the art of front end," *Computational Intelligence and Neuroscience*, Vol. 2010, 7, Hindawi Publishing Corporation, 2009.

Wave V Detection Using Continuous Wavelet Transform of Auditory Brainstem Response Signal

M. M. Rushaidin, **Sh.-Hussain Salleh**, **O. Hafizi**, **H. Mahyar**, **C. M. Ting**, **and A. K. Ariff**
Centre for Biomedical Engineering, Transport Research Alliance
Universiti Teknologi Malaysia, UTM Skudai, Johor 81310, Malaysia

Abstract— Auditory brainstem response (ABR) audiometry is well known tools for detection of hearing loss. It is a neurologic test of ABR in response to the stimuli such as click sound, tone burst or chirp. The non-invasive electrodes are used to obtain the ABR signals. In ABR, wave V of the ABR signals is used as indicator of hearing loss because it is the most dominant and robust peak wave. In current device, there are about 2000 sweeps of the ABR signals have to be averaged in order to get the meaningful signal which required about 4 minutes for one single stimulation level, which is consumed a lot of time. Therefore it is compulsory to have a fast detection method to reduce the recording time. Several types of signal processing techniques have been introduced by researchers to obtain the best technique to detect the ABR signals such as Fast Fourier Transform (FFT) and discrete wavelet transform (DWT). In this study, the continuous wavelet transform (CWT) of ABR signal had been introduced as a marker to identify the ABR waves. Study showed that the CWT of auditory brainstem response can be used a marker to identify the ABR waves with the sensitivity, 0.63 and the specificity, 0.83.

1. INTRODUCTION

Conginetal hearing loss is the most common neurosensory handicaps in newborns and children [1, 2]. Early detection of hearing loss is important especially for newborn because a serious delay in the speech, intellectual and emotional development is expected if the therapies were not one to the deaf babies during the first 6 months [1–3]. Therefore, hearing screening is a compulsory test to detect hearing ability. Prevalence of permanent hearing impairment is about 1 to 3 per 1000 live births, differs from country to country. There is no published data in Malaysia on the actual prevalence of hearing impairment in children. However, case study at Hospital Universiti Malaya shows that the prevalence is 0.42% [4].

Even though there should be universal hearing screening implement to every newborn, but for certain developing country and remote areas, a lack of resources might limit the development of this programme. Therefore, the screening is only involved the high risk neonatal. The Otoacoustic Emissions (OAEs) and Auditory Brainstem Response (ABR) are commonly used to screen hearing loss. OAE testing evaluates the integrity of the inner ear (cochlea). In response to noise, vibrations of the hair cells in a healthy inner ear generate electrical responses, known as otoacoustic emissions. The absence of OAEs indicates that the inner ear is not responding appropriately to sound [5]. The ABR is an electrophysiological response in the Electroencephalograph (EEG) generated by the brainstem in response to auditory signals such as clicks or tones. The stimulus is delivered via earphones or an inserted ear probe and scalp electrodes are used to pick up the signal. ABR evaluates the integrity of the peripheral auditory system and the auditory nerve pathways up to the brainstem and is able to identify infants who have normal cochlear function but abnormal eighth-nerve function (auditory neuropathy) [5].

There were several methods have been introduced for detection of ABR waves, a smart single sweep analysis system has been introduced by Strauss et al. [6], a Discrete Wavelet Transform by Wilson and Aghdasi [7] and instantaneous energy by Rushaidin et al. [8, 9].

2. MATERIALS AND METHODS

The hardware system setup is shown in the Figure 1. It consists of (A) gTec USBamp, a biosignal amplifier and data acquisition machine, (B) gPAH, a programmable attenuator, (C) trigger box, (D) headphone, (E) laptop, (F) MP3 player and (G) electrodes.

In order to capture the brain signal, there are three electrodes were used in the experiments. The positive electrode (channel 1) was connected to vertex, the negative electrode (reference) was connected to mastoid and ground electrode was connected to forehead. The electrodes configuration for the experiments is shown in Figure 2.

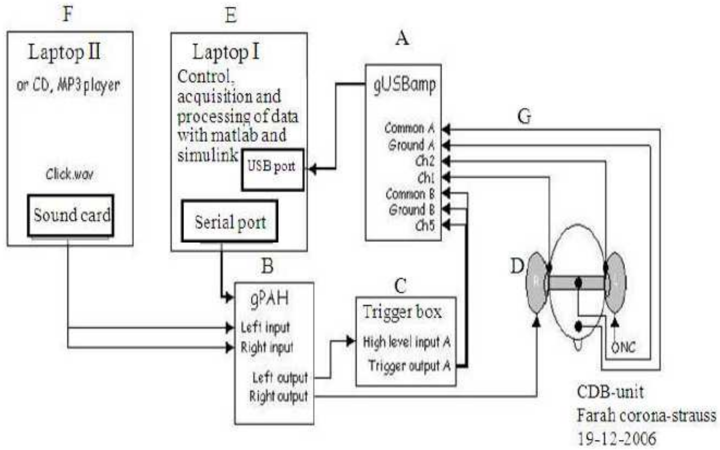

Figure 1: Diagram of the hardware system setup.

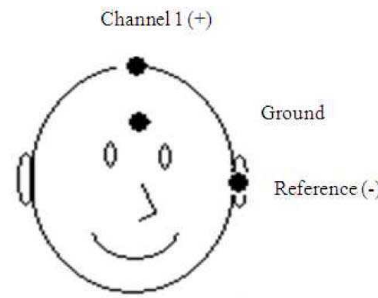

Figure 2: Electrodes configuration.

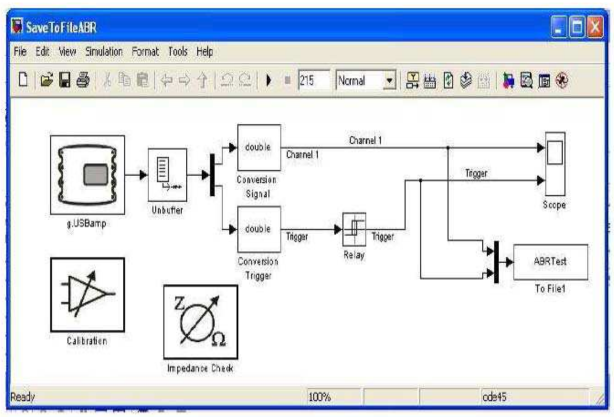

Figure 3: Matlab model configuration.

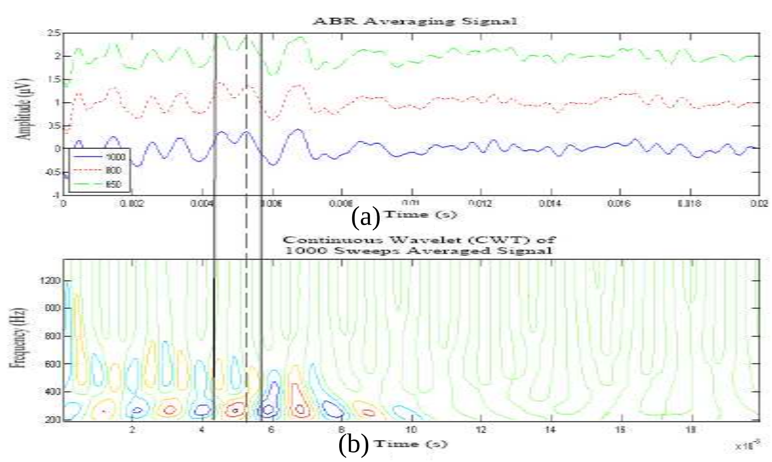

Figure 4: Normal (a) Averaged signal, (b) CWT of 1000 sweeps averaged signal.

The system was used Matlab R2006a simulink software to capture the raw ABR signals from the gTec USBamp and analyze the signals. Some configurations need to be carried out using the Matlab model. The model configuration is shown in Figure 3. The analysis algorithm was written in Matlab M-file format.

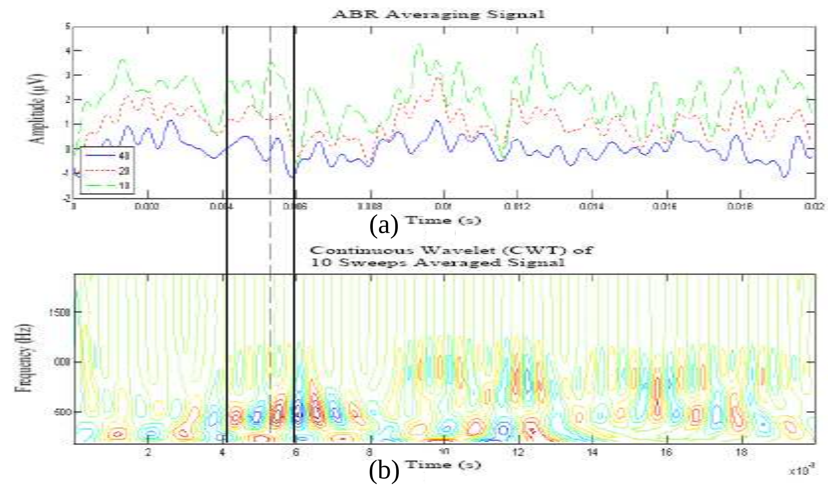

Figure 5: Normal (a) Averaged signal, (b) CWT of 10 sweeps averaged signal.

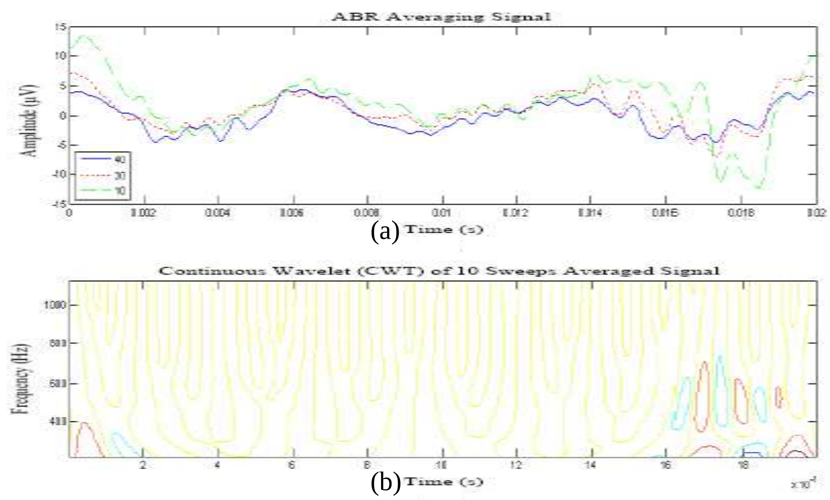

Figure 6: Abnormal; (a) Averaged signal, (b) CWT of 10 sweeps averaged signal.

3. RESULTS AND DISCUSSION

Figures 4, 5, and 6 show the representation of the ABR averaged signal and the continuous wavelet of the ABR signal with different number of sweeps for normal and abnormal subjects. The continuous wavelet was observed between the time ranges from 4 to 6 milliseconds post stimulus. This is because the study focused on the wave V. Figures 4 and 5 show the normal data and Figure 6 shows the abnormal. In Figure 4(b), it can be seen that the high level contours appeared in the regions of 200 Hz and Figure 5(b), in the region of 500 Hz. For the abnormal, it can be clearly seen that the contour levels are mostly at the same level as shown in Figure 6(b). It is different compared with normal signal, which contains various levels of contours.

Sensitivity and specificity of a test relate to the ability of the test to identify correctly both with the disease (sensitivity) and those without the disease (specificity). Sensitivity is the ratio of the number with the disease who are positive on the screening test to the number of all those with the disease. In other words, sensitivity represents the percentage labeled positive on the screening test of all those who truly have the target condition. Specificity is the ratio of the number of those without the disease who are negative on the screening test to the number of all those without the disease. In other words, specificity is percentage labeled negative on the screening test of all those who are truly free of the target condition [3].

Table 1 shows the sensitivity and specificity of CWT technique. It shows that the highest sensitivity of CWT technique is 0.75 and the lowest sensitivity is 0.5. The highest specificity

Table 1: Sensitivity and specificity of CWT technique.

Sweeps	Sensitivity	Specificity
1000	0.5	1
800	0.5	1
625	0.5	1
500	0.75	0.92
250	0.5	0.92
125	0.75	0.83
100	0.5	0.92
80	0.75	0.92
50	0.5	0.83
40	0.75	0.67
20	0.75	0.5
10	0.75	0.5
Average	0.63	0.83

of CW technique is 1 and the lowest is 0.5. After averaged all twelve values of sensitivity and specificity, CWT technique has the sensitivity (0.63) and specificity (0.83).

4. CONCLUSION

In conclusion, this paper discussed about new method of the ABR wave's detection using continuous wavelet transform. The result shows that continuous wavelet can be used as marker in order to detect ABR waves. However, comparison with other techniques has to be done.

ACKNOWLEDGMENT

This research project is supported by CBE (Center for Biomedical Engineering) at University Technology Malaysia and funded by University Technology Malaysia (UTM), Malaysia under grant "Universal Hearing Screening in Malaysia Based On A Cost Efficient Organization Structure Using An Innovative ABR Technology: The Johor Screening Scheme" Vot 77013.

REFERENCES

1. Yoshinaga-Itano, C., "Benefits of early intervention for children with hearing loss," *Otolaryngol. Clin. North Am.*, Vol. 32, 1089–1102, 1999.
2. Minnesota Department of Health, Minnesota Early Hearing Detection and Intervention (EHDI) Program, Guideline for Organization and Administration of Universal Newborn Hearing Screening Programs in the Well Baby Nursery, 2008. http://www.health.state.mn.us/divs/phl/newborn/docs/nhswbnguidelines.pdf.
3. American Speech-Language-Hearing Association (ASHA), Guidelines for Audiologic Screening, 1997.
4. Abdullah, A., M. Y. S. Hazim, A. Almyzan, A. G. Jamilah, S. Roslin, et al., "Newborn hearing screening: Experience in a Malaysian hospital," *Singapore Med. J.*, Vol. 47, 60–64, 2006. http://www.sma.org.sg/smj/4701/4701a9.pdf.
5. Helfand, O. M., D. C. Thompson, R. Davis, H. McPhillips, C. J. Homer, and T. L. Lieu, "Newborn hearing screening: Systematic evidence review," *AHRQ Publication*, No. 02-S001, Agency for Healthcare Research and Quality, Rockville, MD, 2001, http://www.ncbi.nlm.nih.gov/books/bv.fcgi?rid=hstat3.chapter.1787.
6. Strauss, D. J., W. Delb, P. K. Plinkert, and H. Schmidt, "Fast detection of wave V in ABRs using a smart single sweep analysis system," *Proceedings of the 26th Annual International Conference of the IEEE Engineering in Medicine and Biology Society*, 458–461, IEEE Xplore Press, Sep. 2004.
7. Wilson, W. J. and F. Aghdasi, "Fast fourier transform analysis of the auditory brainstem response: Effects of stimulus intensity and subject age, gender and test ear," *AFRICON IEEE*, Vol. 1, 285–290, 1999.

8. Rushaidin, M. M., S.-H. Salleh, T. T. Swee, J. M. Najeb, and A. Arooj, "Wave V detection using instantaneous energy of auditory brainstem response signal," *American Journal of Applied Sciences*, Vol. 6, No. 9, 1669–1674, 2009.
9. Arooj, A., M. M. Rushaidin, S.-H. Salleh, and M. H. Omar, "Use of instantaneous energy of ABR signals for fast detection of wave V," *Journal of Biomedical Science and Engineering*, Vol. 3, No. 8, 816–821, 2010.

Malay Speech Digit Recognition for Speech Therapy Application

Tan Tian Swee, Sh-Hussain Salleh, Ahmad Kamarul Arif, Cheng Wei Lip, and Lau Chee Yong
Center for Biomedical Engineering (CBE), Transportation Research Alliance (TRA)
Universiti Teknologi Malaysia, Skudai 81310, Johor, Malaysia

Abstract— Disorder of speech is defined by the American Speech-Language-Hearing Association (ASHA) as one type of communication disorder. The most difficult task in speech language pathologist is to diagnose the speech disorder. This diagnostician looks on aspect of an individual's communication ability rather than their communication. It required involvement of speech-language pathologists (SLPs) who provide an assortment of service that relate to communication disorder. Therefore, research on applications of speech recognition to speech and language development has been widely conducted since 1990. The improvement in technology has replaced the traditional speech therapy with more attractive tools for diagnostic and training of speech disorder. This paper proposes a method for detecting speech stuttering using speech recognition technique. Stuttering shows break in the usual time sequence of utterance where the usual flow is interrupted. There also conspicuous oscillations and fixations, repetitions and prolongations of sounds and syllables. Stuttering always varies with emotional stress where stuttered increase as in situations invest with fear and shame. Stuttered people may speak perfectly when they are alone and start to stutter when talking to listener. This paper focuses on all Malay digits from kosong (zero) through sembilan (nine). The system is tested using speech data recorded in word-based unit and syllable-based unit. Two experiments on monophones-based and syllable-based have been conducted to find the optimum setting for phoneme recognition. The overall results show that monophones-based unit system is able to do recognition with 90.18% accuracy for monophones-based network and 100% accuracy for word-based network, while syllable-based unit system is able to do recognition with 63.89% accuracy for syllable-based network. Through this paper it can be concluded that this system able to be used as diagnostic software for speech disorder.

1. INTRODUCTION

Stuttering is a speech fluency disorder that can affect our life in many aspects. The most obvious aspect in this disorder is the production of certain types of disruption in the forward flow of speech. For example like repetition of part of words, prolongations and blocks [1]. Stuttering shows break in the usual time sequence of utterance where the usual flow is interrupted [2]. There also conspicuous oscillations and fixations, repetitions and prolongations of sounds and syllables. Stuttering always varies with emotional stress where stuttered increase as in situations invest with fear and shame. Stuttered people may speak perfectly when they are alone and start to stutter when talking to listener. Stuttering behavior can be found when the stutterers were still a child. Incipient, or early stuttering is a distinctive form of stuttering that can be observed from pre-school children. Incipient stuttering is still not the fully developed stuttering yet. Somehow they are different such as the frequent repetition of whole words at the beginnings of utterance [3] and the frequency with which stuttering involves function words [4]. The hypothesis of the cause of incipient stuttering is due to the uncertainty in the formulation of syntactic structures such as sentences and phrases. This uncertainty may due to hesitation while this hesitation would make them repeat or prolong some words in the speaking speech. The incipient or early stuttering is tractable from the consultation of speech therapist. But if this condition is not treated immediately, incipient stuttering would become fully developed stuttering.

Previously, stuttering was viewed as a major impairment. General population always sees stuttering as a peculiar, but not dangerous, speech phenomenon that was occasionally stigmatized [5]. But in fact, stuttering is a curable behavior with proper treatment. Some studies have shown that the people who stutter have elevated anxiety level if compared to the general population [6]. So the treatment must be given to them so that they can be cured from stuttering and lead to stress free life. An assistive tool for tracing stuttering should be developed as the diagnostic process for every patient is human resource consuming and require a lot of time and energy. Relapse following treatment for stuttering is common among stutterer. It is due to the patient's difficulties to adjust themselves to a new role as a fluent speaker [7]. Diagnostic process has to be run again to identify if the relapse of stuttering is really happen. So, it is beneficial to have a diagnostic tool available for stuttering. Clinically result shows that the stutterer would choose the speech therapist that is

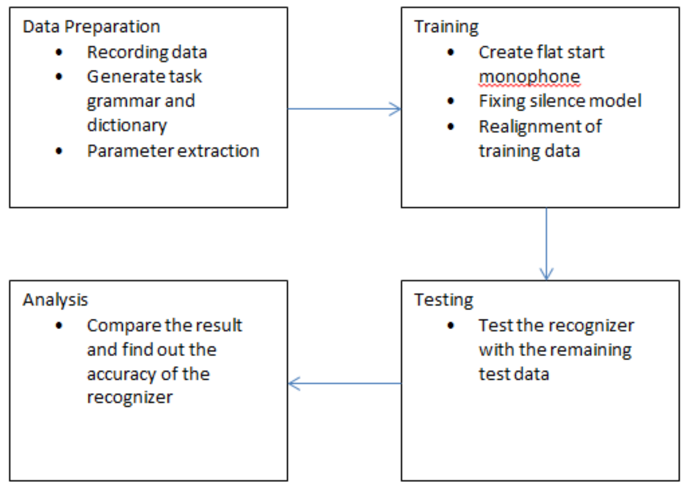

Figure 1: Block diagram of the construction of recognizer.

same gender with them [8]. For example male stutterer tends to choose male speech therapist for their treatment. Due to the lack of human resource at the instance, an assistive diagnostic tool would be a great help.

2. METHODOLOGY

The purpose of this paper is to develop a syllable recognition system which is able to be a diagnostic tool to assist therapist to diagnose articulation disorder. The Hidden Markov Model Toolkit (HTK) is used and also Visual C++ 6.0 was used to create the graphic user interface. The overall process can be categorized as data preparation, training, testing, and analysis. The flow of the procedure is illustrated in the block diagram below.

For the data preparation, the speech data collected were divided into two categories which are word-based and syllable-based. 300 normal speech data were recorded for word-based data. 200 of them were used for training and the rest were used for testing. The words were constituted from 'kosong' (zero) to 'sembilan' (nine). On the other hand, 408 syllable-based speech data was recorded for stuttering experiment. From the database, 300 were used for training purpose and the rest were used for testing purpose. All the data was recorded using Goldwave software in wave file format in 16 K sampling rate, mono channel and five seconds of duration.

After the data was recorded, then the task grammar was defined. The task grammar consist of the words to be recognized by the system. From the task grammar, the word network can be created. The next step is to create the word list in order to create the dictionary. The words are extracted from the database. Then, a pronunciation dictionary is constructed with short pause added to the end of every pronunciation. To extract the sequence of feature vectors, the Mel Frequency Cepstral Coefficient was used. The frame period was set to 10 ms. The window size was set at 25 ms and Hamming window was used. The cepstral filter was set at 22.

For the training part, first step is to define a prototype model. Then the flat start monophones are ready for the first re-estimation using embedded re-estimation tool. The re-estimation uses Baum Welch algorithm to update the HMM states with new parameter. Next step is to add short pause as the word boundary. The purpose of adding short pause is to define the word boundary so the system would be able to observe silence in normal speech. The embedded re-estimation was applied again after this step to update the HMM states with new parameter consists of short pause. Then, realigning process was taken place to align the phone model and the re-estimation was again update the HMM states.

At the testing stage, a new recognition network was created and also as the dictionary. A task grammar target for this testing process was also created meaning that the task grammar only consists the phoneme found in this project. After all the required files were created, the recognizer was executed.

For the analysis, the result from the testing stage was compared with the original transcription file. The comparison would point out the word which wrongly pronounced by user.

In this project, three experiments were carried out which are monophones based recognition, syllable based recognition and phoneme based recognition. For monophone and syllable based recognition, another three sub experiments were conducted by changing the number of state, number of Gaussian mixture and the MFCC target kind.

3. RESULT AND DISCUSSION

In this project, two main experiment were conducted which are monophone based recognition and syllable based recognition. The percentage of recognition was calculated by dividing the correct recognition by the total recognition to get the percentage of accuracy.

For the experiment of syllable based recognition, syllable was used as the model. In this project the syllables are /sa/ /tu/, /d/ /ua/, /ti/ /ga/, /em/ /pat/, /li/ /ma/, /e/ /nam/, /tu/ /juh/, /la/ /pan/, /Sem/ /bi/ /lan/, /ko/ /song/ with minimal pause between each syllable. The main target of this experiment is to find out the best setting as syllable as the model. 408 speech data were recorded, 300 of them were used for training and the rest were used for testing. Three sub experiments were conducted by changing the state number, the Gaussian mixture number and MFCC. As the result, state 13 was chosen because it gives the highest accuracy which is 59.26%. The percentage rises to 63.89% when the Gaussian mixture number was fixed at 8. For the MFCC, MFCC_0_D_A was chosen because it gives highest accuracy for sentence recognition (63.89%) and word recognition (84.78%).

4. CONCLUSION

From the experiment conducted, the result shows that the training system is able to recognize phoneme based on high percentage of word correct. So it is able to diagnose the articulation disorder. But the system still can be improved with some future works. This system gives low accuracy in recognizing long sentence. So long sentence can be also included in the speech data collection.

ACKNOWLEDGMENT

This research project is supported by Universiti Teknologi Malaysiafis university research grant (GUP-Tier 1, Q.J1300000.7136.01H49).

REFERENCES

1. Scott Yarus, J., "Assessing quality of life in stuttering treatment outcomes research," *Journal of Fluency Disorders*, Vol. 35, 190–202, 2010.
2. Ai, O. C., M. Hariharan, S. Yaacob, and L. S. Chee, "Classification of speech dysfluencies with MFCC and LPCC features," *Expert Systems with Applications*, Vol. 39, 2157–2165, 2012.
3. Bloodstein, O. and N. Bernstein Ratner, *A Handbook on Stuttering*, 6th Edition, Thomson/Delmar Learning, Clifton Park, NY, 2008.
4. Bloodstein, O. and B. F. Gantwerk, "Grammatical function in relation to stuttering in young children," *Journal of Speech and Hearing Research*, Vol. 10, 786–789, 1967.
5. Yairi, E. and C. H. Seery, *Stuttering — Foundations and Clinical Applications*, Pearso, Upper Saddle River, NJ, 2011.
6. Craig, A., K. Hancock, Y. Tran, and M. Craig, "Anxiety levels in people who stutter: A randomized population study," *Journal of Speech, Language, and Hearing Research*, Vol. 46, 1197–1206, 2003.
7. DiLollo, A., R. A. Neimeyer, and W. H. Manning, "A personal construct psychology view of relapse: Indications for a narrative therapy component to stuttering treatment," *Journal of Fluency Disorders*, Vol. 27, 19–42, 2002.
8. Bluemel, C. S., "Primary and secondary stammering," *Quarterly Journal of Speech*, Vol. 18, 187–200, 1932.
9. Ezrati-Vinacour, R. and N. Weinstei, "A dialogue among various cultures and its manifestation in stuttering therapy," *Journal of Fluency Disorder*, 2011.

Comparison of Different Time-domain Feature Extraction Methods on Facial Gestures' EMGs

M. Hamedi, **Sh-H. Salleh**, **A. M. Noor**, **T. T. Swee**, **and I. K. Afizam**
Center for Biomedical Engineering, Transportation Research Alliance
Universiti Teknologi Malaysia, Skudai, Malaysia

Abstract— Electromyography is a bio-signal which is applied in various fields of study such as motor control, neuromuscular physiology, movement disorders, postural control, human machine/robot interaction and so on. Processing of these bio-signals is the essential fact during each application and there still can be seen many challenges among researchers in this area. This paper is focused on the comparison between the classification performances by using different well known feature extraction methods on facial EMGs. Totally ten facial gestures namely smiling with both side of lips, smiling with left side of lips, smiling with right side of lips, opening the mouth like saying 'a' in apple word, clenching the molar teeth, gesturing 'notch' by raising the eyebrows, frowning, closing the both eyes, closing the right eye and closing the left eye are recorded from 6 participants through 3 bi-polar recording channels. In the first step, the signals are filtered to get prepared for better processing. Then, time-domain feature extraction methods INT, MAV, MAVS, RMS, VAR, and WL are applied to signals. Finally, the features are classified by Fuzzy C-Means in order to achieve the recognition accuracy and evaluate the performance of each feature extraction method. This work is carried out by revealing that, RMS gives the most probability amplitude approximation in a steady power and non-tiring contraction when the signal is modeled as Gaussian random process. In contrary, WL proved its weakness in estimating the value of facial EMGs.

1. INTRODUCTION

Gestures recognition is the state-of-the-art which can be added and applied in various fields of research [1]. Gestures usually originate from the face and body. This technology has been done by capturing the images or videos from the body movements or recording the Electromyogram (EMG) of muscles neural activities. Recently, many researchers have been interested in the second method because of observed drawbacks in image-based method. Besides, among all body movements, facial gestures and expressions are focused in different applications especially in the field of human computer interaction (HCI). As examples: facial gestures extracted during speech and transformed as control commands by Arjunan and Kumar [2]; a later proposition of controlling a hands-free wheelchair through the facial myosignals by Firoozabadi et al. [3]; application of five facial gestures by Rezazadeh et al. [4] for designing and controlling a virtual crane training system. Obviously, the most important step in these works is data analysis which many challenges still can be seen.

The main source of data is EMG from the target muscles which are the measurement of their electrical activity. There are two ways to record the EMG which are the invasive by using needle electrodes and noninvasive by applying the surface electrodes. Depending on recording method, the EMG analysis can be varying. Due to surface Electromyography characteristics, this method has been more considered in recent works like stated examples.The amplitude of surface EMG (SEMG) signal is random and the range is 0–10 mV and the frequency range is restricted to the 10 to 500 Hz that both are different in each muscle. So, depending on the muscle under investigation the methods for EMG analysis are diverse. Facial muscles which are considered as a new communication channel with computers and machines in HCI systems produce signal with lower amplitude and almost similar frequency range, Hamedi et al. [5].

Raw recorded EMG signals are quasi random and has complicated form. They also contain significance information as well as contamination and workings with them have been always a tough task. Therefore, EMGs need to be analysis preprocessing, processing and postprocessing of signals can be seen as the three main steps. One of the most important and challengeable part in EMG processing is feature extraction which usually apply on raw signals in order to transform it into reduced representation set of features. There are three types of features in different domain; Time, Frequency and Time-Frequency distribution which each of these categories use in specific application. According to facial EMGs specifications, their accurate and useful features are limited in Time-domain.

Mean Absolut Value (MAV), Maximum Scatter Difference (MSD), Root Mean Square (RMS), Power Spectrum Density (PSD), Absolute Value (AV), Mean Absolute Deviation (MAD), Standard Deviation (SD) and Variance (VAR) are the most popular and well-known methods which have been used by Moon et al. [6], Firoozabadi et al. [3], Ang et al. [7], Gibert et al. [8], Rezazadeh et al. [4], Van den Broek et al. [9] and Hamedi et al. [5, 10]. After feature extraction, they used various techniques of classification for recognition between their chosen facial gestures to prepare them in their own applications such as Support Vector Machine (SVM), Multi-Layer Perceptron (MLP), K-Nearest Neighbors (K-NN) and Fuzzy C-Means (FCM). In these works the number of classes are varies from two to eight and different facial gestures were considered. Hamedi et al. [5] provided the maximum number of classes (eight) and achieved 91.8% recognition by applying RMS and FCM methods for feature extraction and classification respectively.

In this paper, the evaluation between six famous feature extraction methods: Integrated (INT), MAV, Mean Absolute Value Slop (MAVS), RMS, VAR, and Wave Length (WL) on ten facial gestures is described. The goal is the comparison of their performances while FCM classifier used for classification and recognition.

2. METHODOLOGY

The general block diagram of the whole procedure is shown in Figure 1. At first, all six subjects (all healthy male within the range of 20–26 age) get prepared for EMG recording. It was done by cleaning the subjects face from any dust and sweat with using alcohol pad. Then, conductive electrode paste is applied in order to reduce the artifacts as much as possible. In this work three pairs of surface electrodes are used and they positioned in bipolar configuration on the affective muscles involved in chosen gestures. In this study ten predefined gestures: smiling with both side of lips, smiling with left side of lips, smiling with right side of lips, opening the mouth like saying 'a' in apple word, clenching the molar teeth, gesturing 'notch' by raising the eyebrows, frowning, closing the both eyes, closing the right eye and closing the left eye are selected. So, to cover the main muscles in these gestures one pair of the electrodes placed on the Frontalis muscle (Channel 2), two pairs are located on left and right side of temporalis muscles (channel 1&3) and another electrode is situated on the left wrist.

Before signal recording all subjects trained how to perform all ten gestures and then, they rested for 1 minute. After that, they were asked to execute all facial gestures 5 times, as 2 secs performance and 8 secs interval rest between each trial.

2.1. Conditioning of Raw EMGs

All acquired signals were passed through a band-pass filter within the frequency range 30–450 Hz, being the principal frequency range of EMG signals. In addition, in order to avoid from any undesirable artifacts which mostly have low frequency like eye movements, a high-pass filtering at 20 Hz is applied. Moreover, by using a notch filter 50 Hz, power line interferences are removed, Van Boxtel [11].

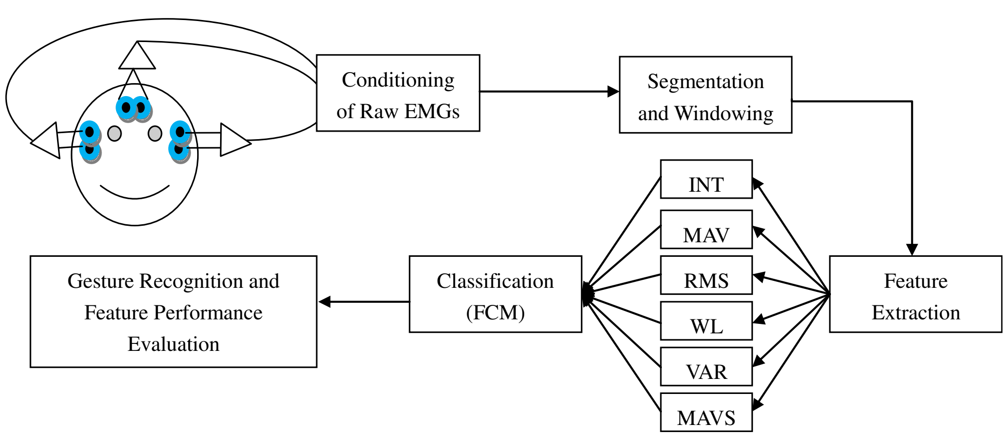

Figure 1: General block diagram of the whole procedure.

2.2. Segmentation and Windowing

In this work all filtered signals are segmented with 256 ms length and the steady-state part of the data were under investigation. Besides, adjacent windowing method is considered prior to feature extraction.

2.3. Feature Extraction

Using entire EMGs as input data for pattern recognition and classification step is not practical because of huge number of data and longtime of processing. So, feature extraction methods have been used to map the real signals into lower dimension feature vectors. The features must contain enough information of signals and must be simple enough for fast training and classification. There have been many experiments in choosing the best method of feature extraction use for facial EMG signals. In this work, six methods INT, MAV, MAVS, RMS, VAR, and WL are chosen to apply on all signals which are explained by Rechy-Ramirez and Hu [12].

2.4. Classification

There are many techniques introduced and proposed in the field of facial EMG signals classification such as Multi-Layer Perceptron (MPL), Fuzzy C-Means (FCM) and Support Vector Machine (SVM). It can be observed that, fuzzy clustering classifiers like FCM performed better in compare with other methods due to its flexibility, fast training, easy to use and low cost of calculation. Besides, the supervised version of FCM led to better classification because of class labels which always provide expedient directions during the training procedure. So, FCM classifier used on all extracted features in order to achieve the discrimination and recognition ratios to find the best feature among proposed methods.

3. RESULTS AND DISCUSSIONS

The main goal of this paper was to find better feature extracted from facial EMGs between INT, MAV, MAVS, RMS, VAR, and WL. Table 1 provided the average classification results of ten facial gestures from all participants of all features. As can be seen RMS and WL features delivered the highest and lowest recognition accuracy amongst all features respectively. Figure 2 demonstrates how the RMS and WL features are distributed in feature space. Obviously, all ten clusters are formed for RMS features and except of two classes Apple and Smile which are overlapped too much, the other classes are discriminated well enough. On the other hand, WL features shown their weaknesses for EMG classification. This is due to the fact that, the WL values for all facial gestures are almost close to each other and there is no way to discriminated them. INT, MAV and MAVS features also provided good distribution with almost similar recognition accuracy results in compare with VAR.

Table 1: Average classification results of all features.

Feature	INT	MAV	MAVS	VAR	RMS	WL
Classification Result	87.5%	84.6%	89.7%	35.7%	90.8%	21.5%

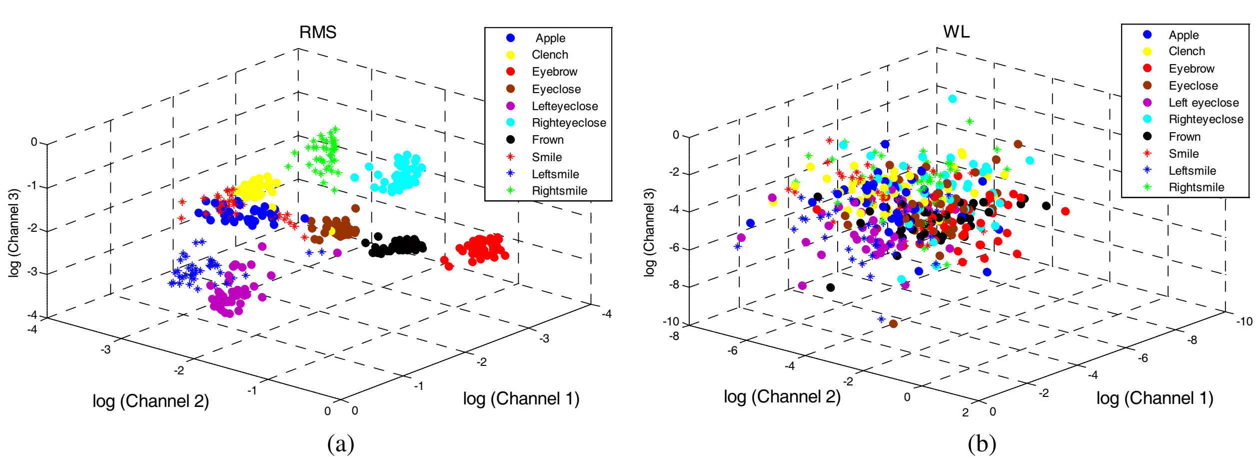

Figure 2: Distribution of RMS and WL features in feature space.

4. CONCLUSIONS

This study highlights an evaluation between six kinds of Time-Domain features which all of them have been already used in various works where EMG signals were involved. Ten facial gestures EMG signals have been recorded form six participants and all considered features were extracted. Then, they were classified by FCM and evaluated by their recognition performances. RMS features shown their abilities in facial gestures EMGs processing and it proved that when a signal is modeled as a Gussian random process, RMS provides the maximum likelihood estimation of amplitude in a constant force and non-tiring contraction. In conclusion, in the field of facial EMG processing, RMS features delivered the best performance while FCM classifier use as pattern recognition technique. In future, all popular classifier performances will be evaluated by applying RMS features as the main feature of EMG signals to find out which classifier is more suitable for facial EMG classification.

REFERENCES

1. Gunes, H., M. Piccardi, and T. Jan, "Face and body gesture recognition for a vision-based multimodal analyzer," *Proceedings of Area Workshop on Visual Information Processing*, Sydney, Australia, 2003; *CRPIT*, Vol. 36, 19–28, M. Piccardi, T. Hintz, S. He, M. L. Huang, and D. D. Feng, Eds., ACS.
2. Arjunan, S. P. and D. K. Kumar, "Recognition of facial movements and hand gestures using surface Electromyogram (sEMG) for HCI based applications," *Proceedings of 9th Biennial Conference of the Australian Pattern Recognition Society on Digital Image Computing Techniques and Applications*, 1–6, Glenelg, Australia, Dec. 3–5, 2008.
3. Firoozabadi, S. M. P., M. A. Oskoei, and H. Hu, "A human-computer interface based on forehead multi-channel bio-signals to control a virtual wheelchair," *Proceedings of 14th ICBME*, 272–277, Tehran, Iran, Feb. 13–14, 2008.
4. Rezazadeh, I. M., X. Wang, S. M. P. Firoozabadi, and G. M. R. Hashemi, "Using affective human machine interface to increase the operation performance in virtual construction crane training system: A novel approach," *Journal of Automation in Construction*. Vol. 20, 289–298, 2010.
5. Hamedi, M., H. S. Sheikh, T. S. Tan, and A. Kamarul, "SEMG based facial expression recognition in bipolar configuration," *J. Comp. Sci.*, Vol. 7, No. 9, 1407–1415, 2011b.
6. Moon, I., M. Lee, J. Ryu, and M. Mun, "Intelligent robotic wheelchair with EMG-, Gesture-, and Voice-based interfaces," *Proceedings of the lEEE/RSJ International Conference on Intelligent Robots and Systems, (IROS)*, IEEE 0-7803-7860-1, Vol. 3, 2453–3458, Las Vegas, NV, Oct. 27–31, 2003.
7. Ang, L. B. P., E. F. Belen, R. A. Bernardo, E. R. Boongaling, G. H. Briones, and J. B. Coronel, "Facial expression recognition through pattern analysis of facial muscle movements utilizing electromyogram sensors," *Proceedings of the TENCON IEEE Region 10 Conference*, IEEE 0-7803-8560-8, Vol. 3, 600–603, Chiang Mai, Thailand, Nov. 21–23, 2004.
8. Gibert, G., M. Pruzinec, T. Schultz, and K. Stevens, "Enhancement of human computer interaction with facial electromyographic sensors," *Proceeding of the 21st Annual Conference of the Australian Computer Human Interaction Special Interest Group on Design Open 247 OzCHI*, 1–4, ACM Press, Melborn, Australia, 2009.
9. Van den Broek, E. L., V. Lis'y, J. H. Janssen, J. H. D. M. Westerink, M. H. Schut, and K. Tuinenbreijer, "Affective man-machine interface: Unveiling human emotions through biosignals," *Biomedical Engineering Systems and Technologies: Communications in Computer and Information Science*, Vol. 52, Part 1, 21–47, Springer Verlag, Berlin, Germany, 2010.
10. Hamedi, M., I. M. Rezazadeh, and S. M. P. Firoozabadi, "Facial gesture recognition using two-channel biosensors configuration and fuzzy classifier: A pilot study," *Proceeding of the International Conference on Electrical, Control and Computer Engineering*, Pahang, Malaysia, Jun. 21–22, 2011.
11. Van Boxtel, A., "Facial EMG as a tool for inferring affective states," A. J. Spink, F. Grieco, O. Krips, L. Loijens, L. Noldus, and P. Zimmerman, Eds., *Proceedings of Measuring Behavior*, 104–108, Noldus Information Technology, Wageningen, Eindhoven, Netherlands, Aug. 24–27, 2010.
12. Rechy-Ramirez, E. J. and H. Hu, "Stages for developing control systems using EMG and EEG signals: A survey," Technical Report, CES-513, ISSN 1744-8050, School of Computer Science and Electronic Engineering, University of Essex, 2011.

Standalone ECG Monitoring System Using Digital Signal Processing Hardware

Goh Chun Seng, Sh-Hussain Salleh, Arief R. Harris, J. M. Najeb, and I. Kamarulafizam
Center for Biomedical Engineering, Transport Research Alliance
Universiti Teknologi Malaysia, Johor, Malaysia

Abstract— This paper describes the implementation of low cost standalone Digital Signal Processing (DSP) hardware for ECG monitoring in order to assist physician or cardiologist to carry out their visual observation in ECG monitoring. The visual observation is in real time, where the acquired ECG from the subject can be seen on the graphic LCD and it is important to ensure the signal is stable and consistent before the pre-recording session take place which would help the cardiologist's or physician's in analysis and diagnosis, accurately. The design of the DSP hardware based stand alone system are divided into three hardware units, first the digital signal processor with memory unit, second is the signal monitoring displays unit and third is analog front end unit. Firmware development in this system design is to attach each hardware unit to perform specific functions in carrying out operation on the stand alone system. The advantages of this system are the ability to run in stand-alone operation and as well as eligibility of updating on board pre-program algorithm for ECG analysis which existing ECG monitoring equipment are lacking, which means that this stand alone system could be programmed to suit a particular need.

1. INTRODUCTION

Non-invasive ECG approach has become the standard practice in clinical environment, after it is first made known by Eithoven [1]. Then, the discovery of ECG brings forward the opportunities for further research and development. So, in year 1947, modern ECG recording machine is introduce by Norman Jeff holter, later it is called Holter Ambulatory Electrocardiography [2]. Hence, along the path it gave birth to the ECG recording system which is populated by the invention of microprocessor in the later years. Indeed, ECG recording trend is turning a new leaf when microprocessor is embedded with electronic gadget in various hardware platforms, which allows full assessment to the collected data of electrocardiography [3]. However, in the early microprocessor system, the ECG signal is compressed while the system is in recording mode, then it is stored and the analysis is done on computer [4]. After that, ECG recording also have had evolved throughout the decades with the growth of technology in signal processing [5]. Later on, the impact of the signal processing achievements created a paradigm shift and alters the being of hardware computation when mathematically algorithms are applied in signal analysis.

Since then, the algorithmic activities show favors in non-computer dependant operation with efficiency in numerical processing. Then, it is followed by the influential of its outcome which is ushering the microprocessor step into higher stage by means of doing solo numerical computing. Follow by the pro-active influent, leads the conventional microprocessor to cushion the successor which is succeeded with a greater benefit of achievements when the digital signal processor (DSPs) is introduced and in promotion in year 1971. Thus, the DSPs offers built in and integrated with mathematical capabilities and proficiency of numeric functional [6] as compared with others available non-DSP terms in the general microprocessor. Nevertheless, it is also capable of doing "on chip" analysis, which is, including real time signal processing [7]. Therefore, the advantages of DSPs had open door to enable ECG analysis to be done in real time processing instead of recording and stored for later analysis.

The introduction of DSP processor had brought forward realization for integrating DSP board to computer based for real time ECG analysis [8]. One of the common hardware tools involved ECG in computing is the plug n play DAQ card [9]. In this system, add on hardware such as data acquisition card is required for this purpose. Where the dependency for plug in data acquisition card in the computer itself required software development, such as firmware and application software is necessary to establish communication link with the connected card. Those integrated data acquisition card with software application can provide a magnificent outcome, but lack of mobility, expensive and computer dependant. But a custom build Printed Circuit Board (PCB) with specialty electronics design are more prefer to use in stand alone operation for specific task [10].

However, few drawbacks of connectivity to computer itself are power dissipation, bulky, complexity and waste of resources to perform only single task purpose [11, 12].

By adapting the idea of custom build and stand alone for specific task operation as suggesting in [10–12], we propose an idea based on single board system design to meet the requirements of simplicity, low power consumption, flexibility and low cost. The proposed prototype design is able for standalone ECG monitoring system using digital signal processing hardware. Thus, it provides an effective, specific operation as independence signal processing unit to process the acquire ECG in this paper.

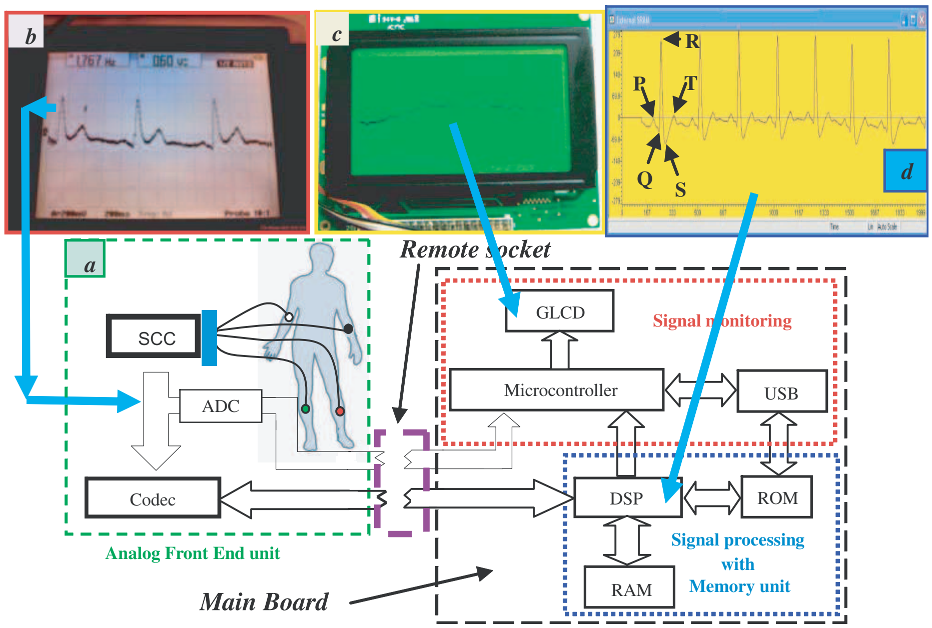

Figure 1: Block diagram of prototype DSP hardware stand alone system with the tapped ECG is checked with oscilloscope and display on the graphic LCD. The tap ECG also captured by the DSP processor and displayed on the window at Code Composer 3x/4x.

2. HARDWARE PLATFORM

Figure 1 shows the DSP hardware based stand alone system design is divided into three functional units. The solid lines with arrows symbol represent the flow of data and information. The dashed lines with green, red and blue color represent the functional hardware units. The DSP hardware consists of three functional hardware units, they are;

a) **Signal processing with memory unit;** this unit provides signal altering, changing, resolving, modification, storage and communication protocol. The mains components are floating point DSP processor (TMS320VC33), Electrical Erasable Programmable Read only Memory — EEPROM (CAT28LV64W) and Static Random Access Memory — SRAM (CY7C1041DV33). The SRAM memory is expandable in both the data bus and address bus width.

b) **Signal monitoring displays unit**; this unit provides input signal observation through the input peripherals. In this unit, the microcontroller, PIC18F452 is configured to interact with graphical liquid crystal displays (GLCD). The ADC chip, ADC0820 received input from the tap ECG signal through signal conditioning circuit (SCC), then the converted ADC data is sent to the output port (DB0 to DB7) of ADC0820.

c) **Analog front End unit**; this unit provides interaction through peripherals connectivity with the real world environment. The peripherals such as in Figure 1 shows that the ECG is delivered to the main board through the custom build AFE device. This AFE input consists of; i) Signal conditioning circuitry (SCC), ii) Codec chip, PCM3003 and iii) Analog to digital converter chip set, ADC0820.

In this DSP hardware design, is utilizing two processors by means of putting a single DSP processor (lack of tasks' oriented but capable of mathematical and algorithm executions) and a single microcontroller (performs best in tasking, but lack of DSP terms) into one system board. Therefore, this will provide separate traffic management for tasking and signal processing without

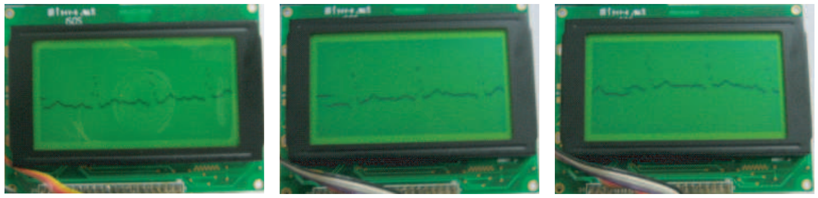

(a) Test Subject: Resting in static condition

(b) Test Subject: Resting in non-static condition

Figure 2: Real time ECG observation from test subject is captured and displayed on the graphic LCD.

over-loading each processor's work load. This approach is depicted in Figure 1, the microcontroller is maintaining to display the tap ECG from ADC chip to the graphic LCD and the DSP processor is focused on reading the tapped ECG signal from the codec chip. However, the Universal Serial Bus (USB) in this DSP hardware design is for downloading the ECG analysis algorithm to the ROM and it is also use for power up the DSP hardware.

3. RESULTS

The operation results for Analog Front End (AFE) unit interface with volunteer subject as shown in Figure 1(a), Figure 1(b) and Figure 1(c) respectively. Figure 1(a) shows the tapped ECG from test subject, it is tapped from the Lead II formation on human body skin surface with four disposable electrodes placed on the right arm (white color), left arm (black color), right leg (green color) and left leg (red color), all the color code were referred to electrodes placement on human body [13]. Figure 1(b) shows the oscilloscope screen display from the output of AFE, this means that it is functional. Then, in Figure 1(c) shows that the output from AFE is able to read by microcontroller, PIC18F452 and display the tap ECG to the Graphic LCD.

Emulator XDS510PP (PLUS) from Spectrum Digital Incorporated was attached to on board JTAG connector at TMS320VC33 by communicate through Code Composer 3x/4x in order to visualized the tap ECG at the graphical windows as depicted in Figure 1(d). The capacity of the graphical windows can only display 2000 data. As a result, 7 cycles of tap ECG data were captured in approximately 7 second, all the captured signal were labeled with its P, Q, R, S and T waves. These collected tapped ECG data are temporary stored in the external RAM as shown in Figure 1(d). Following, in Figure 2 shows the ECG signals monitoring for volunteer subject either resting in static condition or non static condition.

4. DISCUSSION AND FURTHER WORK

In common, the graphic LCD has become the stepping stone along the path for portable device development and it is important for heart rhythm observation on particular subject with routine heart diagnosis. Therefore, the usage of graphic LCD in Figure 2 has significant impact for real time ECG observation; where this will give better preparation and signal stability during pre-recording ECG session begin on the particular subject. Since, with the proposed real time ECG observation, good ECG recording will lead to accurate ECG analysis and diagnosis significantly.

5. CONCLUSION

We have presented the DSP hardware based stand alone system design by using digital signal processor as the core processing unit. The DSP hardware is able to visualize the tap ECG on the graphical LCD (GLCD) as well as the digital signal processor is able to capture the tap ECG as shown on the graphical window in Code Composer 3x/4x. Nevertheless, this system design has laid the ground work for stand alone operation in ECG monitoring purposes by using digital signal processor for real time signal processing. The hardware system is ready to run any processing algorithm related to ECG. The algorithm can be continuously changed and tested to improve system performance and efficiency.

REFERENCES

1. Dijk, J. and B. Van Loon, "Scanning our past from the Netherlands: The electrocardiogram centennial: Willem Einthoven (1860–1927)," *Proceeding of the IEEE*, Vol. 94, No. 12, 2182–2185, 2006.
2. Barold, S. and S. J. Norman, ""Jeff" Holter — Father of ambulatory ECG monitoring," *Journal of Interventional Cardiac Electrophysiology*, Vol. 14, No. 2, 117–118, Springer, 2005.
3. Kara, S., S. Kemaloğlu, and Ş. Kirbaş, "Low-cost compact ECG with graphic LCD and phonocardiogram system design," *Journal of Medical System*, Vol. 30, No. 3, 205–209, Springer, 2006.
4. Watts, M. P. and D. B. Shoat, "Trends in electrocardiograph design," *Journal of the Institution of Electronic and Radio Engineers*, Vol. 57, No. 4, 140–150, IEEE, 1987.
5. Sandham, W., D. Hamilton, P. Laguna, and M. Cohen, "Advances in electrocardiogram signal processing and analysis," *Journal on Advances in Signal Processing*, Vol. 2007, No. 2007, 1–5, Hindawi Publishing Corporation, 2007.
6. Frantz, G., "The DSP and its impact on technology," *Processor Design: System-on-Chip Computing for ASICs and FPGAs*, 101–119, Jari Nurmi, Springer, 2007.
7. Gorup, Ž., D. Štajer, and M. Noč, "Signal analisis system for optimal timing of electrical defibrillation," *10th Mediterranean Electrotechnical Conference, MELECON 2000*, 694–697, 2000.
8. Silva, J., J. R. Caldera, and G. Passariello, "Dsp application for QRS detection, alignment and averaging In ECG signal," *Proceedings of the 1995 First IEEE International Caracas Conference On Digital Devices, Circuits and Systems*, 149–153, 1995.
9. Low, Y. F., I. Binti Mustaffa, N. Binti Mohd Saad, and A. H. Bin Hamidon, "Development of PC-based ECG monitoring system," *4th Student Conference on Research and Development*, 66–69, Selangor, June 27–28, 2006.
10. Trusov, A. A., I. Chepurko, A. R. Schofield, and A. M. Shkel. "A standalone programmable signal processing unit for versatile characterization of MEMS gyroscopes," *IEEE Conferences*, 2007.
11. Tay, E. J., C. F. Lim, and Hemalatha, "DoIP interfacer system: A low-cost alternative to computer for basic network communication in LAN environment," *Journal of Computer Science*, Vol. 5, No. 7, 471–475, 2009.
12. Ray, B., "PC Based Instrumentation versus standalone," *IEEE Conferences*, 1988.
13. Garvey, J. L., "ECG techniques and technologies," *Emergency Medicine Clinics of North America*, Vol. 24, No. 1, 209–225, Elsevier, 2005.

Heart Sound Analysis Using Hidden Markov Models

Hadrina Sh-Hussain, **Sh-Hussain Salleh**, **Tan Tian Swee**,
Ting Chee Ming, **Ahmad Kamarul Ariff**, **and I. Kamarulafizam**
Center for Biomedical Engineering (CBE), Transportation Research Alliance (TRA)
Universiti Teknologi Malaysia, Skudai, Johor 81310, Malaysia

Abstract— This paper purpose is the use of hidden markov models for automatic of heart sounds. Heart Sound is accompanied by both electricity activity and sound. The heart sound clues which can indicate heart murmurs. The heart is divided into 4 chambers. The pumping of the heart will have different effect on the 4 valves which are called aortic pulmonary and mitral valve. The first heart sound can be heard during the closure of the mitral and the tricuspid valve which the S_2 second heart sound due to the closure of the aortic and pulmonary valve. The sound heard is the aortic and pulmonary valve. The sound heard between the S_1 and S_2 is called the systolic murmurs while the sound from S_2 and S_1 is called diastolic murmurs. The raw signals have to be processed first and converted to some form of parametric representation. This parametric representation is further analysed and process to extracts its features.

1. INTRODUCTION

In Malaysia 25.4% of the population have been diagnosed with heart disease in 2010. They were Malaysian due hospitalized owing to cardiac condition compare in 2005 recorded 5,549 case of death [5]. In order to avoid this fearsome condition. Yearly physical examination is recommended. The doctors uses a stethoscope to access the activity of the heart sound. The heart is responsible for the main function of cardiovascular system such as pumping blood through the vast network to all of the tissues and organs of the body. In one loop, blood circulates between the heart and lungs (pulmonary circulation). In the other, blood circulates between the heart and the rest of the body (systemic circulation). These two loops interact to pump blood in a continuous circuit: heart to body, body to heart, heart to lungs, lungs to heart, and heart to body. The goal of this work is to apply hidden markov models for automatic auscultation of heart sound signals. Such device can be used in mostly in rural clinics. The experiment carried out in this paper shows how the proposed method can be are able to classify abnormal sound with high accuracy.

2. METHODOLOGY

The recording used Welch Allyn electronic stethoscope which was placed at the patient chest. The ECG electrode was attached to the left forearm, right forearm and to the left leg. The ECG signals is a non-invasive technique which measure the electrical activity of the heart. Figure 1(a) shows the placement of stethoscope and ECG electrodes for the sound and the electrical activity of the heart. In the acquisition stage both the ECG and the heart sound data are collected simultaneously as shown in. Figure 1(b) the heart sound is recorded using Wellch Allyn software with a 16 bit resolution.

The heart sound signals of patients who suffer heart valve disease were self-record with the assistance of cardiologists using an electronic stethoscope. During recording process, there few factors should be considered in order to obtain a good heart sound. A quiet room and environment is needed to eliminate the background noises.

The work is aimed to perform a Heart Murmur Analysis for detecting abnormalities in the heart sound. The proposed system can be used as a teaching tool with low cost analysis system and its user friendly. The system used mel-frequency cepstrum feature was used as the features for the heart sound. Finally hidden markov model was used to train and recognize the murmurs. The system later can be used by general practioners (GPs) to help in their decision on detecting heart murmurs. The electronic stethoscope was used and placed at the patient chest while ECG electrode was attached to patient's forearm.Ecg electrode are attach to left fore arm, right forearm and the to left leg. The heart sound signals were also taken Hospital Selayang, Malaysia.

HMM model are represented $\lambda = (A, B, \pi)$ in which A represent the state transition matrix, B represent the probability distribution of the observation, and π represents the initial state distribution, and a sequence of observation $O = \{o_1, o_2, \ldots, o_T\}$, classification is carried out by calculating the likelihood score of $P(O\,|\lambda)$ [15].

(a)

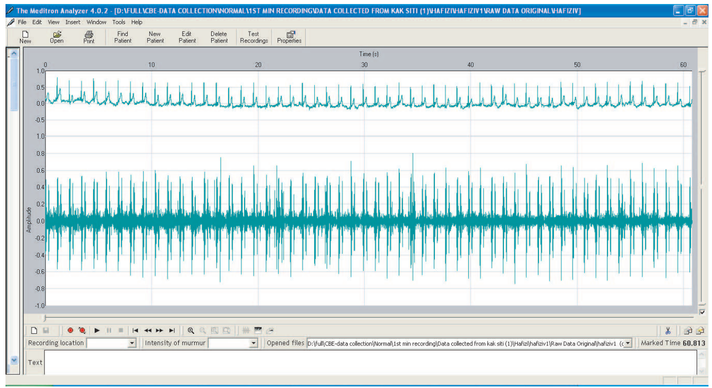

(b)

Figure 1: (a) shows the electronic stethoscope placed on the chest of the patient as well as ECG electrodes placed on the patient hands and leg for the measurement of the heart signals. (b) Normal heart sound with ECG.

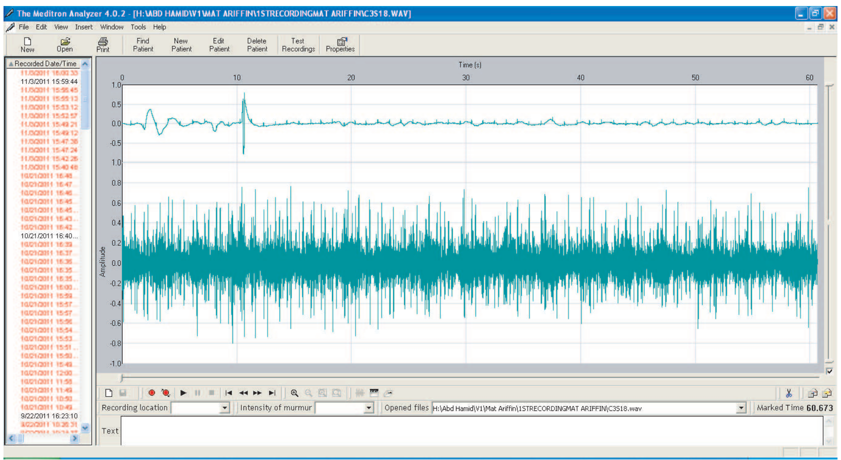

(a)

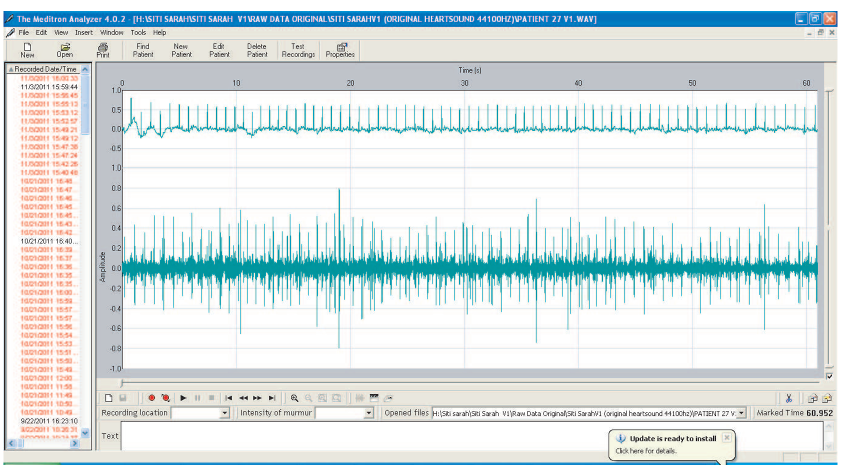

(b)

Figure 2: (a) Abnormal heart sound (Inferior wall and posterior wall infracted area noted but no scar tissue). (b) Abnormal heart sound (Mitral Valve prolapsed Hypokenatic of mid septal wall).

Figure 3 shows the procedure of training and classification to generate HMMs of the heart sound signals. Using the Baum-Welch algorithm with MFCC features obtained from different type of heart diseases is constructed. In the classification procedure, the MFCCs extracted from the test signals are applied to each HMM and calculate the likelihood. The model which gives the highest value is selected as the classification result.

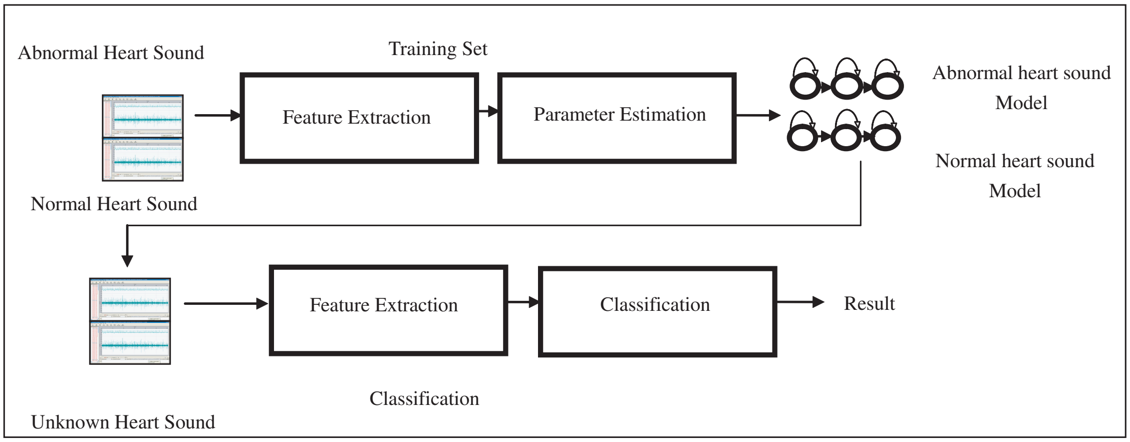

Figure 3: Block Diagram of HMM training and classification procedure.

Table 1: Number of gaussion mixture components.

No of Gaussion mixtures components					
	1	2	4	8	16
state 1	94%	98%	97%	95%	97%
state 2	88%	98%	95%	95%	99%
state 3	93%	94%	99%	98%	100%
state 4	99%	96%	96%	98%	99%
state 5	97%	99%	99%	100%	99%

Table 2: Number of gaussion mixture components.

Training	Normal		Abnormal	
1	50		50	
2	50		50	
3	40		50	
4	50		50	
5	50		50	
Total Cycle	240		250	
6	21		60	
7	32		34	
8	11		8	
9	11		38	
10	29		20	
Total Cycle	104		160	

3. RESULT AND DISCUSSION

Figure 3 shows the procedure of training and classification to generate HMMs of the heart sound signals. Using MFCC with 12 coeffients features obtained from the heart sound signals, each HMM corresponding to the specific heart disease is constructed. In this work, 754 manually segment heart sound cycle corresponding to 5 types of heart diseases such as mitral reguration, mitral valve prolapsed, diastolic dysfunction grade 2, systolic murmurs and tricuspid reguration. The training set for normal and abnormal cycles consist of 240 and 250 whereelse classification consists of 104 and 160 cycles as shown in Table 2. We carried out the comparative experiments with respect to different parameter values of analysis MFCC feature extraction, different number of HMM states and different of gaussion mixtures to investigate the influence of these factors on the classification performance. Table 1 shows the classification result with number of HMM state (S_1, S_2, S_3, S_4, S_5) and each row represent number of mixtures $(1, 2, 4, 8, 16)$. The best performance is achieved when the number of mixture model is set to 16 and 3 state. The best accuracy is 100% wherelse worst result is 42.86%.

By observing each table for each state shown the average calculation different gaussion mixture. Firstly observing one state, we can find 97% is the highest percentage, the two state shown 99%, three state shown 100%, while four state 99.56% and five state model 100%.

4. CONCLUSIONS

The goal of this study was develop a robust algorithm for segmentation heart sound into components using Hidden Markov Models. The detection of S_1 and S_2 in cardiac cycle is the first step towards characterizing murmurs and related heart diseases. In this paper, we have investigated the classification performance of HMM with MFCC features depending on the number of states. HMMs offers significant classification performance to model the sequential cardiological process.

ACKNOWLEDGMENT

This research project is supported by CBE (Center of Biomedical Engineering) at Universiti Teknologi Malaysia.

REFERENCES

1. Meikeng, Y., "Malaysian getting heart disease at younger age," *The Star*, 2, Oct. 26, 2009.
2. http://www.texasheartinstitute.org/HIC/Topics/Cond/murmur.cfm, 2010.
3. Debbal, S. M. and F. Bereksi-Reguig, "Graphic representation and analysis of the PCG signal using the continuous wavelet transform," *The Internat Journal of Bioengineering*, Vol. 2, No. 2, 2007.
4. Barschdorff, D., S. Ester, T. Dorsel, and E. Most, "Neural network based multi-sensor heart sound analysis," *Computers in Cardiology*, 303–306, Sep. 1990.
5. 1,940 maut setiap jam, *Berita Harian*, 1, Sep. 29, 2010.
6. Saha, G. and P. Kumar, "An efficient heart sound segmentation algorithm for cardiac diseases," *India Annual Conference, 2004, Proceedings of the IEEE INDICON*, 2004.
7. Tovar-Corona, B., M. D. Hind, et al., "Effects of respiration on heart sounds using time-frequency analysis," *Computers in Cardiology*, 2001.
8. Lessard, E., M. Glick, et al., "The patient with a heart murmur: Evaluation, assessment and dental consideration," *The Journal of the American Dental Association*, Vol. 136, No. 3, 347–356, 2005.
9. Nakamitsu, T., H. Shino, et al., "Detection and classification of systolic murmur using a neural network," *Proceedings of the 1996 Fifteenth Southern Biomedical Engineering Conference*, 1996.
10. Leedomwong, T. and P. Woraratsoontorn,. "Wavelet entropy detection of heart sounds.," *Proceeding of European Computing Conference*, N. Matorakis, V. Mladennov, and V. T. Kontargyri, Springer, US.27:737-744, 2009.
11. Lehner, R. J. and R. M. Rangayyan, "A three channel microcomputer system for segmentationand characterization of the phonocardiogram," *IEEE Trans. on Biomedical Eng.*, Vol. 34, 485-9, 1987.
12. Iwata, A., N. Ishii, and N. Suzumura, "Algorithm for detection the frist heart sound by spectraltracking," *Med. & Bio. Eng. & Comp.*, 19–26, 1980.
13. Rabiner, L. and B. H. Juang, *Fundamentals of Speech Recognition*, Prentice-Hall, Inc, New Jersey, 1993.
14. Tian-Swee, T., L. Helbin, et al., "Application of Malay speech technology in Malay speech therapy assistance tools," *International Conference on Intelligent and Advanced Systems, 2007. ICIAS 2007*, 2007.

High-Q Transmission Line Stub Resonators Using Interdigital Capacitor Loading for MMIC Applications

T. Katayose[1], **M. Okunogi**[1], **K. Hosoya**[2], **and S. Tanaka**[1]

[1]Shibaura Institute of Technology, Japan
[2]NEC Corporation, Japan

Abstract— Model based design method is presented to reduce the size of high-Q double stub resonators using interdigital capacitor loading. Compared to sophisticated method of transmission line length reduction in the literature, the proposed resonator configuration is compatible with standard GaAs MMIC process and the influence of capacitor loading on resonator characteristics can be minimized if properly designed based on the derived model. Measured results demonstrate successful reduction of the resonator size by 40–50%.

1. INTRODUCTION

Microstrip stub resonators are critical components for MMIC low phase-noise oscillators. It has been shown that by using double open stubs with $\lambda/4 \pm \delta$ length ($\delta \ll \lambda/4$) high-Q can be obtained with well-controlled coupling coefficient which is determined by δ/λ [1]. The large footprint of the resonator, however, hinders chip size shrinking of the MMIC for low cost production. While slow-wave structure is one approach to miniaturizing passive components with long transmission lines (TLs) [2], the complicated structure and the increased loss do not necessarily make it the optimum solution for high-Q resonators.

To cope with these issues, we propose to reduce the size of stub resonators using interdigital capacitor (IDC) which is compatible with GaAs MMIC process. The basic concept of using external capacitors to reduce the size of TL resonator in the UHF bands was reported [3], but there are two major concerns that need be addressed in order to apply this method to the above-mentioned type of high-Q stub resonators in MMICs. First, the amount of capacitance required for sufficient reduction of the stub length may cause self-resonance in such high frequencies as in microwave bands. Second, the capacitor may affect the operating principle of the double stub resonators In this paper, we show the model for analyzing the effect of stub length reduction and discuss the simulated and measured characteristics of the resonator with successful stub length reduction.

2. DOUBLE STUBS RESONATORS

In a two-port resonator with matched source and load at the input and output, the loaded-Q (Q_L) is given as

$$Q_L = \frac{Q_u}{1 + 2\beta_c}, \tag{1}$$

where Q_u is unloaded-Q and β_c is the coupling between the resonator and external circuit. In MMIC low-phase noise oscillators using TL resonators, β_c must be carefully designed to become small enough because Q_u of TLs, such as microstrip lines (MSLs) is very limited. However, it is difficult to control such weak coupling, using capacitor coupling for instance, in a precise and reproducible manner. In our previous work [1], we proposed double stubs resonator with stub length of $\lambda/4 \pm \delta$, shown in Fig. 1(a). In this $\lambda/2$ resonator, theoretical expression for β_c was derived in approximate form [4] as:

$$\beta_c \cong \frac{2}{\alpha\lambda} \sin^2\left(2\pi\frac{\delta}{\lambda}\right), \tag{2}$$

where α is the attenuation constant of the MSL. This result indicates that small β_c can be obtained with good controllability by choosing appropriate δ ($\ll \lambda/4$). The reproducibility of the Q_L is ensured by direct coupling eliminating the need to use capacitors which are potential causes of Q_L variation in real production. Using the same analogy, it is expected that a combination of open-ended stub of length $\lambda/4 - \delta$ and short-ended stub of length δ, as shown in Fig. 1(b), should show high-Q characteristics with $\lambda/4$ resonating mode when δ is sufficiently small compared to $\lambda/4$. It can be shown that β_c for the $(\lambda/4 - \delta, \delta)$ double stub resonator is similar to (1) except that it is has a factor of 4 instead of 2.

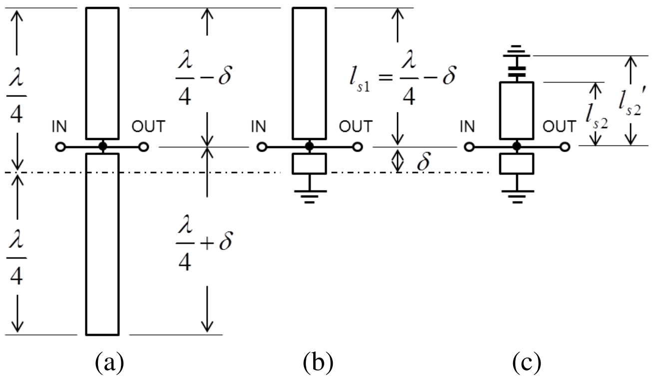

Figure 1: Configurations for double stubs resonators. (a) $\lambda/4 \pm \delta$ double stubs, (b) $(\lambda/4 - \delta, \delta)$ double stubs, (c) double stubs with capacitance loading.

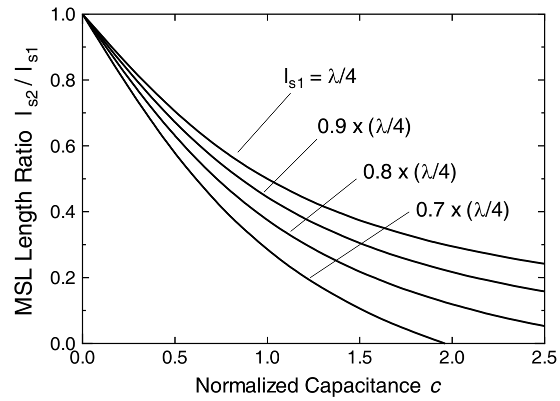

Figure 2: Stub length reduction ratio l_{s2}/l_{s1} versus normalized capacitance.

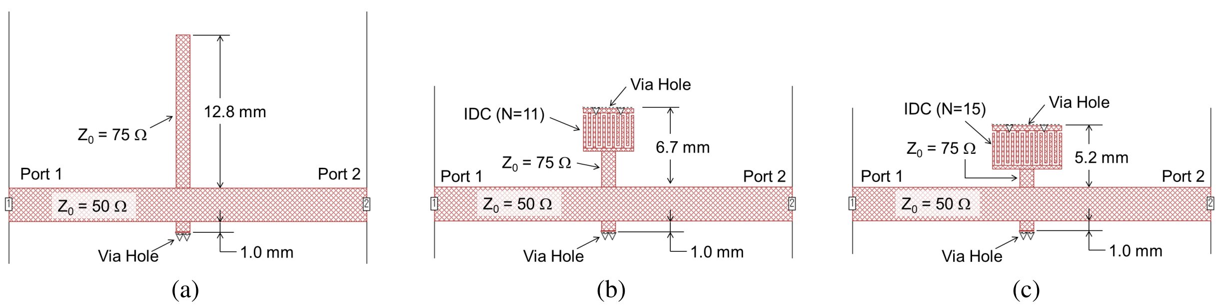

Figure 3: Layout of $(\lambda/4 - \delta, \delta)$ double stub resonators (a) without and (b) (c) with IDC loading.

3. DESIGN MODEL

While the $(\lambda/4 - \delta, \delta)$ double stub resonator is half in size compared to $\lambda/4 \pm \delta$ counterpart, the near quarter wave length TL may still take up large chip area. To further reduce the size of the resonator, we studied to use capacitor loading at the end of the open stub. Instead of using external capacitor [3], we propose to load the open end of the stub with IDC

Figure 2 illustrates schematics of $(\lambda/4 - \delta, \delta)$ double stub resonators before and after capacitor loading. Assuming lossless TL, the admittances of the upper side of the stubs in Fig. 2 are

$$Y_1 = j\,Y_0 \tan\left(\beta l_{s1}\right), \tag{3}$$

$$Y_2 = Y_0 \frac{Z_0 + j\left(1/j\omega C\right)\tan\left(\beta l_{s2}\right)}{\left(1/j\omega C\right) + jZ_0 \tan\left(\beta l_{s2}\right)}, \tag{4}$$

for before and after loading of capacitance C, respectively. Here, β is propagation constant, Y_0 $(= 1/Z_0)$ is characteristic admittance of the stub TLs, l_{s1} and l_{s2} are the length of each TLs. From (3) and (4) it follows that in order for the two admittance values to be equal, the relation

$$\tan\left(\beta l_{s1}\right) = \frac{c + \tan\left(\beta l_{s2}\right)}{1 - c\tan\left(\beta l_{s2}\right)}, \tag{5a}$$

$$c = \omega\, C\, Z_0, \tag{5b}$$

must hold, where c is dimensionless capacitance of C normalized with respect to $1/\omega Z_0$.

Figure 3 plots the ratio (l_{s2}/l_{s1}) for various c values calculated using (5). It can be seen that in overall the length of the open stub decreases with increasing capacitance. Although the ratio, l_{s2}/l_{s1}, levels off at modest value if l_{s1} is close to $\lambda/4$, which is the case with the type of resonator of our interest, l_{s2}/l_{s1} of less than 0.5 is still feasible. Equation (5a) also indicates that it is not the absolute value of capacitance C but the normalized capacitance (5b) that determines the stub length ratio l_{s2}/l_{s1}. Accordingly, by using high characteristics impedance for the stub TL, one can save the capacitance to achieve certain l_{s2}/l_{s1} ratio of design goal, which is important to suppress self-resonance often observed in IDCs with large number of electrode fingers.

4. RESULTS

Based on the above model, resonant characteristics for $(\lambda/4 - \delta, \delta)$ double stub resonators using MSLs on FR4 substrate with thickness of 1.6 mm were designed using EM simulator (Sonnet em). The resonant frequency was 2.5 GHz. The dimensions of the IDC were 2.7, 0.2 and 0.2 mm for the length, width and spacing of the electrode fingers, respectively. Two types of resonators with different characteristic impedance for the stubs ($Z_0 = 50\,\Omega$ and $75\,\Omega$) were compared, while the main TLs were matched to $50\,\Omega$ ports. Typical design layouts of the resonators using stubs with $Z_0 = 75\,\Omega$ are shown in Fig. 3. The open stub lengths without capacitor loading were 11.9 mm and 12.8 mm for $Z_0 = 50\,\Omega$ and $75\,\Omega$, respectively, while the short stub length was fixed at 1.0 mm. In experiments, S-parameters were measured from 0 to 6 GHz using network analyzer (Agilent 8753ES).

Figure 4 plots the effective stub length l'_{s2} before and after capacitor loading for various number of electrode fingers (N). Here, the effective stub length after capacitor loading is defined as l_{s2} plus the IDC size, as shown in Fig. 1(c). As can be seen, although the open stub length before capacitor loading is longer for $Z_0 = 75\,\Omega$ than for $Z_0 = 50\,\Omega$, the stub length in the former case decreases faster with the same increasing number of N. As a result, three to four less number of electrode fingers is required to reduce the effective stub length to a certain level for $Z_0 = 75\,\Omega$ stubs compared with $Z_0 = 50\,\Omega$ stubs. For example, with $Z_0 = 75\,\Omega$ and $N = 11$, l'_{s2} was 6.7 mm (44% reduction with respect to 11.9 mm) without self-resonance seen below 6 GHz. To obtain the same l'_{s2} with $Z_0 = 50\,\Omega$, electrode finger number of $N = 15$ is necessary in which case the self-resonance (shown in the graph) is seen near 5.6 GHz.

Figure 5 compares simulated and measured S-parameters for $(\lambda/4 - \delta, \delta)$ double stub resonators using $Z_0 = 75\,\Omega$ stubs, before and after capacitor loading with $N = 11$ and 15. The agreement between simulation and measurement is relatively good including the self-resonance seen in Fig. 5(c). It can be seen that while the resonant frequency does not change with IDC loading, the attenuation pole slightly shifts to higher frequency with increased capacitor loading, thereby affecting the Q_L of the resonator to some extent Further analysis revealed that the influence of capacitor loading on Q_L can be significant if δ is not small enough, but for our purpose of using small δ for high Q_L the influence is minimum, the detail of which will be discussed elsewhere.

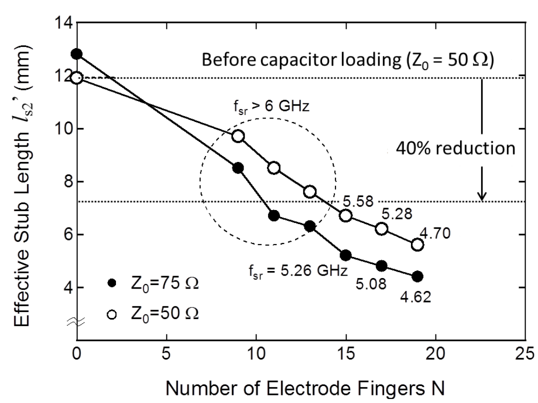

Figure 4: Plots of effective stub length for various number of electrode fingers.

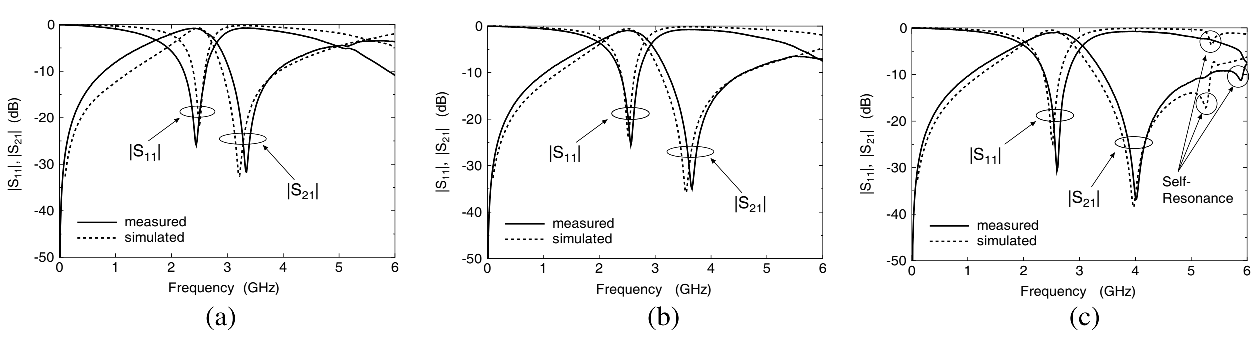

Figure 5: Simulated and measured $|S_{11}|$ and $|S_{21}|$ response for $(\lambda/4 - \delta, \delta)$ double stub resonators of which the layouts are shown in Fig. 4.

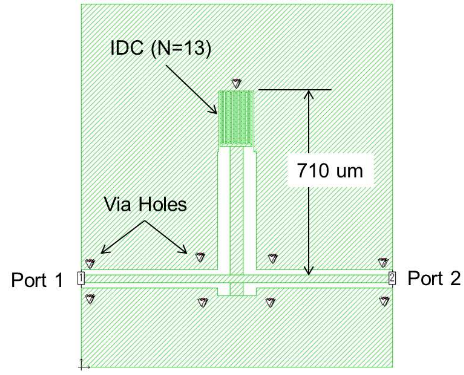

Figure 6: Layout of $(\lambda/4-\delta,\delta)$ double stub resonators ($f_0 = 18\,\text{GHz}$) using grounded CPW in GaAs MMIC process. The open stub length before capacitor loading was 1270 μm.

Use of MSL for $(\lambda/4-\delta,\delta)$ double stub resonators with capacitor loading is somewhat cumbersome because both ends of the stub must be shorted to the ground using via holes, in which case the via hole pads hinder reduction of the total resonator size. In this sense, CPW is more suitable for the type of resonators presented in this work. Fig. 6 shows such example of a resonator layout designed using grounded CPW TLs in GaAs MMIC process for 18 GHz applications. The substrate thickness was 100 μm and the dimensions of the IDC were 200, 5 and 5 μm for the length, width and spacing of the electrode fingers, respectively. No via holes are used for ground shortening the stubs or capacitors but only for suppressing parasitic modes in grounded CPW structure.

5. CONCLUSIONS

We have discussed design method of reducing the size of $(\lambda/4-\delta,\delta)$ double stub resonators using IDC loading. In spite of the simple approach, the method proves successful with 40–50% reduction of resonator size if δ is small enough to ensure that the capacitor does not affect the high-Q performance of this type of resonators. While the major results demonstrated in this paper used MSLs, CPW-based design is most suited for future MMIC applications.

REFERENCES

1. Hosoya, K., S. Tanaka, Y. Amamiya, T. Niwa, and H. Shimawaki, "A low phase noise 18-GHz HBT oscillator utilizing a $(\lambda/4\pm\delta)$ open stubs resonator," *Asia Pacific Microwave Conference Digest*, Vol. 1, 64–67, 1999.
2. Yun, Y., K.-S Lee, C.-R. Kim, K.-M. Kim, and J.-W. Jung, "Basic RF characteristics of the microstrip line employing periodically perforated ground metal and its application to highly miniaturized on-chip passive components on GaAs MMIC," *IEEE Trans. Microwave Theory and Techniques*, Vol. 54, No. 10, 3805–3817, 2006.
3. Henkes, D. D., "Designing short high Q resonators," *Microwaves & RF*, 75–109, Dec. 2003.
4. Hosoya, K., S. Tanaka, Y. Amamiya, T. Niwa, H. Shimawaki, and K. Honjo, "RF HBT oscillators with low-phase noise and high-power performance utilizing a $(\lambda/4\pm\delta)$ open-stubs resonator," *IEEE Trans. Circuit and Systems — I*, Vol. 53, No. 8, 1670–1682, 2006.

Spatial Change of Normalized Radar Cross Section of Ocean Surface for HF Ocean Surface Radar due to the Wave-current Interaction Around Eddy

A. Nadai
National Institute of Information and Communications Technology, Japan

Abstract— The influence of wave-current interaction on the current measurement of HF ocean surface radar (HFOSR) is analyzed by a simulation of the Doppler velocity spectra of the first-order echo. The Doppler velocity spectra is a product of the spatial integration of the radial velocity weighted by the radar sensitivity and the normalized radar cross section (NRCS). As a result of the wavenumber change due to the wave-current interaction and the extension of the wave packet, the NRCS distribution becomes non-uniform. The artificial component is produced around the center of the current phenomena in the simulated radial velocity field because the non-uniformity of the NRCS distribution distorts the spectral shape of the first-order echo. The artificial component flows in the opposite direction of the propagation of the causal ocean waves. The intensity of the artificial component depends on the spatial scale ratio of the radar sensitivity distribution to the current phenomenon. In addition, the spatial averaging effect caused by the radar sensitivity distribution leads the antisymmetric component of the radial velocity difference, which weakens the intensity of the simulated current phenomena.

1. INTRODUCTION

The high-frequency ocean surface radar (HFOSR) is a powerful instrument for measuring the distribution of the radial components of the ocean's surface current over a wide area, in a short amount of time. The principle of radial velocity measurement using HFOSR was established by Barrick [1], Barrick et al. [2]. The multi-site HFOSR system, which consists of two or more radars separated by space, can map ocean surface current vectors using the radial current velocities measured by each radar Barrick et al. [3].

The measurement of the radial components of ocean surface currents using HFOSR is based on the electro-magnetic backscattering from ocean surface waves having one-half the wavelength of the radar wave. The scattering signals cause two strong peaks, called the first-order echoes, in the Doppler spectra of backscattered signal, because these ocean waves satisfy the Bragg resonant condition. Two strong first-order echoes appear as sharp peaks near the Doppler frequencies $\pm f_B$, corresponding to the phase velocities of causal ocean waves on still water. The difference in Doppler frequencies corresponds to the radial current velocity, because the Doppler frequencies of the first-order echoes correspond to the sum of the phase velocities of causal ocean waves on still water and the radial component of the water movement.

The first-order echoes change their spectral shapes with time and space. Heron [4] pointed out the relationship between the broadening of the first-order echo and the spatial change of currents in a radar target cell measured by current meters. Nadai [5] reported the relationship between the broadening of the first-order echo and the spatial change of ocean currents around the eddy on the shear front, between the Kuroshio and coastal region. In this observation, the first-order echoes were not only broadening but also splitting. The ocean area showing the widely broadening and splitting first-order echo agrees with the eddy region, in where the spatial change of current is strong. In Nadai's [6] work, the relation between the broadening of the first-order echo and the current field is analyzed by simulating the radial current velocity spectra, taking into account the spatial distribution of radar sensitivity. However, the difference in spectral shapes between the two first-order echoes is unexplainable with this approach.

The Doppler spectra of the backscattering signal depends not only on the spatial distributions of the radial component of the ocean currents and the radar sensitivity, but also on that of the normalized radar cross section (NRCS). The local value of the NRCS depends on the local spectral density of ocean waves, which is influenced by ocean currents due to the wave-current interaction. For this reason, to discuss the relationship between the spectral shape of the first-order echo and the ocean currents, the spatial distribution of NRCS has to be calculated based on the local spectral density of the ocean waves causing it, which is influenced by the wave-current interaction.

In this paper, the influence of the wave-current interaction on the current measurement by HFOSR is analyzed by numerical simulation. First, the initial parameters of causal ocean waves before being influenced by the wave-current interaction are simulated by backward time integration of the ray equations. Next, the spatial distribution of NRCS of the first-order echo is calculated from the local spectral density of the causal ocean waves. Finally based on the simulated Doppler velocity spectra of the first-order echo using the spatial distributions of the NRCS and the radar sensitivity, the influence of wave-current interaction on the current measurement of HFOSR is discussed.

2. DOPPLER SPECTRA OF FIRST-ORDER ECHO OVER NON-UNIFORM CURRENT FIELD

2.1. HF Backscattering Spectra

The HF backscattering spectra from the ocean's surface are obtained by the surface integration of the radar equation. The attenuation of the radar waves by scattering on the propagation path is assumed to be negligible. When the radar located at the position of $\mathbf{r}_r$ transmits the radar wave with a wavenumber of k_t, the Doppler velocity spectrum P_r of the backscattering signal from a certain area on the ocean's surface centered at $\mathbf{r}_t$ is written with the assumption that the target distance is much larger than the spatial scale of the radar sensitivity distribution, as follows:

$$P_r(v_D, k_t, \mathbf{r}_t) = \frac{P_t}{16\pi {k_t}^2 |\mathbf{r}|^4} \int_{S'} G(\mathbf{r}')\sigma^0(v_D, \mathbf{k}_t, \mathbf{r}')d\mathbf{r}', \text{ and} \tag{1}$$

$$\mathbf{r} = \mathbf{r}_t - \mathbf{r}_r, \tag{2}$$

where σ^0, P_t and G represent the NRCS, the transmission power and the radar sensitivity, respectively.

2.2. Normalized Radar Cross Section of First-order Echo

The first-order echoes are the products of Bragg resonant backscattering. Assuming the incident angle for HFOSR using a ground wave as a right angle, the Bragg resonant condition for the incident radar wave with a wavenumber vector of $\mathbf{k}_t$, is satisfied by the ocean waves with a wavenumber vector of $\mathbf{k}_B^{\pm} = \pm 2\mathbf{k}_t$, where the superscripts $^+$ and $^-$ represent the directions of the wave propagation: receding and approaching to the radar, respectively.

Barrick [1] analyzed the NRCS of the first-order echo as a function of the Doppler frequency. The NRCS σ^0 of the first-order echo for the vertically polarized radar wave with a wavenumber vector of $\mathbf{k}_t$ is described as a function of the Doppler velocity as follows:

$$\sigma^0(v_D, \mathbf{k}_t) = 64\pi|\mathbf{k}_t|^4 \left\{ S\left(\mathbf{k}_B^+\right)\delta\left(v_D - v_R\left(\mathbf{k}_B^+\right)\right) + S\left(\mathbf{k}_B^-\right)\delta\left(v_D - v_R\left(\mathbf{k}_B^-\right)\right)\right\}, \tag{3}$$

where $S(\mathbf{k})$ is the spectral density of ocean waves with a wavenumber vector of $\mathbf{k}$.

The Doppler velocity of ocean waves is the sum of the phase velocity of ocean waves causing the first-order echo and the radial component of the currents. The phase velocity C_p of the ocean waves is determined by the dispersion relation. The radial component v_r of currents is the projection of current vector $\mathbf{V}$ on the line of sight of radar $\mathbf{r}$. As a result, the Doppler velocities v_R of ocean waves with wavenumber vectors of $\mathbf{k}_B^{\pm}$ are described as:

$$v_R\left(\mathbf{k}_B^{\pm}\right) = C_p\left(\mathbf{k}_B^{\pm}\right) + v_r = \pm\sqrt{\frac{g}{|\mathbf{k}_B|}} + \mathbf{V}\cdot\frac{\mathbf{r}}{|\mathbf{r}|}, \tag{4}$$

where g is the acceleration of gravity.

The contribution of the receding and approaching ocean waves on the NRCS of the first-order echo can be separated into σ^{0+} and σ^{0-}, respectively. Then, the spectral shape $P'^{\pm}$ of each first-order echo is described as a function of the discrepancy of Doppler velocity v'_D from the phase velocity of causal ocean waves as

$$P'^{\pm}\left(v'_D, k_t, \mathbf{r}\right) = 64\pi|\mathbf{k}_t|^4 \int_{S'} G\left(\mathbf{r}'\right) S\left(\mathbf{k}_B^{\pm}\right)\delta\left(v'_D - v_r\left(\mathbf{r}'\right)\right)d\mathbf{r}'. \tag{5}$$

2.3. Local Spectral Density of Ocean Waves

When the current field is not uniform, the current field influences the ocean waves through the wave-current interaction. The basic assumptions of the wave-current interaction model are that the ocean waves can be described within the framework of the linear wave theory and that the relative change in the current velocity over the wavelength and the wave period is small. In the presence of current, the governing equation for the wave energy density $E(\mathbf{k})$ can be written as Phillips [7]

$$\frac{\partial}{\partial t}\left(\frac{E(\mathbf{k})}{n}\right)+(\mathbf{V}+\mathbf{C}_g)\cdot\nabla\left(\frac{E(\mathbf{k})}{n}\right)=0 \tag{6}$$

where $\mathbf{k}$ is the wavenumber vector, $n=\sqrt{g|\mathbf{k}|}$ is the intrinsic frequency of waves, $\mathbf{C}_g=dn/dk$ is the group velocity of the ocean wave, and $\mathbf{V}$ is the current velocity. Equation (6) is equivalent to a statement that the wave action density $E(\mathbf{k})/n$ is conserved along the ray paths.

The spectral density of ocean waves is equal to the wave energy density per unit squared. Assuming the imaginary extent A of a monochromatic wave packet, the wave action density can be written using the spectral density S of ocean waves as:

$$\frac{E(\mathbf{k})}{n}=\frac{S(\mathbf{k})A}{n}=\frac{S(\mathbf{k})A}{\sqrt{g|\mathbf{k}|}}. \tag{7}$$

Equation (7) shows that the local spectral density S of the wave packet can be calculated by using the wavenumber vector $\mathbf{k}$ and the imaginary extent A along the ray path, by the conservation law of wave action.

The wavenumber vector $\mathbf{k}$ along the ray paths are obtained by integrating the following ray equations and dispersion relation Liu et al. [8]:

$$\frac{d\mathbf{x}}{dt}=\mathbf{V}+\mathbf{C}_g, \tag{8}$$

$$\frac{d\mathbf{k}}{dt}=-\mathbf{k}\cdot(\nabla\mathbf{V}), \tag{9}$$

$$n^2=g|\mathbf{k}|, \tag{10}$$

where $\mathbf{x}$ is the location of the wave packet. The imaginary extent A is, moreover, obtained by the integration of the divergence of the current field along the ray path:

$$\frac{dA}{dt}=(\nabla\cdot\mathbf{V})A. \tag{11}$$

These equations show that the wavenumber vector and imaginary extent of the wave packet are influenced by the spatial change of the current field.

2.4. Influence of Wave-current Interaction on NRCS

The NRCS of the first-order echo is a function of the local spectral density of causal ocean waves at the moment of radar observation. When the causal wave packet with a wavenumber vector of $\mathbf{k}_B$ has the imaginary extent of A_B at the moment of the radar observation, the initial wavenumber vector $\mathbf{k}_I$ and the initial imaginary extent A_I before being influenced by the wave-current interaction are simulated by the backward time integration. Then, the local spectral density $S_L(\mathbf{k}_B)$ of the causal ocean waves is written as:

$$S_L(\mathbf{k}_B)=\frac{A_I}{A_B}\left(\frac{|\mathbf{k}_B|}{|\mathbf{k}_I|}\right)^{\frac{1}{2}}S_B(\mathbf{k}_I), \tag{12}$$

where S_B is the background spectral density of ocean waves.

The change $\Delta\sigma$ of the NRCS by the wave-current interaction is described as:

$$\Delta\sigma=\frac{S_L(\mathbf{k}_B)}{S_B(\mathbf{k}_B)}=\frac{A_I}{A_B}\left(\frac{|\mathbf{k}_B|}{|\mathbf{k}_I|}\right)^{\frac{1}{2}}\frac{S_B(\mathbf{k}_I)}{S_B(\mathbf{k}_B)}\equiv\Delta\sigma_A\Delta\sigma_k\Delta\sigma_S. \tag{13}$$

Equation (13) indicates that the change $\Delta\sigma$ of the NRCS is the product of contributions from the divergence of current $\Delta\sigma_A$, the wavenumber change $\Delta\sigma_k$, and the background wave spectrum $\Delta\sigma_S$.

The wavenumber change is determined by the velocity shear of the directional component of the ocean currents along the wave propagation. These contributions can be calculated without the time integration when the current phenomena exist in the limited area, because the contributions of the wavenumber change and the background wave spectrum depend only on the wavenumber. The contribution of the divergence of currents, however, is only calculated by the integration along the ray path. For this reason, the integration of the ray equation is needed to calculate the local NRCS on the current field with divergence.

3. SIMULATION

3.1. Current Model

To express the divergence and rotation of the isolated eddy the current model is defined as a function of the radius r and the direction φ of the current vector measured from the radius vector. When the center of the eddy locates at the origin, the tangental and radial velocity components v_θ, v_r at radius r are determined by using the velocity profile v_p as follows:

$$(v_\theta(r), v_r(r)) \;=\; v_p(r)(\sin\varphi, \cos\varphi). \tag{14}$$

Based on an eddy model by Mathiesen [1987], the velocity profile v_p with a maximum velocity V_e at the radius of R_0 is modeled as follows:

$$v_p(r) = \begin{cases} v_p(R_1)r/R_1 & (0 \le r < R_1), \\ V_e \exp\left\{-[(r-R_0)/(bR_0)]^2\right\} & (R_1 \le r \le R_2), \\ v_p(R_2)R_2/r & (r > R_2), \end{cases} \tag{15}$$

$$R_1 = \left[\left\{1 + \left(1 - 2b^2\right)^{\frac{1}{2}}\right\}/2\right] R_0, \tag{16}$$

$$R_2 = \left[\left\{1 + \left(1 + 2b^2\right)^{\frac{1}{2}}\right\}/2\right] R_0, \tag{17}$$

where the parameter b determines the width of the transition region ($R_1 \le r \le R_2$). In the inner region ($0 \le r < R_1$), the absolute velocity v_p linearly increases with the radius, so the divergence and vorticity are constant. Otherwise, in the outer region ($r > R_2$), the absolute velocity decreases proportionally to r^{-1}, so the divergence and vorticity are zero. The radius of R_2, therefore, corresponds to the boundary radius of the eddy. In the transition region, the velocity profile is defined as a Gaussian function and the continuity is kept until the first derivative at the connecting radii R_1 and R_2. In this study, the value of b is set almost to its upper limit as 0.7071067, which is the gentlest way to make the transition. The radii R_1 and R_2 become about $0.5R_0$ and $1.2R_0$, respectively.

3.2. Background Spectral Density Model of Ocean Waves

The spectral density of ocean waves can be expressed as the product of the wavenumber spectrum and the directional spectrum that depend on the wind field. In this study, to simplify the situation, the directional spectrum is assumed to be uniform. Moreover, the wavenumber of ocean waves causing the first-order echo is assumed to belong to the equilibrium region of the wavenumber spectrum before the interaction with the current field. Then, the spectral density $S_B(\mathbf{k})$ of the background wave field becomes the function of wavenumber $|\mathbf{k}|$ as:

$$S_B(\mathbf{k}) = S_0|\mathbf{k}|^{-\frac{7}{2}}, \tag{18}$$

where S_0 is proportional constant. This form of wavenumber spectrum corresponds to the frequency spectrum $\phi(f) \propto f^{-4}$, where f is the wave frequency [Mitsuyasu et al., 1980].

3.3. Radar Sensitivity Distribution

The radar sensitivity distribution is assumed a 2D-Gaussian function to discuss the influence on current measurement using HFOSR generally [Zrnic and Doviak, 1975]. The radar sensitivity G at position $\mathbf{r}$ is assumed a function of the distance from the radar target position $\mathbf{r}_c$ as:

$$G(\mathbf{r}) = G_0 \exp\left(-\left(\frac{|\mathbf{r}-\mathbf{r}_c|}{R_w}\right)^2 \ln 2\right), \tag{19}$$

where G_0 is the maximum radar sensitivity, and R_w is the width of the radar sensitivity, where the radar sensitivity reduces to half G_0. In the simulation of the Doppler velocity spectra of the first-order echo, the radius of the integration area is set to three times the width of the radar sensitivity.

3.4. Normalization

To increase the generality of the simulation, the dimensional units of space $\mathbf{x}^*$ and time t^* are normalized by the radius R_0^* of the eddy and the phase velocity $C_{pB}^* = C_p^*(|\mathbf{k}_B^*|)$ of the ocean waves causing the first-order echo. The relations between the dimensional units ($\mathbf{x}^*$, t^*) and the non-dimensional units ($\mathbf{x}$, t) are described as $\mathbf{x}^* = R_0^*\mathbf{x}$ and $t^* = (R_0^*/C_{pB}^*)t$, respectively. By introducing the relative wavenumber vector $\mathbf{K} = \mathbf{k}^*/|\mathbf{k}_B^*|$, the normalized phase velocity of the ocean waves is described as $C_p(\mathbf{K}) = \sqrt{\mathbf{K}}$.

4. SPATIAL DISTRIBUTION OF NORMALIZED RADAR CROSS SECTION

The simulated results of the initial wave parameters of the wave packets are shown in Fig. 1. The spatial distribution of the initial wavenumber of wave packets agrees with the radial current velocity in the theory. The initial wavenumber becomes smaller than the unity in the negative x-region, because the wavenumber increases by propagating against the current as a result of the wave-current interaction. In the positive x-region, the wave-current interaction works oppositely. As a result, the spatial distribution of the initial wavenumber becomes antisymmetric with respect to the y-axis, at the point where the radial component of the current becomes zero.

On the other hand, the spatial distribution of the initial direction of the wavenumber vector does not show any relation to the radial current velocity. In the area behind the eddy, the wavenumber vectors are rotated counter-clockwise as a result of the refraction inside of eddy region. In the countercurrent side of the positive y-region, there is a narrow area just outside of the eddy boundary showing a strong clockwise rotation of the wavenumber vectors. In other areas, the rotation mostly depends on the y-position. In the positive and negative y-region, the wavenumber vectors rotate clockwise and counter-clockwise, respectively.

The influence of the current field on the ocean waves is limited only to the wavenumber change by the wave-current interaction, because of the non-divergent current model. In the countercurrent area of the eddy, the NRCS increases up to 5 dB. Otherwise, in the following current area, the

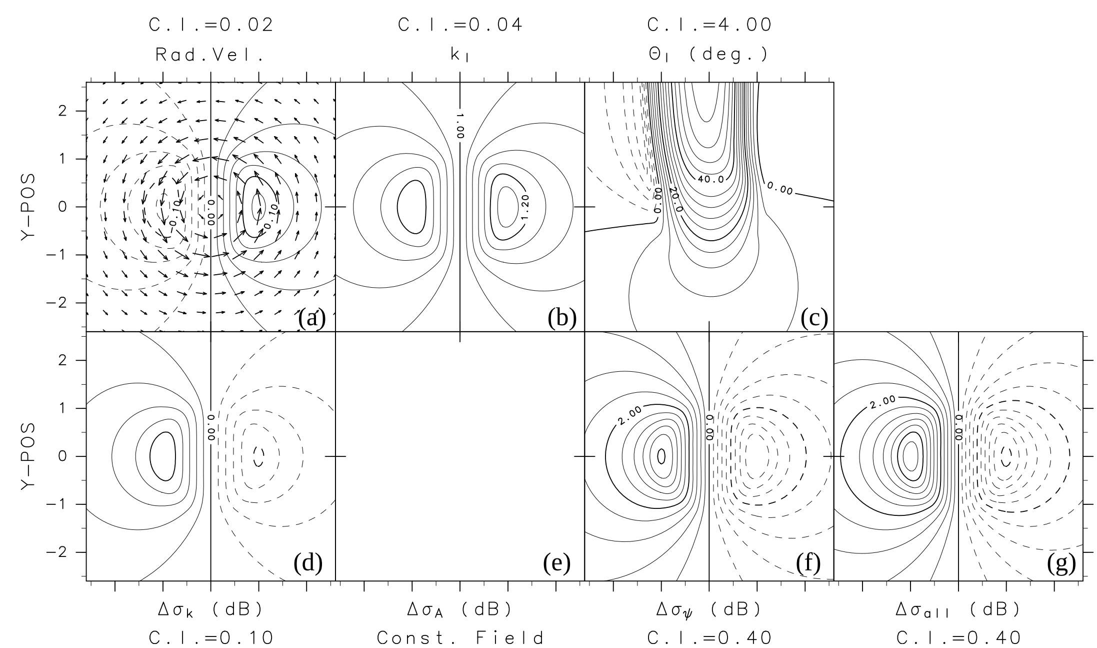

Figure 1: Simulation results of normalized radar cross section (NRCS) around eddy. (a) y-component of the current (radial velocity) of the model with a current vector, (b) an initial wavenumber, and (c) an initial direction of the wavenumber vector of the wave packet. (d) The contribution of wavenumber change, (e) the divergence of the current field, (f) the initial spectral density of the ocean waves, and (g) the total contribution on the NRCS change.

NRCS shows a decrease of about 4 dB at the peak. So, the NRCS discrepancy between both sides of the eddy reaches 9 dB. The spatial distribution of the NRCS is antisymmetric with the radial velocity. The exact value of the NRCS change strongly depends on the spectral model of the background ocean waves, because most of the NRCS change (8 dB) comes from the contribution of the background spectral density. The tendency of spatial distribution, however, does not change as long as the initial wavenumber of the wave packet belongs to the equilibrium region of the background wavenumber spectrum.

5. RADIAL VELOCITY FIELD

Figure 2 shows the distributions of the simulated radial velocity and the difference from the model radial velocity. When the spatial scale of the radar sensitivity distribution is smaller than the eddy scale, the difference between the radial velocities is quite small in all areas. This means that the influence of the wave-current interaction on the radial velocity measurement by HFOSR is negligible, while the spatial scale of the radar sensitivity distribution is smaller than the eddy scale. With the broadening of the radar sensitivity distribution, the difference between the radial velocities enlarges around the eddy region. Moreover, the spatial change of the radial velocity shrinks due to the spatial averaging effect, and the eddy signal on the simulated radial velocity field weakens. The simulated radial velocity at $x = 0$ becomes negative, due to the larger NRCS in the negative radial velocity region.

Although the negative component of the radial velocity difference is stronger than the positive component, the spatial distribution of the radial velocity difference is almost antisymmetric with respect to the y-axis. The intensity and the extent of the radial velocity difference are proportional to the spatial scale of radar sensitivity distribution.

The intensity of the antisymmetric component enlarges with the broadening of the radar sensitivity distribution, because the antisymmetric component of the radial velocity difference comes from the averaging effect caused by the spatial distribution of the radar sensitivity. The spatial distributions of antisymmetric component, calculated using the uniform NRCS field, are also shown in Fig. 2. When the spatial scale of the radar sensitivity distribution is the same as the eddy scale, the maximum velocity of the antisymmetric component reaches about 0.05, which is 40% of the

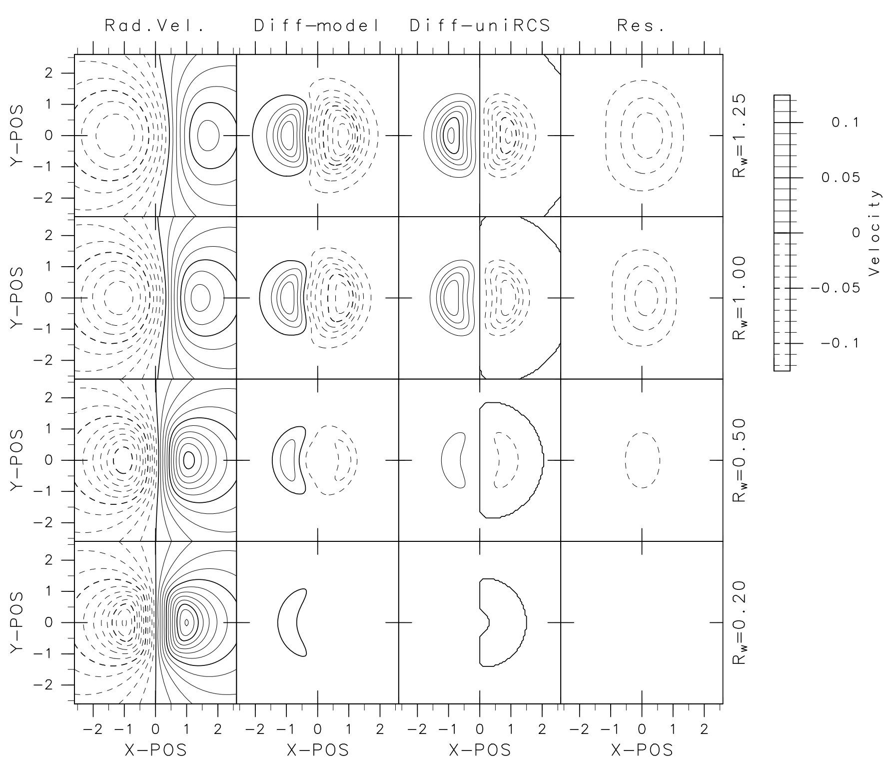

Figure 2: Spatial distribution of simulated radial velocity and difference from model. Rad. Vel.: Ideally simulated radial velocity. Diff-model: Difference of simulated radial velocity from the model. Diff-uniRCS: Difference of simulated radial velocity with uniform NRCS from the model. Res: Residual of difference.

model maximum velocity. With the broadening of the radar sensitivity distribution, the absolute value of the antisymmetric component increases to that of the model current. The extent is, on the other hand, almost the same as the spatial scale of the eddy, regardless of the spatial scale of the radar sensitivity distribution. This means that the HFOSR cannot measure the current phenomena with a smaller scale than the radar sensitivity distribution.

The residual component comes from the non-uniformity of the NRCS distribution as a result of the wave-current interaction. The residual component of the radial velocity difference is negative and localized near the center of the eddy, because of the stronger NRCS in the negative velocity region. While the radar sensitivity distribution is smaller than the eddy scale, the residual component of the radial velocity difference strengthens with the broadening of the radar sensitivity distribution, which is the same as the antisymmetric component. When the spatial scale of the radar sensitivity distribution is comparable or larger than the eddy scale, the intensity of the residual component remains almost constant at about 0.03, that is 25% of the maximum eddy velocity. The extent of the residual component, however, almost agrees with the scale of the radar sensitivity distribution.

6. CONCLUSION

The influence of wave-current interaction on the current measurement of HFOSR is analyzed by the simulation of a Doppler velocity spectra, with not only the radar sensitivity distribution, but also a simulated NRCS distribution. The local spectral density of ocean waves strengthens where the ocean waves propagate against the current, and weaken where the ocean waves propagate along the current, because of the conservation law of wave action. The local spectral density is also influenced by the divergence of the current field. The NRCS of the first-order echo has a non-uniform distribution as a result of wave-current interaction, because the local spectral density of causal ocean waves determines it.

The radial velocity difference between the simulation and the model is able to separate into the antisymmetrical components with respect to the line of zero radial velocity and the residual component. The antisymmetrical component comes from the spatial averaging effect caused by the spatial distribution of the radar sensitivity. As a result, the antisymmetric component of radial velocity difference simply weakens the signal of current phenomena.

The residual component is a result of the distortion of the spectral shape of the first-order echo due to the non-uniformity of the NRCS distribution. The residual component has an opposite signature to the phase velocity of the ocean waves causing the first-order echo, because the larger NRCS appears in the region where the causal ocean waves propagate against the current. The distribution of the residual component is localized around the center of the current phenomena. The residual component deforms the spatial pattern of the current vector field by the creation of the artificial current. So, the spatial distributions of the artificial vorticity and divergence cross each other near the center of current phenomena, because of the localized distribution of the artificial currents.

When the spatial scale of the radar sensitivity distribution is smaller than the current phenomena, variations in NRCS and radial velocity in the radar sensitive area are small. For this reason, the influence does not appear on the simulated radial velocity, but only on the broadening of the first-order echo. With the broadening of the radar sensitivity distribution, the variations in NRCS and radial velocity in the radar sensitive region enlarge and the simulated radial velocity differ from the model.

When the current field is symmetric with a 180° rotation, the distributions of NRCS for two first-order echoes, correspond to the approaching and receding causal ocean waves, also become symmetric with the 180° rotation. As a result, the spatial distributions of the radial velocity difference extracted from each first-order echo become antisymmetric with the 180° rotation. Although the antisymmetric component of the radial velocity difference is independent of the propagating direction of the causal ocean waves, the direction of the residual components become opposite to the phase velocity of the causal ocean waves.

REFERENCES

1. Barrick, D. E., "First-order theory and analysis of MF/HF/VHF scatter from the sea," *IEEE Trans. on Antennas and Propagation*, Vol. 20, No. 1, 2–10, 1972.
2. Barrick, D. E., J. M. Headrick, R. W. Bolge, and D. D. Crombie, "Sea backscatter at HF: Interpretation and utilization the echo," *Proceedings of IEEE,* Vol. 62, No. 6, 673–680, 1974.

3. Barrick, D. E., M. W. Evans, and B. L. Weber, "Ocean surface currents mapped by radar," *Science*, Vol. 198, No. 4313, 138–144, 1977.
4. Heron, M. L., "Line broadening on HF ocean surface radar backscatter spectra," *IEEE J. Oceanic Eng.,* Vol. 10, No. 4, 397–401, 1985.
5. Nadai, A., "Measurement of complicatedness of ocean surface current field by using HF ocean surface radar," *Proceedings of International Workshop on Remote Sensing for Coastal and Marine Engineering, ISPRS WG VII/8,* Hiroshima, Japan, 1995.
6. Nadai, A., "Effects of ocean surface current features on HF ocean surface radar backscatter spectra," *Proseedings of the Fifth International Conference on Remote Sensing for Marine and Coastal Environments,* San Diego, California, 1998.
7. Phillips, O. M., *The Dynamics of the Upper Ocean*, 2nd Edtion, Cambridge University Press, Cambridge, 1977.
8. Liu, A. K., F. C. Jackson, E. J. Walsh, and C. Y. Peng, "A case study of wave-current interaction near an oceanic front," *J. Geophys. Res.,* Vol. 94, No. C11, 16189–16200, 1989.
9. Nadai, A., "Model analysis of influence of wave-current interaction on current measurement of HF ocean surface radar for isolated eddy and upwelling," *J. Geophys. Res.*, Vol. 111, C10012, 2006, doi:10.1029/2006JC003528.

Maxwell Sumudu Based Magnetic Solutions

Fethi Bin Muhammad Belgacem and Eman Al-Shemas
Department of Mathematics, Faculty of Basic Education, PAAET, Shaamyia, Kuwait

Abstract— The Dynamics of a planar, transverse electromagnetic (TEMP) wave propagating in the direction z in lossy media with constant permittivity ϵ, permeability μ, and conductivity $\sigma > 0$, are best described by Maxwell's equations [1, 2],

$$\begin{cases} (i) \quad \nabla \times \mathbf{E} = -\mu \frac{\partial \mathbf{H}}{\partial t}, \\ (ii) \quad \nabla \times \mathbf{H} = \epsilon \frac{\partial \mathbf{E}}{\partial t} + \sigma \mathbf{E}. \end{cases} \tag{1}$$

Various forms of solutions for the electromagnetic couple solutions and profiles of (1) have been found, using various techniques, subject to distinct assumptions on the medium coefficients and fields intial directions.

In view of its advantageous attributes and many quantities preserving properties, the Sumudu turns out to be an ideal tool for many science applications and engineering. Without resorting to a new frequency domain, as in the case of Laplace or Fourier, having units and scale preserving properties, the Sumudu turns out to be the ideal tool, for engineering and many applied mathematics and physics propblems [3, 4]. The Sumudu operator is defined by,

$$G(u) = \mathbb{S}[f(t)] = \int_0^\infty f(ut)\, e^{-t} dt, \; u \in (-\tau_1, \tau_2), \tag{2}$$

over the set of functions,

$$A = \left\{ f(t) \,/\, \exists\, M, \tau_1, \tau_2 > 0, \; |f(t)| < M e^{\frac{|t|}{\tau_j}}, \quad \text{if} \quad t \in (-1)^j \times [0, \infty) \right\}. \tag{3}$$

The function, $G(u)$, is then referred to as *the Sumudu of* $f(t)$. The Sumudu Operator is clearly linear since,

$$\mathbb{S}[af(t) + bg(t)] = a\mathbb{S}[f(t)] + b\mathbb{S}[g(t)]. \tag{4}$$

Computationally, denoting the gamma function by, Γ, wherever, $\Gamma(\alpha+1)$ can be defined (classically for $\alpha > -1$), we then have, $\mathbb{S}[t^\alpha] = \int_0^\infty (ut)^\alpha e^{-t} dt = u^\alpha \int_0^\infty t^\alpha e^{-t} dt = \Gamma(\alpha+1)\, u^\alpha$. So, $\mathbb{S}[1] = 1$, $\mathbb{S}[at+b] = au + b$, and $\mathbb{S}[t^n/n!] = u^n$, for any integer $n \geq 0$. Discretely, $\mathbb{S}[\exp(at)] = \mathbb{S}[\sum_0^\infty (at)^n/n!] = \sum_0^\infty (au)^n = 1/(1-au)$, for $a \in (-1/a, 1/a)$.

Consequently, for any frequency, w, $1/(1+(wu)^2)$, $(wu)/(1+(wu)^2)$, are the respective *Sumudi* of $\cos(wt)$, and, $\sin(wt)$, which may be obtained, $\mathbb{S}[\cos(wt)+j\sin(wt)] = \mathbb{S}[e^{jwt}] = 1/(1-jwu) = (1+jwu)/(1+(wu)^2)$.

Conversly, (with $w = 1$), $1/(1+u^2) = \sum_0^\infty (-1)^n u^{2n}$, with u in $(-1, 1)$, and applying the inverse operator, yields, with t in $\mathbb{R}$, $\mathbb{S}^{-1} \sum_0^\infty (-1)^n u^{2n} = \sum_0^\infty (-1)^n t^{2n}/(2n)! = \cos t$, & $\mathbb{S}^{-1}[u/(1+u^2)] = \mathbb{S}^{-1} \sum_0^\infty (-1)^n u^{2n+1} = \sum_0^\infty (-1)^n t^{2n+1}/(2n+1)! = \sin t$.

Furthermore, for $a \geq 0$, the Heaviside or unit step function, $H_a(t)$, any function shift, $f(t-a)$, has for sumudu,

$$\mathbb{S}[f(t-a)] = \mathbb{S}[H_a(t) f(t)] = e^{\frac{-a}{u}} \mathbb{S}[f(t)], \text{ for } u > a. \tag{5}$$

The TEMP problem, like general field couple problems, can be considered in the Sumudu Transform frame work. Upon Sumudu transformation, Maxwell's Equations are made to yield transient magnetic field solutions. In previous works, Sumudu based techniques were used to deliver transient electric field solutions for electromagnetic planar waves moving in the transversal direction of lossy media, [5, 6]. Here we present a parallel treatment for the magnetic field, using Sumudu established properties.

1. SUMUDU BASED MAGETIC FIELD SOLUTIONS FOR MAXWELL'S EQUATIONS

In this paper, we first albeit briefly, state some Sumdu Convolution, Itegration and Differentiation Properties whose application will help us solve the TEMP problem. The next theorem allows us to use the Sumudu transform efficiently to solve differential equations involving multiple integrals of the dependent variable as well, by rendering them into algebraic ones.

Theorem 1: *Let $M(u)$, and $N(u)$, be the respective sumudi for the functions, $f(t)$ and $g(t)$, with convolution,*

$$(f * g)(t) = \int_0^t f(\tau)g(t-\tau)d\tau, \tag{6}$$

then, the Sumudu of the convolution of the functions, $f(t)$, and $g(t)$, is given by,

$$\mathbb{S}[(f * g)(t)] = uM(u)N(u). \tag{7}$$

Furthermore, the Sumudu of the derivative of the convolution of the functions, $f(t)$ *and* $g(t)$ textitis given by,

$$\mathbb{S}\left[(f * g')(t)\right] = M(u)N(u). \tag{8}$$

Moreover, the Sumudu off the convolution of the derivative of f with itself, is given by,

$$\mathbb{S}[(f * f')(t)] = M^2(u). \tag{9}$$

Finally, the Sumudu of the anti-diderivative, $(f * 1)$, of the function, $f(t)$, is given by,

$$\mathbb{S}\left[\int_0^t f(\tau)d\tau\right] = uM(u). \tag{10}$$

Theorem 2: *Let $G_n(u)$ be the Sumudu Transforms of the n'th derivative, $f^{(n)}(t)$, of $f(t)$, then for $n \geqslant 1$,*

$$G_n(u) = \frac{G(u)}{u^n} - \sum_{k=0}^{n-1} \frac{f^{(k)}(0)}{u^{n-k}}. \tag{11}$$

In particular this means that the Sumudu of the first and second derivatives of the function f are given by,

$$G_1(u) = \mathbb{S}\left(f'(t)\right) = \frac{G(u) - f(0)}{u}, \ \&, \ G_2(u) = \mathbb{S}\left(f''(t)\right) = \frac{G(u) - f(0)}{u^2} - \frac{f'(0)}{u}. \tag{12}$$

In a previous works [7, 8], it was established that, if we set, $a = 1/\sqrt{\mu\epsilon}$, and, $b = \sigma/2\epsilon$.

Theorem 3: *The transient electric field, $E(z,t)$, in the TEMP problem as described in Eq. (1), is given by,*

$$E(z,t) = e^{-\frac{b}{a}z} f(t - z/a) - a\int_{z/a}^{\infty} f(t-\tau)e^{-b\lambda} \frac{\partial}{\partial z} J_0\left(\frac{b}{a}\sqrt{z^2 - (a\tau)^2}\right) e^{-t/u} d\tau. \tag{13}$$

In this work, we set $G(z,u) = \mathbb{S}[h(z,t)]$, and use connected Sumudu properties, such as theorems 1 & 2, to transform Eq. (1), and obtain the second order equation,

$$\frac{d^2G(z,u)}{dz^2} - \gamma^2 G(z,u) = \gamma^2 h_0(z) - \lambda {h_0}'(z)) = V(z,u), \tag{14}$$

the homogeneous solution to which, $G_h(z,u)$, (achieved if $V(z,u) = 0$, i.e., ${h_0}'(z)/h_0(z) = 1+\rho/\lambda = 1 + u\sigma/\epsilon$) is given by,

$$G(z,u) = A(u)e^{\gamma z} + B(u)e^{-\gamma z}. \tag{15}$$

The particular solution, $G_p(z,u)$, of Eq. (14) is then given by,

$$G_p(z,u) = \frac{e^{\gamma z}}{2\gamma}\int e^{-\gamma z}V(z,u)dz + \frac{e^{-\gamma z}}{2\gamma}\int e^{\gamma z}V(z,u)dz. \tag{16}$$

Here, we assume direct values for the magnetic field boundary conditions.

In a lossy medium with conductivity $\sigma > 0$, we assume,

$$\lim_{z \to 0} H(z,t) = H(0,t) = h(t), \quad t \geq 0. \tag{17}$$

In addition, assuming the initial conditions,

$$H(z, t \longrightarrow 0) = h_0(z), \&, \partial H(z, t \longrightarrow 0)/\partial t = {h_0}'(z), \tag{18}$$

and recalling that we have already set,

$$\rho = \frac{\mu\sigma}{u}, \ \lambda = \frac{\mu\epsilon}{u^2}, \ \&, \ \gamma^2 = \frac{\mu\epsilon}{u^2} + \frac{\mu\sigma}{u} = \lambda + \rho, \tag{19}$$

We then get,

$$\begin{cases} A(u) = 0, \ \text{and}, \\ B(u) = G(0,u) = \mathbb{S}\left[h(t)\right] = G(u). \end{cases} \tag{20}$$

In consequence, we have the following result,

Theorem 4: *The transient magnetic field, $H(z,t)$, in the TEMP problem as described in Eq. (1.0), is given by,*

$$H(z,t) = e^{-\frac{b}{a}z} h(t - z/a) - a \int_{z/a}^{\infty} h(t-\tau) e^{-b\lambda} \frac{\partial}{\partial z} J_0 \left(\frac{b}{a} \sqrt{z^2 - (a\tau)^2} \right) e^{-t/u} d\tau. \tag{21}$$

2. CONCLUSION

TEMP like problems field couple solutions can be considered in the Sumudu Transform frame work. In view of its advantageous attributes and many quantities preserving properties, the Sumudu turns out to be an ideal tool for many science and engineering applications. For future work we plan we plan to combine Sumudu Transform with variational techniques such as those developped in the last four decades (see for instance [7, 8]) to analyse & solve TEMP related problems.

REFERENCES

1. Smirnov, Y. G., *Mathematical Methods for Electromagnetic Problems*, Goy Bpo, Moscow, 2009.
2. Kong, J. A., *Maxwell Equations*, EMW Publishing, Cambridge, MA, 2002.
3. Belgacem, F. B. M., "Sumudu transform applications to bessel equations and functions," *AMS*, Vol. 4, No. 74, 3665–3686, 2010.
4. Belgacem, F. B. M., "Introducing and analyzing deeper sumudu properties," *NSJ*, Vol. 13, No. 1, 23–41, 2006.
5. Belgacem, F. B. M., "Sumudu applications to Maxwell's equations," *PIERS Online*, Vol. 5, No. 4, 355–360, 2009.
6. Hussain, M .G. M. and F. B. M. Belgacem, "Transient solutions of Maxwell's equations based on sumudu transform," *Progress In Electromagnetics Research*, Vol. 74, 273–289, 2007.
7. Konnov, I., *Combined Relaxation Methods for Variational Inequalities*, Lecture Notes in Economics and Mathematical Systems No. 495, Springer, New York, 2001.
8. Lions, J. L. and G. Stamppachia, "Variational inequalities, communications in pure and applied mathematics," Vol. 20, 493–519, 1967.

Dual Band Antenna with Paired Excitation for Reduced Cross-polarisation

Gobi Vetharatnam, Koo Voon Chet, and Fabian Kung Wai Lee
Multimedia University, Malaysia

Abstract— Dual L- and C-band antenna with single polarisation is designed for application in synthetic aperture radar (SAR). Shared-aperture antenna systems are increasingly preferred in modern SAR systems. One key requirement in a SAR antenna is low cross-polarisation. In a probe-fed patch, the cross-polarisation reduction depends on the cancellation of fields by adjacent patches. An analysis of the field cancellation with equal-power, unequal-power and different phases was carried out. Good cancellation may be achieved if the adjacent powers are the same. The phases of the adjacent patches do not have significant effect on the cross-field cancellation. Paired excitation may not be immediately possible in a shaped pattern. Modification to the array excitation coefficient must be performed so that adjacent powers in an array are the same even for a shaped beam pattern. Then, the cross-polarisation may be controlled and suppressed to meet the SAR requirements. In this work, the C-band array is made up of three paired radiators in the elevation plane. The azimuth plane has four elements. The L-band patch is made up of two patches placed above the C-band array. The prototype is fabricated with three GML1032 laminates, with two of them being the thicker substrate (1.52 mm) and the other 0.76 mm. A layer of 4 mm low-loss Rohacell HF51 foam separates the radiating layers from each other. The C-band array achieved a cross-polarisation level of 31 dB in the main beam, while the L-band achieved a cross-polarisation level of 25 dB. The C-band achieves a bandwidth of 220 MHz centred at 5.3 GHz. The return loss is about −20 dB. The L-band return loss is about −20 dB at centre frequency with a bandwidth of about 120 MHz. Good radiation pattern was achieved for both the frequency bands.

1. ANTENNA DESIGN

The specification of the antenna is listed in Table 1. The antenna main beam is set to cover about 26° in the elevation direction (cross-track) and 3° in the azimuth direction (along-track). The antenna is single vertically polarised.

For the C-band, the antenna's beam is synthesised using Elliott synthesis method. A total of six elements are required to synthesis the radiation pattern. The coefficients are given in Table 2.

2. ARRAY SIMULATION

The antenna is made up of a C-band sub-array of 4×6 elements and a layer of L-band array with two patches, in a dual-band operation. The C-band patches are rectangular shaped with dimensions of 14.5 mm × 20 mm. The linear array is spaced 38 mm apart and fed via probe offset by 3.2 mm from the centre of patch. The linear array is further extended into a planar array of 4×6 elements. Figure 1 shows the layout of the sub-array antenna. The array is spaced 50 mm apart in the vertical plane. At 5.3 GHz the return loss is −22 dB. The bandwidth achieved is about 250 MHz. The bandwidth achieved is about 4.7% of centre frequency, typical of a patch antenna.

Table 1: Specifications of the SAR antenna.

	L-band	C-band
Frequency	1.25 GHz	5.3 GHz
Bandwidth	80 MHz	200 MHz
Main beam shape Elevation Azimuth	 Pencil beam Pencil beam	 Shaped from 79°–105° Pencil beam
Cross-polarisation	~ -25 dB	< -30 dB
Look angle	30°	
VSWR (Return Loss)	< 2.0 (< -10 dB)	
Polarisation	Single linear	

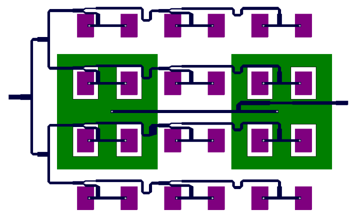

Figure 1: Layout of combined array and its feed network.

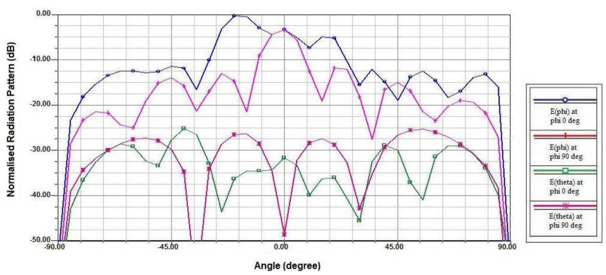

Figure 2: C-band normalized radiation pattern.

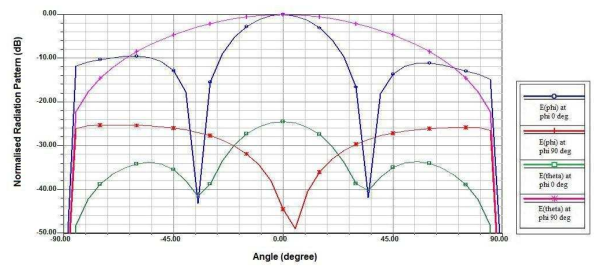

Figure 3: L-band normalized radiation pattern.

Table 2: Array factor.

	Element number					
	1	2	3	4	5	6
Amplitude	5.8	5.8	2.1	2.1	1.0	1.0
Phase (deg)	0	20	48	175	233	14

3. CONCLUSION

The simulated radiation patterns are shown in Figure 2 and Figure 3, respectively, for the C-band and L-band frequencies. The E-plane pattern for the C-band frequency shows the shaped pattern in the main beam with cross-polarisation about -32 dB in the main beam region. The H-plane shows a "sinc" pattern with a cross-polarisation of -25 dB in the main beam region. For the L-band pattern a cross-polarisation of -25 dB is observed in the main beam.

Design of a Digital Synthetic Aperture Radar

W. G. Cheaw, Y. K. Chan, and V. C. Koo
Multimedia University, Malaysia

Abstract— A Synthetic Aperture Radar (SAR) is a complex radar system that requires complex analog signal generation and processing. Real-time processing is now possible with off the shelf computing hardware. A modular analog interface is designed to facilitate the handling of analog signals for processing. This paper describes the architecture for such a system from a concept level and then will describe the implementation and finally the current development progress.

1. INTRODUCTION

Synthetic aperture radar imaging systems are fast becoming the preferred imaging systems for airborne and space borne platforms due to their ability to detect targets without requiring an active heat source or any form of lighting from the system. The properties of electromagnetic waves also allow for a different image property such as the response of electromagnetic waves towards water, metal and moisture that allows it to be used for surveillance on vegetation, landslides, flood and military purposes. Previously, this method of imaging has been quite obscure due to the mathematically complex algorithms required to process the radar signals to generate the images. Current digital systems are rapidly being shrunk due to advances made using various digital systems such as Application Specific Integrated Circuits (ASIC) and FPGA designs [1]. The final products of these systems are often the direct image. This does not allow for research on other algorithms as well as the fine tuning of the processing algorithm. Given that the typical off the shelf computer of today has a considerably increased amount of computing power at a lower power consumption point when compared to its predecessors, it is possible to use today's computer to perform the processing of SAR images in real-time [2].

We will first review the concept of the system in the first section and then discuss the implementation of the system into actual hardware in the second section. We then finally discuss the results obtained so far.

2. PROCESSOR ARCHITECTURE

The system architecture is made up of 2 parts. The first is the FPGA based analogue interface. This part will provide the necessary interfacing for the computer via Ethernet to the analogue inputs and outputs. These analogue interfaces will have to be able to receive a signal of 80 MHz bandwidth. This is by means of a high-speed ADC and DAC. The system is built with a soft-processor. This processor controls the networking interface, data handling and allows for future expansion. The soft-processor also loads the values into the control circuits that control the internal timing of the

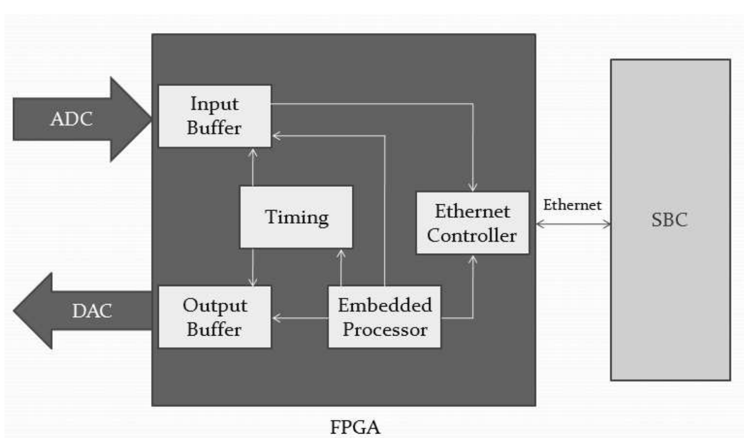

Figure 1: Architecture of digital processor system.

system. This gives the system a way to be controlled precisely as with the requirement of a coherent radar system.

For research purposes, the adjustability of these timing parameters is crucial so that the user can specify the parameters which are crucial to the user. The output buffers are given values from an algorithm run in the processor to generate the output pattern. The timing system then coordinates the sending of signals to the DAC. The values from the ADC are fetched from the buffer and then packaged into a file and then sent to the Single Board Computer (SBC). The computer can then read the data from storage and then process them.

This architecture presents 2 advantages over current systems. The first is that the parameters are controlled via software. The user should be able to control, within reason, the transmission parameters such as chirp duration and bandwidth. This form of system is similar to that of a Software Defined Radio (SDR) system. Since the difference between the 2 is firstly the bandwidth of the signals and secondly the sampling methods reducing the instantaneous bandwidth of the received data. For a radar system, chirp pulsed radar, the instantaneous bandwidth is high but due to the pulsing interval, the average bandwidth is quite low thus allowing the large quantity of data to be sent through gigabit Ethernet (GBe). It can be calculated with the following assumptions:

Chirp band width: 80 MHz
Sampling bandwidth: 100 MHz I, Q
ADC resolution: 14 bits per sample
PRF: Maximum of 1 kHz

$$14\,\text{bits} \times 2 \times 8192 \text{ samples} \times 1000 = 218.75 \text{ Mbits per second}$$

Even when factoring the overheads which are necessary in any communication protocol, as well as latency issues, we still have a 70% surplus in Ethernet bandwidth. This can only be achieved with a pulsed radar system. Time-continuous radar will generate a much larger amount of data which will require some local processing on the analogue receiver.

The SBC consists of a off the shelf computer system with the exception of the inclusion of a Solid State Drive (SSD). The SSD allows the system to withstand the extreme environment that is an airborne platform. SSDs also have a tremendous amount of bandwidth to facilitate the tremendous quantity amount of data a radar system produces.

3. SYSTEM IMPLEMENTATION

The system will have to conform to several parameters in its actualization. They are as follows:

Outer Dimensions: 200 mm × 200 mm × 200 mm
Maximum power consumption: 200 W
Analogue Bandwidth: 80 MHz
Maximum Pulse Repetition Frequency: 1 kHz

The FPGA system will be developed on a Terasic DE3 Development board. This board has an Altera Stratix FPGA and can be attached with DDR SDRAM, Analog interfacing daughter cards and Ethernet daughter cards. This will allow the system to be built with minimal hardware development. Most of the system development will focus on both software and HDL coding.

4. CONCLUSIONS

The software defined radar system in theory can be built. The current system has the processor integrated into the system to and linked to the Ethernet. A small operating system has also been downloaded into the memory of the board and can be linked to the network. The transmission and receiving of data packets have been tested and current research is into the investigation of the system bandwidth and the increasing of the bandwidth.

REFERENCES

1. Langemeyer, S., C. Simon-Klar, N. Nolte, and P. Pirsch, "A architecture of a flexible on-board real-time SAR-processor," *IGARSS*, 2005.
2. McFarlin, D. S., F. Franchetti, M. Püschel, and J. M. F. Moura, "Highperformance synthetic aperture radar image formation on commodity multicore architectures," *Proc. SPIE Conference on Defense, Security, and Sensing*, Vol. 7337, 733708, 2009.

Experimental Studying the Nonlinearity Effects on Adaptive Nulling

Cheng-Nan Hu, Jing-Wei Huang, and Kevin Peng
Communication Research Center (CRC), Oriental Institute of Technology
No. 58, Sec. 2, Sihchuan Rd, Ban-Ciao City, Taipei County, Taiwan, R.O.C.

Abstract— "Beam forming architecture", used in conjunction with an array of sensors to provide a versatile form of spatial filter for space-division multiple accesses (SDMA), becomes one of the enabling technologies to the 4G LTE network [1–3]. This approach features multiple users within the same radio cell to be accommodated on the same frequency and time slot by using internal feedback controlling the amplitude/phase weighting of the adaptive array [4] to modify its time, frequency, and spatial response. However, realization of the beam-forming techniques poses high linearity demands on RF/IF up-/down-conversion chain because nonlinear distortion will degrade the radiation pattern, resulting in the poor signal quality [5, 6]. This study employs a two-element antenna array incorporated with two amplifiers for experimental studying the nonlinearity effects on adaptive pattern nulls shift. Measured results validate the effective proposed method for further analysis on the performance degradation of adaptive array due to multicarrier power amplifiers (MCPA) nonlinearity.

1. EXPERIMENTAL STUDY

Figure 1 shows an adaptive array scheme, each antenna element has its own receiver composed of filters, amplifiers, mixers, etc. to amplify and down-convert the received signals before the A/D converters. During the signal paths on receiver, there exist two principle nonlinearities, present in small-signal amplifiers and mixers to introduce signal's distortion at a receiver, are intermodulation products and gain compression. Of special importance are the third-order intermodulation products since they fall within the signal passband and can not removed by filtering. Since the amount of the harmonic higher-order products is mostly contributed by power amplifiers, this study focuses on studying the power amplifier's nonlinearities effect on nulling performance of the adaptive array. Fig. 2 displays the measured output-power(dBm)/power-gain(dB)/relative-phase against input power (dBm) of two LNAs (Mimi circuits ZEL-0812LN under bias voltage of 15 Volts), showing that the gain (24 dB) and relative phase is declining due to AM/AM and AM/PM conversion as input power is greater than −15 dBm. When amplifiers are derived at nonlinear region, as shown in Fig. 2, at the signal's path of transceiver chains, the radiation pattern will be degraded by shifting nulls on the interference directions. It has been has been investigated numerically by using an 8-element adaptive array [7].

This paper proposed a design concept for experimental study of the nonlinearity effect on adaptive nulling by using an EVB (evaluation board) integrated with a two-element antenna array. As shown in Fig. 3, the EVB includes a coupler (ACX 1608 multilayer coupler [8]), two LNAs (Mimi

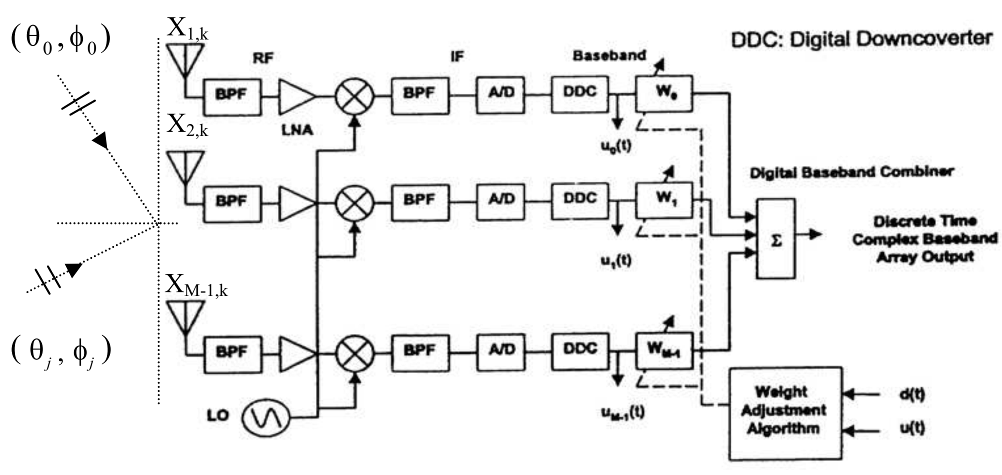

Figure 1: Antenna architecture of an Adaptive Antenna System (AAS) using digital beam-forming.

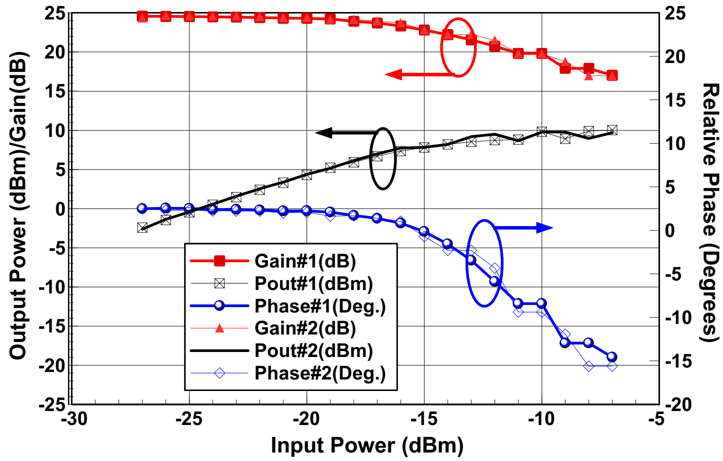

Figure 2: measure output-power/gain/relative-phase against input power of low-noise amplifier (mini circuit ZEL-0812LN).

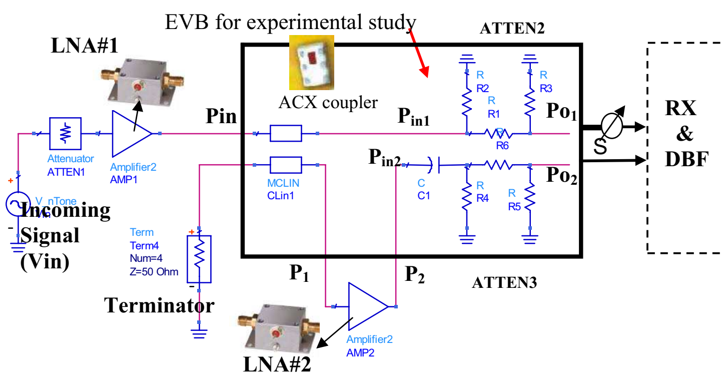

Figure 3: The schematic of the proposed experimental setup.

circuits ZEL-0812LN), and two pi-attenuator networks. The input signal is properly attenuated (ATTEN 1) and then, amplified to simulate a normal incident incoming wave (Vin) with specified power level (Pin). When the signal is received by the input port of the EVB, the receiving signal is divided into two signal paths using chip coupler with coupling value of 14 dB. After that, the trace of the coupling path is connected by an amplifier (LNA 2) and then, followed by a series chip capacitor and pi-attenuator (ATTEN 3); the other trace of through path is directly connected by a pi-attenuator (ATTEN 2). Controlling the power level of the input signal (Pin) to keep LNA operating at linear region, one can obtain two output ports (Po1 and Po2) with equal magnitude/phase by tuning C1 and resistance of two pi-attenuators such that two outputs (Po1 and Po2) can be simulated as two receiving signals with equal amplitude but out-off-phase to form a null at broadside ($\theta = 0°$) at Rx/DBF unit. With increasing the power level of Pin by controlling ATTEN1, the power level of Po1 and Po2 will increase linearly and maintain the in-phase and equal magnitude until the power level of P1 is greater than -15 dBm, resulting LNA#2 derived at nonlinear region. Thus, the receiving signals at two output ports are no longer be equal due to AM/AM and AM/PM conversion at LNA#2 at coupling path. Consequently, the null (at $\theta = 0°$) will be altered because the adaptive processing is based on the information with unexpected distortion. The assessment of the nulling degradation caused by nonlinearities distortion is very complex and cost. Thus, a two-element array equipped with two printed PIFA antennas is used to replace the complex and expansive DBF. Two antennas are placed at opposite direction (see Fig. 4(a)) such that the different pattern can be synthesized to form a depth null at broadside direction without using Balun design provided that two input signals (Po1 and Po2) are equally in both magnitude and phase. Since the null of different pattern is very sensitive to the unbalance between two input signals, any slightly deviation caused by distortion due to nonlinearity of LNA#2 will introduce the null shift from broadside. Thus, the usage of proposed experimental setup, one can clearly observe

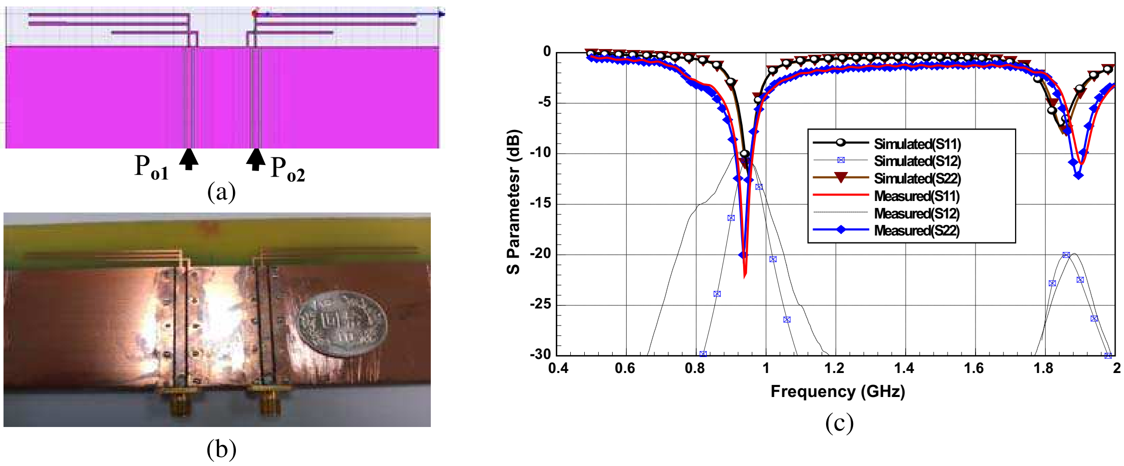

Figure 4: (a) (b) The schematic/photograph of two dual-band PIFA antennas design; (c) The comparison of simulated/measured S parameters.

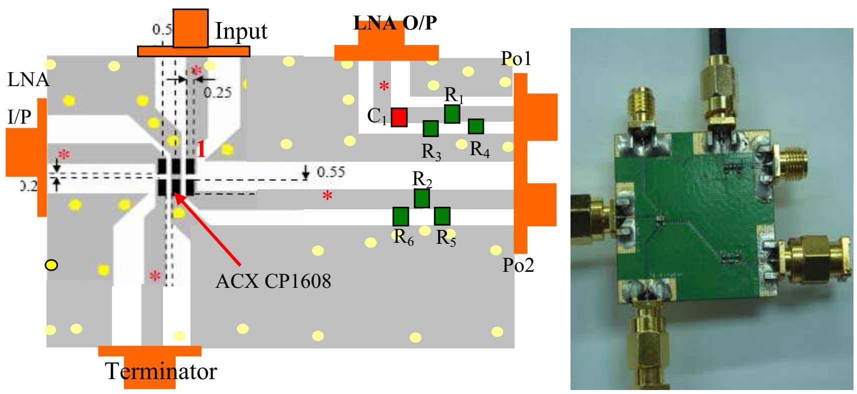

Figure 5: The reference layout/photograph of the experimental EVB.

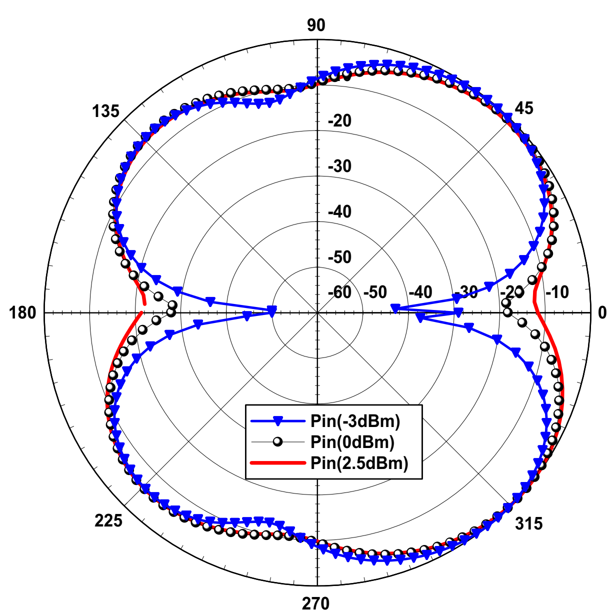

Figure 6: The measured far-field pattern clearly illustrates the null-depth/null-angle degradation from -29 dB/0° dB to -18 dB/2.5° and -12 dB/3.5° corresponding to Pin increasing from -3 dBm to 0 dBm, and 2.5 dBm, respectively.

the effects of nonlinearities on nulling performance of the adaptive array from far-field test range.

2. MEASURED RESULTS

Figures 4(a) (b) show the schematic/photograph of the experimental two-element printed PIFA antenna. Fig. 4(c) plots the comparison of the measured and simulated S-parameters using GEMS software, showing well agreement on the low-band resonant frequency of around 960 MHz for both antennas and acceptable agreement between and measured and simulated data. Figs. 5(a) (b) show the reference layout/experimental photograph for the EVB design for measurement. Three test cased with different input power level are measured at far-field test range, including Pin of -3 dBm, 0 dBm, and 2.5 dBm, respectively, to experimentally evaluate the effect of nonlinearity on nulling performance degradation. The measured far-field pattern (Fig. 6) clearly shows the null-depth/null-angle degradation from -29 dB/0° dB to -18 dB/2.5° and -12 dB/3.5° corresponding to Pin increasing from -3 dBm to 0 dBm, and 2.5 dBm, respectively.

3. CONCLUSION

A design concept for experimental studying the effect of nonlinearities on adaptive performance is proposed, manufactured, and measured to illustrate the adaptive nulling degradation caused by amplifier's nonlinearity using far-field test range.

REFERENCES

1. Tsoulos, G., M. Beach, and J. McGeehan, "Wireless personal communications for the 21th century: European technological advances in adaptive antennas," *IEEE Communication Magazine*, Vol. 35, No. 9, 102–109, Sep. 1997.
2. Parkvall, S., A. Furuskar, and E. Dahlman, "Evolution of LTE toward IMT-advanced," *IEEE Communication Magazine*, Vol. 49, No. 2, 84–91, Feb. 2011.
3. Park, C. S., Y.-P. E. Wang, G. Jongren, and D. Hammarwall, "Evolution of uplink MIMO for LTE-advanced," *IEEE Communication Magazine*, Vol. 49, No. 2, 112–121, Feb. 2011.
4. Widrow, B., et al., "Adaptive antenna system," *Proceeding of IEEE*, Vol. 55, No. 12, 2144–2159, Dec. 1967.
5. Laperle, C., T. Lo, J. Litva, and R. Turner, "Modeling of nonlinearity and their effects on digital beamforming," *IEEE AP-S*, Vol. 1, 124–127, Seattle, USA, Aug. 20–24, 1994.
6. Shimbo, O., "Effects of intermodulation, AM-PM conversion, and additive noise in multicarrier TWT systems," *Proceedings of IEEE*, Vol. 59, No. 2, 230–238, 1971.
7. Schneider, W. K. W., "Efficient simulation of multicarrier digital communication systems in nonlinear channel environments," *IEEE Journal on Selected Areas in Communications*, Vol. 11, 328–339, 1993.
8. http://www.acxc.com.tw/products.php.

Inverse Scattering Experiments for Electric Cable Soft Fault Diagnosis and Connector Location

Florent Loete[1], **Qinghua Zhang**[2], **and Michel Sorine**[3]

[1]LGEP-SUPELEC, 11 rue Joliot Curie 91192 Gif sur Yvette, France
[2]INRIA, Domaine de Voluceau, 78153 Le Chesnay, France

Abstract— Recently published theoretic results and numerical simulations have shown the ability of inverse scattering-based methods to diagnose soft faults in electric cables. The considered soft faults are modeled as spatially smooth variations of the characteristic parameters of electric cables governed by the telegrapher's equations. The purpose of the present paper is to report the experiments made with laboratory equipments confirming previously reported theoretic results and numerical simulations. The tested electric cables are twisted pairs used in trucks.

1. INTRODUCTION

The fast development of electronic devices in modern engineering systems comes with more and more connection cables, and consequently, the reliability of electric connections becomes a crucial issue. This fact has motivated research projects on methods for the diagnosis of faults in electric transmission lines. In this context, a promising technology for transmission line fault diagnosis is the reflectometry, which consists in analyzing the reflection and the transmission of electric waves observed at the ends of a cable. It has been reported that this technology is able to easily detect and locate hard faults (open circuit or short circuit) up to an accuracy of about 10 cm. For soft faults, the problem is much more complicated. Although it has been shown that a degraded connector can influence the reflection coefficient [1], no satisfactory experimental result has been reported for the detection of soft faults in electric cables, to our knowledge.

Recently, the inverse scattering theory has been applied to the reflectometry technology [2, 3]. After completing the theoretic studies initiated by [4], these recently published results show, by numerical simulation, the ability of the method based on the inverse scattering theory to diagnose soft faults in electric cables. The considered soft faults are modeled as spatially smooth variations of the characteristic parameters of electric cables governed by the telegrapher's equations.

The purpose of the present paper is to report the experiments made with laboratory equipments confirming the previously reported theoretic results and numerical simulations. After briefly recalling the inverse scattering-based method in Section 2, Experimental results will be presented in Section 3.

2. THE INVERSE SCATTERING-BASED METHOD

As electric cables of about 10 meters length are considered in this study, the losses in the cables are neglected in the method presented here, though the lossy case can be addressed with a similar method [3]. A lossless cable driven by a harmonic voltage can be modeled by the familiar frequency domain telegrapher's Equation (1) where k is the angular frequency (denoted so because it will play later, the role of a wavenumber), $V(k, z)$ and $I(k, z)$ are the voltage and the current, $L(z)$ and $C(z)$ are distributed inductance and capacitance at the point z along the cable; i is the imaginary unit. Boundary conditions will represent a generator on the left and a load on the right.

$$\frac{d}{dz}V(k, z) - ikL(z)I(k, z) = 0 \tag{1a}$$

$$\frac{d}{dz}I(k, z) - ikC(z)V(k, z) = 0. \tag{1b}$$

We compute now the reflection coefficient $r(k)$ at $z = 0$. Define the electrical distance, the characteristic impedance, and the reflected and direct power waves, as follows

$$
\begin{aligned}
x(z) &= \int_0^z \sqrt{L(s)C(s)}ds, \quad x \in [0, \ell], \quad Z_0(x) = \sqrt{\frac{L(x)}{C(x)}} \\
\nu_1(k, x) &= \frac{1}{2}\left(Z_0^{-\frac{1}{2}}(x)V(k, x) - Z_0^{\frac{1}{2}}(x)I(k, x)\right) \\
\nu_2(k, x) &= \frac{1}{2}\left(Z_0^{-\frac{1}{2}}(x)V(k, x) + Z_0^{\frac{1}{2}}(x)I(k, x)\right).
\end{aligned} \tag{2}
$$

Some direct computations then lead to the following *Zakharov-Shabat equations* [4]:

$$\frac{d\nu_1(k, x)}{dx} + ik\nu_1(k, x) = q(x)\nu_2(k, x) \tag{3a}$$

$$\frac{d\nu_2(k, x)}{dx} - ik\nu_2(k, x) = q(x)\nu_1(k, x) \tag{3b}$$

where

$$q(x) = -\frac{1}{4}\frac{d}{dx}\left[\ln \frac{L(x)}{C(x)}\right] = -\frac{1}{2Z_0(x)}\frac{d}{dx}Z_0(x). \tag{4}$$

Taking $\nu_2(k, 0) \neq 0$, q contains all information upon the reflection coefficient as we have $r(k) = \nu_1(k, 0)/\nu_2(k, 0)$. It is known [2, 4] that the characteristic impedance $Z_0(x)$ can be computed from $r(k)$ measured at $x = 0$ through the following steps:

1. Compute the Fourier transform of the reflection coefficient $r(k)$

$$\rho(x) = \frac{1}{2\pi}\int_{-\infty}^{+\infty} r(k)\exp(-ikx)dk.$$

2. Solve the integral equations (known as Gel'fand-Levitan-Marchenko equations) for their unknown kernels $A_1(x, y)$ and $A_2(x, y)$:

$$
\begin{aligned}
A_1(x, y) + \int_{-y}^{x} A_2(x, s)\rho(y + s)ds &= 0 \\
A_2(x, y) + \rho(x + y) + \int_{-y}^{x} A_1(x, s)\rho(y + s)ds &= 0.
\end{aligned}
$$

3. Compute the potential function $q(x)$ through

$$q(x) = 2A_2(x, x).$$

4. By solving Equation (4), compute

$$Z_0(x) = Z_0(0)\exp\left(-2\int_0^x q(s)ds\right).$$

3. EXPERIMENTAL RESULTS

3.1. Inverse Scattering for a Cable with a Well Known Impedance Profile

In order to experimentally demonstrate the ability of the inverse scattering method presented in this paper to compute the distributed characteristic impedance along a cable, we first had to design an electrical cable with a well known and controlled smooth spatial variation of the characteristic impedance. Furthermore we wanted this soft defect to be as close as possible to a real life defect. The first approach conducted in this study was to use a partially improperly twisted pair. It is known that the inductance L and the capacitance C per unit length of a twisted pair are determined by the radius r of the copper wire, the distance D between the two wires, the magnetic permeability

μ_0 and the dielectric permittivity ε_0 of the air, and the relative dielectric permittivity ε_r of the dielectric insulation, as formultated in the following equations:

$$L(x) = \frac{\mu_0}{\pi} \ln\left(\frac{D(x) - r}{r}\right) \tag{5a}$$

$$C(x) = \frac{\pi\varepsilon_0\varepsilon_r}{\ln\left(\frac{D(x)-r}{r}\right)} \tag{5b}$$

where the distance $D(x)$ between the two wires varies with x so that the characteristic impedance (ignoring the losses in the cable) $Z_0(x)$ as defined in Equation (2) is also a function of x. Consequently, by separating the two wires following some specified function $D(x)$, a spatially well controlled smooth variation of the distributed characteristic impedance $Z_0(x)$ is obtained.

This kind of soft defect was chosen because it is often observed in real life harnesses that, before and after a connector, the twisted line has to be untwisted in order to solder it to the electrical contacts, creating a local variation of the characteristic impedance (Figure 1).

For reasons of convenience we chose a cosine profile for the distance between the two wires:

$$D(x) = d + A\left(1 + \cos\left(2\pi\frac{x}{L} - \pi\right)\right) \tag{6}$$

where d is the diameter of the insulated wire, $A = 4\,\mathrm{mm}$ and $L = 25\,\mathrm{cm}$.

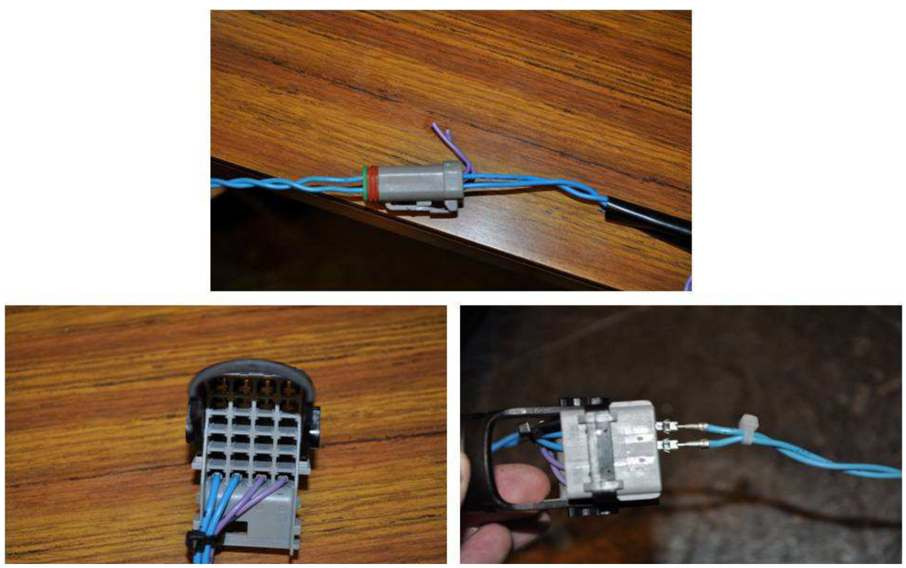

Figure 1: Spatial spacing variation of the two wires of a twisted pair on real life automotive connectors.

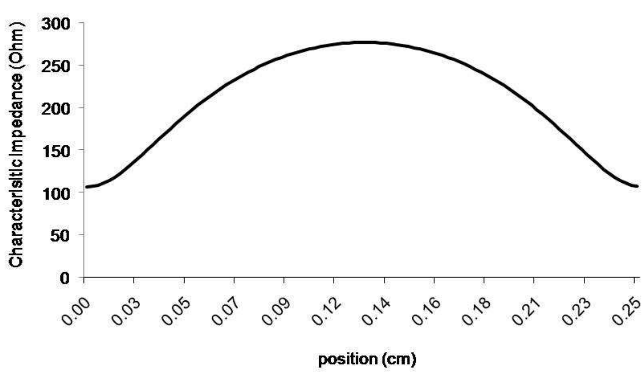

Figure 2: Distributed characteristic impedance $Z_0(x)$ corresponding to the cosine profile.

Following (5), (6) and (2), the computed distributed characteristic impedance corresponding to the cosine profile $D(x)$ is shown in Figure 2. In order to validate this theoretical impedance profile, we tried to compare the experimental and theoretical impulse responses of an electrical cable including the previously described soft defect. The experimental setup is presented in Figure 3. The cable is terminated by a $110\,\Omega$ load. The reflection coefficient measurement is carried out over the 2 MHz–1.102 GHz range using a vector network analyzer (VNA). The impulse response of the line is then obtained by computing the IFFT of the reflection coefficient. The results presented in Figure 4 show a quite good agreement between the theoretical and the experimental impulse responses of the tested cable and therefore validate the models used for $L(x), C(x)$ and $Z_0(x)$.

Now, applying the inverse scattering method presented in Section 2 to the same experimental example, we tried to find back the distributed impedance profile from the measured reflection coefficient. Figure 5 shows the results of the inverse scattering method for two experiments on the same cable with two different loads ($110\,\Omega$ and $220\,\Omega$, respectively in blue and green lines). The

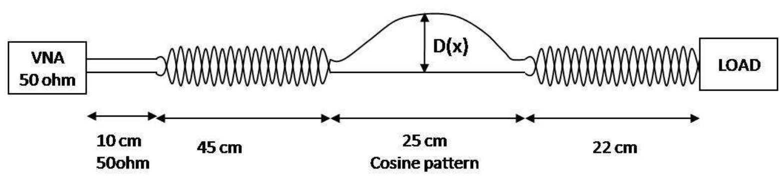

Figure 3: Experimental setup. The cosine profile is inserted in a $110\,\Omega$ twisted pair.

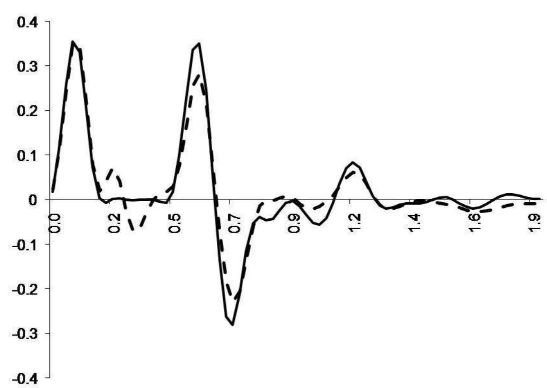

Figure 4: Theoretical (–) and experimental (- -) impulse response of a line including the cosine spacing profile.

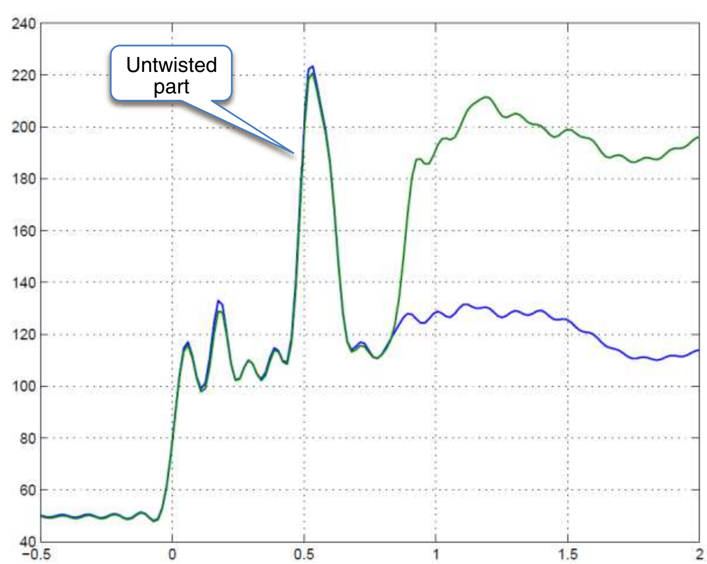

Figure 5: Inverse scattering performed on the cable with a $110\,\Omega$ load (blue line) and with a $220\,\Omega$ load (green line).

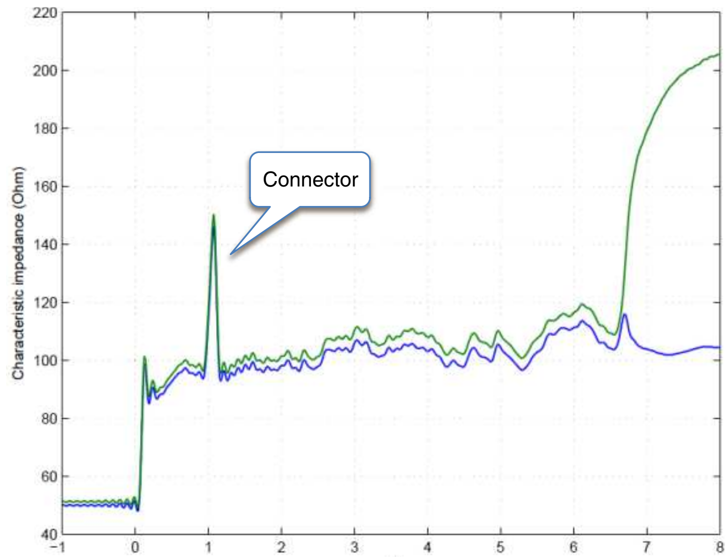

Figure 6: Identification of a connector'slocation using the inverse scattering method. The cable is terminated with a 110 Ω load (blue line) or with a 220 Ω load (green line).

right parts of the two lines that clearly differ from each other represent the estimation of the two loads used in the two experiments. The estimated loads are about 120Ω (blue line) and 200Ω (green line). The left parts of the two lines are almost identical, because they represent the estimated distributed characteristic impedance of the same cable. The location and the form of the untwisted part of the cable are found with a good accuracy for the purpose of fault diagnosis.

3.2. Application to the Location of Connectors on an Automotive Electrical Harness

As previously suggested in Section 3.1, the kind of impedance variation studied in this paper is often observed on a real automotive harness. Therefore we applied the inverse scattering method to a real twisted pair used in trucks. The calbe of 5.4 m long was connected to the VNA through a connector with 0.9 m of the same twisted pair and terminated by a 110 Ω or 220 Ω load directly on the other the end of the cable. As shown in Figure 6, we can observe at the connector's location the impedance variation pattern similar to that observed previously in Section 3.1.

4. CONCLUSION

The experimental results presented in this paper confirm the previously reported theoretic results and numerical simulations. A physical smooth variation of the characteristic impedance was created by spatially constraining the spacing of the two wires of a twisted pair with a well controlled profile, simulating a real life untwisted pair often seen before and after a connector. The inverse scattering method is therefore validated by an experiment with a well known distributed characteristic impedance pattern. Finally the method was applied to the location of a connector on a real life automotive twisted pair with satisfying results.

ACKNOWLEDGMENT

This work has been supported by the ANR SEEDS and 0-DEFECT projects.

REFERENCES

1. Loete, F., S. Noël, R. Meyer, M. Olivas, F. Auzanneau, and D. Chandon, "Feasability of the detection of vibration induced faults in connectors by re ectometry," *24th Int. Conf. on Elec. Contacts (ICEC)*, St. Malo, France, June 2008.
2. Zhang, Q., M. Sorine, and M. Admane, "Inverse scattering for soft fault diagnosis in electric transmission lines," *IEEE Trans. on Antennas and Propagation*, Vol. 59, No. 1, 141–148, 2011.
3. Tang, H. and Q. Zhang, "An inverse scattering approach to soft fault diagnosis in lossy electric transmission lines," *IEEE Trans. on Antennas and Propagation*, Vol. 59, No. 10, 3730–3737, 2011.
4. Jaulent, M., "The inverse scattering problem for LCRG transmission lines," *Journal of Mathematical Physics*, Vol. 23, No. 12, 2286–2290, December 1982.